IAEA-TECDOC-CD-1674

Advances in High Temperature Gas Cooled Reactor Fuel Technology

IAEA
International Atomic Energy Agency

Advances in High Temperature Gas Cooled Reactor Fuel Technology

The following States are Members of the International Atomic Energy Agency:

AFGHANISTAN
ALBANIA
ALGERIA
ANGOLA
ARGENTINA
ARMENIA
AUSTRALIA
AUSTRIA
AZERBAIJAN
BAHRAIN
BANGLADESH
BELARUS
BELGIUM
BELIZE
BENIN
BOLIVIA
BOSNIA AND HERZEGOVINA
BOTSWANA
BRAZIL
BULGARIA
BURKINA FASO
BURUNDI
CAMBODIA
CAMEROON
CANADA
CENTRAL AFRICAN REPUBLIC
CHAD
CHILE
CHINA
COLOMBIA
CONGO
COSTA RICA
CÔTE D'IVOIRE
CROATIA
CUBA
CYPRUS
CZECH REPUBLIC
DEMOCRATIC REPUBLIC OF THE CONGO
DENMARK
DOMINICA
DOMINICAN REPUBLIC
ECUADOR
EGYPT
EL SALVADOR
ERITREA
ESTONIA
ETHIOPIA
FIJI
FINLAND
FRANCE
GABON
GEORGIA
GERMANY
GHANA
GREECE
GUATEMALA
HAITI
HOLY SEE
HONDURAS
HUNGARY
ICELAND
INDIA
INDONESIA
IRAN, ISLAMIC REPUBLIC OF
IRAQ
IRELAND
ISRAEL
ITALY
JAMAICA
JAPAN
JORDAN
KAZAKHSTAN
KENYA
KOREA, REPUBLIC OF
KUWAIT
KYRGYZSTAN
LAO PEOPLE'S DEMOCRATIC REPUBLIC
LATVIA
LEBANON
LESOTHO
LIBERIA
LIBYA
LIECHTENSTEIN
LITHUANIA
LUXEMBOURG
MADAGASCAR
MALAWI
MALAYSIA
MALI
MALTA
MARSHALL ISLANDS
MAURITANIA
MAURITIUS
MEXICO
MONACO
MONGOLIA
MONTENEGRO
MOROCCO
MOZAMBIQUE
MYANMAR
NAMIBIA
NEPAL
NETHERLANDS
NEW ZEALAND
NICARAGUA
NIGER
NIGERIA
NORWAY
OMAN
PAKISTAN
PALAU
PANAMA
PAPUA NEW GUINEA
PARAGUAY
PERU
PHILIPPINES
POLAND
PORTUGAL
QATAR
REPUBLIC OF MOLDOVA
ROMANIA
RUSSIAN FEDERATION
RWANDA
SAUDI ARABIA
SENEGAL
SERBIA
SEYCHELLES
SIERRA LEONE
SINGAPORE
SLOVAKIA
SLOVENIA
SOUTH AFRICA
SPAIN
SRI LANKA
SUDAN
SWEDEN
SWITZERLAND
SYRIAN ARAB REPUBLIC
TAJIKISTAN
THAILAND
THE FORMER YUGOSLAV REPUBLIC OF MACEDONIA
TOGO
TUNISIA
TURKEY
UGANDA
UKRAINE
UNITED ARAB EMIRATES
UNITED KINGDOM OF GREAT BRITAIN AND NORTHERN IRELAND
UNITED REPUBLIC OF TANZANIA
UNITED STATES OF AMERICA
URUGUAY
UZBEKISTAN
VENEZUELA
VIETNAM
YEMEN
ZAMBIA
ZIMBABWE

The Agency's Statute was approved on 23 October 1956 by the Conference on the Statute of the IAEA held at United Nations Headquarters, New York; it entered into force on 29 July 1957. The Headquarters of the Agency are situated in Vienna. Its principal objective is "to accelerate and enlarge the contribution of atomic energy to peace, health and prosperity throughout the world''.

IAEA-TECDOC-1674

ADVANCES IN HIGH TEMPERATURE GAS COOLED REACTOR FUEL TECHNOLOGY

INTERNATIONAL ATOMIC ENERGY AGENCY
VIENNA, 2012

For further information on this publication, please contact:

Nuclear Power Technology Development Section
International Atomic Energy Agency
Vienna International Centre
PO Box 100
1400 Vienna, Austria
email: Official.Mail@iaea.org

Printed by the IAEA in Austria
December 2012

IAEA Library Cataloguing in Publication Data

Advances in high temperature gas cooled reactor fuel technology.
– Vienna : International Atomic Energy Agency, 2012.
CD-ROM. – (IAEA-TECDOC-CD series, ISSN 1684-2073 ; no. 1674)
ISBN 978-92-0-186810-7
Includes bibliographical references.

1. Nuclear power plants. 2. Gas cooled reactors – Technological innovations. 3. Nuclear fuels – Research. I. International Atomic Energy Agency. II. Series.

IAEAL 12-00736

FOREWORD

The coordinated research programmeme (CRP) on Advances in HTGR Fuel Technology was organized in the framework of the technical working group on gas cooled reactors (TWG-GCR) established in 1978 with the purpose of advising the Director General of the IAEA and promoting the exchange of technical information on national programmemes in the field of gas cooled reactors.

The project has been conducted in close cooperation with both the Nuclear Power and the Nuclear Fuel Divisions of the IAEA. Initiated in the TWG-GCR meeting in June 2000, it was actually launched in 2002. The participants were China, France, Germany, Japan, Republic of Korea, Netherlands, Russian Federation, South Africa, Turkey, United Kingdom, and the United States of America. The European Commission and Ukraine qualified as 'observers' according to the IAEA rules. This CRP, being No. 6, was eventually approved by the IAEA as an extra-budgetary activity with an estimated duration of 5 years (2002-2006). Ongoing work of code development and validation and delays in the fuel particle production and distribution with regard to export/import licensing has led to the request for two extensions (2007-2008 and 2009). The CRP-6 officially ended in December 2009, the final RCM was held in May 2010.

The general objectives of this CRP were to:

- Support the development of improved HTGR fuel technology;
- Facilitate the coordination of technology development activities;
- Exchange relevant technical information among the interested Member States.

Based on the successful conduction of CRP-2 on Validation of Predictive Methods for Fuel and Fission Product Behaviour conducted between 1992 and 1997 (IAEA-TECDOC-978), the topical areas and scope of activities in this CRP-6 were to cover all essential aspects of HTGR fuel including fabrication, quality assurance, performance during normal operation and under accident conditions, treatment of spent fuel.

The total CRP-6 programme has turned out to be a very ambitious one. Not only does it comprise a description of the experiences and results of ongoing activities or incorporate the plans for future research programmemes, it also included research efforts which were specifically initiated within CRP-6 providing an ideal platform with all major players participating. These comprised two specific benchmark exercises with the application of HTGR fuel performance and fission product release codes which helped compare the quality and validity of the computer models against experimental data and also against each other, thus being an ideal support for further development and/or refinement. Another major activity was the examination of techniques for fuel characterization and advanced QA/QC. The key exercise included was a round-robin experimental study on the measurements of fuel kernel and particle coating properties of recent Korean, South African, and US coated particle productions applying the respective qualification measures of either participating Member State.

This publication has been prepared through the collaboration of the participants and other experts to the CRP. The IAEA appreciates this support and thanks all contributors who provided their reviews and comments. Especially appreciated is the contribution of K. Verfondern (Germany) in the compilation and preparation of this IAEA-TECDOC. The IAEA officer responsible for this publication was B.M. Tyobeka of the Division of Nuclear Power.

EDITORIAL NOTE

The use of particular designations of countries or territories does not imply any judgement by the publisher, the IAEA, as to the legal status of such countries or territories, of their authorities and institutions or of the delimitation of their boundaries.

The mention of names of specific companies or products (whether or not indicated as registered) does not imply any intention to infringe proprietary rights, nor should it be construed as an endorsement or recommendation on the part of the IAEA.

CONTENTS

1. INTRODUCTION

An earlier report, IAEA-TECDOC-978 [1], documented the results of high quality, low enriched uranium TRISO coated particle fuel production, testing, and fuel performance and fission product transport analysis methods development through the mid 1990s. TECDOC-978 has served as a major international reference for coated particle fuel design and performance. This report documents the results of coated particle development that has taken place since the production of TECDOC-978 and provides additional information in the following areas:

- Plant concepts and fuel designs — Summary descriptions of power plant conceptual design and corresponding fuel designs under consideration in participating member states.
- Fuel production — Coated particle fuel fabrication process development and fuel production including development of product and process specifications, production of the uranium kernels, particle coating and fabrication of fuel elements.
- Fuel characterization and quality control — Techniques used by participating member states and the conduct and results of characterization of reference coated particle materials by project participants.
- Operational monitoring of fuel — Methods for monitoring the performance of fuel in service and examination of irradiated fuel from operating or planned power plants.
- Matrix materials — Experience with carbonaceous matrix materials used to form fuel particles into fuel elements.
- Irradiation testing — Description of facilities (materials test reactors) capable of irradiation of coated particle fuels and experience with irradiation of fuels in MTRs and experimental reactors.
- Post-irradiation examination and testing — Capabilities and future plans for examination of irradiated coated particle fuels and core heatup simulation testing.
- Normal operation and operational transient benchmarking of fuel performance models — Comparison of results of participant fuel performance code predictions for cases ranging from simple first principle calculations to experimental irradiation testing.
- Accident condition benchmarking of fuel performance and fission product transport models — Comparison of results of participant fuel performance and fission product transport code predictions for sensitivity studies, postcalculation of existing tests, prediction of planned future tests.
- Spent fuel treatment and disposal — Experience with shut-down reactors, concepts for present designs, and advanced approaches for future systems.
- Regulatory perspectives on safety and licensing — Considerations regarding fuel design, fabrication and testing, fuel performance and fission product transport analysis methods, fabrication quality assurance, and in-service monitoring.

This comprehensive compilation of data and information on coated particle fuel will be of value to universities, laboratories and design organizations involved or interested in the development and deployment of coated particle fuel technology for electricity and/or process heat production.

2. DEFINITION AND BASIS OF VHTR PLANT CONCEPTS AND FUEL DESIGNS

2.1. ANTARES

2.1.1. General

The ANTARES plant is being developed for complementing the other products of the AREVA NP product line (i.e. EPR and SWR-1000) which are "high output' power plants dedicated to electricity production [2]. The very high or high temperature reactors (V/HTR) are selected because of possible application for process heat including hydrogen production requiring heat at different temperature levels, up to very high temperature. The low power rating of the VHTR power unit also allows diversification compared to the high power rating of the other AREVA NP products. Two concepts are considered for development:

- Electricity production plant dedicated only to electricity production.
- Process heat or cogeneration plant mainly dedicated to applications needing heat at specific temperatures. One of these considered applications is the process heat for hydrogen production by thermo-chemical processes. For this application very high temperature (i.e. in the range of 950°C) could be required. Even if the process heat plant has to produce essentially heat for applications, this can be combined with electricity generation if necessary (e.g. for electrical supply of the plant or the facility using process heat) or if the heat cannot economically be completely used by the process heat application.

During the pre-conceptual design phase, because of the lack of process heat characteristics precisely defined, the electrical plant concept was developed first. The possible extension of the nuclear heat source design optimized for electricity production, to various process heat applications were assessed and the technological limitations identified. Therefore, only one nuclear heat source concept is developed. Differences would exist, but they should be limited, for example due to the difference of operation. In any case, the nuclear heat source (fuel, core, primary circuit boundary, etc.) should be similar. This limits the costs of development and associated R&D.

The ANTARES plants are developed for near term implementation on the market (i.e. around 2020). Nevertheless, for improving their commercial attractiveness, they shall have to be consistent with the international objectives developed for Generation IV (GenIV) nuclear systems. These include economy, safety, sustainability and non-proliferation.

2.1.2. Plant design

The structures and components composing the nuclear heat source are housed in metallic vessels (Fig. 2.1). Another potential candidate was the prestressed concrete cavity. This last concept is rather adapted to high power concepts not consistent with the implementation of the inherent safety oriented design.

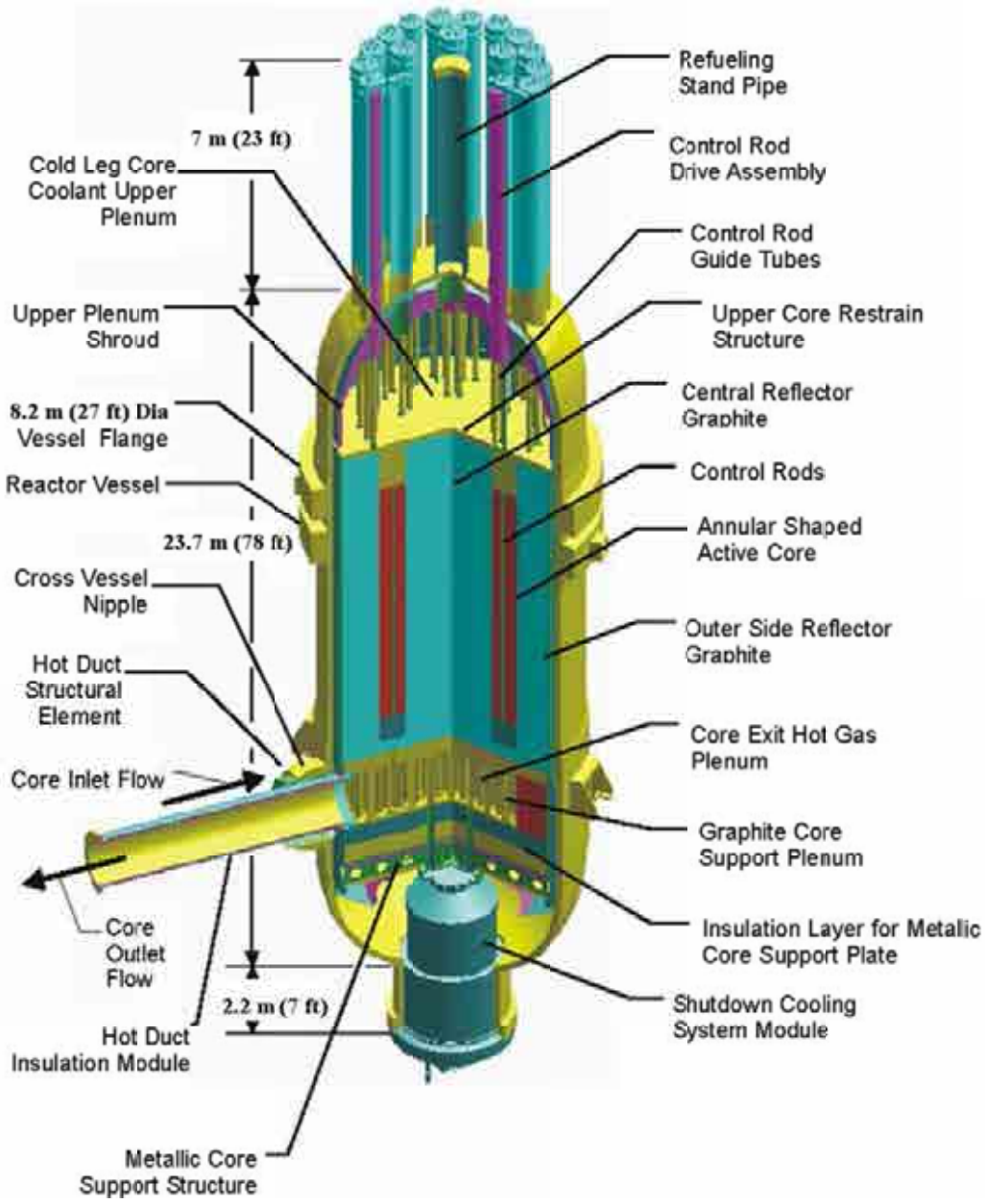

FIG. 2.1. ANTARES nuclear heat source based on the prismatic nuclear reactor.

The indirect cycle concept (i.e. the nuclear heat generated in the core is transferred through an intermediate heat exchanger (IHX) to a secondary circuit for the application) is selected because it allows higher physical and operational separation of the nuclear heat source from the balance of plant. Therefore, the balance of plant equipment may be implemented outside the nuclear island and it need not be nuclear quality equipment (i.e. classical equipment should be used). Compared to a direct cycle concept (i.e. the power conversion system is implemented inside the primary circuit), this is more adequate for application other than electricity production and therefore allows optimization of commonality. This allows avoiding using helium turbo-machinery which requires significant R&D. For electricity production, in the considered range of temperature, the efficiency of the indirect cycle is assessed to be similar to the one expected for direct cycle.

The possibility to implement several power units on a same nuclear island is considered for cost minimization. Optimization studies have not been performed, nevertheless,

implementation of four power units per nuclear island is considered during the pre-conceptual deign phase. The commonality of auxiliary systems to share between several power units is investigated taking into account the safety and availability consequences

- during normal and abnormal operation of a power unit;
- in case of equipment maintenance or failure impacting several power units;
- during the construction phase, including possible accident, of a power unit on the power units in operation.

The design is developed with a target for construction duration of a single power unit, of three years. This value is selected after comparison with the construction duration of EPR and the ones indicated by competitors. More generally, the design is developed in order to facilitate the construction aspects, including operation of other power units during construction of an additional one.

In order to achieve the plant feasibility and its availability with limited R&D possible for near term development, the materials, equipment, systems and structures are based as far as possible on experienced concepts. Nevertheless, innovations are recommended when necessary (e.g. because of the very high temperature environment of certain parts of the plant) or when this could allow a competitive advantage compared to similar products. Where the use of innovative equipment is not necessary, selection of experienced equipment is preferred.

2.1.3. Fuel and core

The fuel of the ANTARES plant is based on enriched uranium with a thermally moderated neutron flux. Even if this fuel cycle is less sustainable than a breeding fuel cycle, it is selected because of its potential capability to develop in the near term. The feasibility of uranium fuel and moderated neutron flux is expected more achievable in the near term compared to breeding cycles. The weak aspect of the uranium fuel with regard to sustainability is nevertheless expected to be reduced by the high efficiency and high fuel burnup which should allow an improved use of natural uranium compared to light water reactors (LWR). The high efficiency allows also minimizing the amount of radio nuclides produced for generating the usable power (in particular plutonium and minor actinides).

The capability to use sustainable fuels based on plutonium or thorium within the nuclear heat source optimized for uranium fuel is assessed. Also, the capability to reduce the toxicity and the volume of minor actinides produced in LWR is evaluated. The capability to reduce the worldwide quantity of weapons-grade plutonium is evaluated. The consequences on the plant design, safety and operation are assessed in order to examine the possibility to adapt the design for improving these capabilities.

The reactor core is a prismatic fuel block core (Fig. 2.2) to generate a thermal power of 600 MW and an electric power of 284 MW, respectively. Compared to a pebble bed concept, block concept allows better control of the local power generation and better control of the fuel burnup. This concept is expected to allow the highest core power density and highest fuel burnup. It allows more limited core pressure drop which limits the power needed for gas circulation. The prismatic core block concept is also more favourable with regard to non-proliferation issues, compared to the pebble bed concept.

The uranium fuel is UO_2 type. In order to possibly improve its performance, UCO fuel is also considered for future development. For limiting the proliferation concerns, the enrichment of uranium fuel is limited lower than 20%. Reprocessing capability of the spent fuels is considered in their design process.

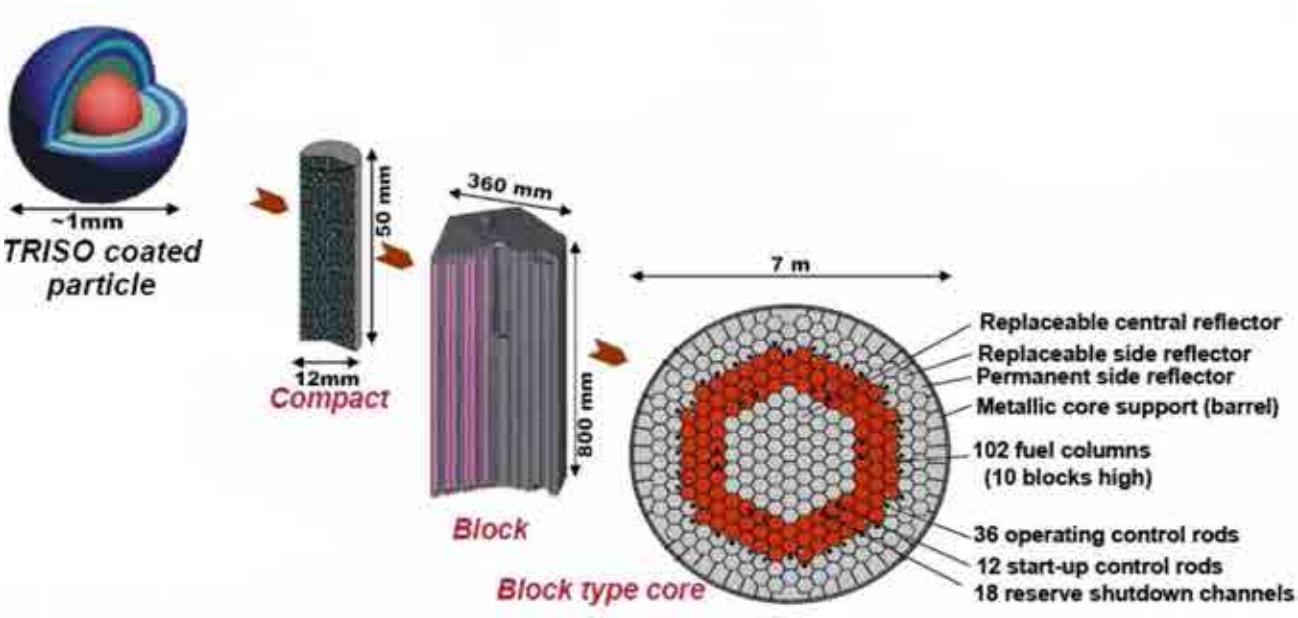

FIG. 2.2. ANTARES fuel design.

Graphite is selected as neutron moderator because of

- its neutronic characteristics allowing the moderation of the neutron flux allowing high neutron fission efficiency and therefore limitation of fissile uranium enrichment.
- its capability to operate in acceptable conditions at high or very high temperature.
- its high thermal inertia allowing the limitation of temperature evolutions in accident conditions.

Major specifications of the fuel for the ANTARES are summarized in Table 2.1.

The safety strategy basically used for designing ANTARES leads to a specific core design:

- annular shape of the core allowing maximizing the capability to radially exchange the heat after reactor shutdown by maximizing the radial exchange surface;
- limitation of the nominal core power and core power density for limiting the peak temperature and slowing the temperature evolution in accident conditions.

TABLE 2.1. MAJOR SPECIFICATIONS OF THE FUEL FOR THE ANTARES

Number of fuel elements	1020
Number of fuel columns	102
Fuel	LEU UO_2
Amount of initial heavy metal in core	4570 kg
Uranium enrichment	14%
Maximum average burnup	150 GW•d/t
Discharged fuel enrichment	5–6%
Fuel element lifetime	1150 efpd
Kernel diameter	500 ± 20 μm
Layer thicknesses Buffer/IPyC/SiC/OPyC	 95/40/35/40 μm
Fuel compact length/diameter	50.0/12.7 mm
Heavy metal loading of compact	1.47 g
Number of coated particles per compact	2500
Packing fraction	16%
Fuel pin length/outer diameter	800/12.7 mm
Number of fuel compacts per fuel pin	15
Fuel element length/width across flat surface	800/360 mm
Number of fuel pins per fuel element	216
Coolant channel diameter	16 mm
Number of coolant channels in fuel element	108

2.1.4. Primary coolant

Helium is selected as primary coolant because

- it has high thermal conductivity;
- it is chemically inert with any other material and at any temperature;
- it is not significantly activated by radiation;
- its cost is reasonably low;
- it is a naturally occurring material that is relatively abundant.

Limited R&D is expected for the development and qualification of equipment containing helium.

2.1.5. Plant operation

The plant is designed considering life duration of 60 years for non-repairable or non-replaceable equipment. It is based on EPR case and information given by competitors. For repairable or replaceable equipment (e.g. IHX), the life duration is optimized taking into account the cost of equipment and its maintenance. The capability to maintain, inspect, repair and replace equipment is maximized.

The plant is designed with an availability factor target of 0.90. This target is based on information given by competitors. It is related to each power unit implemented in the nuclear island. For electricity production plant, load following is required for each power unit. This option is selected as the enveloping case regarding the available utility requirements.

The main parameters defining the normal operation are described in Table 2.2 below. Reference configurations are defined for both the plant dedicated to electricity production and process heat application.

TABLE 2.2. REFERENCE PLANT PARAMETERS OF ANTARES (PRE-CONCEPTUAL DESIGN PHASE)

Configuration	Power (MW(th))	Core inlet temp. (°C)	Core outlet temp. (°C)	Pressure (MPa)	Vessel material	Number of primary loops	IHX type
Electricity production plant	600	400	850	6.0	Mod9Cr	1	Plate
Process heat generating plant	600	400	950	5.5	Mod9Cr	1	Plate

2.1.6. Plant architecture

The plant architecture is defined on the basis of the above requirements and by performing trade studies for comparing the different possible options. The general arrangement of the plant dedicated to electricity production is illustrated in Fig. 2.3.

The main systems defining the nuclear heat source of the ANTARES plant are: reactor building; reactor system; vessel system; primary heat transfer system; shutdown cooling system; reactor cavity cooling system; helium services system; fuel handling and storage system; and power conversion system.

2.1.7. Safety and licensing

The safety options considered for designing the ANTARES plant are consistent with the safety objectives developed by the international GenIV Forum. This means that the safety of the ANTARES plant is enhanced compared to the nuclear power plants currently in operation in particular, the design and the operation of the plant are able to offer the Authorities the possibility of simplifying or not requiring off-site emergency planning zones and associated drills.

Another important path for enhancement is the improvement of the confidence in the demonstration of the safety objectives (e.g. simplicity and good knowledge of the phenomena occurring in any condition, development of a design allowing graduated and progressive defense against potential risks, prevention of cliff edge effects, consideration of bounding degraded plant situations for achieving the exhaustiveness of faults studied as likely to occur, minimization of the complexity of the overall plant architecture and operation).

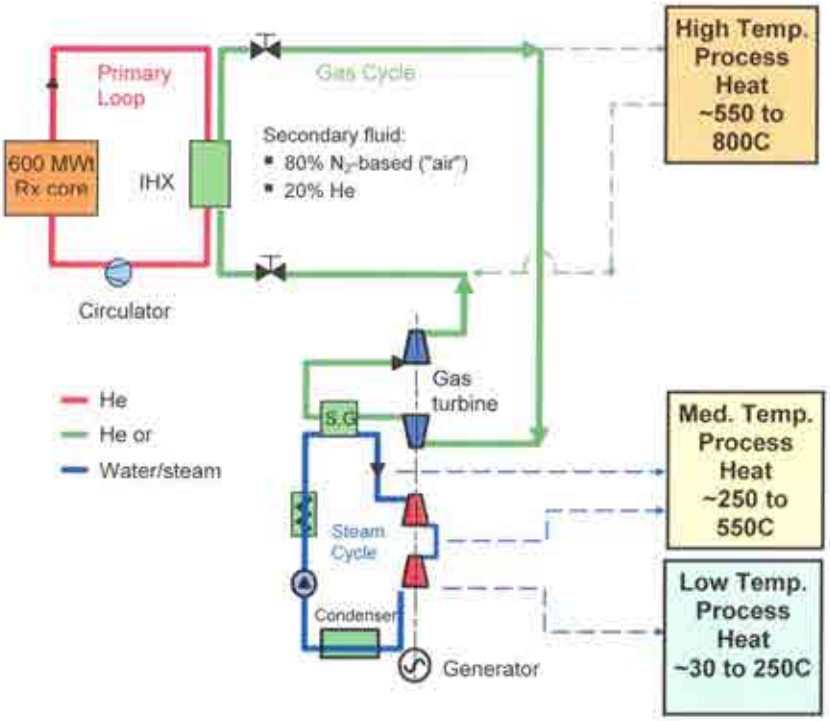

FIG. 2.3. Plant general arrangement.

The ANTARES plant shall be possibly proposed to any customer. It is not developed for some identified countries. During the pre-conceptual design phase, the licensing aspects are taken into account by assessing the licensing constraints in Europe and the USA. Nevertheless, the existing frameworks mainly rely on LWR background, not adapted to the VHTR. Therefore, technology neutral safety objectives have to be anticipated consistently with credible licensing evolution in the representative countries.

Defense-in-depth remains the basic principle to consider for developing the ANTARES safety approach adapted to the ANTARES characteristics. The basis of the design of the ANTARES plant for achieving the safety objective is:

- Prevention of accidents likely resulting in significant radionuclide releases preferably by means of inherent and passive design features for the short term;
- Excellent behaviour of the fuel during normal and accident conditions. The fuel irradiation and performance will be defined consistently with this safety strategy;
- Additional mitigation capability by the slow response of the plant to abnormal situations.

This safety strategy is expected allowing excluding any severe core damage and therefore limiting the requirements concerning mitigation systems (i.e. in particular this is expected allowing to avoid to design a pressure resistance containment as it is for LWR). Also, with this strategy, the number and the associated requirements of safety related systems are expected minimized.

Passive features are preferred, but possibility to use active systems is not excluded. Using active systems for achieving the safety demonstration should be limited and be exceptionally done. This may be done where active systems are significantly more reliable and cheaper than passive systems and where the failure of the safety related active system can be practically

eliminated (i.e. if there are strong and irrefutable arguments proving a very low frequency of occurrence of its failure). The main consequences of this safety strategy are:

- The plant behaviour during any accident combined with the failure of the active shutdown systems is proven acceptable at short term. This is done by the negative feedback coefficient of the core which allows control of the power generation.
- In particular, the heat removal after reactor shutdown in accident conditions has to be achieved by passive and inherent means. Nevertheless, active features may be implemented for lowering the frequency of occurrences of these accident conditions for availability and investment protection.

The fuel performances will have to be consistent with this safety strategy. This means that fuel temperature and burnup could be limited for achieving acceptable accident condition behaviour. This is the main purpose of the experimental fuel qualification programme.

The slow response of the plant to abnormal conditions is a key safety characteristic which has to be verified in any situation. The requested delay for any corrective action has to be defined on a case-by-case basis, taking into account the possibility to analyse the abnormal situation (including external hazards). The design objective is to provide as-long-as-possible grace periods. A delayed response of at least 24 hours is considered during the pre-conceptual design phase.

As a consequence of the safety strategy favouring inherent behaviour and passive systems, no high power electrical supply is rapidly necessary for operating safety-graded systems. For long term accident management, electrical supply may be considered, but only after unavailability duration of at least twenty-four hours.

The radiological releases to the environment, during normal operation are treated according to the principle of ALARA, ‘as low as reasonably achievable’. This is achieved by the limitation of the radionuclide content into helium resulting from

- the fuel characteristics which limit the risk of fuel failure during normal operation;
- the fuel fabrication and its controls which minimize the risk of using failed fuel elements;
- the limitation of helium impurities (i.e. impurities able to be activated);
- the monitoring of the activity into helium with the plant being shut down if abnormal activation is detected;
- the monitoring of any release in the environment during normal operation using dedicated devices as filtering and isolation systems, if needed;
- the limitation of the tritium releases in the environment and in the main secondary circuit.

The design of the plant minimizes the risks to operators. This applies especially to the radiological risk during normal operation according to the ALARA principle. The other potential hazards (chemical, mechanical, etc.) are also considered for the protection of the operators. The risks of malevolence, sabotage and terrorist attack are considered from the pre-conceptual design phase. The selection of the various concepts is performed taking into account this aspect.

2.2. GTHTR300

2.2.1. Reactor core design

As a follow-on project and based on the experience achieved with the Japanese test reactor HTTR so far, the Japan Atomic Energy Agency (JAEA) is currently studying the feasibility of a gas turbine HTGR, called GTHTR300, as a reference concept (Fig. 2.4) with the potential of extension to a nuclear hydrogen production facility in Japan [3]. The GTHTR300 has been designed to meet the requirements of

- highest thermal power and power density with the maximum fuel temperature being kept lower than the limit temperature during loss-of-forced-convection (LOFC) accidents;
- sandwich shuffling of fuel blocks with the proper placement of burnable poison to extend the refueling interval to two years;
- conventional steel material for the reactor pressure vessel (RPV);
- double confinements instead of a containment vessel to prevent air leakage into the reactor core;
- horizontal gas turbine generator installation.

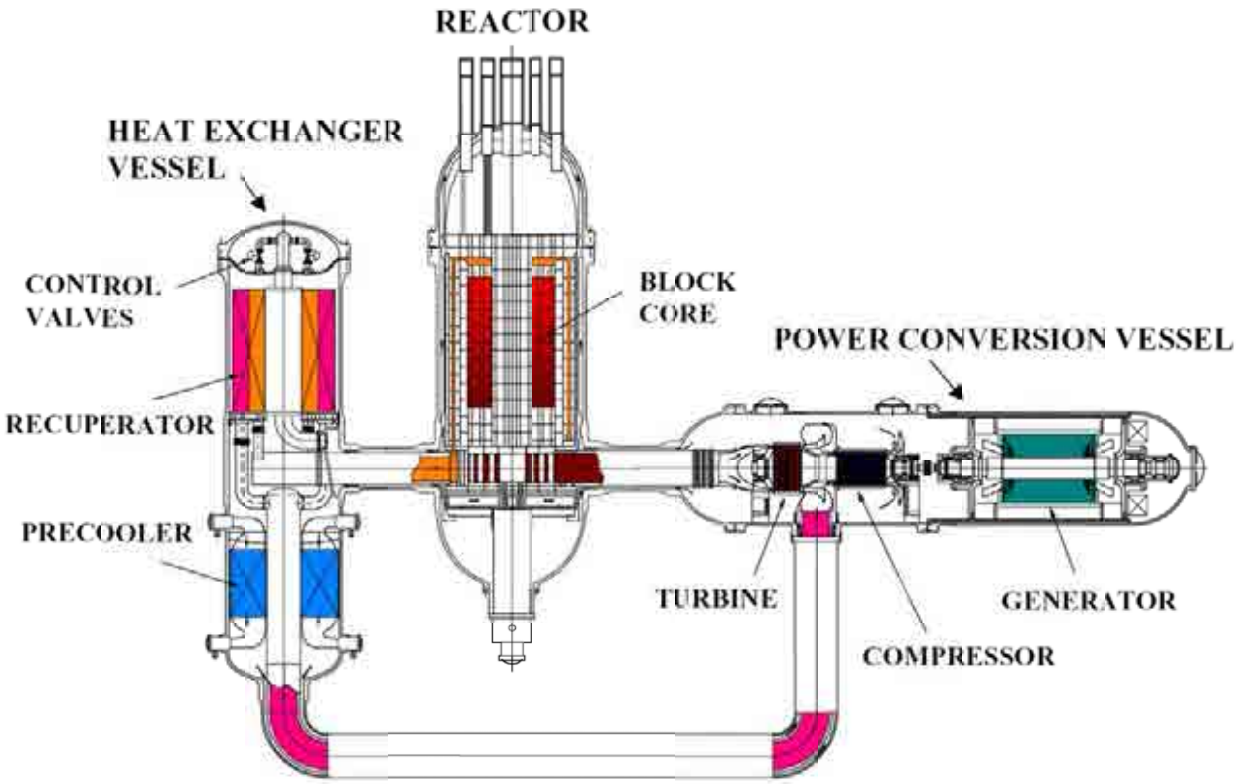

FIG. 2.4. Plant layout of the GTHTR300.

The active core of the GTHTR300 is of an annular shape. It is composed of 720 pin in block type fuel assemblies, hexagonal graphite blocks which are arranged in 90 columns of eight blocks each. The dimensions of the active core are 8 m of total height, the (equivalent) inner and outer diameters are 3.6 and 5.5 m, respectively. The inside of the annular core is filled with 73 graphite columns representing the replaceable inner reflector, and is surrounded by 48 columns of replaceable outer reflector. The outside boundary of the core is given by 18 sectors of permanent side reflector. A horizontal cross-section of this arrangement is shown in Fig. 2.5. Both top and bottom reflector are given by two additional layers of graphite blocks each.

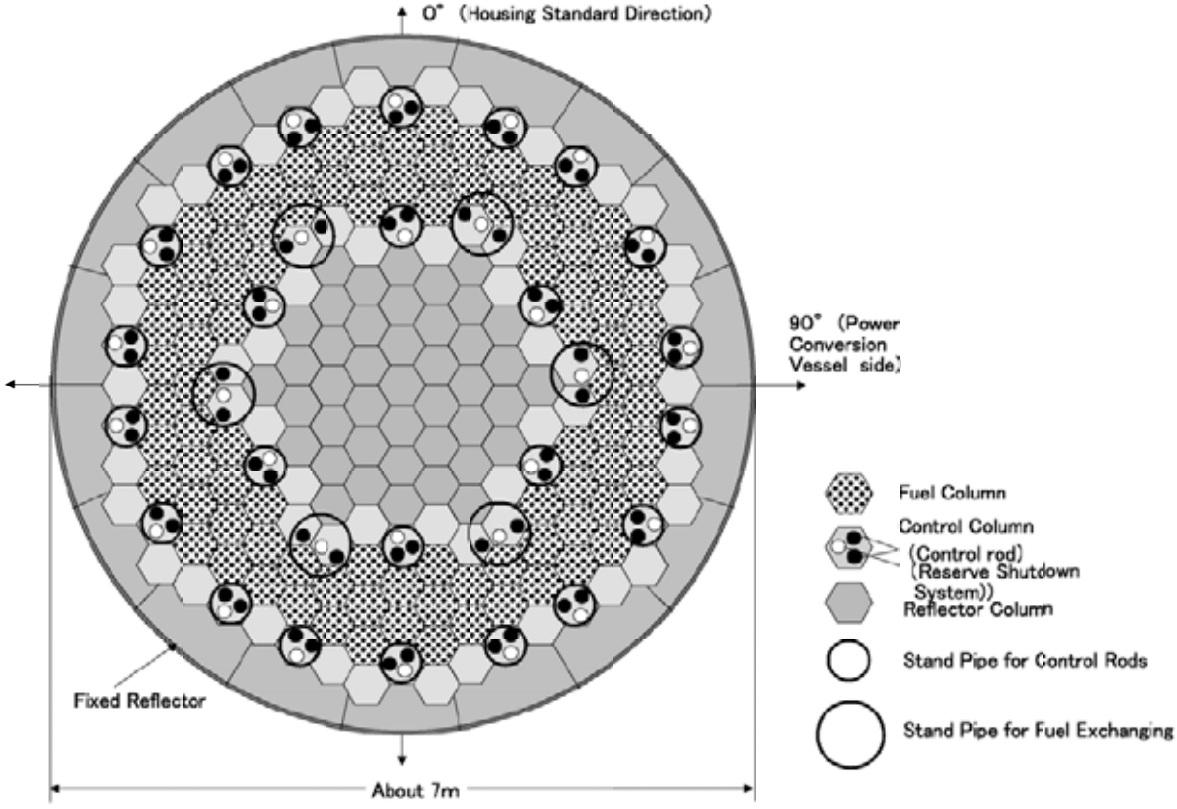

FIG. 2.5. Horizontal view of GTHTR300 core.

The reactor core performance has a big impact on the plant efficiency and the plant cost. For economic reasons and future needs, a two years continuous operation without refueling is deemed necessary. The long refueling interval, which increases the plant availability, and the use of high burnup fuel, which reduces fuel cycle cost. The maximum fuel burnup will reach an average of 120 GW•d/t. The enrichment of the discharged fuel is less than 4.5 wt% and the amount of fissile plutonium is as low as possible. Table 2.3 summarizes the major specifications of the GTHTR300 reactor.

The maximum design temperature during the normal operation was provisionally determined 1400°C that is by 95°C lower than that of the HTTR taking account of the higher average burnup. The fuel temperature limit in the accident was determined 1600°C that is the same temperature limit of the HTTR fuel. However, in order to confirm the integrity of the high burnup fuel for the GTHTR300, further irradiation post-irradiation testing for the GTHTR300 will be conducted.

2.2.2. Fuel reshuffling

A new refueling method is being considered for the GTHTR300 which is called ‘sandwich shuffling’ (Fig. 2.6) where in a refueling process one half of the active core is exchanged for fresh fuel [3].

TABLE 2.3. MAJOR SPECIFICATIONS OF THE GTHTR300

Thermal power	600 MW(th)
Net electric power output	275 MW(e)
Average/maximum thermal power density	5.8/13–15 MW/m^3
Primary coolant	Helium
Reactor coolant inlet/outlet temperature	587/850°C
System pressure (turbine inlet)	7.0 MPa
Coolant mass flow rate	439 kg/s
Active core height	~8 m
Active core inner/outer diameter	3.6/5.5 m
Average burnup	120 GW•d/t
Refueling cycle	730 efpd
Power conversion efficiency	45.8%

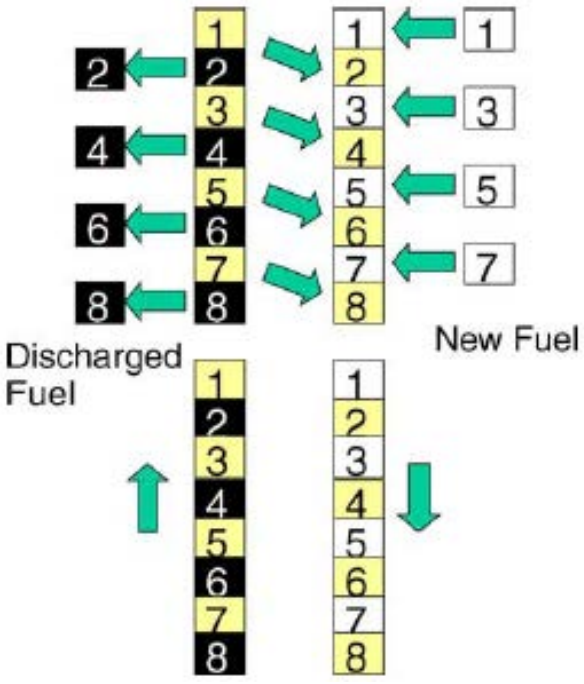

FIG. 2.6. ‘Sandwich shuffling’ scheme for fuel reloading.

The refueling procedure is planned to take place every 550 efpd. At the end of a fuel cycle, all fuel assemblies in core layers 2, 4, 6, and 8 are being removed from the core and go to the fuel waste. They will be replaced by the previously above located fuel assemblies from core layers 1, 3, 5, and 7, respectively. Those layers will then be filled with fresh fuel blocks. Reshuffled fuel blocks do not change their radial position.

This type of refueling means that all core layers with odd numbers always contain fuel within its first fuel cycle only, i.e. with a lifetime ≤ 550 efpd, whereas in all even numbered core layers, the fuel is in its second and final fuel cycle, i.e. having a lifetime ≥ 550 and ≤ 1100 efpd.

2.2.3. Fuel concept

Each fuel block in the fuel column contains 57 fuel rods, and its size is about 0.4 m in across flat and 1 m in height (Fig. 2.7) [3].

A fuel rod consists of 12 hollow fuel compacts with 9 mm in inner diameter and 26 mm in outer diameter where coated fuel particles with uranium enrichment of 14% are bonded with graphite matrix at the packing fraction of 29%. Dowel pins and sockets for fixing fuel blocks are arranged respectively at the top and the bottom of three corners in a block. The burnable poison is stored in holes underneath the dowel pins. The most inner layer of side replaceable reflectors and control rod columns adjacent to the fuel blocks are made of graphite corresponding to IG-110, a fine grained, high purity graphite because impurity largely influences on the control rod worth and the reactivity of the whole core. Coolant helium gas flows downward in annular space around fuel rods and removes the heat from the fuel rods.

Each fuel assembly has a size of ~1 m in height and a ~0.4 m diameter (across flats) as is shown in Fig. 2.7. A block contains 57 fuel pins which are inserted in vertical bore holes. The helium coolant flows through a 6 mm gap between fuel pin outer surface and bore hole inner wall. The fuel pin contains 12 annular fuel compacts in a graphite sleeve with a 9 mm diameter central rod. The hollow compacts have a length of 83 mm and a 9 mm inner and a 26 mm outer diameter. The outer diameter of the fuel pin has been reduced compared to the GTHTR300 reference design (26 mm) in order to allow a higher coolant flow rate around the fuel. A fuel compact consists of approximately 13 000 TRISO particles, which are overcoated by a mixture of graphite matrix powder and binder material. The packing fraction is 29%.

The reference concept for the TRISO coated fuel particles differs from that used in the HTTR core. It is based on a 550 μm diameter UO_2 kernel with low enriched uranium surrounded by a TRISO coating which includes a 40 μm thick SiC layer.

In the electricity generating variant, GTHTR300, the fuel has one degree of initial ^{235}U enrichment (14%), and power inhomogeneities are compensated by proper amounts of burnable poison located in holes underneath the three dowels on the top and bottom surface of each fuel block fixing the assembly. With such a fuel design, the requirement of a two years continuous operation can be met.

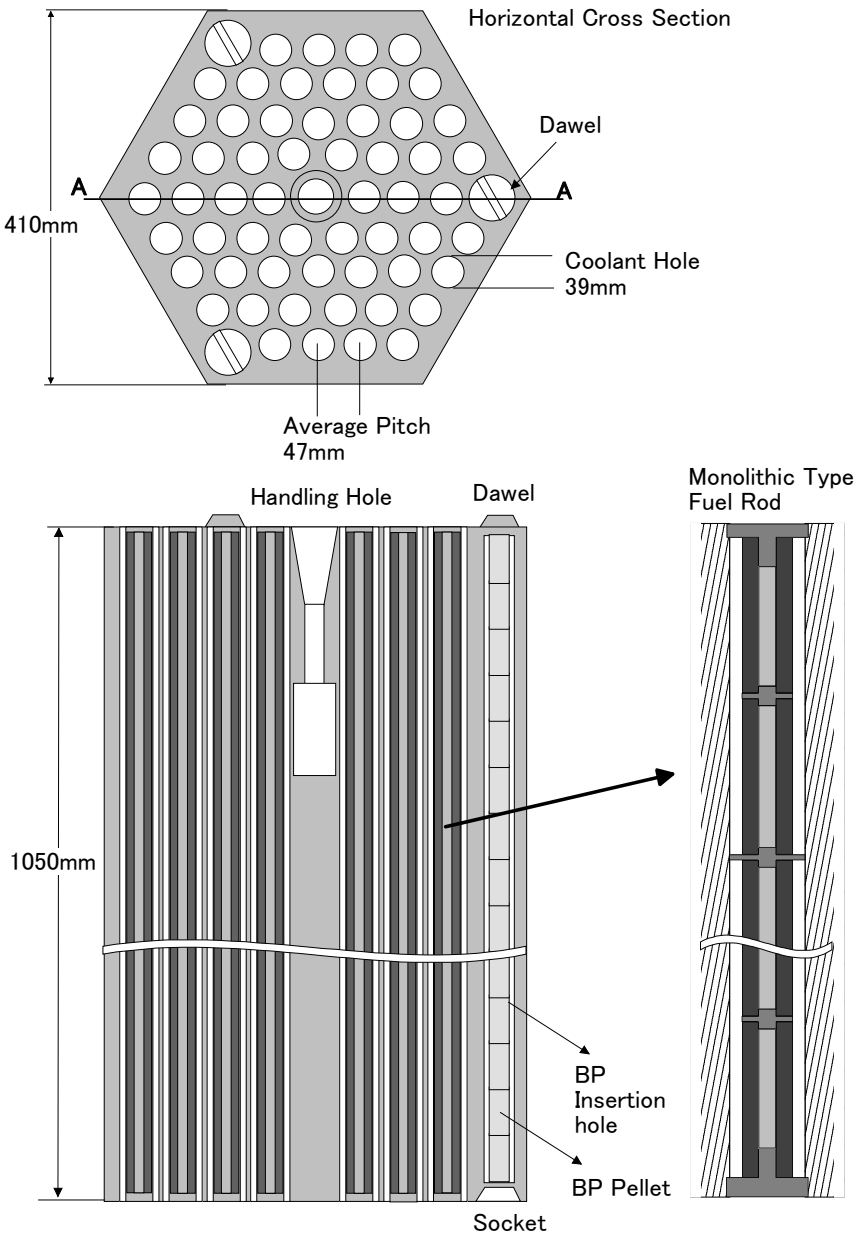

FIG. 2.7. Horizontal and vertical cross-section of a fuel block.

Unlike the GTHTR300, in the GTHTR300C reactor, it is not possible to achieve a sufficiently flat power profile with the use of burnable poison only. Therefore, in addition, the employment of 8 different levels of enrichment is foreseen varying between 7.0 and 16.8% depending on the position in the core, in order to achieve a uniform fuel temperature distribution and coolant outlet temperature, respectively. Also the requirement in terms of continuous operation is with 1.5 years less stringent. The main characteristic data of the GTHTR300 fuel and active core, respectively, are summarized in Table 2.4.

TABLE 2.4. MAJOR SPECIFICATIONS OF THE REFERENCE FUEL FOR THE GTHTR300

Number of fuel elements	720
Number of fuel columns	90
Fuel	LEU UO_2
Amount of initial heavy metal in core	7090 kg
Uranium enrichment	7.0–16.8, average: 14 wt%
Discharged fuel enrichment	4.4%
Fuel element lifetime	550 efpd
Kernel diameter	550 µm
Layer thicknesses Buffer/IPyC/SiC/OPyC	 130/25/40/25 µm
Fuel compact length	83 mm
Fuel compact inner/outer diameter	9/26.0 mm
Fuel compact material	A3-3 matrix
Heavy metal loading of compact	13.5 g
Number of coated particles per compact	13 000
Packing fraction	29%
Fuel pin length/outer diameter	1000/26 mm
Number of fuel compacts per fuel pin	12
Fuel element width across flat surface	405 mm
Fuel element length	1040 mm
Fuel element material	IG-110
Number of fuel pins per fuel element	57
Coolant channel diameter	39 mm

2.2.4. Conditions of reactor normal operation

The reactor core physics analysis was done with 3D calculation models considering a symmetric 60° section of the core. The fuel zone of this 1/6 core region comprises 15 columns. The burnup was calculated for each half of a fuel block corresponding to 30 values per core layer. The average burnup reaches the target value of 120 GW•d/t. The maximum burnup is 155 GW•d/t. The distribution of the neutron fluence is the same as that of the burnup. The maximum neutron fluence in fuel regions is 4.73×10^{25} n/m^2 ($E > 0.183$ MeV) and that of discharged fuels is in the range of ~2.4–4.7×10^{25}.

Despite the high initial uranium enrichment and an effective use of the plutonium during operation, the discharged uranium enrichment is expected to be lower than the target value of 4.5%. The assessed plutonium isotope composition (46% of ^{239}Pu; 17% of ^{240}Pu; 24% of ^{241}Pu; 13% of ^{242}Pu) shows that the plutonium is actively used being the main reason for a stable burnup during the two years of the operation. The factor that brings about such effective use of plutonium is the good point of the sandwich shuffling and effective use of burnable poison.

Although the highest power peaking ratio is from 1.3 to 1.4, the maximum power density is limited to less than approximately 13 MW/m^3 except the last 50 days of the operation without depending much on the control rod movement. However, the diameter of a fuel pin in the

GTHTR300 is 26 mm comparing with 34 mm in the HTTR so that the cooling performance can be improved. Due to the improvement of the cooling performance, the fuel maximum fuel temperature is less than 1400°C. The maximum fuel temperature peak is 1398°C at the beginning of the full power operation.

2.2.5. In-core structure design

The main functions of the in-core structure are

- to support the reactor core and maintain its coolable geometry;
- to limit the heat loss from the reactor core to metal structures, such as the RPV;
- to form the coolant path;
- to limit neutron fluence from the reactor core to prevent excessive irradiation embrittlement of metallic structures.

The reactor core structure consists of graphite structures and metallic structures. The graphite structures are mainly composed of the permanent side reflector blocks and core bottom structures which include the hot plenum blocks, support columns, thermal insulation blocks and bottom blocks.

The support column forms hot plenum and leads coolant flow to the concentric cross duct. The thermal insulation blocks are made of carbon and prevent the heat loss to cold coolant. The metallic structures are composed of a core barrel and an upper plenum shroud. The core barrel supports the graphite structures. The support plate of the core barrel bears the weight of the reactor core and the graphite structures. Its lower surface is cooled by cold coolant to keep its thermal expansion the same as that of the graphite structures.

One of the major functions of the reactor core structures is to form the coolant path for the RPV cooling. The RPV with an inner diameter of 7.6 m can be fabricated of code certified, low cost steel SA533. This is made possible by a plant layout such that the helium gas of 140°C from the compressor flows up cooling the inner surface of the RPV to keep its temperature below the creep range during normal operation. The thickness of the RPV is determined 166 mm so that the initial stress is kept at 140 N/mm^2, and the creep damage remains below 0.9.

2.2.6. The GTHTR300C cogeneration reactor

In the modified version, GTHTR300C (C = Cogeneration) [4], the reactor will be connected to a sulphur–iodine thermochemical water splitting process for hydrogen production. The direct cycle, prismatic block type HTGR with a thermal power of 600 MW provides a coolant inlet/outlet temperature of 594/950°C. In the IHX, the cooling gas at 950°C transfers a part of the thermal power, 168 MW, to the H_2 generation process, while the remaining power in the coolant, now at 850°C, is used for electricity generation of 202 MW(e). Overall efficiency of this cogeneration system is estimated to be 45–50%.

2.3. GT-MHR

The design of the gas turbine modular helium reactor (GT-MHR) is based on rendering the excess weapons-grade plutonium useless for weapons by destroying a large fraction of the fissionable plutonium in a single pass through the reactor [5, 6]. This requires a fuel that can achieve a high burnup of fissionable plutonium in case of fission product release under

normal operating conditions and in design basis accidents at the level allowed for modular reactors with direct gas-turbine cycle.

2.3.1. Programme organization

The programme to develop coated particle fuel for disposal of excess Russian weapons plutonium is being carried out by Russian nuclear labs and industrial organizations with support from US specialists at General Atomics (GA) and Oak Ridge National Laboratory (ORNL). Minatom of the Russian Federation and the US National Nuclear Security Agency each provide 50% of the funds for the programme.

Because of the limited experience with high burnup plutonium fuel, both a reference and alternate fuels are being developed and tested prior to a final selection of the fuel for the initial core for the first GT-MHR module.

The development programme [7] includes fuel design and performance modeling, process development, and irradiation and accident testing. The sequence of these activities and their interrelationships are shown in Fig. 2.8 [7]. The current programme activities are focused on development of the technology for the fuel and the power conversion unit. The main goals of the on-going GT-MHR Fuel Development programme are

- to develop the technology to manufacture fuel for the GT-MHR;
- to qualify fuel for use in the GT-MHR;
- to provide the fuel data base to design, license and operate the fuel fabrication facility and the Prototype module of the GT-MHR.

OKBM (Experimental Mechanical Engineering Construction Office) implements overall control of GT-MHR programme. The A.A. Bochvar All Russian Institute of Inorganic Materials (VNIINM) has technical responsibility for fuel development. RRC-KI and Industrial Association Lutch together with VNIINM develop fuel technology. Irradiation, post-irradiation examinations and testing for safety validation will be conducted at NIIAR (State Scientific Center — Research Institute of Atomic Reactors). It is planned to locate the prototype reactor module fuel fabrication facility near Prototype module site at the Siberian Chemical Combine (SCC). Almost all Russian personnel of the various organizations participating in fuel development were involved in coated particle fuel development programme that was carried out in the Russian Federation from the mid 1960s to the early 1990s.

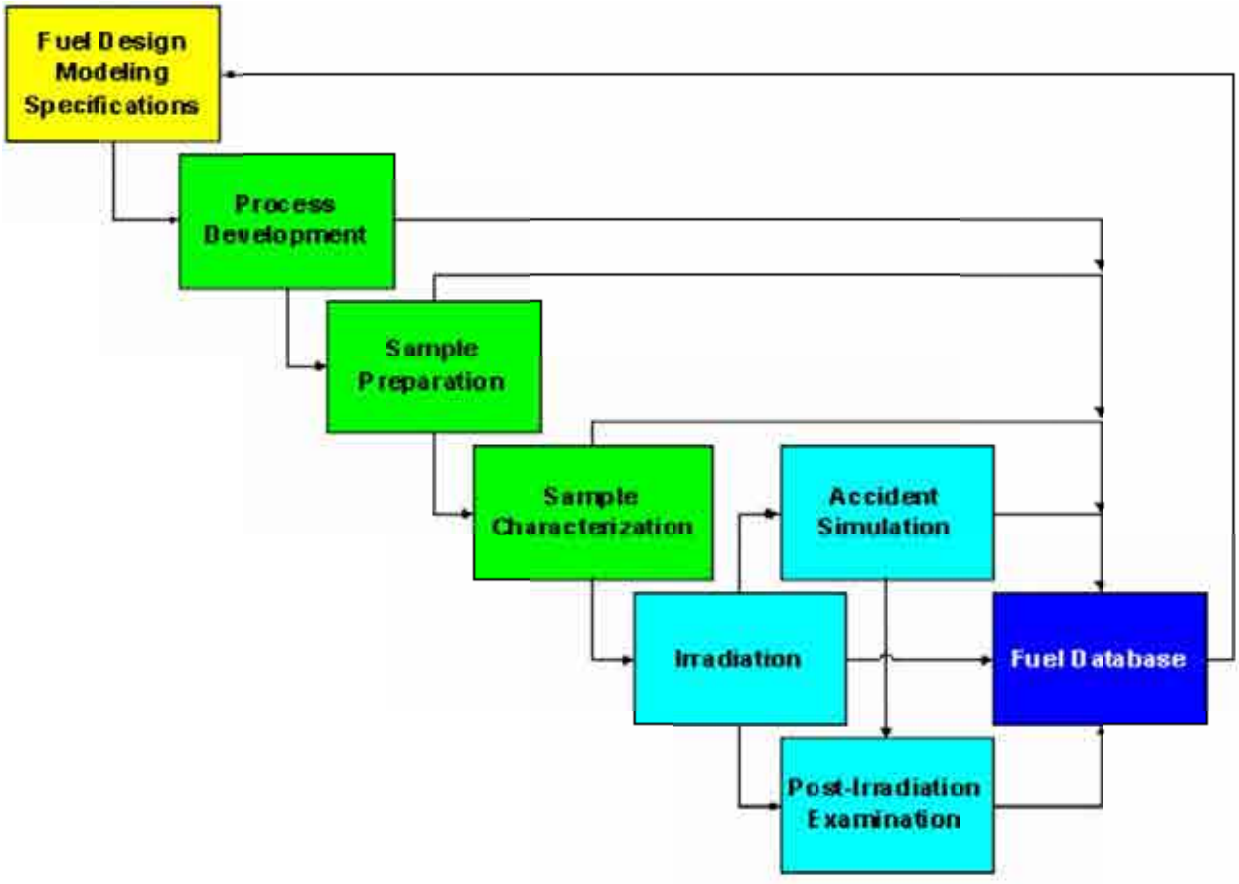

FIG. 2.8. Fuel development programme testing sequence.

2.3.2. Reactor concept

The reactor system couples the MHR directly to a Brayton cycle power conversion system (PCS) as is shown in Fig. 2.9. A GT-MHR module operates with a power level of 600 MW(th) and can produce electricity with thermal efficiencies ranging from 48 to 52% for core outlet temperatures ranging from 850°C to 950°C. High temperature operation of the GT-MHR with passive safety is enabled through the use of graphite fuel elements containing ceramic, TRISO coated fuel in the active core zone which has a height of 7.93 m and inner/outer diameters of 2.96 and 4.83 m, respectively (Figs 2.10 and 2.11). Major core design parameters of the GT-MHR are listed in Table 2.5. Additional information on the MHR design and its technology background is provided in [8].

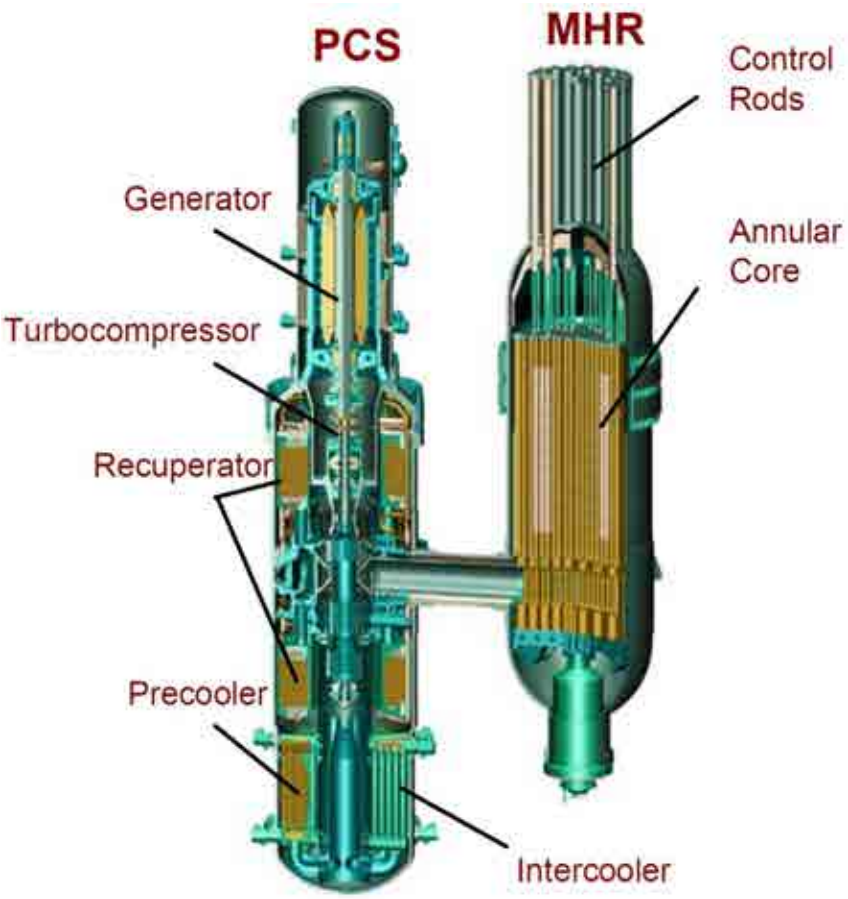

FIG. 2.9. Gas turbine moduler helium reactor, GT-MHR.

2.3.3. Reactor operation

The GT-MHR is designed to operate with coolant inlet and outlet temperatures of 490°C and 850°C, respectively. A potential issue associated with operating at a higher coolant inlet temperature is the impact on the vessel temperature during normal operation and accident conditions. For the GT-MHR, the inlet flow is routed through channel boxes located between the core barrel and the reactor pressure vessel. With this configuration, the vessel temperature during normal operation is approximately 50°C below the core inlet temperature. Additional design modifications are being investigated to further lower the vessel temperatures, such that proven light water reactor vessel materials (e.g. SA533 steel) could be used for the MHR vessel.

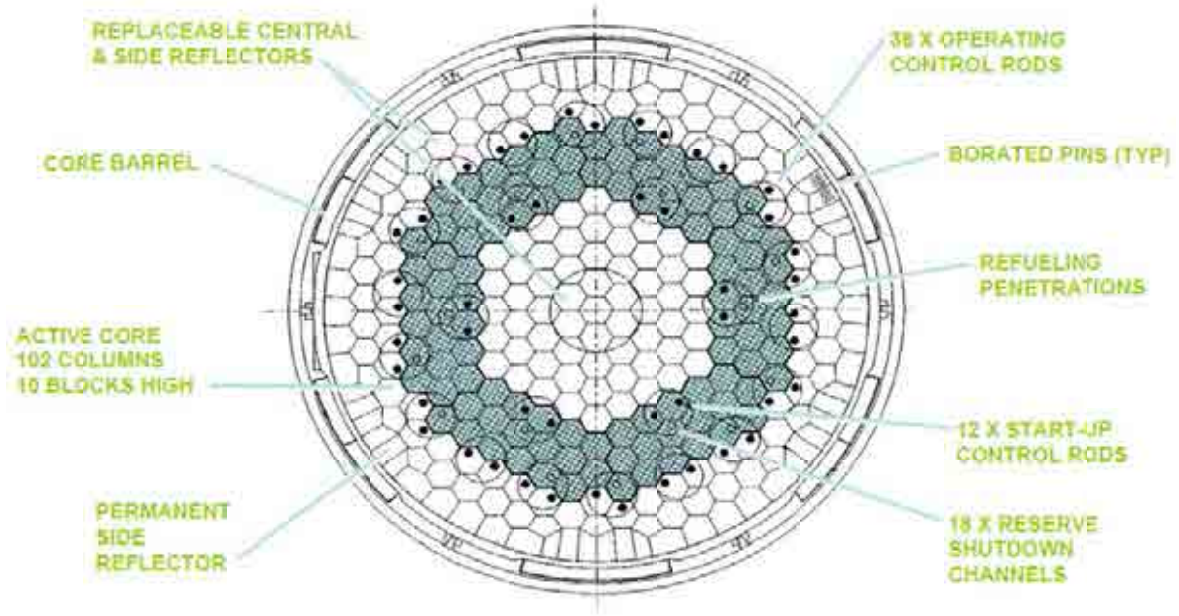

FIG. 2.10. Cross-section of reference GT-MHR plant.

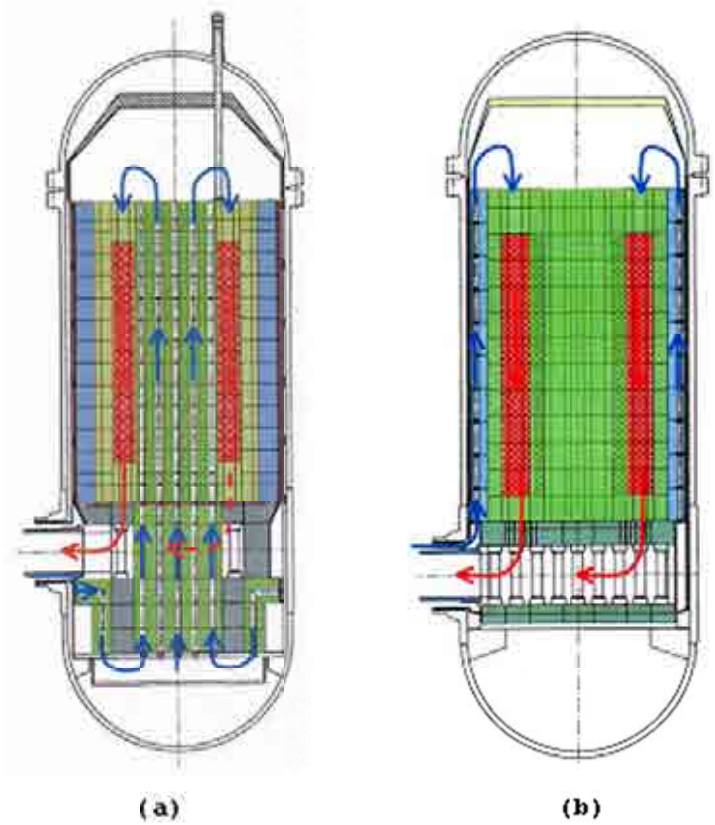

FIG. 2.11. GT-MHR plant with alternative inlet flow configurations (a) inner reflector; (b) permanent side reflector.

TABLE 2.5. CORE DESIGN PARAMETERS OF THE GT-MHR

Thermal power	600 MW(th)
Net electric power output	286 MW(e)
Average thermal power density	6.6 MW/m^3
Primary coolant	Helium
Reactor coolant inlet/outlet temperature	490/850°C
Core upper plenum inlet pressure	6.9 MPa
Core pressure drop	~0.050 MPa
Coolant mass flow rate	320 kg/s
Active core height	7.93 m
Active core inner/outer diameter	2.96/4.83 m
Average/maximum burnup	640/< 930 GW•d/t
Fast neutron fluence	4×10^{25} n/m^2, E>0.18 MeV
Average/peak maximum fuel temperature	1250/1320°C
Refueling cycle	750 efpd
RPV inner diameter	7.23 m
Power conversion efficiency	47.7%

2.3.4. Fuel design

In the conceptual and preliminary design phases of the GT-MHR project, a reference fuel design was developed and the need for including work on alternate fuel designs in the plan to reduce technical and programmatic risks was identified. Both a reference fuel and an alternate backup fuel will be carried in the early process development and in initial irradiations and accident simulation tests before the final fuel selection is made. The reference fuel is TRISO-coated, 200 μm diameter kernels consisting of a mixture of PuO_2 and Pu_2O_3 with an O/Pu atom ratio of < 1.7. This design is based on fuel particles of this type irradiated to high burnup in a test element in Peach Bottom I in the 1970s. Alternate fuels being considered are plutonium oxides diluted with inert or fertile materials and use of ZrC in the coatings. The fuel for the GT-MHR has quality requirements similar to those of commercial coated particle fuels and the GT-MHR core is designed to subject the fuel to in-service irradiation conditions similar to those of the commercial GT-MHR designs. The main fuel design characteristics are listed in Table 2.6, design figures on fuel quality are given in Table 2.7.

2.3.5. Safety and licensing considerations

Passive safety features for the MHR include ceramic, coated particle fuel and an annular graphite core with high heat capacity and low power density. Recently, INL has used the ATHENA thermal hydraulic code to model the response of the MHR during loss-of-flow and loss-of-coolant accidents and has confirmed these passivity safety features work to maintain fuel temperatures well below failure thresholds [9].

TABLE 2.6. MAJOR SPECIFICATIONS OF THE REFERENCE FUEL FOR THE GT-MHR

Number of fuel elements	720
Number of fuel columns	90
Fuel	$UC_{0.5}O_{1.5}$, PuO_{2-x}, x > 0.3
Amount of initial heavy metal in core	Fissile: 1748 kg LEU; Fertile: 514 kg U_{nat}
Uranium enrichment	Fissile: 19.9 wt%, Fertile: 0.7 wt%
Maximum average burnup	Fissile: ≤ 26% FIMA, Fertile: ≤ 7% FIMA
Fuel element lifetime	417 efpd
Kernel diameter	UCO: 350 μm; PuO_2: 200 μm
Layer thicknesses Buffer/IPyC/SiC/OPyC	Fissile: 100/35/35/40 μm Fertile: 65/35/35/40 μm
Fuel compact length	49.3 mm
Fuel compact diameter	12.45 mm
Fuel compact material	H-451 or TS-1240
Number of coated particles per compact	Fissile: 4310, Fertile: 520
Fuel pin length/outer diameter	790/12.7 mm
Number of fuel compacts per fuel pin	15
Fuel element width across flat surface	360 mm
Fuel element length	790 mm
Fuel element material	H-451
Coolant channel diameter	15.9 mm

TABLE 2.7. COATING INTEGRITY REQUIRED FOR GT-MHR FUEL

Parameter	> 50% confidence	> 95% confidence
As-manufactured fuel Quality		
Missing or defective buffer	$\leq 1.0 \times 10^{-5}$	$\leq 2.0 \times 10^{-5}$
Defective SiC	$\leq 5.0 \times 10^{-5}$	$\leq 1.0 \times 10^{-4}$
Heavy metal (HM) contamination	$\leq 1.0 \times 10^{-5}$	$\leq 2.0 \times 10^{-5}$
Total fraction HM outside intact SiC	$\leq 6.0 \times 10^{-5}$	$\leq 1.2 \times 10^{-4}$
In-service fuel performance		
Normal operation	$\leq 5.0 \times 10^{-5}$	$\leq 2.0 \times 10^{-4}$
Core heatup accidents	$(\leq 1.5 \times 10^{-4})$ [a]	$(\leq 6.0 \times 10^{-4})$ [a]

[a] Value is provisional and subject to revision as the design and safety analysis evolve.

Another key consideration for safety and licensing is co-location of the MHR modules with a hydrogen production plant. The *n*th of a kind plants consist of four MHR modules coupled to hydrogen production plants. It is proposed to locate the two facilities as close as possible (e.g. within about 100 m) in order to minimise the distance over which high temperature heat is transferred. INL has recently performed an engineering evaluation for these separation requirements and has concluded separation distances in the range of 60 m to 120 m should be adequate in terms of safety [10]. Other recommendations from the INL study include a 100 kg on-site limit for hydrogen storage, use of double-walled pipes for hydrogen transport, and location of the nuclear plant control room outside of the dispersion zone for chemical release. The below grade installation of the MHR modules, combined with an earthen berm between the MHR modules and the hydrogen production plant for defense in depth, provide additional safety margin for co-location of the two facilities.

2.3.6. The H2-MHR for hydrogen production

For the HTE based H2-MHR, approximately 68 MW of heat is transferred through an Intermediate Heat Exchanger (IHX) to generate superheated steam and the remaining heat is used to generate electricity. For the SI based H2-MHR, nearly all of the heat is transferred through an IHX to a secondary helium loop that supplies heat to the SI process.

For the H2-MHR, the inlet flow is routed through holes in the permanent side reflector, which is similar to the configuration used by the JAEA for their GTHTR300 design [3]. This configuration should provide enough additional thermal resistance between the inlet flow and reactor vessel to maintain vessel temperatures at acceptable levels [11].

The coolant inlet and outlet temperatures are increased to 590°C and 950°C, respectively, for the H2-MHR core. The outlet temperature was increased in order to improve the efficiency and economics of hydrogen production, but was limited to 950°C to avoid any potential adverse impacts on fuel performance during normal operation. Also, a higher coolant outlet temperature could require significant advances in technology to develop a viable IHX design. The coolant inlet temperature was also increased in order to maintain the same coolant flow and convective heat transfer rates within the core as that for the GT-MHR. Peak fuel temperatures during normal operation are maintained below 1250°C as the result of design modifications to optimise the core thermal hydraulic and physics designs [11]. These modifications include using lateral restraint mechanisms and sealing keys to reduce the fraction of flow that bypasses the coolant holes (e.g. through gaps between the graphite blocks), improved zoning of fissile/fertile fuel and fixed burnable poison, and improved refueling schemes.

2.4. HTR-MODUL

2.4.1. Plant design

In the late 1980s, the modular pebble bed reactor concept, the 200 MW(th) HTR-Modul, has been proposed in Germany by SIEMENS-INTERATOM [12]. The HTR-Modul is a pebble bed modular gas cooled reactor with a cylindrical core and passive decay heat removal features. This design formed the basis for the subsequent modular type reactor designs. The HTR-Modul concept was reviewed by the German regulatory agency (TÜV) and approved by the Reactor Safety Commission (RSK) of the German Federal Government. A schematic of the HTR-Modul is shown in Fig. 2.12. The reactor major operating parameters are presented in Table 2.8.

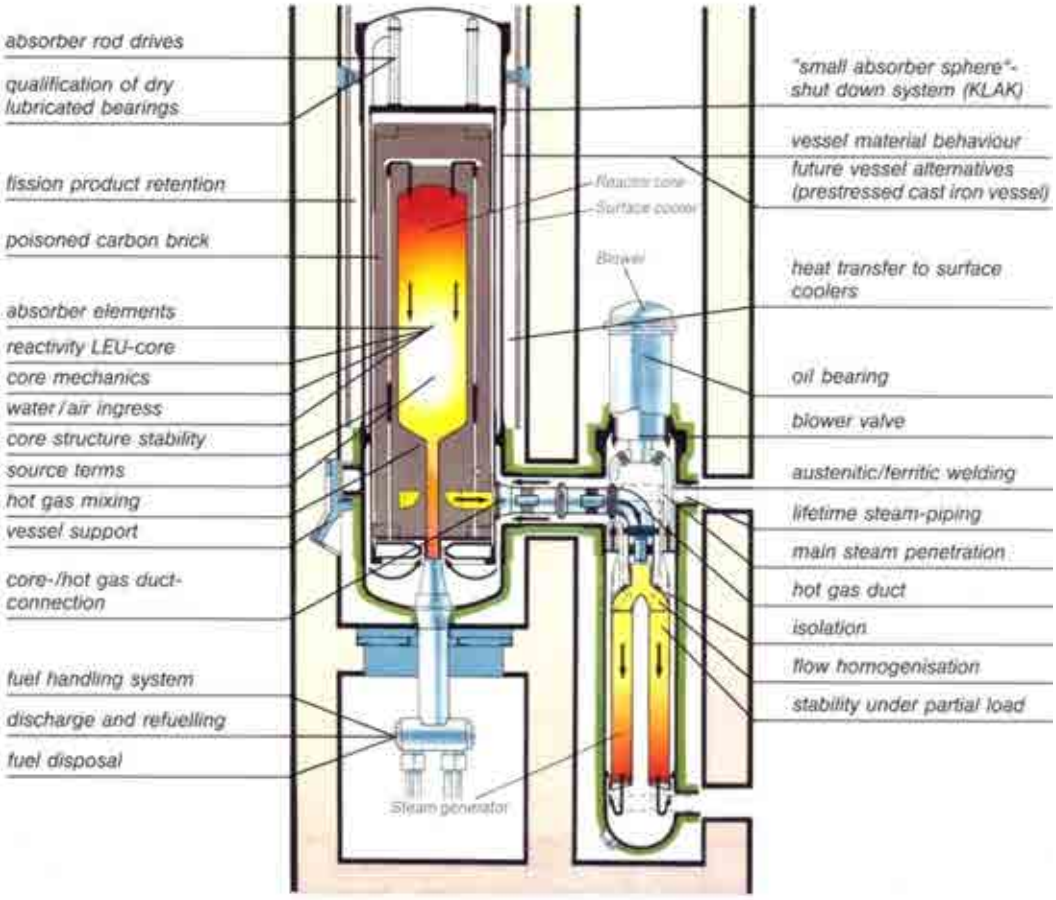

FIG. 2.12. Schematic of the 200 MWt HTR-Modul.

The reactor cylindrical core of the HTR-Modul has a diameter of 3 m and a height of 11 m. With a nominal power production of 200 MW(th), the average power density is 3 MW/m^3. The core enclosure is constructed from graphite blocks that contain approximately 360 000 spherical fuel elements with the first core consisting of 50% fuel elements and 50% moderator and absorber spheres. Each fuel pebble contains approximately 11 600 TRISO coated particles with low enriched uranium, which makes it 4.2×10^9 coated particles in the HTR-Modul. The pebbles are randomly packed in the reactor cavern and move continuously downwards through the core.

After exiting at the bottom, each fuel sphere is examined for structural integrity and burnup level. If it has not yet reached its burnup limit, it is returned to the pebble bed core. A total of 15 cycles are expected for the HTR-Modul fuel sphere before it has reached its 80 000 MWd/t burnup target and is discarded. The low power density in the one-zone core in connection with an average core outlet temperature of 700°C allows heat removal just by the transport mechanisms of conduction, radiation, and natural convection in any state of normal operation or accidents.

TABLE 2.8. CORE DESIGN PARAMETERS OF THE HTR-MODUL

Thermal power	200 MW(th)
Average thermal power density	3.0 MW/m^3
Power density form factor	1.8
Primary coolant	Helium
Reactor coolant inlet/outlet temperature	250/700°C
Core upper plenum inlet pressure	6.0 MPa
Coolant mass flow rate	85.5 kg/s
Bypass flow	6%
Active core height/diameter	9.43/3.0 m
Radial enrichment zones	1
Fuel reshuffling mode	Multiple pass
Number of passes through core	15
Target burnup	80 GW•d/t
Average/maximum fast neutron fluence	$2.1/2.4 \times 10^{25}$ n/m^2, E>0.1 MeV
Maximum fuel temperature + uncertainty range and statistical error	837°C (during first pass) 926°C
RPV height/outer/inner diameter	25/5.9/6.8 m
Reactor building	Vented/filtered

2.4.2. Fuel design

The design of the spherical fuel element has been selected according to the latest German reference concept. It is an A3-3 matrix graphite sphere with 60 mm diameter with an inner fuel-free zone of 50 mm diameter containing approximately 11 600 fissile coated particles. The characteristic fuel data are listed in Table 2.9.

The coated fuel particles consist of a 500 μm diameter oxide fuel kernel with 8% enriched uranium surrounded by subsequent layers of buffer (thickness: 95 μm), inner pyrocarbon (40 μm), silicon carbide (35 μm), and outer pyrocarbon (40 μm). All particles are overcoated with a 200 μm thick matrix graphite layer to prevent direct contact among the particles.

The total heavy metal (uranium) loading in the HTR-Modul fuel element is 7 g. With an enrichment of 8%, it corresponds to a loading of 0.56 g ^{235}U plus ~6.5 g of fertile ^{238}U material in a fuel sphere. This low fissile loading, which is only about half of the 1 g of fissile material per sphere typically used in the German fuel production, was chosen as additional safety margin for the water ingress accident to keep the reactivity increase by the water lower than the increase by withdrawal of all reflector rods. Resulting from the 7 g heavy metal loading is a small volume packing fraction in the fueled zone of the sphere of not more than 8% reducing the chance of manufacture-induced particle defects.

TABLE 2.9. CHARACTERISTIC DATA OF THE HTR-MODUL FUEL ELEMENT

Number of spherical fuel elements in core	360 000
Fuel	LEU UO_x , $x \leq 2.01$
Amount of initial heavy metal in core	2396 kg
Fissile U-235 inventory	107 kg
Uranium enrichment first core/equilibrium	4.2 ± 0.8/8 ± 0.5 wt%
Discharged fuel enrichment	1.4%
Fuel element lifetime in core	1007 efpd
Average duration per pass	67 efpd
Kernel diameter	500 ± 20 μm
Layer thicknesses Buffer/IPyC/SiC/OpyC Overcoating	 95 ± 18/40 ± 10/35 ± 4/40 ± 10 μm 200 μm
Densities Buffer/IPyC/SiC/OpyC	 ≤ 1.05/1.9 ± 0.1/≥ 3.18/1.9 ± 0.1 Mg/m^3
Anisotropy (BAF) iPyC and oPyC	≤ 1.10
Maximum power per particle (mW)	< 250
Fuel sphere material	A3-3 matrix
Fuel sphere diameter	60 mm
Thickness outer fuel-free zone	5 mm
Average/maximum power per sphere	0.6/1.4 (< 4) kW
Heavy metal loading per fuel sphere	7 g
Number of coated particles per sphere	11 600
Packing fraction	8%
Weight of fuel sphere	207 g
Fraction of free uranium	$\leq 6 \times 10^{-5}$
Impurities, boron equivalent	≤ 1.3 ppm

The detection limit is typically at a level of $1–3 \times 10^{-6}$ depending on the U content of the sample, much lower than the U content of a single defective coated particle. In a fuel element with about 1 g of ^{235}U/sphere and 0.07 mg/particle, the content of one defective particle corresponds to an U_{free}/U_{total} value of 7×10^{-5}.

In order to meet the specified limits for the corrosion rate of the fuel element matrix material, the maximum amount of impurities in the helium coolant is limited to ≤ 0.1 vol ppm of H_2O and ≤ 0.5 vol ppm of CO.

A final fuel production campaign was conducted by NUKEM in 1988 to produce spherical elements for a proof test of the HTR-Modul concept. Approximately 200 reference spheres were fabricated from particle productions sets comprising TRISO coated particle batches. The proof test fuel particles had an enrichment of 10.6 wt% ^{235}U. Each proof test spherical element contained 14 600 particles and utilized A3-3 matrix material. A total of eight spherical elements were selected for irradiation in the HTR-Modul proof test rigs HFR-K5 and HFR-K6 (four elements in each test, HFR-Petten). The as-manufactured free uranium fraction value for the proof test spherical elements was $\leq 13.5 \times 10^{-6}$. After irradiation in

Petten, these eight spheres were sent to the Forschungszentrum Jülich for post irradiation examinations (PIE) and later to ITU Karlsruhe for accident condition testing.

Irradiation tests prior to licensing, construction and operation of plant guarantee the required fuel performance and fission product retention in all operating and accident conditions. As one example, the R/B of ^{85m}Kr must remain below 3×10^{-7} during operation. Good performance has been demonstrated both under operational conditions to 12% FIMA and more and under accident conditions to a maximum 1600°C.

2.5. HTR-PM

2.5.1. Programme organization and Chinese HTGR technology progress

The Chinese High Temperature Reactor — Pebble-Bed Module (HTR-PM) is a modular high temperature gas cooled reactor demonstration power plant which is designed by the Institute of Nuclear and New Energy Technology (INET), Tsinghua University of China. The current HTR-PM design falls into the category of 'Innovative Small and Medium-Sized Reactors' of Generation-IV type reactors. It has an electrical output of ~210 MW utilizing two identical reactor units of 250 MW(th) each serving one steam turbine.

The HTGR has attracted many countries for years due to its promise of a high efficiency even for conventional electricity generation (η = 42–45%), but also for its possible application in the heat market. In China, R&D on HTGRs began in the middle of the 1970s. From 1974 to 1985, the INET of the Tsinghua University carried out some basic research on this technology. After 1986, the R&D on HTGR technology was highly intensified by the support of the country's 'High Technology Initiative' and cooperating with the international HTGR community, especially with German institutions. By these cooperations and its indigenous experimental work, China acquired all the technical know-how which has been produced in ~40 years around the world. During 1986–1990, eight key technical research topics, including 43 sub-tasks, were identified and systematic, in-depth experimental studies were carried out.

The keen Chinese interest on HTGRs stems mainly from three goals of the Chinese government for the Chinese nuclear market:

- Develop alternatives to LWRs in nuclear power: The Chinese government has announced to have 40 GW(e) of nuclear power plants in operation and additional 18 GW(e) under construction by 2020. The nuclear power capacity will be expanded to more than 100 GW(e) between the years 2020 to 2040. The HTR-PM could be a supplement to larger LWR plants.
- Develop alternatives to oil and natural gas: China is currently the second largest oil importing country in the world. The HTR-PM could provide a high temperature heat source for hydrogen production, for heavy oil thermal recovery, for coal gasification and liquefaction and for other industrial heat needs. The HTGR would be an ideal nuclear solution for these purposes.
- After the successful operation of the HTR-10, it is an adamant necessity to further improve Chinese HTGR technology and foster HTGR technology innovation. Consequently, the HTR-PM must be the next step; otherwise the vast expertise gained and the large economic expenses during the last 20 years will be lost.

In January 2006, the Chinese national project 'Large Advanced Pressurized Water Reactor and High-Temperature Gas-Cooled Reactor Nuclear Power Plants' became one of the 16 top priority projects of the 'Chinese Science and Technology Plan' for the period of 2006 to 2020.

In November 2003, the ‘Chinergy Company’ was established and designated to be the main contractor of the HTR-PM nuclear island. The preliminary investment agreement was signed in December 2004 by China Huaneng Group, China Nuclear Engineering Corporation and Tsinghua Holding Corporation. One year after the preliminary approval of the project in January 2006, the ‘Huaneng Shandong Shidao Bay Nuclear Power Company’ was founded being the owner of the HTR-PM demonstration plant.

Currently, both the Preliminary Safety Analysis Report and the Environmental Impact Assessment Report have been reviewed and accepted by the National Nuclear Safety Administration.

Extensive preparation work on the construction site of the HTR-PM nuclear power plant has already begun at Rongcheng, Shandong Province. The construction of the HTR-PM reactor was approved by the State Council. The construction of the power plant is foreseen to be finished within 50 months.

2.5.2. Core design of HTR-PM

The HTR-PM is a two modular nuclear power generating unit of 210 MW(e). Being the first industrial HTGR plant in China at present, it is designed for the purpose of electricity generation only. If the market requires, more identical modular reactor units can be constructed in series to form a larger nuclear power plant with appropriate power output. According to the original idea, the plant design is aimed at standardization and modularization.

The HTR-PM demonstration plant adopts the operation mode of two reactor/steam-generator units each of a power of 250 MW(th) being connected to only one steam turbine/generator set (Fig. 2.13). This design allows demonstrating the advantages and key benefits of employing and implementing a design of standardization and modularization. If the construction and operation of the HTR-PM demonstration plant proves to be successful, larger scale HTR-PM plants — using multiple modules feeding one steam turbine only — will become a reality.

The HTR-PM plant will primarily be used for base load operation, but it goes without saying that it can also be operated at lower power (> 25%) if this is demanded for load-following requirements.

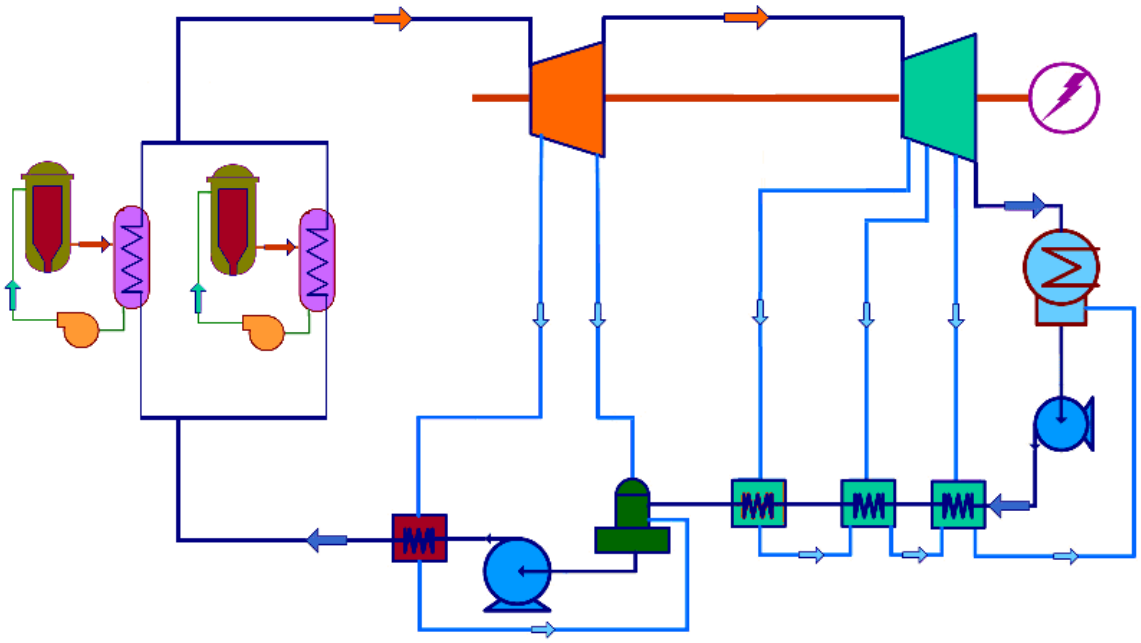

FIG. 2.13. Schematic diagram of the HTR-PM demonstration power plant.

For reasons of utmost simplicity — and thus safety — the pebble bed modular HTR-PM utilizes a one zone core. In addition, the core design obeys strict rules which are mandatory for an inherently safe reactor. Above all, the reactor core is designed around the properties of the spherical fuel elements:

- It must be possible to shutdown the reactor with absorbers from outside the core, so that the rods will not come into direct contact with the fuel elements. This requirement immediately leads to a core diameter of ~3.00 m.
- It must be assured that the fuel temperature limit of 1600°C is never exceeded even in hypothetical accidents. This requirement immediately fixes the maximum power density to ~7 MW/m^3.
- It must be possible to shut down the reactor in a steam atmosphere instead of the usual helium. This requirement for a very hypothetical event immediately leads to a uranium content per pebble of ~7 g.
- The core height is determined by the pressure drop of the core (and the steam generator) which the blower is able to overcome. Currently one-shaft blowers are capable of a pressure drop of ~0.2 MPa. This immediately fixes the maximum core height to ~11 m and dictates a helium pressure of 7 MPa.

The reflectors are made of graphite blocks, which are stapled layer by layer and fixed with graphite wedges. In the circumferential direction, every layer consists of 30 graphite blocks having a height of 300 mm. This graphitic cylindrical structure houses the fuel elements. The side reflector blocks contain the bore holes for the control rods, for the secondary shutdown system of small absorber balls, and for the cold helium entering the reactor from the outer ring section of the coaxial gas duct (Fig. 2.14).

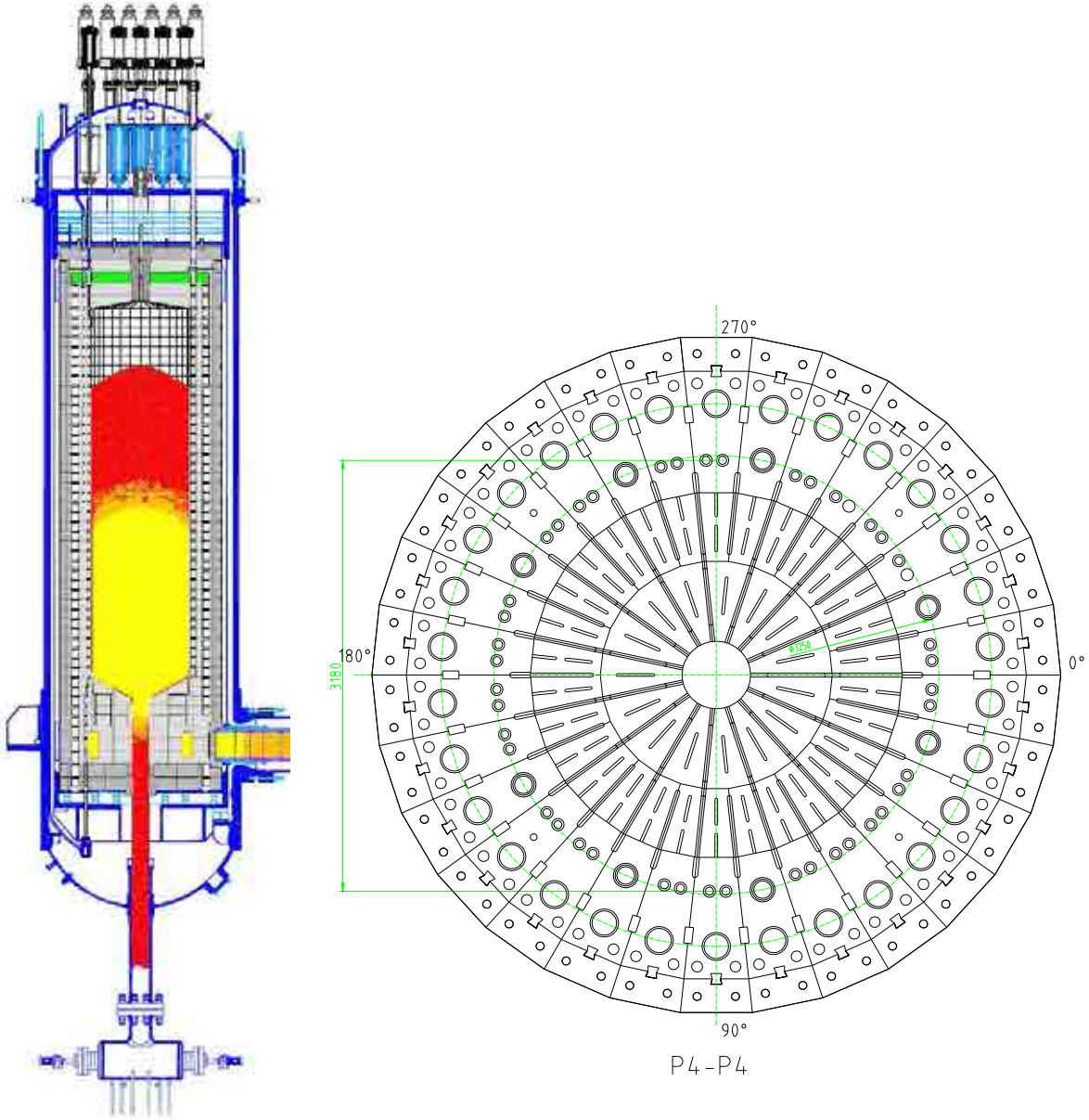

FIG. 2.14. Vertical and horizontal cross-section of the HTR-PM core.

In the centre of the top and bottom reflector, one finds the charging tube and the fuel discharge tube, respectively. The bottom reflector is designed to form a cone shape in order to ensure that all pebbles can easily be extracted from the core without forming stagnant zones. The gas mixing chamber is located below the bottom reflector. This chamber is of absolute necessity since the radial temperature difference of the helium exiting the core amounts to around 140°C. No steam generator would be working properly with this input. From experiments, it is concluded that the mixing chamber reduces this temperature difference to ~10°C. The mixed hot helium is guided to the inner region of the connecting gas duct, the hot gas duct, and delivers its heat to the steam generator.

Helium coolant of 250ºC enters the reactor in the bottom area. From here, the coolant flows upwards in the side reflector's outer 30 channels to the top reflector where it reverses its flow direction and enters the core at the top. During its pass through the core, the helium is heated up to a temperature of 750ºC.

The reactor core and the steam generator are housed in two steel pressure vessels which are connected by the connecting vessel. The coaxial vessel is designed to accept the hot gas in the inside tube, while the cold gas coming from the steam generator flows back in the outside region. Thus, the pressure retaining components of the steam generator vessel and the conducting vessel are in direct contact with the cold gas. The reactor pressure vessel is in close vicinity of the rising cold gas tubes. By this way, it also is protected from the heat of the core and has no contact with hot gases during accident situations.

Some key design parameters of the HTR-PM are given in Table 2.10.

TABLE 2.10. KEY PARAMETERS OF THE HTR-PM CORE

Total thermal power (two units)	500 MW(th)
Electric power turbine generator output	200 MW(e)
Average/maximum thermal power density	3.2/6.6 MW/m^3
Primary coolant	Helium
Reactor coolant inlet/outlet temperature	250/750°C
Core upper plenum inlet pressure	7.0 MPa
Core pressure drop	0.058 MPa
Coolant mass flow rate per unit	96 kg/s
Graphitic core diameter	5.0 m
Active core diameter/height	3.0/11.0 m
Reshuffling scheme	Multi-pass, 15 cycles
Maximum fuel operational temperature	930°C
Average/maximum burnup	90/100 GW•d/t
RPV inner diameter/height	5.7/24.9 m
Power conversion efficiency	42%
Steam temperature at turbine inlet	566°C
Steam pressure at turbine inlet/outlet	13.2 MPa/4.5 kPa
Flow rate of superheated steam per unit	96 kg/s

2.5.3. Steam generator, blower, and absorber systems

The steam generator is a genuine Chinese development and is somehow different from the steam generators used in the reactors Fort. St. Vrain, Peach Bottom, AVR, THTR, and proposed for the HTR-Modul. However, a smaller version of this type of steam generator has been installed into the HTR-10. The steam generator employs the idea of modularization to its highest extent. It consists of 19 separate identical helical tube assemblies; each assembly has five layers and includes 35 helical tubes, as shown in Fig. 2.15. To ensure two phase flow stability, throttling apertures are installed at the entrance of all helical tubes. The assembly type design of the steam generator uses the experiences from the steam generator employed in the HTR-10. In-service inspection is possible. All 19 steam generator modules deliver the steam to a common steam outlet pipe. For full verification of the large steam generator assembly of the HTR-PM, full scale testing will be performed.

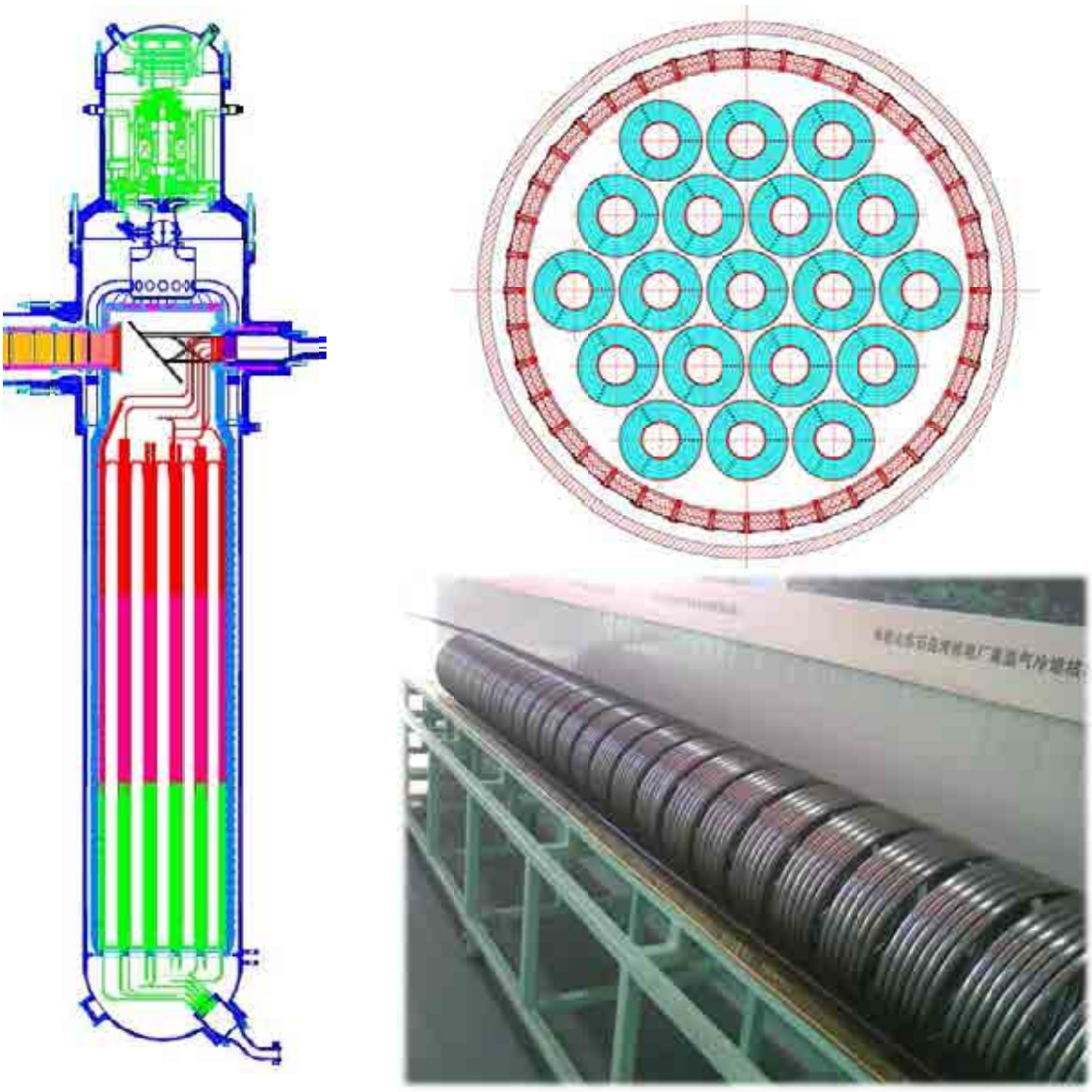

FIG. 2.15. Vertical and horizontal cross-section of the HTR-PM steam generator and a fabricated subassembly.

Due to the favourable temperature features of HTGRs, a superheated high pressure steam turbine is adopted for the HTR-PM. These components are readily available and exhibit high reliability and economical viability. Above all, there are mature experiences in the design, fabrication, serial manufacturing and operation of these systems and components in China.

The main helium blower, designed as a vertical structure, is installed on the top of the steam generator inside the steam generator pressure vessel. The electric motor mounted on an insertable assembly is driven by the converter outside the pressure vessel. A magnetic bearing system is envisaged. The power of the blower is rated to be ~4 MW.

For safety reasons, the blower can be entirely separated from the primary system by a flap. This will ensure that natural circulation in the primary system can be fully stopped. This will protect the core in beyond-design basis water ingress accidents and will mitigate hypothetical air ingress accidents to a large extent.

The control rod system and the small absorber sphere system are two independent control systems of reactivity. These systems fulfill the requirements of diversity and redundancy. There are eight control rods and 22 small absorber sphere (SAS) units, all located in the reflector region. For cold shutdown, the SAS systems as well as the rods are inserted. Both control systems have been adopted for the HTR-10 and the HTR-Modul.

2.5.4. Design of the reactor building

The reactor building houses the two independent modular units each comprising the core pressure vessel, the connecting pressure vessel, and the steam generator pressure vessel with their associated identical internal components. The modular units are heavily protected by four concrete bunkers, the so-called cavities, having a wall thickness of ~2.40 m. The cavities are designed to protect the reactors from external events (Fig. 2.16).

The cavity forms the low pressure vented containment and is designed to withstand an overpressure of 30 kPa. Under normal operating conditions, the cavity exhibits a negative pressure by the HVAC system in order to prevent any radioactive material from entering the environment. The cavity is equipped with filters — during accident condition charcoal filters are put into operation. The cavity's HVAC system is laid out such that in the event of helium leakage from one reactor, the second reactor is not restrained from normal operation. Of course, this is the precondition of operating many modular reactors in one single reactor building. If one reactor suffers a small leak, e.g. a break of a measuring line, the outwards flowing helium will enter the environment via the filters. However, if a pipe rupture occurs, the building will be vented for ~100 s. After that the containment will be closed again and a negative pressure will be installed once more. Hence, the total helium inventory of the primary circuit will enter the environment unfiltered. Since the radioactivity of the helium (including the carried along dust) is very small, the environmental exposure of the public is minimal. Any governmental countermeasures such as evacuation or relocation of the populace can be excluded.

Two independent decay removal systems are installed inside the two circular reactor cavities each having a diameter of 8.5 m. The decay removal systems consist of 300 water filled tubes (diameter: 30 mm) which, in accident conditions, carry away the decay heat, and in operational conditions, the heat losses of the pressure vessels by natural convection to heat exchangers outside the reactor building. In turn, these heat exchangers work also by mere natural convection and deliver the heat into the atmosphere. The design capability of these systems is 0.5 MW for each train, and each reactor has three identical trains. To carry away the decay heat in accident conditions, one needs two trains only.

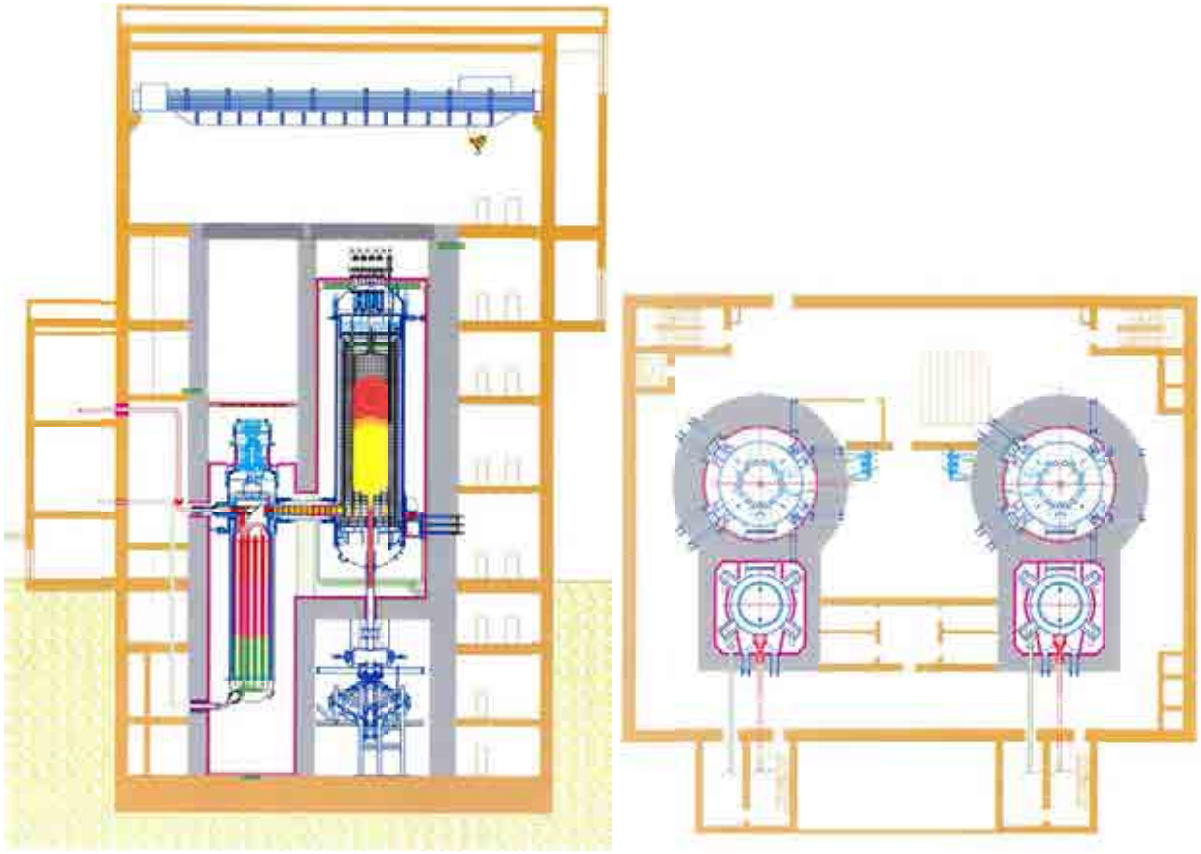

FIG. 2.16. Vertical and horizontal cross-section of the HTR-PM reactor building.

The gas purification plan and the helium storage facilities are bunkered outside the reactor building. The spent fuel is stored in sealed canisters and also in a bunkered zone below the cavities which could be cooled by natural circulation of air.

2.5.5. HTR-PM fuel concept

The HTR-PM is designed to use spherical pebbles according to German design, thus having a diameter of 60 mm. For the chosen power output of 250 MW(th), 420 000 pebbles are needed. The graphitic fuel balls contain the fissile and fertile material in tiny coated particles of approximately 1 mm diameter. In order to avoid an intolerable reactivity increase in case of a water/steam ingress, one fuel sphere is restricted to a uranium content of 7 g. This readily yields ~11 600 coated particles in one fuel ball. Having in mind that the fuel-containing graphitic region of the fuel element has a diameter of 50 mm, one obtains a low packing density of coated particles in the fuel matrix of 9.3%.

The final burnup was chosen to be a high 90 000 MWd/t. This requires an enrichment of ~8.5%, which still falls into the category of low enriched uranium. Uranium oxide has been chosen as fuel.

Every fuel element will pass the core 15 times. This high number had to be chosen to reach the required reactor power of 250 MW(th). To keep the reactor critical, one needs about 400 fresh fuel elements per day. This means on the other hand that 400 × 15 = 6000 fuel elements have to be reshuffled a day. To determine whether an extracted fuel sphere has already reached its design burnup or whether it has to be reinserted into the reactor, gives a maximum

measuring time to determine the burnup of the extracted pebble of only < 14.5 s. It could be shown that this severe requirement can be met by gamma-spectroscopic means to an accuracy of $1\sigma < 2.5\%$.

From experimental evidence, the requirement for the core layout is as follows:

- For normal operating conditions, the fuel temperature must not surpass a temperature of $T_{max,op} = 1200°C$. This temperature holds for a time span of ~1500 days.
- For accident conditions, the fuel temperature must not surpass a temperature of $T_{max,ac} = 1600°C$. This temperature holds for a time span of ~500 hours.

Characteristic fuel data for the HTR-PM are shown in Table 2.11.

TABLE 2.11. MAJOR SPECIFICATIONS OF THE REFERENCE FUEL FOR THE HTR-PM

Number of spherical fuel elements	420 000 per unit
Fuel	LEU UO_2
Amount of initial/equilibrium core heavy metal	2.94/2.8 t/unit
Fuel element residence time	1057 efpd
Kernel diameter	$450–550|_{95/95}$ µm
Kernel density	≥ 10.4 Mg/m^3
Sphericity (D_{max}/D_{min})	$x \leq 1.2|_{95/95}$
Uranium enrichment	4.2 wt% (first load) 8.5 wt% (reload)
Layer thicknesses Buffer IPyC, OPyC SiC	 $50 \leq x \leq 140|_{95/95}$ µm $20 \leq x \leq 60|_{95/95}$ µm $25 \leq x \leq 45|_{95/95}$ µm
Anisotropy factor PyC layers	≤ 1.03 (OAF)
Total/fuel zone diameter	60/50 mm
Number of coated particles	11 600
Packing fraction	9.3%
Initial heavy metal loading	7 g U or 7.942 g UO_2 per sphere (6.65 ≤ x ≤ 7.35 g U)
Free uranium fraction in matrix	$< 3 \times 10^{-5}$

2.5.6. Remarks on modular HTGR safety philosophy and on safety systems

The nuclear safety features engineered into the modular pebble bed reactor HTR-PM can be summarized as follows: Most accidents are controlled by inherent, unchangeable properties of the used components. The consequences of all conceivable accidents will not result in significant offsite radioactive impacts. This is partly achieved by employing the inherent safety features of a gas–graphite system, by observing stringent geometrical restrictions, and — above all — by checking each design step against the properties and limits of the fuel element. A system like this must necessarily have a relatively small power density. However, while this might increase the cost of the pressure vessels and its internals, this effect is largely compensated by the elimination of many common safety systems. In addition, this low power density is extremely important for coping with far beyond design basis accidents. While the intervention time of standard nuclear reactors must start very quickly in the frame of a minute

to an hour, this reaction time is largely increased in modular HTGRs — even for beyond-design basis accidents — to days or even weeks. This gives ample time for deliberating which countermeasures would be appropriate.

Obviously, the heart of a modular HTGR is the fuel element. All design considerations revolve entirely around it. It goes without saying that this design philosophy poses many restrictions to the plant. On the other hand, it eliminates most of the common safety systems. Very few simple systems remain such as absorber rods, blower shutdown, valves to close pipes connected to the primary system, and steam generator dumping.

In effect, the modular HTR-PM represents a change of paradigm in reactor design. Instead of choosing the power of a reactor and then control it by numerous safety systems, the power of a modular reactor is given by geometrical restrictions and by the limitations of the fuel element.

The plant meets already the safety target of Generation-IV nuclear energy systems which stipulates: 'eliminate the need for offsite emergency measures'. The same point of view is clearly put down by IAEA in its report No. NS-R-1 'Safety of Nuclear Power Plants: Design'. Here it is explicitely stated: "An essential objective is that the need for external intervention measures may be limited or even eliminated in technical terms, although such measures may still be required by national authorities." This remark is not restricted to emergency measures but also applies to engineered emergency systems. Up to now, the HTGR development is hampered by these rules which are correct and appropriate, even necessary, for LWRs. But they do no take credit of the unique features of a modular HTGR.

It is clear that the layout of the modular HTR-PM strictly follows the current international rules, such as the 'defense in depth concept', the 'multi barrier principle', the installation of a secondary, diverse shutdown system, etc. Nevertheless, when all these measures fall short, the inherent safety features will never fail. This is evidently illustrated by the self stabilization and limitation of the maximum fuel temperature in a depressurization accident of the HTR-PM (Fig. 2.17). Without any absorber insertion the chain reaction is inherently stopped by the Doppler-Effect. It is not necessary to 'initiate' this effect, and it can not be changed either. It goes without saying that, for demonstration purposes, this example is picked out of many possible examples which clearly show the effect of inherent properties.

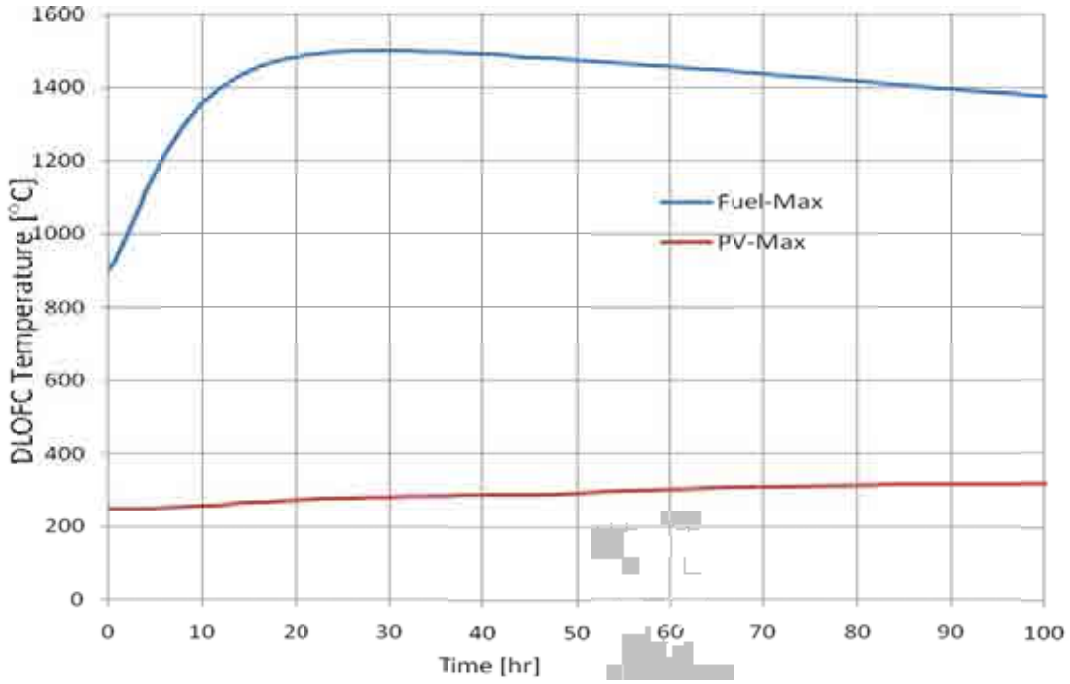

FIG. 2.17. Self-limitation of the fuel temperature during a depressurization accident in the HTR-PM.

2.6. NEXT GENERATION NUCLEAR PLANT (NGNP)

2.6.1. Introduction

The next generation nuclear plant (NGNP) will be a demonstration of the technical, licensing, operational, and commercial viability of high temperature gas cooled reactor (HTGR) technology for the production of process heat, electricity, and hydrogen. This nuclear based technology can provide high temperature process heat (up to 950°C) that can be used as a substitute for the burning of fossil fuels for a wide range of commercial applications. The substitution of the HTGR for burning fossil fuels conserves these hydrocarbon resources for other uses, reduces uncertainty in the cost and supply of natural gas and oil, and eliminates the emissions of greenhouse gases attendant with the burning of these fuels. The HTGR is a inherently safe nuclear reactor concept with an easily understood safety basis that permits substantially reduced emergency planning requirements and improved siting flexibility compared to other nuclear technologies.

The Energy Policy Act of 2005 (EPAct) directed the US Department of Energy (US-DOE) to develop a demonstration of this HTGR technology to economically and reliably produce electricity and hydrogen by the year 2021. The EPAct also stipulated that the task should be undertaken in partnership with the industrial suppliers and end users of the technology. To that end, a working group consisting of suppliers of the technology, nuclear plant owner/operators, other supportive technology companies, and potential end users was assembled. The objective of this working group is to form an alliance that would provide the private sector perspective and direction for completion of the NGNP in partnership with the US DOE. The Alliance will support the selection of the specific operating conditions and configuration for NGNP to ensure it meets private sector expectations, commence management of the project using commercial processes, share the cost of design and construction with the government, and secure a commercial nuclear operating company to operate the plant. Finally, as required by EPAct, the approach for licensing the NGNP is being developed through a joint effort between the US-DOE and the US-NRC.

2.6.2. Pre-conceptual design team recommendations for plant configuration, operating conditions, startup

Three contractor teams with extensive experience in HTGR technology, nuclear power applications, and hydrogen production developed preconceptual designs for the NGNP Project. Westinghouse Electric Company, LLC, AREVA NP, Inc., and General Atomics were the leaders of each of the three teams. The objectives of the pre-conceptual design activities were to

- initiate development of the functional and operational requirements (F&ORs);
- establish a reference configuration of the NGNP;
- provide direction to the NGNP Project R&D programmes to ensure they support design development, licensing, construction, and deployment of the NGNP;
- support development of the licensing strategy for the NGNP and, ultimately, development of a Certification of Design for the use of the HTGR technology in the private sector;
- develop pre-conceptual designs with sufficient detail to provide credible estimates of the schedule and costs for NGNP and an n^{th} of a kind plant;
- perform economic assessments for the n^{th} of a kind plant to confirm the economic viability of the HTGR technology in production of electricity and hydrogen.

Table 2.12 summarizes the key results of each contractor team's evaluation and recommendations for the NGNP operating conditions and configuration. The Westinghouse team selected a 500 MW(th) pebble bed reactor in an indirect cycle configuration (helium secondary loop) that would produce power via a traditional Rankine cycle and hydrogen via the hybrid-sulphur process in series. The AREVA team selected a 565 MW(th) prismatic reactor in an indirect cycle configuration that would produce power via a Rankine cycle (using helium–nitrogen secondary loop) in parallel with hydrogen production (using helium secondary loop) via high temperature electrolysis in the near term and the sulphur iodine process in the longer term. The General Atomics team selected a 550 to 600 MW(th) prismatic reactor in a direct cycle configuration to produce power with a Brayton cycle and via a small intermediate heat exchanger to produce hydrogen in parallel with power. Schematics of the configurations are shown in Fig. 2.18.

Following these preconceptual design efforts, additional special studies were performed to examine high risk areas associated with the design and technology. As part of those studies, the GA team modified their design to have an option in which the vessel is cooled so that SA508/533 (LWR vessel material) can be used. In addition, based on the near term market needs for process heat, the project has selected 750 to 800°C as the reactor outlet temperature. The designs have continued to evolve in response to this change in outlet temperature. While the high level configuration of the Westinghouse pebble bed reactor remained unchanged, the prismatic designs have adopted an indirect power conversion system with a steam generator in the primary loop and in parallel an indirect hydrogen production system. Additional details of the current configurations and operational parameters are shown in Table 2.12. The designs will continue to evolve as the project moves into conceptual design and end user requirements are better defined.

TABLE 2.12. SUMMARY OF DESIGN CONFIGURATIONS AND OPERATING CONDITIONS

Item	Recommended operating conditions & plant configuration		
	Westinghouse	AREVA	General Atomics
Power level (MW(th))	500	565	550–600
Reactor outlet temperature (°C)	750–800	750–800	750–800
Reactor inlet temperature (°C)	350	500	490
Cycle configuration	Indirect — Series hydrogen process and power conversion	Indirect — power conversion system with steam generation in primary loop and parallel indirect hydrogen production	Indirect — power conversion system with steam generation in primary loop and parallel indirect hydrogen production
Secondary fluid	He	He-Nitrogen to PCS He to H_2 Process	He
Power conversion	100% of reactor power	100% of reactor power	100% of reactor power
Hydrogen plant power	10% of reactor power	10% of reactor power	HTE: 5 MW(th) S–I: 60 MW(th)
Reactor core design	Pebble bed	Prismatic	Prismatic
Fuel	TRISO UO_2 1st and subsequent cores	TRISO UCO 1st and subsequent cores	TRISO UCO 1st core, variable subsequent cores
Graphite	PCEA & NBG-18	NGG-17 and NBG-18	IG-110 & NBG-18
RPV design	Exposed to the gas inlet temperature	Exposed to the gas inlet temperature; insulation and vessel cooling options	Exposed to the gas inlet temperature
RPV material	SA508/533	9Cr–1Mo	SA508/533
IHX	Two-stage PCHE, In 617 material	Process — PCHE or Fin-Plate, In 617	Process — single stage PCHE, In 617
Hydrogen plant	Hybrid thermo-chemical plus electrolysis	Initial: HTSE Longer term: S–I	Initial: HTSE Longer term: S–I

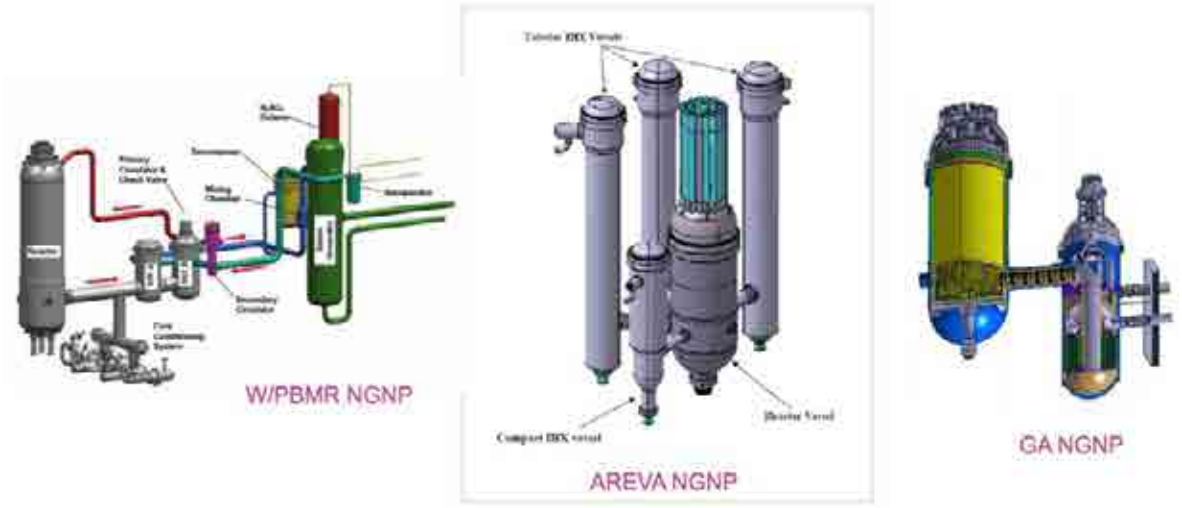

FIG. 2.18. Configurations of pre-conceptual NGNP designs.

2.6.3. Key development risks and associated research and development

The principal technical risks associated with the HTGR technologies anticipated for the NGNP include:

- Qualification and acquisition of reactor fuel (e.g. qualification of fuel production facilities); reactor core ceramics, including graphite and graphite production facilities; and metals in the high temperature regions of the plant (e.g. in the reactor and heat transport system);
- Verification and validation of analysis methods required to support design development; American Society of Mechanical Engineers (ASME) code acceptance; American Society for Testing and Materials (ASTM) standards acceptance; and NRC licensing;
- Availability of materials with acceptable metallurgical and physical properties in the required sizes and thicknesses and the ability to fabricate large vessels on-site using these materials;
- Availability and development of instrumentation (e.g. to monitor the fluence, high temperatures, and gas flow rates in the plant);
- Development of the hydrogen production processes and components;
- Potential contamination of the product streams and meeting acceptable limits .

Research and development activities are planned in the areas of fuels, graphite, high temperature materials, design and safety methods, and heat transport to address these risks. Specifically:

- The Fuel Development and Qualification Programme will qualify TRISO coated particle fuel for use in NGNP. TRISO coated particles will be fabricated at pilot scale for use in the formal qualification testing. The testing programme consists of irradiations, safety testing and post-irradiation examinations that will characterize the behaviour of TRISO coated fuel under both normal and off-normal conditions. The programme also contains out of pile experiments, special irradiations and safety testing to characterize the release and transport of fission products from the kernel, through the coatings, the fuel matrix, the graphite and the primary system (i.e. source term). Formal validation testing is also planned to validate fuel performance and fission product models, required for core performance assessments and safety analysis. The programme is currently considering both UCO and UO_2 and, different from past prismatic core designs, as a one-particle design. Once a design decision is reached by the project, the programme will focus on either UCO for prismatic or UO_2 for pebble bed. Feasible acquisition strategies for fabrication of first core and qualification of the associated production scale fuel fabrication facility for both design concepts have been established and will be executed once the reactor design decision is made.
- The objective of the NGNP Graphite Programme is to develop the qualification dataset of thermomechanical and thermophysical properties for unirradiated and irradiated candidate grades of graphite for NGNP. Where practical, other grades of graphite may be tested/characterized to provide a baseline for comparison or to help understand material property changes for the NGNP graphite grades. The programme consists of statistical characterization of unirradiated graphite material properties to establish the lot-to-lot, billet-to-billet and within billet variability of the material. Irradiations are planned at specified temperatures and doses within the design service condition envelope anticipated for NGNP. Extensive post-irradiation examinations are planned to establish the change in relevant material properties as a function of

temperature and neutron dose. Of particular interest is the irradiation induced creep of graphite, which is critical to determining the lifetime of the graphite under irradiation. From these datasets, constitutive relations will be established for use in a detailed predictive thermo-mechanical finite element model. These data will also support development of relevant ASTM standards and ASME design rules. In the longer term, the programme plans to evaluate processing route and raw material constituent influences on graphite behaviour so that additional large qualification irradiation programmes are not needed when new coke sources are used to make graphite for HTGRs.

- The goal of the High Temperature Materials Programme for NGNP is to establish the relevant thermomechanical performance data to support the development of an intermediate heat exchanger and other high temperature components for an outlet temperature up to 950°C. Creep, creep–fatigue, aging, and environmental degradation testing is planned using the candidate high temperature materials selected for NGNP. Thick and thin sections of base material, weldments and other joints (e.g. diffusion bonding) will be evaluated given the different design options under consideration for the intermediate heat exchanger. (Current candidates are Inconel 617 and Haynes 230). Depending on the outlet temperature selected by the NGNP project, additional high temperature data may be needed to support relevant ASME code cases for the material. R&D to establish requisite in-service inspection techniques will be developed as key components are being designed. Prototype testing of key components is envisioned in a high temperature flow loop to characterize overall behaviour under prototypic flowing HTGR conditions and to validate in-service inspection techniques.
- The goals of the Design and Safety Methods Validation Programme for NGNP are to develop validation experiments and data to validate models and analytical tools for NGNP, to resolve key safety, performance, and technical issues through confirmatory modeling and/or tool development when existing models and/or tools are judged to be inconclusive or inadequate, and to modify, upgrade, and/or develop new analytical tools for future use that will reduce uncertainties and improve the capability of understanding the behaviour and operating margins of the plant. Current areas of focus include developing improved differential cross-sections for plutonium isotopes to reduce uncertainties in the reactivity performance of high burnup low enriched uranium HTGR cores, assessing and improving reactor physics and kinetic methods for prismatic and pebble bed HTGRs, performing physics benchmark studies on past relevant experiments, evaluating important phenomena that influence thermal fluid behaviour in HTGRs and establishing relevant experiments for V&V, evaluating air ingress phenomena in HTGRs and participating in relevant validation experiments, developing experiments to validate reactor cavity cooling system behaviour, and evaluating and establishing system level codes appropriate for HTGR safety analysis.
- The goal of the Component Test Facility project is to design, construct, and startup a test facility to support development of high temperature gas thermal-hydraulic technologies (e.g. helium, helium–nitrogen, CO_2) as applied in heat transport and heat transfer applications in HTGRs. Such applications include but are not limited to primary coolant; secondary coolant; direct cycle power conversion; intermediate, secondary and tertiary heat transfer; and demonstration of processes requiring high temperatures (e.g. hydrogen production, process heat demonstrations at large scale). The initial use of this facility will be in support of the completion of the NGNP. However, this test facility will be open for use by the full range of suppliers, end users, facilitators, government laboratories, and others in the domestic and international community supporting the development and application of HTGR

technology. The facility shall provide for full scale testing and qualification of high temperature fluid flow systems, components, and equipment (e.g. circulators, intermediate and tertiary heat exchangers, piping, and isolation valves) and associated instrumentation.

2.6.4. Conclusions

The NGNP Project will develop and demonstrate a first of a kind very high temperature gas cooled nuclear system with the capability to generate electrical power and produce process heat for hydrogen production and other applications. The NGNP incorporates an inherently safe reactor concept with an easily understood safety basis that permits substantially reduced emergency planning requirements and improved siting flexibility compared to current and advanced light water reactors.

The scope of the project includes development of a very high temperature gas cooled nuclear system, alternative hydrogen production technologies that can efficiently use the process heat from the nuclear system, and power conversion technologies that promise important improvement in electrical power generating efficiencies.

The overall objectives of this project include:

- Developing and implementing the technologies required to achieve the functional performance and meet the design requirements determined through close collaboration with commercial industry end users.
- Demonstrating the basis for commercialization of the nuclear system as a process heat source, the hydrogen production facility, and the power conversion concept.
- Demonstrating as an essential part of the prototype operations that the requisite reliability and capacity factor can be achieved over an extended period of operation.
- Establishing the basis for licensing the commercial version of NGNP by the US Nuclear Regulatory Commission (NRC). This will be achieved in major part through licensing the prototype by NRC and initiating the process for certification of the nuclear process heat system design.
- Fostering rebuilding of the US nuclear industrial infrastructure and contributing to making the US industry self-sufficient for our nuclear energy production needs.

The project will be accomplished though the collaborative efforts of the US-DOE and its national laboratories, commercial industry participants and international government agencies. The Idaho National Laboratory acting as the agent of the US-DOE currently provides project management and technology development leadership for the project.

2.7. PBMR

2.7.1. Introduction

The pebble bed modular reactor (PBMR), being developed in South Africa through a world wide international collaborative effort led by Eskom, the national utility, will represent a key milestone on the way to achievement of the VHTR design objectives. The PBMR project has been progressing rapidly over the past few years to a relatively high level of detail.

The PBMR concept was introduced into South Africa (RSA) in 1993 as exploratory evaluations began to determine the feasibility of small nuclear reactors based on this concept to satisfy the anticipated future growth of electrical demand. Small-sized reactors are of

interest in South Africa because of the widespread distribution of moderate load demand and the high cost of new transmission across this large country. A project team was formed within Eskom to perform a detailed feasibility study. International investors, including British Nuclear Fuels plc, were brought into the project and development efforts were accelerated.

The PBMR is a small, modular pebble bed reactor that is helium cooled and graphite moderated. The genesis of the PBMR design originates with the German HTGR development programme of the 1970s and 1980s. The major innovations for the current PBMR design are the direct coupling of the high temperature reactor system to a gas turbine and the achievement of a very high level of passive safety without the use of active engineered systems. The direct cycle gas turbine eliminates the complex and costly steam cycle for power conversion and results in a significantly higher thermal efficiency. Passive safety is accomplished by the use of high integrity particle fuel which retains its integrity under high temperature accident conditions and has good resistance to chemical attack, e.g. from water or air ingress. Further, the introduction of an annular core allows fuel decay heat to be conducted through the reactor structures to the vessel cavity and then to atmosphere without the need for electric power or early operator intervention.

2.7.2. Physical layout of the PBMR

The PBMR is based on a relatively simple design with passive safety features that require no short term human intervention. While existing commercial reactors use active engineered safety systems, the PBMR achieves its safety through its design approach, the materials used, and the fuel form. The key safety features of the PBMR are:

- radionuclide retention capability of high quality fuel with very low particle failure rates;
- small operational excess reactivity;
- large negative temperature coefficient;
- passive heat removal capability of the reactor design.

The removal of decay heat is achieved by conduction, convection, and radiation heat transfer from the fuel particles through the reactor to the environment. The high surface area to volume ratio of the core promotes this heat transfer process and ensures that the core never reaches a temperature at which significant degradation of the fuel can occur. The combination of the low power density of the core together with the high temperature resistance of the fuel allows this approach to be used.

The power conversion unit of a PBMR module is contained in four steel pressure vessels that house the reactor core, two turbo compressor units, and the power generation turbine. Interconnecting piping allows for recuperation and cooling of the helium returning to the reactor to achieve the needed gas compression and overall improved thermodynamic efficiency. The pressure boundary of the entire PBMR power conversion unit is shown in Fig. 2.19. The thermodynamic cycle of the PBMR is a closed Brayton cycle with recuperation. Helium exits the reactor at 900°C and passes successively through the high and low pressure turbines that drive the compressors and then to the power generation turbine which is coupled to the main electrical generator. The exhaust helium out of the power generation turbine now passes for the first time through the recuperator transferring its heat to the helium returning to the reactor. The helium coolant then passes through two coolers and the compressors, increasing its pressure to 9 MPa before re-entering the recuperator for the second time prior to returning to the reactor at 482°C. The overall efficiency of this cycle is calculated to be approximately 42% with the current conservative bypass flows, including turbine blade clearances, and cooling water temperatures.

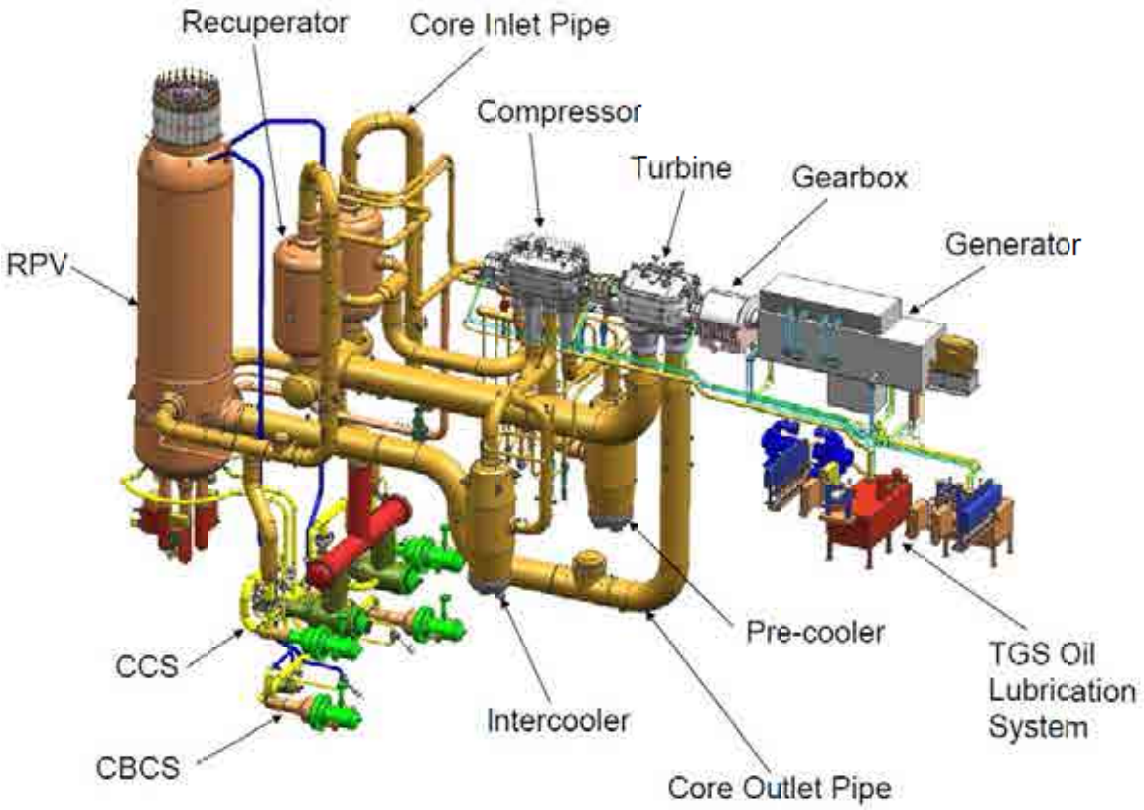

FIG. 2.19. Physical layout of PBMR main power system.

2.7.3. Reactor core design

The PBMR core (Fig. 2.20) consists of approximately 452 000 fuel spheres packed in an annular geometry with an inner radius of 1.0 m and an outer radius of 1.85 m. The active height of the core is 11.0 m, resulting in a relatively low thermal power density of 4.8 MW/m^3.

High plant availability is achieved with on-power refueling. The pebbles gradually move downward in the core bed from top loading locations and exit via one of three defueling chutes at the bottom of the bed. After exiting the core, the pebbles are assayed for burnup and checked for general spherical integrity. If insufficient burnup has been achieved, a pebble is returned to the top of the core by the pneumatic Fuel Handling and Storage System. On average, pebbles make about six passes through the core before being placed in spent fuel storage tanks. Maximum fuel temperature during normal operating conditions is 1080°C. The peak pebble burnup is approximately 95 MWd/t at an equilibrium enrichment of 9.6 wt% of ^{235}U. The maximum fast neutron fluence is 3.7×10^{25} n/m^2, E>16 fJ. Target specifications are summarized in Table 2.13.

The inner and outer reflectors of the annular core are composed of graphite blocks that provide the geometrical boundary of the core and reduce the temperatures that the metallic internals and RPV see. The outer reflector contains 24 control rod system units; the inner reflector houses the eight reserve shutdown system units where small borated graphite spheres are inserted inserted. These systems provide two independent means of achieving reactor shutdown to cold conditions defined as 100°C.

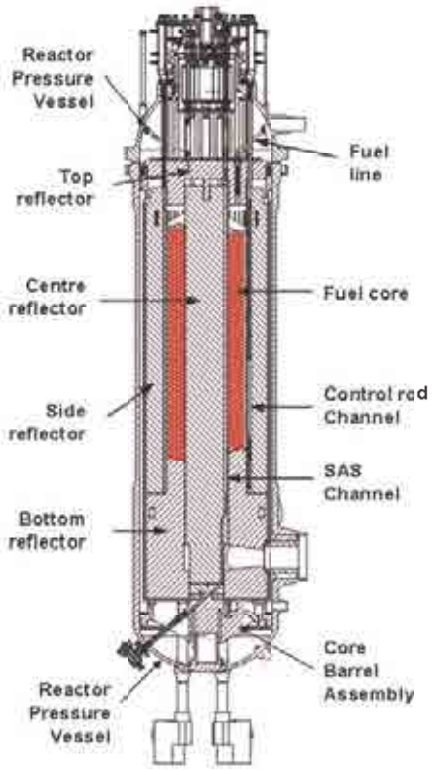

FIG. 2.20. Schematic of the 400 MW(th) PBMR annular core.

TABLE 2.13. CORE DESIGN PARAMETERS OF THE PBMR

Thermal power	400 MW(th)
Electric power output	160 MW(e)
Average/maximum thermal power density	4.8/~12 MW/m^3
Primary coolant	Helium
Reactor coolant inlet/outlet temperature	500/900°C
Core upper plenum inlet pressure	9.0 MPa
Coolant mass flow rate	192 kg/s
Bypass flow	~20%
Active core height/inner/outer diameter	11/2.0/3.7 m
Fuel reshuffling mode	Multiple pass
Number of passes through core	6
Average/maximum burnup	92/100 GW•d/t
Maximum fuel temperature normal op./accident	~1080/~1570°C
Power conversion efficiency	> 41%

2.7.4. PBMR fuel concept

The PBMR fuel concept is practically identical to the German reference fuel concept for the HTR-Modul. Specifications of the fuel are listed in Table 2.14.

TABLE 2.14. CHARACTERISTIC DATA OF THE FUEL ELEMENT FOR THE PBMR

Number of spherical fuel elements in core	452 000
Fuel	LEU UO_2
Amount of initial heavy metal in core	4104 kg
Uranium enrichment first core/equilibrium	4.4/9.6 wt%
Fuel element residence time in core	930 efpd
Kernel diameter	500 μm
Layer thicknesses Buffer/IPyC/SiC/OpyC	95/40/35/40 μm
Maximum power per particle (mW)	< 400
Fuel sphere material	A3-3 matrix
Fuel sphere diameter	60 mm
Thickness outer fuel-free zone	5 mm
Maximum power per sphere	~4.1 kW
Heavy metal loading per fuel sphere	9.0 g
Number of coated particles per sphere	14 440

2.7.5. Plant architecture

The turbo machinery for the PBMR (Fig. 2.21) has been optimized to strike a balance among efficiency, proveness/technological challenge, cost, and ease of performing maintenance. The selection of three separate shafts allows smaller, higher speed turbo machines with simpler rotor dynamics and balancing and also improves maintenance of the different components because there is easier access to each. The principal disadvantage is the higher helium coolant bypass flow, which reduces the overall plant efficiency slightly. Secondly, a more complex control system with multiple bypass paths must be used to compensate for fast transients and load follow operations.

The building for a single PBMR module consists of a reinforced concrete confinement structure, also called the citadel. It is a ‘vented containment with filtering’, which protects the nuclear components of the power conversion unit from external missiles and to retain the vast majority of fission products that might be released in the event of a reactor accident. Release of fission products during a postulated accident is very slow. Thus, it is desirable to vent the pressure from the confinement early in an accident to ensure the confinement’s integrity later in the accident when fission products might be present. Depending on the size of break in the reactor pressure boundary, the venting occurs through the heating, ventilation, and cooling system, through the confinement stack, or through blowout panels.

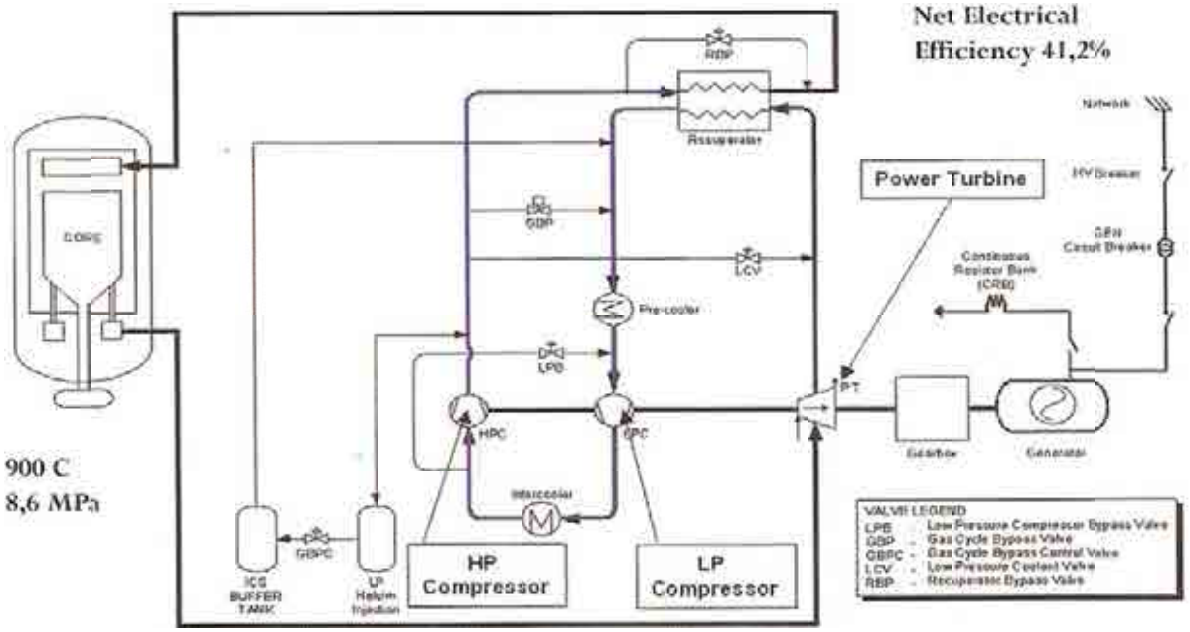

FIG. 2.21. PBMR power conversion cycle.

The fuel handling and storage system is a pneumatic system that uses helium to circulate the fuel pebbles as necessary for refueling or storage. It has been designed to operate for 12 hours per day at a maximum circulation rate of 600 fuel spheres per hour. It is rated at the full power conversion unit operating pressure of 9 MPa and a maximum operating temperature of 260°C. There are three separate defueling chutes and fueling lines that circulate fuel back to the top of the reactor.

TABLE 2.15. PLANT AND FUEL DESIGN PARAMETERS FOR CONCEPTS OF FUTURE VHTR

	ANTARES	GTHTR300	GT-MHR	HTR-PM	PBMR
Thermal power (MW(th))	600	600	600	2 × 250	400
Power density (MW(th)/m^3)	6.3	5.8	6.3	3.2	4.8
Electric power (MW(e))	~300	275	286	200	160
He inlet/outlet temp. (°C)	400/850	587/850	490/850	250/750	500/900
He pressure (MPa)	7.0	7.0	6.9	7.0	9.0
Burnup (GW•d/t)	150	120	121 (LEU)	90	92
No of fuel spheres assemblies	10 × 102	8 × 90	10 × 102	2 × 420 000	452 000
Fuel residence time (efpd)	850	1460	UCO: 834; PuO_2: 750	1057	
Fuel Element					
Fuel type and sphere/compact dimensions (mm)	Prismatic 12.5 dia; 50 length	Pin-in-block (a)	Prismatic 12.5 dia; 50 length	Spherical 60 dia	Spherical 60 dia
No of cp per sphere/compact	2500	13 000	Fissile: 4310; Fertile: 520	12 000	14 440
Packing fraction (vol.%)	16	29	20	7.5	
HM loading in sphere/comp. (g)	1.47	14.4	1.46	7.0	9.0
U-235 content in sphere/comp. (g)	0.21	1.99	0.22	0.595	0.86
Coated Particle					
Kernel composition	UO_2 or UCO	UO_2	Fiss. $UC_{0.5}O_{1.5}$ Fert. $U_{nat}C_{0.5}O_{1.5}$ PuO_2	UO_2	UO_2
Enrichment (^{235}U wt%)	14	14	Fissile: 19.9; Fertile: 0.7	8.5	9.6
Kernel diameter (μm)	500	550	UCO: 350; PuO_2: 200	500	500
Coating layer thicknesses (μm)					
Buffer	95	140	100/65	95	95
IPyC	40	25	35/35	40	40
SiC	35	40	35/35	35	35
OPyC	40	25	40/40	40	40

(a) annular compact: 26 mm outer diameter with 1 mm thick matrix graphite layer, 9 mm inner diameter, 83 mm length.

There are various filters, blowers, and valve blocks that ensure the system operates reliably and that the fuel pebbles are transferred to their proper destination depending on their condition (burnup and/or integrity). The spent fuel is stored in below grade tanks within the conventional module building. The storage capacity is 6 million spheres, which is selected to accommodate all spent fuel on site for the life of the plant.

2.8. CONCLUSIONS

All concepts provide electricity. For most concepts, modified versions for process heat applications are being developed. Table 2.15 provides a summary of the major plant and fuel design parameters of the different VHTR concepts.

3. FUEL PRODUCTION

3.1. KEY FUEL PROBLEMS AND POSSIBLE FABRICATION PROCESSES

Based on nearly five decades of HTGR fuel particle testing under a wide range of in-reactor operating conditions and accident simulations, followed by comprehensive fuel evaluations, a number of potential failure mechanisms have been identified. These mechanisms have been shown responsible for causing damage to, and under extreme conditions, the total failure of the TRISO coating system. Total failure of the TRISO coating results in the loss of volatile gaseous and metallic fission products. The list of potential failure mechanisms applicable under in-reactor or accident conditions, together with the known potential as-fabricated fuel kernel and coating defects is provided in Table 3.1 presenting a summary of the coated particle failure mechanisms with respect to the major in-reactor operating conditions, and key particle design and material property parameters that influence their behaviour [13].

3.2. FUEL PRODUCTION ACTIVITIES IN CHINA

In China, R&D activities for HTGR and its fuel element started from the middle of 1970s and were a part of China High Technology Programme from 1986 to 2000. R&D work of HTGR fuel element was carried out in laboratory scale before 1991. Since 1991, R&D activities have been focused on fabrication technology for the Chinese 10 MW high temperature gas cooled reactor (HTR-10) first-core fuel. The Institute of Nuclear Energy Technology (INET), Tsinghua University, has successfully developed own fabrication technologies of spherical fuel elements for HTR-10. A total of 20 541 fuel balls were fabricated in 2000 and 2001. The performance of the fabricated fuel elements meets the design requirements of HTR-10 fuel.

3.2.1. Design specification of the HTR-10 fuel element

The HTR-10 is a modular pebble bed type of high temperature gas cooled reactor. Spherical fuel elements are used in the pebble bed core. Geometry of fuel element used in HTR-10, as shown in Fig. 3.1, is same as spherical LEU TRISO fuel element of Germany [14].

TABLE 3.1. SUMMARY OF COATED PARTICLE FAILURE MECHANISMS AND KEY DESIGN MATERIAL PROPERTIES

Failure mechanism	In-reactor operating conditions	Particle design and material properties	Comments
Pressure-induced failure	Temperature Burnup Fast neutron fluence	Buffer density (void volume) SiC strength and modulus Fission gas release CO production Fuel kernel composition	UCO fuel eliminates CO
Irradiation-induced PyC failure	Fast neutron fluence Temperature	PyC thickness and density PyC anisotropy PyC dimensional changes PyC irradiation-induced creep	Proper PyC coating conditions
IPyC–SiC interface debonding	Temperature Fast neutron fluence	Nature of interface Interfacial strength PyC dimensional changes PyC irradiation-induced creep	Proper PyC coating conditions
Kernel migration	Temperature Temperature gradient Burnup	Kernel composition CO/CO_2 production PyC, SiC thickness Kernel migration coefficient	UCO fuel eliminates CO
SiC corrosion — CO corrosion	Temperature and time-at-temperature Burnup Fast neutron fluence	Kernel composition IPyC anisotropy IPyC dimensional changes CO production	UCO fuel eliminates CO Proper PyC coating conditions
SiC corrosion — fission product attack (noble metals, rare earths, Cs)	Temperature and time-at-temperature Burnup Temperature gradient	Diffusion coefficient Fission product transport behaviour SiC micro-structure Kernel composition	Concern at high burnups with LEU Pd concern in accident conditions
SiC decomposition	Temperature and time-at-temperature	SiC micro-structure and thickness	Negligible
Non-retentive SiC	Temperature and time-at-temperature Burnup	Kernel composition and enrichment Fission product transport behaviour SiC micro-structure	Concern at high burnups with LEU

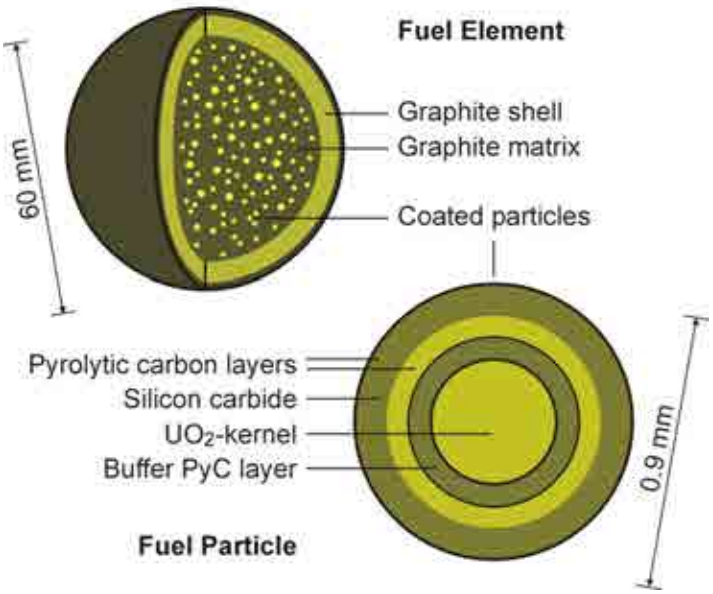

FIG. 3.1. Spherical fuel element with UO_2 TRISO coated particles.

The LEU TRISO coated fuel particle for HTR-10 is composed of a low enriched UO_2 kernel and four layers of (1) a low density porous PyC buffer layer, (2) an inner high density isotropic PyC lager, (3) a SiC layer, and (4) an outer high density isotropic PyC layer. The dimension and function of this TRISO coated fuel particles are listed in Table 3.2.

TABLE 3.2. DIMENSIONS AND FUNCTIONS OF A TRISO COATED FUEL PARTICLE

Component	Dimension (μm)	Main Function
UO_2 kernel	500	1. cause nuclear fission 2. retain fission products 3. be deposition substrate of the buffer PyC
Buffer PyC layer	95	1. provide free volume for gaseous fission products 2. absorb swelling of the fuel kernel due to fission 3. protect the inner dense PyC coating from the damage due to the fission fragment recoil
Inner dense isotropic PyC layer	40	1. protect SiC layer from detrimental reactions with fuel and rare earth fission products 2. prevent reaction between UO_2 and chlorine-containing materials released during SiC deposition 3. take up part of the pressure of CO, CO_2 and gaseous fission products
SiC layer	35	1. play role as pressure vessel for CO, CO_2 and gaseous fission products 2. be barrier against gaseous and solid fission product release
Outer dense isotropic PyC layer	40	1. protect SiC layer from mechanical damage during fuel manufacture 2. be additional barrier against fission gases in case of a failure of the SiC layer

TABLE 3.3. MAIN SPECIFICATIONS FOR THE HTR-10 FUEL

UO_2 Kernel	
Diameter	$(450 \leq x \leq 550)_{95/95}$ μm
Density	$\bar{x} \geq 10.4$ Mg/m^3
Sphericity (D_{max}/D_{min}) [a]	$(x \leq 1.2)_{95/95}$
O/U ratio	$x \leq 2.01$
Equivalent B content	$\bar{x} \leq 4$ μg/g
Coated fuel particle	
Buffer layer thickness	$(50 \leq x \leq 140)_{95/95}$ μm
IPyC layer thickness	$(20 \leq x \leq 60)_{95/95}$ μm
SiC layer thickness	$(25 \leq x \leq 45)_{95/95}$ μm
OPyC layer thickness	$(20 \leq x \leq 60)_{95/95}$ μm
Buffer PyC layer density	$\bar{x} \leq 1.10$ Mg/m^3
IPyC layer density	$1.80 \leq \bar{x} \leq 2.00$ Mg/m^3
SiC layer density	$\bar{x} \geq 3.18$ Mg/m^3
OPyC layer density	$1.80 \leq \bar{x} \leq 2.00$ Mg/m^3
Anisotropy factor of IPyC and OPyC layers	$\bar{x} \leq 1.03$ (OPTAF)[b]
Graphite Matrix Sphere	
Density	$\bar{x} > 1.70$ Mg/m^3
Total ash	$\bar{x} \leq 300$ μg/g
Li content	$\bar{x} \leq 0.3$ μg/g
B equivalent	$\bar{x} \leq 3.0$ μg/g
Thermal conductivity, @ 1000°C	$\bar{x} \geq 25$ W/(m·K)
Anisotropy (coefficient of thermal expansion), $\alpha^{\perp}/\alpha^{\parallel}$ [c]	$\bar{x} \leq 1.3$
Corrosion rate @ 1000°C, He+1vol.% H_2O	$\bar{x} \leq 1.3$ mg/(cm·h)
Erosion rate	$\bar{x} \leq 6.0$ mg/h per sphere
Number of drops (4 m in height)	$x \geq 50$
Breaking force	$x \geq 18.0$ kN
Fuel sphere	
Thickness of fuel-free shell	$x > 4$ mm
U loading	$4.75 \leq x \leq 5.25$ g/ball
U contamination (U_{cont}/U_{total}) [d]	$x \leq 2.5 \times 10^{-5}$
Free U fraction (U_{free}/U_{total}) [e]	$x \leq 3 \times 10^{-4}$
Average discharge burnup	80 000 MWd/(t U)

[a] D_{max} and D_{min} are maximum and minimum diameters of a kernel, respectively;

[b] OPTAF is the Optical Anisotropy Factor;

[c] $\alpha^{\perp}$ and $\alpha^{\parallel}$ are thermal expansion coefficients of the matrix graphite in perpendicular parallel to the equatorial plane of the matrix sphere, respectively;

[d] U_{cont}/U_{total} is the ratio of uranium in the matrix graphite and outer dense PyC layer to the complete U content.

[e] U_{free}/U_{total} is the ratio of measured uranium to the complete U content of the measured sample in the burn-leach test.

x denotes a single value and, and $\bar{x}$ denotes a mean value;

$(\ )_{95/95}$ denotes that with 95% confidence, 95% of measured values shall lie within the range specified in brackets.

This spherical fuel element consists of a spherical fissile material zone, in which the fissile material in the form of low enriched UO_2 TRISO coated fuel particles is embedded in a matrix of graphite material, and a shell of fuel-free pure matrix graphite, surrounding the spherical fissile material zone. The diameter of the fuel zone is approximately 50 mm. The thickness of the shell is about 5 mm. This fuel element is 60 mm in diameter. The matrix graphite serves as a neutron moderator as well as a heat conductor from the fuel to the coolant gas. The specification of HTR-10 fuel element is based on that of HTR-Modul designed by

Siemens/Interatom of Germany [15] and operational requirements of HTR-10. The design specification of HTR-10 fuel element [16] is given in Table 3.3.

3.2.2. Fabrication process of the HTR-10 fuel elements

The fabrication process for the HTR-10 spherical fuel element has been developed through intensive R& D activities in the past 20 years in INET [17]. The testing results showed that the performance of the spherical fuel element manufactured by this process could be qualified for the specification of the HTR-10. The fabrication process including UO_2 kernel preparation, PyC and SiC coating on the UO_2 kernels and spherical fuel element manufacture, as shown in Fig. 3.2, is described below.

3.2.2.1. UO_2 kernel fabrication process

The well known gel precipitation process was used to produce the UO_2 kernels for AVR and THTR-300 by NUKEM of Germany [14] and for the high temperature engineering test reactor (HTTR) at the Nuclear Fuel Industries Ltd of Japan [18]. This process is also adopted to fabricate the UO_2 kernels for the HTR-10, but some modifications were incorporated, i.e. a small amount of urea and hexamethylene tetramine for internal gelation process [19] was added to a solution containing uranyl atmosphere. Finally, UO_2 particles are sintered at 1550°C in H-nitrate and additives, a preparation method which is labeled as the total gelation process of uranium [20].

In this process, the first step is to mix up an acid-deficient uranyl nitrate solution and urea for sol preparation, and then the solution mixed by the tetrahydrogen furfuralcohol-polyvinyl alcohol is added, and finally the sol is prepared by adding hexamethylene tetramine just before dropping. By means of pressurized air, the prepared sol is transported through a piping system to a vibrating nozzle with pre-set frequency. Spherical droplets are emitted from the vibrating nozzle and fall into an ammonia solution to form gel particles. After washing and drying, the gel particles are calcined to UO_3 particles at 500°C in air. The UO_3 particles are then reduced to UO_2 particles at 900°C in H_2 atmosphere. The density of UO_2 kernel reaches about 98% of its theoretical density after sintering. Over- and under-sized particles are separated by using a vibrator sieve. The sorting of fractured and non-spherical particles is performed through a slightly inclined vibrating plate.

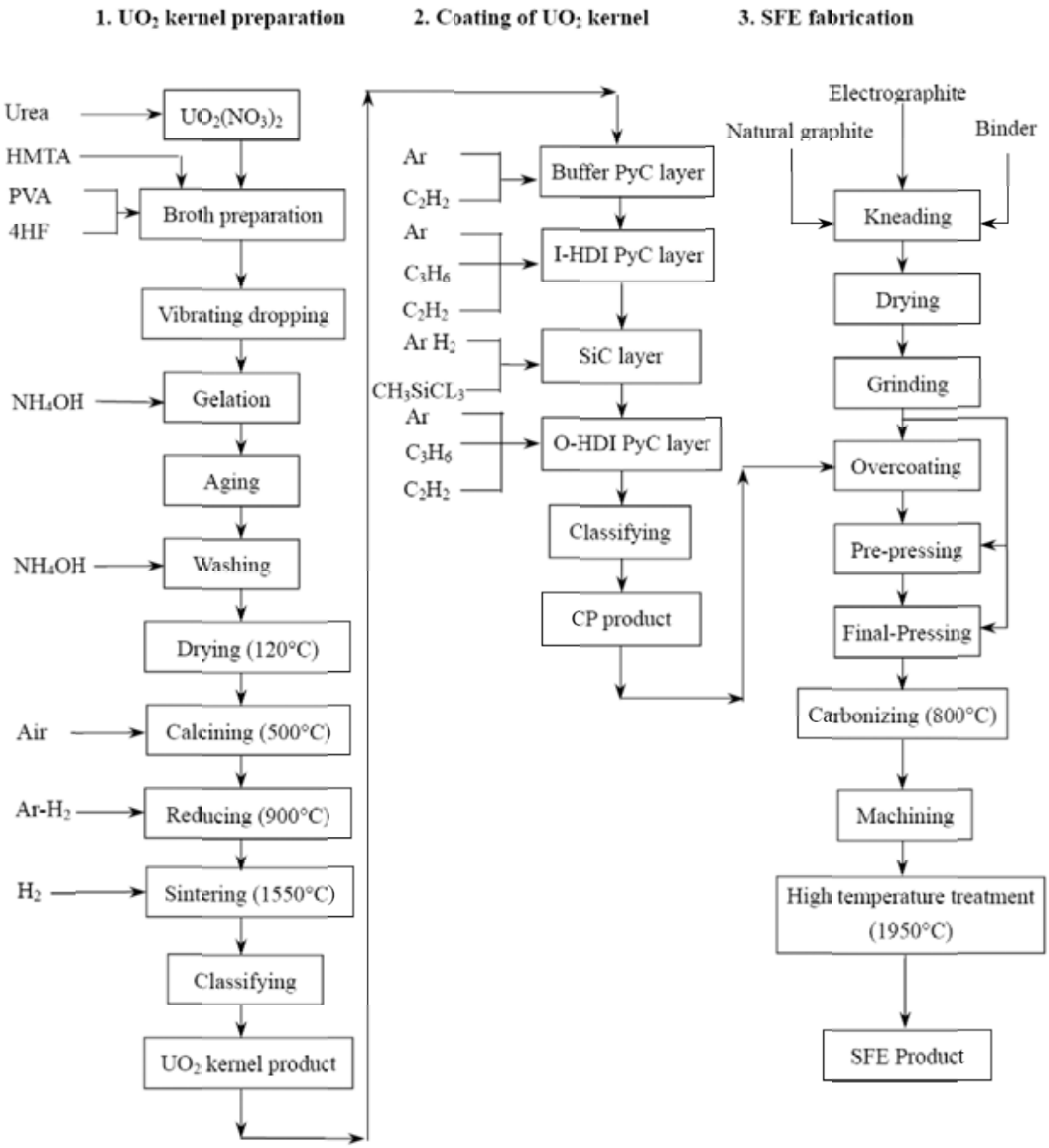

FIG. 3.2. Fabrication flow sheet of HTR-10 first loading fuel.

3.2.2.2. PyC and SiC coating process

The CVD process used in coating process of HTR-10 fuel particles is similar to that applied by all countries engaged in the HTGR [21–24]. The PyC and SiC coatings of the particles are deposited on the UO_2 kernels in a fluidized bed coater by the pyrolytic decomposition of hydrocarbon and methyltrichlorosilane at temperature between 1250°C and 1700°C. In the production of HTR-10 fuel, 3 kg of UO_2 kernels per batch were put into the graphite reaction tube from the top of the coater, reactant and carrier gases were blown from the bottom of the coater. Adjustment of the depositing temperature, reactant concentration, flow rate of the pyrolysis and the carrier gas, and depositing time can be made if required to achieve the specified coating parameters and properties. The buffer layer with porous and low density PyC is deposited from acetylene. The second and fourth high density isotropic PyC layers are

derived from a mixture of acetylene and propylene. The third layer, SiC, is deposited by the decomposition of mithyltrichlorosilane using hydrogen as the fluidizing gas.

3.2.2.3. Manufacture process of the spherical fuel elements

The coated fuel particles are dispersed in the graphite matrix of the fuel zone inside the spherical fuel element. The components of the graphite matrix is the same as the German A3-3 graphite matrix [25], which consists of 64% natural flake graphite, 16% electrographite and 20% phenolic resin binder. The natural flake graphite from Beishu Graphite Mine (Shandong province, China) is purified by means of immersion of HF, HCI and H_2SO_4. The content of ash is ~100 μg/g, that of lithium < 0.005 μg/g, and the boron is < 1 μg/g.

TABLE 3.4. STATISTICAL PERFORMANCE DATA OF SPHERICAL FUEL ELEMENT PRODUCTION OF HTR-10 FIRST-LOADING FUEL

Performance Item	Mean value of lots	Standard deviation of mean value of lots
Graphite Matrix		
Density (Mg/m^3)	1.75	0.01
Total ash (μg/g)	75.6	23.6
Li content (μg/g)	0.0014	0.0022
B equivalent (EBC) [a] (μg/g)	0.902	0.53
Thermal conductivity, @ 1000°C (W/(m·K)) ⊥ ‖	29.3 28.5	1.9 1.7
Corrosion rate @ 1000°C, He+1vol.% H_2O ($mg/(cm^2 \cdot h)$)	0.92	0.18
Erosion rate (mg/h per sphere)	2.6	0.5
Number of drops (4 m in height)	> 100	—
Breaking force (kN) ⊥ ‖	23.4 25.0	1.1 1.4
CTE [b] anisotropy, $\alpha_\perp/\alpha_\parallel$	1.07	0.04
Spherical Fuel Element		
Diameter (mm)	59.6–60.2	—
Thickness of fuel-free shell (mm)	4.0– 6.0	—
Uranium loading (g U/sphere)	5.008	0.041
Uranium contamination of matrix graphite (U_{cont}/U_{total})	6.1×10^{-7}	7.0×10^{-7}
Free uranium fraction (U_{free}/U_{total})	4.6×10^{-5}	6.3×10^{-5}

[a] EBC = Equivalent boron content
[b] CTE = Coefficients of thermal expansion
— data not available

⊥ and || denote perpendicular to and parallel to the equatorial plane of the matrix sphere, respectively.

In the first step of the fabrication procedure for the spherical fuel element, graphitic raw material is processed to resinated powder by means of mixing, kneading, drying and grinding. In the second step, a portion of the resinated powder is used to overcoat coated fuel particles in an overcoating drum. The overcoating layer is about 200 μm in thickness. In the third step, these overcoated particles mixed with the resinated graphite powder are premolded to a 50 mm diameter spherical fuel zone under about 50 MPa pressure. The fuel zone is covered with resinated graphite powder to form an integral spherical fuel element under about 300 MPa pressure in a press line. The press line consists basically of two units, i.e. the pre-

pressure and the high pressure press. The silicon rubber stamps are used in a pressure press in order to maintain an isostatic pressure distribution on the graphite matrix. In the final step, the spherical fuel elements are heated in Argon atmosphere in a coking oven for carbonization of the binder in the resinated powder, and in vacuum at 1950°C to remove out some impurities from the fuel balls.

Table 3.4 shows the inspection results of the spherical fuel element and graphite matrix balls for the first loading of the HTR-10. Compared with the German fuel, many results are similar, but some properties of the HTR-10 fuel, especial the free uranium, need to be further improved.

3.3. FUEL PRODUCTION ACTIVITIES IN FRANCE

3.3.1. Introduction

The Commissariat à l'Energie Atomique (CEA) is a partner of the Generation IV Forum for the development of the very high temperature reactor (V/HTR) system dedicated to massive production of hydrogen and co-generation of electricity. The long term objective of the French V/HTR fuel development programme [26] is to optimize the coated particle design for conditions of high burnup and very high reactor temperature. In this context, CEA, supported by AREVA NP, conducts R&D projects on HTGR fuel. The first step is the mastering of UO_2 coated fuel particle and fuel element fabrication technology.

A review of existing technologies and first laboratory scale experiments have been performed aiming at the recovering of the know-how for HTGR coated particle and fuel element manufacture. The different stages of UO_2 kernel fabrication GSP process have been reviewed, understood and improved. The experimental conditions of the chemical vapour deposition of coatings have been defined on surrogate kernels and a modeling approach to CVD process is now beginning. The study of coated particle quality control methods including innovative characterization methods has been carried out. Former compacting processes used at CERCA have been reviewed and actualized.

In parallel, an experimental manufacturing line, named CAPRI (CEA AREVA PRoduction Integrated) line, is running. The CAPRI line is made up of two parts: the GAIA line at CEA (Cadarache, France) devoted to the production of TRISO particles and the compacting line at CERCA (France, Romans) dedicated to the fabrication of fuel elements. The GAIA line, based on UO_2 and SiC, is versatile in order to explore UCO fuel manufacture and ZrC coating.

The major objectives of the CAPRI experimental manufacturing line are [26, 27]:

- to produce HTGR TRISO fuel particles representative of future industrial fuels and to determine the key parameters for the construction of a modern fabrication plant;
- to permit the optimization of reference fabrication processes for kernels and coatings defined previously and the investigation of alternative (UCO kernel) and innovative fuel sealing layers (ZrC coating);
- to fabricate and to characterize first batches of coated particles and fuel elements (compacts) for irradiation tests (SIROCCO experiments). Data from following post-irradiation examination will feed into the modeling codes.

3.3.2. Current and planned fabrication activities

3.3.2.1. Preliminary fuel specification

The preliminary fuel specifications for coated fuel particles and fuel compacts have been issued by AREVA NP to prepare the SIROCCO irradiation programme in the OSIRIS Reactor at Saclay [26, 28]. These preliminary fuel specifications based on former HTGR achievements [1], given in Table 3.5, are guidelines for the current laboratory scale R&D work [28–31]. Further irradiations supported by fuel modelling will permit to precise and define the final fuel specifications, including alternative fuel design such as UCO kernels or more refractory fission product retention barrier such as a ZrC layer.

TABLE 3.5. PRELIMINARY SPECIFICATIONS OF FUEL FOR THE SIROCCO EXPERIMENT

UO_2 Kernel and coated fuel particle	
Diameter	500 ± 40 μm
Density	≥ 10.4 Mg/m^3
Sphericity (D_{max}/D_{min})	< 1.1
O/U ratio	1.99 ≤ x ≤ 2.02
Buffer layer thickness	95 ± 20 μm
IPyC layer thickness	40 ± 10 μm
SiC layer thickness	35 ± 7 μm
OPyC layer thickness	40 ± 10 μm
Buffer layer density	≤ 1.05 Mg/m^3
IPyC layer density	1.85 ≤ x ≤ 2 Mg/m^3
SiC layer density	≥ 3.18 Mg/m^3
OPyC layer density	1.85 ≤ x ≤ 2 Mg/m^3
Anisotropy factor of IPyC and OPyC layers (BAF)	≤ 1.06
Heavy metal contamination (U_{cont}/U_{total})	≤ 10^{-7}
Defective coating (U_{free}/U_{total})	≤ 5×10^{-6}
Fuel compact	
Diameter	12.6 μm
Length	50 mm
Matrix density	> 1.5 Mg/m^3
Packing fraction	10–15 vol.%

The reference coated particle fuel design consists of a UO_2 kernel, surrounded by a low density pyrocarbon layer, a high density and isotropic inner pyrocarbon layer, a dense SiC and a high density and isotropic. Each layer has to fulfill particular functions [1].

The basic fuel-containing unit for the prismatic core system is the fuel compact, which consists of coated particles bonded in a close-packed array by a carbonaceous matrix. Those compacts are stacked in the fuel holes of the prismatic fuel blocks. A schematic description of coated particles and their embedding in a graphite fuel compact is given in Fig. 3.3.

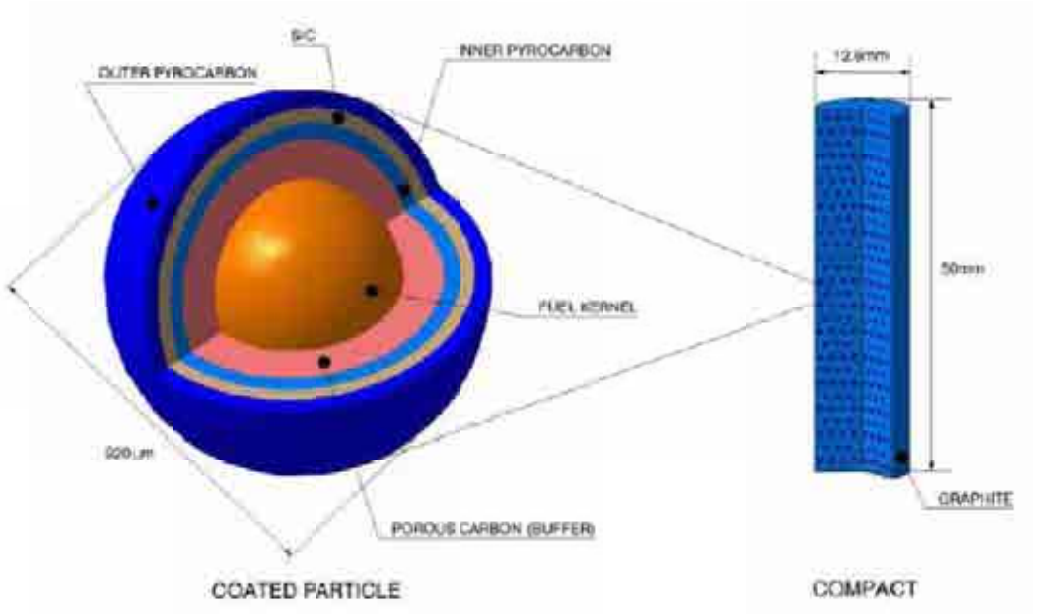

FIG. 3.3. Schematic of fuel coated particles and their embedding in graphite fuel compact (HTGR prismatic core system).

3.3.2.2. UO_2 kernel manufacture

During the early years of HTGR fuel development, different processes for kernel manufacture have been investigated such as the powder agglomeration route used in the DRAGON project [32] or a process based on fusion under vacuum for uranium carbide kernel preparation [33], but rapidly, wet chemical processes studied in Europe and in USA were preferred with two main sol-gel methods coming to the fore [34]:

- the external gelation known as Gel Supported Precipitation (GSP);
- the internal gelation also called the HMTA (HexaMethyleneTetraAmine) process.

Both are based on the precipitation of uranyl nitrate by ammonia into ammonium diuranate. The fundamental difference between GSP and HMTA processes lies in the source of ammonia. In the GSP process, the ammonia is available from an external ammonium hydroxide solution, into which the sol (dispersed as droplets) fall. Whereas, in the internal gelation process, an ammonia precursor added in the solution decomposes thermally to release ammonia internally within the droplet of the sol.

The German experience [14, 35] acquired in the 1980–1990s, has demonstrated high quality manufacturing of UO_2 kernels using the GSP process at an industrial scale with the production of about 400 kg of UO_2 kernels for AVR reloads [35]. The HMTA process has only been studied at a laboratory scale and has as a major handicap the large quantities of organic waste to be retreated. For these reasons, the GSP process has been chosen. It has also been adopted by the Japanese [18] and the Chinese [17] to fabricate UO_2 kernels for the HTTR and the HTR-10, respectively.

The external gelation process is based on the preparation of an uranium feed solution of uranyl nitrate solution in which an organic polymer such as a polyvinyl alcohol (PVA) and a modifier agent such as tetrahydrofurfuryl alcohol (THFA) have been added. This feed solution is then dispersed into droplets through a vibrating nozzle. The spherical droplets are

formed in air from the effect of surface tension, before passing through an ammonia gas layer, hardening the bead surface into the final shape. The droplets are then collected in an aqueous concentrated ammonium hydroxide bath where ammonia induces the precipitation of the uranyl nitrate in ammonium diuranate (ADU). The gelled droplets are aged for a suitable length of time to assure completion of the reaction. The excess ammonium nitrate produced during ADU precipitation is removed from the gelled droplets by washing in water or in a diluted ammonium hydroxide solution. A second washing stage is realized using isopropanol to dehydrate the wet gel beads. After drying, the beads are calcined at 400–600°C in air, then reduced and sintered into UO_2 kernels in $Ar–H_2$ atmosphere at 1600–1700°C.

Investigations led on each stage of the GSP process described above have been performed at CEA, Cadarache using two laboratory scale devices, both equipped with a vibrating nozzle, in vertical and horizontal positions.

Experimental parameters in the broth preparation such as the type of polymer, the concentration of uranium, the polymer/THFA ratio, the influence of acid-deficient uranyl nitrate, the viscosity of the feed solution have been extensively studied. The U based droplet formation has been optimized using a stroboscopic lamp, charge-coupled device (CCD) camera and image analysis software. At the same time, the appropriate conditions of the gelation and ageing stages principally regulated by the temperature and ammonium hydroxide concentration have been determined. The influence of the thermal treatment atmosphere on the micro-structure and the composition of the U based sintered kernels have also been investigated in order to obtain as-specified dense, spherical UO_2 kernels [36].

Preliminary small batches of UO_2 kernels have been successfully manufactured with characteristics (density, sphericity and diameter) fulfilling the guidelines (Fig. 3.4). Presently this R&D work is being transposed to the future GAIA experimental facility.

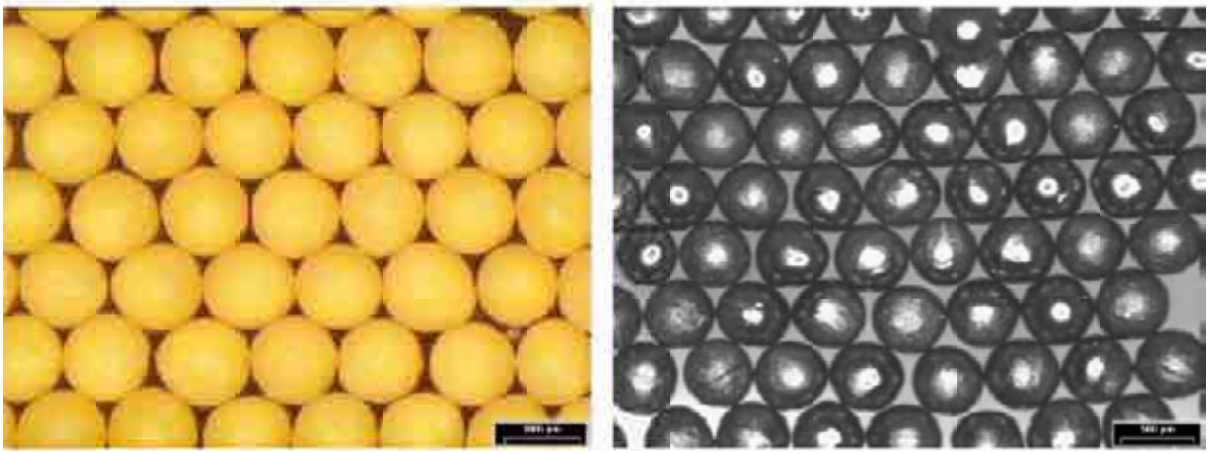

FIG. 3.4. U based kernels produced at CEA Cadarache after drying step (left) and after sintering (right).

3.3.2.3. Coating particle manufacture

(a) Reference HTGR SiC-TRISO coated particle experiments

The SiC and PyC coatings are applied using the Chemical Vapor Deposition (CVD) method which is the same as all countries involved in HTGR programme [14, 17, 18, 37]. The fuel kernels are coated in a fluidized bed using a vertical high temperature furnace. Pyrocarbon

layers are obtained by the cracking of hydrocarbon gases and silicon carbide is deposited by the decomposition of methyltrichlorosilane (MTS) in hydrogen, the fluidisation of the kernels is ensured by argon flow.

Initial experimental trials have been performed at CEA, Grenoble. The primary short term task was to reproduce the reference coated fuel particle as given in Table 3.5. Stabilized zirconia and hafnia have been used as surrogate kernels for the exploration of coating parameters in a laboratory scale coater with 3 inch (76.2 mm) and 2 inch (50.8 mm) inner diameter crucibles. An optical micro-graph of TRISO SiC coated particles fulfilling the guidelines with optimized parameters is shown in Fig. 3.5.

Pyrocarbon coating tests have been performed and adjusted by varying the temperature reaction (1300–1400°C) measured by a pyrometer and the active gas fraction (C_2H_2 or C_3H_6). The low density PyC buffer layer is obtained by decomposition of acetylene (C_2H_2). The density of this layer depends on the gas fraction principally and to a lesser degree on the temperature of deposition. For the high density isotropic layers of IPyC and OPyC, the temperature is the controlling coating parameter. IPyC and OPyC are obtained at lower deposition rate compared to the buffer and the efficiency is varying between 50 to 70%. The use of a gas mixture (C_2H_2/C_3H_6)) is preferable and allows to maintain a constant reaction temperature.

The silicon carbide coating is made at about 1600°C by decomposition of MTS which is carried in an H_2 flow. The MTS flow is controlled by flowing H_2 at fixed pressure and temperature.

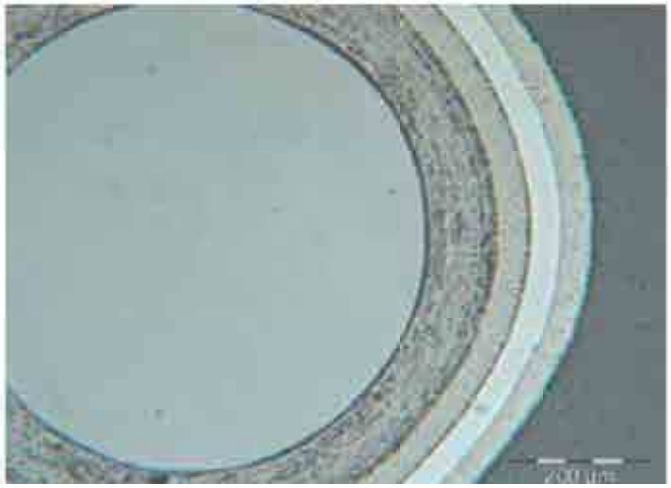

FIG. 3.5. Cross-section of TRISO SiC coated particle produced at CEA Grenoble with ZrO_2 kernel.

The coating parameters tested for the SiC deposition were the temperature, the total flow of reactant and product gases. The deposition temperatures studied were ranged from 1500°C to 1600°C, with different H_2/MTS ratio. The values of deposition efficiency are high and close to thermodynamic predictions near 1600°C. The SiC density measured by a sink-float method was close to the theoretical one (3.2 Mg/m^3). A smooth surface and metallic aspect with a conversion efficiency of 93% were observed for depositions performed at 1600°C. Particles with dull aspect were obtained at 1500–1550°C (Fig. 3.6). Complementary X ray diffraction analysis has showed that the coating temperature should be chosen between 1550–1600°C to prevent hexagonal SiC formation.

FIG. 3.6. Silicon carbide coated particles manufactured at CEA Grenoble at 1550°C (left) and 1600°C (right).

(b) ZrC-TRISO coated particle experiments

In the VHTR concept, ZrC is a candidate to replace SiC because of its physical properties. Zirconium carbide has a melting point at 3540°C and melts eutectically with carbon at 2850°C, whereas SiC begins to decompose above 2000°C [38]. Irradiations of ZrC coated particles studied under normal or accidental conditions have shown good results [38–40]. Zirconium carbide shows higher resistance to chemical attack by the fission product palladium than SiC, a good retention capability of caesium (and less for ruthenium). The method chosen for ZrC deposit is the chloride route, Zr powder is attacked with HCl gas diluted in Ar to form $ZrCl_4$. Hydrocarbons gases such as C_3H_6 or methane (CH_4) are used to provide the carbon [41]. An H_2 atmosphere is used to avoid formation of free chlorine.

Previous study [42] has shown that an increase in the ratio of the hydrocarbon gas to the $ZrCl_4$ in the coating gas results in a co-deposition of carbon (i.e. an increase if the C/Zr ratio in the deposit). In that case, increasing the H_2 concentration inhibits this effect and allows the ZrC to be deposited at higher hydrocarbon gas concentrations which is effective in increasing the coating rate of ZrC.

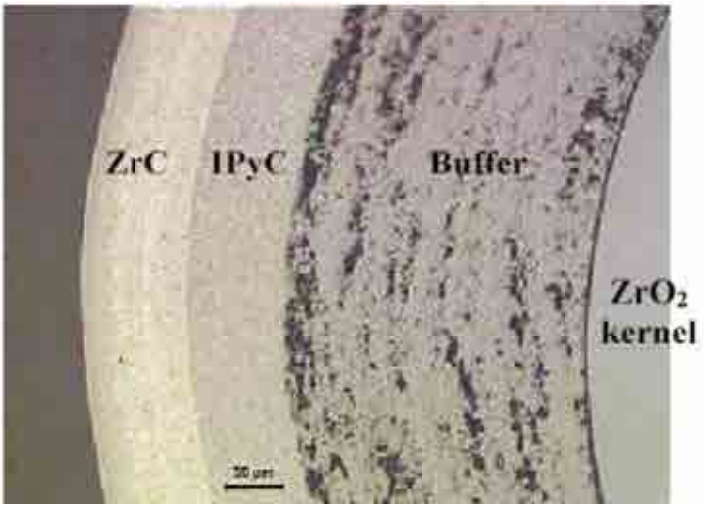

FIG. 3.7. Cross-section of ZrC coated particle produced at CEA Grenoble.

Preliminary ZrC coating trials of about 35 µm thick (Fig. 3.7) have been performed. But during the deposit process, the $C_3H_6/ZrCl_4$ ratio varied due to an uncontrolled increase of temperature in the chlorinator vessel (the chlorination is a very exothermic reaction) and thus it was impossible to master the experimental coating conditions yet. Modifications on the chlorinator vessel are in progress to suppress these technical problems and to focus on the optimization of the ZrC deposit parameters.

(c) Modeling approach

In support to the coating experimental tests, it is essential to develop and experimentally validate computational models for the fuel particle coating process. Models will be designed to account for individual and coupled effects of heat transfer, mass transfer and chemical kinetics on coating formation in order to enhance the understanding of global and detailed aspects of the CVD coating. The approach is based on existing computational models developed for fluidized bed reactors. The long term objective is to define tools able to adapt coating conditions to furnaces of different size (scale up). Associated efforts of coating characterization will permit the improved understanding of the process-product-performance relationships.

3.3.2.4. Coated particle fuel characterization

In the context of re-establishment of a French capability to manufacture high quality HTGR particles, development of accurate characterization equipments is indispensable to ensure, at least, that product specifications are well met, but also to provide pertinent data for fuel performance and fission products models and codes. Well known characterization methods are applied such as thermogravimetric analysis for the determination of the O/U ratio, the He pycnometry or Hg porosimetry for the density measurement of UO_2 kernels. In order to control fuel particle features such as UO_2 kernel diameter and sphericity or coating properties (layer thickness, density, degree of anisotropy of IPyC and OPyC), which are key basic product parameters for HTGR fuel manufacturing, specific characterization tools have been developed at CEA. The outer diameter and sphericity of fuel kernels and coated particles (after each deposit or complete coating) are measured using an optical particle automatic image analysis running with a software dedicated to this task [43]. The thickness of each coating layer can also be determined using this method.

Nevertheless, another specific method based also on image analysis (but in this case, cross-sections of polished coated particles are required) is being developed using a computer controlled platform allowing an efficient sampling with minor effort. The density of each coating layer is determined either by sink-float method on isolated layer or by differential calculations.

Particular attention has also been paid to the anisotropy measurement of the dense OPyC and IPyC layers. The pyrolitic carbon of these two layers must be dense and as isotropic as possible to sustain the high speed neutron irradiation and to avoid shrinkage or creep cracks under neutron irradiation. The anisotropy factor is performed by measuring the change of polarized light reflected from a polished cross-section of dense PyC. Innovative characterization methods such as the weak irradiation and the 3D tomography using synchrotron X ray source are being investigated to measure defective SiC fractions and coating layer density, respectively.

In addition, characterizations of the coating layer micro-structure and chemical composition are carried out by SEM (scanning electron microscopy), TEM (transmission electron

microscopy), XRD (X ray diffraction), EPMA (electron probe micro analysis), SIMS (secondary ion mass spectrometry) and ESCA (electron spectroscopy for chemical analysis) in order to study and to enhance the understanding of relations between coating conditions and properties of the coating layers [44].

3.3.2.5. R&D for compacting programme

The last stage of HTGR fuel fabrication is the manufacturing of the fuel element, consisting of dispersed coated fuel particles in a graphite matrix. The compacting process requires putting pressure on coated particles. This step is thus generally considered as the primary source of particles defects. Special R&D is being made to suppress this. AREVA NP has decided to build a lab scale compacting line for this purpose at CERCA. The aim of this line is to recover past knowledge, to test alternative process options, and to fabricate fuel compacts for the SIROCCO irradiation tests programme in the OSIRIS Reactor, Saclay.

In the 1960's and 1970's, numerous developments have been performed on various compacting processes. Data are available on different techniques such as graphite granulation, overcoating, tar injection, use of recycled graphite. New preparation equipment for matrix material, as well as compacting machine and heat treatment furnace have been designed, according to past experience, with expertise of former HTGR fuel specialists, but using up-to-date components such as electronically controlled stepping motors, high accuracy detectors or measuring devices, computer controlled process supervision. The lab scale line will be installed in a renewed building, designed according to the latest safety and security regulations. Start-up of this line will begin with first tests on surrogate kernels (stabilized ZrO_2 or HfO_2), then fuel compacts will be manufactured with GAIA fuel particles (depleted, enriched uranium) for irradiation purposes.

Three categories of compacting processes can be defined: the overcoating process used, for instance, in the former NUKEM process, the injection process used by GA, and the so called 'CERCA process'. The CERCA process differs from the overcoating process in that the loose coated particles are mixed directly with pre-agglomerated graphite, similar to the shim used in GA process. The main advantage, apart from simplicity, is the very good accuracy in coated particle weighing, and therefore in the quantity of uranium in the fuel compacts. This process was used with great success in the past for the manufacturing of 85 000 fuel compacts for the MARIUS critical experiment at CEA, Cadarache. Great care must be taken with the reliability and reproducibility of the process, and modern experimental methods will be used to cover a very wide variety of parameters, such as volume fraction, matrix density, compacting pressure, heat treatment temperature and duration, quality of graphite powder and resin binder. Work will be focused on the 'CERCA process', which was once considered as the most efficient, but overcoating will also be investigated, although not considered for the moment as the reference process. Overcoating was used extensively for DRAGON fuel (SPITFIRE experiment irradiated in the OSIRIS reactor), and for use with recycled graphite.

The French CERCA compacting process mainly consists of the following steps: manufacturing of the graphite matrix granulates, mixing coated particles with the obtained granulates, pressing and heat treatment. A diagram of fuel compacts manufacturing process is shown in Fig. 3.8. A resinated graphite powder is first prepared by mixing graphite powder and phenolic resin. The mixture is then fed into a rotating drum by a vibrating bowl and alcohol is sprayed directly on the powder, giving small agglomerates of resinated graphite. These granulates are then dried to remove the alcohol and sieved. In order to get a high uniformity of particle distribution, a specific CERCA device has been developed. It essentially consists of two holders, in which granulates and particles are placed. The latter are

then pushed into the dye in order to reach the required packing fraction, before being warm pressed to form green compacts. They are finally sintered in a graphite furnace. Heat treatment temperatures are directly linked with dimensional changes of compacts; final physical properties, structure and density of the graphite matrix. Heat treatment is performed under different atmospheres. First a polymerization of the resin occurs at 200°C, followed by degassing of the volatile organic products coming from the resin in flowing N_2 at 800°C. The final step is heat treatment up to 1800°C in vacuum to insure hardening of the matrix.

Quality control of fuel compacts will include dimension measurement, such as diameter, length, weight, as well as physical characteristics, such as heavy metal contamination or fuel particle failure determination. Characterization methods, such as burn leach test or fuel compact disintegration are under development at CEA and AREVA NP and will be used extensively during this phase of compact fabrication development.

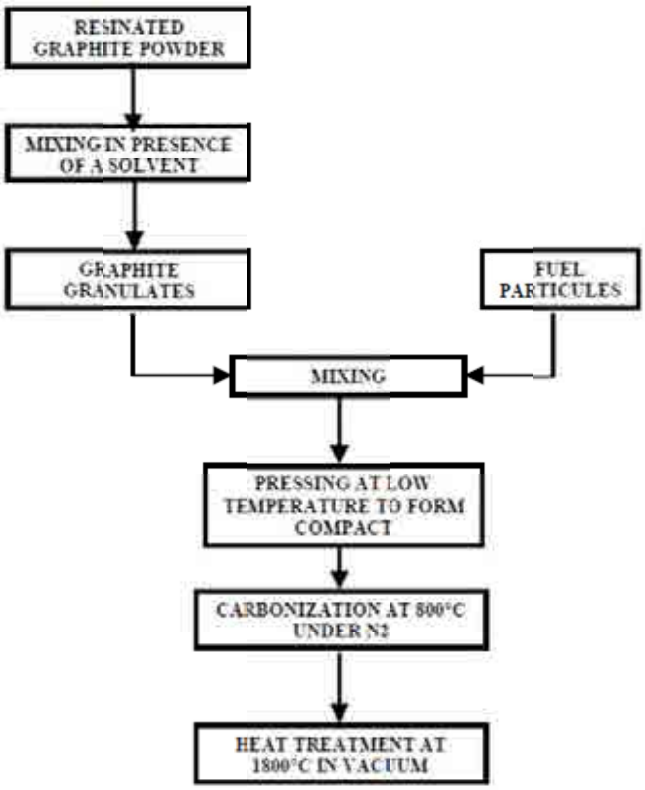

FIG. 3.8. Diagram of the CERCA compacting process.

3.3.2.6. GAIA laboratory VHTR fuel fabrication line

An experimental manufacturing facility, named GAIA, is under operation at CEA Cadarache. The design of GAIA has been focused on the handling of batches large enough to be representative for experimental R&D studies. Batches of 50 to 500 gU of UO_2 kernels will be produced in a 1.5 m high GSP sol-gel reactor (10 litres of volume) using one vibrating nozzle, CVD coatings will be done in a 3 inch (76.2 mm) fluidized bed furnace. A 3D view of the CVD furnace with the glove boxes is given in Fig. 3.9. In this laboratory fuel manufacturing line are assembled the capability to perform the preparation of the feed solution containing depleted, natural or enriched uranium, the U based kernel formation up to the sintering stage, the sieving and shape selection and finally the deposition of PyC and SiC layers. The compacting step will be done at CERCA, Romans.

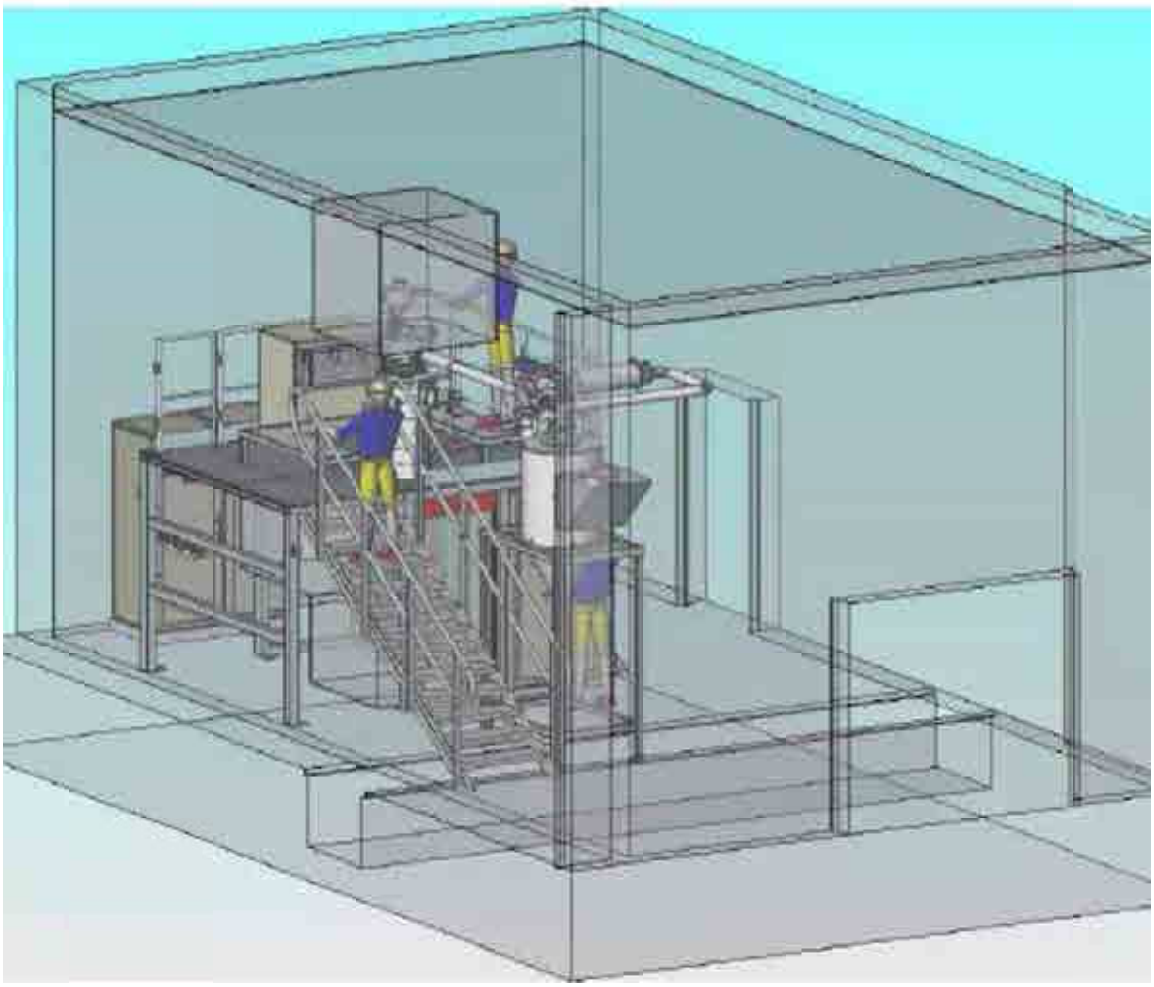

FIG. 3.9. 3D view of fluidized bed furnace of GAIA facility at CEA, Cadarache.

The first objectives of GAIA is to optimize the reference sol-gel and CVD processes for UO_2 kernels and TRISO SiC coatings with parameters in compliance with the guidelines and thus to determine the key parameters for the construction of a modern fabrication plant taking scale-up problems into account. GAIA has also been designed to be as flexible and versatile as possible in order to study different configurations of HTGR fuel fabrication process. In this perspective, the other objectives of GAIA is to allow the manufacture of wide range designs of coated fuel particles and also the investigation of alternative and innovative fuel design such as the UCO kernel and ZrC coating [45].

In the short term, the GAIA installation will produce the batches of coated fuel particles and those latter will be compacted in CERCA for the set of SIROCCO HTGR Fuel irradiation tests foreseen in the materials testing reactor OSIRIS at CEA Saclay. Data on fuel performance under irradiation will feed into the modeling code via the post-irradiation examination results.

3.4. FUEL PRODUCTION ACTIVITIES IN GERMANY

3.4.1. Introduction

As far back as the early sixties, NUKEM Company, working together with Nuclear Research Center Jülich, started work on the development of fuel element for the high temperature reactor. By 1989 NUKEM had already produced over a million fuel elements for the

Arbeitsgemeinschaft Versuchsreaktor (AVR) and the thorium high temperature reactor (THTR). NUKEM's withdrawal from fuel element production was in 1988.

Coated particle development in the Federal Republic of Germany led to a particle design qualified for use in the THTR-300 in 1975. This particle consisted of a mixed oxide, thorium–uranium kernel with a methane derived pyrocarbon coating. The $(Th,U)O_2$ HTI BISO fuel design utilized high enriched uranium.

In the period between 1975 and 1980, the reference particle coating design changed to the LTI TRISO coating which afforded a greater degree of resistance to fast neutron bombardment and a significantly higher degree of fission product retention. The SiC interlayer is the definitive fission product barrier in this design. At first, the kernel material and enrichment remained $(Th,U)O_2$ and high enriched. Then the development work for the low enriched uranium (LEU) cycle started in 1979. The sequence for HTGR fuel particle development is shown schematically in Fig. 3.10 [46].

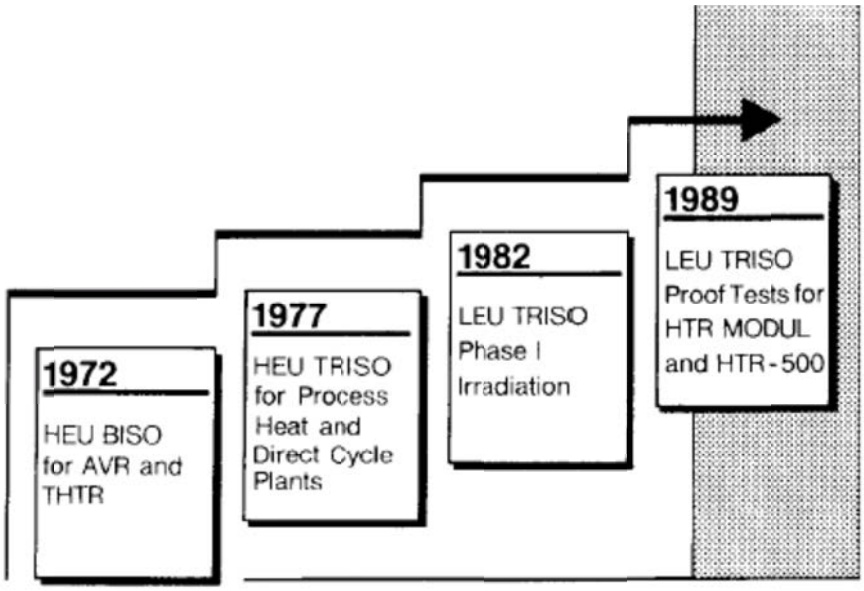

FIG. 3.10. Sequence for German HTGR fuel particle development.

The primary aim of the German HTGR fuel element programme was to develop a unique element valid for all high temperature applications, such as steam cycle/cogeneration, process heat, process steam, and gas turbine reactors.

3.4.2. Fuel production for AVR

One of the main tasks of the AVR experimental power plant was to test the newly developed spherical fuel elements used here for the first time. Since AVR operation started, 12 different fuel element types produced by Germany have been used. They reflect the overall development of spherical HTGR fuel elements in Germany.

The fuel elements of the AVR first core and the first recharges were hollow graphite spheres which were manufactured on a lathe from graphite blocks; the coated particles and graphite powder were filled in and the sphere was closed with a graphite plug. After this, only pressed fuel elements were produced by NUKEM. They had an outside diameter of 60 mm and a 50 mm large inner fuel zone in which the coated fuel particles were embedded. The Tables 3.6

and 3.7 give a survey of all fuel element types produced by Germany and used in AVR [47, 48].

With the exception of the initial core loading (UCC type fuel) and the first reload (T type fuel) which both were machined from graphite blocks, only pressed fuel elements were used produced by NUKEM. Tables 3.6 and 3.7 give a survey of all fuel element variants fabricated in Germany which were used in the AVR [47]. The detailed fuel composition of the reactor core during the operational life is indicated in Fig. 3.11 [49].

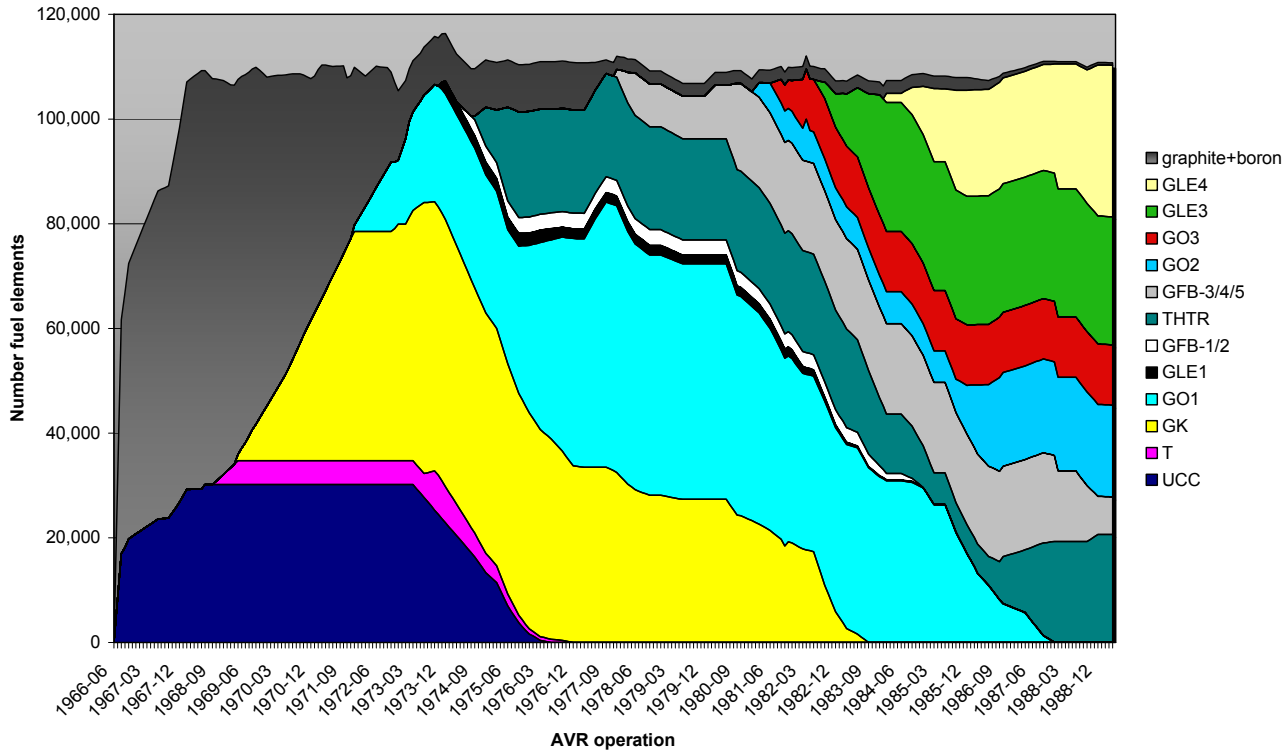

FIG. 3.11. Operational life history of different fuel element types in the AVR.

TABLE 3.6. FUEL ELEMENTS INSERTED IN THE AVR REACTOR

Fuel variant	Reload charge number	Begin insertion	Number of fuel elements	Fuel kernel	Kernel diameter (μm)	U-235 enrichm. (%)	Fuel compos ition			Coating	No. of cp per sphere
							U-235	U_{tot}	Th		
UCC	0	Jul 1966	30 155	$(Th,U)C_2$	200	93.0	1.00	1.075	4.87	HTI BISO	171 000
T	1-1	Oct 1968	4 550	$(Th,U)C_2$	400	93.1	1.00	1.074	4.96	HTI BISO	23 700
	1-2	Aug 1973	2 954								
GK	3	Apr 1969	17 770	$(Th,U)C_2$	400	93.0	1.00	1.075	4.94	HTI BISO	23 700
	4	Jul 1970	6 210								
	5-1	Nov 1970	26 814								
GO-1	5-2	Dec 1971	39 662	$(Th,U)O_2$	400	92.3	1.00	1.083	4.96	HTI BISO	20 800
	7	Jan 1973									
	6-1	Oct 1973									
	12	Mar 1976	11 325								
	14	Nov 1976	9 930								
GO-2	15	Feb 1981	6 083	$(Th,U)O_2$	500	93.0	1.00	1.075	5	LTI TRISO	10 500
	20	Oct 1985	11 850								
GO-3	18	Jul 1981	11 546	$(Th,U)O_2$	400	93.0	1.00	1.075	4.96	HTI BISO	20 800
GO-THTR (22 = KAHTER [a])	9	Sep 1974	5 145	$(Th,U)O_2$	400	93.0	0.96	1.033	10.2	HTI BISO	38 600
	10	Dec 1974	10 022								
	11	Dec 1974	5 000								
	22	Sep 1986	15 248								

[a] KAHTER (‘Kritische Anlage zum Hochtemperaturreaktor’ = critical facility for the high temperature reactor) was an experimental facility at the Research Center Jülich investigating criticality in pebble beds of 10 000–20 000 fuel spheres.

TABLE 3.6. FUEL ELEMENTS INSERTED IN THE AVR REACTOR (cont.)

Fuel variant	Reload charge number	Begin insertion	Number of fuel elements	Fuel kernel	Kernel diameter (μm)	U-235 enrichm. (%)	Fuel compos ition			Coating	No. of cp per sphere
							U-235	U_{tot}	Th		
GFB-1	8-1	May 1974	1440	UO_2 ThO_2	200 600	93.0 n.a.	1.00 n.a.	1.075 n.a.	n.a. 9.99	LTI BISO	24 500 10 100
GFB-2	8-2	May 1974	1610	UO_2 ThO_2	200 600	93.0 n.a.	1.00 n.a.	1.075 n.a.	n.a. 9.99	LTI TRISO LTI BISO	24 500 10 100
GFB-3	13-1	Dec 1977	6076	UC_2 ThO_2	200 500	93.0 n.a.	1.00 n.a.	1.075 n.a.	n.a. 5	LTI TRISO LTI BISO	7500 8000
GFB-4	13-2	Jul 1980	5860	UC_2 ThO_2 + additives	200 530	93.0 n.a.	1.00 n.a.	1.075 n.a.	n.a. 5	LTI TRISO LTI BISO	27 100 8600
GFB-5	13-3	Dec 1977	5354	UCO ThO_2	200 500	93.0 n.a.	0.93 n.a.	1.00 n.a.	n.a. 4.814	LTI TRISO LTI TRISO	— —
GLE-1	6-2	Dec 1973	2400	UO_2	600	14.94 0.7	1.32 0.08	8.6 11.4	n.a.	LTI BISO	8000 9500
GLE-3	19	Jul 1982	24 611	UO_2	502	9.82	1.00	10.2	n.a.	LTI TRISO	16 400
GLE-4	21 21-2	Feb 1984 Oct 1987	20 350 8740	UO_2	502	16.76	1.00	6.0	n.a.	LTI TRISO	9560
			Σ 290 705								

— data not available.
n.a. not applicable .

TABLE 3.7. ALL FUEL ELEMENT TYPES PRODUCED BY GERMANY AND USED IN AVR

Fuel type	Fuel	Particle coating	Fuel per fuel element (g)			Number of fuel elements used in AVR
			U-235	U	Th	
Carbide	$(U,Th)C_2$	HTI-BISO	1.00	1.08	5	50 840
Oxide	$(U,Th)O_2$	HTI-BISO	1.00	1.08	5	72 418
	$(U,Th)O_2$	LTI-TRISO	1.00	1.08	5	6 083
	$(U,Th)O_2$	HTI-BISO	0.96	1.03	10.2	35 415
Separate fissile and fertile particles	UO_2, ThO_2	LTI-BISO LTI-BISO	1.00	1.08	10	1 440
	UO_2, ThO_2	LTI-TRISO LTI-BISO	1.00	1.08	10	1 610
	UC_2, ThO_2	LTI-TRISO LTI-BISO	1.00	1.08	5	6 067
	UC_2, ThO_2	LTI-TRISO LTI-BISO	1.00	1.08	5	5 860
	UCO, ThO_2	LTI-TRISO LTI-TRISO	1.00	1.08	5	5 363
Oxide low enriched	UO_2	LTI-BISO	1.40	20	n.a	2 400
	UO_2	LTI-TRISO	1.00	10	n.a	24 611
	UO_2	LTI-TRISO	1.00	6	n.a	29 090

n.a. not applicable.

3.4.3. Fuel production for the THTR-300

In spherical THTR-300 fuel spheres, the $(Th,U)O_2$ HTI BISO particles were adopted. This particle consisted of a mixed oxide, thorium–uranium kernel with a methane derived pyrocarbon coating. The $(Th,U)O_2$ HTI BISO fuel design utilized high enriched uranium.

Between 1973 and 1980, a total of 380 000 fuel balls were produced for the THTR-300 initial core. From 1980 to 1988, 600 000 reloading fuel spheres were manufactured. Up to the final THTR shutdown (Sept. 1988), approximate 400 000 fresh fuel elements were still on storage [50]. A high production yield was achieved. During the production of 600 000 reloading fuel spheres, only integral 4900 fuel element were rejected as the scrap material. Table 3.8 shows the major quality control data evaluated for the entirety of the initial core fuel elements [50].

3.4.4. LEU-TRISO elements

3.4.4.1. Design specification of the LEU-TRISO elements loaded into AVR and designed for the HTR-Modul

The pebble bed core concept was evolved in the German HTGR development efforts. The pebble bed uses spherical fuel elements with a diameter of 60 mm as shown in Fig. 3.12 [51]. Each sphere consists of an inner 50 mm-diameter fuel region and a 5 mm-thick fuel-free shell surrounding the inner fuel zone. The fuel zone and fuel-free shell are made of the same matrix graphite. The TRISO coated fuel particles are uniformly distributed in the graphite matrix of the fuel zone. The fuel elements are fabricated by the quasi-isostatic pressing process at room temperature [25].

TABLE 3.8. STATISTICAL PERFORMANCE DATA OF COATED FUEL PARTICLES, A3 MATRIX, AND SPHERICAL FUEL ELEMENT PRODUCTION OF THTR-300 INITIAL CORE FUEL

Performance Item	$\overline{X}$	S/$\overline{X}$ (%)
Coated fuel particle		
Kernel diameter (μm)	406	2.6
Buffer layer thickness (μm)	77.4	18
Seal + HTI layer thickness (μm)	100.0	11
O-HTI layer thickness (μm)	78.1	12
Kernel density (Mg/m^3)	9.93	1.4
Buffer layer density (Mg/m^3)	1.12	3.6
HTI layer density (Mg/m^3)	1.84	1.1
Seal layer anisotropy	1.11	—
HTI layer anisotropy	1.14	—
Uranium contamination of HTI layer (wt%)	0.104	15
A3 matrix material		
Density (Mg/m^3)	1.720	0.76
Thermal conductivity (W/(m·K))		
@ 20°C ⊥	63.1	8.2
||	70.1	7.1
@ 1000°C ⊥	37.9	11.6
||	40.9	11.8
Bending strength (N/mm^2) ⊥	24.5	6.6
||	24.3	7.2
Coefficient of ⊥	3.34	6.9
thermal expansion TE (10^{-6}/K) ||	2.93	7.2
E-modulus (N/mm^2) ⊥	9.61	5.2
||	9.98	5.5
Spherical Fuel Element		
Impurities (μg/g B_{equ})	0.26	—
Corrosion rate @ 1000°C in He + 1 vol.% H_2O ($mg/(cm^2 \cdot h)$)	1.00	19
Abrasion rate (mg/h per sphere)	2.82	46
Number of drops (4 m in height)	420	21
Crushing load (kN) ⊥	23.4	6.5
||	22.3	6.0
Free uranium fraction (U_{free}/U_{total})	3.0×10^{-4}	23

$\overline{X}$: mean value of lots.
S: standard deviation of sample.
— data not available.

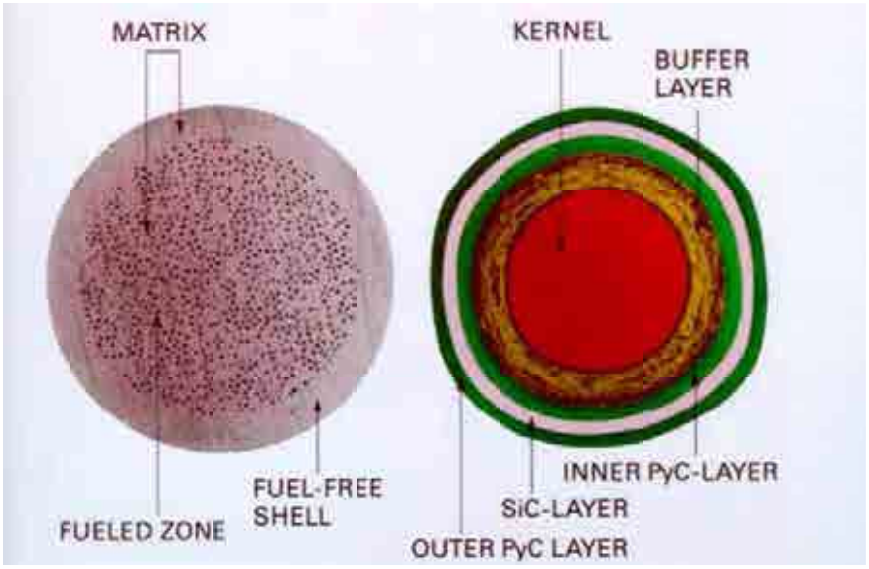

FIG. 3.12. Spherical fuel element configuration developed by Germany.

The German coated particle development started in the mid sixties with its high enriched thorium/uranium fuel cycle (HEU). The $(Th,U)O_2$ fuel kernels are coated with a methane derived pyrocarbon layers only (HTI BISO type). In the period between 1975 and 1980, the mixture of C_2H_2 and C_3H_6 derived pyrocarbon coating (LTI) replaced HTI. Since 1980 fuel particles with UO_2 kernels were developed for the low enriched uranium cycle (LEU). In order to improve the fission product retention capability, the UO_2 fuel kernels were coated with an additional SiC interlayer sandwiched between the high density isotropic layers (TRISO type) [52, 53]. Apart from the fuel particles, the manufacture of the fuel elements is identical for both fuel cycles.

After a thorough study of low enriched fuel particle performance, the Germany adopted low enriched uranium for all future HTGR projects [46]. LEU UO_2 was selected as the reference fuel kernel in 1980. The reference coating design is the TRISO coating. The manufacture of the fuel spheres remained the quasi-isostatic pressing process. The target specification for the HTR-500 and HTR-Modul [15, 54, 55] is listed in the Table 3.9. German HOBEG GmbH had produced more than 50 000 fuel elements of this LEU TRISO type for AVR 19 reloading and Phase 1 experiment in 1981, for AVR 21 reloading in 1983, for AVR 21-2 reloading in 1985 and for proof test in 1988, respectively. The fabrications of these fuel elements had been performed under the requirements of the target specification mentioned above.

3.4.4.2. Fabrication process of the LEU-TRISO fuel elements loaded into AVR

The spherical fuel element was developed by NUKEM [14, 25]. This fuel element consists of a fueled zone, which is about 50 mm in diameter, and a fuel-free shell with a thickness of about 5 mm. The shell and the fueled zone are made of the same matrix graphite. A fuel element contains up to 40 000 coated fuel particles, depending on the specification.

In the period between 1975 and 1980, the German reference particle coating design changed from the HTI BISO coating to the LTI TRISO coating which afforded a greater degree of resistance to fast neutron bombardment and a significantly higher degree of fission product retention. In 1980 LEU was selected as the fuel kernel material, whereas the reference coating design remained the TRISO coating. During the fabrication of AVR reloads 19 and 21, over 50 000 spherical fuel elements with modern LEU TRISO particles were fabricated.

TABLE 3.9. TARGET SPECIFICATION FOR THE HTR-500 AND THE HTR-MODUL

Coated fuel particle	
Uranium enrichment	8.0 ± 0.1 wt% U-235
Stoichiometry	UO_x, $x \leq 2.01$
Diameter (95% confidence)	500 ± 50 μm
Density (average)	$\bar{x} \geq 10.4$ Mg/m^3
Coating thickness (95% confidence)	
Buffer layer	95 ± 22.5 μm
Inner PyC layer	40 ± 20 μm
Silicon carbide layer	35 ± 8 μm
Outer PyC layer	35 ± 20 μm
Coating density	
Buffer layer	$\bar{x} \leq 1.05$ Mg/m^3
Inner PyC layer	$1.8 \leq \bar{x} \leq 2.0$ Mg/m^3
Silicon carbide layer	$\bar{x} \geq 3.18$ Mg/m^3
Outer PyC layer	$1.8 \leq \bar{x} \leq 2.0$ Mg/m^3
Anisotropy factor (BAF)	
Inner PyC layer	$\bar{x} \leq 1.10$
Outer PyC layer	$\bar{x} \leq 1.0$
Spherical fuel element	
Carbon mass	$\bar{x} \geq 190$ g
Thermal conductivity @ 1000°C	≥ 30 W/(m·K)
Anisotropy (thermal expansion)	≤ 1.3
Abrasion [a]	$\bar{x} \leq 6$ mg/h per sphere
Corrosion rate [b]	≤ 1.5 mg/(cm^2·h)
Thickness of fuel-free layer	$4.0 \leq x \leq 6.0$ mm
Drop strength [c]	≥ 50
Crushing strength [d]	≥ 18 kN
Matrix density	≥ 1700 kg/m^3
Defective coating (U_{free}/U_{total})	$\bar{x} \leq 6 \times 10^{-5}$

[a] 20 graphite elements are placed in a drum rotating at 55 revolutions per minute and rotated for 100 h.

[b] Graphite element is heated to 1000°C in a pure helium gas stream at atmospheric pressure. On reaching the target temperature, the gas stream is changed to helium containing 1 volume percent of water and the element is kept at a constant temperature for 10 h.

[c] Fuel element is taken to a height of 4 m and allowed to freefall onto a pebble bed of the same quality and size as the test element until fracture.

[d] Fuel element is pressed between two parallel steel plates at a 10 mm/min rate and breaking force measured.

The fabrication process for spherical fuel elements and their constituents (LEU kernels and TRISO particles) consists of following steps [14]:

(1) gel precipitation technology for LEU UO_2 kernel formation,
(2) chemical vapour deposition of the coating layers, and
(3) preparation of resinated graphitic matrix powder and cold molding of the fuel balls.

(a) Step 1: UO_2 kernel fabrication

In the case of low enriched UO_2 fuel kernels, the well known gel precipitation process [14] is modified as shown in Fig. 3.13.

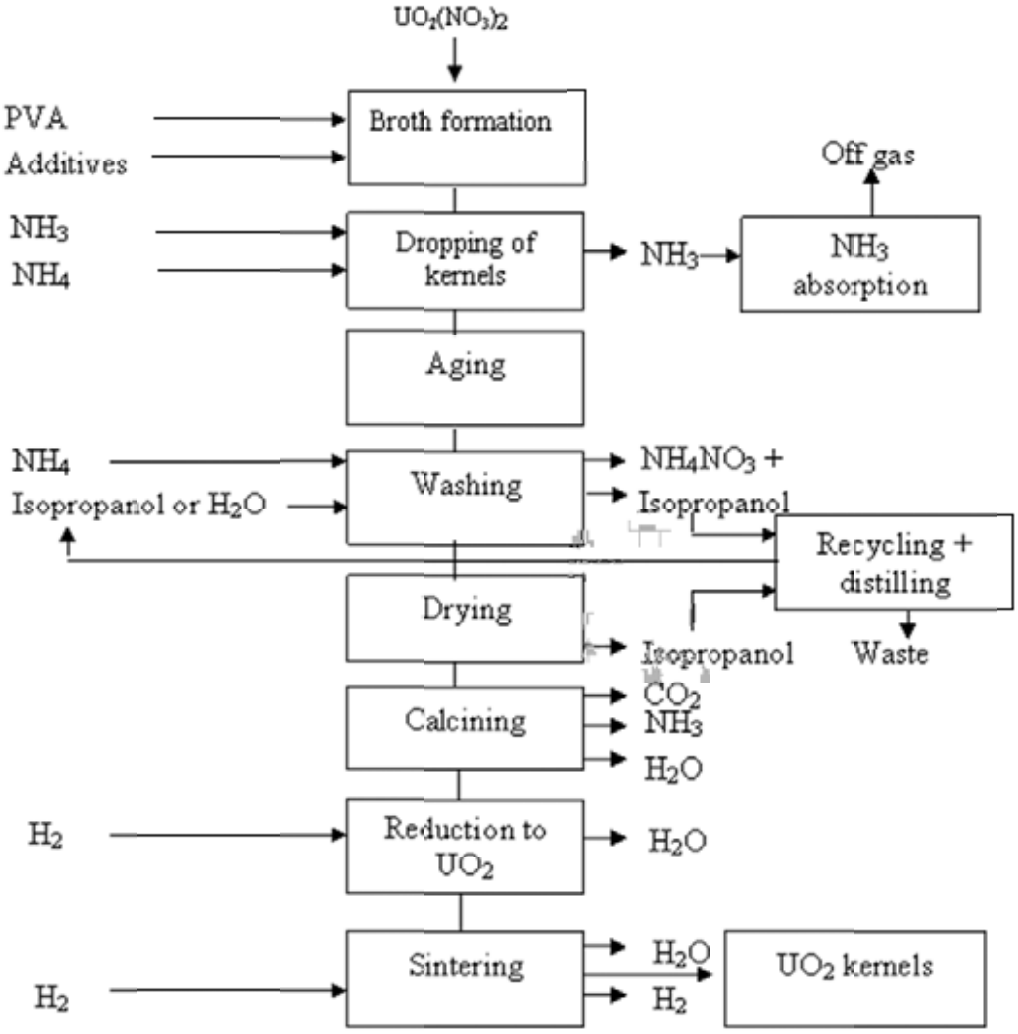

FIG. 3.13. UO_2 kernel formation.

At first uranyl nitrate solution (UN) is prepared by dissolving uranium oxide in nitric acid. The UN is mixed with polyvinyl alcohol (PVA). The spherical droplets are produced by a vibrational dropping technique. These droplets then are aged to improve the internal structure and are washed to remove the nitrate. Following the drying and calcining stages, a UO_2-related step — reduction of the calcined kernels to UO_2 — is inserted. Kernel fabrication is completed by sintering to produce highly dense UO_2 kernels.

The sintered particles are screened, whereby over- and under-sized particles as well as small fragments are separated from the correctly sized product. After the screening, the particles are sorted. Non-spherical particle and larger fragments are removed.

(b) Step 2: PyC and SiC coating process

Coating of the kernels [56–58] is performed in fluidized beds by pyrolysis of adequate hydrocarbons and silane derivatives, as shown in the flow sheet in Fig. 3.14. The pyrocarbon layers are deposited by the pyrolysis of acetylene or acetylene and propane mixture (depending on the layer) at temperature 1000–1400°C. An additional intermediate SiC layer is deposited by the decomposition of methyltrichlorosilane at 1500°C. The variation of the coating parameters allows the production, as required, of differing coats with varying properties. The kernels to be coated are fluidized in a so-called carrier gas. Coating gases are added to the carrier gas, from which the various coats are deposited. Figure 3.15 shows this coater. During the course of the coating process the off-gas are produced (carrier gas and gaseous residues from the pyrolysis). The filtered off-gas is then directed to the stack.

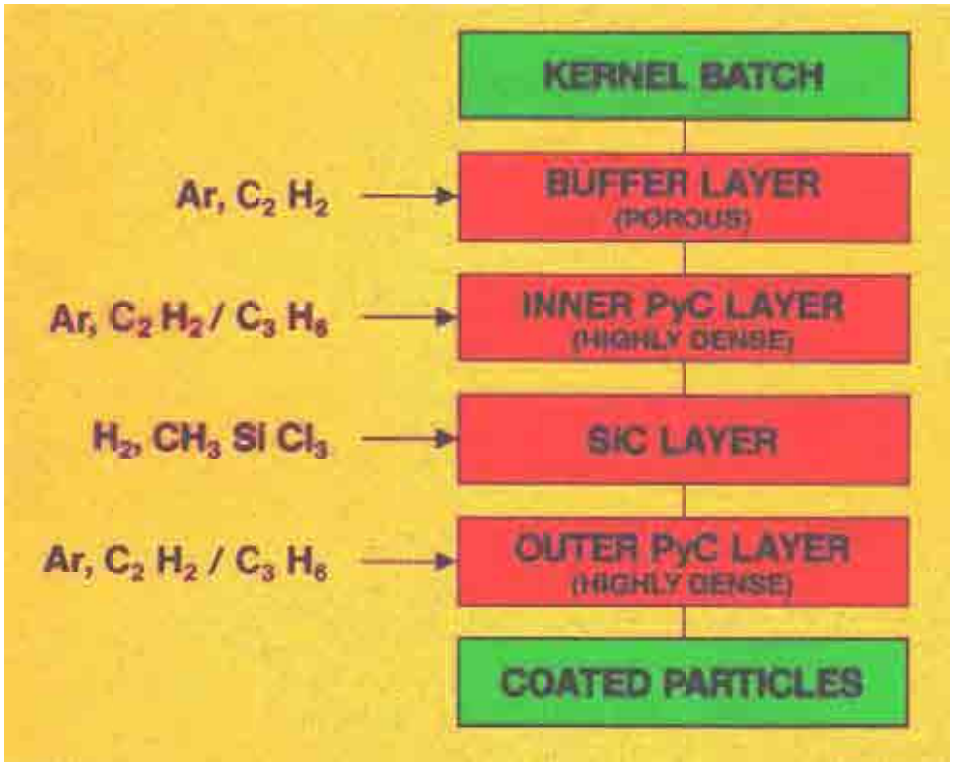

FIG. 3.14. Coating of HTGR fuel kernels.

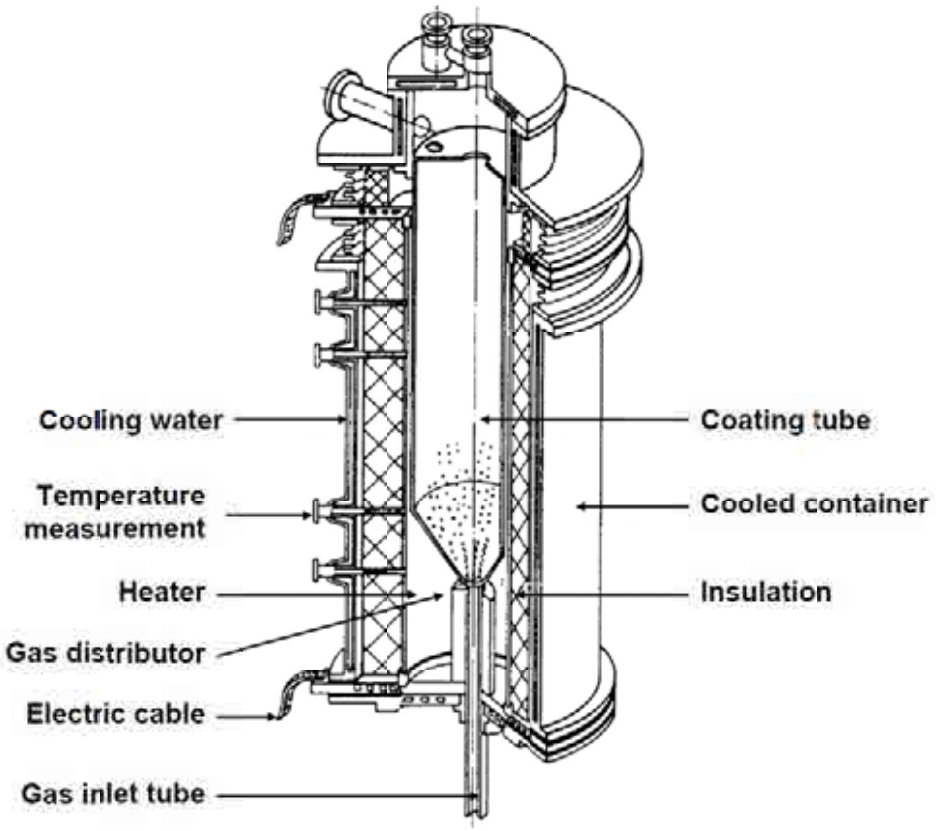

FIG. 3.15. Coater.

(c) Step 3: Matrix fabrication

The best solution for meeting the requirements for the German spherical fuel element was found in the isostatically pressed element with the design of a fueled zone of ≤ 50 mm diameter surrounded by a fuel-free shell of ≤ 5 mm thickness, both based upon A3 matrix material. Raw materials for the matrix production are natural graphites and electro-graphites. There are large resources worldwide for natural graphite with the most appropriate ones, with regard to nuclear purity, being the flake graphites. The electro-graphites are derivates from crude oil or hard coal by distillation and coking of the resulting pitch at a temperature of 3000°C. The composition of raw materials (before heat treatment) is 64 wt% of natural graphite, 16 wt% of petroleum coke graphite, and 20 wt% of resin binder [59]. For the production of 1 million spheres, the raw material demand is approximately 160 t of natural graphite and 40 t of electro-graphite.

The A3 matrix fabrication begins with the cold mixing of natural flake graphite and graphitized coke powder (electro-graphite). This filler material is then mixed with the binder, a pre-fabricated thermoplastic material made of a phenolic resin dissolved in methanol. After the steps of kneeding, drying, grinding, the result is a resinated powder, A3-3, which is then used for the pressing process. In a later modified process, the filler raw materials were mixed with phenol and hexamethylenetetramine at 130°C. The resin itself was no longer pre-fabricated, and rather generated during the matrix manufacture as a duroplastic binder. The result after grinding was A3-27 grade resinated powder, whose properties have more narrow bandwidths compared to A3-3. The composition of the two grades after final heat treatment is given in Table 3.10 [59].

TABLE 3.10. A3 MATRIX MATERIAL COMPOSITION AFTER FINAL HEAT TREATMENT

Component	A3-3	A3-27
heat-treated @	1800 or 1950°C	1950°C
Natural graphite grade FP (%)	72	71.2
Graphitized coke grade KRB (%)	18	17.8
Non-graphitized binder coke (%)	10	11

The process step of isostatic cold moulding is the same for both matrix material grades. It is carried out in silicon rubber dies, which behave like a liquid at high pressures and thus guarantee low anisotropy. The pressing process takes place at room temperature and at 3 MPa during pre-moulding (of the fuel zone) and 300 MPa during final moulding. It is followed by a lathing step to obtain the correct diameter. The coated particles admixed to the graphite material were given an overcoating to reduce the risk of damage during the pressing step. It had a thickness of ~100 μm for BISO particles and ~200 μm for TRISO particles. By testing a wide variety of fuel element variants, an upper limit for the cold pressing process in terms of heavy metal loading was deemed to be at 20–25 g per sphere. At too high a loading, the mechanical strength of the sphere decreases, while the number of defective particles is increasing.

Final step is the heat treatment consisting of two steps which were conducted batch-wise in separate furnaces:

- carbonization of the binder in an inert gas atmosphere by slowly heating up to 800°C with max. 1000 spheres per batch;
- high temperature annealing under vacuum over 1 hour at 1950°C for degassing and purification of the spheres with max. 450 spheres per batch. (Earlier fuel element reload batches for the AVR reactor and other spheres subjected to irradiation testing were based on A3-3 heat-treated at 1800°C. For the AVR reloads 6 to 9, the temperature was raised to 1900°C; for later reloads and THTR and all A3-27 fuel, it was further raised to 1950°C). Purpose was the improvement of corrosion resistance.

The degree of heavy metal contamination of the matrix material is strongly depending on the annealing temperature in the high temperature treatment step, which was especially true for the fuel of the THTR with BISO coated particles. A reduction of the annealing temperature of 100 degrees was observed to decrease the contamination level by 20%. A chlorine treatment of the spherical elements was found to be efficient in removing surface impurities proven in corrosion tests at 1000°C.

Apart from the standard matrix material A3-3, many variants were fabricated and tested, mainly for the purpose of either expanding the raw material data base, or simplifying the fabrication process, or further improving the material properties. The standard A3-3 has been satisfactorily used and proven suitable in the AVR since 1969 and in the THTR-300, the modification A3-27 since 1976 (starting with AVR reload 14) basically within the LEU generic tests. Some statistics on the production of the 850 000 fuel spheres for the THTR-300, which correspond to:

820 times the kernel production capacity per day

3000	coating charges
2100	times the pressing line throughput per day
850	carbonization runs @ 800°C
3400	heat treatment runs @ 1950°C
with < 5%	reject fraction

Within the field of fuel element manufacture, the technology used for the THTR-300 elements was improved [59, 60]. Figure 3.16 shows the fabrication process steps for LEU TRISO fuel that, in principle, do not differ from the THTR fuel element fabrication procedure. In the first step, graphitic raw materials are processed to resinated powder. In this step the process was simplified by using the resin binder components phenol and hexmethylene-tetramine, warm mixing of these binder components with graphite powder, and grinding the product to final grain size. The resin binder is formed by the chemical reaction of the components during the warm mixing process. A portion of the resinated powder is then used to overcoat the coated particles; another portion is premolded together with these overcoated particles to form the fueled zone of the fuel element; and the rest is used for the final molding of the fuel element built up by the fueled zone and a fuel-free shell. Final steps in the process are lathing the elements to obtain the appropriate diameter and heat treatment for binder coating and removal of impurities.

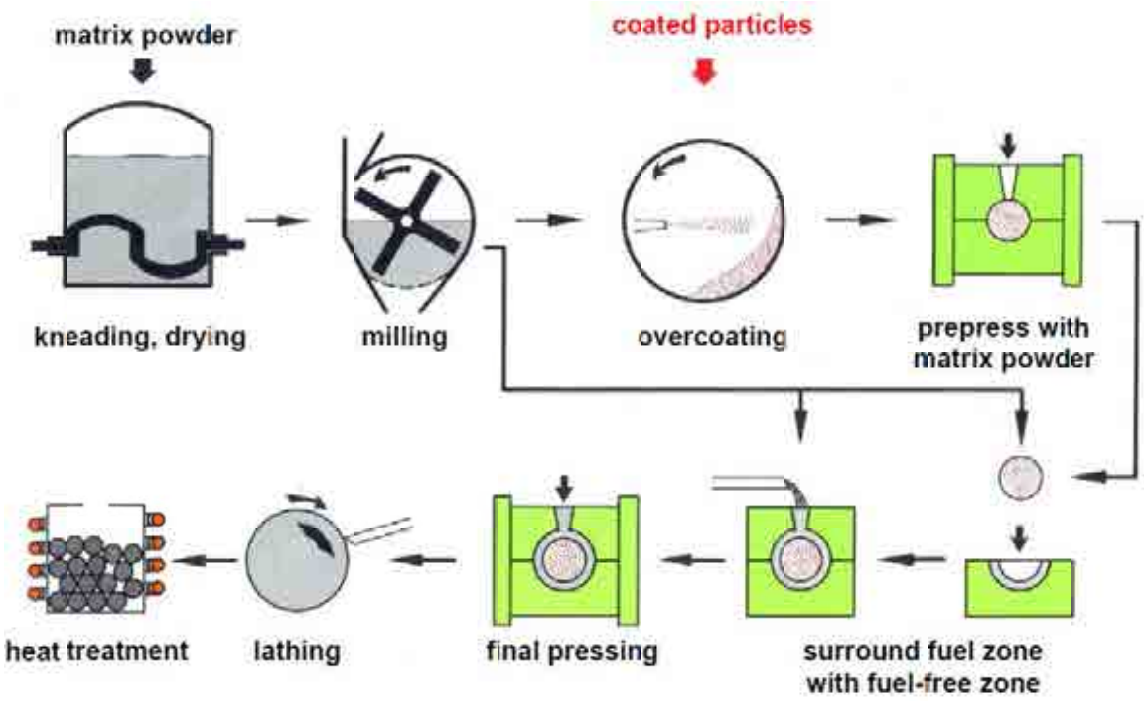

FIG. 3.16. Manufacture process of the spherical fuel elements.

3.4.4.3. Characterization of fabricated LEU TRISO elements

The detailed description of the status of product quality is summarized in Table 3.11 [14]. All data meet the design and target specifications.

TABLE 3.11. PROPERTIES OF UO_2 TRISO COATED PARTICLE AND FUEL SPHERE

		Mean value	Standard deviation
Kernel diameter (μm)		500	11
Kernel density (Mg/m^3)		10.9	0.08
Kernel shape factor (D_{max}/D_{min})		1.07	—
Fraction of odd shaped kernels (twin kernels, cracked kernels, roller shaped kernels	before tabling	5×10^{-4}	—
	after tabling	10^{-5}	—
Layer thicknesses (μm)			
Buffer		92	14
Inner PyC		39	4
SiC		35	2.5
Outer PyC		40 [a]	3
Layer density (Mg/m^3)			
Buffer		0.97	—
Inner PyC		1.91	0.02
SiC		3.20	0.003
Outer PyC		1.91	0.02
Layer anisotropy			
Inner PyC		1.054	0.012
Outer PyC		1.024	0.005
Fraction of defective SiC layers		9×10^{-6}	—
Apparent density of matrix (Mg/m^3)		1.750	0.004
Thermal conductivity @ 1000°C (W/(m·K)) ⊥		39	3
||		40	—
Ash content (μg/g)		40	—
Standard specific corrosion rate ($mg/(cm^2 \cdot h)$)		0.62	0.08
Crushing strength (kN) ⊥		23.7	0.3
||		26.3	0.4
Standard abrasion rate (mg/h)		2.9	0.7
Fraction of particles with defective SiC layers (after tabling)		1.5×10^{-6}	—

[a] Deviation from design (35 μm) intended due to special requests of reloading the AVR reactor .
— data not available.
|| = parallel, ⊥ = with and across orientation of the graphite granules in the sphere.

Two mechanisms exist that can induce particle defects: First, during the molding process, adjacent particles can be pressed against each other. This problem can be overcome by overcoating the particles with layer of resinated graphite powder. Optimum results of overcoating quality have been obtained by classifying the overcoated particles. The second mechanism leading to coating layer cracks are extremely odd shaped particles. These particles are not able to withstand the pressure applied during molding. To exclude this second cause of particle defects, the coated particles are classified before overcoating, using the vibration table. This device ensures a precise separation of the odd shaped material from the good fraction.

With modern TRISO particles, it can be demonstrated that all radiologically relevant fission products are completely retained inside the SiC layer of intact fuel particles. The dominant source term for fission product release will be the small number of particles with defective coatings.

The TRISO particles with defective coatings can be determined by the burn-leach method. Burn-leach data for different TRISO fuel elements are given in Table 3.12 [15]. As shown in the table, the progress in the fuel element quality became evident. The measured values for the total free uranium fraction cover a range between 8 and 51 × 10^{-6}. Therefore the design value has been conservatively fixed at 5 × 10^{-5} (see also Section 4.3.2.5).

TABLE 3.12. EVALUATION OF FREE URANIUM IN GERMAN LEU UO_2 TRISO FUEL

Designation of FE population	LEU I	AVR 19	AVR 21	AVR 21-2	Proof test fuel
Production year	1981	1981	1983	1985	1988
Number of FE lots	n.a.	14	11	8	n.a.
Number of FE produced	< 100	24 600	20 500	14 000	< 200
U-235 enrichment (%)	9.8	9.8	16.7	16.7	10.6
Number of particles per FE	16 400	16 400	9 560	9 560	14 600
Total number of measured particles	82 000	1 148 000	525 800	382 400	146 000
Equivalent free uranium (ppm)	37	49	46	8	21
Upper 95% confidence limit (ppm)	95	61	64	20	53

n.a. not applicable.

3.5. FUEL PRODUCTION ACTIVITIES IN JAPAN

3.5.1. Design specification of the HTTR fuel element

3.5.1.1. Fuel element geometry

The high temperature engineering test reactor, HTTR, is the block type high temperature gas cooled reactor. The HTTR fuel is a pin in block type (fuel block) configuration as shown in Fig. 3.17 [61].

The reactor core of the HTTR consists of replaceable hexagonal reflector and 150 hexagonal fuel blocks, both of which are surrounded by permanent reflector. There are two types of the fuel blocks, one of which is loaded with 31 fuel rods, and the other with 33 fuel rods [62]. The fuel blocks with 33 fuel rods are loaded in the inner region of the core, while the blocks with 31 fuel rods in the outer region.

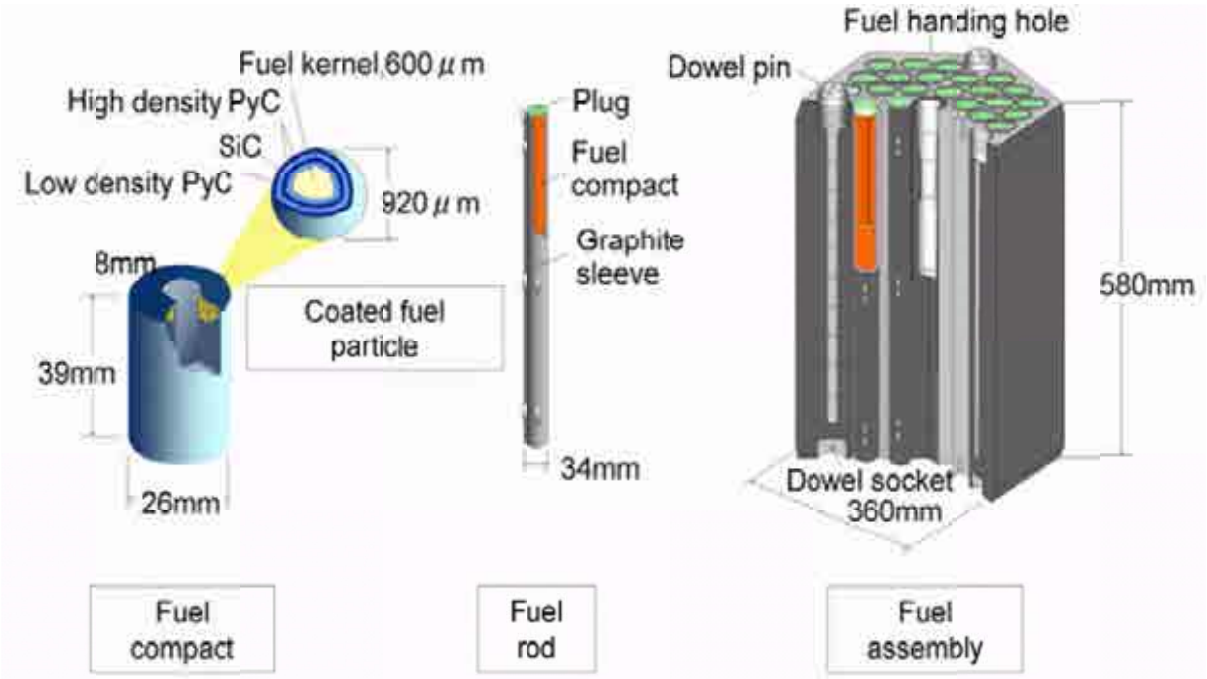

FIG. 3.17. Configuration of HTTR fuel.

The fuel block is a hexahedral prism of 360 mm in width across flats and 580 mm in height. The fuel rods are inserted in a graphite block. The 14 fuel compacts were fitted into a graphite sleeve of 34 mm in outer diameter to form a fuel rod. The fuel compact has shape of annular cylinder which consists of graphite matrix and about 13 500 TRISO coated fuel particles. The coated fuel particle is composed of low enriched UO_2 kernel coated with fourfold layers: low density PyC, high density inner PyC, SiC and high density outer PyC.

3.5.1.2. Design specification

The major specifications of the first loading fuel of the HTTR are listed in Table 3.13 [18, 21, 61].

3.5.2. Fabrication process of the HTTR fuel elements

The fuel fabrication for the HTTR first loading fuel started at the Nuclear Fuel Industries, Ltd (NFI) in June 1995. 4770 fuel rods with 12 kinds of enrichment in total, which correspond to 66 780 fuel compacts, were fabricated through the fuel kernel, coated fuel particle and fuel compact process. 150 fuel elements of 900 kg U of the HTTR first loading fuel were assembled in the reactor building December 1997. The fabrication technology of the HTTR fuel is described below [18, 21].

TABLE 3.13. MAJOR SPECIFICATIONS OF THE FIRST-LOADING FUEL OF THE HTTR

Coated fuel particle	
Diameter	600 ± 12 μm
Density	10.63 ± 0.26 Mg/m^3
Impurity (EBC) [a]	≤ 3 μg/g
Buffer layer thickness	60 ± 12 μm
IPyC layer thickness	30 ± 6 μm
SiC layer thickness	25 +25/-0 μm
OPyC layer thickness	45 ± 6 μm
Buffer layer density	1.10 ± 1.10 Mg/m^3
IPyC layer density	1.85 +0.10/-0.05 Mg/m^3
SiC layer density	≥ 3.20 Mg/m^3
OPyC layer density	1.85 +0.10/-0.05 Mg/m^3
OPTAF of IPyC and OPyC layers	≤ 1.03
Diameter	920 +50/-30 μm
Sphericity	≤ 1.2
Fuel compact	
Coated fuel particles packing fraction	30 ± 3 vol.%
Impurity (EBC[(a)])	≤ 5 μg/g
Exposed uranium fraction	≤ 1.5×10^{-4}
SiC failure fraction	≤ 1.5×10^{-3}
Outer diameter	26.0 ± 0.1 mm
Inner diameter	10.0 ± 0.1 mm
Height	39.0 ± 0.5 mm
Matrix density	1.70 ± 0.05 Mg/m^3
Compressive strength	≥ 4900 N
Fuel rod	
Number of fuel compacts	14
Uranium content	188.58 ± 5.66 g
Total length	577 ± 0.5 mm
Fuel compact stack length	≥ 544 mm
Diameter	34 mm
Fuel block	
Material	IG-110
Distance across flats	360 mm
Length	580 mm

[a] EBC = Equivalent boron contents.

3.5.2.1. UO_2 kernel fabrication process

UO_2 kernels are fabricated by the so-called 'gel precipitation process' shown in Fig. 3.18. Metal solution is prepared with the mixture of the uranyl nitrate solution and additive to control the viscosity of the solution. Droplets of the metal solution are generated at the vibrating nozzles and fall into ammonia water to be aged to ammonium diuranate (ADU) particles. The reaction products of ammonium nitrate etc. are washed off, then the particles are dried and calcinated to UO_3 particles at 500°C in air. The UO_3 particles are reduced and sintered to UO_2 particles with about 97% of the theoretical density at 1600°C under hydrogen atmosphere [63].

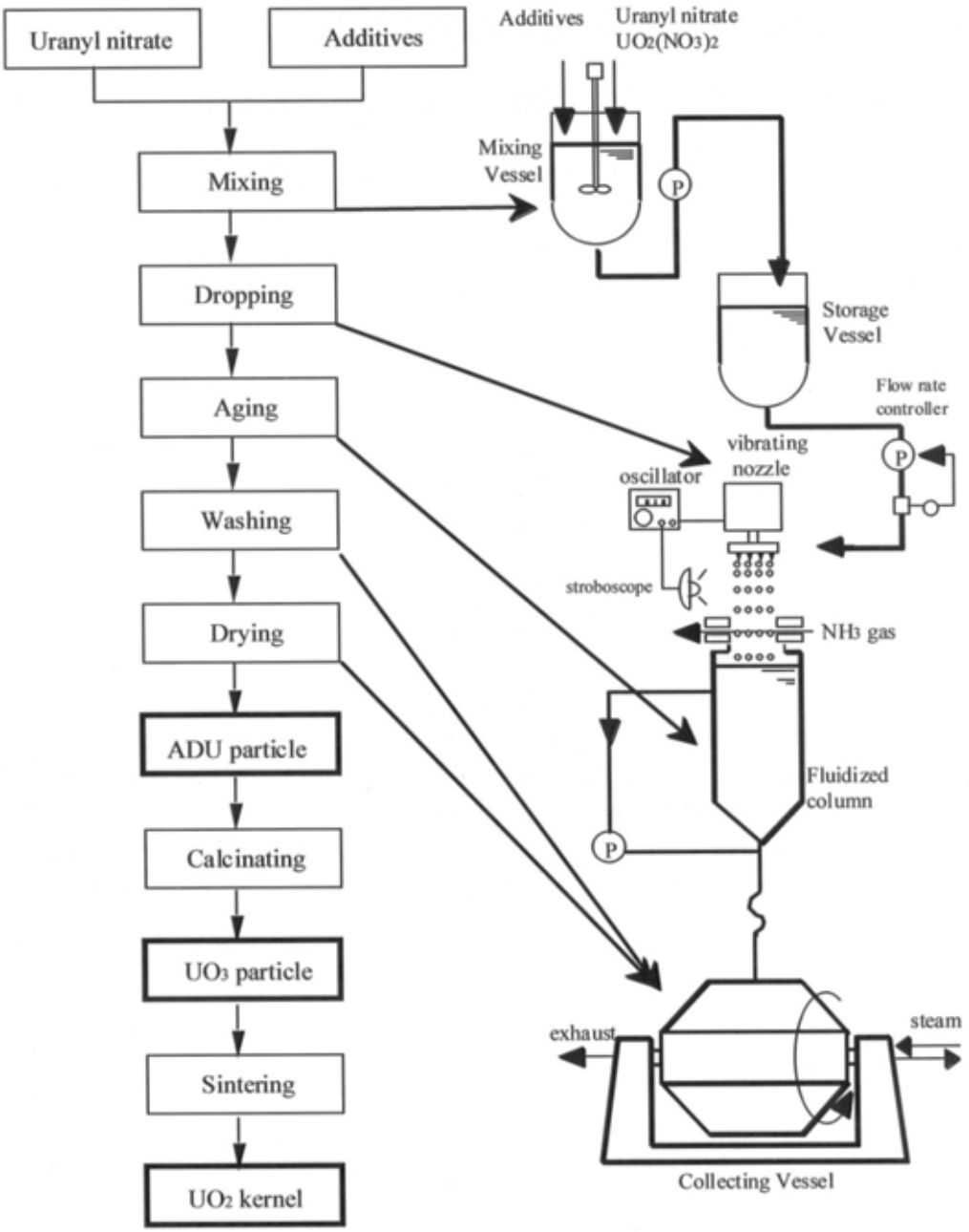

FIG. 3.18. UO_2 kernel fabrication process [63].

Mainly, coated layers of the coated fuel particles have a function to enclose fission products generated in fuel kernel. The mechanical strength of the coated layers depends on their thickness and sphericity. These characteristics strongly depend on the diameter and sphericity of the kernels. Therefore it is essential to establish the fabrication technology to obtain the kernels with more uniform diameter and excellent sphericity. The vibrating nozzles from which droplets are emitted with high speed were developed for such kernels fabrication. The vibrating nozzles can emit droplets with uniform diameter continuously since the diameter of a droplet is determined by the combination of the flow rate of metal solution and the frequency of the nozzles as indicated in the equation (3.1).

The diameter of a droplet is controlled to have same uranium content as that of a fuel kernel.

$$Q = \frac{\pi \cdot D^3}{6} \cdot f \qquad (3.1)$$

where

Q is the flow rate of metal solution (kg/s);
D is the diameter of droplet (m);
f is the frequency of vibrating nozzle (s^{-1}).

Most of the degradation of kernel sphericity is caused by the deformation at the stage of droplet formation and wet ADU particle. At the stage of formation, a process is applied to prevent the deformation of droplets when landing on the ammonia water. In the process, droplets are solidified while falling in ammonia gas blown against the droplets. At the stage of wet-ADU particle, the processes of aging, washing and drying are carried out in the same conical dryer. It is possible to mitigate the impact against the particles by retaining very soft wet-ADU particles in the same conical dryer during the operations, and came to prevent the deformation.

3.5.2.2. PyC and SiC coating process

The coating layers are deposited on the kernels by a CVD process using a fluidized bed type of coater. The TRISO coating process is divided into four coating process for the porous PyC, IPyC, SiC and OPyC layers. Mixing gases of acetylene (C_2H_2) and argon are used for the deposition of porous and low density PyC for the first layer; propylene (C_3H_6) and argon for the deposition of dense PyC for the second and fourth layer; methyl-trichloro-silane (MTS) and hydrogen for the deposition of SiC for the third layer. Figure 3.19 shows the fabrication flow diagram of coated fuel particles [63].

The amount of charged UO_2 kernels corresponds to 3 kg of uranium per coating batch. At a desired temperature, reactants are put into the coater to produce a coating layer on the particles fluidized in the coater. After a certain time to produce the desired thickness of the layer, the reactant gas supply is replaced by argon. The coater and the coated particles are cooled down, and then the coated particles are removed from the coater. All the coated particles are classified by means of a vibrating table to exclude the odd shape particles.

The as-manufactured quality of the fuel has been improved by the modification of fabrication conditions and processes [64]. The coating failure during the coating process is mainly caused by the strong mechanical shocks to the particles given by violent particle fluidization in the coater and by the unloading procedure of the particles. The coating process was improved by

optimizing the mode of the particle fluidization and by developing the process without unloading and loading of the particles at the intermediate coating process.

3.5.2.3. Manufacture process of the fuel compacts

The fabrication flow diagram is shown in Fig. 3.20.

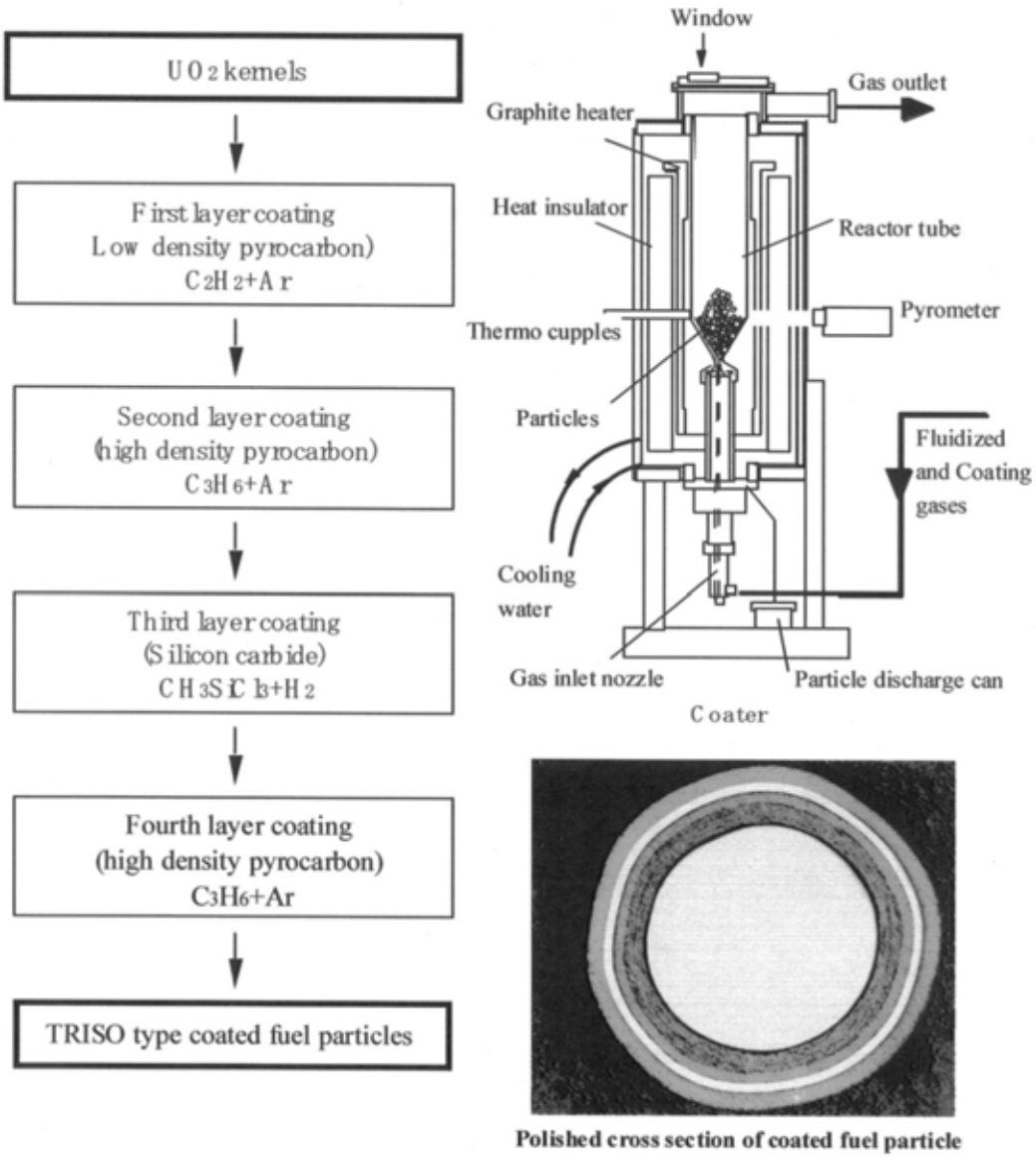

FIG. 3.19. Fabrication flow diagram of coated fuel particles [63].

First, natural graphite powder, electro-graphite powder and a binder are mixed, then the coated fuel particles are overcoated with the graphite matrix and warm-pressed to make annular cylinder of green compacts. The final step of the compaction process is the heat treatment of the green fuel compacts at 800°C in flowing N_2 to carbonize the binder and at 1800°C in vacuum to degas the fuel compacts. Among these processes, the green compact pressing is most complicated, which involves weighing, pre-heating, loading and unloading of overcoated particles and printing an identification number on a green compact, etc. [63].

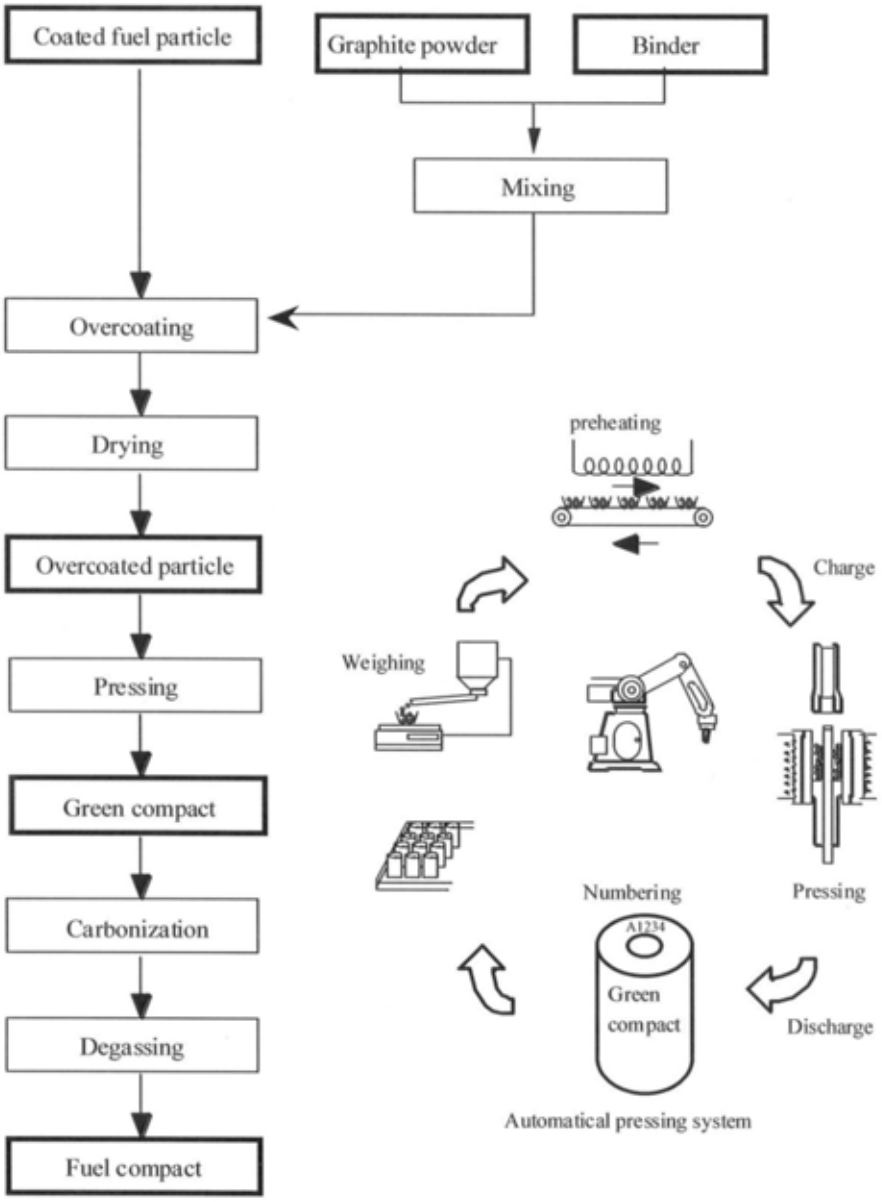

FIG. 3.20. Fabrication process of fuel compact [63].

In order to improve the failure fraction of coating layers at the stage of a fuel com act, it is necessary to disperse coated fuel particles in a green compact as uniformly as possible. From this point of view, the punching speed and the temperature during the warm pressing were optimized to fix the best timing of the softening by heating and the plastic flow of matrix graphite by pressing [64]. As a result, it was realized that average bare uranium function and SiC defective for all fuel compact lots were 2×10^{-6} and 8×10^{-5}, respective [65, 66].

3.5.2.4. Assembling

Fourteen fuel compacts are encased in a long graphite sleeve, making up a fuel rod. The graphite sleeves and the graphite blocks are made of IG-110, a fine grained, low impurity, isostatic-pressed isotropic graphite. The graphite sleeves are transported from Toyo Tanso Co. Ltd. to NFI to assemble the fuel rods. The fuel rods and graphite blocks are transported to the HTTR reactor building. Assembling of the fuel blocks is carried out in the reactor building by insertion of the fuel rods into to the graphite blocks. Assembled fuel blocks are stored in new

fuel storage cells after inspection. The cells are filled with helium gas to keep the fuel blocks in dry condition.

3.6. FABRICATION PROCESS OF HTGR FUEL IN THE REPUBLIC OF KOREA

3.6.1. Introduction

The Korea Atomic Energy Research Institute (KAERI) started the so-called 'Nuclear Hydrogen Key Technology Development (NHTD) Project' in 2006, consisting of VHTR design technology development, fuel technology development, material and component development. The development of technologies relevant to the reactor fuel and materials is one of the important tasks in respect of reactor safety. Work at KAERI has been devoted to develop the fundamental technologies for coated particle fuel, which include the fabrication of uranium kernels, coating technology for pyrolytic carbon and silicon carbide, and for their respective material characterization technology. In the following, the development of laboratory equipment and apparatus to perform experiments for kernel preparation and coating of PyC and SiC, and main results of the fundamental experiments carried out in order to establish the basis of the so-called the TRISO coated particle fuel fabrication technology are described.

3.6.2. Development of fabrication process for coated particle fuel

Even though it has not been decided yet whether pebble or prismatic fuel would be used, it can be rationalized that the development of fabrication technology for coated particle fuel can be started even before the decision for a core configuration is made, since the technology relevant to the coated particle fuel would be commonly utilized both in pebble bed or prismatic fuels and it differs, to a large extent, from a mature LWR fuel technology established with a considerable experience accumulated during its development for several decades in Republic of Korea.

After the work performed on the literature survey and analysis of the current status of the technology for kernel fabrication in the feasibility study, it was decided, in the first place, to perform experimental work with both internal and external gelation methods based upon the so-called wet chemical sol-gel technology in order to observe the mechanism of formation of ammonium di-uranate (ADU) gel and successively to find preliminary desirable conditions for its formation. In order to construct a laboratory scale apparatus, a simple flow diagram and a schematic process flow for the apparatus arrangement were established, based upon the work conducted by literature survey and analysis for both internal and external gelation experiments. After some basic experiments performed on both methods and essential understanding of the methods obtained, only the external gelation method has been focused on for further development, as most of the commercialized process for the large production worldwide involve the external gelation method. Figure 3.21 shows an established flow diagram for both internal and external gelation for comparison.

Based upon these diagrams, a laboratory scale apparatus mostly with glassware was constructed with a capacity of about 50 gU/batch. Figure 3.22 shows an example of the construction of the laboratory sol-gel arrangement for external gelation, which was made use of for the experimental work carried out, in order to find a desirable condition for gel formation and subsequent drying and calcination steps. Developmental work for an alternative was also envisaged and being carried out for kernel preparation using a dry route based on a slurry drop gelation method.

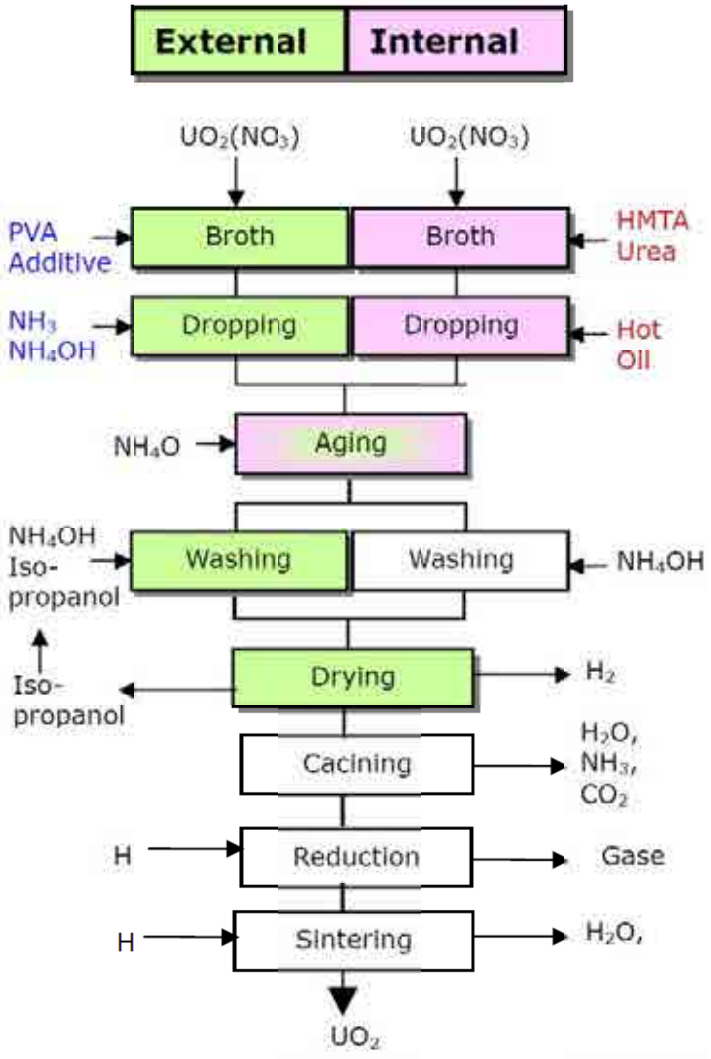

FIG. 3.21. Flow diagram for internal and external gelation [67].

In parallel, experiments were performed on UO_2 formation by calcination after drying of gels formed during gelation. In order to convert the gel product ADU to UO_2 a successive two-step oxidation-reduction step is required for a specified stoichiometric range of UO_2 kernel to be prepared for subsequent sintering. As is well known in HTGR coated particle fuel technology, the coating technologies for pyrolytic carbon and silicon carbide coating layers are the most crucial and delicate. In the past experiences in the USA and Germany, there have been differences in fuel failure between the German NUKEM fuel and fuels supplied by General Atomics in the USA [68].

In order to construct a laboratory scale fluidized bed chemical vapour deposition (CVD) coating furnace, a simple flow diagram and a detailed specification of the furnace to be manufactured were established based upon the work conducted by literature survey and analysis. In the coating process [14], several hydrocarbon gases are involved for the PyC coating and specifically Methyl Trichloro Silane (MTS) gas is to be used for SiC coating which, after coating, gives hydrogen chloride as by-product off-gas to be treated or recovered.

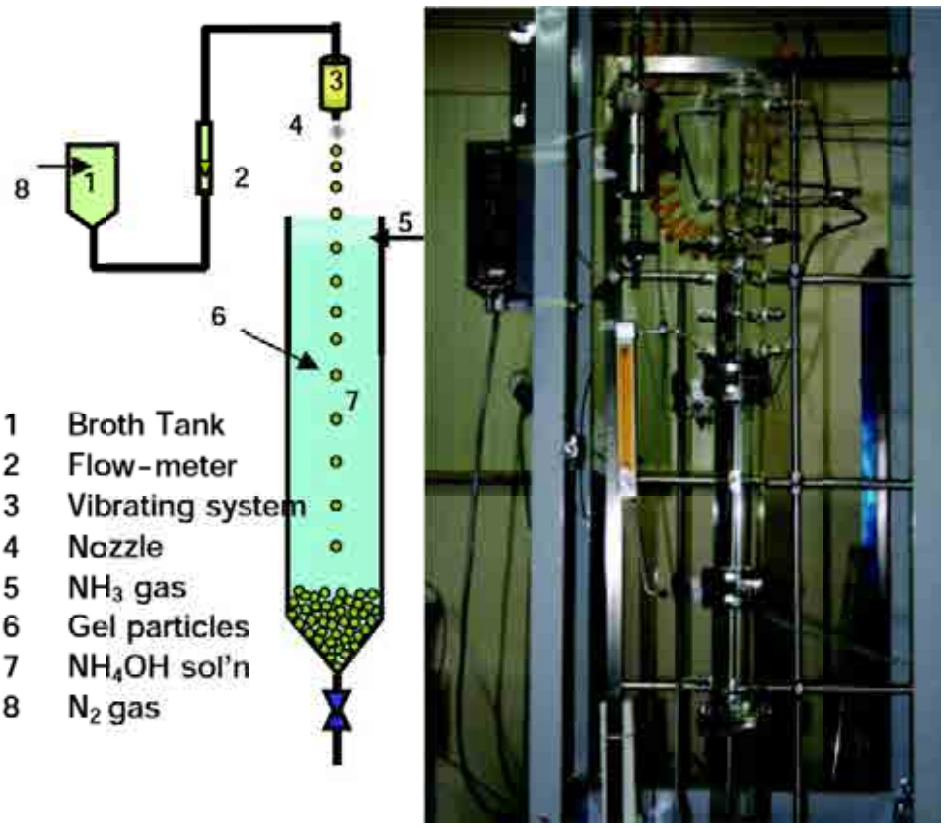

FIG. 3.22. Laboratory scale sol-gel apparatus arrangement for external gelation [67].

The coating conditions for desirable layer thicknesses of respective pyrolytic carbon and silicon carbide by CVD method are different, but these can be more or less optimized by monitoring of coating temperature, reactant gas flow rate and reaction time. However, in order to make more precise coatings, it is found that the design of the furnace with an exact geometrical definition of the gas nozzle would be required. Previous experience was acquired for various research purposes in coating, among others:

- PyC coating of particles of various diameters using zirconia with CVD technique;
- Coating of C/SiC compositionally-graded layer by CVD;
- SiC coating on plate type graphite substrate by low pressure CVD;
- Development of PyC–SiC coating technology for pellet type fuel.

From this experience, coating technology of carbon and SiC by CVD techniques was established. However, difficulty was encountered with coating of particles of very small diameter.

In the coated particle fuel technology, a fluidized bed system is generally employed to coat the entire surface of sphere particles without defects. In order to visibly observe the formation of a fluidized bed with particles of about 600 μm in diameter, a simulation test was carried out to optimize the formation of the fluidized bed, using a transparent cylindrical annular column of about 50 mm (2 inches) inner diameter and ZrO_2 beads with a similar diameter as UO_2 kernels. As a consequence, it was observed that the design of the inlet nozzle for carrier and reactant gases plays an important role in the design of fluidized bed furnaces.

Based upon these kinds of simulation tests and previous experience mentioned above, a laboratory scale fluidized bed reactor was designed, manufactured and installed in KAERI.

Construction of the CVD furnace together with the associated gas supply and control system and the ventilation system for off-gas treatment. The vertical furnace has a graphite heating system with which a maximum temperature of a 1700°C can be attained with a constant heating zone about 100 mm long, and a 50 mm (2 inch) graphite reaction tube with specially designed gas nozzles for carrier and reaction gases at the gas inlet. By utilizing this system, after several successful test runs, experiments on coating of PyC and SiC layers on fluidizing ZrO_2 beads were carried out to observe the formation of the coating layer and to optimize the behaviour of fluidization of the particle bed and the characteristics of the coating layers. Figure 3.23 shows examples of PyC and SiC coatings.

Figure 3.23 (a) shows the macro-graphs of the surrogate kernel material (ZrO_2 bead) before and after coating. In order to develop the coating technology of PyC and SiC layers, experiments were carried out, in the first place, to attempt coating with a single layer of PyC and SiC separately (Fig. 3.23 (b) and (c)). After several runs of the experiments for the control of thickness and densities in a single PyC or SiC layer, attempts were made to coat four different layers at one experiment run with a parametric condition pre-determined in the single layer experiments. Figure 3.23 (**d**) shows a typical ceramographic micro-structure of the TRISO coated particle layers with up-to-dated developmental status, revealed by SEM. It still remains further experiments of the coating of PyC and SiC to establish optimum conditions for the coating process for PyC and SiC within the specified characteristics of respective coating layers.

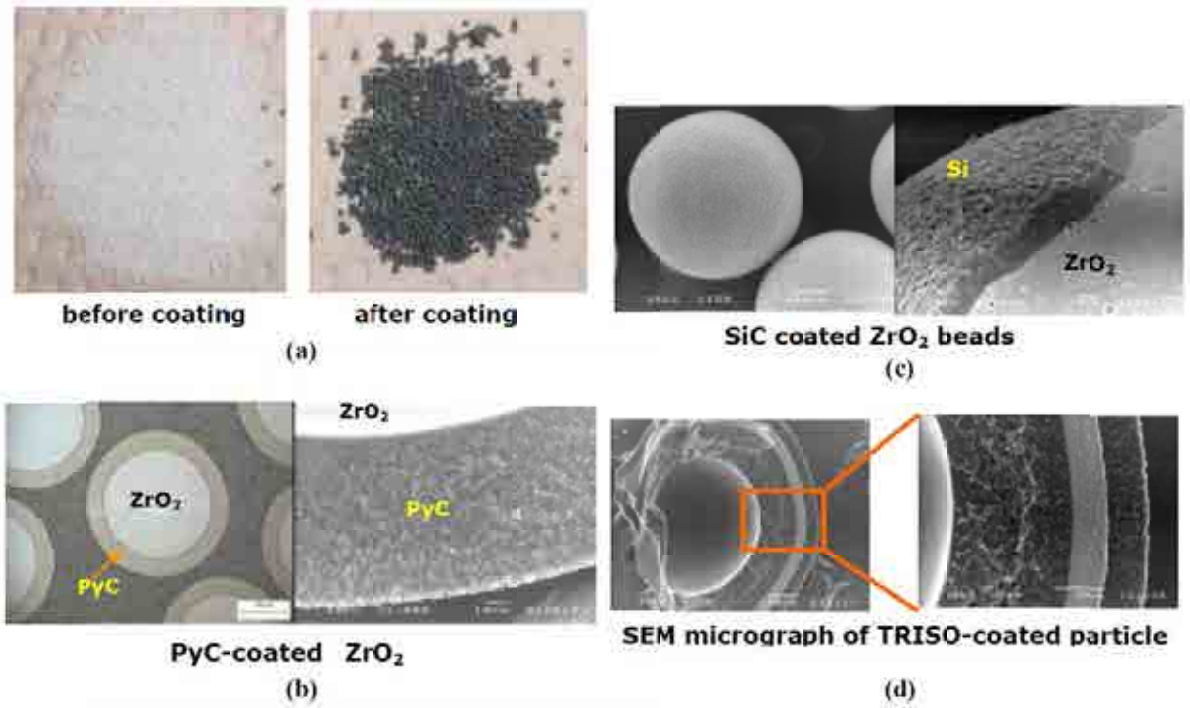

FIG. 3.23. Examples of PyC and SiC coating on surrogate ZrO_2 beads (a) macro-graphs of ZrO_2 before and after coating; (b) PyC-coated ZrO_2 and its coating layer(c) SiC-coated ZrO_2 and its coating layer; (d) micro-graph of the TRISO particle with four coating layers.

3.7. FUEL PRODUCTION ACTIVITIES IN THE REPUBLIC OF SOUTH AFRICA

3.7.1. Introduction

Project for the pebble bed modular reactor (PBMR) is being performed in South Africa. The PBMR is expected to achieve the goals of safe, efficient, environmentally acceptable and economic production of energy at high temperature for the generation of electricity and industrial process heat applications.

The PBMR uses fuel consisting of coated enriched uranium fuel kernels embedded in graphite spheres. Fuel kernels are coated with successive layers. The innermost layer is porous carbon, which allows fission products to collect without creating internal pressure. The next layer is pyrolytic carbon, followed by silicon carbide and a final pyrolytic carbon layer. These outer three layers create a compound barrier against fission product release of which the silicon carbide coating plays the dominant role. A predetermined mass of these already 'contained' fuel particles (each now approximately 1 mm in diameter) is then embedded inside a 50 mm graphite sphere, which is then covered with a 5 mm fuel-free graphite layer. The graphite making up the sphere acts as a moderator, and the outer layer protects the fuel particles from mechanical effects, such as abrasion. Figure 3.24 shows the design of the PBMR fuel sphere [69].

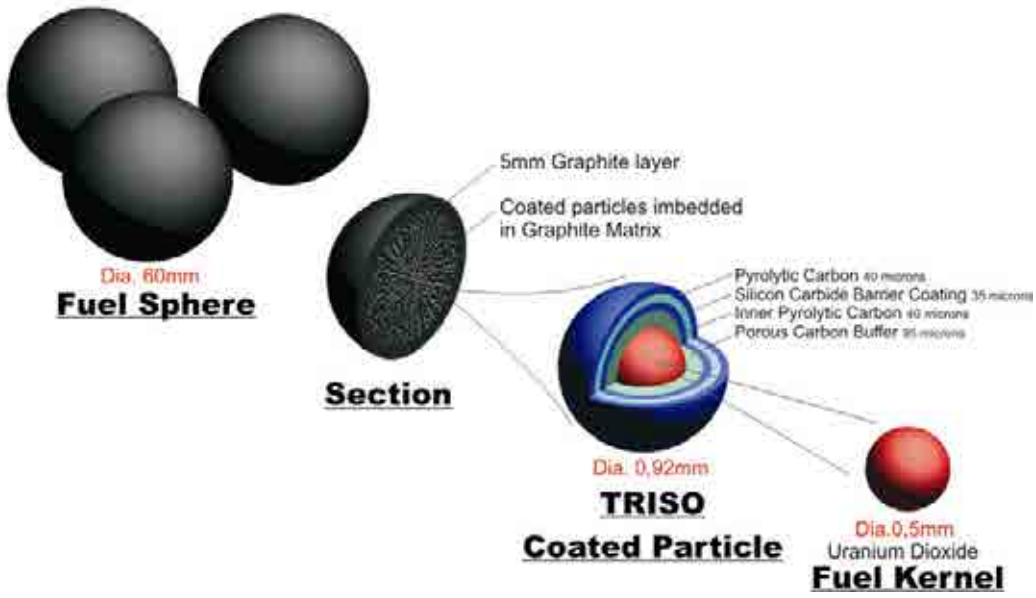

FIG. 3.24. PBMR fuel element.

3.7.2. Manufacturing technology basis

One of the essential points of the PBMR philosophy is to use the well proven and qualified German LEU TRISO fuel element The PBMR fuel manufacturing process steps and principles have been specified to be the same as those that were used in Germany. PBMR purchased the German HTGR fuel manufacturing technology. Access has been gained to the documented German HTGR fuel manufacturing know-how. This includes the following documents, amongst others [70]:

- Specifications for direct materials (matrix graphite constituents);
- Specifications for products and intermediate products;

- Testing and acceptance requirements;
- Fabrication and inspection procedures;
- Production information;
- Plant licensing information.

3.7.3. PBMR fuel development laboratory

3.7.3.1. Purpose and organization of the laboratory

In order to synchronize fuel availability with the planned fuel loading date of the Eskom demonstration plant, PBMR FUEL (PTY) LTD. shall first construct a pilot plant with the production capacity of 270 000 fuel spheres per annum. This plant shall be located at Pelindaba and housed in the PWR fuel manufacturing facility. The purpose of the laboratory work [70–74] is to accomplish the following in advance of commissioning of the PBMR pilot fuel plant:

- Reproduce on laboratory scale the latest German HTGR TRISO fuel manufacturing technology and thereby gain experience and understanding of the processes and materials that will be used in the pilot fuel plant;
- Develop the QC test methods, perform capability studies and qualify the QC test methods;
- Establish and qualify suppliers of materials;
- Train core staff for the pilot fuel plant.

The PBMR Fuel Development Laboratories at Necsa's Pelindaba site includes the following laboratory scale facilities for development of the expertise required to manufacture PBMR Fuel:

- The Kernel Laboratory for uranium dioxide kernels;
- The Coating Laboratory for TRISO coated particles;
- The Graphite Laboratory for PBMR spherical fuel elements (FEs);
- The QC Laboratory to perform the prescribed chemical, physical and dimensional tests.

3.7.3.2. Kernel laboratory for UO_2 kernels

The Kernel Laboratory started manufacturing UO_2 kernels in 2002. Initially the throughput of the Kernel Laboratory was very low, less than 200 g of UO_2 kernels being produced per week. Early in 2005, the throughput was increased to 1 kg of UO_2 kernels per week to confirm that the processes were repeatable and consistent with higher throughput. Once the Advance Coater Facility, with a 5 kg UO_2 kernel batch loading, was being designed and constructed, the Kernel Laboratory throughput increased to 5 kg of UO_2 kernels per week in order to be able to supply the Advance Coater with feed stock.

The laboratory kernel production facility is based on the same process outline and process principles as the reference technology for the external gelation process, as well as the same process parameter values, but with changes as necessary to accommodate the laboratory scale equipment.

Figure 3.25 shows the schematic diagram of the external gelation kernel production process used in the PBMR Fuel Kernel Laboratory. U_3O_8 powder is dissolved in nitric acid to form a uranyl nitrate solution according to the chemical reaction:

$$3\ U_3O_8\ (s) + 20\ HNO_3\ (aq) \rightarrow 9\ UO_2(NO_3)_2\ (aq) + 10\ H_2O + 2\ NO\ (g)$$

The uranyl nitrate solution is pre-neutralized with dilute ammonium hydroxide to just prior to precipitation of the uranium according to the following reaction:

$$2\ UO_2(NO_3)_2\ (aq) + NH_4OH\ (aq) \rightarrow 2\ UO_2(NO_3)_{1.5}(OH)_{0.5}\ (aq) + NH_4NO_3\ (aq)$$

A casting solution is prepared by adding specific amounts of organic additives to the pre-neutralized uranyl nitrate solution. These additives adjust the surface tension and viscosity to ensure proper droplet formation and also assist with later uniform shrinkage of the kernels and to establish the required crystal growth of the uranium.

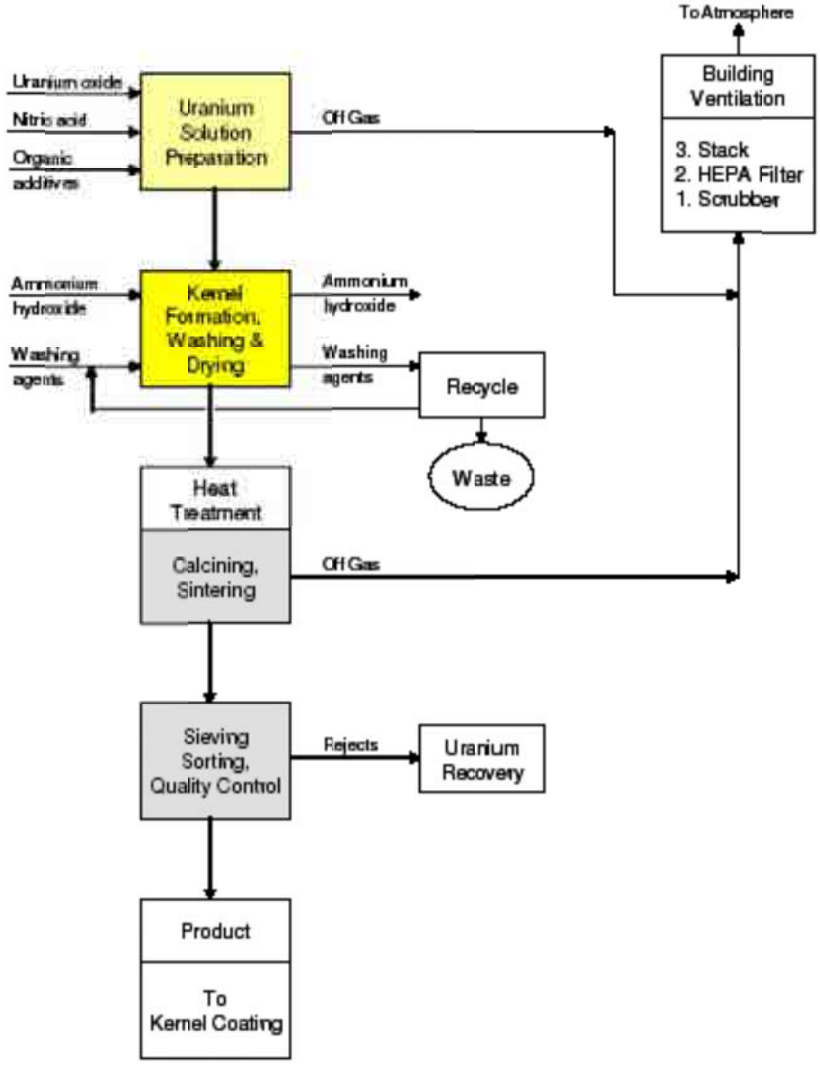

FIG. 3.25. Schematic of the UO_2 kernel production process as followed in the Kernel Laboratory.

Casting is carried out in a glass column filled with the concentrated ammonium hydroxide precipitation solution (Fig. 3.26, left). The casting solution is pneumatically fed to the nozzles at the top of the column where a vibrator 'shakes off' droplets from the feed stream. 100 discrete droplets are formed per second from each nozzle. The droplets fall through air where they attain a spherical shape as a result of surface tension. The spherical droplets then pass through an ammonia atmosphere where ammonia gas is blown directly onto the droplets to create chemical reaction with the uranyl nitrate on the surface of the droplets. The uranyl nitrate precipitates as ADU in the outer layer of the droplet, forming a protective film. This film enables the droplets to retain their spherical shape on impacting precipitation solution without deforming.

As the reaction continues in the casting column, ADU forms throughout the kernels, with ammonium nitrate as by product:

$$2\ UO_2(NO_3)_{1.5}(OH)_{0.5}\,(aq) + 2\ NH_4OH\ (aq) \rightarrow (NH_4)_2U_2O_7\ (s) + NH_4NO_3\ (aq) + H_2O$$

The kernels are kept in the casting column until they are strong enough to be processed further. The diameter of a cast gel kernel is about 1.8 mm.

Once casting is complete, the wet kernels and the accompanying precipitation solution are transferred from the casting column to a rotary flat tank, known as the AWD (Ageing, Washing and Drying vessel). During ageing, the AWD is heated with steam to 80°C. The ageing process fully converts the gel spheres to ADU kernels, and initiates the crystal growth in the kernels.

Initially during the development of the process, ageing had been done in the bottom part of the casting column where the column was heated with silicone oil to 80°C. However, the laboratories were established as the forerunner for the Fuel Plant, with the philosophy of replicating the processes and equipment as close to the German HTGR technology as possible. With this in mind, it was decided to build the rotary flat tank similar to the one used at HOBEG in which ageing, washing and drying of the kernels could be done (Fig. 3.26, right).

After ageing, the solution is drained from the AWD. The ADU kernels in the AWD vessel are washed with water to remove the ammonium nitrate as well as ammonium hydroxide and some of the organic additives. The wash water is drained, and the kernels are washed with alcohol to remove moisture, and any remaining additives.

Following drying, the ADU kernels are calcined in air above 400°C in a batch furnace. The remaining organic additives are cracked and evaporated from the kernels during a gradual temperature increase. From 300°C, the ammonium diuranate is converted to UO_3 according to the reaction:

$$(NH_4)_2U_2O_7\,(s) + O_2\,(g) \rightarrow 2UO_3\,(s) + 2H_2O\ (g) + NO\ (g)$$

The diameter of a calcined kernel is 750 μm and the bulk density ~2 Mg/m^3.

After calcining follows reduction and sintering at high temperature to reduce the UO_3 to UO_2, remove remaining impurities and densify the kernels. The process is carried out under 100% hydrogen:

$$UO_3\,(s) + H_2\,(g) \rightarrow UO_2\,(s) + H_2O\ (g)$$

The reduction of the kernels takes place between 450°C and 650°C where after the temperature is increased to 1600°C in order to form dense, stoichiometric UO_2 kernels that have a diameter of 500 μm and a density just below the theoretical value of 10.96 Mg/m^3. The final production steps are sieving to remove any under and over sized kernels, followed by sorting to remove any odd shaped particles. The latter is performed on a sorting table that is slightly inclined to allow spherical kernels to roll down-hill while odd shaped particles are vibration transported along a perpendicular direction and collected for recycling.

FIG. 3.26. Multi-nozzle casting column (left) and steam jacketed ageing washing and drying vessel.

3.7.3.3. Coating laboratory for TRISO coated particles

In 1999 work was begun to build a one-fifth scale (1 kg UO_2 charge; 20 kW power consumption) coater at the NECSA laboratories. This was embarked upon in order to

- gain understanding of coating processes so as to produce particles that are equivalent to the latest German HTGR technology;
- train personnel;
- provide initial material for the quality control and fuel sphere laboratories, for the further development of their methods and processes.

Only depleted (< 0.7% ^{235}U) UO_2 kernels have been used in the small coater.

In 2003, PBMR decided to build a 'full size' (5 kg UO_2 charge; 110 kW power consumption) coater, also at the Necsa laboratories. This coater was designed to be the prototype for the coaters of the same size in the planned pilot fuel plant. The 5-kg coater is therefore also known as the 'Advance Coater'. Its goals are to

- mitigate the risks for the pilot fuel plant. Coaters and coating technology are seen as the biggest risk due to their complexity. Other coating systems copy inherently simpler proven German systems. The coater was intended to be as close a copy of the German coater as possible, so as to be able to produce fuel that is equivalent to the German fuel.
- train production plant personnel, as the coater will operate eventually with depleted (< 0.7% of ^{235}U) UO_2 kernels.
- enhance the understanding of coater processes and of coatings behaviour.
- demonstrate modifications intended for the production plant that can enhance its productivity.

The four coating layers are deposited on kernels in a heated furnace by a process called chemical vapour deposition (CVD). The process outline to coat kernels with the four layers is shown in Fig. 3.27.

3.7.3.4. Graphite laboratory for PBMR spherical fuel element

The laboratory facility for the preparation of matrix graphite powder, overcoating of coated particles, and manufacture of fuel elements is based on the same principle process steps as those used in Germany. The process outline to manufacture fuel elements is shown in Fig. 3.28.

Generally the equipment designs have been modified to accommodate the laboratory scale production, but key process variables are equivalent; for example:

- Pressing moulds and pressures;
- Carbonizing temperature and atmosphere;
- Annealing temperature and atmosphere.

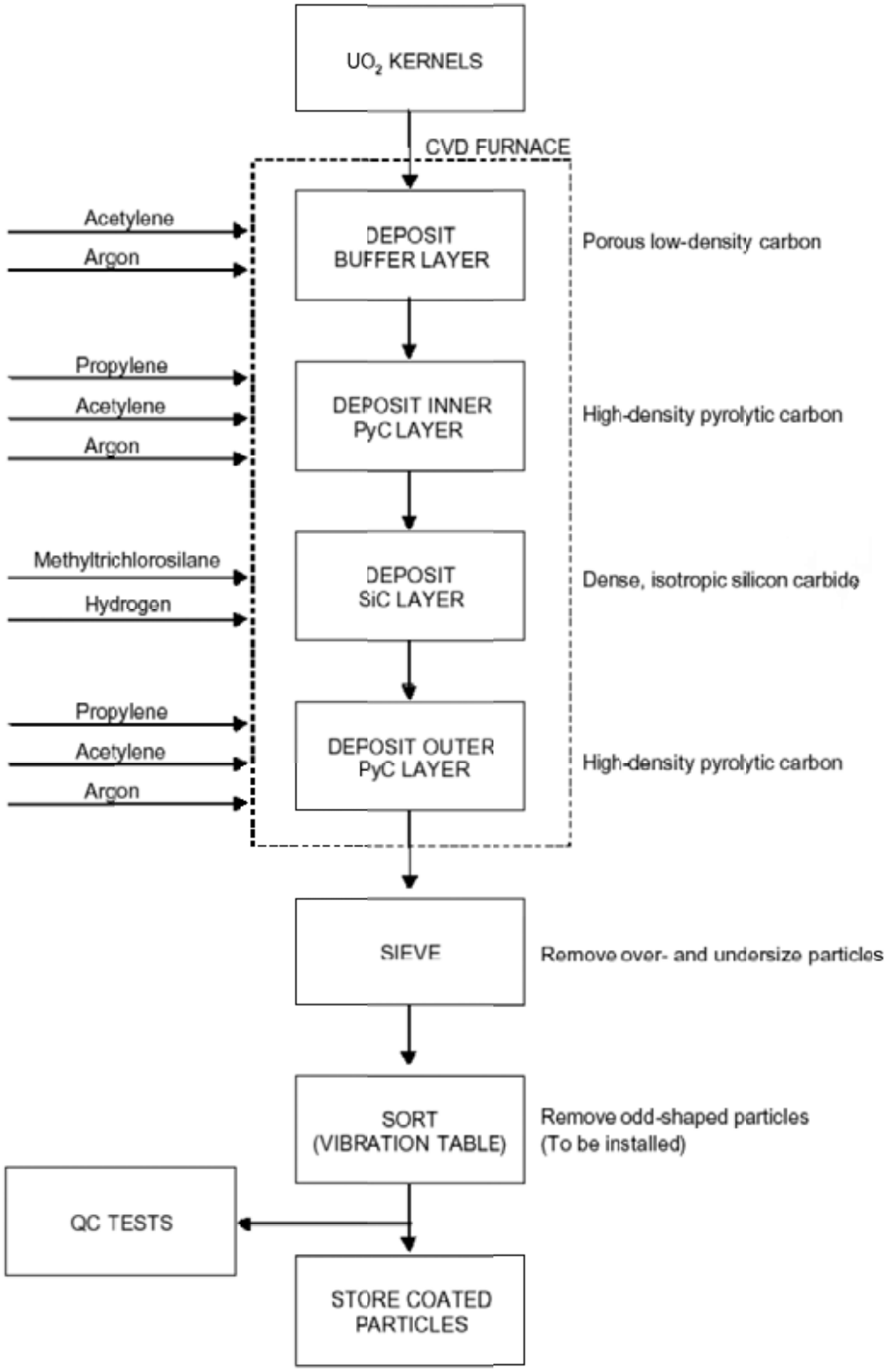

FIG. 3.27. Coating process.

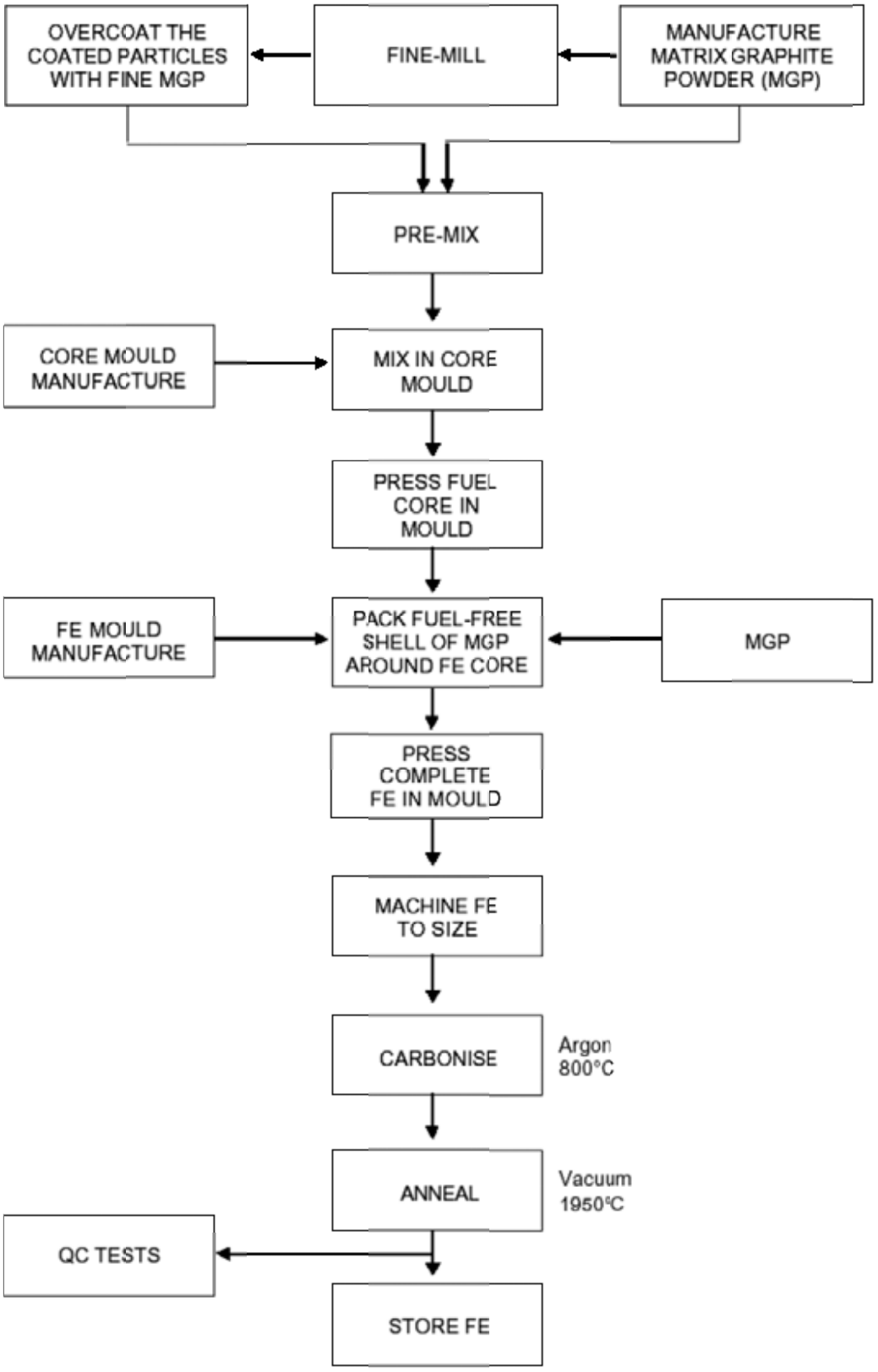

FIG. 3.28. Spherical fuel element manufacturing.

All the equipment needed to manufacture (pressed) graphite spheres and fuel elements are fully operational. Suppliers of natural graphite and electro-graphite powders have produced batches of material for development work in the laboratory. Matrix graphite powder and overcoat matrix graphite powder have been routinely made on laboratory scale (2.5 kg batches). The design of the tooling for the pressing moulds, as well as the material and process for manufacturing the moulds, is sufficiently developed to be able to produce working press moulds.

Technology to pre-press graphite cores and thereafter press graphite spheres at high pressure is sufficiently developed to be able to manufacture small laboratory batches of graphite spheres routinely that conform to density and crushing strength requirements after carbonisation and annealing.

3.7.3.5. Quality control laboratory

The quality control (QC) methods have been specified to be the same as those in the reference technology, but other methods are used if they can be shown by means of capability studies to provide adequately accurate results.

The QC laboratory is being equipped and the test methods developed as required for the pilot fuel plant. Necsa's analytical laboratories are being used for isotopic and impurity analyses of uranic materials. Most of the equipment items needed in the QC laboratory are already available. The test methods are being installed and validated to support the development activities in the process laboratories as well as the selection and pre-qualification of suppliers of materials.

Following the production process, the kernels are sent for extensive analyses to the PBMR Fuel Quality Control Laboratory before being accepted as good quality feed stock for the coater. Table 3.14 contains the results currently obtained for UO_2 kernels produced in the Kernel Laboratory, with a comparison to the specification.

The UO_2 kernels, coated fuel particles and spherical fuel elements manufactured in laboratories at NECSA's Pelindaba site are shown in Figs 3.29, 3.30 and 3.31, respectively [70].

TABLE 3.14. COMPARISON OF THE CURRENT RESULTS WITH THE CURRENT PRODUCT SPECIFICATION

Requirement	Specification	Average results for 2006	Remarks
Stoichiometry	O/U ≤ 2.015	2.014	On average, all kernel batches are within specification
Diameter	95% of kernels within 450–550 μm confidence level of 95%	499 ± 12 μm	All kernel batches are within specification
Sphericity	90% of kernels ≤ 1.2 confidence level of 90%	1.11	All kernel batches are within specification; however, it is aimed to obtain sphericities of below 1.05
Density	≥ 10.5 Mg/m^3	10.77 Mg/m^3	All kernel batches are within specification

FIG. 3.29. Photographs of UO_2 kernels.

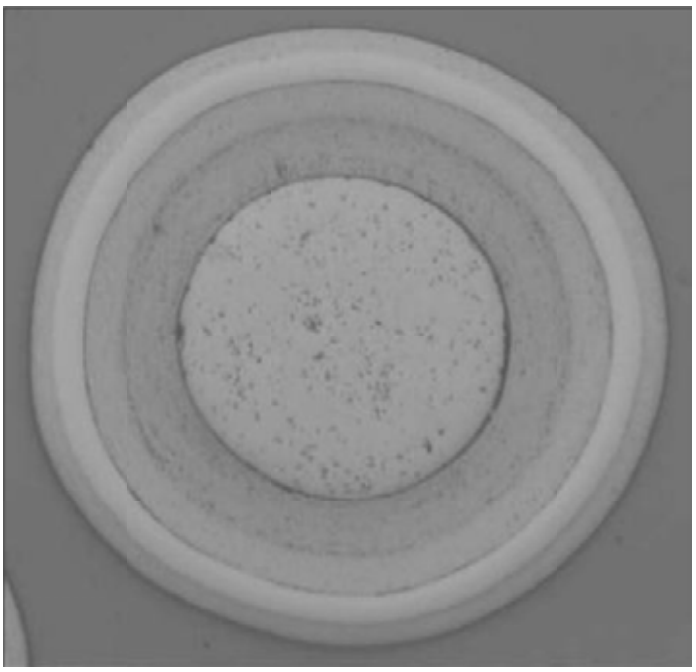

FIG. 3.30. Ceramography of the coated fuel particle.

FIG. 3.31. Photograph of the spherical fuel elements.

3.8. HISTORY OF THE DRAGON REACTOR FUEL DEVELOPMENT IN THE UNITED KINGDOM

This section gives an overview of the historic development of HTGR fuel describing the origin of coated particle fuel for the Dragon Project [32, 75].

3.8.1. Dragon reactor core structure

The Dragon reactor was the first demonstration high temperature gas cooled reactor built in the 1960s. Thirteen OECD countries began this project in 1959 known as Dragon at Winfrith in the UK to serve the growing needs of the HTGR community for irradiation testing of fuels and fuel elements, and technological tests of components and materials. Criticality was achieved in August 1964 and full design power of 20 MW was reached in April 1966. The reactor was finally shut down in September 1975. The core had a maximum thermal power of 21.5 MW (reached in May 1971) with corresponding core inlet and outlet temperatures of 350ºC and 750ºC respectively.

The core of the Dragon reactor was prismatic with an effective diameter of 1.08 m and formed by 37 fuel element clusters held between the top block and bottom ring and arranged in a hexagonal array. Because of the small size of the reactor core and the consequent neutron leakage, a fuel element cluster consisted of six fuel rods containing highly enriched ‘driver’ fuel surrounding a central rod that contained an experimental section. A fuel rod was made up from 30 annular graphite fuel compacts within graphite sleeves. The standard Dragon fuel element had an overall length of 2.54 m with both ends to contain reflector material and a 1.60 m middle section to contain the fuel. With this fuel design, it was possible to irradiate experimental fuels to 1000 days or more by exchanging the driver fuel every 200 days.

Helium coolant was flowing through the annular gap between graphite tube and fuel body. The fuel element clusters could be individually purged from fission gases which proved to be very useful in tracking defective fuel. There was considerable flexibility in the fuel element design. A total of 25 fuel element varieties for the Dragon core were developed during the course of Dragon operation. Three examples are shown in Fig. 3.32 [32, 75].

3.8.2. Stage-I period of fuel development

3.8.2.1. Releasing fuel versus retaining fuel

Back in 1960, HTGR fuel development work was concentrated on fuel, from which it was hoped (!) that fission products would be released, thereby removing parasitic neutron absorbers from the core. The fuel manufacturing process for an 'emitting' type of fuel was comparatively simple involving cold compaction of graphite powder and the appropriate metal or carbide powder into fuel inserts followed by reaction sintering to form the carbides. The annular fuel bodies were then loaded into fuel boxes, which themselves were placed in the graphite tubes of the fuel element cluster. Purging of the clusters was made to remove high neutron cross-section gaseous fission products from the core.

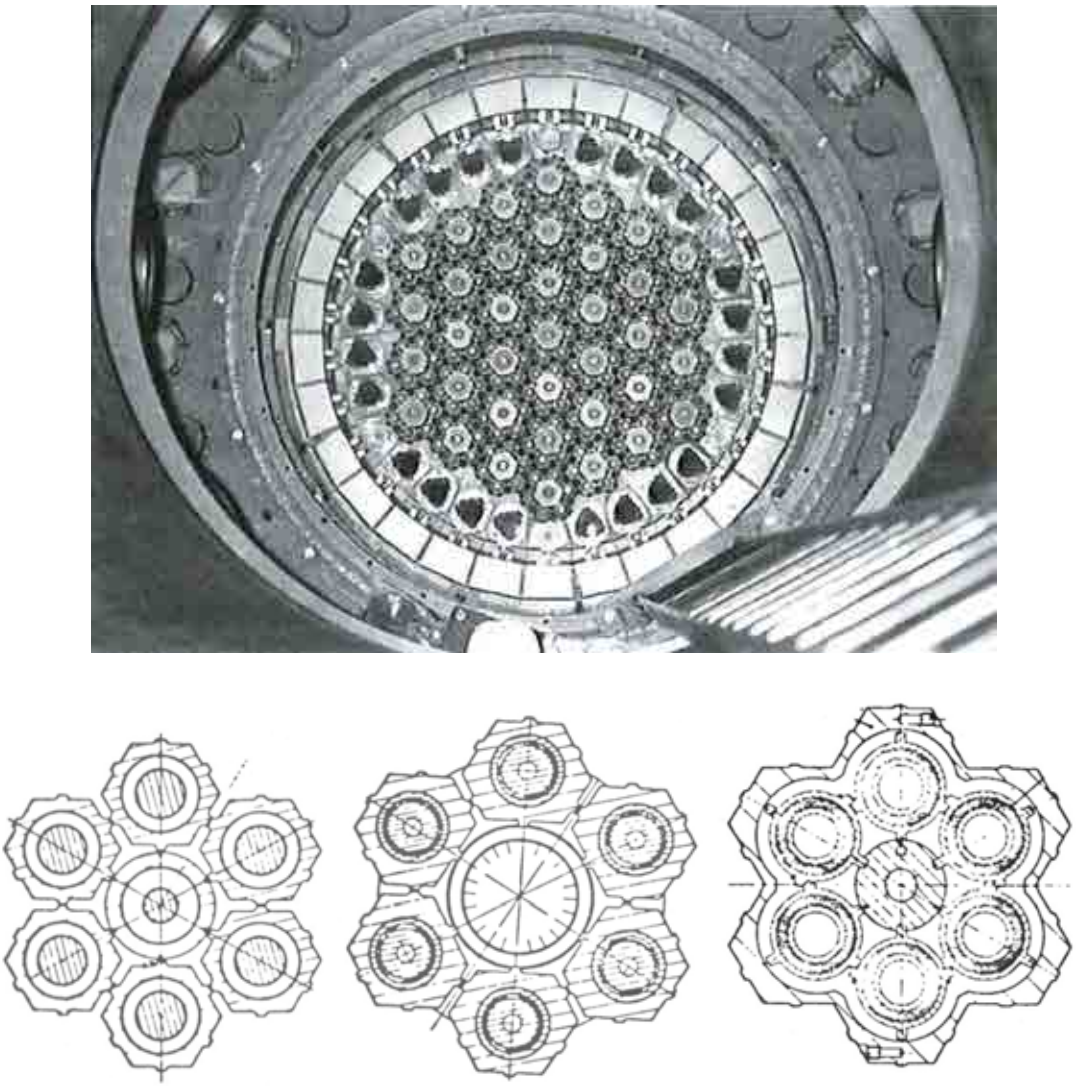

FIG. 3.32. Dragon reactor core (top) and some of the fuel element varieties (bottom); bottom left: D4 with experimental fuel in the centre rod; middle: D9 with enlarged centre rod to allow full-size German fuel spheres; right: D13 reference fuel element design.

Up to the end of 1961, materials development work had concentrated on fission product emitting fuel. But already in the early days of the HTGR it was recognized that a fission product emitting fuel would not be acceptable for a power reactor due to the implied radiation dose to the operators and the consequential maintenance problems resulting from the migration of gaseous or volatile fission products and circuit contamination. Such a fuel concept was not considered viable to progress to a prototype power reactor. Hence a parallel concept was pursued where the fission products are retained in situ.

Originally proposed by Roy A. U. Huddle in October 1957 and patented in March 1959, the particle with a pyrolytic carbon coating as barrier to the escape of fission products became a considerable option. The advantage of a delay in fission product release by a few hours was that most of the heat release would be inside the boxes.

3.8.2.2. Fuel fabrication

Principal objective of the 1st charge loading was to irradiate fuel for the thorium cycle. The fuel was in form of a carbide with 93% enriched uranium arranged in a two-zone core. The

ten centrally located fuel element assemblies contained the fertile material thorium at a $Th/^{235}U$ ratio of ~10 with the remaining 27 fuel elements mainly serving to drive the reactor ('driver' fuel). The highly enriched uranium (or driver) zone of the core should operate for as long as possible, but it was considered unlikely that an unalloyed fissile coated particle could withstand a burnup of 30–50% FIMA. Therefore, it was decided to use zirconium as an alloying diluent to reduce burnup. For the zirconium-containing fuel, uranium monocarbide was ground to powder and then mixed with zirconium monocarbide, formed into micro-spheres by agglomeration, and sintered to form (Zr,U)C driver fuel with a $Zr/^{235}U$ ratio of ~8 [76].

In essence, the method of making particles studied was powder agglomeration. The correct size was achieved by building up the particle as with a snowball. The powder agglomeration process gave spheroidal particles at a reasonable rate and with a yield approaching 100%. It readily gave a porous sintered particle which was thought necessary to provide free space for the fission gases. The process also permitted a wide variety of compositions to be made with ease. A porous kernel made by a dry process became one of the important features of Dragon reference particles, whereas liquid routes to make spheroidal particles, such as the ORNL sol-gel process, were not pursued.

Particle kernel used in driver fuel had a diameter between 251 and 422 μm (defined by passing through respective sieves), while they were sized between 353 and 500 μm for the fertile fuel. For experimentation, the centre rods of three fuel element assemblies were used for the so-called Metallurgical Series I (MET-I) elements each containing 43 varieties of fuel (plus some 2000 graphite specimens).

Work on ceramic coated particle fuel at the Battelle Memorial Institute in the USA had shown that irradiated UO_2 particles coated with alumina in a fluidized bed had favourable gaseous fission product retention characteristics. By the end of 1960, the technique had been adapted successfully to the coating of uranium and thorium carbide micro-spheres with pyrolytic carbon. The success of the fluidized bed process lay in the use of much larger, nearly spherical fuel kernels (> 100 μm diameter) compared to the small irregular particles that came out of the tumbling bed furnace. It could be demonstrated that PyC also provided an effective means of retaining fission products. Although it was recognized that kernels had some retention capability, it was found in experiments that fission products such as caesium, strontium, or barium could diffuse through the pyrolytic carbon layer. Studies on metallic carbides had suggested that a silicon carbide or zirconium carbide intermediate layer could be incorporated into the particle design having the advantages of low neutron capture cross-section, impermeability to fission products, and compatibility with the fuel and pyrolytic carbon.

Soon afterwards, also in the UK at the Royal Aircraft Establishment, Farnborough, a successful coating was carried out on a silica fluidizing reactor using a 1 inch laboratory coater. By the end of 1961, sufficient progress with coated particle fuel manufacture had been made such that the recommendation was given to use coated particle fuel for the initial charge of Dragon. During 1962, a prototype fluidizing apparatus was developed at Winfrith where a 2 inch fluidizing reactor was installed. Coater size eventually increased via 3 inch to 5 inch furnaces.

For the first charge, fuel particles with zirconium/uranium carbide and thorium/uranium carbide were embedded in a resin coated graphite powder matrix to form annular shaped fuel compacts. In the 'admix' process developed for the early fuel loads, the basic ingredients of the fuel compact matrix were a high char yield resin and graphitized petroleum coke filler.

The initial development of a fabrication route for the fuel bodies was dictated by the requirement of coated particle volume fractions as high as 50%. At this level, many particles had direct contact, which allowed only very low forming pressures to avoid particle damage. The process evolved was based on the UK powder casting process which subsequently has been used commercially for the manufacture of high precision moulds. It used graphite powder coated with a thermosetting resin as matrix, a forming pressure of ~0.7 MPa (100 psi) followed by benzene vapour impregnation to densify and strengthen the resulting compact by carbon deposition.

When the fuel particle parameters were finally specified, it was apparent that with a maximum coated particle loading of less than 30% by volume, higher forming pressures were possible. Also the gas impregnation operation could be eliminated, which although practicable, complicated the production route. It was found from experiments on density, strength, and particle damage, that a forming pressure of ~7 MPa (1000 psi) with no impregnation gave satisfactory results, and this route was, therefore, adopted for the initial charge of Dragon.

In May 1963, the important decision was made to use coated particle fuel for the first charge of Dragon. Its manufacture, a total of 18 fuel elements with 'releasing' type fuel containing (UZr)C kernels coated with pyrolytic carbon only, was completed by June 1964, in time for criticality to be achieved on 23 August 1964 (with 16 of the 18 elements of the outer ring). The complete core loading of 37 fuel elements was achieved in February 1965. The mean production rate of the first charge was 1.2 fuel elements per week. For the zirconium-containing driver fuel the apparent loss of ^{235}U was 1.6% and for the thorium-containing fuel 0.7%. Reject fuel was not recovered at the time; nevertheless, the overall yield on a once through basis was impressively high. Fuel charge 1 was operated over 229 efpd.

3.8.2.3. Fuel quality control

From 1963, fuel quality control was gradually beginning to emerge. A Quality Control Worki was set up for the development of suitable quality assurance methods. It was mostly used for the ceramographic examination of coated fuel particles and a non-destructive examination for fuel compacts, graphite fuel tubes, alpha contamination and metrology of the fuel particles. Many other physical properties of fuel body and fuel particle were measured, but only on a very small number of samples. The small size of the particles necessitated a statistical approach to quality during manufacture. Many of the methods developed became well established testing procedures with a high degree of confidence, but a number of physical property measurements were discontinued as a routine after the completion of the first charge. There was, however, initially an important test procedure missing at that time which was the estimation of the broken particle fraction in consolidated fuel, although acid leaching for estimation of broken particles in coating batches was carried out. But once the broken-particle test and associated statistical methods had been developed, examination of the various stages of manufacture enabled to identify the critical parts of the process, and this feedback led to a progressive reduction in the overall broken particle fraction in the reactor. The information on the defective particles assisted in the interpretation of irradiation experiments.

3.8.3. Coated particle development for commercial HTGRs

Following the successful Stage 1 period, which had demonstrated the feasibility of the fabrication of coated particle fuels and their performance and the improvement of fuel quality, work on Stage 2 turned towards the study of these fuels for power producing versions of the HTGR involving a very flexible approach to the fabrication aspects and the development and exploitation of a very extensive irradiation and post-irradiation examination programme. At

this time it was considered that a commercial system would be launched using the thorium high enriched uranium cycle. Thus, 'feed and breed' reference fuels were specified.

During an initial phase, the main factors controlling the performance of coated particle fuels were identified. An extremely wide range of fuels, including Pu fuel, was fabricated and irradiated. Kernels were produced by both melting and sintering and the first comparisons between the behaviour of pyrolytic carbon (PyC) and silicon carbide coatings were made, with the latter clearly superior to plain PyC coated fuels. At this time the development of the replaceable experimental fuel elements in Dragon (such as the D5 design where six driver channels surround one experimental channel) was a key feature of the programme.

For the 2nd charge, the Dragon core needed 32 new fuel element assemblies. Due to the aim of an unpurged fuel element design, a new type, D4 MK II, was developed where only the central rod as an experimental section remained purged, whereas the surrounding six 'driver' fuel rods were unpurged. By January 1967, every fuel element was of this type. Also the new designed 'UC-10' (UC_2 with excess carbon at a $C/^{235}U$ ratio of ~10–12) fuel kernel with a 420–572 μm diameter and a TRISO coating was applied in the driver zone. Furthermore the particles received a thick overcoating. The driver fuel considered the 'Dragon Reference Particle' consisted of fuel particles with an 800 μm UO_2 kernel and a TRISO coating, bonded together in a carbonaceous matrix and pressed to compacts. Fuel charge 2 was operated over 262 efpd.

A significant portion of the 2nd charge was experimental fuel tested in a large scale comparison of fuel compositions and coatings, and also for different irradiation times with the goal of extending fuel lifetime. They contained oxide or carbide mixed compounds, involving low enrichment uranium, thorium and plutonium, and with BISO or TRISO coatings.

Charge 2 included approximately 10 g of plutonium contained in TRISO coated fuel particles which were placed in cartridges. This amount of Pu is about the same as was produced in charge 1 from neutron capture of the ^{238}U during operation [77]. Also interest shifted from the thorium cycle to a LEU fuel cycle in a heterogeneous core which was considered an attractive alternative to the AGR. The first such fuel was fabricated for irradiation in June 1967, and the first experiments were reasonably successful and led to the specification of the so-called LE reference fuel. This switch to uranium fuel cycles was also influenced by doubts over high enriched uranium availability and thorium recycle technology.

In the 3rd charge starting in July 1968, 13 new fuel elements with introduced, with them 26 of the 37 being of the D5 type, where the centre rod and the surrounding driver rods were independently replaceable. Following the new fuel concept, by far most of the driver fuel was oxidic: UO_2+10C, UO_2+5C, UO_2+33C, UO_2+18C. Total production of this oxide fuel was around 650 kg of coated particles used in 43 000 compacts of various types and dimensions, of which some 33 000 compacts were the 'standard D13 type fuel'. With charge 3, a cyclic mode of operation was pursued, which allowed the variation of residence times for the experimental fuel unlike the once-through character of the charges 1 and 2. Cycling was made by exchanging 20% of the driver fuel every 30 efpd [32].

The pin in block design for fuel elements, which was already tested with the earlier fissile–fertile fuel system to avoid high stresses in the main structural components of the core, was also later employed for the LEU fuel tested in the D14 and D16 type fuel elements. With beginning of charge 5, the first integral multi-hole graphite block fuel element (type D22) was introduced into the Dragon core investigating the block design as was used for the US Fort St. Vrain HTGR.

By the end of 1973 a sound basis of knowledge had been reached on the factors limiting the performance of LEU fuels. Large quantities of fuel had been produced and irradiated and some fuels had been irradiated to almost full lifetimes. Design rules for the fuel particles had been quantified for the three main performance limiting features (amoeba failure, pressure failure, fast neutron dose limit for PyC) enabling the designer to specify operational margins.

3.8.3.1. Kernel fabrication

As far as LEU cycle fuel was concerned, the main attention was directed towards the suppression of amoeba failure by development of additives to the kernel to cause gettering of the oxygen released on fission, and thus reduced formation of CO which was involved in the attack of the coating. This was explored in two main developments: (i) the incorporation into the kernel of cerous oxide which could form a solid solution with sub-stoichiometric uranium oxide, and (ii) the addition of another phase to getter the oxygen directly, e.g. ZrC or SiC.

For the advanced fuels in the Th–U cycle, the main areas of development were to produce an improved fully enriched uranium fissile particle from the viewpoint of very high temperature stability and to explore a chemical gettering system for the fission products in the thorium oxide fertile particle. The main variants on the reference UO_2 fuel were by means of dilution with carbon (using the carbon agglomeration route or the WAR process developed by ORNL[1]) or with alumina (UO_2+Al_2O_3), or to alter the composition to uranium carbide with zirconium carbide additions (UC+ZrC, UC+5ZrC). Some experiments also involved uranium carbo-nitride kernels. A large number of oxide getters was examined to explore the possibility of fission product gettering in oxide fuels (Al_2O_3, Ce_2O_3, SiO_2, ZrO_2, $Al_2O_3{\cdot}SiO_2$, Cr_2O_3, Fe_2O_3, MoO_3, MnO_2, Nb_2O_5, TiO_2, V_2O_5, Y_2O_3).

The production of green kernels by the powder route was very simple. The required weights of carbon black, UO and furfuryl alcohol were intimately mixed in an edge runner mill producing a slightly compressed and well dispersed mixture. The mix was then reduced to granules and powder by passing through a series of sieves. The granules and powder were spheroidized on a planetary mill and the required size fraction shape separated on an inclined vibrating plate. Acceptable particles were exposed to hydrogen chloride vapour to polymerize the furfuryl alcohol. Heat treatment of the green kernels was carried out in a static atmosphere of carbon monoxide to minimize the formation of uranium carbide.

The specification of UO_2 particle size was found to be very important in this process. The UO_2 powder available initially consisted of particles up to 250 μm which gave problems of uniform dispersion in a nominally 600 μm diameter kernel and also caused severe segregation of the UO_2 during the spheroidizing process. These problems were immediately eased by sieving out particles greater than 100 μm from the UO feed powder and in the longer term the specification for the supply of new UO was modified.

The liquid route for kernel manufacture was more complicated than the powder agglomeration process and required more elaborate control of the initial stages of kernel heat treatment. Particle shape was better, leading to a reduction in the within-particle variation of coating thickness. Methods of sphere formation needed further development to render them

[1] Presized weak acid resin (WAR) ion exchange materials made from acrylic acid/divinyl benzene copolymers are loaded with uranium from uranyl nitrate solution, dried, and then heat-treated to produce a mixed oxide/carbide particle, typically 360 μm diameter.

less operator sensitive with respect to shape and size distribution. The liquid route process led to a stronger kernel and thereby reduced coating contamination.

3.8.3.2. Coating process

Developments involved improvements to the pyrocarbon, the study of the high temperature performance limits for silicon carbide and the development of a potential alternative in ZrC and, finally, the exploration of new particle designs involving new coating materials. These studies were principally directed towards obtaining fuels which could operate at temperatures above 1400°C for prolonged periods.

Improvements had been indicated in the performance of material derived from propylene and butane at low temperatures (rather than the traditional high temperature methane coatings), high coating rates and uniformity of coating. Since the process is carried out in a fluidized bed coater, it was first necessary to investigate the fluidization process itself by studying particle motion and gas flow patterns. A parallel approach, which was based on the extensive accumulated experience of coating, was the development of a model of the deposition process. The simple concept was that pyrocarbon is formed of initially substantially spherical agglomerates, whose size affects the structure (but not the density) and whose degree of deformation affects the density of the deposit. Before the agglomerate falls onto a coating, its spinning motion and the surface tension of any low viscosity phase give it a spheroidal shape and a tangled internal structure.

The production of the first 'UO_2+10C' driver fuel was started in the second half of 1967. Changes of enrichment, coating layers and procedures led to revised specifications until the accepted standard driver fuel type D13 was specified (Table 3.15).

In almost all cases the coating agents were acetylene for the porous layers and methane for the high density pyrocarbon layers. All driver fuel of this composition was made with a TRISO coating, the silicon carbide layer being derived from methyltrichlorosilane. The coating of all the layers on one batch was carried out in a continuous process.

TABLE 3.15. SPECIFICATIONS OF THE UO_2+10C REFERENCE FUEL USED IN THE D13 TYPE DRAGON FUEL ELEMENT

Enrichment in U-235	typically 93%
Kernel composition	UO_2 + 10C
Kernel diameter	600 μm
Coating layer thicknesses:	
porous	25 μm
inner HDI	50 μm
total inner PyC	75 μm
silicon carbide	35 μm
outer PyC	45 μm

Instances of the deposition of poor quality SiC occurred at times during the driver fuel fabrication. It was usually indicated by a low density and a porous appearance on a metallographic section. Bad quality SiC was traced on several occasions to an incorrect operating temperature. But equipment for SiC deposition was steadily improved. Contamination of coated particles was reduced when changing the unloading procedure of the particles from extraction through a nozzle systen to a particle extraction system by suction through the top of the furnace. Contamination levels were also reduced by sieving the coated particles immediately after removal from the furnace. It was found that the undersize fraction which usually consisted of broken or only partially coated particles had a higher contamination level than the main batch.

Experiments during the LEU period had indicated that the SiC coating became transparent to the fission product ^{110m}Ag at about 1200–1250°C and that at successively higher temperatures the SiC became transparent to strontium and caesium, respectively. It was felt that these phenomena were probably caused by small concentrations of silicon at the crystal boundaries in the SiC and, therefore, experiments were undertaken to examine the effects of varying the structure of the SiC, e.g. through the addition of nitrogen in the coating process to remove silicon and in controlled variation of the SiC grain size. As a back-up, work began on the development of zirconium carbide, a more refractory material, as an alternative coating.

Finally the concept of getters to bind the fission products more strongly within the kernel led to work on the incorporation of getters into the coatings where much higher concentrations could be used. Thus, coating variants using AlO and ZrC as buffer layers were studied.

In the overcoating process, also developed by the Battelle Memorial Institute, the emphasis was on spraying a premixed slurry of matrix material, binder and solvent coupled with a drying process to build up the overcoats. The basic process involved tumbling the coated particles in a rubber-lined copper drum rotating at about 30 rpm. The resin coated matrix powder was then dropped through spraying with Industrial Methylated Spirits, IMS, (ethyl alcohol). At the same time, the resinated matrix powder was vibro-fed onto the particles. Different sizes of drums were used for overcoating, varying from 457 mm (18 in) diameter down to 51 mm (2 in) diameter for overcoating small quantities of coated particles (as low as 200 particles). The overcoated particles were dried in a vacuum oven in a flow of nitrogen at 50°C. During the process, a uniform size range of overcoated particles was maintained by removing the larger particles at certain stages and replacing them at a later time.

By far the largest amount of driver fuel was made to the specification type D13 (see Fig. 3.32) described in Table 3.15. Evidence from the Dragon operation and maintenance testified to the highly satisfactory quality of the driver fuel, sustained over a period of many years. Many variations of the fuel were made for special applications.

3.8.3.3. Fuel element production

The process for compaction of the overcoated particles was considerably improved over the years. The original method of compaction was to use a die placed between the plates of a hand-pumped hydraulic press. The die was heated to approximately 80°C and loaded with the overcoated particles. The die temperature was then increased to above 120°C and the compact pressed. A further temperature increase to 180°C was made to polymerize the resin. The pressed bodies were baked in a semi-continuous nitrogen atmosphere tube furnace to 800°C, the typical heating rate being 75°C/h. Prior to final testing, inspection and assembly the fuel bodies were degassed at 1800°C in vacuum. This process which was adequate for fuel bodies with volume packing fractions of less than ~35% persisted for several years.

The most commonly used matrix powder was British Acheson Electrodes Limited Type 60 which was a premium grade petroleum coke, graphitized as powder with a particle size of about 60 μm. This was resinated with a phenol formaldehyde resin type CS-217 supplied by the Carborundum Co. Ltd., mixed with a hexamine hardener and stearic acid. The heat treatment of the pressed compacts was carried out in two stages. The first stage was a low temperature treatment at about 900°C in a semi-continuous tube furnace. The furnace tube was made of stainless steel with an internal diameter of 127 mm (5 in) and a length of about 4.6 m (15 feet). Compacts passing through the tube were heated from room temperature to 900°C and cooled down to room temperature over a period of about 45 hours. The furnace tube was continuously purged with nitrogen to remove the resin decomposition products. The second stage of heat treatment involved vacuum degassing which was carried out in a batch furnace. Compacts were contained in open ended graphite tubes and heated under vacuum to 1800°C over a period of ~4 hours. The furnace power was then switched off and the compacts were allowed to cool before submitted to the quality control.

3.8.4. Status at termination

The invention and manufacture of coated particle fuel was an extremely important development step in the history of the HTGR. A whole variety of types of fuel particles has been developed, fabricated, tested, and inserted into the Dragon core. They included kernels made of uranium monocarbide, uranium dicarbide, uranium dicarbide/thorium dicarbide, uranium monocarbide/zirconium monocarbide, or uranium dioxide, which were uncoated or coated either with pyrocarbon only or with a sequence of layers pyrocarbon/silicon carbide/pyrocarbon. Also the ratios of U/Th or U/Zr or U/C varied over broad ranges. Furthermore process parameters during the fuel manufacture were changed to develop optimal designs. Fuel kernel diameters were ranging within allowable limits defined by the sieves employed. Between 1963 and 1976, a series of commercial HTGR concepts was studied including a feed-and-breed HTGR using high enriched uranium and ^{233}U bred from thorium, a low enriched homogeneous HTGR a direct cycle gas turbine HTGR, and process heat HTGRs. Correspondingly, a set of basic reference particle designs was established as listed in Table 3.16.

TABLE 3.16. BASIC REFERENCE PARTICLE DESIGNS RESULTING FROM THE DRAGON PROJECT

Particle type	Kernel		Coating type
	Composition	Diameter (μm)	
LEU fuel cycle			
Dragon reference	UO_2	650–800	TRISO
(Th,U) fuel cycle			
Variant 1 Feed	UO_2	200	TRISO
Breed	ThO_2	500	BISO
Variant 2 Feed	UO_2 + 10C	600	TRISO
Breed	ThO_2	800	TRISO
Variant 3 Mixed	$(Th,U)O_2$	400	TRISO

Production of the reference UO_2+10C type fuel was carried out over a period of about eight years. In that time, approximately 250 kg of green kernels of various enrichments were manufactured and these supplied about 700 coating runs producing around 650 kg of coated particles. These coated particles were further fabricated into nearly 43 000 compacts of various types and dimensions. The standard D13 type fuel for Dragon was produced in 344 coating runs and the coating batch rejection rate was about 3%. Such batches were rejected for reasons of high contamination or poor quality silicon carbide. Approximately 33 000 compacts were produced of this type of fuel.

The essential concept of Dragon driver fuel was conservative and this aim was achieved by dilution of the fissile material in the kernel and by trying to obtain maximum protection from a TRISO coating. The normal diluent for the fissile material in the kernel was carbon, the UO_2:C atom ratio being typically 1:10. The method of manufacture was frozen at an early stage and the process did not change markedly thereafter.

The powder agglomeration route for kernel manufacture was simple and variations in composition were easily made. It was economical in labor as well as having low losses. Recycle of reject material was possible up to the stage of hardening the kernels. The shape of the particles was dependent on the operator and the binder content.

Coating requires at least 150 manual operations per batch and since even the best operators tend to be less than 98% efficient in such manual operations, it is clearly a process requiring automation. In the preparation of Dragon fuel, automation would have increased the validity of all fuel testing, both driver and experimental, as well as assisting in a modest way towards the automation of refabrication. LTI pyrocarbons probably require a higher degree of temperature control than HTI pyrocarbons, further emphasizing the need for automatic control. Although control was exercized on the manufacturing process, a proper quality assurance programme was not carried out. It is fortunate that the underlying quality was good and that the product was so conservatively designed that this did not matter.

Although a variety of commercial HTGR developments was being considered, design studies did not lead to a clear definition of the way forward. The extreme flexibility of the HTGR and the array of possible design solutions contributed to the difficulty in defining the basic core design for a prototype system. Good progress being made with some aspects of the work on advanced fuels up to mid 1975.

But the increasing difficulties of the Dragon Project in fulfilling the programme, especially that involving extra-mural irradiation, began to interfere with progress. Unfortunately, a great part of the experimental programme was never completed. Overstretched resources, coupled with a worldwide trend in that era to favour water reactors eventually caused work on the Dragon project to be terminated in March 1976.

3.9. FUEL PRODUCTION ACTIVITIES IN THE USA

3.9.1. Introduction

The primary HTGR programmes in the USA consist mainly of the Peach Bottom HTGR, Fort St. Vrain (FSV) HTGR, and the modular high temperature gas cooled Reactor (MHTGR) [78].

The Peach Bottom project was initiated in 1958 and produced the first electricity from an HTGR on Jan. 27, 1967 [79]. The fuel element design consisted of 3660 mm long, 89 mm diameter, low permeability graphite sleeves which contained annular compacts. The fuel compacts were made by mixing coated particles with graphite powder and pitch binder followed by hot pressing.

The Fort St. Vrain project was initiated in 1965, and the first electricity was produced in late 1976 [80]. The fuel element for FSV HTGR consisted of a hexagonal graphite block 356 mm across the flats and 790 mm high. Coolant and fuel holes were bored into the block, and fuel compacts were inserted into the fuel holes. The fuel compacts was fabricated by filling a mold with coated particles and then injecting a mixture of graphite powder and molten petroleum pitch binder into close packed bed of particles. The compacts were heated to decompose the binder and produce a stable body.

Since the late 1970s several reactor designs have been evaluated based on energy and safety requirements. The MHTGR programme was the culmination of that ongoing development effort [81]. The MHTGR will utilize the same fuel particle and element design employed for the FSV HTGR, with the incorporation of technological advances to reduce initial defects in the fresh fuel. Because of performance and process advantages of UCO, it was selected in 1981 as the reference fissile fuel kernel for the US-DOE HTGR development programme [82].

Peach Bottom Unit 1 and FSV initial cores and reload fuel were manufactured in the USA. For cores 1 and 2 of Peach Bottom Unit 1, about 3500 kg of BISO coated, high enriched uranium (HEU) $(Th,U)C_2$ particles were manufactured and assembled into more than 48 000 annular fuel compacts in cylindrical fuel elements. The FSV initial core required about 20 000 kg of (HEU) $(Th,U)C_2$ and ThC_2 TRISO coated particles into about 1500 hexagonal prismatic fuel elements [1].

3.9.2. Fuel production for the Fort St. Vrain HTGR

3.9.2.1. Introduction

TRISO coated fuel was massively produced by General Atomics (GA) and performed impressively in the FSV [83]. The Fort St. Vrain Nuclear Generating Station [84–86] was a 330 MW(e) (842 MW(th)) HTGR that was operated by the Public Service Company of Colorado from 1974 to 1989. The FSV core used prismatic fuel elements with hexagonal cross-sections. Fuel for the reactor was based on the 93% enriched uranium/thorium cycle (HEU/Th). TRISO coated fissile and fertile particles were separately used. Fuel lifetime in the core was six years, i.e. about one sixth of the fuel elements were removed and replaced at each refueling.

The General Atomics fuel fabrication facility was located on the main General Atomics site in San Diego, California. All fabrication operations were carried out in a 4000 m^2 tilt slab and corrugated metal building with 9 m high ceilings. All processing, quality control operations were carried out in this building. The building also contained offices, the quality control laboratory, maintenance facilities and change-rooms for men and women. In 1982, a 500 m^2, hardened building was added for storage of high enriched uranium in compliance with new Nuclear Regulatory Commission requirements. Air was circulated through the fabrication facility to accomplish four air changes per hour. Operations throughout were conducted for three shifts/day, seven days/week.

General Atomics manufactured fuel for FSV at its facility in San Diego, California (‘SVA’). Manufacturing of Fort St. Vrain fuel began in 1969 and continued until 1985. Fabrication of the initial core, segments 1 through 6, began in 1969 and was completed in 1972, and more than 800 kg of high enriched ^{235}U and 15 000 kg of thorium have been processed [87]. The 1482 fuel elements were shipped to the FSV site 35 miles north of Denver, Colorado, and loaded into the reactor in 1973. The reactor went critical in January, 1974. Subsequently, four reload fuel segments, Segments 7 through 10, were produced between 1972 and 1985. Each reload segment had 240 fuel elements. Between 1974 and 1978, fuel production was shut down because delays in FSV operation precluded the need for reload fuel elements. Segment 10, the last fuel segment, was never irradiated because operations at the FSV reactor were terminated before it was needed.

For FSV, 2448 fuel elements, 7.1 million fuel compacts containing 26 600 kg of fissile and fertile material in TRISO coated fuel particles were produced. The fissile particle kernels contained fully enriched uranium carbide and thorium carbide in a ratio of 1 to 3.6. The fertile particle kernels were 100% thorium carbide.

3.9.2.2. Fuel design specification for fabrication

Fissile and fertile particles were bonded together to form fuel compacts of 12.6 mm in diameter and 50 mm long. Two different diameter fissile particles (‘fissile A’ and ‘fissile B’) and two different diameter fertile particles (‘fertile A’ and ‘fertile B’) were utilized in order to permit different heavy metal loadings in a constant volume fuel compact. In the later reload segments, graphite shim particles were used as well to allow fabrication of compacts with various fissile and fertile loadings.

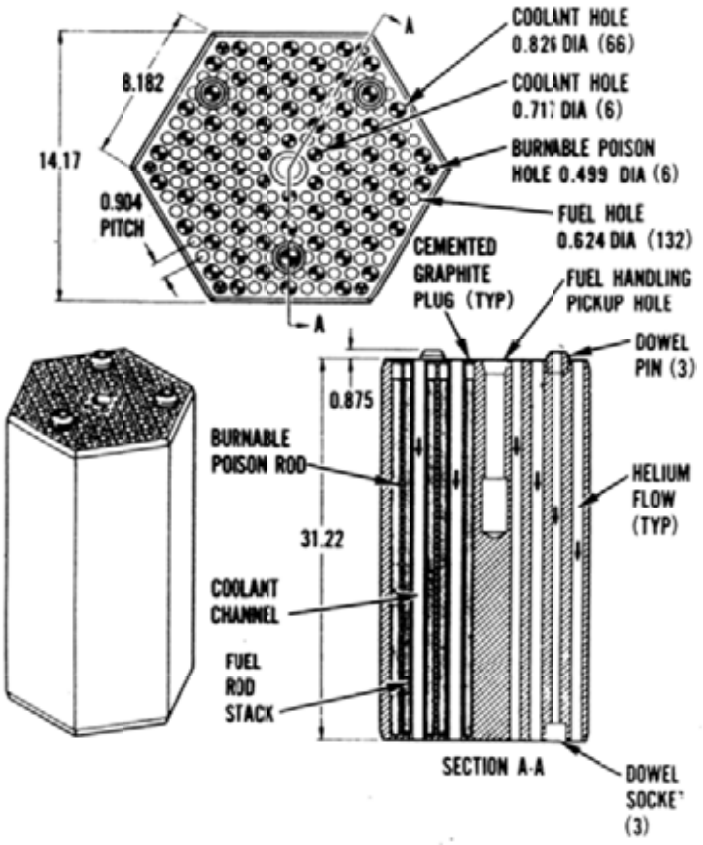

FIG. 3.33. General Atomics prismatic fuel element.

Approximate 3000 fuel compacts were loaded into each graphite fuel block to form a fuel element. The fuel blocks for the initial core and first reload fuel segment were made from machined H-327 graphite that was manufactured by Great Lakes Carbon Corporation. Fuel blocks for subsequent reload segments were made from the more dimensionally stable H-451 graphite that was provided by the same vendor. The fuel blocks were hexagonal in cross-section, 360 mm across flats and 790 mm high (Fig. 3.33 [88]). The core, made from 1482 hexagonal fuel elements, stacked six elements high, was roughly cylindrical in shape, about 6 m in diameter and 4.8 m high. The average core power density was 6.3 MW(th)/m^3. Specifications for the FSV coated particles are shown in Table 3.17.

The fuel cycle using 93% enriched uranium and thorium was the economical optimum cycle for FSV. It was desired to fission the ^{235}U completely, but particles which could sustain the high burnup had not yet been developed. Therefore, a fissile particle containing both fissile and fertile material was used. Coatings on the FSV particles were generally thinner than those used in later designs and the acceptable range of coating thicknesses and kernel diameters were wider than specified in later designs. Later, an all 93% enriched uranium carbide fissile particle was developed and licensed for use at FSV to a burnup of > 70% FIMA and a fast neutron fluence of 8×10^{25} n/m^2. Although the fuel was extensively irradiated in test reactors, it was never used in the FSV core.

TABLE 3.17. SPECIFICATIONS OF FSV COATED PARTICLES

Particle	Fissile		Fertile	
	Smaller (A)	Larger (B)	Smaller (A)	Larger (B)
Kernel				
Material	$(3.6Th,U)C_2$ [a]	$(3.6Th,U)C_2$ [a]	ThC_2	ThC_2
Diameter (μm)	100–175	175–275	300–410	410–500
Enrichment (% U-235)	93	93	n.a.	n.a.
Coating thicknesses (μm)				
Buffer	45–100	45–100	45–65	45–65
Seal	< 5	< 5	< 5	< 5
IPyC	20–30	20–30	20–40	20–40
SiC	20–30	20–30	20–30	20–30
OPyC	> 25	> 35	> 30	> 40
Defective coatings				
Heavy metal migration + missing buffer + missing IPyC	1×10^{-3}		1×10^{-3}	
Defective SiC	3×10^{-3}		5×10^{-3}	
Missing OPyC	1×10^{-3}		1×10^{-3}	

[a] Initial core Th/U = 4.25.
n.a. not applicable.

Fuel compact specifications include dimensions, impurities, matrix coke content, allowable defective particle coatings, and heavy metal contamination. These specifications are shown in Table 3.18.

TABLE 3.18. SPECIFICATIONS OF FSV FUEL COMPACT LOTS

Diameter (ring gauge)	~12.6 mm	
Length (mechanical measurement)	~50 mm	
Coke content (coke + filler)	< 0.36%	
Iron	≤ 20 μg/compact	
Sulfur	≤ 1200 ppm	
Chlorine vapour pressure @ 1600°C	5×10^{-3} Pa	
Contamination (average for all rods in segment)	Uranium	Thorium
Fission gas release (Kr-85m @ 1100°C)	3×10^{-5}	
Heavy metal contamination – burn-leach (contamination + totally exposed kernels)	3×10^{-3}	1×10^{-2}
Fission gas release (Kr-85m @ 1100°C)	Not specified	
Thorium contamination (hydrolysis)		1×10^{-4}
Fuel dispersion	1×10^{-3}	1×10^{-3}
Burn-leach (heavy metal contamination + SiC defects)	3×10^{-3}	1×10^{-2}

3.9.2.3. Fuel fabrication process

FSV fuel production consisted of five major steps:

(1) Fabrication of spherical fissile and fertile kernels;
(2) Application of coatings;
(3) Production of fuel compacts;
(4) Assembly of the compacts into prismatic graphite blocks;
(5) Packaging and shipping the fuel assemblies to the FSV site.

For the FSV assemblies, 25 processing steps were utilized. The steps are shown in Fig. 3.34.

(a) Fabrication of spherical fissile and fertile kernels

Two types of kernels were made. The fertile kernels contain only thorium; the fissile kernels initially contained a mixture of four parts thorium to one part 93% enriched uranium; the ratio was later changed to 3.6 to 1.

For fissile kernel fabrication, thorium oxide (ThO_2) powder, uranium oxide (UO_2) powder, and carbon powder were mixed together with ethyl cellulose and a solvent to form nuggets approximately 1 cm in diameter. The nuggets were dried, ground, and screened to obtain particles of the desired diameter range. Oversize material was reground and screened; undersized material was sent back to the beginning of the process and formed again into 1 cm nuggets. The grinding operation yielded a broad range of particle sizes so about 40% of the material was undersize and had to be recycled back to the beginning of the process. The product material was then converted into thorium/uranium carbide in a vacuum furnace at 2000°C. The rough shaped thorium/uranium carbide particulates were then made into spheres in a drop/melt process at 2700°C.

Because the process made a wide spectrum of kernel sizes, screening was performed between each process step to select the material suitable for further processing. The fertile kernels were produced in larger equipment with the same process starting with thorium oxide powder, ethyl cellulose, and carbon powder.

(b) PyC and SiC coatings

Pyrocarbon and SiC coatings were applied to the kernels in fluidized bed furnaces operating between 1200°C and 1650°C. The TRISO coating was applied in three steps. In the first coating step, three types of pyrocarbon were applied to the kernels (buffer, a thin seal over the buffer, and an inner pyrocarbon). Then the coated particles were removed from the coated and inspected. Next, the SiC coating was applied, and the particle batch was removed and inspected again. In the final step the outer pyrocarbon was applied and a final inspection of the TRISO particles was performed.

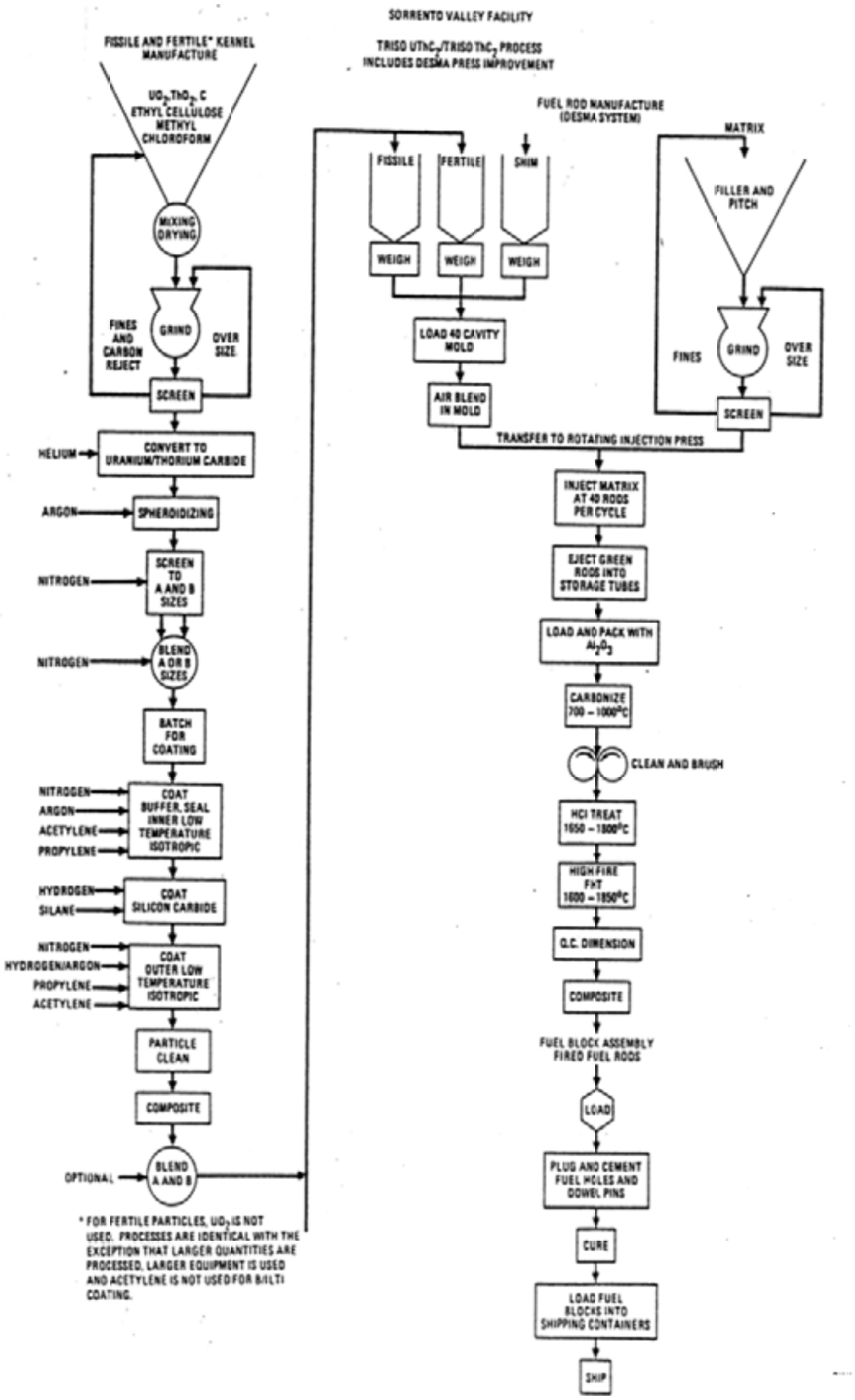

FIG. 3.34. Block flow diagram of the Fort St. Vrain fuel fabrication.

For the initial core, the fissile coating was applied in eleven coaters each having an inside diameter of 120 mm. Fertile coatings were applied in six coaters each having an inside diameter of 240 mm. Using these seventeen coaters, a production record was set in July, 1971, when 308 coating batches were processed in a single 24-hour period. Starting in 1978, a new freon cooled coater (known as the dry coater) was utilized for all of the FSV coating (this process improvement is discussed later); both the fissile and fertile coatings were applied in three steps using this single coating furnace. Table 3.19 describes the coaters used to make the FSV fuel.

(c) Production of fuel compacts

Following coating, the particles were molded into fuel compacts that were 13 mm in diameter and 50 mm long. To form the compacts for the initial core and Segment 7, fissile and fertile particles were metered and transferred to a 20 compact mold where binder was injected and compacts solidified. This compacting machinery was replaced for reload segments 8, 9 and 10 by an improved process discussed below.

TABLE 3.19. COATER DESIGNS USED IN FSV FUEL MANUFACTURING

Segment	Material coated	Number of coaters	Coater design			
			Diameter (mm)	Heating	Coolant	Gas distribution
1–8	Fissile	11	120	200 kW resistance 3 phase 28 Volts phase to phase with split electrode ring	Water	Porous graphite flat frit PyC 60° cone for SiC both with hot unloading feature
	Fertile	6	240	200 kW resistance 3 phase 28 Volts phase to phase with split electrode ring	Water	60° cone with hot unloading feature
9–10	Fissile and fertile	1	240	200 kW resistance 3 phase 28 Volts phase to phase with split electrode ring	Freon	Nozzle and cone with hot unloading feature

After formation the compacts were heat treated in three steps. The compacts were first carbonized in a nitrogen atmosphere in a mold packed with small alumina particles at 900°C, and the pitch volatiles were driven away. Next the compacts were leached with HCl gas at 1650°C to remove uranium and thorium contamination present outside of the SiC coatings; other metallic impurities such as iron were also removed. The compacts then were final heat treated at 1700°C in an argon-purged, graphite-lined, push-through furnace during which the carbonization of the matrix was completed and the residual sulphur and chlorine were removed. Compacts were mass produced in ‘compact lots’; containing about 30 000 compacts. For Segments 8, 9 and 10, compact formation was carried out with an automated, integrated unit.

Following final inspection and quality control release, the compacts were manually loaded into the prismatic fuel blocks to form the fuel assemblies. The prismatic fuel blocks were procured fully machined. Each block contained approximately 3000 compacts. After the compacts were loaded, a graphite fuel hole plug was placed in the top of each fuel hole; the plugs were sealed in place with graphite cement that was cured at a low temperature. The

completed fuel block was engraved for identification and packaged for shipment to the reactor site.

(d) Characterization of fabricated fuel elements

Quality control measurements of the uranium contents in the graphite and in exposed kernels are plotted in Fig. 3.35 for the initial core and reloads.

(e) Fuel fabrication process improvement

In parallel with the production of FSV fuel, GA developed improved fuel fabrication equipment and processes for commercial HTGR fuel. Some of the new techniques were used in production of reload segments for FSV. Following is a summary description of the most significant process improvements introduced.

(i) Desma press

For use on Segments 8, 9, and 10, a new compact forming unit, graphite shim particles, and a new matrix formulation were introduced. A German company, Desma, supplied the new compact formation unit. The Desma Press was a computer controlled thermo-mechanical system that automatically formed the fuel compacts ready for carbonization and heat treatment. The only manual operations required of the operators were loading of particles into feed hoppers, loading matrix into the matrix hopper, and removal of the completed compacts. Fully equipped with eight molds and assuming an 80% on line time, the press could produce 30 720 compacts per 24-hour day. For Ft. St. Vrain production, only two molds were used, and the other six stations were vacant; 7680 compacts were produced each 24-hour day.

In this new process, fissile particles, fertile particle, and graphite shim particles were accurately weighed for each fuel compact with an automatic machine and dropped into one of the holes in a 40-hole transfer cart. The three types of particles were then air blended to provide a homogeneous mixture. The blend was loaded into one of the cavities in a mold that had 40 compact mold cavities. When the 40 cavities were filled, the mold was heated to 160°C and molten matrix was injected into the mold cavities through a matrix manifold. The matrix was a mixture of low sulphur petroleum pitch, graphite flour, octadecanol, and polystyrene. This receipt produces a relatively low density (1.7 Mg/m^3), carbonized matrix. The matrix filled the voids between the particles and bonded the particles together into the compact. The mold was cooled to 30°C and the compacts were ejected from the forty-cavity mold and placed into fuel assembly loading tubes by a harvesting robot.

The compact fabrication process has been significantly improved by the recent work of Besenbruch and colleagues [89] who have shown that compacts with very low defects can be fabricated by controlling the matrix impurity levels, controlling the compact formation and injecting forces, removing the metallic impurities prior to high temperature firing, and performing the high temperature firing in a clean furnace.

(ii) Dry coater

By 1974, General Atomics had built and operated over twenty coaters for mass production of particles with pyrocarbon and silicon carbide coatings. During the initial core, seventeen coaters were used 24 hours a day, five days a week and sometimes seven days a week. The experience gained from production coating was combined to design and build the ‘dry coater.’ The dry coater was to be used for development of the process to be used to fabricate fuel for

the large, commercial HTGRs. Objectives of the coater design were to coat larger batches of particles and retain or improve coating quality. Its first use was for production of reloads 8, 9, and 10.

The inside diameter of the coating chamber was 250 mm. Because this was not a safe geometry for enriched uranium if the coater was cooled with water, a chlorinated hydrocarbon was used for coolant. With the elimination of a coolant with hydrogen, the 250 mm diameter coating chamber could be used for enriched uranium. The coater was made from stainless steel components, resistance heated, and used computer-controlled 'digital valves' for regulating flow rates.

(iii) Other improvements

Improvements were also made in particle homogeniety by air blending, carbonization by better transport of impurities from the heat treating fixtures, and final heat treatment of the compacts by cleaning the furnace components of impurities.

3.9.3. Fuel technology programme supporting the MHTGR

The coated fissile fuel particles for the modular high temperature reactor (MHTGR) consist of a UCO fuel kernel surrounded by the TRISO coating, i.e. a porous buffer layer, a dense inner pyrocarbon layer, a silicon carbide layer, and a dense outer PyC layer. An additional outer protective layer of low density PyC is added to achieve very low breakage during fuel compact fabrication and thus, low as-manufactured defect fraction.

Because of performance and process advantages of UCO (a mixture of UO_2 and UC_2), it was selected in 1981 as the reference fissile fuel kernel for the US-DOE HTGR development programme. The UCO kernel is to be fabricated using the internal gel precipitation process [57, 89]. This process consistently produces high quality kernels with the correct dimensions and specified characteristics, minimizes the environmental processing of wastes and scraps recycle materials, and meets the specific performance requirements. The gelled spheres are stabilized; the kernels are air-dried, calcined and sintered to remove excess oxygen. The kernels are then exposed to argon and argon/CO gas mixture to chemically adjust the ratio of carbon and density of the kernels [1]. The kernels are coated by chemical vapour deposition in a fluidized bed furnace. The buffer and PyC layers are deposited from pyrolysis of hydrocarbon gases and the SiC from methyltrichlorosilane (MTS). TRISO coated ThO_2 kernels produced similarly are also included in the MHTGR to allow varying the local U/Th ratio for core zoning purposes and to decrease the reactivity changes from burnup of fuel.

Activities within the US Fuel Technology Programme in support of the MHTGR are centred in the three main areas: fuel materials development, fuel process development, and fission product behaviour. The majority of the technology development activities for the Process Development are underway at General Atomics (GA), while those in the Fuel Materials and fission product behaviour areas are centred at Oak Ridge National Laboratory (ORNL).

In the fuel process development area, the major emphasis was on the construction and qualification of an improved fuel compact injection press. The LEU UCO fissile and ThO_2 fertile TRISO coated fuels were fabricated by GA as a candidate fuel for the MHTGR, and mean contamination and defect particle fraction were $< 1 \times 10^{-6}$ and 2.3×10^{-5}, respectively [90]. The as-manufactured quality has been improved significantly, resulting in less heavy metal contamination and lower particle defect fraction in fresh fuel (see Fig. 3.35) [83, 91].

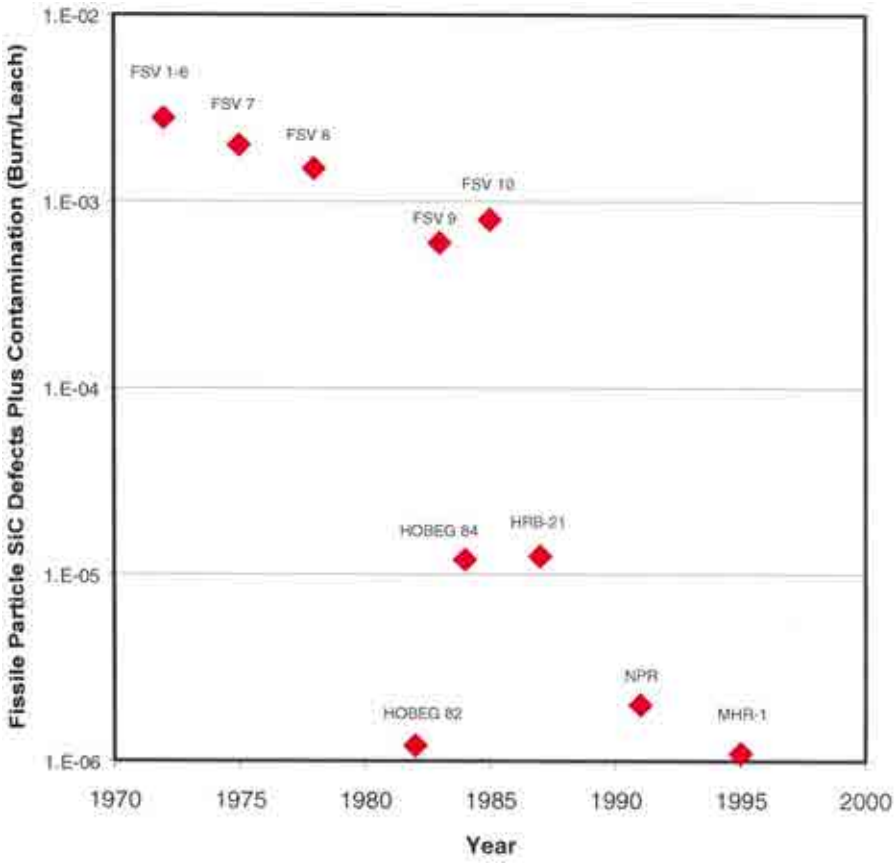

FIG. 3.35. Evolution of HTGR Fuel Quality.

The fuel particles are embedded in a fuel compact composed of the coated fuel particles, a carbon matrix and graphite shim. The matrix is originally 47% petroleum pitch, 38% filler, 10% octadecanol, and 5% polystyrene. The matrix is injected into a mold at 160°C. Afterwards, cooling to below ambient temperature solidifies the compact. The compact, packed in Al_2O_3, is then carbonized at 900°C to decompose organic compounds and to obtain a solid carbon compact. The size of the alumina particles must be controlled to restrain the compact but allow the escape of volatile gases. Thereafter the compacts are heated at 1650°C briefly to stabilize the compact. The diameter of the resulting compact is between 12.37 and 12.72 mm and an adjustable length, expected to be 49.3 mm in most application [1].

3.10. ADVANCED FUEL DESIGN PARAMETERS

3.10.1. Challenges on the road to high temperature, high burnup SiC fuel

3.10.1.1. Introduction

The fuel service conditions proposed for the very high temperature reactor (VHTR) will be challenging [92]. While the highly successful German coated particle fuel programme established an acceptable design envelope for the five key fuel-related parameters (burnup, temperature, fast fluence, particle packing fraction, power density), the German fuel does not adequately envelope the conditions expected for the VHTR for any of these five key fuel-related parameters and neither does any other programme around the world (Fig. 3.36) [93]. Thus, additional fuel development will be required [93].

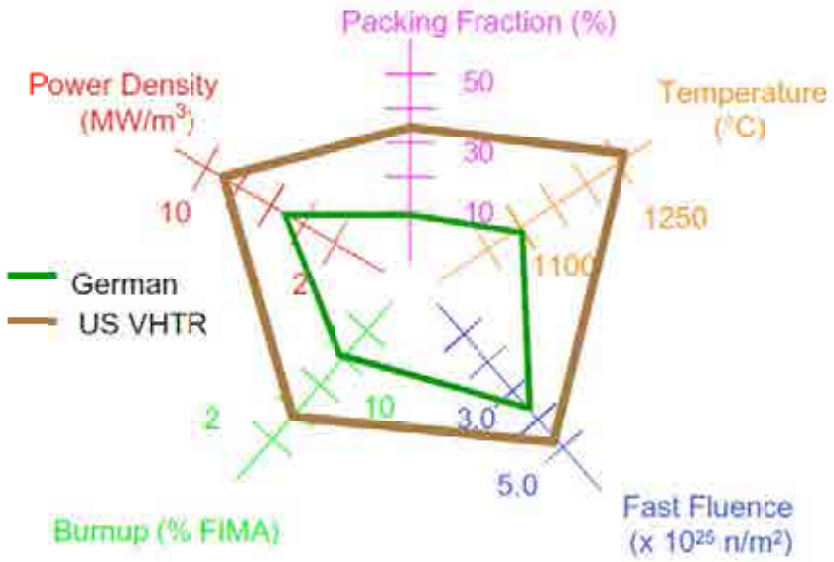

FIG. 3.36. Comparison of US VHTR and German fuel operating envelope.

An assessment has been performed using modeling in the PARFUME code [94] to quantitatively evaluate the challenges associated with high temperature and high burnup with TRISO coated particle fuel. There are a number of known fuel failure and fission product release mechanisms that are temperature and burnup dependent. These include: thermomechanical response of PyC, fission gas release and CO production, amoeba effect, metallic fission product diffusion and Pd attack of the SiC. For each mechanism the effects of increasing burnup and/or temperature were evaluated and where possible the results normalized to results at 1100°C and 8% FIMA. These numerical values then provide a metric to determine how the fuel performance will change as the temperature and burnup are increased.

Fuel development and qualification programmes usually irradiate fuel in test reactors. These high neutron flux irradiations accelerate (or reduce) the time required to reach full design burnup and/or neutron fluence. Accelerated irradiations also result in increased power per particle and increased temperature gradients in the TRISO coated particles. Several fuel-related phenomena are affected by these variations in time and temperature.

The PARFUME code has been used to evaluate some of the most significant effects of accelerated irradiation that are dependent upon time at temperature. These evaluations were based on both German UO_2 and US UCO fuels.

3.10.1.2. Accelerated irradiation

The PARFUME code was used to examine the effects of accelerated irradiation on coated particle fuel performance. Two fuel forms representing typical German particles and US AGR particles were used in the evaluations. German fuel consisted of coated 500 μm diameter UO_2 kernels and the US AGR fuel consisted of coated 350 μm UCO kernels. Particle performance was examined at power levels ranging between 50 and 500 mW/particle which corresponds to approximately real time irradiation up to 10 times acceleration to reach end of life (EOL) service conditions. For these calculations, end of life conditions were 10% FIMA for the German fuel and 20% FIMA for the US AGR fuel, with each fuel form experiencing an EOL fast neutron fluence of 4.0×10^{25} n/m^2 (E>0.18 MeV). Both fuel burnup and fast neutron fluence were accelerated in this analysis, since in many reactors fast and thermal neutron fluxes scale. To simplify the comparisons, these evaluations also assumed that all particles were at the given power throughout its entire life and were held at a thermal boundary condition of 1000°C at the outer surface of the OPyC layer.

As power or acceleration increases, the time required to reach full burnup decreases and fuel temperatures increase. These expected results are illustrated in the Figs 3.37 and 3.38 [93]. For a given power, the US AGR fuel temperature is higher than for the German fuel due to the higher power density associated with the smaller AGR kernels (at 500 mW/particle, the corresponding power density for AGR particles is 22.3 kW/cm^3 and for the German particles it is 7.6 kW/cm^3).

Accelerated irradiation increases total internal gas pressure in both fuel forms as shown in Fig. 3.39 [93]. This pressure increase is primarily due to the increased temperature of the fuel with increasing power. German fuel pressures are higher than AGR fuel pressures due to the formation of CO in the UO_2 fuel which is negligible in UCO fuel. Internal pressures are also affected by the amount of fission product gases released to the void volume which is a complex function of time and temperature. The contributions of CO and fission product gas to the total gas pressure are displayed in Fig. 3.40 [93].

Metallic fission product release is modeled by Fickian diffusion with Arrehnius diffusion coefficients [1]. The calculated results demonstrated that the behaviour is a complex function of time and temperature as illustrated in Figs 3.41 and 3.42 for caesium and silver release [93]. Generally, as power increases, fractional release decreases due to less time available for diffusion. This trend continues until the diffusion rate increases sufficiently (due to increasing temperature and its impact on diffusion coefficients) to dominate over the irradiation time and release begins to increase with increasing power. For some fission products and irradiation conditions, this overall trend may not be displayed as illustrated by Pd penetration in SiC (which is rate limited by diffusive release from the kernel) for German fuel. As shown in Fig. 3.43, Pd penetration continuously decreases with increasing power for German fuel, while for US AGR fuel, Pd penetration initially decreases and then increases with increasing power [93].

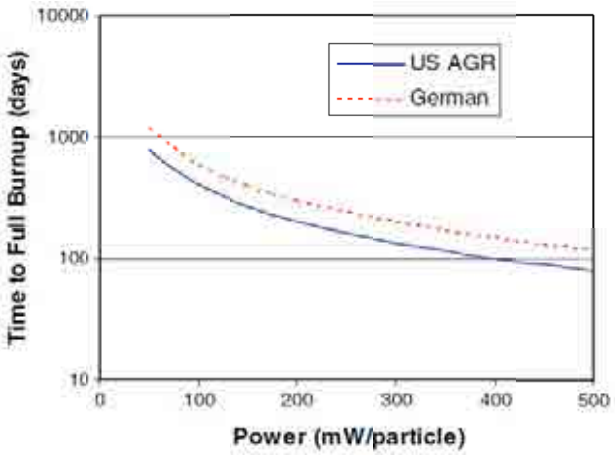

FIG. 3.37. Effect of particle power on time to full burnup.

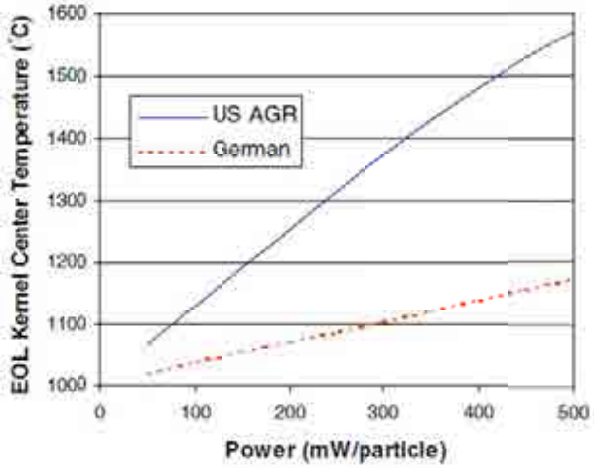

FIG. 3.38. Effect of particle power on particle centre temperature.

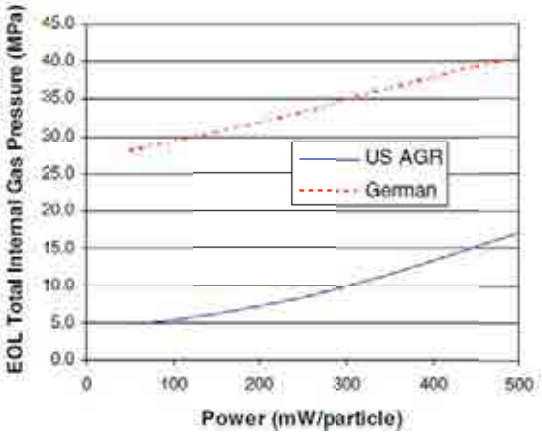

FIG. 3.39. Effect of particle power on internal gas pressure.

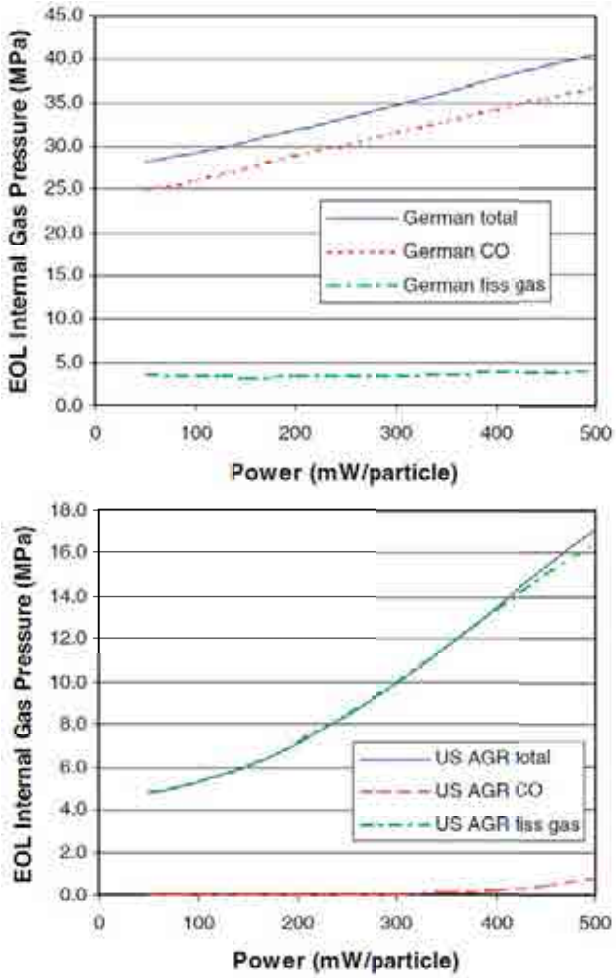

FIG. 3.40. Contribution to internal gas pressure.

Effects of acceleration on fuel performance metrics are complicated due to varying degrees of dependence on temperature, time, burnup and fast fluence. Therefore, fuel performance models are required to accurately predict these effects for a specific fuel form and irradiation history. However, this evaluation has shown the substantial increase in fuel temperatures associated with high levels of acceleration. This gives support to the historic German approach of limiting irradiations to less than three times acceleration.

3.10.1.3. Conclusions

With the exception of the thermomechanical response of the particle, these calculations indicate that high temperature and high burnup will erode existing fuel performance margins in the traditional UO_2 German TRISO coated particle system. Additional fuel development will be required to demonstrate that UO_2 TRISO coated particles will work under VHTR conditions. Irradiations and accident heating tests are proposed as part of the European gas reactor programme to understand the limits of UO_2 at high burnup and high temperature.

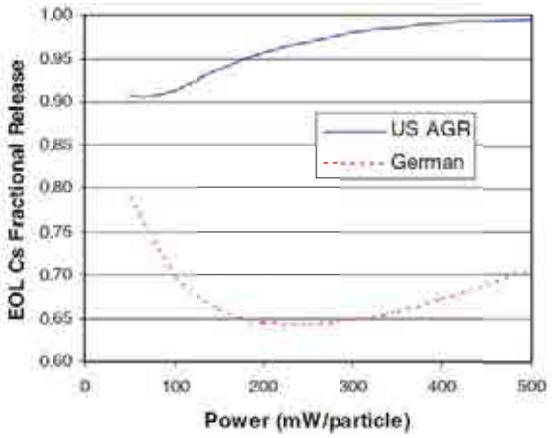

FIG. 3.41. Effect of particle power on caesium release.

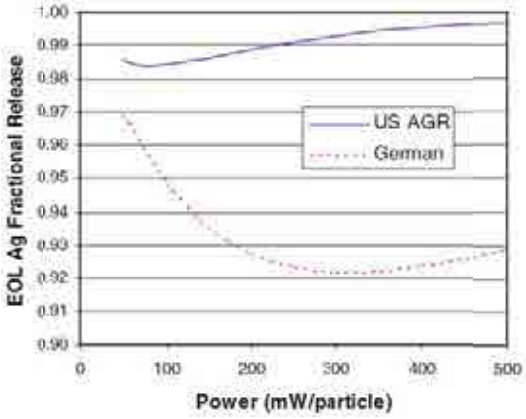

FIG. 3.42. Effect of particle power on silver release.

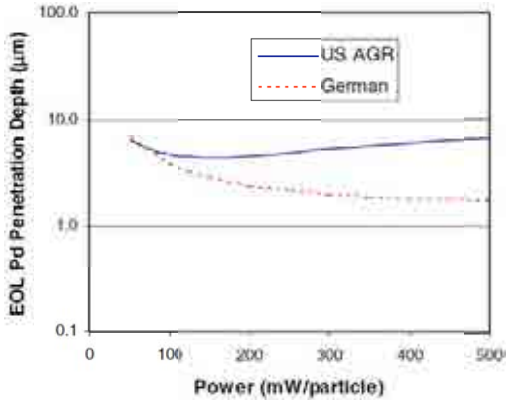

FIG. 3.43. Effect of particle power on Pd penetration into SiC.

Potential solutions exist to recover some of the performance margin that is expected to be lost in going to higher burnup and higher temperature. However, all of them require extensive testing and analysis. The solutions are at different stages of maturity. Some require scoping irradiations and heating tests to demonstrate satisfactory proof of performance while other options are more mature and only require the more extensive set of activities related to formal fuel qualification. These solutions include:

- Reducing kernel size as enrichment/burnup goes up will reduce CO and fission gas pressures but hinders with respect to fission product attack of the SiC.

- The use of UCO will reduce the CO pressure and effectively reduces the potential for kernel migration.
- An alternative fuel kernel is UO_2^* which has shown very promising fuel performance, little kernel swelling, no kernel migration, and improved fission product retention in post-irradiation annealing tests in comparison to conventional TRISO coated particles (see also following Section 3.12.3).
- ZrC as an alternative coating for particle fuel may have higher performance capability than SiC.

3.10.2. Perspective fuel designs

3.10.2.1. UO_2^* fuel concept

A particle design designated UO_2^*, with a dense pyrocarbon seal coat and thin ZrC coating applied directly to a UO_2 kernel followed by the typical SiC TRISO coatings, as shown in Fig. 3.44, was fabricated and tested in the late 1970s and early 1980s. The objective of the thin ZrC layer, which was not expected to survive the irradiation, was to serve as a getter for oxygen to limit CO production and to retard kernel migration. UO_2^* particles from three coating batches with dimensions as shown in Table 3.20, were irradiated and subjected to post-irradiation heating tests alongside standard SiC TRISO particles having kernels of UO_2, UC_2, and UCO. UO_2^* in loose particle, bonded wafer and fuel compact forms were irradiated in the HFIR reactor at ORNL in capsules HRB-15A, HRB-15B, and HRB-16 at temperatures ranging from 860°C to 1210°C, burnups of 19–29% FIMA, and fast fluences of 3.7–6.5 × 10^{25} n/m^2 (E > 29 fJ) [1].

Unexpectedly, the ZrC layers remained intact in all particles observed in post-irradiation examination of fuel from the lower temperature HRB-15B irradiation, and in the majority of particles from the higher temperature irradiations. In addition, kernel diametral swelling was observed to be limited to ~1% for UO_2^* particles with intact ZrC layers versus ~10% for particles with failed ZrC layers as well as UO_2, UC_2 and UCO TRISO particles [95]. As an example of comparative metallic fission product retention, Fig. 3.45 shows autoradiographs of particle trays which contained UO_2^* and UCO loose particles during the HRB-15A irradiation.

The activity on the UCO particle tray was found to be primarily ^{154}Eu. post-irradiation gamma scanning of fuel from HRB-15A [96] and HRB-16 [97] showed superior retention of all metallic fission products, including silver, by the UO_2^* fuel (no release was observed from any of the fuel types for the lower temperature HRB-15B irradiation).

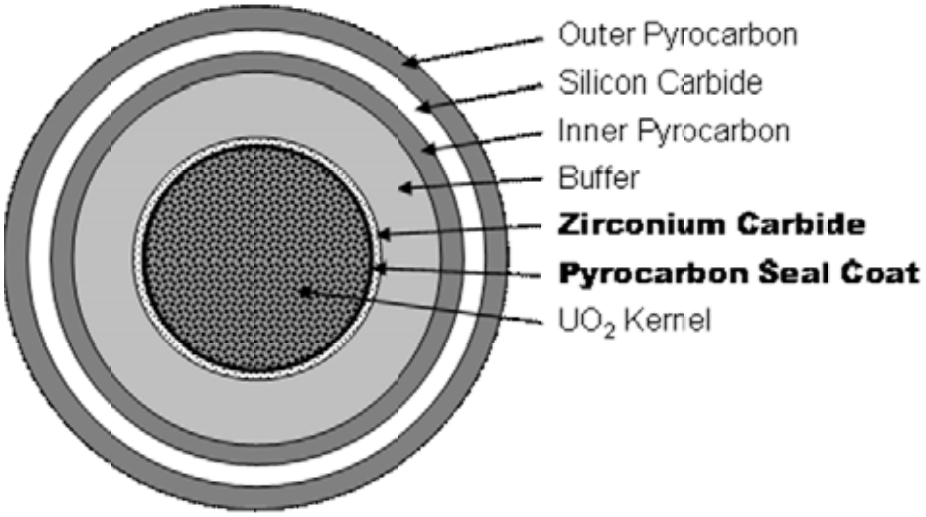

FIG. 3.44. UO_2^* particle.

TABLE 3.20. AS-FABRICATED UO_2^* PARTICLE DIMENSIONS

	Batch 1	Batch 2	Batch 3
Kernel diameter (μm)	312	312	346
Pyrocarbon seal coat thickness (μm)	8.9	7.7	3.0
ZrC layer thickness (μm)	9.1	14	14
Buffer thickness (μm)	82	93	100
IPyC thickness (μm)	35	39	39
SiC thickness (μm)	37	36	35
OPyC thickness (μm)	41	40	49

Three sets of ten particles of each of the four fuel types irradiated in HRB-15B were subsequently annealed for 10 000 hours at temperatures of 1200, 1350, and 1500°C [95]. The results from the 1500°C annealing tests are summarized in Fig. 3.46. The UO_2^* fuel type was the only one that did not release a detectable amount (less than 0.01%) of any fission product in any of these post-irradiation heating tests. In addition to Cs and Ce, this included the more diffusive ^{110m}Ag and ^{154}Eu isotopes for which release from individual particles for all other fuel types at 1500°C ranged as high as 15 to 100%. All ten UO_2 TRISO particles without a ZrC layer released 100% of the silver at 1500°C, so this 9-μm layer applied over the UO_2 kernel in UO_2^* fuel led to a dramatic improvement in retention of this and other important fission products.

Despite the wide range of variation in the pyrocarbon seal and ZrC layer thicknesses of the three UO_2^* particle batches, as shown in Table 3.20, all of the UO_2^* particles exhibited superior performance in the irradiations and post-irradiation annealing. This is an indication that the concept is robust and not sensitive to these primary parameters. The UO_2^* concept was not pursued in the 1980s largely due to the lower fuel temperatures associated with steam cycle designs under development at the time. More recent interest in gas turbine cycles and process heat applications may require development of particle designs such as UO_2^* with enhanced ability to retain fission products at higher operating and accident condition temperatures.

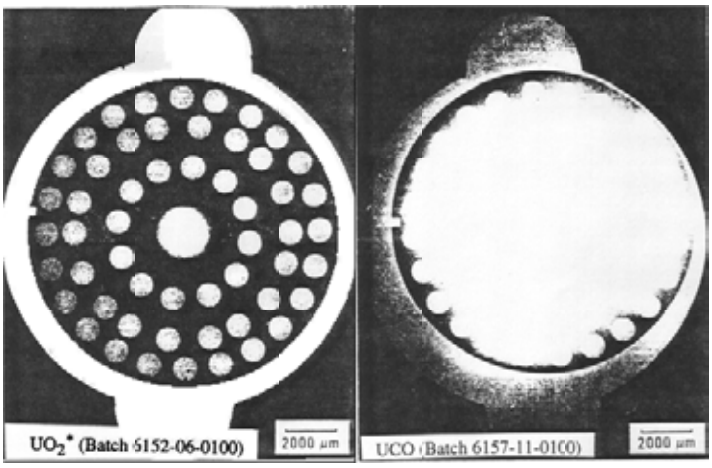

FIG. 3.45. Europium release in HRB-15A irradiation.

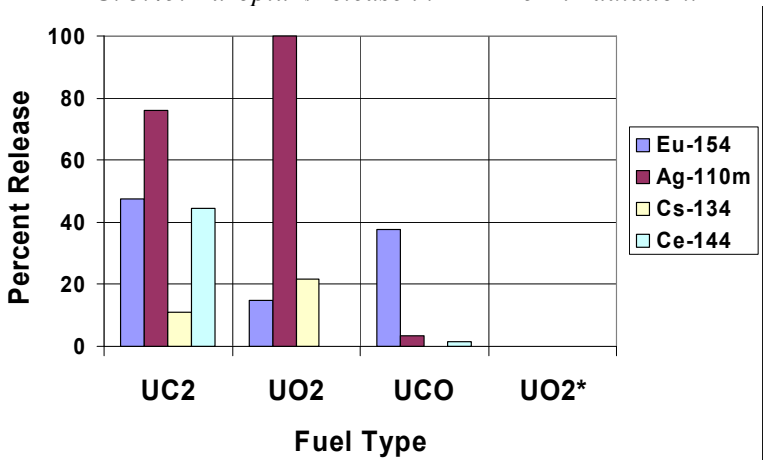

FIG. 3.46. Post-irradiation annealing of HRB-15B fuel.

3.10.2.2. Post-irradiation test programme for high burnup SiC coated fuel particles

The target burnup and fast neutron fluence of the high burnup SiC coated fuel particle are higher than those of the first loading fuel of the HTTR [98, 99]. In order to keep the fuel integrity up to high burnups beyond 5% FIMA, thickness of the buffer and SiC layers of the fuel particle has been increased in the specification. The configuration of the high burnup SiC coated particle is summarized in Table 3.21, comparing with the first loading fuel of the HTTR.

TABLE 3.21. MAJOR CONFIGURATION OF THE HIGH BURNUP SIC COATED FUEL PARTICLE

	High-burnup fuel	First loading fuel of the HTTR
Kernel diameter (µm)	500–550	600
Buffer layer thickness (µm)	90	60
SiC layer thickness (µm)	35	25–30
Target burnup (% FIMA)	5–10	3.6
Fast neutron fluence (10^{25} n/m^2)	3–5	1.5

In order to confirm the integrity of the high burnup SiC coated fuel particle, behaviour of the coating layer should be investigated. PIE techniques required for the investigation of the high burnup SiC coated particle are basically the same as those for the first loading fuel, except handling of the high burnup fuel. The major post-irradiation test items are measurements of the burnup and the through-coatings and SiC layer failure fractions. In addition, we are trying to develop a technique to measure the stress in the SiC layer by, for example, the Raman spectroscopy or the X ray diffraction analysis. The obtained stress data will be used to understand the quantitative relationship between the internal pressure and the coating failure and to develop an improved fuel failure evaluation code.

3.10.2.3. Post-irradiation programme for ZrC coated fuel particle

Major characteristics of the ZrC coated fuel particle are its high temperature resistance (much higher than 1600°C which is the criteria for SiC coated particle) and weakness against oxidation [100, 101]. Considering these characteristics, R&D should be carried out concentrating on ZrC behaviour at high burnups and high temperatures, and on its oxidation behaviour. In development of ZrC coated fuel particle, new PIE techniques should be devised to investigate its irradiation behaviour. Since a ZrC layer is easily oxidized by burning, the burn-leach method can not be applicable to measurement of the failure fraction of ZrC coated particle, while this method is useful for the SiC coated particle. Therefore an alternative method to measure the failure fraction should be developed. In this respect, a plasma oxidation technique was developed in order to remove the OPyC layer of unirradiated ZrC coated particle. Applicability of this method to irradiated ZrC coated particle will also be investigated.

4. CHARACTERIZATION AND ADVANCED QUALITY CONTROL TECHNIQUES

4.1. INTRODUCTION

Most of the high temperature gas cooled reactors successfully operated in the past several decades in the USA, Germany and the UK, and currently in operation in Japan and China have employed coated particle fuels, assembled in graphite matrix with various fuel element forms dependent on reactor design. The so-called pebble bed and prismatic cores are the two typical designs for the HTGR. Although these two different cores have various differences in nuclear and fuel element design, they contain similar coated particle fuels. A fuel element consisting of coated particle fuel in graphite matrix is one of the specific characteristics of HTGR for its inherent safety features.

As the coated particle fuels have features different from other nuclear fuels, fabrication technologies employed are also different from those for other nuclear fuels, which are mostly of pellet and fuel rod type. The fabrication technologies developed so far and currently being utilized involve fabrication of the nuclear fuel material into so-called kernels, which are small spherical particles of uranium oxide (UO_2) or uranium oxide mixed with uranium carbide (UCO), or even Pu- and Th-containing fuel materials. Pyrolytic carbon and SiC layers on the surface of the kernel in four successive layers form the tristructural isotropic coating (TRISO). Specifically, a silicon carbide layer is sandwiched between two dense pyrolytic carbon layers (Inner and Outer PyC), with a buffer layer of porous pyrolytic carbon surrounding the kernel. Layers are deposited by chemical vapour deposition (CVD) of the respective precursors, i.e. hydrocarbons and methyltrichlorosilane (MTS). These fabrication technologies and the relevant processes with adequate process parameters have to be developed and optimized to a certain extent in order to make the coated particle fuel well suited for its design criteria, i.e. the quality of the fuels fabricated with the developed technologies have to be within the design specification of the fuel.

In order to verify the quality, the fabricated coated particle fuel has to be tested in terms of its properties, as required by its fuel specification, which is based on and extended from the design specification. The properties of the fuel should ensure its performance behaviour and should be such that the fuel failure fraction be less than the limit given by the design criteria. An important concern in the inspection of the fuel is the characterization techniques employed, given that the measured properties must be accurate and relevant to the design basis.

In this section, after a short review and identification of the important properties measured for the coated particle, as previously and currently practiced, selection of the characterization items, techniques and measurements for a round robin exercise among the participating member states is described. These results are then summarized with a discussion of the different results of measurement performed among the participating Member States.

4.2. IDENTIFICATION OF IMPORTANT CHARACTERISTICS OF COATED PARTICLES AND THEIR CHARACTERIZATION TECHNIQUES IN HTGR FUEL PRODUCTION

Properties (inspection items for quality control) measured during the fabrication process of the coated particle fuel, though they are used in different fuel designs for pebble bed and prismatic cores, are similar and can be categorized into three groups: (1) fuel kernel inspection, (2) coated particle inspection, and (3) fuel element inspection. The first one is mainly for nuclear design, fuel performance and the coating process, the second one is mainly for fuel performance associated with retention of fission products in the coated particles, and the last group is for the fuel mechanical and chemical integrity. The fabrication processes of the HTGR fuel element in different fuel designs have been discussed in detail in the previous section for various fuel designs and manufacturing technologies employed by the member countries, including their respective schematic flow diagrams. Figure 4.1 shows representatively the schematic process flow diagram of the Chinese HTR-10 fuel manufacturing process for the pebble bed core fuel element [16].

The principal properties measured in quality control (QC) for several different past and present processes together with the QC specifications are summarized and compared in Table 4.1 [16, 68, 102, 103]. As can be seen in this table, different philosophies were adapted to assure the quality of the product.

In the early stages of TRISO processing development, several different characterization techniques were used in parallel to measure key fuel characteristics, as described in detail by Delle et al. [104] In the developmental stage, as many properties as possible were characterized in order to understand the complete material behaviour. However, once the fabrication process was established, routine QC inspection should measure only the specifically representative properties. Delle and Koizlik [105] listed the measured properties for testing of the coated particle fuel including the fuel elements as a final product, mostly for the pebble bed core. The properties they considered to be measured in the developmental phase were not completely identical with those controlled in the modern practice as shown in Table 4.1. The representative properties for kernels and coated particles were essentially the same as those listed in the table, except for the oxidation behaviour of coating layers. Additional items for structural material — and hence the fuel element considered at that time — were, for example, the electrical resistivity and the irradiation-induced creep. These were not considered as quality inspection parameters, and therefore, not specified in the fuel design. Also, Delle and Koizlik [105] further identified in more precise description, the QC

parameters associated with the pyrolytic carbon coating (PyC) layers; these included PyC growth feature size, PyC crystallite size, L_C, and the layer spacing, *c/2*. In addition, they described the available methods by which they attempted to measure the representative properties. They also discussed the characterization techniques in light of their adequateness for routine and timely quality inspection. Some of the examples are described in 4.2.2.

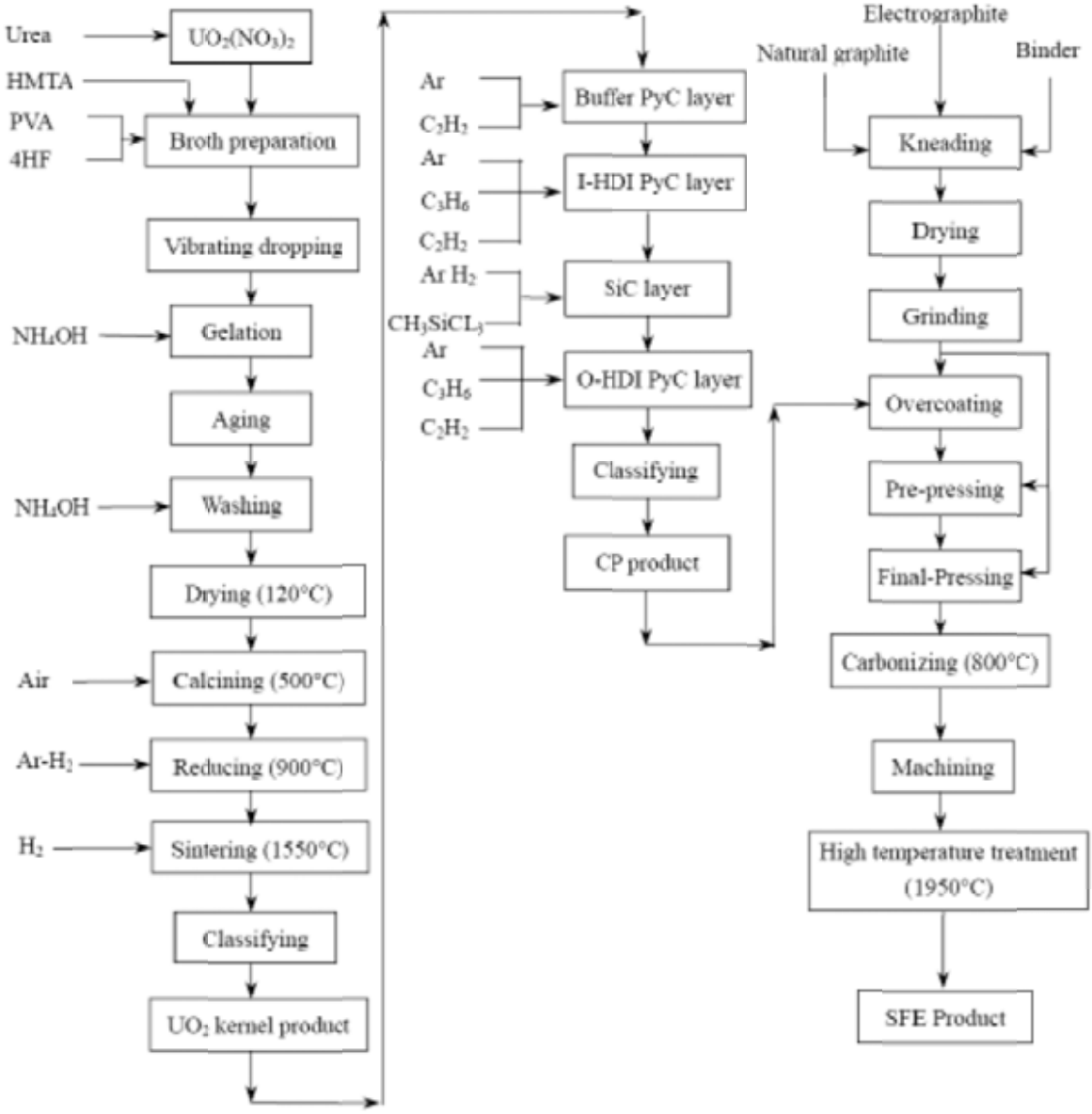

FIG. 4.1. Representative fuel manufacturing flow diagram for HTGR (pebble) fuel.

TABLE 4.1. COMPARISON OF ITEMS TO BE CONTROLLED AND SPECIFICATIONS OF THE COATED PARTICLE FUEL FOR THE DIFFERENT FUEL DESIGNS USED IN HTGR

	USA (NPR fuel)	Germany (HTR-Modul)	China (HTR-10)	Japan (HTTR)
Fuel kernel				
Kernel material	UCO	UO_2	UO_2	UO_2
Enrichment (wt%)	$93.15^{+0.15}_{-1.00}$	8.0 ± 0.1	17	6
Impurities (ppm)	≤ 5000	≤ 1.3 EBC	≤ 3 EBC	≤ 3 EBC
C/U atomic ratio	≤ 0.5	n.a.	n.a.	n.a.
O/U atomic ratio	1.4–1.7	—	≤ 2.01	—
Diameter (μm)	195^{+10}_{-50}	480–520	500 ± 50	600 ± 55
Density (Mg/m^3)	≥ 10.3	≥ 10.4	≥ 10.4	10.63 ± 0.26
Sphericity	—	1.07	≤ 1.2	—
Fraction of odd shaped kernels	—	10^{-5} after tabling	$\leq 5 \times 10^{-4}$	—
Coated particle				
Buffer layer thickness (μm)	90–110	72–108	90 ± 36	60 ± 12
Buffer layer density (Mg/m^3)	0.80–1.10	≤ 1.05	≤ 1.10	1.1 ± 0.1
IPyC thickness (μm)	40– 60	30–50	40 ± 20	30 ± 6
IPyC density (Mg/m^3)	1.85–1.95	1.91 ± 0.1	1.9 ± 0.1	$1.85^{+0.10}_{-0.05}$
IPyC BAF	≤ 1.20	≤ 1.1	—	—
IPyC OPTAF	—	—	≤ 1.03	≤ 1.03
SiC thickness (μm)	35–40	31–9	35 ± 10	25^{+12}_{-0}
SiC density (Mg/m^3)	≥ 3.18	≥ 3.18	≥ 3.18	≥ 3.2
OPyC thickness (μm)	30–50	25–45	40 ± 20	45 ± 6
OPyC density (Mg/m^3)	1.80–1.95	1.91 ± 0.1	1.9 ± 0.1	$1.85^{+0.10}_{-0.05}$
OPyC BAF	Not Specified	≤ 1.1	—	—
OPyC OPTAF	—	—	≤ 1.03	≤ 1.03
PPyC thickness (μm)	40– 60	~200	—	—
PPyC density (Mg/m^3)	0.80–1.10	—	—	—

— data not available.
n.a. not applicable.

In addition, they described for item by item the available methods by which they attempted to measure. They also discussed the characterization techniques for the adequateness to the routine quality inspection for the timely application. Some of the examples are described in 4.2.2.

4.2.1. Characteristics of UO_2 kernels in the kernel fabrication process

During kernel fabrication, the items for quality inspection differ among the fuel producing organizations, as is discussed and shown in the tables in the following sections for measured properties and preferred measurement techniques as well as the sampling rates of some items for HTR-10 fuel, for German LEU TRISO fuel, for HTTR fuel and PBMR fuel, respectively. Among others, important items characterized in kernel production are density of kernel, dimension and sphericity, O/M (heavy metal) ratio and fraction of odd shaped kernel.

Impurities can be checked either in the raw material inspection or after the kernel production and/or both depending on the purpose of the inspection. The odd shaped kernels can be removed during the process by use of a shape sorting table, but this item is again checked after the kernel production and/or after the coating process. The sampling rates are varied among organizations, and the sampling rate are usually established according to the stability of the process, hence the level of the quality confidence that the whole kernel production process can produce.

4.2.2. Characteristics of coated particles during the coating process

After the coating process, coated particles are subjected to inspection. The important items for the coated particles are; density and thickness of the four coating layers, anisotropy factor for IPyC and OPyC, particle dimension and sphericity, as is discussed and shown in the tables in the following sections. For certain items, such as buffer layer density, sampling should be done during the coating process, because the buffer density cannot be characterized accurately after the coating of the three outer layers. Among the inspection items, the most important items are defective SiC layers and surface contamination with uranium, which are usually checked by Burn-leach and leaching methods. Unlike other organizations, the Japanese NFI inspects these items after the fuel compact manufacturing.

4.3. ANALYSIS OF CHARACTERIZATION OF UO_2 KERNEL AND COATED FUEL PARTICLES

This section describes the characterization techniques and QC items currently established and their standard quality for the different production processes for HTR-10 in China, HTTR in Japan and PBMR in South Africa together with the former German HTGR, and compares their differences.

4.3.1. Characterization in the Chinese fuel element production for the HTR-10

4.3.1.1. Inspected parameters

In order to ensure the fuel quality, many properties of product (the spherical fuel element), intermediate products (UO_2 kernel, coated fuel particle and matrix graphite) and main raw materials (uranium, natural and artificial graphite powder, and phenol resin binder) need to be inspected. The inspected items of HTR-10 spherical fuel elements, their intermediate products and raw materials are shown in Fig. 4.2.

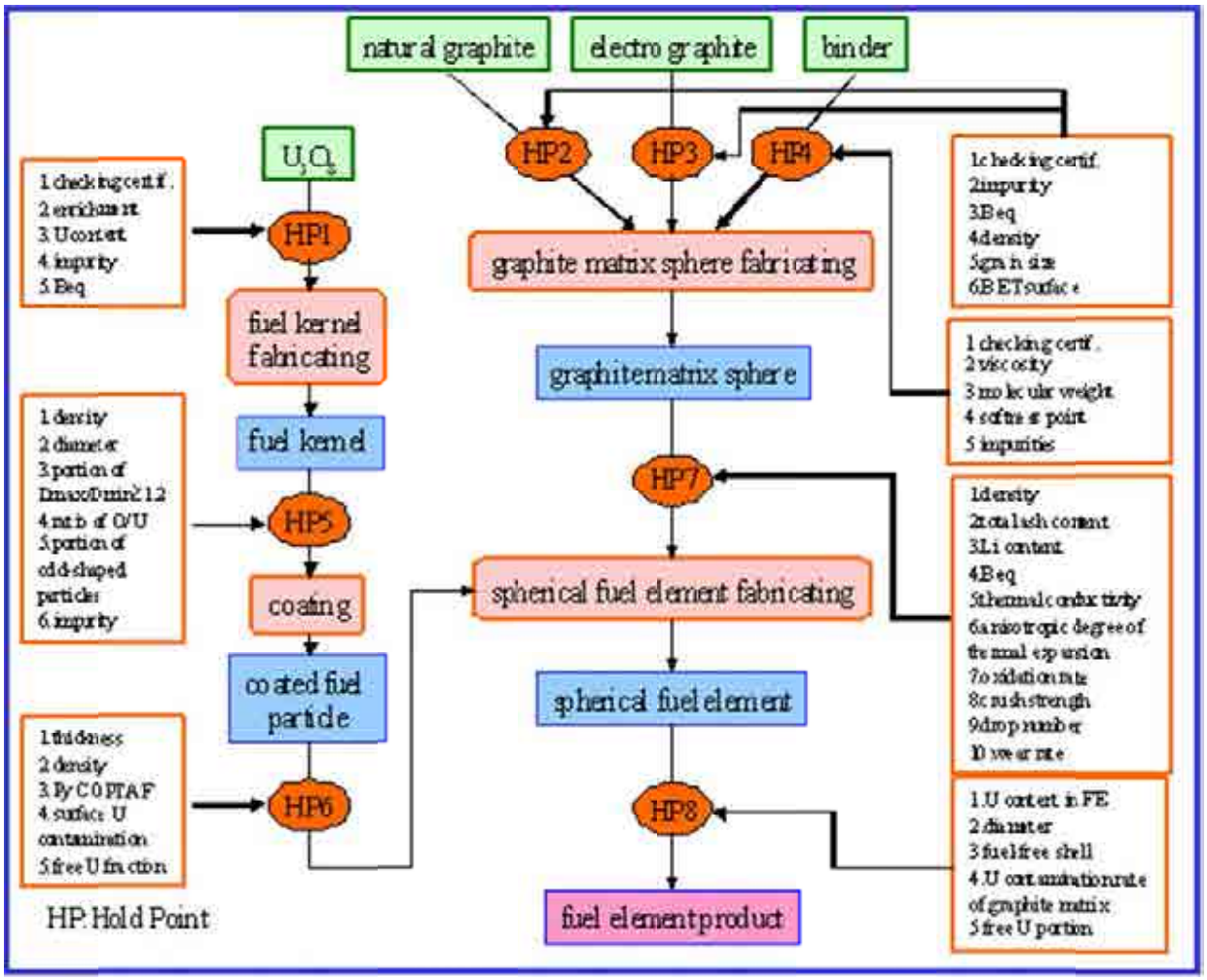

FIG. 4.2. Inspected items of HTR-10 fuel.

4.3.1.2. Used measurement methods

In order to measure all the properties of HTR-10 fuel element, its intermediate products and raw materials, some traditional measurement methods were adopted. However, due to details specific to TRISO fuel manufacturing, some quick, precise and simple measurement methods were researched and developed. Therefore, some new measurement methods and related instruments and devices have been also developed. The measurement methods of all the properties of UO_2 kernels, coated fuel particles for the HTR-10 are listed in Table 4.2.

TABLE 4.2. MEASUREMENT METHODS FOR UO_2 KERNELS AND FOR COATED FUEL PARTICLES IN HTR-10 FUEL PRODUCTION

QC HP	Inspected product	Inspection item	Inspection method, instrument
Fuel kernel			
HP 5	Fuel kernel	Density	Specific gravity bottle
		Diameter	Micro-radiograph, projection instrument
		Portion of $D_{max}/D_{min} \geq 1.2$	Micro-radiograph, digital image method
		Ratio of O/U atom number	Thermogravimetric method
		Portion of odd shaped particles	Vibration, stereoscopic microscope
Coated fuel particle			
HP 6	Low density PyC layer	Thickness	Metalloscope, displacement sensor
		Density	Weighing, size measurement
	Inner high density PyC layer	Thickness	Metalloscope, displacement sensor
		Density	Titration
		Anisotropy degree	Microscope photometer model MPV-2
	SiC layer	Thickness	X ray photograph, projection instrument
		Density	Titration
	Outer high density PyC layer	Thickness	X ray photograph, projection instrument
		Density	Titration
		Anisotropy degree	Microscope photometer model MPV-2
	Coated fuel particle	Surface uranium contamination	Leaching, laser-induced fluorimetric method
		Free uranium content	Burning and leaching, laser-induced fluorimetric method

4.3.1.3. Standard quality

A total of 44 batches of UO_2 kernels and coated fuel particles (3 kg of UO_2 per batch) have been produced for first loading of the HTR-10 in 2000 and 2001. The measured data for all performance items in each batch are summarized in Table 4.3. A metallographic cross-section of the TRISO coated UO_2 particles and the micro-structure of the SiC layer, which has important impact on the SiC strength and the diffusion of the fission products in the SiC layer, is shown in Figs 4.3 and 4.4, respectively. In comparison with NUKEM coated fuel particle, the standard deviation of UO_2 kernel diameter is a little large, but the sphericity of the INET UO_2 kernel and the thickness deviations of the PyC and SiC layers are as good as those of NUKEM.

TABLE 4.3. STATISTICAL PERFORMANCE DATA OF COATED FUEL PARTICLES IN THE PRODUCTION OF HTR-10 FIRST-LOADING FUEL

Performance item	Mean value of lots	Standard deviation of mean value of lots	Standard deviation of all samples
UO_2 kernel			
Diameter (μm)	497.0	7.0	14.8
Density (Mg/m^3)	10.81	0.05	—
Sphericity (D_{max}/D_{min})	1.044	0.009	0.027
O/U ratio	2.00	0	—
Equivalent B content (μg/g)	0.25	0.15	—
Coated fuel particle			
Buffer PyC layer thickness (μm)	99.1	7.4	11.8
IPyC layer thickness (μm)	41.6	3.2	4.3
SiC layer thickness (μm)	36.6	1.8	2.6
OPyC layer thickness (μm)	42.5	1.9	4.8
Buffer PyC layer density (Mg/m^3)	0.98	0.07	—
IPyC layer density (Mg/m^3)	1.85	0.02	—
SiC layer density (Mg/m^3)	3.20	0.00	—
OPyC layer density (Mg/m^3)	1.86	0.03	—
IPyC layer OPTAF [a]	1.025	0.005	—
OPyC layer OPTAF [a]	1.023	0.005	—

[a] optical anisotropy factor.
— data not available.

The radiological fission products released to the primary coolant should be as low as possible. Except ^{110m}Ag, all fission products can be completely retained inside the intact SiC layer of the TRISO coated fuel particles below 1200°C [106, 107]. Therefore the dominant sources of fission product release in the HTR-10 reactor are due to the defective SiC layers of few particles and the contaminated uranium in the matrix graphite and the outer PyC coating. The uncoated uranium in the particles with defective SiC layer and the contaminated uranium are referred to as 'the free uranium'. The free uranium fraction is measured by the burn-leach method. The average free uranium fraction of 44 spherical fuel element lots for the HTR-10 first loading fuel is 4.5×10^{-5}. It is noticeable that the average free uranium fraction in the beginning of fabrication (from F1 to F10) was 1.1×10^{-4} and decreased in the subsequent fabrication (form F11 to F44) to 2.7×10^{-5}. The improvement is attributed to buffering strong mechanical impact and collision of coated fuel particles during the unloading from the fluidized bed, carrying out the sieving and sorting of the UO_2 kernels and coated fuel particles more carefully and reducing odd shaped UO_2 kernels and avoiding twin overcoated particles.

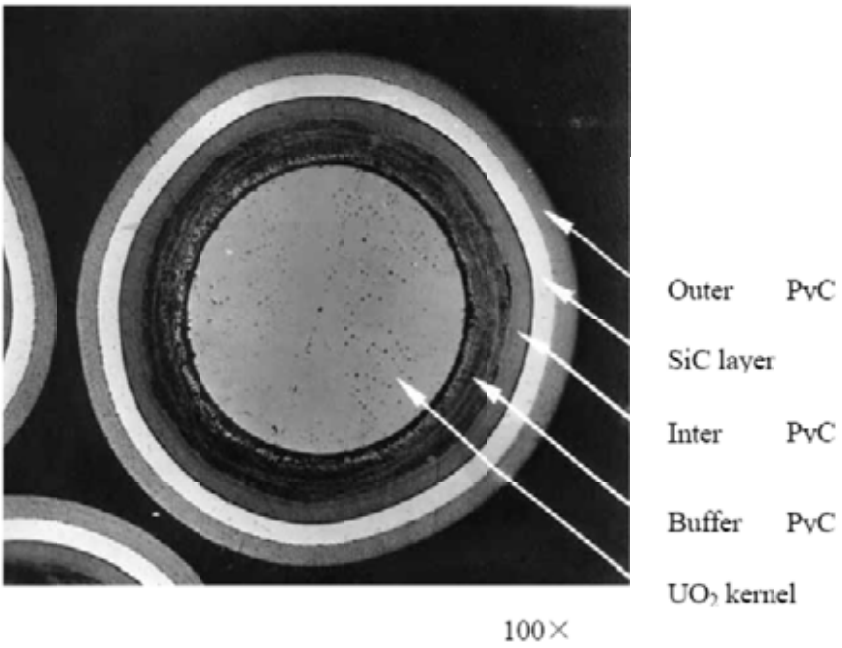

FIG. 4.3. Metallographic section of the coated fuel particle.

FIG. 4.4. Micro-structure of SiC coating (etched).

Each batch contains about 500 spherical fuel elements. Two or four fuel pebbles were inspected through the burn-leach method for measuring free U content in each batch. Table 4.4 shows the number of the fuel pebbles with different number of failed particles in all the inspected spherical fuel elements.

TABLE 4.4. THE HTR-10 MANUFACTURE-INDUCED DEFECTIVE PARTICLES

Fuel pebbles produced for HTR-10	Inspected fuel pebbles/particles in inspected fuel pebbles	Number of fuel elements in burn-leach test with x defective particles						Free uranium (10^{-5})	Design specification (10^{-4})
		X = 0	X = 1	X = 2	X = 3	X = 4	X ≥ 5		
20 451	96/796 800	72	17	3	3	1	0	4.5	3.0

4.3.2. Characterization of the German LEU TRISO fuel element production

4.3.2.1. Principles of German fuel quality assurance procedure

Requirements for the coated fuel particle design are principally defined to address the selected fuel cycle, the chemical behaviour of the fuel kernel during irradiation, and the overall irradiation performance. Since the fuel element plays a central role in retention of radionuclides in an HTGR, quality assurance (QA) and quality control (QC) of as-manufactured fuel will be of utmost importance. Quality is defined as conformity of properties and conditions of items or activities with the specifications. Quality can be measured by identifiable and measurable characteristics. The programme to assure quality consists of programmatic (administrative) and work-oriented (technical) activities and requires an effective management to provide control and verification.

The principal intention of the proof tests is receiving data to demonstrate the feasibility and reliability of fuel elements manufactured by the prescribed procedures and components. The reference tests are intended to ensure that the irradiation results of the previous generic qualification programme for the LEU TRISO fuel can also be transferred to the fuel fabricated on a large production scale and to the operating conditions of the German HTR-Modul. In combination with the post-irradiation examinations, these tests with randomly selected fuel elements fabricated under the conditions of mass production provide the necessary information for the specification and production of licensable fuel spheres for future HTGRs.

In order to transfer the results of the proof tests to fuel elements manufactured later, the exact conformity of manufacturing now and later has to be assured. This is done by describing the manufacturing processes in detailed procedures, by automated process control as far as possible, and by specifying examinations and inspections to scrutinize the manufactured quality with the properties of the standard quality. The requirements for these inspections are described in the work performance and inspection sequence plan dealing with

- raw, auxilliary, and operational materials;
- kernels and coated particles;
- matrix materials;
- fuel elements.

The SiC layer is the most important barrier to keep the fission products inside the coated particles. Damage of the SiC layer during the manufacturing process should therefore be minimized. Defective SiC layers are measured by the so-called ‘burn-leach’ test. Test results are authenticated in certificates in accordance with the German DIN 50049, 3.IB.

4.3.2.2. Inspected parameters

Within the extensive German fuel qualification programme in the past, the procedure was such that certain quality characteristics were specified and then proven by examination. This applied to the fuel kernels, the coated particles, the fuel spheres, and, first of all, to the raw materials. The major characteristics examined and the standard testing methods which were used in Germany are presented in further detail in Table 4.5 [108]. The following sections will describe some of the major techniques of characterizing coated particle fuel [104].

4.3.2.3. The used measurement methods

(a) Particle size analysis

The automated optical particle size analyser (PSA) is a device for measuring kernel and particle diameters and respective volumes. It is considered a reliable, accurate and precise method based on the variation of light intensity when a particle is passing a light beam. The achievable throughput rate is on the order of about 50 particles per second, the feed rate is chosen to match the desired accuracy and precision of the application. The sphericity of kernels and coated particles, i.e. the ratio of a particle's maximum diameter to its minimum diameter, can also be measured by having one particle pass the light beam many times with randomly changed position. Other procedures involve optical image analysis of a photograph of a large number of particles on a tray.

(b) Kernel, buffer and coating layer density measurement

Density is one of the most important parameters with regard to both fission gas retention and irradiation behaviour. SiC and pyrolytic carbon densities are typically measured with the sink-float method (Fig. 4.5) by means of suitable gradient density columns. In a column, two miscible liquids, are mixed such that a uniform density gradient is developed. Representative test samples are obtained by extraction from the coater after completion of the layer considered. Pieces of that layer are then cracked off and allowed to sink and settle in the column. The column is calibrated by means of standards of known density.

This method is neither applicable to UO_2 kernels where density is too high, nor to the porous buffer layer, where liquid infiltration may occur. For these components, the particle size analyser or a mercury porosimeter is used to determine kernel and buffer volume. With regard to the kernel, the mass of a sample of kernels is determined, before it is passed through the PSA and the sum of the volume of all the kernels in the sample is divided by the sample mass to yield the mean kernel 'apparent' density. The density of the buffer layer is determined in a similar way after subtracting the mean kernel volume from the mean total volume and using the appropriate mass values. The real or 'theoretical' density considering a specimen without internal voids is measured by grinding the specimen to powder with ~1 μm sized particles and employing a pycnometer to determine the powder volume. The total porosity can then be calculated by 1 minus the ratio of apparent density over theoretical density.

TABLE 4.5. CHARACTERIZATION METHODS APPLIED IN GERMANY FOR HTGR FUEL

Inspection item	Method	Sampling rate
Starting and raw materials		
Compression density of graphite powder	Density measurement under defined load	Powder in forging die
Rebound of graphite powder	Measurement of height difference of powder column during and after load	Powder in forging die
Specific electric resistance of graphite powder	Measurement of voltage drop along powder column	Powder in forging die
Impurities in graphite powder	Chemical analysis after incineration, emission and absorption spectrometry, photometry, fluorimetry	Representative quantity
Impurities in uranyl nitrate solution	Chemical analysis after incineration, emission and absorption spectrometry, photometry, fluorimetry	Representative quantity
Isotope composition	Mass spectrometry with regard to U-234, U-235, U-238	Representative quantity
Fuel kernel		
Heavy metal loading	Transfer of kernels into a stoichiometrically well defined state and do chemical analysis	
O/M ratio	Potential controlled coulometry	
Isotope composition	Mass spectrometry with regard to U-234, U-235, U-238	
Carbon content	Oxidation of kernels and do chemical analysis of CO_2	
Oxygen content (UCO)	Hot extraction of oxygen, transfer into CO and do chemical analysis of CO, infrared spectrometry	
Doping agent content	Spectral photometry, Atom absorption spectrometry	
Diameter	Optical imaging with particle size analyser, X ray micro-radiography	
Sphericity	Counting of fraction of odd shaped particles, Multiple measurement of maximum and minimum diameter, Micro-radiography, stereo-microscope	
Density	Optical particle size analyser or V-slot to measure mean diameter; Mercury pycnometer or air pycometer to measure volume	Larger number of kernels
Structure	Measurement of reflection on defined lattice planes, X ray with Debeye–Scherrer goniometer	Ground kernels
Sieve fraction	100% sieving with DIN sieves	
Weight	Weight of counted number of kernel and determine mean weight	

Impurities	Spectral photometry, Atom absorption spectrometry	
Coated fuel particle		
Diameter	Optical particle size analyser	
Layer thickness	X ray projection micro-radiography (only OPyC and SiC), X ray contact micro-radiography, Microscopy analysis of ceramographic sections, Optical particle size analyser, Fluid pycnometer (in case of discontinuous coating of single layers at a time)	
Density	Weight of counted number of particles and determine mean weight	
Density of highly dense layers	Liquid density gradient column with calibration bodies, Gas pycnometer	Volume of ~50 g
Optical anisotropy factor OAF (in air) or OPTAF (in oil), Bacon anisotropy factor BAF	Ceramographic sections exposed to polarized light, OPTAF is ratio of reflected light intensity vertically to deposition direction over reflected light intensity in deposition direction; Correlation between OPTAF and BAF	
Growth features size and distribution	Etching of ceramographic sections by wet oxidation, plasma oxidation, or ion bombardment, Scanning electron microscopy (SEM), Transmission electron microscopy (TEM)	SEM on fractured coating, TEM on thinned coating specimens
Polygonity of layers	X ray diffraction, Stereo-microscope, Measurement of layer thickness in 3^{00}–9^{00} position	
Heavy metal content	Grinding of particles and transfer into distinct compounds of U by oxidation, quantitative chemical analysis of U	
Surface contamination	Leaching of particles with HNO_3, quantitative chemical analysis of U	
Defective SiC layers	Burn-leach method	
Heavy metal migration	Micro-radiography, visual inspection of buffer layer	
Tightness of IPyC	Micro-radiography, visual inspection of buffer and IPyC layers after leaching with HNO_3 compared to before	Samples taken after IPyC coating process
Micro-porosity	Determination of fractions of layer, fiber, mosaic components in PyC by X ray small-angle diffraction	Fragments of PyC layers
Pore structure	Quantitative image analysis and determination of pore size distribution	
Ultimate tensile strength of PyC, SiC	Determination of fracture load by crushing between sapphire plates, Hemispherical bursting, Ring compression test	Single SiC or PyC rings prepared from layers, Single SiC half shells
Micro-hardness	Vickers or Brinel hardness	

E-modul of PyC and SiC	Crushing between sapphire plates and recording stress–strain curve	PyC or SiC specimens
Fuel sphere		
Matrix density	Dimension and weight measurements	Matrix specimens 5 × 5 × 35 mm^3
Thermal expansion coefficient and anisotropy	Measurement of temperature and dimensional change with dilatometer; Anisotropy is ratio of coefficient (parallel) over coefficient (vertical)	Matrix specimens 5 × 5 × 35 mm^3
Dynamic elasticity modulus	Elastomat or frequency generator $E = 4 \cdot f^2 \cdot l^2 \cdot \rho$ where f is the resonance frequency, l is length, and ρ is density	Matrix specimens 5 × 5 × 35 mm^3
Bending strength	3-point test on bending device $\sigma = (F_m \cdot l)/W$ where F_m is the fracture strength, l is the support span, and W is the resistance momentum	Matrix specimens 5 × 5 × 35 mm^3
Compressive strength	$\sigma = F_c/Q$ where F_c is the crushing strength, and Q is the cross-section of specimen	Matrix specimens 5 × 5 × 35 mm^3
Tensile strength	$\sigma = F_t/Q$ where F_t is the breaking force, and Q is the cross-section of the specimen	Matrix specimens 8 mm diameter × 30 mm
Specific electrical resistance	$R = (U \cdot Q)/(I \cdot l)$ where U is the voltage drop, Q is the cross-section, I is the electric current, and l is length	Matrix specimens 5 × 5 × 35 mm^3
Thermal conductivity @ RT	Direct measurement	Matrix specimens 5 × 5 × 35 mm^3
Thermal conductivity @ 40°C	Thermo-conductometer after Schröder setting a stationary temperature differenz by means of the boiling temperatures of two liquids and measuring the time required for the vapourization of a certain quantity of liquid, comparison with calibration standard	Matrix specimens 5 × 5 × 35 mm^3
Thermal conductivity @ 1000°C	Radial flux method $\lambda = (Q \cdot \ln(r_2/r_1))/(2 \cdot l \cdot \Delta T)$ where Q is the power of the central heater, r_1, r_2 are the distances of the TC from specimen axis, l is the active length of the specimen, and ΔT is the temperature difference between TC;	Matrix specimens 40 mm diameter × 25 mm
	Modified Kohlrausch procedure by setting an almost parabolic axial temperature profile with maximum in specimen centre and small drop to the sides (< 10°)	Matrix specimens 6 mm diameter × 32 mm with axial bore hole of 1 mm diameter
Impurities, ash contents, B equivalent	Spectral photometer, atomic absorption spectrometry	20–50 g of matrix material
Number of drops	Drop onto pebble bed of the same spheres until fracture	Sphere
Fracture load	Direct measurement of fracture strength with specimen between two parallel steel plates pressed at a rate of 10 mm/min	Sphere
Corrosion velocity	Determination of mass loss after heating up to 900°C or 1000°C in pure flowing helium and then change gas stream to helium plus 1% water contents and heating for 10 h @ constant	Sphere

	temperature and 0.1 MPa $K = \Delta m/(F \cdot t)$ where Δm is the mass loss, F is the sphere surface, and t is time	
Fuel-free zone	Examination of particle-free shell by X ray and visual inspection	Sphere
Abrasion	Determination of mass loss in mg/h in flowing helium in abrasion drum rotating at 55 rpm over 100 h	20 spheres
Surface appearance	Visual inspection	Sphere
Released heavy metal (matrix contamination)	Electrolytical disintegration of matrix material with HNO_3 and quantitative chemical analysis of U in electrolyte and leach solution	Sphere
Defective SiC layers	Burning of spheres in muffle furnace and leaching of U	Sphere
Heavy metal content	Burning of spheres in muffle furnace, destruction of SiC layers	Sphere
Pore size distribution	Quantitative image analysis or determination of pore radius by mercury porosimeter $p \cdot r = 2 \cdot s \cdot \cos\Theta$ where p is pressure, r is the pore radius, s is the surface tension, Θ is the border angle between specimen and mercury	

One method to measure layer thickness is by X ray micro-radiography allowing good statistics of intrinsic layer variation over a large number of particles (100–200). A mono layer of particles is positioned directly on a high resolution photographic film and exposed to an X ray source. Layer thickness analysis of the film is done in a transmission light microscope using standard image processing software. Another option is optical image analysis of a monolayer of particles polished to the midplane.

(c) Anisotropy

High density pyrocarbon is a polycrystalline graphitic material and therefore has anisotropic material properties, such as thermal expansion and fast neutron induced shrinkage. The material should be as isotropic as possible to allow a uniform heat conduction and minimize dimensional changes under irradiation.

A direct measure of the anisotropy in macroscopic material is the so-called Bacon Anisotropy Factor, BAF. According to the method derived by Bacon [109], a frequency distribution J(Θ) of the interference (OO2) is determined where Θ is the angle between deposition normal and c-axis of the particular crystallites.

$$BAF = 2 \frac{\int_0^{\pi/2} J(\Theta) \sin\Theta \cos^2\Theta \, d\Theta}{\int_0^{\pi/2} J(\Theta) \sin^3\Theta \, d\Theta} \qquad (4.1)$$

The BAF is basically defined by the coefficients of thermal expansion at 400°C parallel and perpendicular to the preferred orientation. The BAF cannot be measured easily on coated fuel particles. Usually it is necessary to deposit pyrolytic carbon on graphite and produce small disk type specimens.

Since the structure of PyC on spherical particles is not homogeneous, an optical method can be applied based on the bi-reflection of crystalline graphite. A beam of linear polarized light is sent through the equatorial area of the coated particle onto a ceramographic Section (Fig. 4.5). The ratio of the reflected intensities of the light with polarization and preferred direction being parallel over the case with polarization and preferred direction being perpendicular is called the optical anisotropy factor, OPTAF (or OAF). The OPTAF again is related to the BAF.

(d) Burn-leach testing

One of the essential characterization techniques for quality assurance is the burn-leach testing of HTGR fuel. During a ‘burn-and-leach’ test, the graphite of the sample to be measured (loose coated particles, fuel sphere, fuel compact or coupon) is burnt in a combustion chamber at ~800°C in air down to the SiC layer, until the weight remains constant (about 90 h for a fuel sphere). The residual of ash and particles is treated with a nitric acid solution at ~100°C and the amount of dissolved uranium is analysed. Since the SiC layer is corrosion resistant, the uranium found in the solution includes the natural U-content of the matrix material and the U content of those particles with a defective SiC layer. Also particles with an incomplete coating will be identified. Test results are presented as the ratio of measured free uranium

over the inserted uranium, U_{free}/U_{tot}. The detection limit is typically at a level of 1–3 × 10^{-6} depending on the uranium content of the sample, much lower than the uranium content of a single defective coated particle. In a fuel element with about 1 g of ^{235}U/sphere and 0.07 mg/particle, the content of one defective particle corresponds to an U_{free}/U_{tot} value of 7 × 10^{-5}.

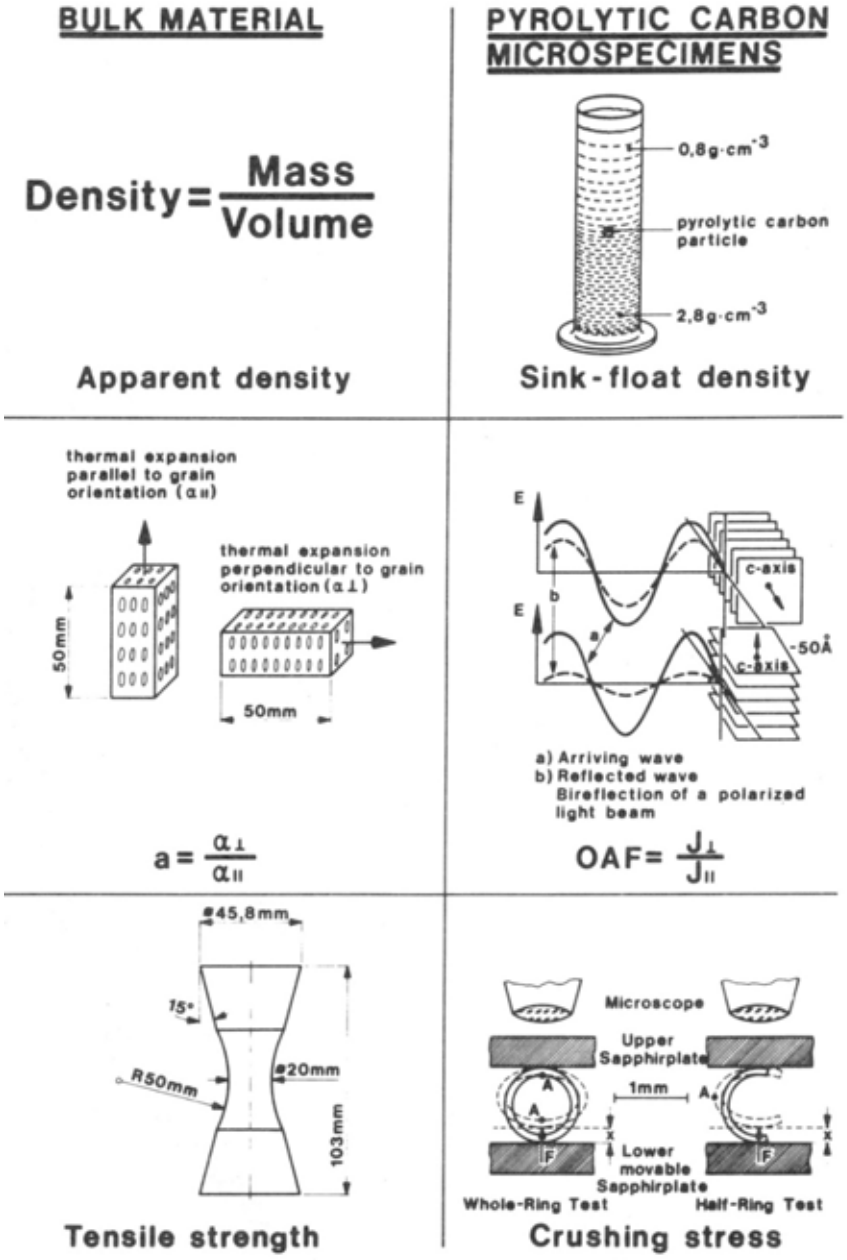

FIG. 4.5. Quality control methods for the determination of density, anisotropy, and strength.

4.3.2.4. Quality of fuel produced for the AVR

Uranium contamination in fresh fuel elements for the AVR was specified to not exceed the limit of 5×10^{-4}. It was measured by leaching and etching. Table 4.6 summarizes the acquired data for different fuel types [110]. The table also indicates a steadily increasing final heat treatment temperature which was used to further reduce the impurity level in the spheres and thus raise its resistance against corrosion. The relatively high contamination for BISO fuel compared to TRISO is due to the manufacturing process where the final heat treatment at high temperatures expels the heavy metal from the kernel into coating and matrix material.

TABLE 4.6. AVERAGE U CONTAMINATION IN AVR FUEL ELEMENTS OF DIFFERENT TYPES

Fuel type	Reload charge	Fraction of U-contamination (10^{-4} U_{free}/U_{tot})	Final heat treatment (°C)
UCC	First core	4.7[(a)]	1450
T	1	0.7 ± 0.5	1450
GK	3, 4, 5	9.6 [a]	1800
GO	5-2, 6-1	1.0 [a]	1800
GO	6-1, 7	1.0 [a]	1900
GLE-1	6	7.0 ± 7	1900
GLE-2	6	11.9 ± 7	1900
GFB-1	8	2.6 ± 7	1900
GFB-2	8	1.6 ± 1.6	1900
GO-THTR-1	9	4.8 ± 0.6	1900
GO-THTR-2	10, 11	2.7 ± 0.6	1950
GO	12	2.9 ± 0.5	1950
GLE-3	19	0.49 [b]	1950
GLE-4	21	0.46 [b]	1950
GLE-4	21-2	0.078 [b]	1950

[a] calculated from comparative measurements.
[b] from [46].

4.3.2.5. Free uranium in modern German HTGR fuel

The TRISO particles with defective coatings can be determined by the burn-leach method. In a study conducted by Interatom [111, 112] evaluating the burn-leach measurements on as-manufactured spherical fuel elements (AVR-19, proof test fuel) with TRISO coated LEU particles, the fraction of free uranium, U_{free}/U_{tot}, i.e. uranium not covered by an intact SiC coating, was generally found to be either below or near the detection limit (typically 1×10^{-6}), or a multiple of the uranium inventory of a single coated particle ($1/16400 = 0.6 \times 10^{-4}$). These measurements indicate that in most cases the measured U_{free} fraction is due to fabrication-induced defective particles, whereas the quasi-homogeneously distributed ^{235}U contamination level in the matrix material is extremely low basically originating from natural contamination of the graphitic raw materials. Figure 4.6 shows all non-zero results from the AVR-19 fuel production.

The total AVR-19 fuel production was done in 14 lots each comprising some 2000 spheres. From each lot, five spheres were taken for the destructive burn-leach test. From these 70 spheres examined, 39 were identified to contain one (26) or two (9) or three (4) particles with a defective SiC coating layer. These data correspond to a Poisson distribution with a mean and variance of 0.80 defects per fuel sphere and a relative defect fraction of 4.9×10^{-5} for the AVR-19 fuel (GLE-3) [112]. Improvements in the fuel manufacture procedure have resulted in lower defect fractions with expected values of 1.1×10^{-5} for the recent fuel and 3.9×10^{-5} for the total manufactured UO_2 TRISO fuel in Germany.

In safety analyses for future HTGR designs regarding modern UO_2 TRISO fuel, an expected value for the free uranium fraction of 3×10^{-5} (which was the initial target of fuel development) was chosen [1]. This value was practically exclusively due to defective particles. Contamination with natural uranium introduced by the graphite raw materials is estimated to be 1×10^{-6}. As a design value for radiological calculations, the recommended assumption for the contamination is 50 µg of natural uranium per sphere, which translates into a U_{free}/U_{tot} fraction of 7×10^{-6} (related to the HTR-Modul fuel element with 7 g of uranium per sphere) [111].

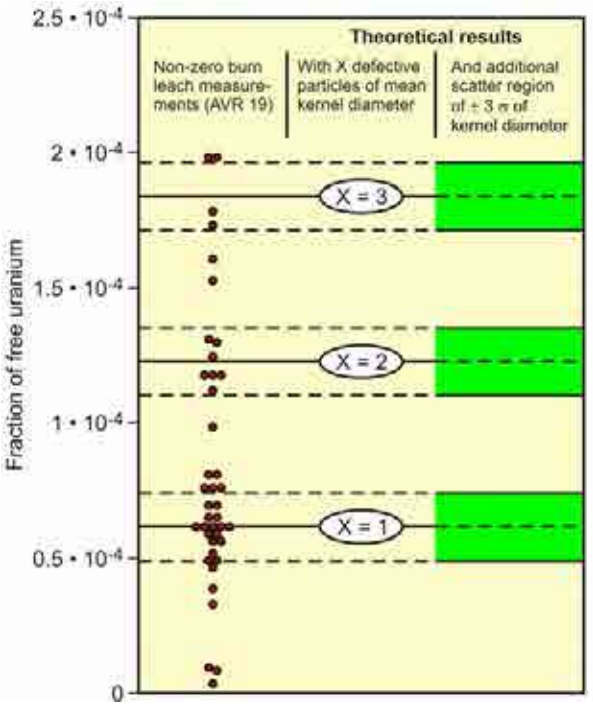

FIG. 4.6. Free uranium measurements from burn-leach tests on GLE-3.

Later productions of LEU TRISO fuel representing the state-of-the-art of German pebble fuel development resulted in a further improvement of the statistics. Table 4.7 shows the results of the quality examination comparing GLE-3 (AVR reload charge 19) and GLE-4 (AVR reload charges 21 and 21-2) with the proof test fuel (= German reference) produced in 1988 on a small scale. The table summarizes the achievements in quality of the German spherical fuel element production showing the improvement in fuel quality when comparing the pre- and post-1985 fuel productions, which is mainly the effect of moving over to automated particle overcoating and of the fact that the kernel, the coated particle, and the coated particle with overcoating were subjected to running over the vibration table, a quality control method which allowed a better separation of odd shaped particles.

The level of heavy metal contamination and the transport of iodine and fission gases in graphite in the temperature range of 1000–1800°C were subject to the heating test series, FRJ2-KA1 and FRJ2-KA2, at the Research Center Jülich [113]. In each test, three AVR spherical fuel elements of type GLE-4 (AVR 21-2) with UO_2 TRISO coated fuel particles were activated at a temperature of about 420°C to 0.6 and 2% FIMA, respectively, to produce short-lived isotopes. Shortly afterwards the spheres were heated at 1000, 1200, or 1400°C over 50 h followed by a 1600 or 1800°C over another 50 h, or even at 2000°C for 2 hours in order to investigate the release behaviour of the short-lived isotopes from the heavy metal contamination. Heating in the high temperature range was expected to release all contamination-related fission gases. Iodine and xenon transient release curves were observed to be similar supporting the interpretation of a release from traps in the matrix graphite. The fact that a burst-like release occurred between 1000 and 1600°C, supports the interpretation of a release from traps within the matrix. In FRJ2-KA1, the ^{131}I activities deposited on the condensing plates were mostly near the detection limit. In contrast, the extremely small amounts of iodine could well be measured in FRJ2-KA2 and traced back to contamination of the matrix with natural uranium of < 0.1 ppm. A burst-like release of iodine between 1600 and 1800°C shows that still at this high temperature level (Fig. 4.7), iodine is being retained to a certain degree. Overall release fractions were very low with an average value of 6×10^{-9} (FRJ2-KA1) and 8×10^{-9} (FRJ2-KA2) as is shown in Table 4.8. Other fission products such as ^{137}Cs or ^{85}Kr could not be measured accurately due to low inventories and low releases. The analysis has shown that the heavy metal contamination level was more than one order of magnitude lower than guaranteed by the fuel manufacturer [113].

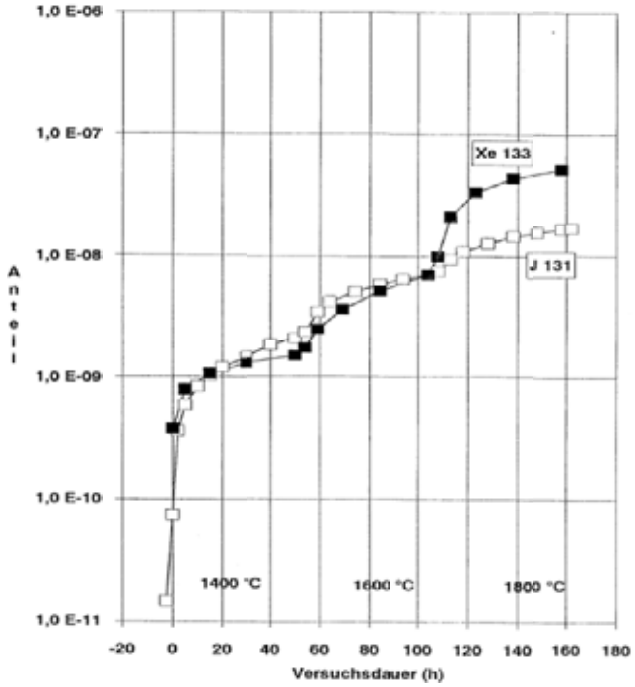

FIG. 4.7. Fractional release of ^{133}Xe and ^{131}I from the sphere FRJ2-KA2/3.

TABLE 4.7. EVALUATION OF FREE URANIUM AND DEFECTIVE SIC IN GERMAN UO_2 TRISO FUEL ELEMENTS

Designation of fuel element (FE) population	LEU Phase I	AVR 19	AVR 21	AVR 21-2	Proof test fuel
Production year	1981	1981	1983	1985	1988
No FEs produced	< 100	24 600	20 500	14 000	< 200
U-235 enrichment	9.8%	9.8%	16.7%	16.7%	10.6%
Number of particles/FE	16 400	16 400	9 560	9 560	14 600
Evaluation of free uranium from burn-leach measurements					
Number of fuel elements tested in burn-leach	5	70	55	40	10
No. of FEs with 0 defective particles	3	31	42	38	8
No. of FEs with 1 defective particle	1	26	8	1	1
No. of FEs with 2 defective particles	1	9	2	1	1
No. of FEs with 3 defective particles	0	4	2	0	0
No. of FEs with 4 defective particles	0	0	0	0	0
No. of FEs with 5 defective particles	0	0	0	0	0
No. of FEs with 6 defective particles	0	0	1	0	0
No. of FEs with ≥7 defective particles	0	0	0	0	0
Total number of defective particles observed	3	56	24	3	3
Total number of measured particles	82 000	1 148 000	525 800	382 400	146 000
Measured free uranium fraction	3.7×10^{-5}	4.9×10^{-5}	4.6×10^{-5}	7.8×10^{-6}	2.1×10^{-5}
Upper 95% confidence limit of U_{free}	9.5×10^{-5}	6.1×10^{-5}	6.4×10^{-5}	2.0×10^{-5}	5.3×10^{-5}
Average number defective particles per FE		0.64		0.12	

TABLE 4.8. FRACTION OF HEAVY METAL CONTAMINATION IN GERMAN HIGH QUALITY FUEL ELEMENTS DERIVED FROM HEATING TESTS WITH ACTIVATED GLE-4 SPHERES

Test	Fractional release after			
	50 h @ 1600°C [a]		50 h @ 1800°C	
Nuclide	Xe-133	I-131 [b]	Xe-133	I-131
FRJ2-KA1/1	5.6×10^{-9}	3.7×10^{-9}	—	—
FRJ2-KA1/2	5.8×10^{-9}	5.2×10^{-10}	—	—
FRJ2-KA1/3	8.7×10^{-9}	2.3×10^{-9}	—	—
Mean value	2.2×10^{-9}	6.0×10^{-9}	—	—
FRJ2-KA2/1	1.1×10^{-8}	9.9×10^{-9}	—	—
FRJ2-KA2/2	6.9×10^{-9}	9.0×10^{-9}	—	—
FRJ2-KA2/3	7.1×10^{-9}	7.1×10^{-9}	5.2×10^{-8}	1.7×10^{-8}
Mean value	8.7×10^{-9}	8.2×10^{-9}	5.2×10^{-8}	1.7×10^{-8}

[a] FRJ2-KA1/2 only 36.5 h.
[b] Values for FRJ2-KA1 relatively uncertain.
— data not available.

4.3.3. Characterization in the Japanese fuel element production for the HTTR

4.3.3.1. Inspected parameters

The inspection items are determined to confirm specifications, which certify nuclear and thermal-hydraulic design, irradiation performance and so on. Considering the purposes for inspections, the inspection items can be divided into three categories [102, 114]:

(1) Compulsory;
(2) user's requirement or optional;
(3) vender's quality control.

The sampling rate is also determined by considering the variability in inspection measurements. Three categories are basically classified as (a) small-scattering data, (b) medium-scattering data and (c) large-scattering data. One sample is measured from an inspection lot with small-scattering data. For the inspection lot with medium-scattering data, three samples are measured and all of them should satisfy criterion. For the large-scattering data, measured data should meet a statistically required criterion with 95% confidence. The inspection item, purpose, method and sampling rate in the HTTR fuel fabrication are summarized in Table 4.9 [102, 114].

TABLE 4.9. INSPECTION ITEM, PURPOSE, METHOD, AND SAMPLING RATE IN THE HTTR FUEL FABRICATION

Inspection item	Major purpose [a]	Method	Sampling rate
Fuel kernel			
U-235 enrichment	B	Mass spectrometer and gamma ray spectrometer analysis	1 sample/enrichment
Diameter	B	Optical particle size analysis	1 sample (100 particles)/fuel kernel lot
Sphericity	A	Optical particle size analysis	3 samples (100 particles/sample)/fuel kernel lot
Density	B	Mercury substitution	3 samples/fuel kernel lot
O/U ratio	A	Oxidation and weighing	1 sample/fuel kernel lot
Impurities	A, B	Emission spectrometer analysis	1 sample/enrichment
Coated fuel particle			
Layer thickness	A	Solvent substitution or sink float	3 samples/cp lot
Optical anisotropy factor	A	Polarization photometer	1 sample (5 cp)/enrichment
Diameter	B	Optical particle size analysis	1 sample (100 cp)/cp lot
Appearance	A	Visula observation	1 sample (2000 cp)/cp lot
Cross-section	A	Ceramography	1 sample (20 cp)/cp lot
Sphericity	A	Selection by vibration table	All cp
Strength	A	Point crushing	30 cp/enrichment
Fuel compact			
U-235 enrichment	D	Mass spectrometer and gamma ray spectrometer analysis	1 sample/enrichment
U content	B	gamma ray spectrometer analysis	All fuel compacts
O/U ratio	A	Oxidation and weighing	1 sample/fc lot
Graphite powder	A	Density, impurities, grain size and water content	1 sample/graphite powder lot
Binder	A	Contents, ash, melting point, and impurities	1 sample/binder lot
Free uranium fraction	A	Deconsolidation and acid leaching	2 samples/fc lot
SiC failure fraction	A	Burn and acid leaching	3 samples/fc lot
Packing fraction	B	Weighing and calculation	3 samples/fc lot
Matrix density	A	Weighing and calculation	3 samples/fc lot
Dimensions	C	Micrometer	All fc
Appearance	A	Visual observation	All fc
Marking	D	Visual observation	All fc
Strength	A	Compression	3 samples/enrichment
Cross-section	A	Ceramography	1 sample/fc lot
Impurities	B	Emission spectrometer analysis	1 sample/enrichment

[a] A: Irradiation performance, B: Nuclear design, C: Thermal-hydraulic design, D: Process control.

4.3.3.2. Measurement methods performed

Uranium content and ^{235}U enrichment in a fuel compact are measured by gamma ray spectrometer analysis as a nondestructive inspection. On the other hand, O/U ratio is measured by the oxidation method as a destructive inspection. The precision of uranium content has been examined [115]. Diameter and sphericity of fuel kernels and the coated fuel particles are measured by optical particle size analysis. An automatic particle size analyser has been installed [116].

The liquid substitution and sink-float technique have been investigated for measurement of pyrocarbon and SiC layer densities [117]. In addition, the density of fuel kernel is measured by a mercury substitution method. Coating layer thickness is measured by X ray radiograph. Suitable selection of the X ray energy, exposure time and geometric factors has been examined to obtain radiographic images with high contrast and resolution [118].

For determination of the exposed uranium fraction in the fuel compact, the electrolytic disintegration/acid leaching method has been developed [119]. The optimum condition of the electric current, leaching time and concentration of the nitric acid has been examined [120]. The SiC failure fraction is measured by burn-leach method where the particles are burnt in air and leached with nitric acid. A correlation between the value of SiC failure fraction and the times of burn and leaching has been examined [121].

4.3.3.3. Inspection results

Figure 4.8 [63] shows the inspection result of kernel diameter for enrichment lots. Almost all standard deviations were less than 10 μm and uniform diameter of kernels were obtained. Figure 4.9 [63] shows the inspection result of sphericity of kernels for enrichment lots. The average of each lot is about 1.05 which indicates excellent sphericity. Figures 4.10, 4.11, and 4.12 [63] show the inspection results of diameter, layer thickness and density of the coated particles respectively. Figure 4.13 [63] shows the final result of SiC defect fraction for all fuel compact lots.

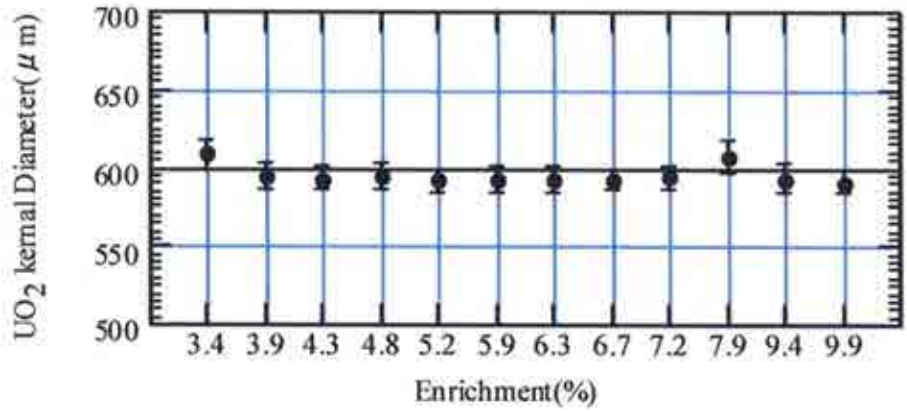

FIG. 4.8. Diameter of UO_2 kernels.

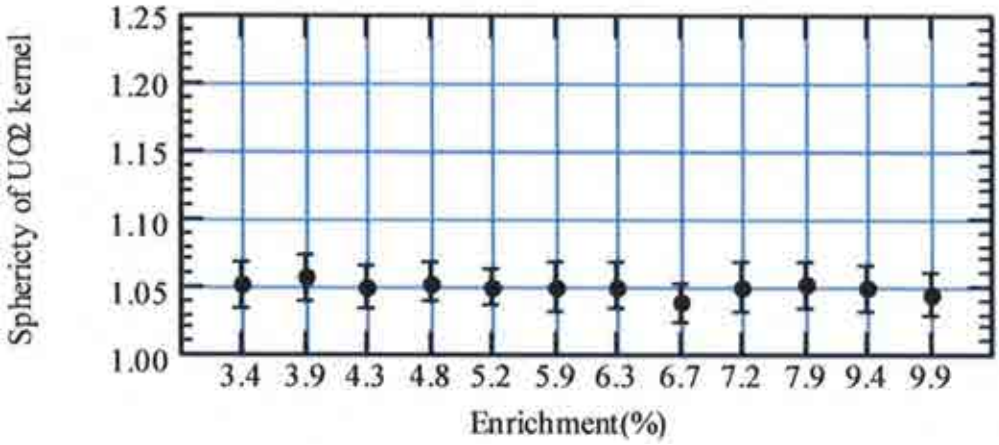

FIG. 4.9. Sphericity of UO_2 kernels.

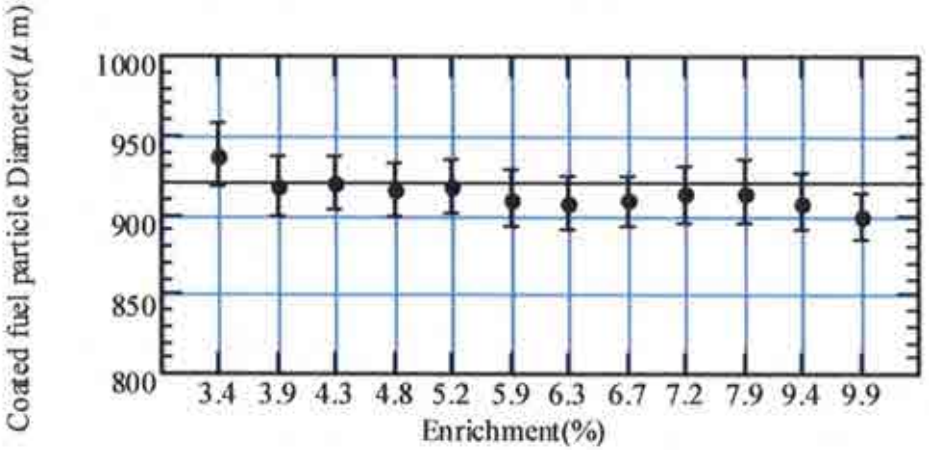

FIG. 4.10. Diameter of coated fuel particles.

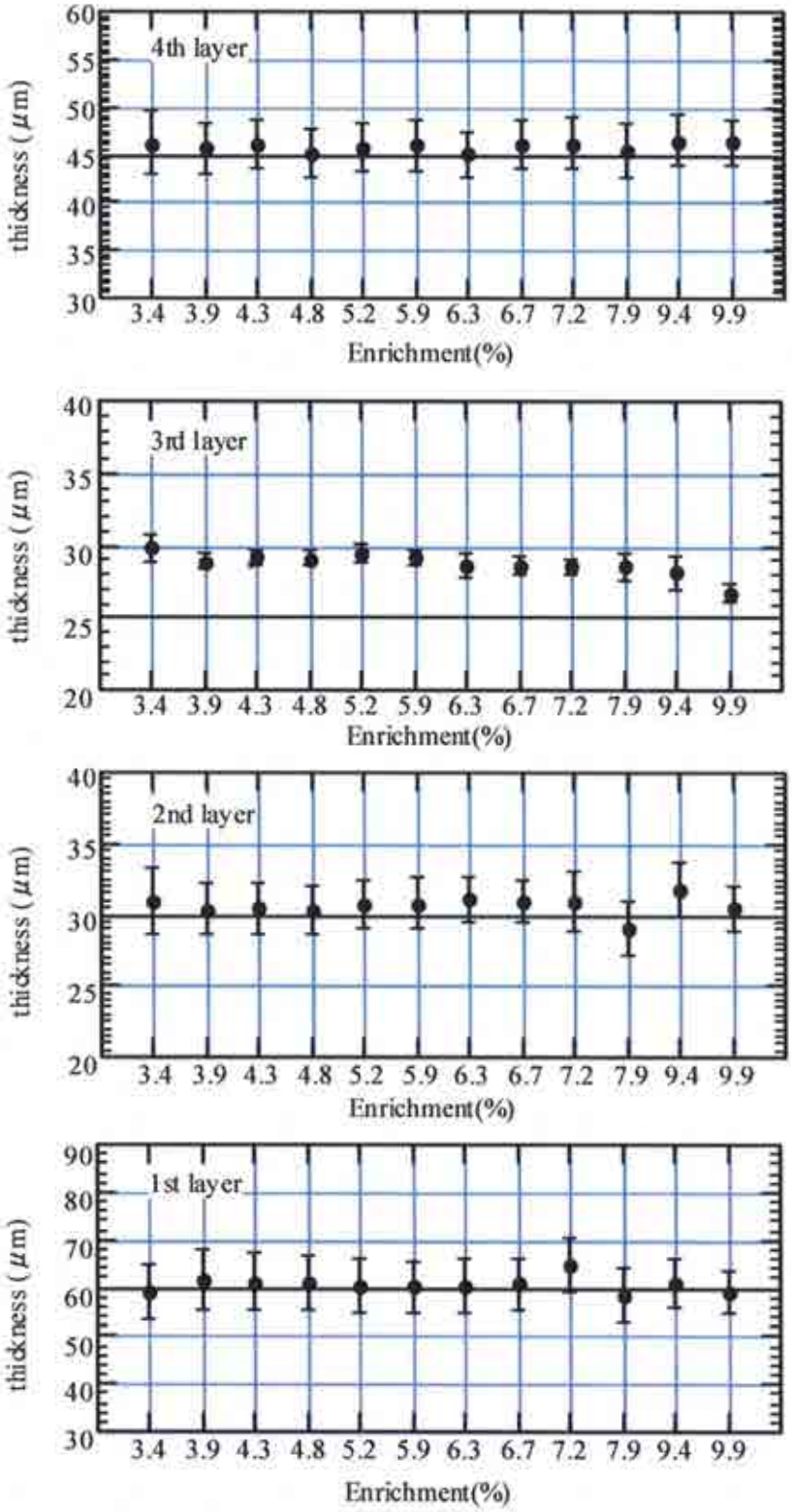

FIG. 4.11. Layer thickness of coated fuel particles.

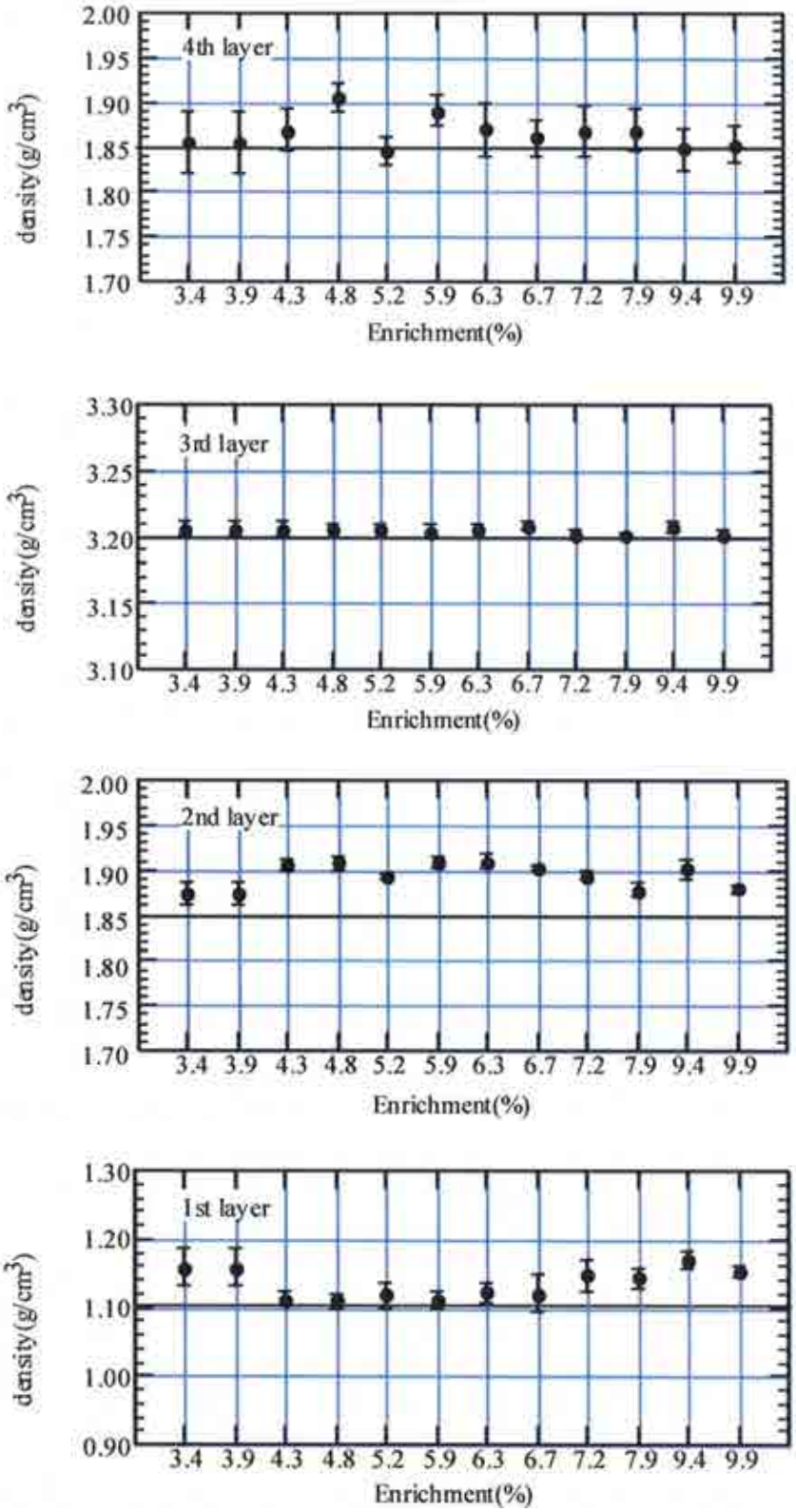

FIG. 4.12. Layer density of coated fuel particles.

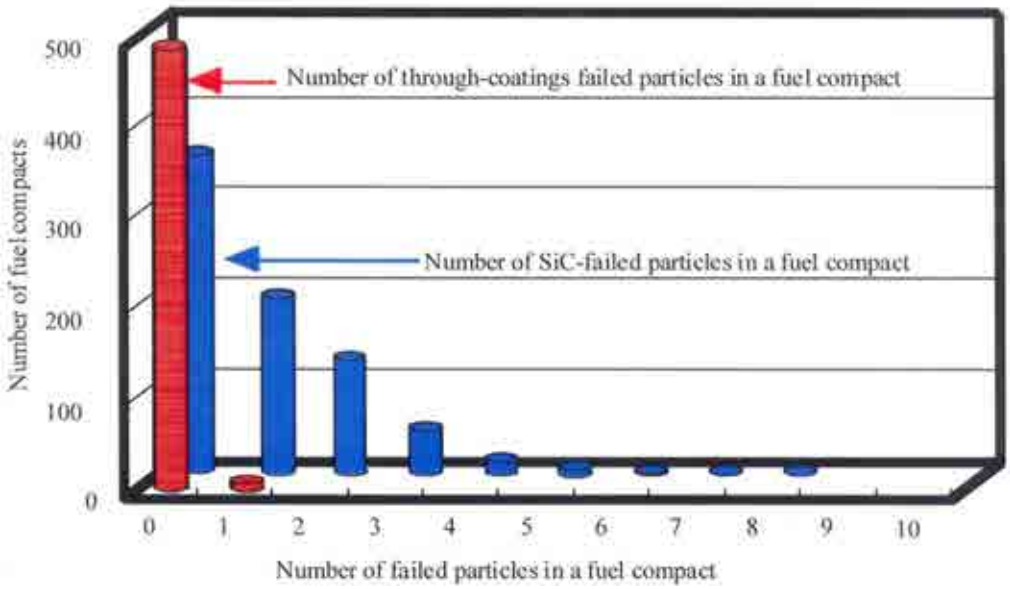

FIG. 4.13. Frequency of fuel compacts having different amounts of particle failures.

4.3.4. Characterization in the fuel element production in South Africa

4.3.4.1. Quality assurance

Coated particles for development and testing purposes must be manufactured and controlled in accordance with a documented QA programme that has been established in accordance with an appropriate standard, for example, ASME NQA 1 (American Society of Mechanical Engineers — quality assurance Requirements for Nuclear Facility Applications). Amongst other things, the QA programme must provide for:

- Product and material specifications to prescribe the technical and quality requirements that must be met;
- Appropriate sampling procedures and acceptance criteria for determining that the specified values have been met;
- Performance of work in accordance with written manufacturing and test instructions;
- Calibration and control of measuring and test equipment;
- Identification and control of materials and product;
- Generation of reports in accordance with established formats and maintenance of appropriate QA records.

4.3.4.2. Statistical quality control

As in any industry, quality assurance, quality control and testing go hand in hand together to ensure the quality of the product and client satisfaction. The nuclear industry, however, is far more rigid and stringent in defining its requirements, standards and specifications as ‘the client’ always involves the safety of the greater public.

Quality control is in essence a set of procedures laid down to evaluate a work product. Products are evaluated by testing against stringent specifications whether they be raw materials, intermediate products or final products. quality assurance is the process by which development and/or production is ’guided’ to ensure the system will attain the objectives set for it.

In the evaluation of a material there are always a multitude of possible errors present — sampling, being perhaps the most critical. The test itself will have a 'random error' present. The development of testing methods strives to reduce all of the errors to a manageable quantity whilst ensuring the parameter value ascribed to any sample is the best possible estimate of the whole batch. This process involves validation of the test method applied to a specific type of material. In order to achieve ultimate confidence in the results of testing, standard statistical processes are used to quantify the uncertainty (of the test value) and the consequences of this uncertainty.

Confidence levels are created by application of statistical processes to ensure that any material in use meets the specification set by the assurance programme. By this process the likelihood of unexpected failure is reduced to a remote probability which can be quantified and accepted in the design. Variability of these critical confidence levels is monitored by the assurance process and manufacturing will be guided by 'trend analyses' of the process. An example of specific information on statistical methods, quality control, and quality assurance as applied to TRISO fuel QA/QC characterization and testing is provided in the reference [122] for the US AGR Fuel Development Programme.

4.3.4.3. QC and characterization test methods

Table 4.10 contains a list of typical QC tests and the preferred techniques used to diagnose TRISO coated particles [123]. Some of the more unique tests are discussed in the sections below.

(a) TRISO particle size and shape analysis (PSA)

The benchmark apparatus for measuring particle diameters (and the associated volumes) for spherical particles in the size range applicable to kernels and coated particles is an automated optical particle analyser with pneumatic particle transport, custom developed by Seibersdorf for NUKEM. It is a reliable, accurate and precise method that relies on the intensity dip observed by a detector when a particle passes through a light beam. For spherical particles, it is possible to achieve a linear response between an appropriately defined function of the intensity dip and the particle diameter. Accurate calibration of the system is achieved by means of standard steel balls. Particles are pneumatically transported, separated and passed through the light beam where they are counted and measured. Although a maximum rate of about 50 particles per second is achievable, the feed rate is chosen to match the desired accuracy and precision of the application.

TABLE 4.10. FUEL KERNEL AND COATING PROPERTIES AND TEST TECHNIQUES

Property	Test technique
Fuel kernel	
Uranium enrichment	Mass spectrometric analysis using thermal ion mass spectrometry or gamma ray spectrometry
Equivalent boron content (impurities)	Spectroscopic analysis using plasma source mass spectrometry or emission spectrometry
Stoichiometry (O/U ratio)	Thermo-gravimetric analysis
Diameter and sphericity	Particle size analyser (PSA) Shadowscope techniques using an optical microscope and image analysis system
Density	Geometrical determination by means of PSA Mass by helium pycnometry or mercury porosimetry
Micro-structure	Microscopy on ceramographic sections
Shape defect distribution (odd shapes)	Sorting table fraction analysis
Coated fuel particle	
Layer thickness and symmetry	Micro-radiography Ceramography using image analysis techniques
Density of buffer layer	Geometrical determination by means of PSA and mass change between the coated and uncoated particles Mercury porosimetry
Density of other layers	Gradient column (sink float method)
Anisotropy of the inner and outer PyC layers	Optical anisotropy measurement Advanced Two-Modulator Generalized Ellipsometry Microscope (2 MGEM)
SiC layer integrity	Burn leach testing Micro-radiography
Micro-structure and chemical composition of layers	Transmission electron microscope (TEM) Scanning electron microscope (SEM) Electron probe X ray micro-analyser (EPMA) Auger electron spectroscopy (AES) Scanning transmission electron microscope (STEM) Ceramography
Uncontained uranium	Burn-leach testing
Shape defect distribution (odd shapes)	Sorting table fraction analysis

Kernels and coated particles are not perfect spheres. Spherical pressure vessels provide maximum strength and therefore sphericity, defined as the ratio of a particle's maximum diameter to its minimum diameter, has to be within specified bounds. To measure sphericity many randomly selected orientations of the same particle are presented to the measurement system by cycling the same particle many times through the light beam. The next particle is then selected and so on. In practice, particle sphericity tends to have a log-normal distribution, indicating that multiplicative accumulation of random errors conspire during manufacture to cause deviation from a perfect sphere.

Particle size and shape is also often determined using a shadowscope technique. In this method, a sample of particles is arranged in a monolayer on a transparent plate. An optical microscope is used in bright field transmitted mode to image the silhouette of each particle. Manual or computer automated image analysis is performed to measure the minimum,

maximum, and average diameters of each particle. The shadowscope technique can provide particle size and shape to an accuracy that is equivalent to or better than the PSA, but sample analysis rate is more limited.

(b) Optical anisotropy

High density pyrolytic carbon is a graphitic material with a complex extended structure. Roughly speaking it behaves in a way similar to a polycrystalline material where each crystallite has inherently anisotropic properties, such as thermal expansion and fast neutron induced shrinkage. It is imperative to strive for isotropic macroscopic orientation in order to have average macroscopic properties that are homogeneous and isotropic. For macroscopic graphite samples, X ray diffraction can be used to define and measure a so-called Bacon Anisotropy Factor (BAF) that directly relates to macroscopic material anisotropy. On the tiny layers of coated particles, normal X ray diffraction is not possible. Fortunately it so happens that the intensity of reflected, polarized light differs depending on the orientation of the polarization direction relative to the crystallographic axes of the graphite crystal. Measurement of the ratio of the reflected intensities of a light beam, polarized first along one direction and then perpendicular to that direction, therefore yields an optical anisotropy factor (OAF). It can be shown that this OAF can be related in a consistent way to the BAF, which in turn relates to actual expected anisotropy and fuel performance. As a light beam can easily be focused onto a polished metallurgical section of a coated particle under a light microscope, an OAF profile across a pyrolitic carbon layer can conveniently be determined. This principle was utilized at Seibersdorf to develop an OAF instrument for NUKEM, which can now be viewed as the primary standard for determination of anisotropy of pyrolitic carbon layers.

Recently, advanced ellipsometry techniques have been applied to the measurement of pyrocarbon anisotropy in TRISO fuels. A system developed by ORNL called the Two-Modulator Generalized Ellipsometry Microscope (2-MGEM), was designed to completely determine the polarization effect on light reflected off a polished pyrocarbon cross-section [124, 125]. This ellipsometer provides very accurate determination of the pyrocarbon anisotropy with a selectable spatial resolution down to a few micrometers.

(c) Kernel, buffer and layer density determination

SiC and pyrolitic carbon densities are measured by means of suitable density gradient columns [126]. A density gradient column is created by filling a glass column with two liquids of different density, where the ratio of the two liquids is varied during filling in order to create a linear density gradient as a function of the column height. This linear density gradient is determined by measuring the zero buoyancy position of calibrated floats. Samples of the IPyC, SiC, and OPyC layers are obtained by fracturing the coatings of individual TRISO particles. Pieces of free-standing OPyC fragments usually can be easily picked out of the fractured coatings because of the weak bonding between the SiC and OPyC layers. Free-standing IPyC fragments usually can not be obtained after deposition of the SiC because of the infiltration of SiC into the open porosity of the IPyC, which results in a strong interface. For this reason, IPyC density must be determined using hot sampling or interrupted batches. Free-standing SiC is obtained by picking out multiple layer fragments and heating in air to about 850°C to remove the attached PyC.

Density of the other two TRISO components (i.e. fuel kernels, and buffer layer) must be obtained by other methods. Suitable liquids spanning the density of the fuel kernels are not available. Liquid penetration of the buffer material results in the determination of the skeletal density of that layer, which is not of interest. A particle size analyser (PSA) can be used to

determine kernel density. The mass of a sample of (pre-sieved and sorted) kernels is determined accurately. The sample is then passed through the PSA and the sum of the volume of all the kernels in the sample is divided by the sample mass to yield the mean kernel geometric density. The geometric density is a reasonable approximation of the envelope density if the particles are close to spherical. The density of the buffer layer can be determined in a similar way after subtracting the mean kernel volume from the mean total volume and using the appropriate mass values. Apart from the relative standard deviation caused by variation in buffer volume, the relative standard deviation in kernel density becomes amplified (by about 6 times for nominal TRISO particles) and adds to the overall relative error. This places a strict upper limit on the required accuracy and precision of kernel density determination. Alternately, Hg porosimetry can be utilized to determine the envelope volume of the kernels and buffer coated particles. This technique can provide improved accuracy, especially for non-spherical particle shapes.

(d) Layer thickness determination: micro-radiography

Although PSA analysis can be used to derive layer thickness, the method becomes increasingly imprecise for outer layers due to error propagation. To achieve good statistics of intrinsic layer variation over a large number of particles (100–200), X ray micro-radiography can be utilized [127, 128]. A single layer of particles is positioned directly on the emulsion of a high resolution photographic film (about 1 μm resolution) and illuminated with an X ray source approximately 300 mm away. With such an arrangement sharp projected images of layers can be achieved even with an X ray tube that does not behave like a true point source, so that there is no need for a fine focus source. To distinguish between the buffer and the adjacent pyrolitic carbon layer, low energy X rays are needed and the exposure must be in vacuum. Tube voltage and current are selected to give the required contrast needed for the intended layers. The developed and mounted film is analysed under a transmission light microscope equipped with a CCD camera. Layer thickness analysis is achieved by means of standard image processing software. Coating thickness is also often determined by preparing metallographic cross-sections and directly imaging with an optical microscope using bright field reflected light [129]. Resolutions of 1 μm can be obtained and analysis can again be performed by standard image processing software.

(e) SiC layer integrity: burn-leach testing

A very important test for SiC layer integrity is the burn-leach test. A representative sample of coated particles of statistically significant size is selected. Under clean laboratory conditions these are burned down to the SiC layers and the remaining particles and ash are leached under reflux for an extended time period in a nitric acid solution. A sample of the liquid is then pre-concentrated in a rotary evaporator and analysed for uranium by an extremely sensitive analytical technique such as fluorimetry, mass spectrometry methods, or delayed neutron counting (after activation in a reactor). When no coated particles leak, the analytical result reflects the unconfined uranium content. The number of broken/leaking particles can be calculated after division of the total concentration by the expected contribution per particle.

The intrusion method has also been applied to determine particle defect or failure fraction. This method involves surrounding the particles with a liquid under pressure. The liquid intrudes into the pores of the particles and the measurement of the extent of the intrusion yields information about the existence or size of the pores. The intrusion liquid can be a wetting or non-wetting liquid e.g. mercury, halogenated carbons or aqueous solutions. For wetting liquids, the liquid will flow into the pores depending on the relative interior/exterior

pressure of the pores and for non-wetting liquids pressure will have to be applied. For mercury (a non-wetting liquid) intrusion, commercial mercury porosimeters are available.

(f) Thermal conductivity

The most important property for predicting the in-pile fuel temperature is the thermal conductivity. For the graphite element (compact or pebble) this property can easily be obtained by the conventional laser flash method. The thermal properties of coated particles must also be evaluated to improve the prediction of the in-pile behaviour.

Photo-thermal experiments are particularly suitable for determining thermal diffusivity between micrometer and millimeter scale simply by varying the modulation frequency [130]. The currently selected technique is thermo-reflectance microscopy, based on detecting a photo-thermal effect and therefore allowing no-contact thermal diffusivity measurement. The thermal conductivity is the product of the experimentally measured thermal diffusivity by the heat capacity and density, according to the following relation:

$$K = \rho \alpha c_p \tag{4.2}$$

where

K is the thermal conductivity (W/(m·K));
α is the measured thermal diffusivity (m^2/s);
ρ is the density (kg/m^3);
c_p is the heat capacity (J/(kg·K)).

(i) Description of the thermo-reflectance microscopy

The thermo-reflectance microscopy technique [131] is based on measuring and analysing the periodic temperature increase induced by the absorption of an intensity-modulated laser beam (pump beam). By detecting the thermally induced reflection coefficient variations with the help of a secondary continuous laser beam (probe beam), the temperature increase is measured at the sample surface with a sensitivity better than 10^{-3} $kHz^{-0.5}$. Unlike other photo-thermal methods, this contactless technique has micrometric spatial resolution.

The experimental set-up (Fig. 4.14) consists of three main parts: an optical system for focusing and positioning the pump and probe beams, a device for measuring the reflected probe beam intensity, and several electronic devices for detecting the signal and driving the experiment [131].

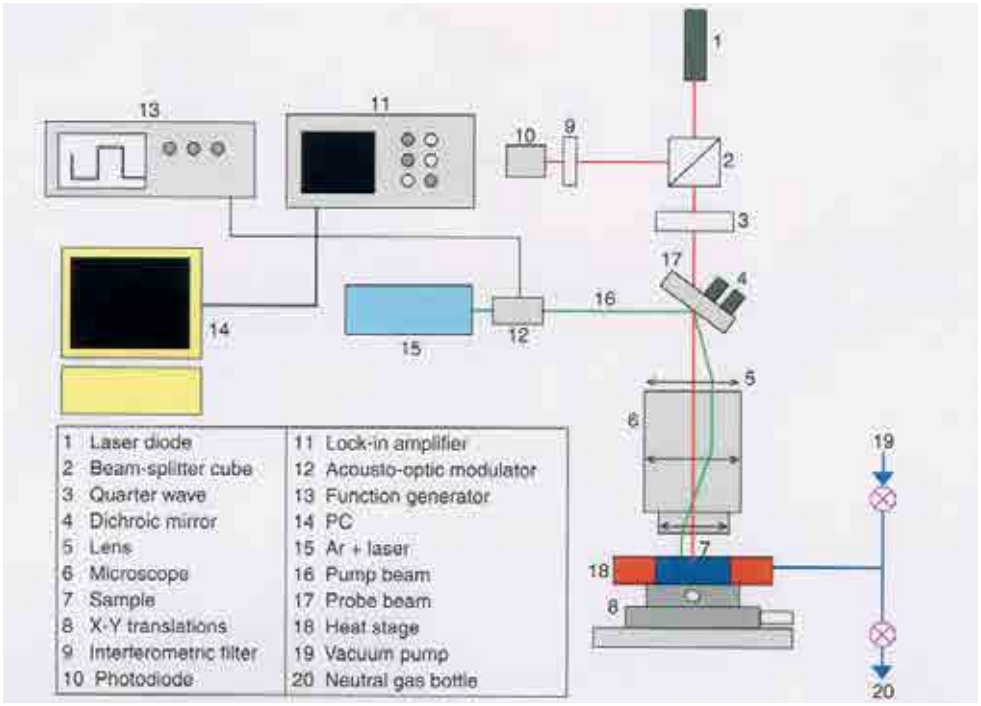

FIG. 4.14. Thermal microscope set-up.

The pump beam is a continuous wave Ar^+ laser with a maximum power of 2 W. Its intensity is modulated by a frequency generator driven acousto-optic modulator operated at frequencies up to 2 MHz. The pump beam is then oriented by a dichroic mirror and finally focused onto the sample surface in the heating stage with a microscope.

The probe beam is a laser diode that passes through a quarter-wave plate and the dichroic mirror, and is then focused onto the sample surface with the same microscope. After reflection, it passes through the quarter-wave plate again and is then sent to the photodiode by a beamsplitter cube. An optical filter prevents any pump beam photons from reaching the detector. A lock-in amplifier extracts the amplitude and phase of the periodic photodiode signal. A PC controls the dichroic mirror orientation and consequently the distance r between probe and pump beam location.

The fused silica heating stage window transmits 93% of the intensities of the two beams. An objective with suitable magnification and a large working distance is used to correct the spherical aberrations due to the heating stage window. The highest temperature that the heating stage can reach is 1500°C with a heating rate of 0.1–130°C/min. The sample must be polished to a mirror finish to ensure good reflection. In our case, the measurements were performed on polished particle cross-sections.

When an isotropic, homogeneous medium is heated by a periodic point-like heat source of power Q, the periodic temperature increase, also called the 'thermal wave', at a distance r from the pump location is described by the following equation:

$$\delta T(r) = \frac{Q}{4\pi k r} \exp\left\{-\frac{r}{\mu}\right\} \cos\left(\omega t - \frac{r}{\mu}\right) \tag{4.3}$$

and

$$\mu = \sqrt{\frac{\alpha}{\pi f}} \tag{4.4}$$

where

μ is the thermal diffusivity length;
f is the modulation frequency of the harmonic heat source;
α is the thermal diffusivity of the material;
k is the thermal conductivity of the material.

The argument of δT (i.e. its phase) is –r/μ; the slope of the phase versus r curve is -1/μ, which is used to estimate the thermal diffusivity of the medium by simple linear regression. The thermal diffusivity can thus be determined with a precision often better than 5%.

(ii) Thermal characterization applied to dense pyrolytic carbon layers

Thermoreflectance microscopy has been applied to characterize dense pyrolytic carbon layers of TRISO particles. Measurements have been performed at room temperature [132], and tests at temperatures of up to 1500°C are currently in progress. The thermal diffusivity is estimated from the 1D least squares fit of the phase profiles. An example for IPyC is illustrated in Fig. 4.15 [132].

The results for the diffusivities obtained on TRISO particles are 7.6 ± 3.2 mm^2/s for IPyC and 3.6 ± 0.2 mm^2/s for OPyC. These results give an order of magnitude of thermal diffusivity values which could be used in modeling of TRISO particles. Differences in the diffusivity values which are observed between IPyC and OPyC may be correlated with the IPyC annealing at around 1500–1600°C during the SiC deposition process tending to increase the diffusivity.

(iii) Thermal characterization applied to buffer layer

Buffer thermal property measurements can be performed at room temperature. The diffusivity obtained for the dense parts of the buffer layer is 5.2 ± 0.5 mm^2/s [132]. A numerical model of steady-state thermal conduction inspired from the guarded hot plate method is used to determine the thermal diffusivity of the buffer layer. This approach, coupling local measurement and numerical homogenization, has been validated as shown in [133]. The diffusivity value obtained on the buffer layer is 4 mm^2/s.

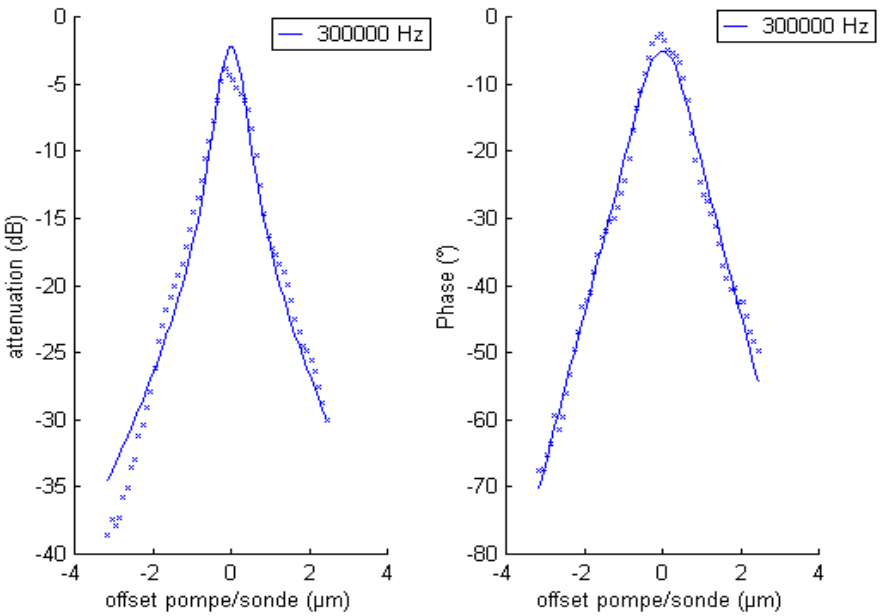

FIG. 4.15. 1-dimensional scanning and its related squares adjustment.

(g) Elasticity modulus

Elastic modulus measurements were performed with a Nanoindenter NT 600 (Micro Materials Limited) that allows indentation displacement of 50 µm. The penetration of the non-deformable diamond indenter is measured by a capacitive sensor with about 0.01 nm accuracy.

Thirty indentations were performed in each layer on a polished equatorial cross-section. The average results for Young's Modulus obtained are 18 ± 1.1 GPa for IPyC and 23 ± 1.4 GPa for OPyC. These values are in agreement with literature data [134–137]. They give an order of magnitude of the IPyC and OPyC Young modulus values which can be used in modeling. Differences are observed between Young's modulus of IPyC and OPyC. As for the thermal properties, this difference may be correlated with annealing of the IPyC during the SiC deposition process.

4.4. ROUND ROBIN EXERCISE OF ZRO_2 KERNEL SURROGATE COATED PARTICLES AMONG PARTICIPATING ORGANIZATIONS

The characterization methods of the coated particle fuel being used by different HTGR coated particle fuel producers have been developed in parallel with their early development of the manufacturing process, and they are being improved with their own technological development in this area. The characterization techniques used for the QC tests are important in view of the quality verification of the fuel production. These should be validated and verified to give evidence that the quality measured by the techniques corresponds to the actual quality of the products.

In this round robin exercise (RRE), four surrogate TRISO coated particle samples were submitted to the participating organizations in the IAEA CRP-6 for testing and the results obtained by the participating organizations were compared. These four surrogate samples, which originated from Korea (KAERI), USA (ORNL and BWXT) and RSA (PBMR), have been distributed to nine participating organizations: INET at Tsinghua University (China),

AREVA (France), JAEA (Japan), KAERI (Republic of Korea), PBMR (RSA), Hacettepe Univ. (Turkey), ORNL (USA), BWXT (USA) and ITU (EU). The purpose of this exercise was the comparison and benchmarking of the characterization methods and results. Test items considered were properties of different coating layers. Namely, 13 items were identified for characterization in this study: particle diameter, sphericity, (surrogate) kernel diameter, four coating layer thicknesses and four coating layer densities (buffer, IPyC, SiC and OPyC), and anisotropy of IPyC and OPyC. However, certain layers, such as buffer layer and IPyC coating layer, were not able to be totally characterized under given conditions, i.e. surrogate kernel instead of uranium kernel and completed TRISO coated particles as samples. Note that these surrogate samples were not necessarily representative of the typical particle quality at the participating organizations or their full range of available characterization methods.

4.4.1. Supply of standard material specimens to the participating Member States

Four surrogate TRISO coated particle samples originating from the Republic of Korea (KAERI), USA (ORNL and BWXT) and RSA (PBMR) were submitted to the participating organizations for testing and compared among the results of characterization obtained by the participating organizations. These four surrogate samples were distributed to nine participating organizations, INET at Tsinghua Univ. (China), AREVA (France), JAEA (Japan), KAERI (Republic of Korea), PBMR (RSA), Hacettepe University (Turkey), ORNL (USA), BWXT (USA) and ITU (EU) in this so-called Round-Robin Exercise. It should be noted that the purpose of this exercise was for the comparison and benchmarking of the characterization methods and results. Also, these surrogate samples were not necessarily representative of the quality and the readiness of the process operation at the participating organizations.

4.4.2. Selection of characteristics to be measured in the coated particle samples

Since the common samples distributed for the test were surrogate (zirconia kernel) coated particles, the characterization items to be measured by each participating organization were limited not only by the samples but also by the methods available up to the time of testing at the participating organizations. At the beginning, some uranium containing coated particles were also considered for this RRE. However, due to the complexity of international transportation, this consideration was abandoned. As a result, the kernel was excluded in this exercise for the characterization items, usually tested for uranium enrichment, uranium content and kernel dimensions including sphericity. Also, there were some participating organizations which did not perform measurements on the buffer and inner PyC layers. For example, INET, JAEA and Hacettepe University measured only on the OPyC and SiC layers both for density and thickness. Figure 4.16 summarizes the items tested by the participating organizations. PBMR samples were not distributed to ITU (EC) and JAEA (Japan).

FIG. 4.16. Characteristics tested by the nine participating organizations.

4.4.3. Characterization methods used by the participating organizations

4.4.3.1. Overview of methods employed

There may be several methods for one characterization item. For example, two methods are currently being used for measuring layer thickness: metallographic examination and non-destructive X ray radiography. For the density measurement, also, there are some alternatives, with precise measurements of weight and volume and mathematical calculations. The methods used in this RRE can be categorized as follows for the items tested and are summarized in Tables 4.11 to 4.14.

TABLE 4.11. TEST TECHNIQUES FOR VARIOUS PARTICLE PROPERTIES

Property	Test technique
Kernel diameter	Ceramography, X ray radiography, particle size analyser (PSA)
Kernel sphericity	Ceramography, particle size analyser (PSA)
Coating layer thicknesses	Ceramography, X ray radiography
Coating layer densities	Sink-float method, X ray radiography
PyC anisotropy	Optical anisotropy measurement (OPTAF), ellipsometry
Coated particle diameter and sphericity	Ceramography, X ray radiography, projection, particle size analyser (PSA)

TABLE 4.12. METHODS EMPLOYED FOR LAYER DENSITY MEASUREMENTS

	Buffer	IPyC	SiC	OPyC
INET	—	—	Sink-float	Sink-float
AREVA	X ray	X ray	X ray	X ray
JAEA	—	—	Sink-float	Sink-float
KAERI	—	—	Sink-float	Sink-float
PBMR	—	—	Sink-float	Sink-float
Hacettepe U.	—	—	—	—
ORNL	—	—	Sink-float	Sink-float
BWXT	—	—	Sink-float	Sink-float
ITU	—	—	—	—

TABLE 4.13. METHODS EMPLOYED FOR LAYER THICKNESS MEASUREMENTS

	Buffer	IPyC	SiC	OPyC
INET	—	—	X ray & projection	X ray & projection
AREVA	X ray	X ray	X ray	X ray
JAEA	Ceramography	Ceramography	Ceramography & X ray	Ceramography & X ray
KAERI	Ceramography & X ray	Ceramography & X ray	Ceramography & X ray	Ceramography & X ray
PBMR	Ceramography	Ceramography	Ceramography	Ceramography
Hacettepe U.	—	—	Ceramography	Ceramography
ORNL	Ceramography	Ceramography	Ceramography	Ceramography
BWXT	Ceramography	Ceramography	Ceramography	Ceramography
ITU	—	—	—	—

TABLE 4.14. METHODS EMPLOYED FOR ANISOTROPY AND PARTICLE DIMENSION MEASUREMENTS

	Anisotropy		Kernel diameter	Particle diameter	Sphericity
	IPyC	OPyC			
INET	OPTAF	OPTAF	—	X ray	—
AREVA	—	—	X ray	X ray	—
JAEA	OPTAF	OPTAF		Projection	—
KAERI	OPTAF	OPTAF	Ceramography & X ray	PSA	PSA
PBMR	OPTAF	OPTAF		PSA	PSA
Hacettepe U.	—	—	Ceramography	Ceramography	Ceramography
ORNL	Ellipsometry	Ellipsometry	—	Shadowscope	Shadowscope
BWXT	—	—	—	Ceramography	Ceramography
ITU	Ellipsometry	Ellipsometry	—	PSA	PSA

All the participating organizations measured coating layer densities by sink float method and or by a titration method only for the OPyC and SiC layers, except AREVA who non-destructively measured the density for all four layers by X ray radiography.

Preparation of the samples for the sink float method involved crushing particles to obtain fragments of multi-layer mixtures and selecting unique outer PyC layers. For the SiC layer samples, these multi-layer sample fragments were oxidized in air above 800°C to get rid of parts of the PyC layers and obtain fragments of the pure SiC layer.

For the anisotropy measurement of PyC layers, most of the organizations used optical anisotropy factor (OPTAF) measurement method except ORNL and ITU which measured the anisotropy of PyC layers by the ellipsometry using the 2MGEM instrument developed by ORNL.

The coated particle diameter and its sphericity were measured by a particle size analyser (PSA), which was a well developed commercialized laboratory instrument using an optical imaging system. They can be also estimated by the ceramography following careful sample preparation by grinding and polishing to obtain the exact mid-plane cross-section of the particles on the surface of the resin mount and direct measurement on an optical microscope or an image analysis system. More detailed explanation for important characterization methods are described in the following subsections, by taking representative methods used in participating organizations as examples.

4.4.3.2. Coating layer thickness measurement

The coating layer thicknesses were measured by ceramography followed either by a direct measurement on a microscope or a (computer-controlled) projector or by an image processing with a software. This needs a careful preparation of samples via embedding the particle samples in a resin, grinding and polishing with a precise control of depth to obtain the exact mid-plane cross-section of the particles on the surface of the resin mount. ORNL applies a mathematical correction to layer thicknesses measurements done by ceramography. Polished mount cross-sections rarely present a planar section that passes exactly through the centre of individual particles because of polishing variability and the particle size range of typical TRISO coating batches. This results in an imaged layer thickness that is greater than the

thickness along the radial direction of the particle. The magnitude of the error can be minimized by polishing the particles as close to the mid-plane as possible. For maximum accuracy, ORNL applies a simple geometric correction to each thickness measurement by calculating the offset of the imaged plane using the polish down distance and the measured particle radius in the plane of polish, with the assumption of a spherical geometry. Figure 4.17 shows a representative micro-photograph example of the ceramography after sample preparation. (KAERI sample taken by JAEA).

AREVA used the X ray radiography method to measure the layer thickness of the four layers. The method relies on X ray Phase Contrast Imaging (PCI) technique: by setting an X ray detector at a finite distance from an HTGR TRISO coated particle, interference fringes at layer interfaces caused by phase distortions occur and are superimposed to the conventional radiographic attenuation image. Due to these fringes, PCI resolves HTGR particle layers where conventional radiography fails. PCI images can be obtained via monochromatic beams (synchrotron) or via polychromatic radiation (conventional X ray sources).

In the AREVA method, a micro-focus tube with a 0.9µm focal spot is used at 40 kV as an X ray source, and the detector consists in a High Resolution X ray Camera with a pixel size of 9.3µm. In order to simulate a TRISO particle PCI intensity profile, preliminary work consisting in characterizing equipment is necessary. In particular, the tube spectrum has to be known accurately, as well as the detector point spread function (PSF). Spectrum characterization is performed by simulation, in inputting in GEANT4 code the tube characteristics such as the electron flux, the electron energy, the target thickness and nature, the distance between the target and the detector taking into account the attenuation of air and of the camera windows prior to the scintillator. Finally, the magnification factor is determined in imaging a metrology pin (diameter measured with an accuracy of 1µm) in the exact same conditions as for the TRISO particles (energy, object to source and detector to object distances). After thresholding the acquired image, a pin intensity profile is extracted and measured in terms of pixels: experimental size of the pixel is then found in dividing the pin diameter by the number of pixels. Magnification factor is then deduced by dividing the real pixel size by the experimental size of the pixel. For each batch, the particles are sorted by sphericity using a vibrating table and then, 30 particles were randomly picked among the most spherical one. Then, one PCI image was acquired per particle (see Fig. 4.18).

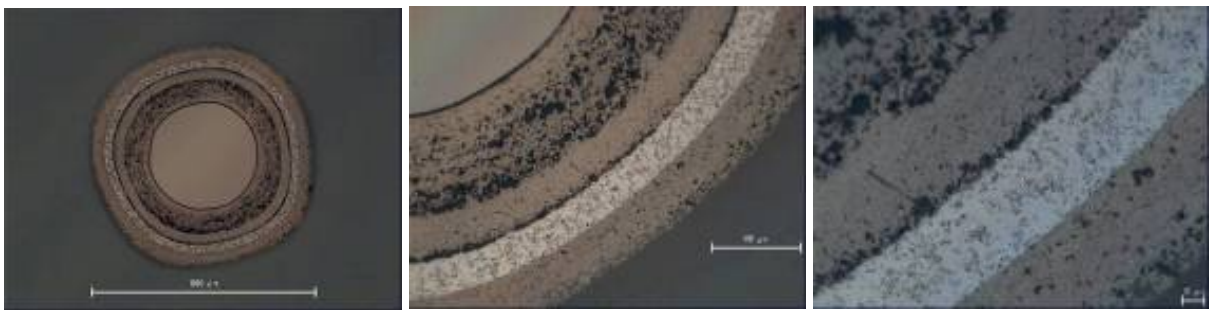

FIG. 4.17. Cross-section of KAERI sample prepared by JAEA (magnitude from left, 100,×400,×1000).

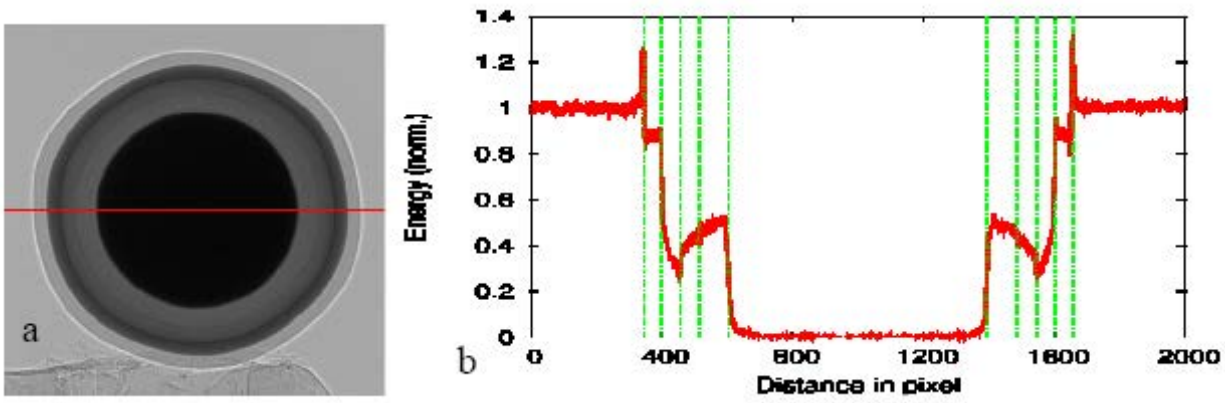

FIG. 4.18. Profile extraction of a BWXT particle. (a) PCI image and (b) extracted profile with approximated layer interface locations.

On each image, 60 intensity profiles were extracted along lines crossing the TRISO particle within angles of ±30° with respect to the horizontal. For each of these profiles, a 'spherical coefficient' is computed corresponding to the sum of the gap between the kernel barycenter and the barycenter of each layer. The first selected profile is the one with the smallest 'spherical coefficient'. The second profile is the one with the second smallest 'spherical coefficient' and away from the first profile with at least angle of 5°. The third profile is extracted with respect to the horizontal.

KAERI used also the X ray radiography method to measure the layer thickness of the four layers. In KAERI, a micro-focus X ray imaging system was used for the coating layer thickness measurement non-destructively, which was developed by KAERI [138]. Although the methodology used is different from that used in the AREVA method, its principle is the same. The focal spot size of the X ray generator was about 2 μm. The number of pixels of the used flat panel X ray detector was 1024 × 1024. The size of a pixel was 48 μm × 48 μm. The distance between the sample and detector screen was adjusted from 40 to 140 cm, and the tube voltage was adjusted from 40 to 80 kV to control the wavelength of the X ray. The coating thickness was measured automatically from the acquired phase contrast X ray radiograph for the coated particles by the developed measurement algorithm based on digital image processing techniques which include a brightness and contrast enhancement, a random noise reduction, an edge detection and a recognition. The X ray power was minimized to obtain a good resolution for an image by maintaining a small size of the focal spot. 50 images were integrated to control the exposure for an object. The random noises were reduced by integration due to an average effect.

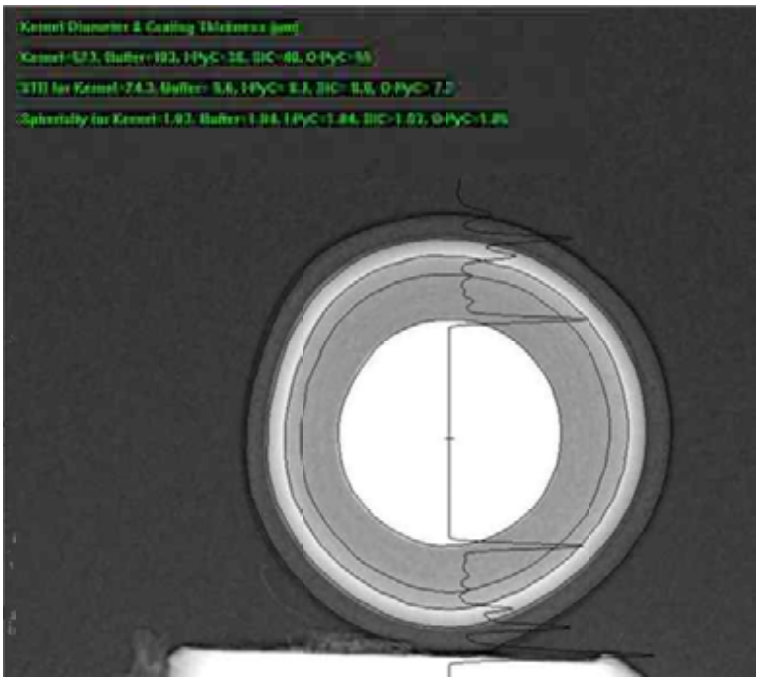

FIG. 4.19. A result of acquisition of PCI image and an extracted profile.

The histogram of the image was adjusted to enhance the brightness and contrast for the integrated image. The intensity of the enhanced image was converted inversely for an image data processing. Here, the intensity of a pixel (picture element) is higher in a region of a higher density for a particle. A higher intensity region is represented by a brighter pixel in an image. Boundary areas can be classified by the gray level differences of the pixels by using the Sobel operator. The result of PCI image acquisition and the developed programme to automatically measure the coating thickness from the X ray image of a coated particle is shown in Fig. 4.19. The distance between the boundary position and the centre of a TRISO particle image is the radius of the coating layer. The radii of the coating layers were circularly measured for the X ray image by rotating it through 360° with a step of 5° and the coating thickness was computed by using the measured radii as shown in Fig. 4.20 (a) and (b).

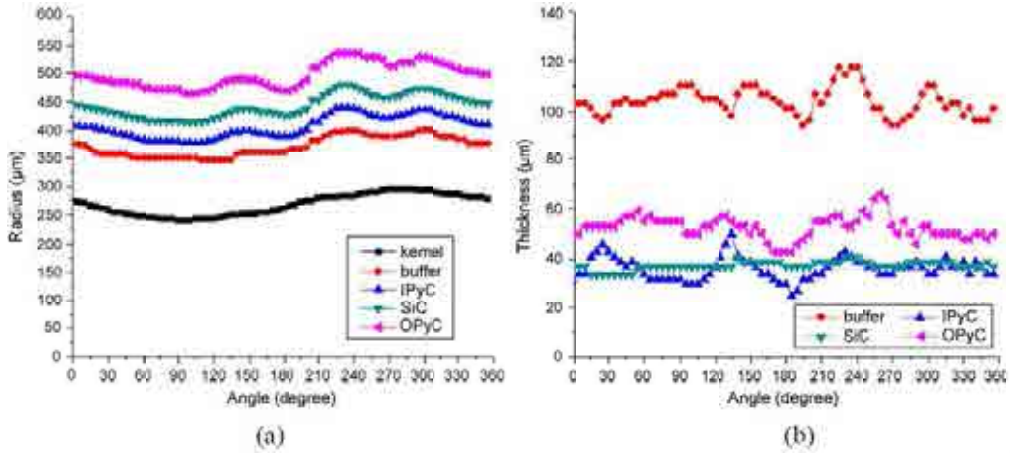

FIG. 4.20. Example of (a) measured radius of the coated particle, and (b) calculated thickness of coating layers.

4.4.3.3. Coating layer density measurement

All the participating organizations measured coating layer densities by sink float method and or by a titration method for the OPyC and SiC layers, except AREVA who measured the density for all the four layers by the X ray radiography non-destructively. The titration method is a derivative method of the sink-float method using the same Archimedes principle. The X ray radiography method has attractive benefits such as less liquid waste generation, sample preparation and timely measurement.

(a) Sink-float method

A liquid density gradient column is used to determine sink-float density of the IPyC, SiC, and OPyC layers. A liquid density gradient column is created by filling a glass column with two liquids of different density, where the ratio of the two liquids is varied during filling in order to create a linear density as a function of the column height. This linear density gradient is determined by measuring the zero buoyancy position of calibrated floats. Different liquid density gradient columns with different density liquids are used to create columns for measuring pyrocarbon (typical range 1.6–2.2 Mg/m^3) and SiC (typical range 3.1–3.3 Mg/m^3). In order to prepare density solution with a gradient, prepare lower density and higher density solutions to cover the range of densities which should include the sample density. In KAERI, as an example, the mixture solutions for the measurement of OPyC (dense PyC) and SiC coating layers were carbon tetrachloride – dibromoethane mixture (density range : 1.60–2.18 Mg/m^3) and bromoform – diiodomethane mixture (density range : 2.90–3.30 Mg/m^3), respectively. The density of buffer layer is generally measured by a geometrical method. For the SiC density measurement, lower and higher density set were 3.1 and 3.3 Mg/m^3, respectively. Figure 4.21 shows (a) general view of a density gradient column, (b) the density solution mixing station, and (c) example of standard floats immersed in the density gradient column to measure SiC layer density The density solution mixing station consists of a low density flask (left, with a magnet stirrer) and a high density flask filled with density solutions which are interconnected with a valve.

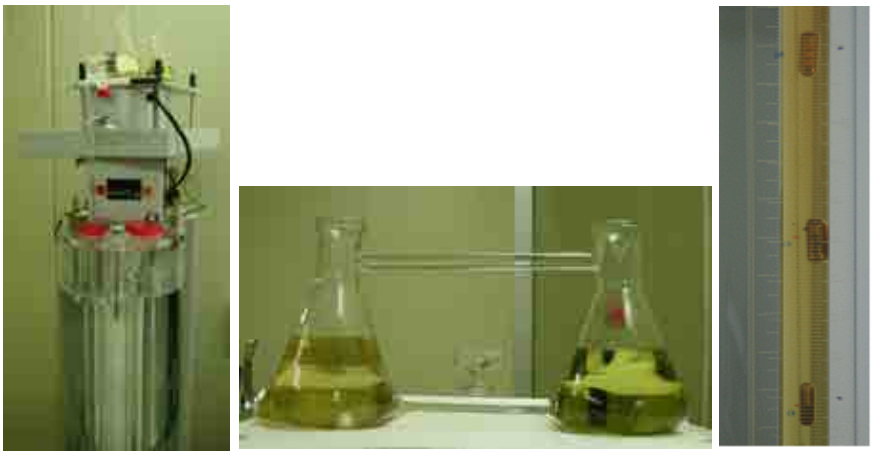

(a) (b) (c)

FIG. 4.21. (a) general view of a density gradient column; (b) density solution mixing station;(c) example of standard floats immersed in the density gradient column to measure SiC layer density (KAERI's example).

Samples of the IPyC, SiC, and OPyC layers are obtained by fracturing the coatings on individual coated particles. Free-standing OPyC layer fragments were picked out of the fractured coatings. A significant quantity of free-standing OPyC layer fragments usually

forms upon fracturing a TRISO particle sample because of the weak bonding between the SiC and OPyC layers. The IPyC density was not measured for this benchmarking exercise because free-standing IPyC layer fragments usually cannot be obtained after deposition of the SiC because of the impregnation of SiC into the open porosity of the IPyC layer. Free-standing SiC was obtained by picking out multiple layer fragments and heating in air to about 850°C for 2 hours to remove the attached pyrocarbon. Care must be exercised to not excessively oxidize the SiC by heating at too high a temperature or for too long a time. Layer fragments were placed in the appropriate liquid density gradient column. The sink-float density of the fragments was determined by measuring the zero buoyancy position in the column.

(b) X ray radiography

AREVA used an X ray radiography method developed in its laboratory to measure coating layer density, using the same principle as when measuring the coating thickness. Each of the obtained intensity profiles is processed in first locating approximately the layer interfaces thanks to the interference fringes.

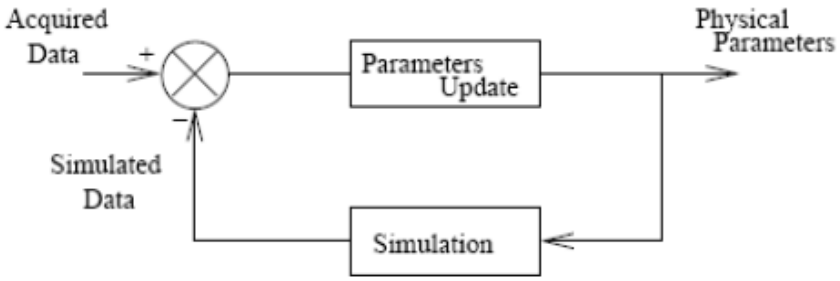

FIG. 4.22. Inverse problem principle.

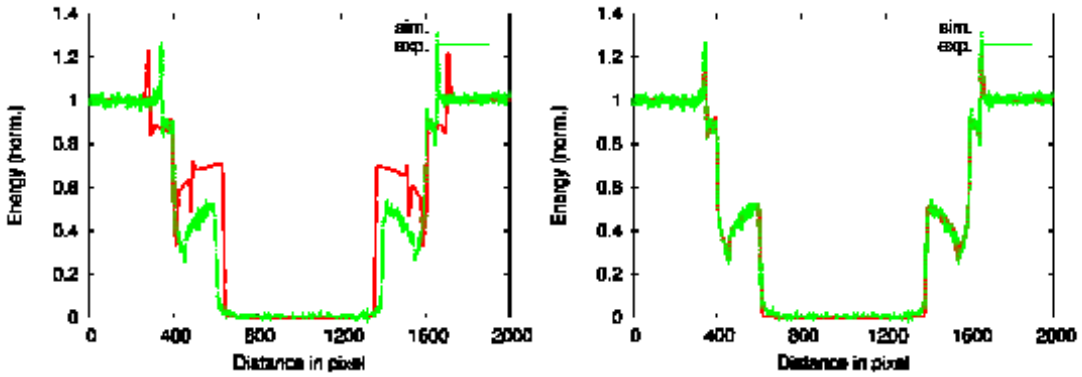

FIG. 4.23. Comparison between the experimental data and the simulation (left) without optimization (bad density and thickness); (right) after stochastic optimization (good densities and thicknesses).

After validation of these locations is performed, another profile is simulated using the previously determined X ray source spectrum, the detector PSF as well as the nominal (specifications) layer densities and the thickness values issued from the validated locations. This simulated profile is then compared to the experimental profile, error calculated and minimized via a stochastic algorithm, layer densities and thicknesses are iteratively adjusted (Figs 4.22 and 4.23). When the error reaches the desired threshold, iteration is stopped and the layer thicknesses and densities are accepted. Then, for each batch, the average and standard deviation of each of the parameters are calculated.

4.4.3.4. Anisotropy measurement

Most of the participating organizations measured the anisotropy of inner and outer pyrolytic carbon layers by a commercially available optical polarimeter attached to an optical microscope. The principle used at these different laboratories is the same, but the measured anisotropy values on a given sample depend on the manufacturer of the equipment and subtle differences in technique.. For example, at KAERI, an optical anisotropy photometer was installed on an optical microscope. Their measured reflectance values, a(θ) are corrected with a cubic zirconia with reflectance of 3.1, to have the corrected values, r(θ). The KAERI equipment consists of an optical (polarization) microscope, anisotropy photometer (polarimeter) and a personal computer, as shown in Fig. 4.24.

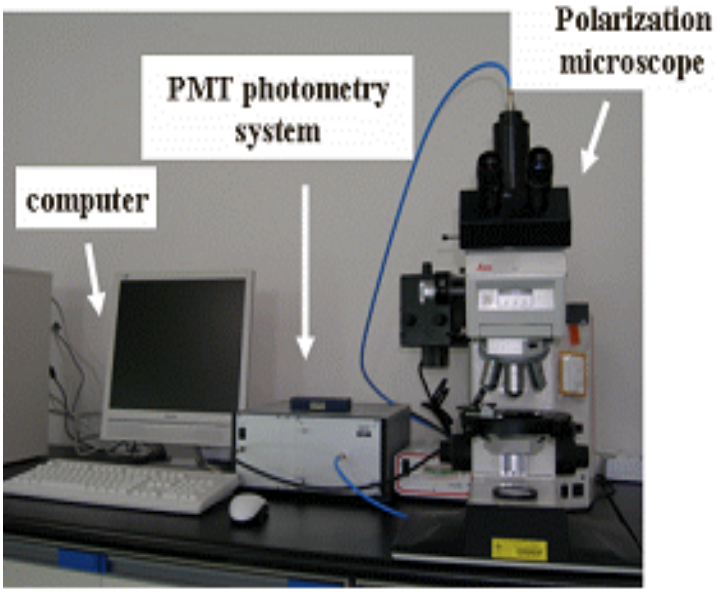

FIG. 4.24. Anistropy photometer installed in an optical microscopy (KAERI's example).

Samples for the optical anisotropy factor measurement are prepared in the same manner as for observation of micro-structure by optical microscopic ceramography. Measurements are automatic by the dedicated software installed in a personal computer. Caution is emphasized with regard to the periodical calibration with a well defined standard. OPTAF is related to the Bacon Anisotropy Factor (BAF) by the following equation:

$$OPTAF = \frac{1 + \eta_c + \eta_c BAF}{2\eta_c + BAF} \tag{4.5}$$

where $\eta_c = 3.52$ (monocrystalline graphite).

ORNL measured the anisotropy of PyC by the 2 Modulator Generalized Ellipsometry Microscope (2MGEM) developed by ORNL as is shown in Fig. 4.25. ITU used also the ellipsometry with the same principle as that used by ORNL. The 2-MGEM uses two polarizer-photoelastic modulator pairs, oscillating at two different frequencies in the kilohertz range, to generate and analyse elliptically polarized light. The 2-MGEM can determine the optical polarization properties of the pyrolytic carbon by reflecting the polarized light beam at near normal incidence from a polished cross-section of the coated particle. This instrument fully determines the change in the elliptical polarization of the light reflected from the pyrocarbon surface and determines all the elements of the Mueller matrix. From this matrix,

the diattenuation (N) can be extracted. The diattenuation is directly related to the Optical Anisotropy Factor (OPTAF) by the equation,

$$OPTAF = \frac{1+N}{1-N} \tag{4.6}$$

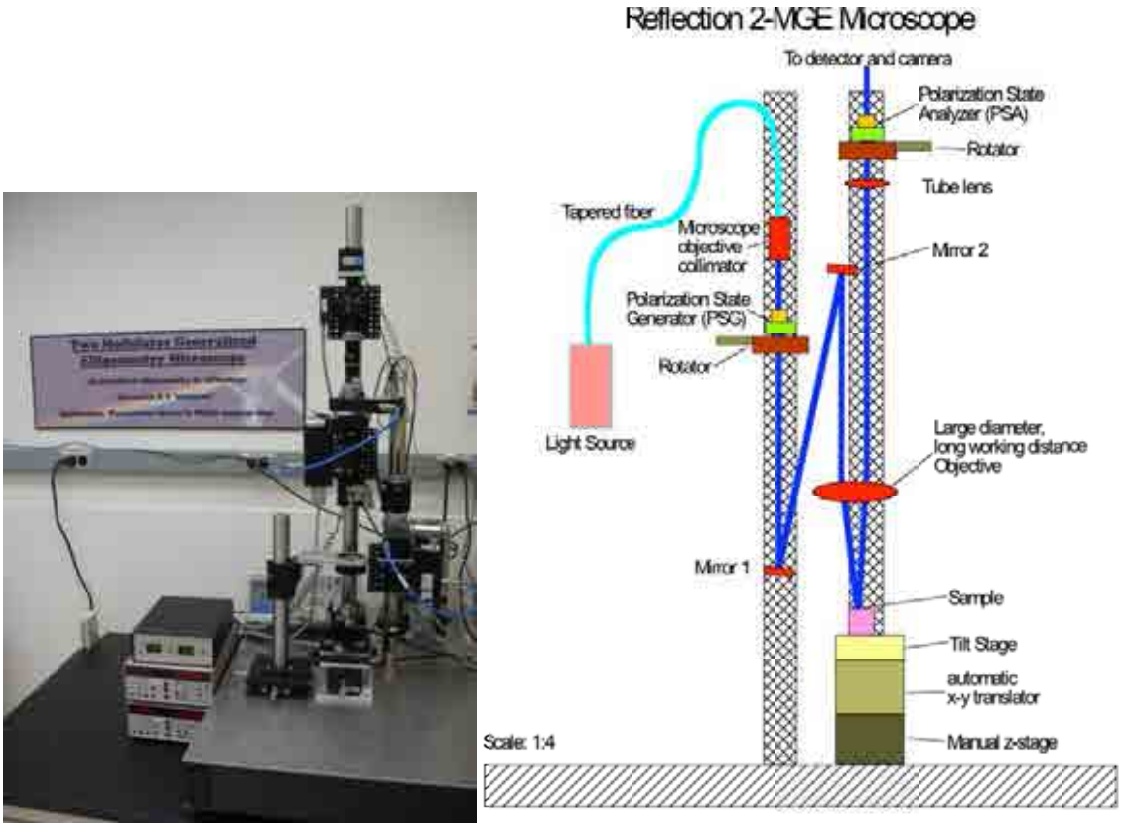

(a) (b)

FIG. 4.25. 2 Generalized Modulator Ellipsometry Microscope (2MGEM, ORNL) (a) general view and (b) schematic structure of the equipment.

Samples are mounted and polished similar to the methods used for imaging with an optical microscope. A computer-controlled stage is used to scan the sample beneath the 2-MGEM. This makes it possible to obtain detailed images of the diattenuation with a resolution as low as 2 μm. Figure 4.26 shows an example of a particle cross-section imaged for reflected light intensity using an optical microscope (Fig. 4.26(a)) and for diattenuation intensity using the 2-MGEM (Fig. 4.26(b)). Figure 4.26(c) shows the distribution of the diattenuation in each of the carbon layers. Typically, the observed variation in diattenuation within each particle is much larger than the variation of the average diattenuation from particle to particle within a batch. The observed variation in diattenuation within each particle is much larger than the uncertainty in the measurement and has been shown to be very reproducible.

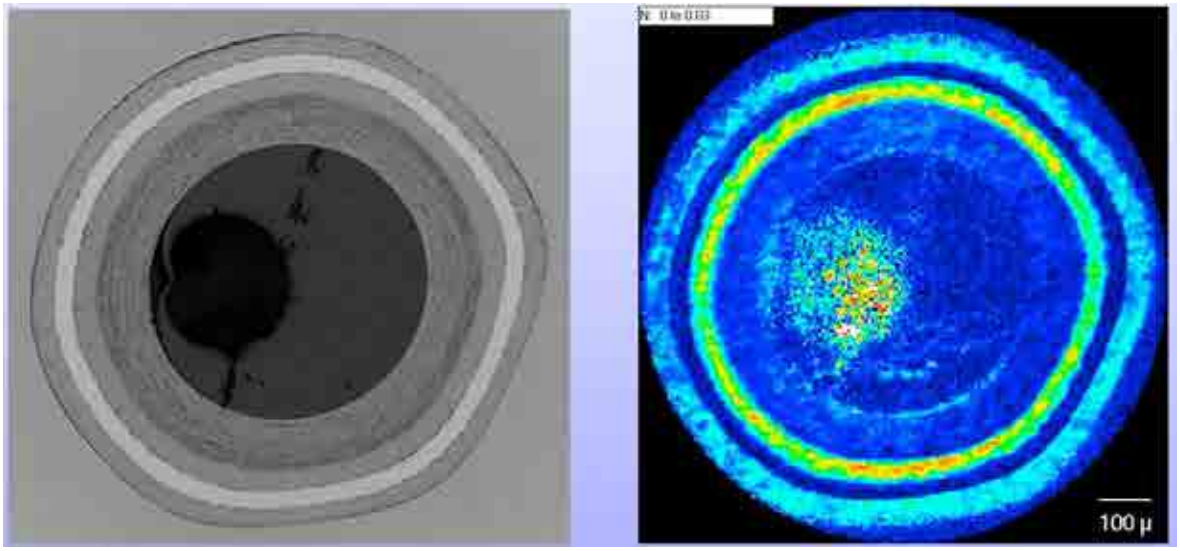

(a) (b)

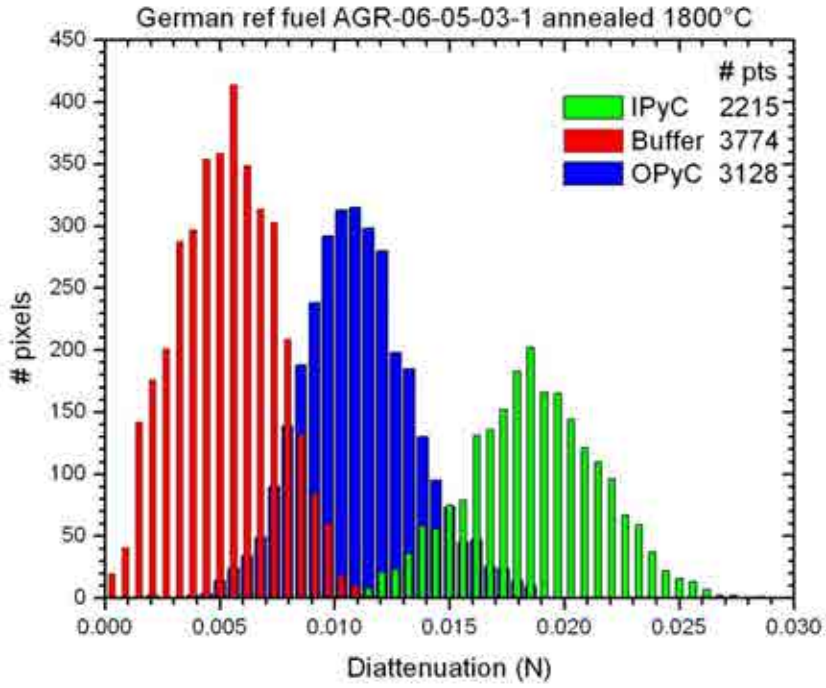

(c)

FIG. 4.26. (a) Image using intensity of reflected light. (b) Image using diattenuation of reflected light with color temperature scaled to the diattenuation. (c) Histogram of the corresponding diattenuation.

4.4.3.5. Particle diameter and sphericity measurement

Optical microscopy was used to measure particle size and shape. Particle size and shape were measured using a shadow graphic technique. Transmitted light was used to produce silhouettes of the particles. Analysis of these images produces information on mean particle diameter and aspect ratio. Aspect ratio is defined as the maximum diameter divided by the minimum diameter. Particles were mounted in a monolayer in a large transparent tray and imaged by acquiring a series of tiled photographs using an automated microscope.

At ORNL, quantified analysis of images obtained for size and shape was done using an ORNL developed image analysis programme. Manual measurements can introduce error from operator bias and tend to be more limited because of the required effort. Automated image

analysis allows for both larger sample size (typically over 1000 particles measured for each particle sample) and for more measurements to be made on each imaged sample. For size and shape determination, the image analysis programme identifies approximately 360 points around the outer boundary of each particle silhouette and calculates average diameter and aspect ratio.

4.4.3.6. Micro-structure observation

Micro-structure of the different coating layers were observed by using optical method and/or scanning electron microscopy to reveal the cross-sectional view and any abnormal appearance such as internal cracks. Ceramography was used by all the participating organizations. The same procedure was applied as for the thickness measurement, i.e. with careful sample via resin mounting, grinding and polishing. In order to reveal the micro-structure such as grain boundaries, some special etching techniques are often used.

4.4.3.7. Open porosity measurement

Among the participating organizations, only ORNL measured the open porosity of the outer PyC layer by using the mercury porosimetry method.

A mercury porosimeter can be used to determine kernel and buffer density, as well as open porosity in the IPyC and OPyC layers. The mercury porosimeter is essentially a volume measurement device. A sample of a few thousand particles is placed in a penetrometer cell with mercury and the air is evacuated. Because mercury does not wet to the sample, the mercury will tend to surround the particles with void space between the particles. The volume not occupied by the mercury is the called the bulk volume. Pressure is applied on the mercury to cause it to surround the individual particles. At some point the majority of void space in between the particles is filled with mercury and under this condition the mercury essentially enshrouds each individual particle in the sample. The volume not occupied by the mercury at this pressure is called the envelope volume. As pressure is increased beyond this point, the open pores at the particle surface are gradually filled, where the size of the penetrated opening is inversely related to the applied pressure. When all open porosity is filled, the volume not occupied by the mercury is called the skeletal volume. The difference between the envelope volume and the skeletal volume is therefore the open pore volume. These various types of volume and density are defined in ASTM standard D3766.

The buffer envelope density is defined as the weight of the buffer divided by the volume of the buffer. This can not be measured directly so it is estimated using the average weight and volume of the buffer coated particles and kernels. The porosimeter is used to measure the average envelope volume of a sample of buffer coated particles. The average envelope volume of the kernels inside the buffer coated particles is then subtracted. The difference, being the envelope volume of the buffer, is then divided by the average weight of the buffer to calculate the envelope density. The average weight of the buffer is determined from the difference between the average weight of the buffer coated particles and the average weight of the kernels inside. As for the kernel measurement, this analysis does not resolve the density of an individual buffer layer. In addition, because it is not feasible to separate the buffer from the IPyC layer in a fully coated particle, this analysis is not performed on the actual coated particle batch, but is instead performed on buffer coated particles either removed during coating by hot sampling or obtained by interrupting the coating process.

Kernel and buffer envelope density were not measured for this QC Benchmark exercise because samples of bare kernels and buffer only coated kernels were not available. OPyC

open porosity was measured on the samples provided from ORNL and B&W. Sufficient material was not available in the samples from KAERI and PBMR. IPyC open porosity was not measured because this cannot be done after deposition of the SiC layer. OPyC open porosity was calculated in units of mL/m^2 from the open pore volume of a sample divided by the surface area of that sample. Surface area was estimated from the approximate number of particles in the sample and the average volume of the particles (with the assumption of a spherical shape). Open pore volume was determined from the mercury intrusion over a pressure range of 1.7 to 69 MPa (~250 to 10 000 psi). Note that this pressure range is only appropriate for OPyC open porosity. IPyC open porosity cannot be measured at higher pressures, typically above 20 MPa (~3000 psi), because of compression of the IPyC/buffer layers.

4.4.4. Test results of the participating organizations

4.4.4.1. Coating layer density measurement

Table 4.15 summarizes the results of the measurements that the participating organizations carried out on the coating layer density. The methods employed by each organization for this test were already given in Table 4.12. The layer densities were measured by two methods; one was the sink float method and the other non-destructive X ray radiography. INET and JAEA used the so-called the titration method which is a variation of the sink float method.

The participating organizations measured the densities only for SiC and outer PyC layers, except AREVA who measured all the four layers nondestructively. However, in the table, the result of buffer and inner PyC layers by AREVA was omitted as there are no other data available to compare with. The values of layer density obtained by AREVA for buffer and IPyC for the four samples are given separately in Table 4.16. ITU and Hacettepe University did not participate in the layer density measurement. In the table, the mean values are also compared between the data obtained with the X ray radiography result and those without the X ray radiography result by designating ‘mean(total)’ and ‘mean(-X)’, respectively. For the SiC layer density, standard deviations of the measurement by each participating organization are narrow compared with that of PyC layer measurements which are about 10 times larger than the former.

It is worth comparing the results obtained by the two different methods. The density values obtained by the X ray radiography are generally higher than the mean values of the data obtained by the sink float method. This is illustrated by Fig. 4.27 where the deviations from the mean values of the densities of outer PyC and SiC layers are shown.

TABLE 4.15. RESULTS OF COATING LAYER DENSITY MEASUREMENTS (Mg/m^3) (STANDARD DEVIATIONS IN PARENTHESES) OBTAINED BY THE PARTICIPATING ORGANIZATIONS

Sample ID	KAERI		ORNL		BWXT		PBMR	
Participant	SiC	OPyC	SiC	OPyC	SiC	OPyC	SiC	OPyC
INET	3.200	1.46	3.200	2.01	3.20	1.89	3.190	1.61
AREVA (X ray)	3.21 (0.02)	1.45 (0.11)	3.21 (0.02)	2.00 (0.13)	3.20 (0.02)	1.98 (0.14)	3.19 (0.02)	1.82 (0.2)
JAEA	3.20 (0.003)	1.45 (0.01)	3.20 (0.004)	1.99 (0.20)	3.20 (0.003)	1.92 (0.04)	—	—
KAERI	3.201 (0.003)	1.435 (0.004)	3.197 (0.002)	2.006 (0.027)	3.192 (0.002)	1.893 (0.009)	3.198 (0.002)	1.615 (0.017)
PBMR	3.198 (0.001)	1.417 (0.011)	3.192 (0.002)	2.011 (0.006)	3.192 (0.002)	1.882 (0.005)	3.196 (0.002)	1.650 (0.006)
ORNL	3.2058 (0.0023)	1.4448 (0.0068)	3.2033 (0.0063)	2.0266 (0.004)	3.1971 (0.0018)	1.8885 (0.0201)	3.2073 (0.0007)	1.633 (0.0067)
BWXT	3.202	—	3.204	2.017	3.194	1.892	3.200	—
mean(-X) [a]	3.203	1.443	3.199	2.012	3.196	1.893	3.198	1.627
mean(total)	3.202	1.443	3.201	2.010	3.196	1.906	3.197	1.666

[a] mean(-X) : mean values calculated without the data of AREVA which measured the density by X ray method.
— data not available.

TABLE 4.16. RESULTS OF BUFFER AND IPYC LAYER DENSITY MEASUREMENTS (Mg/m^3) OBTAINED BY AREVA USING X ray RADIOGRAPHY

Sample ID	KAERI		ORNL		BWXT		PBMR	
Participant	Buffer	IPyC	Buffer	IPyC	Buffer	IPyC	Buffer	IPyC
AREVA	0.99	1.45	1.43	2.00	1.25	1.98	1.06	1.82

4.4.4.2. Layer thickness measurement

The results of layer thickness measurements by the participating organizations are shown in Table 4.17. The methods employed by the participating organizations were given in Table 4.13. The thicknesses are measured mainly by two methods, either by X ray radiography or by conventional ceramography. AREVA measured the layer thickness by use of the X ray radiography PCI (Phase Contrast Imaging) method to measure the four layers. KAERI used the same method and ceramography method as well to compare the results from the two different methods. JAEA used the X ray radiography with an Automatic Visual Measuring System (AVMS) (for outer PyC and SiC layers only) as well as the ceramography to measure all the four layers. INET used a X ray crystalline analyser to take micro-radiographs and measured the thickness with a projector. PBMR used X ray radiography. All the other organizations used the ceramography. Among the participating organizations, only ITU did not measure the layer thickness. Some of the participants measured only the outer PyC and SiC layer thicknesses.

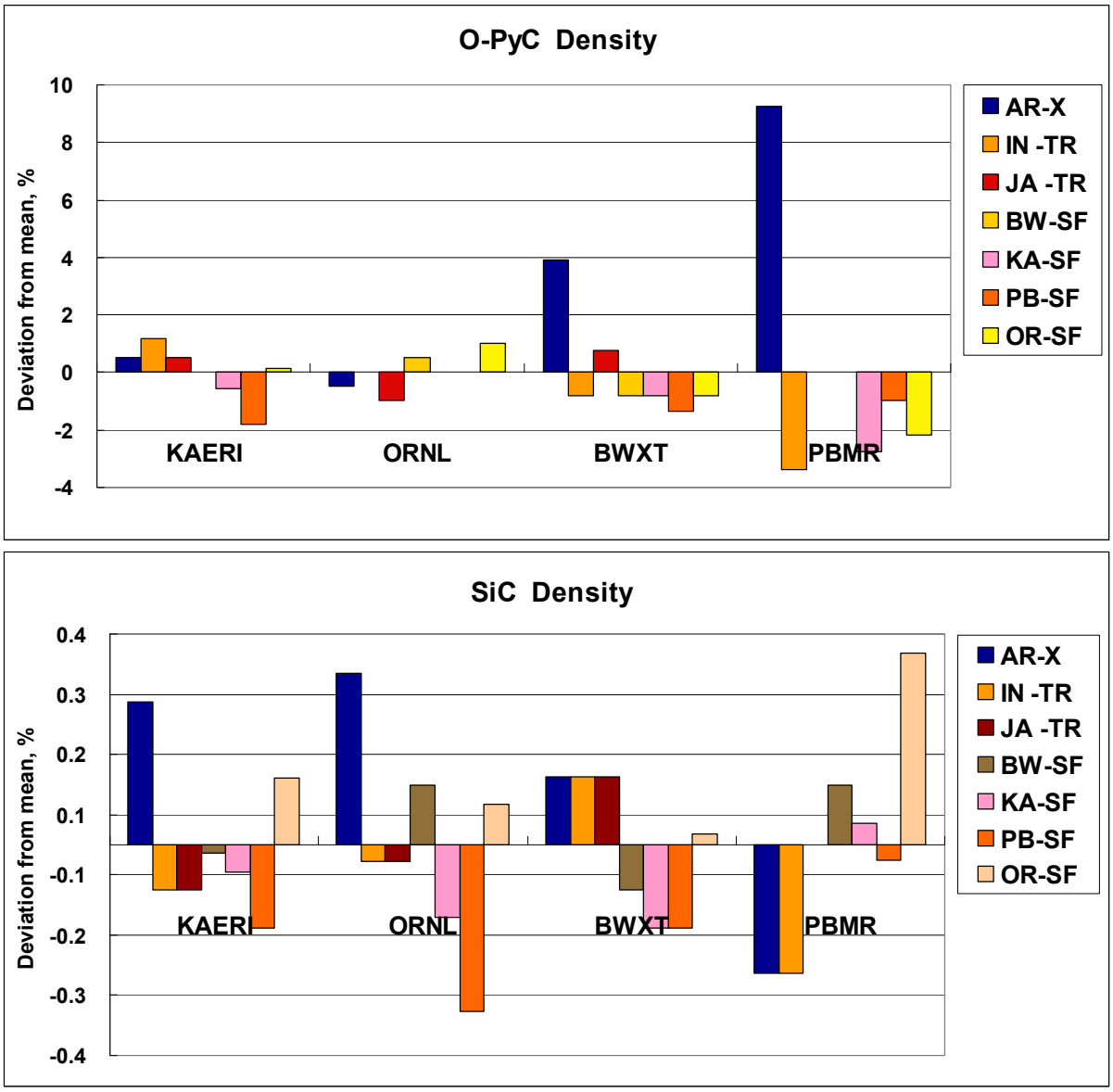

FIG. 4.27. Deviations from the mean values of the densities of OPyC and SiC layers measured by the two different methods. (AR: AREVA; IN: INET; JA: JAEA; KA: KAERI; HU: Hacettepe Univ.; PB: PBMR; OR: ORNL; BW: BWXT. X, TR and SF denote measurement by X ray radiography, titration and sink-float, respectively)

In the table, the mean values are also compared between the data obtained with the X ray radiography result and those without the X ray radiography result by designating 'mean(total)' and 'mean(-X)', respectively. For comparison of the results, deviations from the total mean values of the measurements plotted with the different methods for each sample as shown in Fig. 4.28. Similarly to the density measurement, the layer thickness values obtained by the X ray radiography are generally higher than the mean values of the data obtained by ceramographic method for outer PyC and SiC layers. For buffer and inner PyC layers, this observation is reverse.

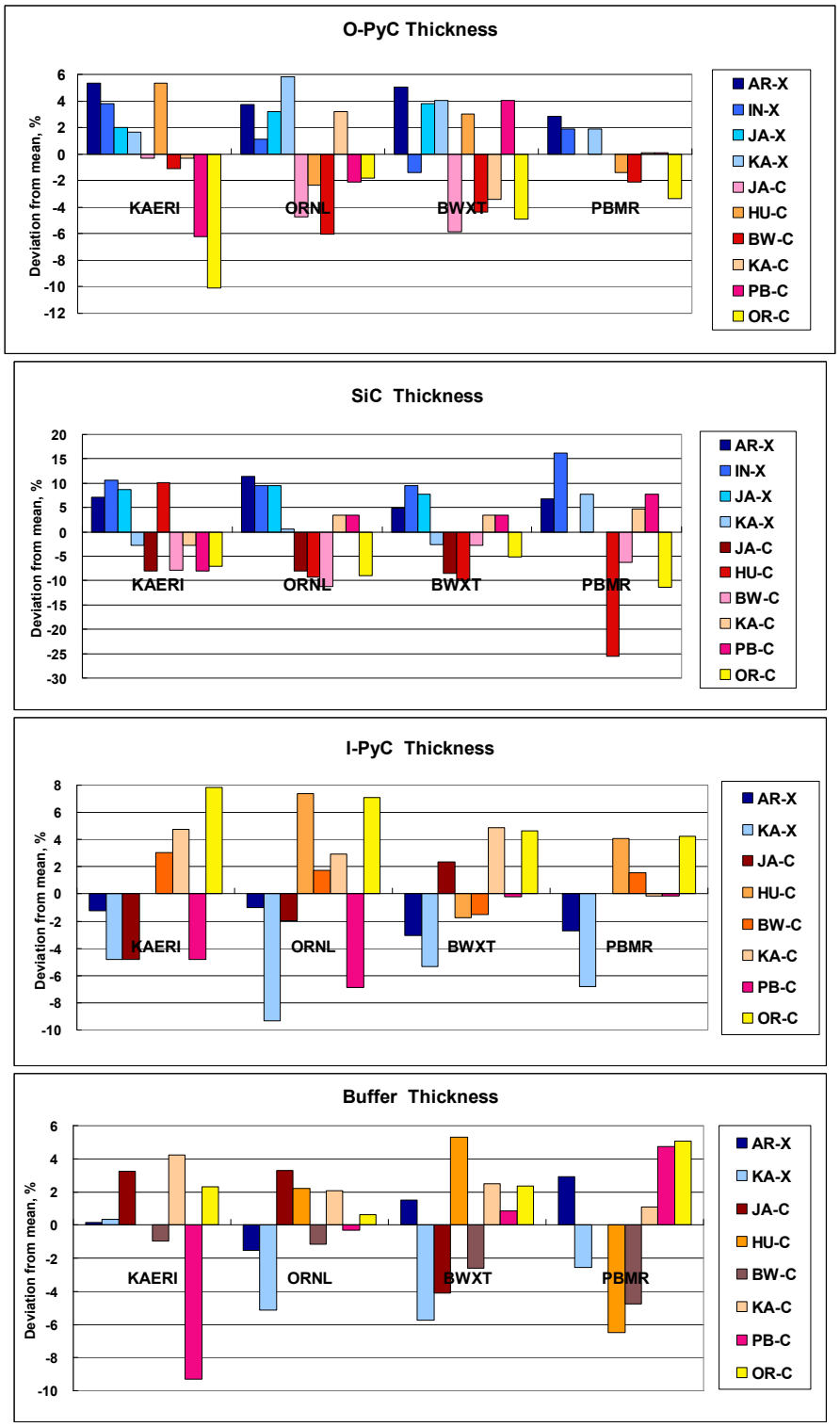

FIG. 4.28. Deviations from the mean values of the layer thicknesses measured by the two different methods (AR: AREVA; IN: INET; JA: JAEA; KA: KAERI; HU: Hacettepe Univ.; PB: PBMR; OR: ORNL; BW: BWXT. X and C denote measurement by X ray radiography and ceramography, respectively).

The layer thickness values obtained by the X ray radiography are generally lower than the mean values of the data obtained by ceramographic method. The dependency of the method of the thickness measurement for this observation is more pronounced than in the case of the density measurement. These differences are certainly due to the black interfaces between the

layers in how precisely the boundaries are determined. An observation to note also is that in the thickness measurement of buffer and iPyC layers, the data for the KAERI TR-64 sample by Hacettepe university were not available separately, and they provided only the combined value of the thicknesses of buffer and iPyC layers since the boundary between he two layers could not be clearly revealed by them.

4.4.4.3. Anisotropy and particle dimension measurements

Anisotropy of PyC layers was measured by ellipsometry at ORNL and ITU using the 2-MGEM instrument and optical polarimetry by INET, KAERI and PBMR. The results of the measurements are summarized in Table 4.18. The precision of the ellipsometry was generally higher than by the optical polarimetry. Kernel diameter, particle diameter and particle sphericity were measured either by X ray radiography or by ceramography as for the thickness measurement. The results of the measurements are also given in the table.

In both measurements, there is no tendency on the deviation from the mean values observed by the difference in the measurement methods as in the thickness or density measurements.

TABLE 4.17. RESULTS OF LAYER THICKNESS MEASUREMENTS BY THE PARTICIPATING ORAGNIZATIONS

Sample ID	KAERI				ORNL				BWXT				PBMR			
Participant	Buffer	IPyC	SiC	OPyC	Buffer	IPyC	SiC	OPyC	Buffer	IPyC	SiC	OPyC	Buffer	IPyC	SiC	OPyC
INET	—	—	42.1	53.1	—	—	38.1	38.2	—	—	37.1	39.8	—	—	38.8	—
AREVA	103.8	41.5	40.8	53.9	82.0	40.4	38.8	39.2	61.4	37.9	35.5	42.4	113.0	73.1	35.7	103.8
JAEA (X ray)	—	—	41.4	52.2	—	—	38.1	39.0	—	—	36.5	41.9	—	—	—	—
JAEA (Ceramo)	107.0	40.0	35.0	51.0	86.0	40.0	32.0	36.0	58.0	40.0	31.0	38.0	—	—	—	107.0
KAERI (X ray)	104.0	40.0	37.0	52.0	79.0	37.0	35.0	40.0	57.0	37.0	33.0	42.0	107.0	70.0	36.0	104.0
KAERI (Ceramo)	108.0	44.0	37.0	51.0	85.0	42.0	36.0	39.0	62.0	41.0	35.0	39.0	111.0	75.0	35.0	108.0
PBMR	94.0	40.0	35.0	48.0	83.0	38.0	36.0	37.0	61.0	39.0	35.0	42.0	115.0	75.0	36.0	94.0
Hacett. Univ.	—	—	41.9	53.9	85.1	43.8	31.6	36.9	63.7	38.4	30.5	41.6	102.7	78.2	24.9	—
ORNL	106.0	45.3	35.4	46.0	83.8	43.7	31.7	37.1	61.9	40.9	32.1	38.4	115.4	78.3	29.6	106.0
BWXT	102.6	43.3	35.1	50.6	82.3	41.5	30.9	35.5	58.9	38.5	32.9	38.6	104.6	76.3	31.3	102.6
mean(X)	103.9	40.8	40.33	52.80	80.50	38.70	37.50	39.10	59.80	37.45	35.53	41.53	110.00	71.55	35.85	103.9
mean(-X)	103.5	42.5	36.57	50.08	84.20	41.50	33.03	36.92	60.90	39.63	32.75	39.60	109.74	76.56	32.60	103.5
mean(total)	103.6	42.0	38.07	51.17	83.28	40.80	34.82	37.79	60.49	39.09	33.86	40.37	109.81	75.13	33.41	103.6

— data not available.

TABLE 4.18. RESULTS OF ANISOTROPY AND PARTICLE DIMENSION MEASUREMENTS BY THE PARTICIPATING ORGANIZATIONS

Sample ID	KAERI					ORNL					BWXT					PBMR				
Participant	Anisotropy		Kernel dia.	Particle dia.	Sphericity	Anisotropy		Kernel dia.	Particle dia.	Sphericity	Anisotropy		Kernel dia.	Particle dia.	Sphericity	Anisotropy		Kernel dia.	Particle dia.	Sphericity
	IPyC	OPyC				IPyC	OPyC				IPyC	OPyC				IPyC	OPyC			
INET	1.016	1.014	—	1004.3	—	1.004	1.009	—	912.5	—	1.024	1.022		884.0	—	—	—	—	1074.1	—
AREVA	—	—	505.6	985.5	—	—	—	510.4	910.1	—	—	—	519.5	873.8	—	—	—	532.7	1089.3	—
JAEA (Ceramo)	—	—	—	987.0	—	—	—	—	896.0	—	—	—	—	875.0	—	—	—	—	—	—
KAERI (X ray)	—	—	531.0	—	—	—	—	525.0	—	—	—	—	536.0	—	—	—	—	537.0	—	—
KAERI (Ceramo)	1.023	1.020	536.0	1027.0	1.057	1.025	1.025	508.0	930.0	1.045	1.029	1.031	524.0	896.0	1.038	1.020	1.024	534.0	1099.0	1.038
PBMR	1.010	1.000	—	1000.0	1.070	1.040	1.010	—	911.0	1.060	1.030	1.020	—	881.0	1.060	1.010	1.010	—	1081.0	1.050
Hacettepe Univ.	—	—	529.0	1011.8	1.161	—	—	530.6	913.4	1.043	—	—	492.8	887.6	1.047	—	—	—	—	—
ORNL	1.004	1.005	—	1001.0	1.055	1.034	1.013	—	907.4	1.044	1.021	1.017	—	881.2	1.039	1.0058	1.006	—	1076.2	1.041
BWXT	—	—	—	1000.8	1.048	—	—	—	909.0	1.042	—	—	—	882.0	1.038	—	—	—	1067.8	1.038
ITU	1.007	1.009	—	1007.0	1.055	1.037	1.027	—	921.0	1.049	1.019	1.016	—	894.0	1.045	—	—	500.7	1062.0	1.048
mean(X)	—	—	518.3	994.9	—	—	—	517.7	911.3	—	—	—	527.8	878.9	—	—	—	534.9	1081.7	—
mean(-X)	—	—	532.5	1004.9	—	—	—	519.3	912.5	—	—	—	508.4	737.6	—	—	—	517.4	1077.2	1.043
mean(total)	1.012	1.010	525.4	1002.7	1.074	1.028	1.017	518.5	912.3	1.047	1.025	1.021	518.1	687.1	1.045	1.012	1.013	526.1	1078.5	1.043

— data not available.

4.4.4.4. Micro-structure observation

For the micro-structure observations, INET, JAEA, KAERI and PBMR used an optical microscope with different magnifications, from 100 up to 1000 to reveal the structure of the coating layers. ORNL used scanning microscope and X ray tomography to reveal the coating layer structure and scanning electron microscopy in the back scattering electron (BSE) mode to reveal the SiC structure.

In the following sections, micro-graphs with different magnifications for the samples taken and analysed by each organization are shown with Figs 4.29 (a)–(d) by INET, Figs 4.30 (a)–(c) by JAEA, Figs 4.31 (a)–(d) by KAERI, Figs 4.32 (a) and (b) by Hacettepe University, Figs 4.33 (a)–(c) by PBMR, and Figs 4.34 (a)–(c) by ORNL. (a) Microscopy images by INET

FIG. 4.29(a). Cross-section of ORNL sample (magnification from left: ×100, ×400, ×1000).

FIG. 4.29(b). Cross-section of BWXT sample (magnification from left: ×100, ×400, ×1000).

FIG. 4.29(c). Cross-section of KAERI sample (magnification from left: ×100, ×400, ×1000).

FIG. 4.29(d). Cross-section of PBMR sample (magnification from left: ×100, ×400, ×1000).

(b) Microscopy images by JAEA

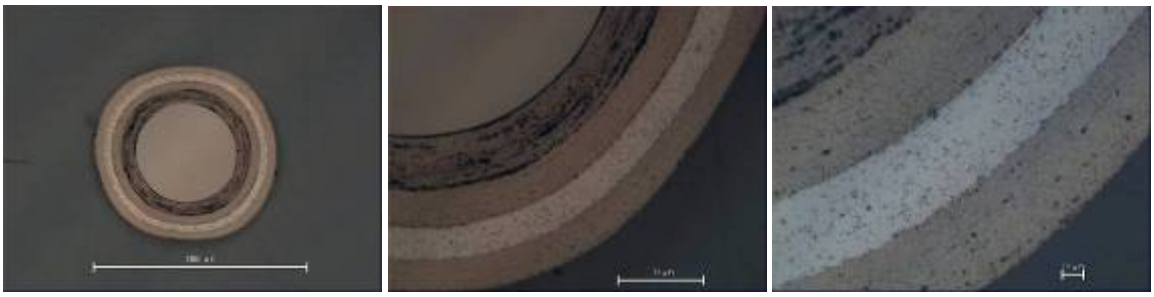

FIG. 4.30(a). Cross-section of BWXT sample (magnification from left: ×100, ×400, ×1000).

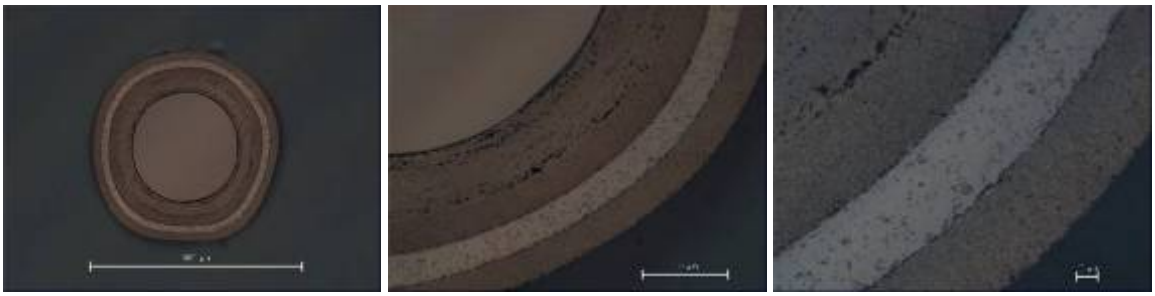

FIG. 4.30(b). Cross-section of ORNL sample (magnification from left: ×100, ×400, ×1000).

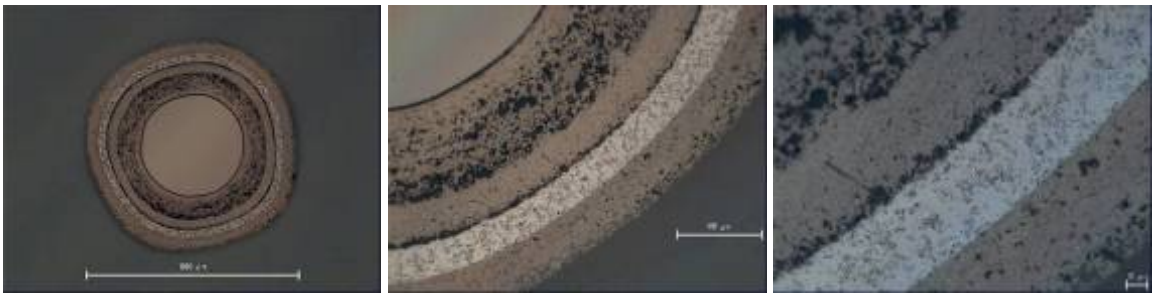

FIG. 4.30(c). Cross-section of KAERI sample (magnification from left: ×100, ×400, ×1000).

(c) Microscopy images by KAERI

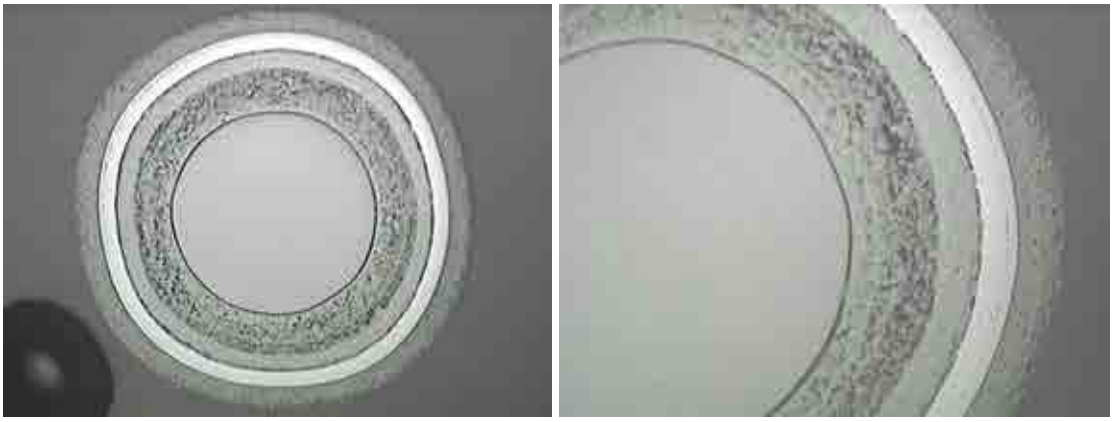

FIG. 4.31(a). Cross-section of KAERI sample (magnification from left: ×100, ×200).

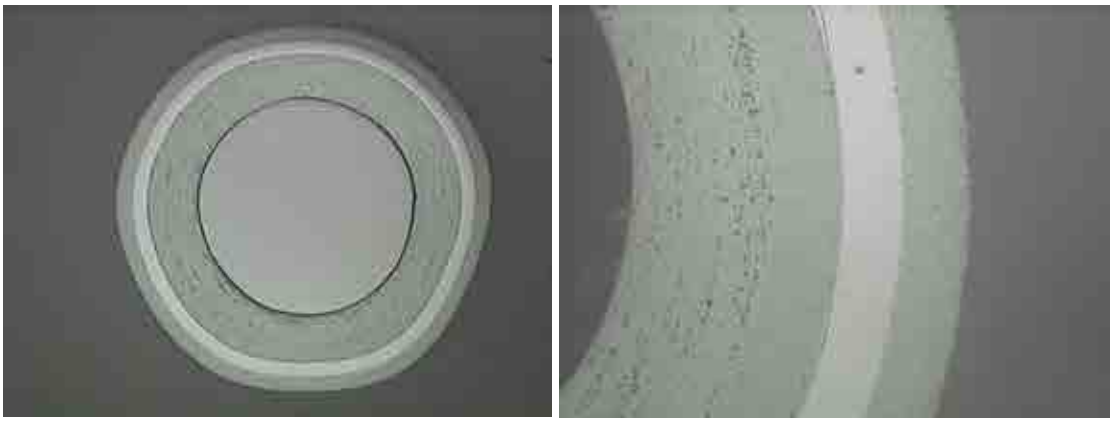

FIG. 4.31(b). Cross-section of ORNL sample (magnification from left: ×100, ×400).

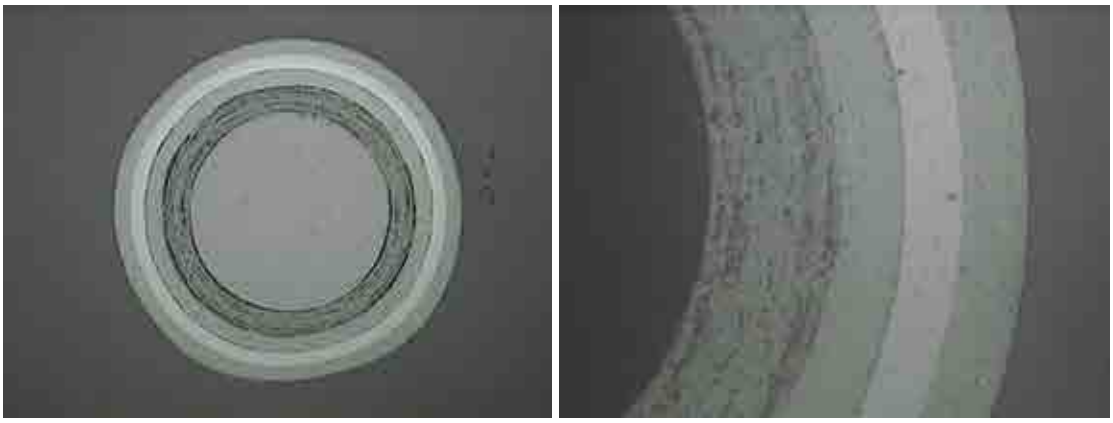

FIG. 4.31(c). Cross-section of BWXT sample (magnification from left: ×100, ×400).

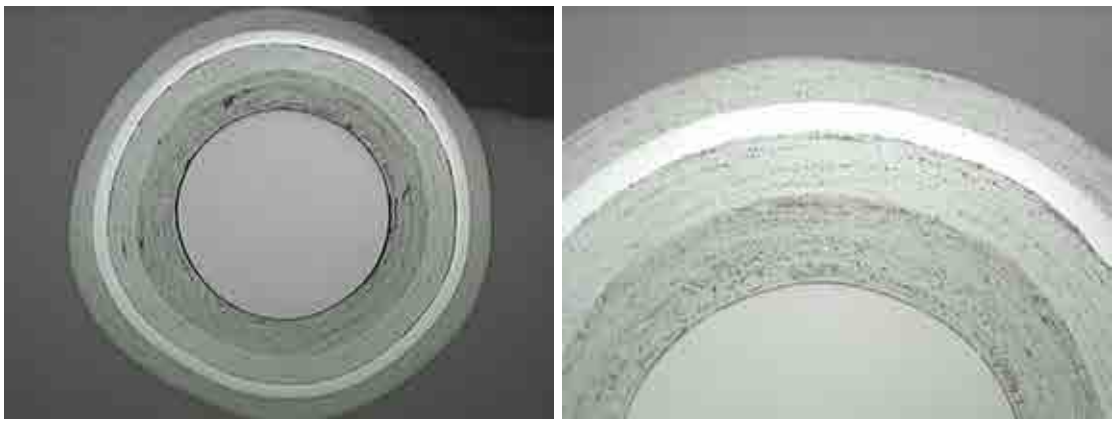

FIG. 4.31(d). Cross-section of PBMR sample (magnification from left: ×100, ×200).

(d) Microscopy images by Hacettepe University

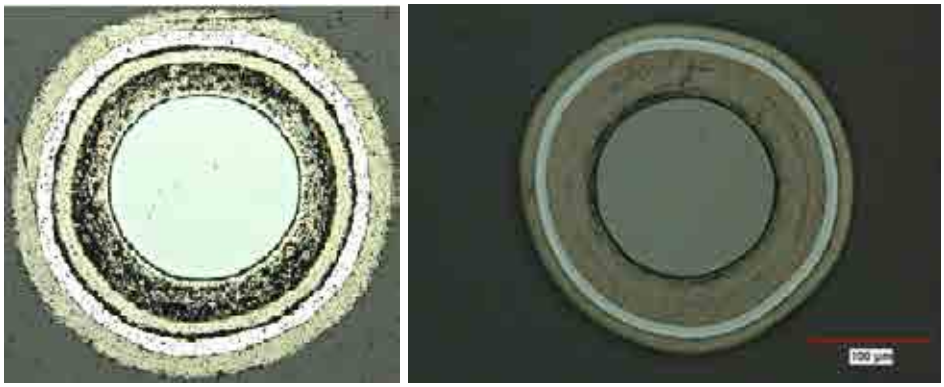

FIG. 4.32(a). Cross-sections of KAERI sample (left) and ORNL sample (right).

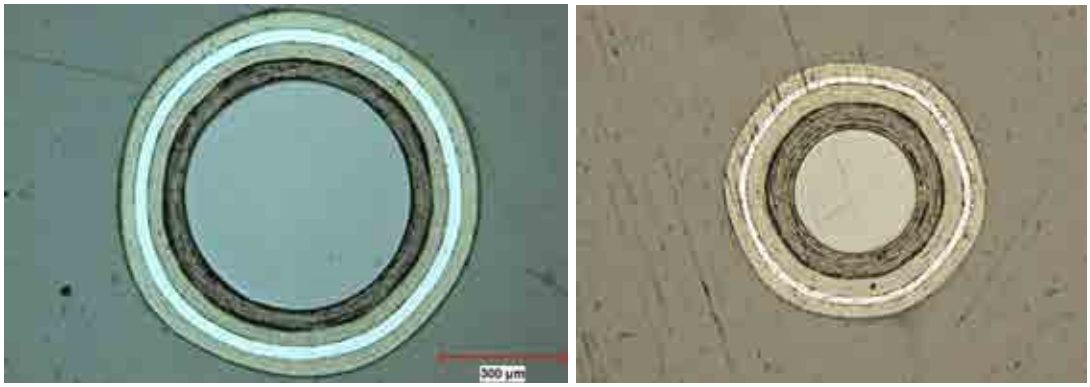

FIG. 4.32(b). Cross-sections of BWXT sample (left) and PBMR sample (right).

(e) Microscopy images by PBMR

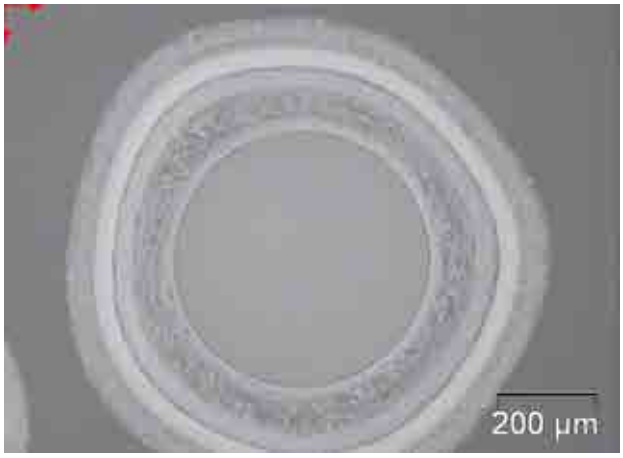

FIG. 4.33(a). Cross-section of KAERI sample.

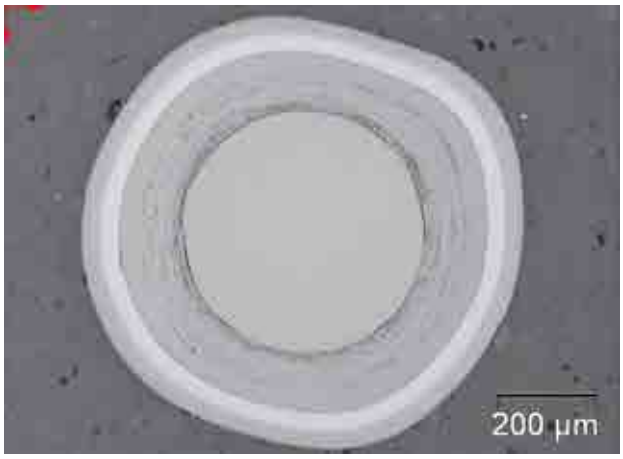

FIG. 4.33(b). Cross-section of ORNL sample.

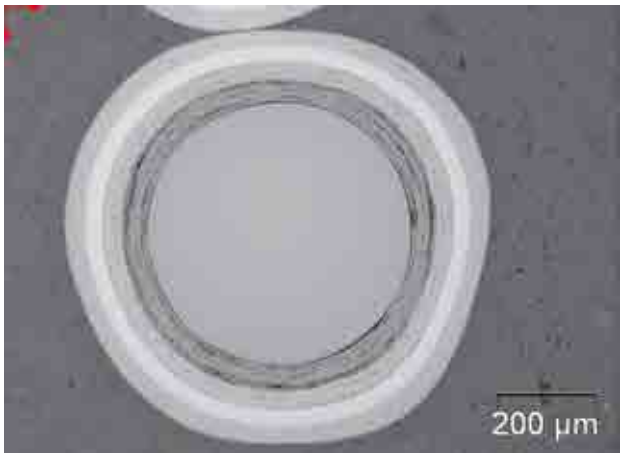

FIG. 4.33(c). Cross-section of BWXT sample.

(f) Scanning electron microscopy images and X ray tomographs by ORNL

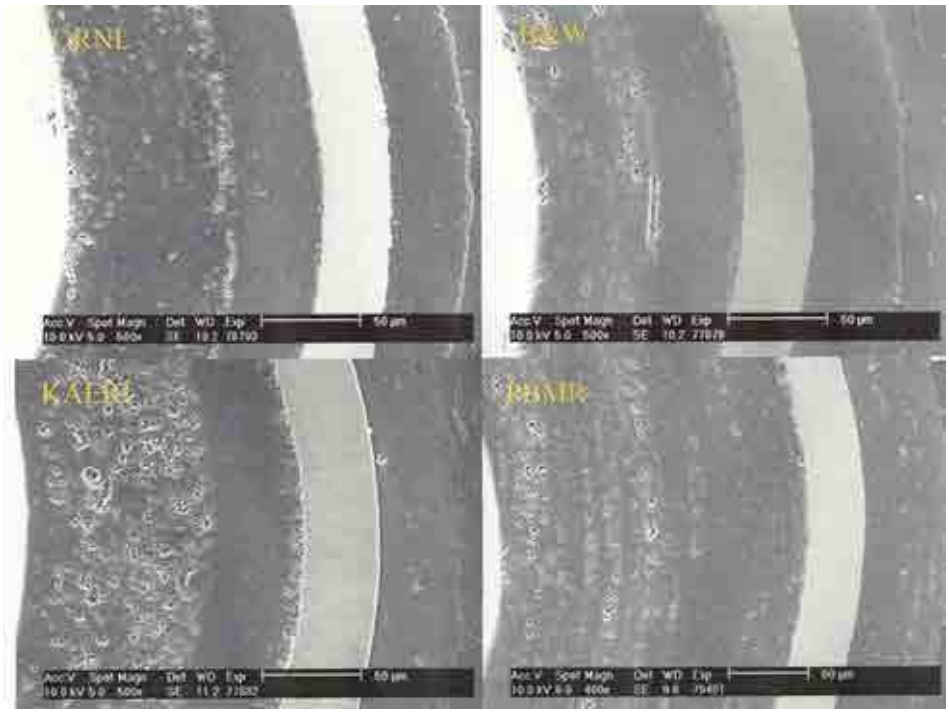

FIG. 4.34(a). Micro-structure observation with secondary electron imaging (ORNL).

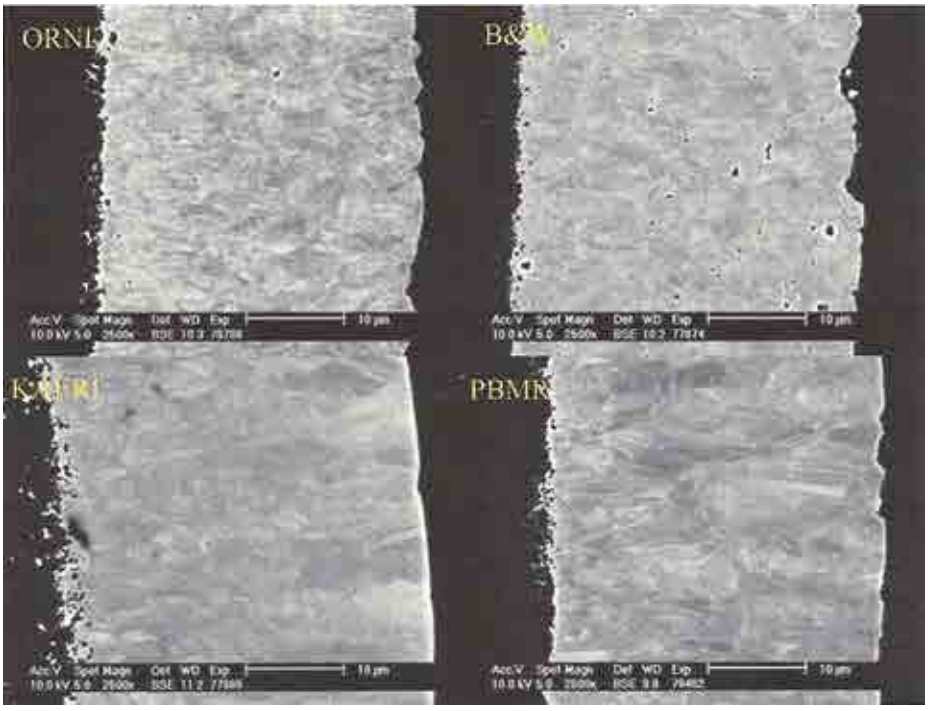

FIG. 4.34(b). Micro-structure observation with backscattered electron imaging (ORNL).

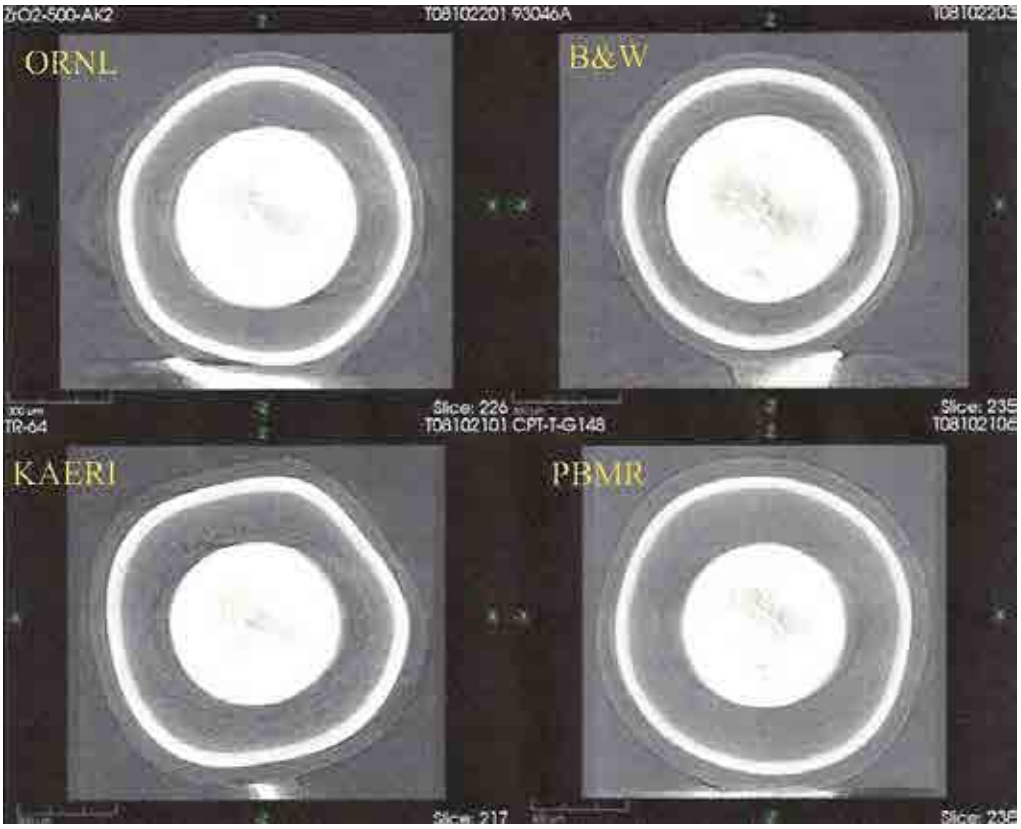

FIG. 4.34(c). X ray tomographic cross-section (ORNL).

In ORNL, micro-structure observation by limited scanning electron microscopy (SEM) and X ray tomography was performed in order to demonstrate the capabilities of those methods. Figures 4.34 (a) and (b) are composites of SEM images from each particle batch. In Fig. 4.34(a), variation in micro-structure such as porosity and interface intercalation can readily be resolved by scanning electron (SE) imaging. In Fig. 4.34(b), back-scattered electron detection (BSE) can be used to resolve differences in SiC grain structure. Figure 4.34(c) is a composite of X ray tomography images presented as two dimension cross-sections through the centre of each particle. Dimensional information such as particle size and shape and coating layer thickness can be extracted using this non-destructive method. Micro-structural variations such as layer porosity can be resolved. Additional SEM and X ray images are included in each data section for the variation particle samples.

4.4.5. Summary

In this round robin exercise (RRE), characterization was carried out among 9 participating organizations on the 4 different surrogate (ZrO_2 kernel) TRISO coated particle samples supplied from KAERI in the Republic of Korea, ORNL and BWXT in the USA and PBMR in South Africa. The participating organizations were INET at Tsinghua University (China), AREVA (France), JAEA (Japan), KAERI (Republic of Korea), PBMR (RSA), Hacettepe Univ. (Turkey), ORNL (USA), BWXT (USA) and ITU (EU).

The purpose of this RRE was for the comparison and benchmarking of the characterization methods employed by the participating organizations and their results obtained by the methods. It should be stressed that the surrogate particle samples are not necessarily representative of the baseline of the process used by each organization and conclusion should

not be drawn regarding fuel performance based on the properties obtained during the characterization of these samples.

The characterization items to be measured were selected after a review of the important characteristics of coated fuel particles in HTR fuel production at fuel producing organizations as described in the Section 4.2. The characterization items to be measured by each participating organization were limited not only by the samples but also by the methods available up to the time of testing at the participating organizations. At the beginning, some U-containing coated particles were also considered for this RRE. However, due to the problems of complexity of international transportation, this consideration was abandoned. As a result, the kernel characterization was excluded in this exercise. Therefore, the selected items for the measurement were mostly limited to the coating layers, i.e. densities of the outer PyC and SiC coating layers, thicknesses of 4 coating layers, anisotropy of inner and outer PyC coating layers and particle dimensions including sphericity.

The characterization methods employed by each organization were established independently by their own technology development. They are both destructive and non-destructive. The characterization methods were discussed fairly in depth in the Section 4.3., by taking examples of both current practice and previous experiences in the former German fuel production activities. The results of the exercise obtained by the participating organizations were quite similar as evidenced in the Section 4.4.5 where the results obtained by different organizations for each item were compared and analysed. However, for certain items, such as layer thickness, the results of the measurement were somewhat different depending on the method employed, i.e. between the destructive ceramography and non-destructive X ray radiography. It should be desirable to perform a further study to elucidate these differences.

4.5. IMPROVEMENT

4.5.1. Why study advanced QA/QC

Due to the number of coated fuel particles in the fuel elements required, i.e. some billions of TRISO particles for each core fuel load, and these are packaged into clusters commonly identified as compacts or pebbles, each of which contains thousands of TRISO particles bound together in a carbonaceous matrix, the standard QC methods for inspection of coated particle fuel during the manufacturing process are labor intensive, as were done manually and in many cases destructive. These methods are not suitable for economically testing large numbers of particles or for providing timely feedback of fuel property measurement data to the manufacturing processes. Therefore, along with the fuel fabrication process, automated inspection technologies are required to enable economic particle fuel production. These need to be high speed, computer controllable, and have outputs compatible with real-time processing to provide rapid feedback to the manufacturing processes. Very high throughput methods capable of 100% inspection, with provision for product sorting to remove defective material, are also attractive for some properties.

4.5.2. Advanced techniques — description and purpose

4.5.2.1. Innovative quality control methods of HTGR fuel particles at AREVA

AREVA NP's Non-Destructive Evaluation Technical Center is engaged in a R&D programme aiming the development of innovative industrial non-destructive evaluation methods for HTGR fuel [139]. After investigating a number of potential techniques, some of them were selected based on their performances and/or their industrial potential. In particular, development has been carried out on high resolution X ray imaging allowing accurate layer thickness, layer density and structural defects characterization, X ray tomography offering the possibility to characterize fuel element homogeneity and determine the number of in-contact particles contained in a fuel element, infrared thermal imaging allowing cracks detection, eddy currents enabling particle diameter measurements as well as crack detection and vision enabling real time automatic crack detection. These techniques were selected either for the richness of their information (X ray tomography), or because of their high throughput rate. For all these techniques, besides the development of a HTGR fuel dedicated control method, equipment and probes were specifically designed, tested and optimized to obtain, in particular for infrared thermal imaging and eddy currents, throughput rates that are compatible with a 100% production control strategy [140].

(a) X ray phase contrast imaging

In contrast to conventional X ray imaging, phase contrast imaging [141] occurs when the object to inspect is placed at a large distance to the film or digital detector. In such a configuration, interference fringes arising at the location of density variations within the object are superimposed to the traditional X ray absorption image. While coupled to tomography, a submicron X ray source focal spot and a very high resolution detector, HTGR particle phase contrast images enable an easy identification of all the particle layers (even though their densities are for some of them very similar), their accurate thicknesses measurement and the detection of flaws such as micro scale porosities or inclusions, layer delaminations and cracks.

As a first stage of the development, images of TRISO particles were acquired at the European Synchrotron Research Facility (ESRF) in Grenoble, France. Thanks to the monochromatic, highly collimated and high flux beam, and the use of a very high resolution X ray camera (0.9 microns per pixel), tomography of TRISO particles was performed (Fig. 4.35).

By developing image analysis tools and image processing algorithms, this high resolution X ray phase contrast imaging method enabled automated measurement of layer thicknesses to an accuracy of ± 1 μm, detection of micrometric porosities or inclusions, detection of layer cracks and interlayer delaminations (Fig. 4.36)

In addition, a dedicated method was developed to retrieve each layer density from phase contrast images, via the iterative reduction of the difference between an image-extracted profile and a simulated one. Results showed a difference of less than 2% with the destructive reference method for HTGR fuel layer density determination, i.e. the sink float method.

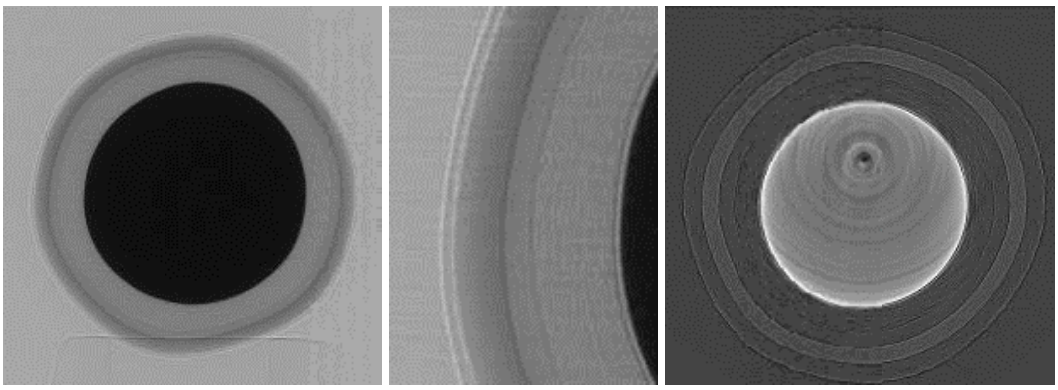

FIG. 4.35. Left: phase contrast image of a TRISO particle at ESRF, middle: zoom on the particle layers, and right: tomographic slide.

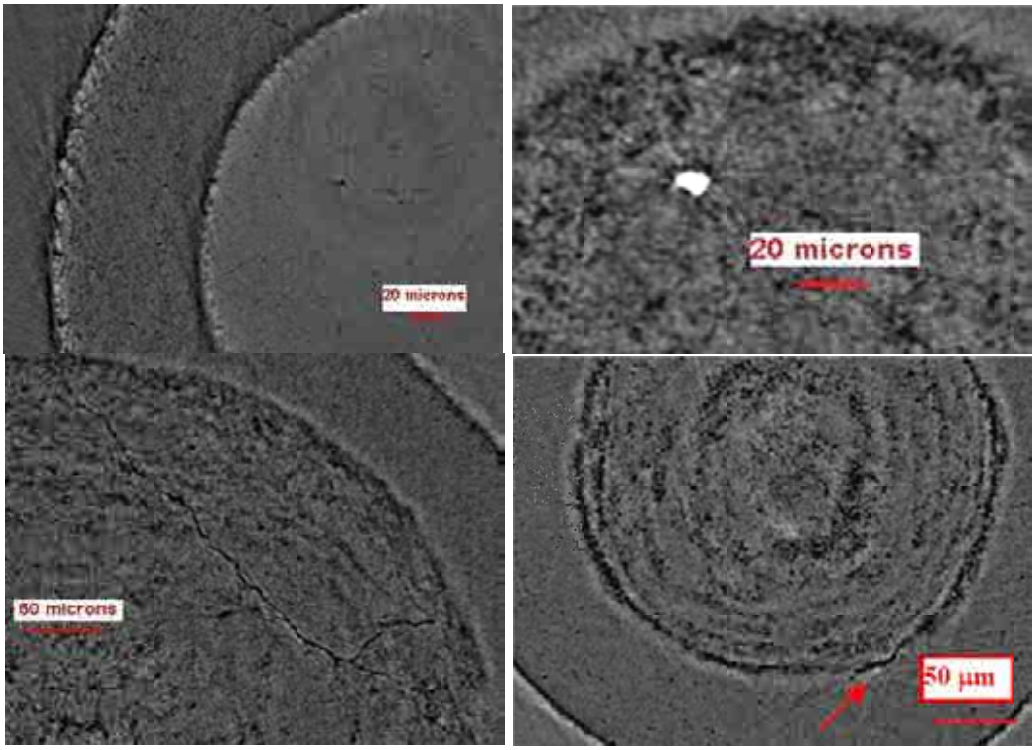

FIG. 4.36. Porosities in OPyC and SiC, kernel inclusion, crack in the buffer and buffer/IPyC delamination detected on ESRF's TRISO particle tomographic slide.

However, even though this technique was more than satisfactory on the technical performance point of view, using a synchrotron facility can obviously not be considered as a potential solution for an industrial quality control method. Thus, in parallel, AREVA NP's Non-Destructive Evaluation Technical Center performed a study aiming the construction of an industrial demonstrator, via, among other activities the benchmarking of different X ray cameras and sources. Although this system is currently still under testing to confirm its technical performances relative to the ESRF equipment (Fig. 4.37), it could be stated that this demonstrator could provide an HTGR fuel particle phase contrast image of extremely good quality in two minutes and that determination of layer thicknesses and densities could be achieved in one supplemental minute.

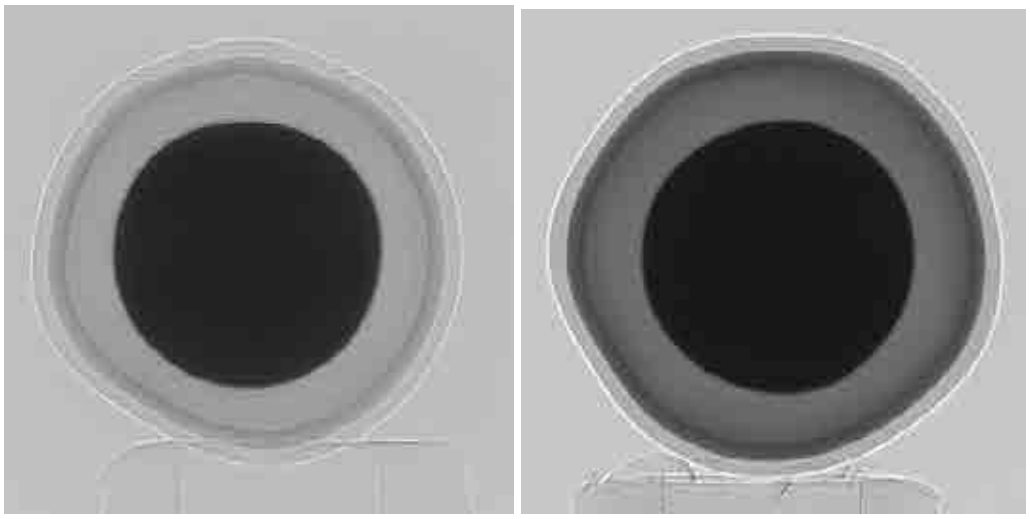

FIG. 4.37. Left: ESRF and right: industrial demonstrator phase contrast image of the same TRISO particle.

(b) Eddy currents

Due to the TRISO particles' reduced size, a high frequency electromagnetic method and equipment had to be developed to assess these objects. A simulation work was first conducted for defining adequate coil parameters, as well as operating conditions. Results showed that the coil inner diameter had to be as close as possible to the TRISO particle diameter, and that the frequency range should lie between 20 to 50 MHz. Knowing that no commercially available eddy current equipment existed in this frequency range, a method was initially developed to measure the impedance module of a particle on an impedance meter in a static configuration, i.e. where the particle was placed manually in different coils. Results confirmed the simulation results, i.e. that the coil having the best sensitivity was the one slightly exceeding the particle diameter, that a direct relation between particle diameter and impedance module existed enabling diameter measurement with an accuracy of 10 μm, and that a variation of the impedance module occurred in the presence of a laser machined notched particle.

However, experiment campaigns led on different TRISO batches and different types of flawed particles revealed that the sole impedance module measurement was not sufficient to discriminate between sound and flawed particles. Indeed, impedance module variation in the case of a flawed particle due to the relative position of the flaw with respect to the coil was so large that its minimal value could match the one of a sound particle. A discrimination criterion was then set, tested and validated, based upon the impedance module 'dispersion', i.e. the difference between the maximum and minimum impedance module values for a flawed particle placed in the coil with different orientations. Such a criterion enabled the undoubtedly discrimination between sound and flawed particles containing real cracked or notched layers with depth ranging from few tens to few hundreds microns (Fig. 4.38).

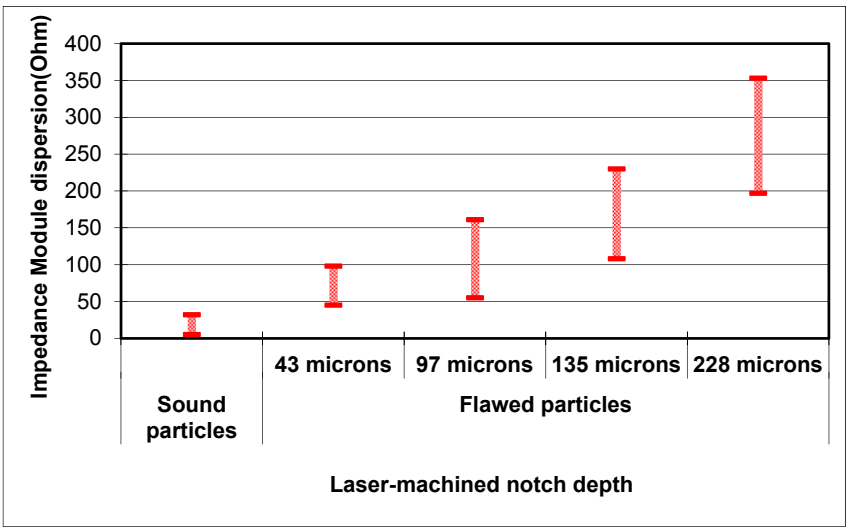

FIG. 4.38. Impedance module dispersion for sound and flawed TRISO particles as a function of laser machined notch depth.

Simultaneously, development was performed to build a device matching the industrial HTGR fuel quality control constraints. The obtained equipment (Fig. 4.39) was proven to fulfill the performances in terms of sensitivity of the static configuration experimental set-up, and exhibited the ability to theoretically control 200 particles per second. Current experimental tests reveal a throughput rate of forty particles per second, with the particle free falling in the coil. Development of a mechanical system enabling active particles injection in the coil is in progress aiming to achieve a throughput rate as close as possible to the theoretical one.

(c) Infrared thermography

In the first step of the development, different infrared thermography techniques were tested, mainly studying crack detection in fuel particles. Infrared thermal microscopy already developed for carbonaceous layer thermal characterization [142], active photothermal camera [143] and flash thermography method were assessed on naturally cracked and on laser machined notched TRISO particles. Whereas the first two methods did not yield positive results, the flash thermography method exhibited a potential for discrimination between sound and flawed particles. This technique relies on particle heating thanks to a light flash whose power and duration are adjusted to provide the best heating efficiency and on the follow up of the particle temperature in time via a high resolution infrared camera.

This technique was further developed via a parametric study aiming, on one hand, to determine the optimal operating conditions and protocol, and on the on the other hand, to define a discrimination criterion. Experimental parameters such as the number of light sources, their power and duration, the nature and shape of the particles sample holder and the required camera resolution were studied and defined. Simultaneously, tests were carried out on sound particles, naturally or micro-flexion induced cracked particles, and laser notched particles issued from different batches, to set and validate a discrimination criterion. Finally, influence of the crack position with respect to the heating source and camera was also assessed.

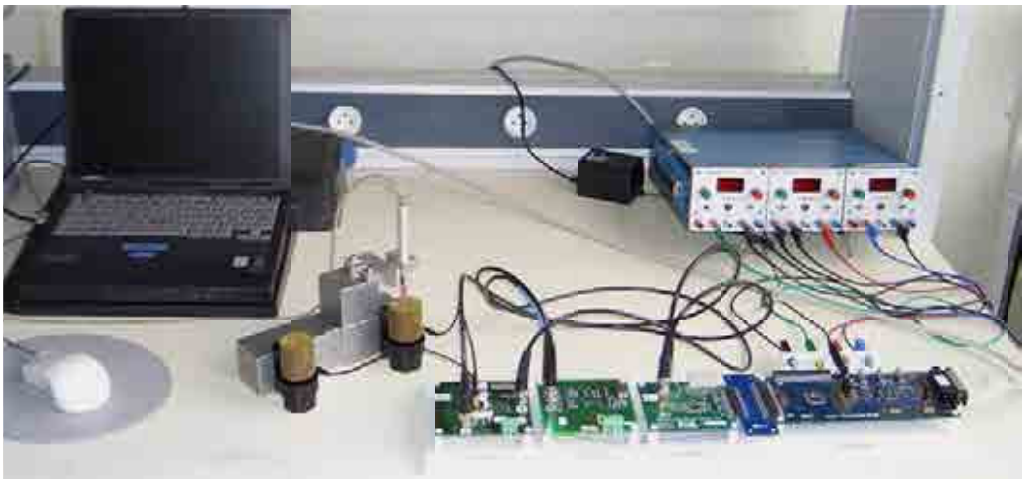

FIG. 4.39. Developed eddy current system.

It was found that flash thermography was a suitable technique for detecting open surface cracks or notches as narrow as few microns and as shallow as few tens of microns, providing a flat particle sample holder, whatever the position of the crack with respect to the heating source and camera. The criterion used to yield such a conclusion is based on the maximum temperature reached by a particle. For a flawed particle, the presence of the crack or notch acts as a thermal barrier to the heat diffusion throughout the particle, leading to a higher maximum temperature than for a sound particle. Whereas this temperature can be measured individually for each TRISO particle, the use of a CCD infrared camera enables the extraction of a thermal false colored cartography at the maximum reached temperature (Fig. 4.40). With this configuration, provided a high resolution camera with a proper magnification, a throughput rate varying from 200 to 600 particles per second could be achieved, positioning the flash thermography method as a 100% production quality control method for open surface crack detection.

(e) Vision

With the need for particles geometrical characterization, vision methods appeared as an obvious characterization technique. Besides, acquisition of particles images with image processing algorithms or light based granulometry techniques that are applicable to HTGR fuel have already been developed in the past for sphericity and diameter measurement. Thus, on the characterization point of view, no specific effort was placed in the development of such a technique.

However, thanks to the recent developments in image acquisition and processing technologies, vision could then be envisaged as a quality control technique for crack detection in HTGR fuel particles. Both high resolution cameras as well as real-time image processing algorithms are nowadays available, enabling industrial quality control. Thus, AREVA NP's Non-Destructive Evaluation Technical Center concentrated its development around the identification of commercially available state of the art vision equipment and on their integration in an industrial demonstrator (Fig. 4.41).

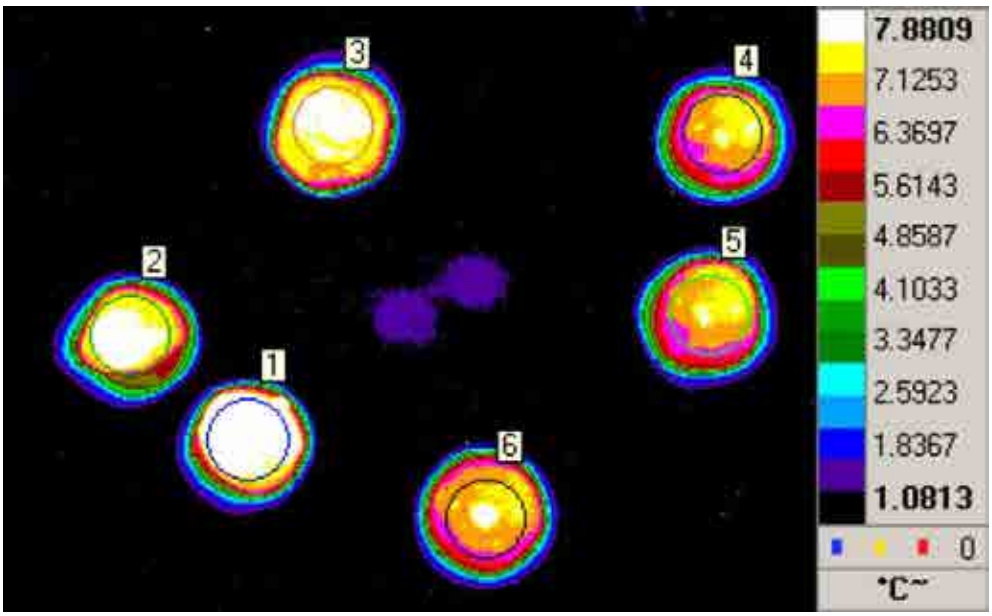

FIG. 4.40. Infrared cartography of sound (1,2,3) and micro-flexion induced cracked (4,5,6) TRISO particles via the flash thermography method.

FIG. 4.41. Developed vision industrial demonstrator.

Nevertheless, whereas the sole integration of existing elements did not constitute a real challenge even if the choice of light source was not trivial to ensure uniform particle illumination, interest of the developed demonstrator lies in the fact that 100% coverage inspection of each TRISO particle surface was performed. A mechanical system based on two rolls rotating in the same direction at different speeds was developed, enabling the quasi-spherical particles to rotate while images were acquired by a high resolution camera.

More precisely, the particles are fed via a vibrating bowl to an inclined ramp where at the end of the latter, an automated system separates them in batches of four particles. Each constituted batch is then propelled by a compressed air mechanism to the cylinder based rotating system located below the camera. While rotating, four images of each batch are acquired, and image

processed with a blob and crack detection algorithm (Fig. 4.42). According to the image processing verdict, each batch is then automatically directed, either to the 'sound particle' or to the 'flawed particle' reservoir via a automated sliding selector.

With this demonstrator, taking into account that 100% coverage inspection is performed on each particle via the acquisition of four images per particle, a throughput rate of 1.5 particles per second is currently achieved. Such a limitation arises from the acquisition cards performances despite being the fastest commercially available ones. One could though envisage that evolution of the semiconductor technology will provide throughput rate improvement in the next years.

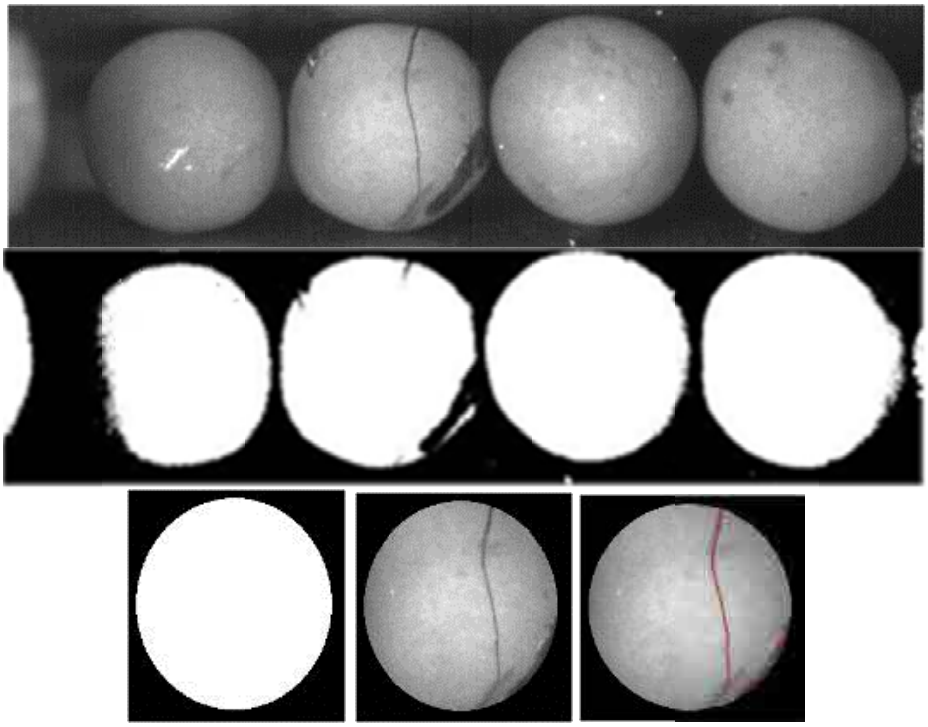

FIG. 4.42. Illustration of the image processing algorithm including blob, mask, and edge detection steps.

(f) X ray tomography

Knowledge of the TRISO particle distributions inside HTGR fuel elements may help manufacturers to improve the quality of their fuel by providing feedback during the development phase. In a joint programme, NRG and JRC-IE developed a fast method to obtain these distributions non-destructively, based on X ray Tomography [144]. The coordinates of the individual TRISO particles are extracted from a tomographic reconstruction of a pebble. The method has been applied to 31 pebbles of types GLE-4 (AVR reload fuel) and HFR-K5/6 (proof test fuel) from the German HTGR fuel programme and TRISO particle distributions have been determined. The 15 GLE-4 spheres contained nominal 9560 coated particles each with 16.76% enriched UO_2 kernels, while each of the 16 proof test fuel spheres contained nominal 14 600 coated particles with 10.6% enriched UO_2 kernels.

The purpose of the tomographic measurements was to obtain the coordinates of the TRISO particles with respect to the center of the pebble. A cone beam set-up has been established at the JRC-IE X ray laboratory, and has been adopted to perform the X ray transmission measurements, on which the tomographic reconstruction was based. Fore each sphere, 720 X

ray transmission images (Fig. 4.43), evenly spaced at 0.5-degree angles, were obtained for each reconstruction. During the measurements a fuel pebble on a sample holder made of perspex was fixed on the rotation axis. The reconstruction performed using the software package COBRA (EXXIM, version 6) resulted in a set of 704^3 voxels, each characterized by an intensity value. The validity of the calibration procedure was checked against small steel spheres at known positions in the sample holder providing accurate position information. A pixel in the tomographic images equals $(70\ \mu m)^2$, a voxel in the reconstruction about $(80\ \mu m)^3$.

The TRISO particles were located by applying a binary intensity filter to the tomographic image and then determining the centres of mass of connected sets of 'on'-voxels, i.e. voxels above a certain intensity level. Using this relatively simple counting method, individual TRISO particles may be located to within a radius of about 40 μm or slightly more than half a pixel. Due to problems remaining with reconstruction artifacts and contrast limits, the number of counted particles fluctuated slightly, depending on the level set on the binary filter. This fluctuation (4–6 for the GLE-4 samples and 7–24 for the HFR-K5/6 samples, or ~0.1% of the total counts) is assumed to be a direct measure for the quality of the reconstruction. Efforts are being made to optimize the experimental set-up and the software for determining the correction parameters to reduce the fluctuations in the number of counted particles.

The average numbers of particles obtained for the two sets of pebbles are 14237 and 9339, equal to volume fractions of 6.6 and 4.3% (Table 4.19). The observed average numbers are therefore below the nominal values (by about 350 and 220, resp.). Destructive measurements of inter-particle distances in a GLE-4 pebble, previously performed at the research centre Seibersdorf, Austria, have returned a particle number of 9251, in agreement with the distribution observed.

TABLE 4.19. STATISTICS OF THE TRISO PARTICLE NUMBERS OBSERVED IN THE INVESTIGATED HTGR PEBBLES

Pebble type	Nominal no. of cp	No. of samples	Mean	Standard deviation	Minimum	Maximum
HFR-K5/6	14 600	16	14 237	181	13 816	14 465
AVR GLE-4	9 560	15	9 339	123	9 081	9 450

The X ray transmission image in Fig. 4.43, left, shows a TRISO particle cloud which contains some areas of low population density, and which is — as a whole — slightly off-centred. This effect has in fact been observed for many of the investigated pebbles. For the population of 31 pebbles, the centres of mass of the TRISO clouds have been determined for the vertical direction. They were found to be evenly distributed around the pebble centre with a standard deviation of 1.6 mm. Both fluctuations of population density and off-centredness of the TRISO cloud will contribute to local temperature variations.

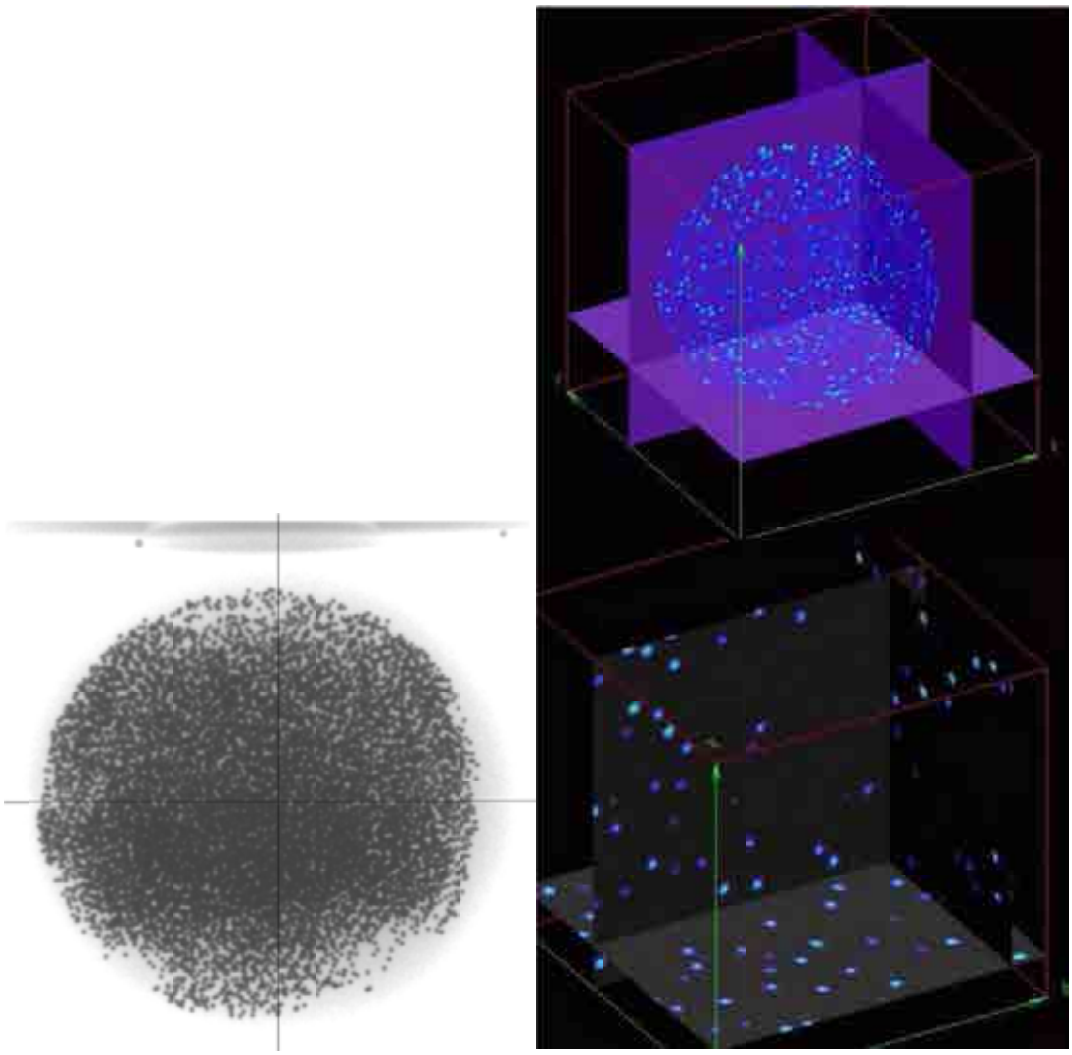

FIG. 4.43. (left) X ray projection after centreing and image correction; (right) Searching through the tomographic reconstruction.

More important with respect to fuel qualification are the distributions of nearest-neighbor distances. Shorter distances could allow for higher particle loadings while keeping the particle failure rate acceptably low. Figure 4.44 presents the resulting distributions. In the top panel, the distributions of three GLE-4 pebbles are given to indicate pebble-to-pebble variations. For the more tightly packed HFR-K5/6 pebbles, this variation becomes negligible. The middle panel shows the normalized average distributions of the two pebble types. As expected, the distribution of nearest-neighbor distances peaks at a lower value and is narrower for the more densely packed pebbles. The same effect was also observed for randomly distributed TRISO particles [145]. In the bottom panel, the tomographic results are compared with those from destructive analysis performed on one GLE-4 pebble at the research centre Seibersdorf. The comparison shows that the Seibersdorf distribution is significantly broader, an indication that the destructive method carries a larger uncertainty in particle positions.

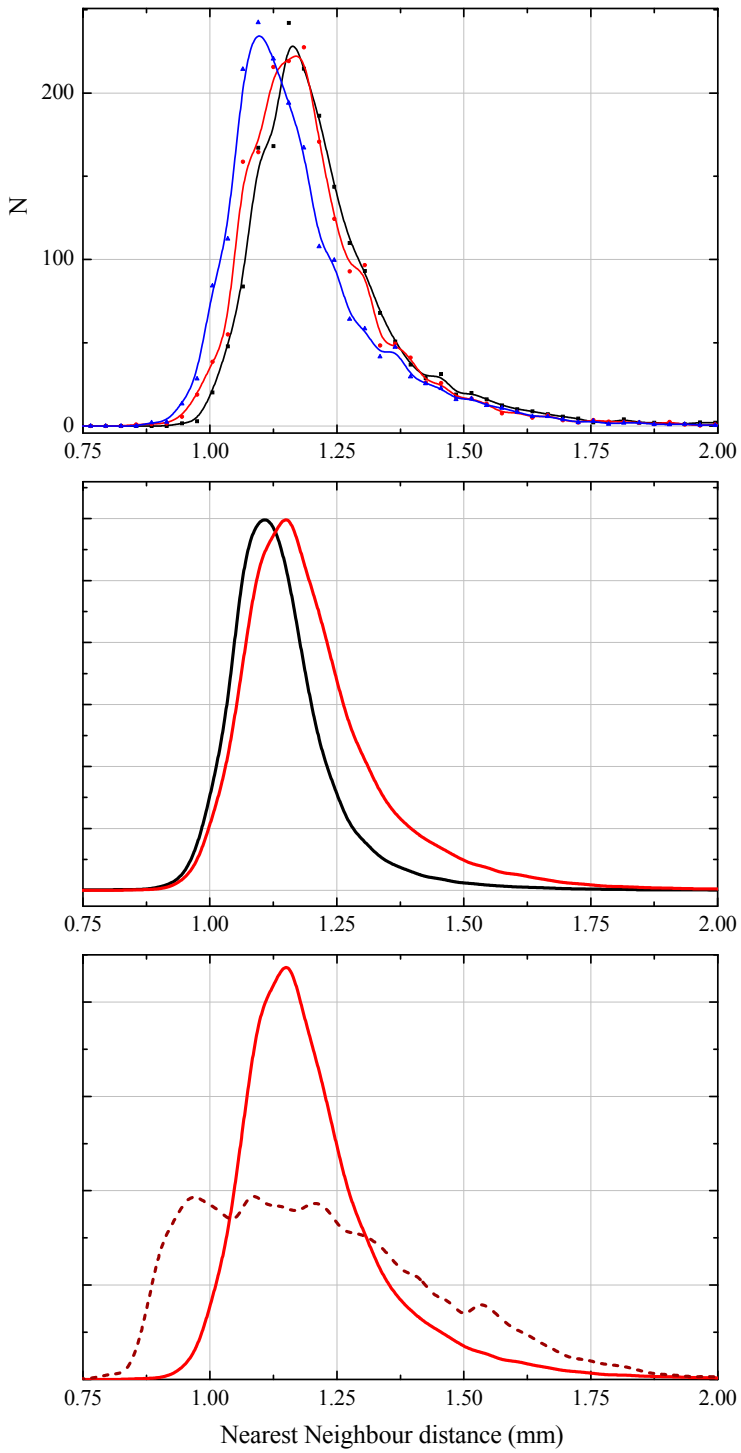

FIG. 4.44. (top) Nearest-neighbor distributions of three GLE-4 pebbles; (mid) Normalized average nearest-neighbor distance distributions for HFR-K5/6 pebbles (black) and GLE-4 (red); (bottom) Comparison of GLE-4 nearest-neighbor distributions as obtained by XRT with results from destructive analysis (Seibersdorf measurement).

(g) HTGR fuel manufacture quality control strategy

Thanks to the development of the above described techniques, and their performances in terms of sensitivity or throughput rate, quality control strategies of HTGR fuel can be suggested.

It is first necessary to mention that all the previously described techniques were compared and validated with the existing characterization techniques. For example, the density retrieval via X ray phase contrast imaging method was tested on particle layers that were characterized via the sink float method. Besides, as already mentioned, all the developed techniques and especially their related criteria were assessed on several types of TRISO fuel during the fuel fabrication process development, i.e. on surrogate and uranium based particles.

To that extent, it could be admitted that these new techniques were validated, but are, most of them being still at a laboratory scale, requiring industrialization development on the way to qualification.

4.5.3. Outlook

Currently, various characterization techniques in nuclear fuel area are being developed for mechanization and automation, along with the development of high tech IT technology, not only for the easy handling of radioactive materials but also for the consistent operation of measuring equipment to reduce sources of human error. Also, for the reduction of radioactive waste in the fuel production stream, it is desirable to utilize non-destructive characterization techniques which can replace destructive methods for easy automation [146].

Considering the large number of the parameters that must be monitored and controlled to produce a large amount of fuel particles with a multitude of specific properties, it seems clear that several nondestructive measurement techniques will be required to determine quality.

For this reason, several methods are being evaluated that can be expected to ultimately provide sufficient QA/QC for particle fuel fabrication. X ray techniques have been used to create a reference library of characteristic particles. Measurement results from electromagnetic signatures and optical imaging inspection methods show that automated detection of some of the defects found in surrogate fuel particles is possible at production throughput rates. These methods are being recommended for further development.

5. METHODS FOR ASSESSING OPERATIONAL FUEL PERFORMANCE

5.1. MEASUREMENT METHODS OF ACTIVITY RELEASE FROM THE REACTOR CORE

5.1.1. HTR-10

5.1.1.1. Introduction

In 1992, China decided to construct the 10 MW(th) modular high temperature gas cooled test Reactor, HTR-10, at the INET site in Beijing [147, 148] to be operated with spherical fuel elements with the LEU TRISO coated fuel particles [14, 149]. The operating pressure of the primary circuit is 3.0 MPa. The helium outlet and inlet temperature are 700°C and 250°C, respectively. The reactor core and steam generator are separately arranged in two pressure vessels which are connected by the hot gas duct pressure vessel. The cross-section of the HTR-10 primary circuit is shown in Fig. 5.1. This project is considered to be the first tangible step of HTGR development in China.

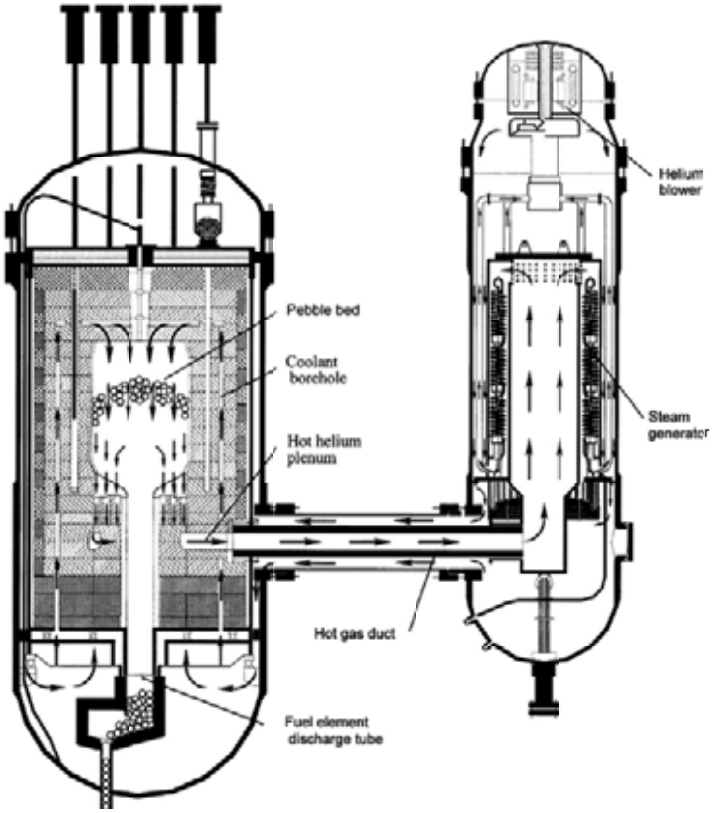

FIG. 5.1. Cross-section of the HTR-10 primary circuit.

The main objectives of the HTR-10 were:

- to acquire the know-how to design, construct, and operate HTGRs;
- to demonstrate the inherent safety features of the modular HTGR;
- to establish an irradiation and experimental facility for fuel elements and materials;
- to carry out R&D work for nuclear high temperature process heat applications.

An HTR-10 fuel element with 60 mm in diameter consists of matrix graphite and about 8300 TRISO coated fuel particles. The fabrication technology for HTR-10 fuel element had been established through a lot of R&D activities in the past 20 years in Institute of Nuclear Energy

Technology, Tsinghua University (INET) [16, 17]. Over 20 000 spherical fuel elements were manufactured for HTR-10 in 2000 and 2001.

In December 2000, the HTR-10 reached its first criticality, and in January 2003 the reactor was successfully connected to the electric grid at full power. From April 2003 to September 2004, INET completed a series of nuclear physics and safety experiments to confirm and verify the claimed crucial inherent safety features of modular HTGRs [150, 151]:

- Loss of offsite power without any counter-measures;
- Main helium blower shutdown without any counter-measures;
- Loss of main heat sink without any counter-measures; and especially
- Withdrawal of all rods without any scram (Fig. 5.2).

The HTR-10 was also used in wintertime to provide district heating for INET.

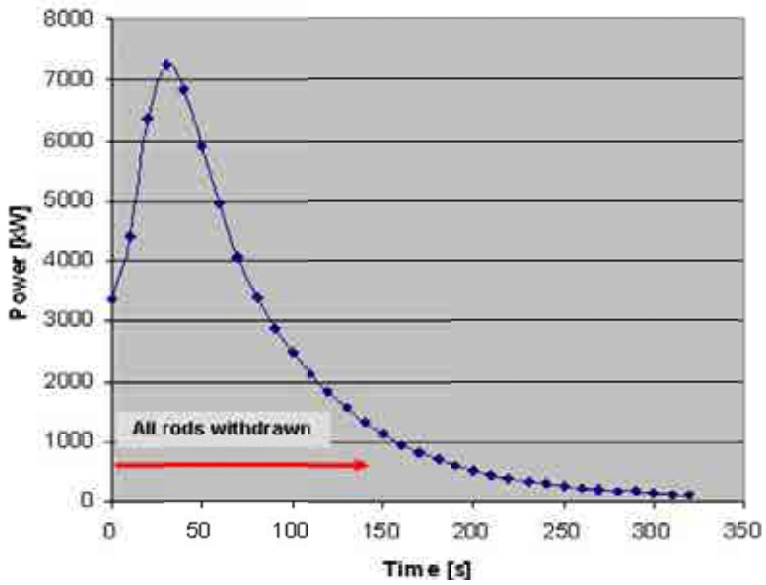

FIG. 5.2. ATWS experiment of the HTR-10.

During this R&D period of the HTR-10, significant achievements were made:

- Manufacture of spherical coated particle fuel elements: The know-how of fabricating fuel elements for the HTR-10 was mastered. The free uranium fraction could steadily be decreased to a value as low as 3×10^{-5};
- Corresponding technologies for pebble bed HTGRs: the technology of fuel element handling and spherical fuel element transportation by pulse pneumatic mechanism;
- Helium process technologies such as helium sealing and purification, the lubrication for rotating equipments in a helium atmosphere, electrical insulation and rotor dynamics;
- Domestic manufacture of key equipments for HTGRs: This mainly covers the reactor pressure vessel, the steam generator pressure vessel, the hot gas duct, the once-through steam generator with helical tubes, the helium blower, the fuel handling equipment; and the reflector graphite components.
- Successful development of fully digital reactor protection systems.

5.1.1.2. Measurement method for the gaseous fission products in HTR-10 primary coolant

In order to monitor the operational performance of the domestic fuel elements, a system measuring gas fission products released from the fuel balls was build in HTR-10. The noble fission gases can be released from particles with a defective or failed coating, and from the uranium contamination in the fuel graphite matrix and outer PyC layer. Since the released fission gases are not deposited in the primary coolant system, the failure fraction of the fuel particles in the core can be excellently monitored using these noble gas concentrations in the cooling gas.

(a) Measurement system

In order to measure the concentrations of the noble gas fission products through their radioactivity, a test loop was installed in HTR-10 as is shown in Fig. 5.3.

The primary coolant is sampled from a tube between the blower outlet and the inlet of primary coolant purification system. The pressure of the primary coolant is decreased from 3 to 0.4 MPa, while the temperature is decreased from 250^{o}C to the room temperature prior to entering the sampling canister. The inner volume of the sampling canister is approximately 0.5 litre. Figure 5.4 shows the sampling canister installed in the test loop. The radioactivity of the fission gas products is measured by HPGe detector, gamma spectrometer and some ORTEC software.

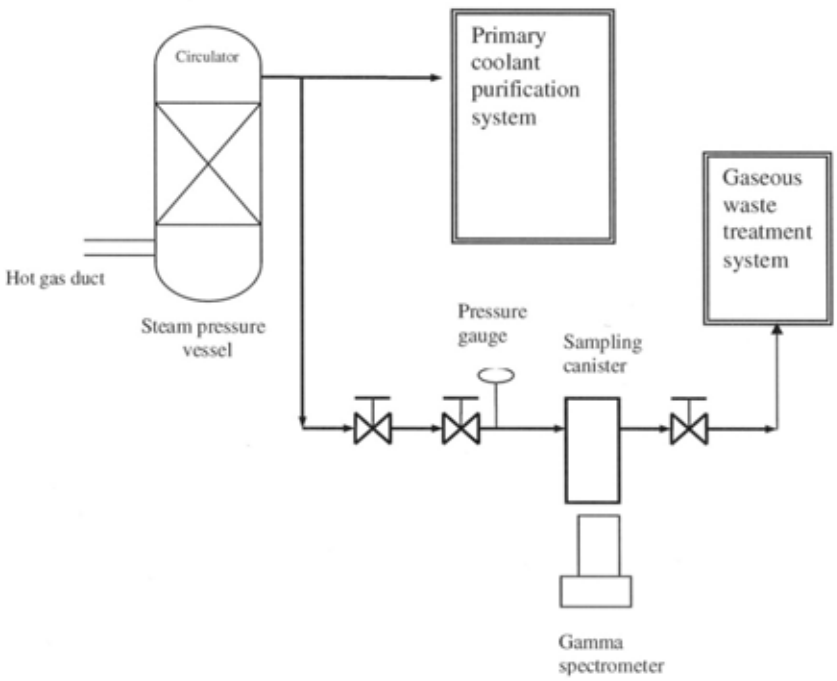

FIG. 5.3. Measurement system of the radioactivity of the gas fission products in the HTR-10 coolant.

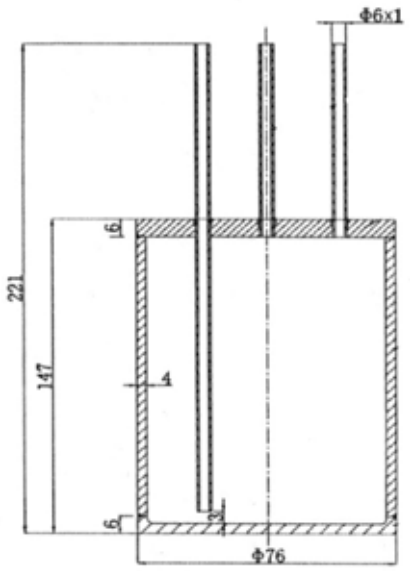

FIG. 5.4. Sampling canister installed in the test loop.

(b) Measurement process

(i) The sampling canister is fixed in the test loop. The HPGe detector is placed just below the sampling canister.

(ii) Open the valves of the sampling canister inlet and outlet for purging the sampling canister, and keep the pressure of 0.4 MPa in the sampling canister for a stipulated time. Then close the valves of the sampling canister inlet and outlet. The He gas inventory in the sampling can be calculated using He gas pressure, temperature, length and diameter of piping.

(iii) Measure the radioactivity of the fission gas products in the sampling canister. The type and activity of the radioactive fission gases can be identified by the energy analysis system using gamma spectroscopy. The isotopes of Kr and Xe in the sampling canister can be detected.

(c) Measurement results

Measurement results have not been obtained yet from this test loop. Currently underway is the purchase of the standard radioactivity gas for calibration of the detector and gamma spectrometer.

5.1.2. AVR

The 46 MW(th) AVR was operated from 1967 through 1988 and generated 1.67×10^9 kWh of electric power. During its operation, the AVR provided invaluable information on spherical fuel element development, fuel particle development with many particle variants (kernel material, enrichments, coating designs) and HTGR fuel cycles. Nearly 290 000 spherical fuel elements of five different types, containing more than 6×10^9 coated fuel particles, were inserted into its core (see also chater 3.4.2.).

5.1.2.1. AVR fuel temperatures

Assessing the operating temperatures experienced by the fuel elements as they traverse, on multiple passes, through the AVR pebble bed core during their irradiation lifetime has been a difficult situation. Predictions based on model calculations were always available, but no experimental measurements were made until the mid 1980s. In 1986, a 'melt-wire experiment' was conducted during the period relevant to when the GLE-3 and GLE-4 fuel elements were present in the AVR [152–156]. This experiment inserted into the AVR specially designed graphite matrix spheres which incorporated a set of 20 quartz capsules, each containing a single melt-wire. The melt-wires were fabricated of a specific alloy composition that would melt if a specific temperature was exceeded. A total of 190 of these monitoring spheres were added into the AVR core through standard fuel loading procedures. At the time of insertion, September 1986, the AVR was operated at full power with a nominal coolant outlet temperature of 950°C.

Upon discharge, 144 of the monitoring spheres were X rayed to assess the momentary maximum peak temperatures experienced during their passage through the AVR. They could be identified uniquely between inner core (IC) and outer core (OC) passage through the core. Results obtained reveal that 21 of the 144 monitoring spheres had seen operating temperatures higher than the maximum melting temperature where all the wires were melted. Using the corrected melting points and proper temperature adjustments [155], the maximum melting temperature value was 1244°C that was exceeded by 15% of the monitoring spheres.

In recent AVR core analyses of power and temperature distributions [157, 158], measured and predicted temperature distributions are in reasonable agreement (Fig. 5.5) when using various modeling assumptions on core modeling and He bypass flows. The designations AVR-1, AVR-3b and AVR-9 in the figure refer to different modeling assumptions in [158].

From the melt-wire test in AVR, the underlying temperature distributions were determined by constructing a Quantile-Quantile (Q-Q) plot [159] based upon the probability properties of the histogram distributions (Fig. 5.6). This was done by ordering the histogram data, calculating probabilities, using these probabilities with a normal distribution to find quantiles. In the Q-Q plot, it can be seen whether the quantiles and the data are linearly related: a single straight line in this type of display would represent a normal distribution of temperatures.

In the case here (Fig. 5.6), there are two parallel straight lines that can be interpreted as two Gaussian distributions with the same standard deviation, but different mean values for the IC and the OC melt-wire spheres. The two normal distributions define the variation of maximum fuel element surface temperatures, centre temperatures of the fuel spheres would be higher by a few dozen degrees dependent on operational history, fissile loading and position in the core.

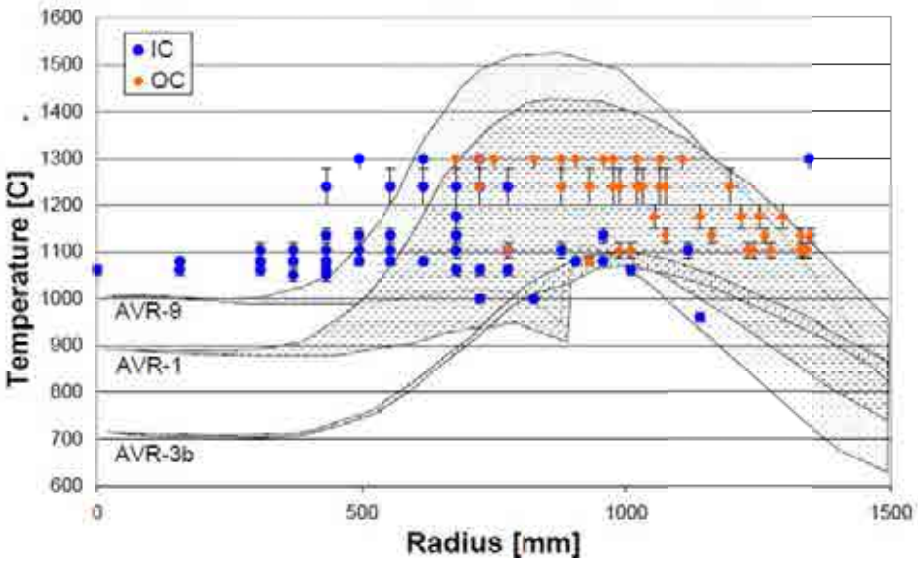

FIG. 5.5. Predicted radial distributions of AVR coolant exit and maximum fuel temperatures compared to experimental melt-wire test results (original, uncorrected data).

The simultaneous least squares fit yields two normal distributions with temperatures of 1097 ± 64°C for the IC meltwire spheres and 1192 ± 64°C for the OC meltwire spheres. These are not random statistical distributions in the thermodynamic sense, but represent variations caused by the AVR basic design, reload mechanism, sphere flow and operational procedures. To a limited extent, these temperatures can be taken as representative maximum fuel temperatures in AVR.

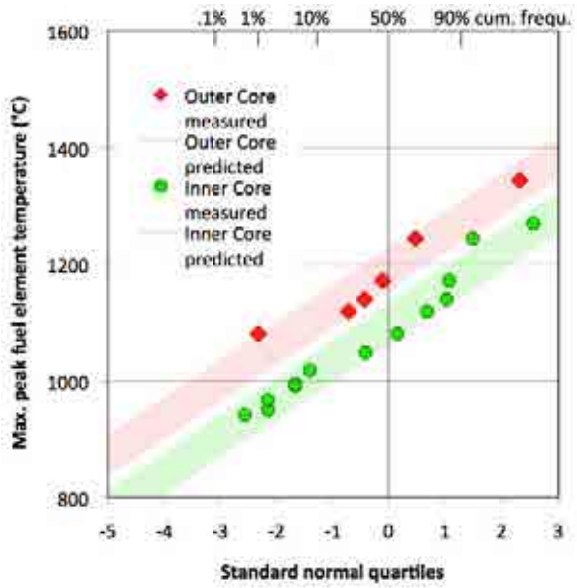

FIG. 5.6. Melt-wire results reproduced by normal distributions for IC spheres (green) and OC spheres (red) with the same spread in the Q-Q plot that shows the measured temperatures versus the (transformed) cumulative frequency.

5.1.2.2. Coolant activity

The activity in the cooling gas was systematically measured at three positions of the AVR primary circuit (Fig. 5.7) [160].

- Activities of totally 12 isotopes of the noble gases Xe and Kr were measured continuously in a bypass flow by gamma analysis. This was accompanied by continuous measurements of total beta-activity.
- Concentrations of solid fission products at the core exit were measured discontinuously in the hot gas sampling loop VAMPYR, where a coolant bypass was routed to a deposition section before passing through filters. After a sampling time of about 6 weeks, filters and deposition tube were analysed.
- At the core entrance behind the blower, coolant activities were measured in cold gas filter tests, which were running parallel to VAMPYR to allow comparison between hot gas and cold gas activities.

Due to a complete retention inside the experimental devices and assuming a constant activity concentration in the hot coolant, the integrated helium mass flow could be taken to derive coolant concentrations and release rates. Original purpose of the cold gas filter was the measurement of dust fractions in the coolant and dust-borne activities of selected isotopes. Early measurements showed graphite dust concenrations in the range of 4–40 μg/Nm^3 [160].

Source of the coolant activity was to a large extent the heavy metal contamination in the matrix material of the fuel elements whose level has changed significantly over the long operation time of the AVR [110]. BISO fuel exhibited with ~10^{-3} a comparatively high level of matrix contamination. The measured coolant activities in the early years of AVR operation were around 1100 GBq (30 Ci).

The testing of TRISO coated fuel in the AVR started as early as 1974 with the fissile particles contained in the GFB-2 variant and, at a larger scale, in 1977 with the GFB-3/4/5 variants. The insertion of mixed oxide TRISO fuel began in 1981 (GO-2), finally followed by the modern LEU TRISO fuel (GLE-3, GLE-4) since 1982.

The first TRISO fuel contamination showed already a lower level of ~10^{-4}. Modern TRISO fuel reduced this level further to the range of contamination with natural uranium (~10^{-5}) making the fraction of fissile material as low as ~10^{-7}. This improvement was verified as one of the reasons for the particularly low coolant activity measurements on the level of 740 GBq (20 Ci) in the final years of operation (Fig. 5.8).

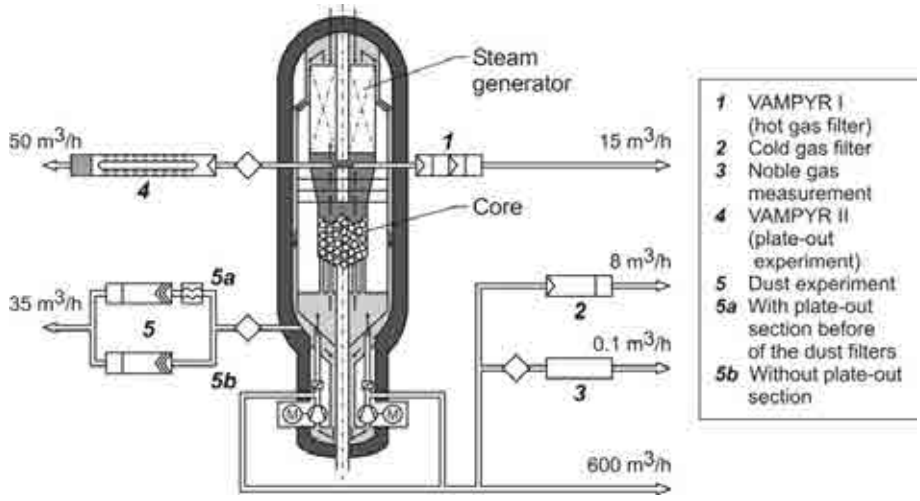

FIG. 5.7. Positions of fission product related experiments in the AVR reactor.

After raising the average coolant outlet temperature to 950°C, fission gas activity stabilized at a level of 1100–1500 GBq (30–40 Ci) or 30 GBq/MW (0.8 Ci/MW) [110]. Activity concentrations valid for full power stationary AVR operation at 950°C, as were measured in the time period 1984–1987 are listed in the following Table 5.1 [153]. The increase of liberated activity with increasing average helium exit temperatures is shown in Fig. 5.9.

TABLE 5.1. COOLANT ACTIVITIES IN THE AVR DURING STATIONARY OPERATION AT 950°C

Radionuclide	Activity concentration (Bq/m^3)
H-3	3.7×10^7
C-14	1.9×10^7
I-131	5.2×10^2
Cs-137	3.0×10^2
Sr-90	2.0×10^2
Ag-110m	4.9×10^1
Co-60	1.0×10^1
Total fission gases	4.6×10^8

5.1.3. THTR-300

During THTR-300 operation, the coolant activity was continuously monitored by beta counting devices to control the fuel quality and detect immediately relative changes and in more detail by gamma spectroscopy of gas samples. Figure 5.10 gives an example for the gas release of short-lived Xe and Kr isotopes into the primary circuit at partial load operation and the comparison with respective calculations [161].

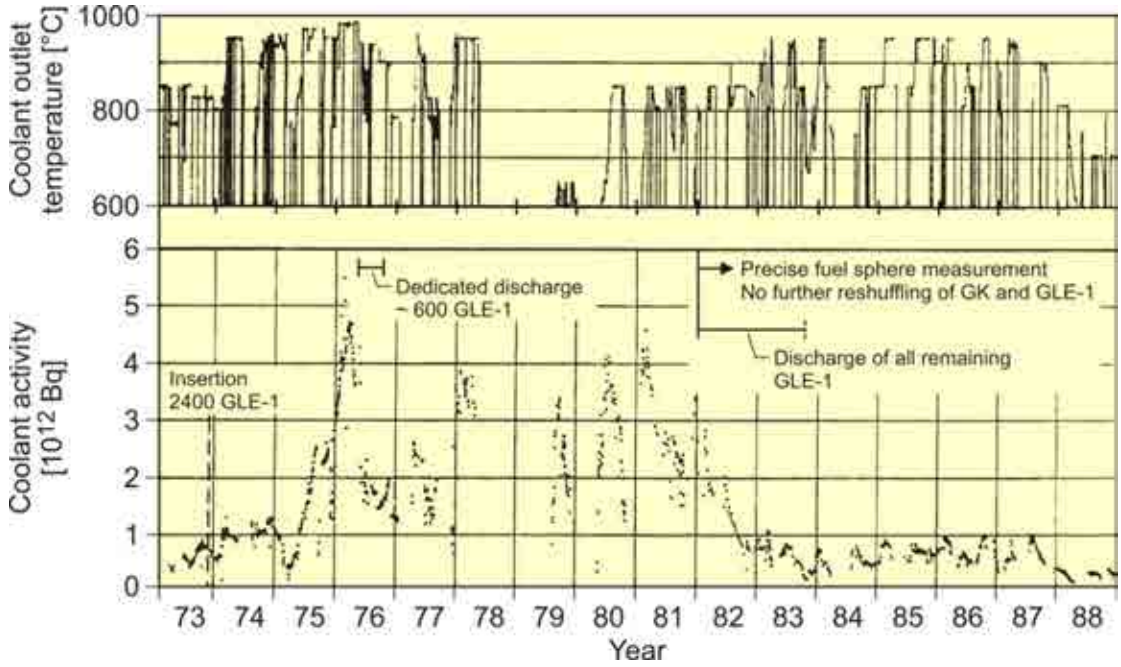

FIG. 5.8. Coolant outlet temperature and activity measurements during the AVR operation history.

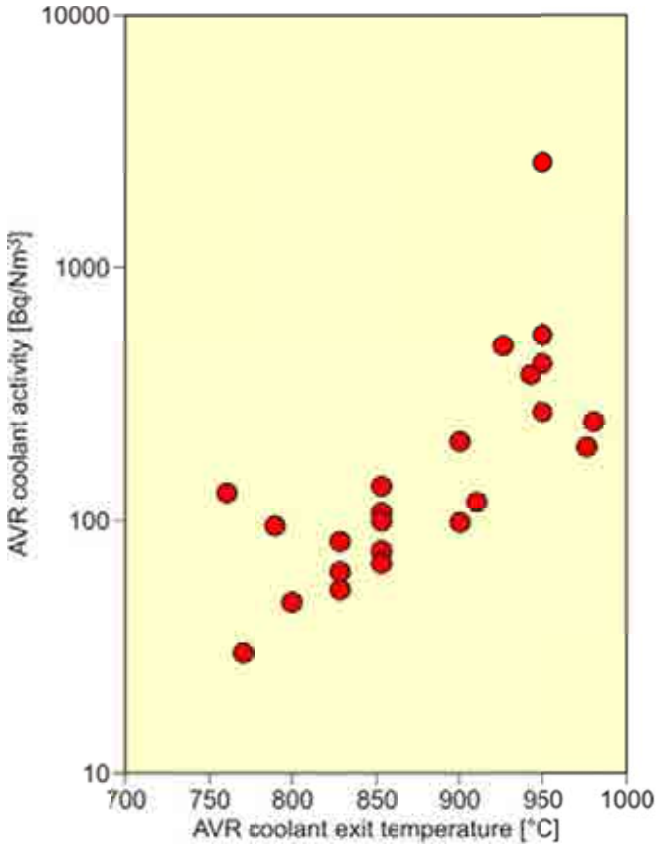

FIG. 5.9. AVR coolant activity vs. medium coolant exit temperature.

Measurements of the specific coolant activity as the sum of nine noble gas nuclides, covering an estimated 90% of the total activity, over the total operating time is shown in Fig. 5.11. A steep rise can be recognized at about 100 efpd (marked with 'SWKP') which was found to coincide with a very high occurrence of damaged fuel elements and a fracture of many BISO coated particles, respectively [50]. Still the measured activity is generally considered to be in good agreement with respective model predictions, not significantly affected by the comparatively high fraction of broken balls.

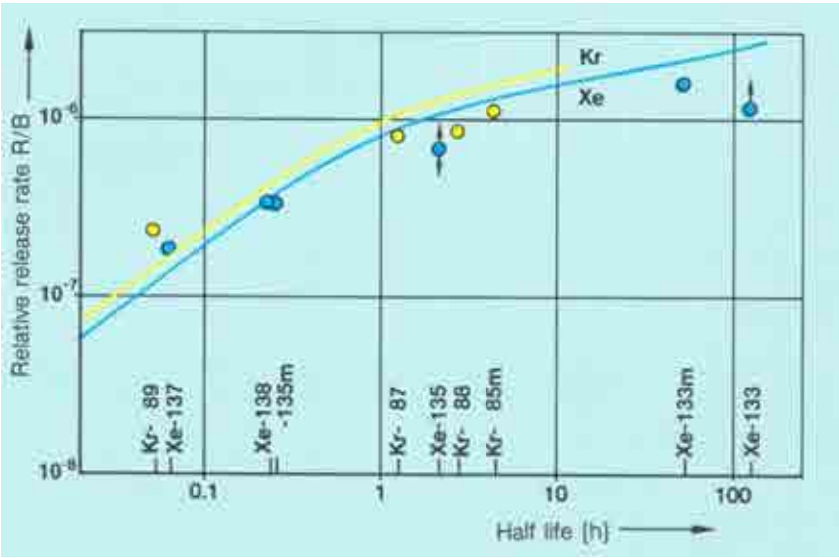

FIG. 5.10. Calculated and measured inert gas release in the THTR-300 at 40% load.

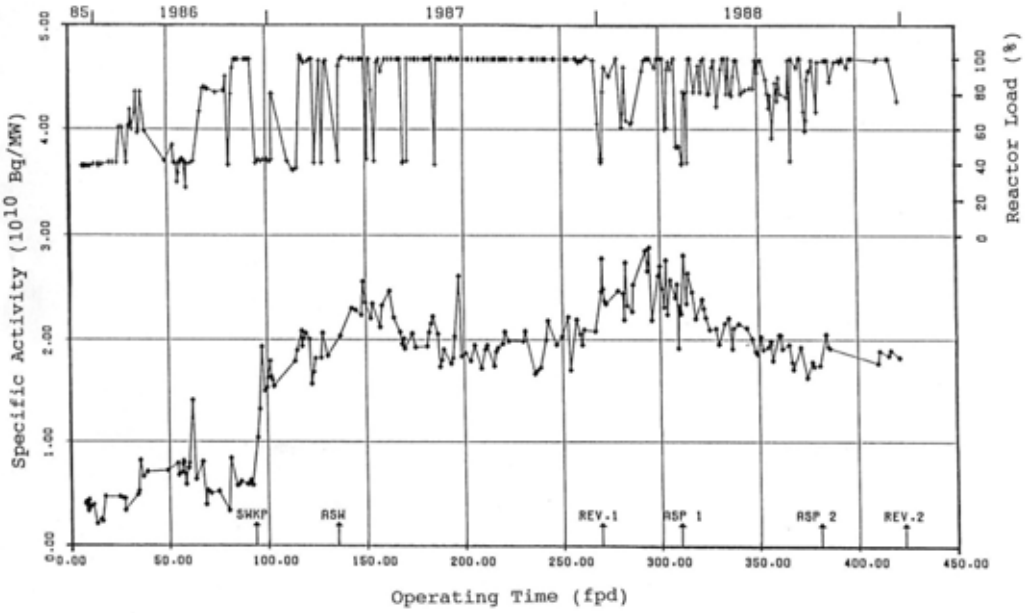

FIG. 5.11. Specific coolant activity (sum of nine noble gas nuclides) in the THTR-300.

5.1.4. HTTR

5.1.4.1. Introduction

In the safety design requirements for the HTTR fuel, it is specified that 'the as-fabricated failure fraction shall be less than 0.2%' and 'the additional failure fraction shall be little through the full service period' [102, 162]. For the safe operation of the HTTR, the continuous and reliable measurement of the coolant activity is required to allow the evaluation of the fuel performance and the radiological assessment of the plant during normal operating conditions [102]. The fission gases are released from the through-coatings failed particle (i.e. there are no intact layers) and from the uranium contamination in the fuel compact matrix [163]. Since the released fission gases do not precipitate on the inner surface of the primary coolant system piping, their concentrations in the primary coolant reflect the core average through-coatings failure fraction and the fuel matrix contamination fraction. Therefore the failure fraction should be evaluated quantitatively during operation.

In order to measure the radioactivity, the primary coolant radioactivity (PCR) instrumentation of the safety protection system, the fuel failure detection (FFD) system and the primary coolant sampling system have been installed in the HTTR.

5.1.4.2. Measurement items and experimental results

(a) PCR instrumentation

The PCR instrumentation is one of the process instrumentations used for the reactor protection system, which consists of three identical channels due to the design requirement for redundancy and physical separation. Figure 5.12 is the diagram of the PCR instrumentation [162].

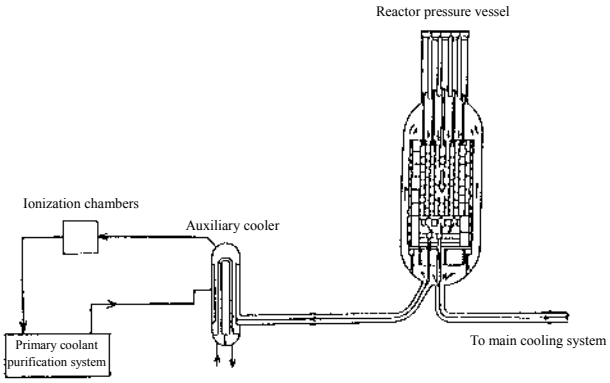

FIG. 5.12. PCR measurement of safety protection system.

The PCR instrumentation assembly consists of three ionization chambers for gamma ray detection which are located between the auxiliary cooling system (ACS) and the primary helium purification system. The sampler has a inner volume of about 200 L, through which the helium gas of the primary helium purification system passes at a flow rate of about 200 kg/h, corresponding to 0.4% of the total flow rate. Each ionization chamber has a detection response to gamma energy in the range of 60 keV to 3 MeV with a sensitivity of 7×10^{-6} (Sv/h)/(MBq/m^3). The signals from the ionization chambers are transferred to the plant computer, in which the PCR is calculated with the factor corresponding to the accuracy of the ionization chamber for 1 MBq/m^3 of ^{88}Kr. The upper limit of the detectors is 3×10^5 MBq/m^3. The signals are used to initiate a reactor scram under abnormal operating conditions. The scram level is 7×10^4 MBq/m^3, corresponding to the concentration of fission gases released from 1% of failed particles. The PCR was measured continuously during the rise to power tests of the HTTR. An example of the measured value in the phase three test of the HTTR is shown in Fig. 5.13 [164, 165]. During the rise to power test, all signals were less than 1×10^3 MBq/m^3.

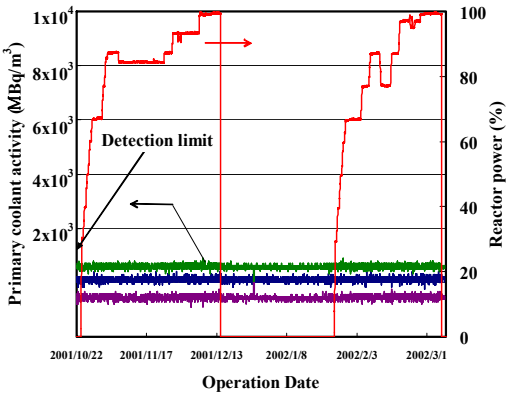

FIG. 5.13. PCR signals in safety protection system in the phase three test.

(b) Fuel failure detection (FFD) system

The fuel failure detection (FFD) system was employed in the HTTR to prevent the additional abnormal failure of coated fuel particles during normal operation. The detection of fuel failure is more difficult compared with that for conventional metal cladded fuel because the amount of fission products released from the failed fuel to the primary coolant system are far smaller than that in LWRs. To solve this problem, the FFD system measures short-lived fission gases released into the primary coolant. Figure 5.14 shows the diagram of the FFD system [162]. In this system, the primary coolant from two of seven regions in the hot plenum are transferred automatically via the precipitating wiring, around which such isotopes as ^{88}Kr and ^{138}Xe are gathered and detected by two NaI (Tl) scintillation counters.

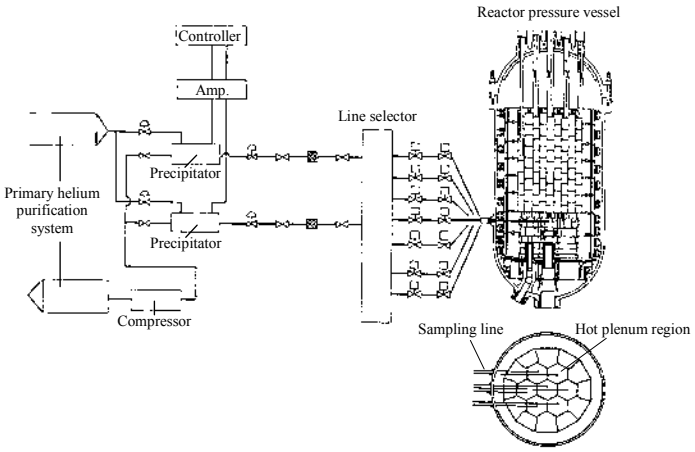

FIG. 5.14. Fuel failure detection system.

For example, the result from the No. 1 fuel region during the phase three test of the rise to power test is shown in Fig. 5.15 [164, 165]. The (S/N) ratio of the FFD system seemed quite good because of its low noise level. In addition, Fig. 5.16 shows the signal from the No. 1 region for the reactor power during the phase-three test [164, 165]. The signal varied in proportion to the reactor power, which increased linearly up to 60% reactor power and exponentially thereafter.

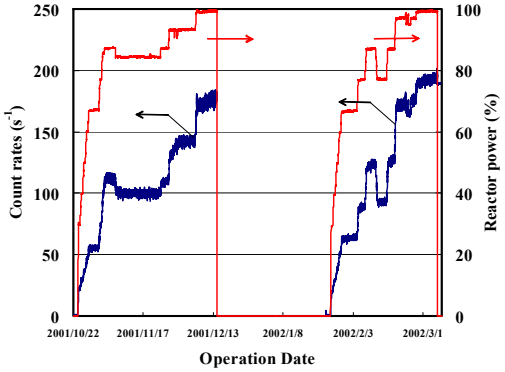

FIG. 5.15. Count rates of the FFD system in the phase-three rise to power test of the HTTR.

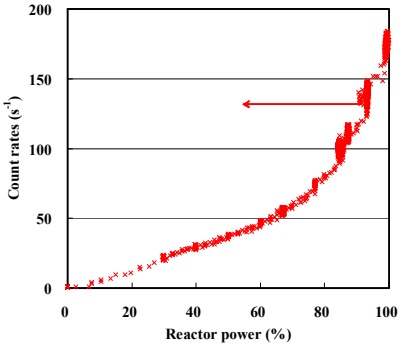

FIG. 5.16. Count rates of the FFD system versus reactor power in the phase-three test.

(c) Primary coolant sampling system

The primary coolant sampling measurement is the only way to determine the fission product gas concentrations. A sample of the primary coolant gas is obtained in a bottle using the grab sample apparatus. Figure 5.17 schematically shows a grab sample line [164, 165].

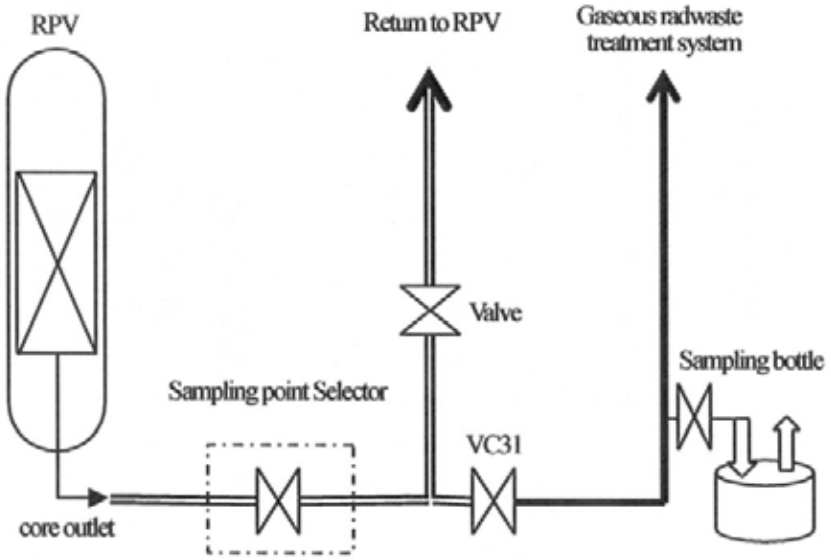

FIG. 5.17. Schematic showing grab sample line.

Grab samples can be taken from ten sampling points in the primary cooling system, such as core inlet, core outlet, primary coolant purification system inlet, etc. Any sampling point can be selected manually by the sampling point selector. In rise to power tests, primary coolant was sampled from the core outlet, which is the nearest point from the fuel region. Pressure of the primary coolant was decreased from 4 to 0.2 MPa (gauge) prior to entering the sampling bottle. The inner volume of the bottle is approximately 1 L, corresponding to about 3 Nl of the sampled gas. Table 5.2 shows the calculated inventories in the sampling line.

TABLE 5.2. HELIUM GAS INVENTORY OF SAMPLING LINES

Line	Inner volume (L)	Pressure (MPa in gauge)	He inventory (Nl)
Core outlet to VC31	1.70	Abs. 4.0	68.0
VC31 to bottle	0.18 [a]	0.2	0.4

[a] calculated value using length and inner diameter of piping.

The helium gas inventory of the sampling line is larger than the volume of the sample, so sampled gas is not taken directly from the core outlet. Each section of the line should be purged before a sample is taken; that is, the sampling line at 4 MPa (gauge) and the line at 0.2 MPa (gauge). In the rise to power test, the flow rates of the first and the second purging were 16.7 and 6 Ndm^3/min, respectively. Both the first and the second purging times were determined by the confirmation test, at more than 10 min and more than 5 min, respectively. Finally, the cooling time from the core outlet to the bottle was about 10 min.

Soon after the sampling, the type and activity of radioactive fission gas in the grab sample was identified by the energy analysis system using gamma spectroscopy. The gamma rays were detected by an intrinsic Ge detector. The detector was calibrated by simulated standards using both ^{133}Xe and a solid mixture of isotopes enclosed in bottles with identical volume and geometry [165]. The acquisition time for the spectrum was 500 s for very short-lived species such as ^{89}Kr (3.18 min), ^{135m}Xe (15.65 min), ^{137}Xe (3.83 min) and ^{138}Xe (14.17 min), and

2000 s for short-lived species such as ^{85m}Kr (4.48 h), ^{87}Kr (76 min), ^{88}Kr (2.8 h), ^{133}Xe (5.29 d) and ^{135}Xe (9.1 h), with a 30 min cooling interval.

Every sampling was performed after the reactor achieved a steady state condition because of the (R/B) measurement discussed below. The measured concentrations of the fission gas i in the primary coolant C_i^{meas} were calculated by the following equation [164, 165]:

$$C_i^{meas} = \frac{A_i^{SV}}{V_{SV}\left(\frac{P_{1atm} + P_{smp}}{P_{1atm}}\right)} \tag{5.1}$$

where

A_i^{SV} is the measured radioactivity (corrected automatically with the acquisition time) (Bq);
V_{SV} is the inner volume of a bottle (m^3);
P_{smp} is the pressure of a sampled gas (Pa);
P_{1atm} is the pressure at room temperature (atm).

Each value of C_i^{meas} is shown in Figs 5.18 and 5.19 as a function of the reactor power [164]. The results revealed that the detected fission gas nuclides in the primary coolant were ^{85m}Kr, ^{87}Kr, ^{88}Kr, ^{133}Xe, ^{135}Xe, ^{135m}Xe, and ^{138}Xe, and concentrations were less than 0.1 MBq/m^3.

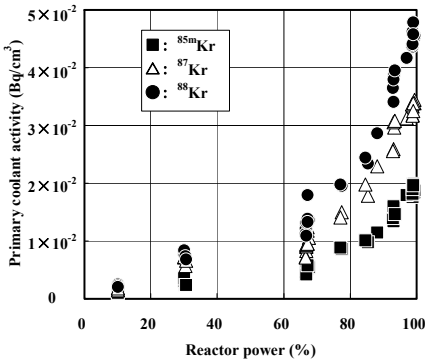

FIG. 5.18. Primary coolant activity concentrations of krypton isotopes during rise to power tests.

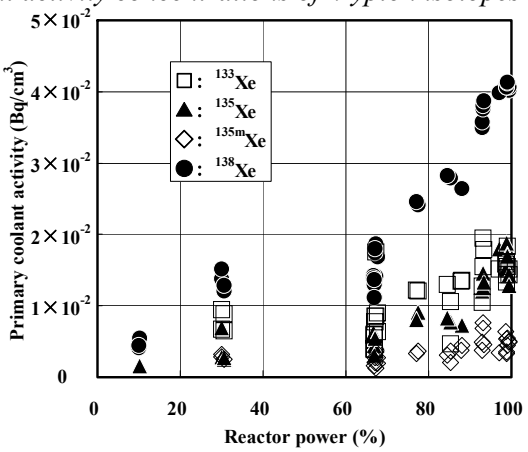

FIG. 5.19. Primary coolant activity concentrations of xenon isotopes during rise to power test.

The concentration of ^{88}Kr varied in proportion to the reactor power, similar to what was observed for the FFD signal in Fig. 5.16. Figure 5.20 shows the relation between FFD count rates in the central hot plenum region and ^{88}Kr concentrations obtained by the primary coolant sampling. The relation is linear. It means that the FFD system properly measured the daughter nuclides of short-lived fission gases such as ^{88}Kr.

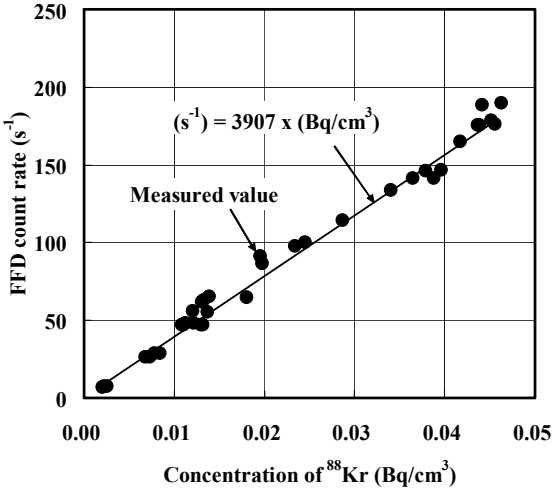

FIG. 5.20. Correlation of the FFD system coun trate and fission gas concentration by sampling.

5.1.4.3. Evaluation of (R/B) values

Fractional releases of short-lived fission gases can be expressed in terms of the (R/B), because the radioactive equilibrium is established quickly in the primary coolant circuit by a flow rate of 45 t/h under normal operating conditions (This corresponds to 1 minute per one circulation.). ^{88}Kr is a candidate to investigate the fuel and the fission gases behaviour in the HTTR, because there is no secondary production from the precursor and it has a sufficiently short lifetime (2.8 h). Sampling measurements were performed more than two days after the reactor achieved the target power. That is about five times longer than the lifetime of ^{88}Kr, when the radioactivity can reach more than 98% of the equilibrium value [164, 165].

The release rate of ^{88}Kr, R, is calculated from the differential equation of the radioactive equilibrium as follows:

$$A(t) = A^{R(sat)}(1 - e^{-\lambda t}) \tag{5.2}$$

$$\frac{dA(t)}{dt} = \lambda A^{R(sat)} e^{-\lambda t} \tag{5.3}$$

$$R = \frac{dA(0)}{dt} = \frac{\lambda A(t)}{1 - e^{-\lambda (t_{smp} - t_a)}} \tag{5.4}$$

where

λ is the decay constant of ^{88}Kr, = 6.88×10^{-5} (s^{-1});
$A^{R(sat)}$ is the radioactivity of ^{88}Kr (Bq);
t_a is the time when the reactor power has been steady (s);
t_{smp} is the time when the sampling was done (s).

$A(t)$ is the radioactivity of ^{88}Kr in the primary circuit at equilibrium, calculated by the following equation:

$$A(t) = C^{sat} V_{He} \tag{5.5}$$

where

C^{sat} is the radioactive concentration of ^{88}Kr (Bq/m^3).

C^{sat} takes into consideration the decay which occurs during transporting of the gas in the sampling line as follows:

$$C^{sat} = \frac{C^{meas}}{e^{-\lambda t_1}} \tag{5.6}$$

where

t_1 is the time taken to transport the sample from the core outlet to the bottle (s);
V_{He} is the inventory of the primary circuit (m^3), written as

$$V_{He} = \frac{P_{initial} \cdot 293\text{K}}{P_{1atm} \cdot 393\text{K}} V_{RPV} \tag{5.7}$$

where

V_{RPV} is the inner volume of the primary circuit (m^3);
$P_{initial}$ is the initial pressure of the primary coolant (Pa), at pre-operation with homogeneous temperature of 393K.

On the other hand, the birth rate of ^{88}Kr, B, is calculated from the number of fissions at the reactor power according to following equation:

$$B = \lambda N_f Y = \lambda \frac{W_{op}}{3.2 \times 10^{-11}} Y \tag{5.8}$$

where

W_{op} is the reactor power measured by the neutron detectors (W);
N_f is the number of fissions at the reactor power W_{op};
Y is the fission yield of ^{88}Kr (= 3.58%) [166].

The fission energy was assumed as 200 MeV in this equation.

The measured (R/B) of ^{88}Kr as a function of the reactor power are plotted in Fig. 5.21 [164, 165]. These are constant at 2×10^{-9} up to 60% reactor power and then increase to 7×10^{-9} at full power.

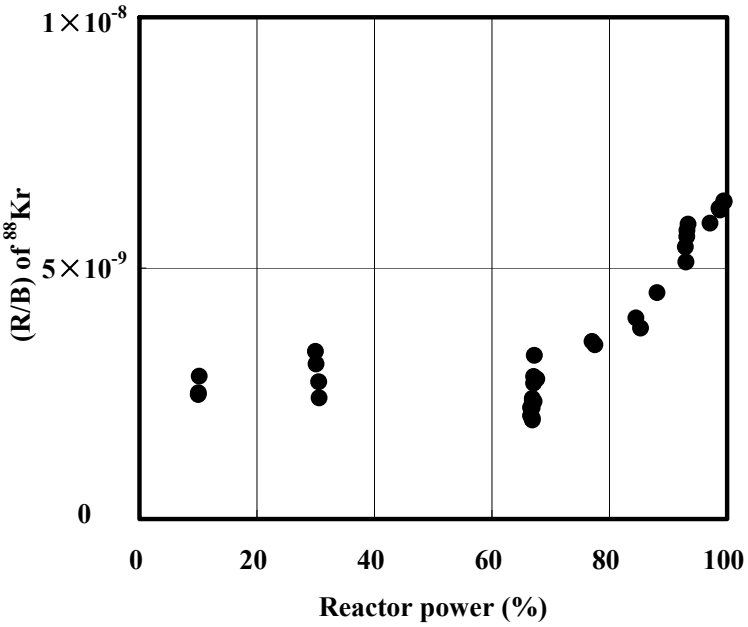

FIG. 5.21. Measured (R/B) of ^{88}Kr during rise to power tests.

5.1.5. DRAGON

Helium samples were taken from the primary circuit for gas analysis, initially Xe and Kr isotopes. The purge system, in the first core applied to all fuel rods, but later only to the central rods with the experimental fuel, served initially the purpose to keep the coolant clean. With the employment of retaining coated particle fuel, it became more or less obsolete, but served then as a diagnostic means to monitor fission gas release from the fuel experiments and individual fuel specimens, respectively. Later DRACULE probe monitoring of coolant borne activities and helium purge from the individual fuel elements; was a sampling device for both hot gas from the core and cold gas downstream a heat exchanger.

With the insertion of the 2nd charge fuel in the Dragon reactor starting in April 1967 and due to the fact that now ~70% of the fuel remained unpurged, the quantity of gas-borne activities rose to an equilibrium level of 56 GBq. Table 5.3 shows the measured R/B for fuel (via purge) and for coolant (via primary circuit) of some fission gas isotopes [167]. The mean purge factor is the ratio of both R/B values.

Iodine release from Dragon fuel elements could not be identified directly due to condensation in the sampling lines. But from MTR testing, a similar release behaviour between xenon and iodine could be deduced, i.e. no significant holdup in the matrix material.

Figure 5.22 shows the R/B of ^{133}Xe measured via the purge system for an experimental fuel rod which was operated at 1800°C, much higher than the nominal fuel temperature of 1250°C. Under these severe conditions, the increase in the gas release was relatively slow [168].

TABLE 5.3. FISSION GAS ACTIVITIES IN THE DRAGON REACTOR

Isotope	R/B fuel	R/B coolant	Mean purge factor
1st charge			
Xe-133	1.22×10^{-4}	1.8×10^{-6}	65
Xe-135	1.10×10^{-4}	1.5×10^{-6}	72
Kr-85m	0.65×10^{-4}	1.2×10^{-6}	53
2nd charge			
Xe-133	8.81×10^{-6}	3.75×10^{-6}	2.4
Xe-135	7.31×10^{-6}	2.34×10^{-6}	3.1
Kr-85m	2.81×10^{-5}	6.97×10^{-6}	4.0

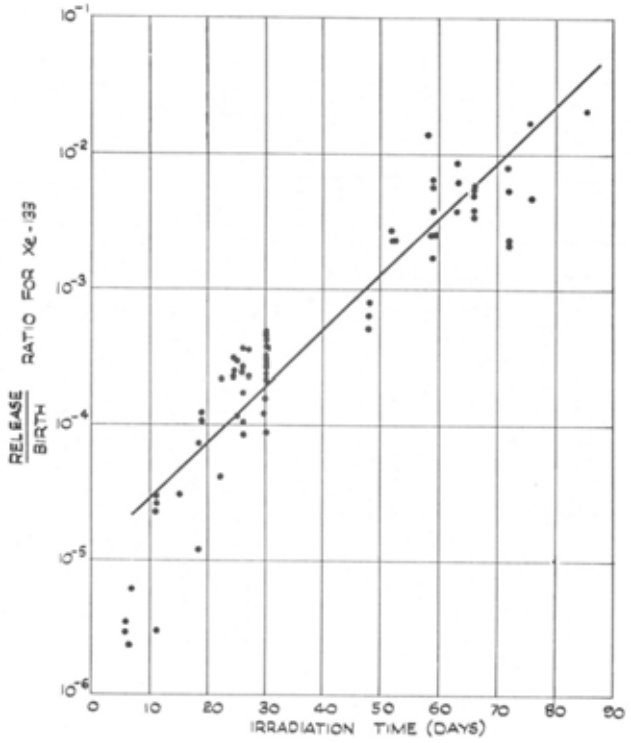

FIG. 5.22. ^{133}Xe R/B for experimental fuel operated at 1800°C.

5.1.6. Peach Bottom

The Peach Bottom Atomic Power Station Unit 1, owned and operated by Philadelphia Electric Company, was a 40 MW(e) HTGR prototype plant. Peach Bottom was the first HTGR to generate electricity and the first to operate at modern steam conditions (540°C at 10 MPa (1450 psi)) with high thermal efficiency (37%). The plant had an overall lifetime availability of 88%. The heart of the nuclear steam supply system was a helium cooled, graphite moderated, 115 MW(th) reactor operating with a 700°C gas outlet temperature on a thorium–uranium fuel cycle.

Peach Bottom began operation in June 1967 with Core 1 and continued until October 1969 accumulating 452 efpd. After the installation of a second core of 804 fuel elements, reactor operation was resumed in July 1970 and terminated in October 1974 after additional 899 efpd. Radioactivity in the main coolant system was controlled by drawing a purge stream of helium

through the fuel elements to the external fission product trapping system. The system consisted of a series of low temperature delay beds and fission product traps to remove and permit decay of fission products. A dehydrator, an oxidizer, and a liquid–nitrogen cooled charcoal trap removed moisture, chemical impurities, and the ^{85}Kr from the main coolant system.

Core 1 operated only about half of its design life. The premature installation of a second core was necessitated by the development of cracks in the graphite sleeves surrounding the fuel compacts of 90 of the fuel elements. The cracked sleeves were caused by swelling of the fuel compacts and rupture of the monolayer coatings on fuel particles. The existence of cracked elements was detected by an increase in circulating primary coolant activity which eventually reached a level of ~10 000 GBq (270 Ci). Although this activity level was well below design activity of 4225 Ci (~156 000 GBq), it was considered prudent to replace the core in view of the accelerating rate of fuel element cracking. The new fuel particle contained in Core 2 was $(U,Th)C_2$ kernels coated with a double layer of pyrolytic carbon (BISO) consisting of an inner low density carbon coating and an outer high density carbon coating. During the entire Core 2 lifetime, the primary coolant has been remarkably clean. Primary circuit activity never exceeded 37 GBq (1 Ci) confirming the improved fission product retention characteristics of the Core 2 fuel particles [169].

Surveillance of fission product release and behaviour was intensified during Core 2 operation to permit a wider range of measurements to be made. In addition to monitoring the noble gas content of the fuel element purge system and the coolant circuit, the programme was extended to include measurements of coolant impurities (including dust) by means of sampling probes in the Loop 1 circuit when entering or exiting the core and steam generator. Monitoring stations were established to measure deposited activity concentrations on the primary circuit surfaces of Loop 1. Gaseous release from Core 2 was predominantly from contamination. The coolant sampling probes were designed to withdraw samples of helium under isokinetic conditions, separate the molecular and particulate impurities, and classify the latter with respect to size [170]. Figure 5.23 shows the reactor plant and the locations of coolant sampling probes and gamma activity monitoring stations [169]. Even at EOL, with a calculated failure fraction of 0.9%, only 15% of the predicted release was from failed particles.

Levels of contamination in Core 2 fuel were high (4.3×10^{-3} fraction of free uranium) relative to the current fuel specification of $\sim 10^{-4}$. (With the fuel element purge system, there was no incentive to impose tight specifications on Peach Bottom fuel.)

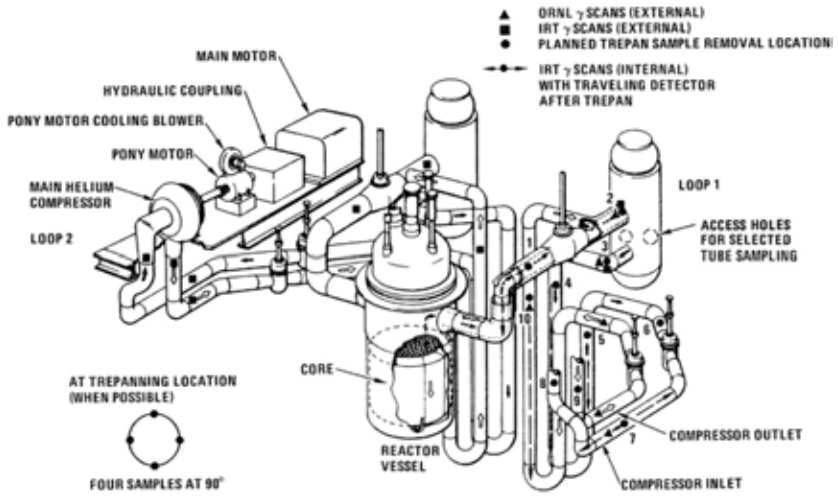

FIG. 5.23. Measuring positions in Peach Bottom plant.

Verification of HTGR design methodology for fission gas release was performed by comparing actual Peach Bottom operating data from Core 2 with design code predictions for noble gas release into the purge stream using the PERFOR code. The calculated and measured R/Bs (release rate into purge divided by birth rate in the fuel) for the reference nuclides ^{85m}Kr and ^{138}Xe are compared in Fig. 5.24 [169]. The agreement is excellent and well within design margins (by a factor of ~5).

Gaseous release into the primary coolant was a factor of 5000 less than into the purge. To further confirm performance predictions, a series of fuel compacts recovered from spent fuel elements was re-irradiated in the GA TRIGA reactor to determine the release characteristics of individual compacts; despite some scatter, these results were also consistent with calculations.

From the measurements of large dust-associated fractions of caesium, it was concluded that caesium behaviour in the coolant circuit was primarily governed by entrainment of deposited caesium released during Core 1 operation, i.e. that the steam generator surfaces might have acted more like a source than a sink for caesium [169].

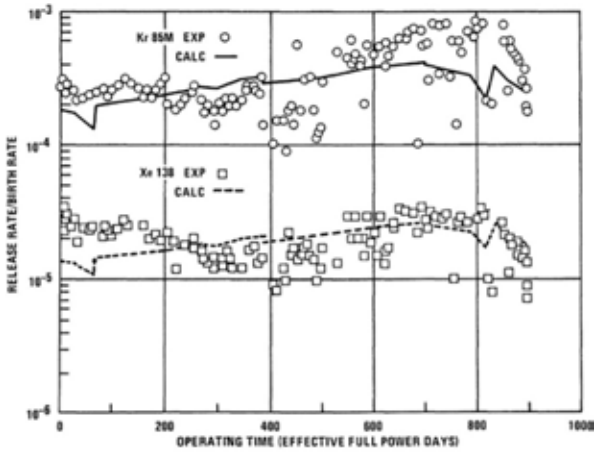

FIG. 5.24. Comparison of measured and calculated fission gas release from Peach Bottom Core 2.

5.1.7. Fort St. Vrain

The release of fission products from the reactor core is monitored routinely as a part of the reactor surveillance programme [171]. Considerable analytical instrumentation has been installed in FSV to measure directly the circulating and plateout activity in the primary circuit. The instrumentation includes a continuous activity monitor, grab sample systems to measure fission gases, including selected iodine isotopes, and plateout probes to measure the coolant concentrations of condensible species, especially iodines and fission metals. Additional information has been obtained by radiochemical examination of components removed from the primary circuit, including spent fuel elements and helium circulators in need of repair.

The FSV primary circuit remained remarkably clean after 657 efpd of operation. The peak circulating activity of 16 240 GBq (439 Ci), measured at 100% power during Cycle 3 operation, was almost two orders of magnitude below the FSAR design activity of 1.14 million GBq (30 900 Ci).

As an indication of the excellent fuel performance experienced to date, the release rate-to-birth rate ratio (R/B) for ^{85m}Kr has remained approximately constant at about 7×10^{-6} since the initial rise to power. In fact, the ^{85m}Kr R/B actually decreased slightly after the first two refuelings when spent fuel from the initial core was replaced with new fuel with lower levels of as-manufactured, heavy metal contamination.

FSV has experienced water ingress into the primary circuit occasionally followed by lengthy drying-out periods, and an adverse effect on fuel performance might have been expected. Laboratory tests have demons trated that water can react wi th the exposed kernels of failed, carbide based fuel particles, and the result of this fuel hydrolysis in an out of pile environment is an order of magnitude increase in the fission gas release rate from failed carbide particles. The periodic water ingresses in FSV have resulted in no discernible increases in fission gas release upon return to power.

5.2. POST-IRRADIATION TEST METHODS FOR UNLOADED FUEL ELEMENTS FROM THE REACTOR

5.2.1. AVR

5.2.1.1. Sampling of AVR fuel for post-irradiation examination

Apart from the previously described in-core measurements in the AVR, PIE was conducted regularly on single fuel spheres, mainly in the Hot Cells at FZJ. Both random and especially selected fuel element samples from the AVR were taken and separated during removal from the core. Sample size was between 33 and 50 spheres with a total number of 92 samples over the whole operation time. Guidelines were established according to which a specific PIE programme was executed. It included

- measurements of ^{133}Xe and ^{85}Kr equilibrium release from single fuel elements during heating tests at constant temperatures of 1050 and 1250°C, respectively, used as indicator for coated particle failure;
- measurements of burnup;
- measurements of concentration profiles of solid fission products in the fuel-free zone;
- metallographic investigations to study the integrity of particles.

After removal from the AVR core, measurements with individual fuel spheres were possible. During operation of the reactor, neither single fuel spheres nor a single fuel element type can

be individually analysed. Only integral statements on the fuel performance over the total core can be given via coolant activity measurements.

5.2.1.2. Release of metallic fission products from the AVR core

Solid fission products were typically deposited on the fuel element surfaces and partially remobilized as dust and transported through the primary circuit. In 1974, after raising the average coolant outlet temperature from 850 to 950°C, a relatively high level of strontium contamination was identified in the AVR core, which has caused a maintenance problem since. The AVR was even quoted as having 'the worst beta contamination of any nuclear installation in the world' [172]. The origin of this strontium could be traced back to enhanced release from carbidic fuel (GK) with $(Th,U)C_2$ HTI BISO coating (UCC, T, GK) and at temperatures > 900°C having reached a maximum burnup of 17% FIMA [173].

The coolant activity increase observed from mid 1975 was presumed to originate from particle failure. It were the routine 1250°C heating tests with all fuel types which eventually identified the small charge of GLE-1 spheres as being responsible for the enhanced activity release. During PIE heating at temperatures < 1200°C, no failures were observed. The failure rate, however, increased significantly when heated at temperatures above 1250°C. When reaching 1500°C, even more than 25% of the particles were found destroyed [110]. As a consequence, it was decided to remove all poor quality GLE-1 fuel elements from the core. The trial not being perfect, however, the circulation strategy was changed so not to re-circulate GLE-1 spheres to the outer core with its higher temperatures. The bulk of this variant was not removed until 1982. The effect of the complete removal on the coolant activities can clearly be seen from the previous Fig. 5.8.

Activities of metallic fission products released into the primary circuit of the AVR vs. operation time are shown in Fig. 5.25 [153]. Table 5.4 lists the fractional release of AVR fuel at EOL [154].

The 'irradiated microsphere gamma analyser', IMGA, is a PIE system to characterize the performance of a large population of coated particles measuring radioisotope inventories of individual coated particles by detecting γ radiation. Among the fuel spheres examined at the ORNL with the IMGA method was the AVR irradiated GLE-3 sphere 76/20 used as a control sphere (vs. irradiated and heated spheres). From the electrolytically deconsolidated AVR ball, some 5000 individual coated particles were given to the IMGA system. The main result was characteristic of no particle failure. No statistical evidence of caesium release from the individual particles and no significant particle-to-particle variation in fission product retention was observed [174].

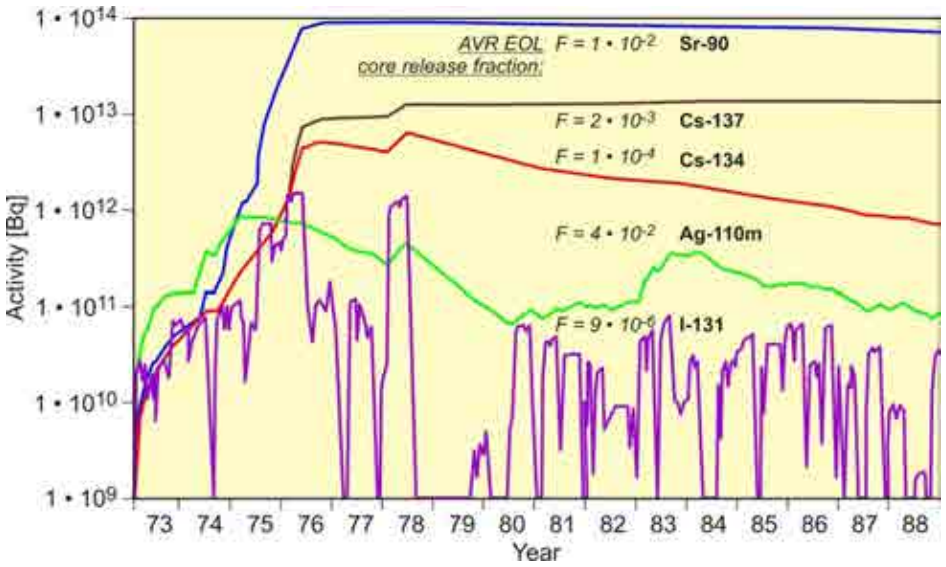

FIG. 5.25. Activities of different radionuclides accumulated in the AVR primary circuit over operation time.

TABLE 5.4. END-OF-LIFE FRACTIONAL RELEASE OF FISSION PRODUCTS FROM AVR FUEL

Radionuclide	EOL fractional release from AVR core
Cs-137	2×10^{-3}
Cs-134	1×10^{-4}
Sr-90	1×10^{-2}
Ag-110m	4×10^{-2}
I-131	9×10^{-6}

5.2.1.3. Fission product profiles in the fuel-free zone

The fuel-free zone of spheres was examined with respect to the long-lived isotopes of caesium, strontium, silver, and others. The procedure of profile measurement was usually such that a 6 mm wide groove was made over the whole circumference of the sphere in 10 steps of 0.4 mm each. Activities for these single graphite powder specimens were then measured and calculated back to the date of discharge from the reactor.

Figure 5.26 shows for the nuclide ^{137}Cs the profiles discovered in GLE-1 spheres with (top curve) and without (bottom curve) defective/failed particles [175]. Surface concentrations are generally higher (for normal particle performance) than further inside the ball. Activity transported with the coolant was obviously deposited on the fuel element surfaces in colder core areas. In contrast, a high concentration level well inside the ball indicates the presence of defective/failed particles having released part of their radionuclide inventory into the matrix material. The ^{110m}Ag profiles were found to be strongly varying for different spheres with sometimes high, sometimes low activities. No burnup dependence on the release behaviour was observed.

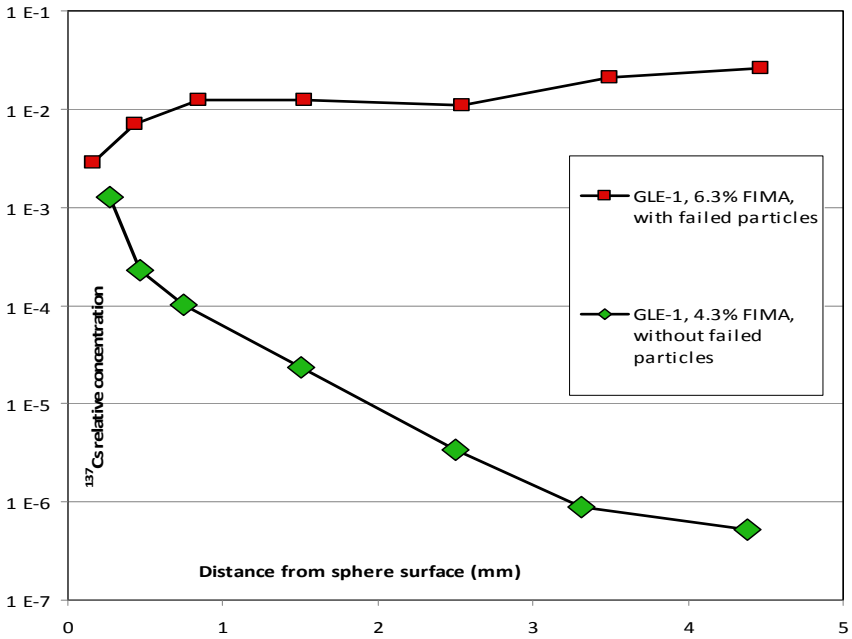

FIG. 5.26. Caesium profiles in the fuel-free zone of AVR fuel elements with and without failed coated particles.

The above typical fission product profiles were also observed in other fuel types and even identified in a moderator sphere. Figure 5.27 shows a comparison of the measured caesium activity ratios (surface over depth of 3.9 mm) [176]. Deviations were only found for silver.

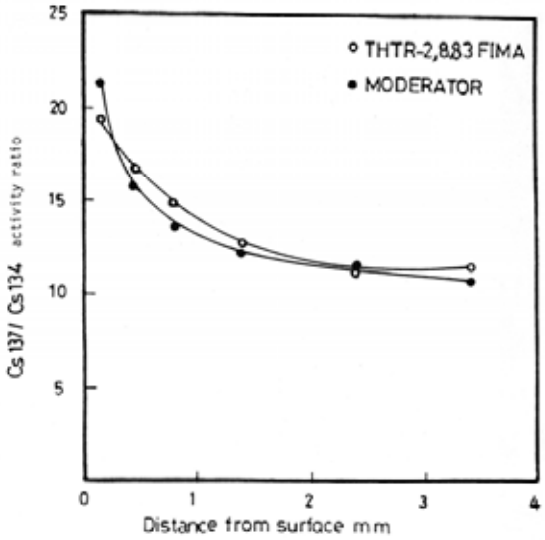

FIG. 5.27. Activity ratios $^{137}Cs/^{134}Cs$ between a GO-THTR sphere and a moderator graphite sphere.

5.2.1.4. End-of-life performance of the modern fuel in the AVR

The AVR fuel reloads of particular importance relative to modern LEU UO_2 TRISO particle performance are GLE-3 and GLE-4. All of these fuel elements were manufactured to high quality requirements. For a seven year period from 1982 to 1988, these fuel elements were inserted into the AVR and experienced real-time HTGR operating conditions. At periodic intervals over this period, a number of irradiated elements would be randomly drawn from the

core for post-irradiation evaluation and accident condition testing. In seven years of irradiation, a total of 240 GLE-3 and GLE-4 elements were withdrawn and evaluated at FZJ. Peak burnups of the withdrawn elements were 9.8% FIMA for the GLE-3 elements and 13% FIMA for the GLE-4 elements. Peak accumulated fast fluence was ~2.9×10^{25} n/m^2 (E > 16 fJ) for the GLE-3 elements and ~2.3×10^{25} n/m^2 (E > 16 fJ) for the GLE-4 elements. PIE included measurements of fission product inventory (burnup), of out-of-reactor gas release, and accident simulation testing.

To assess the EOL performance of GLE-3 and GLE-4 AVR fuel elements, a methodology was developed based upon fission gas release measurement during the temperature increase in the early phase of accident condition testing [177]. The heatup process begins at room temperature, progresses over a series of heating ramps to specific temperatures (300°C, 1050°C, and 1250°C) and hold periods until the desired accident simulation temperature is reached. Two of these hold points, 1050°C, and 1250°C, are designed to equilibrate the irradiated fuel particles in the fuel element at or near their prior irradiation temperature. This allows the fuel to develop a stable internal environment before being heating to an elevated temperature, not previously experienced by the fuel particles. The 1050°C hold point was considered the mean working temperature for fuel specimens from accelerated MTR irradiation tests, and the 1250°C hold point was considered the typical working temperature for AVR fuel elements.

During heating, the test facility is purged with a sweep gas and continuously monitored for release of the long-lived ^{85}Kr noble fission gas. Detection of any significant activity in the sweep gas is an indicator of failed or defective fuel particles present in the irradiated fuel element.

Table 5.5 is a detailed list of 29 GLE-3 fuel elements that have been subjected to accident simulation testing. Of these, 24 from the list were used to analyse AVR EOL irradiation performance. Five were excluded because of the lack of detailed ^{85}Kr release data at testing temperatures near those expected in the AVR. Eleven of the GLE-3 elements were ultimately subjected to isothermal tests from 1600°C or 1800°C, six elements were subjected to a simulated HTR-Modul design basis depressurized event temperature profile up to 1620 or 1700°C; and seven elements were subjected to ramp tests ranging from 1900 to 2500°C.

The ^{85}Kr fractional release data in Fig. 5.28 are indicative of the EOL fuel performance for the GLE-3 elements irradiated in the AVR. For the eleven GLE-3 elements subjected to isothermal accident tests, the release data were measured at the 1250°C hold period during the ramp-up to test temperature and are directly representative of EOL AVR performance. For those elements subjected to a constant heating ramp to temperatures > 1900°C, only release data in the temperature range of 1250°C to ~1400°C were used to estimate EOL performance. And finally, for those elements subjected to a design-basis HTR-Modul depressurization event temperature profile, only the release data along the temperature curve where the furnace temperature was between 1490°C to 1500°C were used as representative of EOL AVR performance [178].

Based on the ^{85}Kr fractional release data from 24 accident simulation tests, the EOL performance of the GLE-3 fuel elements at the time of discharge from the AVR are excellent. Most of the release data, with few exceptions, are < 10^{-6} in the temperature range of 1250°C to well beyond 1400°C. The ^{85}Kr release fraction of a single LEU UO_2 TRISO particle at these temperatures is ~6.1×10^{-5} and those measured from the 24 separate GLE-3 elements are all > 10 times to > 1000 times less. The AVR GLE-3 elements fractional release data also

compares well with ^{85}Kr release data obtained from accident simulation testing of MTR Irradiation and HTR-Modul proof tests specimens [178].

Collectively, the 24 type GLE-3 elements represent a population of ~393 600 LEU UO_2 TRISO coated particles, and with no in-reactor failures their EOL performance is representative of a failure fraction of $\leq 7.6 \times 10^{-6}$ at the upper 95% confidence limit [178].

5.2.2. THTR-300

Unlike the AVR reactor, the THTR-300 was fueled with only one type of fuel element and coated particle design. Also fuel temperatures were lower than in the AVR under normal operating conditions with the average coolant temperature being 750°C at the steam generator inlet.

TABLE 5.5. NOBLE GAS ^{85}Kr RELEASE FRACTION MEASUREMENTS DURING ACCIDENT SIMULATION TESTS ON AVR TYPE GLE-3 FUEL ELEMENTS

Fuel element	Burnup (% FIMA)	Measurement temperature of Kr-85 release (°C)	Kr-85 release fraction
Isothermal accident simulation tests			
AVR 70/33	1.6	1250	3.8×10^{-6}
AVR 73/21 (ITU*)	2.5	n.i.	n.d.r. < 1600
AVR 71/22	3.5	1250	4.5×10^{-8}
AVR 74/18 (ITU*)	4.8	1600	5.9×10^{-6}
AVR 74/10	5.5	1250	$< 8.0 \times 10^{-7}$
AVR 74/11	6.2	1250	1.3×10^{-7}
AVR 76/18	7.1	1250	1.6×10^{-8}
AVR 88/41	7.6	1250	1.3×10^{-8}
AVR 88/33	8.5	1250	$< 4.2 \times 10^{-8}$
AVR 82/20	8.6	1250	5.5×10^{-8}
AVR 88/15	8.7	1250	6.3×10^{-8}
AVR 82/9	8.9	1250	1.3×10^{-8}
HTR-Modul depressurized loss-of-coolant event profile			
AVR 91/31	9.0	1500	1.0×10^{-8}
AVR 89/13	9.1	1490	6.7×10^{-8}
AVR 85/18	9.2	1495	2.6×10^{-8}
AVR 90/5	9.2	1495	5.3×10^{-8}
AVR 90/2	9.3	1495	9.2×10^{-8}
AVR 90/20	9.8	1500	5.7×10^{-8}
Ramp accident simulation tests			
AVR 71/7	1.8	1250	3.1×10^{-7}
AVR 70/19	2.2	1200	1.9×10^{-6}
AVR 74/8	2.9	1250	1.4×10^{-7}
AVR 73/12	3.1	1250	$< 1.4 \times 10^{-7}$
AVR 74/6	5.6	1250	1.3×10^{-7}
AVR 76/28	6.9	1250/n.i.	n.d.r. < 1750
AVR 76/19	7.3	1250	2.3×10^{-7}
AVR 76/27	7.4	1250	4.6×10^{-7}
AVR 80/16	7.8	1250/n.i.	n.d.r. < 1900
AVR 80/14	8.4	1250/n.i.	n.d.r. < 1900
AVR 80/22	9.1	1250/n.i.	n.d.r. < 1600

n.i. not included in EOL AVR evaluation.
n.d.r. no detectable release.

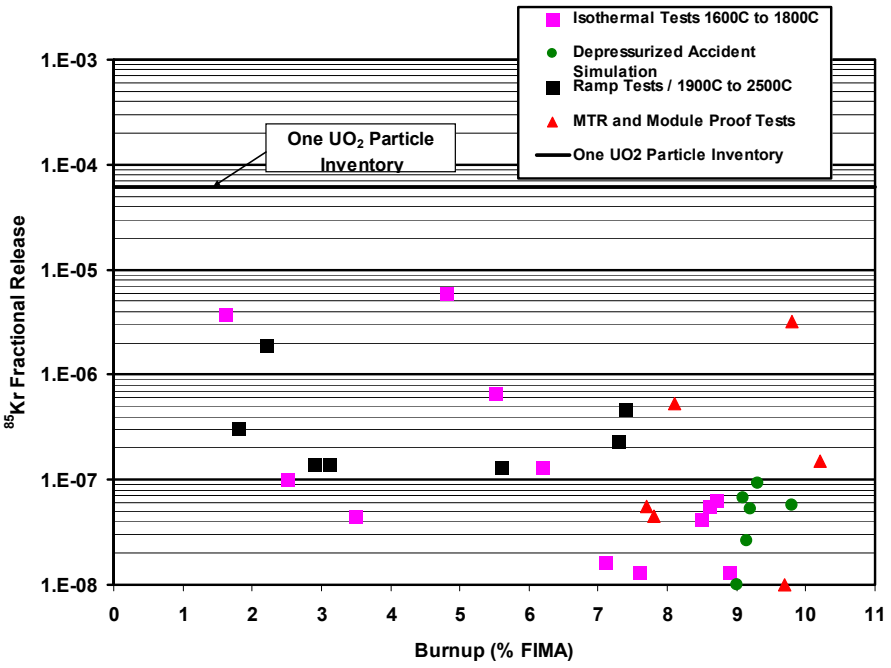

FIG. 5.28. Noble gas ^{85}Kr release fraction monitored during accident simulation testing of AVR type GLE-3 fuel elements and accelerated MTR and HTR-Modul proof tests.Measurements by the FZJ and the JRC-ITU.

Apart from the experience gained from THTR operation, the investigation of the irradiation behaviour of THTR fuel elements was done in respective experiments in MTRs and, as a mass test, in the AVR reactor. The THTR reactor itself was not designed for an intentional discharge of fuel elements for testing purposes. Correspondingly, PIE work was conducted on those spheres tested in the MTRs and on random samples of THTR type fuel taken from the AVR. There were never fuel elements discharged from the THTR to be taken for further PIE.

5.2.3. HTTR

5.2.3.1. Introduction

The future research and development concerning the HTGR development is scheduled in a wide range mainly using the HTTR. The R&D subjects aiming at improving the performance and economy of HTGR are concerned mainly with the advancement of basic HTGR technologies and improvement of the core performance. The R&D using the HTTR is scheduled in a wide range

- to establish the technology basis on HTGRs;
- to upgrade present HTGR technologies;
- to establish high temperature nuclear process application technologies;
- to make the innovative basic research on high temperature engineering.

R&D of HTGR fuel is carried out to establish the technology basis on HTGRs and to upgrade the present HTGR technologies.

5.2.3.2. Post-irradiation test programme for the HTTR fuel

For the R&D of HTGR fuel, it is important to improve fission product retention capability of the fuel with a high power density and a high burnup durability under long term high temperature operation [98, 99]. A modified SiC TRISO coated fuel particle is selected as a high burnup fuel. In order to achieve higher burnups up to 10% FIMA, thickness of the buffer and SiC layers is increased in the design. At the same time, the kernel diameter is somewhat reduced to mitigate the internal pressure in a coated fuel particle increased by the higher burnup. Furthermore, HTGR fuels in the next generation are required for higher temperature utilization and an enhanced safety. For the higher temperature utilization of the HTGR fuels, a key issue is adoption of a new coating material, which is more refractory than SiC used in the conventional coated fuel particles. Since zirconium carbide (ZrC) is one of the promising materials to meet this requirement, development works on the ZrC coating have been conducted at JAEA [179, 180]. The works are going to be upgraded in an engineering scale including production, property and irradiation studies.

On the background described above, JAEA will proceed R&D works in the field of HTGR fuel by the following steps:

STEP-1: Confirmation of irradiation performance of the first loading fuel of the HTTR;

STEP-2: Study on irradiation performance of high burnup SiC coated fuel particle;

STEP-3: Development of ZrC coated fuel particle.

The future post-irradiation programme concerning the first loading fuel of the HTTR is scheduled using the HTTR fuel handling facilities and the Hot Laboratory in Japan Materials Testing Reactor (JMTR).

The post-irradiation test of the first loading fuel of the HTTR is carried out to confirm its irradiation performance and to obtain data on its irradiation characteristics in the core. Hot cells were prepared in the HTTR reactor building to handle spent fuels. General equipments such as those for consolidation of fuel compacts and for handling of coated fuel particles were also installed in the Hot Laboratory of the JMTR.

The fuel assembly of the HTTR is so-called a pin in block type of hexagonal graphite block containing fuel rods. The fuel assemblies will be transferred to the spent fuel storage pool in the reactor building by the fuel handling machine. The irradiated fuel assembly will be disassembled to the fuel rods and a graphite block in the HTTR cells. Then the fuel rods are transferred to the Hot Laboratory of the JMTR by a cask for the post-irradiation examination. In the Hot Laboratory, the following post-irradiation examinations will be carried out:

- Appearance observation of the fuel rods and the fuel compacts to confirm no abnormal crack and corrosion occurs;
- Dimension measurement of the fuel rods and the fuel compacts to confirm no abnormal swelling or shrinkage.
- Fuel failure fraction measurements to confirm there is no abnormal additional failure during irradiation.
- Burnup measurement, X ray radiography, ceramography, etc., will also be carried out to obtain detail irradiation characteristics.

Figure 5.29 shows the flows of fuel failure fraction measurements. Since fission products are almost completely retained by the coating layers, the dominant sources of fission product release are failed particles and contaminated uranium in the fuel compact matrix [163].

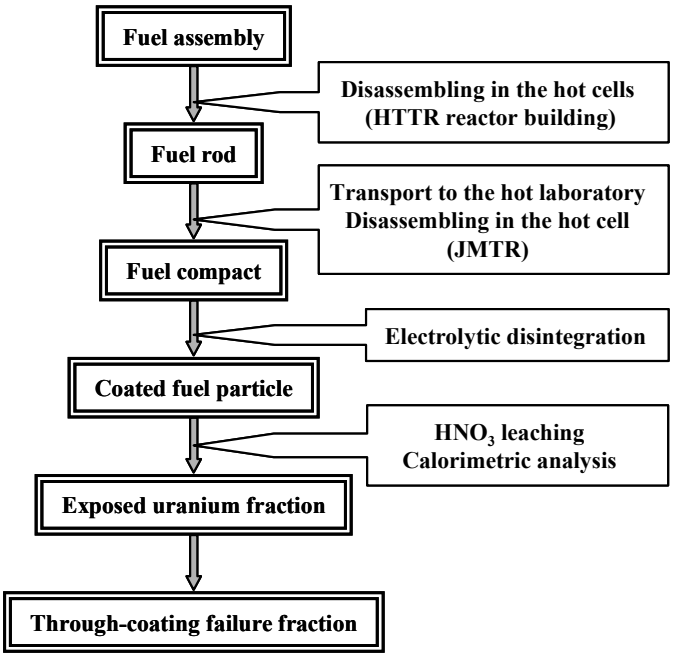

FIG. 5.29. Flows of fuel failure fraction measurements.

The through-coatings failed particle and uranium contaminated uranium in the fuel compact matrix determine the fission gas concentration in the primary coolant during operation. From this point of view, the free uranium fraction is one of the most important post-irradiation test items. On the other hand, since the as-fabricated SiC failed particle does not have the mechanically strongest coating layer, SiC, the as-fabricated SiC failed particle is predicted to result in the through-coatings failed particle by internal pressure during operation. The intact particle is predicted not to fail in the HTTR operating condition [163]. It means that the as-fabricated SiC failure fraction determines the additional through-coatings failure fraction, i.e. increase in fission gas concentration in the primary coolant during operation. The free uranium fractions of the fuel compacts were measured by electrochemical deconsolidation followed by acid leaching [102].

5.2.3.3. Post-irradiation test facility

(a) Hot cells in the HTTR reactor building

Three hot cells named ‘high temperature irradiation materials inspection cells’ are prepared in the HTTR reactor building as shown in Fig. 5.30 [181].

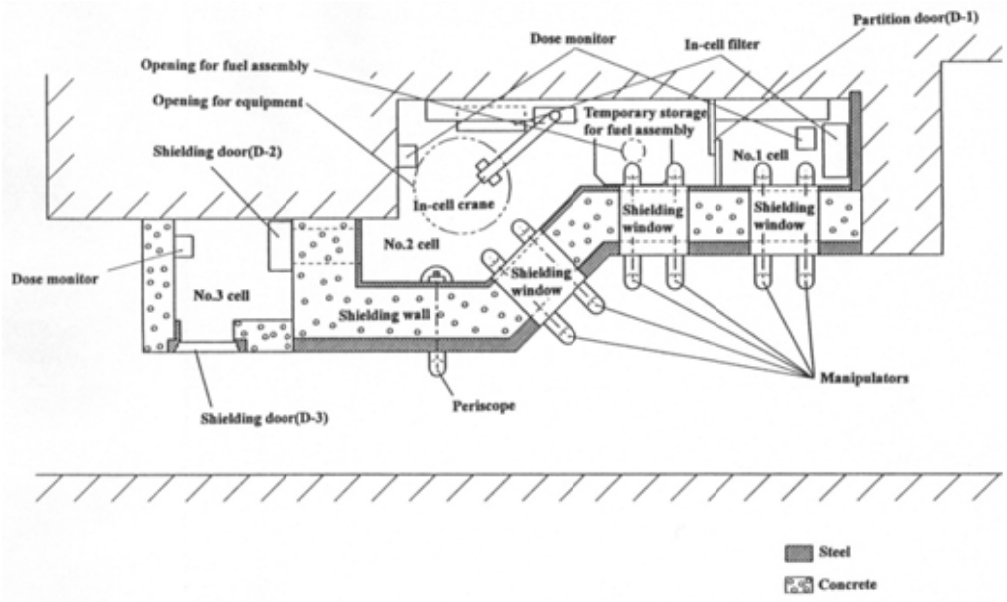

FIG. 5.30. High temperature irradiation materials inspection cells.

The No. 1 and No. 2 cells are designed mainly to dismantle irradiated fuel rods from the fuel assembly. The No. 3 cell is provided for analysis of gaseous fission products and preparation of maintenance works. The irradiated fuel assembly is brought in/out through an opening located on the top of the No. 2 cell. Shielding wall of the No. 1 and the No. 2 cells is 95 cm of concrete and 35 cm of steel to handle an irradiated fuel assembly up to 33 GW•d/t which contains 3.7×10^{15} Bq of activity. Shielding wall of the No. 3 cell is 60 cm of concrete. There are three shielding windows as shown in Fig. 5.31.

FIG. 5.31. High temperature irradiation materials inspection cells.

(b) Hot laboratory in the JMTR

There are three kinds of beta, gamma cells in the JMTR hot laboratory, i.e. concrete cells with microscope lead cells attached, lead cells and steel cells. A lead cell and two concrete cells will be prepared to carry out post-irradiation tests for HTGR fuel development. Tables 5.6 and 5.7 show the items and major apparatuses for the PIE of the first loading fuel of the HTTR.

5.2.3.4. Preliminary post-irradiation examination of the first loading fuel of the HTTR

Preliminary post-irradiation examinations were carried out to confirm post-irradiation examination techniques. Irradiated fuel compacts of the accelerated irradiation test of the first loading fuel of the HTTR were used, of which the irradiation test as 94F-9A capsule irradiation test in the Japan Materials Testing Reactor (JMTR) was performed to confirm the intactness of the first loading fuel during the HTTR operation [182–184]. Fuel compacts irradiated has same dimensions as the first loading fuel and 7.8 wt% of ^{235}U enrichment. Table 5.8 shows irradiation conditions of 94F-9A capsule.

Figure 5.32 shows the items of post-irradiation examination. Irradiation capsule is dismantled and fuel compacts are taken out. Visual observation is carried out by periscope. Dimensions of outer diameters and axial lengths of fuel compacts are measured by laser micrometer and electric micrometer, respectively, to measure dimensional shrinkage of fuel compacts by fast neutron irradiation. Weights of fuel compacts are measured by electric balance. Fuel compacts are dissoluted by electric deconsolidation method and acid-leaching with HNO_3. After that leaching solutions are divided to coated fuel particle and leaching solution. Gamma measurements of coated fuel particles and leaching solution are carried out to measure failure fraction of each fuel compact. If it suggests failed particles exists by failure fraction measurement, X ray radiograph will be carried out to find them. To observe fission product distribution in the cross-section of coated fuel particle, ceramography, scanning electron microscope (SEM) observation and electron probe micro analysis (EPMA) is carried out.

TABLE 5.6. INSPECTION ITEMS IN THE HTTR REACTOR BUILDING

Transport of fuel block	Fuel handling machine
Disassembling of fuel rod	Hot cell in HTTR reactor building Manipulators
Visual inspection	Periscope
Fuel rod canning	Inner capsule Loading cask
Leak test	Leak detector

TABLE 5.7. ITEMS AND MAIN APPARATUSES FOR THE PIE OF THE HTTR FIRST-LOADING FUEL

PIE items	Major apparatuses
Transport of fuel rod	Transport cask Loading lift
Disassembling of fuel compact	Cutter Manipulators
Dimension measurement	Linear scale Periscope
Disassembling of fuel compact	Electrolytic deconsolidate Coated fuel particle handling device
Burnup measurement	Ge detector Fission product inventory measurement
X ray radiography	X ray radiograph
Failure fraction measurement [a]	Electrolytic deconsolidate Acid leaching test FP inventory measurement
Ceramography	Polisher Optical microscope
Non-destructive failure fraction measurement [b]	Sweep gas furnace

[a] The free uranium fractions of the fuel compacts are measured by the deconsolidation followed by the acid leaching. The SiC failure fractions are measured by the burn/leach method.

[b] Post-irradiation heating test identifies failed fuel. We are developing the post-irradiation heating method of a fuel rod and analytical method to quantify failure fraction by measuring released ^{85}Kr from a heated fuel rod.

TABLE 5.8. IRRADIATION CONDITIONS OF 94F-9A CAPSULE

	Lower capsule		Upper capsule	
Compact No.	94FP1-3	94FP1-7	94FP2-7	94FP2-9
Irradiation temperature (°C)	1300–1350			
Irradiation time (h)	8733			
Fast neutron fluence (10^{25} n/m^2, E>0.18 MeV)	1.4	1.6	2.0	1.8
Burnup (% FIMA)	5.5 (lower)		7.0 (upper)	

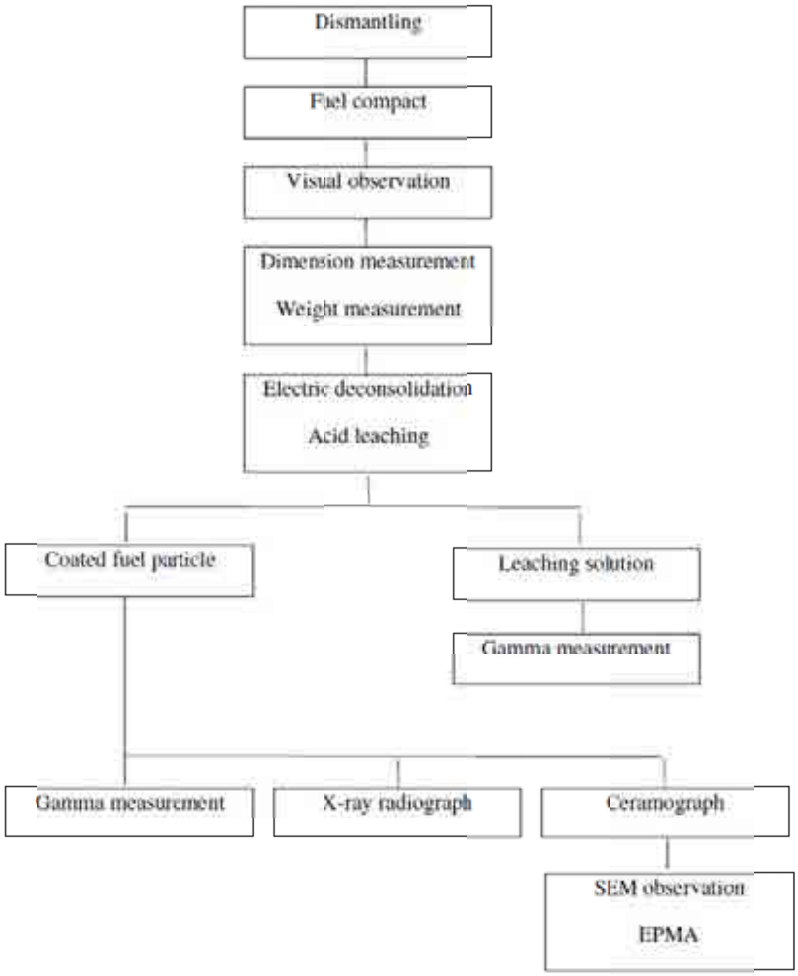

FIG. 5.32. Flowsheet of preliminary post-irradiation examination.

5.2.4. Peach Bottom

As part of the Peach Bottom EOL programme, gamma scanning of 55 driver fuel elements, 21 fuel test elements, 3 reflector elements, and a control rod and sleeve was performed on-site [169]. The major components of the gamma-scanning equipment were a collimator, a charge machine, a Ge(Li) gamma spectrometer, and associated electronic data acquisition equipment. The charge machine driver mechanism was modified to slow movement of the element past the collimator slit (Fig. 5.33) and gamma rays passing through the slit were monitored using a high resolution Ge (Li) detector [169]. The signal from the detector was transmitted to a pulse height multichannel analyser (MCA) and a series of single-channel analysers. The MCA-accumulated gamma ray spectra were stored on magnetic tape for subsequent computer analysis and data processing. Ten different isotopes were monitored.

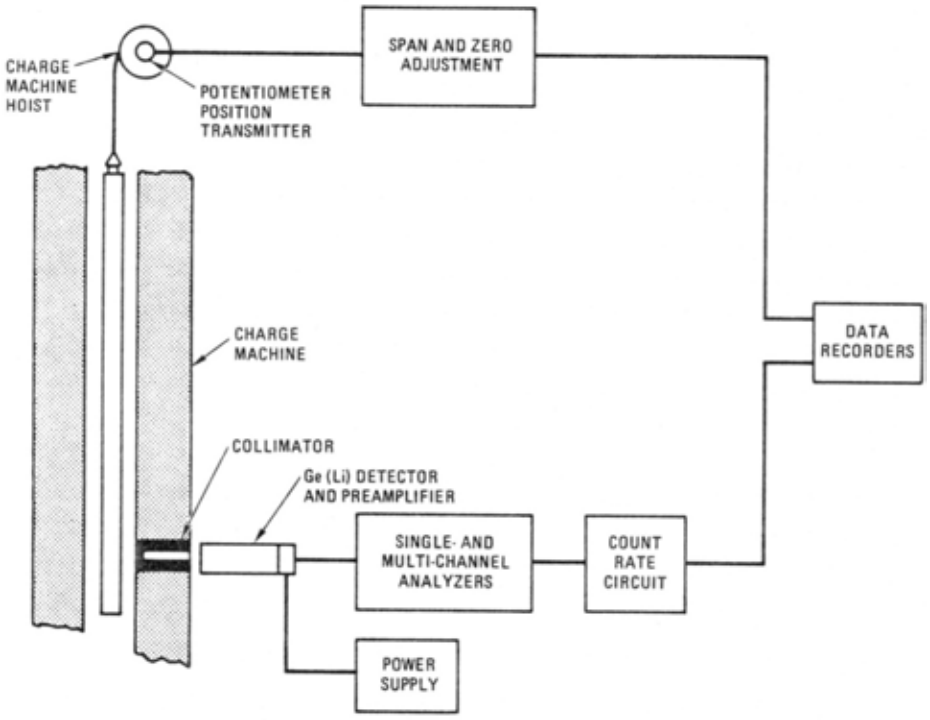

FIG. 5.33. Test arrangement for gamma scanning Peach Bottom test and driver fuel elements.

Normalized axial and radial ^{137}Cs, ^{140}La, and ^{95}Zr profiles in the core were successfully determined from the gamma scans. The ^{137}Cs profiles were subsequently shown to be in good agreement with predicted axial and radial time-averaged power distributions. Also, ^{140}La and ^{95}Zr profiles predicted corresponding power profiles at EOL reasonably well. Of the isotopes analysed, only ^{137}Cs and ^{134}Cs were found to migrate and redistribute within the hotter elements as is shown for an example in Fig. 5.34 [169]. Redistribution is made by the purge flow which is diverted from the upflowing primary coolant through the top of the fuel elements flowing downwards and sweeping the fuel compact surfaces before arriving at the fission product traps and the external cleanup system, respectively.

Fission gas release measurements were made on archive and irradiated Peach Bottom fuel compacts to provide BOL and EOL noble gas release values. The determinations of ^{85m}Kr R/B at 1100°C were made using a TRIGA reactor King furnace facility. The R/B data determined were then employed to refine fission gas release predictions and to check calculated particle failure fractions. Relative caesium sorption determinations were made on archive sleeve graphite, spine graphite, and matrix material. In addition, the diffusivities of caesium in fuel element sleeve and spine graphite archive materials were determined and subsequently employed to refine fuel element and total core metallic release predictions. The major results and conclusions from the radiochemical studies can be summarized as follows:

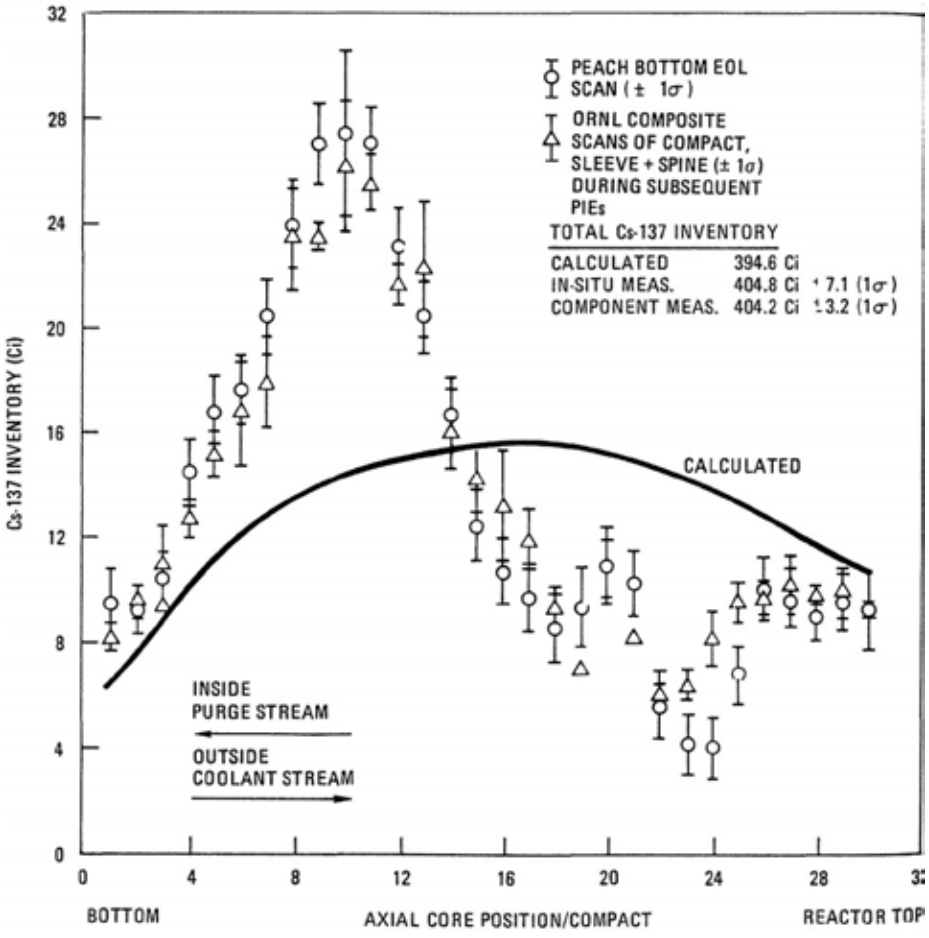

FIG. 5.34. ^{137}Cs inventory vs. axial core position for fuel element F03-01.

- Specific activities in the primary circuit ranged from ~1–8 μCi/cm^2 (40–300 kBq/cm^2) for ^{137}Cs. A decrease in caesium activity in the direction of coolant flow was indicated as anticipated, together with an increase in the ^{137}Cs/^{134}Cs ratio.
- The specific activity levels of ^{90}Sr obtained from leach solution radiochemistry were in the range of 0.02–0.3 kBq/cm^2, several orders of magnitude lower than caesium activities. Activation of leach samples indicated no detectable ^{129}I, indicating that the fuel element purge system was effective in controlling iodine release.
- Compared with H-327 graphite, Peach Bottom fuel element spine graphite was slightly less sorptive and sleeve graphite slightly more sorptive of caesium. Peach Bottom compact matrix material was about 12 times more sorptive than bulk H-327 graphite and about 6 times more sorptive than bulk Peach Bottom sleeve graphite. Peach Bottom fuel element spine graphite was 3 to 4 times more permeable to caesium than H-451 graphite, whereas the sleeve graphite was 10 to 20 times less permeable.

5.2.5. Fort St. Vrain

The 842 MW(th)/330 MW(e) Fort St. Vrain (FSV) reactor, owned and operated by Public Service Company of Colorado (PSCo), was the second HTGR built and operated in the USA [185, 186]. The reactor operated between 1976 and 1989 for about 875 efpd [187]. The reactor core was rated at 842 MW(th), but it was operated well below that rating for much of its lifetime due to chronic water ingress problems associated with the water bearings used in

the helium circulators [188]. For a short time period the reactor operated at 100% design power and achieved a thermal efficiency of 39%.

Figure 5.35 is a cut-away view of the FSV prestressed concrete reactor vessel (PCRV) showing the main primary circuit components. The PCRV acted as a pressure vessel, containment, and biological shield. The primary coolant circuit was wholly contained within the PCRV with the core and reflectors located in the upper part of the cavity, and the steam generators and circulators located in the lower part. The helium coolant flowed downward through the reactor core and was then directed into the reheater, superheater, evaporator, and economizer sections of the 12 steam generators. From the steam generators, the helium entered the four circulators and was pumped up, around the outside of the core support floor and the core barrel before entering the plenum above the core. The superheated and reheated steam was converted to electricity in a conventional, steam cycle, power conversion turbine generator system.

The FSV reactor core was composed of 247 columns of fuel elements, with six fuel elements stacked in each column. The core cross-section in Fig. 5.35, right, shows the locations of the columns in the core, surrounded by one row of replaceable reflector elements, which were in turn surrounded by the permanent reflector blocks. Axial reflector blocks were also located above and below the core. The core columns were grouped into 37 refueling regions with the flow in each region controlled by an adjustable inlet flow control valve on the top of the core to maintain a uniform core outlet temperature as power generation per region changed due to fuel burnup and the attendant control rod repositioning. About one sixth of the 37 regions were refueled each reactor year. The elements in the central column of each of the refueling regions contained two holes for insertion of control rod pairs, and one hole for insertion of reserve shutdown pellets.

Two spent FSV fuel elements, one discharged after one cycle of operation and the other after two cycles, have undergone post-irradiation examination in the GA hot cells. The emphasis during these PIEs has been on gamma scanning and on assessing the mechanical integrity of the fuel elements, and the PIEs confirmed the satisfactory structural performance of these elements. Selected fuel rods and fuel particles from these elements were examined by standard PIE techniques, including sectioning and metallography. There was evidence of limited in-pile failure of the IPyC and OPyC coatings of the TRISO particles, but these types of failures do not result in fission product release. A small number of fuel particles were observed to have completely failed coatings, but these appear to be as-manufactured failures rather than in-service failures because the kernels of these particles had been at least partially leached (FSV fuel rods are HCl leached during manufacture to reduce heavy metal contamination). Moreover, the SiC defect fraction, as determined by metallography, in the irradiated fuel rods was unchanged from that measured by a burn-leach technique in unirradiated rods from the same manufacturing lot.

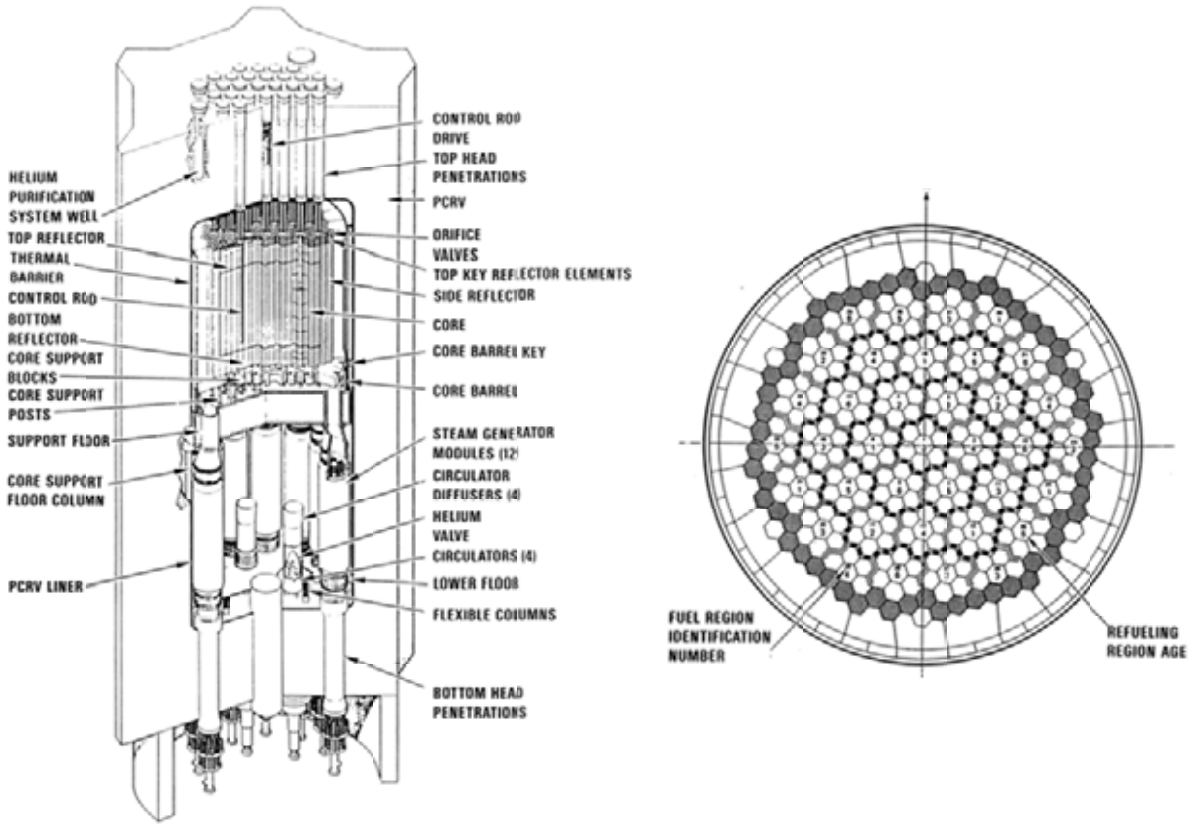

FIG. 5.35. FSV primary coolant circuit.

Fission gas release rates for 17 fuel rods irradiated in fuel element 1-0743, discharged after one cycle of reactor operation, were measured by neutron activation of the rods in the GA TRIGA reactor and compared to R/B measurements for several of these same fuel rods that had been made prior to irradiation; the results are summarized in Table 5.9 [171]. The R/B of ^{85m}Kr for the irradiated rods was nominally lower than forthe unirradiated rods but within one standard deviation for RIS measurements. The implication is that inservice particle failure was negligible which is consistent with the metallographic examinations.

In order to assess these two effects, the performance analysis was repeated for (1) the case with no particle failure wherein the only source of fission gas release is as-manufactured heavy metal contamination, and (2) the case of nominal failure but no fuel hydrolysis. The results are shown in Fig. 5.36, and they indicate that excellent agreement with the data was obtained throughout the first three cycles for both cases [171].

TABLE 5.9. FISSION GAS RELEASE MEASUREMENTS FOR FUEL RODS IRRADIATED IN FSV FUEL ELEMENT 1-0743

Fuel rod ID	Time-averaged max. fuel temp. (°C)	Fast fluence (10^{25} n/m^2, E>29 fJ)	Burnup (% FIMA)		Fission gas release (R/B of Kr-85m @ 1000°C)	
			Fissile	Fertile	Pre-irradiation	Post-irradiation
12-2	690	0.8	6.1	0.3	—	1.1×10^{-4}
12-7	660	0.8	6.2	0.3	—	1.1×10^{-4}
12-13	625	0.8	6.2	0.3	—	1.1×10^{-4}
47-2	685	0.8	6.1	0.3	—	1.1×10^{-4}
47-7	660	0.8	6.2	0.3	—	1.1×10^{-4}
47-14	625	0.8	6.2	0.3	—	1.1×10^{-4}
189-7	695	1.0	6.2	0.3	—	1.1×10^{-4}
285-2	750	1.1	6.1	0.3	—	1.1×10^{-4}
285-7	720	1.1	6.2	0.3	—	1.1×10^{-4}
285-14	680	1.1	6.2	0.3	—	1.1×10^{-4}
47-8	655	0.8	6.2	0.3		
278-8	745	1.0	6.2	0.3	1.3×10^{-4} [a]	9.3×10^{-5}
285-8	710	1.1	6.2	0.3		
189-2	720	1.0	6.1	0.3	—	9.2×10^{-5}
189-14	655	1.0	6.2	0.3	—	5.5×10^{-5}
278-12	745	1.0	6.2	0.3	—	8.2×10^{-5}
278-13	670	1.1	6.2	0.3	—	8.8×10^{-5}
Average	690	0.9	6.2	0.3	1.3×10^{-4}	1.0×10^{-4}

[a] Measured on group of five rods including rods 41-8, 218-8, and 285-8. Rod 157-8, one of the five rods, was broken during disassembly and could not be measured tor fission gas release.

— data not available.

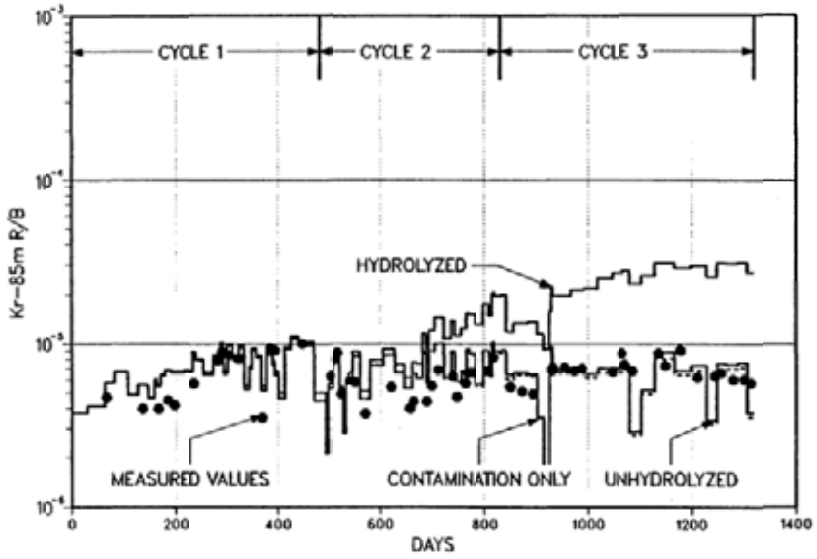

FIG. 5.36. Comparison of measured ^{85m}Kr release data and predictions for Fort St. Vrain.

5.3. BURNUP MEASURING SYSTEM FOR MODULAR PEBBLE-BED HTGR

In a classical stationary nuclear reactor, fuel elements are simply removed from the core after a given time which is determined by predictive calculations and long-time operational experience. In a pebble bed core which employs the multi-pass scheme, the individual spherical fuel element looses its uniqueness after being inserted into the reactor. Therefore it is mandatory to determine the burnup of each pebble after it has been extracted from the core in order to determine whether its design burnup has been reached or whether it has to be reinserted into the core once again (Fig. 5.37) [189].

Many proposals of how to online measure the pebble's burnup have been made; however, only three proposals have been materialized and put into operation.

(1) Measuring the attenuation of a neutron beam by a fuel pebble and drawing from these measurements conclusions on the fuel's burnup. This method had been installed in the AVR for 17 years. However, when looking at the measured 'starry sky' and the keenly drawn relationship of burnup (in FIMA) versus neutron count rate (Fig. 5.38), it is quite obvious that these measurements did not give reliable data. According to an internal AVR report, ~33% of the fuel having reached its very high design burnup were not detected as such and had been reinserted into the reactor again. Obviously, this is intolerable for a reactor whose safety depends on the correct identification of each fuel's burnup.

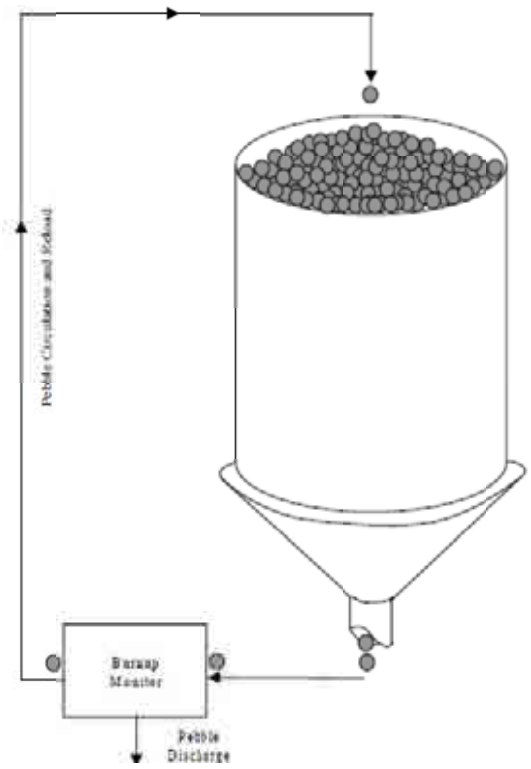

FIG. 5.37. Principle of the multi-pass fueling scheme of a one-zone modular pebble bed reactor.

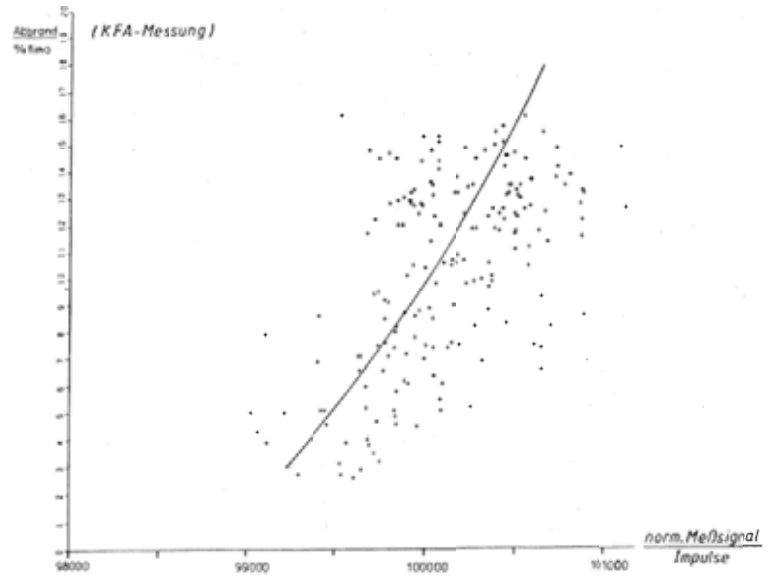

FIG. 5.38. Neutron absorption method; burnup versus neutron count rate. Note: the count rate differs only by ~ 1% between 1 and 10% FIMA [192].

(2) The THTR pebble bed reactor tried to use a different burnup measuring system. It employed a small critical reactor, ADIPCA, situated below the pebble bed reactor. Fuel elements extracted from the THTR core had to roll through the measuring reactor by gravity. The power response of this critical assembly was hoped to be a reliable means to determine the fuel's fissile content. However, due to variables, such as temperature, rolling velocity, graphite content of the fuel, the measurement accuracy was not very convincing.

(3) In 1975, a young Jülich engineer (Helmboldt) proposed the known method of gamma spectroscopy for on-line measurements in pebble bed reactors. Very soon, the gamma line of ^{137}Cs had generally been recognized as the most appropriate candidate [190, 191]. Gamma spectroscopy is foreseen for all planned modular pebble bed rectors since then.

The isotope ^{137}Cs has unique properties that make it an ideal nuclide to measure burnup.

- ^{137}Cs has a long half-life (30a) compared to the time a fuel sphere spends in the reactor core (~ 1000 d); this results in a Cs-activity that increases linearly with the number of fissions and thus the burnup.
- The fission yields of ^{137}Cs for ^{235}U and ^{239}Pu are very nearly the same, so that the ^{137}Cs content is almost independent of the mix of fissile species present in the fuel that changes throughout the lifetime of a fuel sphere in the reactor core. The cross-section of ^{137}Cs for thermal neutrons is negligible.
- ^{137}Cs is very abundant since it has high fission yields of 6.3% and 6.5% per fission for ^{235}U and ^{239}Pu, respectively.
- When ^{137}Cs decays the probability of a gamma emission is very high (84.6%).
- While caesium is considered a volatile fission product, modern HTGR fuels guarantee retention inside the fuel of better than 10^{-5}, therefore placing no restriction on ^{137}Cs as a reliable burnup indicator.

In early 1982, AVR started to replace its old burnup measuring device by the gamma-spectroscopy method (Fig. 5.39) [192].

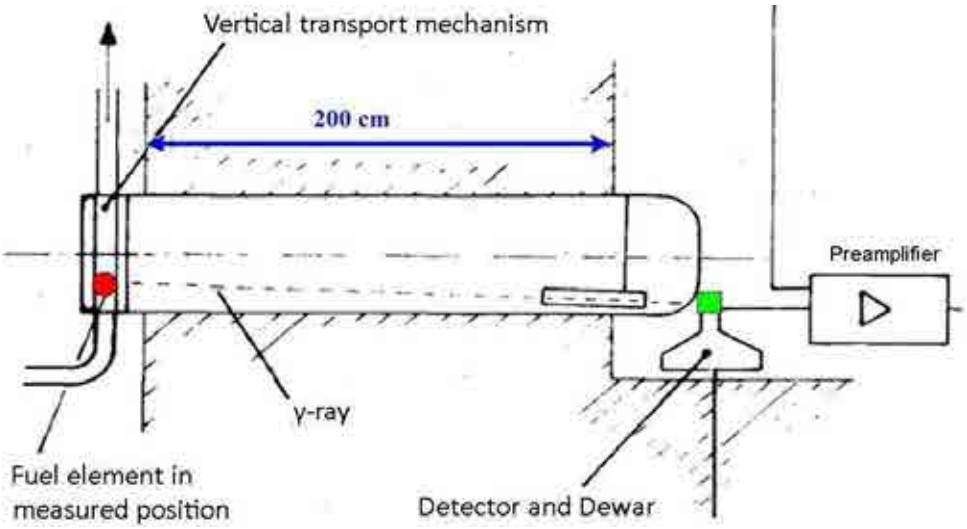

FIG. 5.39. Sketch of the burnup measuring arrangement of the AVR [192].

Here, many peculiar engineering and physical properties of the AVR facilitated the employment of this method. First, the relatively low power of the reactor needs only very few fresh pebbles per day. In combination with a low reshuffling number of the fuel, ample time is available to measure each extracted fuel. More important, however, is the fact that the AVR fuel extraction chute is very long enabling a long decay time (> 14 d) of the irradiated fuel before it reaches its measuring position. It turns out that all gamma peaks neighboring the 661.6 keV ^{137}Cs peak (^{97}Nb, ^{143}Ce, ^{132}I) have already completely decayed rendering measurement very easy (Fig. 5.40).

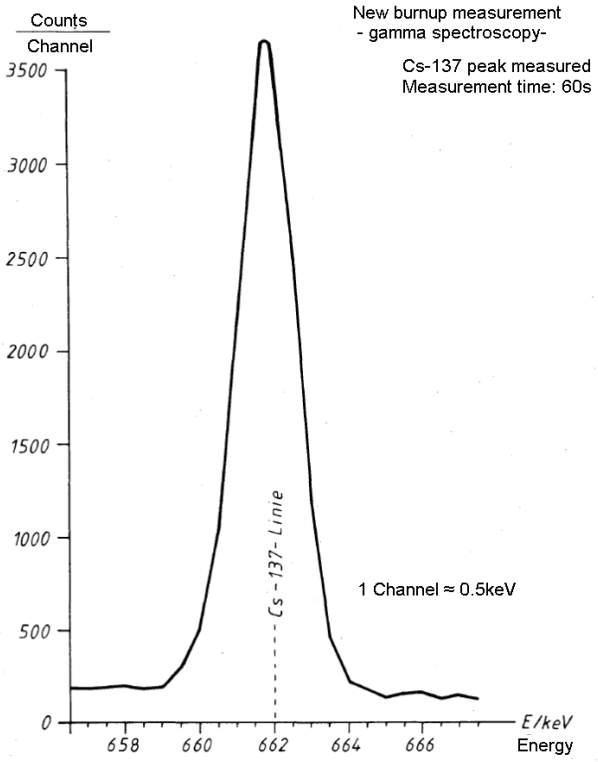

FIG. 5.40. AVR high burnup fuel element, counting time: 60 s; decay time: > 14 d; input count rate: ~20000 cps; channel width: 0.50 keV [192].

When considering gamma spectroscopy for modular HTGRs, it is not as easy to handle as it had been for the AVR. Several reasons must be cited:

- In the very near vicinity of the ^{137}C peak, one finds several peaks which could overlap the Cs peak when measuring systems with a low resolution are used or when not already decayed — as in the case of the AVR. Table 5.10 shows the peaks to be considered, notably ^{97}Nb, ^{137}Cs, ^{143}Ce and ^{132}I, as well as their half-lifes, their peak energies, and their mutual distances when a common Ge(Li)-detector is used (full-width-at-half-maximum FWHM = 1.8 keV, 1σ = 0.76 keV).
- Modern modular HTGR designs have a much higher power than the AVR, a much shorter extraction tube and a higher number of passes of the fuel element through the core. This reduces the decay time considerably and restricts the counting time. For the HTR-Modul, these data are: 200 MW, 55 h decay time and ~10s of mean counting time since the number of fuel passes was chosen to be a high 15 (similar values are found for the Chinese reactor HTR-PM). From Table 5.10, it is obvious that for these very stringent conditions no neighboring peak of the Cs peak has totally decayed at the time the fuel's burnup has to be determined.
- For the above severe conditions, the total count rate of the system is dominated by short-lived fission products with high energy 1–2.5 MeV gammas. Therefore, Compton scattering in the Ge detector produces a broad Compton background which decisively determines the accuracy of measuring the content of the Cs peak.

TABLE 5.10. GLOBAL DATA OF RELEVANT GAMMA PEAKS

Isotopes	Energy (keV)	Distance from neighboring peak (in Sigma)	$T_{1/2}$	Intensity
Nb-97	657.9	4.83	16.8 h	0.982
Cs-137	661.6	3.13	30.1 a	0.846
Ce-143	664.0	4.69	33.6 h	0.058
I-132	667.6	—	78.0 h	0.987

— data not available.

To evaluate the accuracy of gamma spectroscopy under these severe conditions, the experiment FRJ2-KA2 had been carried out between 1989 and 1991 at the DIDO reactor in Jülich. This experiment [193, 194] was explicitly done for the HTR-Modul and shall anew be investigated in the following.

Due to many reactor problems, the in-core irradiation time had been very long; however, for evaluating this experiment to its fullest extent in respect of Cs peak determination, it is important to note that the reactor worked without any interruption for the last 24 days with the designed power of 22.21 MW. Hence, the crucial content of the fission products ^{132}I, ^{97}Nb, ^{143}Ce have definitely reached its saturation values. To a very large extent, this is also true for the important total gamma radiation of the entire fuel sphere.

One fuel element had been extracted from the research reactor ahead of the planned irradiation time to be examined by gamma-spectroscopy method after four different decaying times: 46.7 h, 116.83 h, 180.96 h and 106 days. The measured spectra are shown in Figs 5.41 to 5.44.

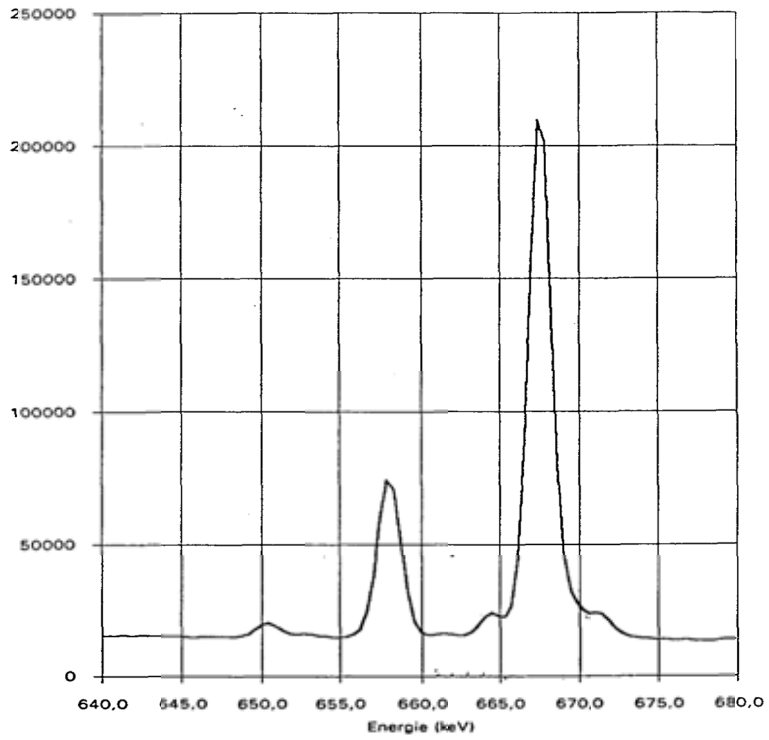

FIG. 5.41. FRJ2-KA2 pebble #3 impulse count vs. energy; 20 mm iron shield, counting time: 5000 s; decay time: 46.7 h; input count rate: 16908 cps; channel width: 0.41 keV.

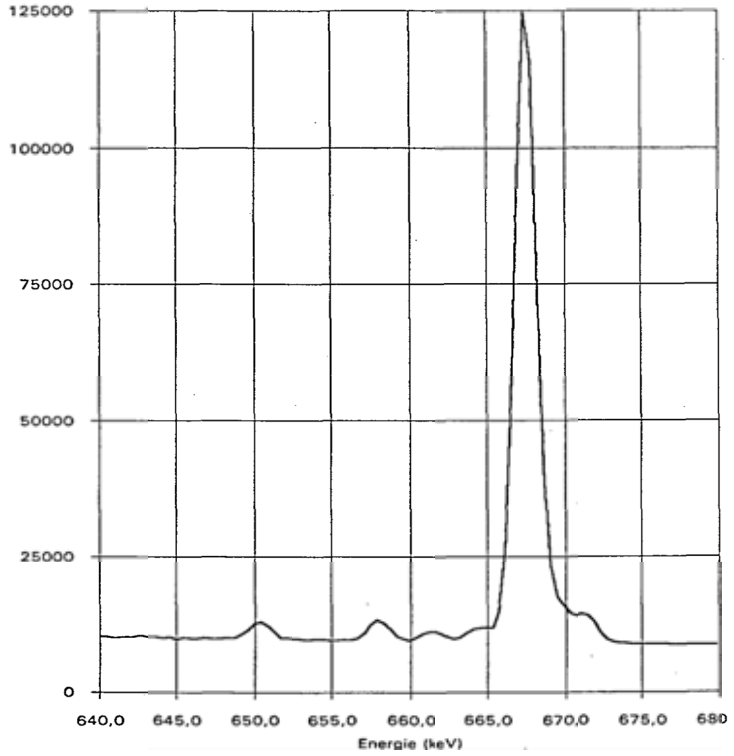

FIG. 5.42. FRJ2-KA2 pebble #3 impulse count vs. energy; 20 mm iron shield, counting time: 5000 s; decay time: 116.8 h; input count rate: 11485 cps; channel width: 0.41 keV.

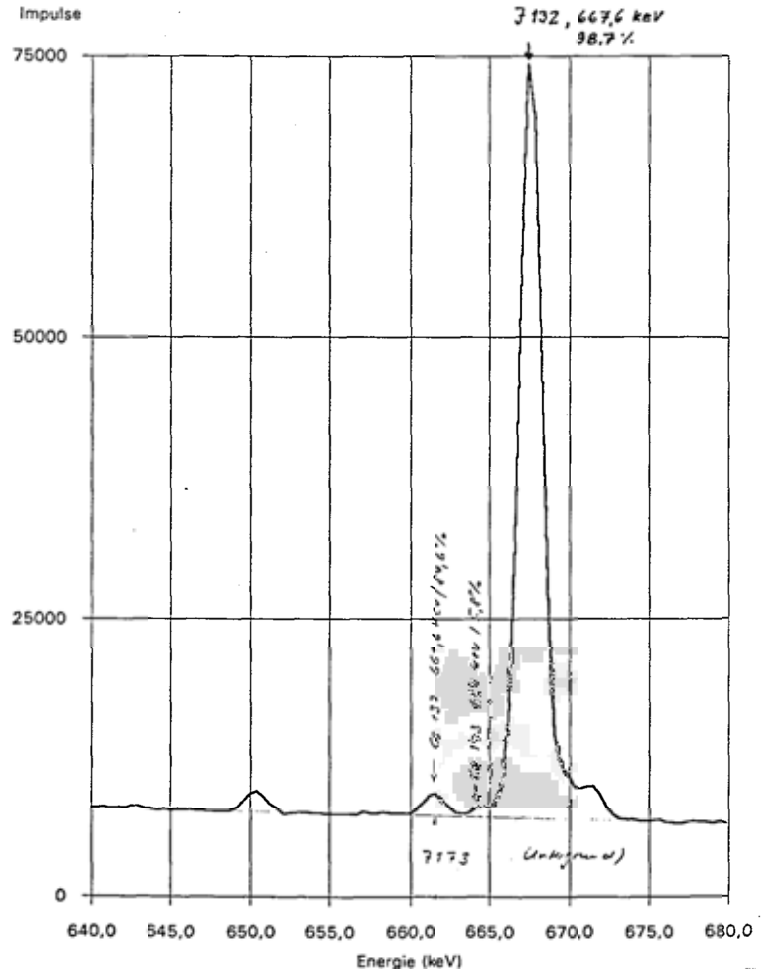

FIG. 5.43. FRJ2-KA2, pebble #3, 20 mm iron shield, counting time: 5000 s; decay time: 181h; input count rate: 9229 cps; channel width: 0.41 keV.

Using different exact laboratory tests, the fuel power had been determined to have been 1450 W. After a lapse of 106 days, i.e. after practically all distorting peaks adjacent to Cs had been completely decayed, the burnup of the fuel was determined to be 2.02% FIMA which is equivalent to 18 900 MWd/t. This value had also been obtained by comparing the fuel's Cs-radiation with appropriate gage elements.

Note, that relevant data for all four measurements are given, such as integral counts, counting time, and the integral pulse rates having to be handled by the detector, and especially by the pre-amplifier and amplifier. Quite obviously, the Cs peak can barely be seen after decay times of 46.32 h and of 117 hours.

Using a detector with a full-width-at-half-maximum of FWHM = 1.8 keV and a channel width of 0.41 keV, the figures show — more or less clearly — the following global data which have been taken from the test records and are collected in Table 5.10.

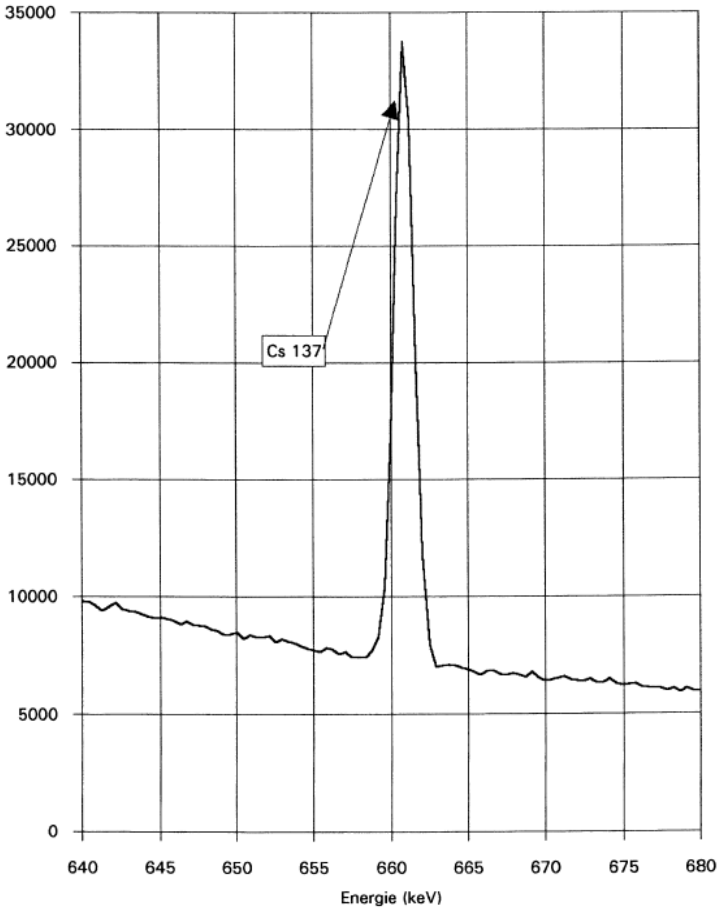

FIG. 5.44. FRJ2-KA2 pebble #3 impulse count vs. energy; counting time: 20000 s; decay time: 2548 h; input count rate: 4090 cps; channel width: 0.41 keV.

TABLE 5.11. GLOBAL TEST DATA OF EXPERIMENT FRJ2-KA2 IN THE DIDO MTR

Mark			I	II	III
Cooling time (h)			46.7	181	2 548 [a]
Counting time (s)			5 000	5 000	20 000
Throughput (cps)			16 908	9 229	4092
Total counts	Isotope	Channel scope			
	Cs-137	1520–1527	—	9 267	102 733
	Nb-97	1511–1518	260 153	—	—
	I-132	1534–1541	862 348	279 372	—
	Ce-143	1528–1531	33 119	—	—
	Background	1520–1531	110 328	57 381	65 680
Relative error of Cs-Peak (%)			—	3.8	0.47
Measured dead-time correction factor			0.880	0.937	0.978

[a] The experiment after 2548 h did not employ the 20 mm thick iron shielding.
— data not available.

From now on, the following further investigations for the burnup measuring system will consider only the test data for the experiments given in Table 5.11. Due to the very stringent conditions, the data of the HTR-Modul were taken as reference.

For reasons of easy comparison, the differences of the fuel irradiation experiment FRJ2-KA2 with the data of the burnt-up fuel from the HTR-Modul are — once again — depicted in Table 5.12.

TABLE 5.12. DIFFERENCES BETWEEN FRJ2-KA2 AND HTR-MODUL

Properties	FRJ2-KA2			HTR-Modul
Fuel power (W)		1450		193
Burnup (GW•d/t)		18.9		80
HM content (g/fuel)		6		7
Decay time (h)	46	181	2548	55
Caesium inventory (GBq)		14.0		77.7
Measuring time (s)	5000	5000	20 000	10

Four differences are immediately striking:

(1) The fuel power in the experiment is approximately 7.5 higher than the power of the 15th pass fuel elements in the HTR-Modul. Since the gamma ray emission of a fuel element is — in the first few days — proportional to the fuel's power and decays with a half-life of ~40 h, the Compton background for an HTR-Modul fuel element of its 15th pass will thus be ~7.5 × 1.15 = 8.6 times lower than in the experiment, if the same experimental parameters were observed. The factor 1.15 takes the different decay times into account (46.7 h versus 55 h).
(2) The Caesium inventory of a burnt-up fuel element in the HTR-Modul will be ~5.6 higher than in the experiment. This increases the Cs peak by the same factor.
(3) The decay time of the fuel extracted from the HTR-Modul will be nearly the same as for the experiment FRJ2-KA2/1 (46.7 h decay time).
(4) The available mean counting time is ~500 times less than the measuring time in the experiment.

When using the same experimental set-up and taking the power ratio of 7.5, one would expect from experiment FRJ2-K15/1 for the HTR-Modul a total number of throughput-counts to be:

$$\frac{16{,}908}{1450} \times 193 = 2250 \text{ counts} \tag{5.9}$$

The background counts below the ^{137}Cs peak are expected to be:

$$B = 110{,}328 \times \frac{193}{1450} \times \frac{10 \times 0.982}{5000 \times 0.880} \approx 33 \text{ counts} \tag{5.10}$$

When considering the somewhat longer decay time, one obtains for the background counts for the HTR-Modul:

$$B = \frac{33}{1.15} = 29 \text{ counts} \tag{5.11}$$

while by taking the measuring data from FRJ2-KA2/2 (see Table 5.11) for a measuring time of 10 s, the net count below the Cs peak would be

$$Cs - peak = 9267 \times \frac{10}{5000} = 19 \text{ counts} \tag{5.12}$$

However, when adjusting for the very different burnups, one finally gets

$$Cs - peak = 9267 \times \frac{10}{5000} \times \frac{2.1}{0.378} = 103 \text{ counts} \tag{5.13}$$

for the net caesium peak of the 15^{th}-pass fuel element.

This would yield an error in measuring the caesium peak of

$$1\sigma = \sqrt{\frac{103 + 2 \times 29}{103^2}} = 12.3\% \tag{5.14}$$

Here one must notice that this error would occur only when using an input count rate of 2250 cps as explained above. But even the equipment used in Jülich for the DIDO irradiation experiment 21 years ago allowed a throughput of at least 17 000 cps. (The preamplifier and amplifier especially built for the HTR-Modul allowed already input rates of >100 000 cps [190]).

Using even only the former Jülich equipment to its fullest extend, the counting error could have been reduced by a factor of

$$\sqrt{\frac{17{,}000}{2250}} = 2.75 \tag{5.15}$$

By using the DIDO counting facility this would already have yielded in 1990 a counting error of the Cs peak of

$$1\sigma = \frac{12.3}{2.75} = 4.5\% \tag{5.16}$$

without having to use the special development of a dedicated preamplifier and amplifier designed for SIEMENS in 1990 [190, 195].

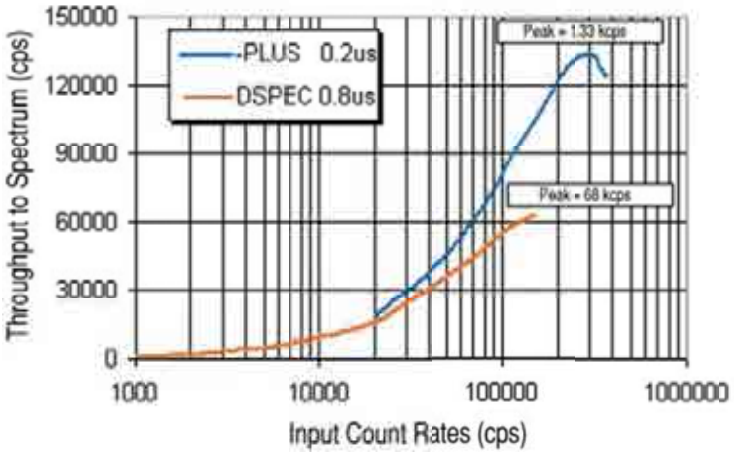

FIG. 5.45. Throughput versus input of the most advanced DSPEC^{PLUS} gamma spectroscopy measuring line (ORTEC) in comparison to the former design DSPEC [196].

Gamma detection systems today have been improved very much, especially the electronic components such as detector, preamplifier, amplifier, analogous to digital converter and the multi-channel analyser. The Ge Digital Gamma Spectroscopy Systems DSPEC^{PLUS} [196] or similar signal processors from CANBERRA [197] are widely used. Figure 5.45 shows the throughput measurements versus the input count rate for two readily available systems. The maximum throughput of the DSPEC^{PLUS} system is about 133 000 cps where the input count rates amount roughly to 300 000 cps having a short shaping or rise time of 0.2 µs corresponding to the blue curve in Fig. 5.45. The energy per channel is ~0.27 keV. This is much better than the equipment used for the FRJ2-KA2 measurements (E = 0.41 keV) and better than the system dedicated to the HTR-Modul in 1990. At this time, one shall carefully deal with the interference from neighboring gamma peaks listed in Table 5.10, which, to unfold overlapped peaks, is not so difficult.

When using a digital spectroscopic system, the point of maximum throughput is the best place to operate. However, for reasons which will become clear somewhat later, for further evaluating the minimum 1σ-error of the Cs peak from the system DSPEC^{PLUS} (see Fig. 5.45) only an input count rate of 100 000 cps is taken. This yields a throughput of ~80 000 cps or a dead-time correction factor of ~0.80.

When using this modern system, the 1σ error for the caesium peak can be further decreased by a factor of

$$\sqrt{\frac{80{,}000}{2250}} = 5.96 \qquad (5.17)$$

instead of the above given factor of 2.75.

For the HTR-Modul, this then would finally yield an error in determining the burnup of the 15th pass fuel element to be:

$$1\sigma = \frac{12.3}{5.96} = 2.1\% \qquad (5.18)$$

Of course, this value covers only the statistical counting error. However, in reality, more errors have to be accounted for, such as equipment stability, shift of counting channels, changes in fuel position, etc. These effects will certainly decrease the accuracy.

However, mainly two effects to further decrease the counting statistics — and, thus, to counterbalance the above mentioned adverse effects — are readily at hand:

(1) Using larger germanium detectors
(2) Determine very early in the counting procedure whether the fuel ball in position will reach the envisaged counts. If not, then the counting time shall be aborted prematurely.

to (1) Using larger detectors

According to the report on FRJ2-KA2 [194], the distance of the collimator from the pebble was set to be 2500 mm, the collimator aperture was 0.8 mm. This yields a solid angle factor of 6.4×10^{-9}. Since the ^{137}Cs inventory of the test fuel was 1.40×10^{10} Bq and the Cs peak was determined to yield 102 733 counts in 20 000 s, the efficiency of the detector can be obtained to be (see Table 5.11)

$$\frac{102733}{20000} \times 1.4 \times 10^{10} \times 6.4 \times 10^{-9} \approx 0.06 \quad (5.19)$$

The used detector had obviously been very small since it detected only ~6% of the incident gamma rays stemming from ^{137}Cs.

Nowadays, one can easily increase this value to ~0.2–0.3 when choosing a larger germanium detector. A larger detector increases the peak-to-Compton ratio decisively and still maintains a favourable resolution. ORTEC gives an increase of this ratio by a factor of 60/40 = 1.5 when increasing the measured efficiency from 5 to 30%. This would reduce the background by the same factor. (Obviously the count rate would increase also; but due to the limitations of the chosen system, the throughput must be kept constant; hence the distance between fuel and detector must be increased accordingly.) A very rough evaluation shows that a reduction in the background by 1.5 would yield an improvement of the 1σ-error of the Cs peak by

$$\sqrt{\frac{103 \times 1.5 + 2 \times 29}{103 + 2 \times 29}} = 1.15 \quad (5.20)$$

This reveals an opportunity to somewhat improve the burnup measurement.

to (2) Premature abortion of counting

Above it was demonstrated from experimental data that one would expect for a burnt-up fuel element of the HTR-Modul a net count for the ^{137}Cs peak when using the nowadays most advanced counting equipment for gamma spectroscopy of

$$Cs - peak = 103 \times \frac{80{,}000}{2250} = 3662 \text{ counts} \quad (5.21)$$

The net background below the peak would be expected to be:

$$Background = 29 \times \frac{80{,}000}{2250} = 1031 \text{ counts} \qquad (5.22)$$

Obviously, in the evolution of passes, the high background for the 1st pass (approximately a factor of 2.27 compared to the final 15th pass, about 2340) gradually decreases, whereas the ^{137}Cs peak gradually increases for each additional pass (approximately by a factor of 10.3 between the 1st pass and the 15th pass, about 355).

The higher background of the first pass is the reason why — even when using the DSPEC^{PLUS} gamma spectroscopy measuring line — the throughput peak of 133 000 cps (corresponding to an input count rates of nearly 300 000 cps) for the 15th pass was not used. Obviously, the spectroscopic measurements would freeze for all passes except for the 15th pass. Therefore only an input count rate of 100 000 cps was used. The needed dead-time correction for higher counts can easily be accounted for by the well known live time correction method.

Nevertheless, it is quite apparent that, e.g. the fuel of the first pass will never reach the expected peak counts of 4693 (= 3662+1031) counts of the 15th pass. Scoping calculations show that the first fuel element will accumulate only ~2695 (= 2340 + 355) counts in the Cs peak region after a counting time of 10 s.

So it is self-evident that one has not to count for 10 s to find out that this fuel element has to be reinserted into the reactor once again. After 1 s, one would expect

$$269 + 1\sigma = 285 \text{ counts}, \qquad (5.23)$$

while for the burnt-up fuel one would expects at least

$$469 - 1\sigma = 447 \text{ counts}. \qquad (5.24)$$

Hence, 9 seconds of counting time can be saved for later use for higher burnt-up fuel elements.

For the second fuel pass, the number of counts expected in the Cs peak region after 10 s is 2933 counts. Here again it is obvious that there is no need to spend 10 s for deciding that also this element must be reinserted into the reactor.

Here, after 1s, one would expect

$$293 + 1\sigma = 310 \text{ counts}, \qquad (5.25)$$

while needing at least 447 counts. Again, one can stop the counting procedure after one second since the count limit of 4693 can not be reached in 10s. Once again, 9 s could be ‘saved’.

Similar arguments hold for fuel elements with only few passes. However, the higher the number of passes the longer one has to count until it is clear whether the fuel element at the measuring position has to be reinserted into the core or whether it has reached its design burnup. However, scoping evaluations reveal that when summing up all the saved counting time from the less burnt-up fuel, one easily gets savings of > 50 s. This time can be used for measuring the high burnt-up fuel more accurately.

This obvious and easy to realize counting technique enables to have much more counting time for the final passes. A factor of 2 should easily be achievable for the last five 'critical' passes. Hence, the 1σ-error in determining the critical burnup can further be reduced by a factor of $\sqrt{2} = 1.44$. This factor can be used to offset the equipment errors mentioned above.

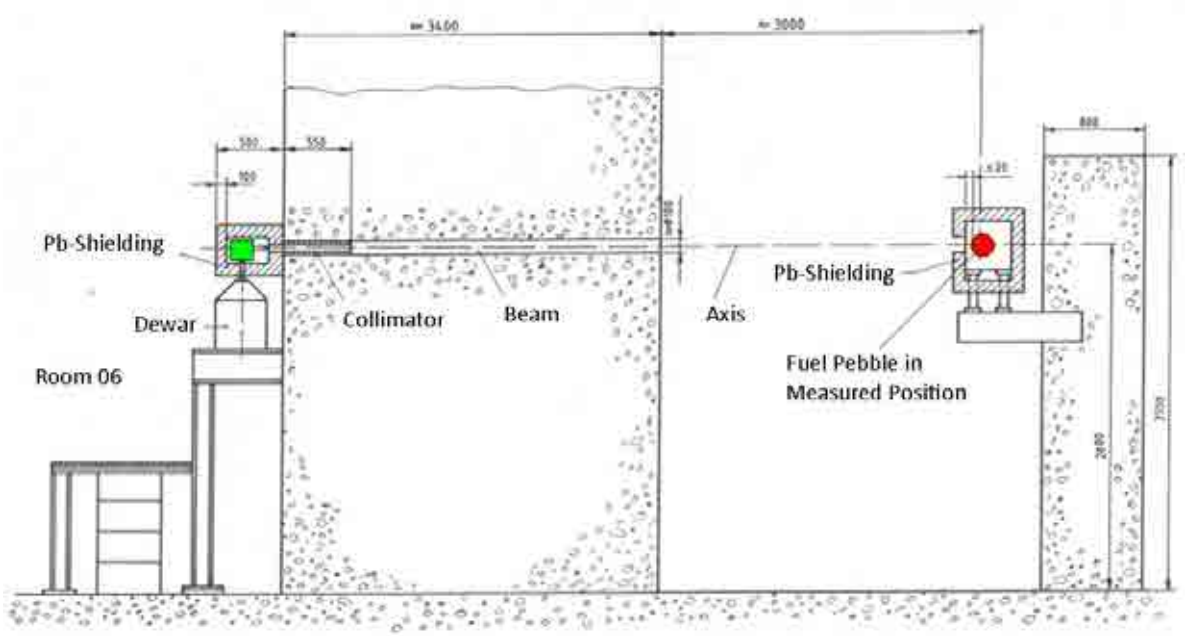

FIG. 5.46. Sketch of the burnup measuring arrangement of the HTR-Modul [195].

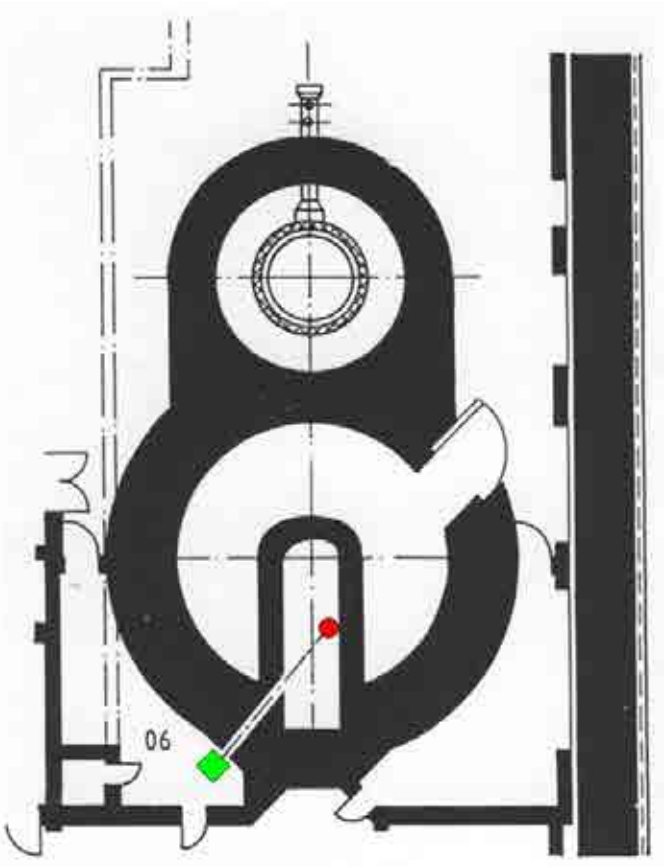

FIG. 5.47. Sketch of the burnup measuring arrangement of the HTR-Modul outside the reactor cavity in a low noise environment [195].

Figure 5.48 shows the theoretical results obtained by INET [198] for the Chinese HTR-PM reactor. One reactor unit has a power of 250 MW and is designed for 15 passes and a decay time of 50 h. These conditions are even slightly more stringent compared to the HTR-Modul since 5978 fuel elements have to be reshuffled per day compared to 5433 for the HTR-Modul. The curve shows very clearly that even for these conditions, the ^{137}Cs peak is unmistakably separated from the neighboring peaks. Its content can readily be determined.

For the used low capacity gamma detection system of 20 000 cps, the error in determining the Cs peak was estimated in [198] to be $1\sigma = 3.5\%$. When using a more modern gamma spectrometer (see above), this value could easily be improved.

As a conclusion, it can be stated that for the very strict conditions of the HTR-Modul, it was demonstrated that the goal set initially for the counting error by the German licensing authorities at $1\sigma < 5\%$ can be met — it even will fall below the set goals by approximately a factor of 2 [195]. The 1σ value of counting statistics for a fully burnt-up pebble, a decay time of 55 h, and an average counting time of 10 s is expected to be $1\sigma \approx 2.5\%$, including not only statistical counting errors but other equipment errors as well.

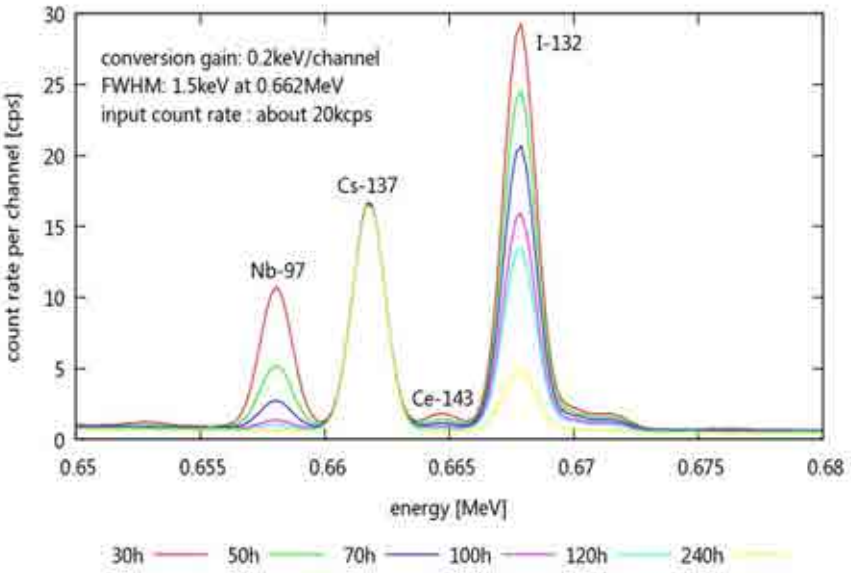

FIG. 5.48. Predicted gamma spectra for the Chinese HTR-PM (using MCNP, KORIGEN) of a pebble after its 15th pass having a burnup of 90 000 MWd/t for various decay times.

Since the Chinese HTR-PM reactor is very similar to the HTR-Modul, the above statement holds also true for this reactor (see Fig. 5.48). It goes without saying that all other proposed pebble bed reactors with less stringed conditions for the burnup measuring device might do even better.

It is significant to note that the obtained results reported here had been derived by experimental results obtained from the German reactor DIDO in Jülich. The experiments had been explicitly carried out in 1990 for the fuel elements anticipated to be used in the HTR-Modul. In 1991, Siemens/Interatom [195] obtained very similar results ($1\sigma \approx 2.1\%$) by using only the data of FRJ2-KA2 with a decay time of 181 h where one clearly can see the Cs peak (see Fig. 5.43 and Table 5.11). In contrast, the above analysis uses many more experimental results given in Table 5.11. However, it is not surprising that the results match very well.

6. PROPERTIES AND PERFORMANCE OF MATRIX MATERIALS

6.1. EXPERIENCE AND DEVELOPMENT IN GERMANY

The graphitic matrix material represents an integral part in the development of the fuel element. It mainly serves as moderator and as structural material protecting the coated particles from outside attacks. But it has also the task of transporting heat from the coated particles to the fuel element surface where it is taken up by the coolant. The key properties of the matrix material are density, strength, and corrosion resistance. Furthermore the neutron irradiation induced shrinkage during operational conditions should be limited.

6.1.1. Matrix properties

The principal properties of the two grades of German matrix materials are summarized in Table 6.1 [59]. Moreover, in special cases, further properties are also investigated.

The desire for the highest possible density of the matrix material results from the need for high mechanical strength of the fuel spheres as structural elements, and also for high thermal conductivity to keep thermal gradients low. A more general reason is to minimize the volume of the moderator material required for a given reactor.

The limitation of the graphitization temperature to < 2000°C requires the use of highly crystalline graphite powder (like natural graphite) as raw material. The mixture of natural graphite with binder was found to be compressible to 1.8–2.0 Mg/m^3, but cracks would occur during the subsequent heat treatment, most probably due to high pressure from gaseous products originating from the binder. Therefore a further component in form of a graphitized powder, which is more difficult to press, was necessary as a filler material with a grain size not too low to avoid to low the mechanical strength (optimal: 50% of grains sized < 32 μm).

For processability, the elastic properties of the natural graphite and graphitized coke powders are of most importance as well as the molecular weight of the resin binder. The elasticity modul and also the thermal expansion coefficient should be low to keep thermal gradients in the material low.

The BET ('Brunauer, Emmett, Teller') surface and porosity are closely associated to the corrosion of the graphite and can be used to identify the type of corrosion. In the case of surface corrosion at high temperatures, BET surface is large in the outer 1–2 mm of the fuel element shell and low elsewhere. In the case of volume corrosion at lower temperatures, BET surface is large in the total sphere.

Material investigations have confirmed that the corrosion resistance of matrix materials is influenced both by the type of binder and by the temperature of heat treatment explaining the differences in the respective data of the table. The porosity of the matrix material, which is formed during the fabrication process can be classified into micro-pores with ≤ 2 nm diameter, macro-pores with ≥ 50 nm diameter, and mesopores as a stage in between. Porosity can be correlated with electrical resistance, thermal conductivity, elasticity modulus, and permeability of the material as well as with the fission product transport behaviour.

Also corrosion has a certain influence especially increasing the open porosity and the BET surface, the latter decreasing again at very high burn-offs. A higher temperature at final heat treatment for the matrix material was found to decrease corrosion rates. With regard to the operational conditions of temperatures varying between 300–1000°C and of pressures between 4–9 MPa, in-pore diffusion is the corrosion rate controlling mechanism. Impurities in the coolant have only a limited effect on the fuel spheres.

TABLE 6.1. A3 MATRIX PROPERTIES COMPARED WITH SPECIFICATIONS

Property	A3-3		A3-27	Required
heat-treated @	1800°C	1950°C	1950°C	
Carbon mass (g)	n.a.	n.a.	n.a.	≥ 190
Geometrical density (kg/m^3)	1700	1730	1740	≥ 1700
Young's modulus (10^4 kN/m^2) ∥	1020	1000	1070	—
⊥	991	970	1020	
Thermal expansion coefficient 20–500°C (10^{-6}/K) ∥	2.80	2.89	2.43	≤ 5
⊥	2.92	3.45	2.69	
Thermal conductivity (W/(m·K))				
@ RT: ∥	59	70	69	
⊥	63	63	64	
@ 1000°C: ∥	38	41	44	≥ 30
⊥	38	37	39	
Specific electrical resistance (10^{-3} Ω cm) ∥	1.56	1.46	1.43	—
⊥	1.60	1.48	1.48	
Falling strength (Number of falls from 4 m height onto A3-3 spheres until fracture)	521	437	652	≥ 50
Corrosion rate (@ 1000°C and 0.1 MPa in helium with 1 vol.% H_2O over 10 h (mg/(cm^2·h))	1.19	0.97	0.73	≤ 1.5
Abrasion (mg/h per sphere)	—	1.81	2.89	
Anisotropy factor	—	1.19		≤ 1.3
Crushing strength (kN) ∥	—	24.9	23.7	≥ 18
⊥	—	23.1	26.3	
Impurities (μg/g)	60 (S:36; Si:6; Ca:4; Cl:3)		32 (Cl:16; Ca:7; Fe:3)	
Ash	50		30	≤ 300
B equivalent	—		—	≤ 1.3
Li	—		—	≤ 0.05

— data not available.
n.a. not applicable.
|| = parallel, ⊥ = perpendicular to the equatorial plane of the matrix sphere.

In a fabrication variant of a cold pre-pressing and a warm final pressing step on laboratory scale, a higher strength of the matrix material was achieved, but a lower thermal conductivity compared to the A3-3 standard. A further drawback, as can be seen in Fig. 6.1, were the relatively large density gradients observed inside the sphere. The difference between minimum and maximum of 0.3 Mg/m^3 was deemed too large such that further R&D efforts were required.

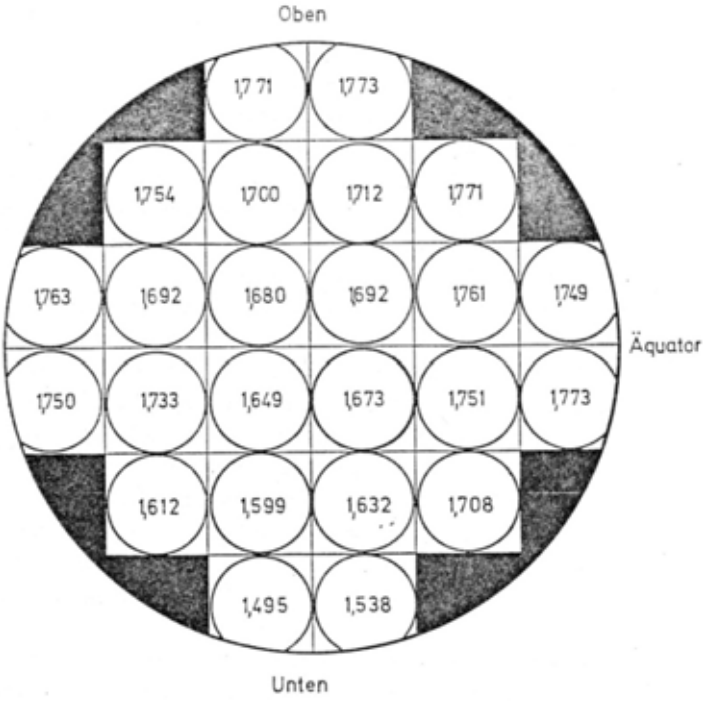

FIG. 6.1. Matrix density (Mg/m^3) distribution measured in a graphite sphere manufactured in a warm-pressing process.

6.1.2. Irradiation behaviour of A3 matrix

Dimensional changes of the matrix material induced by irradiation with fast neutrons occur at temperatures above 300°C primarily depending on fluence, temperature, anisotropy, lattice defects, and the degree of graphitization. The larger the size of the crystallites, which increases with graphitization, the smaller is the dimensional change. The influence of the neutron irradiation on the shrinkage (or swelling) of the matrix material is shown in Fig. 6.2.

Matrix material is geometrically stable with lowest dimensional changes in the temperature range 900–1000°C, whereas shrinkage increases both at lower and higher temperatures. Shrinkage is connected with a density increase. With respect to the THTR operational conditions, shrinkage was found to be changed by 2%, if the irradiation time of 450 efpd at a temperature of 1250°C is reached; the change would even be 2.7% at an irradiation temperature of 1430°C.

The Young's modulus for the matrix material steeply rises at low fluences, passes a maximum, and then decreases again at rates depending on the irradiation temperature.

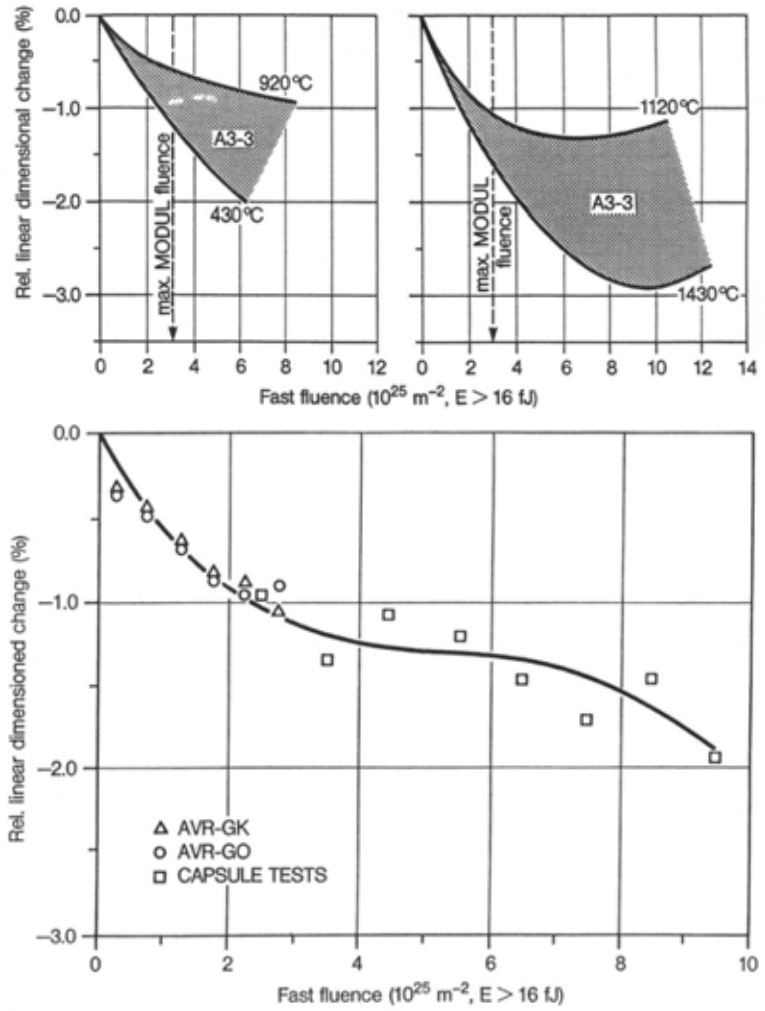

FIG. 6.2. Shrinkage of A3-3 grade matrix as a function of fast neutron fluence at different temperatures (top) and for different fuel spheres (bottom).

The effect of annealing of irradiation-induced dimensional changes is mainly depending on the fast fluence. At lower doses, the annealing causes both the crystallites and the bulk graphite to close cracks and return to their original state. At higher doses, irreversible changes occur due to radiation creep causing plastic flow that cannot be reversed. Internal stresses are then created which may result in more cracks reducing the thermal crystallite expansion.

The total porosity of the matrix material is decreasing upon neutron irradiation, because crystallites are expanding into the micro-pores, and the larger pores serve as buffer volume for the dimensional changes within the bulk material. The extent of the reduction depends on the degree of graphitization. In materials with large crystallites, the reduction is smaller than in less graphitized ones. After passing the turning point of dimensional change, stresses build up which may lead to the formation of new pores and an increase of the porosity, particularly the open porosity. Only beyond a certain neutron fluence depending on material composition and temperature, the open porosity is decreasing again, even below the pre-irradiation value. Figure 6.3 shows the size distribution of the open pore system in the matrix material of a fuel sphere as was measured by mercury porosimetry [199].

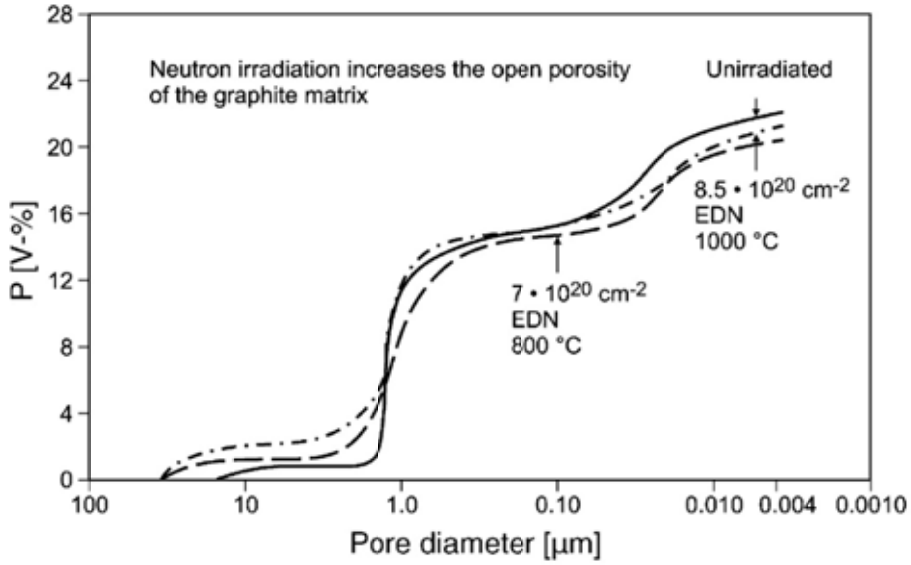

FIG. 6.3. Size distribution of open porosity in unirradiated and irradiated matrix graphite.

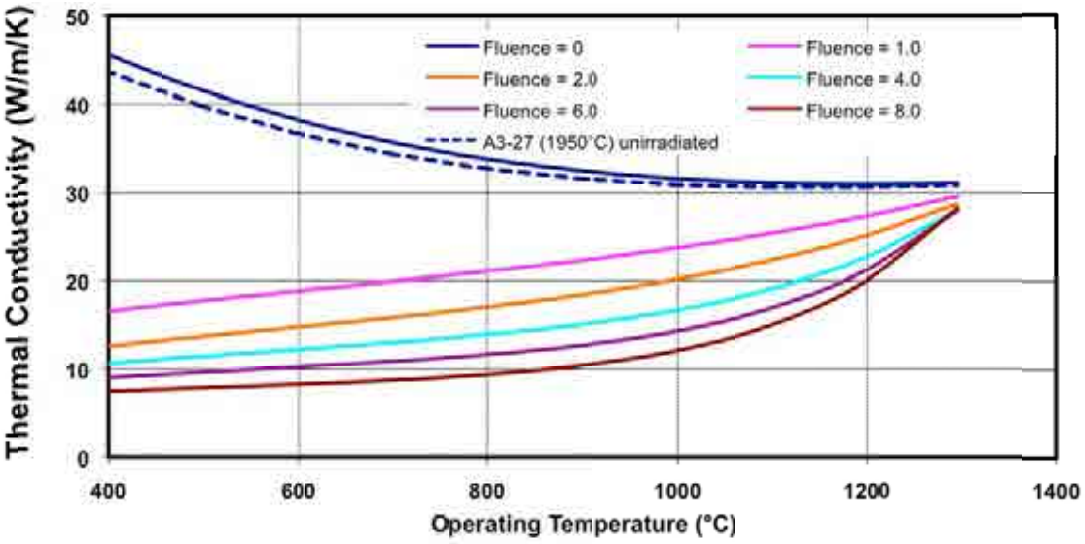

FIG. 6.4. Thermal conductivity of A3-3 heat-treated @ 1950°C as a function of temperature for different neutron doses.

The thermal conductivity which, in the unirradiated state, decreases with increasing temperature, is strongly influenced by neutron irradiation (Fig. 6.4) [53]. It decreases with neutron irradiation due to the increase of lattice defects. As an overall result, it was stated that the behaviour of matrix material under neutron irradiation is well understood. The A3-3 standard material was judged to be of good dimensional stability and behaves isotropically even under extreme irradiation conditions.

6.1.3. Fission product diffusion in A3 matrix

The transport behaviour of fission products by diffusion in matrix material is principally depending on the temperature, but there are various other influencing parameters such as graphite type and nature, coolant gas pressure, state of oxidation, irradiation damage, fission

product concentration, their bonding to the graphite surface, or interference with other fission product species.

The use of effective diffusion coefficients, i.e. the assumption of the Fickian diffusion model, is a simplified simulation of the transport mechanism. At least for caesium, a trapping mechanism was found to describe more realistically the transport process in graphite [200]. The diffusion/trapping/re-emission model assumes that migrating particles are captured in traps for some time, before they are re-emitted and become mobile again. Traps are uniformly distributed, predominantly in the polymeric binder carbon (due to its numerous adsorption sites), and do not lose their trapping character if occupied. The processes are described by a trapping coefficient, μ, and a re-emission coefficient, b, whose reciprocal values indicate average times of a particle to be trapped or mobile, respectively. Under quasi-equilibrium conditions, the trapping-emission process approaches the Fickian diffusion process with the effective diffusion coefficient

$$D'_{eff} = \frac{D_{eff}}{1 + \mu / b} \tag{6.1}$$

It was observed, however, that the traps for caesium disappear, if the matrix material was slightly oxidized (up to a weight loss of 0.3%) due to opening of pores [200].

Comparative measurements with A3-27 type material at 1000°C showed that the diffusion coefficient for caesium was lower by a factor of 20 in relation to A3-3 material. In addition, FRESCO postcalculations of heating tests indicated that for A3-27 materials a reduction of the A3-3 diffusion data for caesium (and strontium) could be reduced by at least a factor of 10 in the accident temperature range 1600–1800°C.

Silver transport measurements were done on ^{110m}Ag-doped specimens of as-received, oxidized, and irradiated A3-3 as well as on as-received A3-27 matrix at temperature values in the range of 850–1300°C [201]. It was observed that Ag mainly concentrates on the binder material rather than the graphite grains. For all types investigated, the silver transport behaviour was found to be conform with the classical Fickian diffusion. Silver transport data in A3-27 were measured to be lower than in A3-3. Also for strontium transport in matrix material, the classical (effective) diffusion behaviour was observed [202].

With regard to iodine, a certain trapping effect in graphite materials has been identified in the lower temperature range mainly based on the perception that the heavy metal contamination and the iodine, respectively, originating from it, is buried in the graphite grains connected with a comparatively slow transport process outwards to the grain boundaries, from where there will be a fast transport, i.e. no hold-up in the fuel element matrix. Under accidental conditions, the iodine transport is usually treated conservatively as to be fast in analogy to fission gases.

As a result of numerous FRESCO postcalculations of heating tests with spherical fuel elements, for safety analysis purposes, the classical Fickian diffusion is considered sufficiently correct and conservative. This could be demonstrated when the ten heated fuel spheres, for which a post-heating deconsolidation was made, was evaluated with respect to caesium and three spheres with respect to strontium. Figure 6.5 shows the calculated concentration profile of ^{137}Cs in the fuel element matrix for the example of three heating tests.

For sphere AVR 71/22, low concentrations were measured indicating no significant release from the coated particles, whereas the particles in both HFR-K3 are at the end of the heating test in a stage of highly releasing caesium. Respective profiles calculated with the FRESCO code (where the caesium release from the coated particles into the matrix was adjusted to the measurements in order to isolate the diffusion transport in the matrix) show a very good agreement with the measurements. It means that the 'effective' diffusion approach is sufficiently well describing caesium transport behaviour in matrix material.

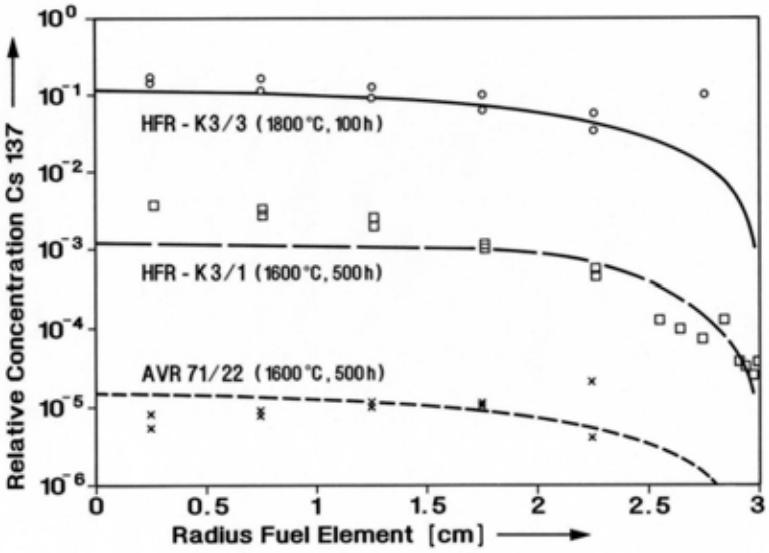

FIG. 6.5. Comparison of caesium profile measurements for heated fuel spheres with FRESCO postcalculations (with adjusted release from coated particles).

6.2. DEVELOPMENT IN FRANCE

A part of the VHTR programme at CEA was to study the aspects of the graphite life cycle including selection of eligible graphite grades, behaviour during operation and post-irradiation management [203]. Requirements for graphite to be used in nuclear applications include mechanical properties, thermal properties and physico-chemical properties, both before and after irradiation. The main items to be studied on selected graphite grades are the mechanical, thermal, structural properties before irradiation, and the physico-chemical properties.

Impurities are a major concern with regard to the nuclear use of graphite. Some impurities can have significant impact on neutron flux, such as boron or cadmium, while others may produce undesirable isotopes. In particular, feedback from the former French CO_2 cooled reactors has driven attention to ^{36}Cl and ^{14}C, which represent the main constraint with regard to graphite disposal as waste. Actually, ^{36}Cl is an activation product of chlorine which is used to remove other impurities from the graphite. On the other hand, it appears that the main production source of ^{14}C in graphite is the activation of nitrogen when its concentration reaches values > 50 ppm. Various graphite grades are already available which may fulfill nuclear standards. These graphite grades can be classified according to the precursor (petroleum or pitch coke), to the process (extrusion, isostatically moulding) and to the grain size. In the project HTR-M, part of the 5th FP of the European Union, some grades were selected as promising for HTGR applications.

6.2.1. Irradiation effects on mechanical and physical properties: present status and needs

Mechanical and thermal properties of graphite are modified under neutron irradiation. Two particularly important property changes for the core lifetime integrity are dimensional changes and irradiation creep. Figure 6.6 shows the irradiation-induced dimensional changes for the graphite grade P3JHAN [203].

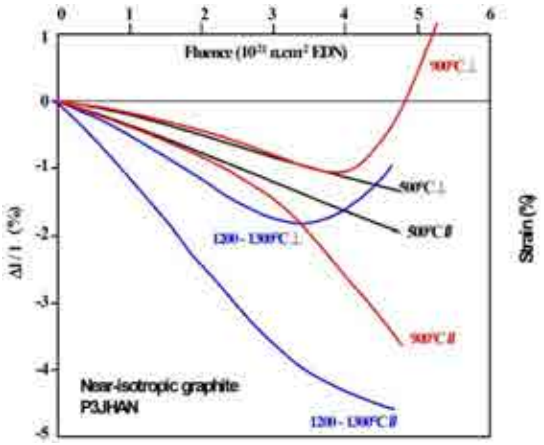

FIG. 6.6. Dimensional changes of P3JHAN graphite under irradiation.

The figure shows that when a near isotropic polycrystalline graphite is irradiated above 300°C, it initially shows a shrinkage in both parallel and perpendicular direction, which increases with neutron fluence. The shrinkage slows down toward a 'turn-around' point, after which the graphite swells back to its original volume and goes beyond.

The graphite dimensional changes depend on irradiation temperature, coke anisotropy, grain size and graphitization temperature. For near-isotropic graphite, minimum shrinkage occurs at an irradiation temperature of about 700°C. The more isotropic the coke, the smaller is its dimensional change.

Dimensional changes are smaller for highly crystalline graphite which implies a large crystallite size and a high graphitization temperature (2800–3000°C). The end-of-life of an old grade of near-isotropic graphite is about 8 dpa (graphite) in the temperature range 1000–1100°C.

While thermal creep of graphite is known to be quite negligible up to about 2000°C, irradiation creep is very significant from temperatures as low as 100°C.

- The so-called primary creep occurs only at low fluences. During this stage, the strain rate of graphite decreases continuously with time and suppression of the applied stress during irradiation implies the elimination of all irradiation creep strains. Thermal annealing leads to the same effects. Only few scattered values for the primary creep constant are known but it seems to increase with temperature.
- The secondary stage of irradiation creep matches with a steady state characterized by a constant strain rate. All strains created during this stage are permanent and cannot be eliminated if the applied stress is suppressed.

Another property which strongly changes with neutron irradiation is the thermal conductivity (Fig. 6.7, left) [203].

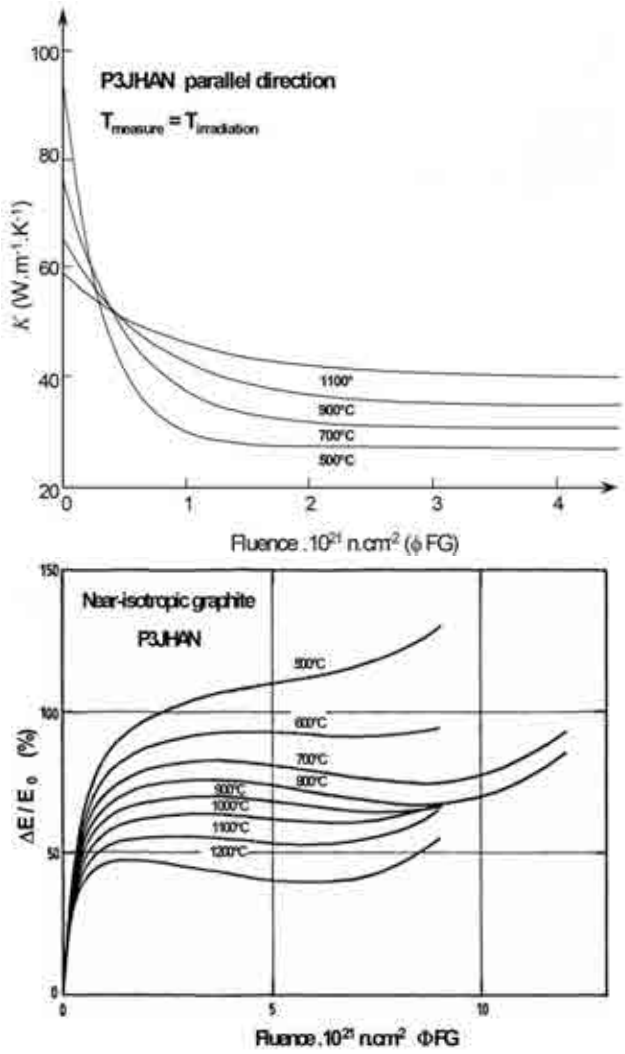

FIG. 6.7. Thermal conductivity (left) and Young's modulus (right) as a function of neutron fluence for graphite grade P3JHAN.

The decrease of thermal conductivity generally observed is due to vacancies in the basal plane and vacancies loops above 500°C. A change occurs already at doses as low as 10^{-3} dpa (graphite) and decreases with increasing irradiation temperature.

Changes of Young's modulus are due to dislocations pinning of by interstitial clusters. As shown in Fig. 6.7, right, Young's modulus increases quickly at the beginning of the irradiation then saturates at a neutron fluence ranging from 0.5 to 2 × 10^{25} n/m^2 [203]. The ΔE/E ratio is higher for the lower irradiation temperatures between 600°C and 1200°C. Generally it is observed that graphite mechanical strength increases under neutron irradiation; strength and Young's modulus are linked by the relation:

$$\frac{\sigma_i}{\sigma_0} = \left(\frac{E_i}{E_0} \right)^n \tag{6.2}$$

where n = 0.5 for 500°C ≤ T_{irr} ≤ 900°C; and n = 1 for T_{irr} > 900°C.

The importance of these irradiation effects demands similar studies on modern grades to be selected for VHTR applications.

6.2.2. Effect of oxidation on graphite behaviour in normal and accidental conditions

One of the key concerns with graphite is its reactivity with oxidizing species, especially at high temperatures. Originally, CEA studies on graphite oxidation were concentrating on accidental conditions, i.e. massive air ingress in the primary coolant. But also new studies were considered to include long term behaviour of graphite in a representative atmosphere of the VHTR. Oxidation studies are performed using thermo-gravimetric analysis and the 'Oxygraph' facility.

The thermo-gravimetric device allows studying graphite samples up to 5 g. The gases produced during oxidation are measured on-line using micro-gas chromatography and mass spectrometry. This facility allows performing parametric studies linked to oxidation kinetics: effect of graphite grade, effect of temperature, effect of gas composition. First results confirmed that the oxidation rate is very small below 600°C (chemical regime), and increases sharply in the diffusion regime of 600–1000°C. At higher temperatures, only a small evolution of corrosion rate is observed.

Grade to grade variations are significant only in the diffusion regime (800°C) where the micro-structure, and particularly the porosity, play an important role. In the 'chemical regime', an effect of the minor elements could be expected via their properties of oxidation catalyst. Indeed, this effect is efficient only if the amount of catalysts is sufficient. In fact, regarding the different grades examined here, the small amount of impurities present in all graphite samples cannot play an important role on oxidation. At high temperatures, and in agreement with the theory, graphite variability has less influence on the oxidation rate, since this is governed by mass transfer in the gas phase.

The 'Oxygraph' facility is devoted to the study of graphite behaviour in case of air ingress in the primary circuit of an HTGR. It consists of a vessel where a graphite sample of about 400 g is oxidized at temperatures up to 1200°C. The sample is actually an electrode, through which a current is sent to reach the expected temperature. Other components in the circulation loop are a cooler (to cool the gas down to 50°C), a circulator, and a heater (to reach 400°C). 'Open-loop' tests simulate oxidation with infinite air source. In this case, the circulating loop is not used, and the oxidizing gas is injected close to the sample, the gas products being released to the outside. In 'closed-loop' tests simulating oxidation with limited amount of air, the intention is to study the equilibrium states in the circuit according to the oxidizing conditions. In these cases, the vessel is connected to the circulating loop. During oxidation, the gaseous products are monitored on-line, using micro-gas chromatography and mass spectrometry. Additionally, gas is periodically sampled during the experimentation and analysed in the laboratory. Preliminary results allow assessing the amount of corrosion that needs to be dealt with in the case of massive air ingress and are in good qualitative agreement with the thermogravimetric analyses.

6.2.3. Post-irradiation management

In terms of quantity, graphite represents the largest amount of waste from an HTGR, with up to 10 000 tons (depending on design and replacement frequency for fuel blocks and replaceable reflectors) to be disposed of during and after reactor life. Two options of disposal have been investigated by CEA: re-use of the irradiated graphite in the nuclear industries, or disposal as final waste. In order to re-use irradiated graphite, various innovative processes have been under investigation, including healing the blocks, or conversion into another carbon based material, such as SiC. Final disposal of irradiated graphite could be done through

graphite destruction (for example, by burning and gas treatment) or direct disposal, as was done for the former French CO_2 cooled reactors.

6.3. EXPERIENCE AND DEVELOPMENT IN JAPAN

6.3.1. Graphitic material for the HTTR

The structural graphite IG-110 produced by Toyo Tanso has been used in Japan for the fabrication of the prismatic fuel blocks and the sleeves of the fuel rods in the HTTR. It is a highly purified, fine-grain petroleum coke graphite with a density of 1760 kg/m^3. It is produced by isostatic rubber pressing at very high pressures and exhibits semi-isotropic properties. The matrix material A3-3 (see section 'Germany' in this section) has been used in the fuel compact fabrication in form of an overcoating for the coated particles. Thickness of the overcoating (~200 μm) was selected such that after pressing of the annular shaped compacts, the required packing fraction of 30% was obtained. Final heat treatment of the fuel compacts is at 800°C in N_2 atmosphere and 1800°C in vacuum to degas the fuel compacts.

The fuel compacts are produced by the warm-pressing of the coated fuel particles with graphite powder. In the first step, coated fuel particles are overcoated by resinated graphite powder with alcohol. The resinated graphite powder is prepared by mixing electrographite powder, natural graphite powder, and phenol resin as a binder in the ratio 16:64:20, followed by grinding the mixture to powder. The aim of the overcoating is to avoid direct contact with neighboring particles in the fuel compact. The thickness of overcoating layer is about 200 μm, which is determined by the specification for the volume fraction of the coated fuel particles in the fuel compact (30 vol.% for Japanese HTTR fuel). Then the overcoated particles are warm-pressed by metal dies to form annular green fuel compacts. The final step of the compaction process is the heat treatment of the green fuel compacts at 800°C in flowing N_2 to carbonize the binder and at 1800°C in vacuum to degas the fuel compacts [18]. The fabrication flow of the fuel compact was already described in Section 3.5.3 [63].

6.3.2. Fuel graphite block of HTTR

The HTTR applies pin in block type fuel element with hexagonal graphite block which is 360 mm in width across the flats and 580 mm in length. IG-110 graphite (Toyo Tanso Co.), fine grained isotropic graphite, is used for the fuel element. It was developed for the core components and core support components of the HTTR with collaboration between the JAEA and Toyo Tanso Co.

Since the in-core graphite components are subjected to various cyclic stresses caused by thermal/irradiation-induced loads during reactor operation, it is necessary to keep enough safety margins for the component design. For this purpose, it is important to use high strength graphite with small variation of material properties [204]. The typical material properties of IG-110 are shown in Table 6.2 [205]. In comparison with medium-to-fine grained PGX graphite, IG-110 has superior thermo-mechanical properties.

TABLE 6.2. TYPICAL THERMO-MECHANICAL PROPERTIES OF GRAPHITE (UNIRRADIATED AND UNOXIDIZED CONDITION

Property	IG-110	PGX
Bulk density (kg/m^3)	1780	1730
Mean tensile strength @ RT (MPa)	25.3	8.1
Mean compressive strength @ RT (MPa)	76.8	30.6
Young's modulus @ RT (GPa) (1/3 Su [a])	7.9	6.5
Mean thermal expansion coefficient (20–400°C) (10^{-6}/K)	4.06	2.34
Thermal conductivity (W/(m·K))	80	75
Ash (wt-ppm)	max 100	max 7000
Grain size (μm)	mean 20	max 800

[a] determined from the joining two points (one point is one third of specified minimum of tensile strength and the other is one third of specified minimum strength) on the stress–strain curve.

The production process of IG-110 graphite is shown in Fig. 6.8 with inspection works defined by the criteria for the HTTR [206] which are determined to meet the specifications as well as to assure the material identification. The process parameters and product characteristics are strictly measured and controlled on each process to meet the requirements. IG-110 graphite blocks for HTTR in-core components were provided through the manufacturing process with stable property, high purification process and highly accurate machining by the Japanese company Toyo Tanso.

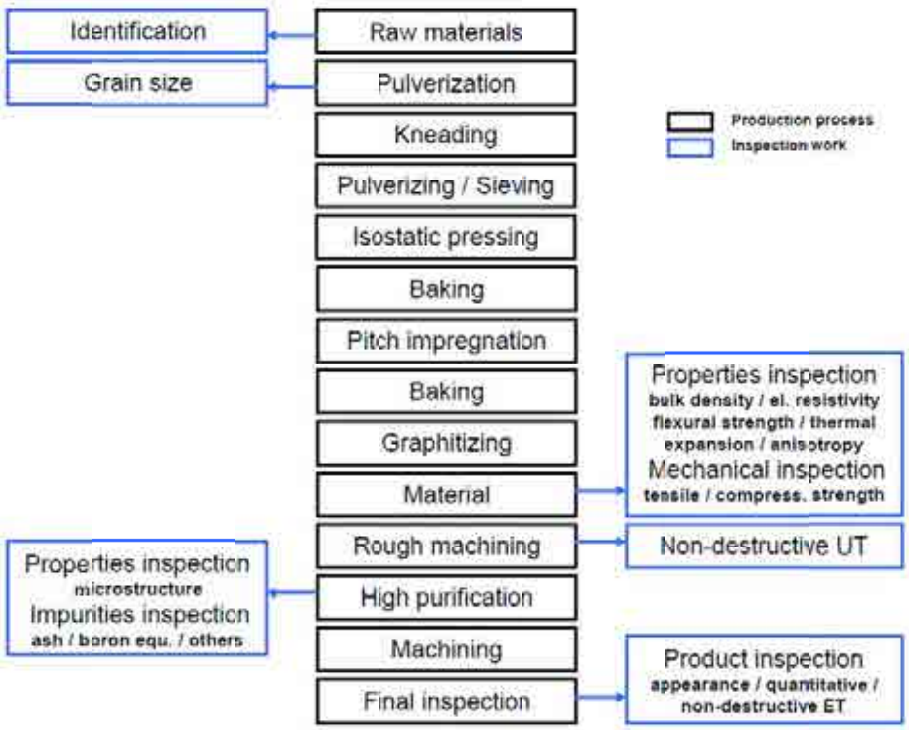

FIG. 6.8. Production process of IG-110 graphite and inspection items.

6.4. EXPERIENCE AND DEVELOPMENT IN RUSSIAN FEDERATION

6.4.1. Previous development of matrix materials

Russian HTGR designs (VGR-50, VG-400, and VGM) were developed in the 1970–1980s with pebble bed core using spherical fuel elements with 60 mm in diameter and evenly distributed TRISO coated fuel particles in a graphite matrix. Fuel elements service conditions and requirements are summarized in Table 6.3.

Operating conditions for the fuel elements are complicated by the presence of friction and contacts between fuel elements, the mechanical influence of absorbing rods, the necessity of frequent transportation by pipelines outside the reactor core (VGR-50), corrosion and erosion attack of the coolant and others [207]. Spherical fuel elements, first of all matrix material, should meet severe requirements on physical, mechanical and thermo-physical properties. It should have a density ≥ 1.8 Mg/m^3, thermal conductivity ≥ 20 W/(m·K) at a temperature of 1000°C, strength (fuel element crushing strength) ≤ 20 kN, high purity (physical factor ≤ 1.6), and radiation stability.

TABLE 6.3. HTGR SPHERICAL FUEL ELEMENTS SERVICE CONDITIONS AND REQUIREMENTS

Characteristics	VGR-50	VG-400	VGM
Fast neutron fluence (10^{25} n/m^2 , E > 0.18 MeV)	1.2	1.7	1.3
Burnup (% FIMA)	10–15	≤ 8	10 (max)
Maximal temperature of fuel (°C)			
Nominal	1300	1250	1250
Accident	1600 (5–10 h)	1600 (5–10 h)	1600 (100 h)
Number of thermal cycles	≤ 2000	≤ 200	up to 15
^{235}U content in a fuel element (g)	0.5	0.4	0.56
Enrichment (%)	21	6.5	8
Compressive stress (kN)	≤ 15	≤ 20	≤ 20
Average erosion rate (mg/(cm^2·h))	$\leq 4 \times 10^{-2}$	—	—
Permissible fission gas products release (R/B)	$\leq 10^{-4}$	$\leq 10^{-5}$	$\leq 10^{-5}$

— data not available.

6.4.1.1. Matrix material

Graphite based compositions consisting of 80% graphite and 20% binder were used for manufacture of a fuel elements matrix material. The matrix material properties are mostly governed by the graphite filler properties [208, 209]. This is a result of that it constitutes the major volume fraction and undergoes minimum modifications in the course of fabricating a fuel element. Simultaneously, also the binder material appreciably contributes to the fuel element final parameters since affects the MM structure obtained after heat treatment, when compacted. Screening of candidate materials for a graphite matrix composition and considering requirements to a matrix material (a combination of high physical, mechanical and thermo-physical characteristics) are required to carry out complex R&D to develop processes of its preparation, compacting, and heat treatment.

(1) Filler graphite

Two grades of Russian artificial graphites having low content of ash residue were investigated: 3OPG (graphite based on calcinated petroleum coke) and MPG (fine-grained graphite based on non-calcinated coke) [208, 209]. In Table 6.4, these materials main characteristics are presented. Analysis has shown that the MPG type graphite filler possesses a higher strength and lower anisotropy in physical properties.

(b) Binder

To fabricate the matrix material, two kinds of coal-tar pitches were used: mid temperature grade with a 65–70°C softening point and high temperature grade (143°C softening point) [208–210]. Both grades of pitches were used either individually or as intermixture.

TABLE 6.4. CHARACTERISTICS OF GRAPHITES

Property	3OPG	MPG
Density, γ (Mg/m^3)	1.80	1.74
Thermal expansion coefficient, α, ||	3.1	5
@ 77–293 K (10^{-6} K^{-1}) $\perp$	3.6	4.8
Effective thermal conductivity, λ_{eff} [a] @ 250°C (W/(m·K))	101	64
Spec. electrical resistance, ρ ($\mu\Omega$·m) ||	9.3	12.4
$\perp$	7.5	10.4
Compression strength, σ_c (MPa)	42	100
Bending strength, $\sigma_в$ (Mpa)	22	45
Anisotropy factor, K_α	0.86	1.04
Graphitization degree	0.85	0.7
Ash content (wt%)	< 0.03	< 0.03
Impurities (wt%) B	3×10^{-5}	1×10^{-5}
Fe	3×10^{-3}	$(1–3) \times 10^{-3}$
Si	5×10^{-3}	$(1–3) \times 10^{-3}$
Mn	1×10^{-4}	1×10^{-4}

[a] λ_{eff} measured by ultrasonic method giving averaged (effective) values without connection to moulding axis.

|| = parallel, $\perp$ = perpendicular to the axis of blank moulding.

6.4.1.2. Preparation of matrix materials and investigation of their properties

The developed scheme includes the steps of preparation of powders (milling and screen-sizing), intermixing of matrix material components, forming press power (milling and bolting). Conventional for the powder metallurgy equipment was employed (jawbreaker, impact-centrifugal mill, ball mill, mixers (Z-shape-paddle mixer, heated rolls) and screen classifiers.

At the stage of investigation of milling conditions of starting coarse ground fillers 3OPG or MPG, the modes providing necessary degree of powders dispersion, in particular, 2-3 powder fractions with particle size from 16 to 1000 μm have been developed (Table 6.5). The following investigation of these powders compactibility has allowed determining the necessary fractional makeup. The compositions B, S, F were approved while fabricating the experimental specimens by technique used for manufacture of the spherical fuel elements

(baking combined with moulding i.e. carbonization under pressure (CUP method). The achieved density of matrix material for the compositions of F and S was 1.76–1.80 Mg/m^3.

Investigations showed a possibility of an additional effect in respect of matrix material properties due to regulating a shape of filler powder particles at the stage of their preparation. The special modes of filler powder treatment permitted to obtain a more isometric and roundish shape of powder particles than usually observed (Fig. 6.9).

TABLE 6.5. FRACTION CONTENT PROVIDING MAXIMAL PACKING OF POWDER PARTICLES

Composition index	Sieve analysis (μm)			
	-1000 +400	-400 +200	-200 +100	-50
B	—	—	40– 60 wt%	60–40 wt%
S	—	45–60 wt%	—	55–40 wt%
F	33–51 wt%	—	17–5 wt%	38–48 wt%

— data not available.

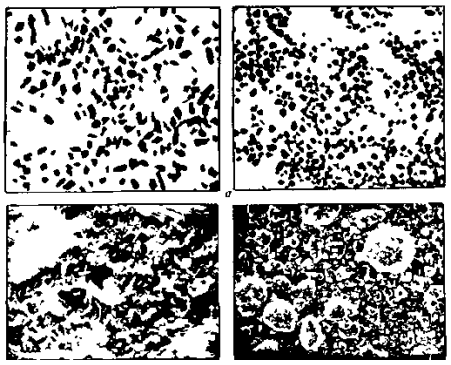

FIG. 6.9. Traditional (left) and improved (right) shape of artificial graphite powder particles: (a) -200 + 400 μm powder (x10) fraction; (b) -50 μm (x400) fraction.

The powder samples microscopic analysis, for example, of fraction -400 + 200 μm, has shown possibility to decrease an anisometry factor from 1.67 (usual powders) to 1.33 (processed) and accordingly to decrease the fraction of particles with irregular shape from 45–85 to 15–40 wt%. Globular structures appear among particles of -50 μm fraction powder (see Fig. 6.9b) . The consequence of particles shape change was the further increase of compactibility and decrease of elastic after-effect of graphite powder filler (for grain composition S example, Fig. 6.10) allowing to increase based on it matrix material density, to decrease change of density in blank volume and to reduce molding pressure necessary for maximum density of green blank.

The press-composition filler formulation for preparation of matrix material was based on the powder with rounded shape particles of S composition (see Table 6.5). Binder content in a matrix composition was from 18 to 20 wt%. Essential influence on affinity of press-composition components alongside with a binder composition is rendered with structural and other characteristics of graphite-filler depending on its technological background. In the context of a press-composition with optimum filler particles size distribution, improved powder particles morphology and a binder composition, the routes of manufacture of spherical specimens 60 mm in diameter from a matrix material by CUP process based on double-action compacting of press-powders has been realized at pressure 10 MPa with the following carbonization under pressure (20 MPa) up to temperature 550°C and final heat treatment in argon atmosphere at 1800°C. The prepared matrix material (indexes compositions of MM-3OPG and MM-MPG) being in essence a carbon–graphite composite with 85% of graphitized filler and 15% of coke (Table 6.6) has high density (γ) and low degree of anisotropy of thermal expansion (K_α). The largest value of the latter (1.15) had MM-3OPG.

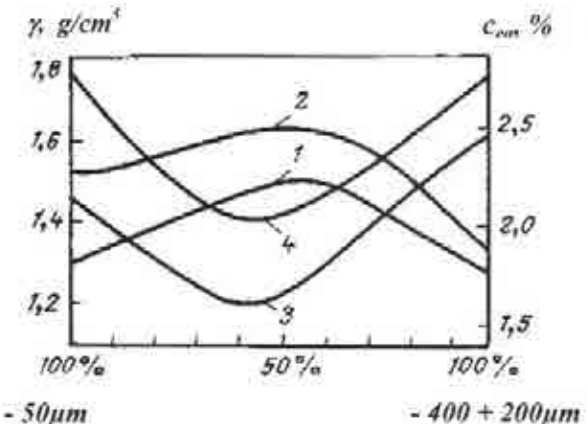

FIG. 6.10. Dependence of powder–filler compactibility on powder particles size distribution and shape at pressure 15 MPa:1, 4: compactibility (density) and elastic after-effect (Cea) of powders with particles of irregular shape; 2, 3: the same for powders with round shaped particles;Cea = (Δh/h) ·100% where Δh is a pure gain of height of powder compact after pressure removal and h the compact height under pressure.

TABLE 6.6. PROPERTIES OF THE MATRIX MATERIALS

Property	Matrix material		Required
	MM-30PG	MM-MPG	
Density, γ (Mg/m^3)	1.89	1.87	≥ 1.80
Modulus of elasticity, E, @ 20°C || (10^4 Mpa) ⊥	0.99 0.93	1.13 1.12	—
Thermal expansion coefficient, α || @ 77-293 K (10^{-6} K^{-1}) ⊥	3.8 3.3	4.0 3.9	—
Effective thermal conductivity, λ_{eff}[(a)], @ 250°C (W/(m·K))	78	82	≥ 20 @ 1000°C
Specific electrical resistance, ρ, (μΩ·m) || @ 20°C ⊥	15.1 12.4	17.3 17.1	—
Bending strength, σ_b, @ 20°C (MPa) || ⊥	24 28	38 45	—
Compression strength, σ_c, @ 20°C (MPa) || ⊥	80 —	90 110	
Crushing strength, P_c (kN)	27	39	≤ 20
Abrasion (mg/h)	1.40	0.93	—
Falling strength (number of falls from 1 m height on steel plate until fracture)	> 3000	—	—
Anisotropy factor, K_α	1.15	1.02	—

[a] λ_{eff} measured by ultrasonic method giving averaged (effective) value without connection to moulding axis.

— data not available.

|| - parallel, ⊥ - perpendicular to the axis of moulding sphere.

Due to the presence of the non-graphitized pitch coke second phase, the specific electrical resistance (ρ) of matrix material is much higher in comparison with initial graphite-fillers. At the same time, the thermal conductivity (λ) correlating with ρ at 250°C is lower for compositions based on 3OPG and is higher for based on MPG compositions in comparison with initial graphite. In the latter case, thermal conductivity of matrix material is better due to its higher density than of filler. Thermal conductivity of matrix material and graphite, as measurements have shown, become approximately the same at temperature near to 1000°C.

CTE (α) values of a matrix material are receivable. Good thermophysical characteristics in a combination with strength, which is higher (matrix material 3OPG) and comparable (matrix material MPG) with initial graphite (see Tables 6.4, 6.6), and isotropy define high thermal strength of matrix material especially based on non-calcinated coke. The results of matrix materials analyses on impurities content limited by neutronics requirements and corrosion stability are shown in Table 6.7.

TABLE 6.7. CONTENT OF IMPURITIES IN MATRIX MATERIAL (wt%)

Material	ММ-30ПГ	ММ-МПГ
B	1.0×10^{-5}	1.0×10^{-5}
Cd	3.7×10^{-5}	2.6×10^{-5}
Gd	2.5×10^{-5}	8.0×10^{-5}
Co	1.9×10^{-5}	7.5×10^{-5}
Mn	2.3×10^{-5}	9.5×10^{-5}
Fe	8.9×10^{-3}	9.8×10^{-3}
Ni	8.4×10^{-5}	1.4×10^{-4}
Ti	5.2×10^{-3}	6.5×10^{-3}
V	1.2×10^{-5}	8.1×10^{-6}
W	1.9×10^{-4}	4.3×10^{-6}

Additional graphite balls chlorine processing followed by finishing heat treatment in vacuum at 1900–1950°C provides decrease in iron content in a matrix material at the level of $< 6 \times 10^{-4}$ wt% and ash residue ≤ 0.01 wt%.

The micro-structure of a matrix material (Fig. 6.11, left) is specified by distinct phase boundary between filler and binder, reminding initial graphite-filler micro-structure. It consists of the same elements (grains, layer of a binder of coke, voids), as graphite filler. Fine voids and uniform structure of MPG type graphite predetermine similar structure of a matrix material on its basis. Due to the greater affinity of pitch coke to this type filler, the phase boundary is blurring, large grains of 200–400 μm fraction are poorly revealed, and the structure looks like fine grain (Fig. 6.11, right).

a b

FIG. 6.11. Micro-structure of matrix materials based on calcinated (a) and non-calcinated coke (b), x70.

The corrosion behaviour in helium (1000°C, He + 1 vol.% H_2O) is characterized by the rate of compositions weight loss: ~1.0 mg/(cm^2·h) based on calcinated coke, ~2.0 mg/(cm^2·h)[2] for non-calcinated coke. Less corrosion resistance of the second group of matrix material is

[2] Corrosion rate for matrix material MPG specimens which have undergone final heat treatment at 2173 K in vacuum, is 1.04 mg/(cm^2/h).

explained, by appreciable intra-grain micro-porosity of MPG type fillers connected with specificity of non-calcinated coke as raw material. At the same time, based on the MPG matrix material during tests at equal conditions has identical loss of weight, but the oxidation front penetration depth is approximately two times smaller than for compositions based on calcinated coke where the binder phase is mainly oxidized and is more expressed loosening the oxidized layer. Uniform character of both phases burning in materials with non-calcinated coke is indirectly proven by measurement of their magnetic susceptibility.

The reactor irradiation of matrix material specimens was carried out at 1000–1270°C and fast fluence 3.4×10^{25} n/m^2 followed by estimation of their irradiation behaviour (Fig. 6.12). Matrix material 30PG tends to anisotropic dimension changes under irradiation (see Fig 6.12(a)). The samples cut along the moulding axis at a fluence higher than 2.2×10^{25} n/m^2 undergo secondary swelling with the rate of ~0.7%/10^{25} n/m^2. Nevertheless properties degradation of this matrix material was not observed. Matrix material MPG in the studied range of fluences undergo nearly isotropic shrinkage with a rate of 0.2–0.5%/10^{25} n/m^2 and dimension stabilization under further irradiation (Fig. 6.12(a)). For the tested matrix material, stabilization (MPG) or slight constant growth (3OPG) of the electrical resistance value is observed (Fig. 6.12(b)).

Values of α of compositions based on non-calcinated coke increase by 40% and are stabilized during further irradiation (see Fig. 6-12(c)). Value of α of compositions 3OPG in a direction perpendicular to compaction axis has practically no change under irradiation, but in opposite direction it decreases in the beginning of irradiation and then is stabilized at a level of -20% of the reference value. The micro-structure analysis of the irradiated matrix material did not reveal any qualitative change in comparison with the initial materials.

The developed matrix materials, in particular matrix material based on non-calcinated coke, possessing good physical, mechanical, and thermo-physical properties and radiation stability, were used for the manufacture of spherical fuel elements for the Russian HTGR designs. A total of 30 000 spherical fuel elements and 25 000 spherical elements (without fuel) for representative bench and reactor tests, as well as for critical facilities and test beds, has been produced in the 1980s in conditions of a pilot production facility. The test results at these stands were used for calculation and experimental substantiation of neutronics characteristics of the Russian HTGR cores and for research of pebble bed movement dynamics.

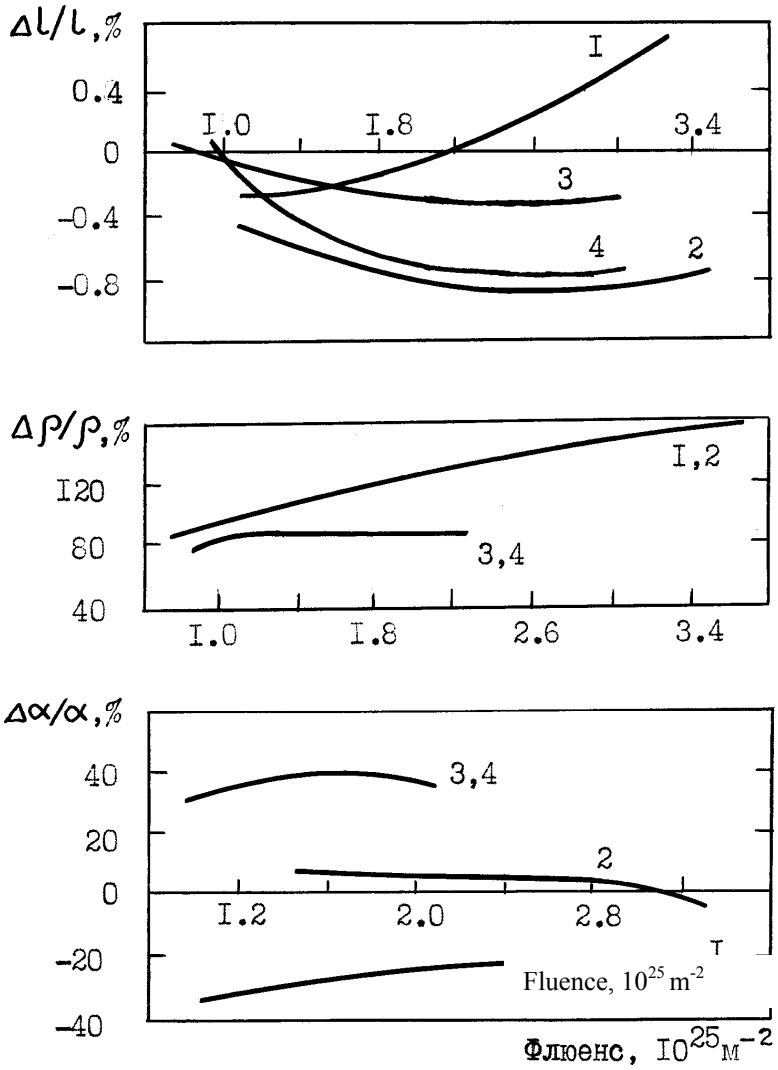

FIG. 6.12. Change of sizes (a), specific resistivity (b) and CTE (c) of irradiated matrix materials. 1: MM-3OPG, || ; 2: MM-3OPG, ⊥; 3: MM-MPG, || ; 4: MM-MPG, ⊥

6.4.2. Present status of matrix materials development

Activity under the modular HTGR project with gas turbine and prismatic core (GT-MHR) containing 3 million of fuel compacts was carried out in the Russian Federation in the last years. Compacts are regular shaped cylinders with 12.5 mm in diameter and 50 mm in length containing 12.6–15.2% of fuel as TRISO coated fuel particles.

The programme of matrix materials development includes the investigation of two versions of material differing by filler where phenol-formaldehyde resin serves as a binder in both versions:

- artificial graphite,
- a mixture of natural (basis) and artificial highly graphitized fillers.

At present, the first stage is implemented within the framework of the investigation programme. Experimental graphite MPG-KS produced by the Russian company 'GraphiteEl Moscow Electrode Factory' is investigated as a filler of compacts. A basis of this graphite is non-calcinated slate coke KS and high temperature pitch as a binder. The structure of this

composition with such coke is the closest to the structure of coke KNPS, a raw material for manufacture of the MPG type graphite [211]. The KS type coke has a slightly higher content of ash residue and more fine-grain structure.

Implemented flow diagram provides preparation of a powder of graphite filler with maximum grain size 100 μm and bulk density 0.5–0.6 Mg/m^3. Its typical characteristics are given in the Tables 6.8 and 6.9.

TABLE 6.8. CHARACTERISTICS OF GRAPHITE POWDER MPG-KS

Graphite type	Maximum size of fraction (μm)	Average size of fraction (μm)	Specific surface (m^2/g)	Bulk density (Mg/m^3)
MPG-KS	100	30–70	8.3	0.52

TABLE 6.9. ASH AND IMPURITIES CONTENT IN THE MPG-KS GRAPHITIZED FILLER

Ash content (wt%)	Contents of impurities (wt%)						
	Fe	Mg	Mn	Al	Si	Cu	B
< 0.03	$\leq 3 \times 10^{-5}$	1×10^{-5}	1×10^{-5}	1×10^{-4}	1×10^{-3}	1×10^{-5}	1×10^{-5}

The second component of a matrix composition is the binder, SFP-011L, representing a powder-like material (< 100 μm) basis on the high purity phenol-formaldehyde novolac type resin. The binder mass fraction is 18–20%. Impurities contents are given in Table 6.10.

Graphite powder is blended with resin for preparation of press-powders. Then the paste like mixture is dried and milled. Green compacts are moulded by method of double-side warm compaction in a die at $P \leq 10$ MPa with use of power press providing to dose precisely a load, to study shrinkage kinetics, and to measure the effort of compact removal from a die. Parameters of moulding and some characteristics of the formed compacts are presented in Table 6.11.

TABLE 6.10. ASH AND IMPURITIES CONTENT IN THE BINDER

Impurity	Contents (wt%)
Fe	$< 1 \times 10^{-3}$
Si	$< 1 \times 10^{-3}$
Co	$< 1 \times 10^{-3}$
Cr	$< 1 \times 10^{-3}$
Ti	$< 1 \times 10^{-3}$
Ni	$< 1 \times 10^{-3}$
Zr	$< 1 \times 10^{-3}$
Ca	$< 3 \times 10^{-3}$
Cd	$< 3 \times 10^{-5}$
Hf	$< 1 \times 10^{-3}$
B	$< 3 \times 10^{-5}$
Ash residue	< 0.01

TABLE 6.11. MOULDING PARAMETERS AND SOME CHARACTERISTICS OF GREEN COMPACTS

Binder fraction in a press-powder	20.0 wt%
Pressure	10.0 MPa
Temperature	105°C
Length	~50 mm
Diameter	12.75 mm
Maximum curvature of surface	0.03 mm
Mean density of matrix material	1.73 Mg/m^3

Further operations of binder polymerization (200°C), carbonization (800–850°C), and high temperature (1800°C) heat treatment in vacuum provide production of compacts with matrix material density at a level of 1.5–1.55 Mg/m^3.

For a validation of a matrix material choice, the programme includes irradiation of specimens in the SM-3 reactor (RIAR, Dimitrovgrad). Matrix material type samples irradiation conditions were:

- temperature $1250 \pm 50^{o}C$
- fast neutrons fluence up to 4×10^{25} n/m^2 (with intermediate ampoule change after fluence equal to 1 and to 2×10^{25} n/m^2).

As the result of this work, it is planned to investigate the following characteristics of matrix materials:

- geometrical sizes;
- weight and density;
- thermal conductivity;
- coefficient of thermal expansion;

- strength at room temperature;
- dynamic elastic modulus;
- thermomechanical interaction of outer PyC layer of coated fuel particles simulators with a matrix material (for fuel compacts simulators).

Complex technology and material science investigations and tests of matrix compositions at pre-reactor, reactor and post-irradiation stages will allow prove the material choice for GT-MHR fuel compacts.

6.5. EXPERIENCE AND DEVELOPMENT IN UKRAINE

6.5.1. New matrix graphite materials

Presently graphite based products are widely used in many branches of engineering and industry. Requirements to graphite, in particular, to the density, strength, purity, isotropy properties and gas density are increasing continuously. Therefore, the electrode methods of graphite production, well worked in the industry, frequently are ineffective that promotes, in its turn, development of new technological processes of carbon–graphite material production.

In the last few decades, in the carbon–graphite material technology there have appeared at least two radically new trends which make it possible to improve essentially their operating characteristics. These are gas phase methods (CVI-chemical vapour infiltration) and the development of carbon fiber and carbon–carbon composite materials (CCCM) with these carbon fibers as a basis. Both trends have been actively developed just for the solution of HTGR problems. However, they have not found wide applications here, although large scale manufactures were realized for other applications, mainly, for space rocket engineering.

At NSC KIPT, research work on fabricating carbon–graphite materials by the CVI methods has been started since early sixties. For this period, much research has been done, production equipment developed, skilled researchers and technicians trained, special technology sections brought into action, where all HTGR core components were fabricated. Simultaneously, the behaviour of the components produced was studied in bench and in-reactor tests. During the last 50 years, the National Science Center ‘Kharkov Institute of Physics and Technology’ was and still remained one of the main designers of materials and components for the HTGR core.

6.5.2. Production technologies of new matrix graphite materials

At present, the worldwide most widespread application is the graphite electrode. The technological process includes the following basic operations: splitting; calcinating without access of air at temperatures of 1100–1300°C; mixing of calcinated and ground coke filler with a pitch binder; forming a billet by extrusion through the die or pressing into the form; complex heat treatment with annealing at 1000–1300°C in gas furnaces and graphitization at 2400–3000°C in electrical resistance furnaces and refining by reaction gases (chlorine, fluorine, etc.) at > 2300°C. For increase of density and improvement of thermal and mechanical properties, impregnation of the graphite billet is applied after annealing or after first graphitization by liquid resin or pitch with subsequent graphitization. For the gas phase, pyrolytic impregnation of porous preforms in once-through, homogenous–heterogeneous reactors is used. In the volume of such a reactor, a convective–diffusive mass transfer of reacting components is realized at a constant low pressure (1.3–2.7 kPa) in the reaction chamber. In the case of isothermal process, the temperature of the preform being compacted and of the reactor walls is practically equal. Here, methane and its homogenous

decomposition products diffuse to the preform surface and into its porous structure. On the heated surfaces, heterogeneous reactions take place forming a solid phase pyrolytic carbon.

The production of GSP graphite (GSP is the Russian abbreviation for pyrocarbon-bound graphite) in NSC KIPT is based on CVI methods the basis of which includes the following technological processes:

- preparation of graphite powder;
- powder mesh on fraction sieving and mixing of various fractions of powder in required proportions;
- formation of billets;
- densification of billets with pyrocarbon;
- billets treatment up to the required sizes and surface finish; heat treatment;
- quality testing.

GSP graphite is obtained from the powder of commercial graphite (for nuclear applications ARV-2 graphite) with a specific granulometric composition, in most cases with a particle size up to 0.63 mm. Powder graphite is produced by cutting of billets on the turning lathe, with subsequent selection and mixing of various fractions in required proportions. This mixture is charged into a porous mould and compacted on the vibrostand to a packed density between 0.8 and 1.0 Mg/m^3. The charged mould is placed into a pyrolysis furnace where binding saturation of the mould with pyrocarbon to a density of 1.65–1.97 Mg/m^3 is carried out.

NSC KIPT developed and introduced a new method of thermogradient pyroimpregnation of porous billets to produce high quality GSP pyrocarbon-bound graphite. Unlike the isothermal method of pyroimpregnation, the thermogradient method provides creation in the preform being treated in a temperature gradient in the direction reverse to the gradient of the carbon-containing gas concentration in the preform, i.e. the temperature is decreasing from the central internal regions of the preform to its surface.

From several variants of the thermogradient method, the most promising is the method of the radially moving pyrolysis zone. It is characterized by the pyrolytic deposition of carbon taking place in a rather narrow zone — the pyrolysis zone. For this method, it is necessary to have a preform comprising a graphite bottom and a porous shell. In the centre of the perform, a current-leading rod is installed. The space between shell and central rod is filled with a powder mix of a required composition. In the pyrolysis chamber, the central rod is resistively heated in a flow of natural gas to 1000–1500°C. A comparatively narrow pyrolysis zone is created around the rod with a temperature from 1000–1500 to 840°C where the powder in this zone is bonded with pyrocarbon. The temperature in the rest of the preform volume is lower than the above indicated. There is no pyrocarbon deposition in that volume and the transport pores are not packed with pyrocarbon. These conditions provide free access of hydrocarbon gas to the pyrolysis zone and a release of hydrogen which is formed due to its interdiffusion in the transport pores.

A principal distinction between the method of moving pyrolysis zone and the above described method consists in that during the initial phase, the temperature of the external surface of the preform is lower than the threshold temperature of the pyrocarbon deposition reaction. In this case, the effective access of methane into the pyrolysis zone is provided; the external surface is packed with pyrocarbon at the last moment. The pyrolysis zone moves along the preform radius from its centre to its surface with a required rate at the expense of gradual increase of the heater temperature that was set in the beginning of the pyroimpregnation process. In this

way, GSP blocks of different sizes (Fig. 6.13) can be produced depending on the type of pyrolysis installation: ranging from small ones to 2500 mm in length and diameter (in GF-3).

6.5.3. GSP graphite properties

A principal feature of GSP graphite is the use of high strength, low temperature pyrocarbon as a binder. GSP type graphite has a characteristic well defined cellular structure. The individual elements of the structure are composed of powder-filler particles with pyrocarbon films deposited on their surface. The structure of GSP graphite consists of powder-filler particles 'cemented' with a pyrocarbon layer (~20 μm thick) and pores of an irregular shape. At points of intersection, the pyrocarbon deposits grow together forming a fully graded multidimensional spatial frame/body involving all powder-filler particles (Fig. 6.14). Annealing of specimens at 1600°C over eight hours does not lead to any observable structure changes.

FIG. 6.13. GSP block: ~900 mm in diameter and ~2600 mm in length (without machining).

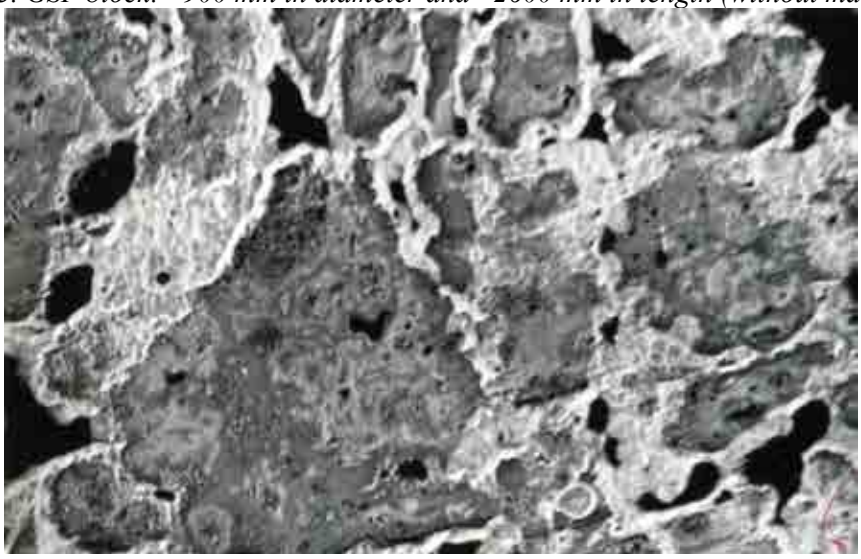

FIG. 6.14. GSP graphite structure, x 70x.

The characteristics of GSP material such as electric resistance, thermal conductivity, thermal expansion and strength are practically isotropic. Due to the feature that gas phase deposited pyrocarbon contains a very small amount of impurities (except hydrogen), and by the use of pure graphite powders as a filler, it is possible to obtain a high purity material suitable for application in the electronic industry.

By milling GSP graphite and subsequent gas phase compaction of the powder obtained, the content of the pyrocarbon component can be increased eventually resulting in a unique material of 'pyrocarbon bound with pyrocarbon' type (Fig. 6.15). The compression strength increases from 120 to 350 MPa with pyrocarbon contents increasing from 30 to 90 wt%.

Some characteristics of GSP graphite with pyrocarbon content ~50 wt% are given in Table 6.12.

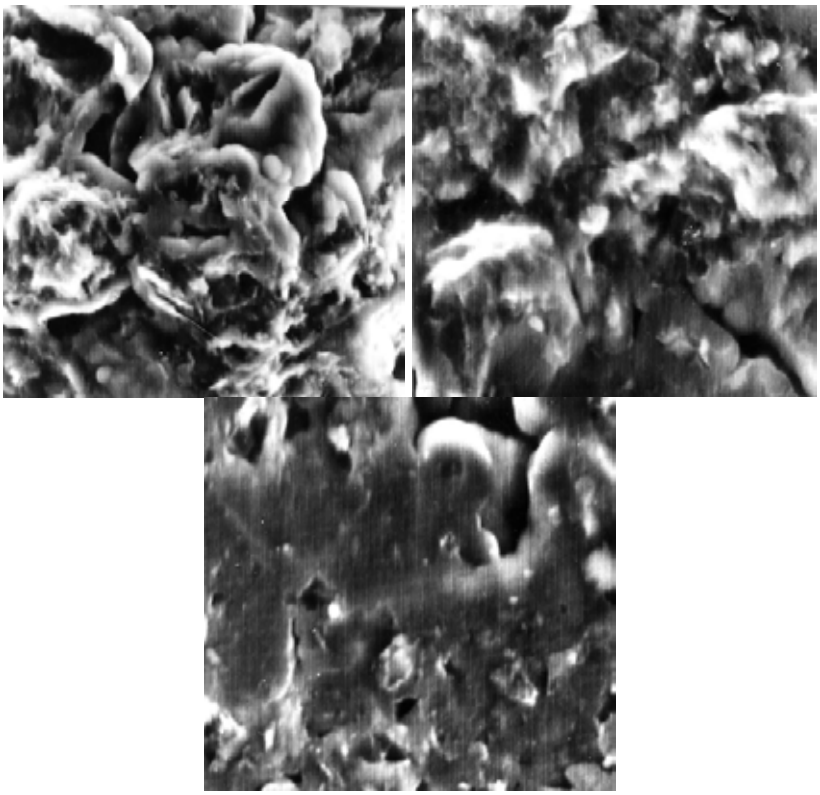

FIG. 6.15. GSP-30 graphite, x 1200x (left); GSP-50 graphite, x 1200x (middle); GSP-90 graphite, x 1200x (right).

TABLE 6.12. PROPERTIES OF GSP GRAPHITE

	Commercial Graphites	GSP Graphite
Density (Mg/m^3)	1.7–1.88	1.7–1.95
Young's modulus (10^3 MPa)	9–12	9–21
Ultimate strength at 20°C (MPa)		
in compression	60–120	160– 400
in bending	30–70	30–70
in tension	20–40	25–35
Thermal conductivity (W/(m·K))		
@ 20°C	90–130	10–80
@ 500°C	70–75	10–60
@ 1000°C	50–55	15–60
Thermal expansion coefficient (10^{-6}/K)		
@ 20–1000°C	5–8	4–5
@ 20–1500°C	8–9	4.5–5.5
Specific electrical resistance @ 20°C ($\Omega \cdot mm^2 \cdot m^{-1}$)	11–16	16–35
Friction coefficient (carbon-copper)	—	0.1–0.3
Anisotropy factor	≤ 1.3	1.03–1.05

— data not available.

According to the data of X ray diffraction analysis, the degree of the GSP graphite crystalline structure perfection is 0.45–0.47, not different from the degree of graphitization of widely applied sorts of reactor graphite. Probably, it is due to the fact that the highly graphitized material-filler exerts the main influence on the formation of X ray diffraction pattern, while the contribution of the pyrocarbon binder is insignificant. To date, the strength and thermal physical properties of GSP graphite are extensively studied [212, 213].

6.5.3.1. Mechanical properties

The strength characteristics of GSP-50 graphite (~50 wt% of pyrocarbon) as a function of the annealing temperature are given in Table 6.13. It can be seen that the values of σ_c and σ_e slightly decrease with increase of the annealing temperature up to ~2300°C.

The σ_b and E_c values of GSP graphite annealed at a temperature of 2800°C are approximately 80% of the initial level. The σ_b and σ_c values are non-monotonously changing with the annealing temperature. Besides, in the temperature range of 2500–2800°C, an appreciable decrease of the strength characteristics is observed. Data for the temperature influence on the strength characteristics of GSP graphite are presented in Figs 6.16 to 6.18.

TABLE 6.13. STRENGTH CHARACTERISTICS OF GSP-50 GRAPHITE (DENSITY 1.91 Mg/m^3)

Annealing temperature (°C)	Strength characteristics (MPa)				
	σ_c	σ_e	σ_b	E_c (10^4)	E_e (10^4)
900 (init.)	205	33	70	1.85	2.35
1600	199	30	57	1.77	2.01
1800	192	32	60	1.53	—
2000	194	30	62	1.42	1.61
2280	187	33	65	1.44	1.51
2500	175	29	67	1.50	1.44
2800	165	27	58	0.96	1.37

— data not available.

The neutron irradiation effect on the mechanical properties of reactor graphite consists in an increase of the strength characteristics and in a decrease of the plasticity. The degree of change in the mechanical properties depends on the dose and the irradiation temperature, as well as on the structural state of the material. There is experimental evidence that with increasing irradiation temperature, the increase rate of reactor graphite strength becomes smaller.

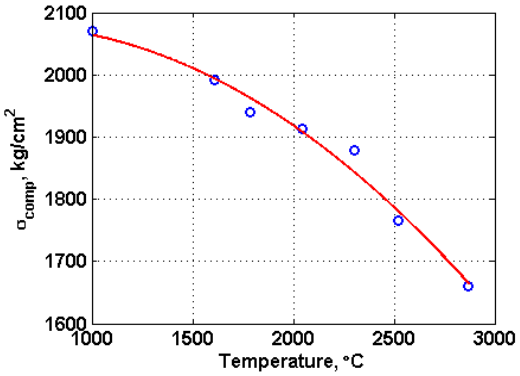

FIG. 6.16. Dependence of durability limit by compression of GSP-50 graphite from processing temperature.

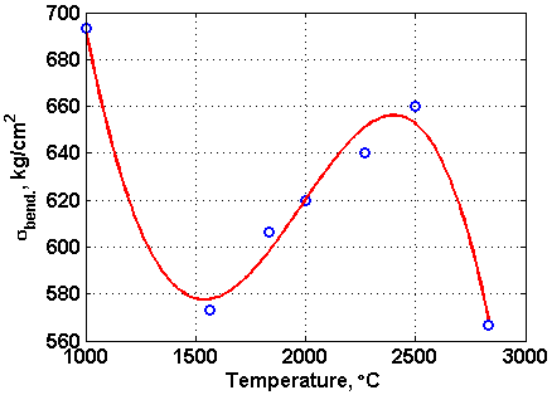

FIG. 6.17. Dependence of durability limit by stretching of GSP-50 graphite from processing temperature.

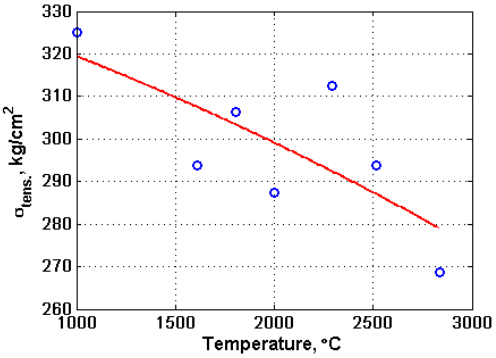

FIG. 6.18. Dependence of durability limit by bend of GSP-50 graphite from processing temperature.

Irradiated GSP specimens show an increase of the strength characteristics in tensile tests, a decrease in compression tests, and very little change in bending tests (see Figs 6.19 through 6.22). As the mechanical properties of GSP graphite in tensile tests are mainly determined by the pyrocarbon binder strength, and in compression tests by the filler strength, the increase of $\Delta\sigma_e/\sigma_e$ values occurs as a result of radiation hardening of the pyrocarbon binder, and some decrease of $\Delta\sigma_c/\sigma_c$ values occurs probably due to internal stresses at the filler–binder interface.

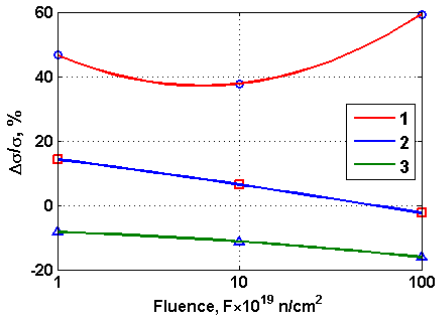

FIG. 6.19. Relative change in the average values of strength characteristics of GSP-50 graphite samples, irradiated at 1200°C, depending on the neutron fluence: 1: Tensile; 2: Bending; 3: Compression.

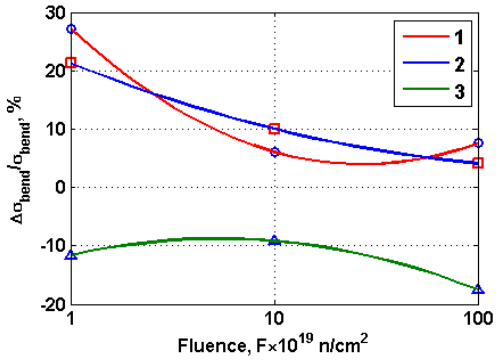

FIG. 6.20. Relative change in bending strength of GSP-50 graphite samples irradiated at 1200°C, depending on the neutron fluence: 1: 315–630 μm; 2: 0–630 μm; 3: 0–315 μm.

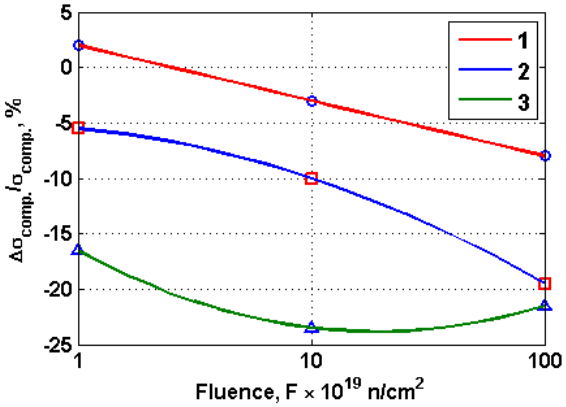

FIG. 6.21. Relative change in compressive strength of GSP-50 graphite samples irradiated at 1200°C, depending on the neutron fluence: 1: 315–630 μm; 2: 0–630 μm; 3: 0–315 μm.

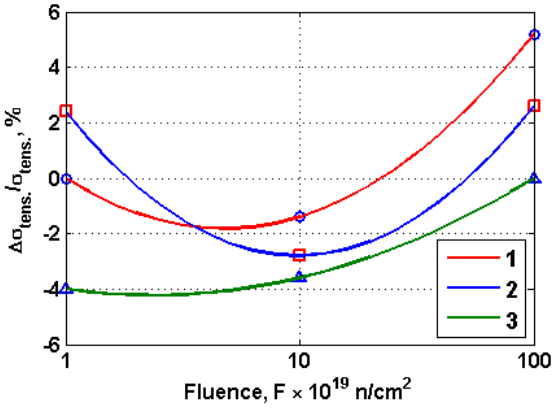

FIG. 6.22. Relative change in tensile strength of GSP-50 graphite samples irradiated at 1200°C, depending on the neutron fluence: 1: 315–630 μm; 2: 0–315 μm; 3: 0–630 μm.

6.5.3.2. Modulus of elasticity

The modulus of elasticity of commercial graphites depends on the porosity and temperature. When the treatment temperature increases to ~1900°C, the modulus of elasticity decreases. During subsequent temperature increase to 2300°C, the modulus of elasticity slightly increases and then decreases again. For GSP reactor graphite, a monotonic decrease of the modulus of elasticity is observed in the range of 1000–2800°C to the value of ~1 × 10^4 MPa. The data on the values of the modulus of elasticity for reactor graphites are given in Table 6.14.

TABLE 6.14. MODULUS OF ELASTICITY OF REACTOR GRAPHITES

Parameter	Graphite grade						
	GMZ [a]	ARV	MPG-6 [a]	GSP-1.65	GSP-1.75	GSP-1.85	GSP-50
Modulus of elasticity E (10^4 MPa)	0.65/ 0.50	0.60	1.05/ 1.06	1.3	1.5	1.6	1.7

[a] In the numerator given are the values for the specimens cut out parallel to the specimen axis, in the denominator perpendicularly.

Data for the temperature influence on the change in the modulus of elasticity of GSP graphite are presented in Fig. 6.23. The relative changes in the value of the modulus of elasticity for irradiated GSP graphite specimens are shown in Fig. 6.24. For GSP graphite, the stage of $\Delta E/E$ decrease is not observed up to a fluence of ~4–6 × 10^{25} n/m^2.

It is known that the change of the elasticity modulus correlates with the change of the material strength: $\Delta\sigma/\sigma = (\Delta E/E_o)^n$, where $\Delta\sigma/\sigma$ is the relative change of ultimate strength of graphite under irradiation; $\Delta E/E_o$ is the relative change of the elasticity modulus of graphite at irradiation; n is the exponent with a value between 0.5 and 1.0, depending on radiation conditions and material properties.

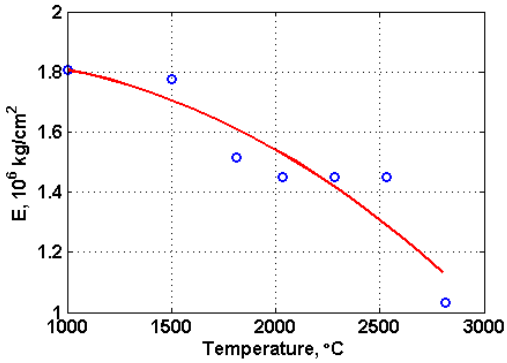

FIG. 6.23. Dependence of GSP-50 graphite elasticity modulus from the processing temperature.

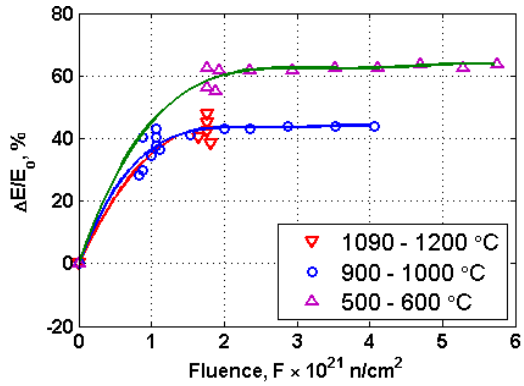

FIG. 6.24. Relative change of the dynamic modulus of elasticity (ΔE/Eo) of GSP material depending on neutron fluence.

Thus, the drop in the radiation increase rate of the elasticity modulus and its decrease to a level lower than its initial value marks the beginning of the stage of material strength loss. This phenomenon is apparently related to the occurrence of the cracking process. This supposition is in good agreement with the changes of other properties like specific electric resistance or thermal conductivity observed under irradiation, as well as with the data of structure analysis. When investigating the neutron fluence, the stage of observable degradation in the values of the elasticity modulus was not reached for GSP graphite.

6.5.3.3. Thermal physical properties

(a) Thermal conductivity

The thermal conductivity coefficient of reactor graphite determines in many respects the thermal stresses and the temperature of the graphite cladding. The thermal conductivity is a very sensitive characteristic of graphite depending on the type of source material, graphitization temperature, anisotropy and other structural and process parameters. There is presently no theory allowing to obtain qualitative data on the thermal conductivity of polycrystalline reactor graphite and its behaviour under irradiation, therefore experimental data are of particular importance.

The thermal conductivity of graphite with a laminar structure is determined by the energy transfer, as a result of elastic wave propagation along the basis planes parallel to the layer direction. Hence, significant changes in the thermal conductivity are caused by local changes in the material density. The results of measurements at high temperatures show that the most drastic decrease of the thermal conductivity is caused by the formation of vacancies. Therefore, also for irradiated graphite, a larger decrease of the thermal conductivity is supposed to be connected with a formation of vacancies arising in the basis planes. Besides, single vacancies are assumed to exert the strongest influence, since they give largest relative variations in the density.

The thermal conductivity values for unirradiated graphite at different temperatures are given in Table 6.15 and in Fig. 6.25. It is seen from the table that the thermal conductivity of the graphite is very much varying from grade to grade and essentially depends on the production technology. For most commercial graphites, the thermal conductivity anisotropy is apparently conditioned by the preferential orientation of some crystallites in the process of billet formation.

For GSP graphite (Table 6-15) the minimum values belong to the material in the initial condition, and the maximum ones to the material after heat treatment at 1800°C for one hour.

The thermal conductivity increases with increasing treatment temperature, and the most intensive changes are observed at temperatures between 2000 and 3000°C. For GSP-1.85 graphite (density: 1.85 Mg/m^3) irradiated at 900–1000°C, a non-monotonic change of the thermal conductivity coefficient with increasing neutron fluence is characteristic: after significant change of λ values at a fluence of 1×10^{25} n/m^2, the thermal conductivity increases at higher neutron fluences (Fig. 6.26). This effect can be explained by the simultaneous action of two processes, heat resistance increasing due to accumulation in the crystallites of radiation defects, the concentration of which reaches a saturation at a fluence of $\sim 1 \times 10^{25}$ n/m^2, and thermal conductivity increasing due to material density increase as a result of shrinkage by ~3%.

TABLE 6.15. THERMAL CONDUCTIVITY OF SOME REACTOR GRAPHITE GRADES

Grade of graphite	Thermal conductivity (W/(m·K))					
	20°C		500°C		1000°C	
	$\lambda_{\parallel}$	$\lambda_{\perp}$	$\lambda_{\parallel}$	$\lambda_{\perp}$	$\lambda_{\parallel}$	$\lambda_{\perp}$
MPG-6	138	125	—	—	—	—
GSP-1.65	10–80	10–80	10–60	10–60	15–60	15–60
GSP-1.75	10–80	10–80	10–60	10–60	15–60	15–60
GSP-1.85	10–80	10–80	10–60	10–60	15–60	15–60

— data not available.

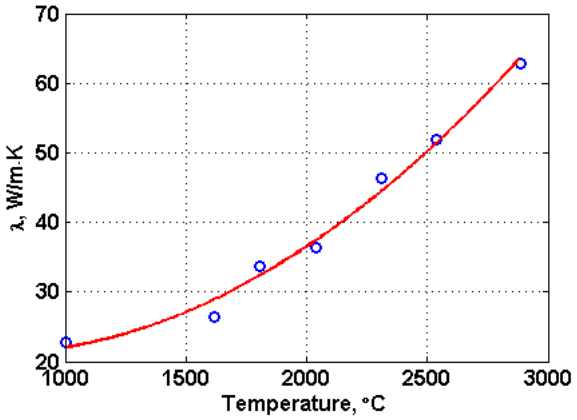

FIG. 6.25. Dependence of heat conductivity coefficient of GSP-50 graphite on annealing temperature.

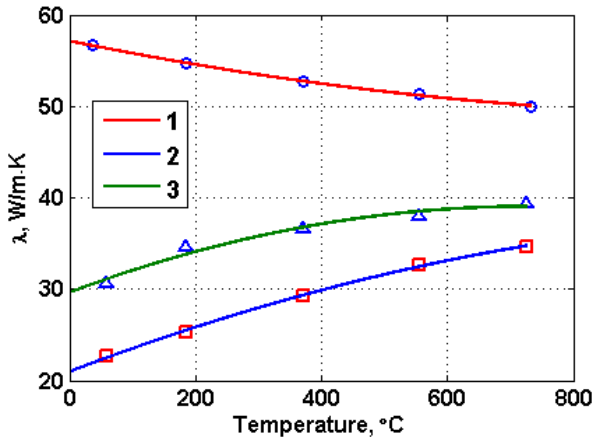

1: Initial; 2: Irradiated to neutron fluence 1×10^{25} n/m^2 at temperature 900–1000°C; 3: Irradiated to neutron fluence 2×10^{25} n/m^2 at temperature 900–1000°C.

FIG. 6.26. Temperature dependence of heat conductivity of GSP-1.85 graphite.

(b) Thermal expansion coefficient

The experience with uranium–graphite reactor operation shows that a destruction due to thermal expansion of graphite must be prevented. The knowledge of temperature and

irradiation effects on the thermal expansion coefficient (TEC) of graphite materials is necessary for the graphite reflectors design.

The thermal expansion coefficient (TEC) of reactor graphite is anisotropic and, to a great extent, depending on the temperature. TEC anisotropy arises as a result of the preferential orientation of anisotropic grains (particles) of the source material (coke) that is revealed in the process of billet forming (forcing or pressing). The process of cracking in reactor graphite exerts the greatest influence on its TEC. The cracks compensate partially the crystallite expansion along the hexagonal axis and thereby decrease the total TEC of graphite. TEC values of reactor graphites are listed in Tables 6.16, 6.17 and in Figs 6.27 and 6.28.

TABLE 6.16. TEC OF DIFFERENT GRADES OF REACTOR GRAPHITE

Parameter	Grade of graphite				
	MPG-6 [a]	GSP-1.65	GSP-1.75	GSP-1.85	GSP-50
TEC ($\alpha_{400°C}$) (10^{-6} K^{-1})	7.3/6.6	—	5.5	5.4	4.4

[a] In the numerator given are the values for the specimens cut out parallel to the specimen axis, in the denominator perpendicular.
— data not available.

TABLE 6.17. TEC VALUES OF GSP GRAPHITE

Density (Mg/m^3)	α (10^{-6} K^{-1})			
	20–1000°C		20–1500°C	
	$\alpha_{\parallel}$	$\alpha\perp$	$\alpha_{\parallel}$	$\alpha\perp$
1.7–1.95	4–5	4–5	4.5–5.5	4.5–5.5

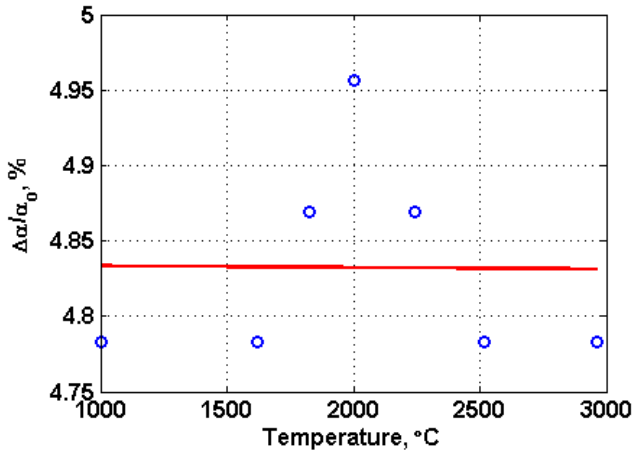

FIG. 6.27. Dependence of GSP graphite TEC at temperature 1000°C on the processing temperature.

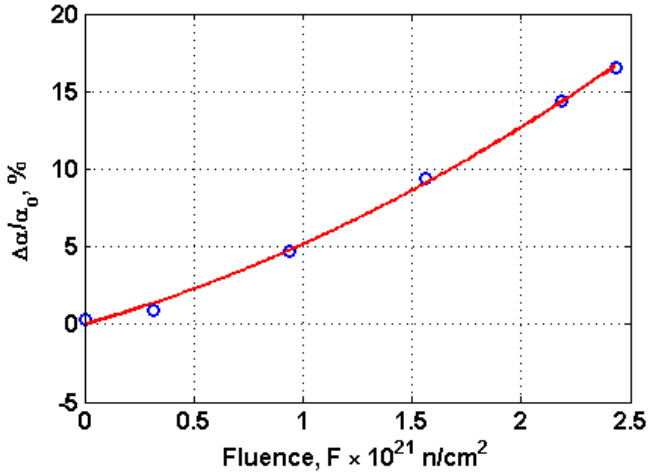

FIG. 6.28. Relative change of GSP graphite TEC, irradiated at temperature of 900–1000°C, depending on neutron fluence.

As a rule, the TEC for most graphites quickly increases up to a temperature of ~100°C, and then the rate of TEC changing sharply decreases. It should be noted that TEC changing for GSP graphite has an isotropic character.

(c) Dimensional change of graphite under irradiation

The radiation dimensional stability of graphite is its most important characteristic which, to a great degree, determines its working efficiency as a material and as graphite based construction on the whole. The rate and behaviour of changes in dimensions of graphite products depend on the irradiation temperature and are varying with neutron fluence accumulation at a fixed temperature. Generally, the dimensional change of carbon materials under neutron irradiation exhibits a complex dependence on the irradiation conditions: the integral flux and the temperature.

At the initial stage of irradiation, an accelerated shrinkage of irradiated graphite is observed. The shrinkage rate slows down with neutron fluence growth, and then the process is reversed — shrinkage is changed by secondary swelling. The swelling rate is higher than the shrinkage rate, and this phenomenon is accompanied by a change in the physical properties of the graphite. Micro-cracks that developed become coarser and join forming macro-cracks. As a result, the material strength decreases, that can limit the operational life of the reactor and, consequently, the entire reactor cladding. The temperature elevation decreases the dose, corresponding to the transition from shrinkage to swelling, and increases the swelling rate. Radiation forming of GSP graphite specimens as a function of the fast neutron fluence (E>0.18 MeV) is presented in Figs 6.29 through 6.37. GSP graphite shows the isotropic shrinkage over the whole investigated temperature range of 300–1200°C. The shrinkage depth depends on the contents of non-graphitized binder in the structure and has a maximum value for the GSP-1.65 material. Shrinkage does not depend on the fractional composition of the powder–filler (in the range up to 630 μm) and on the direction of specimen cutting relative to the GSP billet axis. It weakly depends on the irradiation temperature but sharply increases, especially, at the initial irradiation stage, with density decreasing and pyrocarbon content increasing. The rate of radiation forming after reaching the fluence of 2–3 × 10^{25} n/m^2 sharply slows down and reaches a saturation stage.

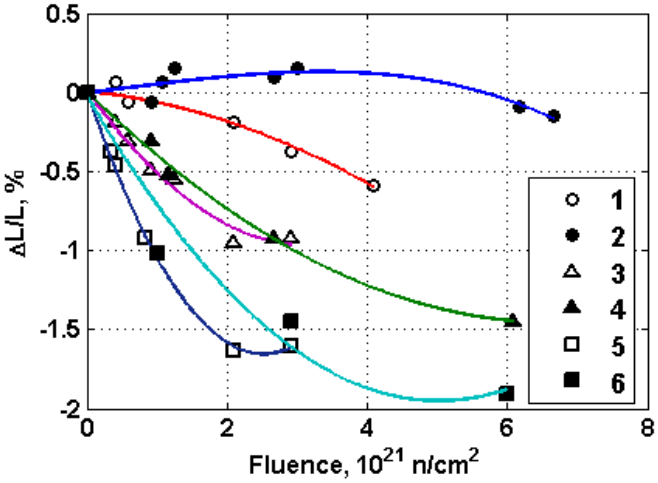

FIG. 6.29. Relative change of the linear dimensions of ARV and GSP graphite samples, irradiated at temperature 600°C (open symbols) and 800°C (closed symbols), depending on neutron fluence: ○● ARV graphite; Δ▲ GSP-30 graphite; □■ GSP-50 graphite.

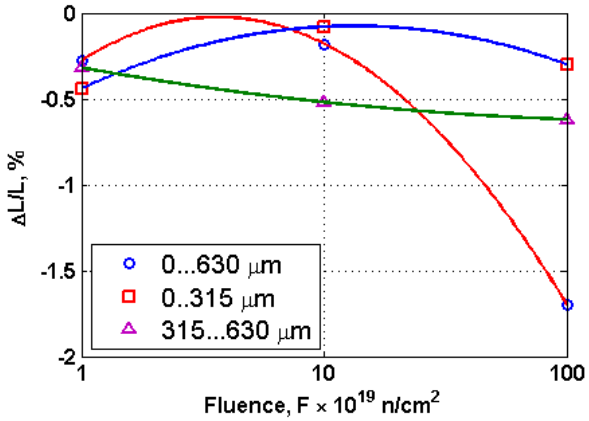

FIG. 6.30. Relative change in linear dimensions of GSP-50 graphite samples with various grain sizes irradiated at 1200°C, depending on fast neutron fluence: ○: 0–630 μm; □: 0–315 μm; Δ: 315–630 μm.

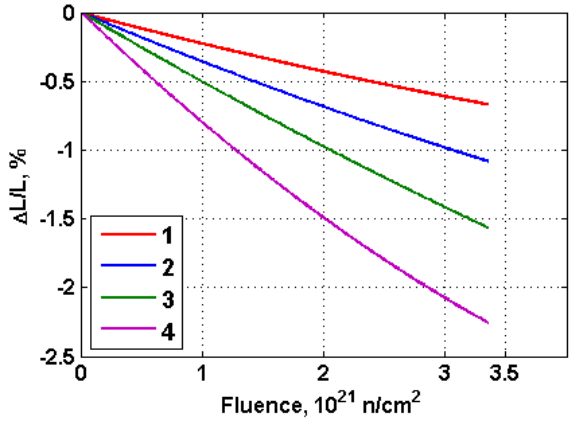

FIG. 6.31. Dependence of shrinkage of GSP-50 graphite samples (1,3; density 1.91 Mg/m^3) and GSP-90 graphite samples (2,4; density 1.75 Mg/m^3) on fast neutron fluence (T_{irr} = 500–600°C): 1,2: Heat treatment under 2800°C, 1 hour; 3,4: Initial material.

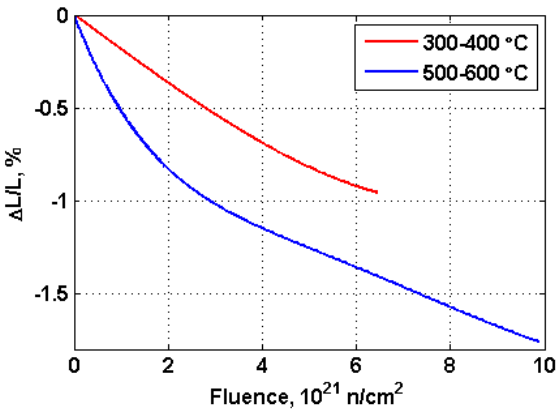

FIG. 6.32. Dependence of shrinkage of GSP-30 graphite the samples with a density of 1.85 Mg/m^3 on fast neutron fluence.

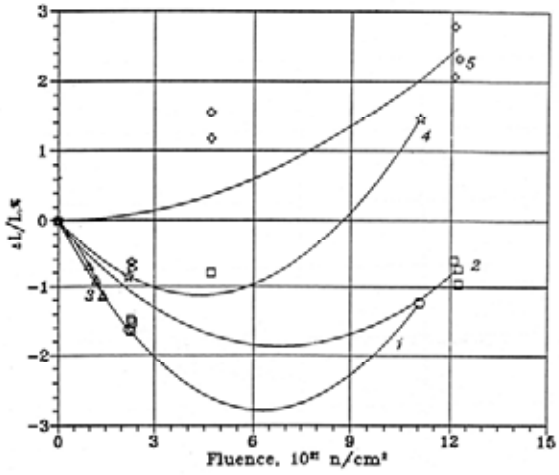

FIG. 6.33. Dimensional changes of GSP-50 matrix graphite samples depending on neutron fluence. Without heat treatment: 1: T_{irr} = 600–700°C, 2: T_{irr} = 700–750°C, 3: T_{irr} = 800–900°C. Heat treatment under 2900°C: 4: T_{irr} = 600–700°C, 5: T_{irr} = 700–750°C.

A degradation in GSP graphite properties up to the investigated neutron fluence of 15 × 10^{25} n/m^2 has not been observed. It is known that the temperature range from 900°C to 1000°C is the most harmful for pressed materials from the viewpoint of material transition into the secondary swelling. GSP graphite shows a maximum shrinkage depth as compared to other materials of this type. In the range from 500°C to 1200°C, the temperature dependence of the GSP graphite shrinkage is more weakly defined than in other materials.

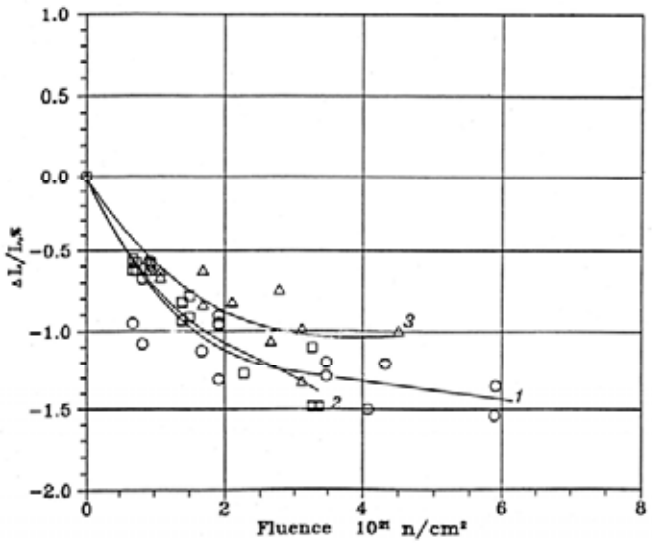

FIG. 6.34. Dimensional changes of GSP matrix graphite samples irradiated under temperature 900-1000°C: 1: GSP-1.65; 2: GSP-1.75; 3: GSP-1.85.

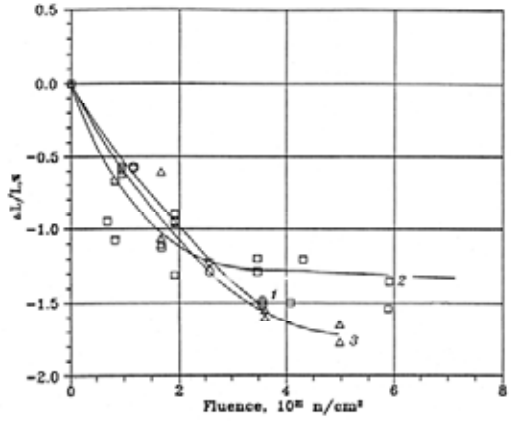

FIG. 6.35. Dimensional changes of GSP-1.65 matrix graphite samples irradiated under temperature: 1: 800–900°C, 2: 900–1000°C, 3: 1000–1200°C.

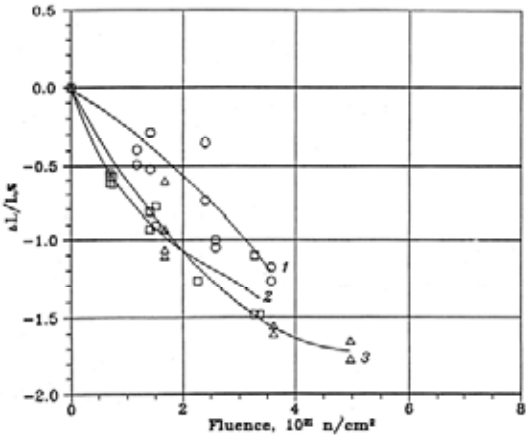

FIG. 6.36. Dimensional changes of GSP-1.75 matrix graphite samples irradiated under temperature: 1: 800–900°C: 2: 900–1000°C; 3: 1000–1200°C.

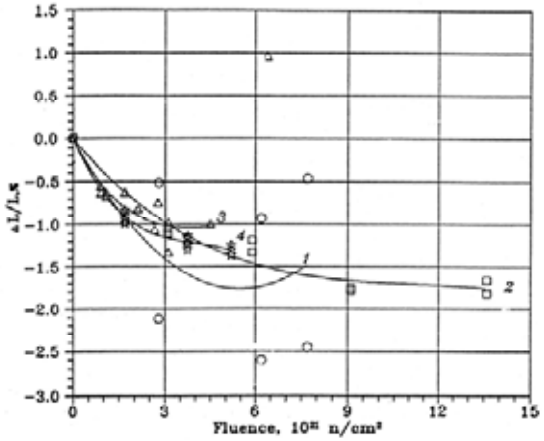

FIG. 6.37. Dimensional changes of GSP-1.85 matrix graphite samples irradiated under temperature: 1: 300–400°C; 2: 500–600°C; 3: 900–1000°C; 4: 1100–1200°C.

GSP graphite has been tested under conditions of in-reactor irradiation at 300–1250°C up to a fast neutron fluence of ~15 × 10^{25} n/m^2. It has been established that the material under irradiation suffers from isotropic shrinkage which does not depend on the fractional composition of the powder–filler (in the range up to 630 μm). This value weakly depends on the irradiation temperature but sharply increases, particularly, at the initial stage of irradiation (up to a fluence of ~1.5 × 10^{25} n/m^2), with density decreasing and pyrocarbon content increasing. The rate of radiation forming after reaching the neutron fluence ~2–3 × 10^{25} n/m^2 sharply slows down and reaches a saturation stage. GSP graphite did not reveal any observable degradation of properties, a result that makes it promising for the use in nuclear reactors cores.

6.5.4. New carbon–carbon composite materials

Carbon–carbon composite materials (CCCM) represent a rather new class of materials. They consist of a cage on the base of carbon filaments and carbon matrix, uniformly distributed in the cage volume. As reinforcing elements for CCCM discrete or continuous fibers are applied. In the latter case the fibers are usually used as threads, containing 10^3–10^4 monofibers of a strand.

Presently there are liquid phase and gas phase production technologies of carbon matrix in CCCM. In the liquid phase process of CCCM technological operations, the know-how adopted from artificial graphites and composites with a polymeric matrix is widely used. The production process mainly consists of

- addition of coke forming hydrocarbon (pitch, bakelite lacquer, furfural spirit, phenol-formaldehyde resin and others) to structure a fibrous cage;
- polymerization of polymeric binding;
- carbonization;
- graphitization.

In the gas phase process of CCCM production with a pyrocarbon matrix, also known as chemical vapour impregnation (CVI) process, the deposition of carbon is conducted from gaseous hydrocarbon (methane, propane, propylene, natural gas, etc.) on a carbon substrate. The essence of the process consists in diffusion of hydrocarbon into the reinforcing cage being the substrate.

Three main methods of formation of a pyrocarbon matrix in the carbon cage in CVI-process have been developed:

(a) Isothermal

While performing the cage saturation, a constant temperature in the volume of the working chamber is maintained and gas is supplied at reduced pressure. The main advantage of this process is the capability to saturate simultaneously several products in the working volume of the chamber. A drawback is the densification that occurs near cage surface. For reaching a high density, it is necessary to remove periodically the dense surface crust.

(b) Thermal gradient

In the thermogradient method, the billet under saturation is placed on a special mandrel heater, where saturation begins from the heated internal part of the billet and spreads in radial direction. Carbon gas diffuses into the billet providing thus densification with pyrocarbon in a significant thickness of the cage. This method is inferior to the isothermal method in the quantity of cages which are being simultaneously saturated. Besides, it is not always possible to achieve the high density of the matrix.

(c) Pressure differential

The process of saturation with a pressure difference is characterized by the fact that gaseous hydrocarbons move inside the cage under excessive pressure relative to the furnace chamber pressure. Over the width of the billet, the pressure difference forces gaseous pyrocarbons to permeate through the pores. During the process, it is necessary to isolate the pressurized internal cavity from the furnace chamber.

CCCM properties may be varied over a wide range by change of the type and volumetric content of carbon fiber filler, reinforcement scheme, type of carbon matrix, processing temperature, etc. As in the case with artificial graphite, CCCM properties, first of all density and strength, depend on features of technological process of matrix production. Also the type of matrix, its manufacturing method, and geometric dimensions, especially the billet thickness, significantly influence the properties of the CCCM products. Massive samples do often not reach the level of characteristics obtained on rather thin billets.

All CCCMs of NSC KIPT are produced in the CVI-process applying one work cycle of fiber cage saturation with pyrocarbon. The production includes concerns thin-walled (~40 mm) and thick-walled (~120 mm) CCCM billets as cylinders, rings and plates. The methods developed at NSC KIPT allow achieve thick-walled cages up to rather high densities.

At the given stage, a CCCM reflector design for an HTGR is not considered. It may not be required to manufacture it completely from CCCM, but rather restrict to its internal part, the most stressed by neutron load. The thickness of such a CCCM shield could comprise tens of percents of the total graphite reflector thickness. As one option of reflector construction, two coaxial CCCM tubes filled with graphite blocks are considered.

6.5.5. Carbon–carbon composite materials properties

The advantages of volume gas phase impregnation are most successfully realized when using fillers of carbon fibers or fabrics. In this case, the moulding of required size structures is substantially simplified,. without the need for binders. The products obtained, after impregnating with pyrocarbon, can be used without any further surface treatment.

The CCCM structure is formed by a system of three filaments in the rectangular coordinates. Monofilaments in bundles are bound with pyrocarbon in the monolith (Fig. 6.38, left). Filling of CCCM cells is incomplete as a consequence of clogging of channels for hydrocarbon gas passage in the process of saturation (Fig. 6.38, right). The thickness of pyrocarbon deposits on the bundle surface inside the elementary CCCM cells reaches ~500 μm, thick enough to reveal the features of the structure of both the laminar formations and the cones of growth. In particular, in Fig.6.38, right, a laminar pyrocarbon structure inside the elementary cell can be seen. Table 6.18 gives the mean values of main properties of CCCM with pyrocarbon matrix and some characteristics of commercial graphites [212, 213].

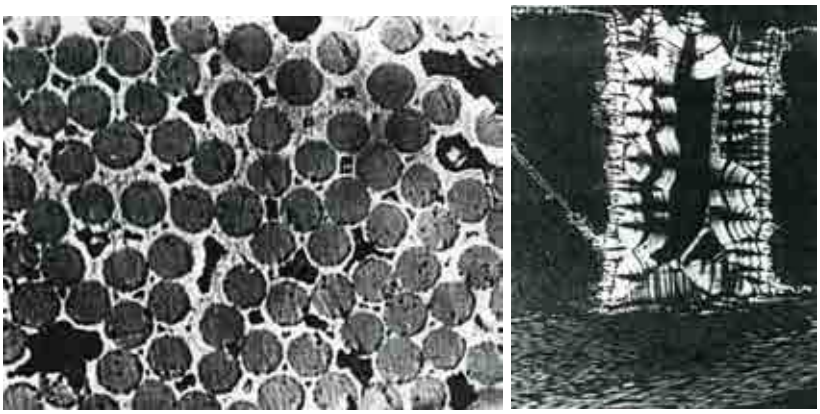

FIG. 6.38. Macro- (left: 50x) and micro- (right: 1000x) structures of carbon–carbon composites with a pyrocarbon matrix.

TABLE 6.18. SOME PROPERTIES OF CCCM WITH PYROCARBON MATRIX

Characteristic	Commercial Graphites	CCCM
Density (Mg/m^3)	1.7–1.88	1.3–1.9
Young's modulus (10^3 MPa)	9–12	12–40
Ultimate strength at 20°C (MPa)		
in compression	60–120	150–400
in bending	30– 70	100–160
in tension	20–40	50–120
Thermal conductivity (W/(m·K))		
@ 20°C	90–130	5–7
@ 500°C	70–75	7–11
@ 1000°C	50–55	10–15
Thermal expansion coefficient (10^{-6}/K)		
@ 20–1000°C	5–8	1–4
@ 20–1500°C	8–9	2–4.5
Specific electrical resistance @ 20°C ($\Omega \cdot mm^2 \cdot m^{-1}$)	11–16	40–65
Friction coefficient (carbon-copper)	—	0.1–0.3
Anisotropy factor	≤ 1.3	—

— data not available.

The limiting (minimum and maximum) values of strength characteristics for the GSP are determined by the final density of the material. In contrast, the CCCM strength is determined by the strength of carbon fibers and the reinforcement pattern depending only weakly on the density.

6.5.5.1. Mechanical properties

In any fiber composite the high strength fibers have to take up the main stresses arising in the material under external loads, and to ensure rigidity and strength in the direction of the fiber orientation. The matrix filling the interfiber space provides joint acting of separate fibers at the expense of own rigidity and interaction existing on the matrix–fiber interphase. Therefore the mechanical properties of a composite are mainly influenced by the strength of reinforcing fibers, the matrix rigidity, and the strong bond on the matrix–filament interphase.

TABLE 6.19. SOME PROPERTIES OF CCCM ON THE BASIS OF WOVEN STRUCTURES

№	Carbon thread		Cage density (Mg/m^3)	CCCM density (Mg/m^3)	Direc tion [a] sample cutting	Tensile strength [b] σ_t (MPa)	Compression strength[(b)] σ_c (MPa)
	Fabrics	Stitching					
1	UN-2 Blade	Ural NSh	0.63	1.60	1	(10.4–13.4) /11.4	(147.9–171.1)/162.6
					2	(8.0–12.0) /10.4	(117.7–176.2)/147.8
2	UN-2 Blade	UNP	0.63	1.62	1	(10.3–14.5) /13.3	(156.7–193.7)/185.2
					2	(9.2–13.6) /11.7	(129.9–171.8)/150.4
3	Ural N-24 Satin stitch	Ural N-24	0.54	1.52	1	(21.8–26.0) /23.5	(167.8–216.0)/185.2
					2	(0.8–39.0) /36.3	(132.9–171.0)/155.2
4	Ural N-24	Ural NSh	0.53	1.56	1	(23.5–30.9) /27.7	(119.7–163.4)/147.2
					2	(19.1–23.2) /21.8	(125.8–159.3)/138.7
5	Ural N-24+ Ural TM-4 Jersey fabric	Ural NSh	0.61	1.51	1	(24.8–33.6) /28.6	(98.1–124.4)/111.9
					2	(20.3–27.7) /23.7	(81.7–112.1)/98.3

[a] 1: cutting along broaching, 2: cutting across broaching;
[b] variations of the characteristics in numerator, average values in denominator.

Table 6.19 lists some characteristics of cages and CCCM billets on the basis of carbon fibers UN-2 and Ural N-24, noticeably different in strength characteristics. Blocks of various carbon fabrics were pierced by a carbon fiber with a distance between stitches of 7–8 mm and a stitch length of 8–10 mm. As can be seen from the table, the tensile strength values σ_t for CCCM samples on the basis of the stronger thread of the Ural N-24 exceed 2 to 3 times the values for CCCM samples based on UN-2 of less strong thread. The difference in the compression strength data σ_c is less noticeable.

An experience from CCCM production is that the strength of carbon fibers is not a unique parameter determining the strength of C–C materials. This is well visible from the data listed in Table 6.20 where substrates on the basis of VMN-4 and Ural-4 carbon fibers exhibit large differences in strength and elastic characteristics. In contrast, CCCMs on the basis of various woven fillers, despite their differences in elastic and strength characteristics of used fibers, differ only insignificantly in the strength characteristics. It is connected with a denser packing of carbon filaments in the reinforcing substrates from low modular filler due to finer pore structure and high stress–strain behaviour of fabrics. Besides, low modular fibers are rather stable against textile processing.

TABLE 6.20. PHYSICAL-MECHANICAL CHARACTERISTICS OF CCCM ON THE BASIS OF PYROCARBON MATRIX

Characteristics	Reinforcing filler			
	Ural TM-4	Ural T-22	'Dnepr' (VMN-4)	TGN-2M
Apparent density of reinforcing cage (Mg/m^3)	0.78	0.62	0.54	0.57
Apparent density of material (Mg/m^3)	1.42–1.48	1.58	1.61–1.67	1.58
Ultimate tensile stress[(a)] (MPa)				
along the warp direction	83/10	76/8	63/6	73/6
along the fill direction	46/12	30/2	—	21/3
Young's modulus[(a)] (Gpa)				
along the warp direction	26/15	24/5	—	21.2/8
along the fill direction	21/10	15/5	29/3	11.5/14
Ultimate compression stress[(a)] (MPa)				
along the warp direction	185/13	155/8	59/6	167/18
along the fill direction	158/10	103/8	—	96/9
Ultimate interlayer shear stress (MPa)	16.0	—	13.0/13	—

[a] denominator desscribes variation (%).
— data not available.

Unlike graphites which are widely used in reactor construction, there is only little data on CCCM irradiation tests. Therefore irradiation of samples without heat treatment was carried out at 300°C and 600°C up to a neutron fluence of 1×10^{23}–1×10^{25} n/m^2, and for samples with thermal treatment at 300°C up to a fluence of ~1.8×10^{24} n/m^2 (E>0.18 MeV). CCCM and CCCM-h/t materials of 3D-structure with a pyrocarbon matrix on the basis of UKN-5000 fiber with the reinforcement scheme x:y:z = 2:2:1 in an initial state (after saturation with pyrocarbon) and annealed have been used at ~2750°C over ~0.5 hours.

The dependence of deformation of CCCM and CCCM-h/t on the fluence of neutrons is given in Fig. 6.39. Each experimental point represents an arithmetical mean of measurements on nine samples. It is obvious that the shrinkage of the material without heat treatment is practically isotropic. The increase of the irradiation temperature from 300°C and 600°C had practically no effect on the CCCM sample shrinkage. A comparison of the data in Fig. 6.30 and Fig. 6.39 shows that with regard to neutron irradiation and shrinkage, GSP and CCCM materials irradiated up to equal fluences (but at different temperatures) are very similar. Some higher shrinkage of CCCM as compared with GSP graphite can be related to different pyrocarbon contents: ~50 wt% in GSP and ~75 wt% in CCCM. Hence, it can be concluded that the main contribution into the radiation CCCM forming is made by the pyrocarbon matrix and not by the fibrous filler.

In Figs 6.40 through 6.43, the irradiation influence on electric resistance and mechanical characteristics of CCCM are shown. It should be noted that irradiation has resulted in a sharp growth of electrical resistance and strength characteristics of CCCM-h/t material (Table 6.21).

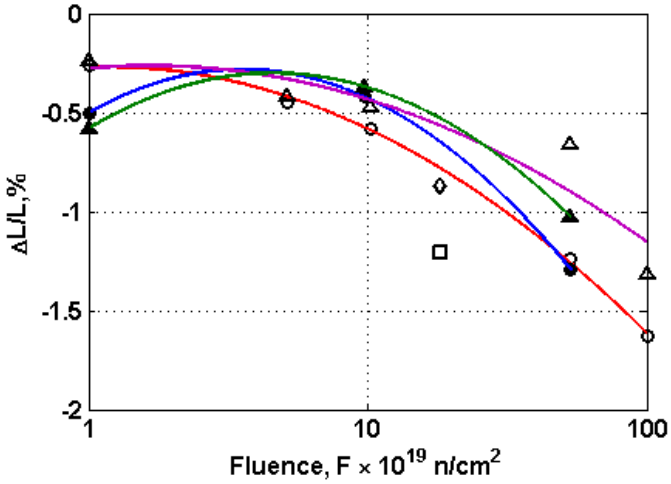

FIG. 6.39. Relative change of the linear dimensions of CCCM samples (○●Δ▲) and CCCM-h/t samples (◊ □), irradiated at temperature 300°C (open symbols) and 600°C (closed symbols), as a function of neutron fluence: ○●□ x,y-cutting samples; Δ▲◊ z-cutting samples.

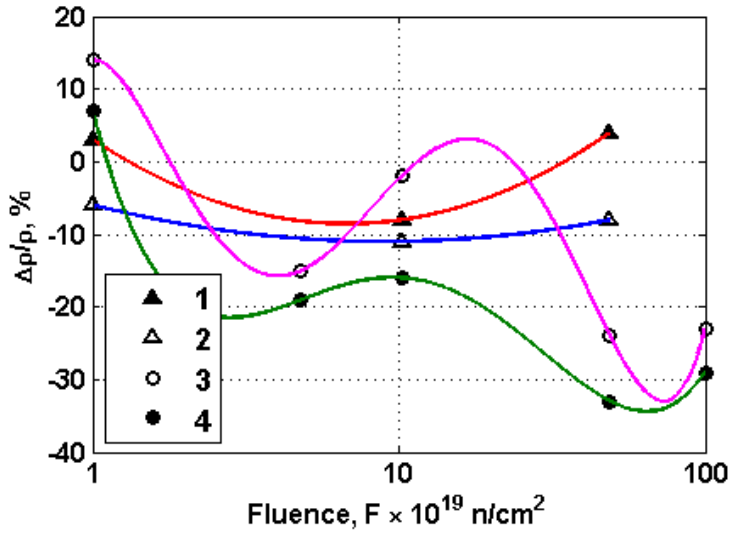

FIG. 6.40. Relative change in electric resistance of CCCM samples, irradiated at 300°C (3,4) and 600°C (1,2), depending on the neutron fluence: 2,3: x,y-cutting samples; 1,4: z-cutting samples.

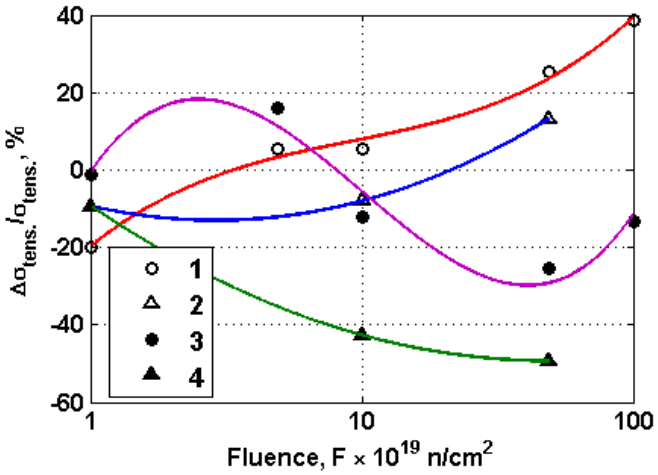

FIG. 6.41. Relative change in tensile strength of CCCM samples, irradiated at 300°C (1,3) and 600°C (2,4), depending on the neutron fluence: 1,2: x,y-cutting samples; 3,4: z-cutting samples.

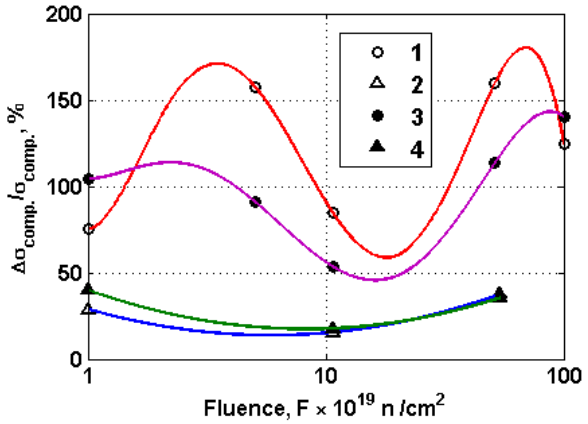

FIG. 6.42. Relative change in compressive strength of CCCM samples, irradiated at 300°C (1,3) and 600°C (2,4), depending on the neutron fluence: 1,2: x,y-cutting samples; 3,4: z-cutting samples.

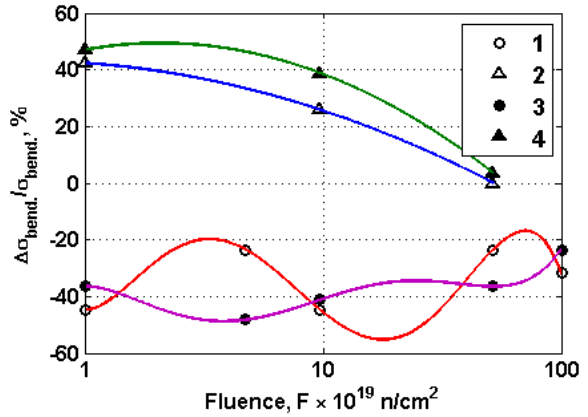

FIG. 6.43. Relative change in bending strength of CCCM samples, irradiated at 300°C (1,3) and 600°C (2,4), depending on the neutron fluence: 1,2: x,y-cutting samples; 3,4: z-cutting samples.

TABLE 6.21. INFLUENCE OF NEUTRON IRRADIATION AT 300°C UP TO A FLUENCE OF ~1.8 × 10^{24} n/m^2 ON RELATIVE CHANGE OF ELECTRICAL RESISTANCE AND STRENGTH CHARACTERISTICS OF HEAT-TREATED CCCM

Characteristic	Direction of cutting							
	x,y				z			
	$\Delta\sigma_t/\sigma_t$	$\Delta\sigma_b/\sigma_b$	$\Delta\sigma_c/\sigma_c$	$\Delta\rho/\rho$	$\Delta\sigma_t/\sigma_t$	$\Delta\sigma_b/\sigma_b$	$\Delta\sigma_c/\sigma_c$	$\Delta\rho/\rho$
Relative change of properties (%)	413	465	83	391	73	323	117	581

The change of strength characteristics of CCCM without heat treatment is illustrated in Figs 6.41 through 6.43. As can be seen, the investigated materials noticeably excel the best grades of reactor graphite in the absolute level of strength characteristics.

When analysing the results of mechanical tests of CCCM, it is necessary to take into account that (i) the strength of CCCM under tensile tests (σ_t) is determined essentially by the strength of carbon filaments, under compression tests (σ_c) by the strength of pyrocarbon matrix, and under bending tests (σ_b) by a complex stressed state with the specimen being partially under tension and partially under compression; (ii) the content of carbon filaments in x,y directions was twice as high as that in z direction.

During the process of irradiation, delaminations around filaments may appear caused by the different character of filler and matrix forming. The increased content of filler (filaments) in the x,y plane leads to an increase of the $\Delta\sigma_c^z/\sigma_c^z$ values and to some decrease of $\Delta\sigma_t^z/\sigma_t^z$ values. Irradiation hardening of the pyrocarbon promotes the increase of the $\Delta\sigma_c/\sigma_c$ values. Appearance of a minimum in the curves of $\Delta\sigma_c/\sigma_c$ at a neutron fluence of 10^{24} n/m^2 is not an experimental error since at the same dose, anomalies in the change of the specific electric resistance are observed (Fig. 6.40).

In total, it can be noted that the level of initial strength of CCCM material is sufficiently high: $\sigma_t \geq 50$ MPa, $\sigma_b \geq 120$ MPa, $\sigma_c \geq 190$ MPa [212, 213], and irradiation softening (loss of strength) is insignificant. Therefore, taking into account the positive results of neutron irradiation tests of GSP graphite having a different pyrocarbon content in a wide temperature range, the efficacy of CCCM material with the given reinforcing structure and manufacturing technique (gas phase technology) can be predicted at least up to a neutron fluence of ~5 × 10^{25} n/m^2.

6.5.5.2. Thermal physical properties

The influence of the reinforcement scheme of the 3D-structure and heat treatment at temperatures of 2700–2800°C over 0.5–1 h on the thermal physical characteristics the CCCM is shown in Table 6.22. As reinforcing component, a carbon UKN-5000 fiber was used and pyrocarbon as matrix.

TABLE 6.22. DEPENDENCE OF CCCM THERMAL CHARACTERISTICS ON THE REINFORCEMENT SCHEME AND HIGH TEMPERATURE ANNEALING OF CAGES

Characteristic	Cage processing	Temperature tests (°C)	Reinforcement scheme on axes x : y : z [a]		
			2:2:4	2:2:2	2:2:1
γ (Mg/m^3)	without h/t	—	1.75	1.72	1.73
λ (W/(m·K))		50	6.9/5.7	5.2–12.0/3.2–7.6	8.0/5.6
α (10^{-6} K^{-1})		20 - 100	1.9/0.3	-3.2–4.3/-4.3–4.3	—
		201-800	2.9/2.5	2.5–3.9/3.2–5.4	3.6/5.8
γ (Mg/m^3)	with h/t	—	1.85	1.80	—
λ (W/(m·K))		50	14.8/16.6	27.0/11.8	—
α (10^{-6} K^{-1})		20–100	0/0	—/0–1.2	—
		20–1800	1.8/1.2	—/1.9	—

[a] numerator contains characteristics in x,y directions , denominator those in z direction.
— data not available.

Table 6.23 shows the temperature dependence of TEC on CCCM billets, measured on initial and on heat-treated at ~2800°C for 0.5 h. The initial density of CCCM billets was 1.74 Mg/m^3 and 1.76 Mg/m^3, after heat treatment 1.65 Mg/m^3 and 1.64 Mg/m^3. The annealing process has obviously a poor influence on the TEC values; the measured α values are almost isotropic. Thermal-physical characteristics of CCCM in the initial state and after heat treatment at ~2750°C for ~0.5 h with the structure reinforcement 2 : 2 : 1 are given in Table 6.24.

TABLE 6.23. TEMPERATURE DEPENDENCE OF TEC α (10^{-6} K^{-1}) FOR CCCM IN AN INITIAL STATE AND AFTER HIGH TEMPERATURE ANNEALING

State of CCCM	Direction of sample cuttings	Temperature of measurement (°C)					
		100	200	400	600	800	1000
Without h/t	x,y	-2.4	-1.3	-0.4	0.2	0.4	0.7
	z	-1.5	-0.9	-0.3	0.1	0.3	0.5
After h/t	x,y	-3.3	-2.1	-0.7	0	0.2	0.4
	z	-1.5	-1.2	-0.2	0.2	0.5	0.7

Note: The reinforcement structure of a cage by UKN-5000 fiber was 2:2:2.

TABLE 6.24. THERMAL CHARACTERISTICS OF CCCM IN THE INITIAL STATE AND AFTER HEAT TREATMENT

State of CCCM	Characteristic		
	γ (Mg/m^3)	λ_{50}[(a)] (W/(m·K))	$\alpha_{20\text{-}1800}$ [a] (10^{-6} K^{-1})
Without h/t	1.73	8.0/5.6	3.6/5.8
After h/t	1.65	32/30	0.8/1.0

[a] numerator contains characteristics in x,y directions , the denominator those in z direction.

Thermal-physical characteristics of CCCM on the basis of WBS cages and pyrocarbon matrix are listed in Table 6.25. The WBS structures were of two types: a fabric package pierced with a Ural-NSh thread, and a tubular structure obtained by spiral winding on TGM-2M fillets mandrel with 6–70 mm in width. For comparison the data of CCCM, where the cage was made by spiral winding on the mandrel of UKN-5000, are also shown in the table.

TABLE 6.25. THERMAL CHARACTERISTICS OF CCCM WITH A PYROCARBON MATRIX

Characteristics	Temperature measurements (°C)	Billet form		
		Plate	Pipe-1	Pipe-2
Cage		Fabric package TGM-2	Fillet winding of TGM-2M fabric	Plait winding of UKN-5000 fiber
Density (Mg/m^3)	—	1.45	1.48	1.49
Sizes of billets (mm)	—	500 × 500 × 80	inner dia: 160 outer dia: 85 length: 1000	inner dia: 140 outer dia: 80 length: 800
$\alpha^{x,y}$ (10^{-6} K^{-1})	20–1500	4.7	—	—
α^{z} (10^{-6} K^{-1})	20–1500	4.3	—	—
α_{rad}, (10^{-6} K^{-1})	1000	—	4.6	5.9
α_{axis} (10^{-6} K^{-1})	1000	—	4.4	1.7
α_{circul} (10^{-6} K^{-1})	1000	—	4.0	0.4
$\lambda^{x,y}$ (W/(m·K))	20	7.8	—	—
λ^{z} (W/(m·K))	20	5.4	—	—
λ_{rad} (W/(m·K))	20	—	5.8	5.5
λ_{circul} (W/(m·K))	20	—	8.1	17.5

— data not available.

6.5.6. Pyrolysis installations and process parameters

Gas phase installations are vacuum steel chambers provided with a vacuum pumping system, gas supply system, electric heating, and automatic control of main process parameters.

A principal characteristic of CVI based carbon–graphite material production is the use of low temperature pyrocarbon (instead of pitch or resin) as a binder. Natural gas (~98% CH_4) is used at a pressure slightly higher than atmospheric pressure to prevent air penetration into the vacuum chamber and formation of explosive mixtures. Saturation of porous fillers is performed at 900°C to 1000°C, duration of the process is between a few hours and thousands of hours depending on the required final density of materials, and, first of all, on the dimensions of articles, i.e. on diameter or thickness, not on length.

For realization of volume gas phase impregnation of porous media, a series of pyrolysis installations have been developed at NSC KIPT (Figs 6.44 through 6.45). The main types and characteristics of the pyrolysis installations are presented in Table 6.26.

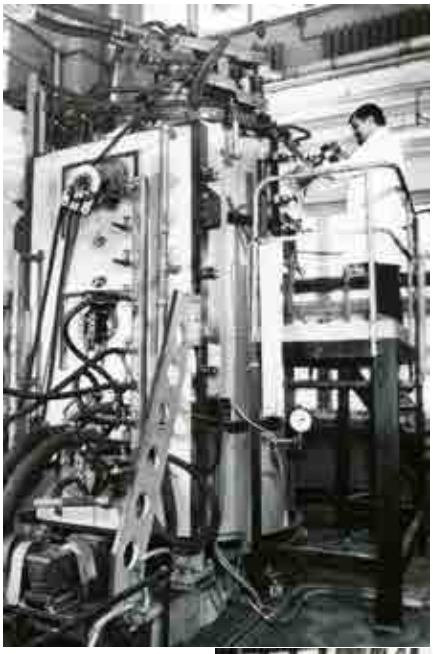

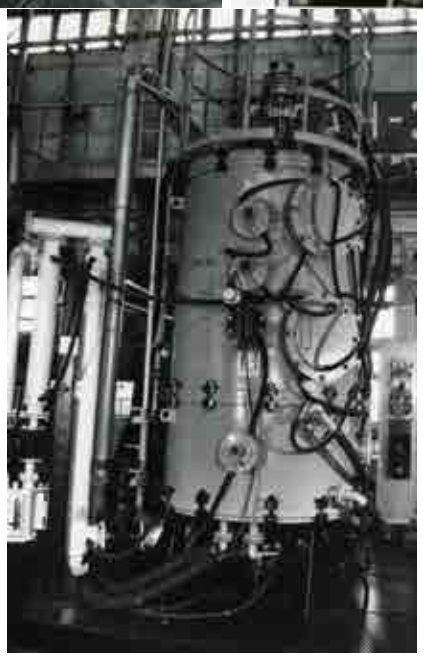

GF-2 GF-3 AGAT-5.0

AGAT-1.6 AGAT-2.0 AGAT-3.2

FIG. 6.44. Pyrolysis installations developed at NSC KIPT.

As can be seen from the table, the smallest of the installations, AGAT-1.6, has been designed for the production of articles of 160 mm in diameter and with a length of up to 1000 mm. At the same time, the largest installation, GF-3, enables to compact articles of 2.5 m in diameter and with a length of up to 2.6 m.

TABLE 6.26. MAIN TYPES AND CHARACTERISTICS OF THE PYROLYSIS INSTALLATIONS

Installation type	Technical characteristics		
	Maximum diameter of product (mm)	Maximum length of product (mm)	Maximum power consumption (kW)
AGAT-1.6	160	1000	100
AGAT-2.0	200	1200	100
AGAT-3.2	320	1200	250
AGAT-5.0	500	2000	500
GF-2	1000	2000	1000
GF-3	2500	2600	1000

FIG. 6.45. General view of the pyrolysis section at NSC KIPT.

Nearly 20 pyrolysis installations of the types listed in Table 6.26 are operating at the NSC KIPT, enabling us to produce up to 100 t per year of high quality carbon materials and to carry out research programmes.

6.5.7. Recommendations for further studies

Since a wide set of graphite based elements of HTGR core will be in operation up to fluence of $\leq 5\times10^{25}$ n/m^2, by now the use of GSP and CCCM can be recommended as basic materials for HTGRs. Particularly promising for this purpose are the CCCM materials with a wide variation of the physical-mechanical and thermo-physical properties depending on the type of binder, reinforcing structure, temperature of treatment of a cage made from carbon filaments, billets etc. The CCCM material being studied belongs to record holders with regard to heat resistance and thermal strength among a wide range of carbon–graphite materials.

The presented technology allows the production of blocks, plates, pipes, cylinders and other structures which may have extensive applications in the HTGR core (Fig. 6.46). It is possible to fabricate CCC cylinders up to 2500 mm in diameter and 2600 mm in height in GF-3 installation (Fig. 6.44) or thick-walled plates, for example, 1500 mm × 1000 mm × (100–150) mm. There is presently no need for larger sizes, but there are no technical or economic barriers expected to the construction of pyrolysis installations capable of producing larger-size structures, e.g. HTGR reflectors. This may offer radically new possibilities of increasing HTGR reliability. Cost of CCCM is presently ~1000.0 US$/kg.

CCCM pipes

GSP graphite blocks

CCCM conic product

FIG. 6.46. Potential applications in an HTGR core.

One of the progressive solutions of reflector production for HTGRs is its manufacture from rings of appropriate sizes (Fig. 6.47). There are no principal difficulties seen in manufacturing thick-walled rings from CCCM of diameter ≥ 3 m and (1.5–2) m in height. It requires, however, the construction of new pyrolysis installations of increased overall dimensions with appropriate energy supply.

Manufacturing of reinforcing cages should be carried out by a method of machine winding of carbon fabric a mandrel with consequent fastening and strengthening of winding structure in a radial direction, by thread piercing, or by rod broaching. For such bulky billets, the method of winding will be one of most economic and simplest in engineering construction.

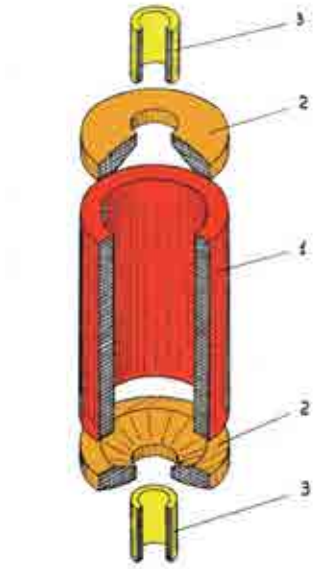

1: side reflector (3–6) m in diameter, 2: bottom and top face reflector, 3: bottom and top discharging tube.

FIG. 6.47. Suggested (forecasted) one-piece large scale unit for HTGR made of composite materials with carbon fiber fillers bound with pyrocarbon:

6.5.8. Conclusions

Analysis of experimental results obtained enables to state the following:

- Under neutron irradiation the carbon–graphite GSP and CCCM materials manufactured by the gas phase technology undergo isotropic shrinkage only slightly dependent on the irradiation temperature and neutron fluence (above 3×10^{25} n/m^2).
- GSP graphite did not reveal any degradation of properties up to the investigated neutron fluence of 10×10^{25} n/m^2.
- Regarding the absolute values, the strength characteristics of irradiated GSP and CCCM materials remain high and significantly exceed those of the presently existing best grades of reactor graphite.
- Materials manufactured by the gas phase technology can be recommended for the use as thermally stressed elements in an HTGR core.
- Supposed the use of gas phase methods allows the manufacture of large-size GSP and CCCM billets possessing a high neutron irradiation resistance, perfectly new opportunities will be opened for the construction of HTGR cores in the form of large scale facilities.

6.6. EXPERIENCE AND DEVELOPMENT IN THE USA

In the USA, a comprehensive programme titled advanced gas reactor (AGR) has been started with the overall goal of VHTR fuel development and qualification. The fuel particle and fuel compact development work was performed at the ORNL. Phase one of the AGR programme (AGR-1) involved fabrication of AGR-1 fuel compacts for irradiation in the INL advanced test reactor (ATR) [214].

6.6.1.1. Matrix production

The matrix was made by mixing natural graphite, synthetic graphite, and a thermosetting resin in the ratio of 64, 16, and 20 wt%, respectively, which is equivalent to the A3 matrix formulation that was developed in Germany. Natural graphite is highly anisotropic, but can be milled into a fine particle size and re-formed into graphite that is macroscopically isotropic. Synthetic graphite is less anisotropic than natural graphite, but also can be milled and re-formed in order to produce an overall isotropic graphite. The resin used in the A3 matrix is added in order to provide adhesion to the mixture and the TRISO particles during overcoating, and to fuse the compact into a solid piece during the carbonization step.

After carbonization and heat treatment, final impurities concentrations were within specification. Based on this requirement, the best natural graphite candidates were the Asbury Graphite Mills sample (RD 13371), and the Graftech natural flake milled grade (GTI-NFM). The synthetic graphites with lowest impurities content were the SGL sample (KRB2000) and the Timcal KS-15 grade. The resin candidates with the lowest impurities were the Borden Durite sample, and the Plenco P-800 resin. The matrix was produced by wet mixing the three raw materials in a jar mill with ethylalcohol. After spinning for one hour, the contents of the container were poured into a large rectangular pan and allowed to dry for 48 hours. After drying, the 'cake' of graphite and resin was broken into smaller pieces and charged to a Holmes pulverizer with a US Sieve 60 mesh screen (250 μm opening) in place. After pulverizing, the matrix production was complete.

6.6.1.2. Overcoating method

The first AGR overcoater utilized a top secured design. Coating of 500 μm surrogate zirconia kernels (outer diameter: ~1000 μm after coating) was initially performed in order to try to replicate the German coating process. The overcoating process developed in Germany involved slowly rotating the TRISO particles and matrix in a large steel drum. Methanol jets were also incorporated into the drum which aided in the matrix adhering to the TRISO particle.

The TRISO coated 500 μm particles produced as part of the first TRISO coating applications were available, so they were used to gain experience with the overcoating process and generate early data. The slow rolling method developed by the Germans was used to successfully overcoat these TRISO coated 500 μm surrogates in the top secured overcoater. Figure 6.48 shows a particle overcoated by this method.

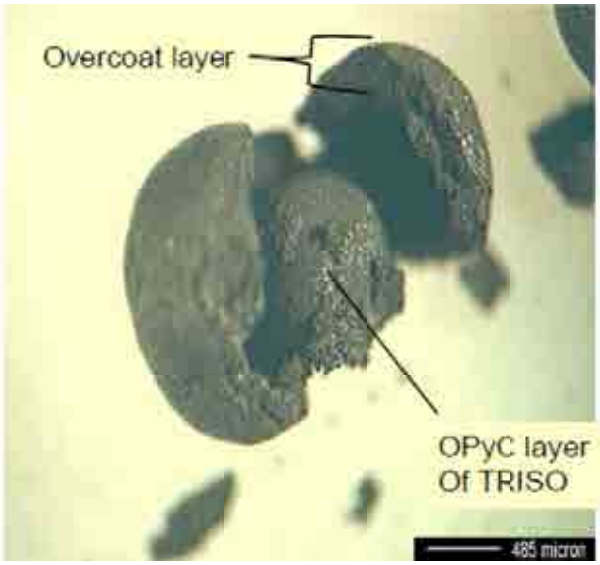

FIG. 6.48. Overcoated particle using top secured overcoater and slow rolling method, overcoat intentionally broken off to show TRISO particle.

In the next step, it was switched from TRISO coated 500 μm particles to TRISO coated 350 μm particles corresponding in size to the eventual LEU UCO TRISO particles for AGR-1 test article fabrication. Interestingly, poor overcoating results were obtained in the top secured overcoater. It was then decided to secure the bottom of the overcoating chamber to the motor, thus allowing easier access to the particle/matrix mixture. Figure 6.49 shows the bottom secured overcoater. After redesigning the overcoating chamber, it appeared that this process change led to successful overcoating of TRISO coated 350 μm particles.

Through experimentation it was found that the best way to create the environment — well mixed particles and matrix with an added agent to aid in the adherence of matrix to the smaller sized particles — would be a centrifugal overcoating method. The key aspects of the centrifugal overcoating method are:

- the particles and matrix are pre-mixed in a set ratio;
- the particle/matrix mixture is spun at high enough speed to force the mixture to the walls of the overcoater;
- upon insertion of the agitator arm, the mixture comes off the wall of the overcoater as a spray which passes through a fine mist of methanol. The mist of methanol is achieved with a syringe pump and ultrasonic atomizer.

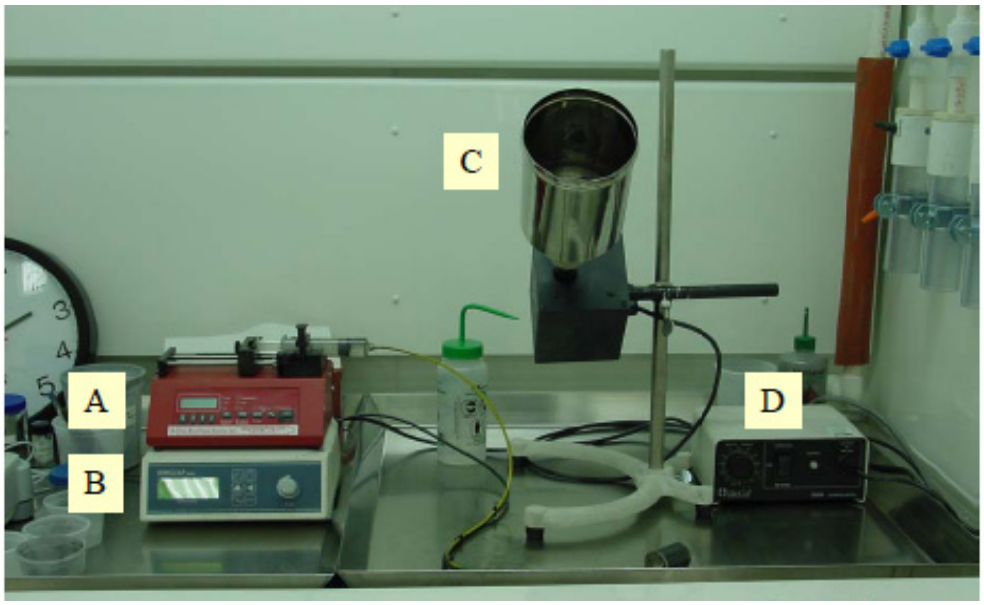

A: syringe pump, B: ultrasonic atomizer, C: overcoating chamber, D: motor.

FIG. 6.49. Overcoater set-up.

A schematic of the centrifugal overcoating process is shown in Figure 6.50.

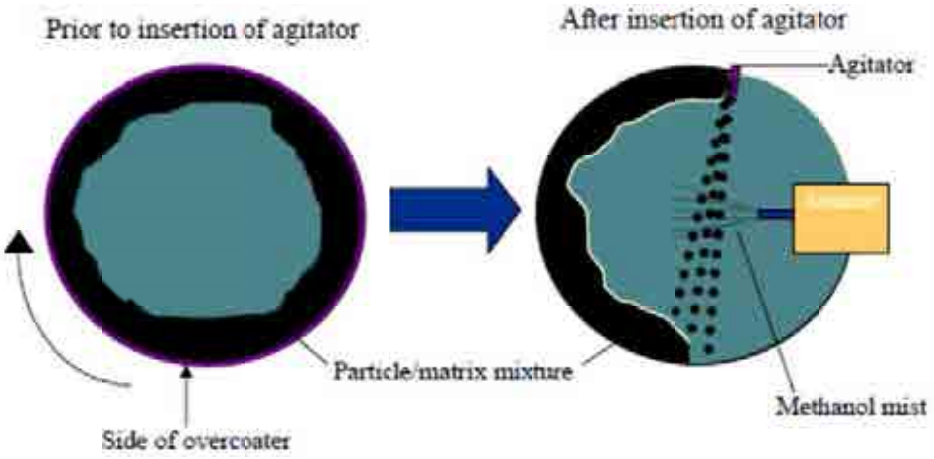

FIG. 6.50. Schematic of the centrifugal overcoating process developed at ORNL.

The pre-mixing of the particles and matrix in a set ratio allows for good contact between the matrix and the particles and a lesser probability that matrix clumps will form because essentially no excess matrix that could lead to clump formation is present. The spinning of the particle/matrix mixture ensures that the set mixture ratio will be maintained during overcoating, as the particles and matrix are not moving because they are pinned to the wall of the overcoater. The use of the agitator arm to spray the particles off the wall and through a mist of methanol ensures that the methanol is delivered at a time when the correct ratio of particles and matrix is present such that the matrix will adhere to the OPyC layers of the particles, and not itself. The mist of methanol helps to evenly coat the particles so that an even layer of matrix is deposited over the entire surface area of the particles. The centrifugal overcoating method proved effective and overcoated particles with the desired overcoat layer thickness were successfully produced. Optimal process variables of quantity of TRISO

particles, quantity of matrix, volume of methanol, angle of the overcoater, and speed of overcoating, were determined experimentally.

6.6.1.3. Compacting method

Once the overcoating method had successfully produced overcoated particles with outer diameters required to meet the fuel particle packing fraction, compacting of those overcoated particles was initiated. As part of the compacting method development, LEU01-46T TRISO (baseline) particles were received after having been characterized [215]. Prior to overcoating, the particles were washed in methanol to reduce the amount of contamination on the particles. After washing, the LEU01-46T particles were overcoated in the above described way.

Figure 6.51, left, shows an image of the outer surface of a compact that was formed without overcoated particle exposure to methanol prior to compacting. Notice the pits and open spaces between particles where the overcoat did not effectively flow into the inter-particle spaces. Figure 6.51, right, shows a compact whose overcoated particles were saturated with methanol prior to compacting. The surface finish of this compact appears smoother and uniform because the overcoat was more malleable and able to fill the void spaces between particles.

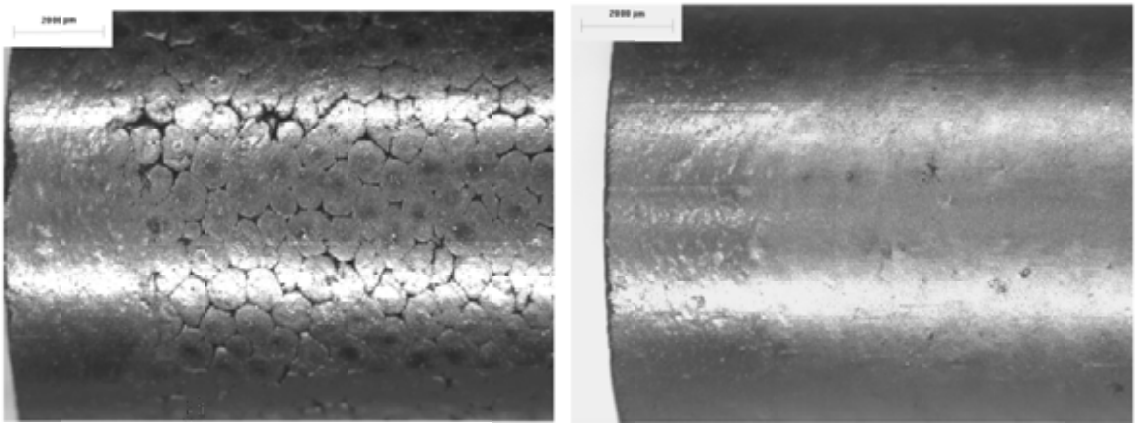

FIG. 6.51. Image of compact side showing complete compression due to proper saturation of overcoated particles prior to compacting (left); incomplete pressing due to lack of methanol saturation in the original overcoated particles (right).

The overcoated particles were sized using sieves and tabled in order to extract the most spherical overcoated particles available. The sieved and tabled overcoated particles were then riffled into aliquots for compacting where one aliquot was used to form one compact. The overcoated particles were saturated with methanol vapour prior to compacting in order to increase the malleability of the overcoat and thus allow it to more effectively migrate and fill inter-particle spaces during compacting. Table 6.27 provides a summary of the relevant overcoating and compacting data used in fabricating the AGR-1 test articles.

TABLE 6.27. OVERCOATING AND COMPACTING SUMMARY

Item	LEU01-46T (Baseline)	LEU01-47T (Variant 1)	LEU01-48T (Variant 2)	LEU01-49T (Variant 3)
Weight TRISO (mg)	0.727	0.733	0.724	0.726
Diameter (μm)	799.7	804	798	795
g of +18 particles, Bin 3	410	424	358	415
Tabler yield (%)	77	96	96	90
Weight overcoated particle (mg)	1.16	1.12	1.19	1.21
Compacting charge overcoated particles used (g)	4.8600	4.7300	4.9400	5.0230
No. of compacts fabricated	84	85	71	82
No. of compacts needed for AGR-1	79	79	67	79

Table 6.28 gives the upper limit of the 95% confidence interval of the defect fraction for exposed kernels. No exposed kernels were detected in any of the compact lots. The table also gives the upper limit of the 95% confidence interval of the defect fraction for particles with defective SiC before and after compacting. No defective SiC was detected in variants 1 and 3. Baseline showed two defective particles and variant 2 showed one. The baseline defective SiC fraction appears to have increased due to the compacting process. This may be due to cracking of the SiC during compacting on particles with abnormally thin regions of SiC (< 15 μm as opposed to a normal thickness of 35 μm).

TABLE 6.28. OVERCOATING AND COMPACTING SUMMARY

Property	Baseline	Variant 1	Variant 2	Variant 3
Exposed kernel fraction	$\leq 3.1 \times 10^{-5}$ (0/99 470)	$\leq 4.1 \times 10^{-5}$ (0/74 699)	$\leq 3.1 \times 10^{-5}$ (0/99 110)	$\leq 3.1 \times 10^{-5}$ (0/99 032)
Defective SiC coating fraction, after compacting	$\leq 1.3 \times 10^{-4}$ (2/49 735)	$\leq 6.1 \times 10^{-5}$ (0/49 799)	$\leq 9.6 \times 10^{-5}$ (1/49 555)	$\leq 6.1 \times 10^{-5}$ (0/49 516)
Defective SiC coating fraction, before compacting	$\leq 2.5 \times 10^{-5}$ (0/120 688)	$\leq 4.0 \times 10^{-5}$ (1/121 117)	$\leq 9.5 \times 10^{-5}$ (1/50 265)	$\leq 4.0 \times 10^{-5}$ (1/120 660)

Note: Values in parentheses are the actual measured defects over the number of particles in the analysed compacts.

7. IRRADIATION TESTING OF HTGR FUEL

7.1. INTRODUCTION

7.1.1. Various types of irradiation tests

There are various types of irradiation testing of HTGR fuel which can basically be categorized in four groups:

(1) Irradiation of the HTGR fuel inside closed capsules. This is the simplest irradiation geometry. Since no information on the fuel behaviour is obtained during the irradiation test, information can only be achieved during the post-irradiation examination (PIE).

(2) Irradiation of the HTGR fuel inside capsules in which the gas is purged during the irradiation. The xenon and krypton fission gas atoms which were released during the irradiation are taken up by the purge gas and the activity of this gas can be measured outside the irradiation experiment.
(3) The HTGR fuel is placed in a gas loop in which high pressure high speed helium gas is purged along the fuel. The fuel is then directly cooled by the flowing helium gas. In the capsules mentioned under the previous two bullets the heat is generally transported from the fuel over a small gas gap surrounding the fuel. The pressure and cooling conditions in a gas loop are therefore more representative for HTGR conditions than the capsules mentioned above. However, the technical and financial complications involved in constructing an in-reactor gas loop are immense and therefore, in the past, capsule irradiations were considered sufficient for fuel qualification.
(4) The irradiation is performed in experimental HTGRs, such as Dragon, AVR, Peach Bottom, or the currently operated HTR-10 and HTTR. These irradiation conditions are the most relevant, but it is more difficult to analyse the irradiated fuel spheres/compacts amongst others because of the imprecise knowledge of the irradiation history.

Besides the irradiation of fuel compacts and fuel spheres with a wide variety of kernel material, there have also been performed a large number of irradiations in which parts of the fuel compacts and fuel sphere have been irradiated:

- irradiation of matrix graphite;
- irradiation of loose coated particles;
- irradiation of designed-to-fail particles;
- irradiation of coating layers that do not contain fissile material.

Besides irradiation testing under normal conditions it is also of crucial importance to study the behaviour of the fuel during accident conditions. Accident simulation testing can be done

- by heating the irradiated fuel in a hot cell in order to study fission product release behaviour during a simulated core heatup accident. One of the devices constructed for accident testing is the KÜFA test facility which will be described in more detail in Section 8;
- by heating the fuel during irradiation. An example of this is described later in this section for the IVV-2M reactor in the Russian Federation;
- by introduction of water vapour into the irradiation capsule to study fission product behaviour under oxidizing conditions simulating a water ingress.

In this section, the focus is on irradiation testing of HTGR fuel in MTRs. Real-time testing in HTGRs was already treated in the previous Section 5.

7.1.2. Short-lived noble gas/halogen release

7.1.2.1. Introduction

The release of noble gases from spherical fuel elements has been extensively investigated by in-pile measurements of irradiation experiments and the regular monitoring of the coolant gas activities of the AVR and the THTR.

The transport mechanisms of the noble gases produced by the finely distributed uranium contamination of the matrix material were clarified by the results from seven irradiation

experiments in the R2 test reactor at Studsvik (seven xenon, six krypton isotopes) [216]. The gas release from artificially failed particles was firstly studied in detail with the irradiation experiments FRJ-P25 ($(Th,U)O_2$ kernels) and FRJ2-P28 (UO_2 kernels) in the FRJ2 test reactor at Jülich [217]. More refined model data of the transport characteristics of production induced defects of TRISO particles with UO_2 kernels were drawn from the German reference irradiation tests for proof test fuel, HFR-K5 and -K6, in the HFR, Petten [218]. A description of internationally applied fission gas release models was given in [1].

In several irradiation experiments, the ^{131}I activity released from the test elements and deposited on the capsule walls was measured out of pile directly after termination of the irradiation. Furthermore, during reactor shut down periods between consecutive irradiation intervals, the 'cold' release of ^{133}Xe and ^{135}Xe atoms (70°C) being produced by their radioactive precursors ^{133}I and ^{135}I were measured in-pile. These data determine upper limits for the iodine release during irradiation, because iodine atoms entirely released from the fuel sphere and still adhering to the surfaces of open porosity cannot be distinguished. All experimental findings confirm that the transport behaviour of the halogens at elevated temperatures is similar to that of noble gases.

Regular measurements of the coolant gas activities in the AVR and the THTR-300 have been conducted and evaluated on the base of above transport models verifying their reliability and applicability under real pebble bed reactor conditions [50, 219]. Not only did these evaluations serve to test the underlying design methods, they also helped identify potential failure mechanisms and supervise the quality of the fuel elements.

7.1.2.2. Radionuclide transport and release phenomena

The relative importance of the phenomena associated with radionuclide transport and release is strongly dependent upon a number of parameters, including birth location within a particle or sphere, particle condition/characteristics, temperature, and radionuclide physical and chemical properties.

The following phenomena are associated with radionuclide transport within a fuel sphere:

- Fission product recoil: The fission products are produced with a high initial kinetic energy and travel through the surrounding material over a finite distance and if near the kernel surface or in a graphite particle may be ejected and deposited in a pore location from which they can be more readily transported to the fuel sphere surface. The average recoil distance varies by radionuclide and by the material. The fraction of fission product released by recoil is independent of irradiation parameters and, in particular, of temperature. For the reference 500 mum diameter UO_2 kernel, the release fraction in the surrounding buffer region is ~2 to 3%. For fissions from heavy metal contamination in the matrix material, the fraction deposited in the intergranular region is approximately an order of magnitude higher [220].
- Diffusion: Radionuclides move within the fuel particles and matrix material of a fuel sphere by diffusion associated with the concentration gradients within the sphere. The rate of diffusion varies by many orders of magnitude and is a strong function of many parameters including chemical and physical properties of the radionuclide, material, location in micro-structure, and temperature. During normal operation, the oxide kernel (and to a lesser degree oxycarbide and carbide kernel) is highly retentive of most radionuclides, the dense pyrocarbon layers are

effective barriers to gaseous fission product diffusion, and the silicon carbide layer is an effective diffusion barrier to almost all radionuclides (silver being a notable exception at elevated temperatures).

- Surface sorption and mass transfer: Graphite has the ability to adsorb metallic atoms. On the surface of the fuel sphere, fission product transport to the coolant gas is controlled by a combination of surface sorption and convective mass transfer [221].

Extensive irradiation and post-irradiation safety testing to measure radioisotope release has been conducted on fuel particles and spheres [15, 71, 222]. The dominant radionuclides released from the fuel were identified by gamma and beta measurements in the course of PIE. In-pile irradiation data were measured in an ex-core loop, with results limited to noble gases because of condensation and plateout of other species in the tubing between the core and detector. Post-irradiation testing data included both gaseous radioisotopes measured in a gas loop, and metallic radioisotopes detected on cold finger deposition plates that were periodically cycled through the furnace in the course of the test. Limited post-irradiation testing data were developed for the more short-lived radioisotopes (e.g. ^{131}I, ^{110m}Ag) in testing conducted shortly after completion of the irradiation, but the majority of data was for the longer-lived species (e.g. ^{85}Kr and ^{137}Cs).

(a) Equivalent sphere model

Notwithstanding the fact that SiC is the primary fission product barrier in HTGR fuel, retention in the UO_2 kernel plays an important role. A set of useful correlations has been derived for kernel retention assuming a delay in the UO_2 grains that are modeled as small spheres with radius a, known as Booth [223] model or 'Equivalent Sphere Model' [224]. These correlations have also been applied for release of fission gases from heavy metal contamination in the matrix material, in which case the equivalent sphere stands for a graphite grain. Applying numerical simulation diffusion codes, a is replaced by the real radius of the fuel kernel, of the coated particle, or of the spherical fuel element.

Some special solutions of the pertinent diffusion equation are given below. Assuming constant production rate and a stable fission product, the in-reactor fractional release is

$$F_{in-reactor} = 1-\frac{6}{D't}\sum_{n=1}^{\infty}\frac{1-e^{-n^2\pi^2 D't}}{n^4\pi^4} = 1-\frac{1}{15D't}+\frac{6}{D't}\sum_{n=1}^{\infty}\frac{e^{-n^2\pi^2 D't}}{n^4\pi^4} \quad (7.1)$$

where

$D'\left[s^{-1}\right] = D/a^2$ is the reduced diffusion coefficient.

$F_{in-reactor}$ is efficiently approximated by

$$F \approx 4\sqrt{\frac{D't}{\pi}}-\frac{3}{2}D't \quad \text{for } D't \le 0.35\text{, and} \quad (7.2)$$

$$F \approx 1-\frac{1}{15D't} \quad \text{for } D't > 0.35\text{.} \quad (7.3)$$

The predicted release curve, applicable to the irradiation of a defective or failed particle is shown as the lower term in Fig. 7.1 displayed versus a dimensionless kernel diffusion time given by the product of the reduced diffusion coefficient with heating or irradiation time. It is compared with the respective release curve for the heating condition [224].

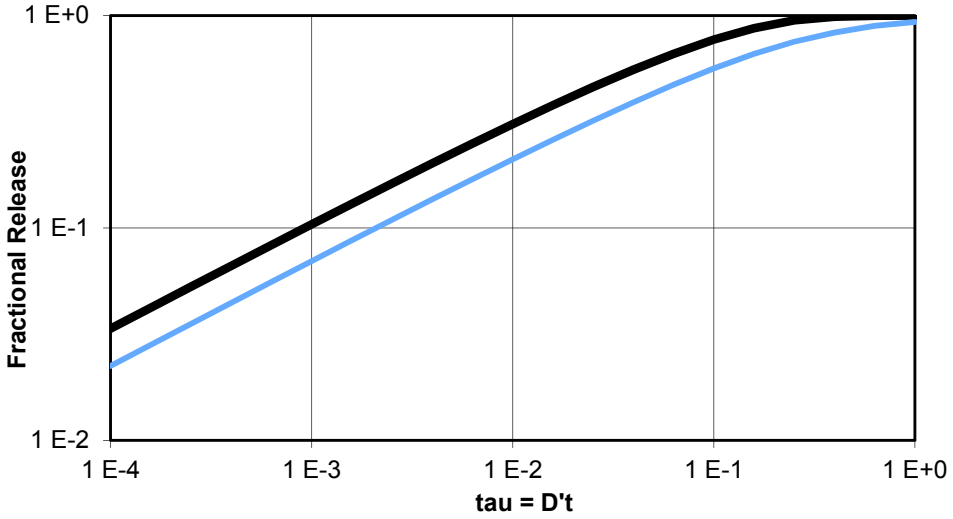

FIG. 7.1. Fractional release of long-lived fission products during heating (upper curve) and during irradiation (lower curve) as a function of diffusion time t=D't according to the equivalent sphere model.

Kernel retention is mainly due to fission product slow-down in UO_2 grains. Further delays in grain boundaries, intergranular bubbles, etc., are usually neglected in high burnup (> 8% FIMA) HTGR fuel. Because numerical diffusions codes like GETTER [225] and FRESCO [221, 226] treat the whole kernel as one representative unit, the equation

$$D' = \frac{D_{grain}}{a^2} = \frac{D_k}{r_k^2} \tag{7.4}$$

is valid with a being the equivalent grain radius and $r_k = 250\mu m$ kernel radius.

Usual tables [1, 227] contain D_k values. Recommended kernel diffusion coefficients are given in Table 7.1.

TABLE 7.1. RECOMMENDED REDUCED KERNEL DIFFUSION COEFFICIENTS OF KEY FISSION PRODUCTS IN UO_2

Species	D_o' (s^{-1})	Q (kJ/mol)	Reference
Caesium	0.90	209	row „FRG' in [1]
Strontium	3.5×10^{4}	488	
Silver	0.107	165	
Xenon, krypton	2.1×10^{-5}	126	
Xenon, krypton [a]	5×10^{-3}	155.4	[228]

[a] for prediction of the release of stable and long-lived fission gases.

The release equations (7.1), (7.2), (7.3) can also be used to predict ^{137}Cs, ^{90}Sr, and ^{110m}Ag release from the kernel into the buffer layer or, vice versa, to derive the effective mean irradiation temperature from the measurement of internal fission product release.

(b) Short-lived fission gases Xe and Kr

To determine in-reactor release rates of short-lived fission gases, the steady state solution of the diffusion equation

$$0 = D\frac{1}{r}\frac{\partial^2(rc)}{\partial r^2} - \lambda c + p \tag{7.5}$$

is solved to give the release rate (R) to birth rate (B) ratio

$$\frac{R}{B} = 3\sqrt{\frac{D'}{\lambda}}\left(\coth\sqrt{\frac{\lambda}{D'}} - \sqrt{\frac{D'}{\lambda}}\right) \tag{7.6}$$

Figure 7.2 shows the good agreement of this model with a calibration experiment for gas release and also the comparison to the more sophisticated NOBLEG code [216].

By comparing in-reactor measured R/B data to predicted R/B for one bare kernel from the formula above, one can estimate the fraction of manufacture-induced defective or in-reactor failed particles. The full transient solution of the diffusion equation results in the R/B ratio is given by

$$\frac{R}{B} = 3\sqrt{\frac{D'}{\lambda}}\left(\coth\sqrt{\frac{\lambda}{D'}} - \sqrt{\frac{D'}{\lambda}}\right) - 6e^{-\lambda t}\sum_{n=1}^{\infty}\frac{e^{-n^2\pi^2 D't}}{n^2\pi^2 + \lambda/D'} \tag{7.7}$$

and cumulative fractional release given by

$$F(t) = 3\sqrt{\frac{D'}{\lambda}}\left(\coth\sqrt{\frac{\lambda}{D'}} - \sqrt{\frac{D'}{\lambda}}\right) - \frac{6}{\pi^2}\cdot\frac{\lambda}{D'}\cdot\frac{1}{e^{\lambda t}-1}\cdot\sum_{n=1}^{\infty}\frac{1-e^{-n^2\pi^2 D't}}{n^2\left(n^2\pi^2 + \lambda/D'\right)} \tag{7.8}$$

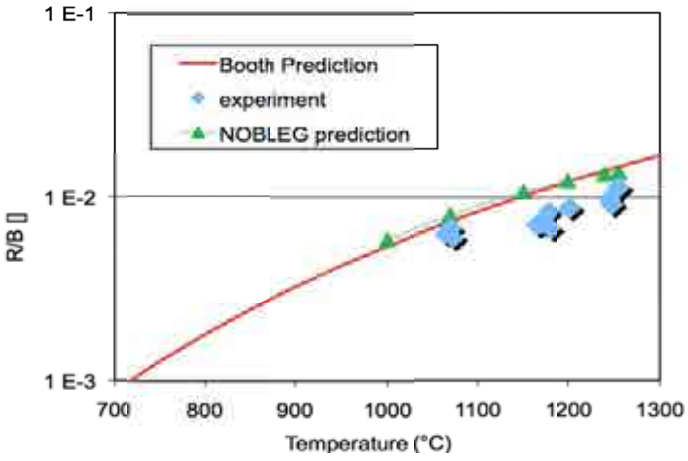

FIG. 7.2. Kr-85m release rate from UO_2: model predictions and measurements in capsule 2 of the release calibration experiment FRJ2-P28.

(c) Uranium contamination of the matrix material

The transport model describing the release of fission gases from the uranium contamination of the matrix material is outlined in Fig. 7.3 [216]. The graphitic matrix material is treated as a three-component system. Component 1 may be attributed to the graphite grains of the raw material and component 2 to the amorphous, non-graphitized binder coke between the grains. The open pore system filled with helium constitutes the gaseous component 3.

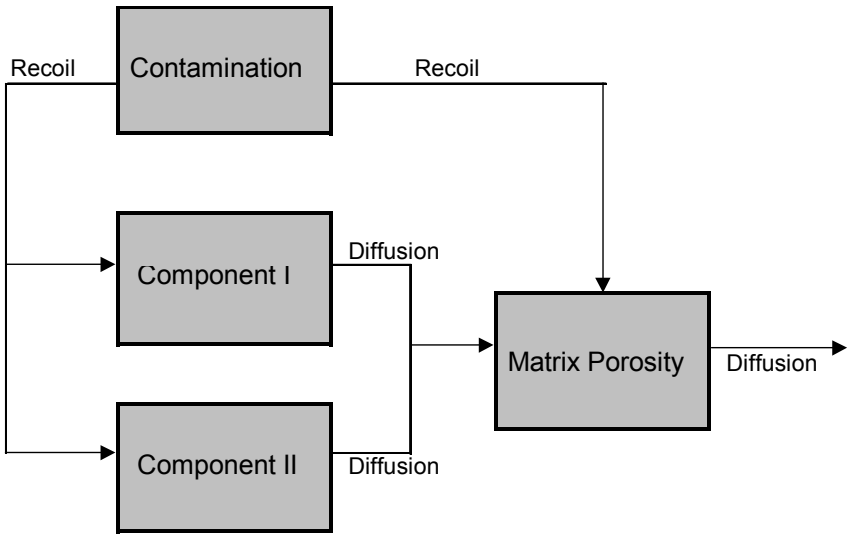

FIG. 7.3. Transport model for noble gas release from contamination of the matrix material.

The primary fission products are distributed homogeneously in these components by direct recoil. The gas atoms diffuse from the recoil sites in the grains of the solid components to the open porosity of the fuel sphere. The steady state fractional release due to this diffusion in each solid component is determined by the above described equivalent sphere model according to

$$\frac{R}{B} = 3\,U_c \sqrt{\frac{D_r}{\lambda}} \left(\coth \sqrt{\frac{\lambda}{D_r}} - \sqrt{\frac{D_r}{\lambda}} \right) \tag{7.9}$$

where

R is the release rate into the open porosity (atoms/s);
B is the fission (birth) rate in the fuel sphere (atoms/s);
U_c is the ratio of uranium finely distributed in the matrix material to total uranium inventory of fuel sphere ('U-contamination of the matrix material');
λ is the decay constant of noble gas nuclide (s^{-1});
$D_r = D/r^2$ is the reduced diffusion constant of noble gas element in component 1 or 2 (s^{-1});
D is the diffusion constant of xenon or krypton in component 1 or 2 (m^2/s);
r is the equivalent sphere radius of component 1 or 2 (m).

The two solid state diffusion processes and the direct recoil into the pore system are followed by the pressure and temperature dependent gas phase transport through the open porosity of the fuel sphere to the coolant. This process is also described by the Booth equation (7.9) where r equals the radius of the fuel element and D equals the effective diffusion constant for the combination of Knudsen and binary gas diffusion given by the Bosanquet equation:

$$\frac{1}{D} = \frac{1}{(k_1 v)} + \frac{1}{(k_2 D_{1,2})} \tag{7.10}$$

where

k_1, k_2 are structural parameters of A3 matrix material;

$v = \sqrt{\frac{8RT}{\pi m}}$ is the mean thermal velocity of gas atoms (m/s);

m is the atomic weight;
T is the absolute temperature (K);
R is the absolute gas constant, = 8.3145 (J/(mol·K);
$D_{1,2}$ is the binary diffusion constant of xenon or krypton in helium.

The parameters k_1 and k_2 were measured for unirradiated A3 matrix material using a hydrogen permeation method. The binary the gas-in-gas diffusion coefficient is approximately proportional to $T^{1.5}$ following the Chapman–Enskog theory of gases.

The release from the grains of the material components and the recoil into the pore system are working in parallel followed in series by the gas phase transport through the porosity. Consequently, the total gas release from the fuel sphere is given by the addition of two terms according to equation (7.1) and a constant term multiplied with the same equation (U_c being omitted) where $D_r = D/r^2$ and D is given by equation (7.10) with r = 0.03 m.

7.1.2.3. Release from MTR experiments

In general, analytical solutions of the diffusion equation are not available for the complex situation of a coated particle with several coating layers embedded in spherical fuel or compacts elements. Therefore, numerical simulation codes have been developed to predict and postcalculate irradiation tests in material test reactors and post-irradiation heating tests (see also Section 9). Then, theses codes are also used for release predictions in planned reactors like the Siemens HTR-Modul and the Chinese HTR-PM, or for the analysis of the core releases from operating reactors like AVR, THTR, and Fort St. Vrain.

All models have to be verified and — together with an appropriate data set — they have to be validated by suitable experimental material. This is most reliably done on the measured releases from complete spherical fuel elements. Fission gases are measured throughout irradiation. The release of metallic fission products is determined after irradiation by gamma and beta spectrometry of all components outside the fuel element. A compilation of the most representative results [229] is given in Table 7.2 and shown in Fig. 7.4 versus an average irradiation temperature.

It can be observed that silver release becomes significant at irradiation temperatures above 1000°C. This is a well known phenomenon even in particles with high quality SiC coatings [106, 230, 231].

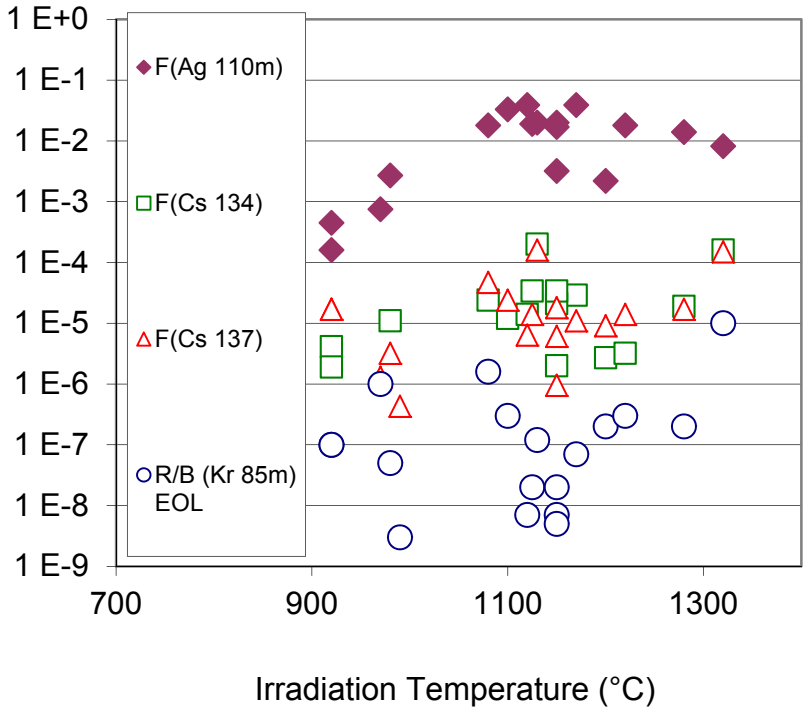

FIG. 7.4. Fractional release of ^{110m}Ag, and ^{134}Cs, ^{137}Cs as a function of temperature in 230–530 d irradiation tests as measured in post-irradiation examination work, also included end-of-irradiation gas release rates R/B.

Caesium releases shown in the table are insignificant below the 2×10^{-5} level, because this is the lower detection limit when working in a hot cell environment. In the case of in-reactor caesium release, the ^{137}Cs and the ^{134}Cs release fractions should be identical, because the two caesium isotopes have the same chemical behaviour. If this is not the case, caesium comes from external contamination sources.

In several irradiation experiments with R/B values of ^{133}Xe in the range from 10^{-7} up to 10^{-2} covering contamination and failed particle dominated releases, an approximate 1:1 relation between the ^{133}Xe (half life: 5.3 days) and ^{131}I (half life: 8.0 days) R/B values was found. For R/B values below 10^{-5}, the ^{131}I data lie by a factor of about 3 below the ^{133}Xe R/B values. This indicates the effect of an adsorption/desorption equilibrium on the surfaces of the open porosity at low iodine partial pressures which reduces the effective gas phase diffusion constant of iodine. In total, it can be concluded that it is conservative to use the same diffusion data for iodine as for xenon. The same applies to bromine and krypton.

7.1.3. Some fundamental considerations pertaining to modeling the mechanical behaviour of coated fuel particles during irradiation

7.1.3.1. Introduction

A number of important features that are required in a computer code to model the irradiation performance of coated fuel particles during irradiation are identified. Amongst these are the following:

- A suitable equation of state to calculate the internal gas pressure is necessary since the perfect gas law is inadequate.
- An allowance for the presence of CO_2 should be taken into account when calculating gas pressures.

- The code should be able to model the whole life of a particle, from manufacture, followed by a complex irradiation history and then on to long term storage.
- Kernel–coating mechanical interaction (KCMI) as a possible cause of particle failure must be taken into account.
- Execution times must be sufficiently fast to enable statistical calculations, involving many computer runs, to be feasible.

These features are illustrated in the modeling of a number of experiments using the computer programme STRESS3 and the associated statistical code STAPLE. The modeling of two Japanese irradiation experiments illustrated (a) the need for a statistical code, and (b) to be able to model monotonic changes in temperature over the course of an irradiation, in order to reproduce the experimental observations.

Pre-irradiation modeling of German fuel in the HFR-EU1 experiment demonstrated that KCMI is predicted to be the predominant failure mechanism, and that statistical variations in the burnup at which failures occur are governed, almost entirely, by the variability in the buffer layer thickness. KCMI was also identified as a failure mechanism in the US NPR-1 irradiation, but only after the IPyC layer had failed first. This was identified as being due to a rather subtle IPyC Poisson ratio effect.

TABLE 7.2. EXPERIMENTAL END-OF-IRRADIATION ^{85m}Kr RELEASE RATE R/B AND CUMULATED FRACTIONAL METALLIC RELEASE F FROM FUEL ELEMENTS WITH HIGH QUALITY (Th,U)O_2 AND UO_2 TRISO PARTICLES. RESULTS ARE ARRANGED WITH INCREASING AVERAGE IRRADIATION TEMPERATURE

Test	Irradiation time (efpd)	Irradiation temp. (°C)	Burnup (% FIMA)	R/B Kr-85m	F Cs-137	F Cs-134	F Ag-110m
HFR-K3/2	359	920	10	1×10^{-7}	1.7×10^{-5}	4.1×10^{-6}	4.5×10^{-4}
HFR-K3/3	359	920	10.6	1×10^{-7}	1.7×10^{-5}	1.9×10^{-6}	1.6×10^{-4}
FRJ2-K15/1	533	970	14.1	1×10^{-6}	1.3×10^{-6}	—	7.5×10^{-4}
R2-K13/4	517	980	9.8	5×10^{-8}	3.2×10^{-6}	1.1×10^{-5}	2.7×10^{-3}
FRJ2-K15/3	533	990	14.8	3×10^{-9}	4.3×10^{-7}	—	—
FRJ2-P27/1	232	1080	7.6	2×10^{-6}	4.7×10^{-5}	2.4×10^{-5}	1.8×10^{-2}
R2-K12/1	308	1100	11.1	3×10^{-7}	2.4×10^{-5}	1.2×10^{-5}	3.3×10^{-2}
FRJ2-K13/4	396	1120	7.6	7×10^{-9}	6.4×10^{-6}	1.4×10^{-5}	3.9×10^{-2}
FRJ2-K13/1	396	1125	7.5	2×10^{-8}	1.4×10^{-5}	3.4×10^{-5}	1.9×10^{-2}
FRJ2-P27/3	232	1130	7.6	1×10^{-7}	1.6×10^{-4}	2.0×10^{-4}	2.0×10^{-2}
FRJ2-K13/3	396	1150	7.9	7×10^{-9}	6.1×10^{-6}	3.4×10^{-5}	1.7×10^{-2}
FRJ2-K13/2	396	1150	8	2×10^{-8}	1.8×10^{-5}	2.1×10^{-5}	2.0×10^{-2}
FRJ2-K15/2	533	1150	15.3	5×10^{-9}	9.5×10^{-7}	2.0×10^{-6}	3.2×10^{-3}
R2-K13/1	517	1170	10.2	7×10^{-8}	1.1×10^{-5}	2.9×10^{-5}	3.9×10^{-2}
HFR-K3/1	359	1200	7.5	2×10^{-7}	9.1×10^{-6}	2.7×10^{-6}	2.2×10^{-3}
HFR-K3/4	359	1220	9	3×10^{-7}	1.4×10^{-5}	3.2×10^{-6}	1.8×10^{-2}
R2-K12/2	308	1280	12.4	2×10^{-7}	1.7×10^{-5}	1.9×10^{-5}	1.4×10^{-2}
FRJ2-P27/2	232	1320	8	1×10^{-5}	1.5×10^{-4}	1.6×10^{-4}	8.2×10^{-3}

— not measured.

A modeling of the comprehensive Dragon Project Charge III Centre Rod experiment is reported. A reasonable correlation with experimental observations was obtained provided there was included the option that the outer pyrocarbon (OPyC) layer had failed first, due to interaction with the retaining meniscus bonded resin. The modeling was performed using STRESS3 [232], a code which models stresses in individual particles, and STAPLE which calculates particle failure statistics by running STRESS3 many times.

7.1.3.2. Some important features desirable in an advanced fuel performance code

(a) Equation of state

Because it is known that failure of coatings will occur if the internal gas pressure exceeds some critical value, it is clearly important that an appropriate equation of state be employed to calculate pressures. Amongst the many equations of state which have been proposed, the one by Redlich and Kwong [233] appears to combine the advantages of both a simple formula and a high level of accuracy for the current application. Figure 7.5 compares some experimental pressure–volume values for xenon, due to Harrison [234], at three temperatures, with the corresponding Redlich–Kwong isotherms. It is apparent that agreement is excellent over the temperatures and pressures that are relevant to coated particle modeling.

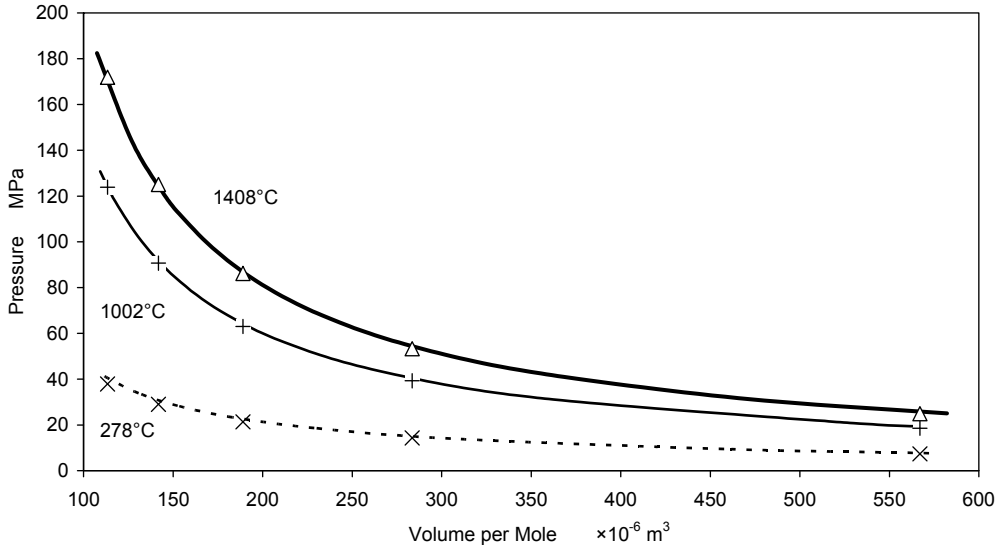

FIG. 7.5. A comparison between the Redlich–Kwong equation of state (lines) and experimental values (symbols) for xenon.

The Redlich–Kwong equation of state is

$$\left[P + \frac{a}{T^{1/2}V(V+b)}\right](V-b) = RT \tag{7.11}$$

where

P,V,T,R represent pressure, volume per mole, temperature, and the universal gas constant, respectively;
a,b are constants whose values are obtained by noting that at the critical point

$$\left(\frac{\partial P}{\partial V}\right)_T = \left(\frac{\partial^2 P}{\partial V^2}\right)_T = 0 \qquad (7.12)$$

implying that

$$a = \frac{R^2 T_c^{2.5}}{9\xi P_c}, \quad b = \frac{\xi R T_c}{3P_c} \qquad (7.13), (7.14)$$

where

T_c, P_c are the critical temperature and pressure;
$\zeta = 2^{1/3} - 1$.

In the case of a gas mixture mean values of a and b, $\overline{a}$ and $\overline{b}$, are required, given by

$$\overline{a} = \left[\sum_{m=1}^{\mu} \zeta_m a_m^{0.5}\right]^2 \text{ and } \overline{b} = \sum_{m=1}^{\mu} \zeta_m b_m \qquad (7.15), (7.16)$$

where

μ is the number of gas species comprising the mixture;
ζ_m is the fraction of gas molecules in the mixture that consist of species m.

Figure 7.6 illustrates the inadequacy in using the perfect gas law to calculate gas pressures within coated particles. The abscissa represents the gas pressure of a Xe and Kr fission gas mixture that would be calculated, knowing the temperature, the number of moles of gas present and the volume they can occupy, using the perfect gas law. Ordinate values show the factor by which this pressure needs to be multiplied in order to obtain the corresponding Redlich–Kwong equation of state value. Figure 7.6 demonstrates that during irradiation gas pressure values could be underestimated by up to ~40% if the perfect gas law is used in the calculation.

This is mainly because it ignores the volume occupied by the gas molecules. By contrast, when irradiated particles are cooled to room or ambient temperatures, pressures could be overestimated by a factor of ~2 if the perfect gas law is employed. This is because these temperatures are close to the critical temperature, when the gas will be attaining more liquid-like properties. It also implies that stresses in the silicon carbide (SiC) layer during the long term storage of irradiated particles will be lower compared with those derived using the perfect gas law.

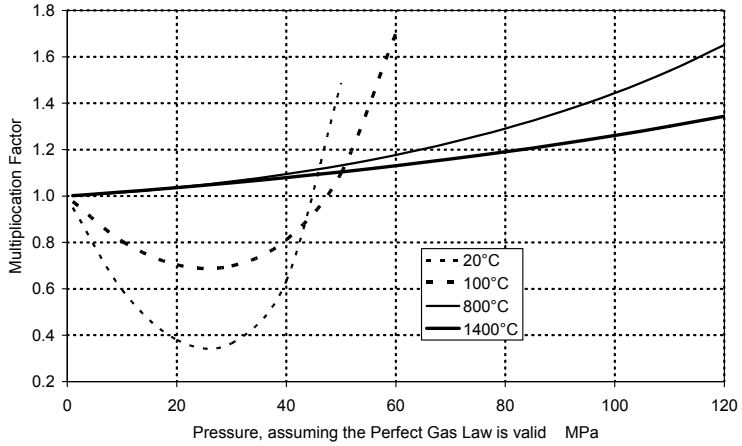

FIG. 7.6. Correction of fission gas pressures, calculated assuming the perfect gas law.

(b) Gas pressure contributions due to CO and CO_2

Let us assume that as a result of irradiation a hypothetical pressure P_O of oxygen atoms is created in the voidage. In practice this oxygen will react virtually completely with carbon to produce equilibrium concentrations of CO and CO_2 in accordance with the Boudouard reaction

$$C + CO_2 \leftrightarrow 2\ CO \tag{7.17}$$

If f is the fraction of oxygen atoms that react to form CO, the partial pressures of CO and CO_2 are given by

$$P_{CO} = f\ P_O \tag{7.18}$$

$$P_{CO_2} = \frac{1}{2}(1-f)P_O \tag{7.19}$$

so that the total pressure is

$$P_{CO} + P_{CO_2} = \frac{1}{2}(1+f)P_O \tag{7.20}$$

The equilibrium constant, K_P, defined as

$$K_P = \frac{[P_{CO}]^2}{P_{CO_2}} \tag{7.21}$$

is equal to [235]: $\exp\left(18.36 - \frac{1.997\times10^4}{T}\right)$ MPa

to an accuracy of better 2.2%. From equations (7.18) through (7.21), it follows that

$$\frac{P_{CO}+P_{CO_2}}{P_O}=\frac{1}{2}+\frac{\sqrt{K_P^2+8K_PP_O}-K_P}{8P_O} \tag{7.22}$$

Figure 7.7 shows a plot of this fraction and also of f as a function of P_O for a number of temperatures. It is apparent that in many situations a significant fraction of the oxygen reacts with carbon to form CO_2 and that this will lower the additional pressure from the oxygen released during fission compared with the situation in which it reacted to produce only CO.

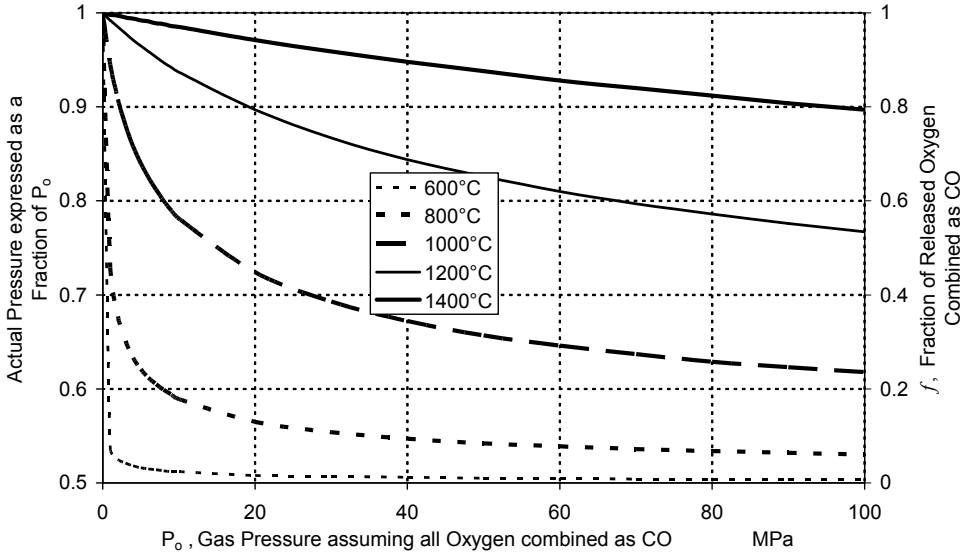

FIG. 7.7. Effect of CO_2 production on gas pressure.

Finally, from the point of view of establishing the composition of the gas, which will be required in the calculations described above, we note that if no moles of oxygen atoms are created by irradiation, then the number of moles of CO and CO_2, are given by

$$\frac{P_{CO}}{P_O}=\frac{n_{CO}}{n_O}=\frac{\sqrt{K_P^2+8K_PP_O}-K_P}{4P_O} \tag{7.23}$$

and

$$\frac{P_{CO_2}}{P_O}=\frac{n_{CO_2}}{n_O}=\frac{1}{2}-\frac{\sqrt{K_P^2+8K_PP_O}-K_P}{8P_O} \tag{7.24}$$

(c) Other desirable features of a computer code

In addition to being able to calculate gas pressures reasonably accurately, a few of the other desirable features that should be incorporated into an advance computer code are presented here.

An adequate model should be able to handle the history of a coated particle, from its manufacture, during irradiation, and finally throughout its long term storage in a repository. Amongst other things this implies that during irradiation changes in the neutron flux and temperature are capable of being modelled, for example as particles pass through and are then

re-inserted into a pebble bed reactor, and also during shut-downs. This is not to say that simpler models have no use. For example, analytical models that assume constant neutron flux and temperature values enable stresses in the layers to be calculated readily by hand. Furthermore they enable a scientific understanding of how the various material properties influence these stresses [236]. The same is also true of simple models which calculate the stresses that are introduced due to a change in temperature [237].

Another feature which a coated particle performance code should be able to model is the possibility that particles may fail due to kernel–coating mechanical interaction (KCMI) [238], a mechanism which to date has received little attention. Failure by this means rather than because of a sufficient buildup of gas pressure may occur if the buffer layer possesses adequate voidage, or if the fraction of gas released from the kernel is small as will occur at sufficiently low irradiation temperatures. It is well known that fuel kernels will swell during irradiation; as a result, once gaps between the kernel and IPyC layer have closed, this will enhance considerably stresses in the SiC layer due to its high (compared with PyC) elastic modulus. Failure of this layer will then occur at burnup values only slightly in excess of that at which KCMI is initiated. Not many experimental irradiations appear to have been reported where failure of particles has been attributed to KCMI. The one clear case is an unpublished report by Horsley and Brown (Harwell Laboratory, 1971) relating to the irradiation of some gas cooled fast reactor particles to 11.7% FIMA burnup at around 925°C. An obvious way of postponing the onset of KCMI is to increase the early in life gas gap between the kernel and IPyC layer by enhancing the thickness of the buffer, since the gap is caused by its shrinkage in the radial direction during irradiation. However, a sizeable gap containing low thermal conductivity fission gases will result in a significant temperature drop between the fuel and cladding. Bearing in mind that in practice the kernel is unlikely to remain in a perfectly symmetrical position within the particle, temperature variations around the periphery of the IPyC layer would then be expected, which could promote appreciable carbon transport (the amoeba effect). So clearly there must be a limit to how much the thickness of the buffer layer can be increased in order to avoid KCMI.

Computer codes which calculate stresses in the layers of particles during the course of an irradiation are invaluable in determining the burnup at which failure will occur. However, such calculations only refer to individual particles, whereas in practice one is interested in the fraction of a batch of particles that have failed as a function of burnup. The most satisfactory way to calculate failure fractions is to run the code many times (in practice 10^5–10^6 runs), varying for each run the particle specifications in accordance with the statistical variation of items such as the layer thicknesses.

7.1.3.3. Some practical examples that illustrate a number of important factors in modeling particle endurance

(a) HRB-22 irradiation

In the Japanese sponsored irradiation HRB-22 [136] in the high flux isotope reactor (HFIR) at Oak Ridge National Laboratory, 32 000 particles were irradiated up to a maximum burnup of 7% FIMA. Four failures were observed, two each in the region of 2.5 and 6% FIMA respectively. STRESS3 calculations, using mean particle specifications, predicted that up to 7% FIMA burnup the SiC layer was always under compression, implying that no failures would occur. This conclusion was in agreement with a previous calculation using a Japanese fuel performance code [18]. Even if both PyC layers were to fail very early in the irradiation, another STRESS3 run showed that tensile stresses at the end of life were extremely modest, and so unlikely to cause failure of the SiC layer.

These calculations employed mean particle dimensions and fracture stress values. However, when particle statistics are included in a STAPLE calculation two failures were predicted to occur over the burnup range of 6 to 7% FIMA. Therefore, to a first approximation, the third and fourth failures that were observed have been modelled successfully, but not the first two, which tentatively may be attributed to these particles being defective. It was through STRESS3 runs that in other irradiations, such as in some reported below, failures were identified to have been caused by KCMI.

(b) 91F-1A irradiation

The irradiation 91F-1A [136] in the Japanese materials test reactor comprised two capsules, upper and lower, each containing 4400 particles. The upper capsule was irradiated at 1300°C to a burnup of 8% FIMA, by which time two failures were observed. Modeling of this irradiation produced results that were rather similar to those discussed above relating to the HRB-22 irradiation. It predicted two failures, in keeping with the experimental observations.

Although the lower capsule experienced a higher rating compared with that of the upper capsule, so that a burnup of 9.5% FIMA was achieved, no failures were observed. It was speculated that this was because of the irradiation temperature history. During the first half of the irradiation particles were irradiated at 1250°C. However at this point, due to a malfunction of the temperature controller, the temperature decreased monotonically with time, falling to 820°C by the end of the irradiation. A STAPLE run was able to support this suggestion because, up to 9.5% FIMA burnup, no failures were predicted.

(c) HFR-EU1 irradiation

The HFR-EU1 irradiation experiment that took place in the Petten HFR reactor included three spherical fuel elements of German origin, each containing 9500 particles. The original intention was to irradiate them to a burnup of ~20% FIMA exploring the limiting burnup that presently manufactured coated particles can attain (see also Section 7.2.4).

First, a STRESS3 run was performed, using mean values of the particle specifications and with fracture stresses set artificially high in order to avoid failure of any of the layers. Figure 7.8 shows tangential stresses in the SiC layer over the course of the irradiation. The noteworthy feature is the abrupt increase in the rate at which stresses increase with burnup at about 18% FIMA. This is due to the onset of KCMI. (The decrease in the slope at burnups above ~20% FIMA is due to creep of the SiC which makes a contribution at very high stresses even though the creep constant was assumed to be about two orders of magnitude lower than

that of PyC.) This is demonstrated in Fig. 7.9, which shows the kernel–coating radial gap over the course of the irradiation. Initially the gap increases owing mainly to the shrinkage in the radial direction of the buffer and IPyC layers. Next, the effect of the swelling kernel, thereby closing the gap, predominates until at ~18% FIMA burnup, the gap becomes closed. Note that the maximum radial gap is predicted to be ~14 μm. A gap of this size could result in an appreciable temperature drop between the kernel and coatings. For example, if the kernel were located (unrealistically) symmetrically in the centre of the particle, then the temperature drop for this particle design would be in the region of 150°C if the kernel is generating a power of 0.25 W. Fortunately, gaps of this size only occur over a comparatively small burnup range, but nevertheless they could be the cause of significant carbon transport, as observed in the amoeba effect.

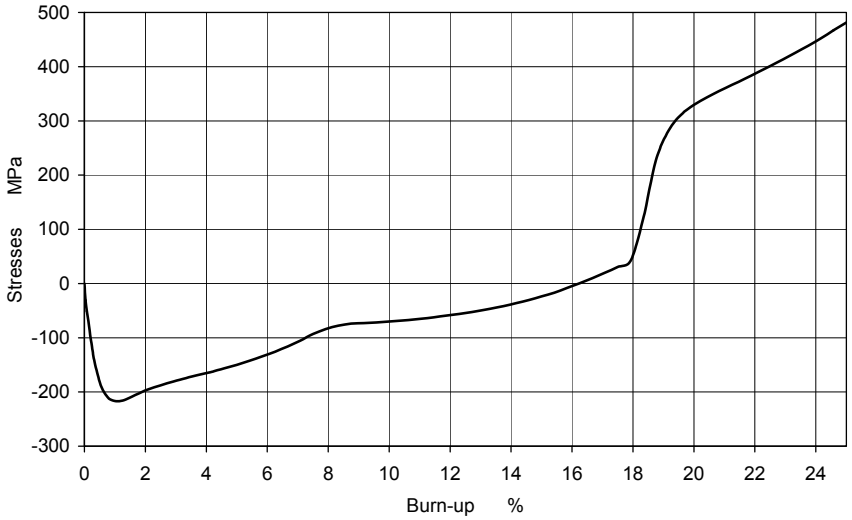

FIG. 7.8. Stresses in the SiC layer during irradiadion.

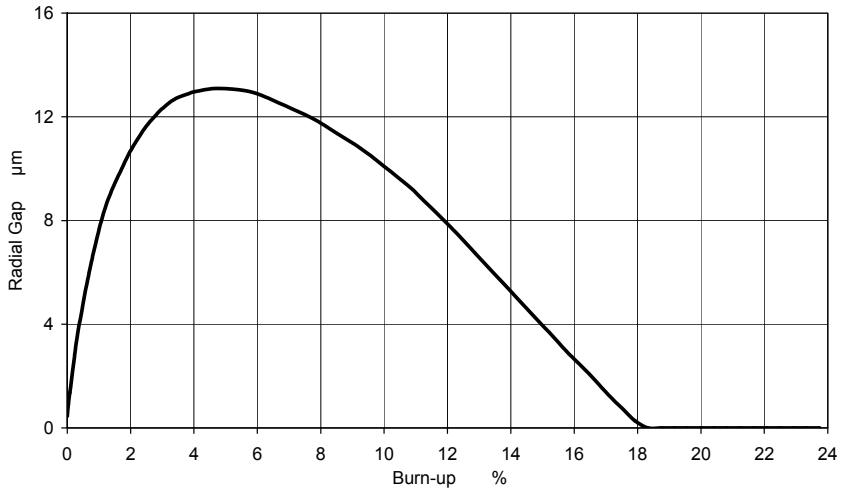

FIG. 7.9. Kernel–coating radial gap during irradiation.

The heavy solid line in Fig. 7.8 shows the failure fraction as a function of the burnup from a STAPLE run when all the known statistical variations of the particle specifications are included. However, it is instructive to explore how some of the individual statistical variations affect this result. For example, if all particle specifications, including fracture stresses of the layers were to adopt their mean values, all particles would fail at ~22.5% FIMA burnup (from Fig. 7.8), because the mean fracture stress of the SiC layer in the calculation was assumed to

be 400 MPa. The light solid line in Fig. 7.10 shows how that result is modified when Weibull statistics for the three load bearing layers are introduced into the calculation. Up to ~18% FIMA burnup, a few failures occur due to stresses created by the internal gas pressure. However, from Fig. 7.8 it is known that at ~18% FIMA burnup, KCMI will be initiated and stresses will then increase rapidly as the irradiation continues, thereby causing the sharp rise in the failure fraction with burnup. The dotted line in Fig. 7.10 shows the results of a calculation in which all particle specifications adopted their mean values, apart from the buffer layer thickness. This implies that there will be a particle to particle variation in the burnup value at which KCMI is initiated. As a result, burnup values at which failure fractions of practical interest occur are lowered compared with the situation when the buffer layer thickness of all particles in the batch are assumed to be the same. However, what is significant is that this dotted line, corresponding only to a variability in the buffer layer thickness is very close to the heavy solid line, for which all particle specifications were included in the calculation. This is because KCMI predominates over all other factors that affect the failure of particles.

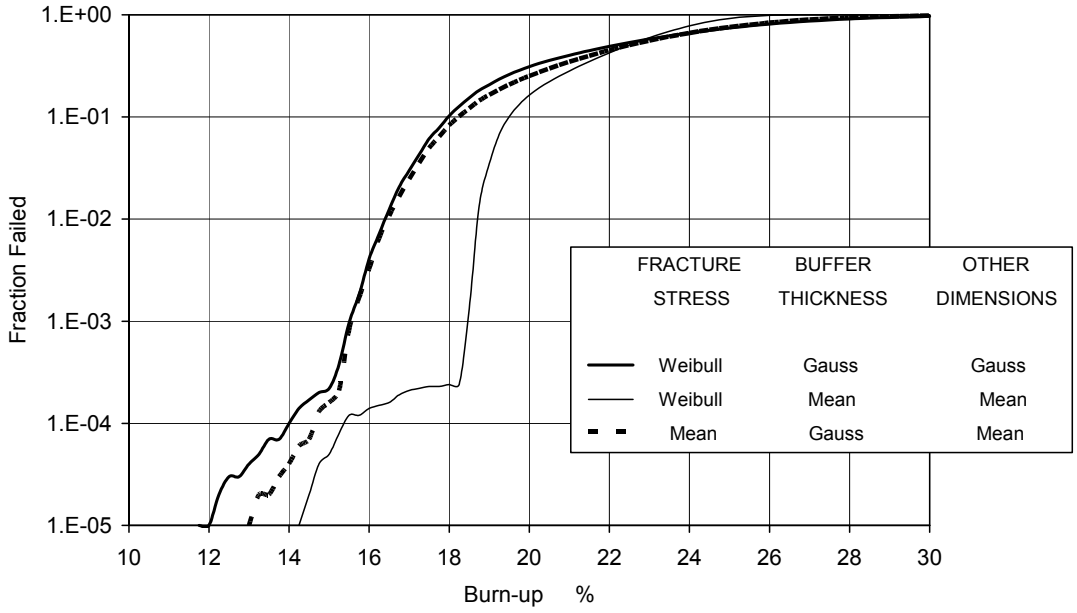

FIG. 7.10. Effect of variability in fracture stresses and buffer thicknesses and other dimensions on failure fractions.

(d) NPR-1 irradiation

In the USA irradiation NPR-1 [239] in HFIR, particles were irradiated at ~950°C to a burnup of 79% FIMA. A number of compacts were irradiated; that labelled A5 is considered here. A STAPLE run predicted failure of the SiC in 2.4% of the particles. Experimentally, 0.6% with a 95% confidence in the range 0–3% was observed, so reasonable agreement between the two sets of results was obtained.

However, the interesting feature of this modeling exercise emerged from a number of exploratory STRESS3 runs. It was found that provided the IPyC and OPyC layers remain intact over the course of the irradiation the SiC coating was always under compression. On the other hand, if the IPyC layer fails during the early part of the irradiation KCMI can occur, resulting in possible failure of the SiC layer. Further STAPLE exploratory runs indeed demonstrated that the predicted failures referred to above occurred by KCMI. The explanation

why KCMI occurs when the IPyC has failed but not when it is intact is due to Poisson ratio dimensional changes in the latter case. At appreciable neutron doses a failed, unrestrained, IPyC layer will expand radially, thereby contributing to the closure of the kernel–coating gap. By contrast, an intact IPyC will be highly stressed in the tangential direction as it creeps in order to nullify the shrinkage that a corresponding unrestrained layer would undergo. From Poisson ratio considerations this will result in shrinkage in the radial direction, thereby contributing to a delay in the burnup value at which KCMI will be initiated.

(e) Charge III centre rod experiment

The 'Charge III Centre Rod Experiment' irradiation [240] in the Dragon reactor was a realistic demonstration of particle performance under power reactor conditions. Eight particle designs were irradiated at two temperatures, namely 1250 and 1400°C. For each of these 16 combinations, several batches of 104 particles were irradiated at a number of burnup values, up to 12% FIMA. Particles in each batch were held in position in their containing box by means of resin, to which they were meniscus bonded. At the end of the irradiation, PIE on a number of boxes was performed to determine the failure fractions. Results for two of the designs, LE 10 and FB 3, are shown as data points in Figs 7.11 and 7.12.

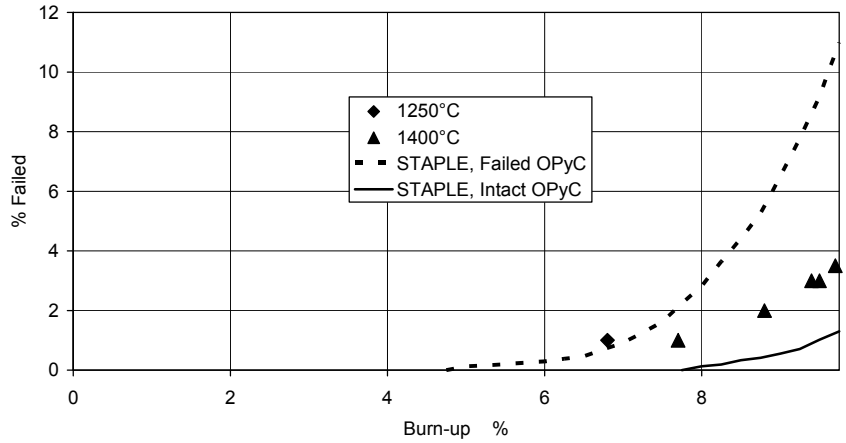

FIG. 7.11. Modeling particle design LE 10.

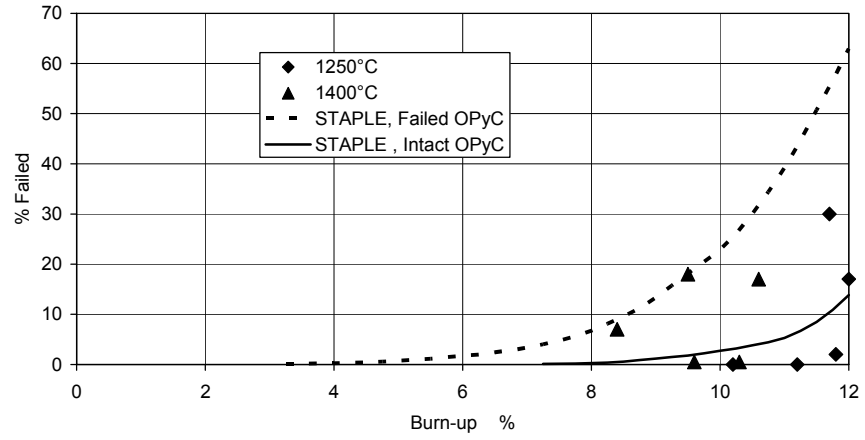

FIG. 7.12. Modeling particle design FB 3.

The solid lines in these figures are the results of STAPLE calculations, assuming an irradiation temperature of 1300°C. It is evident that many of the experimental results lie

above these lines. STAPLE calculations were repeated, but now with the OPyC layer made to fail, to produce the dotted lines in Figs 7.11 and 7.12. It is apparent that many of the experimental results lie between the two lines.

One can advance plausible arguments to justify the supposition that OPyC layers may fail during the irradiation. For example, failure of OPyC layers deposited from methane has been reported in the past [241]. Again, during the early stages of the irradiation, the resin holding the particles in position is expected to undergo large dimensional changes, which could cause such failures. If only a fraction of the OPyC layers were to have failed, then the appropriate failure line should lie somewhere between the two shown in the above figures.

7.1.3.4. Concluding remarks

It is highly desirable for there to be a close collaboration between experimentalists and modellers in the development of fuel that will perform to the desired specifications. This is because, for example (a) both experimentalists and modelers are able to identify failure mechanisms; (b) experimental work can point to inadequacies in a fuel performance code, thereby leading to its improvement; (c) modeling can greatly assist in the experimental work, both concerning the particle design and the irradiation conditions to aim for; in addition what sort of PIE should be undertaken.

Probably the biggest limitation in modeling studies lies in inadequacies in the available input data. This is especially the case with regard to the properties of the PyC and buffer layers. But despite these limitations, advanced models are able to provide valuable insights into the underlying mechanisms that affect particle endurance.

7.2. IRRADIATION TESTING IN THE HFR AT JRC PETTEN

7.2.1. Reactor description of the HFR

7.2.1.1. HFR reactor in Petten

The high flux reactor (HFR) in Petten, the Netherlands, is a 45 MW multi-purpose research reactor that is owned by the European Union and that is operated by NRG (Nuclear Research and Consultancy Group). NRG is also the license holder for the HFR. The reactor has many irradiation locations for materials testing (Fig. 7.13) [242]. It has been the work-horse for irradiation of spherical fuel elements for the German HTGR project in the 1970–1995 time frames. It has also been used to irradiate GA compacts for the US programme in the late 1980s.

The HTGR fuel irradiation activities that have been performed at the HFR Petten were described in 1990 as follows by reference [243]: “Because of its favourable design and operational characteristics and the availability of dedicated experimental equipment the high flux reactor at Petten has been extensively used as a test bed for HTGR fuel and graphite irradiations for more than 20 years. Earlier fuel testing programmes contributed to the development of the coated fuel particle concept by extended screening tests. Now these programmes concentrate on performance testing of reference coated fuel particles and reference fuel elements for the German HTR-Modul, the HTR-500 and to a lesser extent for the US HTGR concepts. It is shown with representative examples that these fuels have excellent fission product retention capabilities under normal and anticipated off-normal operating conditions. Extended irradiation programmes in the HFR Petten have significantly contributed to the database for the design of HTGR graphite structures. The programmes not

only comprise radiation damage accumulation in the temperature range from 570 to 1570 K up to very high fast neutron fluences and its influence on technological properties, but also irradiations under specified load conditions to investigate the irradiation creep behaviour of various graphites in the temperature range 570 to 1170 K."

7.2.1.2. 'BEST' sample holder in the HFR Petten

For the HTGR fuel irradiation, two different types of irradiation rigs/locations are available: one that can accommodate compacts, and one that can accommodate spheres. The REFA and BEST rigs are multi-cell capsules, 63 to 72 mm in diameter, which can handle four to five spheres in up to four separate cells. The TRIO or QUATTRO rigs/locations are ~32 mm in diameter and 600 mm in useful length. They can handle three or four parallel stacks of compacts. For the three-stack configuration, about 30 compacts could, in principle, be irradiated in the rig. There is a large axial flux gradient across the useable length (40% spread maximum to minimum) that must be considered in the design of any experiment.

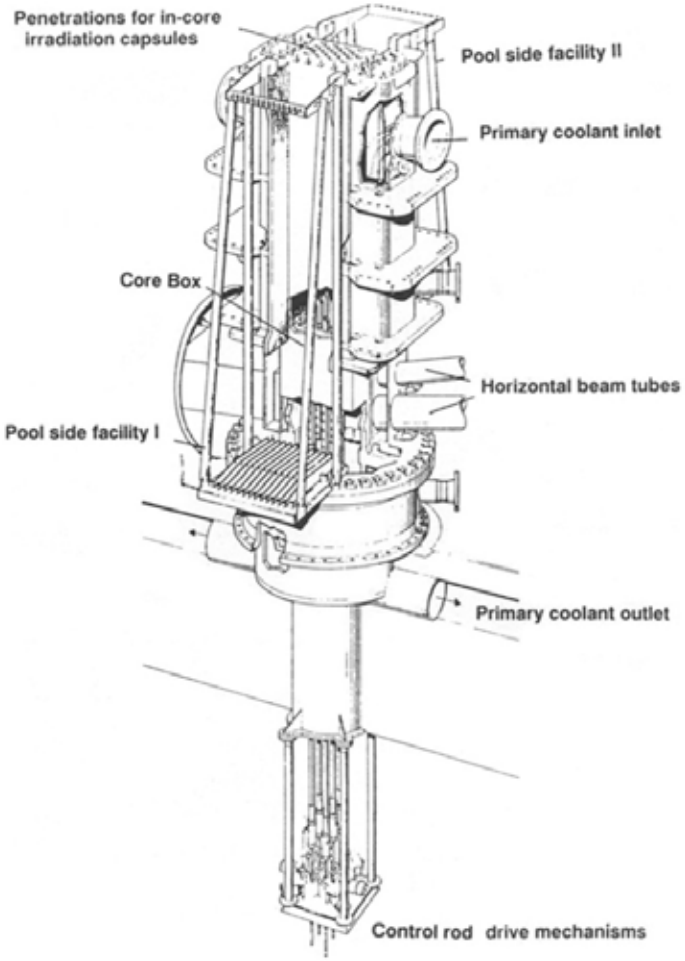

FIG. 7.13. HFR Petten reactor vessel.

Most of the HTGR fuel irradiations that were performed in the HFR in the period until the early nineties were performed in a sample holder based on the 'BEST' concept [244]. The irradiation rig BEST can accommodate full size spherical fuel elements or cylindrical segments of the prismatic block fuel element with a maximum outer diameter of 65 mm in up

to four independent capsules. The basic design of the BEST rig (Figs 7.14 and 7.15) is the use of up to four independently and individually monitored and operated single contained capsules, arranged in line [244].

The capsules are surrounded by a protection tube which also forms the water cooling gap. The instrumentation cables of the lower capsules are passed through this gap to the upper rig head in the central reactor top lid. The connection between the capsules and the rig head is formed by the extension tube. The heat, generated by fissions and gamma absorption is dissipated radially by conduction and radiation through the material layers. Temperature control is obtained by a binary gas mixture of helium and neon. The control range is greater than 300 K. The complete in-pile section of the BEST rig can be moved vertically in the irradiation channel. Additionally, the upper and lower capsule can be displaced relative to the rig. Both independent movements are operated remotely by a displacement unit inside the rig head. This feature allows compensation of the shift of the vertical neutron fluence rate pattern during the run of an irradiation cycle and allows power and/or temperature cycling. Methods and instrumentation are in use for power and/or temperature cycling and transient experiments, as well as for in-situ fuel hydrolyzing and graphite oxidation irradiation experiments. Instrumentation for injection of water vapour into the purge gas (range 10–2000 Pa) is in regular use.

All relevant process data, such as temperature, mass flow, gas pressure, downstream radioactivity, up- and downstream gas impurities, neutron fluence rate and reactor power, etc., are recorded by the central computerized data logger and stored on tape for on-line and off-line data evaluation. Experimental data as temperature field, neutron fluences, fission power, burnup and fractional fission gas release data are reported cycle by cycle. The BEST type sample holders are connected to a gas sweep loop facility which is similar to the one that has been used for the irradiation experiment HFR-EU1 (see Section 7.2.4).

The main difference between the BEST type sample holder and the sample holders of the HFR-EU1 is that these latter two have a double containment, while the BEST type sample holder has a single containment.

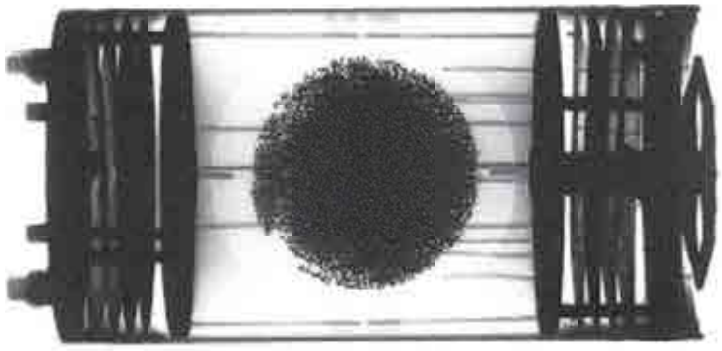

FIG. 7.14. BEST rig: pre-irradiation X ray photo of a capsule with one spherical fuel element of the HTR-Modul proof test.

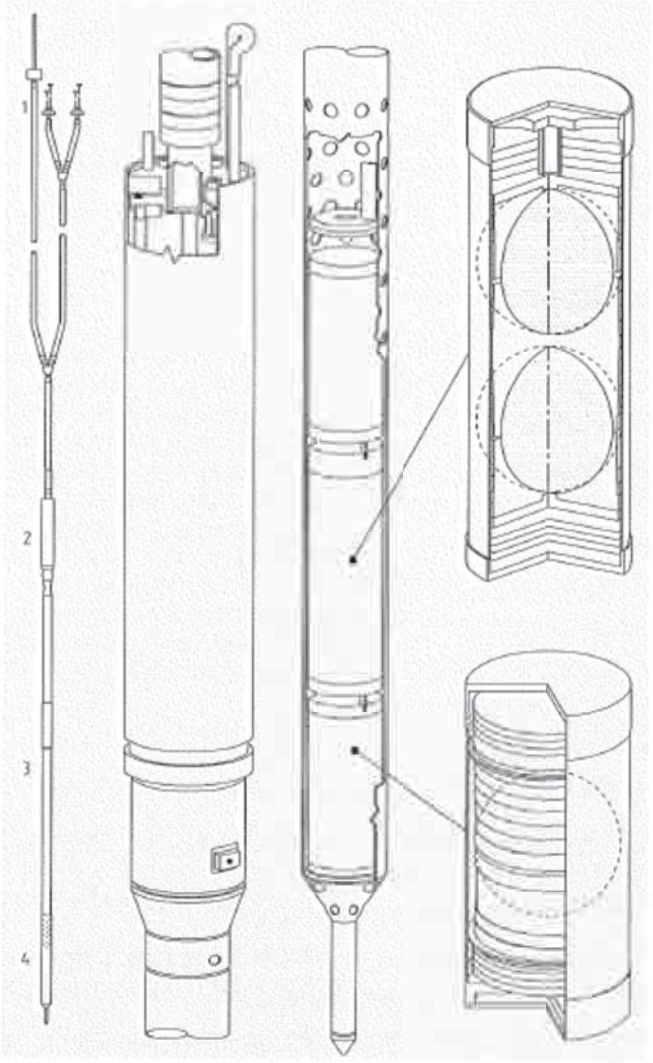

FIG. 7.15. General arrangement drawing of a 'three-capsule' BEST rig for spherical HTGR fuel elements of 60 mm diameter.

7.2.2. Proof test fuel irradiation experiment HFR-K5 and -K6

7.2.2.1. Reference irradiation testing of LEU UO_2 TRISO fuel

The development of the reference fuel cycle for future pebble bed reactors was performed by the German companies HOBEG, HRB and INTERATOM until approximately 1990 [54]. Qualification of this fuel was performed by production and quality control experience, irradiation testing and accident simulation experiments. The results of the qualification programme fully supported the new safety concepts of advanced HTGR designs.

After having developed a new type of fuel element, it must be demonstrated and proven that all the properties required by power reactor design, remain unchanged or are at least only modified to a tolerable extent under the conditions of normal reactor operation or even design base accidents. This irradiation testing (together with appropriate post-irradiation examination) is performed in two phases:

Phase I: Irradiation experiments with simplified but in general covering conditions with regard to target burnup, fast neutron fluence and fuel temperature, aiming at information concerning different objectives, such as particle failure function, fission product transport and fuel element integrity.

Phase II: Power reactor plant specific 'reference tests' (or proof tests) to demonstrate the transferability of Phase I results to the specific demand of a commercial power reactor project. 'Near to production' fuel is investigated under conditions as close as is reasonably achievable to HTGR power plant operation, e.g. including simulation of a multi-pass fuel reloading system.

To obtain reliable thermal design data for different reactor positions, a pre-runner experiment was performed for Phase II. The unique feature of this test was that the spherical fuel elements were equipped with more than 20 thermocouples each to determine the temperature distribution within the spheres for each test reactor position. Based on these data, the thermal irradiation history for the Phase II tests has been recalculated and the core position in the MTR for each cycle has been selected.

For the actual German reference LEU TRISO fuel, several irradiation experiments have been realized in the framework of Phase I. Tests with the reference type of coated fuel particles are listed in Table 7.3 [54]. In some cases, it was impossible for technical reasons to irradiate full-size (60 mm diameter) elements. To meet the experimental requirements, 'small spheres' were installed in the irradiation capsules, which are identical to the original fuel elements with respect to materials and methods employed for their manufacture, but have a fueled zone of only 20 mm diameter with a corresponding 20 mm thick fuel-free shell. From this sphere, a cylindrically shaped irradiation specimen was machined.

In some other cases, hot pressed cylindrical compacts and flat coupons (with a monolayer of coated particles) have been used. In these Phase I experiments, a total of approximately 212 000 particles have been irradiated. Up to the final values for burnup and fast neutron fluence, given in the table, not a single particle has failed in the sense of irreversibly increased fission gas release. This was determined by the quasi-continuous control of fission gas release during irradiation of the specimens. Fission gas release always stayed below values which would have been obtained if one particle were defective in the capsules. The specific fission gas release from defective particles — necessary to interpret the measurements — was determined by an additional experiment with intentionally inserted defined amounts of 'designed-to-fail' fuel particles.

TABLE 7.3. CHARACTERISTIC DATA OF PHASE I IRRADIATION EXPERIMENTS WITH LEU TRISO FUEL

Experiment	Capsule	Specimen number and type	Number of particles		Irradiation time (efpd)	Burnup (% FIMA)	Fluence (10^{25} n/m^2, E>0.1 MeV)	Nominal fuel temperature (°C)
			capsule	experiment				
HFR-P4	A/01	12 small spheres	19 572	39 144	351	11.1–14.7	5.5– 8.0	900
	C/03	12 small spheres	19 572			9.9–14.7	5.5–8.0	1050
SL-P1	-	12 small spheres	19 572	19 572	330	8.6–11.3	5.0–6.8	800
HFR-K3	1/A	1 fuel element	16 400	65 600	359	7.5	4.0	1000
	2/B	2 fuel elements	32 800			10.2	5.9	800
	3/C	1 fuel element	16 400			9.0	4.9	1200
FRJ2-K13	1	2 fuel elements	32 800	65 600	396	7.5–8.0	< 0.2	1200
	2	2 fuel elements	32 800			7.6–7.9	< 0.2	1200
FRJ2-P27	1	3 compacts, 2 coupons	7340	22 020	232	9.4	1.4	900
	2	3 compacts, 2 coupons	7340			10.9	1.7	1300
	3	3 compacts, 2 coupons	7340			8.8	1.3	1100

The HTGR fuel irradiation testing in the HFR can be categorized in two time periods:

(1) The period from the seventies until the early nineties. In this period a large number of fuel irradiations have been performed, mainly within the German HTGR programme. This involved, amongst others, the HFR-K5 and -K6 irradiation experiments, for which the BEST type sample holder was also used.
(2) The period starting around 2004 in which, amongst others, the European HTGR research activities restarted. This involved the HFR-EU1bis (Section 7.2.3), HFR-EU1 (Section 7.2.4), and the PYCASSO (Section 7.2.5) irradiation experiments.

7.2.2.2. Preparation

The fuel proof test HFR-K6 [245] was originally designed to test the fuel elements for the planned HTR-Modul, and the proof test HFR-K5 for the validation of fuel for the HTR-500**.** Before the start of HFR-K5 irradiation, it was decided to abandon the HTR-500 project. HFR-K5 was therefore performed with the same fuel under the same conditions as HFR-K6. The fuel elements were manufactured under similar conditions and standards as the AVR-21 reload batch consisting of LEU TRISO particles at NUKEM. Four 60 mm reference fuel elements with LEU TRISO coated particles were selected and inserted into a three-capsule BEST rig for irradiation in the HFR Petten. Capsule A contained the test element HFR-K6/1, capsule B the test elements HFR-K6/2 and HFR-K6/3, and capsule C test element HFR-K6/4. A similar arrangement was chosen for the irradiation test HFR-K5.

7.2.2.3. Conduction

The irradiation temperature was automatically adjusted by gas mixture technique (He/Ne). The heat transfer characteristics for neon are lower than for helium, and by adjusting the helium/neon gas mixture, the temperature of the test elements can be regulated. In order to simulate the multi-pass core circulation of the fuel elements, the central fuel temperatures were planned to be set to ~800°C for one third of the irradiation time and ~1000°C for the remainder for each HFR cycle. A total of 36 thermocouples, 17 neutron fluence detectors, 9 gamma-scanning detectors and 4 self powered neutron (SPN) detectors were attached to the fuel elements and capsules to determine the temperature distribution and history with respect to neutron fluence and burnup. The downstream gas from each capsule was analysed quantitatively and qualitatively by a 4096 multi-channel analyser with two Ge (Li) detectors. The release of noble gas nuclides ^{85m}Kr, ^{87}Kr, ^{88}Kr, ^{89}Kr, ^{133}Xe, ^{135}Xe, ^{135m}Xe, ^{137}Xe, and ^{138}Xe was measured and recorded during irradiation for each capsule.

The neutron fluence, burnup and plant specific temperature targets were all met including operational transients and water ingress investigations. Not a single coated particle failed in the sense of irreversible increased fission gas release. For HFR-K6 (Table 7.4), the test elements were irradiated over 26 HFR periods between 21 June 1990 and 8 April 1993 for 633.6 efpd.

TABLE 7.4. HFR-K6 TEST ELEMENT SPECIFICATION AND IRRADIATION DATA

Parameter	Fuel element designation			
	HFR-K6/1	HFR-K6/2	HFR-K6/3	HFR-K6/4
Specification	capsule A	capsule B		capsule C
Fuel element No.	2953-56	2953-98	2953-38	2953-26
Uranium content (g)	9.44	9.44	9.44	9.44
U-235 enrichment (%)	10.6	10.6	10.6	10.6
Number of coated particles	14 600	14 600	14 600	14 600
Failed coated particles	0	0	0	2(a)
Irradiation data				
Burnup (% FIMA)	8.3	10.6	10.9	9.9
Neutron fluence (10^{25} n/m^2, E>0.1 MeV)	3.2	4.6	4.8	4.5
Max centre temp(b) (°C)	1090	1130	1140	1130
Max power(c) (kW/FE)	1.82	2.51	2.70	2.48

TABLE 7.5. HFR-K5 TEST ELEMENT SPECIFICATION AND IRRADIATION DATA

Parameter	Fuel element designation			
	HFR-K5/1	HFR-K5/2	HFR-K5/3	HFR-K6/4
Specification	capsule A	capsule B		capsule C
Fuel element No.	2953-12	2953-42	2953-68	2953-72
Uranium content (g)	9.44	9.44	9.44	9.44
U-235 enrichment (%)	10.7	10.7	10.7	10.7
Number of coated particles	14 600	14 600	14 600	14 600
Failed coated particles	0	0	0	1 a
Irradiation data				
Burnup (% FIMA)	7.8	10.1	10.3	9.3
Neutron fluence (10^{25} n/m^2, E>0.1 MeV)	4.0	5.8	5.9	4.9
Max centre temp. b (°C)	1020	1070	1010	1030
Max power c (kW/FE)	2.21	3.03	3.19	3.06

a Fabrication-induced defects.
b Calculated from the measured surface temperature and fuel element power output.
c Fission power and gamma heat.

The parallel HFR-K5 (Table 7.5) under nominal identical conditions started on 8 January 1991 and ended on 16 May 1994 after 23 completely measured irradiation periods for a total of effective 564.3 days. The HFR-K5 irradiation time was 69 days shorter than HFR-K6, resulting in lower burnup and fast neutron fluence values.

7.2.2.4. Results

In accordance with the multiple core passage of the fuel in the HTR-Modul, the test elements were subjected to 17 temperature cycles [247]. Figures 7.16, 7.17, and 7.18 show the R/B

values from the three HFR-K6 capsules for various fission gas isotopes during the final 200 days of irradiation. While gas release for capsules A and B started at a very low level and gradually increased to the level of 10^{-8}–10^{-7}, data of capsule C remained, on the whole, in the 10^{-7}–10^{-6} range. This is a strong indication for the presence of 1, probably 2, manufacture-induced defective coated particles in sphere HFR-K6/4. It is supported by the satisfactory agreement found when comparing with a postcalculation of the gas release assuming two defects (Fig. 7.19) [246]. The three spheres in the other two capsules reveal a release level far below the level expected from a defective particle. Table 7.6 summarizes the fission gas (krypton) release data for both HFR-K5 and HFR-K6.

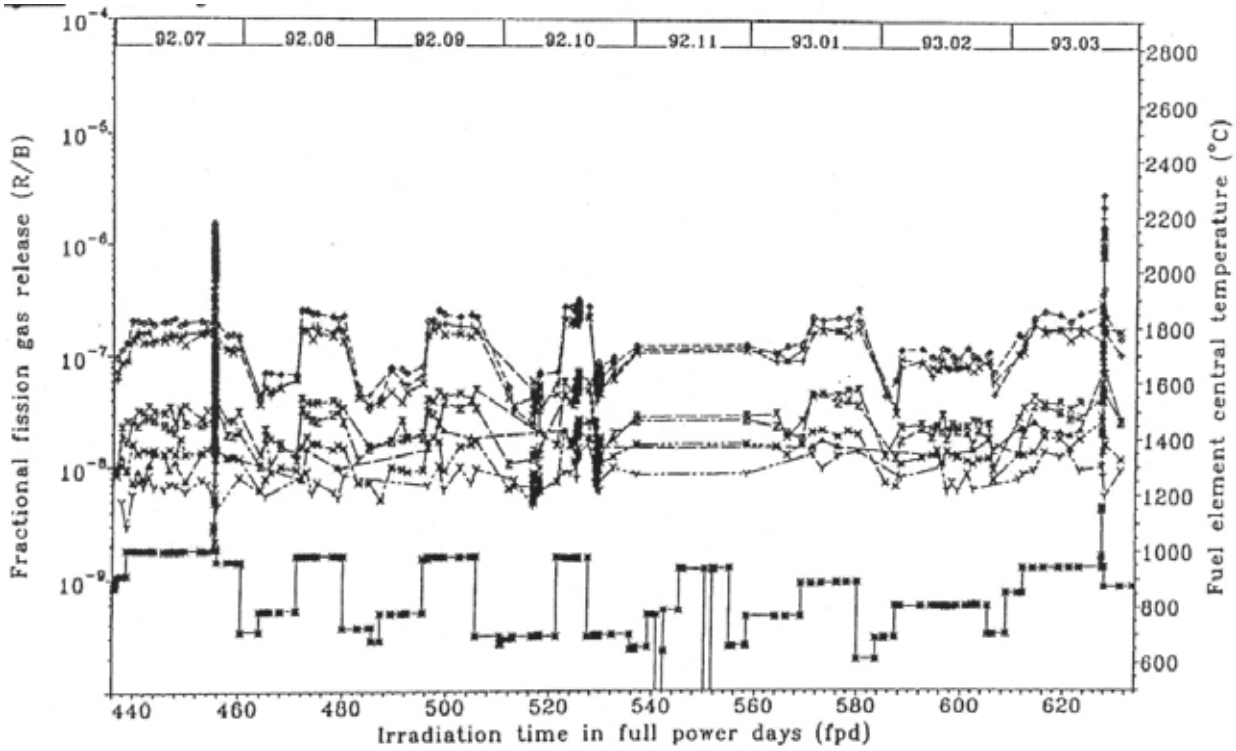

FIG. 7.16. R/B values from capsule A of HFR-K6 based on centre temperatures.

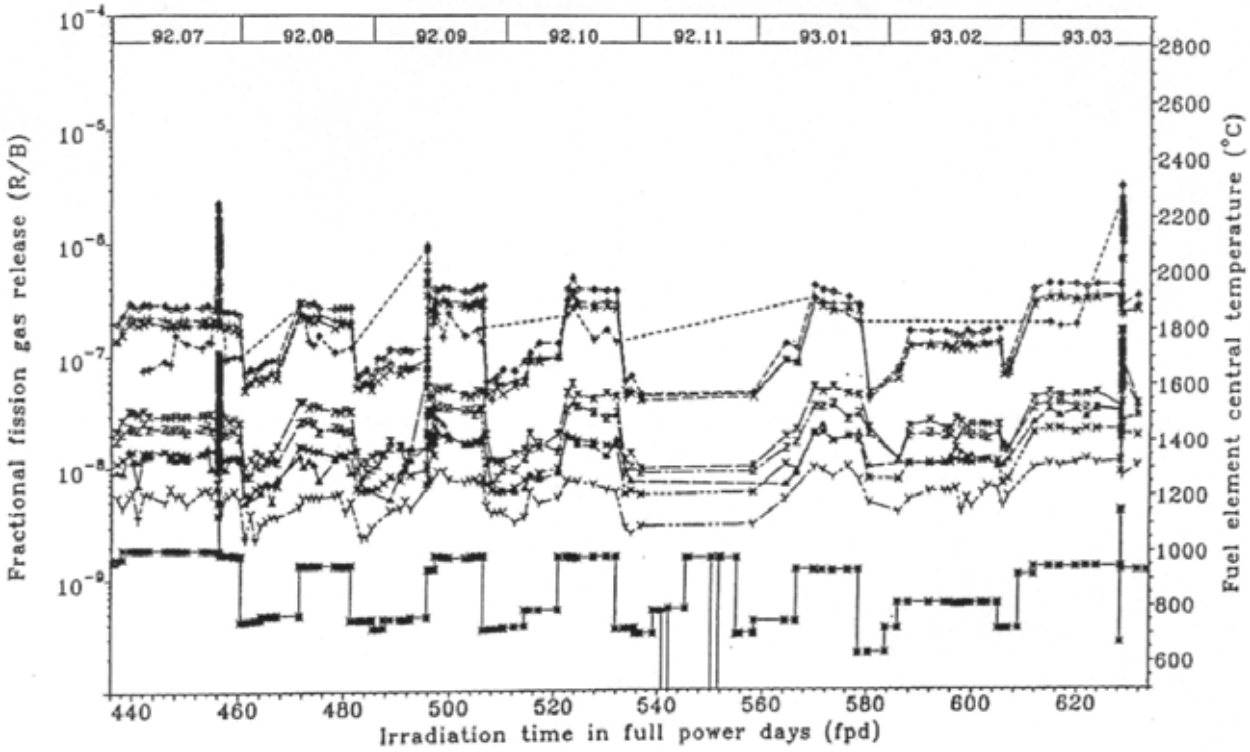

FIG. 7.17. R/B values from capsule B of HFR-K6 based on centre temperatures.

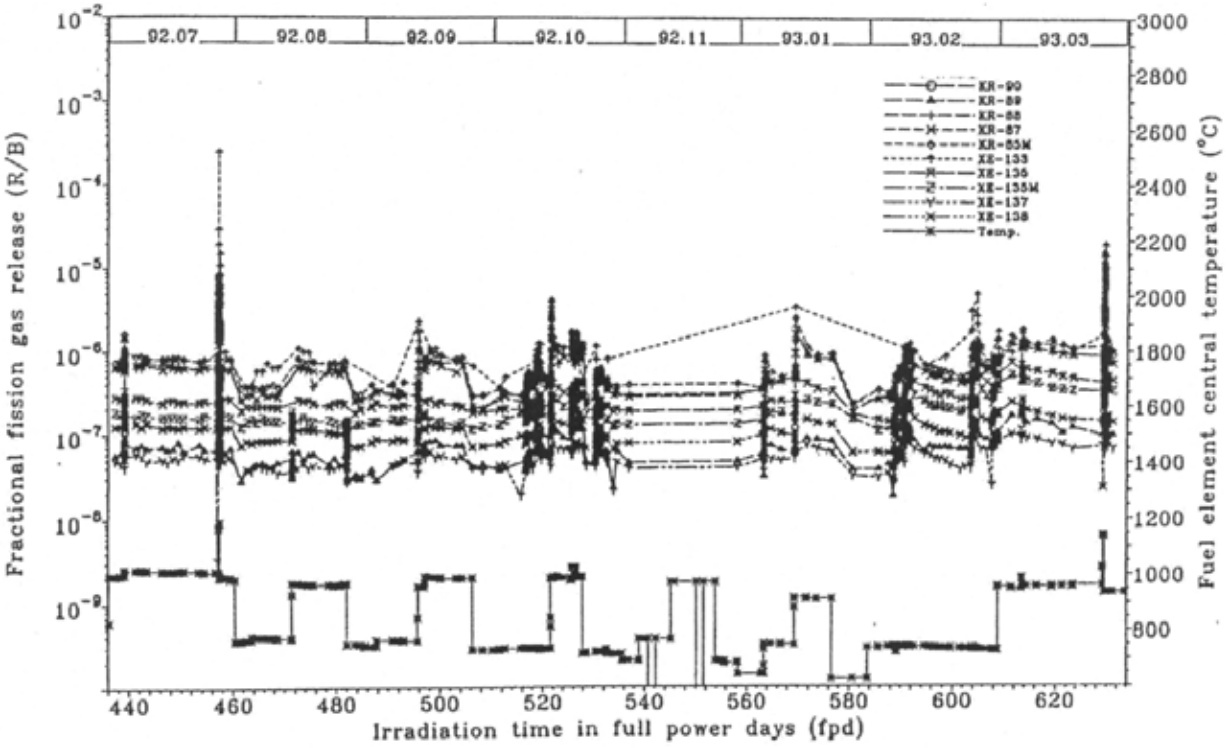

FIG. 7.18. R/B values from capsule C of HFR-K6 based on centre temperatures.

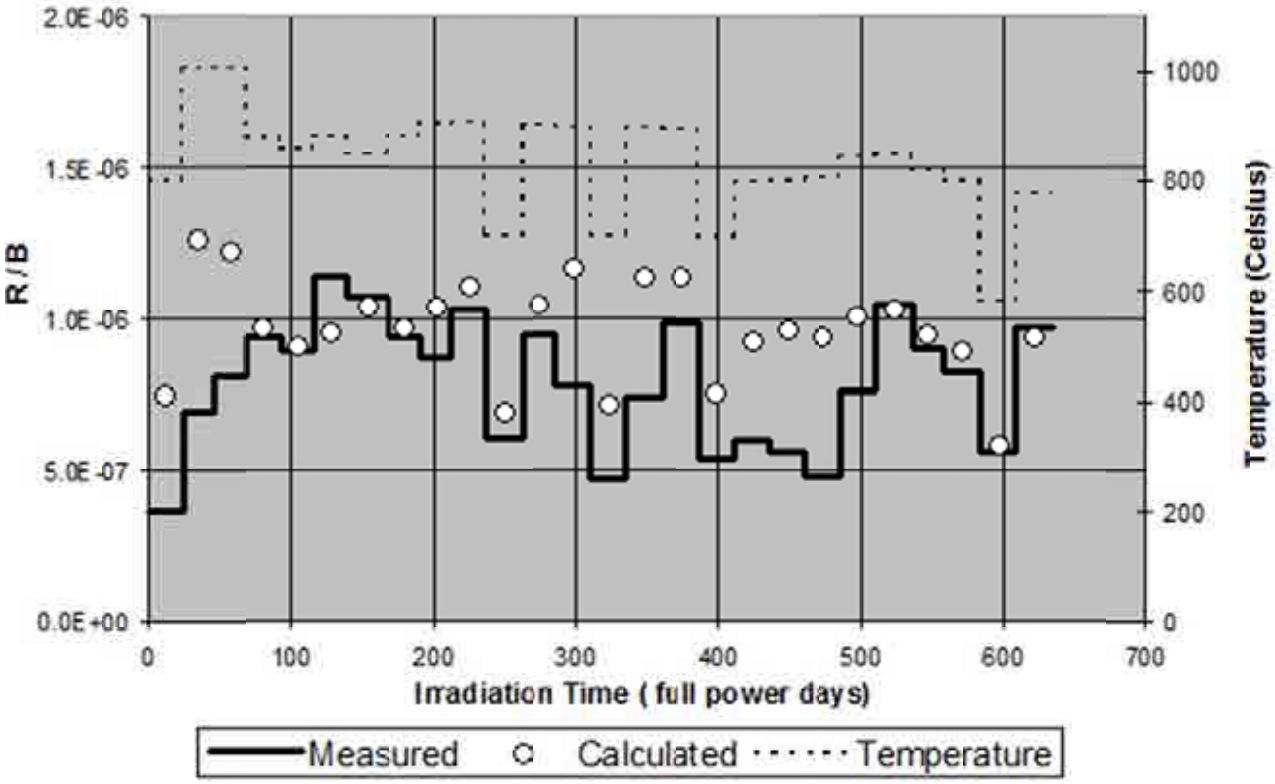

FIG. 7.19. R/B of ^{88}Kr from capsule C of HFR-K6 and comparison with a calculation assuming two defective particles.

TABLE 7.6. SUMMARY OF HFR-K5 AND HFR-K6 KRYPTON RELEASE RESULTS

Fuel Sphere Designation	R/B			
	Kr-85m	Kr-88	Kr-85m	Kr-88
HFR-K5/1	4.76×10^{-10}	3.67×10^{-10}	1.64×10^{-7}	1.35×10^{-7}
HFR-K5/2+3	2.69×10^{-10}	1.47×10^{-10}	3.11×10^{-7}	2.56×10^{-7}
HFR-K5/4	2.51×10^{-7}	1.95×10^{-7}	3.5×10^{-7}	2.9×10^{-7}
HFR-K6/1	5.0×10^{-10}	4.95×10^{-10}	1.52×10^{-7}	1.73×10^{-7}
HFR-K6/2+3	3.0×10^{-10}	2.07×10^{-10}	4.38×10^{-7}	3.44×10^{-7}
HFR-K6/4	4.5×10^{-7}	3.66×10^{-7}	1.22×10^{-6}	9.7×10^{-7}

The HFR-K6 test spheres were also exposed to temperature transients with short term increase of the temperature by 150–200°C within 1–2 h, in one case within 0.1 h. Figure 7.20 shows the releases spikes created by the temperature increase for sphere 4 with the two particle defects. These bursts seem to be characteristic for the behaviour of transient gas release from defective/failed particles indicating some spontaneous release of gas atoms stored in bubbles or pores of the particle kernel or the buffer layer.

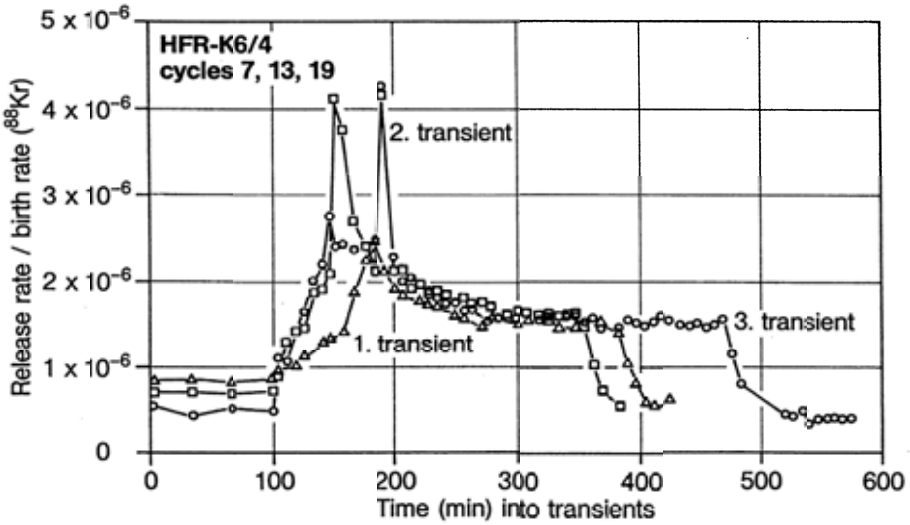

FIG. 7.20. Kr-88 release from capsule C with fuel sphere HFR-K6/4.

Water ingress effects were also investigated by water vapour injection tests into capsules A (no defective particels) and capsule C (two failed particles) [218, 247, 248]. The ^{88}Kr release from capsule C during the first 2000 Pa water vapour injection test is presented in Fig. 7.21 where the R/B values are plotted against injection time. The ^{88}Kr R/B progression can clearly be distinguished. The first peak occurs after one and a half hours, as the krypton gas is quickly extracted from the matrix material by the water vapour. This corresponds with the peak observed for capsule A where only fission product release from matrix release was measured. This release peak for capsule C is much larger than the corresponding peak from capsule A, which shows that fission gas trapped in the matrix material was predominantly released by the failed particles of test element K6/4 prior to the 2000 Pa water injection. The krypton gas trapped in the matrix material is quickly exhausted and only fission products trapped in the failed particles are further released. The second peak starts shortly after the beginning of the water vapour injection, and continues until the water vapour injection is stopped after about 24 h. The krypton release then slowly decreases for the next 48 h until the release rate before the injection started, is reached.

By comparing fission product release profiles from test elements containing no failed particles, it is suggested that water vapour has an effect on both fuel kernel diffusion rates and to a lesser extent on matrix material graphite diffusion rates. The theory is that water vapour has only a significant effect on fuel elements containing failed particles by affecting the diffusion characteristics of the materials of the fuel elements. There is little difference between the effects on small (Kr) and large (Xe) nuclides, and it can be assumed that the increase in fission product release due to water vapour is similar for all gaseous fission products. Increases in gas release in subsequent water injection tests of similar water vapour pressures suggest that some permanent damage occurred in the UO_2 kernel structure that have no effect on normal operation release.

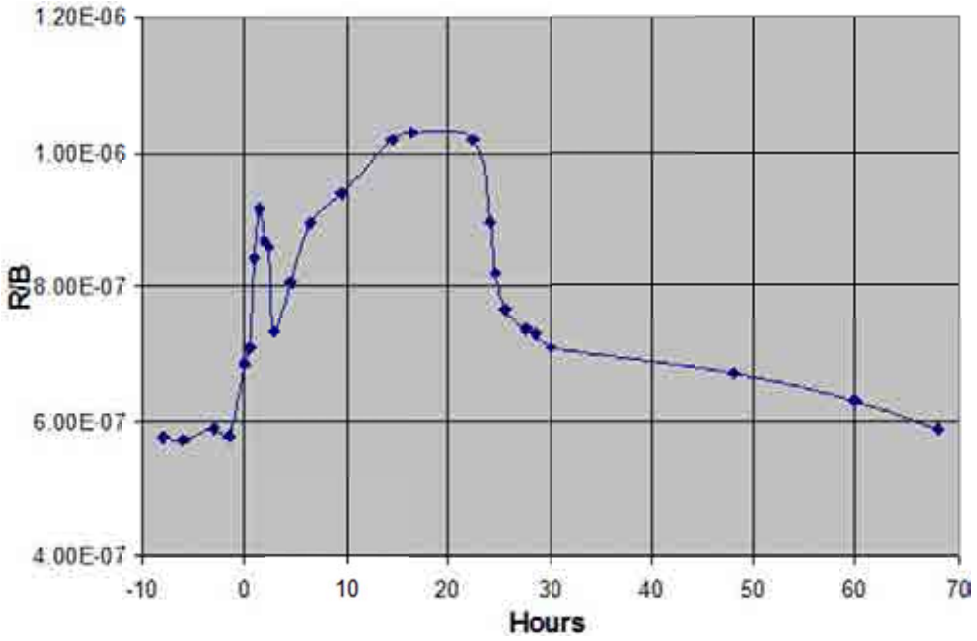

FIG. 7.21. Kr-88 release behaviour during the first 2000 Pa p_{H2O} water ingress test on capsule C of HFR-K6.

7.2.3. European Union irradiation experiment HFR-EU1bis

7.2.3.1. Objectives of HFR-EU1bis

The irradiation experiment HFR-EU1bis [249, 250] aimed at demonstrating the feasibility of low coated particle failure fractions under normal operating conditions and more specifically:

- increased central fuel temperature of 1250°C compared to 1000–1200°C in earlier irradiation tests;
- irradiation to a burnup close to 16% FIMA, which is double the license limit of the HTR-Modul; due to a neutronics data processing error, the experiment was prematurely terminated at 11.07% FIMA maximum so that this objective was not fully achieved;
- confirmation of low coated particle failure fractions at increased temperature, burnup, and neutron fluence conditions.

7.2.3.2. Preparation

HFR-EU1bis contained five fuel spheres stacked along the centre line in a closely fitting graphite holder (shroud) composed of two half shells for each sphere. On either axial side of the fuel sphere section, a thermal barrier in the form of a 5 mm axial gas gap was present between the fuel section and graphite filler blocks. The two graphite filler blocks on either side of the fuel section were axially fixed by means of a TZM (a standard titanium–zirconium–molybdenum alloy) plate and a heat shield section.

This assembly was placed in a containment tube made of AISI 321 stainless steel. The containment tube is placed in the so-called 'Full Size HTR Fuel Element Rig', REFA-170, which is a standard HFR core insert, consisting of a 316 L stainless steel tube cooled by water flow at the outside. Between the graphite section and the containment and between the containment and the REFA two radial gas gaps were present. The irradiated pebbles were 60 mm in diameter with LEU TRISO coated particles and were of former German production, type AVR GLE-4/2 produced as batch AVR 21-2 in October 1987.

The sample holder (Fig. 7.22) was equipped with 24 thermocouples of type N (Nicrosil/Nisil wires, MgO insulator, Inconel 600 sheath) with an outer diameter of 1.05 mm, a gamma scan wire and the fluence detector sets. The heat generated by fission and photons dissipated mainly radially through the materials by conduction and through the gas gaps by conduction and radiation to the outside containment which was cooled by the downstream primary cooling water.

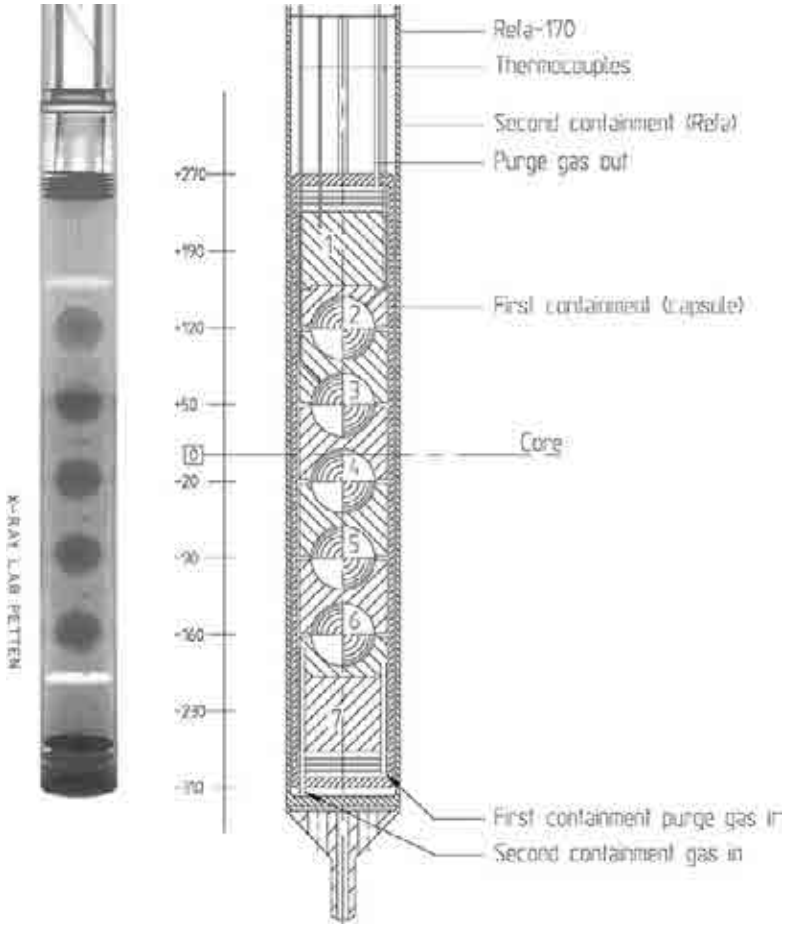

FIG. 7.22. Conceptual sketch of the HFR-EU1bis experiment and an inverted X ray picture prior to irradiation.

The temperature of the fuel surface was controlled by adjusting the He/Ne mixture in both first and second containment. This temperature adjustment was required to compensate for changes of time and fluence dependent operating parameters such as fission power depletion (burnup), dimensional changes of specimen assembly, changes in thermal conductivity and thermal expansion, changes in nuclear characteristics from cycle to cycle, and movement of the reactor control rods. The predicted useful range of temperature change by these gas changes was approximately 120 K. A schematic of the sample holder is shown in Fig. 7.22. Fuel sphere numbers 2 to 6 correspond to pebbles HFREU1bis/1 to HFR-EU1bis/5 [249].

7.2.3.3. Conduction

The HFR-EU1bis irradiation was performed for 10 reactor cycles in core position G3 (Fig.7.23) [249].

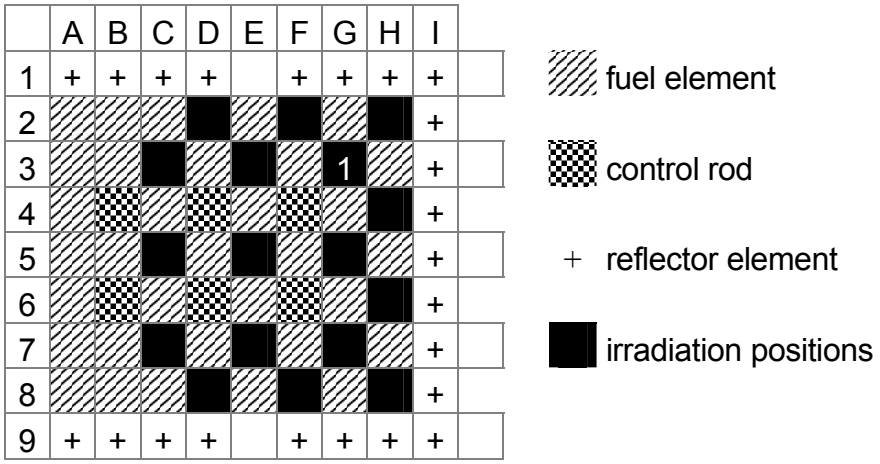

FIG. 7.23. Standard HFR core configuration showing HFREU1bis in core position G3.

The first and second containment normally remained closed (stagnant gas) during the first two reactor cycles (venting only for weekly gas sampling) and was purged with a constant gas flow during the remaining cycles which facilitated temperature adjustment and gas sampling.

The central fuel temperature could not be directly measured because drilling a hole for the thermocouple would have damaged several particles. Therefore the irradiation was conducted by controlling the surface temperature of the pebbles such that the calculated central temperature remained as constant as possible. Due to power depletion with burnup, the surface temperature had to be raised during the experiment from initially 1015°C to 1109°C on the upper hemisphere of pebble No. 4 which was used as a reference temperature. Measured temperatures in the sample holder were stored in the standard HFR data acquisition system. Figure 7.24 shows the average temperatures during the 10 irradiation cycles without correction for thermal drift and neutron-induced decalibration. The pebble surface temperatures are encircled. At the end of irradiation, 11 out of the 24 thermocouples (46%) provided physically impossible or unreliable signals, most of them being situated in the graphite between pebbles where the measured temperature was routinely between 50 and 100 K higher than on the pebble surface. Such thermocouple dropouts are frequently encountered in high temperature irradiation tests. Several mechanisms are suspected to have acted such as exposure to high temperature and neutron flux for extended periods of time, contact problems in connectors, vibrations in the experiment, and movement of thermocouples due to differential thermal expansion.

The temperatures have been analysed in [251] and show that the centre of the fuel pebbles has indeed been successfully kept approximately at 1250°C. This test thereby stretched well beyond the intended operational limits of AVR fuel, in terms of temperature, but also flux, pebble power, and spectrum hardness.

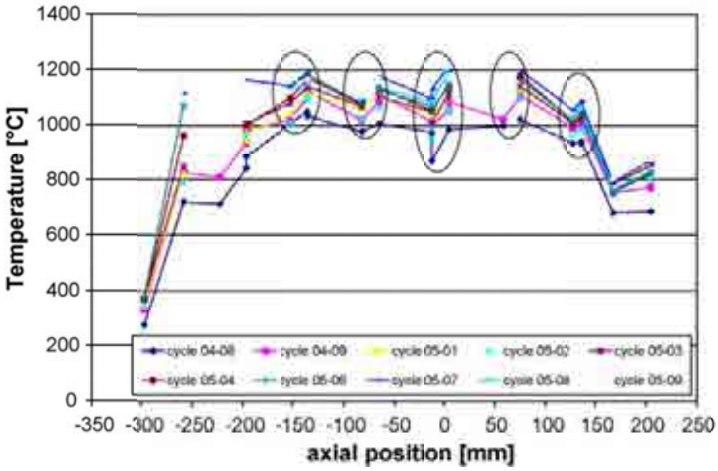

FIG. 7.24. HFR-EU1bis cycle-averaged temperatures measured in irradiation rig for all 10 irradiation cycles. Ellipsoids mark axial pebble positions.

7.2.3.4. Fission gas release measurements

For the performance of HFR-EU1bis, a gas panel installed in a glove box was used for gas mixing, flow and pressure control, and for gas sampling, in general performed once per week. The gas panel was operated from a PLC-controlled command cabinet which also contained a number of alarm functions such as the automatic cut-off of all gas lines to and from the irradiation rig in case of excessive radioactivity release. The gas flow coming from the sample holder was normally routed through an activated charcoal filter to minimize radioactivity release to the HFR off-gas system. For gas sampling, this filter was bypassed and the gas rather sent through a detachable sampling vessel with a volume of 100 cm^3. This sampling vessel was then removed from the glove box and placed on an external multi-channel gamma spectrometer calibrated for the measurement of five different isotopes, ^{85m}Kr, ^{87}Kr, ^{88}Kr, ^{133}Xe and ^{135}Xe. Of each sample, several measurements were made with the counts corrected for decay to determine the specific isotope concentration in the purge gas at the moment of gas sampling. The statistical error of this measurement was between 4 and 9%. With the knowledge of gas flow, pressure, and temperature, the fission gas release rate R from the five pebbles could be determined and related to the birth rate B from neutronics calculations (error 10–15%), thus yielding the characteristic R/B value (Fig. 7.25) [249, 252].

In the beginning of the second irradiation cycle, an operating error had caused a strong unwanted temperature excursion due to filling of the sample holder with pure Ne instead of He. After the excursion, a leak was detected between the inside and the outside of the sample holder. A neutron radiograph attributed this leak to a partly molten steel minitube running all along the inside of the sample holder to provide gas for the second containment outside the capsule. Also, the built-in gamma scan wire and the sheath of one fluence detector set were partly molten. After some modification of the gas panel, the irradiation could safely be resumed with a single containment. Even with a single containment, i.e. same gas mixture on inside and outside of the sample holder, there was sufficient temperature control margin left to maintain the target temperatures. Continuous purging as opposed to occasional venting was chosen to perform gas sampling in steady-state conditions.

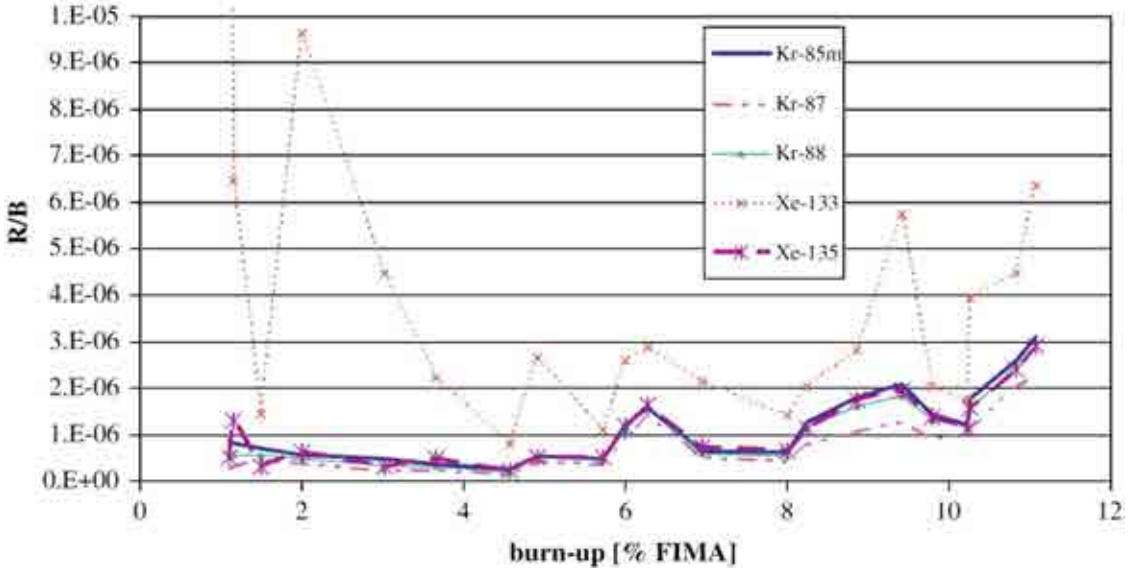

FIG. 7.25. HFR-EU1bis R/B results for the five fission gas isotopes measured.

From the five scanned isotopes, four were generally consistent. The ^{133}Xe counts were systematically higher, probably due to its additional precursors ^{133}I and ^{133m}Xe. An upward trend could be observed at the end of the irradiation. Only a few dubious results were scrapped which could be linked to thermal transients in the sample holder during the gas sampling.

A first evaluation of the fission gas release in HFR-EU1bis was performed [253]. It was found that for centre fuel temperatures below 1300°C, the gas release is attributed mainly to the contamination in fuel and irradiation rig materials and only partly to the release from coated particles. For temperatures above 1300°C, the fission gas release increases beyond what can be expected from contamination only and the presence of failed particles is the only possible explanation. R/B vs. half-life graphs suggest that the high releases at temperatures above 1300°C in HFR-EU1bis may be from a failed coated particle that does not release its full kernel released inventory of fission gases below 1300°C. It appears that an additional in-pile coated particle failure occurred during the second last irradiation test as the fission gas release for all nuclides significantly exceeded the release of contamination and one failed particle only. Whether or not the two (or more) failed particles occurred in the same fuel sphere or different spheres cannot be deduced from the data. The results were obtained by applying the above assumptions to the krypton R/B calculation and compared to R/B from contamination sources only and actual measurements.

7.2.3.5. Post-irradiation examination

PIE on the five irradiated spheres was conducted in the hot cells at NRG Petten which included dismantling, metrology, gamma scanning of graphite shells and pebbles, weighing, visual inspection of the pebbles, gamma scanning of the outer stainless steel containment (to confirm burnup calculations), X ray photography, neutron metrology on the fluence detector sets, ceramography and electron probe micro-analysis (EPMA) on one pebble.

The diameter of the pebbles measured in three perpendicular axes was found to have decreased by 1.29 mm (2.16%) on the average, corresponding to a 6.3% volume decrease. As

expected, the pebbles having received the highest fast fluence showed the most significant shrinkage.

Gamma scanning of the graphite half shells allowed detecting a significant amount of ^{110m}Ag, ^{134}Cs and ^{137}Cs. Gamma scanning of the pebbles showed the existence of significant inhomogeneities in the coated particle distribution inside the pebbles. Visual inspection of the pebbles revealed that their shiny surface was maintained hinting at the absence of corrosion phenomena.

After completion of non-destructive PIE on the five pebbles irradiated in Petten, four have been subjected to safety-relevant tests at the JRC Institute for Transuranium Elements (JRC-ITU) in Karlsruhe in the KÜFA facility to verify fission product retention by out of pile heating tests beyond 1600°C (see Section 8.3.2). The pebble designated HFREU1bis/2 has been used for PIE at the NRG Hot Cell Laboratories and investigated destructively including both ceramography and EPMA.

(a) Burnup determination

Several methods can be applied to non-destructively determine the burnup of irradiated fuel elements. One is gamma scanning for the fission product inventory of ^{137}Cs as monitor isotope. Fuel burnup determination using wet chemistry is a destructive technique usually done by measuring the content of an accumulating fission product. The ^{148}Nd isotope proved to be an ideal monitor, because it is a stable fission product, it has a well known fission yield independent of neutron energy and similar to that of ^{235}U and ^{239}Pu, is not volatile and has no volatile precursors. To determine the burnup, two different methods have to be employed to measure the required U, Pu and Nd vectors. For U and Pu, thermal ionization mass spectrometry (TIMS) is extensively used. For the determination of the Nd vector, ion chromatography (IC) is used on-line to separate this element from the other fission product isotopes, which can cause isobaric interferences. Subsequently, the isotopic composition of Nd is determined by isotopic dilution inductively coupled plasma mass spectrometry (ICP-MS). For this purpose, a hollow drill will extort a cylinder of pebble material (Figs 7.26 and 7.27) [249]. Burnup and neutron fluence data are listed in Table 7.7 [254].

FIG. 7.26. Carottage of an irradiated pebble after KÜFA test.

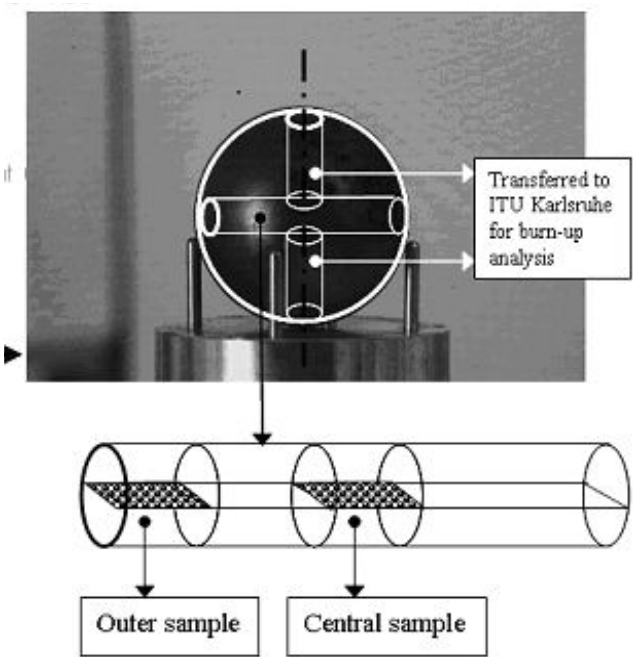

FIG. 7.27. HFREU1bis destructive PIE procedure.

Dust from this carottage process may serve as a first integral burnup indicator. From the extracted cylinder, samples can be taken at different radial positions and be powdered prior to dissolution for creating a radial burnup profile.

While the intrinsic uncertainty from wet ^{148}Nd analysis is smaller (0.5–2%) than for ^{137}Cs gamma spectrometry (5–10%), it is probable that the extraction of aliquots from the pebble required for ^{148}Nd analysis induces errors such that ^{137}Cs measurements can only be confirmed but not improved. The PIE in combination with fuel performance code evaluation by IRSN has been reported in [250]. The HFR-EU1bis samples continue to provide interesting results, considering the samples have been subjected to extreme conditions, and have shown to be of very high quality.

TABLE 7.7. BURNUP AND NEUTRON FLUENCES IN HFR-EU1bis SPHERES

Designation	Burnup (% FIMA)	Thermal fluence (n/m^2, E < 0.683 eV)	Fast fluence (n/m^2, E > 0.1 MeV)
HFR-EU1bis/1	9.34	1.34×10^{25}	2.41×10^{25}
HFR-EU1bis/3	11.07	1.59×10^{25}	2.86×10^{25}
HFR-EU1bis/4	11.07	1.59×10^{25}	2.86×10^{25}
HFR-EU1bis/5	9.70	1.40×10^{25}	2.51×10^{25}

(b) Non-destructive PIE (half shell gamma scanning)

- The release of silver (^{110m}Ag) shown in Fig. 7.28 has been significant. The image shows the ^{110m}Ag counts when moving along the graphite half shells that encased the pebbles during irradiation, but without pebbles inside.

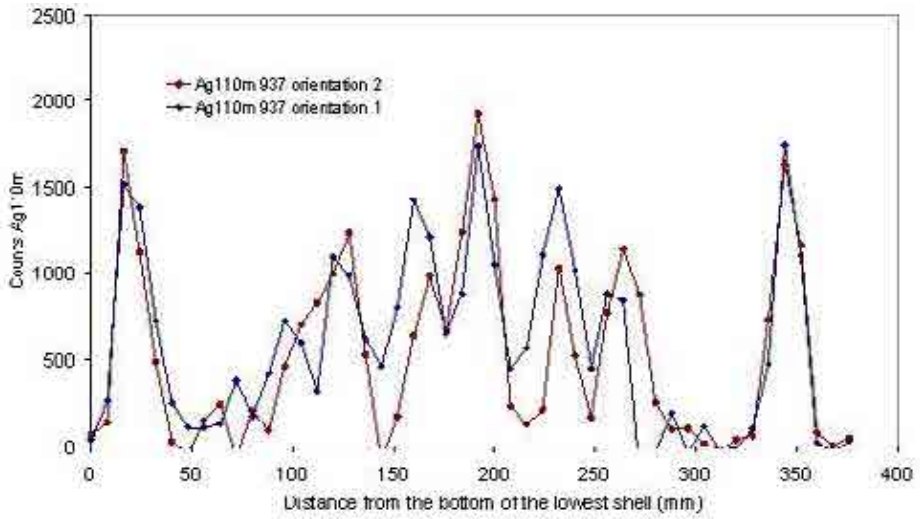

FIG. 7.28. Ag-110m gamma scan profile of the graphite half shells that encased the pebbles in the HFREU1bis experiment.

Two conclusions can be drawn:

- Agglomerates of silver can be identified: high concentrations of silver appear as count peaks, but these peaks are uncorrelated to pebble position, half shell volume or other experiment characteristics. Additionally, the scans in two directions show a similarly irregular silver distribution.
- Although the silver distribution is irregular, a profile can be identified in which the highest amount of silver is found in the centre of the experiment, and the number of counts detected decrease to either side. At the very end of the half shell stack, the counts suddenly peak.

The profile can be explained by the temperatures at the outer radius of the half shells during irradiation. The test requirement was a high and constant pebble centre temperature of 1250°C. The temperature gradient depends on the power, and therefore on the position of the pebble in the HFR core flux profile. In the middle, the flux and power was maximal, therefore the temperature gradient was maximal, compared to locations at either side where the temperature gradient in the pebble was lower. The design of the experiment adjusted for this, and ensured by appropriate gas gap insulation that the outer half shell temperatures were reached. The temperature gradient in the pebble was thus compensated to ensure the central temperature requirement (all pebbles with 1250°C central temperatures) was met.

At either end, beyond the lowest and highest pebble in the test, the temperatures dropped quite quickly. Therefore the profile measured can be explained by silver deposition at relatively low temperature locations (at maximum fluence and at either end of the experiment) and more and more evaporation from the half shells to the containment at increasing half shell temperatures (at either side of the maximum flux/pebble power). An illustrative example of the half shell outer radius temperature profile can be found in [251].

The amount of silver released in the middle of the experiment has been quantified. In the maximum flux region, the fractional release of silver amounts to 7.6%. Because the level of silver detected in the centre of the experiment compares well to the level at either end of the experiment, it can be assumed that not much of the silver released and accumulated at these locations has moved from the half shells to the containment. The release rate is therefore considered a reliable estimate of the silver release from the pebble with highest burnup.

The half shell gamma scan for caesium as shown in Fig. 7.29 indicates a regularly distributed caesium presence in the half shells, similar for both perpendicular directions in which the scans have been performed. The half shells contain a spherical cavity in which the pebbles have been encased during irradiation. The most caesium is counted at the solid parts of the half shells, i.e. in between pebbles, because more graphite is present at those locations. In case the counts are corrected for volume, the caesium release profile shows peaks at the pebble locations, indicating highest caesium density there, and this proves clearly the origin of the caesium is from the pebbles and not due to uranium/thorium contamination of the half shell graphite.

This is also confirmed by detailed gamma scanning of parts of the half shells, showing no other gamma emitters in significant quantities than ^{110m}Ag, and ^{134}Cs/^{137}Cs (in case of contamination other fission products would have been detected). Additionally, neutron activation analysis has shown the contamination levels have been very low.

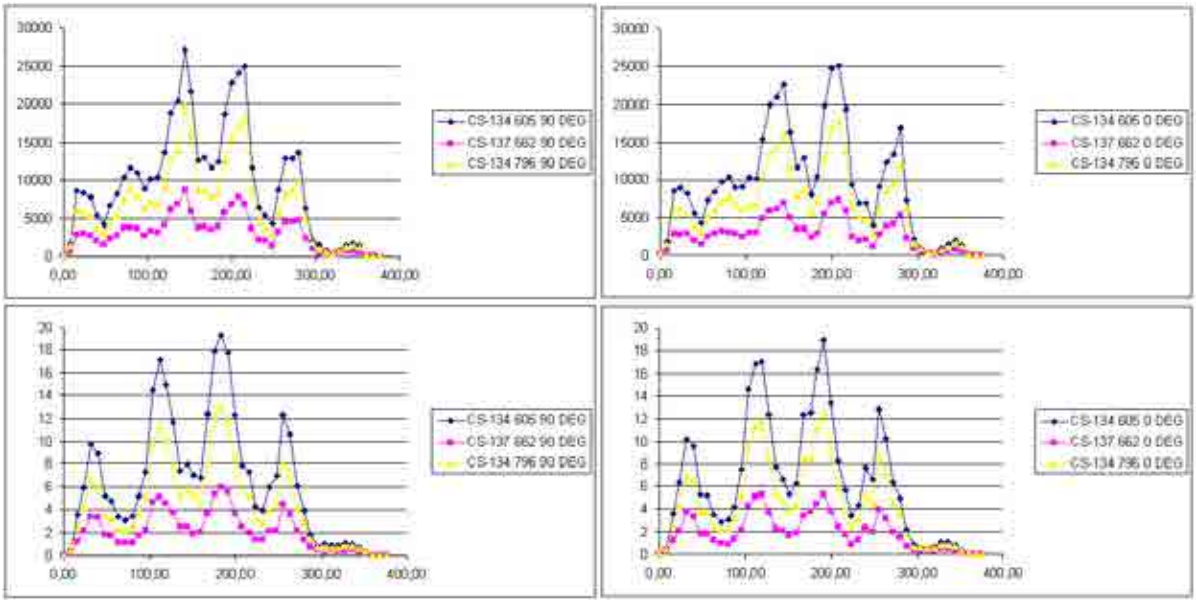

FIG. 7.29. Caesium profiles (one isotope 137, and two isotope 134 gamma energies) in the graphite half shells in the HFREU1bis experiment in two perpendicular directions (0 DEG, and 90 DEG), as measured in counts (upper), and after volume correction in counts/mm^2 (lower).

The caesium profile also shows that the upper pebble (most right pebble) has a very low release, while the other four pebbles show a high release that can be correlated to the HFR flux buckling profile and therefore can be correlated to power, burnup, and/or temperature gradient. It should be noted that the most right pebble (upper pebble) has had the lowest central temperature throughout the irradiation as shown in [251].

The almost identical distribution of caesium in two perpendicular directions in the half shells is remarkable, especially in combination with the very low caesium counts at the most right (upper) pebble. Supposed the caesium release is from failed particles, it should be from a significant amount to lead to this regular caesium release distribution. In that case, at least some failed particles would have been expected in the upper pebble, but this is apparently not the case.

An attempt has been made to quantify the amount of caesium present in the half shells, which amounts to a fractional release of caesium of 0.012%. It should be noted that considering the low melting temperature of caesium, much of the caesium is likely to have evaporated and has moved from the graphite half shell to the cooler inside of the containment tube. This is confirmed by very high activity levels of a sweep test taken from the containment inside surface, gamma scanning of which revealed significant presence of ^{110m}Ag, ^{134}Cs/^{137}Cs only.

(c) Destructive PIE (ceramography)

Ceramography examples from the centre and outside of the HFR-EU1bis pebble are shown in Figs 7.30 and 7.31, respectively. Typical kernel overview images from the centre and outer radius of the fuel zone are given in Fig. 7.32.

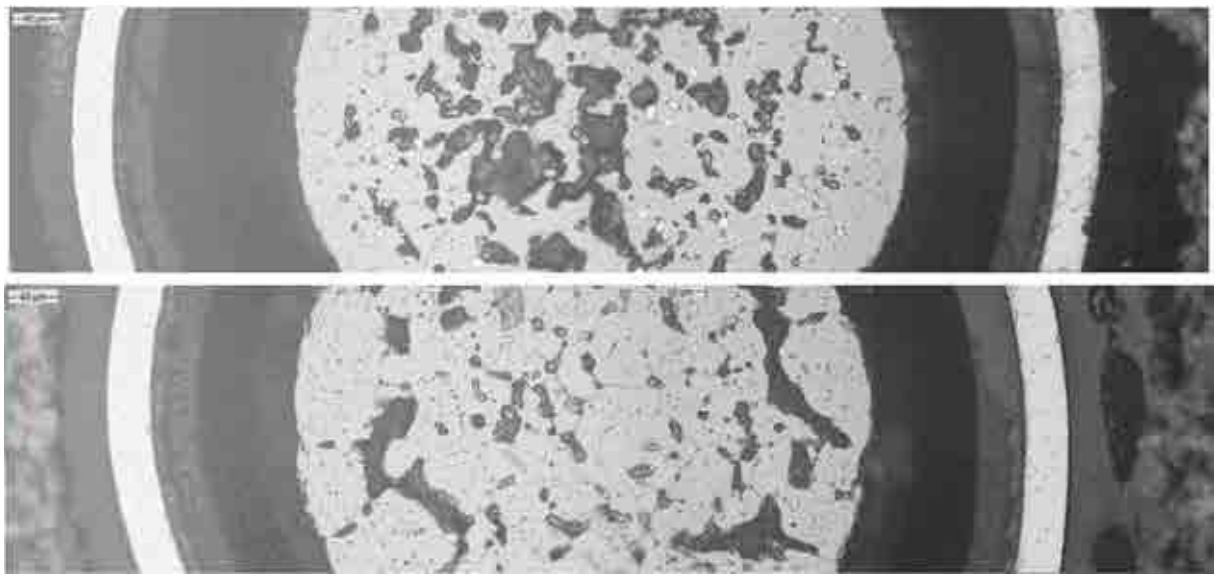

FIG. 7.30. Ceramography of particles from the fuel zone centre (buffer blackened by ion etching).

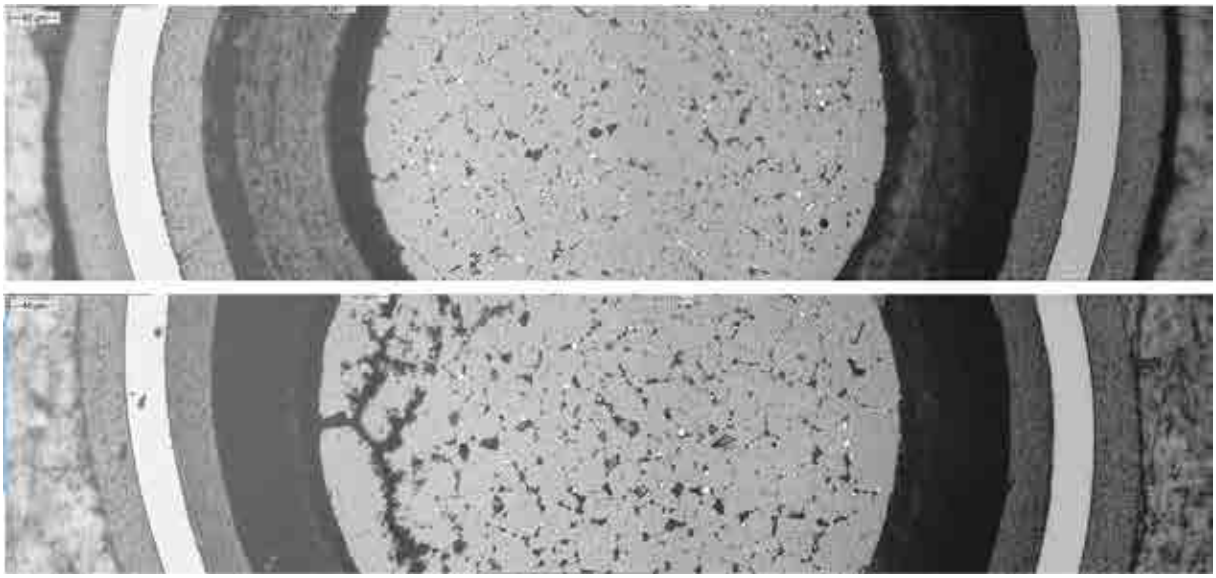

FIG. 7.31. Ceramographies of particles from the outer radius of the pebble fuel zone (buffer is blackened by ion etching).

EPMA analyses have been performed to investigate the distribution of fission products in the particles. An example is shown in Fig. 7.33. For more examples and evaluation, it is referred to [250]. Remarkable conclusions from EPMA have been that palladium, renowned for attacking SiC, had accumulated near, but not at the SiC layer (no Pd attack was observed), and that most caesium was present in the buffer layer, and not in the kernel or the other coatings. The presence of caesium in the buffer coincides with the presence of xenon, also in the buffer.

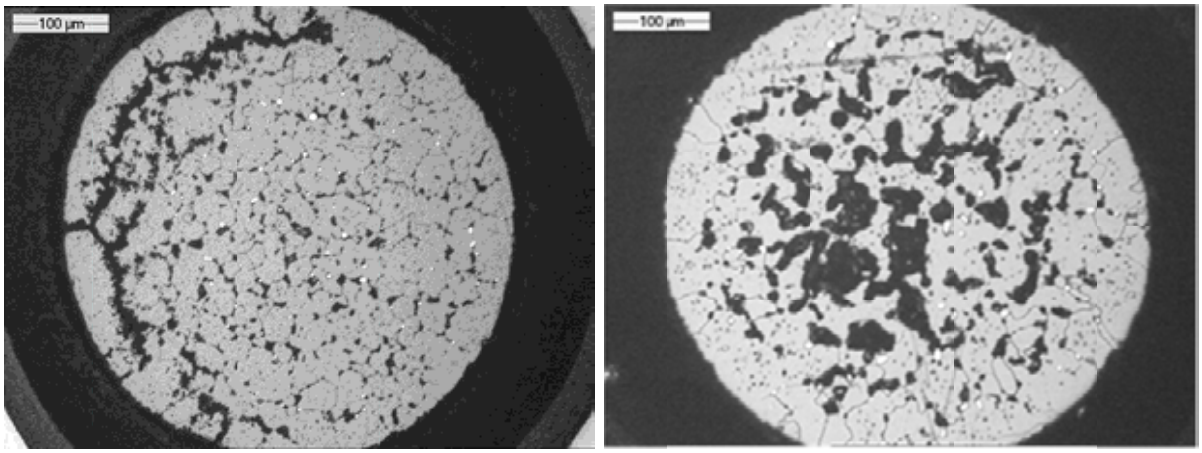

FIG. 7.32. Typical examples of fuel kernels after ion etching from the pebble periphery (top) and the pebble centre (bottom). The left side of the left picture was directed to the pebble surface.

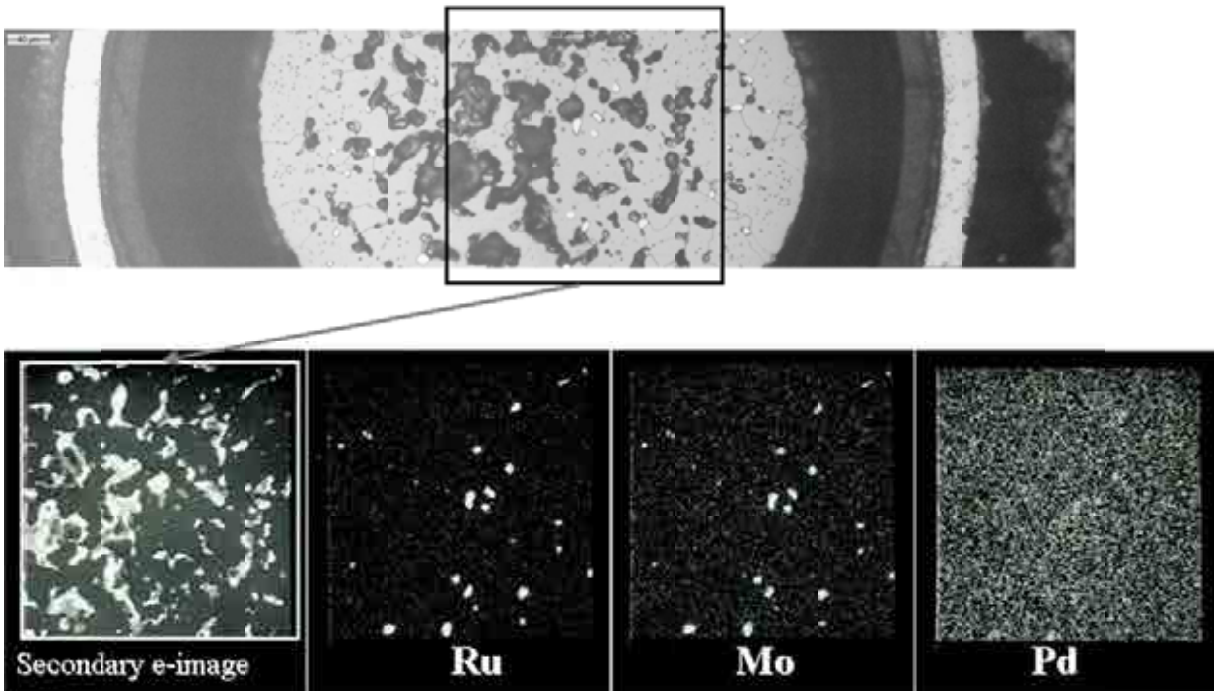

FIG. 7.33. Kernel ceramography and corresponding EPMA of a particle from the centre of the pebble, considering Ru, Mo and Pd.

Destructive PIE from the samples taken from the centre and the outside of the fuel zone of the pebble (Figs 7.34 and 7.35) shows a significant difference in response to an identical preparation procedure: break-out from the SiC coating is apparent and significant in the central high temperature zone of the pebble, but almost absent in the outer part of the fuel zone. This indicates that the SiC coatings have deteriorated more in the high temperature

region of the pebble. This is in line with investigations on SiC behaviour under irradiation, both from past and ongoing activities showing that the SiC micro-structure is significantly weakened by void swelling under (high energy) neutron irradiation at temperatures beyond 1250°C.

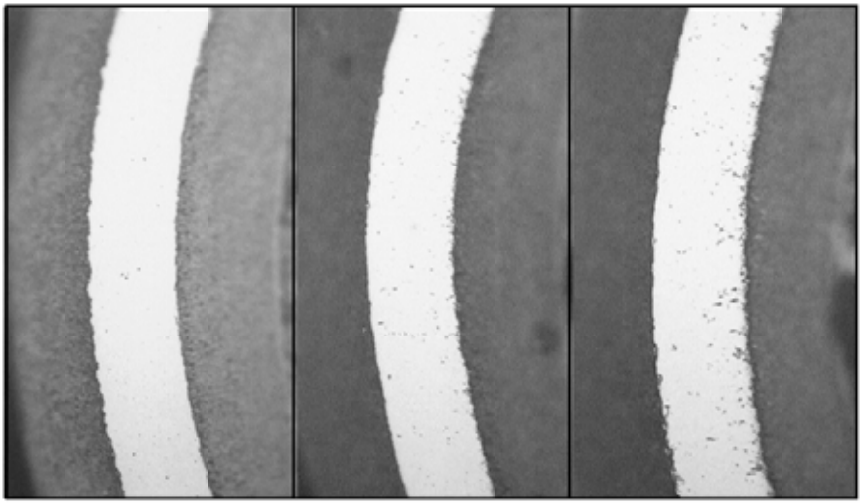

FIG. 7.34. Typical ceramography details of the SiC coating, unirradiated (left), HFREU1bis irradiated at 1000–1150°C (middle), and HFREU1bis irradiated at 1250°C (right).

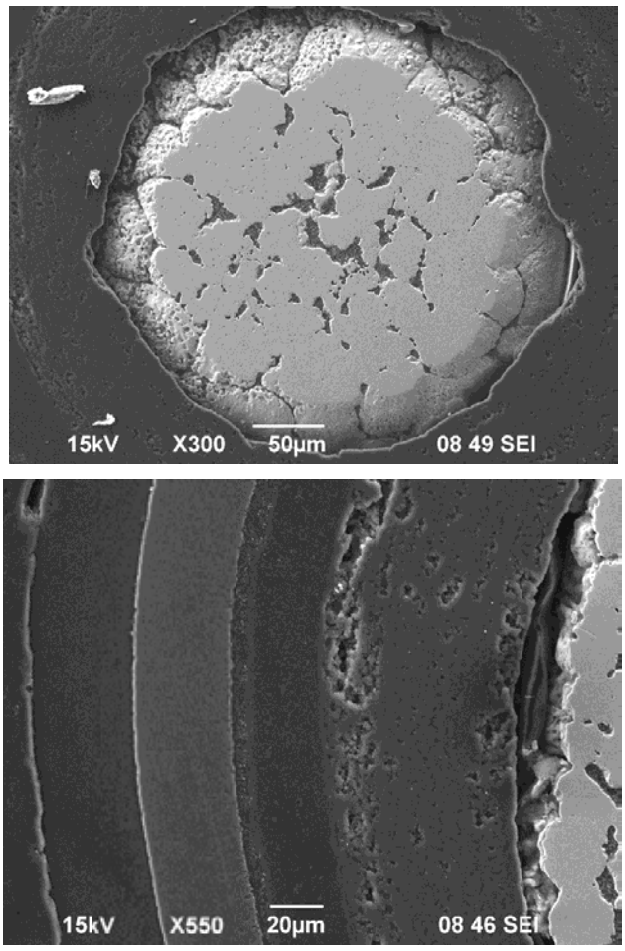

FIG. 7.35. SEM images.

(d) HFR-EU1bis preliminary evaluation

Although speculative, fission product diffusion through SiC coating could be enhanced by deterioration under high energy neutron irradiation (HFR-EU1bis has been irradiated in a relatively hard spectrum) at high temperatures, especially for metallic elements, whose diffusion is dominated by transport through gaps, (micro-)cracks and voids. The explanation of the uniform release could be that caesium diffusion through the SiC layer is enhanced at (very) high temperature irradiation due to this mechanism. This mechanism becomes apparent quite abruptly at a certain temperature, and therefore also the release of caesium by enhanced diffusion through SiC could take place from a distinct temperature onwards. Possibly it has therefore not been observed in previous tests. It should be noted that HFR-EU1bis has been operated at conditions well beyond expected conditions in HTR systems, and conditions of tests performed in the past. More investigations on the samples will be conducted at NRG where a recently installed SEM, with add-ons is being adopted to gain more insight in fission product distributions, SiC micro-structure development, etc. (see Fig. 7.35).

7.2.4. European Union irradiation experiment HFR-EU1

7.2.4.1. Objectives of HFR-EU1

The irradiation experiment HFR-EU1 [255] conducted in two phases between 2006 and 2010 had the objective of exploring the potential for high performance and high burnup of the existing German AVR fuel pebbles and newly produced fuel for advanced applications such as the conceptual GenIV very high temperature reactor (VHTR). Irradiating fuel under defined conditions to high burnups and testing it afterwards in thermal ramp tests to simulate cooling accidents is a licensing requirement for new fuel and provides better understanding of fission product release and failure mechanisms should coating failure occur.

7.2.4.2. Preparation

The irradiated pebbles were 60 mm in diameter with LEU TRISO coated particles. The three German pebbles were of type AVR GLE-4 produced as batch AVR 21-2 in October 1987. They were manufactured by HOBEG. The two Chinese pebbles were produced by INET for the operation of the HTR-10 test reactor.

The design of HFR-EU1 is based on previous experience of HTGR fuel irradiations within the European Union, namely HFR-P4, HFR-K5, HFR-K6 and SiC coated graphite spheres. The five pebbles and six mini-samples (10 coated particles each, packed in graphite powder and contained in a niobium tube) were tested in a standard re-usable REFA-172 rig, slightly larger than the REFA-170 rig used in the HFR-EU1bis test. This change was required to accommodate the two different capsules and gas lines. A schematic drawing is shown in Fig. 7.36 [256]. The sample holders (1st containment) are made of AISI 321 capsules containing several graphite cups (SGL R6650) holding the pebbles in place. The REFA-172 rig forms the 2nd containment. The upper sample holder (INET fuel) is equipped with 14 thermocouples, while the lower one (AVR fuel) has 20. Thermocouples are of type N made by Thermocoax with Inconel 600 sheaths.

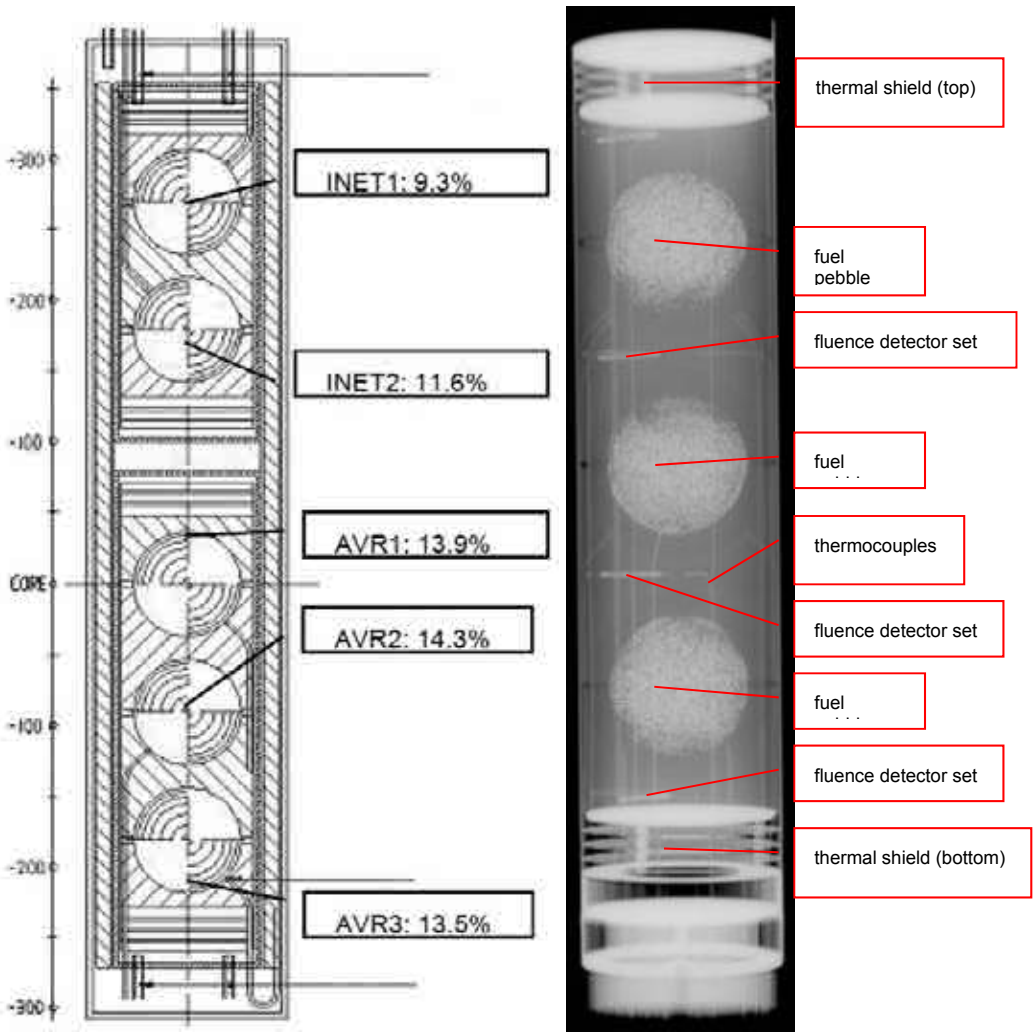

FIG. 7.36. Cross-section of the HFR-EU1 sample holder with upper Capsule 1 containing two Chinese spheres and lower Capsule 2 containing three German spheres (left); pre-irradiation X ray of German capsule (right).

Nuclear instrumentation includes 12 neutron fluence detector sets, 4 self powered neutron detectors and 4 gamma scan wires. The heat generated by fission and photons dissipates mainly radially through the materials by conduction and through the gas gaps by conduction/radiation to the outside containment, which is cooled by primary cooling water. The temperature of the fuel surface could be controlled by adjusting the He/Ne blend in both the 1st and 2nd containments. This temperature adjustment was required to compensate for changes of time and fluence dependent operating parameters such as fission power depletion (burnup), dimensional changes of specimen assembly (graphite shrinkage, typical turn-around dose (10–15) × 10^{25} n/m^2, typical shrinkage at turn-around approximately -2% at 470–500°C), changes in thermal conductivity and thermal expansion, changes in nuclear characteristics from cycle to cycle, and movements of reactor control rods.

With two independent capsules containing the fuel elements in HFR-EU1, this experiment was more complex in terms of design and operation than HFR-EU1bis which had accommodated five pebbles in a single sample holder. Moreover, it was connected to a new gas handling facility [257] that enabled continuous instead of batchwise fission gas release analysis. The 1st and 2nd containments were continuously purged with a constant gas flow of 50 mL/min during the whole irradiation which facilitated temperature adjustment and gas

sampling. This set-up with a higher gas pressure in the 2nd containment enabled permanent integrity surveillance of the 1st containment using pressure alarm units. Cycle-by-cycle turning of the experiment by 180° was applied to flatten neutron fluence and radial burnup gradients across pebbles.

The experiment was designed such that despite the decrease in power with time the desired surface temperature could be kept as constant as possible for all pebbles over the entire irradiation. This was achieved by sizing the gas gaps between graphite cups and 1st containment tube and 1st and 2nd containment tubes such that a suitably adjusted He/Ne blend enabled obtaining the required pebble temperatures. Unlike HFR-EU1bis where constant central temperature was desired, HFR-EU1 was conducted with constant surface temperature. While this approach eliminates uncertainties in thermal conductivity data (order of 10%) for the calculation of the evolving temperature profile across the pebble, power depletion with burnup continuously decreases the central temperatures during the experiment.

7.2.4.3. Conduction

HFR-EU1 was initially designed to be slower (lower neutron flux and fission power, thus lower acceleration factor) than HFR-EU1bis with an initially estimated 22 calendar months in position H2. However, the HFR conversion from HEU to LEU finished only a few months before the start of the experiment required two position changes inducing significant power variations. The irradiation test was performed in two campaigns from 29 September 2006 to 24 February 2008 (12 reactor cycles of 28 days each) and continued from 19 October 2009 to 19 February 2010 (4 reactor cycles) totaling 445 efpd. The interruption of the test was imposed partly by reactor outage and partly by unexpectedly high thermocouple failure in the capsule with the German spheres, which required construction of a new safety case. The irradiation of HFR-EU1 was done in the HFR core positions H2, H4, and F2; Figure 7.37 displays the successive moves.

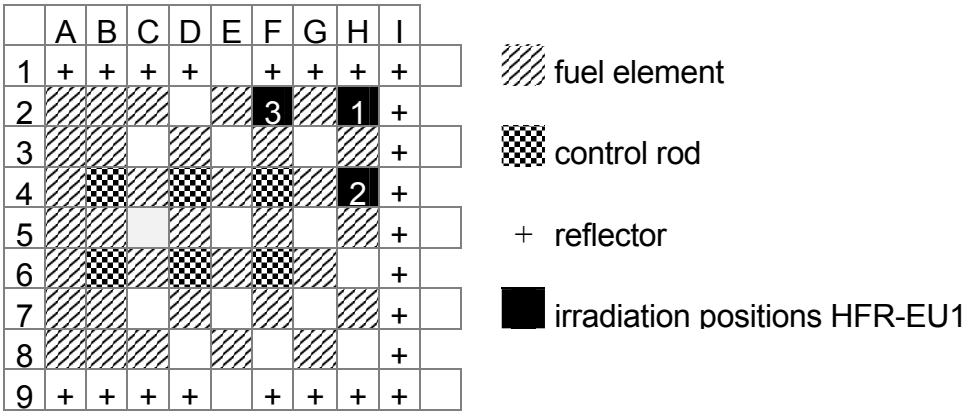

FIG. 7.37. Standard HFR core configuration showing HFR-EU1 in core positions H2, H4 and F2.

Measured temperatures in the sample holder were stored in the standard HFR data acquisition system.

Figure 7.38 shows the time-averaged temperatures for all 16 irradiation cycles without correction for thermal drift and neutron induced de-calibration of thermocouples [257]. Typically, circumferential temperature differences of approx. 50 K were observed, mainly due to the unexpectedly strong axial flux buckling on the top of the capsule. This same axial flux buckling was too strong to adjust both INET pebbles to the same temperatures despite the

provisions foreseen in the capsule design. In agreement with INET, the target temperature for a reference thermocouple in the INET capsule was thus changed to obtain approx. 940°C on pebble INET 2. The 950°C target for the AVR pebbles was maintained. Still, the fuel surface temperatures were sensitive to HFR power fluctuations, experiment loading and control rod movements.

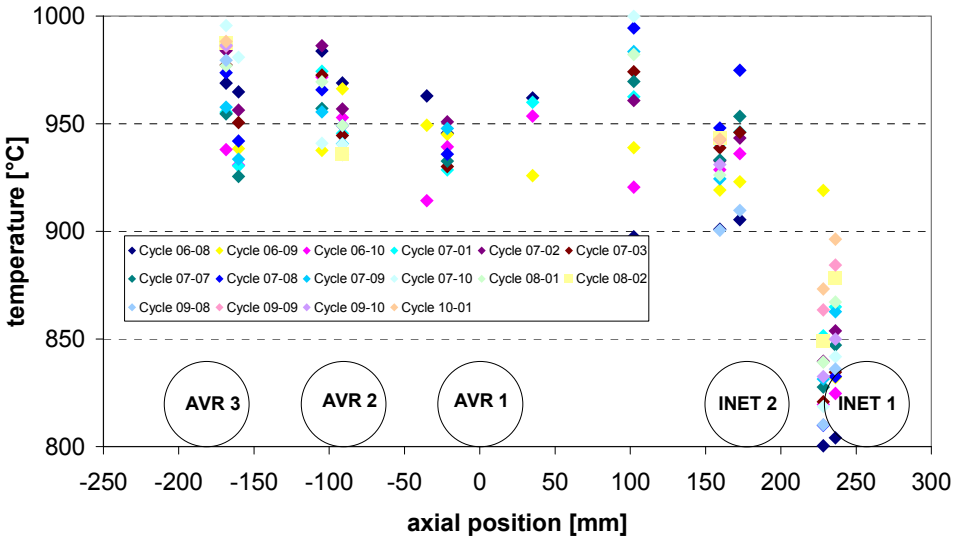

FIG. 7.38. Cycle-averaged temperatures measured in irradiation rig.

Thirty-four thermocouples (TC) were built into the experiment. They were supplied by Thermocoax and were of type N (Nicrosil/Nisil wires, MgO insulator, Inconel 600 sheath) with an outer diameter of 1.05 mm. Already after 12 irradiation cycles, 4 out of the 14 INET and 16 of the 20 AVR TC provided physically impossible or unreliable signals. The experiment ended with 6 out of 14 damaged TC in the INET capsule and 18 out of 20 damaged TC in the AVR capsule. Because in this test TC were considered safety instrumentation, the unexpectedly massive failure imposed a complete review of the safety documentation of this experiment. Several mechanisms are usually quoted to have acted such as exposure to high temperature and neutron flux for extended periods of time, carburization of the sheath, and movement of TC due to thermal expansion. But because of the accumulation of defects in the lower AVR capsule, a common cause failure is suspected, either the high temperature brazing process for the bottom lid transition or the U-bend of the TC before they enter the capsule from below. Specific PIE is planned to elucidate this question.

7.2.4.4. Fission gas release measurements in HFR-EU1

HFR-EU1 was conducted using a newly built gas handling station, the so-called ‘sweep loop facility’, SLF (Fig. 7.39) [256]. This installation was the follow-up installation of the old sweep loop which was used, amongst others, for the HFR-K5 and HFR-K6 installations.

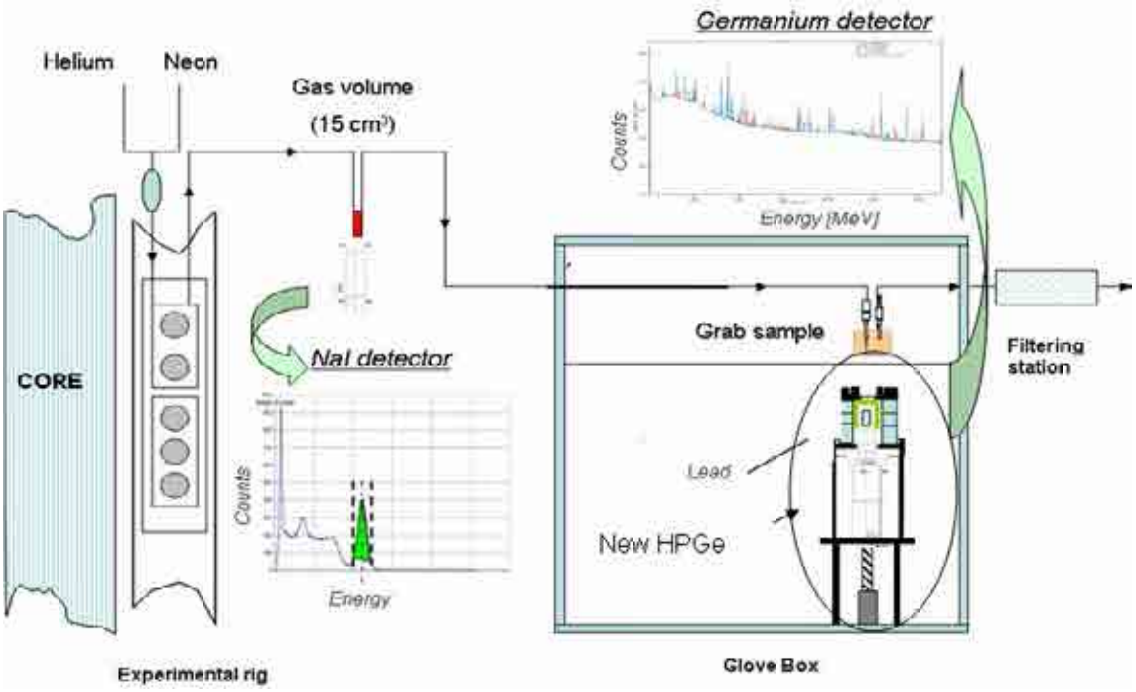

FIG. 7.39. HFR-EU1 — The new sweep loop facility for gamma spectrometry (Courtesy of JRC).

This installation provides all containments with variable gas blends for temperature control and enables permanent surveillance of containment integrity as well as gas sampling for fission gas release measurements by gamma spectrometry with the associated alarm functions. Gas sampling was in general performed once per week per capsule. The SLF was operated from a PLC-controlled command cabinet which also contained a number of alarm functions such as the automatic cut-off of all gas lines to and from the irradiation rig in case of excessive radioactivity release. Temperature was adjusted by mixing He and Ne while keeping the total gas flow rate constant, typically 50 mL/min. For gas sampling, the gas flows from the 1st containment were routed through a detachable grab sample with a volume of 100 cm^3. This grab sample was then removed from the glove box and placed on a multi-channel gamma spectrometer calibrated for the measurement of five different isotopes, namely ^{85m}Kr, ^{87}Kr, ^{88}Kr, ^{133}Xe and ^{135}Xe. Of each sample, several measurements were made and the counts were corrected for decay to determine the specific isotope concentration in the purge gas at

the moment of gas sampling. The statistical error of this measurement ranged between 4 and 9%. Together with the known gas flow, pressure and temperature, the fission gas release rate R from the two capsules could be determined and related to the birth rate B from neutronics calculations (error approx. 10%) thus yielding the characteristic R/B value which is considered a good health indicator of coated particle fuel. The burnup shown in Fig. 7.40 is the one pre-calculated for the experiment (capsule averaged). Later adjustments will be made once the burnup measurements of the pebbles and the analyses of gamma scan wires and fluence detectors will be available.

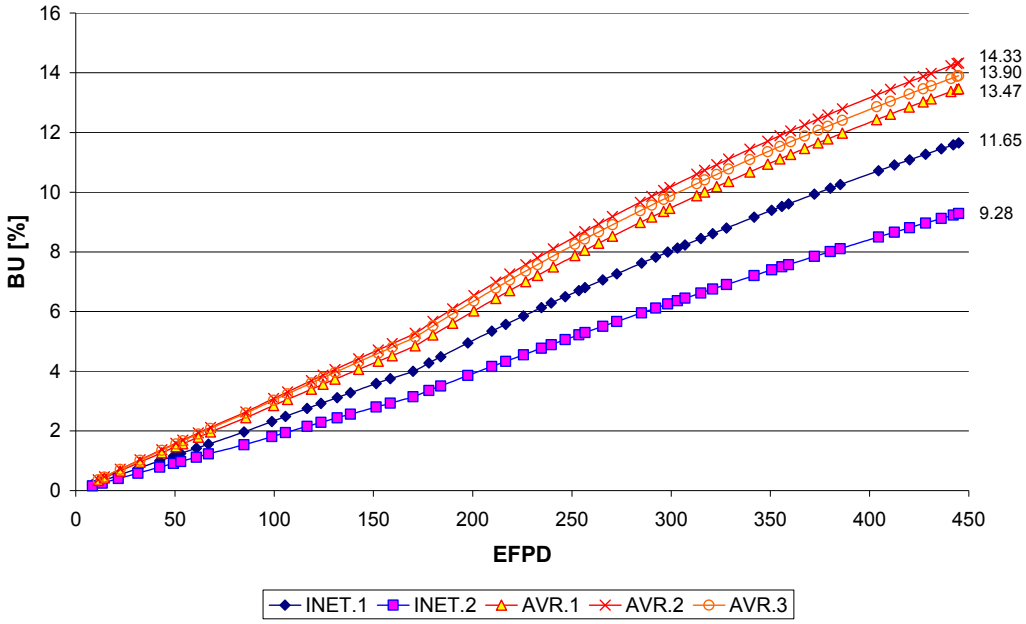

FIG. 7.40. Burnup vs. irradiation time for all five HFR-EU1 pebbles.

At end of irradiation, based on ^{85m}Kr, an R/B of approx. 8×10^{-8} for INET fuel and 2.5×10^{-7} for AVR fuel was measured (Fig. 7.41) [257], which is at least two orders of magnitude lower than the R/B corresponding to a theoretical full fission gas release of a single particle in the capsules (approx. 1.7×10^{-4} and 2.8×10^{-4} for INET and AVR capsule, respectively). In the earlier experiments HFR-K5 and HFR-K6, R/B values of 5×10^{-7} had been measured on fresh fuel. More recently and at very high temperature, HFR-EU1bis produced higher R/B of approx. 4×10^{-6} [249, 258].

This suggests that in none of the HFR-EU1 pebbles particle failure has occurred. Instead, the measured fission gas release probably originates from uranium and thorium impurities in the matrix graphite of the pebbles and in the graphite cups used to hold the pebbles in place. To validate this assumption, the same neutronic method used for the pebbles was applied to the graphite cups considering a probable graphite contamination of 50 wt-ppb of natural uranium and of 250 wt-ppb of thorium [259]. Figure 7.42 shows the ratio of fission rate from contamination to the one from a single particle calculated up to 332 efpd [257]. One can deduce from this figure that after 332 efpd, contamination accounts for > 11% of one INET particle and > 22% of one AVR particle. Measured fission gas release must thus be higher than this value before one may conclude on full particle failure.

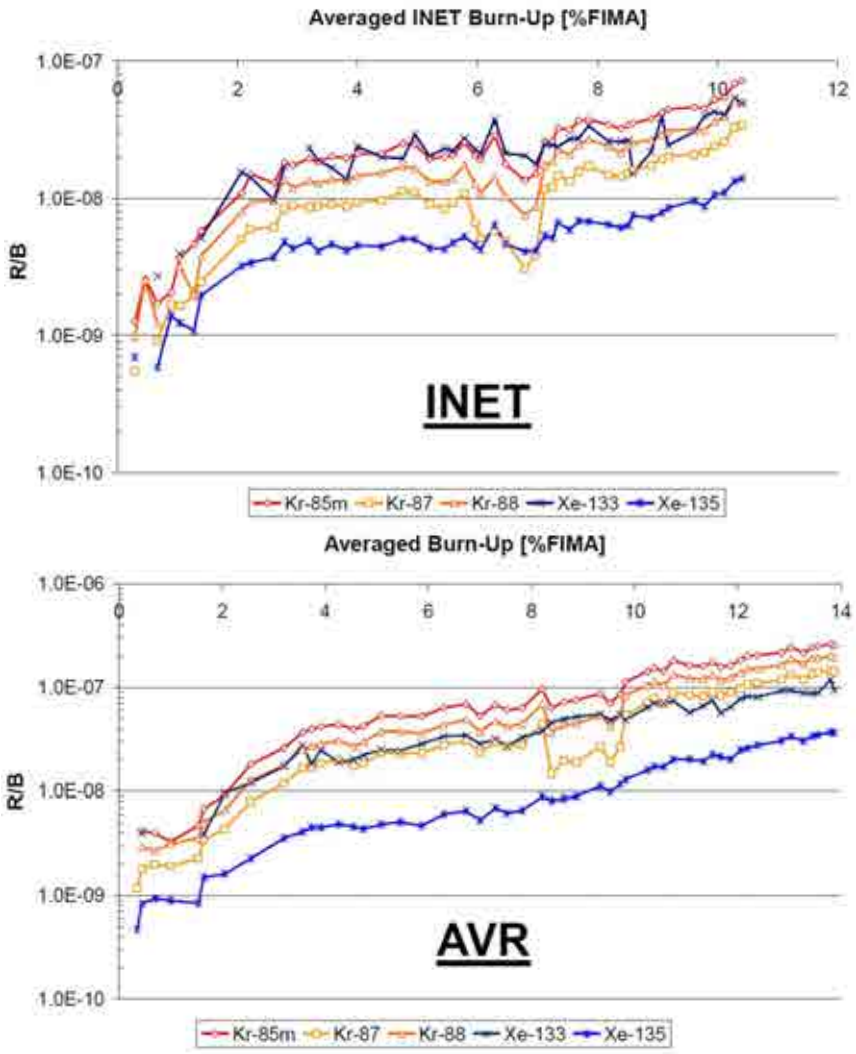

FIG. 7.41. R/B vs. burnup for INET spheres (top) and AVR pebbles (bottom).

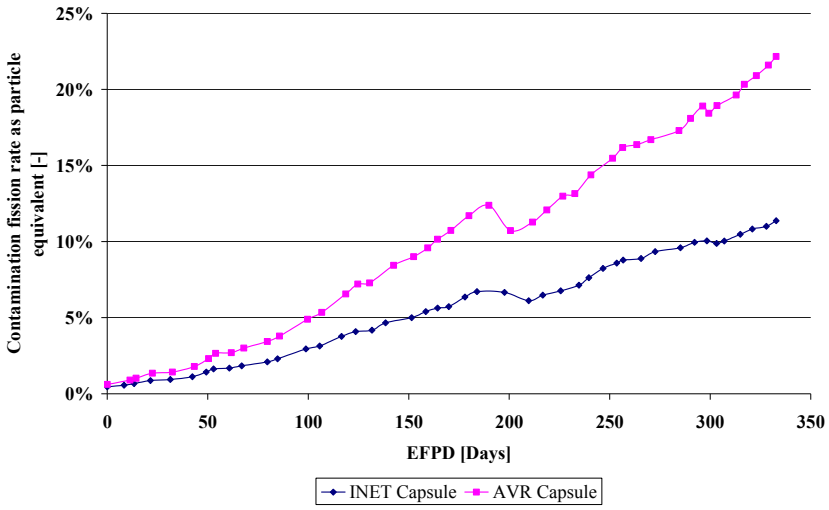

FIG. 7.42. Relative significance of fission gas release from graphite contamination compared to a single fuel kernel.

During 445 efpd, a pre-calculated maximum burnup of 14.3% FIMA was achieved with a fast neutron fluence of approximately 4.95×10^{25} n/m^2. Fission gas release from both fuel types was consistently low thus hinting at absence of fuel damage.

The experiment is planned to be completed with further extensive PIE at NRG Petten and JRC-ITU in Karlsruhe including KÜFA tests. Dismantling, PIE, transport and safety tests are planned to take place in the EU project ARCHER starting in 2011 [260].

7.2.5. European Union irradiation experiment PYCASSO

7.2.5.1. Objectives of PYCASSO-I and PYCASSO-II

The 'analytical' PYCASSO (PYrocarbon irradiation for Creep And Swelling/Shrinkage of Objects) irradiations focus on determining the effects of neutron irradiation in the temperature range of 900–1100°C, excluding effects due to the presence of fuel. These irradiations can therefore be considered separate-effect tests where only the influence of neutron fluence and temperature on coatings and coating combinations are investigated. Within the RAPHAEL (V)HTR 6th FP of the EU, the PYCASSO experiments have been devised to investigate coating behaviour under irradiation. Samples have been included from CEA (France), JAEA (Japan), and KAERI (Republic of Korea). The partnership for PYCASSO was initiated by the RAPHAEL project and is integrated in the Generation IV International Forum VHTR Fuel and Fuel Cycle project.

The PYCASSO experiment is a separate-effect test where the influence of fuel (coating corrosion or micro-structural change due to fission products), thermal gradients, and variation in coating micro-structure and dimensions have been minimized by the use of dummy kernels (Al_2O_3 and ZrO_2), high conductivity particle holder material combined with low energy production of the kernels, and strict (fabrication) quality control and selection procedures, respectively. The purpose of the experiment for the partners involved was:

- for CEA to determine the behaviour of pyrocarbon under irradiation, especially the interaction of pyrocarbon swelling and creep with SiC coating layers, with the results being used to validate and improve HTGR fuel performance modeling;
- for JAEA to investigate the behaviour of ZrC coatings which have been successfully manufactured, but require characterization and PIE;
- for KAERI to determine the influence of fabrication of pyrocarbon layers with different densities on the behaviour under irradiation.

For these purposes, dedicated particles have been manufactured consisting of surrogate kernels (ZrO_2 and Al_2O_3) with different types of PyC/SiC/ZrC coatings and coating combinations. All specimens delivered have been extensively characterized such that even potentially small changes due to the irradiation in dimensions, micro-structure and density can be determined accurately after irradiation. The three partners involved in the PYCASSO irradiations have the following irradiation targets:

- CEA: Two drums have been irradiated until two different fluences of 2.05×10^{25} n/m^2 (E>0.18 MeV) and 1.65×10^{25} n/m^2 (E>0.18 MeV) in PYCASSO-I, confirmed by Post-irradiation neutron metrology. In PYCASSO-II, fluences of 2×10^{25} n/m^2 and 3×10^{25} n/m^2 (E>0.18 MeV) are targeted for two drums. Target temperature is 1000°C.
- For KAERI and JAEA specimens, two drums with identical content have been irradiated at two different temperatures, 900°C and 1100°C, with approximately the

same fluence with a maximum of 2×10^{25} n/m^2 (E>0.18 MeV), and 3×10^{25} n/m^2 (E>0.18 MeV) for PYCASSO-I and PYCASSO-II, respectively.

For each separate tray and samples therein, the achieved fast neutron fluence can be determined with high accuracy, which facilitates correlating material changes with fluence.

The PYCASSO irradiations are performed in the high flux reactor (HFR) in Petten, the Netherlands, under NRG coordination. A detailed description of the PYCASSO irradiation objectives, the samples irradiated, and irradiation performance can be found in [261] and [262].

The PYCASSO irradiations are of a completely new and complex design. The route from the concept definition via feasibility studies, fabrication and assembly, up to the irradiation took only 1.5 years. The PYCASSO-I irradiation was conducted between April 2008 and April 2009 and has been successfully de-assembled in the meantime. The follow-up test, PYCASSO-II, has been irradiated for eight cycles and was terminated in December 2010.

7.2.5.2. PYCASSO layout

Since PYCASSO was a first of a kind experiment for NRG, a significant amount of time has been invested in the design phase of the experiment. Important technical requirements of the irradiations were:

- constant specimen temperature throughout irradiation;
- accurate fluence determination of the samples;
- minimum specimen activation for easy handling and post-irradiation examination, preferably in glove box;
- minimal chemical interaction, e.g. between samples and sample holder material.

These boundary conditions have led to the design of flat disk-like sample holders (diameter approx. 25 mm) as is shown in Fig. 7.43 where one layer of particles can be accommodated per sample holder in a hexagonal cavity.

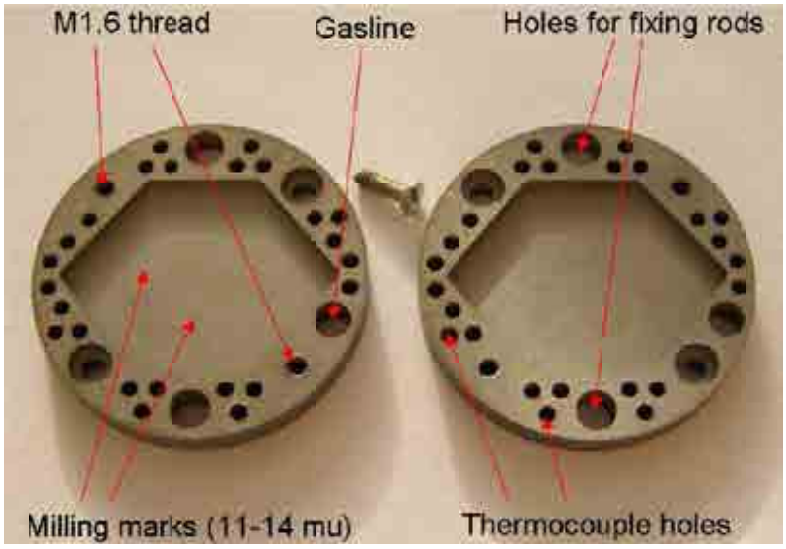

FIG. 7.43. Prototype hexagonal sample holder cup for PYCASSO irradiations.

Sample holders were made of a tungsten alloy, with high density and high thermal conductivity such that sufficient heat is generated through gamma radiation for the temperatures desired to be reached, whilst maintaining low thermal gradients in the sample holder. Radially, PYCASSO-I consisted of the assembled sample holder disks, a heat shield, a containment tube, and the so-called TRIO tube which is standard HFR equipment. It is cooled at the outside by the HFR cooling water. The three gas gaps between the sample holders and the cooling water thus established, have been adjusted to achieve the temperatures desired tailoring the radial heat resistance by gas gaps and compensating for the nuclear heating profile of the HFR.

CEA preferred two different fluence levels at similar temperatures, whereas JAEA and KAERI preferred similar fluence levels at two different temperatures. JAEA and KAERI sample holders have therefore been combined, and the locations of the sample holder stacks have been chosen to best meet the conditions desired within the limits of the HFR flux and heating profiles.

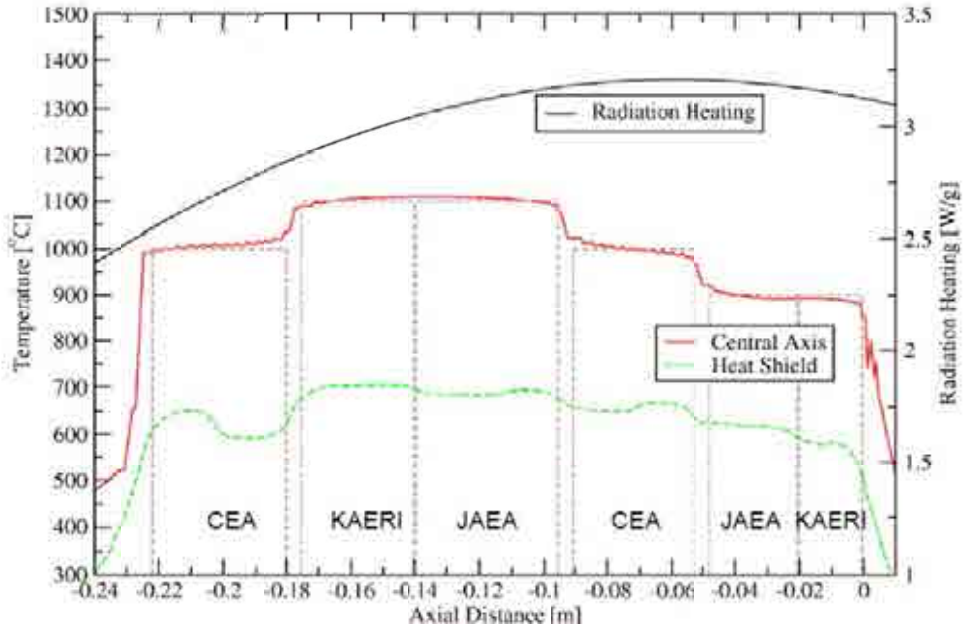

FIG. 7.44. PYCASSO-I pre-calculated temperature profile and radiation heating along central axis.

In Fig. 7.44, a preliminary temperature calculation result is shown together with the nuclear heating profile (also an approximate measure of location of the partners' samples. High temperature fluence measurement sets have been applied that can withstand the high temperatures in PYCASSO-I. These monitor sets were a novel design, and the 900°C region contained a regular monitoring set for reference.

The resulting PYCASSO-I design contained a total of 76 sample holders. Heat generation and radial gas gap width have been tuned by adjustment of the disk thicknesses and diameters respectively, resulting in a total of 40 different types of sample holder disks. Axially, the temperature regions in PYCASSO-I were established by axial gas gaps.

FIG. 7.45. PYCASSO-I (lower X ray image and photograph) and -II (upper X ray image) assembly showing sample holder disks of the three partners involved. Photograph shows the complete PYCASSO-I stack of sample holder disks prior to placement of radial heat shield and containment and a finite element model of the assembly.

In addition to the sample holder disks, seven dedicated tungsten alloy components have been designed as sample stack bottom and top plates, and axial separator disks. At either side of the total sample holder stack, reflective heat shields have been placed for reducing the axial heat flow at these locations. After manufacture, the disks were cleaned by heating, before the samples were put in the sample holder disks, separated from the sample holder by refractory metal foil. Examples are shown in Fig. 7.45 including an overview of the assembled PYCASSO-I stack.

7.2.5.3. Conduction

The PYCASSO-I experiment has been performed successfully and the required fluences have been reached within 3%. Temperatures during the HFR cycles are shown in Fig. 7.46. First activity measurements after de-assembly have shown promising results for a PIE campaign in a glovebox outside hot cells. A cell de-assembly impression is given in Fig. 7.47.

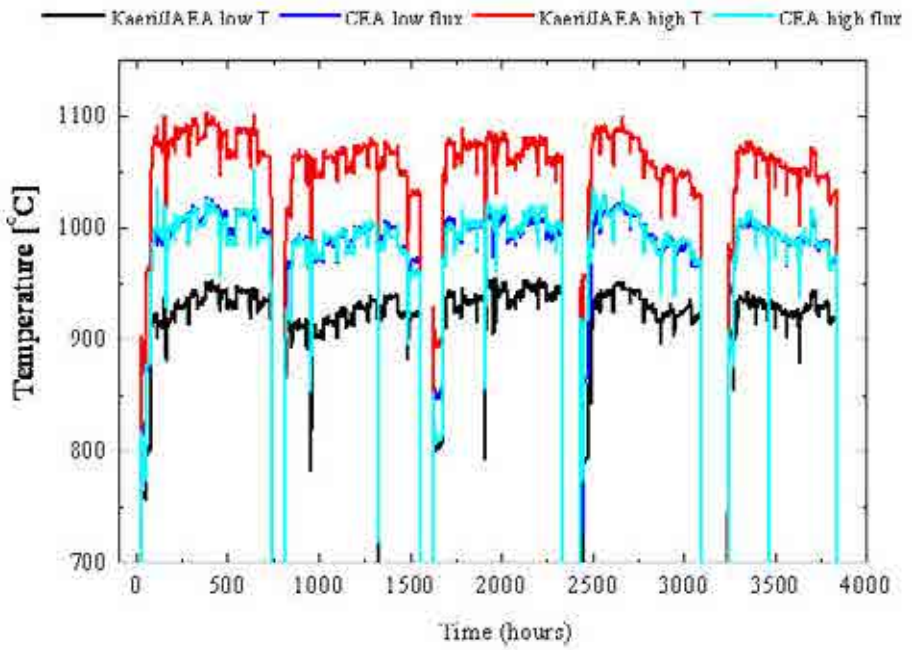

FIG. 7.46. PYCASSO-I average drum temperatures during the six HFR cycles of irradiation.

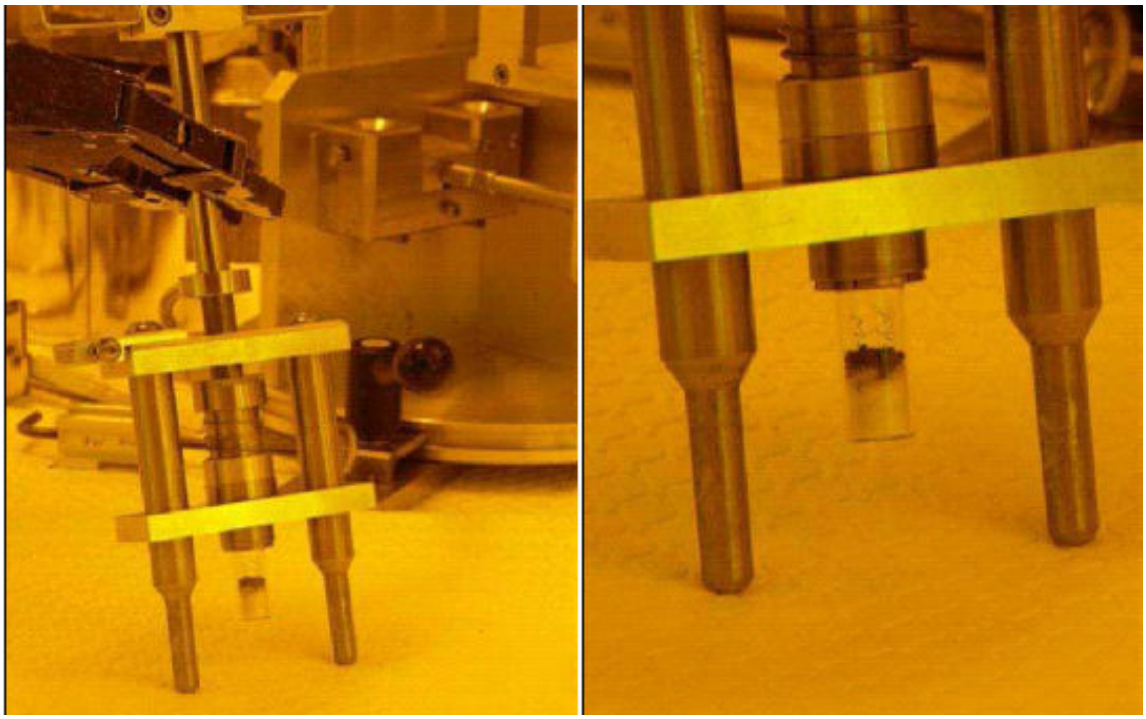

FIG. 7.47. PYCASSO-I de-assembly in hot cell impression, showing de-assembly apparatus (left), and retrieved particles of one tray collected in a glass container (right).

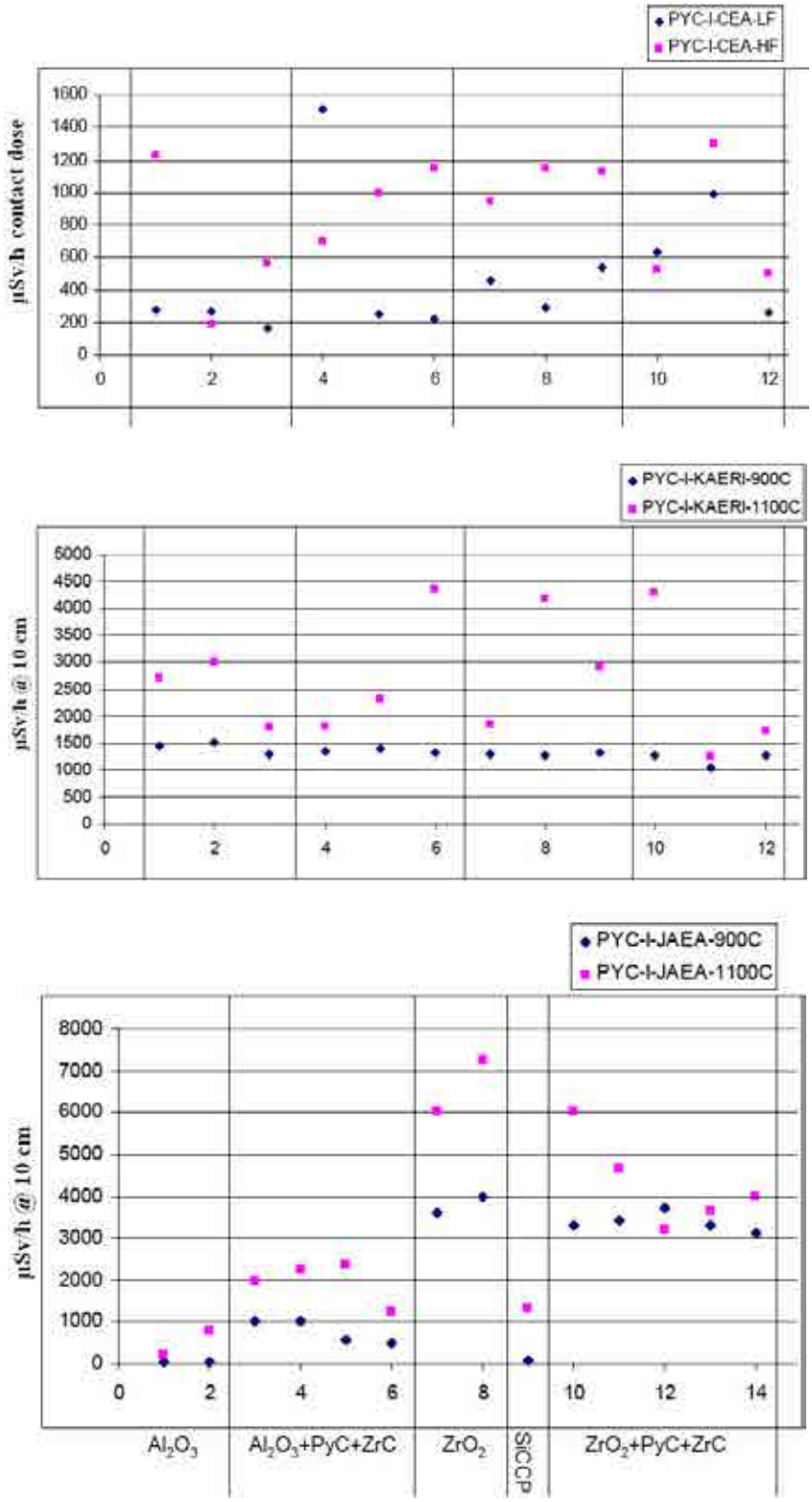

FIG. 7.48. Dose rate at 10 cm per tray for the JAEA samples of CEA (top), KAERI (middle), and JAEA (bottom).

The low fluence CEA samples show low activity (Fig. 7.48, top), and the high fluence stack is expected to be lower after an additional cleaning of the samples. The KAERI and JAEA samples show consistently higher activation (Fig. 7.48, middle and bottom, respectively) by activation of the samples themselves, especially of zirconium and hafnium impurities therein. Possibly a longer cooling time and a cleaning procedure to remove highly active sample holder debris from the container or handling of limited amounts of samples could reduce the activity to a level appropriate for investigation in a glovebox.

The following PIE will be useful for the PYCASSO samples:

- Diameter and sphericity measurement by image analyses and tomography;
- Coating thickness by tomography;
- Density by tomography and helium pycnometry of coating fragments;
- Anisotropy by ellipsometry;
- Micro-structural examinations by XRD, SEM, EBSD, TEM and high resolution tomography;
- Mechanical properties by crush tests and nano-indentation.

A PIE campaign for the PYCASSO irradiations has been proposed for the European FP 7 ARCHER project [260] and will comprise high precision metrology and detailed micro-structural evaluation. One high potential PIE methodology has been proposed which is X ray tomography, by which coating dimensions can be measured accurately in a non-destructive way. An example of this is shown in Fig. 7.49, in which a cross-section of an unirradiated CEA particle is shown, created by non-destructive X ray tomography. Average drum temperature readings of the first six cycles are given in Fig. 7.50. Dismantling and PIE is part of the ARCHER project.

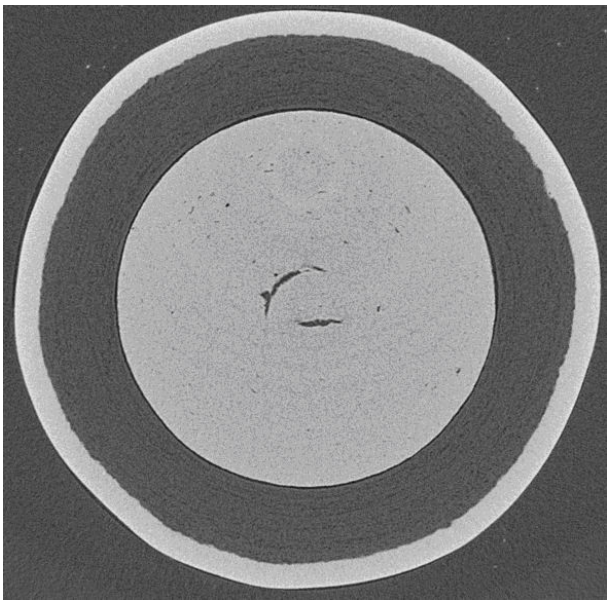

FIG. 7.49. Example of tomography on a CEA particle: this cross-section is generated non-destructively, from a full 3D tomography database of one particle.

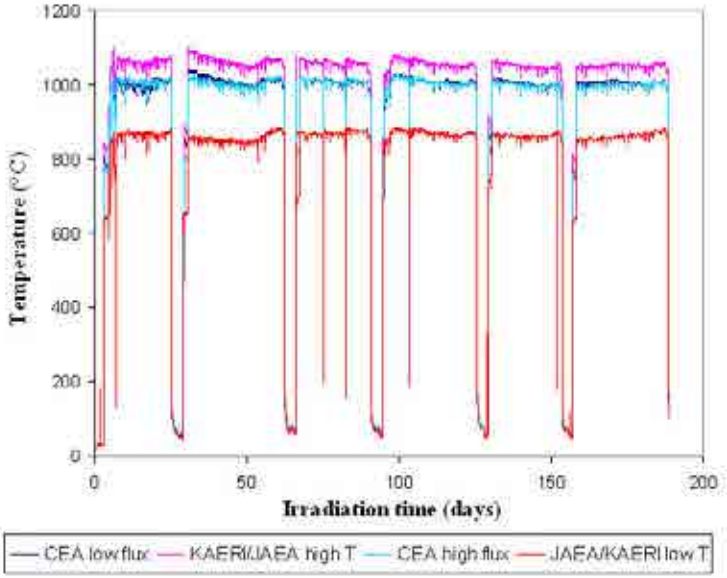

FIG. 7.50. PYCASSO-II average drum temperatures during the first six HFR cycles of irradiation.

7.2.6. Irradiation of Chinese HTR-PM fuel

7.2.6.1. Introduction

The HTR-PM is a modular pebble bed high temperature gas cooled reactor. The spherical fuel elements for the HTR-PM will consist of a spherical fissile material zone, in which 7 g of uranium in the form of ~12 000 low enriched UO_2 TRISO coated fuel particles is embedded in a matrix of graphite material, and a shell of fuel-free pure matrix graphite, surrounding the spherical fissile material zone. The diameter of the fuel zone is approximately 50 mm. The thickness of the outer fuel-free shell is about 5 mm.

The specification of HTR-PM fuel element is based on that of HTR-Modul designed by Siemens/Interatom of Germany and operational requirements of HTR-PM. R&D work of HTGR fuel element was carried out in experimented scale before 1991. Since 1991, R&D activities have been focused on fabrication technology for the HTR-10 first core fuel. During long term R&D activities, the INET has successfully developed own fabrication technologies of spherical fuel elements for the HTR-10. In 2000, approximately 20 000 spherical fuel elements have been fabricated. The performance of the fabricated fuel elements meets the design requirements of HTR-10 fuel.

Although the existing HTR-10 fuel production line in INET is at laboratory scale, the HTR-PM fuel production can be based on the successful fabrication technology of HTR-10 fuel. The existing lab scale fuel plant at INET is being upgraded for the throughput of 100 000 fuel spheres per year.

The main purpose of upgrade of the existing lab scale fuel plant at INET is to:

- fabricate HTR-PM irradiation test samples, and to
- provide successful technology of fabrication process and equipment for the HTR-PM fuel plant.

To study irradiation performance of the fabricated fuel, an in-pile irradiation test will be performed to qualify the fabricated fuel for application in the HTR-PM. Fuel qualification is an essential part of the licensing process for the HTR-PM. This irradiation test is scheduled to start in 2011.

7.2.6.2. Irradiation test plan

Samples for irradiation testing will be five fuel spheres characterized by the following features:

- Moulded spherical fuel element of 60 mm diameter with a fuel-free shell of **>** 4 mm thickness;
- low enriched uranium (17%), 7 g of uranium per fuel sphere;
- UO_2 fuel kernel;
- TRISO coating;
- A3-3 matrix graphite.

Irradiation testing of these fuel elements will be made under the following conditions:

- The central temperature of the fuel spheres will be kept in 1050±50°C.
- The irradiation will be continued until ≥ 100 GW•d/t U.
- Fast neutron fluence (E ≥ 0.1 MeV) is between 2×10^{25} n/m^2 and **~** 7×10^{25} n/m^2.
- Initial (about 20 days) maximum power per fuel sphere and particle is 3.5 kW and 300 mW, respectively. Later, the maximum power per fuel sphere and particle will be limited to about 3.0 kW and about 250 mW, respectively.
- The impurity contents of sweep gas (helium and neon) should be as low as possible.
- Temperature measurement will be performed in the fuel-free zone. Isothermal fuel sphere surface temperature should be achieved by stepped gas gaps between graphite body and capsule wall.

7.3. IRRADIATION TESTING IN THE JMTR AT JAEA OARAI

7.3.1. Irradiation testing in OGL-1

Irradiation experiments for the HTTR fuel development were performed mostly by using Oarai Gas Loop-1 (OGL-1) and capsules in Japan materials test reactor (JMTR) of JAERI. Various research efforts have been carried out to confirm the integrity of the HTTR fuel [263–265].

7.3.1.1. OGL-1

The Oarai Gas Loop-I, OGL-I, is an in-pile helium gas loop, installed in the reflector region of the Japan Materials Testing Reactor (JMTR), for irradiation of high temperature gas cooled reactor fuels at high pressure and temperature. Most irradiation experiments for the HTTR fuel had been performed in OGL-1 from 1977 until 1995 and capsules, in the range of temperature and burnup required. Figure 7.51 shows the position of OGL-1 in the JMTR core [266]; characteristic data are given in Table 7.8 [264]. The loop was composed of a concentric double pipe at a part of the JMTR core [267]. A schematic of the OGL-1 loop is shown in Fig. 7.52.

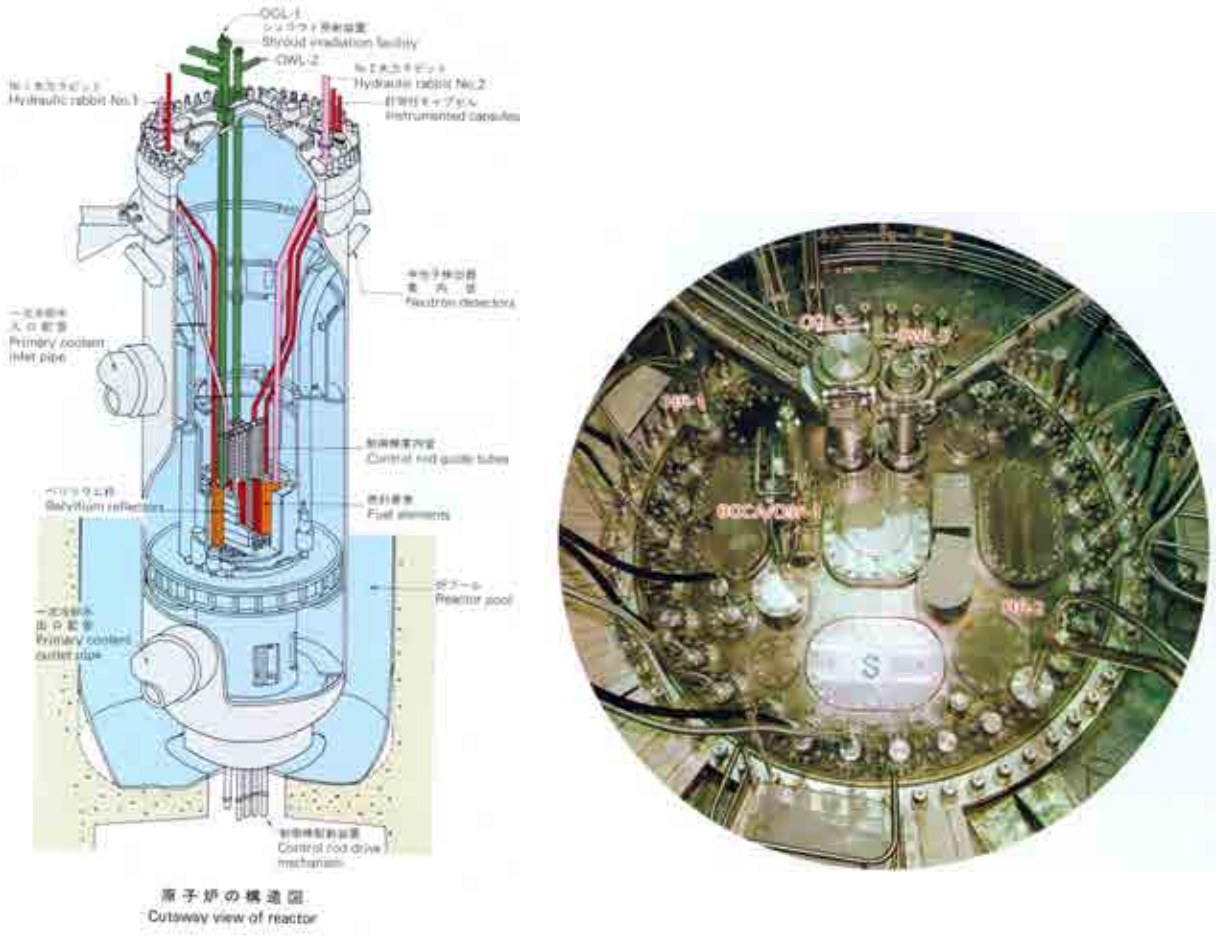

FIG. 7.51. Top view on the OGL-1 in the JMTR.

TABLE 7.8. CHARACTERISTICS OF THE OARAI GAS LOOP-1 (OGL-1)

Core position in JMTR	G, H-3,4
Effective dimension in core	82 (dia.) × 750 mm^2
Thermal neutron flux, average	5.5×10^{17} n/(m^2·s)
Fast neutron flux	1.1×10^{17} n/(m^2·s), E>1 MeV
Specimen power	< 135 kW
Helium coolant flow rate	0.1 kg/s
Maximum operating temperature	1000°C
Operating pressure	3 MPa
Impurity content	< 10 vol.ppm

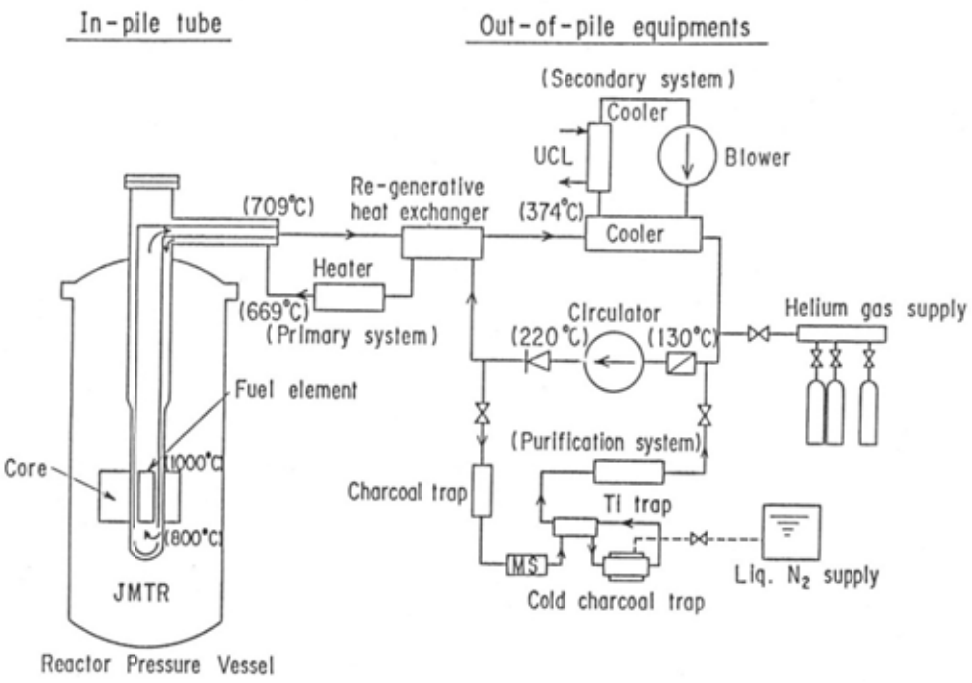

FIG. 7.52. Layout of the OGL-1 loop and the measuring points of the fission product plateout measurements .

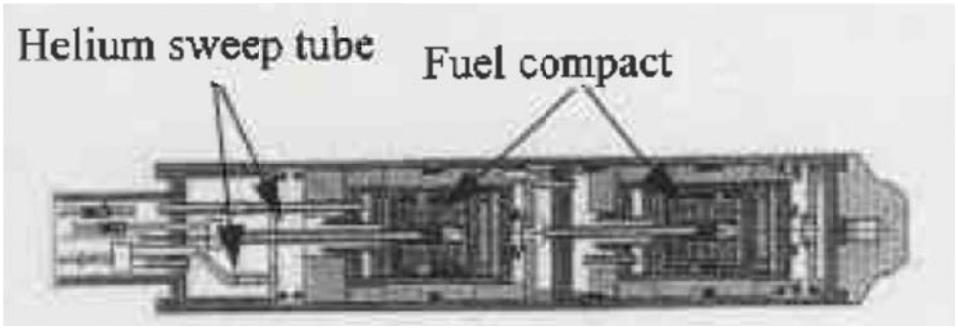

FIG. 7.53. Gas sweep capsule.

Figure 7.53 shows a gas sweep capsule, one of the capsules of JMTR which is able to measure fission gas release rate for the evaluation of the fuel failure fraction of specimens [265].

The helium gas loop OGL-1 simulating VHTR coolant conditions was also used for plateout studies in order to conduct

- measurements of plateout distribution in the primary circuit of OGL- 1,
- plateout measurements in small-size specimens,
- hot gas filter and dust filter experiments,
- development and validation of a plateout computer model.

The distribution of fission product plateout was measured by a non-destructive method using the handy type pure germanium (Ge) detectors.

TABLE 7.9. IRRADIATION HISTORY OF THE OGL-1 FUELS

OGL-1 cycle	JMTR cycles	Irradiation time (efpd)	Burnup (% FIMA)	Fast neutron fluence (10^{25} n/m^2, E>0.18 MeV)	Irradiation temperature of fuel compact (°C)	R/B Kr-88	Objective
1	39, 40	39.0	0.6	0.12	1380	—	Commissioning of OGL-1
2	42–45	71.6	0.9	0.20	1430	—	1st irradiation of VHTR fuel
3	46, 47	40.7	0.5	0.09	1320	—	Short term irradiation
4	48–51	78.0	2.0	0.23	1340	—	Medium term irradiation
5	52–58	142.3	3.3	0.38	1350	—	Long term irradiation
6	59	21.9	0.4	0.04	1480[(a)]	1.4×10^{-6}	High-temperature transient
7	60, 61, 63	58.0	1.4	0.16	1380	4×10^{-7}	Matrix graphite test
8	64–66	53.8	1.0	0.12	1390	2.6×10^{-7}	Metallic FP behaviour
9	67–73	145.5	2.7	0.28	1340	1.5×10^{-5}	Mass production
10	74–79	130.2	2.8	0.24	1330/1500 [a]	3×10^{-6}	Mass production-transient
11	80–82	62.3	1.6	0.17	1350	1.0×10^{-6}	Mass production-short irradiation
12	83–91	195.0	3.9	0.31	1340	2.3×10^{-6}	Mass production-long irradiation
13	92–102	243.0	3.7	0.49	1340/1500 [a]	—	High quality fuel
14	103–106	65.0	1.2	0.14	1350/1500 [a]	—	High burnup fuel
15	107–115	216.0	3.1	0.44	1345	—	HTTR fuel demonstration
HTTR	n.a.	660	3.6	1.2	1320	—	n.a.

[a] transient.
— data not available.
n.a. not applicable.

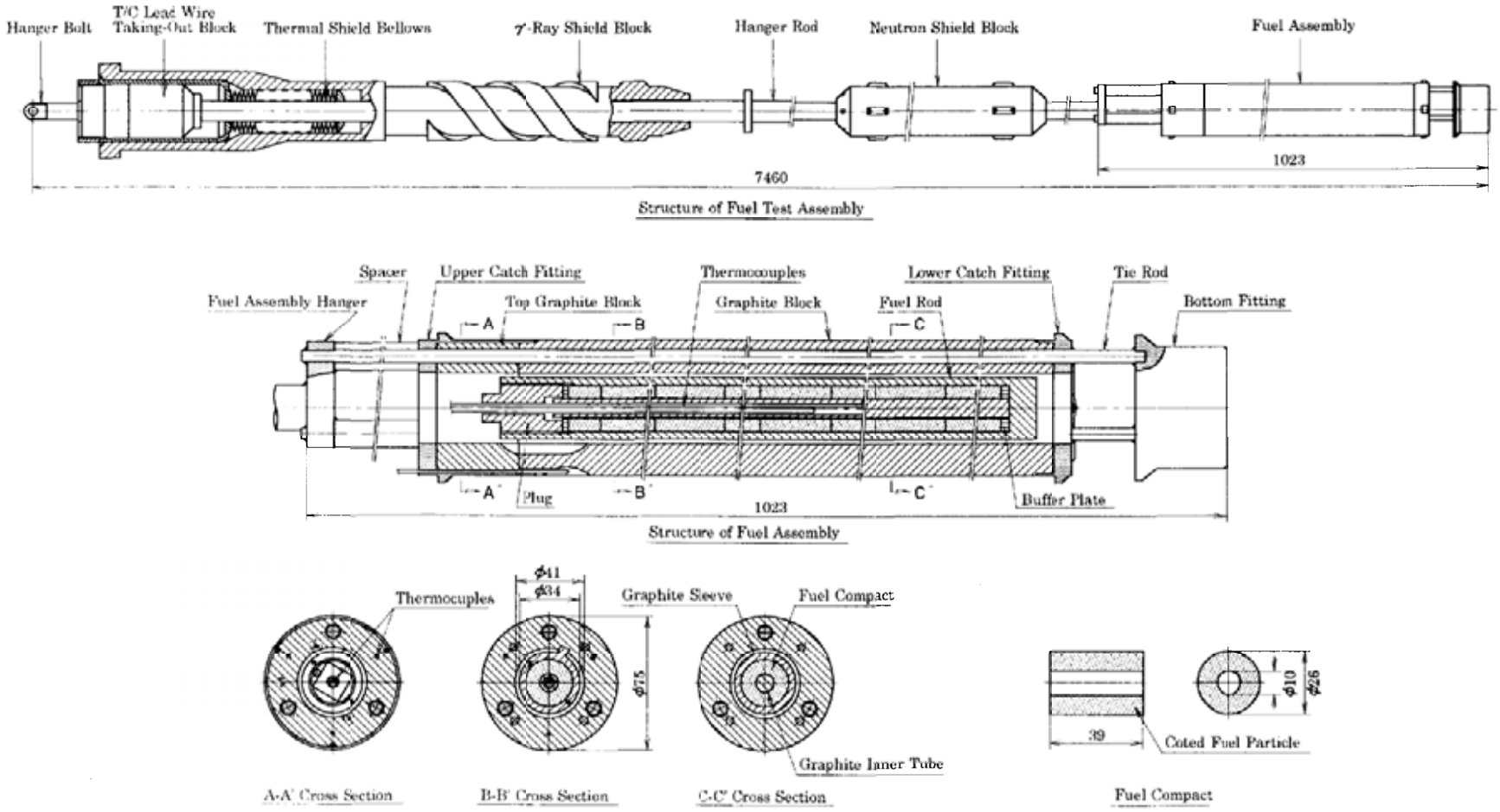

FIG. 7.54. Schematic of 15th OGL-1 fuel assembly for HTTR fuel irradiation testing.

7.3.1.2. Results

Table 7.9 shows the irradiation experiments for the HTTR fuel in Japan materials test reactor (JMTR) [267].

The coated fuel particles used in the OGL-1 fuel assemblies No. 6 to 8 were produced in a small scale fluidized bed coater, while in the assemblies No. 9 to12, trial manufacturing fuels were used, produced with a large scale fluidized bed for mass production to be applied for HTTR fuel production. For the 9th assembly loaded with the first mass production fuel, the fission gas release, R/B of ^{88}Kr, was found to be relatively high with 1.5×10^{-5}. Also various defects were observed in ceramographic sections of the irradiated coating layers.

Later, in the 12th fuel assembly, a decrease in the fabrication-induced through-coating defect fraction could be achieved. Correspondingly, the R/B of ^{88}Kr for was reduced here to an excellent value of 2×10^{-6}. Thus, the production technology and the irradiation performance of the HTTR design fuels were successfully demonstrated,

The fuel assemblies No. 13 to 15 employed the first-charge fuel of the HTTR. The 13th assembly was loaded with high quality fuel, whose as-produced defect fraction could be drastically decreased compared with previous fuels. The 15th assembly (Fig. 7.53) was loaded with fuel which had been manufactured in the same apparatus that was used afterwards for the first charge HTTR fuel production. Both fuel assemblies gave good results in fission gas release rates during irradiation and in PIE [264].

The fuel compact was irradiated up to 7% FIMA at a temperature of 1200°C. The measured release rate to birth ratios (R/B) of ^{88}Kr in both inner capsules were less than 10^{-6} as shown in Fig. 7.55, top [268], a level which corresponds to one particle failure. These results are far smaller than the safety design value of the HTTR, set at 5.35×10^{-4}, a value that corresponds to 1% fuel particle failure.

In order to investigate fuel behaviour at extended burnup, irradiation tests were performed by using so-called extended burnup fuel, whose target burnup and fast neutron fluence were higher than those of the first loading fuel of the HTTR. In order to maintain fuel integrity at burnups up to over 5% FIMA, thickness of buffer and SiC layers of the fuel particle were increased to 90 μm and 35 μm, respectively. The fuel compacts were irradiated at the HFIR reactor at ORNL (HRB-22) up to 7% FIMA, and at the JMTR over 9% FIMA, respectively [268].

The fuel assembly No. 14 in OGL-1 indicated a spike release of fission gas during irradiation at 1500°C after a transient temperature increase up to this value (Fig. 7.55, bottom) [268]. But overall, these three assemblies demonstrated good performance of the loaded fuels giving significantly lower values in fission gas release rates during irradiation and in particle failure fractions after irradiation compared to the corresponding design limits for the first charge fuel of the HTTR.

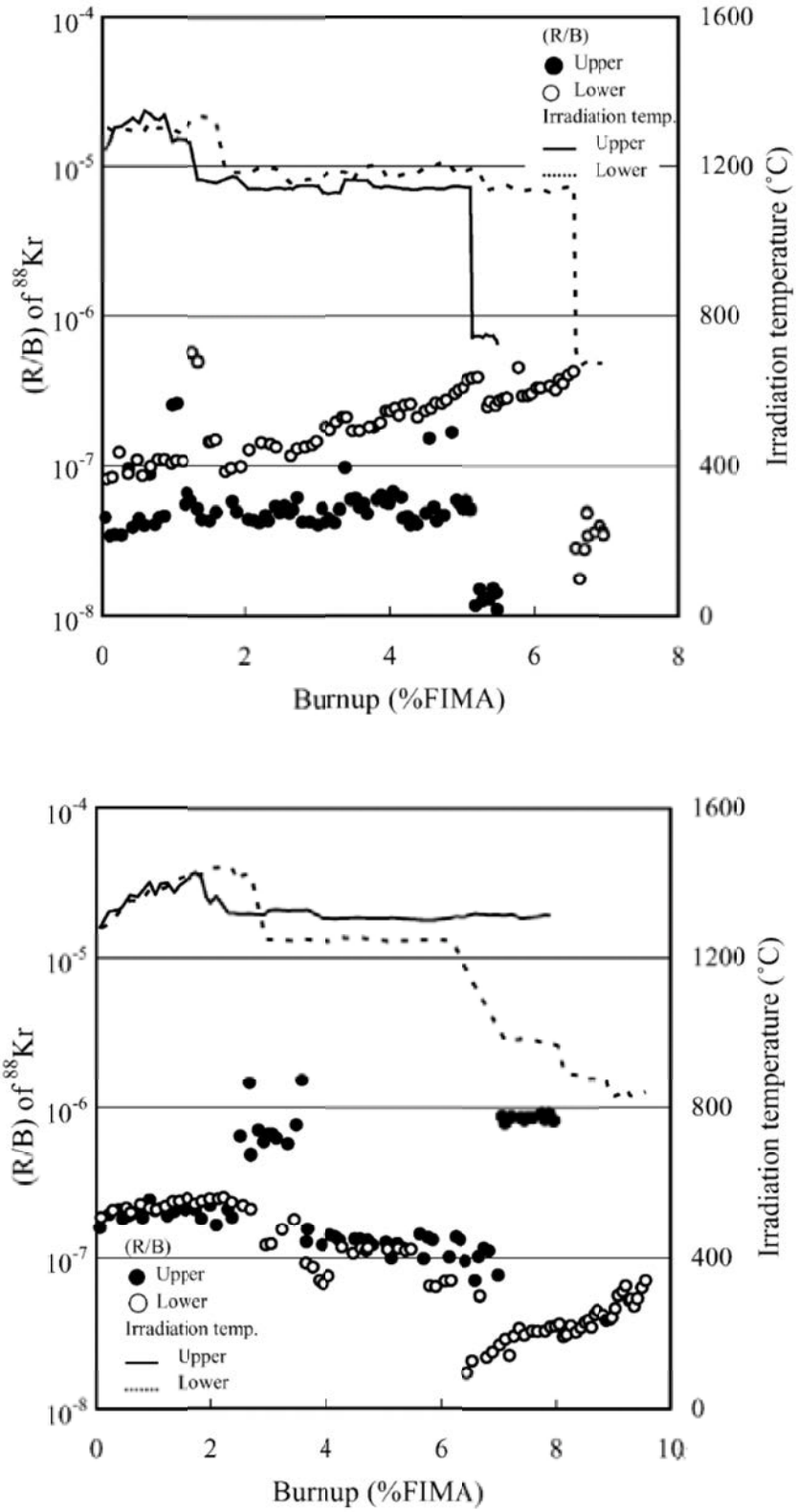

FIG. 7.55. Measured fractional releases and irradiation temperatures in the accelerated irradiation test of the first fuel of the HTTR (top); Capsule irradiation test of extended burnup fuel in OGL-1 (bottom).

7.4. IRRADIATION TESTING IN THE HFIR AT ORNL OAK RIDGE

7.4.1. Reactor description of the HFIR

The high flux isotope reactor (HFIR) at ORNL is a light water cooled, beryllium-reflected reactor with a thermal power of 85 MW that uses HEU U-Al fuel to produce high neutron fluxes for materials testing and isotope production. It has been used extensively in the US gas reactor programmes to irradiate coated particle fuel. Two specific materials irradiation facilities are of note. The large 'removable beryllium' (RB) positions (of which there are eight) are 46 mm in diameter and 500 mm long and can accommodate capsules holding up to 24 compacts, (three in each graphite body, eight bodies axially) in a single purged cell. The 16 small vertical experimental facilities (VXF) positions are 40 mm in diameter and 500 mm long. They can accommodate capsules holding up to 16 compacts (eight in each graphite body, two bodies axially) in a single purged cell. There is a large axial flux gradient that must be considered in the design of any experiment in any of these locations.

7.4.2. US testing of NP-MHTGR fuel

In August 1988, the Secretary of Energy announced a strategy to acquire new production reactor (NPR) capacity for producing tritium. The strategy involved construction of a new production modular high temperature gas cooled reactor (NP-MHTGR). Specially designed reference fuel for the NP-MHTGR was successfully manufactured, but — against all model predictions — unsuccessfully performed in irradiation testing. In total, about 700 out of the 230 000 fuel particles contained in the three tests had failed. Shortly after the completion of the irradiation tests, DOE announced in September 1992 the closeout of the NP-MHTGR programme [269].

7.4.2.1. Fuel Design for NP-MHTGR

The NP-MHTGR fuel element consists of a stack of cylindrical fuel compacts containing the fuel particles inserted into a graphite block. The reference fuel particle, the so-called TRISO-P particle (with P for protective) schematically shown in Fig. 7.56 [269] is a high enriched (93%) UCO fuel kernel surrounded by an eight layer TRISO coating which is composed of concentric layers of low density pyrocarbon (buffer), high density pyrocarbon (IPyC), silicon carbide (SiC), high density pyrocarbon (OPyC), and low density pyrocarbon (PPyC) with thin layers of extra high density pyrocarbon (seal coats) between the buffer and the IPyC and between the OPyC and PPyC. An additional seal coat was added to the outside of the PPyC to reduce any possible interaction between the fuel compact material and the fuel particle surface. Specified fuel particle dimensions and densities together with the as-fabricated values are presented in Table 7.10.

Fuel manufactured for the NP-MHTGR programme was manufactured to full ASME-NQA-1, 1989, standards and achieved a higher quality level than had been produced previously in the USA. Fuel quality variables and attributes were measured extensively between fabrication steps to ensure conformance to fuel specification requirements. The NP-MHTGR test fuel was, therefore, predicted to perform with low fission product release in reactor service.

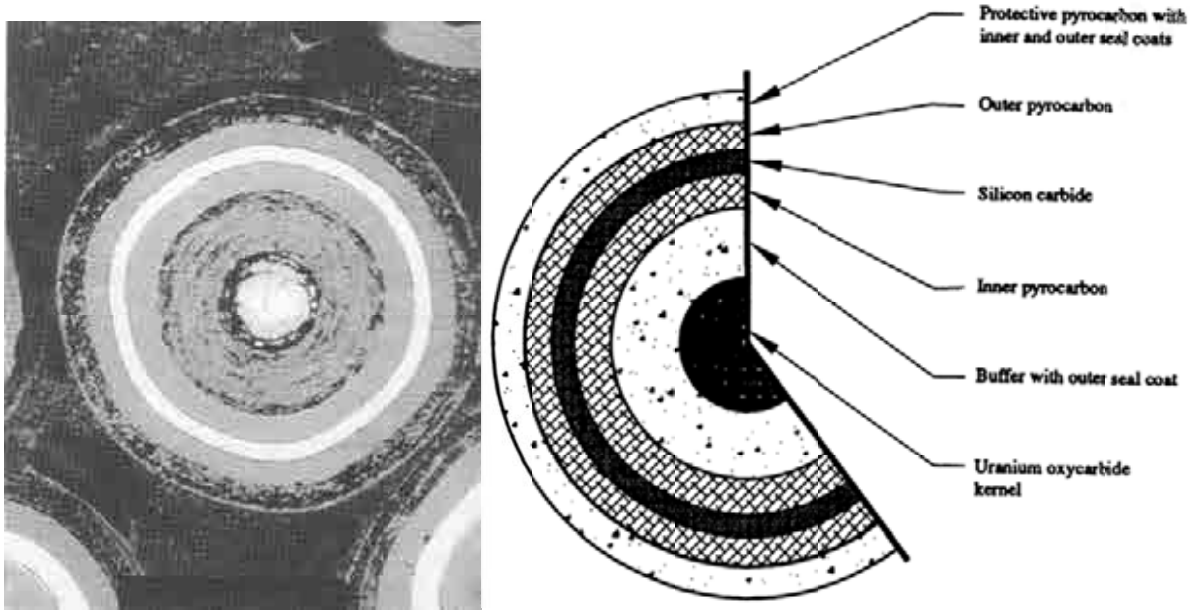

FIG. 7.56. Cross-section of an as-fabricated NP-MHTGR fuel particle.

TABLE 7.10. PERFORMANCE TEST FUEL DIMENSIONS AND DENSITIES

	Particle thickness (μm)		Density (Mg/m^3)	
	spec. mean	as fabricated	spec. mean	as fabricated
UCO kernel	145–205	200	> 10.3	10.51
Buffer carbon coating	90–100	102	0.8–1.10	0.96
IPyC + seal carbon coats	40–60	53	1.85–1.95	1.92
Silicon carbide	30–40	35	≥ 3.18	3.23
OPyC + seal carbon coats	30–50	39	1.80–1.95	1.86
PPyC + seal carbon coats	40–60	47	0.80–1.10	1.06

The NP-MHTGR fuel particle configuration included four major changes from the previous evolution (Fort St. Vrain) fuel particle:

(1) Fuel kernel was UCO rather than UC_2;
(2) The PPyC layer was added to reduce mechanical damage of the fuel particles during the compacting process;
(3) The IPyC layer was made thicker for added protection of the fuel kernel from HCl attack during SiC application;
(4) Seal coats were added to both sides of the PPyC (for the NP-MHTGR and the inside only for the NE-MHTGR), and between the buffer and the IPyC.

7.4.2.2. Fuel capsule irradiation

Three irradiation tests were conducted to demonstrate that the proof test fuel would meet the performance goals for the NP-MHTGR. One test, designated NPR-1, was to demonstrate maximum service life conditions for temperature, burnup, and fast neutron fluence. The second test, NPR-2, was conducted at a lower temperature which was to be more representative of the core average temperature. These two tests were performed in the HFIR at

ORNL. The third test, designated NPR-1A and a backup test to NPR-1, was performed in the ATR at the INL. Each experiment consisted of approximately 75 000 fuel particles in 16 to 20 compacts. The experiments were designed such that fuel compacts could be irradiated at or near the NP-MHTGR design service conditions for temperature, burnup, and fast fluence. The design parameters for the three capsules are listed in Table 7.11.

The NPR-1A capsule (Fig. 7.57) contained 20 compacts, each with about 3770 particles [269]. The fuel compact stack was approximately 1.22 m long, 0.017 m in diameter, and was positioned within an instrumented graphite sleeve.

TABLE 7.11. KEY EXPERIMENTAL PARAMETERS IN NPR CAPSULES

Test	Capsule average/peak temperature (°C)	Peak fluence (10^{25} n/m^2)	Peak burnup (% FIMA)	Number of particles
NPR-1	974/1246	3.7	79	77 500
NPR-1A	977/1119	2.0	64	75 360
NPR-2	753/1024	3.7	79	77 500
NP-MHTGR core	600/1250	3.7	75	1.8×10^{10}

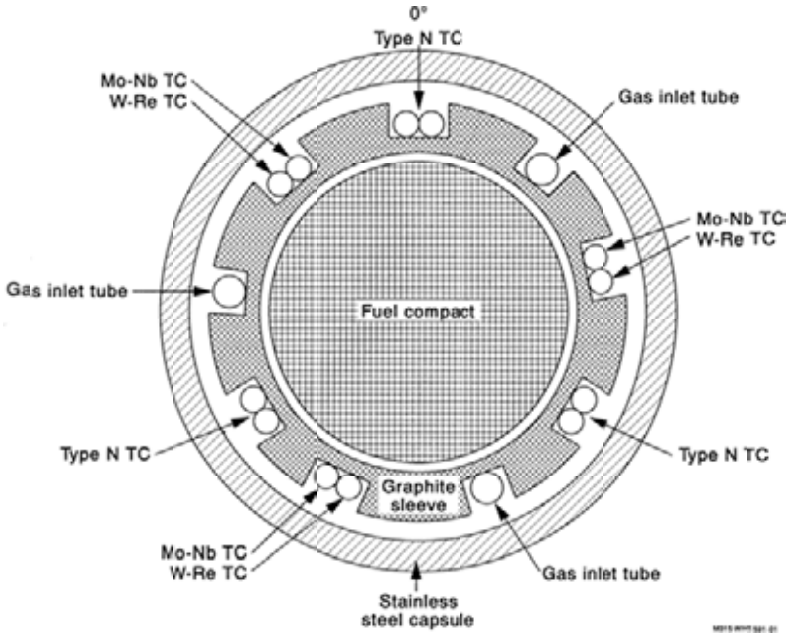

FIG. 7.57. Cross-section of NPR-1A capsule.

Irradiation of the NPR-1A capsule began on October 2, 1991, and was terminated after 64.2 full power days. Fuel performance models predicted no particle failures in each of the tests. However, after reaching a burnup of 48% FIMA, the on-line monitoring system detected a single particle failure in NPR-1A. Continued monitoring indicated about two additional particle failures each day until the irradiation was terminated after reaching 64% FIMA, instead of its original goal of 75% FIMA. It was decided to remove NPR-1A early to allow for the earliest possible assessment of the particle failures.

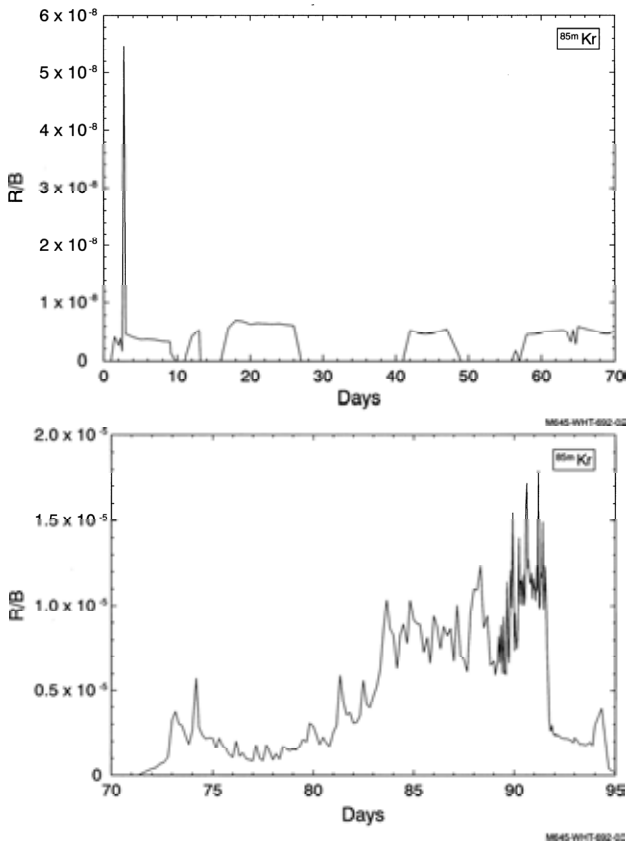

FIG. 7.58. NPR-1A release-to-birth ratio for ^{85m}Kr before and after first particle failure.

Figure 7.58 is a plot of the ^{85m}Kr R/B during the experiment. The R/B remained low during the first 42 full power days of the experiment. However, after 71.4 elapsed days (Figure 7.58, right), the R/B increased from a value of 4×10^{-9} to 3.8×10^{-7}, indicating particle failure. The initial particle failure occurred at a peak fluence of 1.27×10^{25} n/m^2, a peak burnup of 47% FIMA, and a peak temperature of 1133ºC. The ^{85m}Kr R/B continued to increase over time to a peak value of 1.8×10^{-5}. Based on the peak R/B, the total number of particle failures in NPR-1A is estimated to be ~48.

The NPR-1 and -2 experiments were irradiated in the HFIR for a total of eight cycles. The capsules were instrumented to provide measurements of temperature, gas flow, neutron fluence, and fission gas release. A radial schematic of the capsule is shown in Fig. 7.59. The irradiation capsule consists of a double contained, single, purged cell containing 16 fuel compacts surrounded by H-451 graphite fuel bodies.

Irradiation on NPR-1 capsule began July 25, 1991, and was completed on May 29, 1992, at a peak fluence of 3.7×10^{25} n/m^2. The calculated temperatures ranged from 727 to 1027ºC. Temperatures remained fairly constant over the first three cycles with a gradual decrease during the last three cycles as the uranium was depleted from the compacts. Most of the burnup was attained in the first three cycles, while in the last five cycles, the fuel saw a high fast fluence and a lower burnup rate. NPR-1 experienced its first particle failure at a burnup of 72% FIMA. About 526 particles were estimated to have failed after the fuel reached a burnup of 79% FIMA.

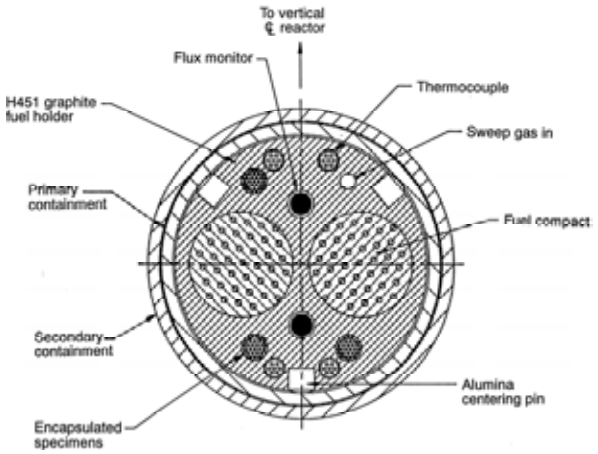

FIG. 7.59. Schematic cross-section of the NPR-1/2 irradiation capsule.

Figure 7.60 is a plot of the ^{85m}Kr R/B during the NPR-1 experiment [269]. The R/B remained low (~10^{-8}) during the first 120 full power days. However, at a peak fluence of 1.7×10^{25} n/m^2, the R/B increased to 1.7×10^{-7} indicating particle failure. The peak burnup and temperature at the time of the first particle failure were 72% FIMA and 1123ºC, respectively. The ^{85m}Kr R/B continued to increase during the irradiation and reached a final value of ~3×10^{-4} at the end of the experiment. Based on these results and activity spikes recorded by the ionization chamber, 526 particles were estimated to have failed.

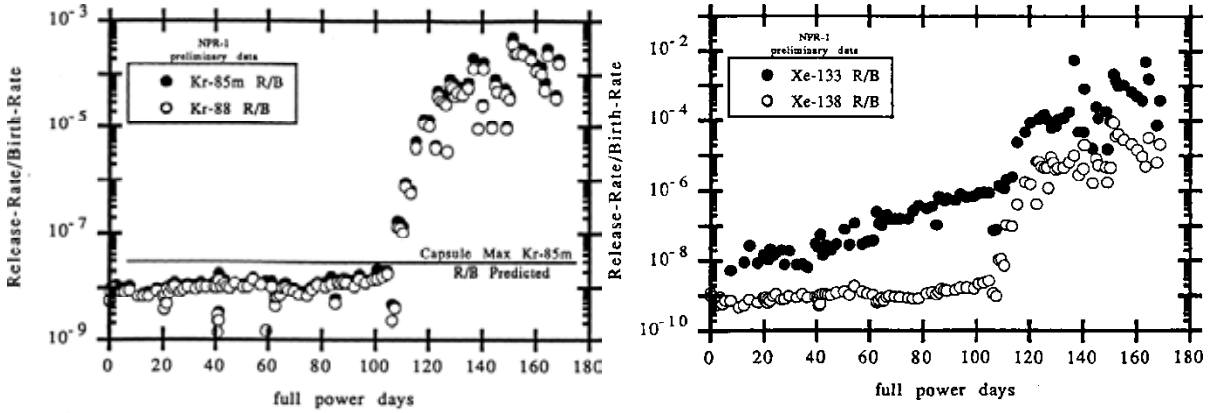

FIG. 7.60. NPR-1 measured R/B ratios as a function of full power days for ^{85m}Kr and ^{88}Kr (left); for ^{133}Xe and ^{138}Xe (right).

Irradiation of the NPR-2 capsule began August 28, 1991, and was completed on May 29, 1992, at a peak fluence of 3.7 × 1025 n/m^2. NPR-2 operated at a lower temperature than NPR-1. The calculated temperatures ranged from 597 to 897ºC. NPR-2 experienced its first particle failure at a burnup of 75% FIMA. About 135 particles were estimated to have failed at 79% FIMA.

Figure 7.61 is a plot of the ^{85m}Kr R/B during the experiment [269]. The R/B remained low (< 10^{-8}) during the first 120 full power days. However, at a peak fluence of 2.0×10^{25} n/m^2, the R/B increased to 7×10^{-7}, indicating particle failure. The peak burnup and temperature at the time of particle failure were 75% FIMA and 960ºC, respectively. The ^{85m}Kr R/B continued to increase during the irradiation and reached a final value of ~6×10^{-5} at the end of experiment. Based on these results and activity spikes recorded by the Geiger–Müller monitors, 135 particles were estimated to have failed.

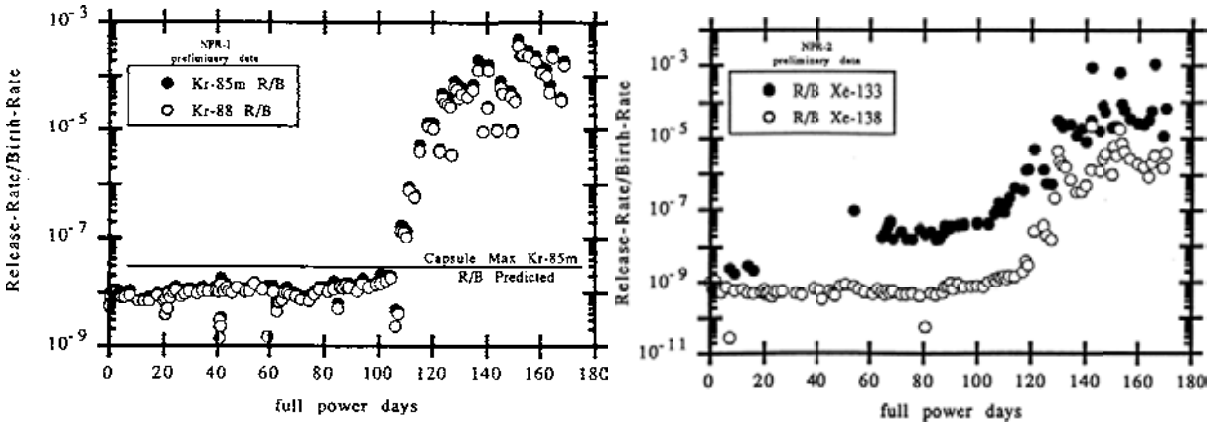

FIG. 7.61. NPR-2 measured R/B ratios as a function of full power days for ^{85m}Kr and ^{88}Kr (left); for ^{133}Xe and ^{138}Xe (right).

In total, about 700 out of 230 000 particles contained in the three tests failed (Table 7.12) in contrast with model predictions of no failures.

Within the new production modular high temperature gas reactor (NP-MHTGR) programme, an extensive particle fuel and irradiation programme was conducted. As a part of this irradiation programme several capsules were irradiated. Among these were capsules NPR1, NPR2, and NPR1A. A total of 221 136 particles were irradiated. Of these approximately 700 failed.

TABLE 7.12. FAILED PARTICLES IN THE NPR IRRADIATION TESTS

Test	Irradiation time (efpd)	Burnup (% FIMA)			Total number of failed particles
		Targeted	Achieved	First failed cp observed	
NPR-1	165	—	79	72	526
NPR-1A	64.2	75	64	48	48
NPR-2	175	—	79	75	135

— data not available.

7.4.2.3. Post-irradiation examination of NPR fuel

A variety of examination techniques including burn-leach and IMGA were used to obtain information on the failure fraction of fuel particles in individual compacts and on the nature of the failures. Optical ceramography and scanning electron microscopy (SEM) were used to thoroughly characterize as-manufactured fuel particle quality. NP-MHTGR SiC was determined to have a larger columnar grain structure than other SiC samples. In some cases,

single grains extended nearly through the coating. The evaluation found evidence of lenticular voids and flaws in the SiC (called gold spots because of their appearance) that slightly decreased the structural strength of the SiC. The gold spot formation was determined to be the result of fuel particles leaving the reaction zone of the furnace during coating and contacting furnace surfaces to get contaminated with SiC ash, which was then sealed in the coating when the particle re-entered the reaction zone.

Metallic inclusions (primarily Cr and Ni) in the SiC also accounted for low strength. Gold spot particles were tested as a group, but did not show a large decrease in measured strength. Flaws associated with the gold spots however, appear to contribute to a low strength tail to the strength distribution.

Eight of the 16 compacts from each of the NPR-1 and NPR-2 capsules and all 20 of the compacts from capsule NPR-1A were given a standard fission gas release test in the TRIGA Mark 1 Reactor Facility at General Atomics. In this test, fission gas release was measured under irradiation for 30 minutes while the compact was held at 1100ºC. The fraction of exposed kernels in each compact was obtained by dividing the measured R/B values by the R/B for an exposed kernel (varied from 0.030 to 0.043, depending on the irradiation exposure of the compact) under the conditions of the TRIGA R/B testing. The capsule average values of exposed kernel fraction are compared with values based on end-of-life (EOL) in-pile R/B and counting radiation spikes. The agreement between values derived from EOL R/B and radiation spikes is remarkably good.

A leach-burn-leach procedure was carried out on compact NPR-1 B6. It consisted of a 24-hour leach in boiling concentrated nitric acid (14 M), plus hydrofluoric acid (0.03 M) to dissolve kernels that had been exposed by the failure of all the coating layers. This was followed by a burn in air at 750ºC for 48 hours to remove all compact matrix and PyC layers (including any intact IPyC beneath failed SiC), and finally a 48-hour leach (under the same conditions as before) to dissolve any kernels exposed by the burn, providing a measure of the fraction of particles with failed SiC but intact IPyC layers. The ^{95}Zr and ^{144}Ce contents of the leach solutions were determined by radiochemical analysis. These fission products were expected to remain with the kernel and serve as a measure of the fraction of the kernels in the compact dissolved in the leach solutions. The results show reasonable agreement with results of SiC failure fraction based on other measurements. Although used to a very limited extent in this PIE, LBL showed promise as a method for determining exposed kernel fraction and SiC failure fraction in irradiated compacts, and is a candidate for continued development.

Compacts from the NPR-1 and NPR-2 capsules were deconsolidated by an electrochemical process, and compact NPR-1A 13 was deconsolidated by burning to obtain particles for IMGA examination to determine the fraction of particles with failed SiC. The IMGA measured the content of gamma-emitting nuclides in individual particles. The ratio $^{137}Cs/^{144}Ce$ was used as a measure of SiC integrity. ^{144}Ce remained within exposed kernels, whereas ^{137}Cs could only be retained by an intact SiC layer. Agreement between values of exposed kernel fraction and SiC failure fraction was expected, given the large fractional failure of the PyC layers discussed below.

Kernels were observed to contain large gas voids and to have undergone swelling at the high burnups in the NP-MHTGR irradiations (up to 79% FIMA). Generally, the kernels retained a spherical shape and were contained in the densified buffer coating. Occasionally, the buffer cracked radially and the swelling kernel extruded through the crack to the IPyC layer. No chemical attack of the IPyC by the kernel or by fission products was observed.

Most often, shrinkage of the buffer led to the opening of an annular gap between the buffer and the IPyC. In only about 5% of the buffers did irradiation-induced densification of the buffer lead to the formation of radially oriented shrinkage cracks. Radial cracks were observed in IPyC layers with increasing frequency as a function of fast fluence, occurring in up to 65% of the particles in a compact cross-section at the highest exposure.

7.4.2.4. Most probable causes of fuel particle failure

Evidence from as-manufactured characterization, irradiation, and post-irradiation examination data indicates that irradiation-induced changes in material properties of the pyrocarbons played a dominant role in the failure of fuel particles to retain fission gases. The as-manufactured particle characterization data indicate that the level of as-manufactured defects in the SiC prior to irradiation (4×10^{-4}) was two orders of magnitude too low to account for the level of particle failures (up to 4×10^{-2} in high fluence compacts). Particle failures were a strong function of neutron fast fluence, as evidenced by the increase in in-reactor fission gas release with irradiation time. IMGA data indicates caesium release from fuel particles was a function of both fast neutron fluence and irradiation temperature. Fission gas release data from post-irradiation TRIGA testing indicate fuel particle failure strongly depended on fast neutron fluence and less strongly depended on irradiation temperature.

These observations are in accordance with the well known behaviour of pyrocarbons to undergo dimensional changes with fast neutron fluence, sometimes leading to failure of coating layers [270]. In contrast, SiC is relatively stable under neutron irradiation [271]. The experimental evidence strongly implicates irradiation-induced changes in the pyrocarbon layers as having played a leading role in the NP-MHTGR fuel particle failures. Direct observation by metallography in the PIE confirmed the large scale failure of pyrocarbon layers and the fluence dependence of these failures.

The PPyC is expected to shrink and fail early under irradiation and widespread PPyC failure (85 to 100% above a fluence of 1.9×10^{25} n/m^2) was measured by metallography. The OPyC is also expected to shrink under irradiation, but the extent of OPyC failure observed above 1.9×10^{25} n/m^2 (47–90%) was unexpected and is mostly likely attributable to crack propagation from the PPyC. The inner seal coat between the PPyC and the OPyC was expected to separate the two layers and prevent crack propagation. However, the seal coat acted as a strong bond and facilitated crack propagation.

The most probable of the causes identified was mechanical failure of the SiC induced by the concentration of tensile stresses in the SiC in the vicinity of cracks in the IPyC, where an IPyC layer was apparently strongly bonded to the SiC. In compact metallography IPyC failures were observed without SiC failures, but all through-wall cracks in the SiC were found to be in the vicinity of the IPyC cracks.

7.4.3. Reference irradiation testing for the Japanese HTTR fuel at HFIR

7.4.3.1. HRB-22 irradiation experiment

The irradiation of the Japanese HTTR fuel was carried out as HRB-22 capsule irradiation test, which was a part of a cooperative effort between the United States Department of Energy (US-DOE) and the Japan Atomic Energy Research Institute (JAERI, now JAEA) [272]. The fuel for the irradiation test was called high burnup fuel, whose target burnup and fast neutron fluence were higher than those of the first loading fuel of the HTTR [273]. In order to keep fuel integrity to high burnup over 5% FIMA, thickness of buffer and SiC layers of fuel particle were increased.

7.4.3.2. Irradiation capsule

The irradiation capsule HRB-22 was a test capsule containing advanced Japanese fuel to be later used in the HTTR [274, 275]. Its function was to obtain fuel performance data at HTTR operating temperatures in an accelerated irradiation environment. The irradiation was performed in the HFIR reactor at ORNL operated at a nominal power of 85 MW(th) throughout most of the irradiation period. The capsule was irradiated for 88.8 efpd in position RB-3B of the removal beryllium facility over four reactor operating cycles starting with HFIR cycle 325. The maximum fuel compact temperature was maintained at or below the allowable limit of 1300°C for most time of the irradiation. Included in the data collected during the irradiation test are TC and gas flow data, the calculated maximum and volume average temperatures based on the measured graphite temperatures, measured gaseous fission product activity in the purge gas, and associated release rate-to-birth rate (R/B) results.

The HRB-22 capsule consisted of a doubly contained, single purge cell with 12 fuel compacts held in a graphite fuel body. The fuel compacts were annular right circular cylinders with an outside diameter of 26.05 mm, inside diameter of 10 mm and a height of 39 mm. The fuel body was fabricated from grade 2020 graphite which was a fine grain graphite manufactured by the Stackpole Carbon Company. The fuel body with fuel compacts was placed inside a double-walled Inconel 718 containment. The radial gap between the graphite fuel body and the containment wall was sized to maintain the temperature as uniformly as possible over the length of the capsule by machining a steep outer surface to the sleeve. The capsule includes a facility for introducing a purge gas. Capsule temperatures were adjusted by changing the composition of the sweep gas, a mixture of helium and neon, flowing in the gap. A typical radial cross-section of the capsule is shown in Fig. 7.62 [274].

The temperature of the graphite fuel body was monitored by 24 thermocouples (TC) located at axial positions corresponding to the axial midpoints of each fuel compact. Twenty one of the thermocouples were arranged in three thermocouple army tubes (TCATs) with seven TC’s in each tube. The capsule includes facility for introducing a purge gas. Capsule temperatures were adjusted by changing the composition of the sweep gas flowing in the gap between the graphite fuel body and the inconel pressure vessel. A mixture of helium and neon was used to control the temperature. Greater fractions of helium, which has the higher thermal conductivity, decrease thermal resistance in the gap resulting in lower fuel temperatures. The same gas mixture occupies the gap between fuel compact and graphite fuel body, and the central cavity in the fuel compact.

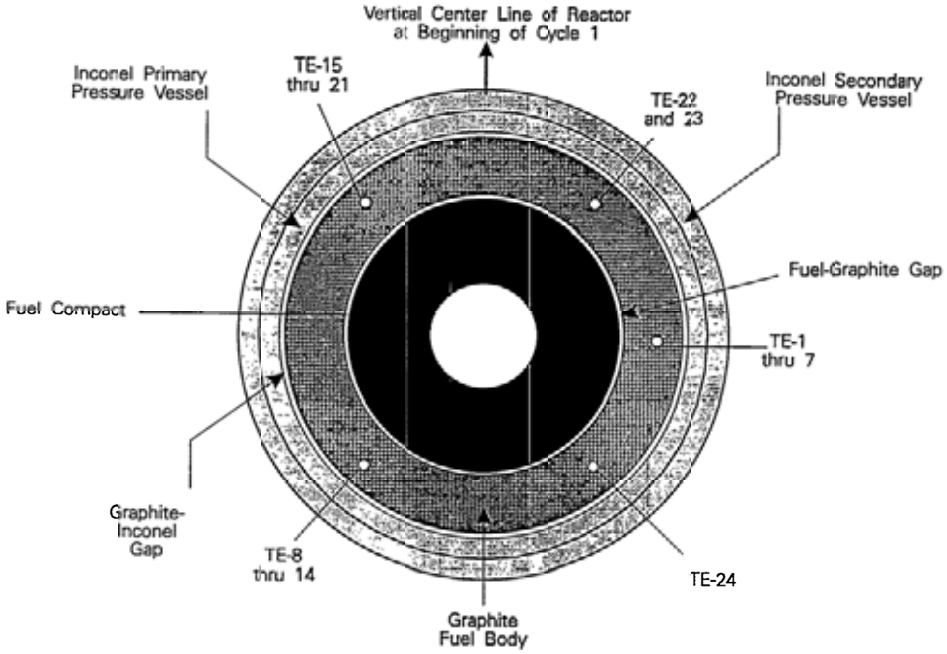

FIG. 7.62. Schematic drawing showing the radial cross-section of capsule.

7.4.3.3. Fuel design and fabrication

The fuel for the HRB-22 capsule irradiation test were TRISO coated fuel particles dispersed in graphite matrix to form annular fuel compacts. The design of the particles was different from that for the initial core fuel of HTTR [21, 162]. The fuel design for the HRB-22 capsule irradiation tests is called 'advanced fuel'. A target burnup of the advanced fuel is 10% FIMA, whereas that of the HTTR fuel is 3.6% FIMA. Since the advanced fuel must retain larger amounts of gaseous and solid fission products, together with carbon monoxide, for a longer time than HTTR fuel, the dimensions of the advanced fuel were changed from those of the HTTR fuel. In the advanced fuel design, the diameter of the fuel kernel is smaller, and both buffer layer and SiC layer are thicker than those of the HTTR fuel. The dimensions of the fuel compacts for the HRB-22 capsule irradiation test were the same as those of the HTTR fuel: 26 mm outer diameter, 10 mm inner diameter, and 39 mm length. Fuel loading for the HRB-22 capsule was calculated based on a single constant loading scheme along the length of the capsule. The loading was based upon a maximum linear heat rate of 65.6 kW/m (20 kW/ft). Inventory requirements for ^{235}U, ^{238}U, and total uranium of each fuel compact were 0.0948, 2.2499, and 2.3447 g, respectively [272].

The fabrication process of the high burnup fuel irradiated in the HRB-22 capsule was basically same as that of the first loading fuel of the HTTR. Major results of the pre-irradiation characterization are described below. Table 7.13 shows measured dimensions of as-fabricated coated fuel particles.

TABLE 7.13. COMPARISON OF MAJOR SPECIFICATIONS AND IRRADIATION TARGET OF EXTENDED BURNUP FUEL AND FIRST-LOADING FUEL OF THE HTTR

Parameter	Extended burnup fuel	First loading fuel of HTTR
Kernel diameter (μm)	500–550	600
Buffer layer thickness (μm)	90	60
SiC layer thickness (μm)	35	25–30
Target burnup (% FIMA)	5–10	3.6
Fast neutron fluence (10^{25} n/m^2)	3–5	1.5

Burnup and fast neutron fluence for the fuel compacts are shown in Figs 7.63 and 7.64, respectively. The fuel temperatures were evaluated based on measured TC temperatures. Time dependent maximum fuel temperatures are shown in Fig. 7.65. For measurement of the release rate-to-birth rate ratios (R/B) a sample of the sweep gas was obtained in a bottle using the grab sample apparatus. The sample was obtained by first evacuating the bottle and grab sample manifold and then backfilling the system with the sweep gas. The type and activity of radioactive fission gas in the grab sample were measured using gamma spectroscopy. The gamma rays were detected by an intrinsic Ge detector. The measured R/B values are shown in Fig. 7.66.

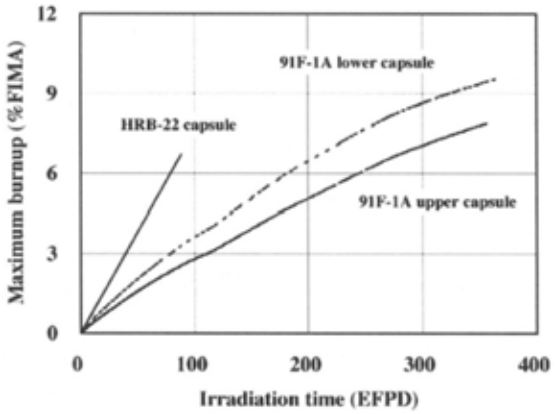

FIG. 7.63. Burnup in irradiation tests.

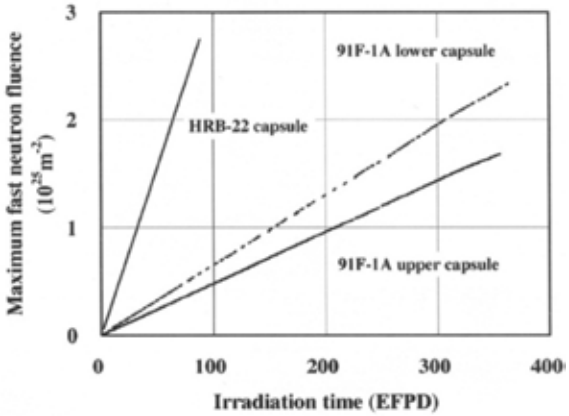

FIG. 7.64. Fast neutron fluence in irradiation tests.

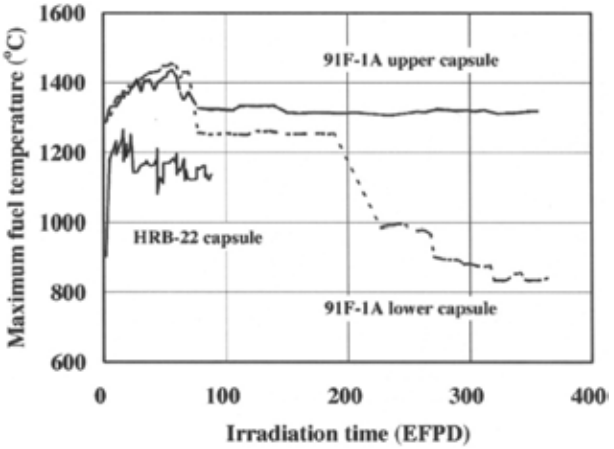

FIG. 7.65. Maximum fuel temperatures in irradiation tests.

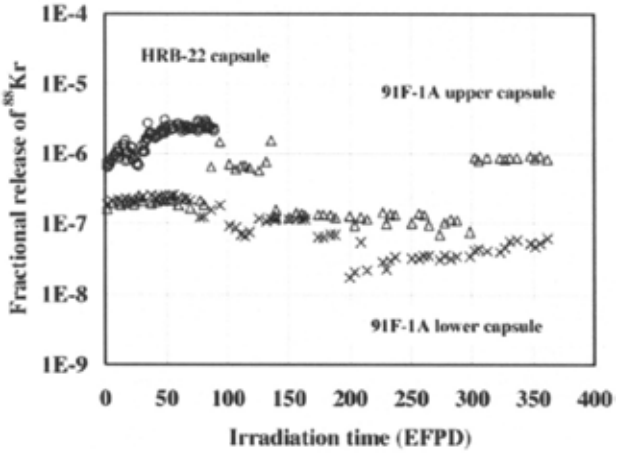

FIG. 7.66. Kr-88 fractional release in irradiation tests.

7.5. IRRADIATION TESTING IN THE HTTR AT JAEA OARAI

7.5.1. Reactor description of the HTTR

The status of operation and tests of the HTTR, and research on nuclear heat application has been described in [266]. In the HTTR, fuel and material irradiation tests will also be carried out employing superior characteristics of the HTTR. A full scale sample of fuel, that is, a full block size irradiation sample, for the advanced fuels will be irradiated in the central fuel column of the core. Pebble balls can also be tested using the graphite basket as shown in Fig. 7.67 [266].

A fuel failure test in block size will also be carried out in the centre column of the core. Batch and capsule irradiation tests of fuels and materials as well as tritium recovery test will be performed in the irradiation test hole in the replaceable reflector region. Furthermore, batch material irradiation tests will be carried out in the permanent reflector region. The thermal and fast neutron fluxes in irradiation region as of the order of 10^{17} n/(m^2·s), and the temperatures are between 400 and 1100°C, depending on the axial and radial positions in the core and reflector.

7.5.2. In-reactor performance of HTTR fuel

Since the first loading fuel of the HTTR is the first mass production HTGR fuel in Japan, their quality should be carefully inspected. In addition to the quality control and assurance of the fabrication process, the irradiation test was carried out confirm the intactness of the first loading fuel during the HTTR operation [183].

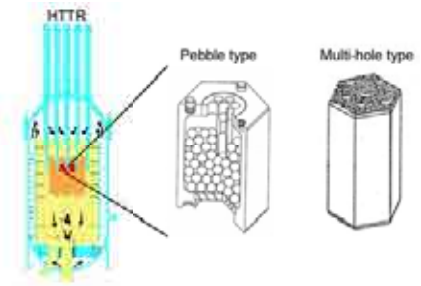

FIG. 7.67. Proposed fuel irradiation in the HTTR core.

The irradiation was carried out as the 94F-9A capsule irradiation test in the JMTR. In order to investigate fuel intactness, the fuel compact was irradiated over 7% FIMA although the maximum burnup in the HTTR design (3.6% FIMA which corresponds to 33 GW•d/t). The fuel compacts were irradiated at the temperature of 1300–1350°C. The maximum burnup and fast neutron fluence for the fuel compacts are 7% FIMA and 2.7×10^{25} n/m^2, respectively. The measured release rate to birth rate, (R/B), of ^{88}Kr in both inner capsules was less than 10^{-6} as shown in Fig. 7.68 [184], which corresponds to one particle failure in the inner capsule. This result is far smaller than 5.35×10^{-4} which is the safety design value of the HTTR. Thus, it was concluded that no significant additional irradiation-induced failure occurred up to 6% FIMA that is about two times higher than 3.6% FIMA of the maximum burnup in the HTTR core.

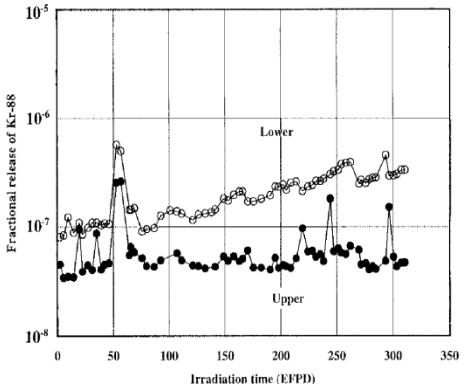

FIG. 7.68. Measured (R/B) of ^{88}Kr in the acceleration irradiation of the first loading fuel.

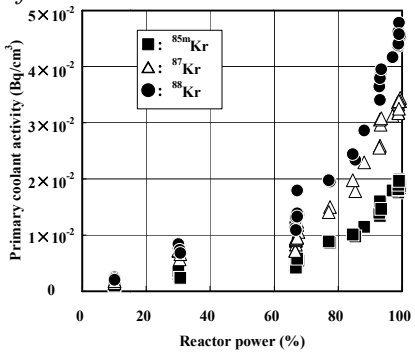

FIG. 7.69. Primary coolant activity concentrations of Kr isotopes during rise to power tests.

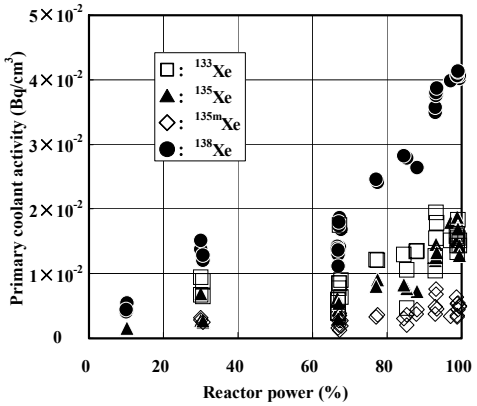

FIG. 7.70. Primary coolant activity concentrations of xenon isotopes during rise to power tests.

During the rise to power test of the HTTR, which started in September 1999, primary coolant sampling measurements were carried out to measure fission gas concentrations [276]. The concentrations of fission gas nuclides of ^{85m}Kr, ^{87}Kr, ^{88}Kr, ^{133}Xe, ^{135}Xe, ^{135m}Xe, and ^{138}Xe were less than 0.1 MBq/m^3 as shown in Fig. 7.69 and 7.70 [164, 165]. The measuring method of radioactive concentrations of fission gases in primary coolant is mentioned in section 5.1.3.

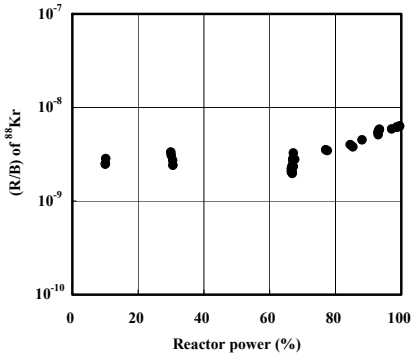

FIG. 7.71. Measured (R/B) of ^{88}Kr during HTTR operation.

The R/B ratio of fission gases was calculated based on the measured concentrations. Figure 7.71 shows the R/B of ^{88}Kr as a function of the reactor power [164, 165]. The (R/B) values are as low as 2×10^{-9} up to 60% of the reactor power, then increase to 7×10^{-9} at full power operation. This result suggests that in lower reactor power, the fission gas release mechanism is recoil from the contaminated uranium in the fuel compact matrix. Beyond 60% of the reactor power, the R/B increases presumably because diffusion release becomes the main release mechanism.

7.6. IRRADIATION TESTING IN THE ATR AT INL IDAHO

7.6.1. Reactor description of the ATR

The advanced test reactor (ATR) at INEEL is a light water cooled, beryllium-reflected reactor that uses HEU U-Al fuel in a four-leaf clover configuration to produce high neutron fluxes for materials testing and isotope production (Fig. 7.72). The clover leaf configuration results in nine very high flux positions, termed flux traps. In addition, numerous other holes of varying size are available for testing. Of interest here are several holes that can be used to irradiate coated particle fuel. The large B holes in ATR (of which there are four) are 38 mm in diameter and 760 mm in length. They can accommodate five individually purged cells, with two graphite bodies per cell, containing up to three compacts per body. Thus, a total of 30

compacts can be irradiated in this location. Of special note are the very flat burnup and fluence profiles available axially in the ATR over the 760 mm length. This allows for nearly identical irradiation of large quantities of fuel.

FIG. 7.72. Schematic of the advanced test reactor (ATR) at INL.

7.6.2. Irradiation experiment AGR

7.6.2.1. AGR fuel development and qualification programme

The US Department of Energy has embarked on a series of tests of TRISO coated particle reactor fuel intended for use in the VHTGR as part of the advanced gas reactor (AGR) programme. The AGR-1 experiment is the first in this series of fuel tests to be irradiated in the advanced test reactor (ATR). The AGR fuel development and qualification programme was established to address the following overall goals:

- Provide a baseline fuel qualification data set in support of the licensing and operation of the next generation nuclear plant (NGNP). Gas reactor fuel performance demonstration and qualification comprise the longest duration research and development (R&D) task for the NGNP feasibility. The baseline fuel form is to be demonstrated and qualified for a peak fuel centreline temperature of 1250°C.
- Support near term deployment of an NGNP by reducing market entry risks posed by technical uncertainties associated with fuel production and qualification.
- Utilize international collaboration mechanisms to extend the value of DOE resources.

The AGR fuel development and qualification programme consists of the elements fuel manufacture, fuel and materials irradiations, post-irradiation examination (PIE) and safety testing, fuel performance modeling, and fission product transport and source term evaluation.

The AGR fuel irradiations will be conducted over the next ten years to demonstrate and qualify new particle fuel for use in high temperature gas reactors. The goals of the irradiation experiments are to provide irradiation performance data to support fuel process development, to qualify fuel for normal operating conditions, to support development and validation of fuel performance and fission product transport models and codes, and to provide irradiated fuel and materials for PIE and safety testing [277, 278]. The experiments, which will each contain

several separate capsules, will be irradiated in an inert sweep gas atmosphere with individual on-line temperature monitoring and control of each capsule. The sweep gas will also have on-line fission product monitoring on its effluent to track performance of the fuel in each individual capsule during irradiation.

The AGR fuel experiments belong to a category of experiments designated at the INL as instrumented lead experiments, which derives its name from the instrument leads utilized to provide continuous monitoring (and typically control) of experiment parameters during irradiation. Each instrumented lead experiment test train may contain several vertically stacked capsules, and is typically designed, as the AGR experiments were, for a specific irradiation position in the ATR. Therefore the design is unique for the irradiation position location and size, irradiation parameters (e.g. temperature, fluence, monitoring requirements, etc.) and the umbilical tube routing necessary to connect the experiment to the monitoring, control and data collection equipment. This section reviews the design of the AGR-1 experiment [279, 280], and discusses the preliminary irradiation results obtained to-date.

7.6.2.2. AGR-1 fuel specimens

The fuel is comprised of 350 μm diameter low enriched uranium (LEU) fuel kernels, coated with traditional TRISO coatings (i.e. a layer of silicon carbide sandwiched between two pyrolytic carbon layers) to make up the 780 μm nominal diameter TRISO coated fuel particles. Next the fuel particles are overcoated with a thermo-set resin and pressed into fuel compacts that are then sintered to remove the volatile compounds in the resin. Each compact contains approximately 4150 fuel particles with a mean uranium content of approximately 0.9 grams. For AGR-1, four different types of TRISO coatings were produced (baseline, variant 1, variant 2, and variant 3) to study the impact on key fuel fabrication processing variables on fuel performance. Table 7.14 presents pertinent attributes of the fuel that is being irradiated in AGR-1 [281].

7.6.2.3. Experiment capsules

The experiment test train consists of six separate stacked capsules vertically centred in the ATR core. Each capsule has its own custom blended gas supply and exhaust for independent temperature control and fission product monitoring. Temperature control of the capsules is accomplished by adjusting the mixture ratio of two gases with differing thermal conductivities to control the heat transfer across an insulating gas jacket between the heat source (fuel fissions and gamma heating of capsule materials) and the relatively cold reactor coolant (52ºC). Helium is used as the high (thermally) conductive gas and neon is used as the insulating gas. A horizontal capsule cross-section at the top of the test train is shown in Fig. 7.73, left, and a vertical section of a capsule is shown on the right-hand side of the figure. The capsules are approximately 35 mm (1 3/8 inches) in diameter and 150 mm (6 inches) in height — including the plenums between adjacent capsules. Each capsule contains 12 prototypical right circular cylinder fuel compacts nominally 12.3 mm (½ inch) in diameter and 25 mm (1.0 inch) long.

The compacts are arranged in four layers in each capsule with three compacts per layer nested in a triad configuration. A nuclear grade graphite spacer surrounds and separates the three fuel compact stacks in each capsule to prevent any fuel particles on adjacent compacts from touching each other, which could possibly cause a premature particle failure. Boron carbide was dispersed in the graphite spacer to serve as a consumable neutron poison. In addition to the boron carbide, a thin (0.25 mm) hafnium shield next to the outside capsule wall surrounds the two fuel compact stacks facing toward the centre of the ATR core (stacks 2 and 3 in the figure). A thin (0.25 mm) stainless steel shield next to the outside capsule wall blankets the

other fuel compact stack (stack 1 in the figure) located on the side of the capsule facing away from the ATR core.

Stainless steel was used for this shield (versus hafnium) in order to minimize the effects on the neutron flux to these already lower powered fuel compacts while retaining the same insulating gas jacket to maintain the proper irradiation temperature. The neutron poisons were necessary to limit the initial fission rate in the fuel and thereby provide a more consistent fission rate/power production during irradiation. As the boron carbide is consumed in the graphite, the fission rate in the fuel will reach a peak at about the mid-point of the irradiation. The fission rate will then slowly decrease as the fuel continues to burnup. Reducing and controlling the initial fission rate in this manner decreased the ratio of the maximum to minimum heat generation rates in the fuel, which will provide better temperature control over the length of the rather long 2 year irradiation.

There are nominally three thermocouples in each capsule (the top and bottom capsules have five and two thermocouples respectively for different reasons) located in the top, middle, and bottom areas of the graphite spacer measuring the temperature of the graphite. Since no metal could touch the fuel particles, the thermocouples measure the graphite temperature and the corresponding fuel temperatures are calculated. type N thermocouples are utilized in the coolest portion of the capsule (away from core centre), and the INL developmental thermocouples [282] are used in the higher temperature positions within the capsule (towards core centre). Flux wires were also installed in the graphite to measure both the thermal and fast neutron fluence.

An umbilical tube (termed a lead-out) houses and protects the gas lines and thermocouple leads from the experiment capsules to the reactor vessel wall penetration. Outside the reactor vessel wall, the gas lines and thermocouple leads are connected to their facility counterparts in the temperature monitoring, control and data collection system. The lead-out also vertically locates the experiment in the east large B irradiation position in the ATR core, shown in Fig. 7.74.

The large B positions (38 mm or 1.5 inch diameter) were chosen for the AGR fuel irradiations due to the rate of fuel burnup and fast neutron fluence accumulation in these positions providing an acceleration factor of between one and three times that expected in the very high temperature reactor (VHTR). This acceleration factor was high enough to accomplish the irradiation within a reasonable time, but yet low enough to avoid possible premature fuel particle failures similar to those experienced in past highly accelerated particle fuel tests.

TABLE 7.14. FUEL ATTRIBUTES FOR AGR-1

Property	Specific range for mean value	Actual mean value ± Population standard deviation			
		Baseline	Variant 1	Variant 2	Variant 3
Kernel diameter (μm)	350 ± 10	349.7 ± 9.0			
Kernel density (Mg/m^3)	≥ 10.4	10.924 ± 0.015			
Buffer thickness (μm)	100 ± 15	103.5 ± 8.2	102.5 ± 7.1	102.9 ± 7.3	104.2 ± 7.8
IPyC thickness (μm)	40 ± 4	39.4 ± 2.3	40.5 ± 2.4	40.1 ± 2.8	38.8 ± 2.1
SiC thickness (μm)	35 ± 3	35.3 ± 1.3	35.7 ± 1.2	35.0 ± 1.0	35.9 ± 2.1
OPyC thickness (μm)	40 ± 4	41.0 ± 2.1	41.1 ± 2.4	39.8 ± 2.1	39.3 ± 2.1
Buffer density (Mg/m^3)	0.95 ± 0.15	1.10 ± 0.04	1.10 ± 0.04	1.10 ± 0.04	1.10 ± 0.04
IPyC density (Mg/m^3)	1.90 ± 0.05	1.904 ± 0.014	1.853 ± 0.012	1.912 ± 0.015	1.904 ± 0.013
SiC density (Mg/m^3)	≥ 3.19	3.208 ± 0.003	3.206 ± 0.002	3.207 ± 0.002	3.205 ± 0.001
OPyC density (Mg/m^3)	1.90 ± 0.05	1.907 ± 0.008	1.898 ± 0.009	1.901 ± 0.008	1.911 ± 0.008
IPyC anisotropy[(a)] (BAF)	≤ 1.035	1.022 ± 0.002	1.014 ± 0.001	1.023 ± 0.002	1.029 ± 0.002
OPyC anisotropy[(a)] (BAF)	≤ 1.035	1.019 ± 0.003	1.013 ± 0.002	1.018 ± 0.001	1.021 ± 0.003
IPyC anisotropy post compact anneal (BAF)	Not specified	1.033 ± 0.004	1.021 ± 0.002	1.036 ± 0.001	1.034 ± 0.003
OPyC anisotropy post compact anneal (BAF)	Not specified	1.033 ± 0.003	1.030 ± 0.003	1.029 ± 0.004	1.036 ± 0.002
Sphericity (aspect ratio)	≤ 1% of the particles shall have an aspect ratio ≥ 1.14.	1.054 ± 0.019	1.056 ± 0.019	1.053 ± 0.019	1.055 ± 0.018
Mean uranium loading (g U/compact)	0.905 ± 0.04	0.917	0.915	0.904	0.912
Compact diameter (mm)	12.22–12.46	12.36 ± 0.01	12.36 ± 0.01	12.36 ± 0.01	12.34 ± 0.01
Compact length (mm)]	25.02–25.40	25.066 ± 0.080	25.123 ± 0.030	25.077 ± 0.065	25.227 ± 0.037
Defective SiC coating fraction	≤ 2.0×10^{-4}	4.0×10^{-5}	0	2.0×10^{-5}	0
Defective IPyC coating fraction	≤ 2.0×10^{-4}	0	0	0	0
Defective OPyC coating fraction	≤ 1.0×10^{-2}	0	9.6×10^{-4}	0	0

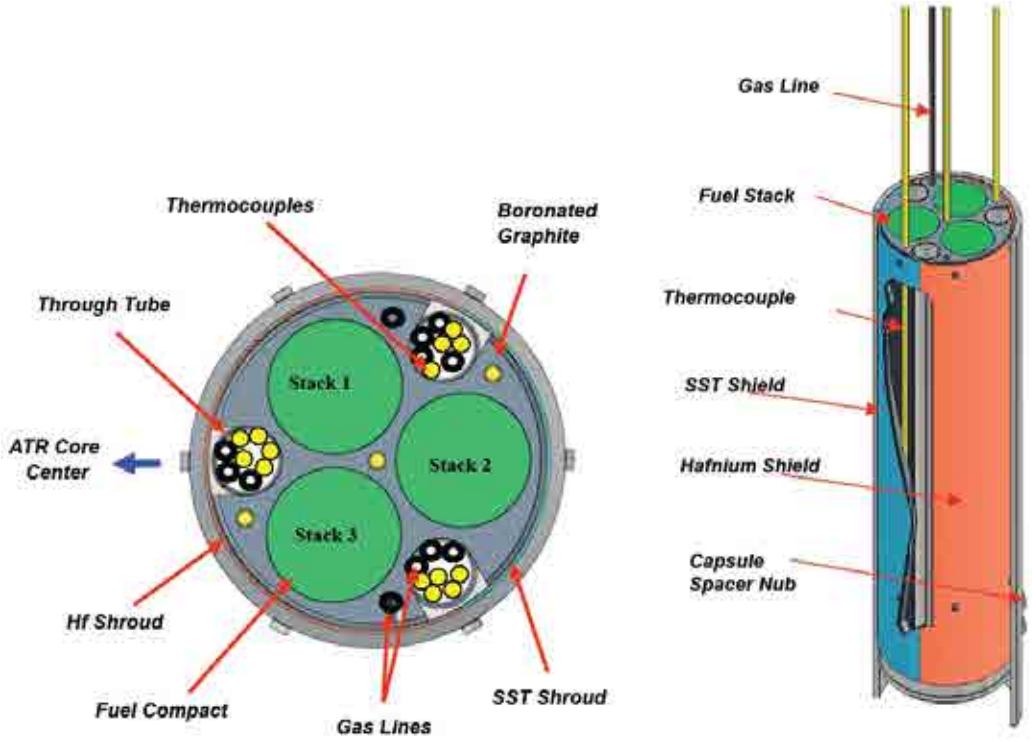

FIG. 7.73. Horizontal cross-section (left) and vertical section (right) of an AGR experiment capsule.

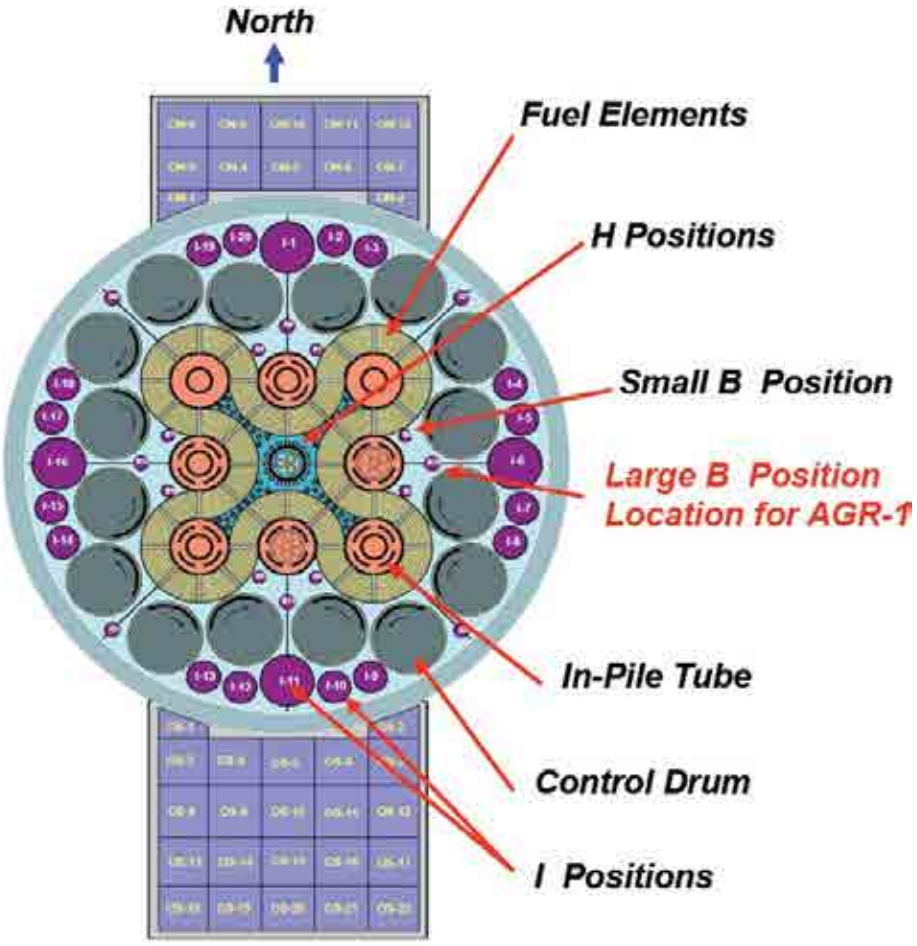

FIG. 7.74. ATR core cross-section.

The irradiation time for the AGR-1 experiment was determined by the neutron flux rate in the large B position and the average burnup goal of 18% FIMA for all fuel compacts, and a minimum of 14% FIMA for each fuel compact [281]. This requirement in combination with the slightly less than 20% fuel enrichment resulted in a rather long irradiation time, and a significantly reduced heat generation rate towards the end of the irradiation.

As indicated earlier, every effort was made to flatten the temporal heat generation rate curve to increase the controllability of the temperatures at the end of the irradiation. This controllability was necessary to meet the time-average volume-average temperatures of 1150 +30/-75ºC for the irradiation while staying below the time-average peak temperature of 1250ºC and maximum instantaneous peak temperature of 1400ºC. These requirements provided some significant challenges in the design of the AGR-1 experiment and control systems.

(a) Temperature control system

The temperature of each experiment capsule is controlled by varying the mixture of two gases with differing thermal conductivities in a small insulating gas jacket between the specimens and the experiment containment. The combination of helium and neon, which is the typical gas combination currently used at ATR, is also being utilized in the AGR fuel experiments. Computer controlled mass flow controllers are used to automatically blend the gases (based upon feedback from the experiment thermocouples) to control the temperatures.

(b) Fission product monitoring

Fission gases are the most common materials monitored in lead experiment temperature control exhaust gases, and the AGR fuel experiments are no exception. The experiment flow path is shown in Fig. 7.75.

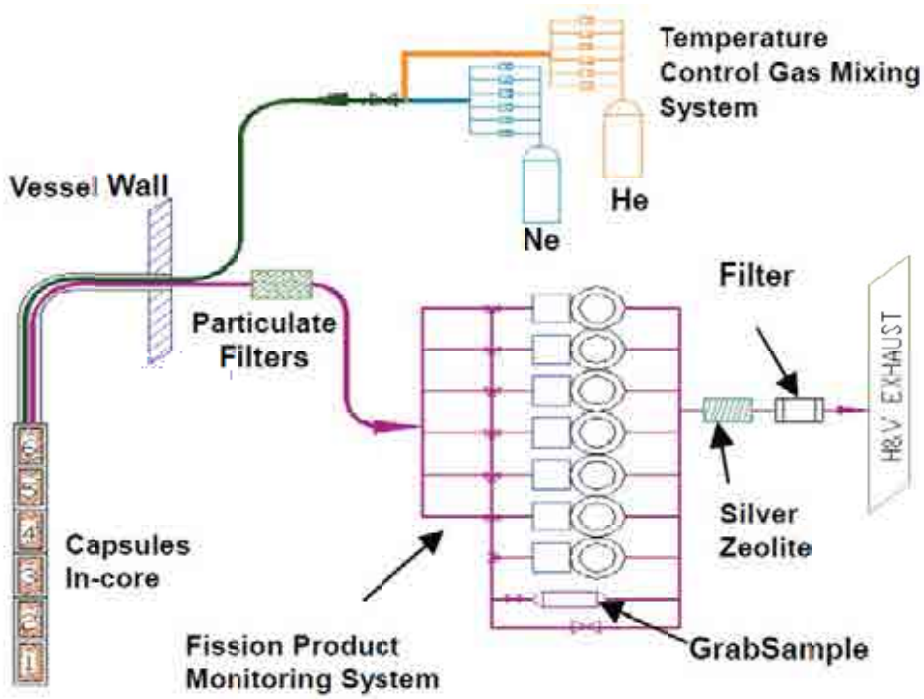

FIG. 7.75. AGR-1 experiment flow path.

The outlet gas from each capsule is routed to individual fission product monitors. The capsule outlet flows can be rerouted to an online spare monitor if any monitors experience detector or other failures. There is also the capability to take a grab sample of the effluent gas from each capsule. The fission product monitors consist of a spectrometer for identifying and quantifying the fission gas nuclides and a gross gamma detector to provide indication when a puff release of fission gases passes through the monitor. The gross gamma detector also provides the release timing. With the combination of a gross gamma detector and a spectrometer being continuously on-line, the gross gamma detector results can be scanned quickly to establish which portions of the voluminous spectrometer data need to be closely scrutinized. A puff release of fission gases typically indicates when a TRISO fuel coating failure may have occurred. Through identification and quantification (with uncertainties) of the isotopes, the spectrometer can be used to determine the isotopic R/B of the fission gases being detected. The system was designed and response modeled to detect and quantify each individual fuel particle failure up to and including a very unlikely 250th fuel particle failure.

7.6.2.4. Experiment irradiation and status

The experiment was inserted in the east large B position (B-10) of the ATR core in mid December 2006. Final flow testing of the temperature control and fission gas monitoring system installations were accomplished after the experiment had been inserted. Irradiation of the experiment was initiated on December 24, 2006, and continued until completion on November 6, 2009, reaching 620 effective full power days of irradiation.

Following initial shakedown of the capsule during the first irradiation cycle [283], the AGR-1 experiment went very well. The fission product monitors had been stable and provided data reliably for all six capsules. After six irradiation cycles, three out of the eight installed type N thermocouples had failed, and five out of the ten installed INL developmental Mo–Nb thermocouples had failed.

Figure 7.76 is a waveform plot of the gas flows from Capsule 3 during the 4th cycle and Fig. 7.77 the corresponding thermocouple measurements. As indicated in the figure, the capsule was on mostly neon to keep the control temperature within the allowable operating band. Of the three thermocouples installed in that capsule, only one was still operating by the end of the cycle and is plotted in the figure. These on-line data have been gather and stored in the SAS computer programme and will serve as the AGR programme's database for official qualification of all AGR fuel data for the NGNP.

Table 7.15 provides a summary status of the AGR-1 experiment at the end of irradiation. Detailed as-run physics and thermal analyses were performed cycle by cycle to track fuel burnup, fast neutron fluence damage and fuel temperatures during the irradiation. After 620 efpd, peak burnups ranged from 15 to over 19% FIMA and fast fluences were between 3.1 and 4.4×10^{25} n/m^2 (E>0.18 MeV). The temperature distribution of the fuel in Capsule 3 calculated at the end of the 4th irradiation cycle is shown in Figure 7.78. The mean temperature of the fuel is about 1140°C and the peak fuel temperature during that cycle was about 1250°C.

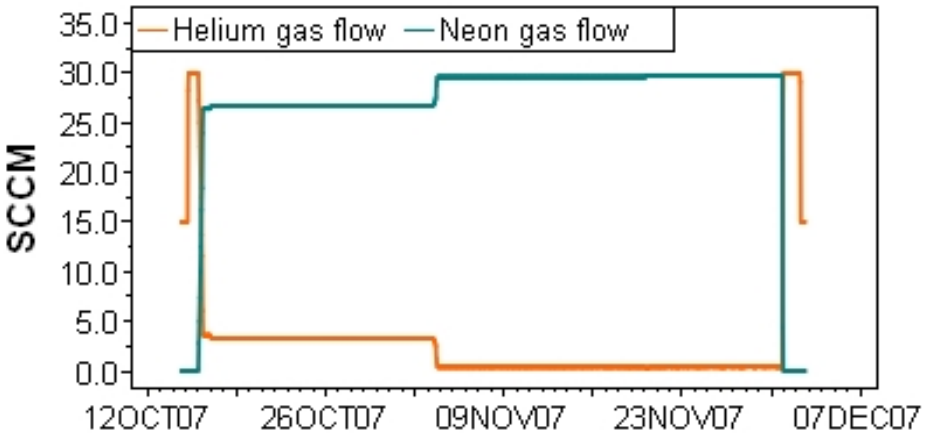

FIG. 7.76. Gas flow measurements from Capsule 3 during the 4th irradiation cycle.

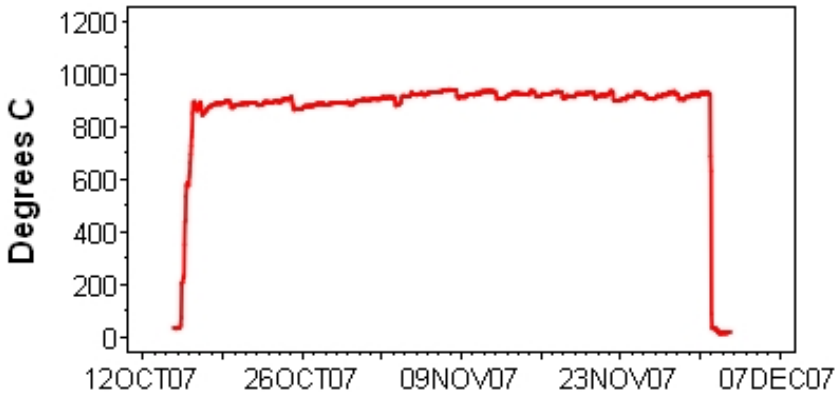

FIG. 7.77. Thermocouple measurements from Capsule 3 during the 4th irradiation cycle.

TABLE 7.15. SUMMARY OF AGR-1 IRRADIATION CONDITIONS AFTER 13 CYCLES (620 efpd), PRELIMINARY DATA

Capsule	Peak compact burnup (% FIMA)	Peak compact fast neutron fluence (10^{25} n/m^2, E>0.18 MeV)	Time-average peak temperature (°C)	Time-average volume-average temperature (°C)
6	15.0	3.1	1180	1080
5	18.4	3.9	1230	1100
4	19.5	4.3	1250	1120
3	19.6	4.4	1210	1080
2	19.1	4.1	1240	1100
1	17.2	3.4	1160	1040

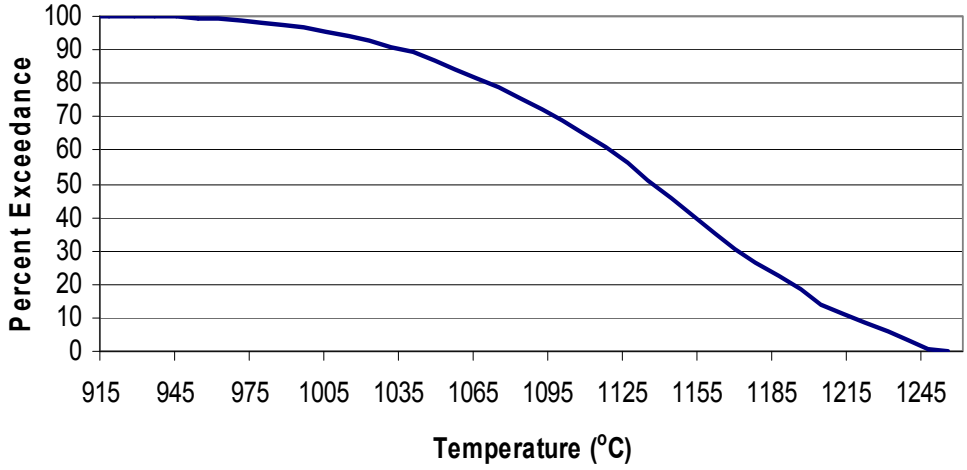

FIG. 7.78. Fuel temperature distribution in AGR-1, capsule 3.

Based on the fuel temperature distributions during each cycle, time-averaged peak and time-averaged volume-averaged temperatures were calculated as the irradiation progressed. After 620 efpd, the time averaged peak fuel temperatures ranged between 1160 and 1250°C and time average volume temperatures were about 100 to 140°C lower depending on the capsule.

Release to birth rate ratios have been calculated for many of the short-lived fission gases [284]. Representative results from the six capsules for ^{85m}Kr, ^{88}Kr and ^{135}Xe are shown in Fig. 7.79. In all cases, the R/B is less than about 1×10^{-7} indicative of release from heavy metal contamination. A failure of one particle in a capsule would result in an R/B of about 3.5×10^{-6} based on 4150 particles per capsule and a release of about 1.5% from the kernel which is a typical value at these temperatures and burnups.

Expressions for release to birth rate ratios (R/B) of short-lived isotopes are often approximated as:

$$\frac{R}{B} = 3\sqrt{\frac{D'}{\lambda}} \tag{7.25}$$

where

R is the fission product gas release rate (s^{-1});
B is the fission product gas birth rate (s^{-1});
D' is the effective reduced fission gas diffusivity (s^{-1});
λ is the fission gas decay constant (s^{-1}).

At constant temperature, this correlation can be expressed as

$$\log\left(\frac{R}{B}\right) = cons\tan t + n\cdot\log\left(\frac{1}{\lambda}\right) \tag{7.26}$$

where n is the a variable exponent which has replaced the 0.5 square root power relation.

For diffusive release, values of n have been observed to vary between approximately 0.1 and 0.5 and are dependant upon fuel form, temperature and burnup, while values near 1.0 are indicative of failure induced release of stored inventory [285]. A typical plot of AGR-1 R/B values versus 1/λ is shown in Fig. 7.80, which displays an exponent value of 0.39 for krypton isotopes and a value of 0.36 for xenon isotopes. These values are consistent with diffusive release from uranium contamination in the fuel matrix.

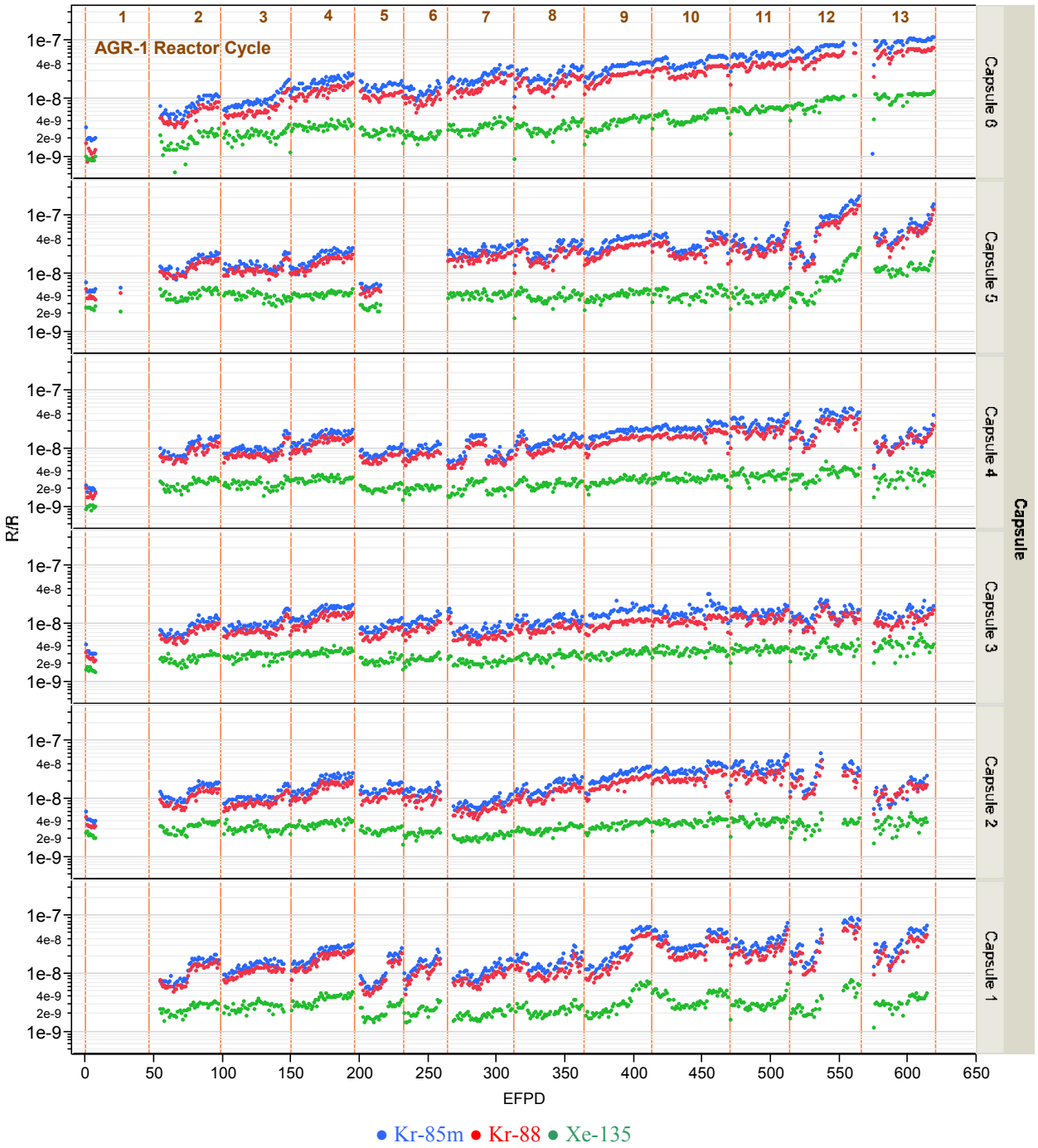

FIG. 7.79. R/B for AGR-1, Capsules 1 through 6.

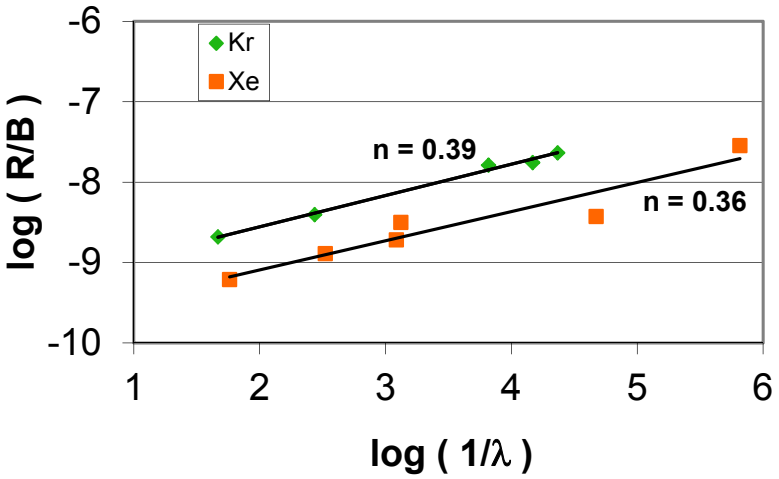

FIG. 7.80. AGR-1 R/B values versus decay constant from Capsule 1 after 188 efpd.

7.6.2.5. Post-irradiation examination of AGR-1

The main objectives of the AGR-1 PIE campaign are [286]:

- Assessment of the overall performance of the test train and components and provide data to verify the test train thermal analyses;
- Evaluation of fission product retention of the fuel during the irradiation and during post-irradiation accident tests;
- Characterization of the compacts and individual particles to assess the condition of the matrix material, kernels, and coatings.

Advanced PIE capabilities for coated particle fuel developed at the INL include high temperature accident testing, compact deconsolidation and leach-burn-leach testing, irradiated particle visual examinations and gamma spectrometry, and detailed dimensional measurements of fuel and capsule components. The PIE of the AGR-1 experiment is currently in progress, and will be performed using facilities at both INL and ORNL.

The AGR-1 irradiation test train was shipped in March 2010 to the Hot Fuels Examination Facility (HFEF) at the INL. It was loaded into the hot cell, visually inspected, and then examined by gamma spectrometry to get an initial indication of the condition of the interior capsule components. Complete axial gamma scans of the test train were performed using the HFEF precision gamma scanner. The test train was scanned in a vertical orientation. Three different rotational orientations were used so that each scan included only a single compact stack.

The gross gamma results for fuel stack 3 are shown in Fig. 7.81. The fuel compacts and interior components of the test train (e.g. capsule heads, Nb gas lines, Hf shrouds) could be easily resolved from gross and isotopic data.

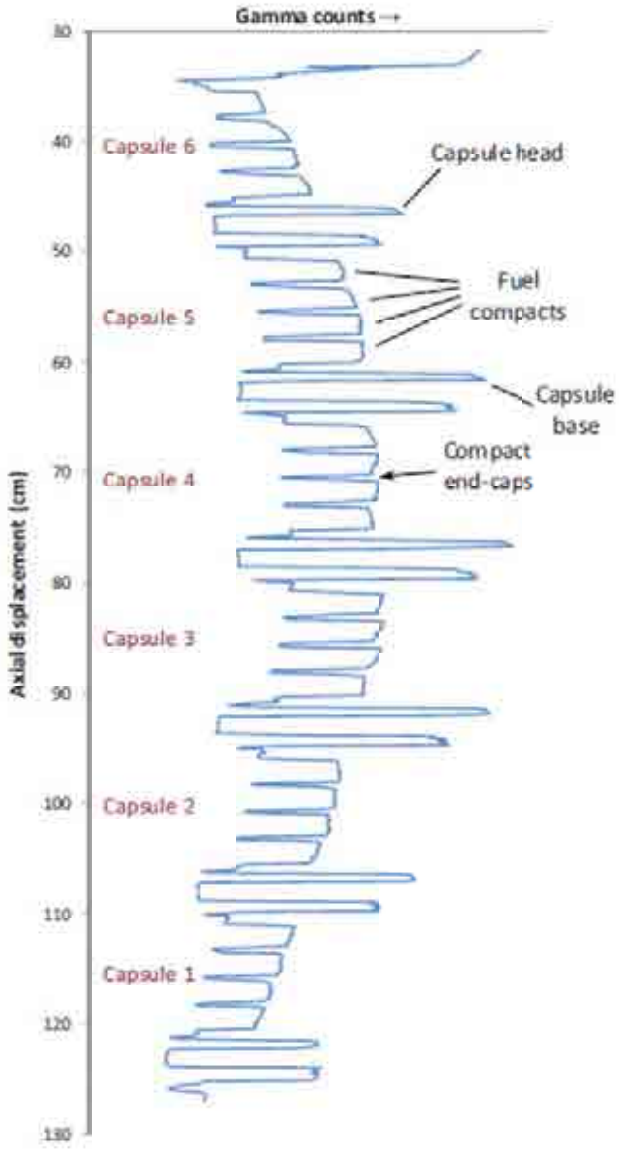

FIG. 7.81. Gross gamma scan results for AGR-1 fuel stack 3, showing the location of some interior components of interest.

After the non-destructive test train exams, the test train and capsules were disassembled to remove the fuel compacts and other components of interest. To quantify the amount of irradiation-induced dimensional change that has occurred during the experiment, a non-contact photo-visual inspection system was designed so that digital images with a high degree of detail could be taken of the fuel compacts and graphite holders, from which dimensional measurements with an uncertainty of < 0.025 mm could be made. Images are then processed for dimensions by measuring between defined points at the edge of the imaged components using image analysis software. The image of an irradiated AGR-1 compact from Capsule 4 acquired with the in-cell camera is shown in Fig. 7.82.

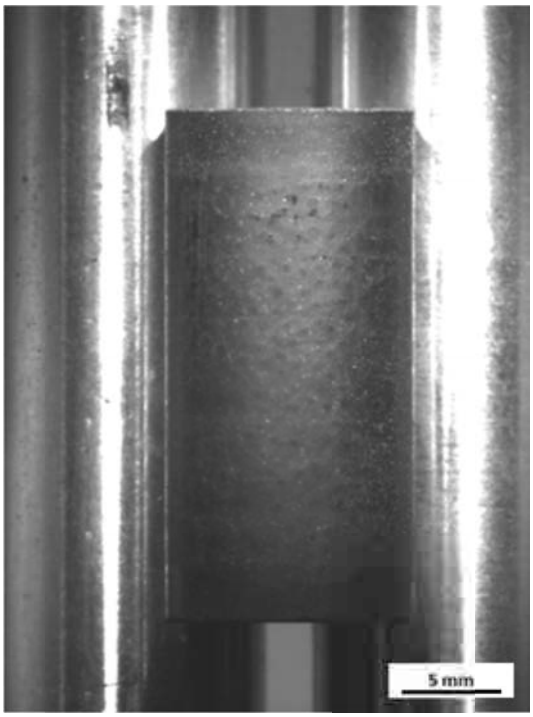

FIG. 7.82. Irradiated fuel compact from AGR-1 Capsule 4.

Preliminary dimensional data from several of the capsules indicates net shrinkage for the compacts. Diametrical dimensional change was in the range of -0.9 to -1.2% with an average of -1.0%, while length change was between -0.2% and -0.9% with an average of -0.6%. The graphite holders exhibited very different behaviour depending on the specific capsule. Preliminary data indicate shrinkage of the graphite in the outer two capsules (capsules 1 and 6) and swelling in the inner four capsules (capsules 2, 3, 4, and 5). The graphite holders from capsules 1 and 6 contained 5.5 wt% boron carbide, those in the remaining capsules 7 wt% boron carbide.

Further PIE works still to be done include [286]:

- The irradiated AGR-1 compacts will be characterized with gamma spectroscopy to determine inventories of key fission products and the burnup. Burnup measurements from spectroscopy data will be compared with values determined from destructive measurements.
- Fuel compacts will be cross-sectioned and examined with optical microscopy. Analysis will focus on kernel and coating micro-structures (including signs of coating damage or delaminations), kernel migration, and fission product corrosion of SiC.
- The extent of metallic fission product release from the fuel compacts during the irradiation will be determined by measuring the radionuclide inventories of the various capsule components, including the graphite fuel holders and the metal capsule parts (e.g. the capsule shell), during post-irradiation examination. The graphite holders and graphite end spacers will be quantitatively gamma counted to determine the inventory of fission products including ^{110m}Ag, ^{137}Cs, and ^{154}Eu. Fission products on metal capsule parts will first be stripped using an acid treatment, and the leach solution will then be analysed using radiochemical methods for the fission products of interest. In addition, the graphite holders will

be gamma scanned in both the axial and radial directions with a narrow collimator slit in an attempt to locate the spatial distribution of selected fission products.

- Compacts will be electrolytically deconsolidated in order to obtain individual particles for subsequent analysis. The deconsolidation process is made by electrolytic oxidation in concentrated nitric acid where individual fuel particles can then be collected and separated from any fines or larger matrix debris by sieving.
- At INL a system has been developed to allow inspection of particles and selection of individual particles for specific experiments. It will be used to perform initial visual examination on large batches of particles, to select specific particles by means of a vacuum needle, and to load particles into glass vials for subsequent analyses.
- The 'leach-burn-leach' procedure will be applied as a method for detecting failed coating layers in large batches of particles. The method involves a preliminary concentrated nitric acid leach on a batch of deconsolidated particles after compact deconsolidation and using the particles that have through-coating cracks to dissolve the uranium oxycarbide kernels. In addition, this method will also be used to look at the inventory of fission products that have been released from particles but retained in the compact matrix.
- Gamma spectrometry will be used to determine fission product inventories in individual irradiated particles, which allows the degree of fission product release to be measured. To accommodate variations in kernel size and burnup, this is best accomplished in practice by looking at the ratio of the fission products of interest to one that is known to be relatively immobile within the fuel kernel, e.g. cerium. A relatively low $^{137}Cs/^{144}Ce$ ratio would indicate a particle that has experienced high caesium release. Selected particles can be examined in more detail to evaluate the SiC coating micro-structures (e.g. grain size, grain orientation, quantity and types of defects) that may have contributed to increased release rates. At ORNL, a dedicated Advanced irradiated microsphere gamma analyser (Advanced IMGA) has been designed that will enable automated gamma counting of large batches of particles.
- Fuel specimens will be characterized by microscopic methods both after irradiation and after post-irradiation heating tests. Optical and electron microscopy will be used to characterize compact and particle cross-sections. Elemental analysis (wavelength dispersive spectroscopy) will be used to examine kernel micro-structures and phase heterogeneity and migration of fission products in the various coating layers, including corrosion of the SiC layer by palladium or other fission products. Additional SiC micro-structure information will be obtained from electron backscatter diffraction analysis (EBSD). Coating micro-structures and coating interface phenomena will be explored using TEM or atom probe tomography.

7.6.2.6. Conclusions

After 13 cycles, AGR-1 has been successfully irradiated for about 620 effective full power days with no fuel particle failures. The experiment has reached a peak burnup of 19.6% FIMA and a peak fast neutron fluence of 4.4×10^{25} n/m^2 (E>0.18 MeV).

Fabrication and assembly as well as initial irradiation of the experiment has provided some valuable insight into the design and operating characteristics of the test train as well as the temperature control and fission product monitoring systems. It is anticipated that irradiation

of this experiment will produce more valuable insights and lessons learned that may be applied to the future AGR experiments. These insights and lessons learned from AGR-1 can then be utilized to improve the experimental results and data from the future AGR irradiation experiments to support qualification of particle fuel for use in high temperature gas reactors.

post-irradiation examination has begun and will focus on evaluating differences in performance for the various AGR-1 fuel types. This will include an examination of fission product releases and particle failure fractions during irradiation and during post-irradiation high temperature accident testing, and detailed characterization of kernel and coating micro-structures and fission product migration within the particles.

7.7. IRRADIATION TESTING IN RUSSIAN MATERIAL TEST REACTORS

7.7.1. Description of various Russian MTRs

Several Russian test reactors had been developed to perform irradiation tests and post-irradiation examination of HGTR fuel. Irradiation tests and post-irradiation examination of uranium dioxide fuel spheres and coated particles had been performed at several Russian experimental bases [287]:

- Russian Research Center “Kurchatov Institute” (Moscow);
- Institute of Nuclear Materials (Zarechny);
- Research Institute of Atomic Reactors (Dimitrovgrad);
- Research Physics and Chemistry Institute (Obninsk).

7.7.1.1. IVV-2M reactor

The water cooled water moderated test reactor ‘IVV-2M’ with a 15 MW thermal power output was commissioned in 1966. The IVV-2M core is composed of fuel assemblies and beryllium reflector. Each fuel assembly consists of five tubular three layered hexagonal fuel elements which are placed co-axially between two case tubes. The core is arranged as sections. Each section comprises six fuel assemblies and a water cavity (a trap) with a diameter of 60 mm. There is also a cavity with a 120 mm diameter in the centre of the core and those with diameters of 60 mm and 130 mm in the Be reflector. The reactor operates by cycles with a length of 300 effective power hours each, with shutdowns of approximately two days between cycles, and is shut down twice yearly for refueling. The effective time of operation at the rated power of 15 MW is approximately 7500 effective hours per year [287]. Its maximum thermal and fast neutron fluxes are 4×10^{18} n/(m^2·s) and 1×10^{18} n/(m^2·s) , respectively. Fuel sphere irradiation tests are performed in irradiation rigs that can accommodate four full-sized fuel spheres per rig.

The IVV-2M FA (Fig. 7.83) consists of five tubular three layer hexahedral FE which are arranged coaxially between two jackets. The fuel elements rest on the ribbed bushing welded into the tail end. Each fuel element face has a longitudinal rib in the middle. An aluminum alloy was used for manufacturing the fuel element can as in the rodlike fuel assembly. Fuel is UO_2 dispersed in an aluminum matrix. The outside case tube dimension is about 62.5 mm to receive wrench. The fuel layer is 500 mm in length, the fuel element wall is 1.35 mm thick.

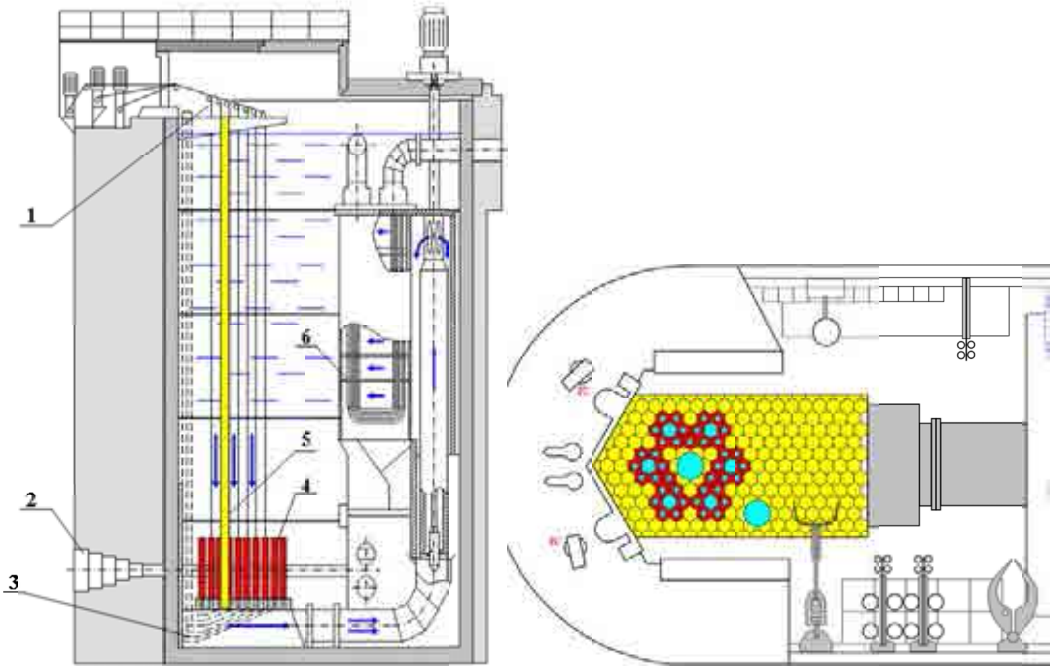

FIG. 7.83. Schematic of IVV-2M reactor 1: shim-and-scram system, 2: horizontal experimental channel, 3: fuel-cladding integrity control system, 4: core, 5: irradiation rig(s), and 6: heat exchanger.

7.7.1.2. SM-3 and RBT-6 reactors

Facilities for irradiation of coated particle fuel are being established at the Russian Research Institute of Atomic Reactors (RIAR), Dimitrovgrad, RF, as part of the DOE/MINATOM International GT-MHR programme. The use of two RIAR reactors is planned: the SM-3 reactor and the RBT-6 reactor. These reactors provide a variety of test channels and operating environments. The SM-3 reactor has higher neutron flux locations and can be used for testing of statistically significant numbers of particles in compacts and to produce irradiated compacts for accident testing. The lower flux RBT-6 can be used to test fuel compacts and loose particle samples and fuel material samples to obtain specific fuel material irradiation characteristics, fission product transport information, and produce irradiated material for special tests. Full burnup and full fast neutron fluence can be reached in a short time in the inner positions of SM-3.

Coated particle fuel irradiation capsules can be fitted into test 'channels' in these reactors. Each apparatus is made up of 'ampoules' (cells). Four channels in SM-3 are suitable for irradiation testing of coated particles. The irradiation capsule currently being designed for the GT-MHR programme consists of three ampoules; each of the ampoules can accommodate four compacts; consequently, a maximum of 12 compacts can be tested in each channel and a maximum of 48 compacts can be tested simultaneously in the four SM-3 channels. Ampoules are currently being designed for the RBT-6 reactor the International GT-MHR programme. These new facilities will permit multi-cell irradiations of loose particles and compacts; design details are not available at this writing. To reach full burnup and full fast fluence simultaneously, it is necessary to reduce the thermal flux by using neutron shields of materials such as hafnium.

7.7.2. Russian irradiation experiments

In the Russian Federation, the concept of fuel for an HTGR core was accepted to be the spherical fuel element [287]. The design of spheres with UO_2 fuel sphere has been developed since the end of 1960s for several Russian reactors, namely: VGR-50 (50 MW(e)), VG-400 (400 MW(e)) and VGM (200 MW(e)). Key parameters of HTGR fuel irradiation tests performed in these research centres are given in Table 7.16.

7.7.3. Irradiation technology at the Institute of Nuclear Materials

The Institute of Nuclear Materials (INM in Zarechny) operates the water cooled water moderated test reactor 'IVV-2M' which has a thermal power of 15 MW. Three means were used to insert coated particles into the irradiation rigs (Figs 7.84 and 7.85):

- a loose ordered location of coated particles as one layer in graphite disks of the 15 mm diameter and the 2 mm thickness each ((a) in Fig. 7.84);
- a uniform volume distribution of coated particles (hereinafter a compact of a cylinder form), of a 12 to 18 mm diameter and a 20 to 25 mm height in a graphite matrix ((b) in Fig. 7.85);
- a loose location of coated particles in axial holes of 1.2 mm diameter ((c) in Fig. 7.85).

The ampoule 'MT' is a non-instrumented irradiation rig to be placed in the cells of the 27 mm diameter. In the ampoule, there are three tight capsules. Each capsule has five specimens with coated particles. Every specimen is made of 10 to 13 graphite disks, each containing approximately 50 coated particles. Any disk has coated particles of only one modification. Each sample in a capsule has similar sets of modifications. There is a graphite thermal insulation between a sample and a capsule's body. Coated particles are exposed to irradiation under the temperatures from 1000 to 2000°C to attain the fuel burnup of 5, 10 and 15% FIMA.

The 'MT' type irradiation rig of the 27 mm diameter is designed to test 6 to 8 tight capsules where 2 or 3 are provided with gas service lines. The channel is to control a gas and volatile (caesium) fission product release. One specimen in each capsule is in the form of a cylinder or compact. In order to study a fission products' release the cavity between the samples and capsules' body is filled with micro-spheres of high purity carbon being a good absorbent of volatile fission products. Gaseous fission products are sampled by purging with inert gas which consumption is insufficient to transport carbon micro-spheres. During the scheduled reactor outage, and volatile fission products are sampled by purging when carbon micro-spheres are moved to the place of their analysis. The tests are performed at a neutron flux density of about 5×10^{17} n/(m^2·s) and temperatures of up to 1500°C.

TABLE 7.16. PARAMETERS OF IRRADIATION TESTS OF FUEL SPHERES AND COATED PARTICLES IN RUSSIAN TEST REACTORS

Reactor	Irradiation rig	Object under test	^{235}U loading (g)	Thermal neutron flux (10^{17} n/(m^2·s))	Fast neutron flux (10^{17} n/(m^2·s))	Irradiation temperature (°C)	Power per coated particle (W)	Fuel burnup (% FIMA)	Fast neutron dose (10^{25} n/m^2)
IVV-2M (INM, Zarechny)	MT-1, MT-2	Loose cp fuel pellets	1.5–3	5–8	10–13 (E>0.1MeV)	1100–1950	0.54–0.84	1.4–14	0.21–2.7 (E>0.1MeV)
	MTI	Loose cp fuel pellets	2	5–8	10–13 (E>0.1MeV)	800, 1200, 1400	0.55–0.65	4–12	0.6–2.0 (E>0.1MeV)
	MT-3	Fuel compacts fuel coupons	2	5–8	10–13 (E>0.1MeV)	750–1400	0.55–0.65	11–17	1.5–2.3 (E>0.1MeV)
MR (RRC 'KI', Moscow)	ASU-8	Loose cp fuel coupons fuel spheres	1.5	7–10	12–16 (E>0.1MeV)	1000–1300	0.76–0.96	5–15.3	0.7–2.2 (E>0.1MeV)
	Vostok	Fuel spheres	up to 6	9–10	13 (E>0.1MeV)	900–1400 (1600 shortly)	0.11–0.83	8.8–21.5	0.4–2.2 (E>0.1MeV)
	PG-100	Fuel spheres	8–50	5.0	1.5 (E>0.2MeV)	440–1350	500–5300 [a]	1.5–18	0.075–2.3 (E>0.2MeV)
VVR-C (НИФХИ, Obninsk)	Cashtan	Fuel spheres	up to 10	1.0	0.6 (E>0.2MeV)	1000–1700	400– 1300 [b]	6.8–41	0.22–0.57 (E>0.2MeV)
SM-2	Carat	Loose cp fuel coupons fuel pellets	4–6	8.5	5.0 (E>0.5MeV)	800–1700	300–700 [b]	3–24	0.75–2.2 (E>0.5MeV)
RBT-6 (НИИАР, Dimitrov-grad)	Udar	Fuel spheres	up to 25	0.28	—	300 (1200 [c]) up to 2000 cycles	200–800(1)	1.0	0.1 (E>0.18MeV)
	BKS	Loose cp fuel sphere protot. (10 mm dia.)	0.25–0.34	36	1.9	1250–1400	0.6–1.2	4.5–11	2.0–5.1
	RBT	Fuel spheres	up to 4	3.1	3.6	1250–1400	0.10–0.17	10–12	1.6–2.1

[a] per fuel sphere
[b] per ampoule (set of pellets and loose coated particles)
[c] Maximum cycling temperature
— data not available

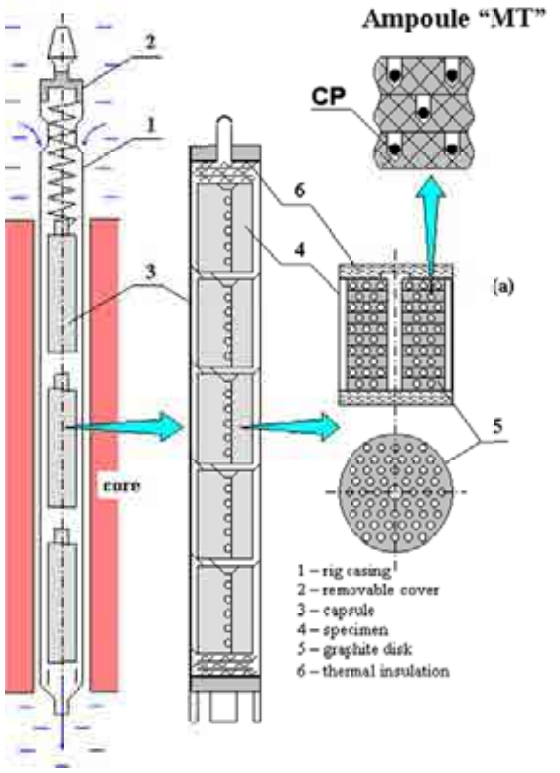

FIG. 7.84. Irradiation rig for testing HTGR coated particles in the IVV-2M reactor.

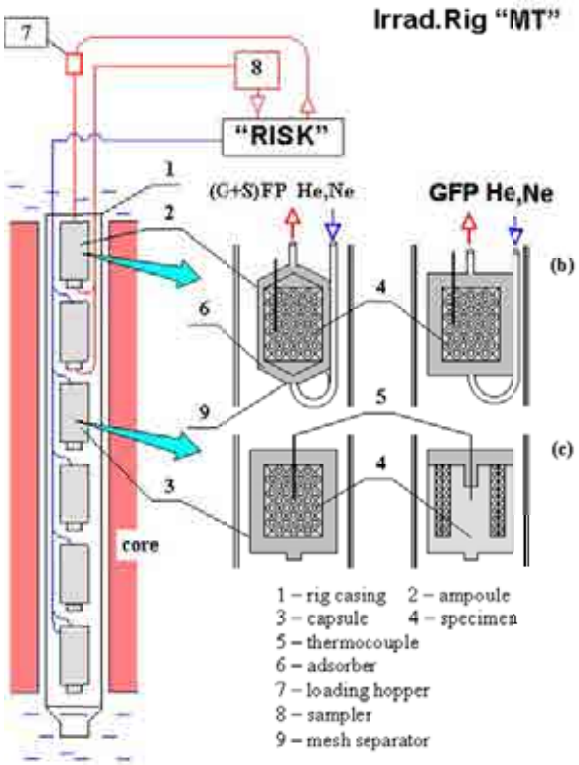

FIG. 7.85. Irradiation rigs for testing HTGR coated particles in the IVV-2M reactor.

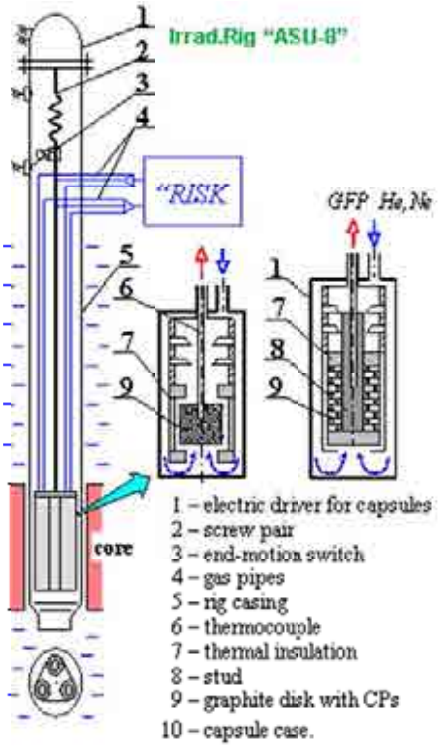

FIG. 7.86. Irradiation rigs for testing HTGR coated particles and fuel spheres in the IVV-2M reactor.

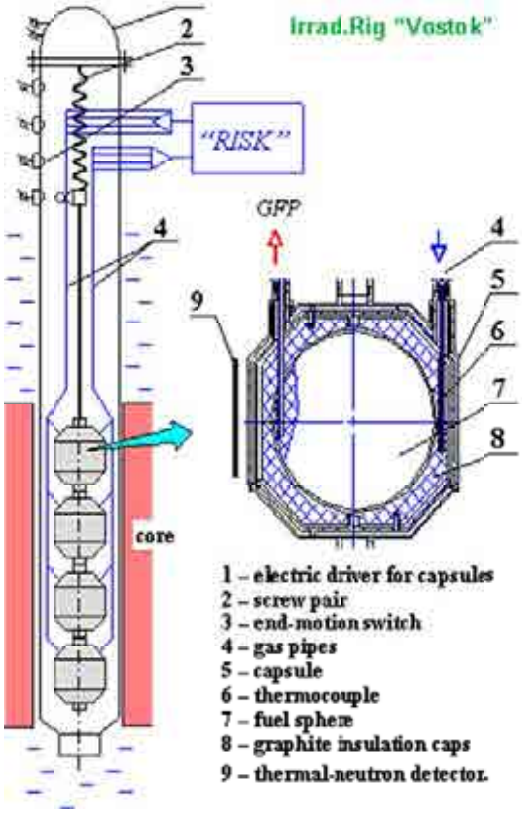

FIG. 7.87. Irradiation rigs for testing HTGR coated particles and fuel spheres in the IVV-2M reactor.

The ‘ASU-8’ type irradiation rig (Fig. 7.86) of the 60 mm diameter is intended to study gaseous fission products’ release from three batches of coated particles exposed to irradiation in separate capsules and under similar conditions. These capsules are of the same design as the capsules of the ‘MT’ ampoule. They contain the specimens either as sets of 7 to 10 graphite disks with coated particles or one fuel compact. A temperature of coated particle irradiation is regulated within 600 to 1400°C by traveling the specimens along the core height. The maximum neutron flux density is 7×10^{17} n/(m^2·s).

The ‘Vostok’ type irradiation rig (Fig. 7.87) is capable for testing of four full scale fuel spheres in the central core cell of the diameter of 120 mm. Fuel spheres are located in individual capsules. A fuel sphere is placed into a graphite cap with a gas gap of 1 to 2 mm between the fuel sphere and graphite cap. Besides, there is another gas gap to regulate temperatures in the capsule components and fuel sphere. The fuel sphere temperature of 1000 to 1400°C is regulated by varying a gas carrier composition in the gas gaps. The design of the irradiation rig provides a travel of capsules along the core height. The maximum thermal neutron flux density in fuel spheres reaches the value of 1.2×10^{18} n/(m^2·s).

7.7.4. Irradiation test of fuel spheres

7.7.4.1. Nominal and transient temperatures

Fuel spheres were tested under irradiation both cyclically (Vostok-1, -2, -3, -4, -5) and in the long term (Vostok-6) at specified fuel temperatures and up to target fuel burnups and fast neutron doses. In these irradiation tests the following basic dependencies were obtained:

- at irradiation temperatures of 1000°C, it was detected an insignificant increase of gaseous fission products’ release. At that, the critical fuel burnup was not reached (its value is greater than 15 to 20% FIMA); R/B values usually do not exceed 1×10^{-6};
- at irradiation temperatures of 1200°C, some coated particles can be depressurized at fuel burnup of 10 to 15% FIMA which leads to increasing of R/B values up to 1×10^{5};
- at irradiation temperatures of 1400°C, R/B values were increased up to 1×10^{-5} at fuel burnups of 5 to 13% FIMA.

The obtained results witness about satisfactory serviceability of the fuel spheres tested.

7.7.4.2. Accident temperatures

For a series of experiments, a short term in-pile heating of fuel spheres (up to 1550 and 1720°C for hundreds or tens hours) was performed at fuel burnups of 9 to 14% FIMA which simulates emergency cooling-down of a HTGR core (Fig. 7.88).

When fuel temperatures had returned to their nominal irradiation values, a significant increase of gaseous fission products’ release were not obtained in two experiments, but in another experiment, the R/B value for ^{88}Kr was 4×10^{-3} with failure of an appreciable fraction of coated particles.

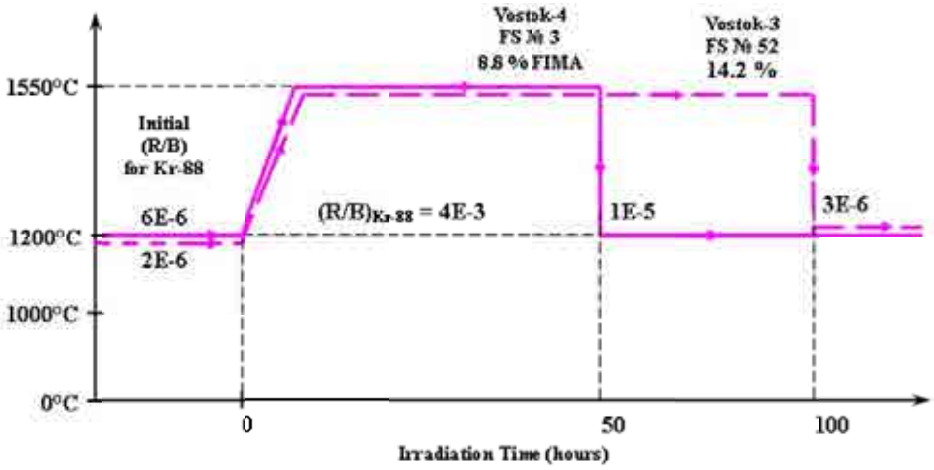

FIG. 7.88. Release of ^{88}Kr from a fuel sphere at accident temperatures.

7.7.5. Reference irradiation testing for the Chinese HTR-10 fuel

Qualification tests on the Chinese HTR-10 fuel have been performed in the Russian IVV-2M reactor [288, 289]. An irradiation test of four spherical fuel elements (SFE) had been performed in the Russian reactor IVV-2M. The elements were sampled randomly from the first and second product batches which were manufactured for the HTR-10. The maximum burnup of the irradiated fuel elements reached 107 GW•d/t and the maximum fast neutron fluence was 1.31×10^{25} n/m^2. The release-to-birth rate ratio (R/B) did not increase significantly during irradiation. However, an in-pile heatup test of element SFE 7 in capsule 5 led to a failure of approximately 6% of the coated particles. After the test it was estimated that the fuel temperature had very likely been much higher than the intended 1600°C.

7.7.5.1. Irradiation rig

The irradiation rig contained five independent capsules as shown in Fig. 7.89 [288]. From top to bottom, these capsules are numbered capsules 1 to 5. Capsule 1 (Fig. 7.90) contained about 13 500 loose coated fuel particles and 60 samples of matrix graphite of the fuel balls. The spherical fuel elements SFE 5 and SFE 7 from the first batch were located in Capsules 2 and 5 (Fig. 7.89), respectively, while elements SFE 12 and SFE 8 from the second batch were located in Capsules 3 and 4. Each capsule was controlled independently. It was continuously swept and monitored for gas fission products releases. The irradiation temperature was adjusted by gas mixture ratio of He and Ne.

7.7.5.2. Irradiation testing

The irradiation test started in July 2000, and ended in February 2003. The irradiation temperature was kept at 1000 ± 5°C. The burnup of the irradiated elements SFE5, SFE12 and SFE7 reached 97.3, 107 and 95 GW•d/t U, respectively. The fast neutron fluence reached 1.10×10^{25}, 1.31×10^{25} and 1.06×10^{25} n/m^2, respectively.

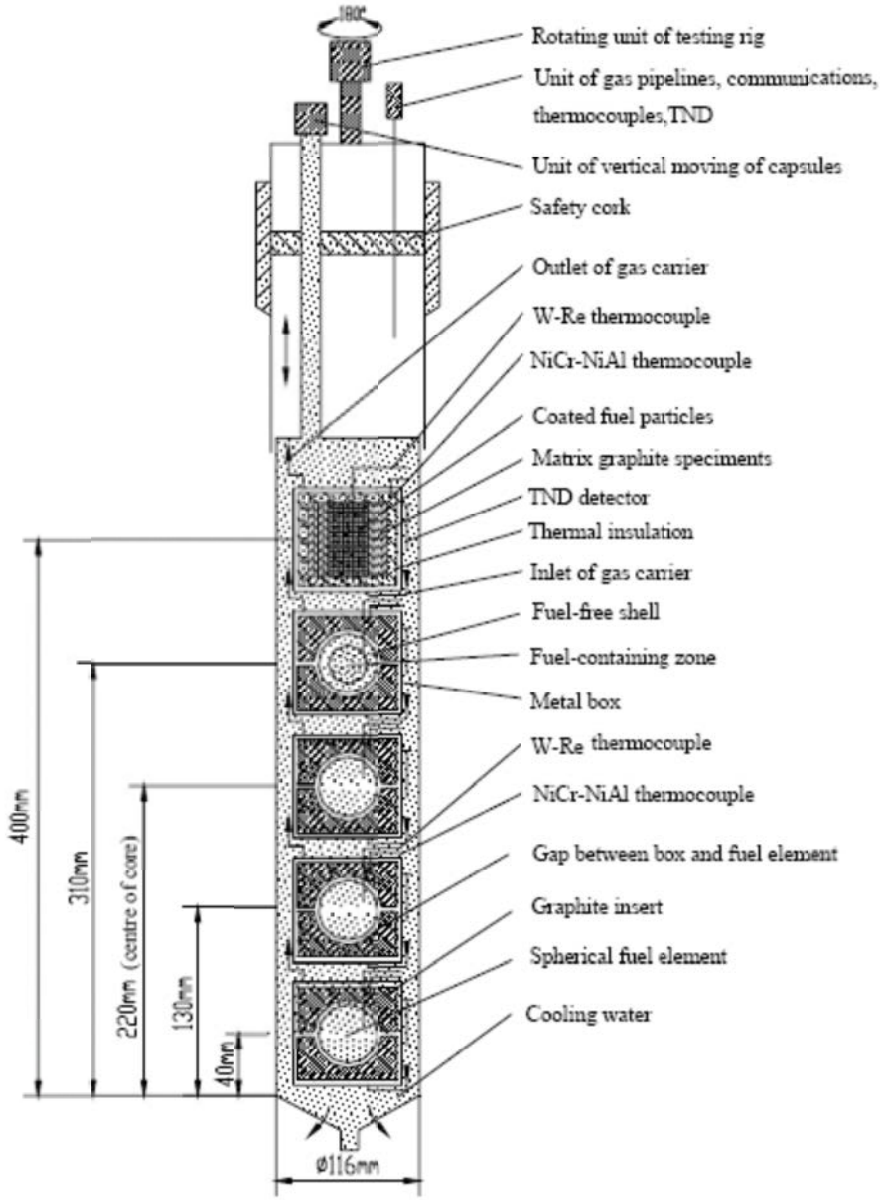

FIG. 7.89. Irradiation testing rig for HTR-10 fuel.

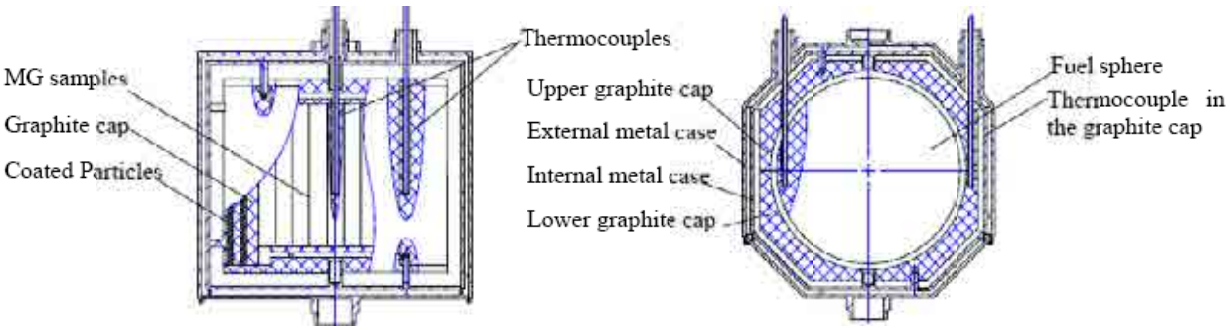

FIG. 7.90. Side view of Capsule 1 (left) and Capsule 5 (right).

The levels of the R/B of ^{135}Xe from four irradiated fuel elements as a function of the burnup are given in Fig. 7.91. The figure shows that the R/B values did not increase significantly during irradiation indicating that most likely irradiation-induced failures of coated particles did not occur. The high R/B levels were mainly due to the presence of fabrication-induced defects.

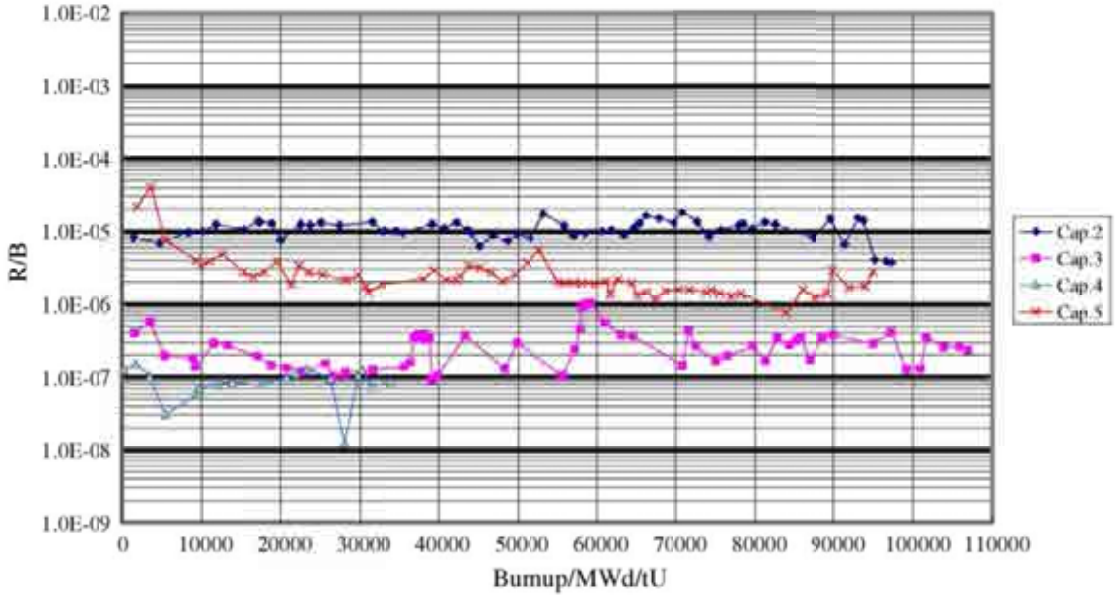

FIG. 7.91. R/B of ^{135}Xe of four irradiated fuel elements as a function of the burnup.

From burn-leach measurements on two batches, the average free uranium fraction was estimated to be 1.4×10^{-4} and 2.3×10^{-4}, respectively. The R/B ratio of ^{135}Xe of element SFE8 in capsule 4 was only recorded up to 37 000 MWd/t U (about 5980 effective hours) when the measurement was terminated due to a sudden increase of fission gas release from below 10^{-6} to more than 10^{-3} (Fig. 7.92) indicating a massive failure of coated particles in this element [289].

The maximum temperature of the HTR-10 fuel under accident conditions is 1200°C. To understand the irradiation performance at this condition, the temperature of element SFE12 in Capsule 3 was adjusted to 1200 and 1250°C for 200 h by changing the ratio of He and Ne when its burnup reached 38.7 and 57.3 GW•d/t U, respectively. Increasing the temperature of element SFE12 in the capsule 3 from 1050 to 1200°C and to 1250°C caused an increase of fission gas release. When the temperature returned to 1050°C, the R/B ratio was restored to its initial level.

For any off-normal reactor condition, the fuel temperature of a modular HTGR is limited by design to be below 1600°C. To test the irradiation performance of HTR-10 fuel at 1600°C, an in-pile heating test was arranged. However, since no furnace for external testing at 1600°C was available, the fuel element was heated in the reactor itself by increasing the thermal neutron flux. Moving capsule 5 to the central part of the core of maximum thermal neutron flux was the most practicable choice. Thus, capsules 1 to 3 were transferred to the upper region of the core with low thermal neutron flux; here the fuel temperatures were not beyond 1000°C.

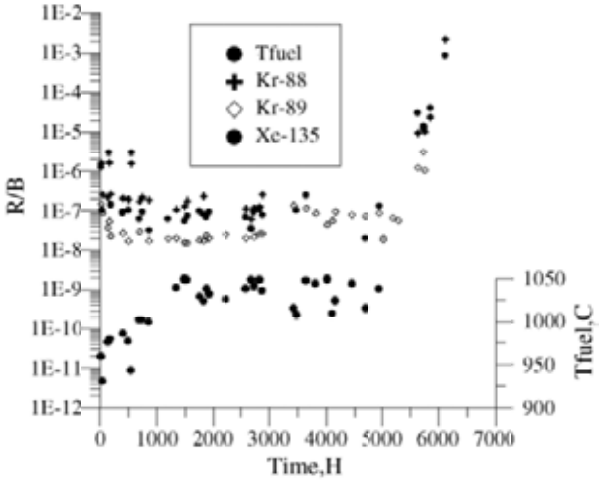

FIG. 7.92. Gas release fraction measurement of SFE 8 in Capsule 4.

7.7.5.3. Results and discussion of post-irradiation examination

The post-irradiation examination started in February 2004, and contains visual inspection, dimension and weight measurement for the irradiated fuel elements, deconsolidation of the irradiated balls and determining the distribution of the solid fission products in the matrix graphite along the ball diameter, measuring the failure fraction of the loose coated fuel particles obtained from the ball deconsolidation by the irradiated microsphere gamma analyser (IMGA), ceramography examination of the failed and non-failed particles, and determining the distribution of the solid fission products in the coating by chemical layer-by-layer analysis.

(a) Visual inspection and diameter measurement

Figure 7.93 shows the photographs of the irradiated fuel elements [290]. It can be seen that the appearance of the SFE5 in capsule 2 fixed at 1000°C, SFE12 in capsule 3 fixed at 1000°C with 1200°C for 200 hours and 1250°C for 200 hours and SFE7 in capsule 5 fixed at 1000°C with the high temperature heating at the end of the test is similar to that before the irradiation test.

The diameter of SFE5, SFE12 and SFE7 perpendicular and parallel to pressing direction were measured before and after the irradiation test, respectively. The measured results are shown in Table 7.17, and are not abnormal.

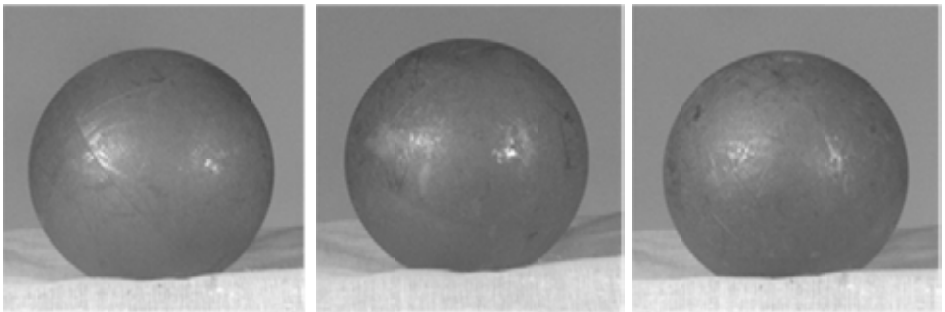

(a) SFE5 in capsule 2 (b) SFE12 in capsule 3 (c) SFE7 in capsule 5

FIG. 7.93. Appearance of irradiated fuel elements.

TABLE 7.17. DIAMETER CHANGE OF IRRADIATED FUEL ELEMENTS

Fuel element		Before irradiation (mm)	After irradiation (mm)	Relative change (%)
Perpendicular to pressing direction	SFE5	60.03	59.68	-0.58
	SFE12	60.04	59.62	-0.70
	SFE7	60.06	59.66	-0.67
Parallel to pressing direction	SFE5	59.90	59.67	-0.38
	SFE12	60.06	59.62	-0.73
	SFE7	60.19	59.68	-0.70

(b) Electrolytic deconsolidation of irradiated fuel elements

SFE5, SFE12 and SFE7 were electrolytically deconsolidated to obtain loose coated fuel particles for further analysis and to determine the distribution of solid fission and activation products in the matrix graphite. The principle of this deconsolidation process is anodic oxidation of the matrix graphite by electrolysis. The anode of a DC voltage supply is directly connected to the matrix graphite of the fuel element. A Pt metal acts as the cathode and is dipped into the electrolyte solution. A nitric acid solution is used as the electrolyte solution.

By rotating the spherical fuel element in the electrolyte solution, a cylinder remaining of 60 mm length by 20 mm diameter of the fuel element was obtained. This cylinder was then inserted into the electrolyte solution (perpendicular to the solution surface) and deconsolidated in ~5 mm steps to obtain the loose coated particles and graphite powder along an axis through the centre of spherical fuel element. After each step of deconsolidation coated particles were removed by the screening. The graphite powder and electrolyte were also separated, and their relative solid fission and activation products were measured by a high resolution G(Li) detector. The ratio of activity measured in the graphite and electrolyte solution of each step represents of the distribution of fission and activation products along the spherical fuel element diameter. Fig. 7.94 gives the radioactivity distribution of nuclides determined during the axial deconsolidation of SFE12 and SFE7, respectively [290].

Figure 7.94 reveals low radioactivity and uniform distribution of the solid and activation products in SFE12 under constant temperature for a long time, and high radioactivity of the solid and activation products in SFE7 and relatively higher concentration in the centre of the fuel element due to the failure of the particles under too high heating temperature at the end of the in-pile test.

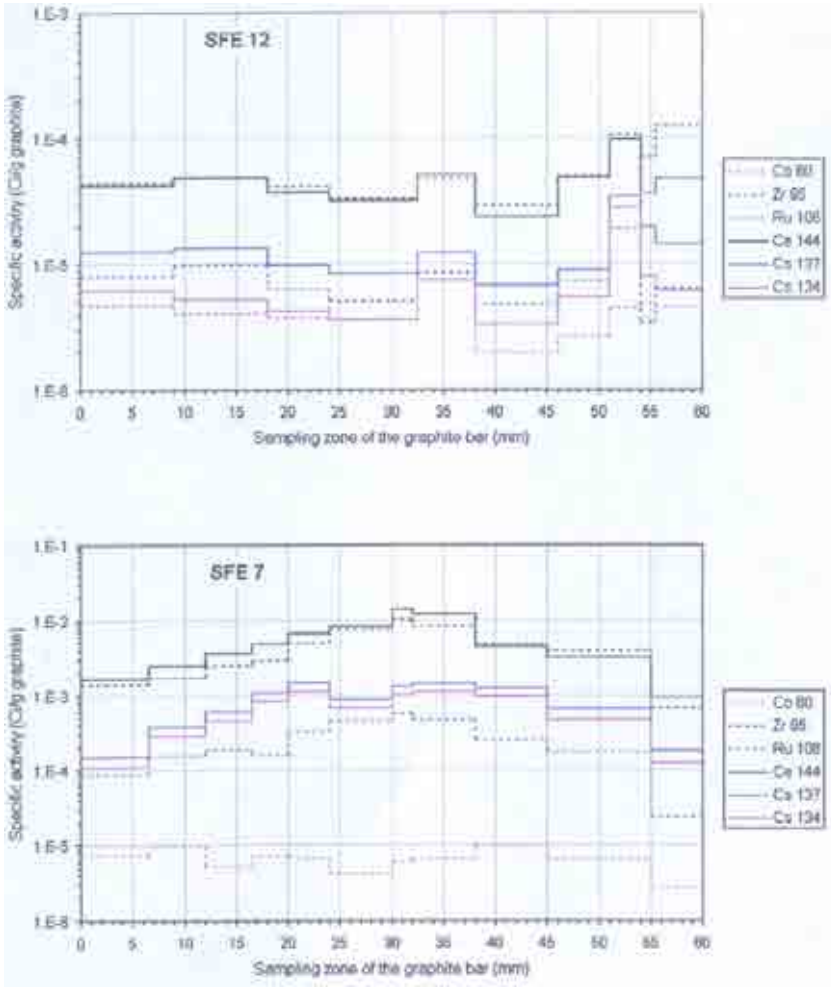

FIG. 7.94. Radioactivity distribution of nuclides determined during the axial deconsolidation of SFE12 and SFE7.

(c) Measurement of failed particles

The IMGA system records the gamma ray energy spectra of individual irradiated fuel particle from a large population and performs quantitative analysis on those spectra. Judgement between intact particle and failed particle is based on the activity ratio of two isotopes of caesium (^{134}Cs and ^{137}Cs) and ^{144}Ce. Therefore, IMGA provides the capability of making statically accurate failure fraction measurement on irradiated HTGR coated fuel particles. As mentioned above, the actual failure fraction is based on a ratio of the activity of a volatile fission product to a non-volatile fission product. The boiling point of the element caesium is 678°C, but it is 3470°C for the element cerium. The caesium will therefore escape more readily from a defective coating than cerium. Thus, the measurement of a low activity ratio of ^{137}Cs or ^{134}Cs to ^{144}Ce can indicate the failure of a particle.

The IMGA system utilized in the examination of irradiated HTR-10 fuel particles is similar to the IMGA equipment at ORNL [291] in structure of the system. It consists of three major components: an automated singularizing particle handling system, a high resolution gamma detector, and a computer based pulse height analyser. Each fuel ball contains about 8300 coated fuel particles. The 2014 and 1670 particles sampled at random from SFE12 and SFE7, respectively, were inspected by IMGA. Inspection results are shown in Fig. 7.95 and 7.96, resp.

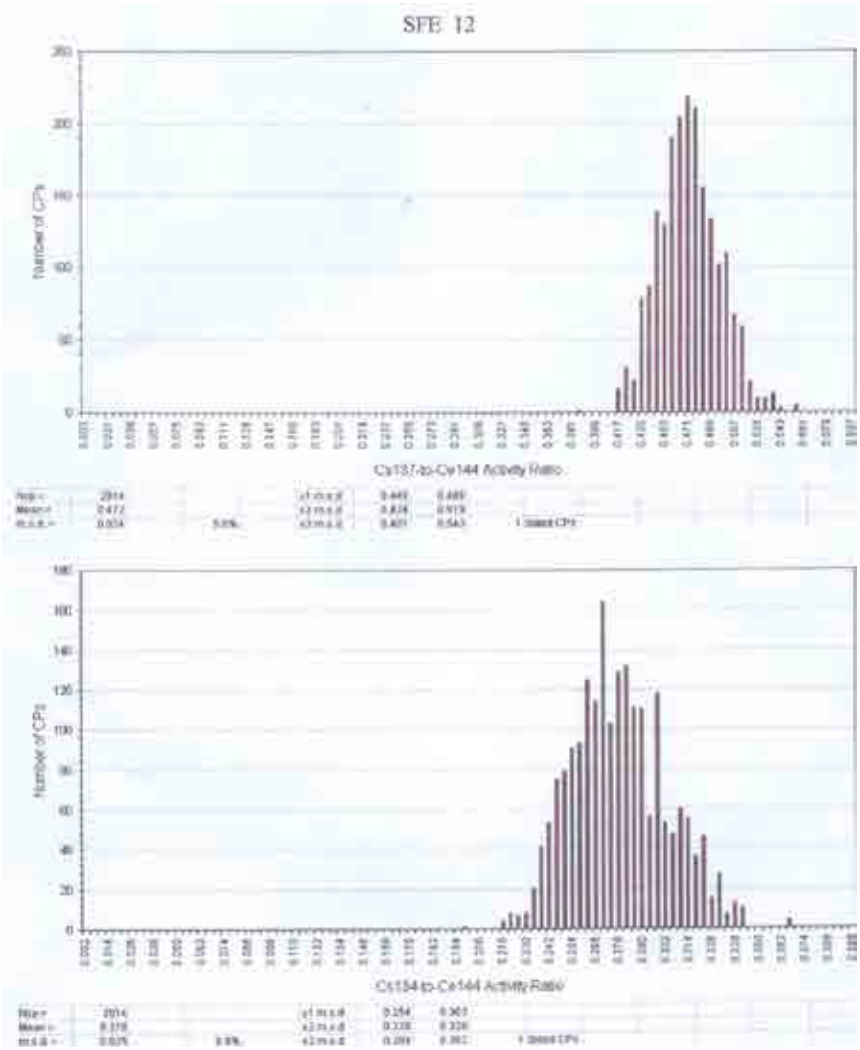

FIG. 7.95. Activity ratios of ^{137}Cs and $^{134}Cs/^{144}Ce$ determined on particles of SFE12.

If the activity ratio of ^{137}Cs or $^{134}Cs/^{144}Ce$ in a particle is less than A_{mean} - 3S (where A_{mean} is the mean value of the activity ratios in determined particles, S the standard deviation), this particle is considered failed. One of 2014 particles in SFE12 and 47 of 2014 particles in SFE12 were found failed. In accordance with the R/B curve in Fig. 7.91, failure of one particle for SFE12 may be caused by manufacture. The failure of the particles in SFE7 was caused by too high nuclear heating temperature (much more than 1600°C).

Table 7.18 gives the gas fission products release and expected temperature raising process in the heating testing of SFE 7 [290]. During several hours at 1570°C listed in the table, the particles in SFE7 began to fail quickly. Because a thermocouple was failed, actual fuel temperature in SFE7 was much more than 1600°C. Too high nuclear heating temperature for SFE7 caused the failure of the coated fuel particles in SFE7.

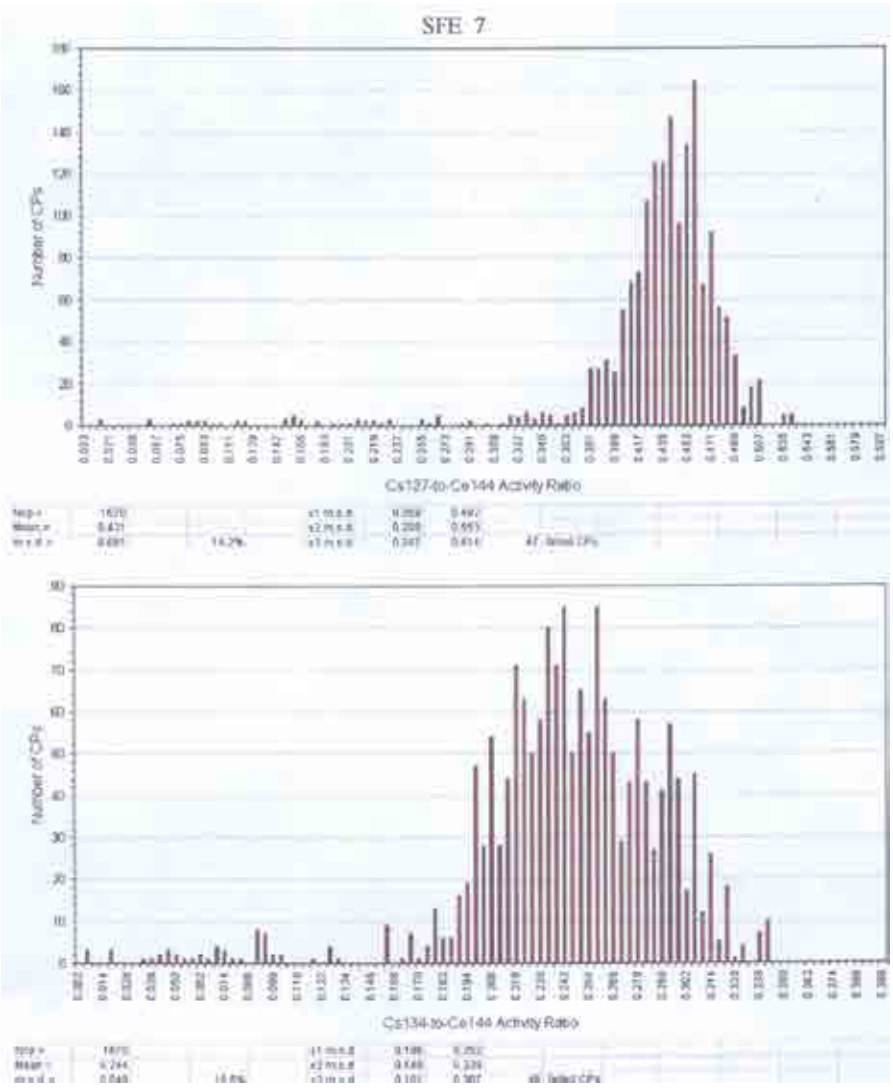

FIG. 7.96. Activity ratios of ^{137}Cs and $^{134}Cs/^{144}Ce$ determined on particles of SFE7.

TABLE 7.18. GASEOUS FISSION PRODUCT RELEASE FROM SFE7 IN HEATING TESTS

Heating sequence	Date	Test time (h)	Expected T_{FUEL} (°C)	(R/B) of nuclides					
				Kr-85m	Kr-87	Kr-88	Kr-89	Xe-135	Xe-138
			1000	7.76×10^{-6}	2.48×10^{-6}	4.53×10^{-6}	1.17×10^{-6}	2.77×10^{-6}	8.53×10^{-7}
Heating test									
(1)	2003-03-02	5	1440	9.78×10^{-5}	4.71×10^{-5}	5.23×10^{-5}	2.27×10^{-6}	9.11×10^{-5}	4.85×10^{-6}
(2)	2003-04-02	14	1470	1.36×10^{-4}	6.61×10^{-5}	7.91×10^{-5}	2.76×10^{-6}	1.10×10^{-4}	6.64×10^{-6}
(3)	2003-04-02	22	1570	5.85×10^{-2}	2.25×10^{-2}	2.07×10^{-2}	3.15×10^{-3}	9.27×10^{-2}	5.35×10^{-3}
(4)	2003-05-02	42	1280	1.28×10^{-2}	4.00×10^{-3}	3.98×10^{-3}	5.64×10^{-4}	2.39×10^{-2}	1.01×10^{-3}

(d) Summary

The following conclusions can be drawn from the post-irradiation examination:

- One failed coated fuel particles was found by IMGA method in the 2014 particles sampled at random from the irradiated SFE12 in capsule 3. This particle may have become defective already during manufacture.
- About 3% coated fuel particles failed in fuel sphere SFE7 in capsule 5 based on the measurement results of 1670 particles by IMGA. The main reason of failure is probably the too high fuel temperature which is presumed to have largely exceeded 1600°C.

7.7.6. Irradiation programme for South African fuel

Apart from own irradiation capabilities in the SAFARI reactor at Pelindaba, South Africa has also been considering irradiation testing of PBMR fuel in the following facilities:

- IVV-2M — The test reactor planned to be used for the PBMR production plant fuel irradiation programme and a portion of the PBMR laboratory produced fuel irradiation programme is the IVV-2M reactor located at Zarechny in the Russian Federation.
- HFR — A portion of the PBMR laboratory produced fuel irradiation programme will be conducted in the HFR reactor located at Petten in the Netherlands.
- ATR — A coated particle irradiation of the PBMR laboratory fuel will be conducted in the advanced test reactor (ATR) reactor located at Idaho National Laboratories in the USA, as part of the AGR irradiation programme.

7.7.6.1. Testing of laboratory-produced fuel spheres

In order to provide early confirmation of the validity of the PBMR manufacturing process, a total of nine 'pre-production' fuel spheres manufactured in the PBMR fuel laboratory was planned for irradiation. Of those spheres, five were to be irradiated in the HFR Petten and four in the IVV-2M reactor. The fuel spheres for these tests contain coated particles produced in a full-sized coater prototypical of the coaters to be installed in the PBMR pilot fuel plant. Main goal of these tests is to confirm the performance of fuel produced in the full scale pre-production or 'advance' coater as part of the manufacturing assurance programme.

7.7.6.2. Overview of testing of production plant fuel spheres

A pilot fuel plant will be constructed in South Africa to produce fuel in sufficient quantities to support the startup and continued operation of the PBMR demonstration plant. This portion of the testing is on equilibrium fuel spheres manufactured on a fully qualified production line from the pilot fuel plant. PBMR will be started up with fuel enriched to approximately 4.2 to 4.5% ^{235}U to control startup reactivity, and will then be transitioned to the use of equilibrium fuel whose ^{235}U enrichment will be approximately 9.6%. The first test, using four equilibrium fuel spheres, will be ended when the spheres reach a burnup of approximately 5% FIMA (which corresponds to the maximum expected burnup of startup fuel in PBMR). In the second test, a total of 12 fuel spheres will be irradiated until the maximum burnup of approximately 11.6% FIMA is reached.

The fuel spheres manufactured on a qualified PBMR production line will meet all specified requirements and is to be verified independently during pre-irradiation characterization. Test objective is to confirm that the behaviour of PBMR fuel spheres under irradiation and post-

irradiation heating test conditions meets PBMR requirements for normal operating and accident conditions regarding:

- Fission gas release — to be measured in an external gas loop during irradiation/heating;
- Metallic fission product release — to be determined in the PIE by measuring deposition in the irradiation capsules that surround the fuel spheres during irradiation; it will be periodically determined during heating tests by removing and replacing deposition plates in the test furnace;
- Failure of coated particles — to be quantified by means of fission gas release analysis during irradiation and during heating tests.

(a) Pre-irradiation characterization

Fifteen fuel spheres, in addition to the 16 to be irradiated, have been produced for independent pre-characterization. This will form part of an independent assessment of the as manufactured properties of coated particles, fuel spheres and matrix graphite. Pre-irradiation characterization for fuel spheres and coated particles consists of:

- Determination of geometrical sizes of kernels, coated particles, and layer thickness;
- Determination of kernel density, coated particle density, and density of all coating layers;
- Kernel and coated particle mass determination;
- Determination of kernel impurities;
- Ceramography of coated particles to
    - investigate the structure of the kernel, buffer, PyC, and SiC layers;
    - determine anisotropy of dense PyC layers, including in particles removed from a heat treated fuel sphere;
    - determine uranium distribution in coated particle layers;
- Determination of free uranium content in spheres;
- Determination of U/O ratio in kernels;
- Determination of compression strength of coated particles.

(b) Testing of production plant fuel spheres — partial burnup

The purpose of the test is to confirm that fuel manufactured for use in the PBMR demonstration power plant can be burned to approximately 5% FIMA, the maximum burnup calculated for the startup fuel, and will perform satisfactorily under DBA conditions. Four equilibrium fuel spheres containing a total of approximately 57 800 coated particles will be loaded into an irradiation rig and inserted into the IVV-2M test reactor. At a burnup of nominally 5% FIMA, the fuel spheres will be removed from the test reactor and subjected to PIE and heating tests. The successful completion of this test will confirm production fuel integrity for normal operation and DBA conditions to a burnup of 5% FIMA.

The irradiation target for the production fuel in the irradiation rig is a burnup value of ~5% FIMA (48.2 GW•d/t) at a constant centre temperature of 1200°C. The fast neutron dose at this burnup is $\sim 1.7 \times 10^{25}$ n/m^2. The duration of this irradiation will be approximately one year.

(c) Post-irradiation examination

PIE work to be performed on the four fuel spheres from the irradiation rig should include appearance and the measurements of mass, diameter, burnup, and fission product inventory. Furthermore, all irradiated fuel spheres will be subjected to heating tests simulating DBA transient temperatures, first at 1600°C for 100 h and then at 1800°C for 100 h. Following the heating tests, all heated fuel spheres will be visually examined and their fission product inventories measured.

One heated fuel sphere will then be deconsolidated to provide coated particles for ceramography and fission product distribution measurements including the following:

- Fission product distribution in fuel sphere.
- Optical ceramography of coated particles.
- Irradiated Microsphere Gamma Analysis (IMGA) on coated particles.
- Fission product distribution in coated particles.

7.7.6.3. Testing of production plant fuel spheres — full burnup proof test

The purpose of the proof test is to demonstrate, using a test sample that is statistically sufficient, that production fuel spheres meet all coated particle failure and fission product release requirements under normal operation, anticipated operational occurrences, and DBA conditions, including DLOFC and PLOFC temperature transients. It is planned to irradiate 12 production fuel spheres containing a total of approximately 173 400 coated particles in the IVV-2M reactor.

(a) Irradiation target

The average target burnup for PBMR fuel spheres is approximately 9.6% FIMA, which was calculated based on six cycles through the reactor core. In PBMR operation, a small number of fuel spheres could be recycled near the maximum Burnup Measurement System setpoint with uncertainty, and pass through the high burnup path near the inner reflector. Therefore, depending on the setpoint of the Burnup Measurement System and the measurement uncertainty, a fuel sphere could achieve a burnup as high as approximately 11.2% FIMA (109 GW•d/t). For this reason, the value of 11.6% FIMA is listed in Table 7.19 (test summary). The maximum fast neutron dose estimated in a similar manner is approximately 3.6×10^{25} n/m^2. Normal temperature cycles in the reactor core will be simulated by irradiation at two representative core temperatures — one interval at a temperature representative of the low temperature part of the PBMR temperature cycle and a second interval at a temperature representative of the high temperature part of the PBMR temperature cycle. At the end of irradiation, the fuel spheres in one of the irradiation rigs will be subjected to a temperature transient simulating the first part of a PLOFC transient. In Table 7.19, nominal irradiation targets are compared to parameter values.

TABLE 7.19. COMPARISON OF NOMINAL PROOF TEST IRRADIATION TARGETS WITH CORE DESIGN PARAMETERS

Parameter	Design limits	Design	Nominal proof test irradiation target
Number of Cycles	6	6	8
Maximum power per fuel sphere (kW)	4.5	2.76	3
Average residence time (days)	n.a. [a]	925	731
End of life fast neutron dose (10^{25} n/m^2, E>0.1 MeV)	n.a. [a]	2.72	3.63
Average discharge burnup (GW•d/t/% FIMA)	92/9.5	91/9.4	111.9/11.6
Maximum temperature (°C)			
Normal operation	1130	1068	900/1150 cycles
DLOFC (transient peak)	n.a. [a]	1593	1600/1800
PLOFC (transient peak)	n.a. [a]	1319	1350

a not applicable.

TABLE 7.20. SUMMARY OF PBMR FUEL IRRADIATION TESTS

Test	Fuel to be tested			Test description					Technical objective
	Production route	Number	Reactor	Burnup (% FIMA)	Temperature (°C)	Cycle	Post heat	PIE	
Production plant fuel, partial burnup demonstration	Pilot fuel plant	4	IVV-2M	5	1200	no	Four fuel spheres to 1600°C, then to 1800°C	yes	Qualification to 5% FIMA Zero or low number of coated particle failures
Production plant fuel, full burnup demonstration	Pilot fuel plant	12	IVV-2M	11.6	900/1150	yes	Eleven fuel spheres, five to 1600°C, six to 1800°C	yes	Full fuel proof test including simulated PLOFC in test reactor, detailed PIE

(b) Post-irradiation examination

PIE work to be performed on one or more of the 12 irradiated fuel spheres should include appearance and the measurements of mass, diameter, burnup, and fission product inventory. A deconsolidation should also be done to determine fission product distribution in the fuel sphere and allow optical ceramography of coated particles and determine fission product distribution in coated particle.

Following irradiation, irradiated fuel spheres will be externally examined and their burnup measured. One fuel sphere will be deconsolidated to enable ceramography of coated particles to be carried out and to measure the fission product distribution through the fuel sphere.

Of the remaining 11 fuel spheres, five spheres will be subjected to heating tests simulating maximum reactor fault transient temperatures, nominally 1600°C for about 100 h, and six spheres will be subjected to temperatures of approximately 1800°C for about 100 h. Following heating tests all heated fuel spheres will be visually examined and their fission product inventories measured. A summary of the planned irradiation tests for PBMR production plant fuel spheres is provided in Table 7.20.

7.8. IRRADIATION TESTING IN THE OSIRIS REACTOR AT CEA SACLAY

7.8.1. Reactor description of OSIRIS

OSIRIS is an open-core pool type, experimental reactor with a thermal power of 70 MW based on a light water reactor, and located within the French Atomic Energy Commission (CEA) centre at Saclay. It is a multi-purpose reactor, used for technological irradiation for the purposes of the nuclear power industry or those of fundamental research, production of radioelements and doped silicon, and analysis by activation. The reactor started operation in 1966 and functions on average 200 days a year, in cycles of varying lengths from 3 to 5 weeks. A shutdown of about 10 days between two cycles is necessary to reload the core with fuel, carry out light maintenance operations and the handling operations required for the experiments. The basic principle of design of an open-core, pool type of reactor enables direct access to the core, facilitated by the absence of any pressurization vessel. The core of the OSIRIS reactor is loaded with 38 standard fuel elements with plates, six control elements, and seven reflectors made of beryllium. At the end of each cycle, approximately one element out of six is unloaded to be replaced by a new fuel element. Furthermore, the core houses five slots for experimental devices.

An OSIRIS fuel element consists of 22 plates, each plate made of alloy U_3Si_2Al (silicide), 0.51 mm thick, with an aluminium sheath of 0.38 mm thickness in between. The thickness of the coolant channel is 2.46 mm. The uranium is enriched to 19.75%. The two edge plates contain boron (a burnable neutron poison) to comply with the regulatory safety margins to control the reactivity available at the beginning of cycle. It is thus possible to have long operating cycles (4 to 5 weeks). Each control element comprises 17 plates similar to the standard elements and with a coolant channel thickness of 2.79 mm.

The OSIRIS irradiation facility is designed to allow irradiation of HTGR fuel compacts or loose fuel particles in the core of the reactor to study damage effects or to apply thermal transient conditions at the periphery. Being on-purpose-designed for compacts, the present device is limited to a maximum diameter of 15 mm. The internal component of the sample holder is designed and manufactured for each type of new loading. The out of pile facility is generic and can be supplemented for specific requirements. In steady-state conditions, the

device reaches a maximum temperature of 1300°C on the surface of the fuel. In transient conditions, it can reach 1600°C. The atmosphere of the samples is a binary mixture of high purity rare gases, helium and neon. The out of pile part can track the irradiation, the thermal conditions and the fission products release of the two independent fuel columns in quasi-identical conditions.

The temperature is controlled in two independent ways. The first involves operating a bank of six electrical furnaces automatically controlled by temperature sensors. The second involves acting upon the composition of the gas mixture to adjust the heat conductivity and thus to control heat transfer to the fuel. The concentration of helium is adjusted initially by the operator to place the device in good thermal conditions.

The gamma spectrometry measurements are based on the analysis of Xe and Kr releases. Volatile fission products are transported by the rare gas flow from the in-pile capsule to the shielded compartment. The transit time is adjusted according to the period of the considered isotope. The design of the circuit avoids deposition of solid elements whose decay can produce Xe or Kr, together with complicated post-interpretations. In the shielded compartment, a first gamma sensor measures the total release rate and the monitoring checks if the experiment can continue in safety conditions. After this overall measurement of activity, standard filters fix all the volatile fission products except rare gases.

The high level detection mode proceeds by measuring the gas mixture with the flow. The low level detection mode is performed on cold traps where the Xe and Kr are continuously fixed. These cold traps allow integral measurement and avoid sending the released Kr and Xe into the core by the recirculation of the carrier gas.

After each activity measurement, the cold trap is bypassed and purged, and the second cold trap is switched to the loop. This measurement procedure can be followed for each of the two independent capsules. One measurement can be done each day on each capsule. Different types of calculations can be done on line to determine the R/B rate. Several storage tanks ensure radioactivity decay before transfer after gas mixture replacement.

7.8.2. Irradiation experiment SIROCCO

7.8.2.1. Objectives

The SIROCCO programme is planned by Commissariat à l'Énergie Atomique (CEA) and AREVA NP [27]

- to provide data on fuel performance under irradiation under normal operating conditions, non-operating conditions and accident conditions;
- to support development and validation of fuel performance and fission product transport models and codes;
- to support the fuel licensing programme.

7.8.2.2. Preparation

The first irradiation tests will mainly be conducted at the materials testing reactor OSIRIS in Saclay, France, with HTGR fuel coming from the French fuel line named GAIA in Cadarache, France, and compacted at CERCA, AREVA NP subsidiary in Romans, France. The objectives of these irradiation campaigns are to verify, on the one hand, the quality of the fuel in terms of integrity and fission products retention and, on the other hand, the ability of

the reference particle to withstand VHTR conditions. The objectives of the first irradiation campaign (SIROCCO-1) are to verify the quality of the fuel in terms of integrity and fission product retention. The fuel to be irradiated in SIROCCO-1 and the irradiation conditions are described in Tables 7.21 and 7.22.

TABLE 7.21. THE HTGR FUEL TO BE IRRADIATED IN SIROCCO-1

Type of particle	UO_2/Buffer/OpyC/SiC/IPyC
Particle geometry	500/95/40/35/40 μm
Matrix geometry	Compact
Origin of particles	German past manufacture and CAPRI production
Enrichment	9.8 wt%
Packing fraction	~10%, which is ~1500 particles per compact

TABLE 7.22. SIROCCO-1 IRRADIATION CONDITIONS

Fuel surface temperature	~1000°C
Fluence	$> 2 \times 10^{25}$ n/m^2
Power density	< 0.2 W/particle
Duration	~150 days

The fuel quality verification will consist of a direct comparison between new French particles and German particles: the German best particle past fabrication will be compacted with the same CERCA process, the same packing fraction and enrichment, and irradiated in the same device (with separate fission gas release measurement system) under the same conditions (Fig. 7.97).

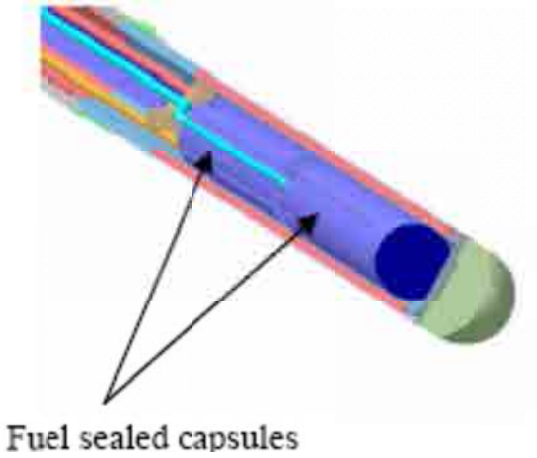

FIG. 7.97. 3D view of a two capsules sample holder.

This will allow comparison of the French new manufacture quality with the German reference with a high degree of confidence in terms of fission gas release, PIE and safety tests. In addition, these two sets of particles will be characterized before and after irradiation with the same CEA improved characterization methods. The valuable data coming from the out of pile consoles and allowing the continuous monitoring of the fission product release measurements of the whole in-pile containment and the PIE will be the basis of the industrial fuel qualification programme.

7.9. IRRADIATION TESTING IN THE HANARO REACTOR AT KAERI DAEJEON

7.9.1. Reactor description of HANARO

The HANARO reactor at KAERI, Daejeon, is an open-tank-in-pool type reactor with a maximum thermal power of 30 MW (Figs 7.98 and 7.99). The core is composed of a light water cooled and moderated inner core and a light water cooled, heavy water moderated outer core.

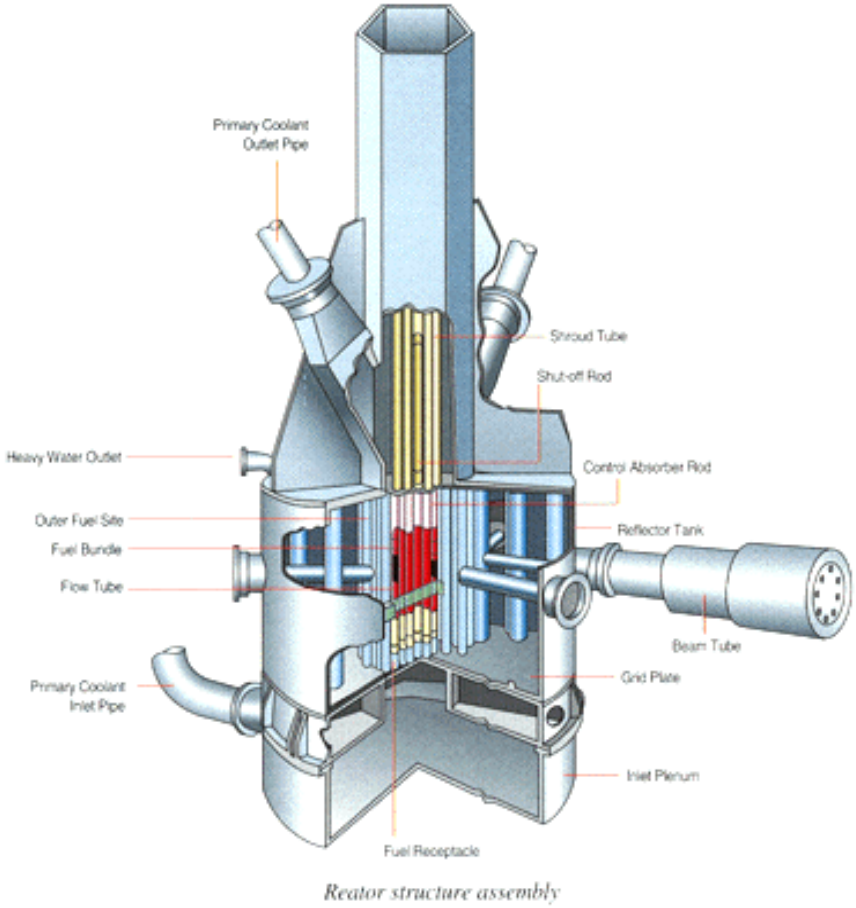

FIG. 7.98. Schematic of the HANARO reactor at KAERI.

The inner core has 28 fuel sites to contain low enriched uranium of 19.75 wt% in uranium silicide compound which is dispersed in the aluminum matrix and three test sites for capsules. The outer core consists of four fuel sites and four test sites, which are embedded in the reflector tank surrounding the reactor core and filled with heavy water. The tank, which provides a large region of high thermal neutron flux, accommodates various vertical and horizontal experimental holes. The reactor operation cycle is 28 days. The reactor has inherent safety characteristics such as heat removal by natural circulation and reactor trip by gravity drop of shut-off rods.

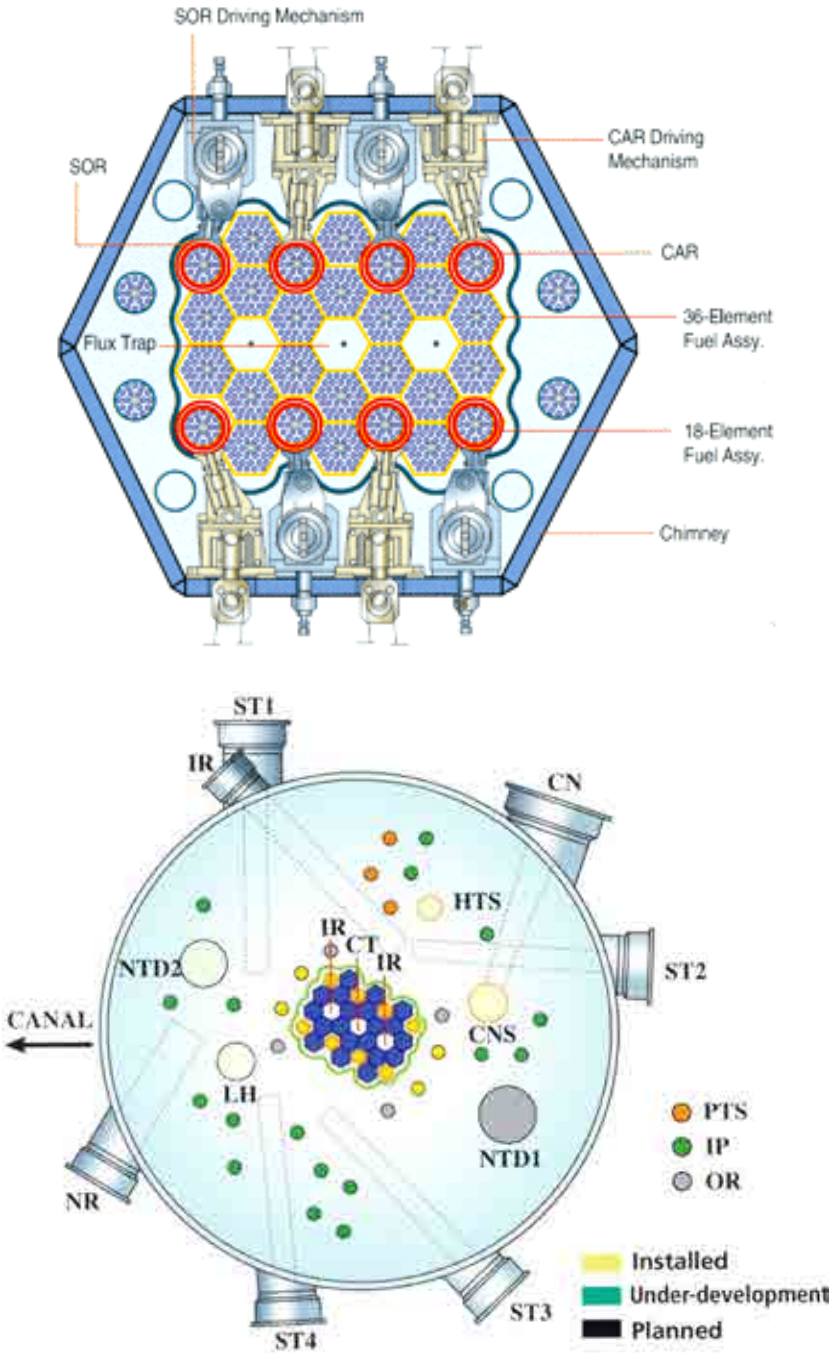

IR+CT: capsule irradiation; SOR: shut-off rod ; CAR: control absorber rod ; NTD: neutron transmutation doping.

FIG. 7.99. Hanaro core cross-section.

The primary coolant enters the inlet plenum and flows upward through fuel channels for cooling. The coolant is gathered in the chimney, and then exits through two outlet nozzles. Each of the two loops has a 300 kW pump, a 14 MW plate type heat exchanger, and a check valve. The two loops combine at a returning line into the core. For the removal of decay heat, two natural circulation modes are available; loop and pool natural circulation. When the density driving force is not enough for natural circulation, the core is cooled by pool natural circulation through two flap valves. The secondary coolant is cooled by a cooling tower with four cooling fans.

The quantity of uranium in one fuel element is 69.1 grams in a standard core element and 51.4 g in a reduced core element. The reduced core elements are introduced to have a uniform power distribution within a fuel assembly and located at the outermost ring of the hexagonal fuel assembly. There are two types of fuel assemblies required for HANARO, hexagonal fuel assemblies having 36 elements and circular ones having 18 elements.

7.9.2. Irradiation programme for Korean HTGR fuel

Within the framework of the Korean Nuclear Hydrogen Production Technology Development and Demonstration (NHDD) Project [292], a series of irradiation tests will be required for a qualification of the technology and the products [67]. In KAERI, long term plan for the irradiation tests of the coated particle fuel is currently being evaluated and established along with the technology development for fuel manufacturing and design as well as performance analysis.

Recently, KAERI performed a preliminary analytical work for the feasibility of irradiation test of coated particle fuel in HANARO which is the only research reactor in Republic of Korea. Figure 7.100 shows one of the results obtained from the preliminary analytical work performed for the temperature distribution in the graphite rod clad with Zircalloy-4 or stainless steel where the coated fuel particles would be loaded in nine evenly arranged holes. More detailed irradiation condition is currently being established and evaluated.

A non-instrumented capsule for use in the irradiation test should be designed to provide a high temperature condition for the TRISO coated particle fuel held in the capsule and to withstand the thermal load imposed to the metallic tubes surrounding the test specimen. Moreover, the capsule should satisfy a variety of requirements related to the nuclear and the geometrical characteristics of the reactor core. The capsule considered in this design study has a cylindrical shape and mainly consists of the end plugs, external tubes, and specimens. The cross-sectional schematic view of the test capsule is shown in Fig. 7.101, left [293]. Test fuels in their compact forms are located in the middle of the capsule. The encapsulating tubes are made of molybdenum, and the gaps are filled with neon gas. When the capsule is loaded into the reactor, it works as a heat source by gamma ray irradiation. Temperature of the moderator surrounding the capsule is 40ºC. The irradiation test capsule with a diameter not to exceed 16 mm should provide a temperature circumstance as high as 950°C to assure the actual core condition for the TRISO compact fuel. The tubes that encapsulate the test specimen should withstand the thermal load imposed to the metallic tubes.

The heat flux from the TRISO compact fuel was the sum of gamma heat from the matrix and the decay heat from the TRISO fuels retained in the compact. Figure 7.101, right, shows a 2D finite element model for a thermal analysis of the test capsule. For a heat transfer analysis of the capsule, the gap conductance between the gaps and the convective heat transfer to the moderator should be considered. The gap conductance depends on the gap size, surface roughness, gas conductivity, surface temperatures, and the gas pressure.

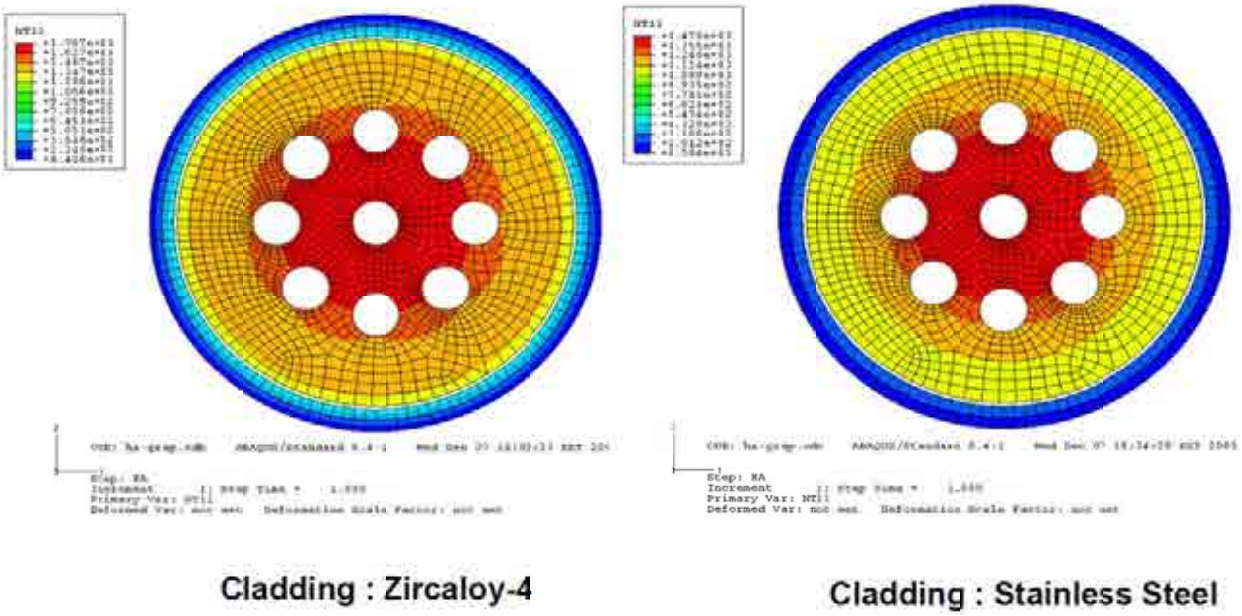

FIG. 7.100. Temperature distribution in graphite rod with different cladding materials and with coated fuel particles in holes.

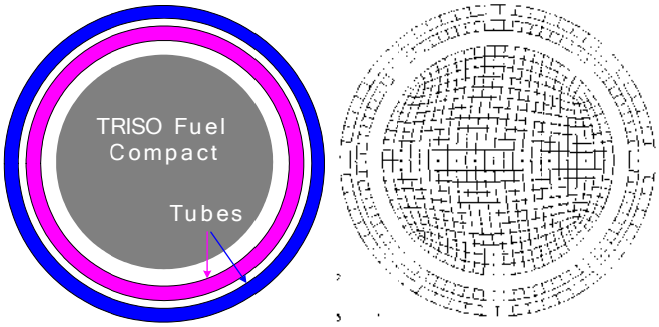

FIG. 7.101. Schematic view of capsule considered for irradiation test (left) and finite element model of capsule.

Thermal sensitivities of the compact fuel and the inner tube were investigated as a function of the heat flux and the diameter of the compact fuel. The design variables considered in this parametric study, the heat flux and the diameter of the compact fuel were chosen as they had been proven critical in a previous design study which had been carried out with loose particles. The results showed that a capsule with a compact fuel with the radius of 5.4 mm and the heat flux of 7.64 MW is most desirable in terms of the thermal integrity of the capsule. A heat flux of 7.64 MW can be obtained from a compact fuel with 21 TRISO particle fuels. The capsule with this design assured a temperature of 956°C for the compact fuel. The temperature of the inner tube was 345°C [293].

8. CORE HEATUP SIMULATION TESTING AND OTHER PIE OF HTGR FUEL

8.1. TEST BACKGROUND

The central aspect of the safety philosophy for an HTGR is the retention of fission products — particularly those of the iodine nuclides — in the fuel elements during operation and accidents. For this reason, the determination of the number of damaged particles constitutes

the central objective of measuring the fission gas release in the reactor and in the extensive post-irradiation examinations under accident conditions. In modern production methodologies, the heavy metal contamination of fuel elements is kept very low. Consequently, solely the number of defective particles establishes fission gas or iodine release.

During a loss-of-forced-convection accident, the temperature in the core of an HTGR will increase. The amount of this increase depends on the geometrical design of the reactor and the nature of the accident. The KÜFA facility was designed specifically to simulate these accident conditions and to quantatively measure fission product release in this environment. For the case of the German HTR-Modul concept, relatively low accident temperatures of less than 1600°C have been anticipated.

With the increase of the core temperature above normal operation, fission products may be released from the fuel elements into the primary circuit. For a conservative assessment of the fission product release, the peak temperature conditions of a fuel element in the reactor core have to be simulated. The relevant fission products to be measured and their relevance in case of accident are given in Table 8.1.

TABLE 8.1. RADIOLOGICALLY RELEVANT FISSION PRODUCT NUCLIDES

Fission product	Half life	Relevance
I-131	8.021 days	Greatest significance for design and licensing, important for heatup accident conditions
I-133	20.81 hours	
Cs-134	2.066 years	Long term behaviour after extreme accidents and in risk analyses
Cs-137	30.07 years	
Sr-90	28.78 years	Long term behaviour after extreme accidents and in risk analyses, formed by Kr-90 in the primary circuit
Ag-110m	249.8 days	Small inventory, important for maintenance
Ag-111	7.454 days	Important for normal operation and accident conditions
Kr-85	10.783 years	Indicator of particle coating failure and conservative upper limit for iodine release, important for waste management
Kr-90	32.32 seconds	Precursor of Sr-90
Xe-133	5.247 days	important for normal operation conditions
Xe-137	3.818 min	Precursor of Cs-137
H-3	12.323 years	important for waste management
C-14	5730 years	important for waste management

The relative characteristics of the metallic fission products of radiological interest for LEU UO_2 TRISO fuel under HTGR service conditions are as follows:

- Silver is known to begin to be released from TRISO fuel at temperatures above 1000°C of normal operating temperatures, and to be released from intact particles in significant fractions after several days at 1600°C. A part of the silver may be released from the fuel in form of the stable (inactive) ^{109}Ag and no longer be subjected to an activation to ^{110m}Ag. Silver deposits in graphite at 900°C and plates out on metallic surfaces at temperatures of 800°C and diffuses into the bulk metal, where it is effectively captured. As a result, silver does not present an important concern with regard to offsite dose, but can be a dominant contributor to occupational dose depending on component maintenance requirements.
- Strontium is retained to a large extent in oxide kernels during normal operation even when coatings are defect and is slowly released at temperatures beyond modular HTGR accident conditions (i.e. approaching 1800°C for several days). Additionally, it is strongly adsorbed in matrix material and little is released from spherical fuel elements. Different from other species, it is difficult to measure and the results shown have an uncertainty of an order of magnitude compared to around 10% for others.
- Caesium is also released from particles with defective silicon carbide layers in normal operation and can be released from the fuel spheres depending on the local conditions. However, there is a significant delay in release from the sphere due to holdup in the matrix. In the AVR, the LEU UO_2 TRISO spheres were typically net absorbers of caesium due to the low silicon carbide defect fractions.

The primary isotopes of caesium of interest are ^{134}Cs and ^{137}Cs, whose inventories developed differently as a function of burnup, but whose release fractions under accident conditions are very similar. The combination of ^{85}Kr and ^{137}Cs data in the early phase of the heating tests allow determination of both through-coating failure fractions and failure fractions of particles with silicon carbide defects and an intact pyrocarbon layer.

8.2. FUTURE PIE PROGRAM IN CHINA

8.2.1. Post-irradiation examination (PIE) for the irradiation test of HTR-PM fuel

To study irradiation performance of the fabricated fuel, an in-pile irradiation test will be performed to qualify the fabricated fuel for application in the HTR-PM. Fuel qualification is an essential part of the licensing process for the HTR-PM. This irradiation test will start in 2011. After in-pile irradiation test, the following post-irradiation examinations will be performed:

- Three irradiated fuel pebbles will be investigated using the KÜFA facility at ITU, Karlsruhe. The heating curve will be decided before the beginning of the tests. The maximum heating temperature will be 1800°C up to 150 hours.
- One KÜFA-tested and one non-KÜFA-tested fuel pebbles will be characterized. Ceramography samples will be obtained by drilling a bore hole through the centre of the pebble. The drilled-out cylinder shall be cut into three sections representative of outer, mid-radius and central zones of the pebble.
- Furthermore, intact and defective coated particles, possibly from both a KÜFA-tested and a non-KÜFA-tested pebble will be characterized. Sorted-out particles suitable for ceramography will be obtained by electrochemical deconsolidation and

IMGA measurements. Ceramography samples with intact particles or defective particles will be mounted and polished for OM and SEM examination.

- Burnup measurements will be performed using ^{137}Cs gamma spectrometry.
- The pebble will be bored with two small holes for the mounts to aid uniform dissolution in nitric acid under anodic polarization. The deconsolidation of one pebble will include two stages. In the first stage, a cylinder through the fuel sphere centre with approximately 20 mm diameter will be obtained. In the second stage, this cylinder will be deconsolidated step by step. In each step, the content of various solid fission products will be determined after separating the graphite matrix powder and the coated particles. The coated particles will be washed, dried and collected. Some particles will then be selected for ceramographic embedding, polishing and examination.
- The coated particles from electrochemical deconsolidation will be characterized by IMGA. This should reveal the number of failed particles and their condition/fission product release.

8.2.2. PIE for the future HTR-PM fuel

In order to study the post-irradiation performance of HTR-10 fuel, HTR-PM fuel, and some irradiation tests of HTGR fuel, the construction of a hot cell facility for PIE of the HTGR fuel is currently planned. This hot cell facility includes burnup measurement, electrochemical deconsolidation of fuel pebble, KÜFA test system on fuel pebbles, ceramography on fuel pebbles and coated fuel particles, and optical and scan electron microscopes, and will be built in INET of Tsinghua University.

8.2.2.1. Hot cell line

This hot cell facility will consist of five hot cells:

Cell 1: Receiving and burnup measurement cell
The PIE in this cell will include:

- Containers with radioactive samples will be transported into the cell. After opening the box from inside by manipulator, the top lid of the transport container can be removed by the cell crane and the samples will be unloaded;
- Burnup measurement of the irradiated fuel spheres;
- Dimensional measurement of the irradiated fuel spheres;
- Weight measurement of the irradiated fuel spheres;
- Visual inspection of the irradiated fuel spheres;
- Equipment for cutting and lathing.

Cell 2: KÜFA test cell on fuel spheres
In order to study the fuel performance under the accident conditions, the irradiated fuel pebbles will be investigated using the KÜFA in this cell.

Cell 3: Electrochemical deconsolidation of fuel pebble and IMGA for the irradiated
The electrochemical deconsolidation of the irradiated fuel pebble will be carried

out in this cell. The coated particles will be washed, dried and collected. Some particles will then be selected for IMGA. The coated particles from electrochemical deconsolidation will be characterized by IMGA in this cell. This should reveal the number of failed particles and their condition/fission product release.

Cell 4: Metallography cell
Rotating grinders, polishers, ultrasonic cleaning bath, small cutting device, etc will be installed in this cell.

Cell 5: Microscope cell
One scanning electron microscope and some optical microscopes will be installed in this cell.

8.2.2.2. Operating and service area

The operating area is in front of the hot cell line. This area has a personal entrance/exit leading to the change rooms. A connection to the first floor gives access to the area for auxiliary systems for running the cell equipment such as cooling systems, pressure supply, pumps, ventilation system etc. For material reception the access is via the main lock and the door in the side of cell 1. The materials access can be done by a monorail crane.

The service area behind the hot cell line can be used for the storage of containers and contaminated materials. The decontamination shop for repairing contaminated equipment will be in this area.

8.3. PIE ACTIVITIES IN THE EUROPEAN UNION

8.3.1. Former tests in the KÜFA at FZJ

Demonstrating the capability of spherical fuel elements to withstand a severe depressurization accident with no measurable loss of fission product was a primary objective of the German fuel development programme. Since the 1970s, irradiated fuel elements retrieved from AVR and from MTR tests have been investigated in accident simulation tests. Prior to the mid 1980s, the temperature margins explored were up to 2500°C where fission product release was massive [294].

In response to the reactor designer's requirement for a passively safe HTGR, the KÜFA (= KÜhlFingerApparatur, i.e. cold finger device) furnace was designed and installed at the Hot Cells of the Forschungszentrum Jülich for high precision, on-line measurements of fission product release from HTGR fuel under simulated accident conditions. Using this device, the release behaviour of fission gases (Xe, Kr) and solid fission products (Cs, Sr, Ag, etc) from irradiated fuel under off-normal conditions could be tested and evaluated up to 1800°C [177, 295, 296]. This facility made it possible to demonstrate that modern LEU UO_2 TRISO coated fuel particles retain all safety relevant fission products up to 1600°C at a level not exceeding release under normal operating conditions, which in itself is very low.

The maximum expected fuel element temperature evolution in a depressurized loss-of-forced-coolant accident in a small modular HTGR is shown in Fig. 8.1 [12]. The maximum fuel temperature limit is set at 1600°C based upon the estimated maximum core temperature of ~1500°C plus a reasonable estimate of the effect thermal property uncertainties have on this maximum temperature estimate. The figure shows the temperature programme, with which

the conditions in a core heatup accident after depressurization were generally simulated in the heating experiments given in Table 8.2. For testing purposes, of interest for core heatup simulation testing is the temperature range of 1600–1700–1800°C as illustrated in Fig. 8.1.

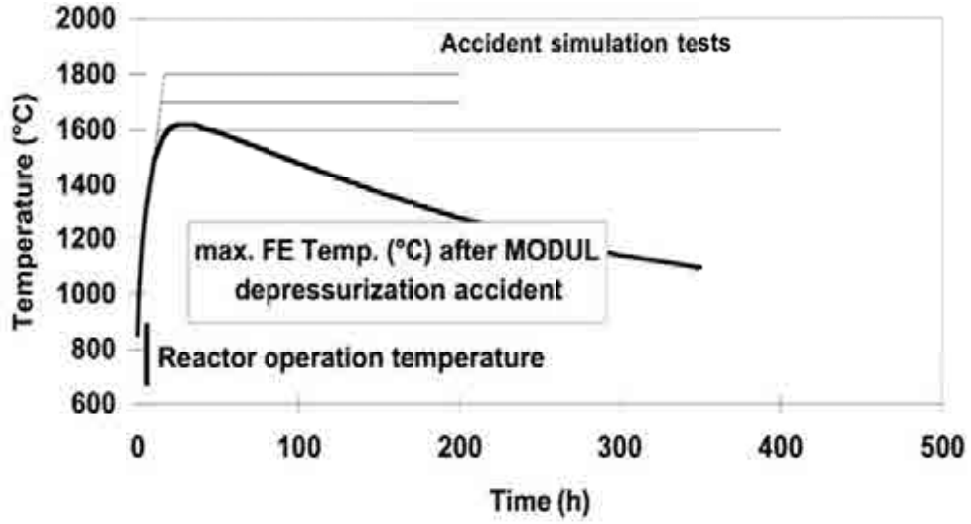

FIG. 8.1. Temperature evolution during a loss-of-coolant accident in a small HTGR and in the heating tests.

8.3.1.1. Release from bare fuel particle kernels

Little fission product retention can be expected in exposed UO_2 fuel kernels at elevated temperatures. Figure 8.2 shows that the release of silver, xenon, iodine and caesium quickly approaches 100% during a 1600°C heating test [177]. Beginning in the 30 hours heatup phase to the test temperature, significant release already begins to occur for ^{131}I, ^{133}Xe and ^{137}Cs. After 50 to 100 hours at 1600°C nearly all of the inventories of these fission products have been released from the exposed UO_2 fuel kernels. Only the fission product ^{90}Sr is strongly retained within the oxide kernels at this temperature (but this is not the case for carbide kernels). The primary barrier to the volatile fission products such as iodine, xenon and caesium is by the coating layers on TRISO coated particles, especially the SiC layer.

Measurement of ^{131}I ($T_{1/2}$ = 8.02 d) release from various fuel configurations during heating at 1600°C shows three different types of release behaviour:

(1) exposed UO_2 fuel kernels with ~100% ^{131}I release;
(2) irradiated fuel elements with TRISO coated fuel particles that were contaminated in the AVR by old failed fuel from the 1960s and 1970s; ^{131}I release behaviour is at 10^{-5} level;
(3) fuel elements with modern TRISO coated fuel particles; ^{131}I release behaviour is at the 10^{-9} to 10^{-8} level.

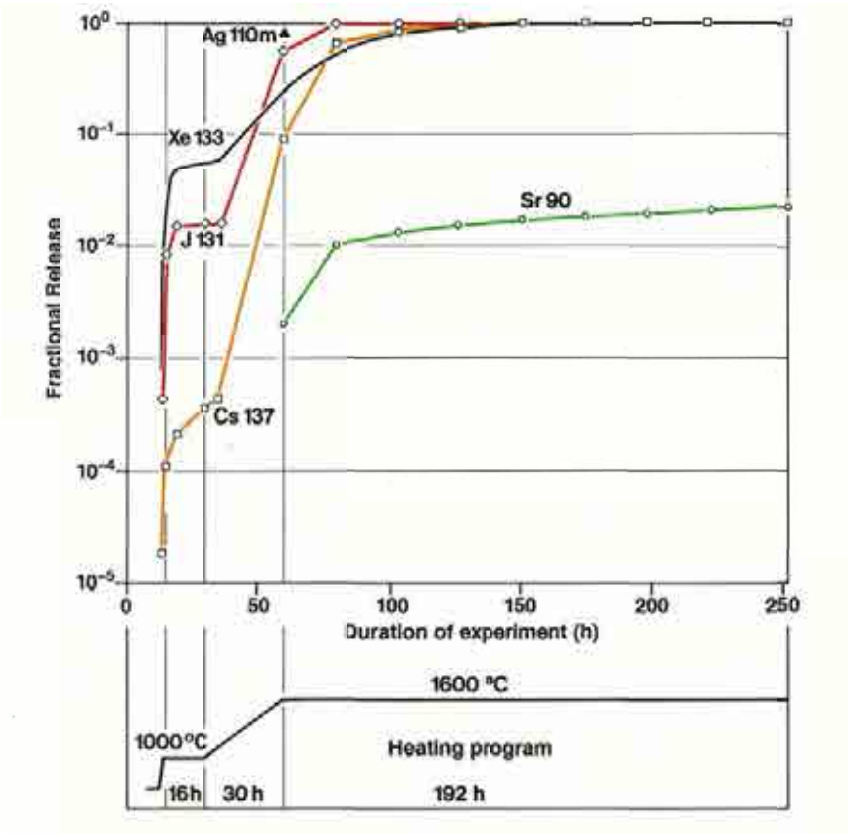

FIG. 8.2. Fission product release from exposed UO_2 kernels during heating test at 1600°C.

8.3.1.2. Release from irradiated spherical fuel elements

In the period 1985 to 1994, a number accident simulation tests in the range of 1600° to 1800°C were carried out in the KÜFA facility. Eighteen of these tests, four on irradiated fuel elements from accelerated irradiation tests (HFR-K3 and FRJ2-K13) and 14 on GLE-3 fuel elements irradiated in the AVR, are listed in Table 8.2. This table identifies the fuel elements tested, their irradiation history, accident temperature simulation and duration, and the fission product results of the accident simulation testing. All of the fuel elements identified here contained modern LEU UO_2 TRISO coated fuel particles.

In the unrestricted core heatup simulations tests with irradiated spherical fuel elements, no single particle failure or any noticeable caesium or strontium release were observed during the first few hundred hours in any of the 1600°C heating tests. The number of particle failures and fission product release do increase as the accident simulation temperatures rises to 1700° and 1800°C. Figures 8.3 and 8.4 show the measured time dependent krypton and caesium release profiles during isothermal heating tests at 1600° to 2100°C. As representatives for a whole series of fission products, there is full retention at 1600°C for the accident specific first hundred hours or more (with ^{110m}Ag being an exception). In particular,

- caesium is retained at 1600°C in kernel, by SiC and by the A3 matrix of the fuel element with SiC providing for the strongest retention. This retention, however, can only be guaranteed by modern high quality TRISO coatings. At 1800°C, there is no delay by the kernel and the matrix, but SiC also becomes more permeable to most fission products.

- krypton is always released later than caesium, because of the additional retention by dense, intact pyrocarbon layers. Krypton releases indicate zero particle failures at 1600°C and one single particle failure in the 1700°C test. At ~1800°C, more failures are observed.
- strontium is retained much better in oxide kernels and the sphere matrix than caesium. Therefore, strontium release comes generally later than caesium, although its retention by SiC might not be as good.
- even in high quality SiC of modern TRISO coatings, silver is already released at irradiation temperatures above 1100°C and release fractions are approaching 100% in the accident condition heating tests.

An attempt to interpret fission product release in terms of particle defects (manufacture) and accident specific failure is given in Table 8.2 [177].

If the maximum burnup in the fuel element is kept strictly below 11% FIMA, as is typical for current pebble bed concept HTGR designs, the allowable fuel temperature limit may be higher than 1600°C. This remains to be established with new experiments. If the burnup of UO2 TRISO coated particle fuel is pushed to ~15% FIMA, fuel temperature must be rigorously limited to ≤ 1600°C (Fig. 8.5) [296].

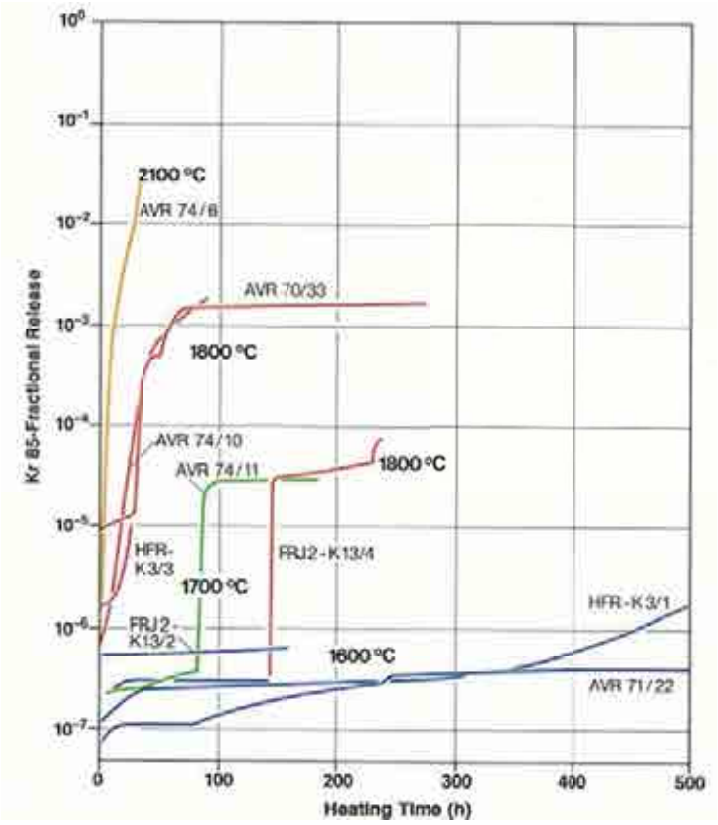

FIG. 8.3. Krypton release during tests with irradiated spherical fuel elements at 1600 to 2100°C.

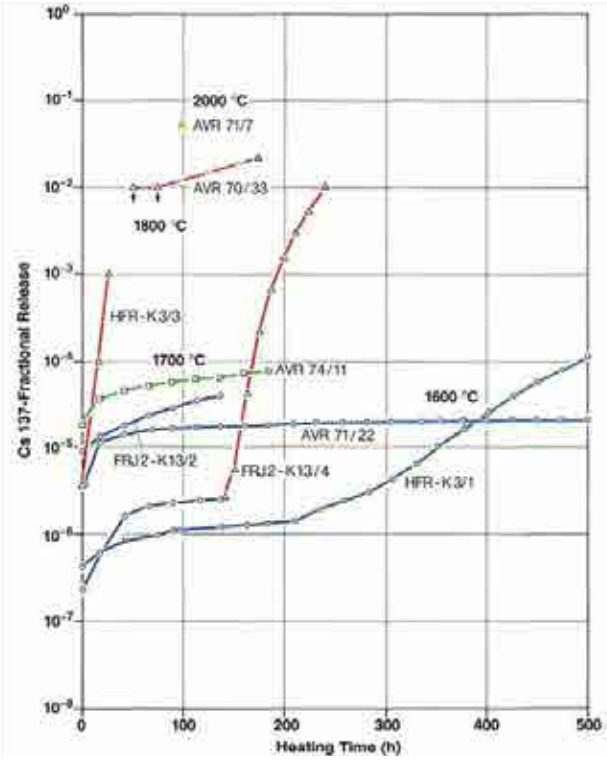

FIG. 8.4. Caesium release from heated spheres as a function of heating times up to 500 hours.

TABLE 8.2. RESULTS OF ACCIDENT SIMULATION TESTS WITH IRRADIATED FUEL ELEMENTS CONTAINING UO_2 TRISO PARTICLES

Fuel element	Burnup (% FIMA)	Fast fluence (10^{25} n/m^2 E>0.1 MeV)	Heating test		Number of failed particles[b]		Fractional release			
			Temp (°C)	Time (h)	manuf.	heating	Kr-85	Cs-137	Sr-90	Ag-110m
AVR 71/22	3.5	0.9	1600	500	no	no	4.0×10^{-7}	2.0×10^{-5}	5.3×10^{-6}	9.0×10^{-4}
HFR-K3/1	7.7	3.9	1600	500	no	no	1.8×10^{-6}	1.1×10^{-4}	1.8×10^{-7}	2.7×10^{-2}
FRJ2-K13/2	8.0	0.1	1600	138 (160)	no	no	6.4×10^{-7}	3.9×10^{-5}	3.3×10^{-7}	2.8×10^{-3}
AVR 82/20	8.6	2.4	1600	100	no	no	1.5×10^{-7}	6.2×10^{-5}	3.8×10^{-6}	4.4×10^{-3}
AVR 82/9	8.9	2.5	1600	500	no	no	5.3×10^{-7}	7.6×10^{-4}	8.3×10^{-5}	1.9×10^{-2}
AVR 89/13	9.1	2.6	1620[a]	~10	no	no	2.0×10^{-7}	1.1×10^{-5}	—	8.3×10^{-4}
			1620[a]	~10		no	1.3×10^{-9}	1.4×10^{-6}	—	1.5×10^{-2}
AVR 85/18	9.2	2.6	1620[a]	~10	no	no	1.4×10^{-7}	1.3×10^{-5}	—	6.5×10^{-3}
AVR 90/5	9.2	2.7	1620[a]	~10	no	no	1.9×10^{-7}	9.0×10^{-6}	—	1.1×10^{-3}
			1620[a]	~10		no	6.6×10^{-9}	3.3×10^{-6}	—	9.0×10^{-4}
AVR 90/2	9.3	2.7	1620[a]	~10	1	2	1.0×10^{-4}	4.6×10^{-5}	—	3.7×10^{-2}
AVR 90/20	9.8	2.9	1620[a]	~10	2	3	2.4×10^{-4}	6.5×10^{-6}	—	7.6×10^{-2}
AVR 74/11	6.2	1.6	1700	184.5	1	no	3.0×10^{-5}	7.6×10^{-5}	8.3×10^{-5}	3.2×10^{-2}
AVR 91/31	9.0	2.6	1700[a]	~10	2	18	1.2×10^{-3}	2.4×10^{-3}	—	6.2×10^{-1}
FRJ2-K13/4	7.6	0.1	1600	138	no	no	3.0×10^{-7}	2.5×10^{-6}	2.0×10^{-8}	4.5×10^{-4}
			1800	100		2	7.2×10^{-5}	9.9×10^{-3}	1.4×10^{-3}	5.3×10^{-1}
AVR 88/33	8.5	2.3	1600	50	no	no	1.0×10^{-7}	1.2×10^{-4}	8.4×10^{-6}	1.2×10^{-3}
			1800	20		~4	1.8×10^{-4}	4.6×10^{-4}	2.3×10^{-4}	2.1×10^{-1}
AVR 88/15	8.7	2.4	1600	50	no	no	6.3×10^{-8}	1.2×10^{-5}	—	9.1×10^{-3}
			1800	50	1	~6	2.9×10^{-4}	1.4×10^{-2}	1.1×10^{-2}	8.1×10^{-1}
AVR 70/33	1.6	0.4	1800	175	no	28	1.7×10^{-3}	2.2×10^{-2}	—	—
AVR 74/10	5.5	1.4	1800	90	no	30	1.8×10^{-3}	7.9×10^{-2}	—	—
AVR 76/18	7.1	1.9	1800	200	no	~3	1.2×10^{-4}	4.5×10^{-2}	6.6×10^{-2}	6.2×10^{-1}
AVR 88/41	7.6	2.0	1800	24	no	no	2.4×10^{-7}	1.5×10^{-4}	1.2×10^{-4}	7.7×10^{-2}
HFR-K3/3	10.2	6.0	1800	100	no	~12	6.5×10^{-4}	5.9×10^{-2}	1.5×10^{-3}	6.7×10^{-1}

[a] simulating calculated core heatup curve [b] out of 16 400 particles — data not available

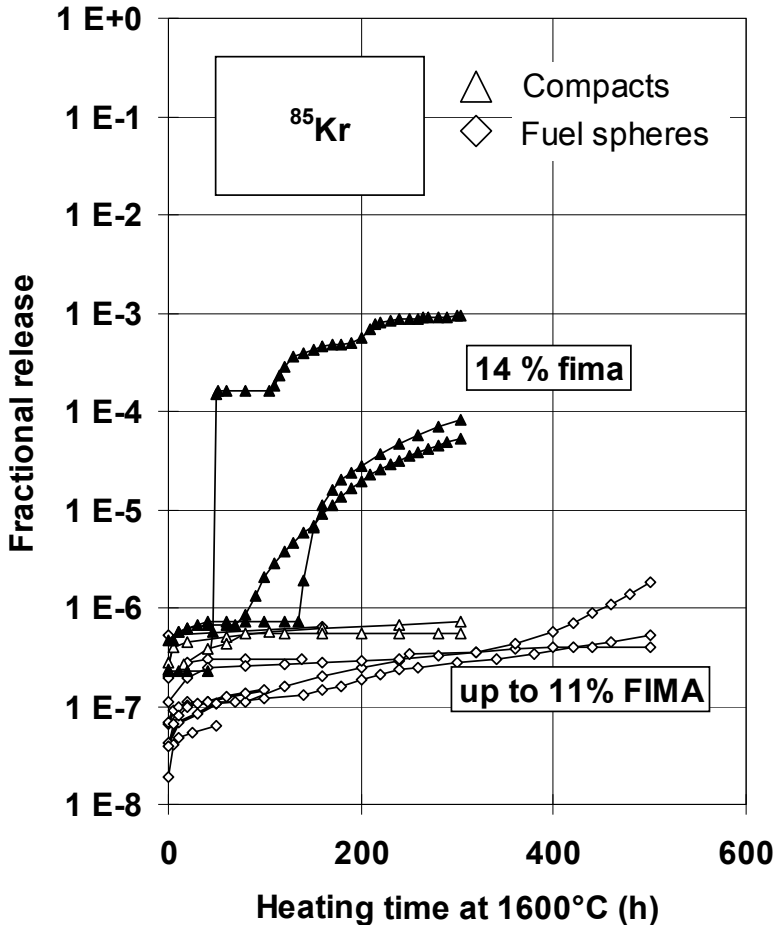

FIG. 8.5. Krypton-85 release at 1600°C from compacts with 11 to 14% FIMA burnup in comparison to spherical fuel elements with 3.5 to 9% FIMA burnup.

8.3.2. New KÜFA facility for heating tests

8.3.2.1. Description of facility

An upgraded version of the KÜFA has been installed in the hot cells of the Institute for Transuranium Elements (ITU), Karlsruhe, Germany. After commissioning between 2002 and 2005 and several cold tests on all subsystems, the new KÜFA facility is in operation since 2006.

The basic function of the KÜFA (Fig. 8.6) is to heat the fuel elements up to the expected temperature in a dynamic helium atmosphere, and to collect and measure the fission product release during a specified time period. In the current upgraded version, temperatures up to 2000°C can be achieved.

The fuel element is supported by three pins in the centre of a tantalum tube (gas stream cylinder) placed inside the furnace. Helium flows through this tube from the bottom to the top. The tantalum tube and the fuel element are heated by an electrical resistance heater likewise made of tantalum. A W/Re thermocouple placed near the specimen measures the actual temperature during the heating tests. This thermocouple can be replaced if needed and serves simultaneously for the electronic control of the temperature of the furnace.

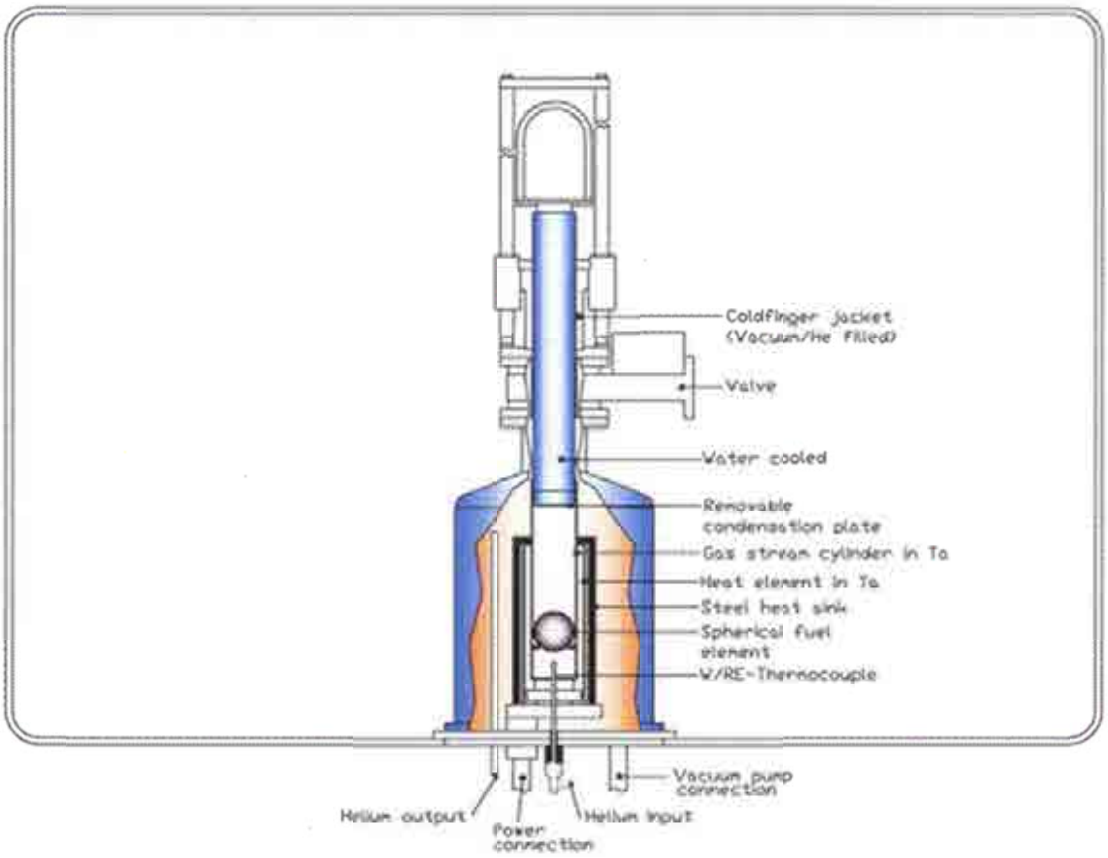

FIG. 8.6. Cold finger apparatus (KÜFA).

8.3.2.2. Measurement of fission gas release

Through the analysis of the release curves, individual failed particles in the fuel element time can be detected as a function of temperature and heating time. The relevant gaseous radioactive isotope ^{85}Kr (see Table 8.1) is important for this measurement. The release of krypton fission gas is also indicative of the release of other fission products, like iodine, which are difficult to measure directly but is conservatively assumed to be released to the same extent as krypton.

The furnace is installed in an alpha-tight box in a hot cell which also contains the filters for the helium circuit (Fig. 8.7). Helium carries the fission gases into cold traps where ^{85}Kr and other stable noble gases are trapped. Here they are adsorbed on active charcoal filters at liquid nitrogen temperature. The activity in the cold trap is measured by on-line gamma spectrometry continuously throughout the test. In principle, only the long-lived ^{85}Kr can be detected. However, as long as the cooling period of the fuel elements is less than 4 to 8 weeks, measurements of ^{133}Xe are possible as well. The cold traps are installed outside the hot cell. After the noble gases are removed, the helium is routed back into the hot cell and released, in a controlled manner, through the ventilation system. The two cold traps are placed in a room beneath the hot cell. The second cold trap is to ensure all the ^{85}Kr activity is collected and measured. As soon as activity is detected in the second cold trap, the first is changed.

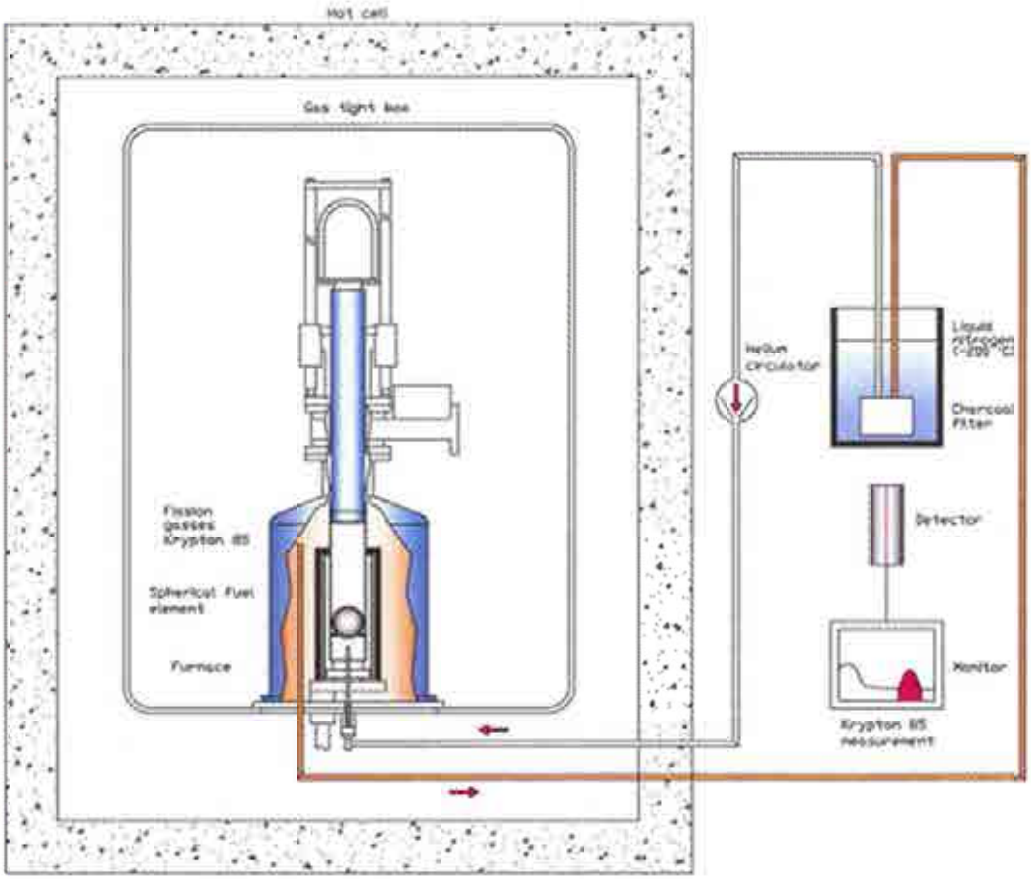

FIG. 8.7. Schematic of the gaseous fission products release measurement.

8.3.2.3. Measurement of solid fission product release

The determination of solid fission product release is slightly more difficult than that of the chemically inert fission gases. At high temperatures, they can get into the coolant by migration/diffusion and subsequent gaseous desorption, first from the surface of the coated particles and afterwards from the surface of the fuel element. On the other hand, such fission products are re-deposited by adsorption on cooler surfaces, and this deposition mechanism is exploited for trapping solid fission products in the cold finger test rig.

To detect the release of solid fission products, a water cooled cold finger (Fig. 8.8) protrudes into the hot tantalum tube just above the hot cell [254]. At the end of this cold finger, a replaceable condensation plate is held in place. Solid fission products released from the fuel element are deposited on this plate which is held at a temperature of less than 100°C, typically 40–80°C depending on the testing temperature. This temperature is much lower than the specimen temperature which is in the range of 1600–2000°C.

During testing, the cold finger can be removed from the furnace through an air lock system without requiring cool-down of the specimen. Helium circulation is maintained during the condensation plate changes, which assures the continuous monitoring of fission gas relrease from the specimen and the detection of any coated particle failure.

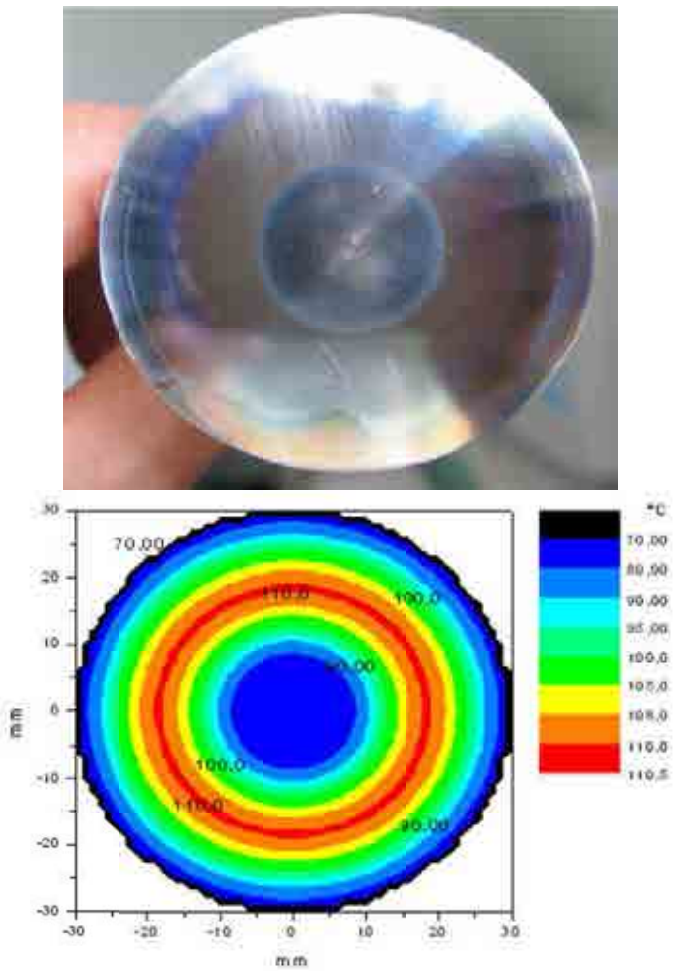

FIG. 8.8. Water cooled cold finger in KÜFA.

After replacing the condensation plate, the cold finger is returned to its position just above the hot zone of the furnace. The plate is normally changed once or twice a day but may be changed more frequently, if necessary. The changing procedure lasts only few minutes and requires relatively easy manipulation.

The used condensation plates are taken out of the hot cell to be measured by gamma spectrometry in a low background laboratory (Fig. 8.9). Measurement of gamma emitters such as ^{137}Cs, ^{134}Cs and ^{131}I is relatively simple, because their individual energy lines can identify them. Strontium-90, a beta-emitter nuclide, has to be separated chemically from other fission products for this determination. Since strontium emits beta rays with the highest energy, the activity can also be estimated using a scintillation counter after a special calibration. This procedure is relatively complicated and in the past has not yielded satisfactory results [296]. Alternatively, the condensation plates can be leached in nitric acid and the resulting solution analysed using an 'inductively coupled plasma mass spectrometer' (ICP-MS). Based on past experience gathered at FZJ, the KÜFA facility can detect very low fractional releases down to 10^{-8} [296].

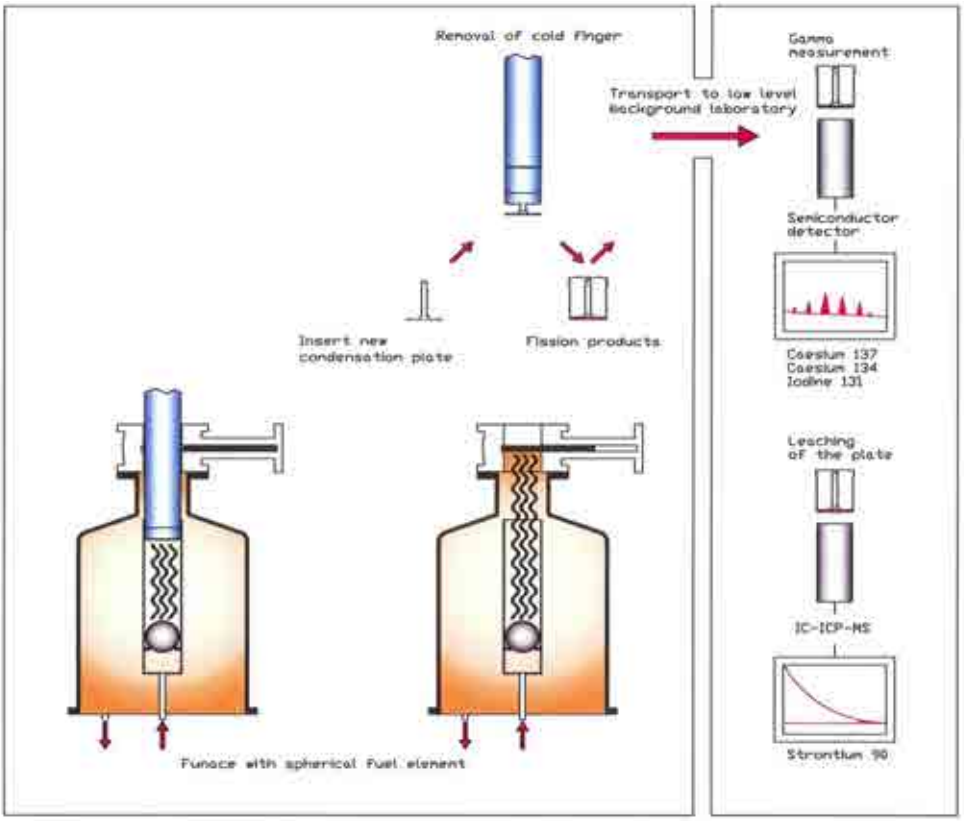

FIG. 8.9. Schematic of the solid fission products measurement.

8.3.2.4. Current heating programme at ITU

(a) Delivery of irradiated samples

Samples already irradiated in the Dido and AVR reactors in Jülich and in the HFR Petten, have been transferred to the hot cell installation of the ITU in Karlsruhe, to be tested using the new KÜFA installation. Irradiation details are given in Table 8.3.

(i) AVR 73/21

A first spherical fuel element irradiated in the AVR reactor over estimated 235 efpd with low burnup (2.5% FIMA) was loaded into the furnace and a heating programme up to 1800°C was started. The fuel element with the code name AVR 73/21 was from the GLE-3 production with 10 g of heavy metal. Objective of the test was to prove that all systems and the data acquisition work properly under hot conditions and to gain an initial experience of the KÜFA operation. The heating programme was divided into two phases — one phase at 1600°C for 5 h and a second phase at 1800°C for 5 h. Since, burnup, irradiation temperature and fast fluence were relatively low and since this type of fuel was known to have excellent retention ability for fission products, no significant release of fission products was expected. The ^{85}Kr release during the test was below the detection limit of the apparatus. In order to detect solid fission products, two cold plates were introduced and analysed by gamma spectrometry after the test. Results could be obtained for ^{137}Cs but apparently there was a contamination of the cold plate container originating from the hot cell floor. After this test the procedure was changed by implementing the replacement of all containers after transferring the cold plates from the hot cell into a clean environment.

TABLE 8.3. FUEL ELEMENTS TRANSFERRED FROM FZJ TO JRC-ITU

Sample No	Type	Fuel element No	Enrichment (%)	End of irradiation	Burnup (% FIMA)	Fast fluence (10^{25} n/m^2)
1	HFR-K5	1	10.6	16.05.94	6.7	4.0
2		2	10.6		8.8	5.8
3		3	10.6		9.1	5.9
4		4	10.6		8.7	4.9
5	HFR/K6	1	10.6	04.05.93	7.2	3.2
6		2	10.6		9.3	4.6
7		3	10.6		9.7	4.8
8		4	10.6		9.2	4.5
9	FRJ2-KA2	1	16.76	27.04.90	1.84	~0.0
10		2	16.76		2.00	~0.0
11		3	16.76		2.02	~0.0
12	AVR-GLE 3	74/16	9.82	08.02.85	3.2	0.5
13		74/18	9.82		4.8	0.8
14		73/21	9.82	07.02.84	2.5	0.3
15		73/23	9.82		2.7	0.3
16	AVR-GLE 4	73/22	16.76	07.02.84	3.4	0.3
17		87/6	16.76	19.11.88	3.51	0.3
18		87/7	16.76		3.53	0.3
19		87/8	16.76		3.53	0.3
20		87/9	16.76		3.56	0.3
21		87/10	16.76		3.51	0.3

(b) First heating tests with the new KÜFA at ITU.

(ii) AVR 74/18

A second AVR GLE-3 fuel element, AVR 74/18, with a medium burnup of 4.8% FIMA was heated in two phases up to 1600°C for 100 h and then up to 1800°C for 100 h (red curve in Fig. 8.10) [297].

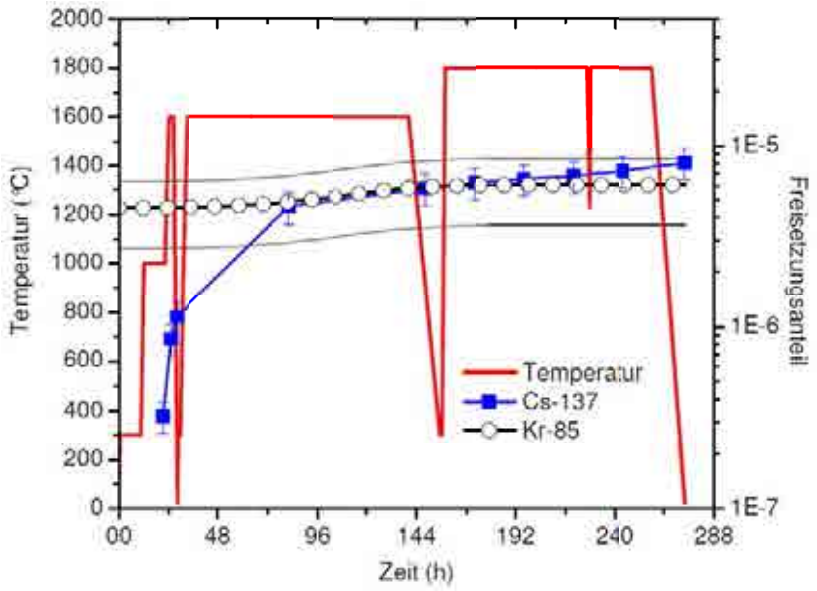

FIG. 8.10. KÜFA-II heating test AVR 74/18.

The heating programme followed the full testing procedure including the reactor simulation at 1050°C for 10 h. From 1050°C, the temperature was increased at 47°C/h to 1600°C according to the HTR-Modul accident simulation. The ^{137}Cs inventory of AVR 74/18 at the beginning of the KÜFA test was determined using gamma spectrometry. As can be seen in the figure, a slightly increasing release of ^{85}Kr could be detected reaching 5.9×10^{-6} after the 1600°C and 6.1×10^{-6} after the 1800°C heating phase. This krypton probably originates from contamination in the matrix graphite grains. The release of ^{137}Cs increased following a typical curve during both heating phases up to 10^{-5} fractional release.

(iii) HFR-K6/2

The irradiation test HFR-K6 (see Section 7.2.2) was conducted from 1990 to 1993 in the HFR Petten [247] in order to qualify the final fuel element design for the HTR-Modul reactor (proof test). Four spherical fuel elements were irradiated for 633 efpd. The fuel element HFR-K6/2 had a nominal burnup of 9.3% FIMA and HFR-K6/3 had a nominal burnup of 9.7% FIMA.

The heating test of HFR-K6/2 was performed in two phases. The first heating phase was at 1600°C for 100 h, during which the furnace inadvertently shut down twice; the second heating phase was at 1800°C for 200 h (see red curve in Fig. 8.11) [297]. The ^{85}Kr activity (black curve in the figure) remained at an extremely low level of ~10^{-8} over about 250 h into the test, when a sudden increase of ^{85}Kr release was observed reaching 1.0×10^{-5} of fractional release. There was presumably the failure of one or several SiC layers with subsequent slow diffusive transport of the krypton through the OPyC layer. The overall release fraction is still below the inventory of one particle. The ^{137}Cs activity (see blue curve in Fig. 8.11) also remained at a comparatively low level reaching 4.5×10^{-5} after 100 h at 1600°C, and only with the beginning of SiC failure did caesium release increase more rapidly eventually reaching 2.1×10^{-3} at the end of the additional 200-hours heating at 1800°C.

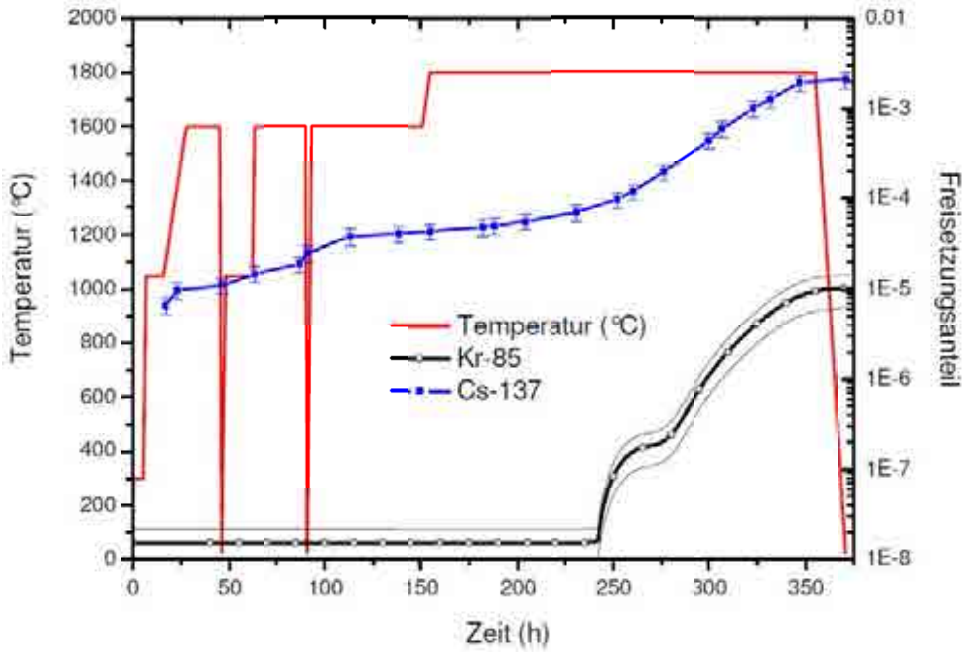

FIG. 8.11. KÜFA-II heating test HFR-K6/2.

(iv) HFR-K6/3

For the heating test of HFR-K6/3, Figure 8.12 illustrates the heating schedule and the measured release of ^{137}Cs and ^{85}Kr. The test was performed in four phases. The first phase constituted 1600°C for 100 h, the second phase 1700°C for 100 h, and the third phase 1800°C for 100 h. After the third phase, a fourth heating phase at 1800°C for a further 300 h followed (see red curve in Fig. 8.12) [298]. After 100 h at 1600°C, the ^{85}Kr activity detected in the cold trap was at a low value of 5.2×10^{-6}. Until the end of the third phase after ~400 h into the test, the ^{85}Kr release was still low with 8.1×10^{-6} indicating that no particle had failed until that moment. After starting the fourth phase, a significant release of ^{85}Kr began reaching 5.5×10^{-4} fractional release and indicating failure of several particles. Later PIE using a scanning electron microscope (SEM) could verify this assumption. The ^{137}Cs release can be divided into two phases. Up to the end of the 1700°C (second heating phase) only small amounts of ^{137}Cs were released with 5.5×10^{-7} after 100 h at 1600°C and 2×10^{-6} after additional 100 h at 1700°C. At 1800°C, large releases start following a typical diffusion curve reaching a fractional release of 9.3×10^{-4} after the third heating phase. At the end of the test, a fractional release of 4.3% has been measured. It can be seen from the figure that the ^{85}Kr and ^{137}Cs release curves follow the same shape in the 4th heating phase.

As a first conclusion it can be said that the fuel element HFR-K6/3 showed an excellent coated particle performance with late particle failure at 1800°C and a low caesium release up to 1700°C. It is not clear whether the cooling and re-heating of the sphere induced additional failures on the coated particles. However, such an effect would explain the sudden release of fission gas at the beginning of the fourth phase. It is assumed that the performed heating programme represents a conservative case with respect to any possible accident scenario.

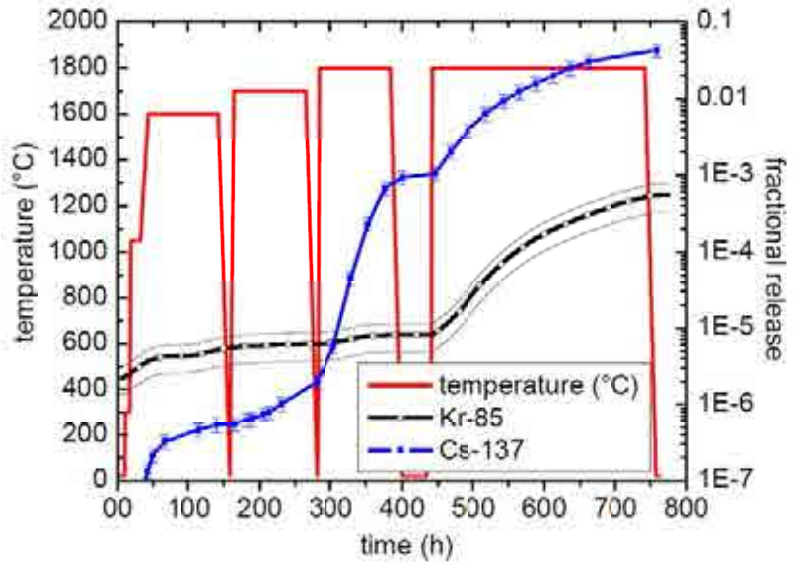

FIG. 8.12. KÜFA-II heating test HFR-K6/3.

8.3.2.5. PIE for pebbles irradiated in HFR-EU1bis

(a) HFR-EU1bis/1

The irradiation test HFR-EU1bis (see Section 7.2.3) was conducted from September 2004 to October 2005 in the HFR Petten in order to examine present HTGR fuel under VHTR conditions. Five spherical fuel elements of GLE-4.2 type were irradiated for 249 efpd. Of the five fuel spheres, four have been heated in the meantime in the new KÜFA furnace.

The heating test of HFR-EU1bis/1 with a burnup of 9.3% FIMA was performed in three phases. The first heating phase was at 1250°C for 200 h, the second heating phase at 1600°C for 200 h, and the third phase at 1700°C for 150 h (see red curve in Fig. 8.13) [254]. The ^{85}Kr activity (black curve in the figure) remained at a low level reaching 1.4×10^{-6} of fractional release after the 1250°C heating phase. Further increase during the following heating at 1600°C and 1700°C to a fractional release of 2.4×10^{-5} seems to originate from single particles with a failed SiC layer and still intact OPyC layer. The overall release fraction is still below the inventory of one particle meaning that there was no pressure vessel failure of a coated particle during the test.

The ^{137}Cs activity (see blue curve in the figure) is on a relatively high level already during the 1250°C heating with 7.2×10^{-5} at the end of this phase. This is presumably the result of partly the high temperature during irradiation with enhanced diffusion through the particle coatings and partly release from particles with an SiC layer that failed during irradiation 100 h at 1600°C, and only with the beginning of SiC failure did caesium release increase more rapidly eventually reaching 2.1×10^{-3} at the end of the additional 200-hours heating at 1800°C. The measured silver release was 2.3×10^{-3} after the 1250°C phase and 7.2×10^{-3} at the end of the 1600°C phase.

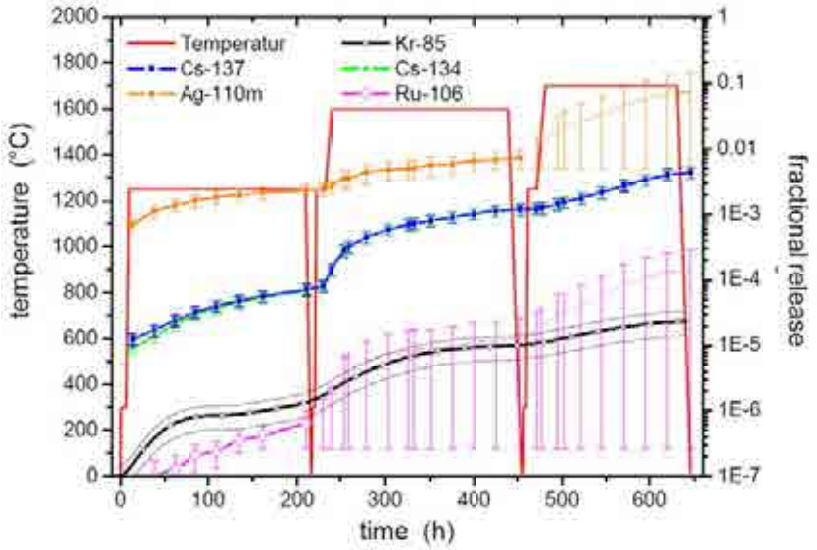

FIG. 8.13. KÜFA-II heating test HFR-EU1bis/1.

(b) HFR-EU1bis/3

The heating test of HFR-EU1bis/3 with a burnup of 11.1% FIMA was performed in two phases. The first heating phase was at 1250°C for 100 h followed by a heating phase at 1600°C for 200 h (see red curve in Fig. 8.14) [297]. The ^{85}Kr activity (black curve in the figure) was gradually increasing, but remained at a low level reaching 2.3×10^{-6} at the end of the test. The overall release fraction is still below the inventory of one particle.

Similar to the previous test, the ^{137}Cs activity (blue curve in the figure) increased from the beginning to a comparatively high level already during the 1250°C phase reaching 3.9×10^{-5} after 100 h. Further strong increase at 1600°C finally led to a fractional release of 2.7×10^{-3}. Since no pressure-induced particle failure was observed during the test, this high caesium release value could be explained by SiC failure in quite a number of coated particles and the high temperature during irradiation. Silver release reached the 10^{-3} level at the end of the 1250°C heating and 3.6×10^{-3} at the test end.

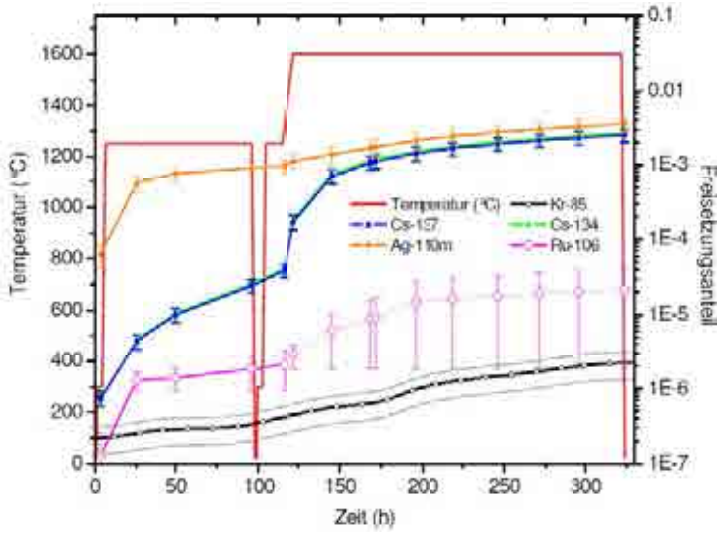

FIG. 8.14. KÜFA-II heating test HFR-EU1bis/3.

(c) HFR-EU1bis/4

The heating test of HFR-EU1bis/4 with a burnup of 11.1% FIMA was performed in three phases. The first heating phase was at 800°C for 50 h followed by a short (10 h) second heating phase at 1250°C, and a third phase representing a core heatup transient with a maximum temperature of 7120°C after 70 h and then remaining constant at that level for 140 more hours (see red curve in Fig. 8.15) [297].

The ^{85}Kr activity (black curve in the figure) remained below the detection limit during the initial phase, increased to 1.6×10^{-6} during the 1250°C phase, and then further to 1.7×10^{-5} at the end of the test. The overall release fraction is still below the inventory of one particle. The ^{137}Cs activity (blue curve in the figure) starting from the 10^{-5} level was steadily increasing and eventually a fractional release value of almost 1% at the test end. Final fractional release measured for silver was 2.5%.

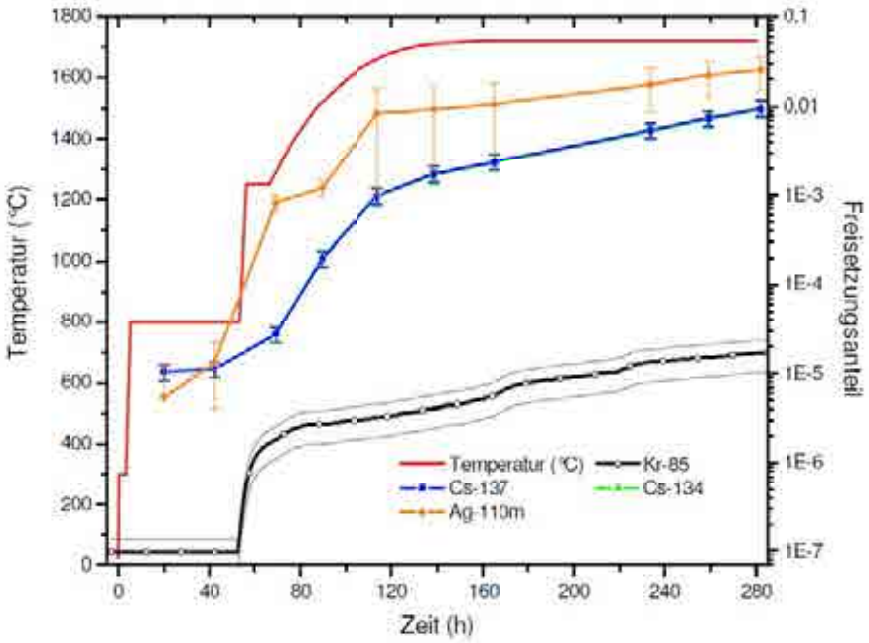

FIG. 8.15. KÜFA-II heating test HFR-EU1bis/4.

All heating tests conducted so far in the new KÜFA-II furnace at ITU are summarized in Table 8.4 [297, 298].

8.3.2.6. Post-irradiation examination on sphere HFR-K6/3

Following the HFR-K6/3 heating test, further PIE works were conducted after boring out and segmenting a 10 mm diameter central part of the sphere [297, 298]. Ceramographic sections were made from four coated particles disintegrated from different locations. The two sections shown in Fig. 8.16 indicate high porosity in the UO_2 kernel with visible debonding of the buffer layer from both UO_2 and IPyC layer, and also between IPyC and SiC. Two of the four particles exhibit cracks in the SiC in radial direction [297].

Another six coated particles were investigated by means of electron microscopy showing higher-quality pictures confirming the occurrence of debonding, but leaving the micro-structure basically intact (Fig. 8.17) [297].

TABLE 8.4. RESULTS OF ACCIDENT SIMULATION TESTS IN THE KÜFA-II FURNACE AT JRC-ITU

Fuel element	Irradiation			Heating		Fractional release of		
	Burnup (% FIMA)	Fast fluence (10^{25} n/m^2, E>0.1 MeV)	Temperature (°C)	Temperature (°C)	Time (h)	Kr-85	Cs-137	Ag-110m
AVR 74/18	4.8	0.8	820	1000	10	4.5×10^{-6}	3.2×10^{-7}	—
				1600	100	5.9×10^{-6}	5.8×10^{-6}	—
				1800	100	6.1×10^{-6}	8.1×10^{-6}	—
HFR-K6/2	9.3	4.6	940	1050	10.5	— [a]	6.6×10^{-6}	—
				1600	100	— [a]	4.3×10^{-5}	—
				1800	200	1.0×10^{-5}	2.1×10^{-3}	—
HFR-K6/3	9.7	4.8	940	1050	13.5	3.2×10^{-6}	1.3×10^{-7}	—
				1600	100	5.2×10^{-6}	5.5×10^{-7}	—
				1700	100	6.2×10^{-6}	2.0×10^{-6}	—
				1800	100	8.1×10^{-6}	9.3×10^{-4}	—
				1800	300	5.5×10^{-4}	4.3×10^{-2}	—
HFR-EU1bis/1	9.3	3.0	1250	1250	210	1.4×10^{-6}	7.2×10^{-5}	2.3×10^{-3}
				1600	200	1.0×10^{-5}	1.2×10^{-3}	7.2×10^{-3}
				1700	150	2.4×10^{-5}	4.3×10^{-3}	—
HFR-EU1bis/3	11.1	4.0	1250	1250	100	3.4×10^{-7}	3.9×10^{-5}	9.6×10^{-4}
				1600	200	2.3×10^{-6}	2.5×10^{-3}	3.6×10^{-3}
HFR-EU1bis/4	11.1	4.0	1250	800	48	— [a]	1.1×10^{-5}	1.3×10^{-5}
				1250	10	1.6×10^{-6}	2.8×10^{-5}	8.2×10^{-4}
				transient	70	4.1×10^{-6}	1.7×10^{-3}	9.4×10^{-3}
				1720	~140	1.7×10^{-5}	9.6×10^{-3}	2.5×10^{-2}
HFR-EU1bis/5	9.7		1250					

[a] below detection limit.
— data not available.

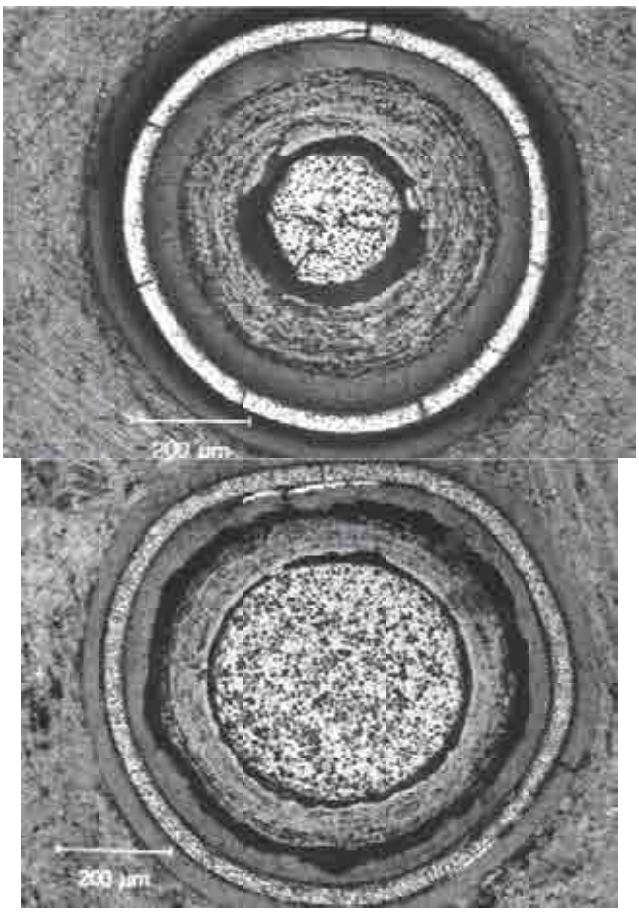

FIG. 8.16. Ceramographic section from two coated particles taken from HFR-K6/3 after 400 h heating at 1800°C.

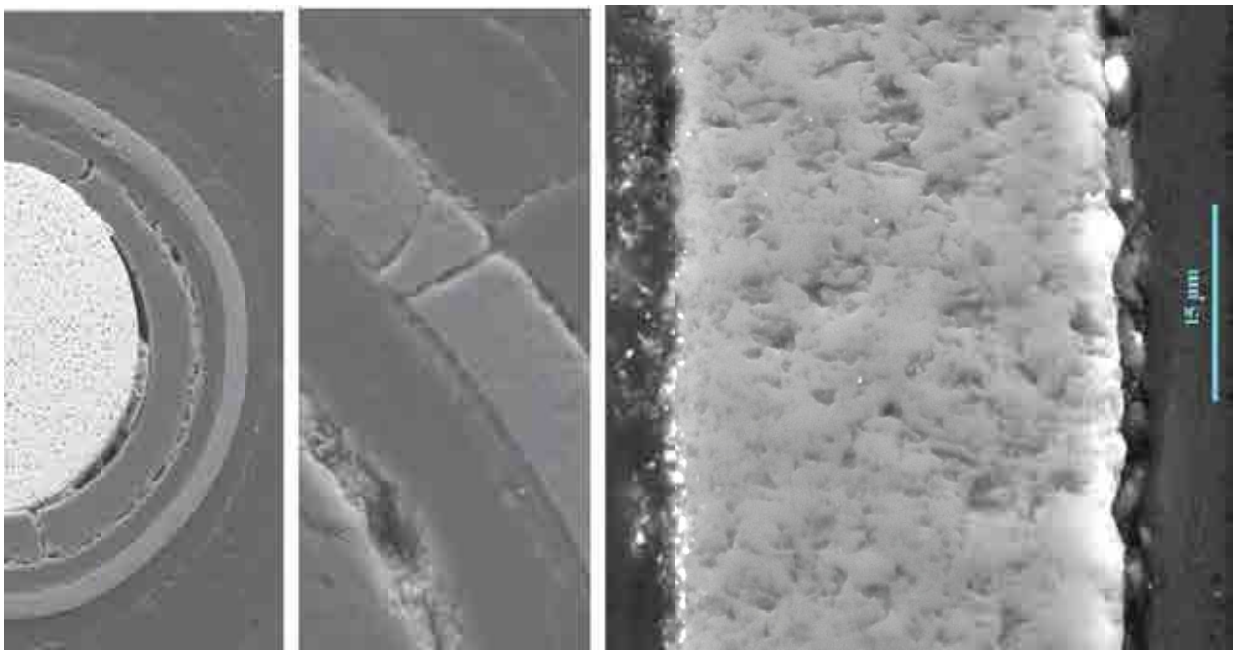

FIG. 8.17. SEM frame of a particle from HFR K6/3 heated 400 h at 1800°C.

Measurements of the Vickers hardness on one particle have shown good agreement with literature data for beta-SiC indicating a basically undamaged micro-structure of the material.

A hardware & software development of an IMGA device at the ITU Karlsruhe has been recently completed (Fig. 8.18) and verified in a small scale operation on ^{137}Cs-activated ceramic beads [299].

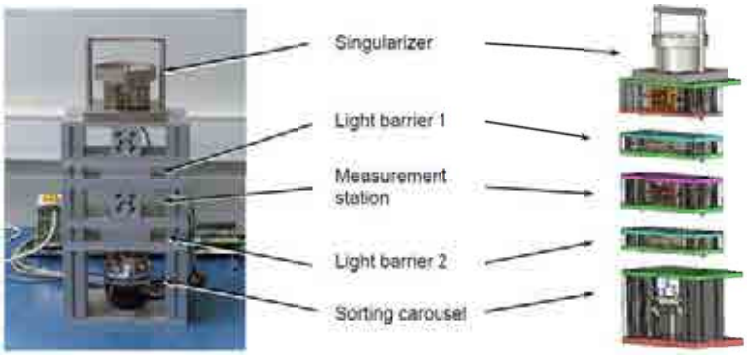

FIG. 8.18. Set-up of the IMGA at JRC-ITU.

In order to assess fuel behaviour and fission product release in accidents under oxidizing conditions, the so-called 'KORA' furnace facility was designed and installed at the ITU, Karlsruhe. Similar to the facility of the same name which was successfully operated at the research centre Jülich, KORA enables the simulation of both steam ingress, typically at 800°C, and air ingress effects on TRISO coated particles in the range from 1300° to 1500°C. A 'cold' version of KORA-II has been assembled and connected (electrical, cooling, steam & gas lines) in the meantime and will start cold testing in 2011. The 'hot' version will require further substantial modifications to furnace [254].

8.3.2.7. Conclusions from the heating tests in the new KÜFA furnace

Several conclusions can be drawn from the first series of core heatup simulation tests in the new KÜFA-II furnace [297, 298]:

- The previous observation that no coated particle failure occurs during isothermal heating at 1600°C was confirmed by the new tests.
- The heating tests HFR-K6/2 and HFR-K6/3 representing proof test fuel for the HTR-Modul have shown excellent retention behaviour for fission products. Coated particles remained intact even at 1800°C over 100 hours before significant particle failure occurred. Metallic fission product release remained well below the expected levels from previous experience. Analysis of the SiC micro-structure has shown that it remained intact even after 400 h of heating at 1800°C.
- In contrast, the heating tests with the spheres irradiated in HFR-EU1bis revealed worse retention behaviour for caesium. Although obviously no pressure-induced particle failure occurred, caesium release level was comparatively high already at heating temperatures as low as 1250°C and reached the 10^{-3} range at the end of the tests. Main reasons for this behaviour are believed to be on the one hand the high irradiation temperature of 1250°C and on the other hand the occurrence of a temperature excursion during the irradiation experiment that presumably caused impairment of quite a number of coated particles.
- With the conditions of high irradiation temperature (~1250°C) and high burnup (~11% FIMA), the limits of coated particle performance may have been exceeded.

Further heating tests will be required to confirm the good retention behaviour of fuel typical for the operational conditions of the HTR-Modul.

8.4. INVESTIGATION OF TRISO FUEL UNDER RIA CONDITIONS IN JAPAN

For the development of high performance HTGR fuels, it is necessary to acquire data concerning fuel behaviour in reactivity-initiated accidents (RIA) where fuel temperatures could exceed 1600°C for short durations of 1–10 s. At the Nuclear Safety Research Reactor (NSRR) of the JAEA in Tokai-mura, eight pulse irradiation tests were performed with unirradiated coated fuel particles with the objective to determine the failure limit and clarifying the failure mechanism of the HTGR fuel under RIA conditions [300].

8.4.1. RIA experiments

The fuel particles consisted of a spherical fuel kernel of low enriched UO_2 and the TRISO coating. Figure 8.19 shows the test fuel and test capsules for the pulse irradiation tests [300]. Seven fuel particles were embedded in a graphite disk of 10 mm outer diameter, 4 mm inner diameter, and 3 mm height. Thirty-six disks were piled up to form a fuel segment. Thus, 252 fuel particles were contained in one fuel segment. A test fuel rod was composed of two fuel segments and a zircaloy-2 cladding tube of 12.27 mm outer diameter and 0.86 mm thickness. K type (chromel/alumel) thermocouples were attached to the fuel segments and R type (Pt-13%Rh/Pt) thermocouples were welded onto the surface of the cladding tube for the temperature measurements. The test fuel rod was inserted into the inner capsule which was filled with nitrogen gas at standard conditions. The inner capsule was mounted in the test capsule and the inside of the test capsule was filled with water.

The inner capsule has two different diameters in order to obtain data under two conditions by one pulse irradiation. The diameter of the inner capsule was 60.5 mm for the upper part and 30 mm for the lower part as is shown in Fig. 8.19. Due to the two different thicknesses of water between inner capsule and test capsule, thermal neutron flux and energy deposition during the pulse irradiation were different between the upper and lower fuel segments.

The conditions of the four pulse irradiation tests are shown in Table 8.5. In the NSRR, the pulse shape depends on the inserted reactivity. The pulse width at half maximum of power in the experiments conducted was 4–10 ms.

Test 522-1 aimed at confirming that no fuel failure occurs at 1600°C which is the fuel temperature limit during AOO. Therefore the inserted reactivity was determined such that the fuel temperature in the upper segment position (1U) reached approximately 1600°C. The energy deposition in the lower segment (1L) was higher since the amount of the moderating water was larger around the lower segment. Tests 522-2 and 522-3 aimed at the study of the fuel behaviour during failure and the failure mechanism at higher temperatures. The target fuel temperatures of the lower segment (2L) in test 522-2 and upper segment (3U) in test 522-3 were near the melting point of UO_2 (3113 K). Under these conditions, the expected fuel temperature of the upper segment (2U) in test 522-2 was below and that of the lower segment (3L) in test 522-3 was above the melting point of UO_2. In test 522-4, the inserted reactivity was selected such that for both segments (4U and 4L), the fuel was sufficiently heated beyond the melting point of UO_2.

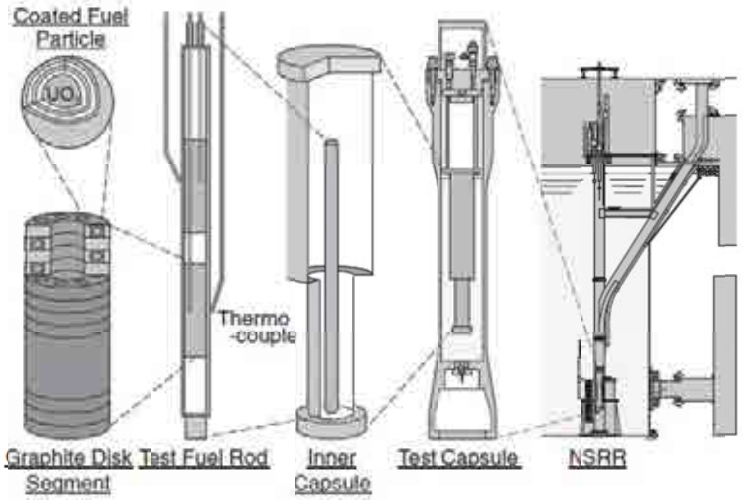

FIG. 8.19. Configuration of test fuel and capsules.

TABLE 8.5. TEST CONDITIONS AND MAIN RESULTS

Test ID	Inserted reactivity ($)	Segment	Energy deposition (kJ/g of UO_2)	Estimated peak temperature (K)
522-1	2.16	1U	0.578 ± 0.003	1510 ± 20
		1L	0.695 ± 0.003	1830 ± 20
522-2	3.07	2U	1.053 ± 0.005	2660 ± 20
		2L	1.254 ± 0.006	3000 ± 20
522-3	3.82	3U	1.436 ± 0.007	3240 ± 20
		3L	1.702 ± 0.008	3650 ± 20
522-4	4.14	4U	1.642 ± 0.006	3490 ± 20
		4L	1.869 ± 0.007	3950 ± 20

The energy deposition on the fuel during the pulse irradiation was evaluated on the basis of the number of fissions which can be derived from the gamma ray measurements. As a result, the energy deposition ranged from 0.578 to 1.869 kJ/g of UO_2 during the pulse irradiations.

8.4.2. Post-irradiation examination results

8.4.2.1. Post-test appearance

The test fuel rods were disassembled after the pulse irradiation tests. Visual observation, X ray radiography, gamma ray analysis, and ceramography were carried out on the fuel particles, disks, segments and test rods.

Visual change was not seen on the outside of the tested fuel rods. Oxidation of the fuel rod surface due to the temperature rise was also not observed. The X ray radiographs of the fuel rods indicated that the fuel particles kept their position in the fuel disks. Furthermore, no particular changes were found on the external of the fuel segments (Fig. 8.20) [301].

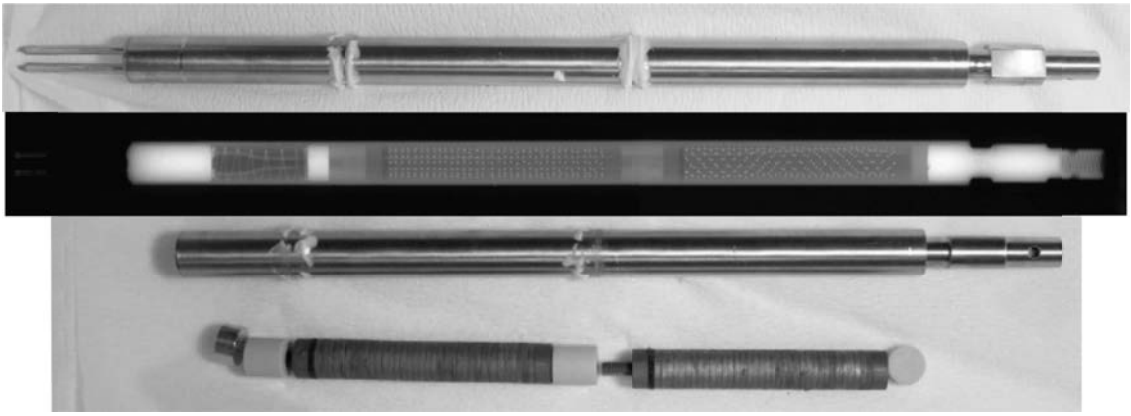

FIG. 8.20. Visual observation of fuel rod (top), X ray radiography of fuel rod (middle), and visual observation of a segment (bottom) with no particular change on appearance observed.

After disassembling the fuel segments, the fuel disks were visually observed. The appearances of the fuel disks were just like before the pulse irradiation. Since there was no radioactive contamination detected on the disk surfaces, it was confirmed that the UO_2 of the fuel kernels did not leak out of the graphite disks. The fuel kernels mostly kept the globular shape. However, it was observed that a small amount of UO_2 was released from the coating layers due to fuel particle failure in Segments 3L and 4L where the fuel was exposed to very high temperatures.

8.4.2.2. Temperature history during pulse irradiation

In the temperature histories recorded at the inner disk surface and cladding surface, very sharp peaks could be seen at the beginning of the pulse irradiation in the cladding surface temperatures. This is mainly traced back to the gamma heating of the thermocouples which is generally observed in the NSRR experiments. On the other hand, the gamma heating was rather small at the inner disk surface which could not clearly be explained at that stage of the study. The temperature at the inner disk surface generally reaches the maximum after ~2 s, which becomes higher with increasing energy deposition. Temperature increase rates at the inner disk surface were smaller in the two segments 2U and 2L compared to the other segments. It is likely that the thermocouples in the two segments were not properly attached to the inner disk surface. The maximum temperatures at the cladding surface are almost the same as those at the disk inner surface, the maximum generally being reached at ~5 s.

The temperatures at the centre of the fuel particles were estimated with the ABAQUS code using the obtained transient data of the heat generation density, surface temperatures at the inner disk and cladding. Since the fuel reached its peak temperature within several tens of milliseconds after start of the pulse irradiation, the temperature data at the disk inner surface in segments 2U and 2L were appropriately used for the estimation. The heat generation density was calculated from the NSRR reactor power. Transient data that were obviously affected by the gamma radiation were excluded from the estimation.

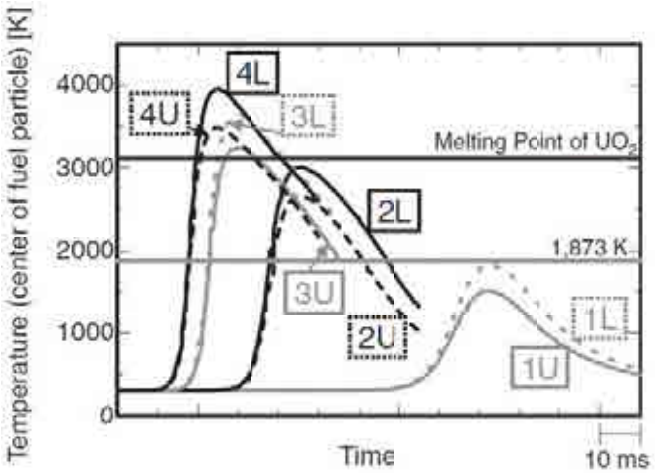

FIG. 8.21. Calculated temperature histories at centre of fuel particles during pulse irradiations.

Figure 8.21 indicates the calculated temperature changes in the eight fuel segments during the pulse irradiations. The temperatures increased rapidly and reached peak values from 1510 to 3950 K at 20–40 ms after the initiation of the pulse irradiation. Temperatures in the segments 1U and 1L were lower than 1600°C, while those in the segments 2U, 2L, and 3U were close to the melting point of UO_2, and those of segments 3L, 4U, and 4L were obviously higher than the UO_2 melting point.

8.4.2.3. Micro-structure change and fracture behaviour

Ceramography was performed in order to clarify the behaviour of the fuel particles during the pulse irradiations. Figure 8.22 shows some results of the ceramography. No cracks were identified in both coating layers and fuel kernels of segment 1U where the fuel peak temperature reached 1237°C during the pulse irradiation. Cracking of the fuel kernel could be seen in segment 1L which saw a peak fuel temperature of 1557°C. A release of UO_2 from the fuel kernel through the coating layer, however, was not observed in that fuel segment. The cracks in the fuel kernel were thought to be generated by the tensile stress as the heated fuel kernel was cooled after the pulse irradiation from the periphery inwards.

Cracks in the fuel kernels were also observed in segments 2U and 2L, in which the fuel temperature reached 2660 and 3000 K, respectively. The number of cracks increased with increasing energy deposition. Voids were seen at the centre of the fuel kernels in segment 3U in which the fuel temperature reached 3240 K. The formation of the central voids is an evidence of the melting of the fuel kernel. In segments 3L and 4U, in which the peak fuel temperature reached 3650 and 3490 K, respectively, cracks propagated into the coating layer and a void was formed in the centre of the fuel kernel. Moreover, traces of UO_2 released from the fuel particle were observed in these segments. In segment 4L with the highest energy deposition and a fuel temperature of 3950 K, the formation of cracks penetrating the coating layer and of large central voids was remarkable.

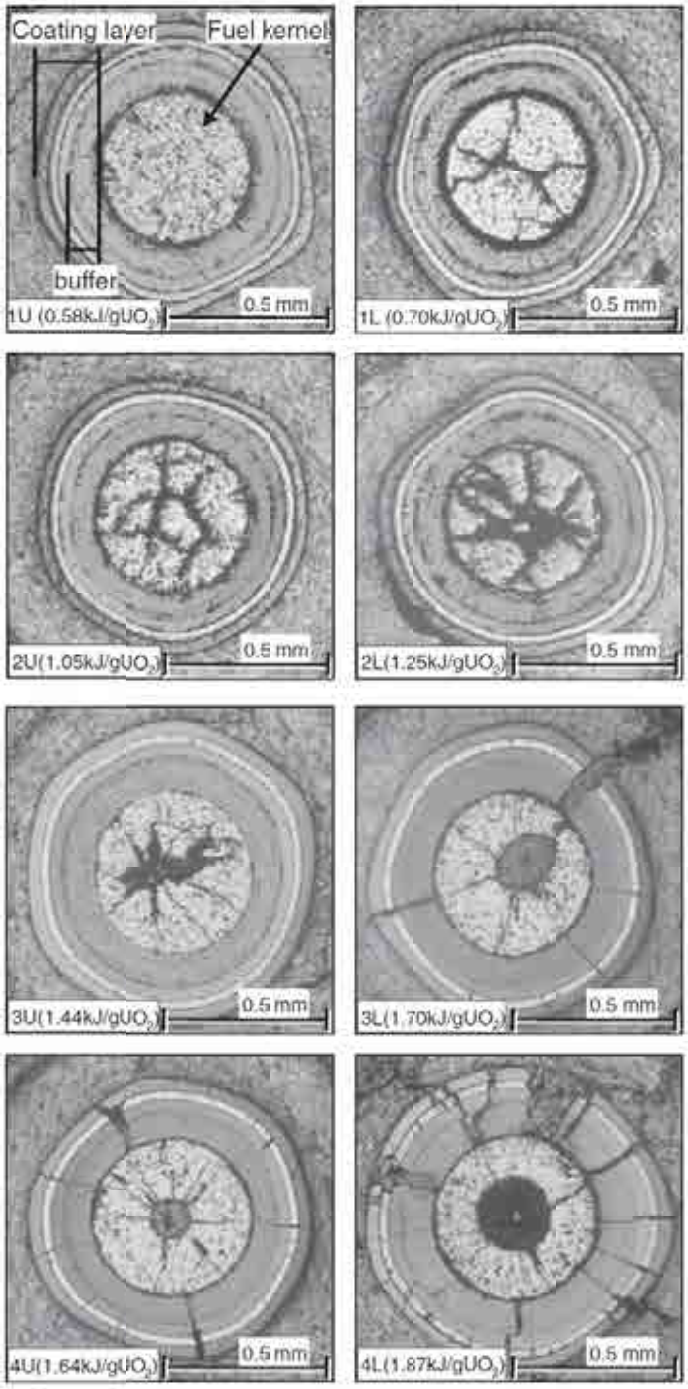

FIG. 8.22. Ceramographs of fuel particles pulse-irradiated with different energy depositions.

From chemical etching studies, it was concluded that significant UO_2 grain growth did not occur in segments 1U, 1L, 2U, and 2L. The extent of the grain growth was judged to be mainly dependent on the temperature since the periods at high temperatures were very short during the pulse irradiation. Therefore, the very small grain growth indicated that the fuel temperature in these fuel segments was well below the melting point of UO_2 in consistence with the calculated fuel temperatures. As the grain size became larger toward the centre of the fuel kernels in segment 3U, it was presumed that the fuel temperature was higher and the duration at high temperatures was relatively longer in the centre region of the fuel kernels. A columnar grain growth was seen in the vicinity of the void in the centre of the fuel kernels in segments 3L, 4U, and 4L. Central void formation and columnar grain growth indicate melting

of the fuel kernel during the pulse irradiation. The micro-structure of the buffer layers appeared to be different between intact (1U, 1L, 2U, 2L, 3U) and failed fuel particles (3L, 4U, 4L). The buffer layers from intact particles were porous and those of failed particles were dense. The difference in the buffer layer density may be related to the failure mechanism.

8.4.2.4. Fraction of failed fuel particles

For the determination of the fraction of failed fuel particles, all pulse-irradiated particles were given into boiling nitric acid and then subjected to X ray photography. Since UO_2 is dissolved by the acid, while the coating layer is not, only UO_2 kernels of the intact particles could clearly be observed and counted in the photographs. The results of the failure fraction measurements are listed in Table 8.6 [301].

Figure 8.23 shows the fraction of failed fuel particles as a function of energy deposition. The particles began to fail above an energy deposition of 1.40 kJ/g of UO_2 and the failure fraction increased as the energy deposition increased. Almost all particles failed above 1.869 kJ/g of UO_2. This relation between energy deposition and failure fraction is in accordance with the results of former studies. At a level of 1.436 kJ/g of UO_2, just above the failure threshold, the fuel temperature was estimated to have reached more than 3240 K, which is a little higher than the melting point of UO_2. Therefore, the failure of the fuel particles was thought to be induced by the melting of the UO_2 fuel kernels. The failure threshold obtained from this study is beyond the safety limits of the present HTGR fuel.

The density of UO_2 decreases discontinuously when the phase of UO_2 changes from solid to liquid. Theoretically, this phase change causes a volume and diameter increase of approximately 17 and 6%, respectively. Therefore, the failure of the particle may be explained by the melting and swelling processes in the fuel kernel leading to a compression of the low density buffer layer in the radial direction, and subsequently to a kernel–coating mechanical interaction, when the energy deposition during the pulse irradiation is higher than 1.40 kJ/g of UO_2.

TABLE 8.6. IDENTIFICATION OF THE NUMBER OF FAILED PARTICLES IN THE DIFFERENT SEGMENTS

Segment	Number of failed particles (out of 196)	Fraction of failed particles
1	0	0.
2	0	0.
3	0	0.
4	0	0.
5	3	0.016
6	73	0.372
7	145	0.740
8	190	0.969

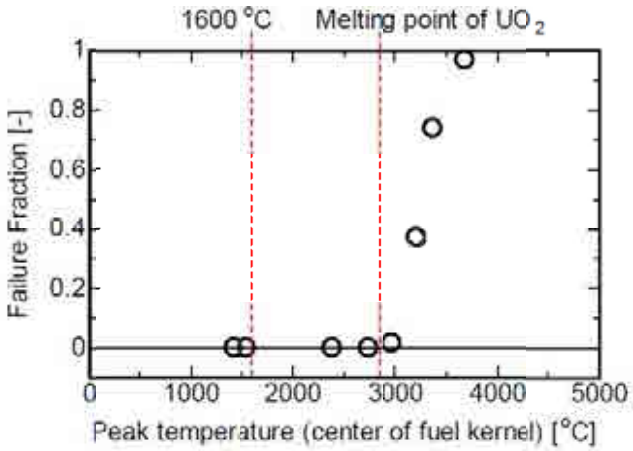

FIG. 8.23. Fraction of failed fuel particles as a function of energy deposition.

8.5. PIE AND ACCIDENT TESTING PLANS FOR THE NGNP PROJECT IN THE USA

As part of the NGNP fuel development and qualification programme, eight fuel irradiation experiments are planned in the ATR reactor at the INL. The first of these irradiation tests, AGR-1, was terminated in November 2009. This experiment is intended to act as a shakedown test of the multicapsule design and to provide early data on fuel performance from lab scale fuel that will be used in fuel fabrication process development. This test will also provide samples for post-irradiation accident testing where fission product retention of the fuel at high temperatures will be experimentally measured.

8.5.1. Post-irradiation examination and accident testing

8.5.1.1. PIE for AGR experiments

At the conclusion of the AGR-1 irradiation the test train will be removed from the reactor and shipped to the hot fuel examination facility at the materials and fuels complex at the INL for inspection and disassembly. The large number of fuel compacts involved in the AGR irradiations and the need to compile a substantial fuel performance database for NGNP licensing will require the collaborative efforts of the INL and ORNL for the post-irradiation examination of the fuel and capsule components. The PIE for the NGNP fuel will focus on (1) characterizing the compacts and individual particles to observe the micro-structure of the matrix material, kernels, and coatings, and (2) evaluating the fission product retention of the fuel during irradiation and during post-irradiation accident testing. In addition, the PIE of the AGR-1 test will include an assessment of the multi-capsule instrumented irradiation test train performance and provide data to verify the test train thermal analyses. The PIE for the AGR-1 experiment will include the following key activities:

- Test train inspections and nondestructive analyses (including isotopic gamma scanning) to determine the overall condition of the test train exterior and the condition and location of internal components;
- Test train disassembly, extraction of fuel and other interior components (including the graphite fuel holders, melt wires, and flux wires), and evaluation of test train performance by characterization of thermocouples, melt wires, and flux wires;
- Dimensional measurements of the fuel compacts and graphite holders;
- Measurement of fuel and graphite properties, including fuel burnup determinations, and measurement of fuel and graphite thermal conductivity and thermal expansion;

- Postirradiated fission metals release analysis by measurement of fission metal inventories on metal capsule components and gamma scanning of graphite fuel holders;
- Deconsolidation of compacts to provide particles for subsequent analyses and leach-burn-leach analysis to quantify SiC failure fractions and evaluate fission product inventories in the compact matrices;
- Micro-analytical characterization of fuel compacts and particles using optical metallography, scanning electron microscopy, and electron probe micro-analysis to investigate fuel micro-structures, the condition of coatings, and fission product migration;
- Accident testing to investigate release of selected fission products (including radioisotopes of Ag, Cs, I, Sr, Te, Eu, Kr and Xe) at elevated temperatures in pure helium;
- Irradiated microsphere gamma analysis (IMGA) to measure fission product inventories and evaluate fission product retention for individual particles.

These experiments will provide the programme with data on uranium oxycarbide particle fuel performance and on the fundamental effects of irradiation on fuel properties. The results will indicate if the programme's current approach to fuel fabrication has been successful in producing high quality fuel that exhibits good irradiation and accident performance.

In subseqent planned irradiation experiments, the focus will be on demonstrating successful performance of fuel produced at the production scale, selecting a reference fuel, qualification of the fuel, and validating fuel performance codes. In addition to the experiments planned for the AGR-1 fuel, future post-irradiation work will include accident release tests under air and steam ingress conditions. Several irradiation tests will be dedicated to experimental measurements of fission product transport within the fuel matrix material and core structural graphite and validation of fission product transport codes.

8.5.1.2. Accident testing

A critical component of the fuel evaluation for the NGNP programme will be verification of the fission product retention behaviour at elevated temperatures, similar to those experienced during a depressurized conduction cooldown accident scenario. Accident test results will demonstrate the robustness of the AGR fuel and the data will be a key element in the fuel qualification process.

The performance of fuel under accident conditions will be evaluated by heating compacts and particles in helium and measuring the release of fission products in dedicated furnaces at both INL and ORNL. Specific heating temperatures will range from 1400 to 2000°C. The systems at the two laboratories are similar in their fundamental operation. Condensable fission products (e.g. Ag, Sr, Cs, I, Eu) will be collected on a metallic surface attached to a water cooled cold finger located near the heated fuel compacts or particles. The fission products evolved from the fuel at high temperatures are swept by flowing helium to the condensation surface. The collection surfaces can be changed periodically during a heating test (typically several hundred hours) so that time dependent release data are collected. Fission gases swept from the furnaces will be collected throughout the tests in cryogenic traps and measured by gamma spectrometry.

The ‘fuel accident condition simulator’ (FACS) furnace has been recently designed and fabricated for fuel accident testing at INL (Fig. 8.24) [286]. This system uses a graphite heating element and a tantalum hot zone and is capable of sustained temperatures of up to 2000°C in a helium atmosphere. The peak current through the heater is 1250 A at 28 V. The system is designed to facilitate remote operation in a shielded hot cell, with an automated condensation plate exchange capability that requires no direct operator manipulation of the system. The condensation plate can be kept at a temperature of approximately 60°C during a 1600°C test. The furnace will accommodate samples with maximum dimensions on the order of 75 mm in diameter and 200 mm in length. The samples will be supported on a tantalum holder that enters the furnace chamber from the bottom and the vertical location of the sample within the hot zone can be adjusted as necessary. The system involves multiple water cooled circuits for the furnace components and the cold finger.

The furnace is currently undergoing extensive remote operation and maintenance engineering and qualification prior to installation in the hot cells at the hot fuel examination facility (HFEF) at INL. Calibration tests will then be performed to determine fission product collection efficiencies on the condensation plate. The fission gas monitoring system for this furnace will consist of two identical carbon-filled cryogenic traps in the helium sweep gas line, each with a high purity germanium detector to measure accumulated fission gases (Kr, Xe). The system will be equipped with in-line particulate and moisture filters to minimize fouling problems and interferences with the cryogenic traps. The fission gas system is currently being designed and will be installed and tested along with the furnace in HFEF in 2009.

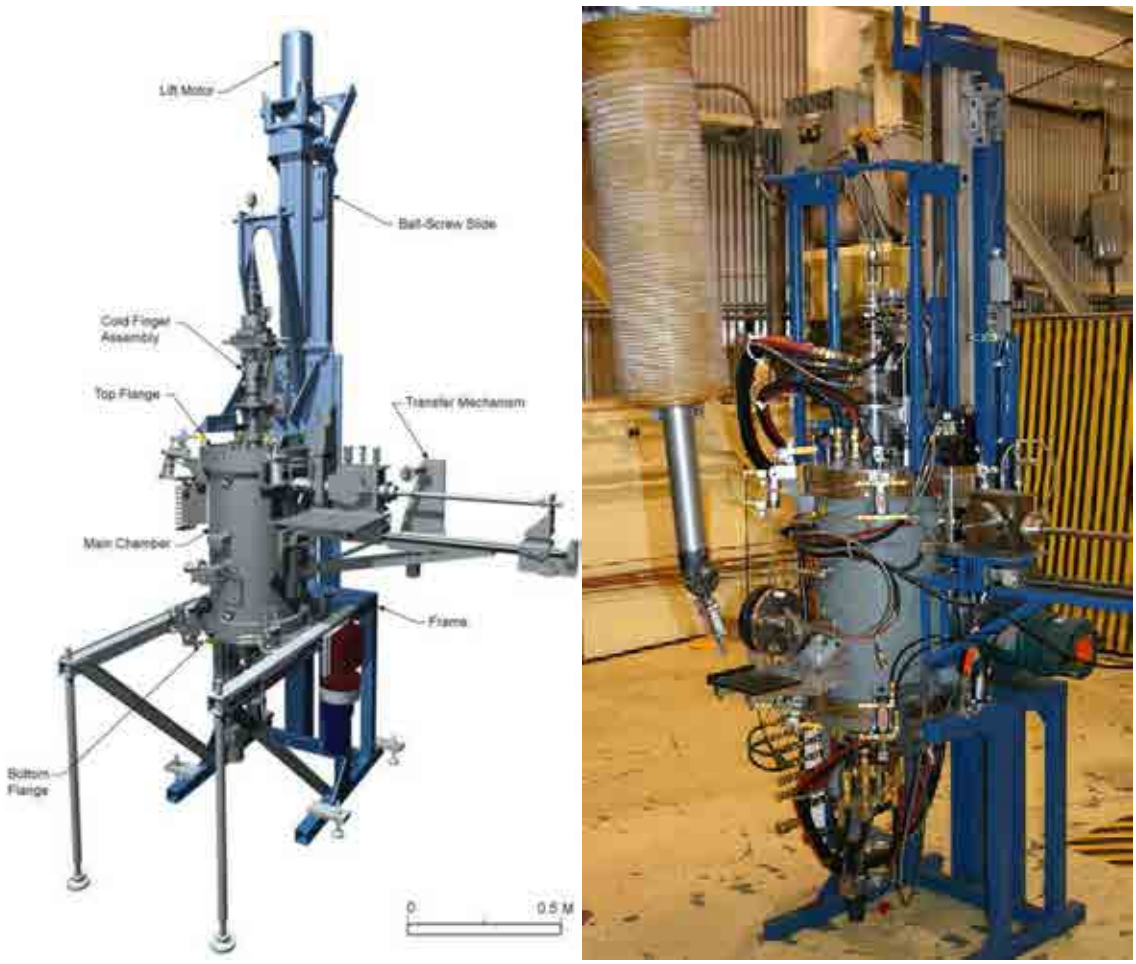

FIG. 8.24. Fuel accident condition simulator furnace module during remote engineering work at INL.

The core conduction cooldown test facility (CCCTF) will be used for accident performance testing at ORNL. This system has been utilized in past US HTGR fuel PIE programmes and is specifically designed for heating irradiated coated particle fuel compacts [302]. The CCCTF is a special purpose free standing hot cell that houses a high temperature furnace (Figs 8.25 and 8.26) [303]. The furnace is fully programmable with a range from room temperature to 2000ºC.

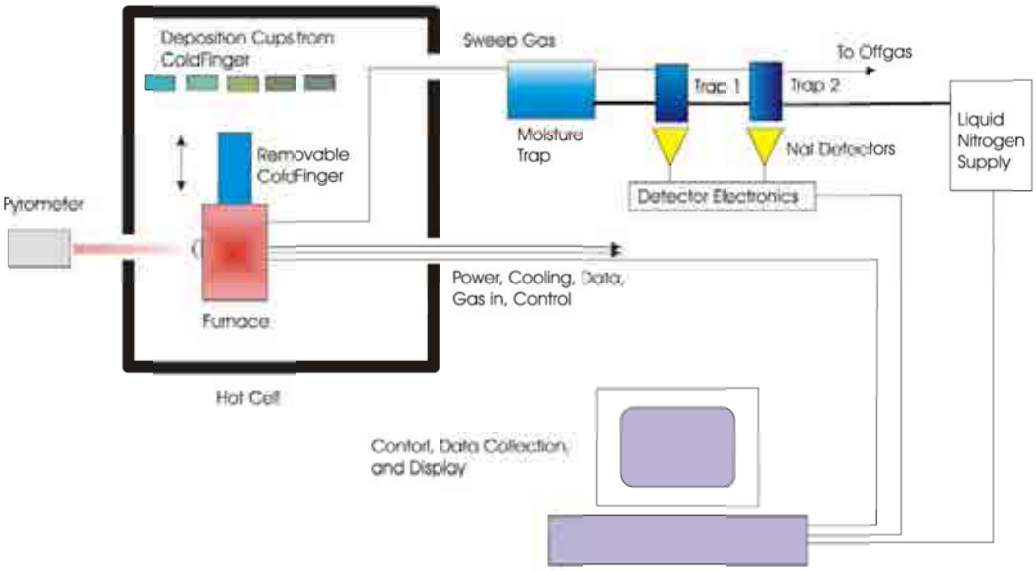

FIG. 8.25. CCCTF at ORNL for core heatup simulation testing.

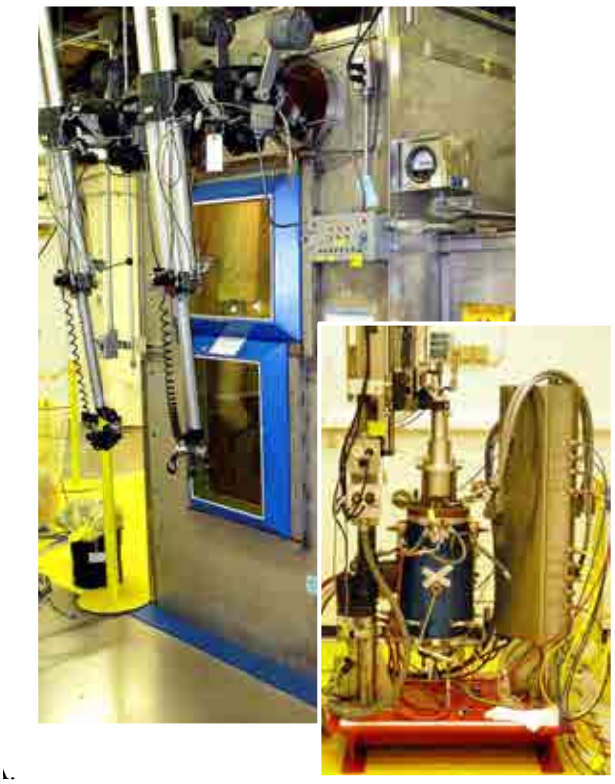

FIG. 8.26. The core conduction cooldown test facility shielded cubicle and high temperature furnace at ORNL.

Testing is performed with the fuel housed in a refractory metal container that separates it from the surrounding furnace. Ultra-high purity helium is used as a sweep gas to purge the furnace through a series of liquid nitrogen cooled charcoal traps. The traps are continuously monitored with NaI detectors to provide real time measurement of fission gas (^{85}Kr) release. An air lock at the top of the furnace will allow for the insertion of the water cooled cold finger assembly. The cold finger has a replaceable deposition cup on the end which attracts volatile fission products while it is inside the furnace. Some of the irradiated fuel compacts will need to be reactivated prior to heating in order to produce measurable quantities of radiologically important radionuclides, such as the 8-day ^{131}I.

The entire left side of the hot cell is a shielded door that allows personnel access to the cell between experiments. The furnace itself is mounted on a steel platform and can be removed from the cell for maintenance and upgrades. The versatility of the CCCTF hot cell allows for many different experimental assemblies to be installed with relatively minor alterations for remote operation. The cell is stainless steel lined and contains a minimum of 4 inches of lead shielding.

An auxiliary chamber has shielding equivalent to the cell walls and allows for storage of radioactive samples while experimental assemblies are installed in the cell. The cells interior dimensions are 1.22 m (48 in) wide, 1.78 m (70 in) deep, and 2.13 m (84 in) tall.

The NGNP programme currently plans to design and build an additional furnace that can be used for accident tests under air or steam ingress conditions. This system will have a 1600°C max temperature capability and will allow injection of controlled air or air/steam mixtures into the helium supply. The system will utilize a fission gas monitoring system similar to those currently employed for the existing systems to monitor the release of fission gases during heating tests.

Because of the importance of ^{131}I in dose calculations for postulated reactor accidents, the high temperature release of iodine is an important fuel attribute that should be evaluated during post-irradiation accident tests. Because of the short (~8 day) half life of ^{131}I, the inventory in the irradiated fuel will be essentially zero when PIE begins, several months after the end of the test irradiation. Re-irradiation of the fuel in a test facility (to generate ^{131}I by fission) followed immediately by accident testing is the proposed method for acquiring iodine release data. To accomplish this, the fuel will be re-irradiated in the Neutron Radiography (NRAD) reactor in the HFEF facility. The NRAD reactor is a 250 kW TRIGA reactor located below the hot cells. A pneumatic transfer system is currently being designed and fabricated to shuttle samples from the HFEF hot cell to the reactor core and back inside an aluminum canister. The samples can then be quickly transferred to the FACS furnace for accident testing.

Metal condensation plates from the furnaces will be analysed for deposited fission products including ^{137}Cs, ^{110m}Ag, ^{154}Eu by direct gamma spectrometry. It is expected that the quantities of ^{131}I on the plates will be too low relative to other radioisotopes to resolve their gamma emissions by direct gamma analysis. Therefore both ^{90}Sr (beta emitter) and ^{131}I will be stripped from the plates using an acid wash following the gamma spectrometry. Strontium and iodine will then be chemically separated from the leachate solution. Strontium-90 will be measured by liquid scintillation and ^{131}I will be analysed by gamma spectrometry.

8.5.1.3. Deconsolidation, leach-burn-leach, and irradiated micro-sphere gamma analysis

Compacts will be electrolytically deconsolidated in nitric acid to release individual particles from the matrix material for subsequent analyses. A radiochemical analysis of the deconsolidation solution will be performed to gather information about fission products retained in the compact matrix. The burn-leach technique will then be used on the loose particles to assess the SiC failure fractions of the irradiated fuel.

Loose particles from the deconsolidation and/or burn-leach experiments will undergo irradiated microsphere gamma analysis (IMGA) to measure the fission product inventories. After gamma counting, the particles will be sorted based on the observed results. This analysis will be performed on fuel after irradiation (to examine in-pile fission product behaviour) and after accident testing (to examine high temperature fission product behaviour). The data will primarily be used to gauge the relative fission product retention in each of the analysed particles. The data may also be used to screen particles based on radionuclide inventories prior to performing other detailed analyses, such as electron microscopy of particle cross-sections.

A new generation of IMGA instrument is being designed for the NGNP fuel work. This system will utilize a computer controlled vacumm needle to select a single particle from a bin and position the particle in front of the gamma detector. This method minimizes the probability of particle damage and provides a high level of reliability. The system will be fully automated to allow continuous operation and maximize the number of particles analysed. The specific count time will be influenced by the particular radionuclides of interest and the measurement geometry. Typical use will involve taking the ratio of various fission products of interest to one that is known to be relatively immobile within the kernel (such as ^{144}Ce) to obtain the fraction of the fission product that is retained in the particle. This can provide data on whether a particle contains coating failures (e.g. by observing high Cs release resulting in a low ^{137}Cs/^{144}Ce ratio) or whether a particle has abnormally low retention of various fission metals (e.g. by observing high Ag release resulting in a low ^{110m}Ag/^{144}Ce ratio).

The radionuclides to be included in the analysis for specific particles will be determined prior to the experiment based on the experimental objectives and data needs. Measurements aimed at determining fission metals release will include ^{110m}Ag, ^{137}Cs, and ^{154}Eu. The number of particles to be analysed from each compact or capsule will also depend on the radionuclides to be counted, which will dictate count times. After IMGA, individual particles of interest can be selected as appropriate for various micro-analyses such as SEM or EPMA.

8.5.1.4. Micro-analysis

Polished cross-sections of irradiated compacts and individual particles will be analysed using an array of micro-analytical techniques, including optical ceramography, electron microscopy, and electron probe micro-analysis (EPMA). These techniques will be used to characterize the micro-structure of the kernels, coatings, and matrix, and assess any observed coating failures. Properties of particular interest include fuel kernel porosity, kernel migration, buffer layer degradation, fractures in the TRISO coating layers, and delaminations between coating layers. Elemental analysis using EPMA will be used to characterize fission product migration and distributions within the kernel and coating layers and determine the effects of fission product corrosion on SiC layer integrity. Micro-structural characterization of the SiC layers, including the use of electron backscatter diffraction for information regarding crystallographic orientation of SiC grains and grain boundary alignment, will be used to aid in the

interpretation of fission product release behaviour and understand the relationships between SiC micro-structure and release.

8.5.1.5. Fuel and graphite dimensional measurements

Several fundamental analyses of the fuel compact and graphite fuel holder properties will be performed to aid in the evaluation of the irradiation conditions.

- Accurate dimensional measurements of fuel compacts and graphite fuel holders from the irradiation capsules will be made using a custom vision measuring system in the HFEF hot cells. The system is being designed to measure the dimensions with a combined uncertainty no larger than ±25 μm. The data will be used to determine the irradiation-induced dimensional changes of the components and refine the capsule thermal analyses based on updated gas gap widths.
- The graphite fuel holders will be gamma scanned in multiple dimensions in order to map the distribution of fission products and potentially identify specific compacts from each capsule that have failed particles. The analysis will focus on local 'hot spots' in the graphite formed by fission product release (e.g. ^{137}Cs) from the fuel compacts into the graphite.
- Individual fuel compacts will also be gamma scanned to determine critical fission product ratios for burnup calculations. To augment these burnup measurements, selected fuel compacts will undergo destructive burnup measurements using the ASTM E321-96 method.
- The thermal properties (including bulk thermal conductivity and thermal expansion) of the fuel compacts and graphite holders will be measured experimentally.

8.5.2. Conclusion

The post-irradiation examination of NGNP fuel will assess fuel performance during normal operation and under accident conditions. The experiments will focus on the fission product retention of fuel particles and on the micro-structural condition of kernels and coatings. This work will support the fuel fabrication effort by providing feedback on the performance of kernels, coating, and compacts. Ultimately this data will contribute significantly to the technical basis for fuel qualification for the very high temperature gas cooled reactor.

9. BENCHMARKING OF FUEL PERFORMANCE MODELS DURING NORMAL OPERATION AND OPERATIONAL TRANSIENTS

9.1. CALCULATION MODELS FOR NORMAL OPERATIONAL CONDITIONS

9.1.1. International code development

A key part of this CRP-6 includes benchmark calculations with fuel performance models under normal HTGR operating conditions. The normal operation benchmarking has been structured in two phases:

(1) In the first phase, a series of simplified analytical benchmarking problems have been established as a way to 'calibrate' the codes and/or models. This first phase is divided into three steps. In the first step (cases 1 to 3), it begins with simple analytical cases to test simple thermo-mechanical behaviour. Pyrocarbon layer behaviour is tested in the second step (cases 4a to 4d). The third step (cases 5 to 8) represents a single particle

with more complexity added with each subsequent case. These three steps should allow testing different segments of code structural models under controlled conditions.

(2) In the second phase, the codes and/or models will be used to calculate more complicated benchmarks of actual experiments (cases 9 to 12) that have been completed and of planned experiments (case 13).

Current participants in the benchmark include France, Germany, Japan, Republic of Korea, the Russian Federation, Turkey, the United Kingdom, and the USA.

9.1.2. Codes used in benchmark exercise

All computer models that were applied in this benchmark exercise are described in the following in more detail. For direct code-to-code comparison, the Tables 9.1 and 9.2 at the end of this section synthesize the code description and the input parameters.

9.1.2.1. France: ATLAS code description

The ATLAS module should be able to conduct:

- Thermal and mechanical deterministic calculations on an free particle using a finite element method. The models are one-dimensional for intact particles or particles with fully debonded layers (V1.0) or two-dimensional for shaped (V1.0), partially debonded or cracked particles (V2.1).
- Diffusion calculations of gaseous and metallic fission products through the particle layers (V2.0).
- Calculations of fuel elements of compact (V2.1) or pebble type.
- Probabilistic calculations to estimate the probabilities of failure of the layers during an experiment (V2.1) or even in a whole core using former calculations.

The ATLAS code is able to perform thermal and mechanical calculations on a free particle and has been applied to cases 1 to 13 (no failure fraction is given in this document). Version V2.1 allows calculating the corresponding failure fractions for cases 9 to 13.

The properties which are needed for the kernel are specific heat c_p, density ρ, thermal conductivity λ, expansion coefficient α, Young's modulus E and the Poisson coefficient ν.

The properties which are needed for the buffer, the PyC and SiC dense layers are specific heat c_p, thermal conductivity λ, expansion coefficient α, Young's modulus E, Poisson's coefficient ν and the irradiation induced creep factor K. The creep Poisson's coefficient is equal to 0.5.

The thermal loading has two components:

(1) The power released by fission in the kernel. At that time, the input data for the code is the dFIMA/dt (FIMA: fissions per initial metal atom) as a function of time.

(2) The imposed temperature to the outer surface of the model.

The loads of the mechanical calculations are of imposed pressure or deformation type and result from the following physical phenomena:

- Release of fission gases (Xe and Kr) and production of CO depending on burnup, temperature, and time.
- Influence of the graphite matrix on the particle. This influence is, for the time being, taken into account by a pressure imposed on the outer surface of the model.
- Fuel swelling. This includes the solid and gaseous swelling.
- Fuel densification.
- PyC and SiC layer irradiation-induced dimensional change depending on temperature and fast neutron fluence.

A finite element method is used and is followed by:

- A thermal calculation giving the temperature field in the meshing nodes. The thermal model treats the conduction in the particle. Between kernel and buffer, buffer and the first dense layer, and between layers if needed, meshes simulate a gaseous joint.
- A mechanical calculation allows access to the displacements fields, stresses and strains in the meshing nodes. The mechanical model treats the visco-elasticity with a large displacement resolution in the particle. The non-linearities are of three types: (a) the large displacement resolution, (b) the material non-linearity through irradiation induced creep laws, and (c) the geometrical non-linearity through a contact condition between disconnected surfaces.

The main characteristics of the model are as follows:

- The thermal load is the temperature field resulting from the thermal calculation. The thermal calculation is performed on the deformed geometry coming from the former mechanical calculation.
- The pressure load is calculated at each time step from the free volume (calculated from the deformed geometry), the temperature, and the quantity of gas (Xe, Kr, CO) present.
- The swelling of the kernel and the irradiation induced dimensional change of the layers are considered as loads of imposed deformation type.

9.1.2.2. Germany: PANAMA code description

The FZJ computer code PANAMA [228] simulates the mechanical performance of TRISO coated fuel particles under given normal operation and accident conditions. The failure probability, Φ_p, which is of importance under the conditions of normal reactor operation and core heatup accidents for modular type HTGRs, is based on a pressure vessel model and includes a degradation effect on the SiC layer due to fission product corrosion.

In the pressure vessel model, the SiC layer represents the wall of a simplified pressure vessel, while all other layers are ignored. This pressure vessel is assumed to fail as soon as the stress induced in the SiC layer by the internal gas pressure, σ_t, exceeds the tensile strength of the SiC, σ_o. The probability for a pressure vessel failure of a particle is a function of time and temperature and can be described according to the following Weibull equation:

$$\Phi_p(t,T) = 1 - \exp\left\{-\ln 2 * \left(\sigma_t / \sigma_o\right)^m\right\} \quad (9.1)$$

The tensile strength is a material parameter whose mean value and statistical Weibull modulus, m, can be derived, e.g. from SiC ring crack tests [304]. The SiC layer is weakened

under irradiation; its strength is assumed to decrease as a function of the fast neutron fluence as was derived from measurements on the German particle batch EO 1607.

The effect of fission product corrosion is transformed into a thinning of the SiC layer, i.e. the pressure vessel wall, at a volume corrosion rate $\dot{v}$ according to [305], thus leading to a sooner failure of the coated particle at given conditions. The stress induced in the SiC layer, σ_t, is determined with the following equation valid for a 'thin shell' or 'soap bubble' pressure vessel of radius r, which is equivalent to the mean radius of the SiC layer, and initial thickness d_o:

$$\sigma_t = \frac{r^* p}{2 d_0} * \left(1 + \dot{v} t / d_0\right) \quad [Pa] \tag{9.2}$$

The internal gas pressure p is calculated by applying the ideal gas law to the generation of fission gases Xe, Kr, and reaction gas CO. The amount depends on the yield of stable fission gases F_f, burnup Bu, the number of oxygen atoms produced in the kernel O_f, and the temperature T:

$$p = \frac{\left(F_d * F_f + O_f\right) * Bu}{V_f / V_k} * R * T / V_m \quad [Pa] \tag{9.3}$$

where

F_d is the release fraction of fission gases (Xe and Kr) from the kernel into the void volume [306];
V_f is the void volume (m^3), typically 50% of the buffer volume;
V_k is the kernel volume (m^3);
V_m is the molar volume of the heavy metal in the kernel (m^3/mole).

Oxygen production in the particle kernels as a result of the fissioning of ^{235}U or ^{239}Pu is strongly dependent on the irradiation history and to a great extent on the type of kernel. Corresponding relationships for O_f were derived from tests at Seibersdorf, Austria, covering an irradiation time up to 550 efpd and a temperature range between 950–1525°C [307]. In case of a transient irradiation temperature history, O_f will be stepwise integrated (upper limit: 0.625). After integration, the total O_f value can be taken to derive, in reverse, a fictive average irradiation temperature corresponding to that temperature, which would result in the same O_f value, if it were kept constant over the same irradiation time.

The validation of the PANAMA model has been made against numerous experiments with spherical fuel elements heated at accident temperatures in the range of 1600–2500°C. Good agreement with the Kr release measurements was found in many cases. For fuel exposed to extreme irradiation conditions, however, the calculated failure fraction has shown the tendency to overpredict failure.

The material property 'mean SiC strength' and its Weibull distribution as well as their fast fluence dependence are highly significant input parameters. The reference data for SiC strength (836 MPa) and respective Weibull modulus (8.02) for the unirradiated state, typically used in predictive calculations, correspond to a former German coated particle batch production, EO 1607, which appears to represent some kind of average data. It was also the only particle batch, for which SiC strength and Weibull modulus were measured after

irradiation in HFR-GM1. In this experiment, the fast fluence achieved was 1.8×10^{25} EDN at an irradiation temperature of 1185°C. The analysed strength degradation and modulus reduction with fast fluence were 687 MPa and 5.98, respectively. That relationship is usually in PANAMA calculations interpolated or extrapolated to the fast fluences considered, however, with no assured data basis.

Further improvement of PANAMA is planned for the future considering the following aspects:

- ideal gas law to be replaced by the Redlich–Kwong equation of state;
- include statistics by conducting a sequence of calculations with varying layer thicknesses over a given statistical range;
- incorporate the effects of PyC prestressing on the SiC (depending on shrinkage and creep in pyrocarbon, the tensile stress in the SiC layer can be reduced significantly);
- presently free volume in kernel is assumed constant, also no kernel swelling.

For the benchmark calculations here, the PANAMA model — due to its feature of ignoring all coating layers except for the SiC — cannot be applied to the cases 1 through 8, but has been applied to the cases 9 through 13.

9.1.2.3. Japan: RIGID-SIC code description

In Japanese fuel failure modeling, the so-called 'Rigid SiC' model [98, 308, 309] is employed for the stress calculation. In this model, the failure probability of each coating layer of the coated fuel particle follows the Weibull distribution. The model consists of three calculation parts, 1) internal pressure calculation, 2) stress calculation, and 3) failure fraction calculation, as described below.

(a) Internal pressure calculation method

The internal pressure is assumed to be generated from stable gaseous fission products and CO gas due to excess oxygen by UO_2 fission. It is simply assumed that the free volume of the gases is calculated from the densities of as-fabricated porous buffer layer and of theoretical PyC. Finally the internal gas pressure is calculated by using the ideal gas equation.

(b) Stress calculation method

In this model, the following stresses are calculated as input to the failure fraction calculation (see 'Failure Fraction Calculation Method').

For the intact particle, the tangential and radial stresses at the inner surface of the SiC layer at the time τ, $\sigma_t^a(\tau)$ and $\sigma_r^a(\tau)$ (MPa), are calculated by the following equations:

$$\sigma_t^a(\tau) = \frac{1}{r(4)^3 - r(3)^3} \cdot [\sigma_r^b(\tau) \cdot r(4)^3 - \sigma_r^a(\tau) \cdot r(3)^3 + \frac{1}{2} \cdot [\sigma_r^b(\tau) - \sigma_r^a(\tau)] \cdot r(4)^3] \tag{9.4}$$

$$\sigma_r^a(\tau) = \frac{-3 \cdot (1 - \nu_{PyC})}{1 + \nu_{PyC} + 2 \cdot (1 - 2 \cdot \nu_{PyC}) \cdot W_a} \cdot P(\tau) + \frac{2}{3 \cdot C} \cdot \frac{(W_a - 1) \cdot [\dot{S}_r(\tau) + 2 \cdot \dot{S}_t(\tau)] + 3 \cdot G_a \cdot [\dot{S}_r(\tau) - \dot{S}_t(\tau)]}{2 W_a \cdot (2 \cdot \nu_{PyC}^c - 1) - (1 + \nu_{PyC}^c)} \tag{9.5}$$

$$\sigma_r^b(\tau) = \frac{2}{3 \cdot C} \cdot \frac{(W_b - 1) \cdot [\dot{S}_r(\tau) + 2 \cdot \dot{S}_t(\tau)] + 3 \cdot G_b \cdot [\dot{S}_r(\tau) - \dot{S}_t(\tau)]}{2 W_b \cdot (2 \cdot \nu_{PyC}^c - 1) - (1 + \nu_{PyC}^c)} \tag{9.6}$$

$$W_a = \{r(3)/r(2)\}^3,\ G_a = \ln\{r(2)/r(3)\},\ W_b = \{r(4)/r(5)\}^3,\ G_b = \ln\{r(5)/r(4)\} \quad (9.6a)$$

where

r(n), r(n+1) are the inner and outer radius of the IPyC (n=2), SiC (n=3) and OPyC (n=4) layer (m);
$P(\tau)$ is the internal pressure at the time τ (MPa);
$\dot{S}_r(\tau)$, $\dot{S}_t(\tau)$ are the radial and tangential swelling rate of PyC at the time τ ($(\Delta L/L)/10^{25}$ n/m^2);
C is the creep constant of PyC ((MPa·10^{25} n/m^2)$^{-1}$);
ν_{PyC}^{c} is the Poisson ratio of the creep of PyC.

For the SiC failed particle, the internal pressure at time τ, $P(\tau)$, MPa, works for the tangential stress at the inner surface of IPyC layer, $\sigma_t^I(\tau)$, MPa, to be described below ;

$$\sigma_t^I(\tau) = P(\tau)(Wa+2)/\{2(Wa-1)\} \quad (9.7)$$

For the both SiC and IPyC failed particle, the internal pressure at time τ, $P(\tau)$, MPa, works for the tangential stress at the inner surface of OPyC layer, $\sigma_t^O(\tau)$, MPa, to be described by

$$\sigma_t^O(\tau) = P(\tau)(2W_b+1)/\{2(1-W_b)\} \quad (9.8)$$

(c) Failure fraction calculation method

The model is based on the following assumptions:

- the intact particle never fails unless the SiC layer is failed;
- outer PyC layer never fails unless SiC and inner PyC layer are failed;
- the failure of each layer is a function of only the tangential stress at the inner surface of them;
- each layer never fails unless the tangential stress at the inner surface of them is > 0 MPa.

The failure probability of each layer is calculated by the following basic equation:

$$f_i(t) = 1 - \exp(-\ell n2 \times (\frac{\sigma_i(t)}{\sigma_{0,i}})^{m_i}) \quad (9.9)$$

where

f_i is the failure probability of i layer at irradiation time t;
$\sigma_i(t)$ is the stress on the i layer at irradiation time t (MPa);
$\sigma_{0,i}$ is the strength of the i layer (MPa);
m_i is the Weibull modulus for the i layer strength.

Probability that the intact particle becomes the through-coatings failed particle (F_{TC}) can be expressed as follows ;

$$F_{TC} = f'_{IPyC} \times f_{SiC} \times f'_{OPyC} \quad (9.10)$$

where

f'_{IPyC} is the failure probability of the IPyC layer in the SiC failed particle;
f_{SiC} is the failure probability of the SiC layer in the OPyC intact particle;
f'_{OPyC} is the failure probability of the OPyC layer in the SiC failed particle.

The probability that the intact particle becomes the SiC-failed particle (F_{SiC}) becomes same as the failure probability of the SiC layer.

$$F_{SiC} = f_{SiC} \tag{9.11}$$

In the fabrication of coated fuel particles, a few particles are made as initially SiC-failed particles (i.e. defective SiC coating). In this model, the SiC-failed particle is defined as a particle that has failed SiC layer but has an intact OPyC layer. The probability that as-fabricated SiC-failed particle becomes the through-coatings failed particle (F'_{TC}) is written as following equation:

$$F'_{TC} = f'_{OPyC} \tag{9.12}$$

The tensile stress induced in the coating layer is calculated based on a thick-walled spherical pressure vessel model [310]. The internal pressure is generated by stable gaseous fission products and CO gas due to excess oxygen by UO_2 fission. The free volume in the buffer layer is calculated from as-fabricated porous buffer layer density and theoretical density of the PyC.

9.1.2.4. Republic of Korea: COPA code description

The COPA (COated PArticle) code consists of nine modules as follows [311]:

- COPA-BURN. This calculates the neutron flux and fluence with time, and then burnup, fission rate per volume, power generation and fission product inventory throughout a fuel element and a fuel particle at a location in a core. This is inserted into the COPA-MECH, COPA-FAIL, and COPA-FPREL modules.
- COPA-TEMTR. This calculates the temperature distribution in a coated particle by using an implicit point-scheme finite difference method [312]. The numerical modeling is one-dimensional. The geometric elements for the numerical modeling are a kernel, a gap between a kernel and a buffer, a buffer, a gap between a buffer and an IPyC, an IPyC layer, a SiC layer, and an OPyC layer.
- COPA-TEMPEB. This calculates the temperature distribution in a pebble by using the implicit point-scheme finite difference method. This model is one-dimensional for a pebble. The geometric elements are a fuel region and a matrix graphite region. The fuel region is assumed to be a mixture in which matrix graphite and coated particles are homogenously blended.
- COPA-TEMBL. This calculates the temperature distribution in an equivalent slab of a block in a prismatic modular reactor by using the implicit point-scheme finite difference method. The equivalent slab is an approximation to a symmetry element in a fuel block and was devised to calculate the fission product migration in a fuel block more easily [313]. The numerical model is one-dimensional for the equivalent slab. The geometric elements considered are a fuel compact, a graphite slab, and a gap between the compact and the graphite slab. The fuel compact is assumed to be a mixture in which matrix graphite and coated particles are homogeneously blended.
- COPA-MECH. This performs mechanical analyses on an intact coated fuel particle by using a finite element method utilizing the Galerkin form of the weighted residuals

procedure [314]. The models are one-dimensional. The geometric elements for a numerical modeling are a fuel kernel, a buffer, and three coating layers. This calculates the contact forces or pressures acting on interfaces between the layers of a coated particle. This is inserted into the COPA-FAIL to calculate the failure fraction of the coated particles during a reactor operation.

- COPA-FAIL. This calculates the failure fractions of coated fuel particles under reactor operational conditions. This uses a Monte Carlo method for a random particle sampling in which a sample is equivalent to a coated fuel particle. The particle has different dimensional sizes, material properties, and fracture strengths of the coating layers through the Monte Carlo sampling. Kernel diameter, thicknesses of a buffer and three coating layers, and densities of a kernel, a buffer and three coating layers show the standard normal distribution. The strengths of the SiC and PyC layers are expressed in the Weibull distribution. In order to calculate the stresses of the coating layers of a coated particle and check the particle integrity, the COPA-FAIL uses the COPA-MECH for an intact coated particle and the statistical correlations obtained in the COPA-ABAQ for a particle with debonded or cracked layers.
- COPA-FPREL. This analyses the fission product migration in a coated fuel particle, a pebble and a fuel block under reactor operational conditions, and during heating and irradiation tests. The implicit point-scheme finite difference method is applied to a coated fuel particle, a pebble and a fuel block. In a fuel block, the analysis of a fission product migration is applied to the equivalent slab. The equivalent slab is sized so that thermal resistances in the slab and the symmetry element are the same. Migration mechanism is assumed to be diffusion only.
- COPA-ABAQ. This analyses the crack and debonding of the coating layers by using ABAQUS. These models are two-dimensional. This produces the maximum SiC stresses in the cracked or debonded particles according to several parameters such as particle sizes, material properties and irradiation temperature. A statistical correlation can be developed through a statistical method which correlates the maximum SiC stress to the particle parameters. The correlation is inserted into the COPA-FAIL to calculate the maximum SiC stress for particles with debonded or cracked layers.
- COPA-MPRO. This calculates or provides 1) the material properties of the kernel material, buffer, high density pyrocarbon, silicon carbide, matrix graphite, and structural graphite, 2) a heat conductance in a gap, 3) the partition factors at the layer interfaces of a coated particle, 4) the diffusion coefficients of fission products, 5) the sorption isotherm data of fission products on the surfaces of a pebble, a compact, and a fuel block, 6) heat and mass transfer coefficients of fission products in helium.

Each module is a stand-alone programme. It is inserted into other modules or is used to generate the input data for other modules.

9.1.2.5. The Russian Federation: GOLT code description

The code GOLT (Gazo-OhLajzdaemoe Toplivo — Gas-Cooled Fuel) [315] is intended for predicting performance of single as well as a batch of fuel coated particles under normal conditions irradiation and accidents. The code is developed for different types of HTGR coated particles including fuel based on PuO_{2-x}.

The version GOLT-v1 is capable to calculate temperature distribution along particle radius, formation of fission gases, CO, CO_2 and internal pressure, fuel kernel swelling, irradiation induced dimension changes and creep of all coating layers, development of stresses and deformations in each coating layer, probability of failure of each dense coating layer, behaviour of coated particles with all probable combinations of failed and intact TRISO coating layers and total probability of SiC layer and through-coating failure.

Version GOLT-v2 takes into account additional failure mechanisms: KCMI (kernel–coating mechanical interaction) [238], amoeba effect, corrosion and thermal decomposition of SiC layer, improved model of buffer behaviour including possibility of its cracking and debonding from IPyC, as well as possibility of IPyC–SiC debonding.

Version GOLT-v2a is intended for predicting the performance of a single coated particle at accident or heating test conditions and includes special procedures for transition from normal to accident mode of calculations.

Version GOLT-v3 accumulates capabilities of version GOLT-v2 and includes Monte-Carlo procedure to estimate the fraction of failed particles by conducting a sequence of calculations with varying layer thicknesses, kernel diameter and strength of dense coating layers over a given statistical range.

Version GOLT-v2 has been applied to calculate cases 1 to 8, version GOLT-v3 to calculate cases 9–13 of the Normal Operation Benchmark and GOLT-v2a to some cases of the Accident Condition Benchmark.

(a) General algorithm of calculation

The thermo-mechanical model for single coated particle is based on standard equations of mechanics of a viscous-elastic body. Boundary conditions on outer surface of a coated particle depend on whether free particles or particles in a fuel compact or spherical fuel element are considered. The initial set of differential equations is solved by finite difference approximation. The coated particle is divided into a set of small spherical sub-layers, including kernel and buffer, and each sub-layer has individual temperature and properties. Properties of coating materials (pyrocarbon, silicon carbide, zirconium carbide etc.) depend on temperature, fast neutron fluence, and time. For all coating layers, anisotropic irradiation-induced dimension changes (IDC) and creep are taken into account. For IDC of pyrocarbon, available approximations are used which depend on initial anisotropy and irradiation temperature. The effect of fission product corrosion and thermal decomposition is transformed into a thinning of SiC layer [316].

Calculation of temperature profile over particle radius is performed sequentially from fuel kernel centre through all sub-layers to the particle's outer surface for each time step. For the current time step, the following sequence of calculation is performed: burnup, fluence of fast neutrons, properties of materials, swelling of kernel, generation of fission gases, generation of CO and CO_2, shrinkage of buffer, IDC of dense layers, free internal volume for gases, internal pressure, current thickness of SiC layer, stresses and deformations in each mesh node (including kernel and buffer), failure probability for each coating layer. Calculations are performed step-by-step on time, thus, formation of stresses in coated particles during manufacturing is possible.

All calculations listed above are repeated four times to obtain results for all possible variants of TRISO coated particle behaviour depending on combination of intact and failed dense

layers of coating. Then the total probability of SiC layer and through-coating failure is calculated.

(b) Internal pressure

The internal pressure is assumed to be generated from fraction of stable gaseous fission products, xenon and krypton, released to open porosity of the kernel and to buffer as well as from generation of CO and CO_2 in oxide fuel UO_2 or PuO_{2-x}. Internal voidage in the particle is calculated with account of kernel swelling, thermal deformations and IDC of IPyC layer. Code GOLT includes two independent subroutines intended for calculation of internal pressure in fuel based on UO_2 or PuO_{2-x}, correspondingly. Generation of CO and CO_2 in UO_2 fuel is evaluated by Homan's approximation. For PuO_{2-x} fuel, joint analysis with thermodynamical code ASTRA [317] or analytical approximation [318] is used. Finally the Redlich–Kwong or ideal gas equation of state (choosing of equation depends on available initial data) is applied to calculate the overall internal pressure.

(c) Model of TRISO coating failure

The probability of failure of single spherical coating layer is described according to the Weibull equation:

$$P(s) = 1 - \exp\left\{\ln(0.5) * (s / \sigma_m)^m\right\} \qquad (9.13)$$

where

s is the maximal stress in layer (Pa);
σ_m is the median strength ($P(\sigma_m) = 0.5$) (Pa);
m is the Weibull's modulus.

In the code GOLT, automatic calculation of SiC and through-coating failure probability for TRISO coated particles is performed. Total probability of SiC layer failure is derived from the results of calculations of the complete set of possible variants of coated particle behaviour:

V_1: all layers of coating remain intact: $P(V_1) = (1-P_1) \cdot (1- P_0)$

V_2: IPyC fails, OPyC remains intact: $P(V_2) = (1-P_1) \cdot P_0$

V_3: IPyC remains intact, OPyC fails; $P(V_3) = (1-P_0) \cdot P_1$

V_4: IPyC becomes failed, OPyC becomes failed; $P(V_4) = P_1 \cdot P_0$

where

V_i is the i-th variant of TRISO coated particle behaviour;
$P(V_i)$ is the probability of i-th variant of TRISO coated particle behaviour;
P_1 is the probability of IPyC failure;
P_0 is the probability of OPyC failure.

Then the total probability of SiC (or any other material) layer failure can be calculated by:

$$W_{SiC} = \sum_{i=1}^{i=4} P(V_i) \cdot P(W / V_i) \quad (9.14)$$

where $P(W/V_i)$ is the conditional probability of SiC layer failure at i-th variant which is automatically calculated for each variant.

The probability of through-coating failure is calculated by the expression:

$$P_{thc} = P(W / V_4) \cdot P(V_4) \quad (9.15)$$

Version GOLT-v3 performs these calculations with account of statistical dispersion of design parameters: diameter of kernel and layers thicknesses as well as of strength of dense coating layers. The direct Monte-Carlo procedure is used to calculate fraction of particles having failed SiC layer and through-coating damage. In the first case, the data obtained are needed to evaluate metal fission product release and in the second to calculate release of gaseous fission products.

9.1.2.6. Turkey: TRFUEL code description

CRP-6 study is performed to verify the finite element model of the coated fuel particle. The study involves cases starting from simple one-layer particle to a real TRISO particle. As the number of layers increase, the particle faces different loads that simulate irradiation conditions.

Steady state calculations are performed for Cases 1 to 4c, for internal pressures, temperature and swelling/shrinkage rate do not change with time. For Cases 4d to 14, transient calculations are performed. Cases 1 to 8 assume constant pressure inside the IPyC layer. For Cases 9 to 14, gas pressure inside the IPyC is calculated and presented as a comparison metric. Tangential and radial stress as a function of fast neutron fluence are other items of the comparison metric for analysing the performance of different coated fuel particle models. Also, for Cases 9 to 14, particle failure probability is calculated and compared for different models. Individual layer failure probabilities are calculated for the relevant cases.

One approach for prediciting the particle failure probability is assuming the SiC as the principal barrier and considering its failure probability as the representative of the particle failure probability. This approach is employed for the analysis. Since tension (not compression) of the SiC is the main contributor to the failure, tensile stress values of the tangential stress in the SiC layer is used in the probability calculations.

Main approaches and assumptions for the CRP-6 study are as follows:

- Under irradiation conditions or reactor operation, the particle is under pressure load from fission gases and CO formed outside the kernel. Ambient pressure is assumed outside the OPyC layer.
- Under irradiation, PyC shrinks in both radial and tangential directions. At modest fluences depending on the density, temperature and anisotropy of the material, it begins to swell in the radial direction and continues to shrink in the tangential direction. This behaviour puts the PyC layers into tension in the tangential direction. At longer irradiation times, irradiation-induced creep works to relieve the tensile stress on the PyC layers. Creep is also modeled in the present study.

- The anisotropy of PyC layers affects swelling as a function of neutron fluence.The IPyC and OPyC layers behave differently in radial and tangential directions as a result of this anisotropy, which is represented by the Bacon Anisotropy Factor (BAF). Anisotropy of the PyC layers is taken into consideration starting from case 4a. Radial and tangential swelling/shrinkage rates as a function of fast neutron fluence are presented in this section. These equations change according to the initial BAF of the case and also depend on material properties and irradiation conditions.
- Thermal expansion is another load factor affecting the SiC and PyC layers taken into consideration.

ANSYS finite element commercial code is employed in the analysis. User defined code packages are added as necessary if models provided by the code. Two dimensional axisymmetric models are employed to simulate the coating layers of the cases. Internal gas pressure and ambient pressure are the boundary conditions of the model. Transient and steady state structural models with material properties of CRP-6 cases are used to calculate the stressess on the coating layers and failure probabilities.

For cases 9 to 14, internal gas pressure due to fission product gases and CO is calculated. Xe and Kr are assumed to be the representative of the gaseous fission products. Stable gaseous fission products xenon and krypton compose 31% of the fission products. The diffusion of these gases are assumed to be well represented by the Booth equivalent sphere release model and which is used explicitly in this study. The release fractions are calculated based on diffusion calculations using the simple Booth model.

Free oxygen from the kernel immediately reacts with the carbon in the buffer and forms CO and a few percent of CO_2. The following experimental correlation of oxygen release is employed in this study to calculate the amount of CO formed inside the IPyC layer:

$$\log\{(O/f)/t^2\} = -0.21 - 8500/(T+273) \qquad (9.16)$$

where

O/f is the oxygen release at the end of irradiation (atoms per fission);
t is the irradiation time (days);
T is the time-averaged particle surface temperature during irradiation (°C).

The ideal gas law is employed to calculate the pressure on the inner side of the IPyC layer as a function of burnup. The free volume on the inner side of the IPyC consists of the empty volume of the buffer, which is 50% of the full dense material, and the free volume created by CO formation within the buffer. On the other hand, this volume is decreased by the swelling of the kernel, which is assumed to be 0.47% per % FIMA.

9.1.2.7. United Kingdom: STRESS3 code description

In the UK, stresses in an individual particle are calculated by means of the STRESS3 code [232, 319]. The statistics of particle failure are obtained by performing STRESS3 runs on many particles that have been randomly selected, using the code STAPLE [232].

In the code STRESS3, the whole irradiation history is divided up into a sequence of consecutive finite neutron dose steps. Values of stresses and strains are known at the beginning of each step (and assumed to be zero at the start of the calculation). The requirement therefore is to calculate changes in stresses and strains, $\Delta\sigma$ and $\Delta\varepsilon$, for each layer

over the neutron dose step being considered currently, which then enable stresses and strains to be updated for the start of the next step. Spherical symmetry is assumed. As a result, although all materials comprising the particle may be treated as anisotropic, there are only either two or four independent values for each property. (With subscripts 1 and 3, or alternatively 11, 12, 13 and 33 in reduced tensor notation where 1 and 2 denote directions in the surface of the layer and 3 normal to it.)

For each specific layer the displacement equations, defining the change in strain during the current neutron dose step is given by

$$\Delta\varepsilon_l = \sum_{m=1}^{3}\left[S_{lm}\Delta\sigma_m + K_{lm}\left(\sigma_m + \frac{1}{2}\Delta\sigma_{\mathrm{m}}\right)\Delta\Gamma\right] + T_l\Delta\theta \qquad + G_l\Delta\Gamma \qquad (9.17)$$

where

l=1,3;
first term in brackets is the elastic strain;
second term in brackets is the irradiation creep;
first term following brackets is the thermal expansion;
last term is the dimensional change under irradiation.

In equation (9.4), S represents the compliance constant, K the irradiation creep constant, Γ the neutron dose, T the thermal expansion coefficient, Θ the temperature and G the dimensional change that occurs per unit neutron dose. The Δ preceding each variable denotes the change in its value over the course of the dose step. (Additional time dependent factors, relating to thermal creep and sintering are incorporated into the code, but for the sake of simplicity are omitted from equation (9.4) since in practice their numerical values so far have assumed to be zero.) It will be noted that the stress employed in defining the creep strain is the value that occurs approximately half way through the step (i.e. an implicit–explicit solution is employed).

In spherical symmetry, increments in radial displacements and strain are related by the compatibility relation

$$\Delta\varepsilon_1 = \frac{\Delta u}{x};\quad \Delta\varepsilon_3 = \frac{\mathrm{d}\,\Delta u}{\mathrm{d}x} \qquad (9.18),\ (9.19)$$

and stress increments by the equation of equilibrium

$$\Delta\sigma_1 = \Delta\sigma_3 + \frac{1}{2}x\frac{\mathrm{d}\,\Delta\sigma_3}{\mathrm{d}x} \qquad (9.20)$$

where

u is the radial displacement;
x is the radial coordinate.

Eliminating $\Delta\sigma_1$, $\Delta\sigma_3$, $\Delta\varepsilon_1$, $\Delta\varepsilon_3$ from Equations (9.17) and (9.20) produces a differential equation in Δu

$$x^2 \frac{\mathrm{d}^2 \Delta u}{\mathrm{d}x^2} + 2x \frac{\mathrm{d}\,\Delta u}{\mathrm{d}x} - 2\gamma\,\Delta u = 2(\delta + \xi)x \tag{9.21}$$

where

γ, δ, ξ are complex expressions derived from the material properties;
γ and δ are constants.

ξ is a function of x since it depends on the known stresses at the start of the step. The solution has two constants of integration; these are derived from a set of simultaneous equations from all the layers which define the boundary conditions (continuity of displacements and radial stresses at the interfaces).

If, at the end of a neutron dose step, the radial stress between two layers is found to exceed the specified debonding stress, the step is repeated with the boundary conditions modified appropriately by way of recognising that a gap now exists between the layers; similarly if a previously opened gap is found to have closed. Again, if at the end of a step the tangential stress in a layer is found to exceed the fracture stress, failure is simulated by means of a number of additional pseudo time steps during which creep relaxation is allowed to occur until the stress in the layer has decreased to some low, residual value. During subsequent steps the compliance constant of this failed layer is set very high.

The change in voidage during irradiation, due to swelling of the kernel and volume changes of the layers, is taken into account. Because the voidage in the particle and the gas pressure are interdependent variables, the gas pressure must be calculated iteratively. In order to calculate gas pressures the Redlich–Kwong equation of state is used and the presence of CO_2 as well as CO is taken into account.

STRESS3 requires details of the relevant properties of the different materials which comprise the particle. They may be specified as functions of the neutron dose by providing numerical values at user specified doses. Values of properties at doses corresponding to the various steps in the calculation are then derived by interpolation. Alternatively, the value of any property may be chosen to remain constant throughout the irradiation.

Information relating to the particle design is then required. This includes the diameter of the kernel and thicknesses of the various layers, a specification of the material employed in each layer together with its fractional porosity and fracture stress; also the stress at which debonding between layers can occur.

Details of the irradiation that need to be specified include the following: the relation between neutron dose, burnup and time, the fraction of fissions that occur via plutonium versus burnup, and a wide range of parameters which can vary with neutron dose, including the irradiation temperature, fuel swelling rate, and the relevant information required to calculate the quantity and composition of gas in the voidage. As a result complex irradiation histories, including shut-downs and transients, can be modeled.

The output after each neutron dose step consists of the following information:

- the maximum tangential stress in each layer;
- the radial stress at each coating interface;
- a message when a layer has failed, debonded, or a previously open gap has closed;

- the maximum (elastic + creep) strain in each layer;
- the size of gaps between layers;
- the internal voidage;
- the change in the overall radius of the particle.

Calculations can proceed until all layers have failed.

It is perhaps worth emphasizing that one of the strengths of STRESS3 is that it does not rely on any specific models to define the input data. The user simply inserts numerical data from a preferred model. For example, this enables the way different PyC dimensional change recommendations affect the results to be readily studied. Again, the user is not tied to one specific model to describe the release of oxygen over the course of the irradiation.

The STAPLE code (STAtistics of Particle LifE) [232] simulates the selection of numerous particles from a batch, performs a STRESS3 run on each of them, and records the burnup at which a user specified layer fails. These burnup values are stored in bins, thereby enabling a histogram of the number of failures in each bin to be obtained, and from them the cumulative increase in failure fractions with burnup.

For the purpose of selecting particles, any of the following variables may be varied statistically, assuming a normal distribution: kernel diameter, thicknesses of all the layers, open porosity of the kernel and layers, and closed porosity of the kernel. All these selections of property values were performed using a random number generator and a simple algorithm. Likewise fracture stresses of any or all the layers may be specified in accordance with Weibull statistics. The output comprises a standard STRESS3 output, obtained by assuming that all variables adopt their mean value. Finally details of the statistics of particle failure are printed out.

9.1.2.8. USA: PARFUME code description

The INL integrated mechanistic fuel performance code for TRISO coated gas reactor particle fuel is called PARFUME (PARticle Fuel ModEl). PARFUME describes both the mechanical and physico-chemical behaviour of the fuel particle under irradiation, while capturing the statistical nature of the fuel and also calculates fission product transport under postulated accident conditions. Material properties used in PARFUME to represent the shrinkage, creep, thermal expansion, and elastic behaviour of the coating layers were obtained from a report prepared by the CEGA Corporation in July 1993 [320].

The PARFUME thermal model is based on a finite difference heat conduction approach with internal heat generation capabilities for either fuel spheres or cylindrical compacts. Based upon input boundary conditions, time dependent fuel element temperature profiles can be calculated for either steady-state or transient conditions. The resulting fuel element temperature profiles are then used to calculate particle temperature profiles. This model accounts for the factors that result in the development of a gap between the buffer and IPyC. These factors include the net effects of kernel swelling; shrinkage and creep in the buffer, IPyC, and OPyC layers; and the associated kernel/buffer contact pressure. Furthermore, the model accounts for changes in gap conductivity with changes in particle geometry, gap gas composition, pressure, and temperature.

Particle internal gas pressures are calculated according to the Redlich–Kwong equation of state [233]. Parameters utilized by this equation of state are derived from the critical temperature and pressure of each gas species [321] occupying void volume within the

particle. PARFUME considers the generation of CO and the release of the noble fission product gases, xenon and krypton, in this pressure calculation. Either of two algorithms may be chosen for calculating CO production. A simple temperature dependent General Atomics (GA) correlation [322] is used primarily for comparison to historic evaluations. The other algorithm is a detailed model derived from thermochemical free energy minimization calculations performed by the HSC code [323]. Input to the HSC code consisted of elemental fission product inventories generated by the MOCUP [324] code which couples the MCNP [325] and ORIGEN2 [326] codes. This CO production model considers burnup, temperature, uranium enrichment, and fuel composition in the calculation.

PARFUME calculates fission product gas release due to both recoil and diffusion. Direct fission recoil from the kernel to the buffer is accounted for by geometrical considerations and fission fragment ranges derived from compiled experimental data [327]. Diffusive release is calculated according to the Booth equivalent sphere diffusion model [223] which utilizes an effective diffusion coefficient formulated by Turnbull [328]. This effective diffusion coefficient accounts for intrinsic, athermal and radiation-enhanced diffusion.

A model accounting for release of short-lived fission product gases from failed particles and from uranium contamination in the fuel matrix material is incorporated into PARFUME. This correlation calculates release rate to birth rate (R/B) ratios for several prominent fission product nuclides. Also based upon the Booth equivalent sphere gas release model [329], this correlation uses different reduced diffusion coefficients for release from failed particles [52] and from uranium contamination [330].

Kernel migration (amoeba effect) occurs within the presence of a macroscopic temperature gradient and is calculated according to a standard formulation. This algorithm utilizes kernel migration coefficients derived from experimental data. For UCO fuel where kernel migration is expected to be miniscule, a General Atomics derived correlation [285] is used. For UO_2 fuel, where kernel migration can be significant, recent data (from the last 20 years) [97, 331] were fitted to an Arrhenius function to derive a kernel migration coefficient correlation. Particle failure is assumed to occur when the kernel comes into contact with the SiC layer. A Pd–SiC interaction model is based on fitting all available in-reactor data for Pd penetration in SiC [305, 332–334] to an Arrhenius function. The resulting penetration depth correlation is folded with finite element stress analyses of corroded, or thinned, SiC to develop a failure algorithm.

A key element of the PARFUME programme is a closed form solution that calculates stresses in the coating layers of a one-dimensional (symmetrical) spherical particle [335]. This solution accounts for the irradiation-induced creep and swelling in the pyrocarbon layers in addition to the elastic behaviour of the three layers of a TRISO coated particle. To treat situations where the particle temperature varies throughout irradiation, the solution has been enhanced to include the effect of differential expansion among the layers. Failure of a one-dimensional particle occurs if the internal pressure is high enough that the tangential stress in the SiC layer reaches the SiC strength for that particle.

PARFUME also considers multi-dimensional behaviour that may contribute to particle failures, such as (i) cracking of the IPyC layer, (ii) partial debonding of the IPyC from the SiC layer, (iii) an aspherical geometry, and (iv) thinning of the SiC due to interaction with fission products. To model the first three of these multi-dimensional effects, PARFUME utilizes the results of detailed finite element analysis on cracked, debonded, or aspherical particles in conjunction with results from the closed form solution for a one-dimensional particle to make

a statistical approximation of the stress levels in any particle. Using this approach [336], numerous parameters can be varied statistically about a mean value, and failure probabilities may be calculated [137, 337, 338]. Failure due to thinning of the SiC caused by SiC/fission product interaction is based on the size of the thinned area.

The various failure modes are implemented in PARFUME such that a particle fails only in one mode, that which occurs first. The code uses the Weibull statistical theory to determine whether particles fail, using a mean strength for the SiC layer that is based on a stress distribution corresponding to the failure mechanism under consideration. PARFUME retains the time at which failures occur, allowing for the construction of a time evolution of the failure probability for a batch of particles.

The failure probability for a batch of fuel particles can be calculated in PARFUME using the traditional Monte Carlo method or an alternate approach using an integral formulation. The integration treats each statistically varying parameter as a dimension in parameter space. The integral convolves density functions representing the statistical distributions for the varying parameters with the failure probability as it varies over the parameter space. An advantage of the integration method is that it calculates a very small failure probability as quickly as a large failure probability, and thus, can be much faster than the Monte Carlo method. Because this is a multiple integration, the speed of the probability calculation depends largely on how many parameters are given a statistical variation.

9.1.2.9. USA: GA code description

The approach employed by General Atomics (GA) in this benchmark study was to use the GA proprietary codes named PISA to calculate IPyC, SiC and OPyC stress related failure, and CAPPER to calculate SiC failure due to thermo-chemical effects during the irradiation phase defined for each benchmark case. The OPyC failure fraction obtained from PISA and the SiC failure fraction obtained by combining the results from PISA and CAPPER were input to SORS to define the failure fractions at the start of the heating phase. Coating failure, fission gas (e.g. ^{85}Kr) release and fission metal (e.g. ^{137}Cs, ^{90}Sr, and ^{110m}Ag) release during the heating phase were calculated by SORS.

(a) The PISA code

Fission gases are generated within the kernel of the fuel particle with burnup and accumulate in the porous low density buffer layer. The resulting internal gas pressure can be as high as several tens of MPa which leads to tensile stresses in the coating layers. PISA [339] is a one-dimensional finite element computer code that performs thermal-stress history calculations for coated particles under irradiation conditions and calculates failure probabilities using a two-parameter Weibull model. The PISA code has built-in functions that calculate the fission gas pressure as a function of burnup, temperature, fuel enrichment and other parameters. The fission gas pressure is typically applied at the interface between the buffer and the IPyC layers. PISA can also perform calculations with the assumption that one or more layers have failed, with failure being defined as the loss of load carrying capability in the tangential direction while retaining the radial stiffness of the material.

PISA calculates the stress distribution in the coating layers by numerically solving coupled thermal-stress equations. Three material models are considered in PISA to model material properties: linear elastic, linear viscoelastic materials with stationary creep, and linear viscoelastic materials with stationary and transient creep. The first material model is for rigid and dimensionally stable silicon carbide (SiC) and the other two are for pyrocarbon (PyC),

which shrinks and creeps in preferred orientation directions (tangential and radial) during irradiation. Mechanical failure of a fuel particle coating layer is defined as the stress loading on the coating layer exceeding the material strength of the coating. Presently, the PISA code does not perform thermo-chemical calculations to determine the CO partial pressure. For the benchmark cases, an Excel spreadsheet model was used to calculate the CO pressures based on a mass balance with number of oxygen atoms released per fission as an input parameter, which was set at 1.7. The CO partial pressures calculated using the Excel spreadsheet were provided as input to PISA. The material properties used in PISA were those defined for the benchmark.

(b) The CAPPER code

The CAPPER ('Capsule Performance') code [340] was developed by GA to predict fuel performance and fission gas release (Kr, Xe and I isotopes) for irradiation test capsules and fuel performance (but not fission product release) in out of pile heating tests of irradiation test fuel using the fuel failure and fission gas release models given in GA's Fuel Design Data Manual (FDDM) [341]. It has the capability of modelling test conditions (temperature, burnup, fluence, and dimensions) that vary arbitrarily with time and position. CAPPER contains component models for each of the fuel failure mechanisms and fission gas release models for failed particles and heavy metal contamination. CAPPER provides options for using FORTRAN subprograms for specific correlations (such as kernel migration in UO_2 fuel particles) to be used in place of the FDDM correlations.

Inputs to CAPPER include the fraction of particles having four types of manufacturing defects: (1) a missing buffer layer (fB), (2) a missing or defective IPyC layer (fI), as indicated by excessive uranium dispersion in the buffer layer, (3) a missing or defective SiC layer (fS), and (4) a missing or defective OPyC layer (f_O). The fraction of the particle population in the various defect categories are normally obtained from the fuel product specification or from quality control measurements performed on the as-manufactured particle population. The sum of these defective particle fractions is FM. CAPPER calculates the following failure probabilities using the failure models in the FDDM [341]:

POP	Irradiation induced OPyC failure
PIP	Irradiation induced IPyC failure
PIO	Pressure vessel failure in particles with initially intact buffers, SiC and OPyC
PFO	Pressure vessel failure in particles with intact buffer and SiC but a failed or defective OPyC layer
PKM	SiC failure due to kernel migration
PSR	SiC failure due to SiC corrosion from fission product attack
PSD	SiC failure due to SiC thermal decomposition
PHM	SiC failure due to heavy metal dispersion

For the benchmark cases, the probability for SiC failure due to heavy metal dispersion is zero because the fraction of particles having excessive uranium dispersion is defined to be zero. Thermal gradients have not been defined as inputs for the benchmark cases, but thermal

gradients in German fuel spheres are small so a default value of zero was used in CAPPER for the sensitivity cases and the heating test cases, with the exception of the HRB-22 cases. For the HRB-22 heating test cases, a conservative thermal gradient of 104 K/m was used for the irradiation phase; nevertheless, the calculated values for PKM were negligible.

The fission product release behaviour in TRISO particles depends on the condition of the silicon carbide (SiC) and the outer pyrocarbon (OPyC) layers, and to a lesser extent the condition of the inner pyrocarbon (IPyC). Each of these layers can be either intact or failed, thus there are 2^3 (eight) coating failure condition categories (one of which is all three layers intact), each of which has different fission product release characteristics. CAPPER calculates the fraction of the fuel particle population in each of these failure categories. However, the IPyC failure fraction is assumed to be 1 in SORS (i.e. no credit is taken for fission product retention by the IPyC coating layer), so there are only four failure categories of interest with the following characteristics:

(1)	Intact Sic, intact OPyC	No gas release, Some Ag diffusive release at high temperature accident conditions
(2)	Intact Sic, failed OPyC	No gas release Some Ag diffusive release at high temperature accident conditions
(3)	Failed Sic, intact OPyC	Some diffusive gas release at high temperature accident conditions No resistance to release from pyrocarbon layers. The fuel kernel provides some resistance to release
(4)	Failed Sic, failed OPyC	No resistance to gas release by coating layers. Only the fuel kernel provides resistance to gas release No resistance to release by coating layers. Only the fuel kernel provides resistance to release

The fraction of particles in categories 3 and 4 were calculated using the failure probabilities calculated by CAPPER, except that the value of POP obtained using PISA was substituted for the corresponding value obtained by CAPPER.

TABLE 9.1. CODE DESCRIPTION SUMMARY, PART I

Participant country/organization	FRANCE	GERMANY	JAPAN	REPUBLIC OF KOREA	RUSSIAN FEDERATION
Code name	ATLAS	PANAMA	RIGID SIC	COPA	GOLT
Code statistical methodology	Weibull, Importance Sampling	Weibull	Weibull	Monte-Carlo calculation	Weibull, Monte-Carlo calculation
Thermal model:					
Fuel element	Yes	No	No	Yes	No
Fuel particle layers	Yes	Yes	No	Yes	Yes
Buffer densif., gap formation	Yes	No	No	Yes	Yes
Gap conductance effects	Yes	No	No	Yes	Yes
Kernel burnup effects on conductivity	yes	No	No	Yes	No
Thermomechanical particle structures modeled:					
Intact	Yes	Yes	Yes	Yes	Yes
Any number of coating layers	Yes	≤ 4	4	Yes	Yes
Cracked layers	Yes	No	SiC	Yes	Yes
Debonded layers	Yes	No	No	Yes	Yes
Faceted particles	yes	No	No	No	No
Influence of buffer on stress history in dense layers	Yes	No	No	Yes	Yes
As-manufactured defects (missing or failed) layers	Yes	No	Yes	Yes	Yes

TABLE 9.1. CODE DESCRIPTION SUMMARY, PART I (cont.)

Participant country/organization	FRANCE	GERMANY	JAPAN	REPUBLIC OF KOREA	RUSSIAN FEDERATION
Code name	ATLAS	PANAMA	RIGID SIC	COPA	GOLT
Physio-chemical related models:					
Short-lived fission gas release	Yes	No	No	Yes	No
Long-lived fission gas release	Yes	Yes	Yes	Yes	Yes
CO/CO_2 production	Proksch	Proksch	Proksch	Homan	Homan or Proksch for UO_2 code ASTRA or analytical approach for PuO_{2-x} based fuel
Equation of state for fission gases, CO and CO_2	Ideal gas law	Ideal gas law	Ideal gas law	Redlich–Kwong	Redlich–Kwong or Ideal gas law
Kernel swelling	Yes	No	No	Yes	Yes
Buffer densification	Yes	No	No	Yes	Yes
Layer interaction models:					
Amoeba effect	Yes	No	No	No	Yes
Fission product/SiC interactions	Pd corrosion model	As SiC thinning rate after Montgomery	No	Yes	As SiC thinning rate after Montgomery
Thermal decomposition of SiC	No	As SiC thinning rate after Benz	No	Yes	As SiC thinning rate after Benz

TABLE 9.1. CODE DESCRIPTION SUMMARY, PART I (cont.)

Participant country/organization	Turkey	USA (INL)	USA (GA)	UK
Code name	TRFUEL	PARFUME	PISA, CAPPER	STRESS3
Code statistical methodology	Weibull	Weibull, Monte-Carlo or Direct integration calculation	Deterministic	Weibull Monte-Carlo
Thermal model:				
Fuel element	Yes	Yes	Yes	Yes
Fuel particle layers	Yes	Yes	Yes	Yes
Buffer densif., gap formation	No	Yes	No	Yes
Gap conductance effects	No	Yes	No	No
Kernel burnup effects on conductivity	No	Yes	No	No
Thermomechanical particle structures modeled:				
Intact	Yes	Yes	Yes	Yes
Any number of coating layers	4	≤ 4	No	6
Cracked layers	No	Yes	No	Yes
Debonded layers	No	Yes	No	Yes
Faceted particles	No	Yes	No	No
Influence of buffer on stress history in dense layers	No	No	No	Yes
As-manufactured defects (missing or failed) layers	Yes	Yes	Yes	Yes

TABLE 9.1. CODE DESCRIPTION SUMMARY, PART I (cont.)

Participant country/organization	Turkey	USA (INL)	USA (GA)	UK
Code name	TRFUEL	PARFUME	PISA, CAPPER	STRESS3
Physio-chemical related models:				
Short-lived fission gas release	No	Yes	Yes	Yes
Long-lived fission gas release	Yes	Yes	Yes	Yes
CO/CO_2 production	Yes	Chemical equilibrium	No	Chemical Equilibrium
Equation of state for fission gases, CO and CO_2	Redlich–Kwong	Redlich–Kwong	Programmable	Redlich–Kwong
Kernel swelling	No	Yes	No	Yes
Buffer densification	No	Yes	No	Yes
Layer interaction models:				
Amoeba effect	No	Yes	No	No
Fission product/SiC interactions	No	Yes	No	No
Thermal decomposition of SiC	No	No	Yes	Yes

TABLE 9.2. CODE DESCRIPTION SUMMARY, PART II

Parameter	FRANCE	GERMANY	JAPAN	REPUBLIC OF KOREA	RUSSIAN FEDERATION	TURKEY	USA (INL)	USA (GA)	UK
Type of kernel	UO_2	UO_2 $(U,Th)O_2$ UCO	UO_2	UO_2	UO_2, PuO_{2-x}, PuO_{2-x} in ZrO_2 matrix	UO_2	UO_2 UCO	UO_2 UCO	UO_2 $(U,Pu)O_2$
Oxygen/uranium ratio	Yes	No	No	Yes	Yes	Yes	Yes	No	Yes
Oxygen/plutonium ratio	Yes	No	No	No	Yes	No	No	No	Yes
carbon/uranium ratio	No	No	No	No	Yes	No	Yes	No	Yes
^{235}U enrichment	Yes	No	No	Yes	Yes	Yes	Yes	Yes	Yes
Kernel diameter	Yes	Yes	Yes	Yes	Yes	Yes	Yes	Yes	Yes
Buffer thickness	Yes	Yes	Yes	Yes	Yes	Yes	Yes	Yes	Yes
IPyC thickness	Yes	Yes	Yes	Yes	Yes	Yes	Yes	Yes	Yes
SiC thickness	Yes	Yes	Yes	Yes	Yes	Yes	Yes	Yes	Yes
OPyC thickness	Yes	Yes	Yes	Yes	Yes	Yes	Yes	Yes	Yes
Kernel density	Yes	No	Yes	Yes	Yes	Yes	Yes	No	Yes
Buffer density	Yes	No	Yes	Yes	Yes	Yes	Yes	No	Yes
IPyC density	Yes	No	No	Yes	Yes	Yes	Yes	No	Yes
SiC density	Yes	No	No	Yes	Yes	Yes	Yes	No	Yes
OPyC density	Yes	No	No	Yes	Yes	Yes	Yes	No	Yes

TABLE 9.2. CODE DESCRIPTION SUMMARY, PART II (cont.)

Parameter	FRANCE	GERMANY	JAPAN	REPUBLIC OF KOREA	RUSSIAN FEDERATION	TURKEY	USA (INL)	USA (GA)	UK
IPyC BAF	Yes	No	No	Yes	Yes	No	Yes	No	Yes
OPyC BAF	Yes	No	No	Yes	Yes	No	Yes	no	Yes
Irradiation duration	Yes	Yes	Yes	Yes	Yes	Yes	Yes	Yes	Yes
EOL burnup	Yes	Yes	Yes	Yes	Yes	Yes	Yes	Yes	Yes
End of life fluence	Yes	Yes	Yes	Yes	Yes	Yes	Yes	Yes	Yes
Irradiation temperature	Any history	Any history	Time-volume average	Any history	Any history	Any history	Any history	Any history	Any history
Ambient pressure	Yes	No	No	Yes	Yes	Yes	Yes		Yes
SiC strength	Yes	Yes	Yes	Yes	Yes	Yes	Yes	No	Yes
Weibull modulus	Yes	Yes	Yes	Yes	Yes	Yes	Yes	No	Yes
Yield of stable fission gases	Yes	Yes	Yes	Yes	No	Yes	Yes		Yes
Molar volume of heavy metal	Yes	Yes	No	No	Yes	No	No		Yes
Void volume of buffer layer	Yes	Yes	No	Yes	Yes	Yes	Yes	Yes	Yes
Diffusion coeff. of fission gases in kernel	No	Yes	Yes	Yes	No	Yes	Yes	No	Yes

9.2. BENCHMARK CALCULATIONS FOR A SINGLE COATED PARTICLE

9.2.1. Description of cases

Benchmark cases 1 through 8 are for single particles while the remaining cases represent a population of particles within an experiment. Input parameters for the simple analytical cases 1 through 3, are listed in Table 9.3. Table 9.4 lists the input parameters for the analytical pyrocarbon layer cases 4a through 4d. These cases do have unrealistic input parameters such as zero burn up and a finite internal gas pressure. This is intended to reduce the model variability among the different codes. Input parameters for the single particle cases 5 through 8, are listed in Table 9.5. A brief description of each benchmark case follows.

9.2.1.1. Case 1 — elastic SiC

This particle has a kernel diameter of 500 μm and a buffer thickness of 100 μm. It has only one coating layer, a 35 μm thick SiC layer. The coating behaviour is elastic.

9.2.1.2. Case 2 — simple BISO

This particle is the same as in case 1, except that the single coating is a 90 μm thick IPyC layer.

9.2.1.3. Case 3 — IPyC/SiC composite without fluence

This particle has two coating layers, an IPyC and SiC layer.

9.2.1.4. Case 4a — IPyC/SiC composite with no creep and constant swelling

This is the same particle as in case 3, except that it experiences a fast neutron fluence with the IPyC layer imposed to swell. The internal pressure of 25 MPa is assumed to be constant.

9.2.1.5. Case 4b — IPyC/SiC composite with constant creep and no swelling

This is the same particle as in case 3, except that it experiences a fast neutron fluence with the IPyC layer imposed to creep. The internal pressure of 25 MPa is assumed to be constant.

9.2.1.6. Case 4c — IPyC/SiC composite with constant creep and constant swelling

This is the same particle as in case 3, except that it experiences a fast neutron fluence with the IPyC layer imposed to creep and swell at constant rates. The internal pressure of 25 MPa is assumed to be constant.

9.2.1.7. Case 4d — IPyC/SiC composite with constant creep and fluence dependent swelling

This is the same particle as in case 3, except that it experiences a fast neutron fluence with the IPyC layer swelling at a variable rate. The internal pressure of 25 MPa is assumed to be constant.

9.2.1.8. Case 5 — TRISO, 350 μm kernel

This is a full three layer (TRISO) coated particle with a 350 μm diameter kernel under realistic service conditions.

9.2.1.9. Case 6 — TRISO, 500 μm kernel

This TRISO coated particle has a 500 μm diameter kernel with all other parameters the same as in case 5.

9.2.1.10. Case 7 — TRISO, high BAF

This particle is the same as in case 6 except that the Pyrocarbon BAF is increased to 1.06 (correlation (b)).

9.2.1.11. Case 8 — TRISO, cyclic temperature history

This is a TRISO particle subjected to a cyclic temperature history characteristic of fuel in a pebble bed reactor. It is assumed that the particle experiences ten cycles where the temperature is initially 873 K, increases linearly to 1273 K and then decreases immediately back to 873 K. The period for each cycle is one tenth of the total irradiation time, or 100 days (see Fig. 9.1).

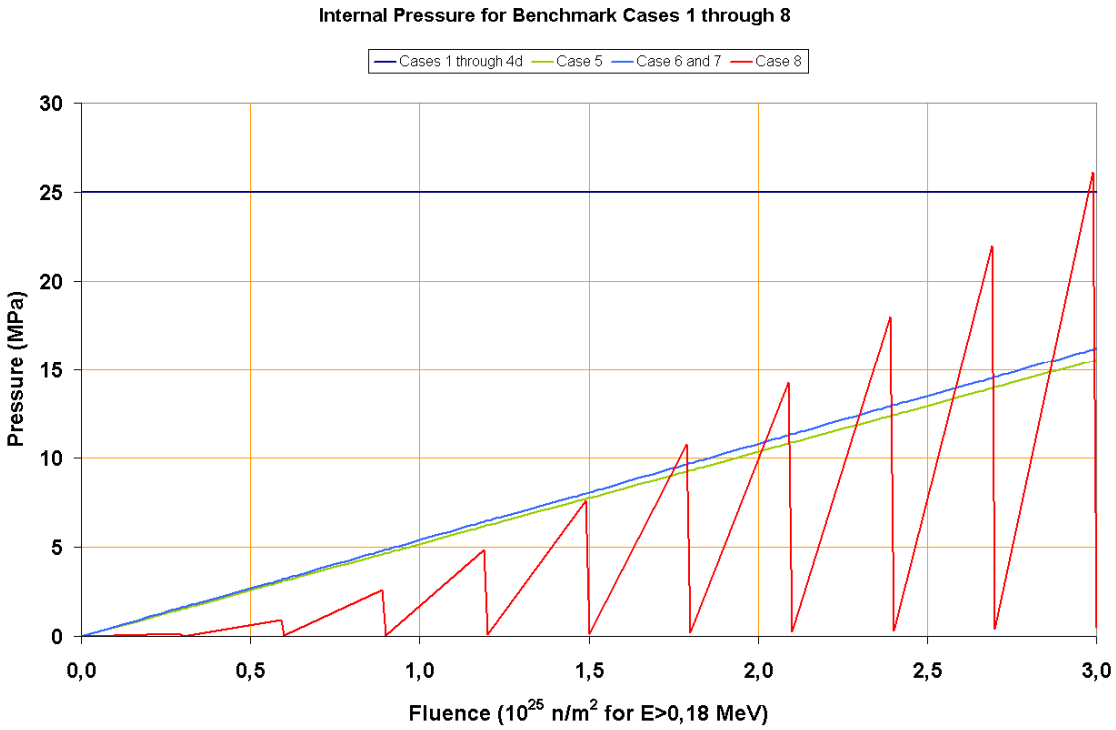

FIG. 9.1. Internal pressure for Cases 1 through 8.

TABLE 9.3. INPUT PARAMETERS FOR ANALYTICAL THERMO-MECHANICAL BENCHMARK CASES

Parameter	Case 1: Elastic SiC	Case 2: Simple BISO	Case 3: IPyC/SiC without fluence
Oxygen to Uranium ratio	2	2	2
Carbon to Uranium ratio	0	0	0
U-235 enrichment (wt%)	10	10	10
Kernel diameter (μm)	500	500	500
Buffer thickness (μm)	100	100	100
IPyC thickness (μm)	n.a.	90	40
SiC thickness (μm)	35	n.a.	35
OPyC thickness (μm)	n.a.	n.a.	n.a.
Kernel density (Mg/m^3)	10.8	10.8	10.8
Buffer density (Mg/m^3)	0.95	0.95	0.95
IPyC density (Mg/m^3)	n.a.	1.9	1.9
SiC density (Mg/m^3)	3.20	n.a.	3.20
OPyC density (Mg/m^3)	n.a.	n.a.	n.a.
IPyC BAF	n.a.	1.0	1.03
OPyC BAF	n.a.	n.a.	n.a.
Irradiation duration (efpd)	0	0	0
End of life burnup (% FIMA)	0	0	0
End of life fluence (10^{25} n/m^2, E > 0.18 MeV)	0	0	0
Constant temperature (K)	1273	1273	1273
Internal pressure (MPa)	25	25	25
Ambient pressure (MPa)	0.1	0.1	0.1
Results to be compared	max. SiC tangential stress	max. IPyC tangential stress	max. tangential stresses for SiC and IPyC

n.a. not applicable.

TABLE 9.4. INPUT PARAMETERS FOR ANALYTICAL PYROCARBON LAYER BENCHMARK CASES

Parameter	Case 4a: No creep/constant swelling	Case 4b: Constant creep/no swelling	Case 4c: Constant creep/constant swelling	Case 4d: Const. creep/fluence-dep. swelling
Oxygen to Uranium ratio	2	2	2	2
Carbon to Uranium ratio	0	0	0	0
U-235 enrichment (wt%)	10	10	10	10
Kernel diameter (μm)	500	500	500	500
Buffer thickness (μm)	100	100	100	100
IPyC thickness (μm)	40	40	40	40
SiC thickness (μm)	35	35	35	35
OPyC thickness (μm)	n.a.	n.a.	n.a.	n.a.
Kernel density (Mg/m^3)	10.8	10.8	10.8	10.8
Buffer density (Mg/m^3)	0.95	0.95	0.95	0.95
IPyC density (Mg/m^3)	1.9	1.9	1.9	1.9
SiC density (Mg/m^3)	3.20	3.20	3.20	3.20
OPyC density (Mg/m^3)	n.a.	n.a.	n.a.	n.a.
IPyC BAF	1.03	1.03	1.03	1.03
PyC creep coefficient (MPa 10^{25} n/m^2 E>0.18 MeV^{-1})	n.a.	2.715×10^{-4}	2.715×10^{-4}	2.715×10^{-4}
PyC swelling rate ($(\Delta L/L)/10^{25}$ n/m^2 E>0.18 MeV)	-0.005	n.a.	-0.005	correlation (a)
Irradiation duration (efpd)	0	0	0	0
EOL burnup (% FIMA)	0	0	0	0
End of life fluence (10^{25} n/m^2, E > 0.18 MeV)	3	3	3	3
Constant temperature (K)	1273	1273	1273	1273
Internal pressure (MPa)	25	25	25	25
Ambient pressure (MPa)	0.1	0.1	0.1	0.1
Comparison metric	inner surface tangential IPyC stress, inner surface tangential SiC stress as a function of fast neutron fluence			

n.a. not applicable.

TABLE 9.5. INPUT PARAMETERS FOR SINGLE PARTICLE BENCHMARK CASES

Parameter	Case 5: TRISO 350 μm kernel	Case 6: TRISO 500 μm kernel	Case 7: TRISO High BAF	Case 8: TRISO Cyclic temp.
Oxygen to Uranium ratio	2	2	2	2
Carbon to Uranium ratio	0	0	0	0
U-235 enrichment (wt%)	10	10	10	10
Kernel diameter (μm)	350	500	500	500
Buffer thickness (μm)	100	100	100	100
IPyC thickness (μm)	40	40	40	40
SiC thickness (μm)	35	35	35	35
OPyC thickness (μm)	40	40	40	40
Kernel density (Mg/m^3)	10.8	10.8	10.8	10.8
Buffer density (Mg/m^3)	0.95	0.95	0.95	0.95
IPyC density (Mg/m^3)	1.9	1.9	1.9	1.9
SiC density (Mg/m^3)	3.20	3.20	3.20	3.20
OPyC density (Mg/m^3)	1.9	1.9	1.9	1.9
IPyC BAF	1.03	1.03	1.06	1.03
OPyC BAF	1.03	1.03	1.06	1.03
Irradiation duration (efpd)	1000	1000	1000	1000
End of life burnup (% FIMA)	10	10	10	10
End of life fluence (10^{25} n/m^2, E > 0.18 MeV)	3	3	3	3
Constant irradiation temperature (K)	1273	1273	1273	873 to 1273 (10 cycles)
Ambient pressure (MPa)	0.1	0.1	0.1	0.1
Results to be compared	Inner surface SiC and IPyC tangential stress histories			

9.2.2. Imposed properties fixed for the benchmark

Table 9.6 summarizes the material properties to be used in cases 1 through 8. The internal pressure history for case 8 is listed in Table 9.7 and is shown graphically in Fig. 9.2. The internal pressure to be used at any fluence value between fluence values listed is determined by interpolating linearly between the pressures listed for the surrounding fluence values. The change in pressure in this interpolation is in linear proportion to the change in fluence. The pressure cycles given in Table 9.7 for case 8 are not necessarily realistic. The actual pressure is likely to drop off almost instantaneously at the end of each cycle. Spreading the pressure drop over a finite time interval in these calculations is intended to alleviate convergence problems that could occur when solving for an instantaneous change in pressure. If an instantaneous change in temperature poses difficulties when solving for case 8, it may similarly be assumed for this exercise that the temperature drop at the end of each cycle occurs over a finite time interval.

TABLE 9.6. MATERIAL PROPERTIES FOR BENCHMARK CASES 1 THROUGH 8

Case	PyC Young modulus of elasticity (MPa)	PyC Poisson ratio	PyC Poisson ratio in creep	PyC coefficient of thermal expansion (K^{-1})	PyC creep coefficient (MPa/(10^{25} n/m^2, E>0.18 MeV))	PyC swelling strain rate (10^{25} n/m^2]$^{-1}$, E>0.18 MeV)	SiC modulus of elasticity (MPa)	SiC Poisson ratio	SiC coefficient of thermal expansion (K^{-1})
1	n.a. [a]	n.a. [a]	n.a.	n.a. [a]	n.a.	n.a.	3.70×10^5	0.13	4.90×10^{-6}
2	3.96×10^4	0.33	n.a.	5.50×10^{-6}	n.a.	n.a.	n.a.	n.a.	n.a.
3	3.96×10^4	0.33	n.a.	5.50×10^{-6}	n.a.	n.a.	3.70×10^5	0.13	4.90×10^{-6}
4a	3.96×10^4	0.33	n.a.	5.50×10^{-6}	n.a.	-0.005 (isotropic)	3.70×10^5	0.13	4.90×10^{-6}
4b	3.96×10^4	0.33	0.5	5.50×10^{-6}	2.71×10^{-4}	n.a.	3.70×10^5	0.13	4.90×10^{-6}
4c	3.96×10^4	0.33	0.5	5.50×10^{-6}	2.71×10^{-4}	-0.005 (isotropic)	3.70×10^5	0.13	4.90×10^{-6}
4d	3.96×10^4	0.33	0.5	5.50×10^{-6}	2.71×10^{-4}	correlation (a)	3.70×10^5	0.13	4.90×10^{-6}
5	3.96×10^4	0.33	0.5	5.50×10^{-6}	2.71×10^{-4}	correlation (a)	3.70×10^5	0.13	4.90×10^{-6}
6	3.96×10^4	0.33	0.5	5.50×10^{-6}	2.71×10^{-4}	correlation (a)	3.70×10^5	0.13	4.90×10^{-6}
7	3.96×10^4	0.33	0.5	5.50×10^{-6}	2.71×10^{-4}	correlation (b)	3.70×10^5	0.13	4.90×10^{-6}
8	3.96×10^4	0.33	0.5	5.35×10^{-6}	correlation (d)	correlation (c)	3.70×10^5	0.13	4.90×10^{-6}

n.a. not applicable.

TABLE 9.7. INTERNAL PRESSURES FOR BENCHMARK CASES 1 THROUGH 8

Case	Fluence (10^{25} n/m^2)	Internal pressure (MPa)
1	Independent	25 (constant)
2	Independent	25 (constant)
3	Independent	25 (constant)
4a	Independent	25 (constant)
4b	Independent	25 (constant)
4c	Independent	25 (constant)
4d	Independent	25 (constant)
5	Linear ramp	From 0 to 15.54
6	Linear ramp	From 0 to 26.20
7	Linear ramp	From 0 to 26.20
8	0	0.
	0.29	0.14
	0.30	0.02
	0.59	0.94
	0.60	0.04
	0.89	2.59
	0.90	0.07
	1.19	4.87
	1.20	0.10
	1.49	7.64
	1.50	0.14
	1.79	10.79
	1.80	0.20
	2.09	14.26
	2.10	0.26
	2.39	17.99
	2.40	0.33
	2.69	21.96
	2.70	0.41
	2.99	26.13
	3.00	0.50

Material properties are generally obtained from CEGA's report [320]. Pyrocarbon creep coefficients of the CEGA report are increased by a factor of 2, based on correlations with NPR experiments [336]. Correlations for pyrocarbon swelling strain rates are given Table 9.8 and corresponding swelling strain (or 'irradiation induced dimensional change', IIDC) are plotted Fig. 9.3. In case 8, the pyrocarbon creep coefficient is assumed to vary over the temperature range of 873 K to 1273 K according to correlation (d) given in Table 9.8 and Fig. 9.3.

Thermal expansion coefficients shown are obtained from CEGA data. In cases 1 through 7, the particle is considered to be thermally stress-free. Therefore expansion coefficients are not actually needed for these cases. In case 8, the particle is considered to be thermally stress-free at the initial temperature of 873 K. Differential expansion stresses occur as the irradiation temperature changes. The PyC thermal expansion coefficient given in Table 9.6 for case 8 is representative of the average temperature of 1073 K. The PyC swelling is assumed to be isotropic for cases 4a and 4c. Because cases 1 through 8 address only a single particle, mean strengths and Weibull moduli do not apply.

It is intended that cases 1 through 8 focus only on the behaviour of the outer coating layers (IPyC, SiC, OPyC). There is no temperature variation assumed through the coating layers. Except for the internal gas pressure that is applied to the inner surface of the IPyC, kernel and buffer are assumed not to interact with the outer layers. Internal pressures for each case are provided in Table 9.7.

For cases 1 through 8, dFIMA/dt is equal to zero, meaning that there is neither heat production nor fuel swelling or densification. Also fission product release and CO production models are not applicable.

For cases 1 through 8, the buffer is disconnected from the kernel and the IPyC and its stiffness is close to zero in order to avoid any mechanical interaction with the layers. The irradiation-induced dimensional change is neglected.

Correlation (a) through (c) and (e) through (f) — PyC swelling rate

$$\dot{g} = \sum_{i=0}^{5} A_i x^i \tag{9.22}$$

where

x is the fast neutron fluence (10^{25} n/m^2, E > 0.18 MeV). [3]

Correlation (d) is the PyC creep coefficient

$$K = \sum_{i=0}^{2} A_i T^i \tag{9.23}$$

where

T is the temperature (°C).

The coefficients A_i (I = 0,…5) are listed in Table 9.8.

[3] Divide fast neutron fluences for E > 0.10 MeV by a factor of 1.10 to obtain fast neutron fluences for E > 0.18 MeV.

TABLE 9.8. PYC CORRELATIONS FOR BENCHMARK CASES 4D THROUGH 14

	A_0	A_1	A_2	A_3	A_4	A_5
Correlation (a)						
radial	-2.22642×10^{-2}	2.00861×10^{-2}	-7.77024×10^{-3}	1.36334×10^{-3}		—
tangential	-1.91253×10^{-2}	2.63307×10^{-3}	1.69251×10^{-3}	-3.53804×10^{-4}		
Correlation (b)						
radial	-2.12522×10^{-2}	1.83715×10^{-2}	-5.05553×10^{-3}	7.27026×10^{-4}		—
tangential	-1.79113×10^{-2}	-3.42182×10^{-3}	5.03465×10^{-3}	-8.88086×10^{-4}		
Correlation (c)						
radial	-1.80613×10^{-2}	9.82884×10^{-3}	-2.25937×10^{-3}	4.03266×10^{-4}		—
tangential	-1.78392×10^{-2}	1.71315×10^{-3}	2.32979×10^{-3}	-4.91648×10^{-4}		
Correlation (d)	4.386×10^{-4}	-9.70×10^{-7}	8.0294×10^{-10}			—
Correlation (e)						
radial for $x < 6.08$	-1.43234×10^{-1}	2.62692×10^{-1}	-1.74247×10^{-1}	5.67549×10^{-2}	-8.36313×10^{-3}	4.52013×10^{-4}
radial for $x > 6.08$	0.0954					—
tangential for $x < 6.08$	-3.24737×10^{-2}	9.07826×10^{-3}	-2.10029×10^{-3}	1.30457×10^{-4}		—
tangential for $x > 6.08$	-0.0249					—
Correlation (f)						
radial	-2.13483×10^{-2}	1.64999×10^{-2}	-3.80252×10^{-3}	4.73765×10^{-4}		
tangential	-1.83549×10^{-2}	-3.29740×10^{-3}	5.47396×10^{-3}	-1.03249×10^{-3}		

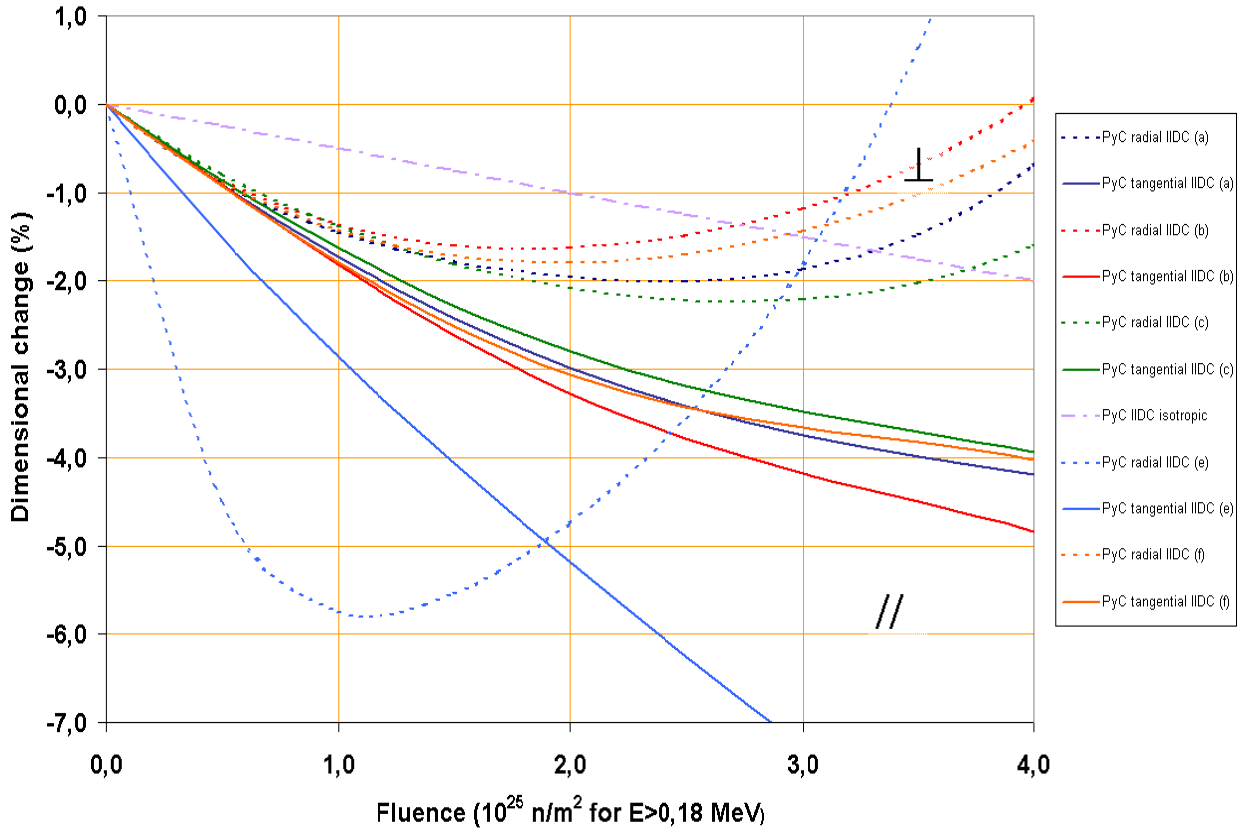

FIG. 9.2. PyC swelling strain rate for cases 4d through 14.

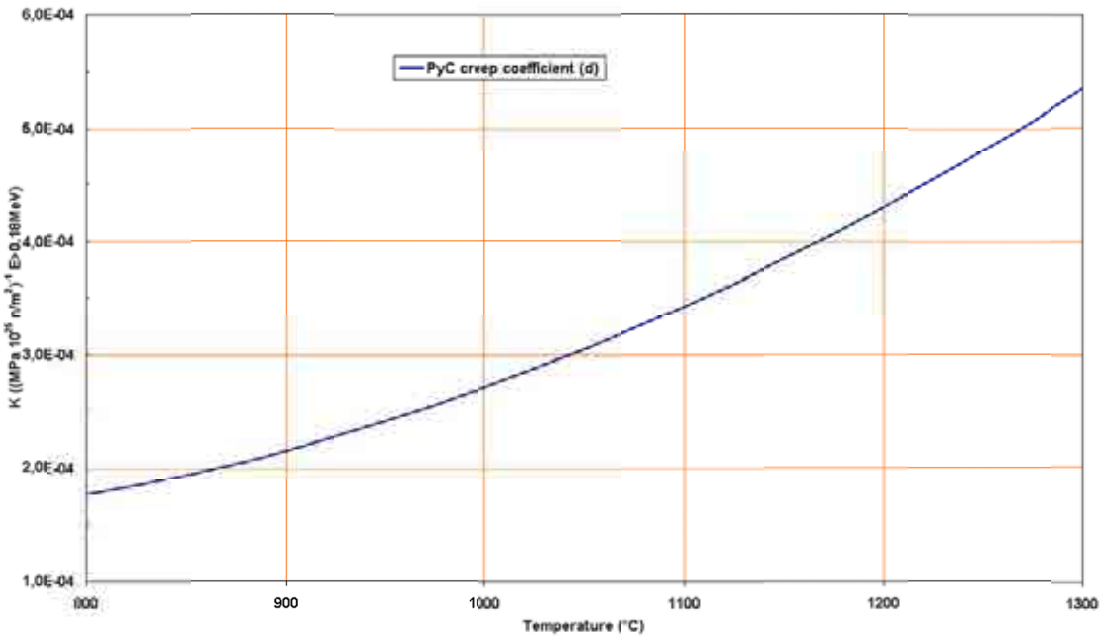

FIG. 9.3. PyC creep coefficient for case 8.

9.2.3. Results from participating countries

9.2.3.1. Case 1: elastic SiC

The results are listed in Table 9.9 and shown in Fig. 9.4.

TABLE 9.9. RESULTS FOR CASE 1: ELASTIC SIC

Case 1	Maximum SiC tangential stress (MPa) at the inner surface of SiC
France	125.4
Japan	125.79
Republic of Korea	125.19
Russian Federation	125.2
Turkey	125.2
United Kingdom	125.1
USA/GA	125.9
USA/INL	125.2

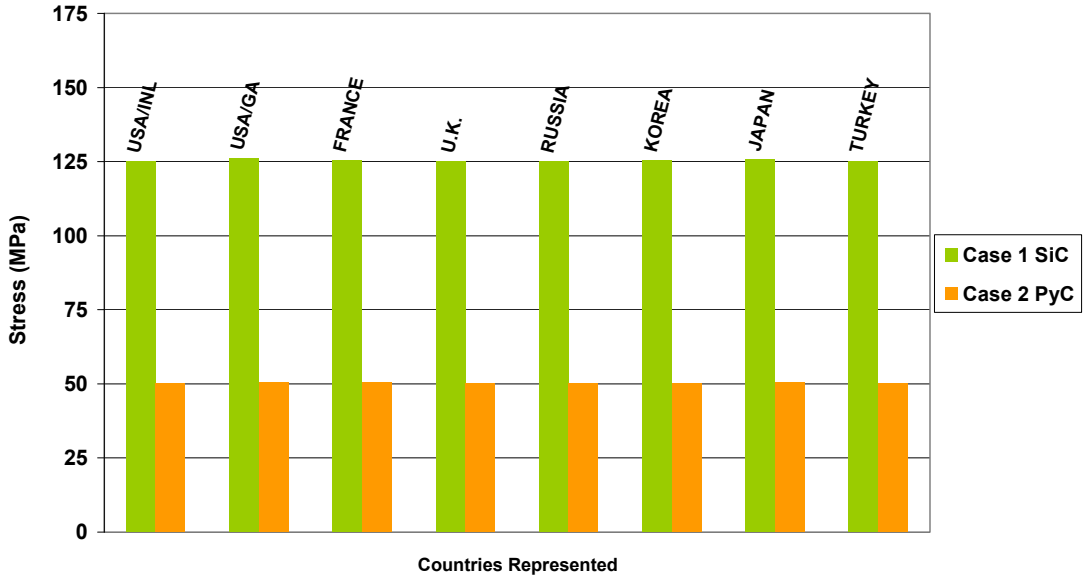

FIG. 9.4. Case 1 and 2 — Maximum tangential IPyC and SiC stresses.

Analytically, the tangential stress in the thickness of a spherical shell is given by:

$$\sigma_t(r) = P_i \cdot \frac{r_i^3 \cdot (2 \cdot r^3 + r_o^3)}{2 \cdot r^3 \cdot (r_o^3 - r_i^3)} - P_o \cdot \frac{r_o^3 \cdot (2 \cdot r^3 + r_i^3)}{2 \cdot r^3 \cdot (r_o^3 - r_i^3)} \quad (9.24)$$

where

r_i, r_o are inner and the outer radius of the shell (m);
P_i, P_o are the pressures acting on the inner and outer surfaces of the shell (Pa).

With r_i = 350 μm and r_o = 385 μm, the tangential stress at the inner surface is equal to 125.19 MPa, in good agreement with all codes.

9.2.3.2. Case 2

The results are listed in Table 9.10 and were shown also in Fig. 9.4. With r_i = 350 μm and r_o = 440 μm, the tangential stress at the inner surface is equal to 50.20 MPa, in good agreement with all codes.

TABLE 9.10. RESULTS FOR CASE 2: SINGLE BISO

Case 2	Maximum tangential stress (MPa) at the inner surface of IPyC
France	50.4
Japan	50.5
Republic of Korea	50.2
Russian Federation	50.2
Turkey	50.2
United Kingdom	50.2
USA/GA	50.6
USA/INL	50.14

9.2.3.3. Case 3: IPyC/SiC without fluence

The results are listed in Table 9.11.

An analytical expression is given in [342] as follows:

Analytically, the tangential stresses at the inner and outer surface of a spherical shell are given by:

$$\sigma_{ti} = \frac{(2+m)P_i - 3mP_o}{2(m-1)} \text{ and } \sigma_{to} = \frac{3P_i - (2m+1)P_o}{2(m-1)} \qquad (9.25), (9.26)$$

where

$m = (r_i/r_o)^3$;
r_i, r_0 are the inner and outer radius of the shell (m);
P_i, P_o are the pressures acting on the inner and outer surfaces of the shell.

The pressure between the IPyC and SiC layers, Π is given, with the help of equations (9.25) and (9.26) by the following relation which equates the radial displacements in the two layers at their interface:

$$\frac{3P_i - (2m_a+1)\Pi}{2(m_a-1)} \cdot \frac{1-\mu_a}{E_a} + \frac{\Pi\mu_a}{E_a} = \frac{(2+m_b)\Pi - 3m_bP_o}{2(m_b-1)} \cdot \frac{1-\mu_b}{E_b} + \frac{\Pi\mu_b}{E_b} \qquad (9.27)$$

where

subscripts a and b refer to the IPyC and SiC layers, respectively;

E is the Young Modulus;
μ is Poisson's ratio.

The radial stress, -Π, between the two layers is found to be -18.8 MPa. Then, using Equation (9.25), tangential stresses in the IPyC and SiC are calculated to be 8.8 and 104.4 MPa respectively, in good agreement with all codes.

TABLE 9.11. RESULTS FOR CASE 3: IPYC/SIC WITHOUT FLUENCE

Case 3	Maximum tangential stress for SiC	Maximum tangential stress for IPyC
France	104.6	8.8
Japan	123.3	—
Republic of Korea	104.38	8.78
Russian Federation	106.7	9
Turkey	104.2	8.7
United Kingdom	104.3	8.7
USA/GA	104.5	9.3
USA/INL	104.3	8.77

— data not available.

9.2.3.4. Case 4a: IPyC/SiC composite with no creep and constant swelling rate

Results are given in Fig. 9.5 for radial stresses and in Fig. 9.6 for tangential stresses. At the start of the irradiation, case 4a is equal to case 3.

The irradiation induced dimensional change of the pyrocarbon layer is countered by the SiC layer, which is about 10 times more rigid. This pyrocarbon dimensional change quickly creates circumferential compression stresses in the SiC layer and tensile stresses in the pyrocarbon layer.

In order to calculate these stresses from analytical relations, equation (9.27) may be used, as in case 3. The only difference being that an extra term g_a should be added to the left hand side of that equation. g_a is defined as the overall fractional change in linear dimensions at a specific neutron dose (being -0.0005 × dose in units of 10^{24} n/m^2. Tangential stresses in the IPyC and SiC are calculated to be 926.80 MPa and -845.71 MPa, respectively, at the dose of 3×10^{25} n/m^2, in good agreement with all the codes.

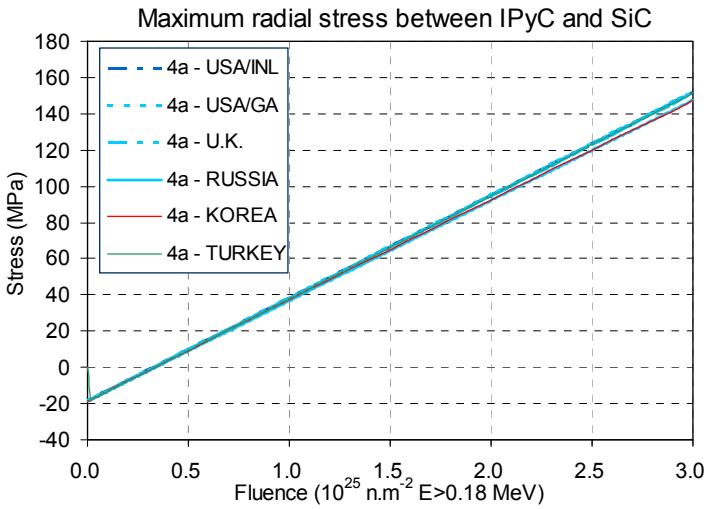

FIG. 9.5. Case 4a — Inner surface radial stress between IPyC and SiC as a function of fast fluence.

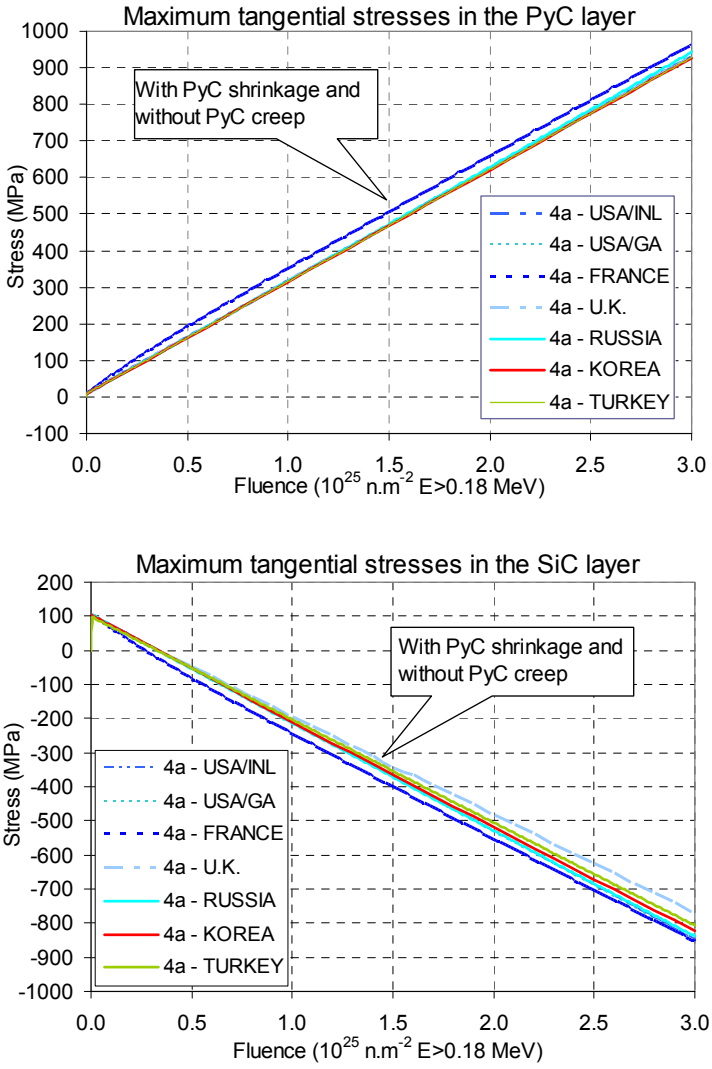

FIG. 9.6. Case 4a — Inner surface tangential IPyC and SiC stresses as a function of fast fluence.

9.2.3.5. Case 4b — IPyC/SiC composite with constant creep and no swelling

Results are given in Fig. 9.7 for radial stresses and in Fig. 9.8 for tangential stresses. At the start of the irradiation, case 4b is equal to case 3.

Because the IPyC creep Poisson's ratio is equal to 0.5, it is expected that, since the volume will be conserved, stresses in that layer will decay from the initial value reported in case 3 to a constant hydrostatic stress of -25 MPa, in good agreement with all the codes.

At the same time, the relaxation of PyC stresses reload the SiC layer and the tangential stress at the equilibrium is equal to the stress given by equation (9.25), that is to say, with r_i = 390 µm and r_o = 425 µm, at the inner surface, 139.34 MPa, in good agreement with all the codes.

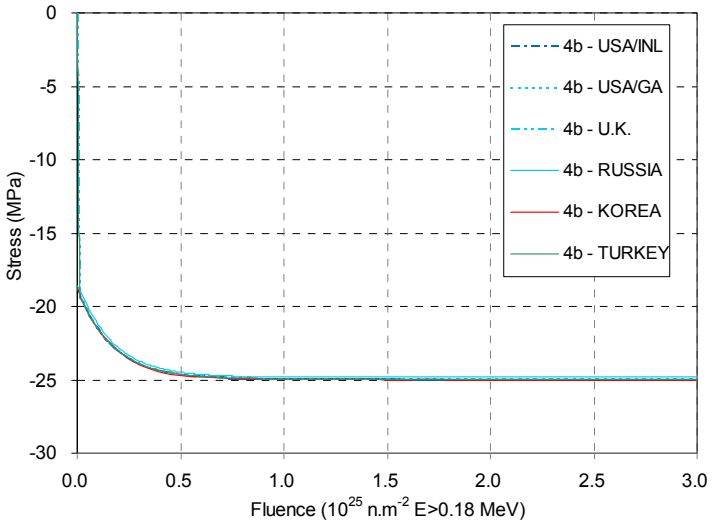

FIG. 9.7. Case 4b — Inner surface radial stress between IPyC and SiC as a function of fast fluence.

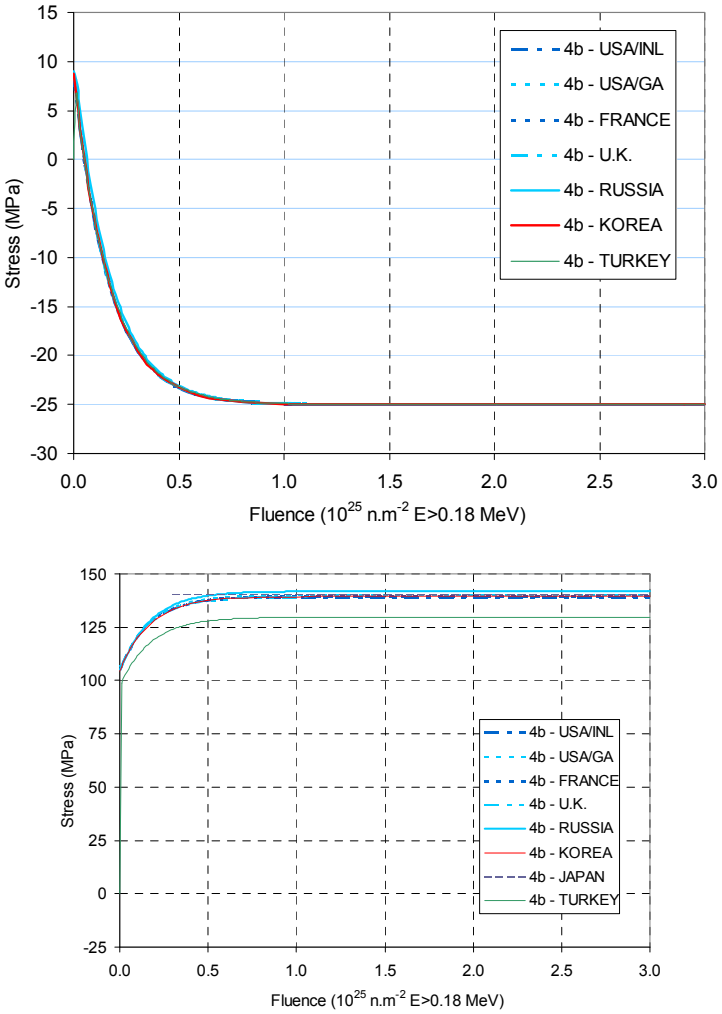

FIG. 9.8. Case 4b — Inner surface tangential IPyC and SiC stresses as a function of fast fluence.

9.2.3.6. Case 4c — IPyC/SiC composite with constant creep and constant swelling

Results are given in Fig. 9.9 for radial stresses and in Fig. 9.10 for tangential stresses. At the start of the irradiation, case 4c is equal to case 3. The irradiation induced dimensional change of the pyrocarbon layer is countered by the SiC layer which is about 10 times more rigid. This pyrocarbon dimensional change quickly creates circumferential compression stresses in the SiC layer and tensile stresses in the pyrocarbon layers. The irradiation induced creep in the pyrocarbon layers tends to relax the stresses before the latter becomes too great, and an equilibrium is created between densification and relaxation because the swelling rate is constant.

Stresses in the equilibrium state may be calculated analytically, making the approximation that the elastic constant of SiC is infinite and considering the irradiation induced dimensional change isotropic and the creep Poisson's ratio equal to 0.5. The IPyC tangential stress, σ_{ta} is given by

$$\sigma_{ta} = -\frac{2m_a \dot{g}_a}{K_a} - P_i \qquad (9.28)$$

where $\dot{g}_a$ is the swelling rate of the IPyC layer.

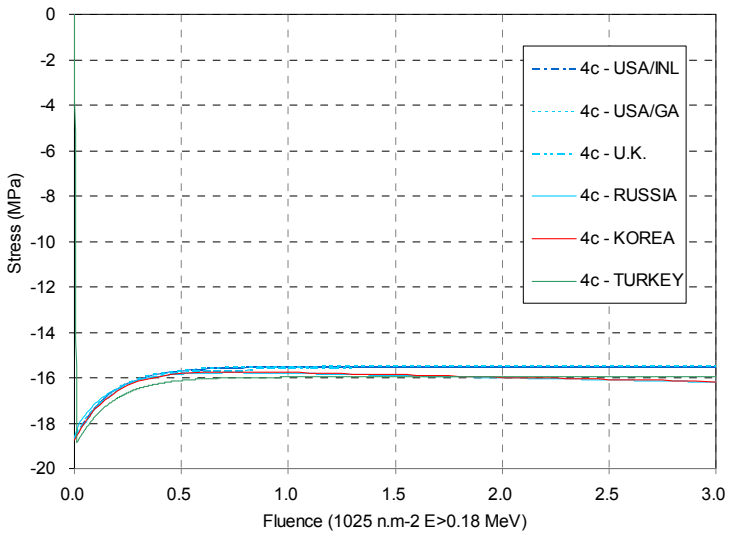

FIG. 9.9. Case 4c — Inner surface radial stress between IPyC and SiC as a function of fast fluence.

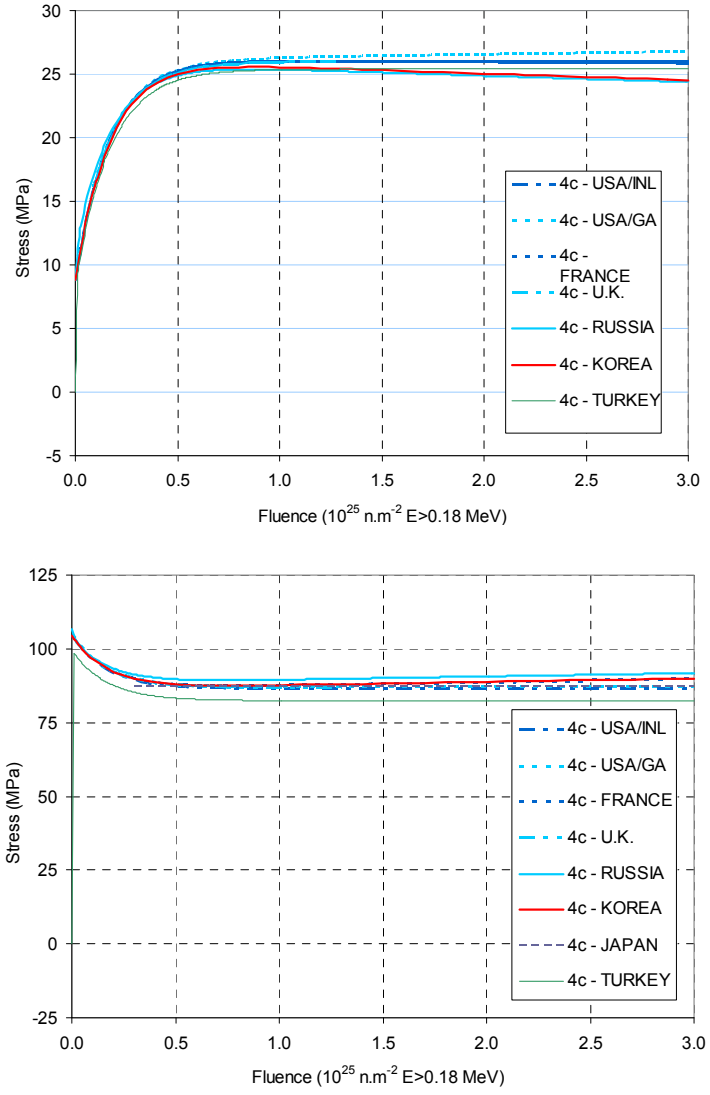

FIG. 9.10. Case 4c — Inner surface tangential IPyC and SiC stresses as a function of fast fluence.

The radial stress at the IPyC/SiC interface, σ_r is

$$\sigma_r = -\frac{4\dot{g}_a(m_a - 1)}{3K_a} - P_i \tag{9.29}$$

The value of σ_r is used in Equation (9.25) to derive the tangential stress in the SiC layer. Tangential stresses in the IPyC and SiC are calculated to be 26.05 and 86.5 MPa, respectively, in good agreement with all the codes.

9.2.3.7. Case 4d: IPyC/SiC composite with constant creep and neutron dose dependent swelling

This case is similar to case 4c except that the swelling of the IPyC layer is both anisotropic and a function of the neutron dose. Results are given in Fig. 9.11 for radial stresses and in Fig. 9.12 for tangential stresses. At the start of the irradiation, case 4d is equal to case 3. According to the equation (17) in [236] (see equation (9.34) in Section 9.3.3), once a quasi equilibrium state has been achieved, the IPyC tangential stress is given by

$$\sigma_{ta} = -\frac{4.5m_a\hat{\dot{g}}_{1a} - 1.5(m_a - 1)\left(\hat{\dot{g}}_{1a} - \hat{\dot{g}}_{3a}\right)}{2.25K_a} - P_i \tag{9.30}$$

where subscripts 1 and 3 refer to the tangential and radial directions, respectively, and

$$\hat{g} = \dot{g} - \frac{\ddot{g}}{C} + \frac{\dddot{g}}{C^2} - \cdots \tag{9.31}$$

where C is a relaxation time (or rather neutron dose) constant, taken to be 1.7×10^{24} n/m^2.

Good agreement between IPyC stress values calculated from equation (9.30) and those obtained from the codes was observed. Likewise good agreement was also obtained for stresses in the SiC layer and at the IPyC/SiC interface, in these cases with the use of equation (9.30) and equation (9.32) [236].

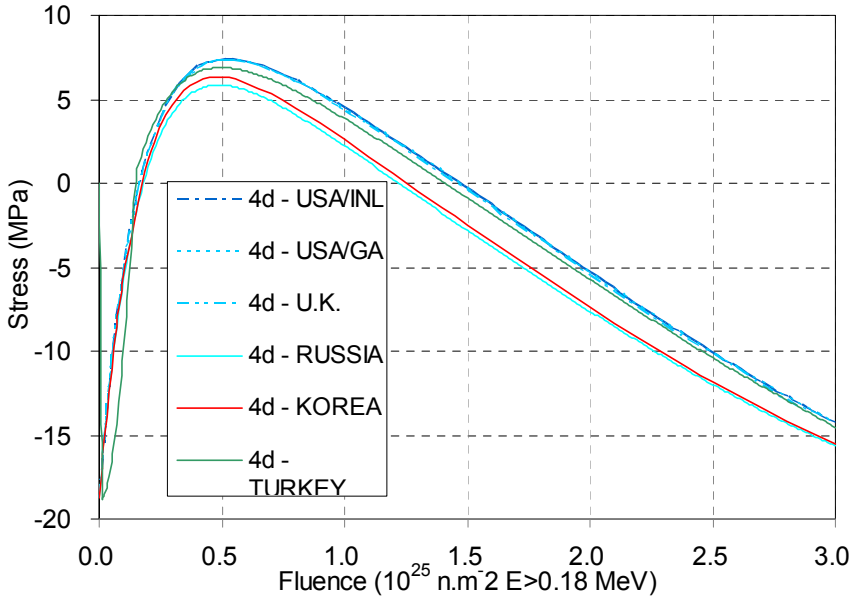

FIG. 9.11. Case 4d — Inner surface radial stress between IPyC and SiC as a function of fast fluence.

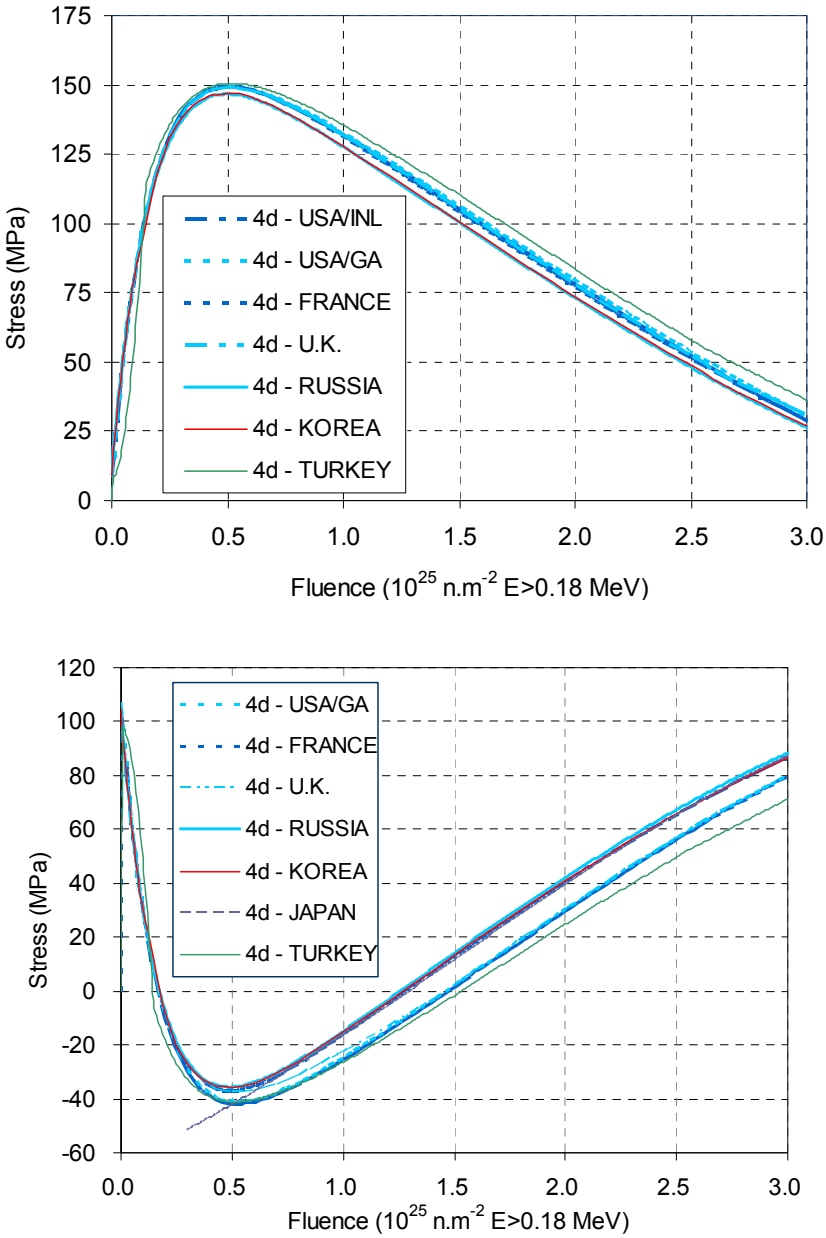

FIG. 9.12. Case 4d — Inner surface tangential IPyC and SiC stresses as a function of fast fluence.

9.2.3.8. Case 5

Case 5 is similar to case 4d except that the particle dimension is different, with a smaller kernel and an additional outer pyrocarbon layer, and that the pressure is not constant but rises linearly with burnup from 0 to 15.54 MPa. Results are shown in Fig. 9.13.

9.2.3.9. Case 6

Case 6 is similar to case 4d, except for the additional outer pyrocarbon layer and that the pressure is not constant, but rises linearly with burnup from 0 to 26.20 MPa. Results are shown in Fig. 9.14.

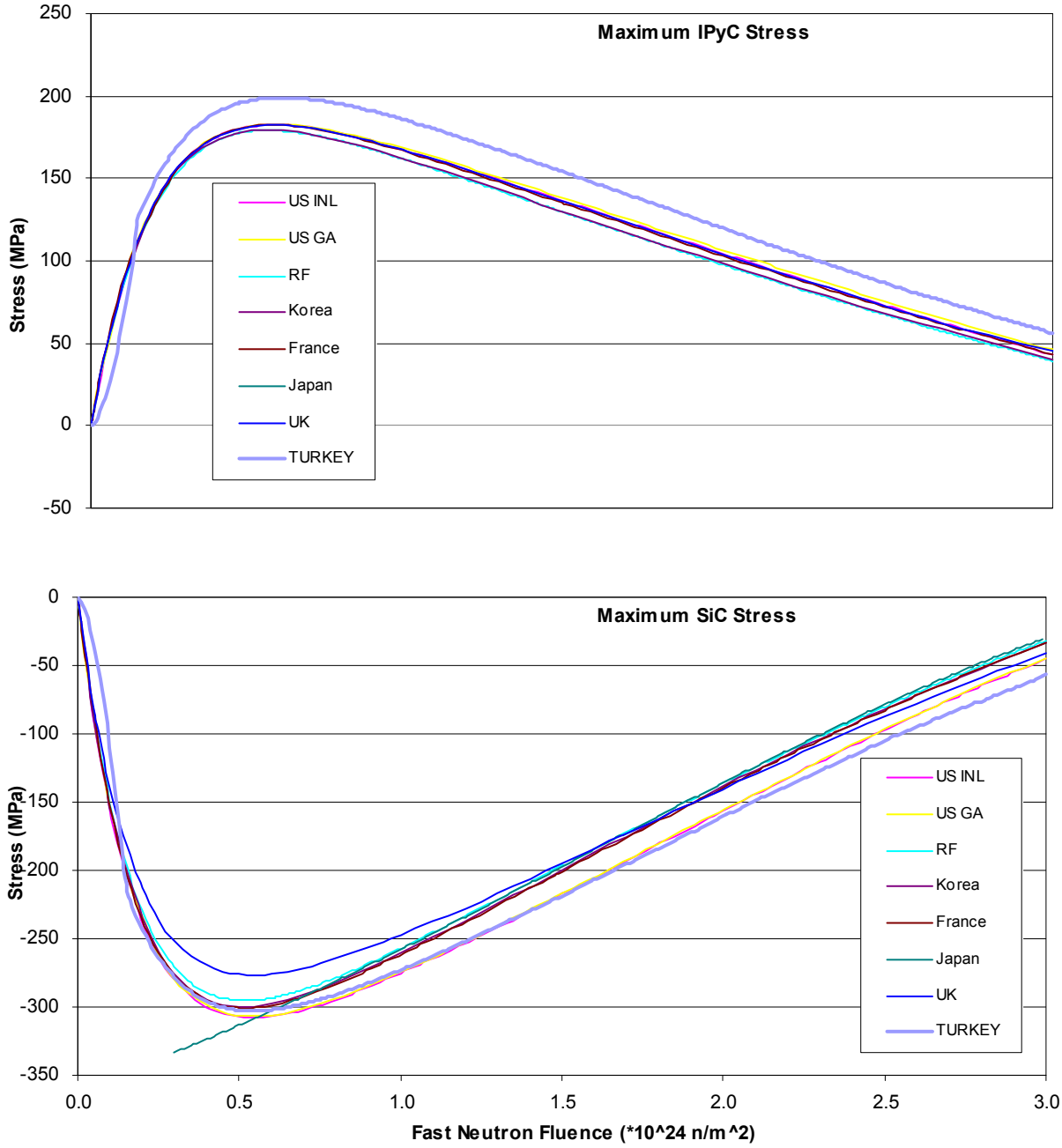

FIG. 9.13. Case 5 — Inner surface tangential SiC stress as a function of fast neutron fluence.

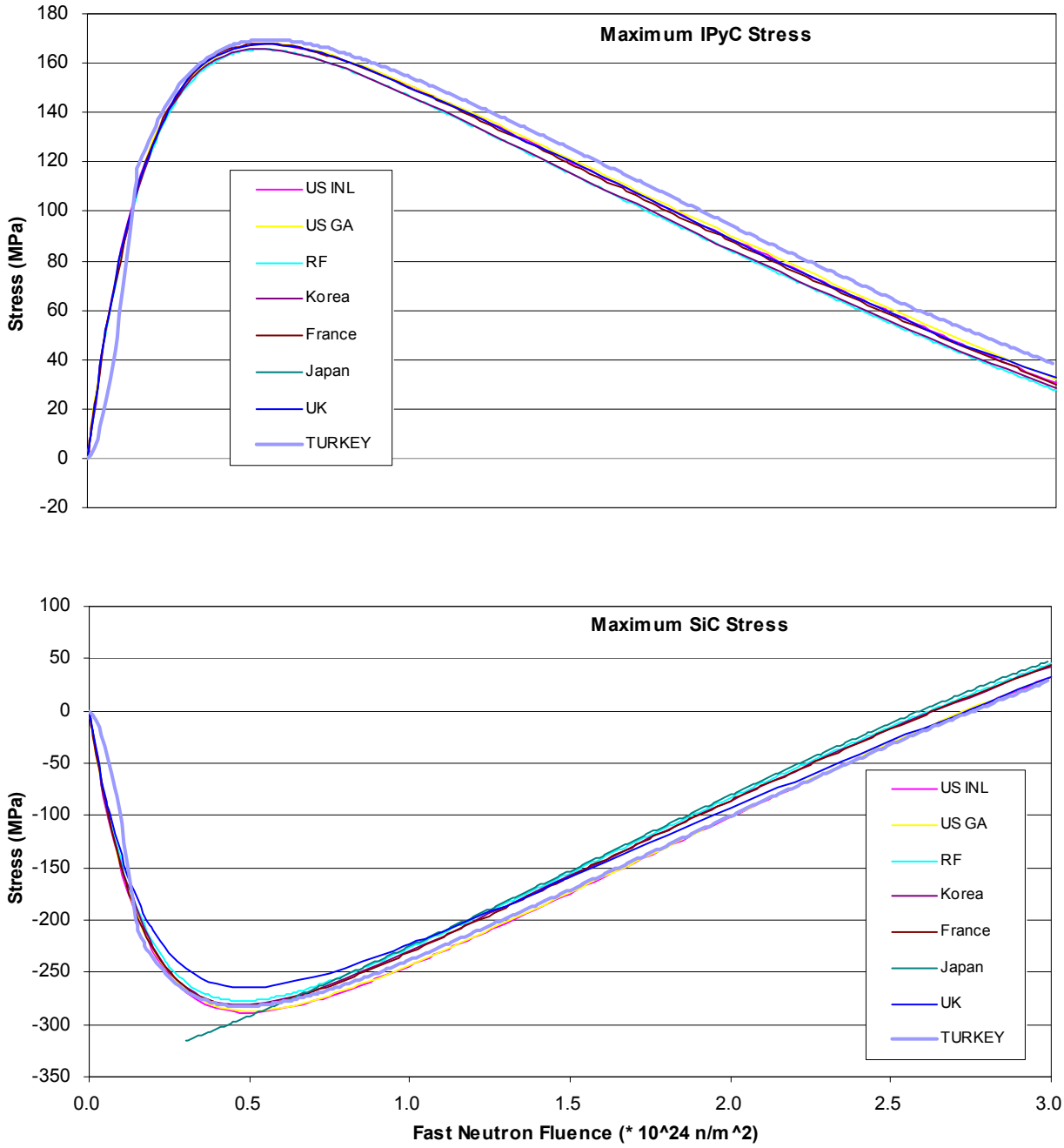

FIG. 9.14. Case 6 — Inner surface tangential SiC stress as a function of fast neutron fluence.

9.2.3.10. Case 7

Case 7 is similar to case 6 except that the swelling rate is a little bit higher due to the change of initial anisotropy (correlation (b) instead of correlation (c)). Results are shown in Fig. 9.15.

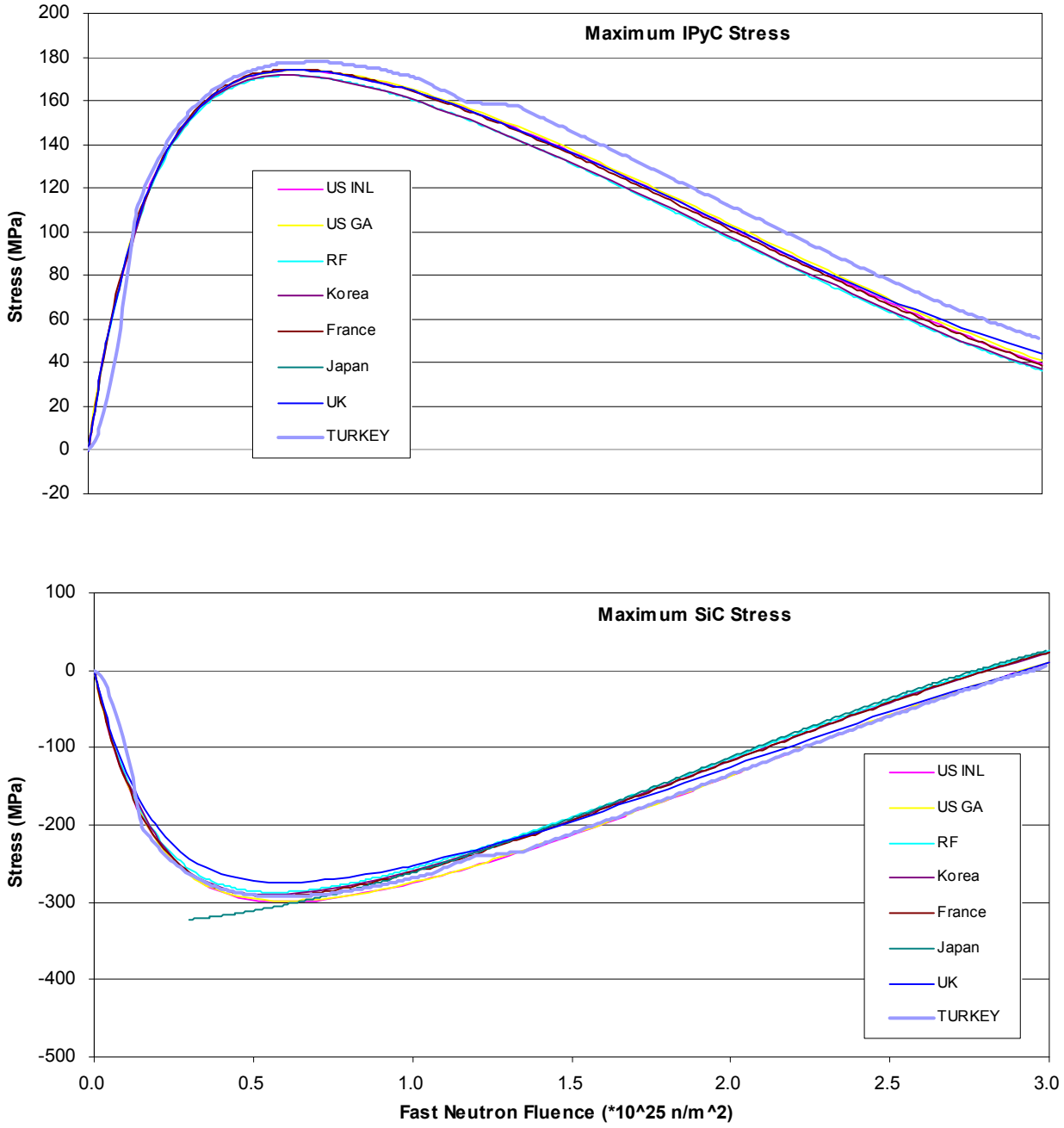

FIG. 9.15. Cases 7 — Inner surface tangential IPyC stress as a function of fast neutron fluence.

9.2.3.11. Case 8

It is assumed that the particle experiences ten cycles where the temperature is initially 873 K and increases linearly to 1273 K, and then decreases immediately back to 873 K. The period for each cycle is one tenth of the total irradiation time, or 100 days.

Figure 9.16 shows the tangential stresses in the IPyC and SiC layers as a function of neutron dose. They illustrate how the effect of temperature cycling modifies the long term evolution of stresses over the course of the irradiation. A very good agreement between the codes is noted.

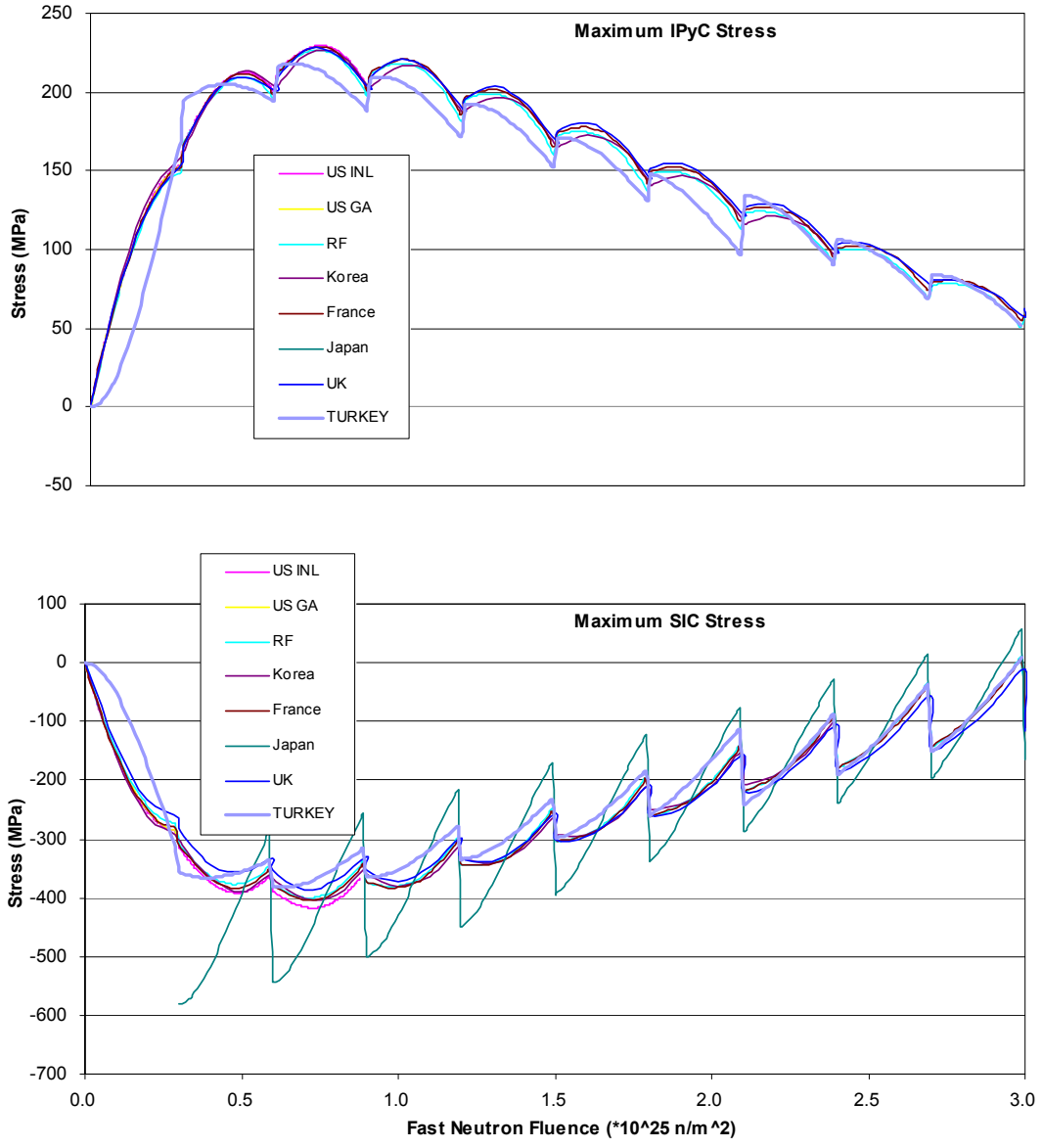

FIG. 9.16. Case 8 — Inner surface tangential IPyC (top) and SiC stresses (bottom) as a function of fast neutron fluence.

9.3. POSTCALCULATION OF IN-PILE FUEL TESTS

9.3.1. Input parameters and test conditions

The cases regarded here characterize fuel particles from past irradiation experiments. These include the HRB-22 (Japanese) experiment, HFR-K3 (German) experiment, HFR-P4 (German) experiment and the NPR-1 (US) experiment. Parameters for these cases are listed in Table 9.12.

With regard to cases 1 through 8, the main differences are

- the internal pressure, which is not fixed but rather determined by fission product release and CO production;
- the geometry of the particle which describes a population (mean value and standard deviation).

9.3.1.1. Case 9 — HRB-22 experiment

These are LEU TRISO coated particles with a mean kernel diameter equal to 544 μm in compacts irradiated 89 days until 4.79% FIMA and 2.1×10^{25} n/m^2 (E > 0.18 MeV).

9.3.1.2. Case 10 — HFR-K3 experiment, pebble B/2

These are LEU TRISO coated particles with a mean kernel diameter equal to 497 μm in a pebble irradiated 359 days until 10% FIMA and 5.3×10^{25} n/m^2 (E > 0.18 MeV).

9.3.1.3. Case 11 — HFR-P4 experiment, fuel element 3

These are LEU TRISO coated particles with a mean kernel diameter equal to 497 μm in a mini-pebble irradiated 351 days until 14% FIMA and 7.2×10^{25} n/m^2 (E > 0.18 MeV).

9.3.1.4. Case 12 — NPR-1 experiment, compact A5

These are HEU TRISO coated particles with a mean kernel diameter of 200 μm in a compact irradiated 170 days until 79% FIMA and 3.8×10^{25} n/m^2 (E > 0.18 MeV).

9.3.1.5. Case 13 — HFR-EU1 experiment

These are LEU TRISO coated particles with a mean kernel diameter equal to 502 μm in a pebble assumed to be irradiated 600 days until 20% FIMA and 5.4×10^{25} n/m^2 (E > 0.18 MeV). Input for the 'future' irradiation experiment, case 13 (HFR-EU1), is listed in Table 9.13.

9.3.2. Imposed properties fixed for the benchmark

Table 9.14 summarizes the material properties to be used for cases 9 through 13. For the PyC modulus of elasticity, PyC Poisson's ratio, SiC modulus of elasticity, and SiC Poisson's ratio, the values were given in Table 9.6 (cases 3 through 8).

TABLE 9.12. INPUT PARAMETERS FOR PAST IRRADIATION EXPERIMENTS

Parameter	Case 9: HRB-22	Case 10: HFR-K3/B/2	Case 11: HFR-P4/3	Case 12: NPR-1 A5
Oxygen to Uranium ratio	2	2	2	1.51
Carbon to Uranium ratio	0	0	0	0.36
U-235 enrichment (wt%)	4.07	9.82	9.82	93.15 ± 0.01
Kernel diameter (μm)	544 ± 9	497 ± 14	497 ± 14	200 ± 5
Buffer thickness (μm)	97 ± 13	94 ± 10	94 ± 10	102 ± 10
IPyC thickness (μm)	33 ± 3	41 ± 4	41 ± 4	53 ± 4
SiC thickness (μm)	34 ± 2	36 ± 2	36 ± 2	35 ± 3
OPyC thickness (μm)	39 ± 3	40 ± 2	40 ± 2	39 ± 4
Kernel density (Mg/m^3)	10.84	10.81	10.81	10.52 ± 0.01
Buffer density (Mg/m^3)	1.10	1.00	1.00	0.96 ± 0.05
IPyC density (Mg/m^3)	1.85	1.88	1.88	1.92 ± 0.01
SiC density (Mg/m^3)	3.20	3.20	3.20	3.23
OPyC density (Mg/m^3)	1.85	1.88	1.88	1.86 ± 0.01
IPyC BAF	1.00	1.053	1.053	1.058 ± 0.005
OPyC BAF	1.00	1.019	1.019	1.052 ± 0.006
Irradiation duration (efpd)	89	359	351	170
End of life burnup (% FIMA)	4.79	10	14	79
End of life fluence (10^{25} n/m^2, E > 0.18 MeV)	2.1	5.3	7.2	3.8
Time-average, volume-average irradiation Temperature (°C)	1303	1073	1335	1260
Ambient pressure (MPa)	0.1	0.1	0.1	0.1
Comparison metric	end of life failure fraction			

TABLE 9.13. INPUT PARAMETERS FOR THE FUTURE IRRADIATION TEST HFR-EU1

Oxygen to uranium ratio	2
Carbon to uranium ratio	0
U-235 enrichment	16.7 wt%
Kernel diameter	502 ± 11 μm
Buffer thickness	95 ± 14 μm
IPyC thickness	41 ± 3 μm
SiC thickness	35 ± 2 μm
OPyC thickness	40 ± 4 μm
Kernel density	10.81 Mg/m^3
Buffer density	1.01 Mg/m^3
IPyC density	1.87 Mg/m^3
SiC density	3.20 Mg/m^3
OPyC density	1.87 Mg/m^3
IPyC BAF	1.02
OPyC BAF	1.02
Irradiation duration	600 efpd
End of life burnup	20% FIMA
End of life fluence	5.4×10^{25} n/m^2, E > 0.18 MeV
Time-average, volume-average irradiation temperature	1298 K
Ambient pressure	0.1 MPa
Comparison metric	end of life failure fraction

Properties are generally those used in the STRESS3 code (except for case 12). The SiC mean strength and Weibull modulus are based on data used in German standard calculations (except for case 12). Properties for case 12 are based on data from [336]. The pyrocarbon creep coefficients of [336] were amplified by a factor of 2 (in case 12), based on correlations with NPR experiments. Correlations for pyrocarbon swelling strain rates are given in Table 9.8 and corresponding swelling strain (or irradiation-induced dimensional change, IIDC) were plotted in Figs 9.2 and 9.3.

TABLE 9.14. MATERIAL PROPERTIES FOR BENCHMARK CASES 9 THROUGH 13

Case	PyC creep coefficient (MPa-10^{25} n/m^2)$^{-1}$, E > 0.18 MeV	PyC Poisson's ratio in creep	PyC swelling strain rate (10^{25} n/m^2)$^{-1}$, E > 0.18 MeV	PyC mean strength (MPa)	PyC Weibull modulus	SiC mean strength (MPa)	SiC Weibull modulus
9	4.93×10^{-4}	0.4	correlation (e)	200	5.0	873	8.02
10	4.93×10^{-4}	0.4	correlation (e)	200	5.0	873	8.02
11	4.93×10^{-4}	0.4	correlation (e)	200	5.0	873	8.02
12	2.70×10^{-4}	0.5	correlation (f)	218	9.5	572	6.0
13	4.93×10^{-4}	0.4	correlation (e)	200	5.0	873	8.02

For cases 9 through 13, dFIMA/dt is constant and equal to the ratio burnup over irradiation time, making active heat production, fuel swelling and densification, fission product release (CEA model) and CO production (Proksch model) models. Also for cases 9 through 13, the buffer is disconnected from kernel and IPyC and its stiffness is close to zero in order to avoid any mechanical interaction with the layers, as it seems to be the case in the German experiments. The irradiation-induced dimensional change of the buffer is made inactive, too, in order to avoid at the beginning of the irradiation an important gap between the buffer and the IPyC (increasing the temperature of the kernel), as it seems to be the case in the German experiments.

These assumptions are due to the lack of knowledge concerning buffer properties and have consequences on the results: kernel coating mechanical interaction (KCMI), which is intentionally avoided here, is modeled in STRESS3 [232] and has a great influence on the results of cases 9 through 13 given in [342].

9.3.3. Results from participating countries

Figs 9.17 to 9.21 show for cases 9 through 13 the calculation results of

- the tangential stresses in the SiC layer as a function of irradiation time for a particle having the mean geometry;
- the total gas pressure as a function of irradiation time;
- the failure fraction as a function of irradiation time.

For cases 9 through 13, given the greater complexity associated with simulating a real irradiation experiment the calculations showed major differences that can largely be attributed to the physico-chemical models used to calculate fission gas release and CO production in the kernel.

The effect of creep factor is discussed hereafter.

Figure 9.22 shows for case 10 (HFR-K3) a comparison of the tangential stresses in the SiC layer as a function of irradiation time between ATLAS and the same calculation with the UK code STRESS3. The two curves are globally in good agreement, because there is no KCMI with the STRESS3 model. The maximum stress is about 220 MPa for STRESS3 and 280 MPa for ATLAS indicating a divergence of about 30%.

It appears that the different values assumed for the creep Poisson' ratio, ν, (0.4 and 0.5 in STRESS3 and ATLAS, respectively) explains these differences. Thus a glance at the analytical expressions defining stresses in the various layers [236] reveals how dependent they are on the value assumed for ν. As a simple illustration of this assertion, equation (9.30) was derived from equation (15) in [236] where, for the OPyC layer, these stresses at the inner and outer surfaces are given by:

$$\sigma_{1o}\left(a_o\right) = -\frac{3\dot{g}_{1o}(1-\nu_o)\,(m_o-2)+2\Delta\dot{g}_o\nu_o\,(m_o-1-m_o\ln m_o)+9m_o\nu_o(1-\nu_o)K_o\Pi}{3K_o(1-\nu_o)[m_o(1+\nu_o)+2(1-2\nu_o)]} \quad (9.32)$$

and

$$\sigma_{1o}\left(b_o\right) = -\frac{9\dot{g}_{1o}(1-\nu_o)+\Delta\dot{g}_o\left[(1+\nu_o)(m_o-1)+2(1-2\nu_o)\ln m_o\right]}{3K_o(1-\nu_o)[m_o(1+\nu_o)+2(1-2\nu_o)]} - \frac{m_o(1+\nu_o)-(1-2\nu_o)}{m_o(1+\nu_o)+2(1-2\nu_o)}\Pi$$

(9.33)

assuming ν = 0.5. Values of the coefficients in the first and second terms of equation (9.30) are 4.5, -5.4, -1.4, 3.24, and -0.67, respectively.

According to [236], the corresponding stresses for the IPyC layer are given by:

$$\sigma_{1i}\left(a_o\right) = -\frac{9\dot{g}_{1i}m_i(1-\nu_i)-\Delta\dot{g}_i\left[(1+\nu_i)(m_i-1)+2(1-2\nu_i)m_i\,\ell n\,mi\right]}{3K_i(1-\nu_i)[2m_i(1-2\nu_i)+(1+\nu_i)]} - \frac{(1+\nu_i)-m_i(1-2\nu_i)}{2m_i(1-2\nu_i)+(1+\nu_i)}P$$

(9.34)

where

ν is the Poisson coefficient of irradiation creep;
$\dot{g}$ is the shrinkage rate;
K is the uniaxial creep constant;
a, b are the inner and outer radius;
1 = radial, 3 = tangential.

The creep Poisson's factor is taken 0.5 and isotropic swelling is assumed. The above equation takes into account the effect of the creep Poisson's factor and the non-isotropic swelling of the pyrocarbon. If only the main term of that equation is considered, proportional to the tangential swelling rate, the coefficient taking into account the creep Poisson's factor is

$$\frac{3(1-\nu)}{(1-\nu)[2m(1-2\nu)+(1+\nu)]} \quad (9.35)$$

where

$m = (r_i/r_o)^3$ with r_i and r_o being inner and outer radius of the shell (m).

With ν = 0.5, this coefficient is equal to the factor 2 of equation (9.13). If ν = 0.4 is considered, then this coefficient is equal to 1.54, which is about 30% less. Thus, the divergence between the two calculations is likely mainly due to the creep Poisson's factor.

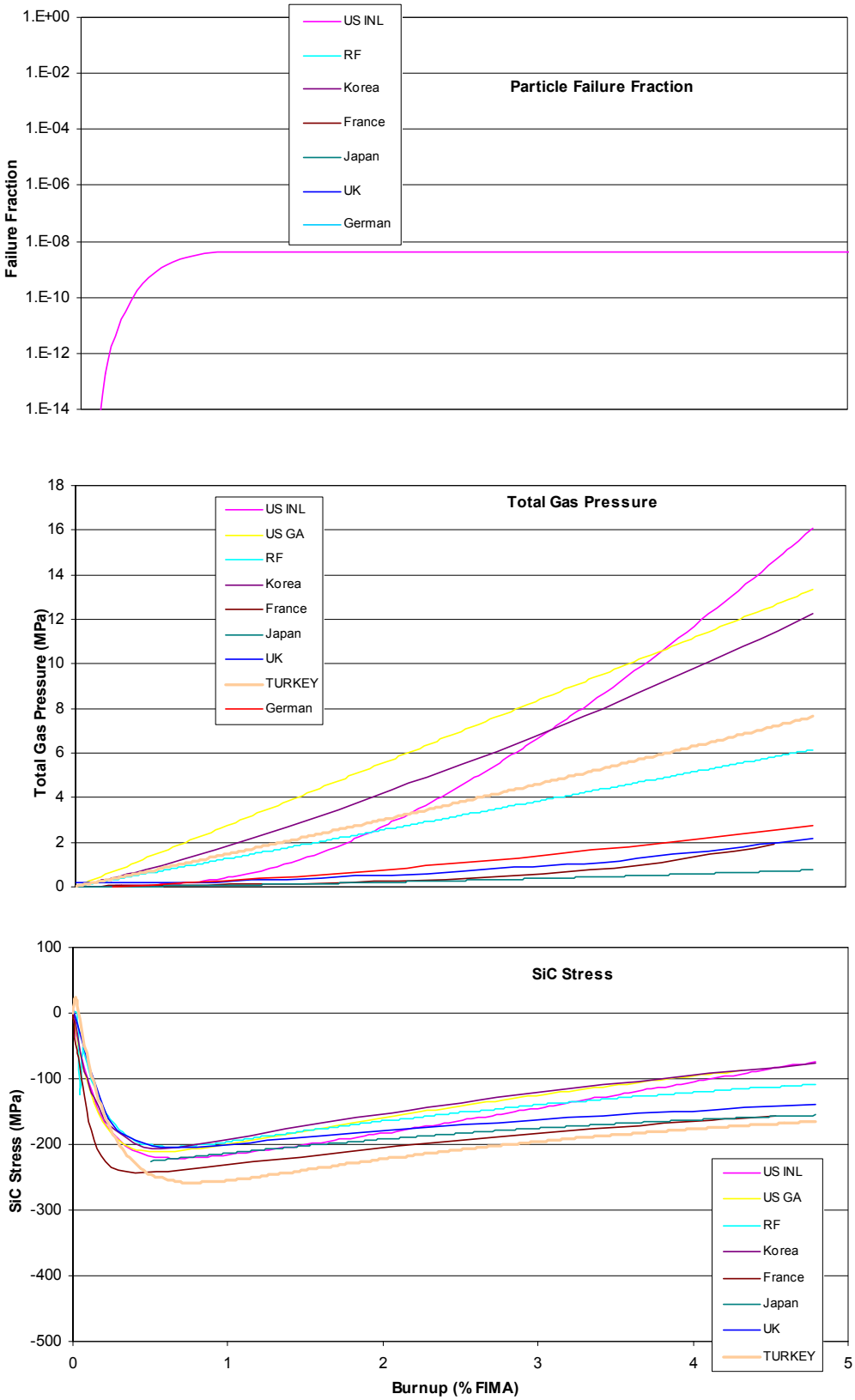

FIG. 9.17. Case 9: HRB-22 — total gas pressure, SiC stresses and failure fraction as a function of burnup.

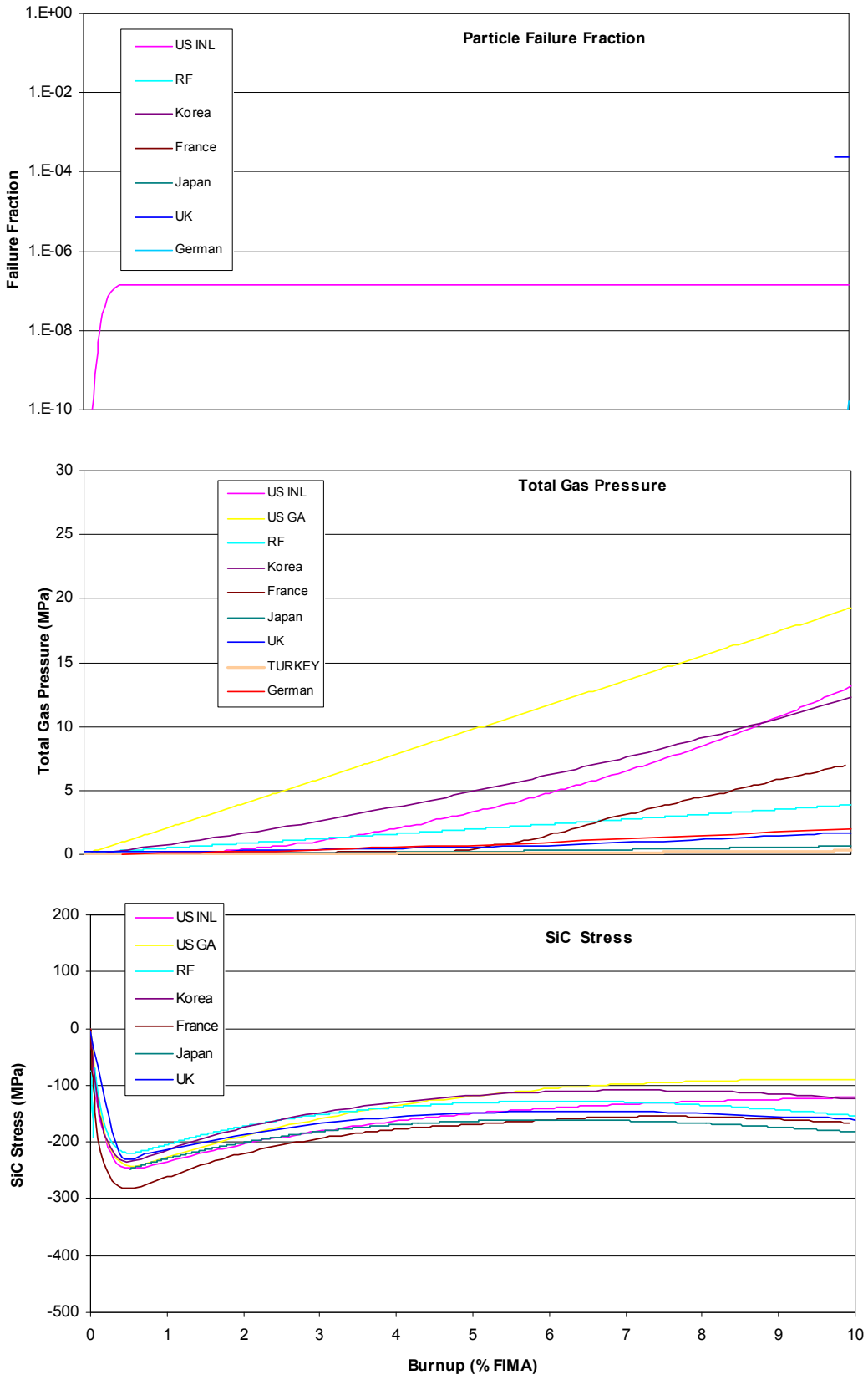

FIG. 9.18. Case 10: HFR-K3/2 — Total gas pressure, SiC stresses and failure fraction as a function of burnup.

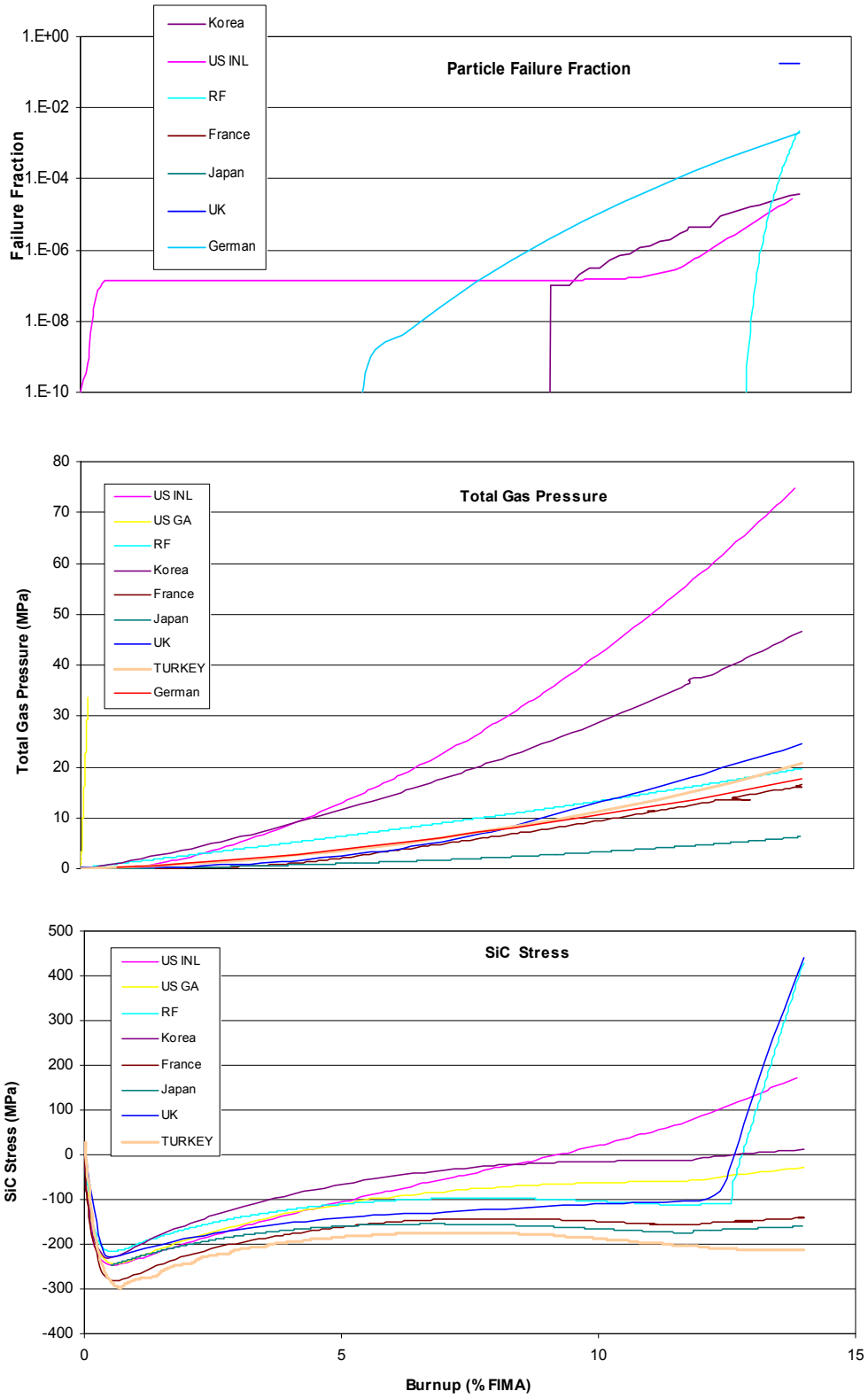

FIG. 9.19. Case 11: HFR-P4-3 — total gas pressure, SiC stresses and failure fraction as a function of burnup.

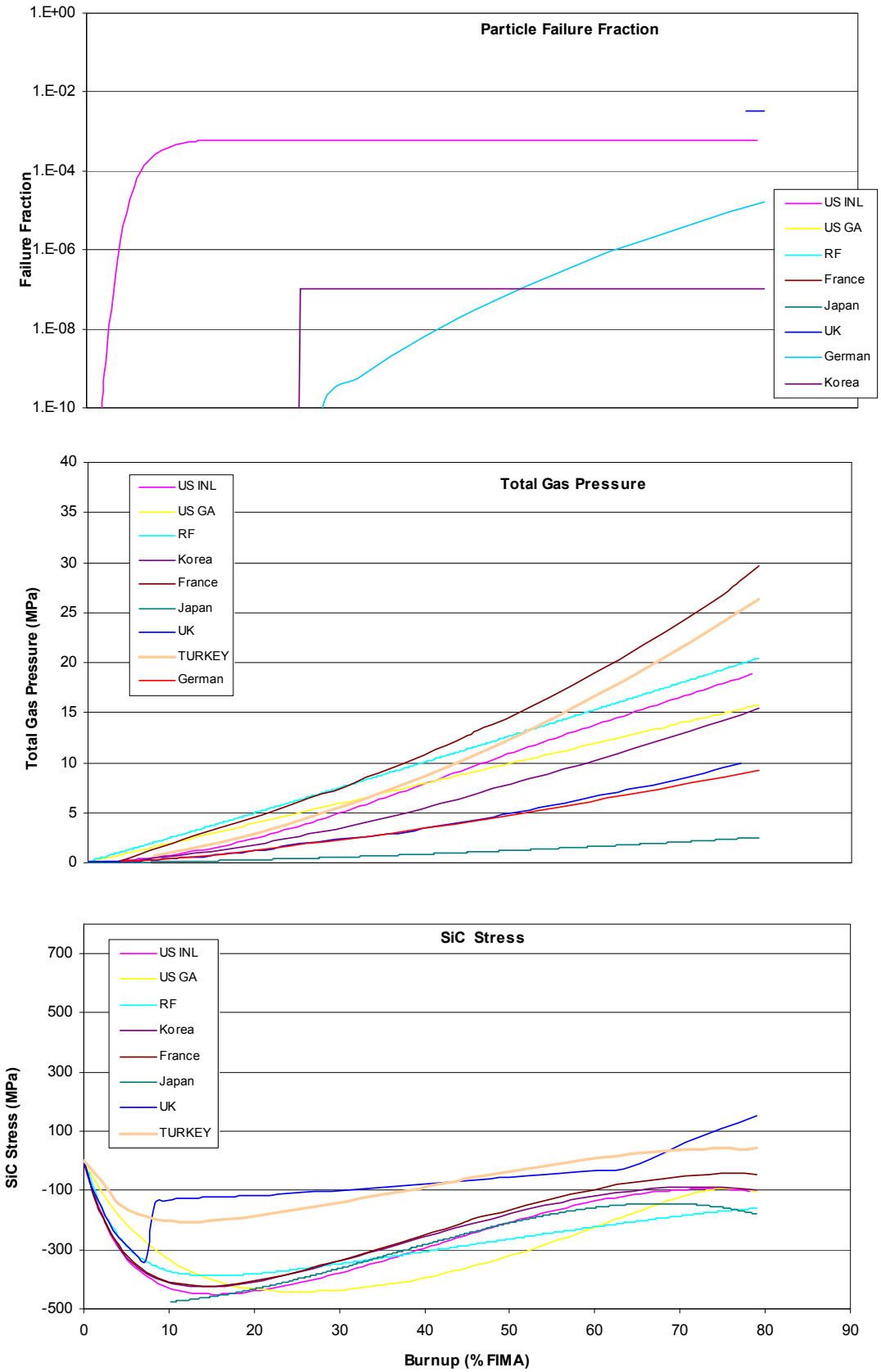

FIG. 9.20. Case 12: NPR-1A — total gas pressure, SiC stresses and failure fraction as a function of burnup.

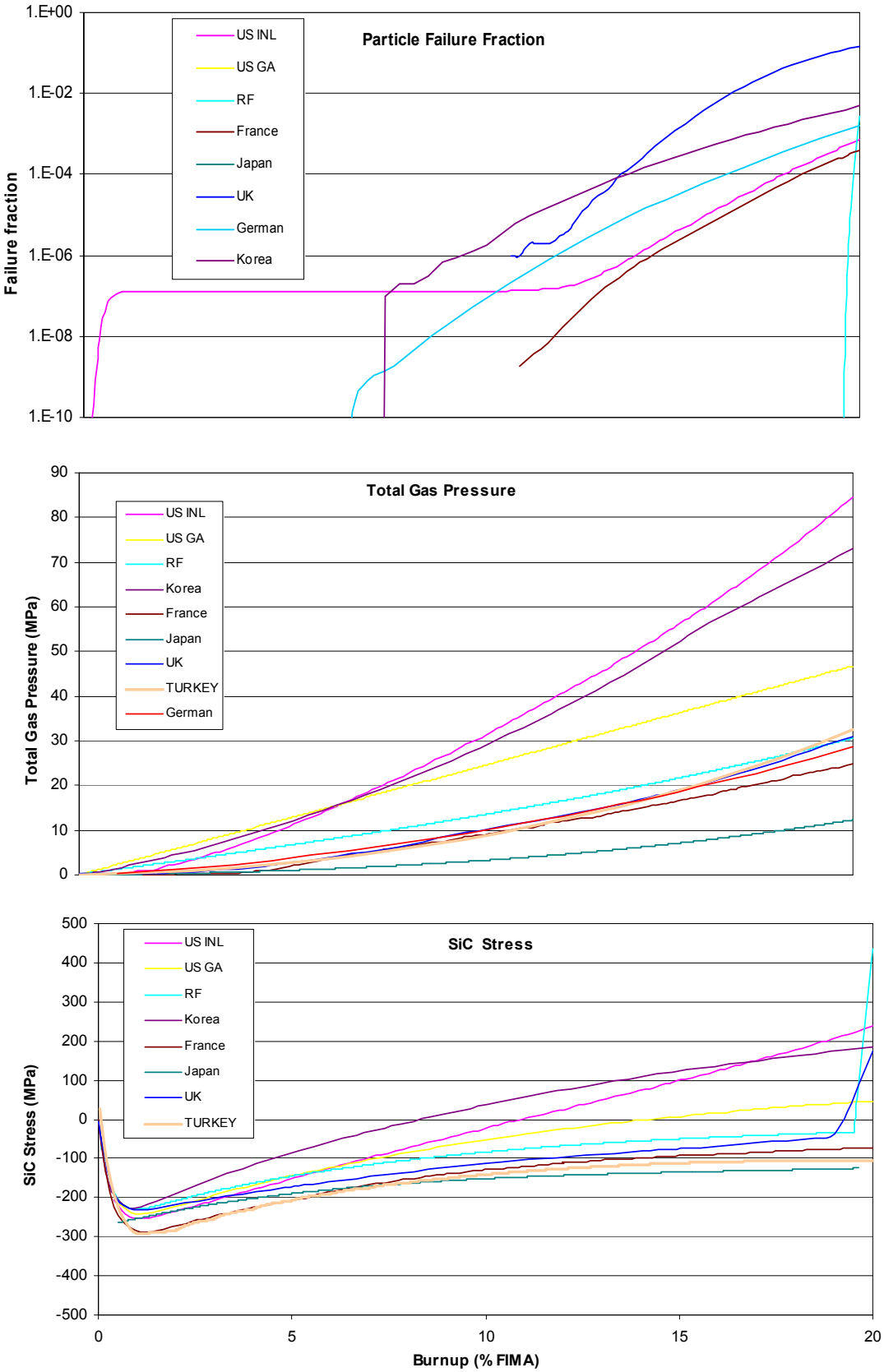

FIG. 9.21. Case 13: HFR-EU1 — total gas pressure, SiC stresses and failure fraction as a function of burnup.

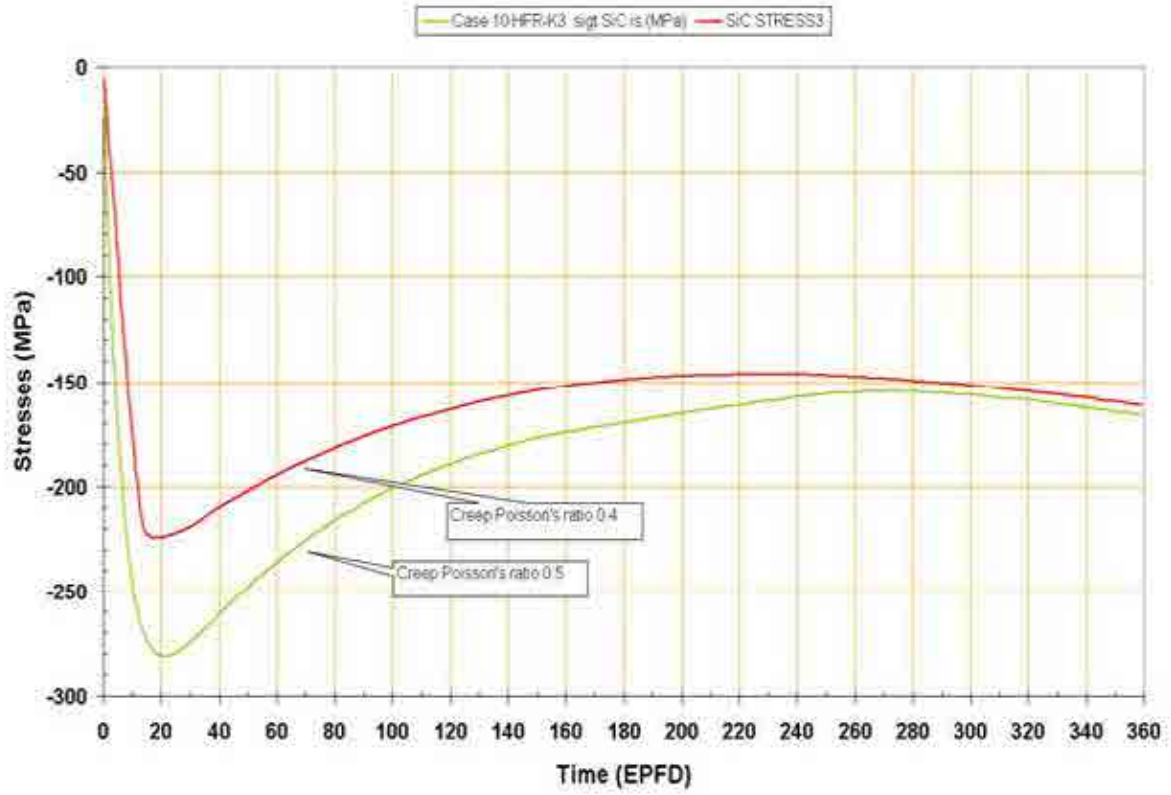

FIG. 9.22. Case 10: HFR-K3/2 — Comparison STRESS3–ATLAS of tangential stresses in SiC layer.

9.4. SUMMARY AND CONCLUSIONS

This section presented the calculations of the benchmark of fuel performance models under normal conditions.

Cases 1 to 7, simplified analytical benchmarking problems to 'calibrate' the codes and/or models, have been compared with analytical formulations. The results from cases 1 through 8 were all very good. Excellent agreement was observed among many of the codes.

The stresses in case 8, which is more complex, taking into account cyclic temperature history characteristic of fuel in a pebble bed reactor, have been compared and again excellent agreement was observed among many of the codes.

For cases 9 through 13, given the greater complexity associated with simulating a real irradiation experiment the calculations showed major differences that can largely be attributed to the physico-chemical models used to calculation fission gas release and CO production in the kernel. For German type particles where gas pressures are low, the stress in the SiC layer is dominated more by the PyC shrinkage than by the internal gas pressure in the particle. Thus, for low burnup and low temperatures, the degree of accuracy needed in calculating the internal gas pressure in the particle is less because of this lower impact on stress in SiC.

10. BENCHMARKING OF FISSION PRODUCT RELEASE BEHAVIOUR MODELS UNDER ACCIDENT CONDITIONS

10.1. MODELING OF FISSION PRODUCT RELEASE UNDER ACCIDENT CONDITIONS

10.1.1. Introduction

The transport of any metallic fission or activation product could be calculated if the transport parameters of the nuclide were available. But it is impractical (and unnecessary) to evaluate production, transport and release of all species generated in a nuclear reactor. Therefore, only the radiological most significant nuclides are analysed. Key radionuclides are selected based on the combination of their fission yield, their transport and release properties and their radiological hazard level.

The radiologically most relevant radioisotopes monitored during accident simulation testing include the long lived strontium (^{90}Sr), silver (^{110m}Ag), caesium (^{134}Cs, ^{137}Cs), and krypton (^{85}Kr) activation and fission products, and the short lived iodine (^{131}I) and xenon (^{133}Xe) fission products (see also Table 8.1). Isotopes of the same chemical species are assumed to result in same release fractions. More nuclides may be considered depending on the expected fuel conditions.

10.1.2. Codes used in benchmark exercise

A total of eight codes from France, Germany, the Republic of Korea, South Africa, and the USA have been applied to all or a part of the proposed benchmark cases. From the historic perspective, the comparison is between three 'old' (Germany, South Africa, USA/GA) and five newly developed models.

10.1.2.1. France: ATLAS code description

The ATLAS code as has been used in the normal operation benchmark was already described in Section 9.1.2. For the assessment of fission product release, the long-lived fission products behaviour in the different constitutive materials is handled by taking into account [343]:

- Production of the fission products in the Kernel. A simplified model from calculations using the codes APOLLO2 and DARWIN/PEPIN of Commissariat à l'Energie Atomique is used.
- Diffusion of the fission products through the kernel and the layers, using a single transport law with effective diffusion coefficients.
- Radioactive disintegration.

The whole diffusion mechanism is modeled as follows for each fission product species:

$$\frac{\partial c^{(i)}}{\partial t} = -div\left(D^{(i)} \cdot grad\left(c^{(i)}\right)\right) - \lambda \cdot c^{(i)} + \dot{s} \qquad (10.1)$$

where

$D^{(i)}$ is the diffusion coefficient in the layer i (m^2/s);
$c^{(i)}$ is the concentration of the fission product in the layer i (kg/m^3);
$\dot{s}$ is the fission product source term (kg/(m^3·s));

λ is the radioactive disintegration constant (s^{-1}).

10.1.2.2. Germany: FRESCO-II code description

The FZJ computer model FRESCO actually exists in two versions. The 'core' version [226] was developed first to describe the fission product release behaviour in a pebble bed core during a core heatup accident phase taking account of redistribution of fission products by the coolant flow and sorption effects at the graphite surfaces of both the fuel elements and the top and bottom reflectors. This FRESCO(-I) version requires the input of transient temperature and coolant flow distribution as the result of a thermodynamic model calculation.

A follow-up version, FRESCO-II [221], concentrates on a single, representative spherical fuel element and includes, in addition to the heating/accident phase, also the phase of irradiation/normal operation. Main purpose of this version was to simulate a complete irradiation and heating experiment for a spherical fuel element. The important input data comprise, apart from the fuel geometry and the temperature–time history, the effective diffusion coefficients for kernel, coating layers, and graphite, as well as a particle failure function given in form of a step function.

The FRESCO diffusion model distinguishes between two types of particles, intact particles and defective/failed particles. From the moment of failure, a particle is treated in the model as a bare kernel which releases activity immediately into the fuel element matrix graphite; the inventory present in the layers at this time is regarded as released. Since the moment of failure is important, the particles which fail at a certain time are treated in a separate, independent diffusion calculation. For this reason, the number of steps in the failure function is limited to 10. The transport of metallic fission products through the fuel materials is modeled as a transient diffusion process. The transient diffusion equation is typically solved numerically in discrete steps of time and locations with appropriate boundary and interface conditions.

The rate of migration of a species through a homogeneous medium is defined by its mass flux and a concentration gradient as the driving force. According to Fick's first law as described in [344], the flux of atoms diffusing through a medium is proportional to the concentration gradient:

$$J_x = -D\frac{\partial c}{\partial x} \tag{10.2}$$

where

J is the diffusion flux (atoms/(m^2·s));
D is the diffusion coefficient (m^2/s);
c is the concentration (atoms/m^3);
x is the position or length (m).

The second Fickian law describes the time dependent change of the concentration field by diffusion. Assuming the diffusion coefficient D to be a constant and including source (e.g. production from nuclear fission) and sink (e.g. radioactive decay) terms, Fick's equation reads as follows:

$$\frac{\partial c}{\partial t} = D\frac{\partial^2 c}{\partial x^2} - \lambda c + S \tag{10.3a}$$

or in spherical coordinates:

$$\frac{\partial c}{\partial t} = D\left(\frac{\partial^2 c}{\partial r^2} + \frac{1}{r}\frac{\partial c}{\partial r}\right) - \lambda c + S \qquad (10.3b)$$

where

λ is the decay constant (s^{-1});
S is the fission product production rate (atoms/(m^3·s)).

The following boundary conditions apply:

- Concentration gradient is 0 at radius r = 0

$$\left.\frac{\partial c}{\partial r}\right|_{r=0} = 0 \qquad (10.4a)$$

- Continuity of flux and concentration is given at the interface between two adjacent materials with diffusion coefficients D_1, and D_2:

$$c_1 = c_2 \text{ and } -D_1\left.\frac{\partial c}{\partial r}\right|_1 = -D_2\left.\frac{\partial c}{\partial r}\right|_2 \qquad (10.4b)$$

- For fission product transport in the fuel element matrix graphite, a third boundary condition applies describing the mass transfer at the fuel surface which is given by

$$-D\left.\frac{\partial c}{\partial r}\right|_{r=r_s} = \beta\left(c_{bl} - c_{gas}\right) \quad with\ c_{bl} = f\left(c_w, T\right) = \alpha c_w \qquad (10.4c)$$

where

β is the mass transfer coefficient from the surface to the coolant;
c_{bl} is the concentration in the coolant immediately above the graphite surface (atoms/m^3);
c_{gas} is the mean concentration in the coolant (atoms/m^3);
c_w is the concentration in the graphite near the surface (atoms/m^3);
α is the ratio between boundary layer and wall concentration and is determined by sorption isotherms.

This third boundary condition defines the release rate from the surface of the fuel sphere into the coolant. In most cases, free evaporation from the surface can be assumed expressed by

$$\beta \to \infty \text{ or } c_w = 0 \qquad (10.4d)$$

The transport speed is determined by the diffusion coefficient D, m^2/s, which is typically depending on the temperature. For gas-in-gas binary diffusion, the diffusion coefficient is approximately proportional to T1.5. For transport in solids, an Arrhenius type temperature dependence [345] of the form is assumed

$$D = D_o \exp\left\{-\frac{Q}{RT}\right\} \quad (10.5a)$$

where

D_o is the pre-exponential factor (m^2/s);
Q is the activation energy (J/mol);
R is the universal gas constant, = 8.3145 (J/(mol·K));
T is the absolute temperature (K).

The transport of mobile fission metals is certainly structure-sensitive and more complex than classical Fickian diffusion and likely a combination of lattice diffusion, grain boundary diffusion, pore diffusion, etc., further complicated by effects like irradiation-enhanced trapping and adsorption. Consequently, any quoted diffusion coefficient should be called an 'effective' diffusion coefficient which implies that the overall migration process is approximately described by Fick's laws [224].

An effective diffusion coefficient can be deduced experimentally for specific temperatures or temperature ranges, since the diffusion of fission product atoms increases as the temperature is raised according to the Arrhenius equation. Sometimes experimental findings suggest the incorporation of additional dependencies like neutron fluence, Γ, or concentration of the considered species, c, or the use of two temperature ranges with different activation energies like one for the normal operation phase and another one for the accident temperature range:

$$D_{eff} = D(T,\Gamma,c,...) = \sum_{i=1,2} D_{o,i} \exp\left\{-\frac{Q_i}{RT}\right\} \quad (10.5b)$$

The procedure of calculation within a time step is performed in two consecutive parts: first the diffusive release from intact and defective particles and from the graphite grains is determined. The sum of those single releases is the overall source term for the fuel element matrix graphite (grain boundaries). In the second part, the diffusive transport through the matrix and release into the coolant is calculated. The diffusion calculation is conducted based on relative values. The inventory of a fission product is built up during the normal operation phase according to its decay constant until reaching 100% at the end of irradiation and beginning of the accident phase, respectively. For long-lived species, the buildup is (almost) linear with irradiation time, while short-lived species quickly reach the equilibrium state.

10.1.2.3. Republic of Korea: COPA code description

The COPA-FPREL code [346] analyses the fission product migration in the coated fuel particle, pebble, compact and structural graphite of a HTGR fuel under reactor operational conditions and during irradiation and heating tests. The code uses a finite element method using the Galerkin form of the weighted residuals procedure [347]. The numerical method in COPA-FPREL was originally a finite difference method, but it was changed to the finite element method for easier control of interval size.

In the finite element method, the kernel, buffer and the coating layers of a coated fuel particle are divided into specified number of intervals, respectively. The diffusion coefficient is assumed to be constant in the interval. A Fickian diffusion equation including birth rates is applied to these intervals. The birth rate is the generation rate of the fission products per volume. The fission products are generated through a nuclear fission in the kernel material

and a uranium contamination in the coating layers, and are transferred from adjacent layers through recoil. The initial concentration distribution in a particle is expressed by a function of the radial coordinate, only. The diffusion current is zero at the particle centre. The concentration is assumed to be zero at the particle surface. At the layer interfaces, the currents in two layers are the same and there exist concentration ratios.

The fuel and graphite regions of a pebble are divided into specified numbers of intervals, respectively, in which the diffusion coefficient is assumed to be constant. The fission product transport within a pebble can be described by the Fickian diffusion equation including source terms. The source terms are the fission product generation rate per volume through nuclear fissions in a heavy metal contamination and the fission product release rates per volume from the intact and failed coated fuel particles. The initial concentration distribution in a pebble is expressed by a function of the radial coordinate, only. The diffusion current is zero at the pebble centre. The fission products evaporate on the pebble surface. The concentration at the pebble surface is in equilibrium with the vapour pressure on the pebble side of the boundary layer which forms between the pebble surface and the bulk coolant. The equilibrium is expressed by a sorption isotherm. The mass transfer occurs through the boundary layer into the bulk coolant. The resulting system of finite element equations becomes nonlinear because of the boundary conditions at the pebble surface. An iterative solution scheme is applied to solve the system of algebraic finite element equations.

There are many symmetrical parts in a fuel block of a prismatic reactor. A symmetrical part consists of a fuel compact, a gap between compact and structural graphite, structural graphite, and a coolant hole. For a simple calculation, a symmetrical element is approximated by a one-dimensional equivalent slab [313, 348]. The graphite length in an equivalent slab is determined so that the slab and the symmetrical element have the same thermal resistance. The fission product transport within the compact and graphite in a slab can be described by the Fickian diffusion equation. The numerical modeling is the same with that for a pebble except a gap. It is assumed that the vapour pressure in the gap is in equilibrium with the concentrations on the compact and graphite surfaces simultaneously. The resulting system of finite element equations becomes nonlinear because of the gap conditions and the boundary conditions at the graphite surface facing a coolant.

COPA-FPREL takes the fluence, fuel burnup and coolant temperature in the form of piecewise functions of time. At a certain point of time, it calculates the temperature distribution in a fuel element using the coolant temperature or uses a constant temperature value according to an input option. The material properties such as the diffusivity, sorption isotherm parameters, mass transfer coefficient, thermal conductivity are updated according to the temperature distribution in a fuel element. Source terms including the fission product release rates from the intact and broken coated fuel particles and the fission product generation rate from the uranium contaminations are calculated. New concentration distribution in a fuel element is calculated iteratively since a system of finite element equations is nonlinear. In order to calculate a source term due to the fission product release rates from the coated fuel particles, a finite element analysis is applied to the coated fuel particles, too. The temperature and concentration distributions in the coated fuel particles are calculated through the same finite element method as one applied to a fuel element. The temperature at the particle surface is the temperature of a fuel element where the particle is located. The temperature distribution in a coated fuel particle is calculated using the particle surface temperature or assumed to be constant according to an input option. The time dependent failure fraction of the coated fuel particles is inputted into COPA-FPREL in the form of a piecewise function of time.

10.1.2.4. South Africa: GETTER code description

The GETTER code [225] calculates the time dependent release of caesium, silver and strontium from the fuel elements of the PBMR equilibrium core under normal operating conditions. The code was developed at HRB and used to analyse and model the AVR, THTR and HTR-Modul reactors, as well as irradiation tests of spherical fuel.

The exact theory can be found in the reference [225]. Standard coated particles within the specification limits demonstrate highly efficient retention of the metallic fission products, with notable exceptions of strontium and the activation product ^{110m}Ag. The particle failure fraction is calculated from a conservative empirical correlation of failure fraction as a function of temperature, with instantaneous incremental failure assumed when a given temperature is reached. The GETTER code is also used for calculations of the release of noble gases, halogens and metallic fission products under accident conditions.

The GETTER code contains thermo-hydraulic and burnup subroutines in order to calculate fuel temperatures, fission powers and all inventories throughout the history of a fuel sphere in the core. GETTER calculates the transport of fission products from their birth sites to eventual release from the fuel surface. Gas precursors and activation products are taken into account.

The input data to GETTER include:

- Reactor core geometry (flow channels and core regions).
- CFD analysis output (core geometry and dimensions, helium pressure, flow speeds and circulation times through the core and main power system (MPS)).
- VSOP analysis output (fuel residence times, coolant and fuel surface temperatures, fast and thermal neutron fluxes and cross-sections).
- Cross-sections derived from MCNP analyses.
- Material data (fuel sphere data: uranium loading, enrichment, dimensions, particle failure fraction, uranium contamination; transport data for all fuel materials).
- Fission product yields (^{235}U, ^{239}Pu and ^{241}Pu).
- Reactor specific data (thermal power, number of fuel spheres, etc.).

The output data from GETTER include:

- Calculated fuel temperatures.
- Fission powers from U and Pu, as well as burnup.
- Radionuclide inventories in different fuel components.
- The release rates from different fuel components.
- Single sphere weighted core average release.

10.1.2.5. USA/INL: PARFUME code description

The PARFUME computer code is being developed at the Idaho National Laboratory to support the very high temperature reactor (VHTR) programme. PARFUME is an integrated mechanistic code that evaluates the thermal, mechanical, and physic-chemical behaviour of coated fuel particles and the probability for fuel failure given the particle-to-particle statistical variations in physical dimensions and material properties that arise during the fuel fabrication process. PARFUME calculates fractional fission product release based upon the diffusion model extracted, and then modified, from the TMAP4 computer code. The original coding was derived to represent the one-dimensional transport of atoms in plane geometry using

finite difference techniques. This coding was modified for use within PARFUME and was also extended to include the capability to simulate transport in cylindrical or spherical coordinates. The spherical coordinate extension allows increase fidelity in modeling transport within fuel particles and pebble bed fuel spheres, while the cylindrical coordinate extension allows for modeling of prismatic fuel compacts.

Fuel performance is continuously modeled by PARFUME from an irradiation phase through a postulated accident (or heatup) phase. Both the normal irradiation and accident phase conditions are user defined. The timing and number of fuel particle failures are tracked whereby PARFUME then separately considers fission product transport from uranium contamination, intact fuel particles, particles with initially failed SiC layers, and particles with induced layer failures.

10.1.2.6. USA/GA: SORS code description

The SORS code was developed by GA for use in calculating the release of fission products, transuranics, and other radionuclides from the reactor fuel to the coolant for postulated core heatup scenarios in an HTGR core. SORS calculates the fractional release of fission products from the fuel particles based on diffusion in a one-dimensional spherical geometry using data and formulations from GA's Fuel Design Data Manual (FDDM). In calculating the fractional release of fission products from the fuel, SORS considers the presence of various types of defects in the fuel particles at the onset of the accident, failure of one or more of the fuel particle coating layers by a number of mechanisms during the accident, the heavy metal contamination fraction, diffusion of volatile and metallic fission products through the fuel kernel, diffusion of metallic fission products through intact SiC coatings, and diffusion of volatile fission products through intact OPyC coatings. The calculations account for the influence of burnup, fast neutron fluence, irradiation and accident condition temperatures, and radionuclide concentrations.

Fuel particle defect fractions at the onset of an accident (heating phase) are provided as input to SORS (in data statements within the code) based on the fuel performance results calculated using the PISA and CAPPER codes. PISA is used to calculate OPyC and SiC coating failure due to thermo-mechanical effects, and CAPPER is used to calculate SiC failure due to thermo-chemical effects. Accident scenario parameters are provided as input data to SORS, including the time averaged temperature during the irradiation phase preceding the accident, the burnup and fast neutron fluence at the onset of the accident, and the time-dependant temperature during the accident.

SORS calculates the SiC failure probability as a function of time during the accident and uses the values along with the initial failure probabilities and particle defect fractions input to the code. The fuel particle failure fractions calculated in SORS provide the source terms for fission product release from the particles, which is calculated using the fission product release models in the FDDM. These include models for diffusion of gaseous and metallic fission products from the kernel in failed fuel particles, diffusion of gaseous fission products and metallic fission product through intact OPyC coating layers in particles having a defective SiC layer, and diffusion of metallic fission products through the SiC in intact fuel particles. The SORS calculations, which are for prismatic HTGR cores, do not account for hold up of fission products in the matrix material of fuel spheres.

10.1.2.7. USA/NRC: NRCDIF code description

NRCDIF solves the general diffusion equation in the form

$$\frac{\partial C}{\partial t} = \frac{1}{r^m}\frac{\partial}{\partial r}\left(r^m\, D\,\frac{\partial C}{\partial r}\right) - \lambda C + S \qquad (10.6)$$

where

C is the species concentration;
D is the diffusion coefficient;
λ is the decay constant;
S is the generation term;
m is the type of geometry (m=0 for cartesian, m=1 for cylindrical, and m=2 for spherical).

The code is programmed in MATLABTM where the partial differential equation is converted to ordinary differential equations using a second order accurate spatial discretization on a fixed set of user-specified nodes. For the TRISO particles, the boundary conditions are symmetry at the particle centre and zero concentration on the surface. The model is intended only to describe the fission product distribution and release from the fuel particles.

The code can model different particle types, namely, 'intact' particles (with all outer layers), 'failed' particles with only the fuel kernel, and particles with missing layers. There is no temperature variation within a fuel particle. The particle temperature can be a function of time with user-defined Arrhenius type diffusion coefficients for each layer.

The code can calculate the fission product release from particles during normal operation by appropriate choice of initial conditions (temperature and concentration), and evaluation of the source term using an effective fission yield for each fission product. Following the normal operation calculation, the distribution of the fission products in each layer is known which can be used as initial condition for the accident calculation. The model can be extended to take into account diffusion in the matrix and graphite block with user defined temperature histories for each component.

10.1.2.8. USA/SNL: MELDIF code description

MELCOR is a fully integrated, engineering level computer code that was originally developed to model the progression of light water reactor severe accidents. The code is being modified to include models for HTGR safety analysis. The fission product release model for HTGRs, termed MELDIF, is a finite difference diffusion model, containing models for the major categories of fuel particles (intact, failed, SiC layer failed, for example) coupled to a graphite matrix model. Temperature and power conditions for the model are provided by MELCOR for each core cell. The model is to be used both for release under accident conditions and during normal operation. Geometries are included in MELCOR both for the pebble bed reactor (PBR) and the prismatic modular reactor (PMR).

MELCOR nodalizes the active core into axial levels and radial rings in a cylindrical geometry to define a core cell location. Within a core cell, there are separate temperatures for each component, such as fuel particles, graphite matrix, surrounding graphite structures, etc. Within a core cell, there is one average temperature per component, although there is a temperature profile considered for some components, such as fuel (pebbles or compacts), graphite block for a PMR, or reflectors. The component temperatures are used as the temperature of the TRISO particles and graphite matrix in the cell.

The HTGR fission product model for MELCOR is designed to calculate the released amounts and distribution of fission products in the modeled HTGR reactor system. To do this, it is necessary to calculate the amount of fission products generated and released during normal power operation. This includes the amount of fission products generated in the fuel kernels, the amount recoiled and diffused to the buffer layer, the amount diffused through the dense coating layers, the amount released from the kernels of particles with failed coating layers , the amount which diffuses through the graphitized matrix (and for PMRs the graphite fuel block) and the distribution of fission products released and distributed to the reactor system and adsorbed on dust and other surfaces in the reactor system.

There are two general populations of TRISO particles considered: those with intact coating layers and those with failed coating layers. A small fraction of fresh fuel particles are also modeled as failed from the start owing to manufacturing defects, consistent with the design specification.

For intact particles, the gaseous fission products released accumulate in the buffer; for failed particles, fission products are assumed to go directly to the graphitized matrix. The condensable (metallic) and non-condensable (gaseous) fission product release will be calculated using diffusion based release models. This calculation is performed during normal operation, to determine the partition of the fission product inventory between the kernel and the buffer layer, and the amount released from failed particles. There are also contributions to fission products from uranium contamination in the graphite matrix. In HTGRs, fission products are not just present in the fuel; they may also accumulate, via adsorption, in graphite dust that is generated and subsequently distributed in the reactor system, and via plateout in the primary system. For a PBR, graphite dust is generated primarily due to abrasion during the circulation of the pebbles through the core and transport within the fuel pebble recirculation system. Dust is also present, but to a lesser degree, in the PMR reactor system. The quantity and distribution of dust during normal operation could be calculated by a stand-alone model or determined from MELCOR calculations of the operating reactor system. A liftoff model for the dust and fission products is necessary for calculation of the accident consequences. Existing MELCOR aerosol transport models provide the framework for calculation of dust and fission product transport in the reactor system.

MELCOR uses a steady-state calculation for normal operation, followed by the accident simulation. The normal operation calculation is used to generate initial conditions for the accident simulation and would be done in three stages: (1) establishment of thermal steady-state using an ‘accelerated steady-state’ option; (2) calculation of fission product distribution and release to the coolant using a diffusion model, and; (3) distribution of the released fission products in the reactor system, using an ‘accelerated’ run to establish deposition rates and locations. To do the reactor normal power operation calculation, MELCOR requires the rate of fission product generation, rate of release of fission products from failed TRISO particles and fuel matrix contamination, and graphite dust generation rate and size distribution. During normal operation, there would be releases of metallic fission products, notably ^{110m}Ag and Cs, from both intact TRISO coated fuel particles, failed TRISO coated particles, and U contamination. The radionuclide transport models in MELCOR would distribute the dust in the primary system, and released fission products would accumulate on the dust and surfaces of the reactor system. For a typical particle burnup of three years and the reactor operating lifetime of 40 years, it is necessary to run an ‘accelerated’ steady state calculation, as mentioned above, to reduce computation time. Once the trends in the distribution of dust and rate of deposition are established, the results would be scaled up to the full operating time.

The final step before the transient run is to scale the fission product distributions to the reactor inventory provided by ORIGEN.

For accident conditions, the finite difference model for the failed particles is replaced with an analytic model. Release fractions from the failed particles are convoluted with a failure rate to give the total fission product release. Since MELCOR is not a fuel performance code, the empirical fuel failure fraction is provided by a user input particle failure fraction versus temperature curve or particle failure fraction versus temperature and burnup.

10.2. BENCHMARK DEFINITION

Similar to the benchmark for normal operation, the accident condition benchmark also consists of three parts:

(1) a sensitivity study to examine fission product release from a fuel particle starting with a bare kernel and ending with an irradiated TRISO particle;
(2) the postcalculation of some well documented irradiation and heating experiments;
(3) the prediction of heating tests which are planned in future.

A total of 24 cases have been suggested.

10.2.1. Fuel particle data

Tables 10.1 and 10.2 give an overview of the benchmark cases to be studied providing the general characteristics of the fuel spheres/compacts and the coated particles, respectively.

10.2.2. Diffusion coefficients

The diffusive transport of fission products (caesium, strontium, silver, fission gases) is calculated assuming that the fuel materials are homogeneous. Therefore, effective diffusion coefficients are used in code calculations. The set of data to be applied corresponds to the diffusion coefficients for ‘Germany’ as listed in [1].

10.2.3. Initial distribution in accidents

The initial distribution of the specific fission product nuclide considered is equivalent to the initial fissile uranium distribution. By far most of the fissile material is concentrated in the particle kernels surrounded by an intact coating. The particles are homogeneously dispersed in the fuel zone of the spherical fuel element. However, there are small fractions of uranium outside the kernel in the coating and matrix graphite due to the manufacturing process or natural contamination, respectively. The data to be assumed (Table 10.3) are typical to the German reference fuel element and have been used in the calculations. The complement to 100% of the sum of the above fractions is set as the initial kernel inventory.

10.2.4. Sorption effect of metallic fission products on graphite surfaces

At the boundary between fuel element and coolant, transition of diffusing atoms occurs due to adsorption and desorption (evaporation) processes, respectively. Both are connected by a steep concentration difference of several orders of magnitude. These concentrations are put into relation by the so-called sorption isotherms, which are a function of the temperature and at high surface concentrations (in the so-called Freundlich regime, also of the surface concentration itself.

The sorption effect is strongly depending on the concentrations of the nuclide considered in bulk and coolant, on the type of radionuclide and the thermodynamic conditions, but also on the type of graphitic material. The sorption effect is furthermore influenced by the coolant velocities being more significant at low gas velocities. Fuel element matrix graphite has a high sorption capacity for caesium and strontium. This potential increases with fast neutron irradiation at temperatures below ~1100°C and decreases, if irradiation temperatures reach ~1400°C [349]. In contrast, the sorption capacity of graphite for silver and iodine is much smaller.

Since the heated spheres considered here were not in a reactor environment, the assumption is that no credit should be taken from the sorption effect and that rather transition of the fission products from the fuel element surface into the coolant is unhindered.

10.2.5. Code properties comparison

Table 10.4 summarizes and compares some essential code properties including also some input data which are related to the codes solution method.

10.3. SENSITIVITY STUDY

10.3.1. Input parameters and test conditions

Table 10.5 lists all 15 cases selected for the sensitivity study and the corresponding boundary conditions with regard to irradiation and heating conditions.

The cases 1a, 1b refer to caesium release from a fuel kernel at two different temperatures, while the cases 2a, 2b consider the same heating conditions, but for a particle consisting of kernel, buffer, and dense PyC layer. All other cases of the sensitivity study are based on a complete TRISO coated particle.

In the five cases 3a–e, the TRISO particle is exposed to heating temperatures of 1600°C and 1800°C. Distinction is made with regard to a broken SiC layer (3d) and a through-coating failure (3e). The four cases 4a–d correspond to the previous cases 3a–c, 3e with the difference of assuming now a realistic irradiation phase of 500 efpd at 1000°C preceding the heating phase. The two cases 5a, 5b finally are focusing on a modified irradiation phase assuming 10 temperature cycles to simulate the multi-pass feature of fuel in a pebble bed reactor.

TABLE 10.1. CHARACTERISTICS OF THE FUEL ELEMENT IN THE ACCIDENT BENCHMARK CASES

Parameters	Sensitivity study	Conducted heating tests				Planned heating tests	
		HFR-P4	HRB-22	HFR-K3	HFR-K6	HFR-EU1bis	HTR-PM
No of cases for benchmark	15	2	2	2	1	1	1
Fuel	Particle	Small sphere	Compact	Sphere	Sphere	Sphere	Sphere
Fuel element type	n.a.	LEU phase 1	91 OPB-7	GLE-3 LEU phase 1	GLE-4 (AVR 21)	GLE-4-2 (AVR 21-2)	HTR-PM
Matrix graphite grade	n.a.	A3-27	—	A3-27	A3-3	A3-3	A3-3
Matrix density (kg/m^3)	n.a.		1690	1750	1750	1750	1730
Total FE dimension (mm)	n.a.	32 length 23–29 dia	39.0 length 26.0 outer dia 10.0 inner dia	59.98 dia	60 dia	60 dia	60 dia
Fuel zone diameter (mm)	n.a.	20 dia	n.a.	47 dia	50 dia	50 dia	50 dia
No of cp per sphere/compact	n.a.	1631	2800	16 350	14 580	9560	11 240
Packing fraction (%)	n.a.	14.6	6.8 (fuel) 17.1 (dummy)	10.2	9.6	6.2	7.0
Heavy metal loading (g/FE)	n.a.	1.018	2.323	10.22	9.4346	6.0	7.0
U-235 content (g/FE)	1.0×10^{-4}	0.10016	0.095	1.004	1.0	1.005	0.62
Fraction of free uranium	0.	n.a.	4.2×10^{-7}	3.5×10^{-5}	0.	7.8×10^{-6}	6×10^{-5}

— data not available.
n.a. not applicable.

TABLE 10.2. CHARACTERISTICS OF THE COATED PARTICLE IN THE ACCIDENT BENCHMARK CASES

Parameters	Sensitivity study	Conducted heating tests				Planned heating tests	
		HFR-P4	HRB-22	HFR-K3	HFR-K6	HFR-EU1bis	HTR-PM
Coated particle batch	n.a.	EUO 2308	—	EUO 2308	EUO 2358-2365	HT 384-393	n.a. [a]
Kernel composition	UO_2	LEU UO_2	LEU UO_2	LEU UO_2	LEU UO_2	LEU UO_2	LEU UO_2
Enrichment (U-235 wt%)	8.0	9.82	4.07	9.82	10.6	16.76	8.9
Kernel diameter (μm)	500	497 ± 14.1	544 ± 9.1	497 ± 14.1	508 ± 10.0	501 ± 10.8	500
Buffer layer thickness (μm)	100	94 ± 10.3	97 ± 12.9	94 ± 10.3	102 ±11.5	92 ± 14.3	95
IPyC layer thickness (μm)	40	41 ± 4.0	33 ± 3.4	41 ± 4.0	39 ±3.9	38 ± 3.4	40
SiC layer thickness (μm)	35	36 ± 1.7	34 ± 1.6	36 ± 1.7	36 ± 3.4	33 ± 1.9	35
OPyC layer thickness (μm)	40	40 ± 2.2	39 ± 3.1	40 ± 2.2	38 ± 3.5	41 ± 3.8	40
Kernel density (M/m^3)	10.81	10.81	10.84	10.81	10.72	10.85	≥ 10.4
Buffer density (M/m^3)	1.00	1.00	1.10	1.00	1.02	1.01	≤ 1.10
IPyC density (M/m^3)	1.9	~1.9	1.85	~1.9	1.92 ± 0.005	~1.9	1.90
SiC density (M/m^3)	3.20	3.20	3.20	3.20	3.20	3.20	≥ 3.18
OPyC density (M/m^3)	1.88	1.88	1.85	1.88	1.92	1.88	1.90
IPyC anisotropy BAF	1.053	1.053	1.00	1.053	1.042	1.029	≤ 1.10
OPyC anisotropy BAF	1.019	1.019	1.00	1.019	1.023	1.020	≤ 1.10
Fraction of defective SiC	0	$< 1 \times 10^{-6}$	3.4×10^{-7}	4×10^{-5}	1.3×10^{-5}	—	$\leq 6 \times 10^{-5}$

— data not available.
n.a. not applicable.

TABLE 10.3. URANIUM INVENTORIES OUTSIDE THE FUEL KERNELS

Uranium outside fuel kernel	Inventory fraction		Uranium outside fuel kernel	Inventory fraction
U in buffer	1.0×10^{-3}		U in SiC	1.0×10^{-6}
U in IPyC	1.0×10^{-4}		U in OPyC	1.0×10^{-6}
U in matrix graphite	1.0×10^{-7}			

TABLE 10.4. CODE PROPERTIES

	ATLAS	FRESCO	COPA	GETTER	PARFUME	SORS	NRC Code	SNL Code
Calculates Cs, Sr, Ag, fission gases from cp	yes	yes	yes	yes	yes	yes	Yes	Yes
Considers retention in matrix graphite	no	yes	yes	yes	yes	yes	No	Yes
Considers initial inventory distribution	yes	yes	yes	yes	yes	yes	Yes	Yes
Considers defective/failed particles as function of time	yes	yes	yes	yes	yes	yes	No	Yes
Number of nodes assumed in kernel	9	39 case 1: 150	25 case 1: 50	1–50	~5 µm radial steps	1	45	45
Number of nodes assumed in layers	5–7	39 each	5 buffer: 1	1–50 each	~5 µm radial steps each	1 each	10 each	10 each
Number of nodes assumed in fuel element	n.a.	fuel zone: 9 fuel-free zone: 20	fuel zone: 5 fuel-free zone: 4	fuel and fuel-free zone: 1–20 each	fuel zone: 18 fuel-free zone: 3	1	N/A (only cases 1–3)	N/A (only cases 1–3)
Time step irradiation (s)	auto-adjustable < 300 000	36 000 case 5: 8640	0.864–86 400	10^3–10^6	170 000– 350 000	n.a.	N/A (only cases 1–3)	N/A (only cases 1–3)
Time step heating (s)	auto-adjustable < 300 000	360 case 5: 120	86.4–8640	10^2–10^4	3600	10^3–10^5	N/A (only cases 1–3)	N/A (only cases 1–3)

n.a. not applicable.

TABLE 10.5. CASES OF THE SENSITIVITY STUDY

Sensitivity study / Case	Particle type	Irradiation phase				Heating phase			Radio-nuclides to be calculated
		Time (efpd)	Temperature (°C)	Burnup (% FIMA)	Fast neutron fluence (10^{25}, E>0.1 MeV)	Temperature T (°C)	Ramp rate to reach T (K/h)	Time at T (h)	
1a	Bare kernel	n.a.	n.a.	n.a.	n.a.	1200	n.a.	200	Cs-137
1b						1600		200	
2a	Kernel + buffer + IPyC	n.a.	n.a.	n.a.	n.a.	1200	n.a.	200	Cs-137
2b						1600		200	
3a	TRISO coated particle	n.a.	n.a.	n.a.	n.a.	1600	n.a.	200	Cs-137
3b						1800	n.a.	200	
3c						1600 + 1800	Step	200 + 200	
3d	As 3a–c, crack in SiC @ 1800°C					1600 + 1800	Step	200 + 200	Cs-137
3e	As 3a–c, crack in SiC @ 1600°C, crack in IPyC and OPyC @ 1800°C					1600 + 1800	Step	200 + 200	Cs-137 Kr-85
4a	TRISO coated particle	500	1000	10	2	1600	n.a.	200	Cs-137 Ag-110m
4b						1800	n.a.	200	
4c						1600 + 1800	Step	200 + 200	
4d	As 4a–c, crack in SiC @ 1600°C, crack in IPyC and OPyC @ 1800°C					1600 + 1800	Step	200 + 200	Cs-137 Kr-85
5a	TRISO coated particle	10 cycles of 100 each	600 →1000	10	2	n.a.	n.a.	n.a.	Cs-137 Ag-110m
5b						1600	Step	200	

n.a. not applicable.

10.3.2. Results on fission product release for case 1

10.3.2.1. Comparison case 1

The simplest case is the release from a spherical particle kernel with homogeneously distributed fission products. This case can also easily be calculated analytically by applying the fractional release term derived from the 'equivalent sphere model' [224]:

$$F = 1 - 6\sum_{n=1}^{\infty} \frac{\exp\left(-n^2\pi^2 D't\right)}{n^2\pi^2} \quad (10.7)$$

where

D' = D/r^2 is the reduced diffusion coefficient based on the Arrhenius expression for the diffusion coefficient above and divided by the square of the kernel radius (s^{-1});

t is the heating time (s).

The dimensionless fractional release, F, can be easily computed with the approximations

$$F \cong 6\sqrt{\frac{D't}{\pi}} - 3D't \text{ for } D't \le 0.15 \quad (10.8a)$$

and

$$F \cong 1 - \frac{6\exp\left(-\pi^2 D't\right)}{\pi^2} \text{ for } D't > 0.15 \quad (10.8b)$$

The calculated fractional release values for ^{137}Cs at the end of the 200-hour heating phase at 1200°C (case 1a) and 1600°C (case 1b), respectively, are listed in Table 10.6.

TABLE 10.6. FRACTIONAL RELEASE OF ^{137}CS AFTER 200 H FOR CASE 1

Participant	Fractional release of Cs-137 from a bare kernel	
	Case 1a (1200°C)	Case 1b (1600°C)
France	0.472	1.000
Germany	0.456	1.000
Republic of Korea	0.473	1.000
South Africa	0.498	1.000
USA/GA	0.453	0.970
USA/INL	0.467	1.000
USA/NRC	0.463	0.998
USA/SNL	0.465	1.000
Analytical solution	0.4673	0.99999959

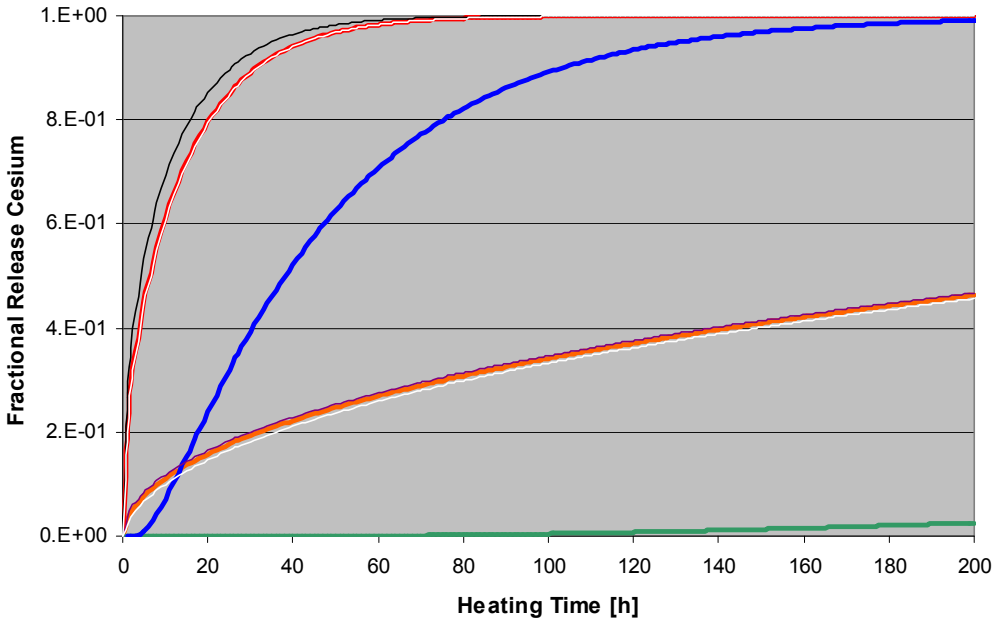

FIG. 10.1. FRESCO-II transient fractional release of ^{137}Cs for case 1 (red, black, white curves) and case 2 (blue, green curves) (linear scale!).

10.3.2.2. Findings from comparison case 1

The comparison of the fractional caesium release results shows that most codes come close to the analytical solution. The three 'old' codes (FRESCO-II, GETTER, SORS) are a little bit off in the 1200°C case, although it is only about 2% deviation; the latter code was also somewhat off in the 1600°C case. GETTER requires an irradiation phase to precede a heatup phase so that transport during the irradiation phase (recoil and knock-out effects) influences the release fraction during heatup causing GETTER to overestimate the release when compared with heatup diffusion only.

One problem in FRESCO-II has been identified to be the limited number of spatial discretization steps for the diffusion calculation. Figure 10.1 shows the transient caesium release calculated with FRESCO-II for 1200°C (lower red curve) and 1600°C (upper red curve). Both red curves are sandwiched between a black curve above representing the analytical solution and a white curve below, where a smaller number of nodes in the kernel was chosen (35 as standard vs. 150 for case 1 here). There is also a deviation in the 1600°C case, which is clearly visible especially in the first 50 hours of heating.

10.3.3. Results on fission product release for case 2

10.3.3.1. Comparison case 2

The results of the calculations for case 2, caesium release from a particle kernel plus buffer plus dense PyC layer after 200 h heating at 1200°C and 1600°C, respectively, are listed in Table 10.7.

TABLE 10.7. FRACTIONAL RELEASE OF ^{137}CS AFTER 200 H FOR CASE 2

Participant	Fractional release of Cs-137 from a bare kernel + buffer + pyrocarbon layer	
	Case 2a (1200°C)	Case 2b (1600°C)
France	0.028	0.995
Germany	0.026	0.991
Republic of Korea	0.029	0.995
South Africa	0.030	0.993
USA/GA	0.006	0.968
USA/INL	0.026	0.996
USA/NRC	0.026	0.989
USA/SNL	0.026	0.995

10.3.3.2. Findings from comparison case 2

The comparison shows that most codes arrive at a fractional release of 2.6–2.9% in the 1200°C case and more than 99% for the 1600°C case. The GA code SORS remains below these figures with less than 1% and less than 97%, respectively.

The transient release curves as calculated with FRESCO-II were already included in Fig. 10.1, the green curve for 1200°C and the blue curve for 1600°C. Their respective differences to the red curves represent the retention potential of the buffer and PyC layers during heating showing a certain delay in the release. Similar to case 1, GETTER slightly overestimates the release fraction due to irradiation phase transport. For the SORS calculations, it can be seen that the retention effect of the two layers is much stronger compared to the other codes in the 1200°C case, whereas the release values calculated for 1b and 2b are practically the same, i.e. no retention effect of the PyC layers in the 1600°C case.

10.3.4. Results on fission product release for case 3

10.3.4.1. Comparison case 3

The results of the calculations for case 3 are listed in Table 10.8 considering caesium release from a TRISO coated particle after 200 h heating at 1600°C (3a) and 1800°C (3b), heating at 1600°C following by 1800°C (3c), in addition assuming SiC crack at 1800°C (3d), and finally assuming SiC failure from the beginning plus through coating failure at 1800°C (3e). The through coating failure in the last case allows also the calculation of fission gas release.

TABLE 10.8. FRACTIONAL RELEASE AFTER 200/400 h FOR CASE 3

Participant	Fractional release from a TRISO coated particle					
	Case 3a	Case 3b	Case 3c	Case 3d	Case 3e	
	Cs-137	Cs-137	Cs-137	Cs-137	Cs-137	I, gases
	after 200 h		after 400 h			
France	6.59×10^{-5}	0.207	0.222	0.999	0.97	0.98
Germany	1.15×10^{-3}	0.218	0.239	1.000	1.00	1.00
Republic of Korea	4.72×10^{-4}	0.210	0.224	1.000	1.00	1.00
South Africa	1.14×10^{-4}	0.203	0.230	1.000	1.00	1.00
USA/INL	1.32×10^{-4}	0.208	0.222	1.000	1.00	1.00
USA/NRC	1.25×10^{-4}	0.207	0.22	—	—	—
USA/SNL	1.00×10^{-4}	0.208	—	—	—	—

— data not available.

The fractional release curves as calculated with FRESCO-II are given in Fig. 10.2 for all five cases 3a–e. For the first 200 h, the red and orange curves (identical) represent heating at 1600°C (3a, 3c, 3d), the blue curve heating at 1800°C (3b), and the green curve heating at 1600°C, but with a failed SiC layer. This latter case (3e) is similar to the previous case 2b, both heating at 1600°C, but with the difference that the caesium has to pass now two dense PyC layers.

For the second 200 h, which is heating at 1800°C, the red curve represents the intact TRISO particle (3c), while the orange curve is based on the assumption of a failed SiC (3d), and the through coating failure (3e, green curve) is not visible since release fraction has reached already 100%.

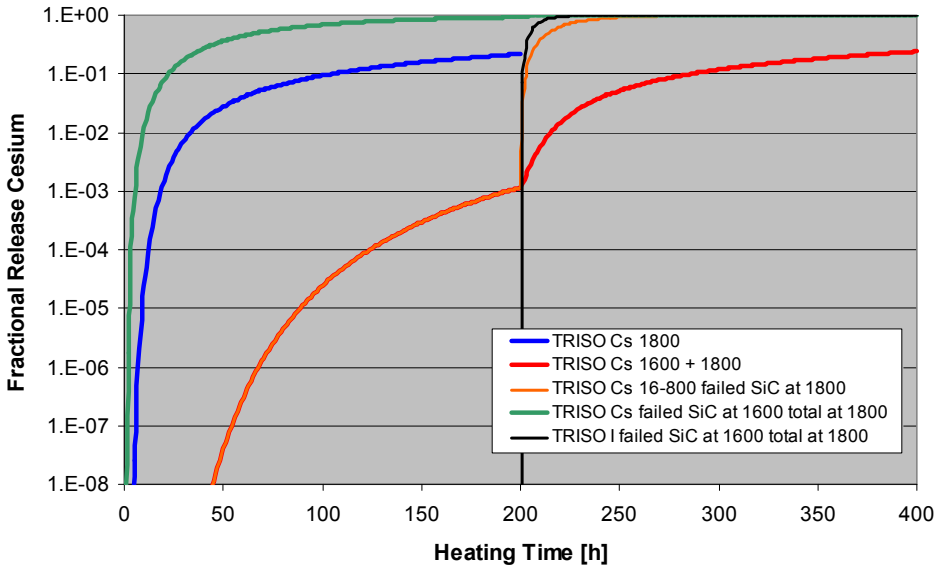

FIG. 10.2. FRESCO-II transient fractional release of ^{137}Cs for case 3.

10.3.4.2. Findings from comparison case 3

Case 3a representing the 'classical' 1600°C accident case exhibits surprisingly diverging fractional release values after 200 h for the different models as is shown in Fig. 10.3 raising doubts about the applied diffusion coefficients in SiC. The recommended diffusion coefficient of caesium in SiC as generally understood is at a temperature of 1600°C:

$$D = 5.5\times10^{-14}\exp\left\{\frac{\Gamma}{5}\right\}\exp\left\{-\frac{125{,}000}{RT}\right\} + 1.6\times10^{-2}\exp\left\{-\frac{514{,}000}{RT}\right\} = 1.011\times10^{-16}\ \frac{m^2}{s} \quad (10.9)$$

where

Γ is the fast neutron fluence, = 2 (10^{25} n/m^2, E>16fJ).

A re-check of the FRESCO-II calculation revealed that a higher value of D = 1.477 × 10^{-16} m/s^2 has been used instead leading to higher release data.

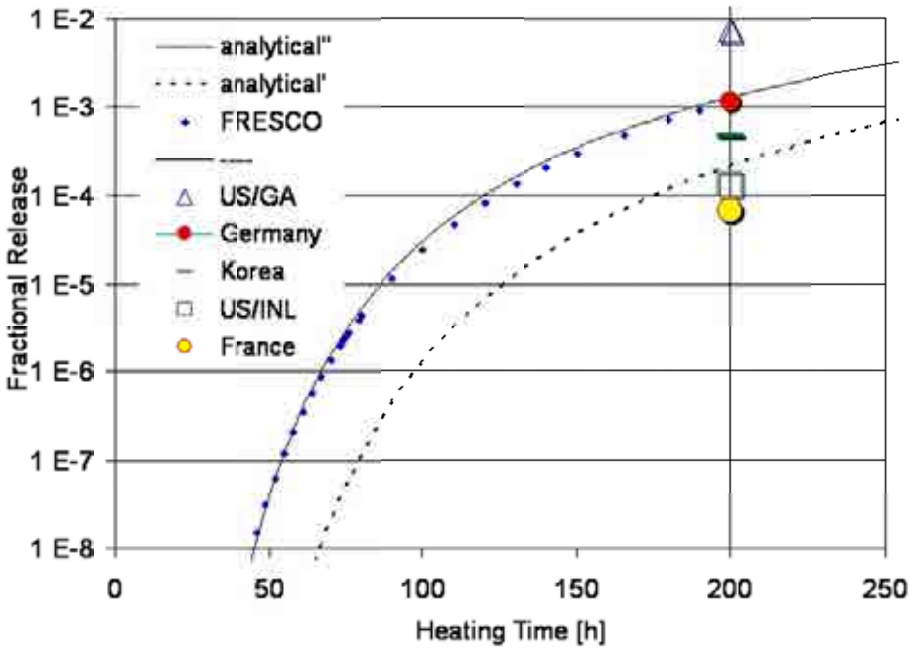

FIG. 10.3. Fractional release of ^{137}Cs for case 3a from different codes.

The higher diffusion coefficient is not in disagreement with the recommendation in [1] as can be interpreted from Fig. 10.4. The figure shows the Arrhenius diagram of the diffusion coefficient for caesium in silicon carbide including the previous recommendation derived by Allelein [350] for normal operation (lower dashed line) and by Myers [351] for accident conditions (dashed line composed of two branches). These old reference curves are compared with the new recommendation for normal operation (lower solid line plus the parallel lines) derived by HRB [352] and for (the high temperature branch of the) accident conditions (steep solid line) derived by Verfondern [353]. FRESCO-II now has implemented a diffusion coefficient which is, for accident conditions, composed of the new (Verfondern) high temperature branch and the old (Myers) low temperature branch. There is obviously an ambiguity in the interpretation of the recommendation in [1].

According to Minato [39], the fractional release of caesium after 200 h at 1600°C should be 2.1×10^{4}. Most codes reach this value within a factor of 2 or less. FRESCO-II is off because of the above given reason. For the 1800°C heating over 200 h, all codes predict a release fraction of ~21%.

In case 3c, the combined 1600/1800°C heating, the predicted result should be 0.236. It is also pretty well met by all codes. Cases 3d and 3e assuming failed SiC and through coating failure, respectively, will certainly result in a practically complete release of caesium, which is predicted by all codes. In case 3e assuming a through coating failure with beginning of the 1800°C heating phase, fission gases will be released also. The black curve in Fig. 10.2 indicates a spontaneous, steep increase of the fractional release reaching very soon 100%.

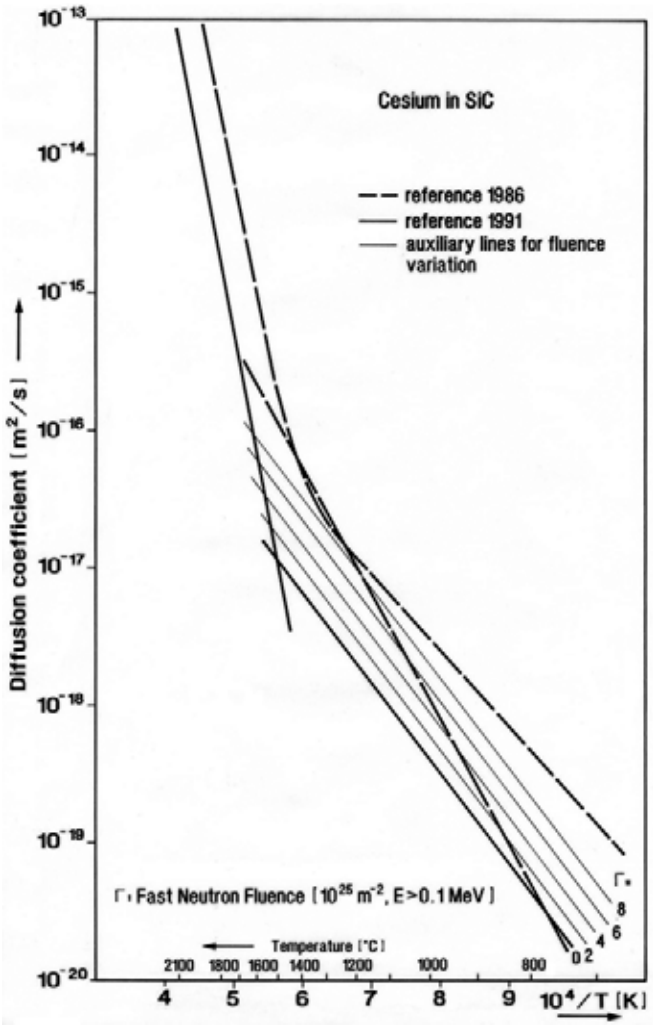

FIG. 10.4. Derivation of a new diffusion coefficient for caesium in SiC from heating tests with modern HTGR spherical fuel elements.

10.3.5. Results on fission product release for case 4

10.3.5.1. Comparison case 4

Case 4 also treats a complete TRISO particle, but now includes a preceding irradiation history. Fractional release results at the end of the heating phase are listed in Table 10.9 for both ^{137}Cs and ^{110m}Ag. In Fig. 10.5, the transient release curves as calculated with FRESCO-II are given for caesium, silver, and fission gases/iodine.

Assuming a crack of the SiC layer at 1600°C, i.e. with beginning of the heating phase, caesium release will immediately steeply rise, since the retention in the still existing PyC layers is small at 1600°C. The additional assumption of cracked PyC layers at 1800°C merely has a further influence on the caesium release from the particle. It does, however, decisively influence the release of fission gases, since they will escape the particle only upon a through-coating failure as is shown with the black curve in Fig. 10.5 starting at time 200 h.

TABLE 10.9. FRACTIONAL RELEASE AFTER 200/400 h FOR CASE 4

Participant	Fractional release from an irradiated TRISO coated particle			
	Case 4a	Case 4b	Case 4c	Case 4d
	after 200 h		after 400 h	
Cs-137				
France	2.55×10^{-4}	0.20	0.21	1.00
Germany	1.47×10^{-3}	0.22	0.24	1.00
Republic of Korea	8.25×10^{-4}	0.21	0.23	1.00
South Africa	1.64×10^{-4}	0.21	0.23	1.00
USA/INL	4.10×10^{-4}	0.23	0.23	1.00
Ag-110m				
France	0.27	0.58	0.98	0.98
Germany	0.41	0.87	0.92	1.00
Republic of Korea	0.55	0.95	0.98	1.00
South Africa	0.42	0.88	0.93	1.00
USA/INL	0.43	0.89	0.93	1.00

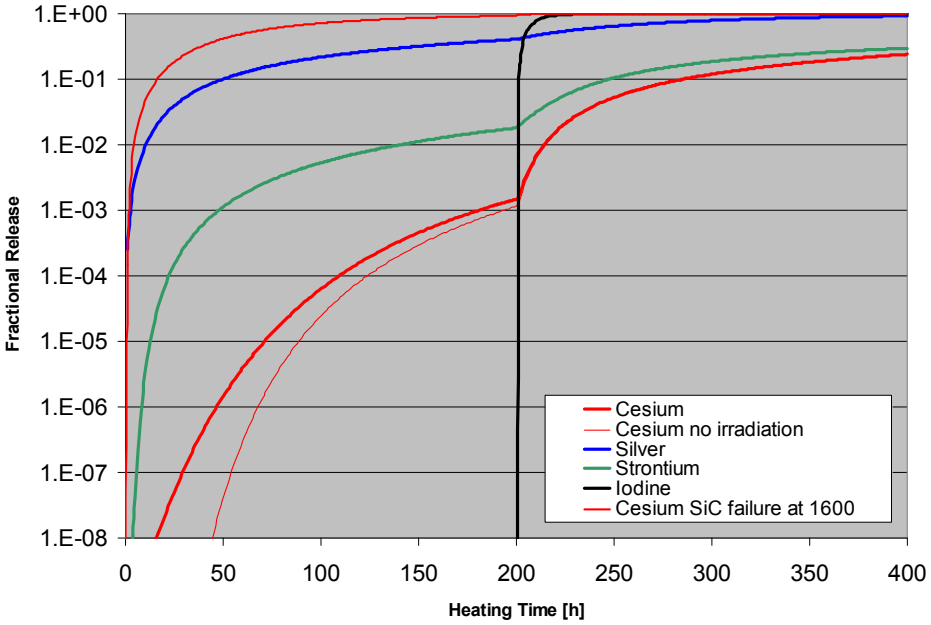

FIG. 10.5. FRESCO-II fractional release of ^{137}Cs for cases 4a, 3a, and 4d (red), of ^{110m}Ag and ^{90}Sr for case 4a (blue and green), and of fission gases/iodine for case 4d (black).

10.3.5.2. Findings from comparison case 4

Unlike the case 3 with no significant irradiation phase, the diffusion process from the kernel into the coating over 500 days at 1000°C has further proceeded into the coating with fission products being sooner released during the heating phase. This effect can be seen from the difference of the two lower red curves in Fig. 10.5; it is, however, less pronounced with progressing time and increasing heating temperature.

Comparing the 1600°C case 4a with the corresponding case 3a without irradiation, the increase of fractional release after 200 h is for all codes approximately the same, the difference being $\sim 3 \times 10^{-4}$. Silver release data are as expected much higher compared to caesium and are ranging between 27% (ATLAS) and 55% (COPA), while calculated caesium release values are ranging between 2.55×10^{-4} (ATLAS) and 8.25×10^{-4} (COPA), ignoring the SORS result (very high) and the FRESCO-II result (input mistake for Cs diffusion coefficient).

For the 1800°C case (4b), calculation results for caesium are with 20–23% in a narrow range, for silver with 58–95% in a somewhat wider range. Similar results were obtained for the combined 1600/1800°C heating case 4c.

10.3.6. Results on fission product release for case 5

10.3.6.1. Comparison case 5

Case 5 describes heating at 1600°C, but with a preceding irradiation phase consisting of 10 temperature cycles in the range 600–1000°C with a total irradiation time of 1000 days. Fractional release data after irradiation (5a) and after the subsequent heating phase (5b) are given in Table 10.10.

TABLE 10.10. FRACTIONAL RELEASE AFTER 200/400 h FOR CASE 5

Participant	Fractional release from a cycles-irradiated TRISO coated particle			
	Case 5a		Case 5b	
	Cs-137	Ag-110m	Cs-137	Ag-110m
	after irradiation		after 200 h heating	
France	3.78×10^{-12}	1.57×10^{-5}	6.44×10^{-4}	0.14
Germany	2.19×10^{-19}	5.55×10^{-6}	1.22×10^{-3}	0.39
Republic of Korea	1.92×10^{-11}	1.25×10^{-5}	6.63×10^{-4}	0.54
USA/INL	6.45×10^{-14}	5.06×10^{-5}	3.07×10^{-4}	0.42

10.3.6.2. Findings from comparison case 5

Due to the low irradiation temperature, the fractional release data for caesium at end-of-life are very low and should not be taken too seriously, since they may be dominated by effects of the numerical calculation method rather than the physical model. Only silver release reaches a level which is within the typically displayed release range. Calculated values differ by one order of magnitude between 5.6×10^{-6} (FRESCO-II) and 5.1×10^{-5} (PARFUME).

To see the difference compared to higher operating temperatures, the calculation was repeated with FRESCO-II for a maximum cycle temperature of 1250°C. Figure 10.6 shows the release of the metallic fission products ^{137}Cs and ^{110m}Ag. An additional curve (thin blue line) for the silver radionuclide illustrates the difference to the original case 5a of cycles with a maximum temperature of 1000°C.

For the subsequent heating phase over 200 h at 1600°C as shown in Fig. 10.7, transient silver release for the two different temperature curves (blue lines) is compared showing that for 1000°C maximum temperature, silver release is starting at a much lower level, but is quickly approaching the 1250°C release curve. For caesium (red lines), the transient release for 1250°C maximum temperature (upper red line) is compared with case 4a with shorter irradiation at lower temperatue (middle red line), and also with case 3a (lower red line) where no irradiation was assumed.

10.4. POSTCALCULATION OF HEATING EXPERIMENTS

10.4.1. Input parameters and test conditions

For this postcalculation part of the accident benchmark study, a total of seven heating experiments with fuel samples from four irradiation experiments have been selected. Table 10.11 summarized the irradiation and heating conditions of these heating experiments.

For the purpose of easy comparison, the heating temperature/time history was precisely defined including the heatup phase. Furthermore, the krypton release records from the heating tests were translated into failures of coated particles as a pre-defined boundary condition for the fission product release calculations.

One aspect that should be mentioned here was not treated the same in all codes: for a fractional release in a heating test, the reference inventory is the inventory at the beginning of the test. Therefore, in a calculation, the released amount of a fission product species at the end of irradiation should be subtracted from the calculated fractional release during heating.

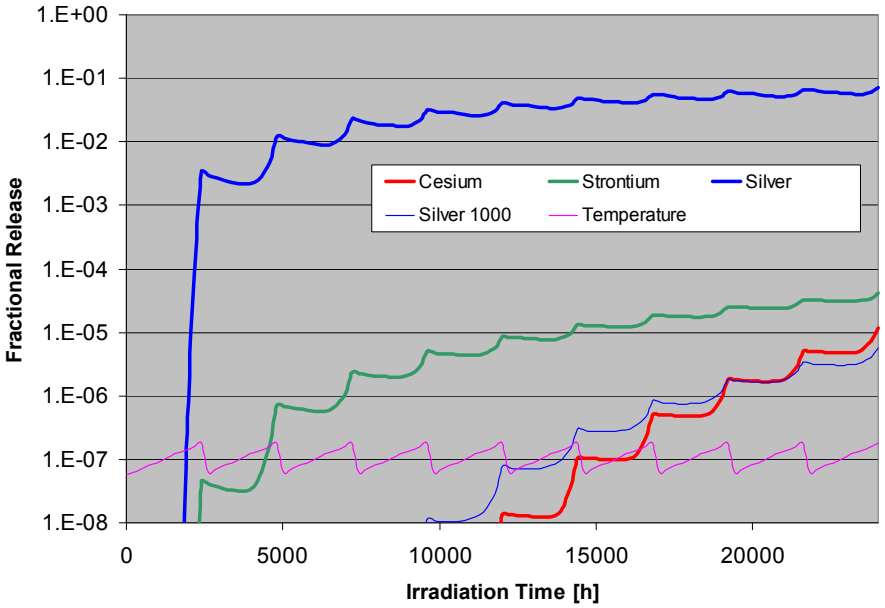

FIG. 10.6. Fractional release of metallic fission products for case 5, irradiation phase.

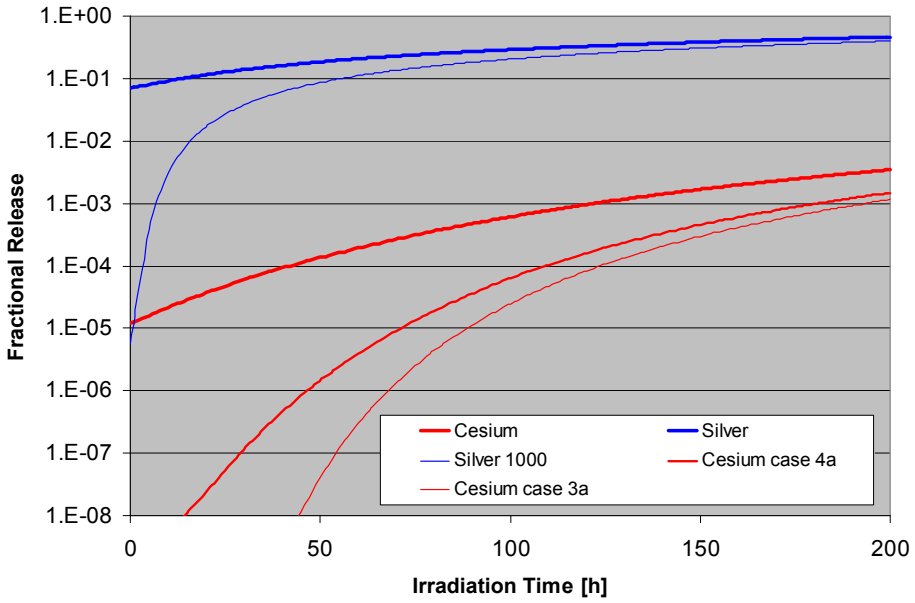

FIG. 10.7. Fractional release of metallic fission products for case 5, heating phase.

TABLE 10.11. POSTCALCULATION OF HEATING TESTS

Case	Irradiation phase				Heating phase		
	Time (efpd)	Temperature (°C)	Burnup (% FIMA)	Fast neutron fluence (10^{25}, E>0.1 MeV)	Temperature T (°C)	Time to reach T (h)	Time at T (h)
6a	351	940	11.1	5.5	300		0.5
HFR-P4-1-12	(8424 h)				1050	1.5	5.5
					1250	0.5	13.5
					1600	7.5	304
							Total: 333
6b	351	1075	13.9	7.5	300		0.5
HFR-P4-3-7	(8424 h)				1050	1.5	5.5
					1250	0.5	13.5
					1600	7.5	304
							Total: 333
7a	88.9	1103 (time av max)	4.8	2.1	20		0.8
HRB-22	(2134 h)				1650	5.4	
Test 3		1031 (time/vol av)			1700	0.8	270
							Total: 277
7b	88.9	1103 (time av max)	4.8	2.1	20		0.4
HRB-22	(2134 h)				1750	5.8	
Test 4		1031 (time/vol av)			1800	0.8	222
							Total: 229

(s) = surface temperature; (c) = centre temperature.

TABLE 10.11. POSTCALCULATION OF HEATING TESTS (cont.)

Case	Irradiation phase				Heating phase		
	Time (efpd)	Temperature (°C)	Burnup (% FIMA)	Fast neutron fluence (10^{25}, E>0.1 MeV)	Temperature T (°C)	Time to reach T (h)	Time at T (h)
8a	359	1020(s)–1216(c)	7.5	4.0	300		0.5
HFR-K3/1	(8616 h)				1050	1.5	5.5
					1250	0.5	16.5
					1550	6.5	
					300	1	
					1600	9	500
							Total: 541
8b	359	700(s)–983(c)	10.6	5.9	300		0.5
HFR-K3/3	(8616 h)				1050	1.5	5.5
					1250	0.5	13.5
					1800	12	25.5
					300	1	
					1050	1.5	19.5
					1250	0.5	19
					1800	12	74.5
							Total: 187
9	634	1140 (s)	10.9	4.8	300		7
HFR-K6/3	(15 216 h)				1050	2	13.5
					1600	11	99
					20	17	
					1700	5.5	100
					20	17	
					1800	2	100
					20	17	
					300	7	
					1800	1	300
							Total: 699

10.4.2. Results on fission product release for case 6: HFR-P4

The irradiation test HFR-P4 was conducted to explore the potential limits of the German high quality UO_2 LTI TRISO fuel beyond the target limits of the HTR-Modul. Particles were embedded in cylindrical compacts machined from spherical fuel elements with a reduced spherical fuel zone. Low in-pile R/B values of fission gases indicated no particle failure during irradiation. Two of the irradiated compacts considered here, HFR-P4/1-12 and/3-7, have achieved burnups of 11.1 and 13.9% FIMA and fast neutron fluences of 5.5 and 7.5 × 10^{25} n/m^2, E>0.1 MeV. Both compacts were heated at 1600°C over 300 h [296].

Since it was heating of compacts, the curves represent release from the coated particles neglecting retention of the compact matrix material.

Due to the small number of coated particles per compact, the level corresponding to one failed particle is 6 × 10^{-4}.

10.4.2.1. Comparison case 6: HFR-P4/1-12

Figures 10.8, 10.9, 10.10 show the fractional release of caesium, strontium, and silver, respectively, as a function of heating time for the different codes and the comparison with the corresponding measurements indicated by the red symbols. No experimental data are available for silver release.

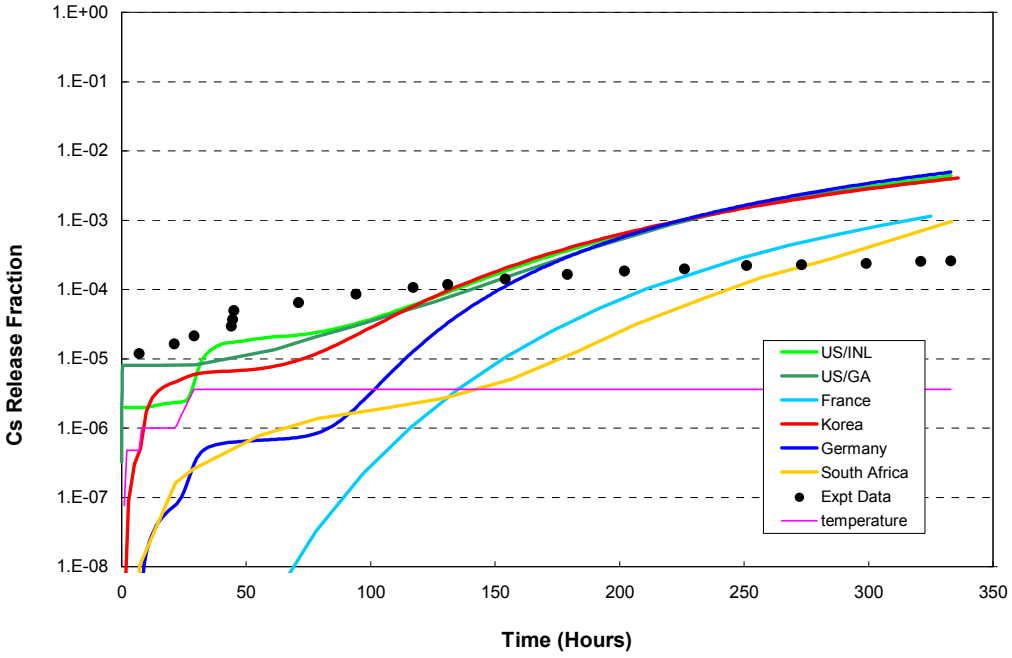

FIG. 10.8. Fractional release of ^{137}Cs from HFR-P4/1-12.

Caesium release measurements (Fig. 10.8) start at a relatively high level > 10^{-5}, which may be an indication of the presence of a coated particle with a defective/failed SiC layer. The calculated release curves remain below the measurements in the first half of the test, but are rising at a higher rate and eventually exceeding the measurements. Calculations of three codes are almost identical in the second half of the test, while there are some larger differences in the first phase. The plateau section in the curves results from the quick release of contamination outside the SiC.

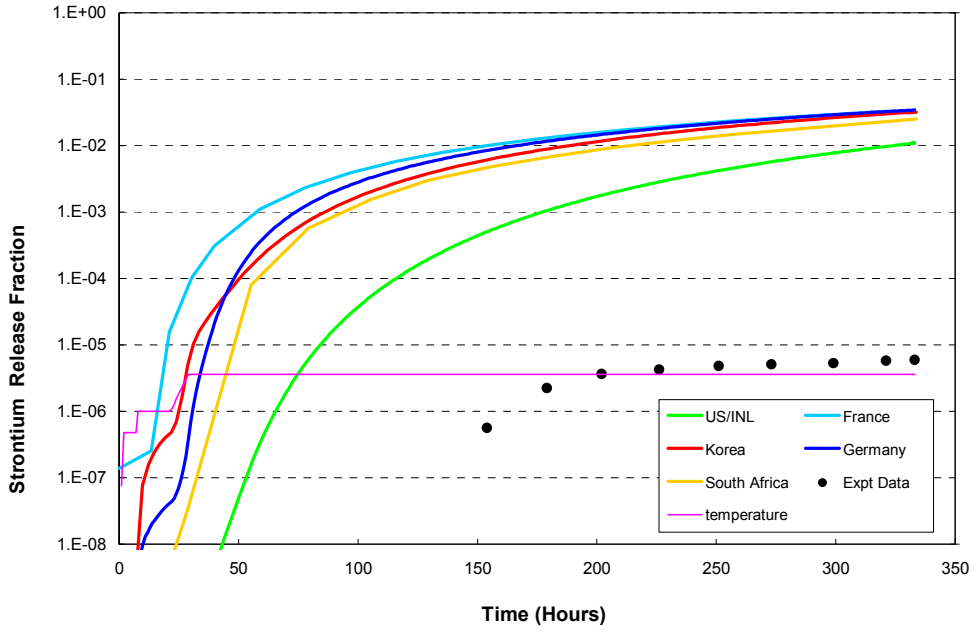

FIG. 10.9. Fractional release of ^{90}Sr from HFR-P4/1-12.

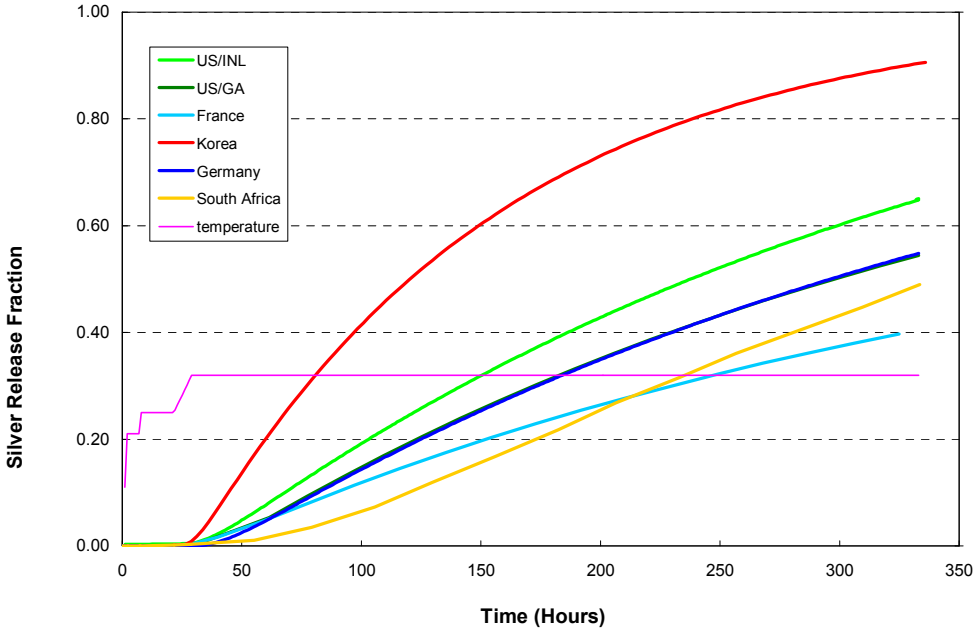

FIG. 10.10. Fractional release of ^{110m}Ag from HFR-P4/1-12 (linear scale!).

With regard to strontium (Fig. 10.9), all codes predict nearly the same transient fractional release within a range of a factor of about 5, but are by more than three orders of magnitude above the measurements. Silver release predictions shown in Fig. 10.10 in a linear scale vary between 40 and 90% at the end of the heating test.

10.4.2.2. Comparison case 6: HFR-P4/3-7

In this 1600°C test, three particle failures have been observed. The assumption to be considered in the postcalculation was that the 1st coated particle failed after 49 h @ 1600°C, the 2nd after 115 h, and the 3rd after 200 h.

Figures 10.11, 10.12, 10.13 show the fractional release of caesium, strontium, and silver, respectively, as a function of heating time for the different codes and the comparison with the corresponding measurements indicated by the red symbols.

The observed release of caesium, which is significantly higher compared to 1600°C heating tests with fuel of lower burnup < 10% FIMA, is in much better agreement with the calculations than compact HFR-P4/1-12. The particle failures can be clearly identified in the caesium release curve of FRESCO-II from the sudden puff releases (Fig. 10.11). PARFUME and COPA are already above these steps, the steps may therefore not be visible, whereas ATLAS obviously has not taken into account the three particle failures.

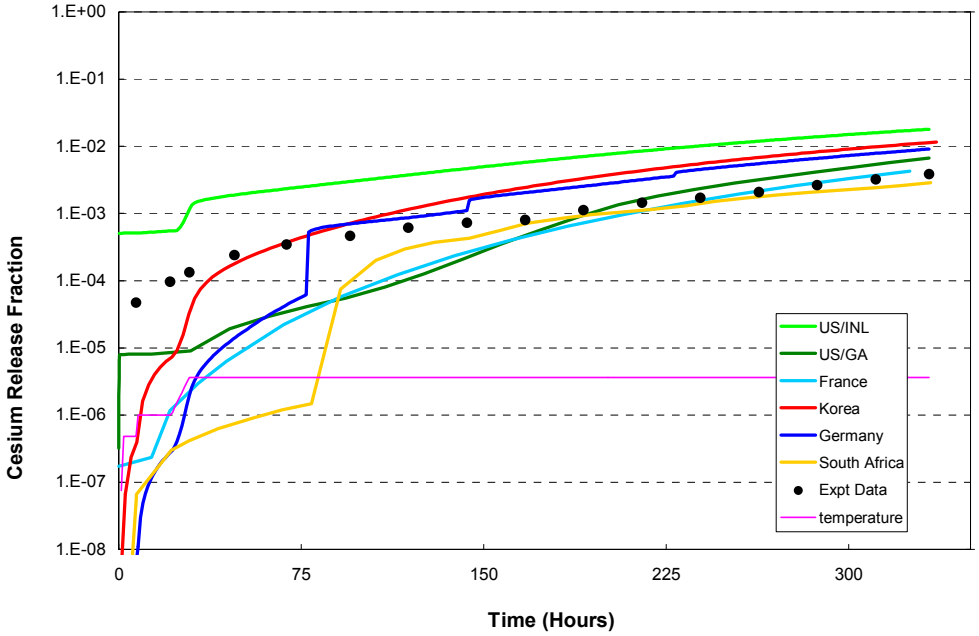

FIG. 10.11. Fractional release of ^{137}Cs from HFR-P4/3-7.

For strontium (Fig. 10.12), there is again a good agreement among the codes and a large discrepancy to the measurements. The fact that PARFUME and ATLAS start at a high level is probably because the release value at the end of irradiation was not subtracted from the calculated release during heating. For silver (Fig. 10.13), calculations overestimate the measurements. They are matched well at the beginning, but the measured silver release flattens abruptly after 50 h and remains almost constant, a behaviour that can hardly be reproduced by a diffusion calculation.

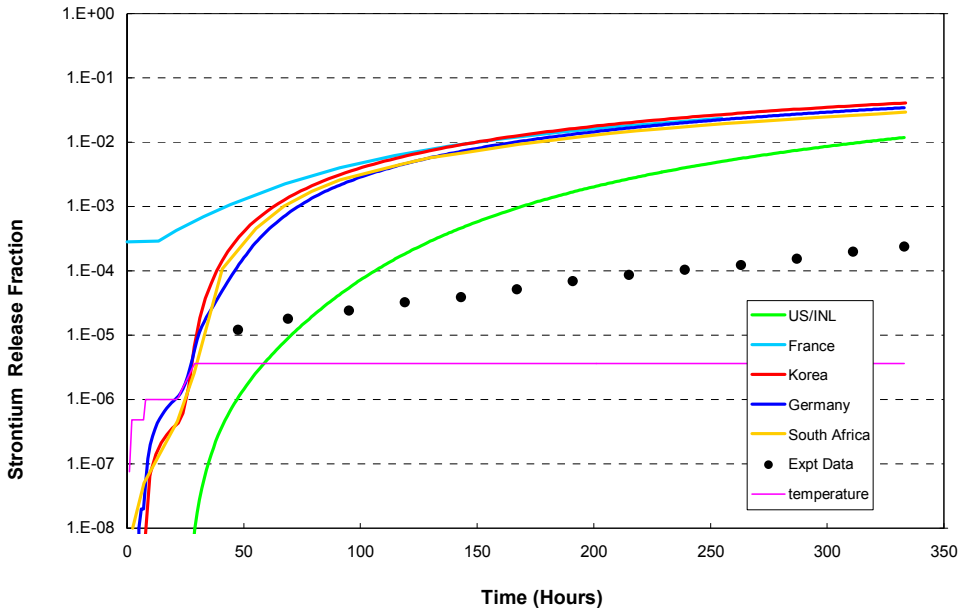

FIG. 10.12. Fractional release of ^{90}Sr from HFR-P4/3-7.

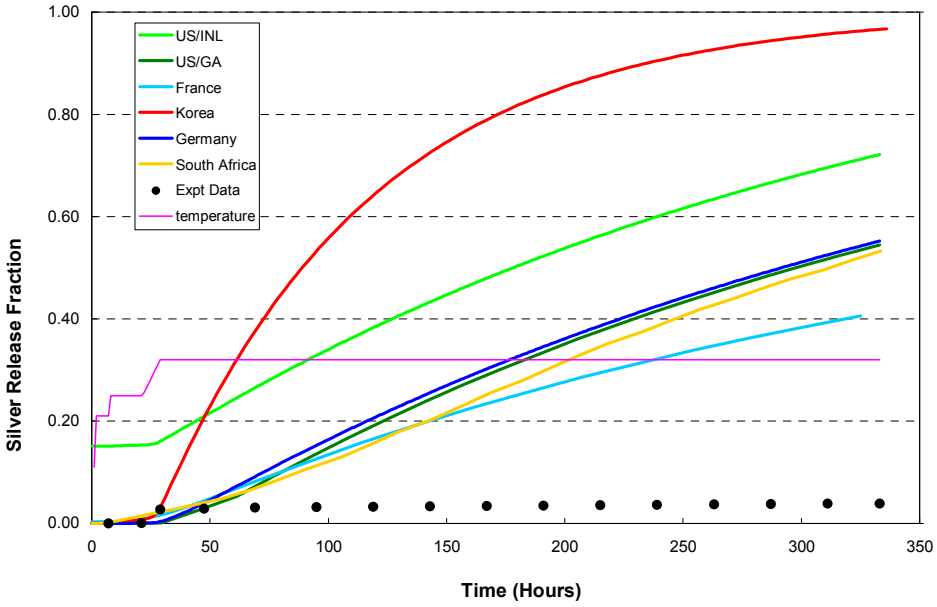

FIG. 10.13. Fractional release of ^{110m}Ag from HFR-P4/3-7 (linear scale!).

10.4.3. Results on fission product release for case 7: HRB-22

The HRB-22 was an irradiation experiment at the HFIR in Oak Ridge dedicated to the advanced Japanese fuel [275]. Four heating tests with unbonded coated particles, which were extracted from selected compacts, were conducted in the Oak Ridge CCCTF furnace. Two of these tests have been selected as benchmark examples. Only three codes have been applied for postcalculating these two heating tests.

10.4.3.1. Comparison case 7: HRB-22, test 3

For the accident condition test 3 (ACT 3), compact 10 was chosen to extract 25 coated particles to be heated for 270 h at 1700°C. There was a little amount of fission gas release

observed during the test which, however, never reached a level to justify the assumption of a particle failure. Postcalculations for caesium are in very good agreement with the experimental data (Fig. 10.14). The results for silver, here shown at a linear scale, conservatively cover the experimental data with a difference of less than a factor of 2 (Fig. 10.15).

10.4.3.2. Comparison case 7: HRB-22, test 4

For test ACT 4, again 25 individual coated particles were taken from compact 10 for heating in CCCTF. Heating time was 220 h at 1800°C. The results given in Figs 10.16 and 10.17 show again a conservative coverage of the experimental data by the postcalculations.

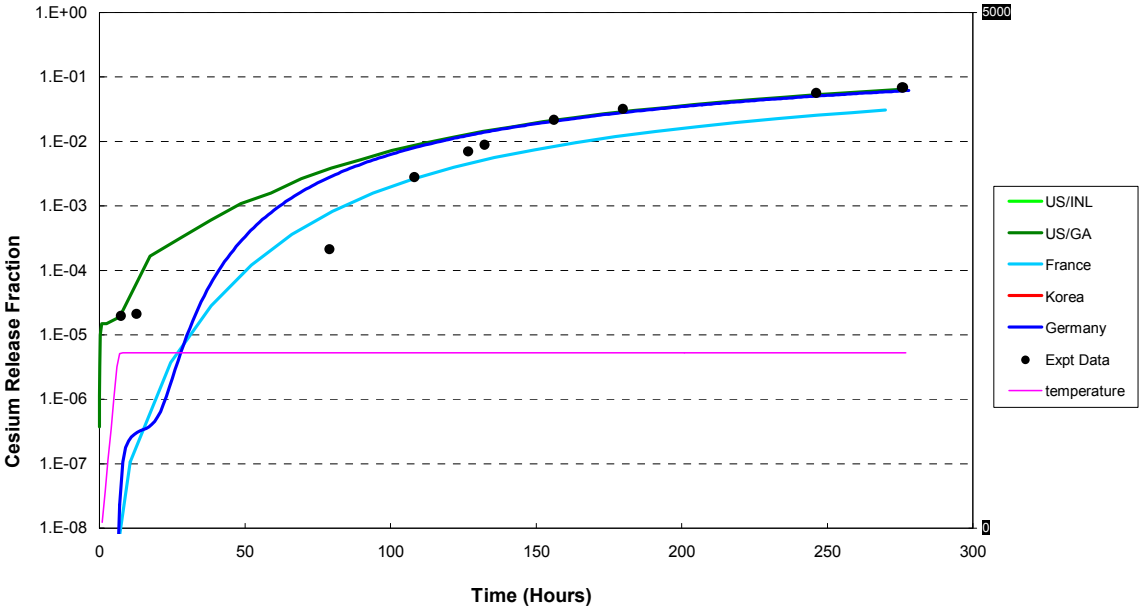

FIG. 10.14. Fractional release of ^{137}Cs from HRB-22, test 3.

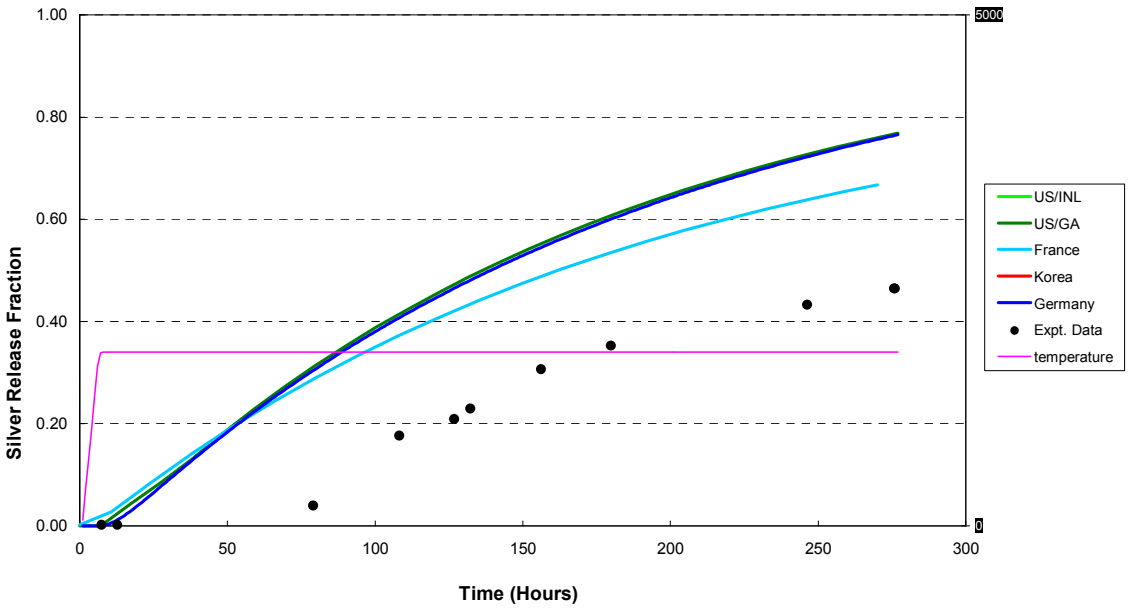

FIG. 10.15. Fractional release of ^{110m}Ag from HRB-22, test 3 (linear scale!).

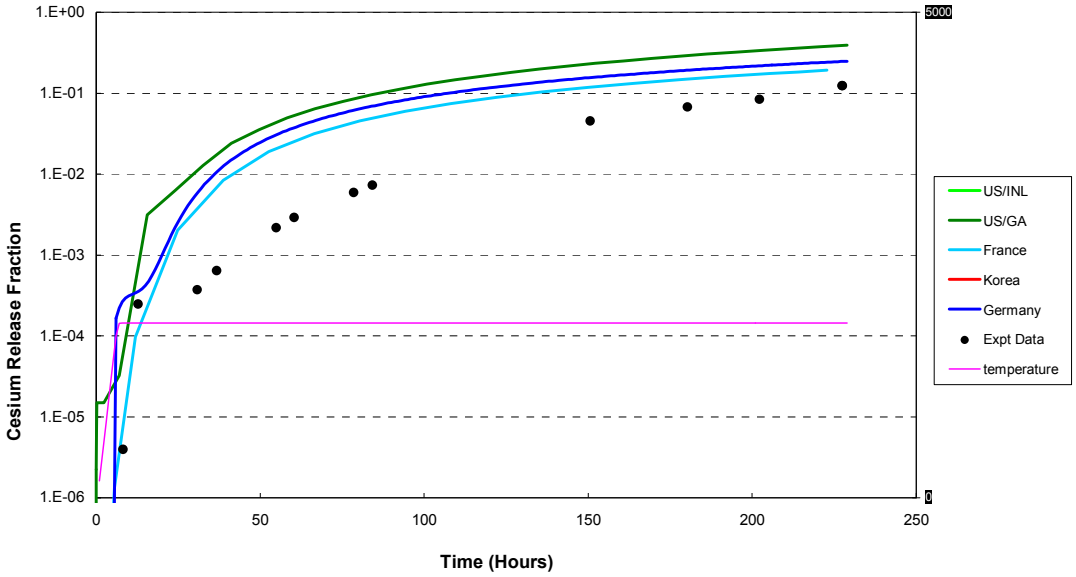

FIG. 10.16. Fractional release of ^{137}Cs from HRB-22, test 4.

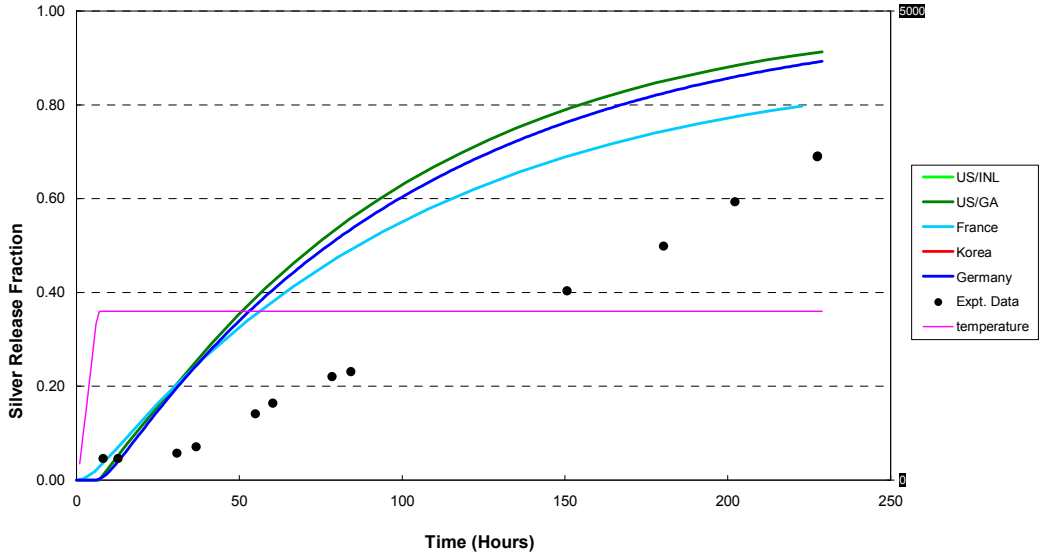

FIG. 10.17. Fractional release of ^{110m}Ag from HRB-22, test 4 (linear scale!).

10.4.4. Results on fission product release for case 8: HFR-K3

The HFR-K3 irradiation experiment was considered a reference test for a steam-cycle HTGR using fuel of the AVR-19 reload charge. This test with four spherical fuel elements, of which two were heated after irradiation [107], belongs to the most well documented of the German HTGR fuel programme.

It should be mentioned here that both heating tests were part of the analysis study conducted in 1989 where caesium release from 44 heating tests and strontium release from 10 heating tests were taken to derive new recommendations for a diffusion coefficient in silicon carbide.

10.4.4.1. Comparison case 8: HFR-K3/1

Sphere 1 was heated over 500 h at 1600°C. Despite severe irradiation conditions with a 7.5% FIMA burnup and a fast neutron fluence of 4.0×10^{25} n/m^2, E>0.1 MeV, the observed krypton gas release remained below the inventory of one particle, therefore no particle failure was assumed.

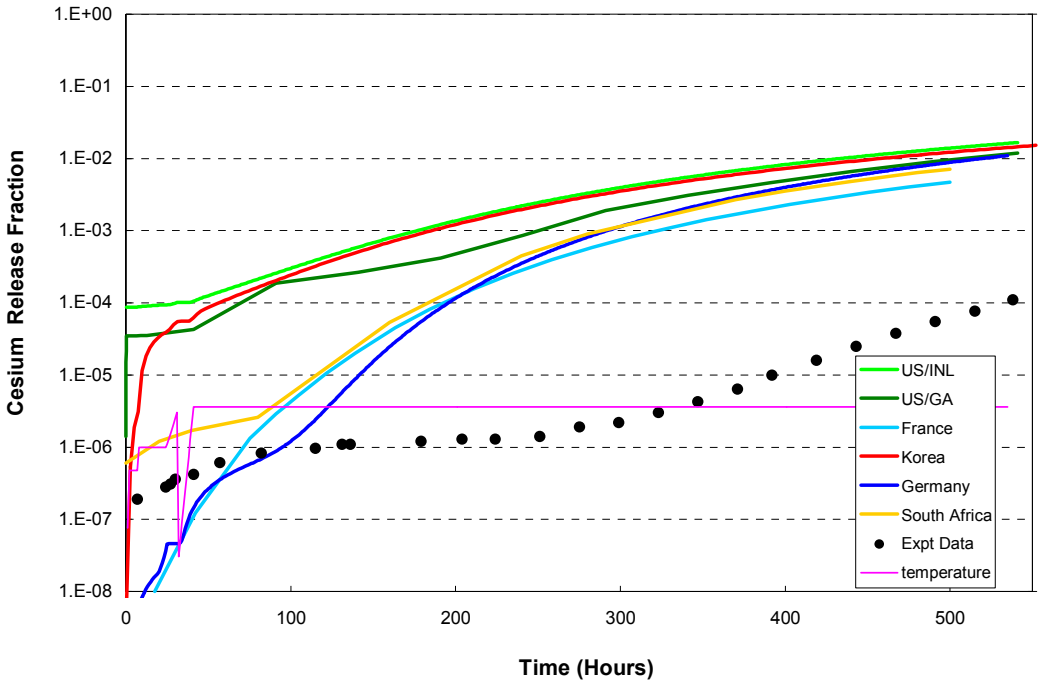

FIG. 10.18. Fractional release of ^{137}Cs from HFR-K3/1.

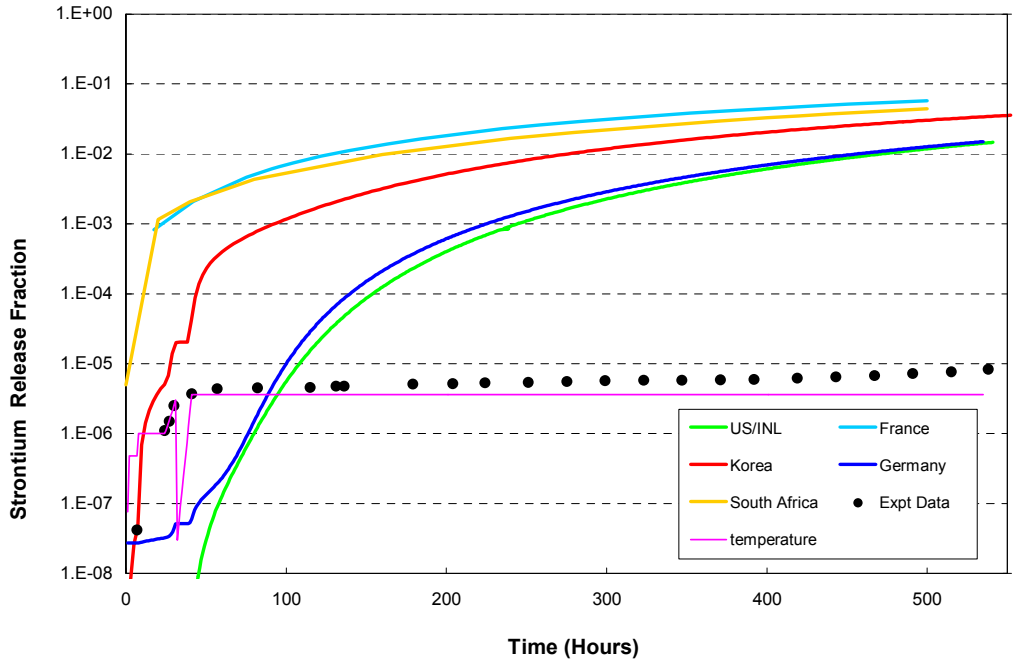

FIG. 10.19. Fractional release of ^{90}Sr from HFR-K3/1.

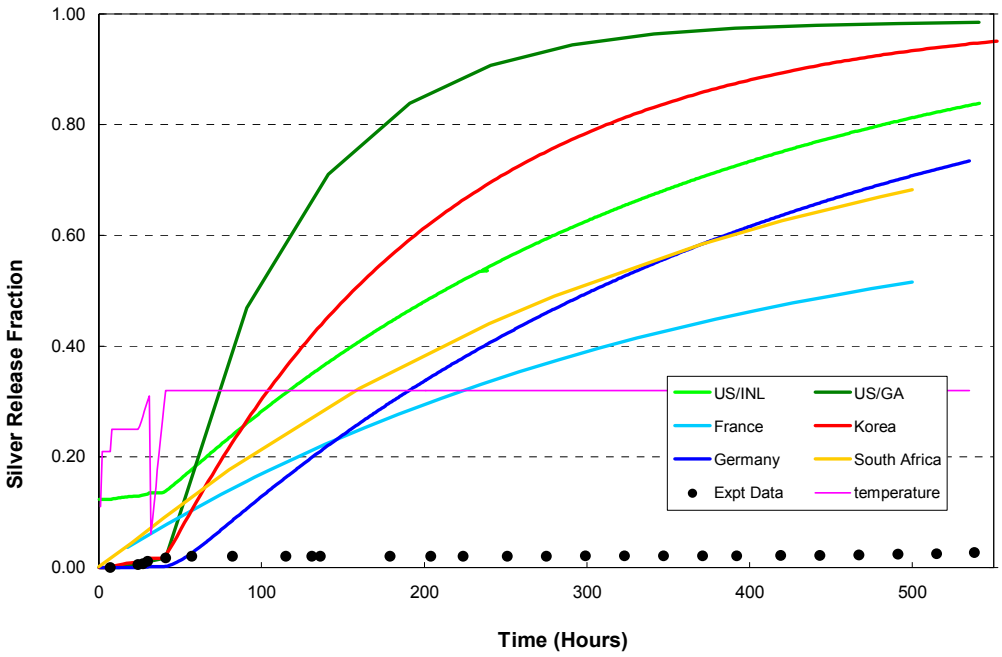

FIG. 10.20. Fractional release of ^{110m}Ag from HFR-K3/1.

The measured transient release curves for the metallic fission products (Figs 10.18, 10.19, 10.20) show that, after an initial increase, the release remains more or less constant, before — in the case of caesium — the release fraction starts to increase and reaches at the end of the heating test a value of about 1×10^{-4}. Strontium remains below the 10^{-5} throughout the whole test, while silver, after rapid increase to a level of ~3%, remains practically constant.

Postcalculation of this test with the various models reveals a tremendous overestimation by all codes. Measurements are hardly reproducible with a diffusion model using a simple effective diffusion coefficient.

10.4.4.2. Comparison case 8: HFR-K3/3

Sphere 3 of the same irradiation test was heated at 1800°C over 100 h, where after 25 h, the test was accidentally interrupted and later resumed. In contrast to sphere 1, heating of sphere 3 has shown a much more diffusion-like transient behaviour as can be seen from the Figs 10.21, 10.22, and 10.23, respectively. A steadily increasing Kr release was observed after 10 h heating at 1800°C exceeding the level of one failed particle (6×10^{-5}) after about 50 h at 1800°C. For the postcalculation, it was assumed that 10 particle failures occurred during heating at 1800°C after 50 h, 55 h, 65 h, 70 h, 75 h, 80 h, 85 h, 89 h, 92 h, and 97 h.

Corresponding postcalculations with diffusion codes — consequently — results in better qualitative agreement with the measurements. But also the quantitative agreement is much better in this case, even for silver, for which a more or less diffusion-like behaviour was recorded (which is not always the case). Largest discrepancy is again with the strontium overestimated in the calculation by more than an order of magnitude.

The massive overprediction of strontium release in the HFR-K3 heating tests suggests to possibly adjust downwards the Sr diffusion coefficient in silicon carbide. This, however, can only be done by taking all experimental evidence together.

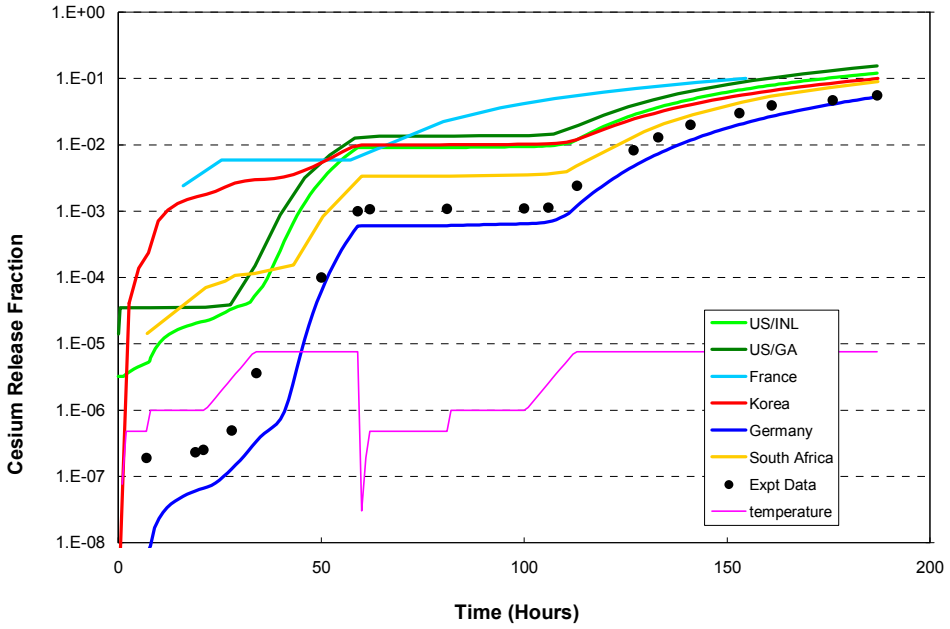

FIG. 10.21. Fractional release of ^{137}Cs from HFR-K3/3.

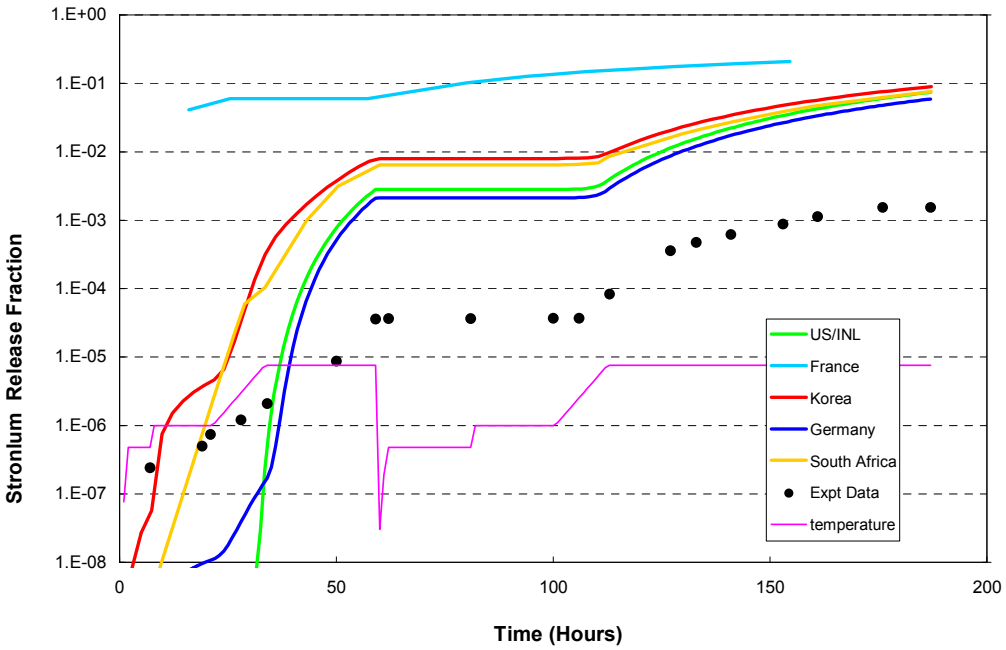

FIG. 10.22. Fractional release of ^{90}Sr from HFR-K3/3.

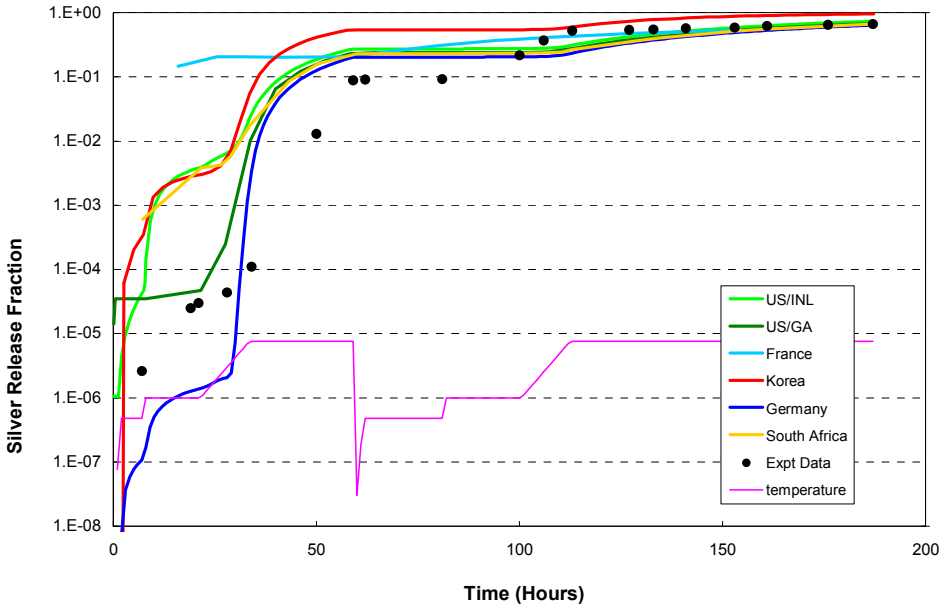

FIG. 10.23. Fractional release of ^{110m}Ag from HFR-K3/3.

10.4.5. Results on fission product release for case 9: HFR-K6/3

The irradiation experiment HFR-K6 with four GLE-4 fuel spheres was, in conjunction with HFR-K5, considered to serve as proof test for HTR-Modul fuel, where respective operational and transient conditions were to be simulated during the test. Due to the decline of nuclear activities in Germany, it was not until 13 years after irradiation that post-irradiation examination work was resumed.

The heating test with an HFR-K6 irradiated sphere was one of the first in the new KÜFA-II furnace operated at the ITU in Karlsruhe (see Section 8.3.2). The test was conducted with sphere 3 which had reached a burnup of 10.9% FIMA (after revision: 9.7% FIMA) and a fast neutron fluence of 4.8×10^{25} n/m^2, E>0.1 MeV. Heating temperature levels chosen were 1600, 1700, and 1800°C over periods of 100 h each followed by a fourth heating phase again at 1800°C over additional 300 h [297, 298].

The measured krypton release remained surprisingly low, even below the level of 10^{-5} during the three heating phases. Only with beginning of the 4th heating phase, the release increased significantly. The assumption with regard to the postcalculation was the failure of 5 particles: after 119 h, 174 h, 214 h, 258 h, and 288 h, respectively, of the final 1800°C heating phase.

Also the observed caesium behaviour (Fig. 10.24) has shown extremely low fractional release data which remain during the 1600°C and 1700°C heating phases near the 10^{-6} level, before the release starts to increase with the 1800°C phase and eventually reaches ~4%. The ^{110m}Ag isotope was, due to the long time after the irradiation, no longer present in the sphere, while strontium has not been measured so far.

The postcalculations with the various codes exhibit good agreement among each other, but a strong overestimation of the caesium release with a difference of several orders of magnitude during the first few hundred hours of heating, and reduced to about a factor of 10 at the end of the test. The effect of the few failed particles on the caesium release is not visible due to the much larger total release (both measured and calculated). The calculated silver release (Fig. 10.25), again shown for a linear scale, is ranging between 60 and 100% fractional release at test end.

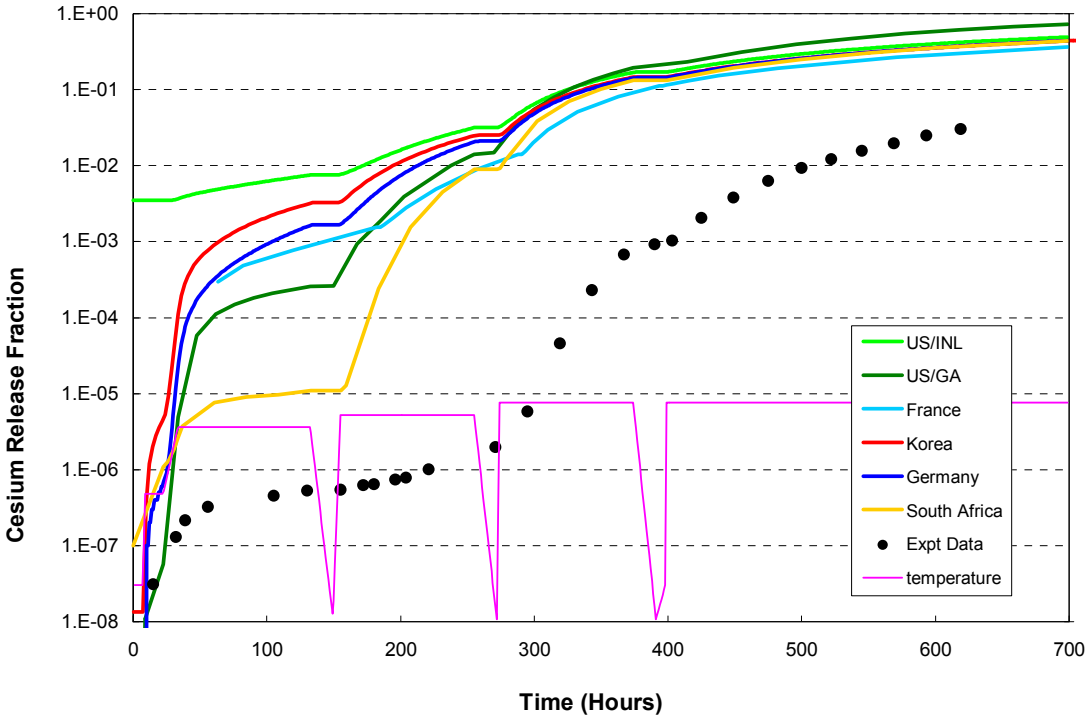

FIG. 10.24. Fractional release of ^{137}Cs from HFR-K6/3.

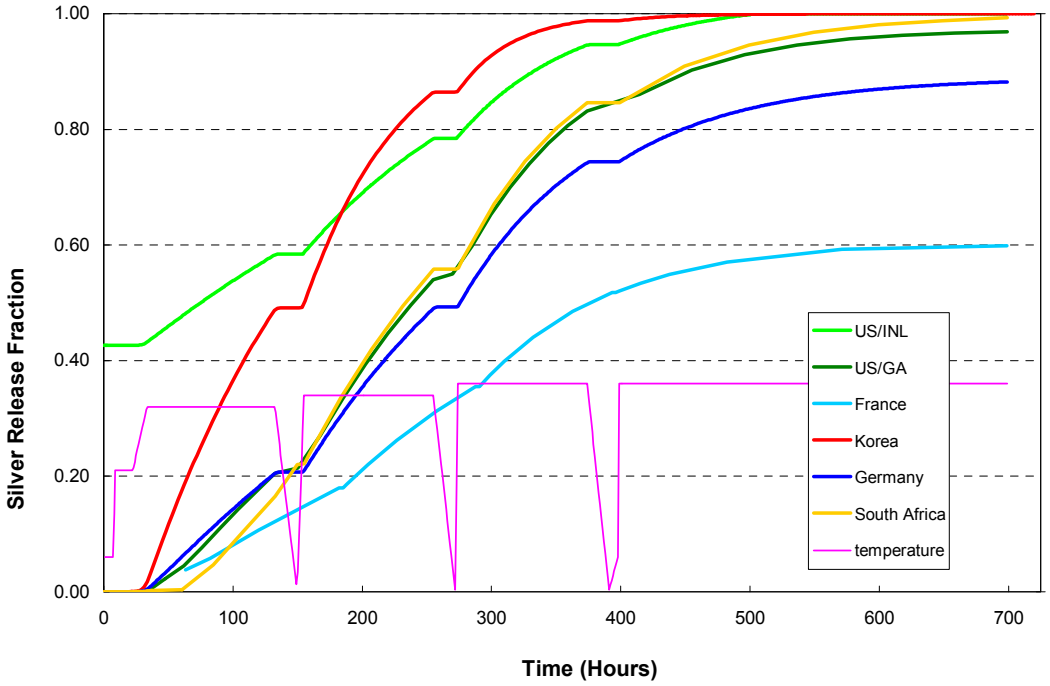

FIG. 10.25. Fractional release of ^{110m}Ag from HFR-K6/3 (linear scale!).

10.5. PREDICTION OF FISSION PRODUCT RELEASE BEHAVIOUR DURING HEATING

10.5.1. Input parameters and test conditions

Two examples have been suggested for the prediction section, for which the respective boundary conditions are listed in Table 10.12. The heating experiment with sphere 1 of the irradiation test HFR-EU1bis was, at least at the time of definition of the accident benchmark, in the planning stage and therefore considered a prediction. Experimental caesium and silver release data have been made available in the meantime. The 'HTR-PM' called test has actually no direct relation to the Chinese HTR-PM design. It is a simple code-to-code comparison where fuel sphere data assumed are those of the German reference fuel exposed to a fictive irradiation history.

10.5.2. Results on fission product release for case 10: HFR-EU1bis/1

As part of the revitalized irradiation programme for HTGR fuel irradiation testing in the European Union, the so-called HFR-EU1 irradiation experiment was initiated with the goal to explore the performance limits of the presently existing German and Chinese high quality fuel (see Section 7.2.4.). This test with a focus on high burnup (towards 20% FIMA) was terminated in February 2010. A parallel, congenial test, called HFR-EU1bis, with a focus on high operation temperature was conducted under simplified conditions and was terminated in October 2005 with post-irradiation examination work having started soon afterwards (see Section 7.2.3.).

Sphere 1 out of the five fuel spheres inserted in the EU1bis test, which reached a burnup of 9.3% FIMA and a fast neutron fluence of 3×10^{25} n/m^2, E>0.1 MeV, was planned to be heated at temperature levels of 1250, 1600, 1700, and 1800°C over 200 h each. The first, relatively low temperature level was chosen to account for the analysis of the release behaviour of silver, of which still plenty is available. In the real heating test, there was no 1800°C heating phase. Another difference was the assumption in the calculations to proceed to the next temperature level immediately, whereas in the real heating test, the fuel sphere was cooled down to room temperature after each heating phase. These cooldown and heatup interim phases took a longer time than the 2 hours assumed in the calculations.

Furthermore, in the release calculations, no particle failure was assumed. For the heating test itself, this was found to be in agreement with the experiment, since measured krypton release during heating remained below the level of the inventory of a single coated particle. What may not be in agreement with the real experiment, is the high chance of presence of irradiation-induced failures of an SiC layer or even the whole coating that could be concluded from the high R/B gas release measured particularly toward the end of irradiation. To what extend sphere EU1/1 had contributed to the overall gas release could not be distinguished during the irradiation test. The transient fractional release curves for the metallic fission products are plotted in Figs 10.26, 10.27, and 10.28.

The measured ^{137}Cs activity (see symbols in Fig. 10.26) is on a relatively high level already during the 1250°C heating. This is presumably the result of the high temperature during irradiation with enhanced diffusion through the particle coatings and release from particles with an SiC layer that failed during irradiation.

TABLE 10.12. PREDICTION OF HEATING TESTS

Case	Irradiation phase				Heating phase		
	Time (efpd)	Temperature (°C)	Burnup (% FIMA)	Fast neutron fluence (10^{25}, E>0.1 MeV)	Temperature T (°C)	Time to reach T (h)	Time at T (h)
10	249	1100 (s)	9.3	3.0	300		6
HFR-EU1bis/1	(5976 h)				1250	19	200
					1600	7	200
					1700	2	200
					1800	2	200
							Total: 836
11	1000	1000	9	2–5	300		0.5
HTR-PM	(24 000 h)				1250	2	10
					1600	7.5	200
					1650	1	200
					1700	1	200
					1800	2	200
							Total: 824

(s) = surface temperature.

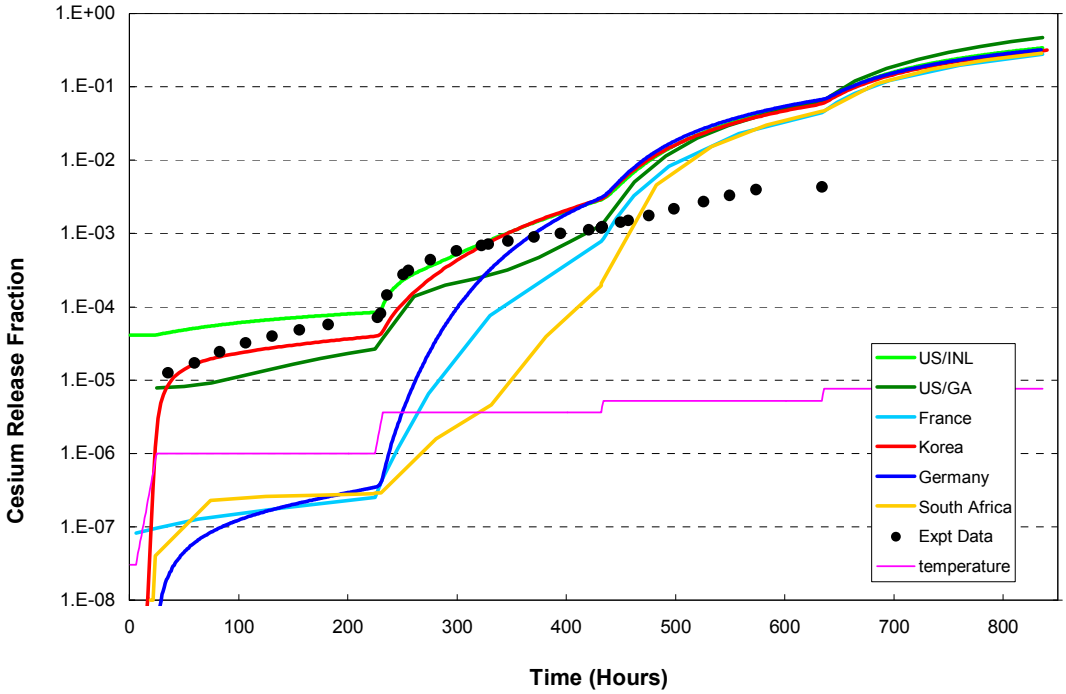

FIG. 10.26. Fractional release of ^{137}Cs from HFR-EU1bis/1.

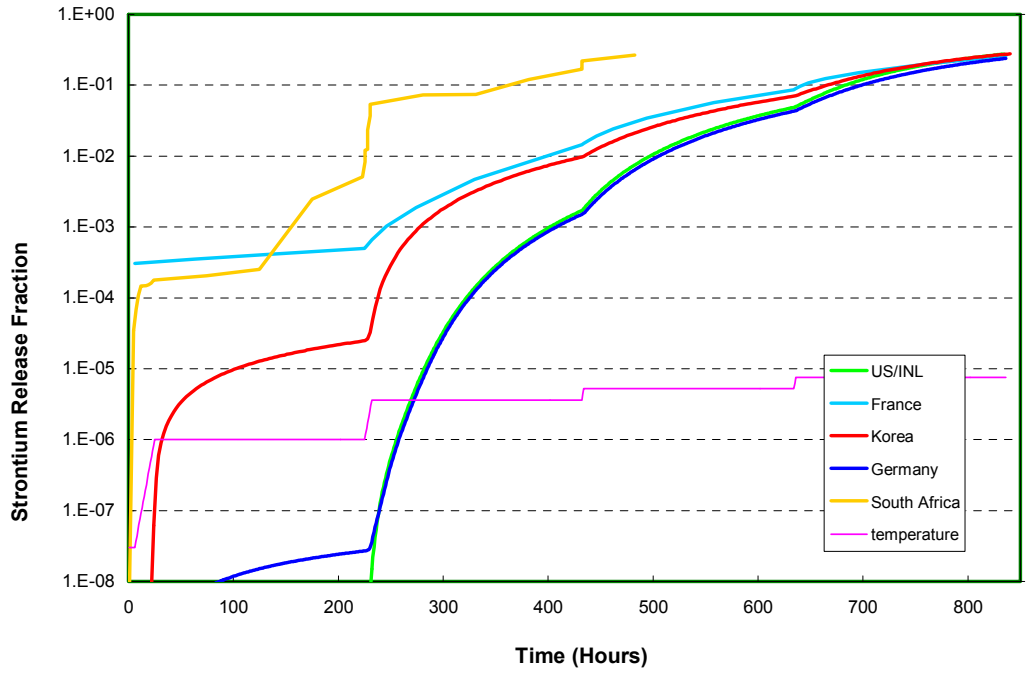

FIG. 10.27. Fractional release of ^{90}Sr from HFR-EU1bis/1.

In agreement with the experience with high silver release at temperatures above 1000°C, the calculated fractional release of ^{110m}Ag is reaching already the percentage range towards the end of the 1250°C heating phase, followed by the expected steep increase at higher temperatures. Also ^{137}Cs and ^{90}Sr are predicted to escape significantly from the sphere at an early stage.

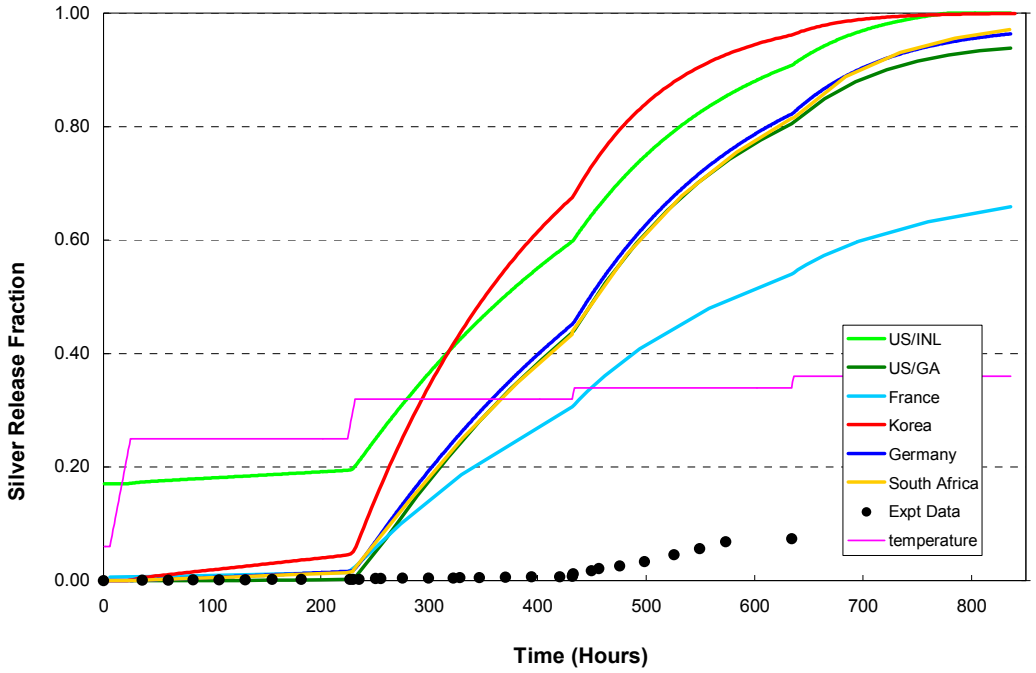

FIG. 10.28. Fractional release of ^{110m}Ag from HFR-EU1bis/1 (linear scale!).

10.5.3. Results on fission product release for case 11: HTR-PM fuel sphere

The calculations for the heating experiment with an HTR-PM fuel sphere were made based on the assumption of no particle failure during the heating. Results are shown in Fig. 10.29 with all codes being in fairly good agreement with each other.

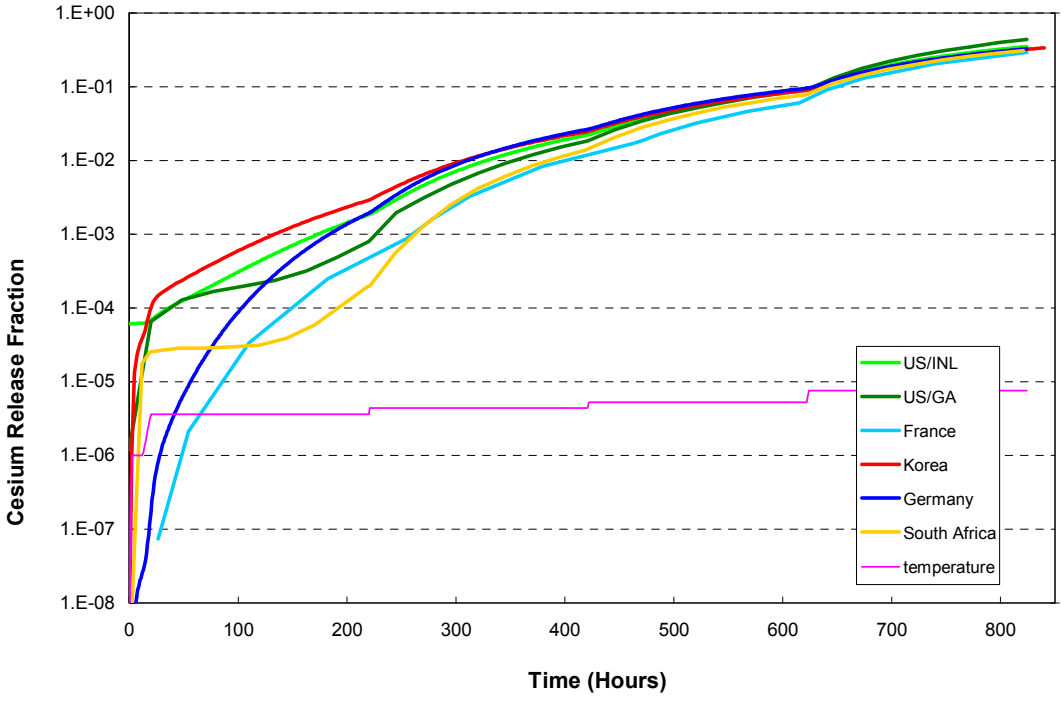

FIG. 10.29. Fractional release of ^{137}Cs from the 'HTR-PM' fuel sphere.

10.6. SUMMARY AND CONCLUSIONS

National engagement as well as bilateral or multi-national cooperation in HTGR fuel development is ongoing and is expected to further improve fuel performance and the ability to make reliable predictions. The accident condition benchmark exercise has successfully demonstrated to be a useful basis for verification and validation in establishing the reliability of code predictions. The confidence in the applicability of these codes is strengthened by validation along the experimental programmes that include both irradiation and heating tests.

Any new HTGR fuel development programme will, however, have to ascertain that the fuel is consistent with the internationally established standards as described here. Additional irradiation and post-irradiation testing and examination will be required for newly manufactured fuel, in order to expand and improve the existing statistical data base for fuel performance analysis. The additional data will demonstrate successful fuel designs, cover the full range of design and operating requirements of future reactors, strengthen the statistical viability of the performance base, and confirm expected in-reactor performance. Fuel test programmes will be continual efforts in that it may be open to new test requirements or new understandings of fuel performance.

From the codes that have been applied to all or part of the cases suggested for the accident benchmark, most represent developments from the recent years to be compared with some older codes, where development was often constraint by requirements of computer technology at that time. This valuable accident benchmark exercise is beneficial to both types of models since it provided the opportunity for confirmation/validation and identified the areas for further improvements, some conclusions can be drawn:

- In the sensitivity study, most codes have shown good agreement among each other. Some differences can be explained by different assumptions for input data or boundary conditions. With regard to the sensitivity identified for the number of nodes in the diffusion calculation for the kernel, the application of the analytical solution offered by the Booth model appears to be more accurate method. Time step length may also influence the calculational results.
- From the postcalculations of heating tests and comparison with the measurements, it appears that the diffusion coefficient for caesium in silicon carbide, which was recommended following the evaluation of 44 heating experiments, is still varying over a broad range.
- The ambiguity in the explanation of the recommended diffusion coefficient of caesium in silicon carbide of [1] should be eliminated by saying (as most seem to understand it) that the formula recommended is the sum of the low temperature ‘HRB-branch’ with the high temperature ‘FZJ-branch’:

$$D = 5.5\times10^{-14}\exp\left\{\frac{\Gamma}{5}\right\}\exp\left\{-\frac{125{,}000}{RT}\right\} + 1.6\times10^{-2}\exp\left\{-\frac{514{,}000}{RT}\right\} \quad \frac{m^2}{s}$$

  where Γ is the fast neutron fluence (10^{25} n/m^2, E>16fJ).
- It is obvious that in particular the strontium data are largely overpredicted in most cases. While the retention capability of UO_2 and the matrix material of the fuel spheres is visible, it is most probably the diffusive transport through the silicon carbide layer that appears very conservative and should undergo a thorough review.
- Silver release measurements are often unusual and inconsistent, and therefore extremely difficult for postcalculation. There are presumably other mechanisms for transport and

retention working than treated by a simple diffusion model. The diffusion coefficient recommended in [1] was derived from a 1500°C heating test at Harwell.

- One of the most recent heating tests, HFR-K6/3, has shown supremely low krypton and caesium release values, which are largely overpredicted by the model calculations. This extremely good accident condition performance of the very latest manufacture of German TRISO fuels should be the starting point of further studies: if results of this type can be substantiated reproducibly, new HTGR designs might benefit from potentially higher accident temperatures than the presently established 1600°C limit. The new limit has to be quantified taking account of the burnup and neutron fluence levels reached during irradiation.
- Problems that arose with validation along experimental results may require expansion of postexamination after irradiation and heating.

11. SPENT FUEL TREATMENT AND DISPOSAL

11.1. EXPERIENCE WITH SPENT FUEL TREATMENT FOR SHUT-DOWN HTGR

Every nuclear facility must be decommissioned at the end of its lifetime. Decommissioning includes clean-up of radioactivity and subsequent demolition of the plant. According to internationally acknowledged definitions by the IAEA, there are three options for decommissioning:

- Immediate dismantling or early site release or decon where the facility will be decontaminated and dismantled soon, i.e. a few months or years after shutdown;
- Safe enclosure or safestore where the facility is put into a safe storage configuration for a period of 40–60 years before contamination and dismantling activities will start;
- Entombment where all radioactive material will remain on-site with no requirement for total removal. The radioactive parts of the facility will be encased in a long-lived structure, e.g. concrete, and maintained until radioactivity is no longer a concern and site license can be terminated.

Which one of the above options will be selected, is usually determined by individual national policy and the owner's strategy.

Between the 1960s and 1980s, HTGR spent fuel processing was extensively studied in the USA and in Germany at laboratory scale and later at pilot scale. The experience achieved in the past was mainly on ^{233}U recovery from mixed $(Th,U)O_2$ coated fuel particles.

These works have essentially dealt with the head end process to recover the kernels of uranium and thorium oxides by elimination of the successive layers of carbon and silicon carbide (SiC). After this step, the uranium and the thorium were recovered and separated from the fission products by the THOREX process (dissolution of the oxide by HNO_3/HF, then extraction of the thorium and uranium by tributylphosphate (TBP) and used for the re-fabrication of the oxide.

11.1.1. Germany

11.1.1.1. Decommissioning strategy for gas cooled reactors

Since the end of the 1970s, the HTGR fuel strategy was guided by the need to meet non-proliferation aspects and to find a convincing publicly accepted spent fuel concept. The

German reference spherical fuel element with its safety related properties has many positive features, which are effective not only during normal operation and during accidents, but also under conditions of intermediate storage and final disposal:

- Efficient use of uranium and in-situ generated plutonium in LEU fuel due to high burnup;
- Isotopic composition of the spent fuel which is non-proliferation friendly;
- TRISO coating of the fuel particles providing an effective long term barrier against fission product transport and reduces the need for additional barriers;
- Passive air cooling systems being sufficient from the beginning of intermediate storage due to the low power density of the fuel;
- Disposal techniques developed for medium active waste applicable to spent HTGR fuel;
- Homogeneous graphite matrix minimizing any spent fuel conditioning effort;
- Corrosion resistance of both matrix graphite and particle coatings against repository relevant salt brines allowing a simple fuel disposal packaging concept;
- Small and easy to handle equipment in intermediate and final storage.

For these reasons, the concept of spent fuel treatment was selected in Germany in 1985 for the two HTGRs which were operated, the AVR test reactor in Jülich and the prototype reactor THTR-300 in Hamm-Uentrop. This option of direct disposal, which is presently the only accepted method of spent HTGR fuel management in Germany, involves the two steps of

- intermediate dry storage in appropriate containers and facilities;
- transfer to a deep-mined salt dome repository for final disposal utilizing techniques of treatment similar to heat generating medium level active waste (MLW).

But also for the period of longer term interim storage, until a final disposal site has been selected, dry storage in casks is to be applied.

11.1.1.2. Handling of spent fuel from the AVR

At the end of 1988, after 21 years of operation, the AVR reactor was permanently shut down. Application for the license for decommissioning was submitted in December 1987. Until the license was granted, the reactor was held at ‘zero power operation’. Safestore decommissioning of the AVR began in 1994. It was split into two phases [354]:

(1) Defueling of the reactor, dismantling of plant systems outside the reactor building;
(2) Dismantling of components, alteration of components, installation and operation of new facilities for the state of safe enclosure as well as operation in the state of safe enclosure.

Originally a strategy for a complete removal was investigated consisting of a step-by-step dismantling, which allowed the plant to be transferred into a configuration of safe enclosure after either step [354].

In 2003, the AVR GmbH was taken over by the ‘Energiewerke Nord’ (EWN) in Lubmin, Germany, and the decommissioning strategy was changed. In an agreement between the Federal Government and the State of NRW, it was decided to not only have a safe enclosure of the AVR reactor, but to have the site returned to green-field status by the year 2012. The

plan is to lift the grouted reactor pressure vessel including all internals with a weight of some 2100 t as a whole out of the reactor building and store it in a separate building.

The AVR was primarily used to test the HTGR concept, the fuel, and the components. Fueling of the first core loading started on July 14, 1966, with about 30 000 first core fuel elements, 70 000 moderator (graphite) balls, and 3000 absorber balls. In sum, more than 290 000 spherical fuel elements of five different types and 15 variants (carbide/oxide, BISO/TRISO, HEU/LEU) with more than 6 billion coated fuel particles plus about 80 000 graphite (moderator) balls were inserted into the core. Fuel element design also changed soon with reload charge 3 from machined graphite shells to pressed matrix materials.

Using high enriched mixed carbide/oxide fuel at the beginning, the reactor core was, since mid 1982, gradually converted to low enriched fuel. By the end of operation, a total of 2.4 million spheres were recycled in the core, some 180 400 fuel elements were removed from the core. The detailed fuel composition of the reactor core during the years of operation was described already in Section 3.4.2. The composition of the reactor inventory of totally ~110 000 fuel spheres remaining in the reactor at the end of operation was about 50% of HEU and 50% LEU fuel. The exact fuel composition after terminating the operation of the reactor is given in Table 11.1 [48, 355]. At present, all fuel is stored in CASTOR casks at an interim dry storage facility at FZJ.

TABLE 11.1. FUEL INVENTORY OF AVR AT THE END OF OPERATION

AVR fuel			Number of fuel elements (rounded)
Type		Variant	
HEU	5 g Th	GO, GFB-3, -4, -5	39 300
	10 g Th	THTR	17 400
LEU	10% enrichment	GLE-3	24 500
	16.7% enrichment	GLE-4	29 000
		Total:	110 200

Defueling started in April 1994 with HEU fuel only. Due to the fact that a particular license was required for LEU fuel handling in the Hot Cells of FZJ, all LEU fuel identified was reshuffled back into the core. Selection was made by measurement of the ^{232}U isotope which is practically present in the thorium containing HEU fuel only. During operation, a perfect distinction by ^{233}Pa in the gamma scan was possible. The defueling process was interrupted after having discharged 35 000 HEU fuel elements with a HEU share in the circulated elements reduced to 17%. After the LEU license was finally granted, defueling was resumed in March 1996. It was restricted at the beginning by the fact that upper limits for heavy metal and ^{239}Pu contents had to be obeyed. After obtaining the permission for considerably higher limits, unselective defueling could begin with still 63 000 spheres in the core. The defueling process was accompanied by regular criticality measurements to ensure in-time countermeasures in case of too high a fuel concentration in the core centre conceivably resulting from the fresher fuel of the outer zone displaced to the inside during defueling. The defueling was completed by the middle of 1998 [356].

Table 11.2 lists the book balance of charged and discharged AVR fuel elements [48]. The figure of ‘12’ as the overall difference should not be taken too seriously due to the uncertainties in counting spheres in cases of misidentifying fuel types, broken spheres, or

problems with the charging system. As a result of an inspection for residual fuel in the core, the equivalent of 197 fuel elements was said to be unretrievable [48]. It is an estimated upper limit of fuel loss in the core, but was considered by the regulator to be sufficiently low and safely enclosed to remain in the reactor during its interim storage. All lost fuel is classified as HEU fuel with originally 5 g of thorium. Total heavy metal left in the core was calculated to be 486 g of uranium (including 71 g of ^{235}U and 24 g of ^{233}U), 7.2 g of plutonium, and 1180 g of ^{232}Th [48].

TABLE 11.2. BOOK BALANCE OF CHARGED AND DISCHARGED AVR FUEL ELEMENTS

Fuel type	Fuel variant	Charged	Fraction of total fuel (%)	Charged	Discharged	Difference
HEU	UCC	30 155	10.4			
5 g Th	T	7 504	2.6			
	GK	50 794	17.5			
	GO	90 396	31.1			
	GFB-3,4,5	17 290	5.9			
		total:		196 139	201 945	-5 806
HEU	GFB-1,2	3 050	1.0			
10 g Th	THTR	35 415	12.2			
		total:		38 465	32 978	5 487
		Total HEU:	80.7	234 604	234 923	-319
LEU 7% enr	GLE-1	2 400	0.8	2 400	2 327	73
LEU 10% enr	GLE-3	24 611	8.5	24 611	24 412	199
LEU 16.7% enr	GLE-4	29 090	10.0	29 090	29 031	59
		Total LEU:	19.3	56 101	55 770	331
		Total:	100.0	290 705	290 693	12

The book discharge deviations were corrected not until after final defueling. It was, however, known by sphere measurements before the so-called KAHTER fuel loading (reload 22 inserted September 1986) that in the last years of operation, GLE-1 elements were no longer in the reactor, and that the number of the old HEU elements with 10 g of Th was only around 2000 (instead of over 5000 as in the book). Both were confirmed in the defueling process.

Steel cans with a capacity of 50 fuel spheres each were filled at the AVR site and transported to the hot cells at FZJ, where they were sealed and stored in a water pool serving as buffer storage. The steel cans were then opened and the fuel from those, which did not indicate water penetration, was repacked into larger, dry storage canisters with a capacity of 950 balls (Fig. 11.1 top) [357]. Fuel elements which were found wet due to leaky sealings of the steel cans, were also given into the dry storage canisters, but then sealed with a particular leak-tight welding. The dry storage canisters are filled with helium of 0.1 MPa, their specified leak tightness is $< 10^{-2}$ Pa L/s. The employment of the 950-ball canisters was considered to ease the future repackaging step to the reference 400 L final disposal drums.

For the intermediate storage, two concepts are being applied:

- canister storage behind a concrete shielding; or
- storage directly in shielded containers.

A natural convection type, dry storage facility, which is operated since 1981 without any disturbance, took up 72 of the dry storage canisters in 36 positions up to now (Fig. 11.1 bottom left). Heat removal designed for 7.2 kW is supported by an air venting system of 2000 Nm^3/h. According to the second concept, two of the canisters are inserted into a CASTOR THTR/AVR type storage cask closed by a double lid system.

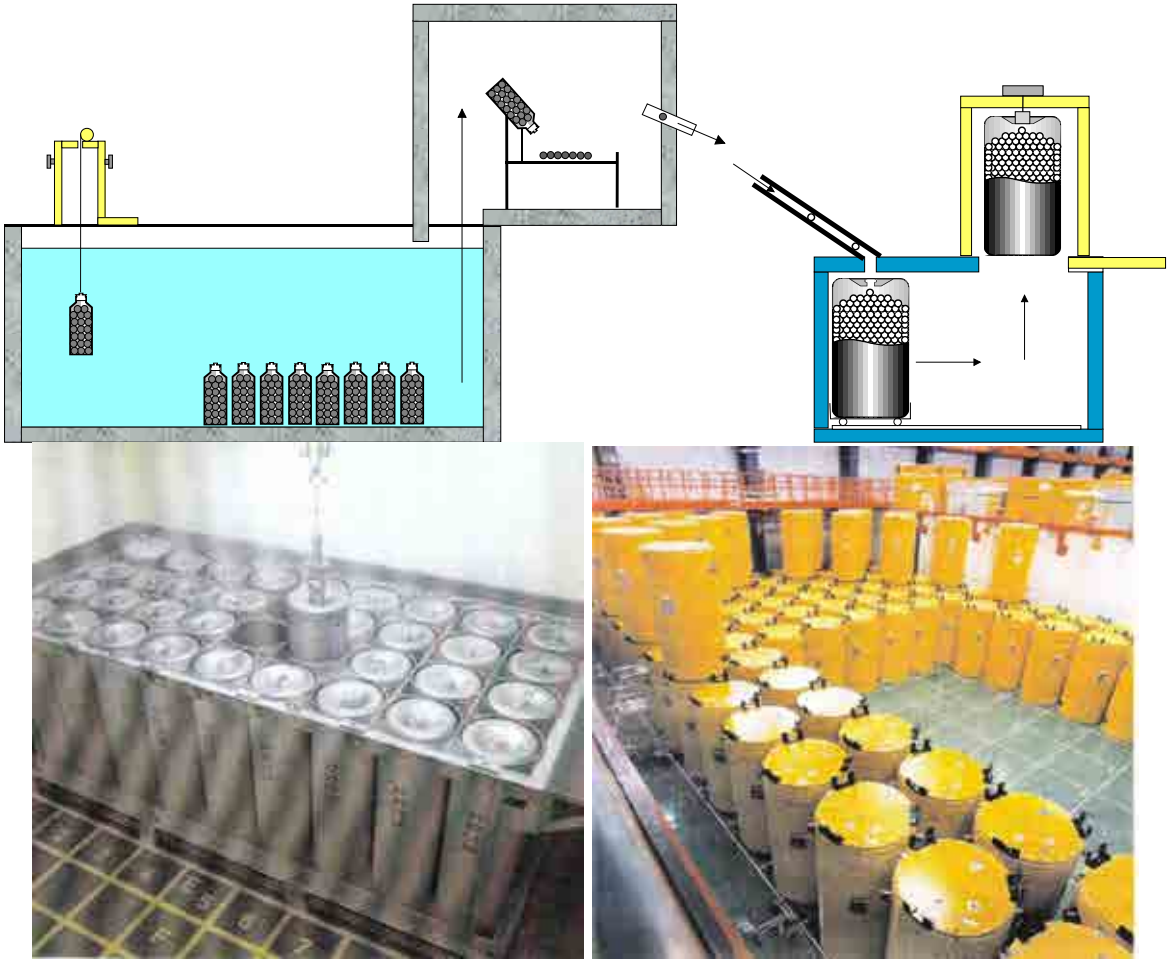

FIG. 11.1. AVR spent fuel management in the hot cells at FZJ (top), AVR canister storage (bottom left), storage in CASTOR casks (bottom right).

The CASTOR casks are stored at FZJ in the intermediate dry storage facility licensed to take up a total of 158 casks (Fig. 11.1, bottom right). The maximum heat production of 15 kW (if completely filled) is passively removed by natural convection [358].

This procedure has been done for all fuel discharged during reactor operation and after reactor shutdown, which are approximately 290 000 fuel spheres in (presumably) 153 CASTOR casks. Last transport to the storage site was in August 2000. As of September 2004, the AVR container store contains 132 CASTOR casks with a total of 250 560 spheres and the dry storage facility contains 34 fuel canisters with a total of 32 264 spheres.

11.1.1.3. Handling of spent fuel from the THTR-300

The concept of the 'Thorium Hochtemperatur-Reaktor', THTR-300, in Hamm-Uentrop dates back to the end of the 1960s. The THTR-300 with a thermal power of 750 MW was operated for a total of 16 410 hours or an equivalent time of 423 days of operation at full load.

Construction (1971–1983) and operation (1983–1988) of the reactor were characterized by various licensing-technical and political obstacles which eventually ended up in the decision by the operator in September 1989 for decommissioning the reactor.

The decommissioning procedure is conducted in four consecutive steps [359]:

(1) Shutdown operation; primary circuit depressurized; helium substituted for nitrogen; shutdown rods fully inserted and locked; removal of decay heat (< 20 kW) by natural convection and radiation;
(2) Unloading the reactor and spent fuel storage as a prerequisite for safe enclosure; reactivity < 0.95 during unloading by addition of 7000 absorber balls; core inspection device for visual control of fuel-free state;
(3) Establishment of safe enclosure; residual radioactivity sealed from environment and controlled; effective dose from release into environment < 0.1 mSv per year; all buildings except for reactor hall, reactor building, and auxiliary building to be released from the validity of the Atomic Act;
(4) Operation of passively 'safe enclosure' over 30 years; largely no maintenance; monitoring the few remaining systems to be operated from adjacent fossil power plant.

Steps 2, 3, and 4 require a license according to the German Atomic Act.

The establishment of the configuration of safe enclosure was achieved in February 1997 (comparable to the IAEA passive SAFE STORAGE option). The operation of the safely enclosed plant will last for 30 years, before a complete dismantling may take place.

The THTR fuel concept was designed for a high enriched uranium–thorium fuel cycle. The reference fuel particle consists of a homogeneous U–Th mixed oxide kernel surrounded by a BISO coating. Total particle diameter is about 760 μm. The spherical fuel element contains approx. 34 100 of those BISO coated fuel particles. The total heavy metal content amounts to 1.032 g of 93% enriched uranium and 10.2 g of thorium per fuel sphere.

The initial THTR core contained a total of 674 200 spherical elements, of which 358 200 (or 35%) were fuel elements, 272 500 (40%) were graphite elements, and 43 500 (7%) were B and Hf-doped absorber elements. During THTR operation, 1.3 million spheres were circulated, 235 000 of which were permanently removed and replaced by fresh fuel [360]. At the time of termination of operation on September 1, 1989, a total of 704 426 operating elements were in the core and the loading facility [361]. In addition, the internal operating element storage contained about 240 000 operating elements. From the core itself, approximately 670 000 operating elements (Table 11.3) had to be finally removed, 84% of which were fuel elements [362].

TABLE 11.3. COMPOSITION OF THTR CORE.

Number of operating elements in the core at beginning of unloading process	
563 000	Fuel elements
76 000	Graphite elements
31 000	Absorber elements
Σ 670 000	Operating elements

Unloading of the THTR pebble bed core was initiated in December 1993 with a concept based on detailed calculations and tests with a core model. The unloading process was completed in October 1994 achieving the state of a 'nuclear fuel free' reactor. The unloading process is, in principle, similar to the discharging process during normal operation except for some process engineering modifications concerning the replacement of the helium gas by nitrogen and air as well as the reduced temperature in the depressurized reactor. Absolutely subcritical conditions during the unloading process were guaranteed by insertion of both reflector and in-core control rods and by the addition of 4200 absorber elements.

The unloading of the THTR pebble bed was monitored by means of the burnup measuring system, a graphite moderated 500 W 'Small Burnup Measuring Reactor' (SMR), containing 3.6 kg of ^{235}U in form of 20% enriched U–Al fuel in 767 strip shaped fuel elements with rectangular cross-section (15 × 1.1 mm^2) and 89–711 mm length. In the SMR, a reactivity effect was created when a THTR fuel element was passing. Operating elements were sorted by this way and transferred to steel canisters each containing 2100 elements. The flow pattern of the spheres during the unloading procedure was examined in experiments using a 1:2 core model showing that a central funnel is formed leading to a mixture of fuel elements with different burnups [363].

The diagram in Fig. 11.2 shows the number of discharged absorber elements (AE) and graphite elements (GE), respectively, per each of the 268 'unloading steps', which corresponds to 2100 discharged fuel elements or one filled steel canister [364]. Furthermore, the mean burnup of the removed fuel elements is plotted exhibiting different phases during the unloading process. The minimum in burnup around unloading step 150 is due to fuel elements from the surface of the outer upper core with a low irradiation history, whereas the later increase in burnup is from highly irradiated fuel from the bottom edge of the core [364].

The efficiency of the selection process was about 97%, meaning that from the total of about 300 000 graphite elements and 43 500 absorber balls, approximately 3% have gone with the fuel elements into the fuel canisters [362]. The inventory of fissile material remaining in the core after completion of the unloading process was estimated to be 0.976 kg, significantly lower than the required value of 2.5 kg. Between start and end of plant operation, ten containers were filled with about 17 000 damaged operating elements mainly due to control rod operation, four more were filled until the end of fuel unloading.

An at-reactor canister storage for spent THTR fuel (Fig. 11.3) with 72 storing positions for three canisters each plus nine more positions for high active waste was licensed in 1982. It received its first regular spent fuel in 1988. All fuel canisters were stored there for 1–2 years. Shielding is given by concrete walls of 1.9 m thickness. The store is designed for a heat removal of 232 kW which is realized by a forced convection cooling [358].

For the following step of storage and transport of the fuel elements to an external interim store, respective casks of the CASTOR THTR/AVR type have been used with one CASTOR to contain one fuel canister with approximately 2100 fuel elements. Maximum burnup per fuel element container was about 8.8% FIMA, maximum decay heat per fuel element container was about 100 W, both values significantly lower than the design values. Neutron dose rates at the loaded transport and storage cask were shown to be less than 1 μSv/h. Two more CASTOR casks were filled with the SMR fuel elements.

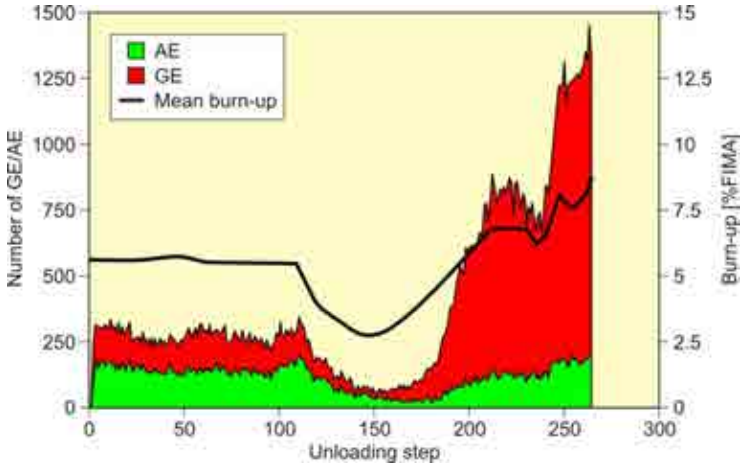

FIG. 11.2. Discharged absorber (AE) and graphite elements (GE) per unloading step (= 2100 fuel elements) and mean burnup of fuel elements.

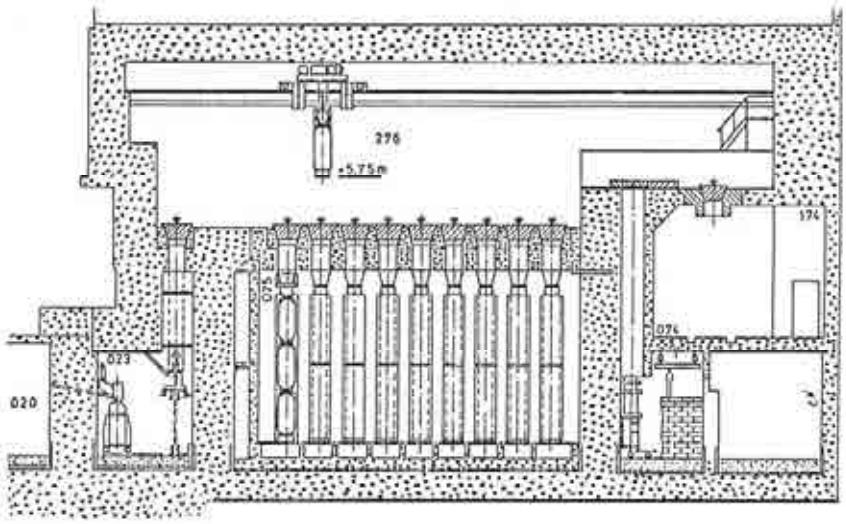

FIG. 11.3. THTR-300 store for spent fuel.

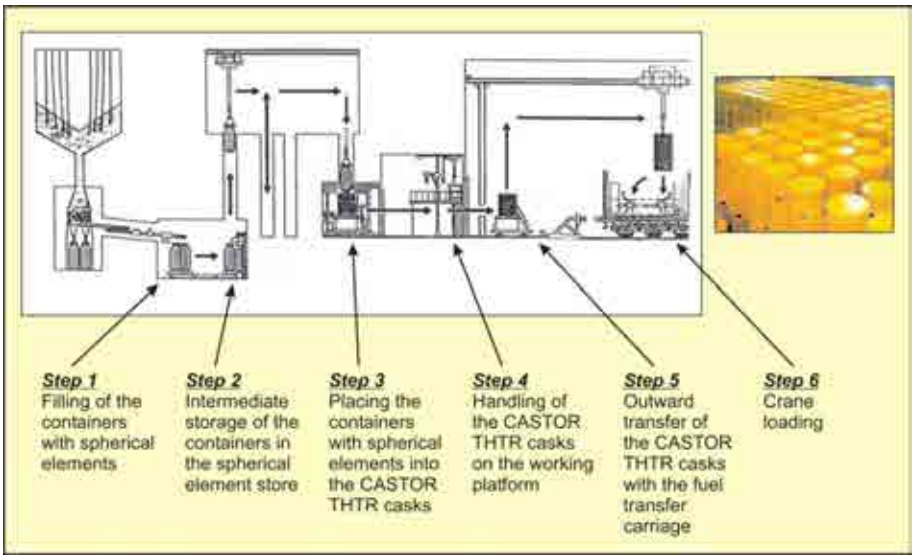

FIG. 11.4. THTR-300 spent fuel management.

The storage license for the casks in the interim storage site Ahaus (BZA) was issued in 1992. Special six-axle railway wagons were available to carry three casks each. By April 1995, a total number of approximately 620 000 spent fuel elements had been transported in 306 CASTOR casks in 57 shipments from the THTR site to the BZA. A schematic of the complete spent fuel management is shown in Fig. 11.4 [359].

11.1.1.4. Transport and storage container CASTOR THTR/AVR

With the development of transport and storage casks, the tendency was towards away-from-the-reactor storage facilities having the advantage of increasing the storage capacity as needed. Transport and storage containers of the CASTOR type have already been proven good for LWR fuel elements. The development of CASTOR THTR/AVR casks began in 1982. The CASTOR for HTGR fuel as shown in Fig. 11.5 [362] is a massive cast iron cask to be closed by a primary and a secondary lid and a protection sheet. The lid system is designed such that the required control of leak tighness can be done at the storage site. Dimensions of the cask are given in Table 11.4 [362]. A transport license for these CASTOR casks was issued in 1987.

11.1.1.5. Heat and acivity release from spent fuel spheres

Most of the activity of spent fuel exists in a solid, non-releasable form. From the gaseous fission and activation products, only the long-lived isotopes are of importance with regard to spent fuel storage. During transfer of spheres from the small to the larger storage canisters, fuel specific data (type, burnup) were collected to know about the exact amounts of fuel and radioactivity contents in the dry storage. ^{3}H, ^{14}C, and ^{85}Kr have been identified as the only considerable contributors to radioactive release from spent HTGR fuel at inert storage conditions [357].

An aqueous solution can penetrate the A3 matrix graphite of a fuel element through its open pore system. Under normal conditions, a sphere takes up about 8 ml. Under pressurized conditions and dissolution of the pore gases in the liquid, this amount raises to conservatively estimated 23 mL [199]. Hydrogen atoms in the water may be substituted by tritium leading to HTO molecules accounting for 95% of the tritium inventory in the storage container. In combination with radiolysis, HT or T_2 gas will be formed. The ^{85}Kr is a fission product and mainly contained in the fuel particles. Its amount is directly related to the uranium contamination in the matrix and the number of failed particles.

TABLE 11.4. DIMENSIONS OF CASTOR THTR/AVR CASK

Outer/inner length	2780/1964 mm
Outer/inner diameter	1380/640 mm
Material	Nodular graphite cast iron
Weight	26.1 t
Integral tightness of either lid	10^{-5} Pa L/s
Contents	1900 fuel spheres (AVR) or 2100 fuel spheres (THTR)

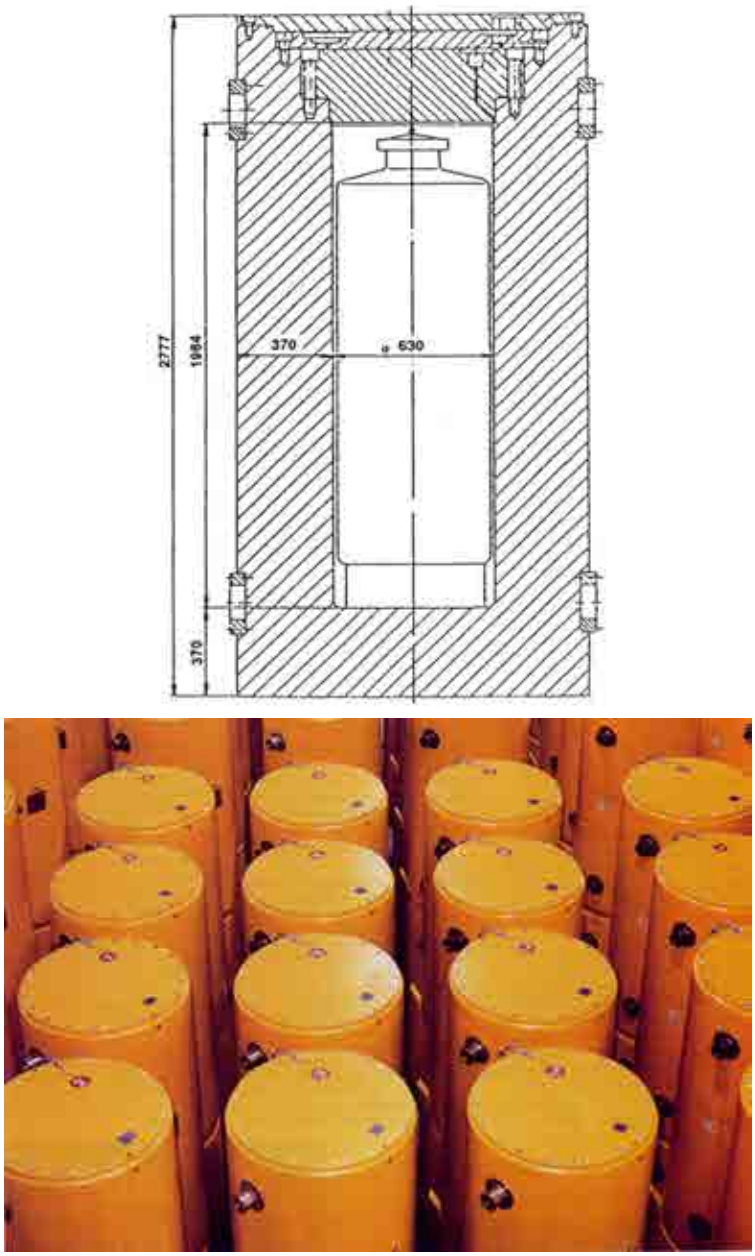

FIG. 11.5. CASTOR THTR/AVR cask to take up one THTR fuel canister.

FZJ conducted an experimental programme to test the storage behaviour of spent AVR fuel measuring activities and decay heat production of 17 spheres with a burnup between 4 and 16% FIMA and decay periods of 150 to 1700 d showing good agreement with respective ORIGEN predictions [366].

First measurements of activity release from AVR spent fuel were conducted in the 1970s in a facility simulating dry storage conditions [367]. It consisted of a furnace with a capacity of five spheres and two gas-tight storage containers which could take up 20 spheres each. These were connected to a sweep gas circuit including traps for the gaseous species. The furnace could be heated up to 400°C, while the two containers were kept at temperatures of 140°C (maximum temperature at dry storage) and 40°C (nominal operating temperature of disposal site), respectively. Fuel types investigated were UCC with 16.7–18.0% FIMA burnup for testing carbide fuel and GO-THTR with 5.1–6.5% FIMA for testing oxide fuel [367].

As is shown in Fig. 11.6, tritium was found to be released at rates independent of the fuel type explained by the fact that its origin is mainly from ^{3}He and impurities in the graphite [367]. A repetition of these measurements a few weeks later exhibited reduced rates, a depletion effect showing that only a part of the tritium adsorbed on the pore surfaces is available for release. The activities released into the containers were found to show no significant further increase after 50 d at 40°C and after 10 d at 140°C, respectively, due to the depletion of the inventory and increasing partial pressure in the void volume [367]. The isotope ^{226}Ra can be neglected under interim storage conditions. Unlike the ^{3}H and ^{85}Kr release rates into the container were observed to significantly increase during the investigation time. The depletion effect was not observed for ^{85}Kr.

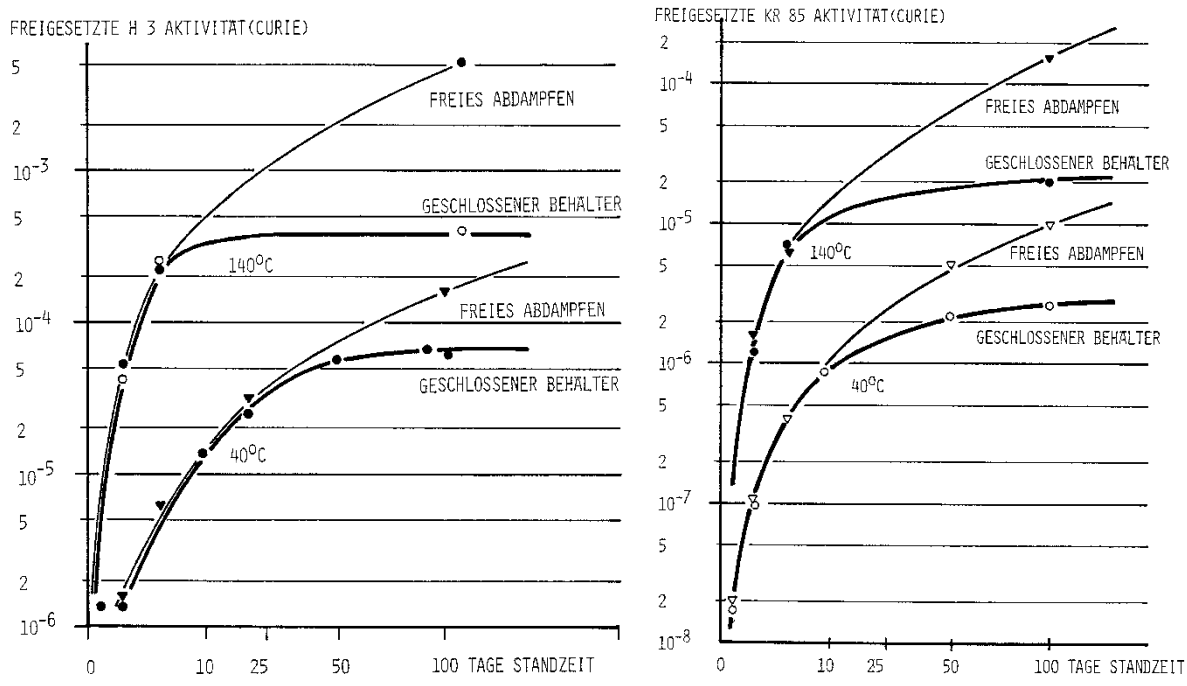

FIG. 11.6. H-3 (left) and Kr-85 activity released from 20 GO fuel elements in open and closed container (7 L void volume) over 100 d.

Furthermore measurements on the release of ^{3}H and ^{85}Kr were made using two specially prepared canisters. One canister is filled with GK type (average burnup 15% FIMA), the other one with GO type fuel balls (12.4% FIMA), with all fuel discharged from the AVR at the end of 1976. The canisters were equipped with valves to allow sampling of the inside gas atmosphere. The void volume of the canisters is 118 L initially consisting of normal air (at 25°C) with a relatively high moisture content (10–20 mg of H_2O per litre of air), which originated from the former interim storage in a water basin.

Tritium and krypton-85 activities were measured during storage over several years. For the first three years, the observed increase in ^{3}H activity corresponds to an average of 7.4×10^{-3} GBq/a for both GO and GK fuel, whereas for ^{85}Kr, the average release rate was 3.7×10^{-3} GBq/a for GO fuel and 1.9×10^{-3} GBq/a for GK fuel [368]. Activity release rates from AVR spheres into the canister gas atmosphere are shown in Fig. 11.7 in an Arrhenius type diagram for ^{3}H and ^{85}Kr [362].

Also the release from te two AVR canisters inside a CASTOR cask into the cask atmosphere was experimentally investigated. Between 1987 and 1992, one CASTOR THTR/AVR cask and one TN-AVR 2 cask were externally heated up to 55°C. The higher temperature resulted in the release of moisture and thus of tritium in form of HTO. Since leakage rates from a cask lid are by three orders of magnitude lower than those from a canister plug, activity release from CASTOR casks, which are closed with two lids, into the environment is expected to be negligibly low.

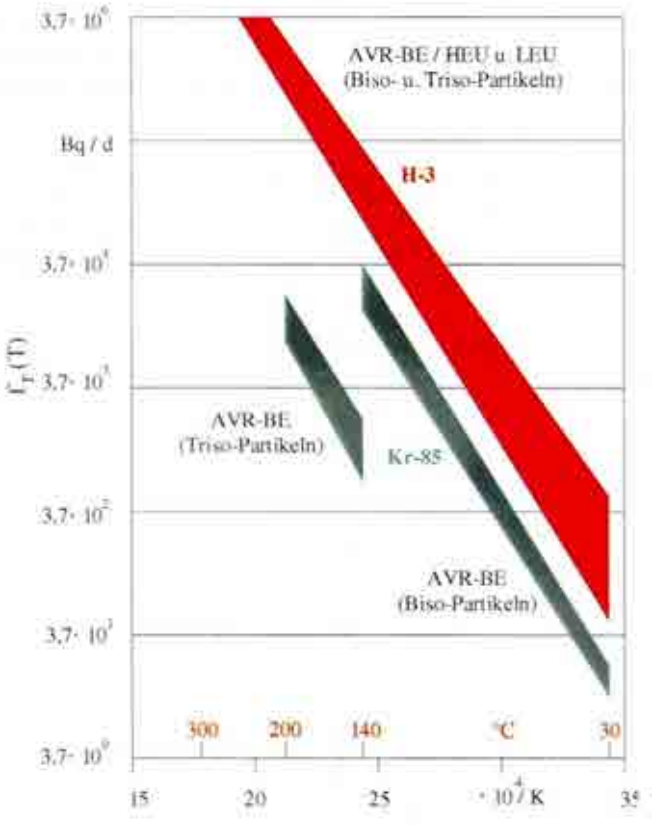

FIG. 11.7. Arrhenius diagram of ^{3}H and ^{85}Kr release rates from experimental data.

With regard to ^{14}C, an activation product from ^{14}N and ^{13}C, high concentration values are typically found near the sphere surface resulting from coolant deposition. It can be released as CO_2 during oxidation processes. The ^{14}C is bound to the binder material in the matrix graphite and, at presence of moisture in the storage container, is liberated as gaseous CO_2 during corrosive reactions. For the ^{14}C activity measurements conducted on the same two canisters in the time 1986–1989, the fractions of O_2 and CO_2 and the ^{14}C concentrations are listed in Table 11.5 [369].

The decreasing amount of O_2 and the concomitant increase of CO_2 show the corrosive origin of the ^{14}C. The accumulated CO_2 corresponds to a carbon loss of averaged 7.7 mg per GK sphere (after 5.3 years) and 6.5 mg per GO sphere (after 6.4 years). Considering an averaged ^{14}C inventory of 5.5×10^{6} Bq per fuel sphere, the fractional release rate of ^{14}C into the canister atmosphere is 8.6×10^{-4} per year. It is a conservative figure used for the first 10 years. For longer times, the depletion of oxygen in the container atmosphere can be taken into account [369].

TABLE 11.5. CARBON-14 CONCENTRATIONS AND O_2 AND CO_2 FRACTIONS IN THE CANISTER GAS ATMOSPHERE FOR GK AND GO FUEL ELEMENTS

GK fuel elements				GO fuel elements			
Time (years) 0=Oct 1983	O_2 (vol.%)	CO_2 (vol.%)	^{14}C (Bq/mL)	Time (years) 0=Sep 1982	O_2 (vol.%)	CO_2 (vol.%)	^{14}C (Bq/mL)
0.	21.	0.	0.	0.	21.	0.	0.
2.7	10.2	5.7	—	3.8	7.4	7.0	—
3.8	6.6	7.8	129	4.9	6.1	8.5	72
4.1	6.3	8.6	137	5.2	5.7	8.6	81
4.6	6.0	8.9	166	5.7	5.0	9.2	99
5.3	4.2	10.9	228	6.4	4.3	9.2	108

— data not available.

To judge upon the ^{14}C activity in the storage canisters of THTR fuel, the experimental data gathered with the stored AVR fuel is taken and transferred to the conditions of THTR fuel. For a fuel lifetime of 1000 efpd in the THTR core, the ^{14}C inventory is 0.015 GBq per fuel sphere (to be seen as an upper limit). With a void volume of 206 L in the (one) canister initially consisting of a helium–air atmosphere (at 200°C), the ^{14}C activity in the canister gas accumulates to 0.27 GBq after 10 years of storage time. This is conservative with respect to the smaller amount of oxygen available to each fuel element in the THTR canister [369]. A ^{14}C inventory of 0.004 GBq per spent THTR fuel sphere was calculated with the ORIGEN-S 2 code based on a target burnup of 11.4% FIMA and three years of cooling time [362]. Since 1988, also ^{14}C activities of the gas atmosphere inside the CASTOR cask for the AVR spheres, but outside the two canisters are being measured. These values, however, are much lower because of the low leakage rates of the canisters [369].

A tritium inventory of 0.53 GBq per sphere spent was calculated with the ORIGEN-S 2 code for THTR fuel elements for a target burnup of 11.4% FIMA and 3 years of cooling time [362]. For the tritium activity inventory in a HEU fuel element from the AVR, an upper limit has been estimated to be 2.5 GBq with about 20% inside the coated particles and 80% inside the matrix material. A respective value for the ^{85}Kr inventory in a HEU fuel element, considered as an upper limit for all AVR fuel spheres, was assessed to be 17.3 GBq, almost everything inside the coated particles. The estimated figure for ^{14}C in the matrix material is 0.045 GBq [362].

After shutdown of both German HTGRs, a more detailed analysis has been made to estimate the realistic radioactive inventory of all spent fuel. With respect to the AVR fuel with its different types, it is wise o further subdivide fuel types into burnup classes to avoid a calculation based on an inappropriate averaging of the burnup and allow for a more precise assessment of the single nuclide activities. For this purpose, 12 reference fuel elements have been defined representing all spent AVR fuel [370]. Table 11.6 summarizes the results listing for each reference group the total activity (sum of all individual activities $> 10^6$ Bq from fission and activation products and actinides) as of the year 2003 as well as for a selection of nuclides their relative contribution to the total activity [371]. The results of a respective study for the spent THTR fuel are shown as well in the table. Activity data are here based on the year 1998 corresponding to a 10-years cooling period [362].

The MLW concept involves stabilization by cementing and the use of thin-walled containers. The reference design provides for 400 L canisters (1500–1800 spheres) stapled up to a height of 8 m to resist a rock pressure of 25 MPa in a < 100°C temperature environment. Release of activity is limited to 0.41 GBq of ^{3}H and 1.10 GBq of ^{85}Kr, respectively, per canister and year. Mechanical tests with (unirradiated) single spheres and sphere arrangement and later, on a pilot scale, with 180 litre canisters containing 800 spheres have shown the strong influence of a backfilling. Utilizing cement or quartz sand backfilling, neither sphere failure nor a remarkable volume change of the package was observed when imposing a pressure of 25 MPa. Only slight failures (< 3%) in the upper region were found for a rock salt grout backfilling. In contrast, the pebble bed with no backfilling was crushed to small pieces by more than 90% [372].

An accident scenario to be considered for final storage of spent fuel is the event of a water ingress into the salt mine where the evolving salt brine would start corroding the waste package and may reach the fuel particles. Since intact coatings have excellent long term chemical resistance, a release of activity from leaching is only possible with defective particles. In an experimental series, single bare fuel kernels — HEU $(U,Th)O_2$ TRISO of 12.1% FIMA irradiated at 900°C, LEU UO_2 TRISO of 10.7% FIMA irradiated at 1000°C, unirradiated UO_2 — were leached with a saturated brine at pressures of ambient/13 MPa and temperatures of ambient/90°C (Fig. 11.8) [373]. The results for the higher temperature and pressure reveal a nuclide specific leachability with Cs, Sb, or Eu being well mobilized in contrast to Ru or Am. A rapid release of activity was observed for UO_2 with almost 100% within 100 d, and for $(U,Th)O_2$ a 30–50% fraction within 1–2 years. Under these storage typical conditions, some of the kernels had partly disintegrated and released a large portion of their inventory [373].

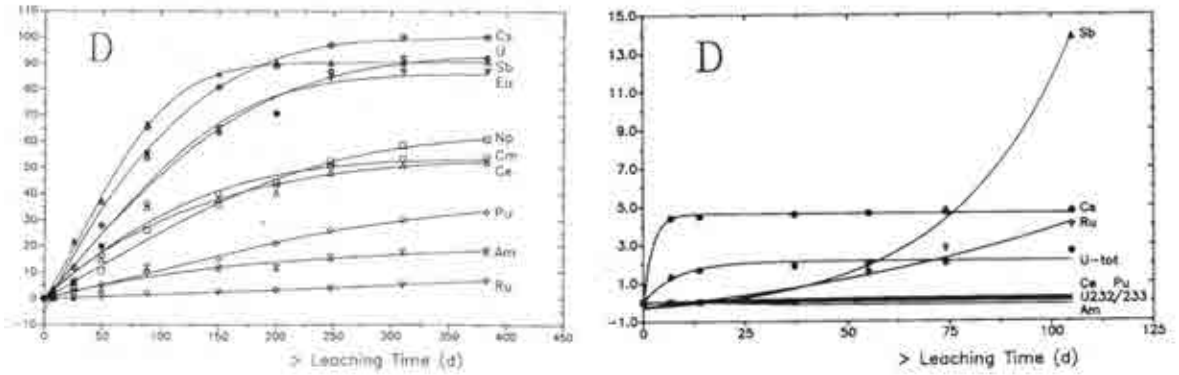

FIG. 11.8. Radionuclide leaching from irradiated UO_2 (left) and $(U,Th)O_2$ (right) kernels with Q brine at 13 MPa pressure and 90 °C temperature.

TABLE 11.6. PREDICTED TOTAL ACTIVITY OF AVR SPENT FUEL FOR THE YEAR 2003

Fuel type	No. fuel elements rounded	Burnup (%FIMA)	Operation time (years)	Total activity (Bq)	Fraction of total activity (%)							
					H-3	Kr-85	C-14	Sr-90	Cs-134	Cs-137	Pu-238	Pu-241
AVR												
HEU-1		(av 14.9)										
1.1	90 000	13.6	5.0	2.35×10^{16}	0.3	1.1	0.004	24.0	0.03	25.2	0.6	0.3
1.2	24 400	21.0	13.6	9.39×10^{15}	0.2	0.9	0.006	24.1	0.04	24.8	1.2	0.3
1.3	42 000	18.2	9.7	1.63×10^{16}	0.3	1.3	0.004	24.0	0.2	24.5	0.9	0.4
1.4	11 400	7.5	2.4	1.78×10^{15}	0.6	1.6	0.002	24.2	0.1	24.7	0.1	0.2
1.5	28 300	16.0	7.9	9.57×10^{15}	0.3	1.3	0.004	24.0	0.2	24.5	0.7	3.3
HEU-2		(av 6.7)										
2.1	21 100	10.0	8.8	7.60×10^{15}	0.2	1.2	0.003	24.4	0.1	24.6	0.7	0.2
2.2	15 200	2.0	1.4	1.15×10^{15}	0.1	1.6	0.003	24.1	0.05	24.5	0.006	0.1
2.3	2 000	12.0	13.0	9.40×10^{14}	0.2	1.3	0.004	24.3	0.2	24.5	0.8	0.3
LEU-3	2 400	8.0	7.7	1.29×10^{15}	0.2	0.7	0.002	16.2	0.03	22.3	0.5	20.4
LEU-4	24 600	8.5	5.5	7.45×10^{15}	0.3	1.1	0.002	19.2	0.2	22.4	0.3	11.9
LEU-5		(av 8.6)										
5.1	8 700	3.5	0.8	6.30×10^{14}	1.1	1.5	0.001	22.8	0.05	23.9	0.03	2.6
5.2	20 400	11.0	3.7	4.71×10^{15}	0.4	1.3	0.002	21.1	0.1	23.7	0.2	7.6
Total	290 700			8.43×10^{16}	0.3	1.2	0.004	23.3	0.1	24.5	0.7	2.0
THTR												
HEU-2	617 606	5.0		1.31×10^{17}	0.6	2.0	0.002	22.9	0.5	23.1	0.1	0.2

The leak resistance of complete spent AVR fuel spheres of different types and also one of the non-heated spheres of the HFR-K3 experiment in a salt brine was experimentally investigated at pressures up to 30 MPa and temperatures up to 150 °C over up to 1230 days. Leached activities were mainly given by ^{137}Cs, ^{134}Cs, ^{90}Sr, ^{144}Ce, ^{133}Ba, ^{154}Eu, ^{60}Co. The tests have revealed a gradual release of the matrix contamination into the brine, for Cs about 10–20% of its inventory in the matrix. Figure 11.9 shows the ^{137}Cs release rate under final storage typical conditions revealing lower figures for TRISO fuel [374]. Total release fraction is $< 10^{-4}$ after more than four years. Release from defective particles is by orders of magnitude higher. Long term relevant nuclides like ^{129}I, ^{99}Tc, ^{237}Np, are expected to exhibit much lower release rates [375].

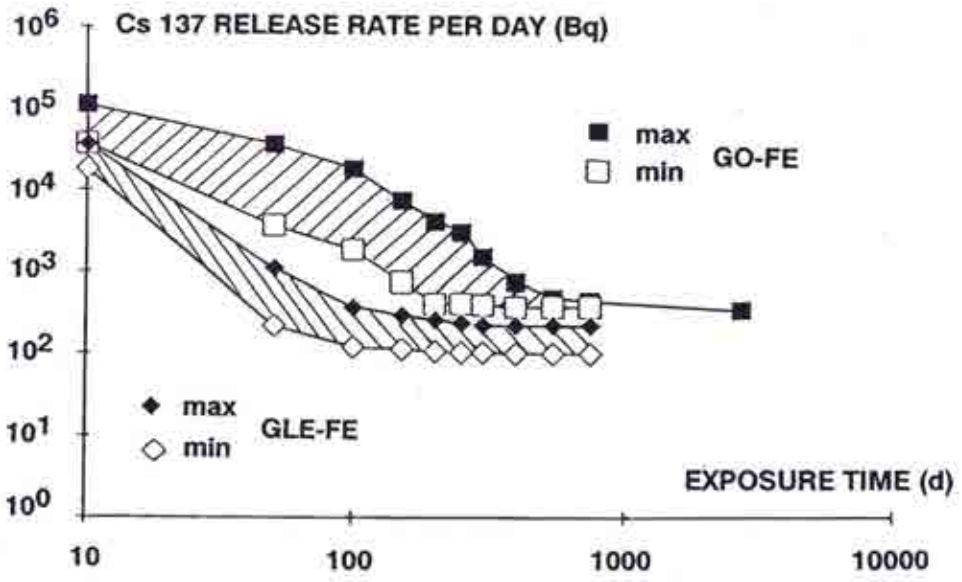

FIG. 11.9. Caesium release in leach tests with irradiated AVR fuel elements at 13 MPa pressure and 90 °C temperature GO: BISO coated (U,Th)O_2 fuel; GLE: TRISO coated UO_2 fuel.

The release behaviour of HTR fuel elements under final disposal conditions was experimentally examined for spent AVR fuel spheres which were given into a saturated quinary alkaline solution (Q brine) representative of salt repository conditions [376]. The leaching process at 90°C temperature and 13 MPa pressure exhibited two distinct phases: removal of surface activity on a short term (~weeks), and removal of activity from uranium contamination and defective/failed particles on a longer term. The experiments have shown that leaching rates did not significantly differ from those at higher pressures (30 MPa) in previous tests. Major differences in the release behaviour were given between BISO and TRISO coated fuel. TRISO fuel with the lower uranium contamination of the matrix showed a respective lower long term release [376].

Apart from the above 'integral' tests, further investigations were also concentrating on the understanding of the behaviour of the single components under respective conditions. These included the measurements of corrosion rates of the fuel materials matrix, pyrocarbon, silicon carbide, as well as the leaching of uranium and thorium from particle kernels. Results have shown that corrosion rates for A3 matrix are higher at the presence of oxygen. The significant increase in an argon atmosphere under gamma radiation is due to the generation of radiolysis products. Respective results for pyrocarbon are similar to those for matrix material. Corrosion rates for silicon carbide were found to be strongly related to the corrosive environment and

the temperature. Leaching tests with different types of unirradiated kernels in Ar at 90°C for more than one year exhibited lower dissolution rates for $(Th,U)O_2$ kernels by one to two orders of magnitude compared to UO_2 kernels [199].

Visco-plastic behaviour in rock salt will eventually close gaps/voids, so-called convergence, around the storage arrangement and imposes a hydrostatic pressure buildup according to the depth of the disposal location which, after all gaps are closed, corresponds to the total mountain pressure. Convergence is enhanced with increasing temperature. For a depth of 800–1000 m and a maximum temperature of 200°C, a temporarily and locally limited maximum pressure of about 30 MPa has to be taken into consideration [377].

If there are gaps between coating layers or between particle and overcoating, they may interrupt the transfer of the pressure load from the outside to the particle. Convergence was measured in the ASSE salt mine at a rate of about 0.3 mm per year. The annular gap around the waste barrels in a bore hole is expected to close after approximately 200 years [377].

Crushing tests with thin-walled 180 L drums containing graphite spheres and various kinds of back-filling materials at loads up to 25 MPa (= maximum rock pressure) have shown that a back-fill with quartz sand fully stabilized the volume with hardly any sphere damage. In contrast, a salt grout filling has led to considerable sphere breakage, and packages with only fuel spheres inside were size-reduced with all fuel elements cracked.

In the 1970s, an in-situ demonstration test of direct final storage with about 100 000 AVR fuel elements in 100 canisters was planned and prepared at the Asse salt mine in Germany. The retrievable canisters with 950 spheres each were intended to be placed into four 36 m deep bore holes at the 750 m level of Asse [378]. Before starting the experiment, however, the project was stopped in 1978 for political reasons [379].

Resuming respective works in 1983, the project MHV (MLW and HTR Fuel Element Test Storage in Bore Holes) was started focusing on the retrievable in-situ disposal for demonstrating respective handling techniques. Five 1 m diameter bore holes with a depth of 10 m were drilled in the Asse salt mine (Fig. 11.10). One hole was considered to contain four gas-tight stainless steel canisters with 950 spent AVR fuel elements each.

The material to be controlled according to IAEA standards were 444 ‘effective g’, where ‘effective grams’ for enriched uranium are defined as the U_{tot} (in grams) multiplied by the square of the enrichment (which was 52.4%). Therefore the test site was classified as ‘location outside facilities’ which can handle < 1 ‘effective kg’, the lowest level of IAEA control [380]. The project also included an electrical heating to keep the temperature at a level of 70°C and comprehensive devices for measuring geo-mechanical parameters, gas release and heat development (see Fig. 11.10). The test was planned for a duration of 5 years [374]. This project, however, was also discontinued for financial reasons, the demonstration storage test never did materialize.

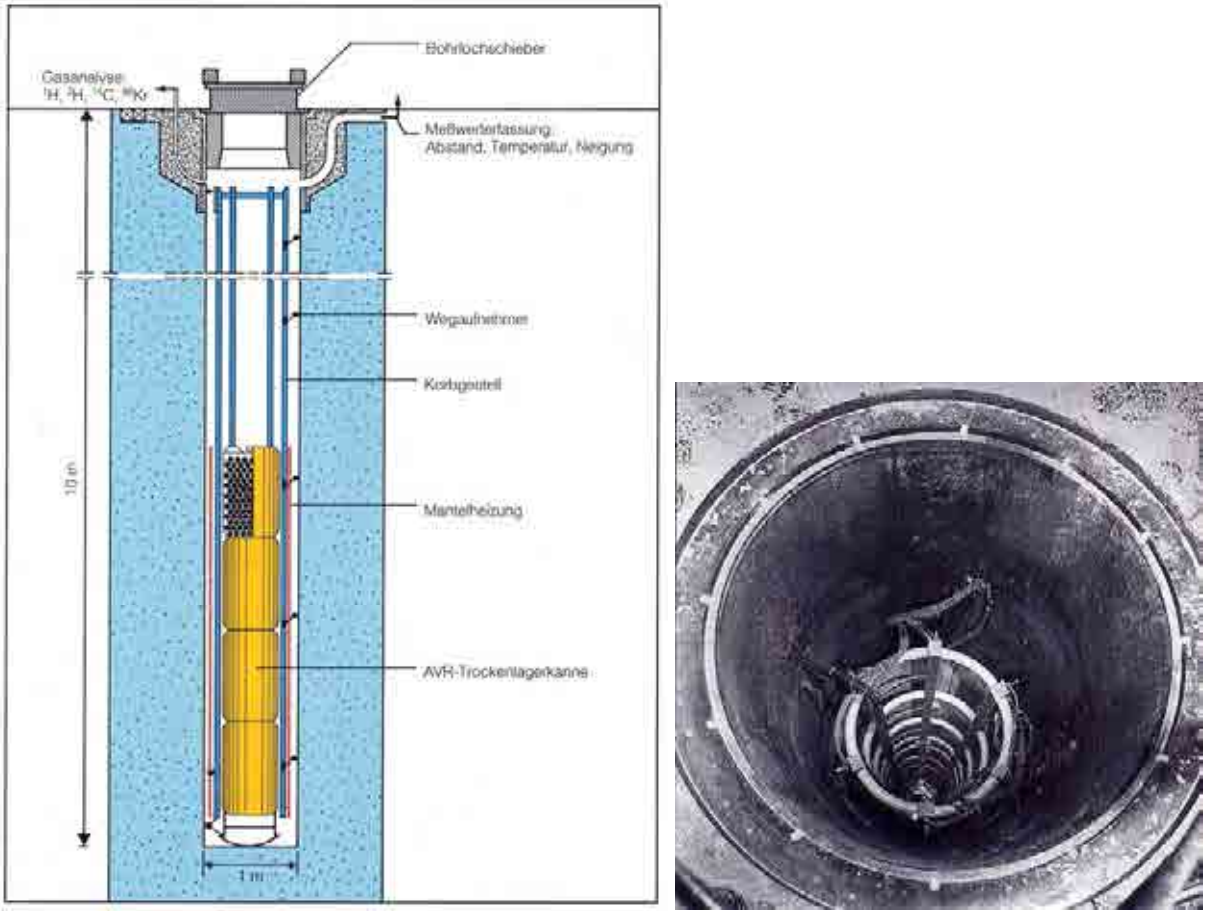

FIG. 11.10. Planned demonstration test for final disposal of spent HTGR fuel spheres.

11.1.2. United Kingdom

Late in the Dragon project, a programme of fuel recovery from still unirradiated fuel particles and compacts was initiated [75]. The amount of fuel to be treated was estimated to be about 31 kg of ^{235}U, its conversion into a saleable asset was considered a useful addition to the funds available. The first stage of the recovery process involved oxidation of the carbon of the fuel bodies and the outer carbon layers of the fuel particle coatings. For the particles with a TRISO coating, which was the majority of the fuel to be recovered, this meant a burning down to that layer. In the second stage, the particles were crushed and the product oxidised to remove any residual carbon from the particle kernels and the inner pyrocarbon layers. The residue was transferred to the Winfrith Analytical Chemistry Group for chemical purification of the U_3O_8. The retrieved fissile fuel was eventually shipped back to Germany.

There have been several studies of the options for decommissioning the Dragon reactor. In the absence of a United Kingdom disposal site for the disposal of high and medium level radioactive waste, the cost estimates resulting from these studies must be viewed as very approximate. It was anticipated that two factors would dominate the rate of decommissioning of the Dragon Reactor: the supply of finance and the ranking of the order in which the UKAEA's liabilities might be decommissioned. As Dragon was a gas cooled reactor with a low inventory of radioactive contamination, it was virtually certain that it will not rank highly for whatever funds are available for decommissioning.

The Dragon spent or partially spent fuel consisted of small uranium carbide or oxide spheres, approximately 1 mm diameter, coated with layers of carbon and silicon carbide. The particles were consolidated into compacts, small annuli ~45 mm long with a 30 mm central hole. Various other types of fuel and geometry were used during the 16 years of the experimental programme but due to the small size of the Dragon core, the amount of spent fuel was dominated by the amount of driver fuel needed to keep the reactor in operation.

These waste packages contain fuel consisting of uranium and uranium/thorium oxide and carbide kernels, graphite and some ZrC, covered with carbon and SiC layers to give particles of 0.1–0.25 mm. The fuel particles are mixed with graphite and compressed into compacts and some of the fuel has disintegrated. Chemically, the composition of the packages is

- ~95% graphite/pyrocarbon;
- ~5% heavy metal oxides and carbides (U/Th/Zr);
- ^{14}C — graphite and pyrolytic carbon;
- Th — Thorium oxide & thorium carbide (ThC & ThC_2);
- U — Uranium oxide and uranium carbide (UC & UC_2);
- Pu — Plutonium oxide and plutonium carbide (PuC).

Following defueling of Dragon, 75 000 fuel compacts were placed untreated in mild steel storage containers 2.62m long (Fig. 11.11) stored on-site in the Dragon fuel store, considered an interim measure. Long term storage in such containers, however, was inappropriate because of the possibility of corrosion of the cans. It was also considered that shorter stainless steel containers were easier to handle for transport off-site. Because of timing uncertainties, any new stainless steel canisters needed to be compatible with confirmed storage on the Dragon site. After it became obvious that corrosion could potentially affect the container integrity for long term storage, UKAEA required sorting and repackaging of the Dragon fuel into stainless steel containers to be then relocated to Harwell. The total number of containers shipped to Harwell was 85.

There is no detailed publically available experimental characterization or inventory data for the Dragon waste packages, and published inventories are based on calculations using inventory codes. The Dragon waste packages are the property of the Nuclear Decommissing Authority (NDA), and are classified in the UK as medium level active waste as their heat generation rates are low enough not to require engineered cooling [381]. The situation with regard to the Dragon spent fuel is untypical because of the low heat generation rates as fuel waste streams arising from the treatment of spent HTGR fuel would be generally classified as high level radioactive waste (HLW).

Since the core of the Dragon reactor was unloaded in December 1975, the installation is being held in a care and maintenance state. With the removal of all fuel and moderators, Stage 1 decommissioning of Dragon is considered complete. Currently, Stage 2 decommissioning of the secondary containment structures is expected to begin in 2038, with Stage 3 decommissioning of the reactors complete by 2053 [381].

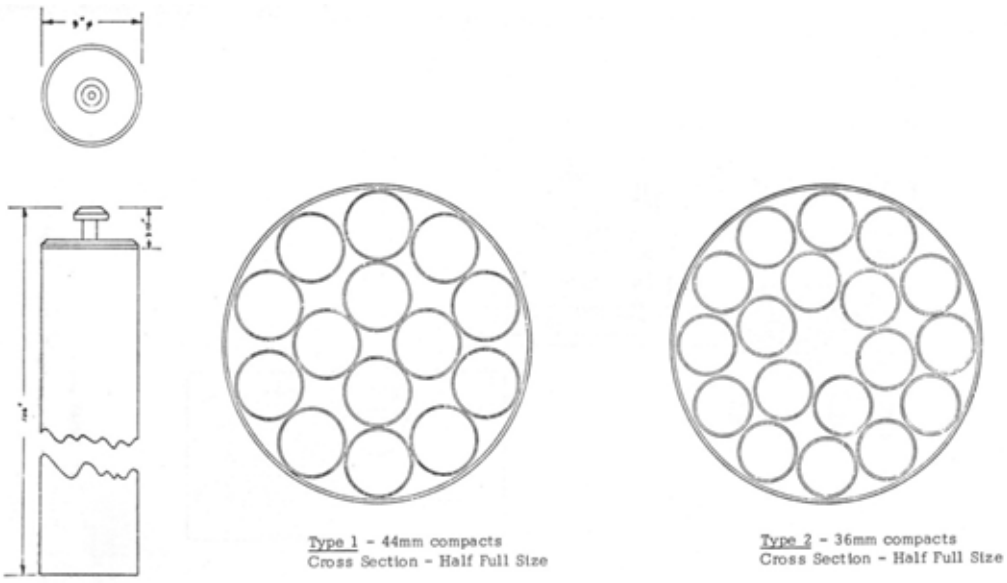

FIG. 11.11. Dragon irradiated fuel storage container.

11.1.3. USA

11.1.3.1. Peach Bottom

Peach Bottom (see also Section 5.1.6) operated successfully for seven years until it was shut down for decommissioning in late 1974 because it had completed its demonstration mission [382]. An extensive and highly successful end-of-life (EOL) R&D programme, jointly sponsored by US-DOE and EPRI, was conducted with the primary goal of generating real-time integral data to validate HTGR design methods with emphasis on reactor physics, core thermal/fluid dynamics, fission product transport, and materials performance, especially performance of the Incoloy 800 used for the steam generator superheaters [169].

(a) Plant D&D

The decision to decommission the Peach Bottom HTGR was based on a study of the benefits to be derived from further operation beyond depletion of Core 2 relative to the investment necessary to satisfy the NRC's requirement for a full term license. Based on technical and economic evaluations of several options, a mothballing (SAFESTOR) of the facility under a Part 50 Possession Only License was selected [383]. An important consideration in this decision was that Peach Bottom Unit 1 is co-located on a site with two much larger 1060 MW(e) BWR IIIs (Peach Bottom Units 2 and 3) which will undergo D&D beginning in ~2015 on the current schedule [384]. At that time, it should be a relatively small incremental task to complete the D&D of Unit 1, especially since the radioactivity will have decayed over several decades by that time. The following decommissioning activities for Peach Bottom unit 1 were accomplished [385]:

- Shipment off-site of all fuel and source materials for storage and eventual permanent disposal;
- Removal of liquids, pressurized gases, and flammable materials from the containment building;
- Decontamination and retirement of major equipment;

- Removal and burial of fission product traps, delay beds (parts of the He purification system) and other contaminated materials;
- Complete closure of the primary system;
- Release of the control room, laboratories, etc., for unrestricted use.

As indicated above, Peach Bottom decommissioning offered a unique opportunity to conduct EOL research and surveillance in a prototype HTGR. With the agreement of Philadelphia Electric Company, a contract was negotiated between General Atomic, ERDA (precursor to DOE), and EPRI, and in March 1975, the Peach Bottom EOL programme was initiated.

Three consecutive phases of the programme provided input to the HTGR design methods validation [169]:

(1) Nondestructive fuel and primary circuit gamma scanning;
(2) Destructive removal of materials samples from a steam generator and other primary circuit components;
(3) Laboratory examinations of removed components.

Component removal activities were performed largely by Catalytic, Inc., under subcontract to General Atomic, with site support services provided by Philadelphia Electric [386].

Component removal site work commenced with the establishment of restricted access areas and installation of controlled atmosphere tents to maintain a relative humidity < 30%. Mock-ups were used extensively to test and develop the tooling and to train operators under simulated working conditions. Examples are shown in Figs 11.12 and 11.13. Primary circuit ducting samples were removed by trepanning, and steam generator access was achieved by a combination of arc gouging and grinding.

Tubing samples were removed using internal cutters and external grinding. The special tooling used was developed by Power Cutting, Inc., under subcontract to Catalytic, Inc. Throughout the component removal phase, strict health physics, safety, and quality assurance programmes were implemented. Dose rates for certain operations, especially those involving the removal of steam generator tube samples, were significant (Fig. 11.14).

A total of 148 samples of primary circuit ducting and steam generator tubing were removed with no significant health physics or safety incidents. These samples were packaged in special inerted containers for shipment to General Atomic. Additionally, component removal served to provide access for determination of caesium plateout distributions by gamma scanning inside the ducts and for macro-examination of the steam generator from both the water and helium sides. Subsequent evaluations at General Atomic indicated excellent performance of the steam generator and other materials, together with close correlation of observed and predicted fission product plateout distributions [169].

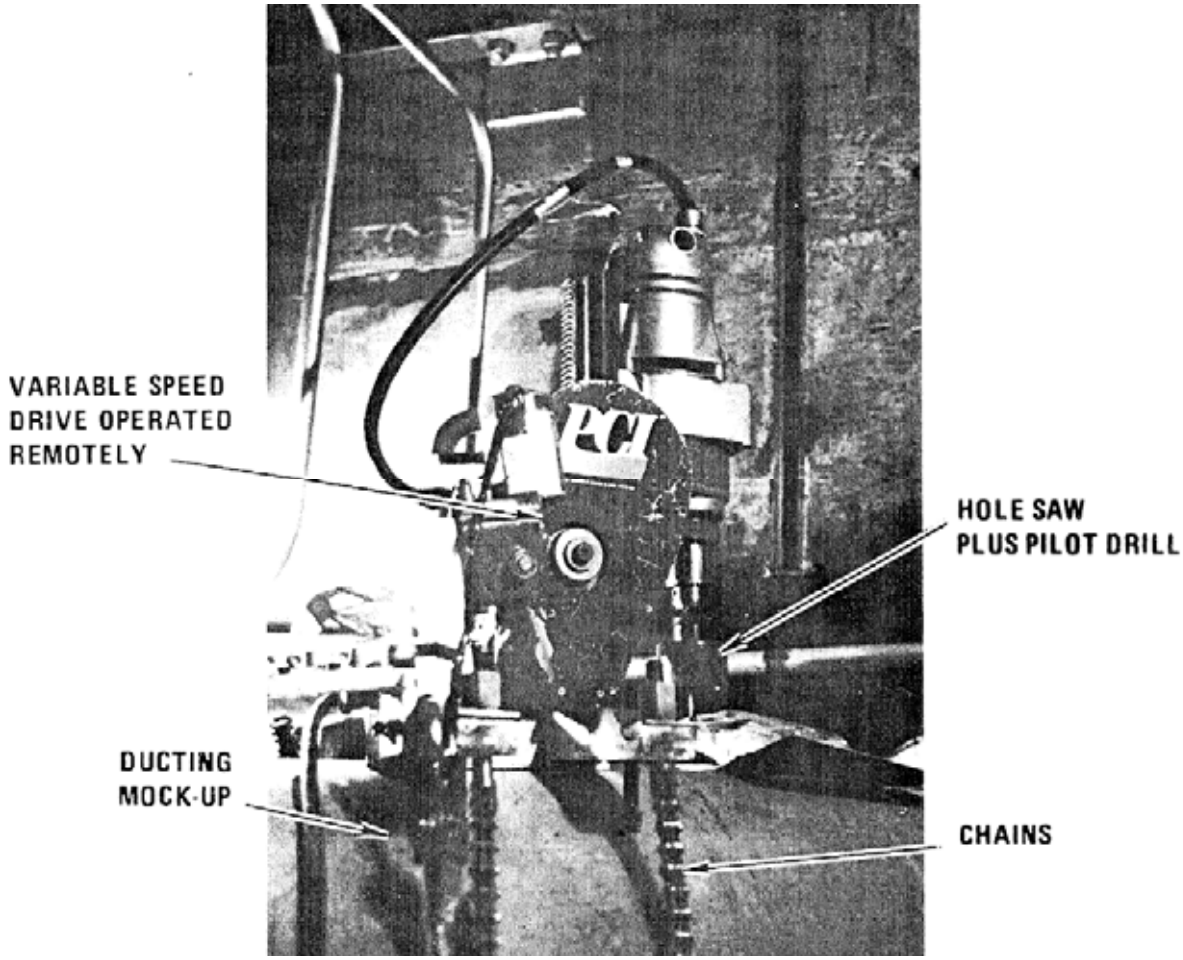

FIG. 11.12.Trepan cutting tool mounted on duct mock-up.

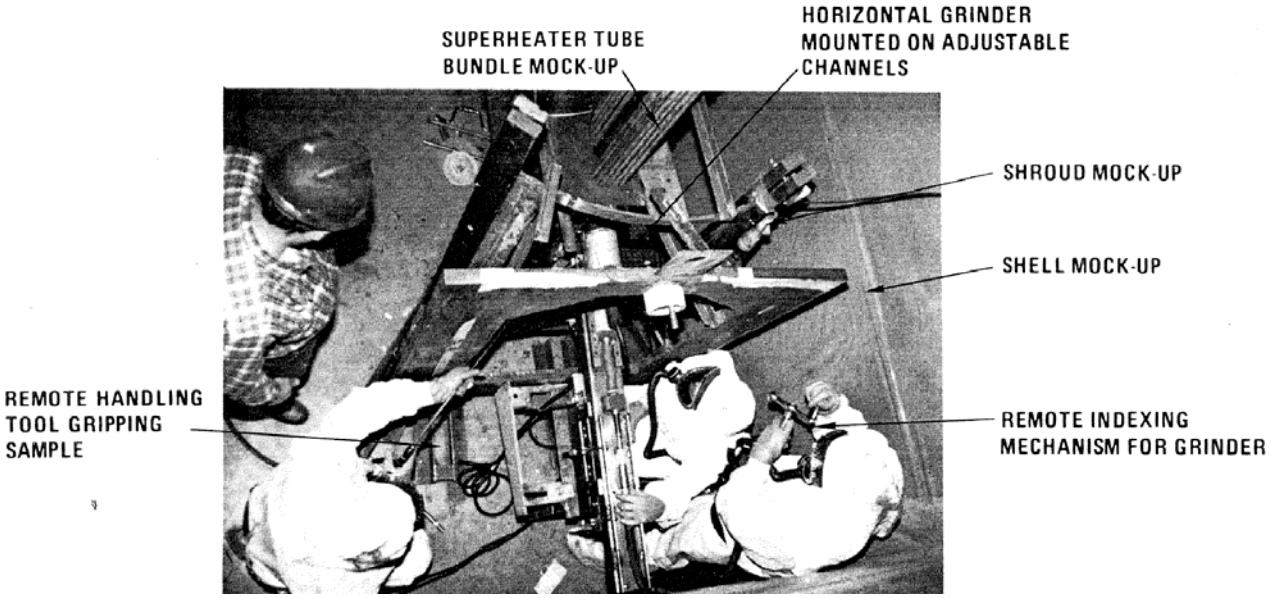

FIG. 11.13. Steam generator tub bundle mock-up showing practice tube sampling.

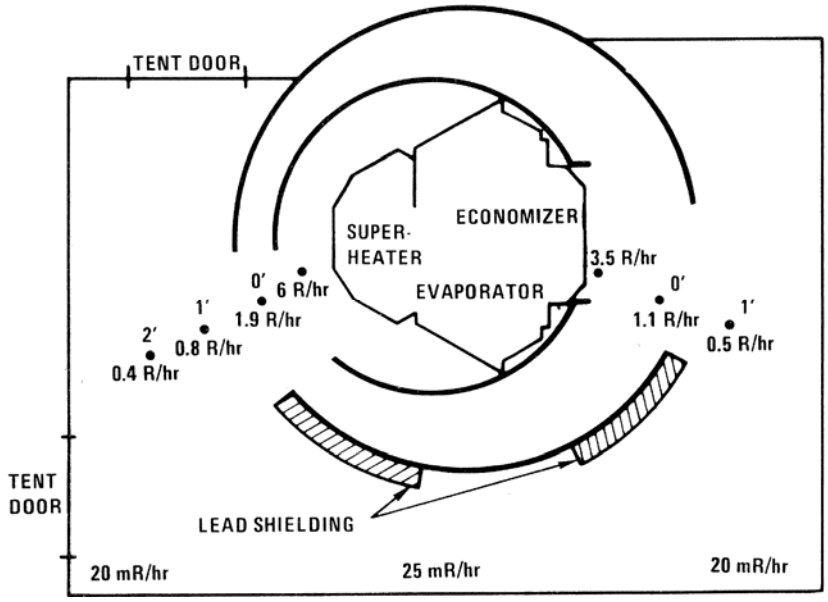

FIG. 11.14. Radiation levels during steam generator tube tampling.

(b) Spent fuel storage/disposal

Peach Bottom Unit 1 was operated with two batch-loaded cores, each consisting of 804 fuel elements. The basic Peach Bottom fuel element consisted of a graphite cylinder 89 mm (3.5 in) in diameter and 3.66 m (12 ft) long as shown in Fig. 11.15. Within each fuel element were 30 annular fuel compacts, each 76 mm (3 in) long, consisting of pyrocarbon coated fuel particles bonded in a carbonaceous matrix. The compacts were stacked on a graphite spine which was surrounded by a low permeability 89 mm (3.5 in) diameter graphite sleeve as shown in Fig. 11.16. The uranium (93.15% enriched in ^{235}U at BOL) and thorium within the compacts were in the form of carbides uniformly dispersed as coated particles in a carbonaceous matrix. Top and bottom reflectors were attached to the ends of the sleeve. The fuel elements were made of graphite and ceramic materials except for a stainless steel screen located near the bottom (cold end) of the fuel elements.

Core 1 operated from March 1966 (initial criticality), until October 1969, when it was shut down to replace the core [382]. In July 1970, the second core of Peach Bottom started commercial operation and in October 1974, having successfully completed its design lifetime of 900 efpd, it was shut down. Plant operation with additional new cores could have been routinely continued; however, since the research objectives had already been achieved, and commercial power generation alone from the plant was not sufficiently economical, the plant was permanently shut down. All spent fuel elements from both cores were stored in individually sealed canisters when they were shipped from the Peach Bottom site. Most of the spent fuel was shipped to INL. Some fuel test elements were sent to ORNL.

(i) PB core 1 spent fuel elements

As of October 1986 [387], there were 814 PB core 1 elements stored in open-field drywells at the Idaho Chemical Processing Plant (ICPP), Fermi-1 Blanket Storage Facility, at INL. These elements included 813 regular fuel elements and one fuel test element. Each element was placed in a sealed aluminum canister with a stainless steel liner at the plant site after removal from the reactor.

Because of fuel compact swelling in core 1 fuel elements, the outer graphite sleeve was fractured in ~78 fuel elements, and two elements were broken during removal. It was necessary to remove these fuel elements with a special failed fuel element tool. A salvage canister was also used at times to handle leaking canisters. A standard core 1 storage canister is shown in Fig. 11.17. The canisters were shipped to the INL in the PB shipping casks. The elements were positioned within the cask with a basket assembly. At INL, the entire basket assembly loaded with canisters was lowered into a drywell. A loaded basket normally holds 18 fuel elements.

(ii) PB core 2 spent fuel elements

As of October 1986 [387], there were 785 PB core 2 elements at the Irradiated Fuel Storage Facility (IFSF) at INL placed in special core-2 storage containers (Fig. 11.18). The remaining irradiated elements, including 33 test elements which were irradiated in core 2, were either shipped to GA or to ORNL for PIE. All spent fuel shipped to GA for PIE was subsequently shipped to INL. The spent fuel shipped to ORNL has been consigned to irradiated waste or placed in long term storage. The exact disposition of these elements can be determined from the shipping records at ORNL.

11.1.3.2. Fort St. Vrain

The FSV reactor (see Section 5.1.7) had many design features similar to the GT-MHR, e.g. graphite moderation, helium coolant, and very similar designs for coated fuel particles, fuel elements, and control rods (see Table 11.7 for a detailed comparison). The fuel compacts, which were inserted into machined blind holes in the fuel elements, were composed of TRISO coated fuel particles bonded together with a carbonaceous matrix into fuel compacts. Coolant holes, slightly larger in diameter than the fuel holes, were drilled in parallel through the block to allow the helium to be circulated through the fuel element to remove the heat generated in the fuel. A standard FSV fuel element, prototype for the GT-MHR, is shown in Fig. 11.19.

In 1973, Fort St. Vrain began operation under DOE sponsorship to demonstrate gas cooled reactor technology. By 1979, ownership of the plant had transferred to PSCo. The plant's operating life was cut short by poor performance, especially because of chronic water ingress problems associated with malfunctioning of the water-lubricated bearings used in the helium circulators [188]. The utility shut down Fort St. Vrain permanently in 1989, and began decommissioning activities in November 1992 (e.g. [388]). During the next three-plus years, 4000 m^3 (140 000 cubic feet) of irradiated waste — graphite blocks, support structures and concrete — were removed and shipped to the Hanford disposal facility in Richland, Washington. By early 1996, decommissioning was completed several months ahead of schedule and under the estimated $189 million budget [389]. The NRC released PSCo from its operating license in mid 1997 [185].

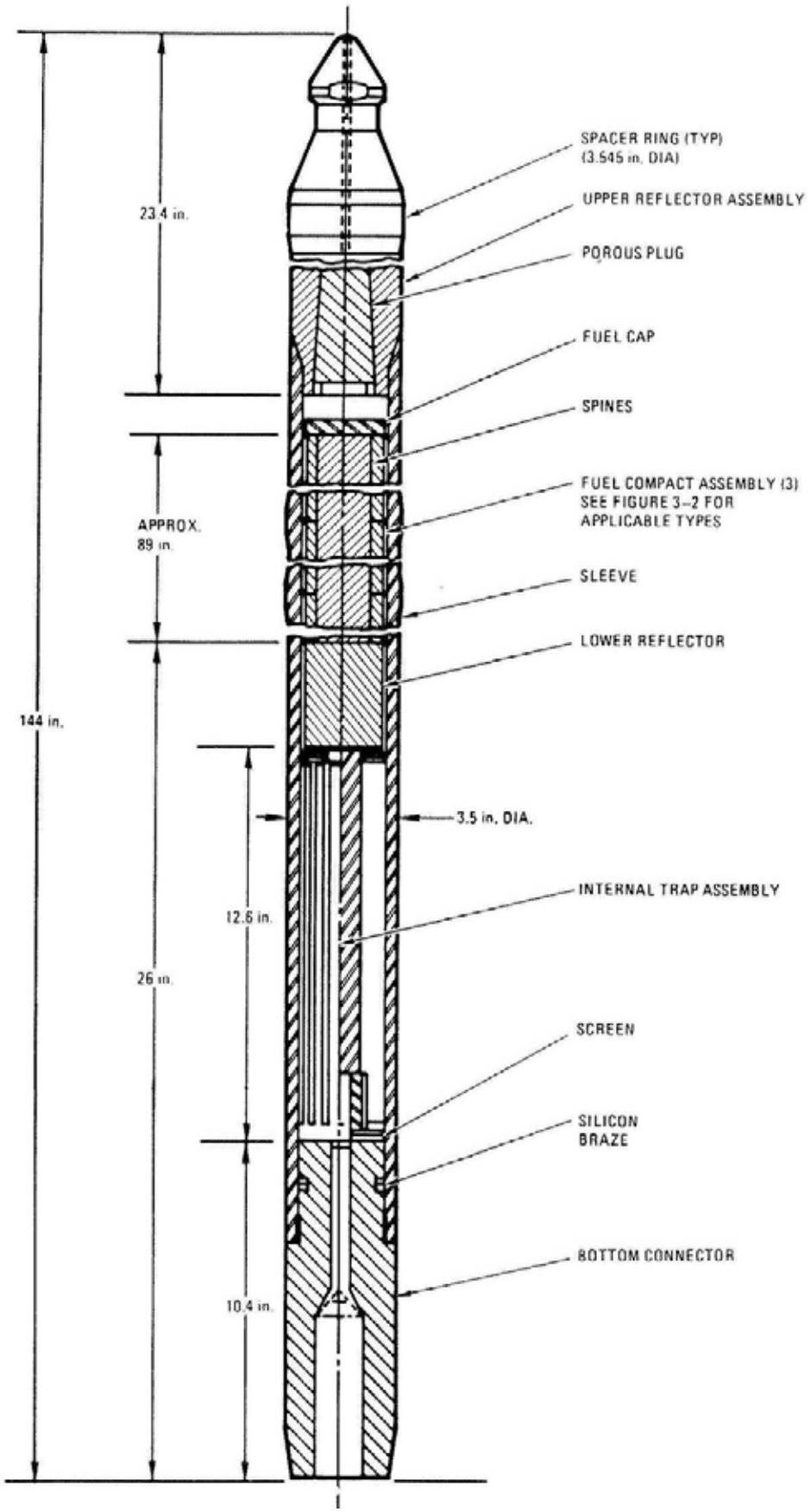

FIG. 11.15. Peach Bottom fuel element.

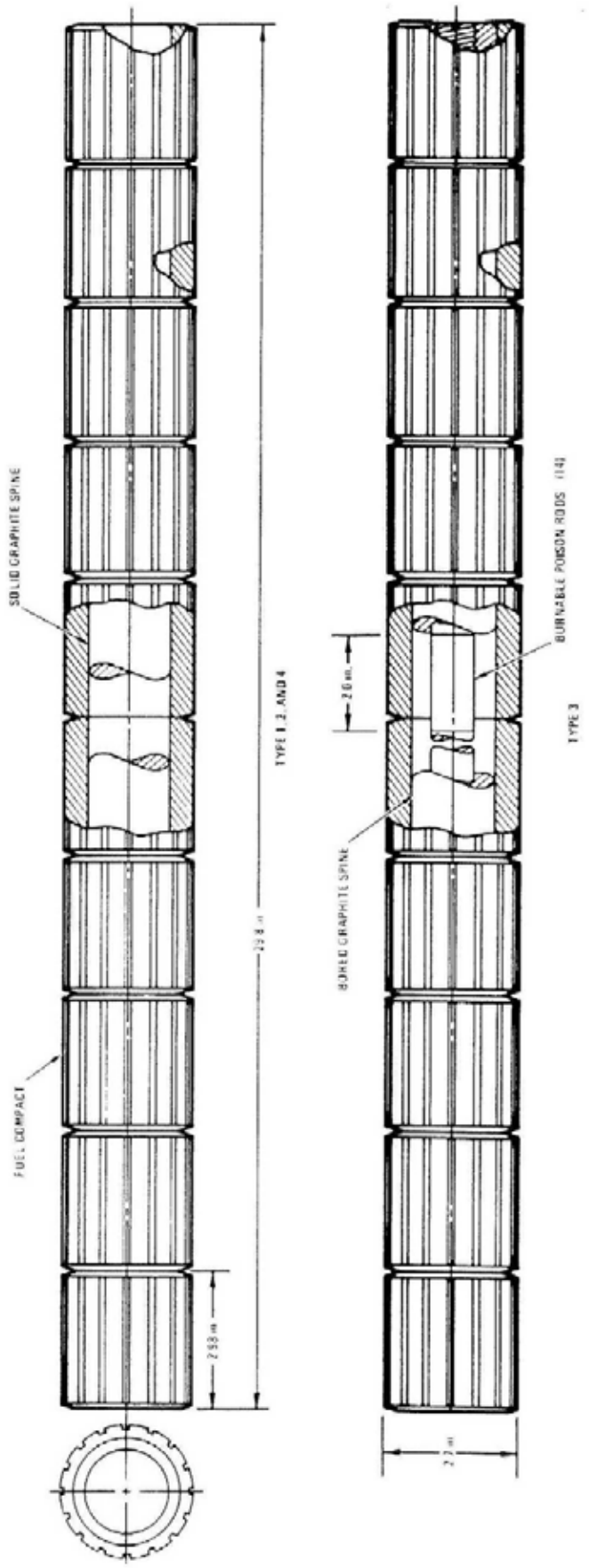

FIG. 11.16. Peach Bottom fuel compact assembly.

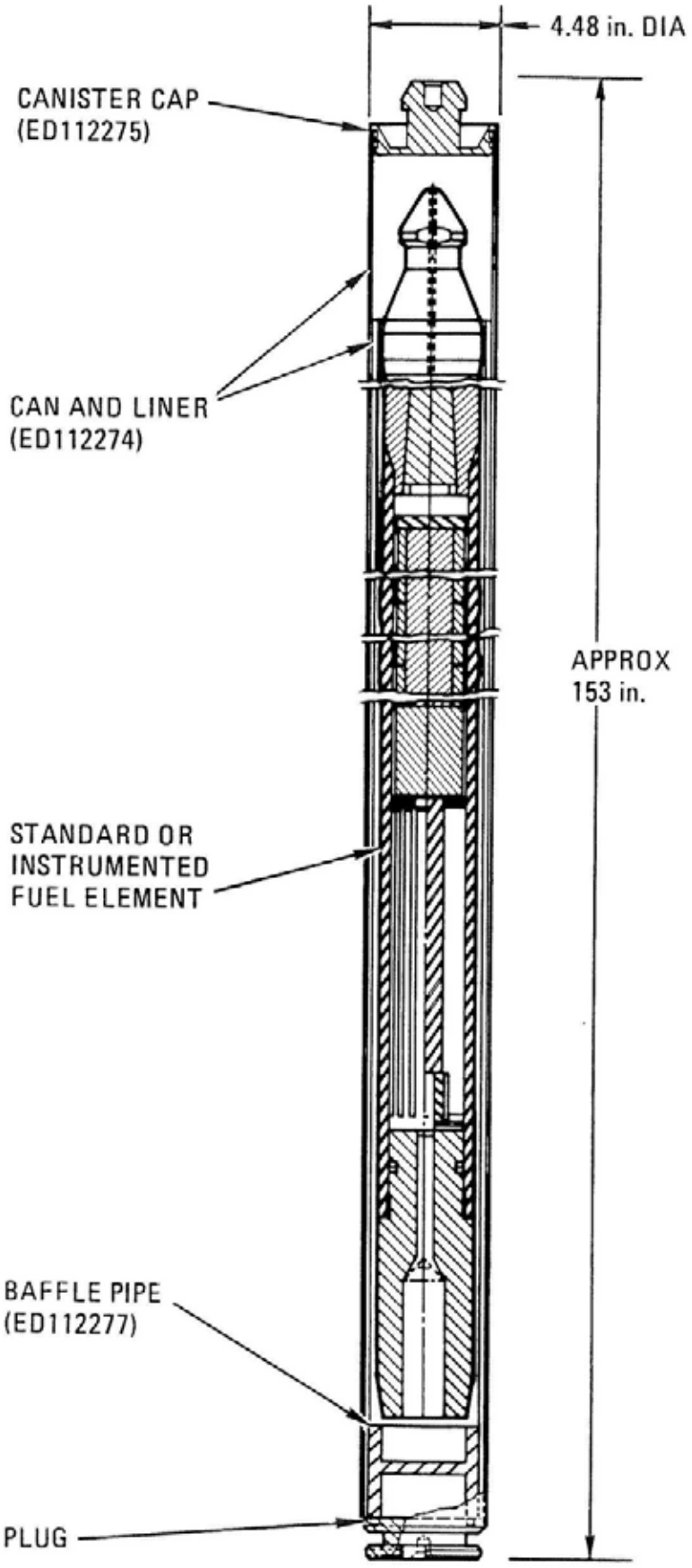

FIG. 11.17. Peach Bottom core 1 non-failed fuel element storage canister.

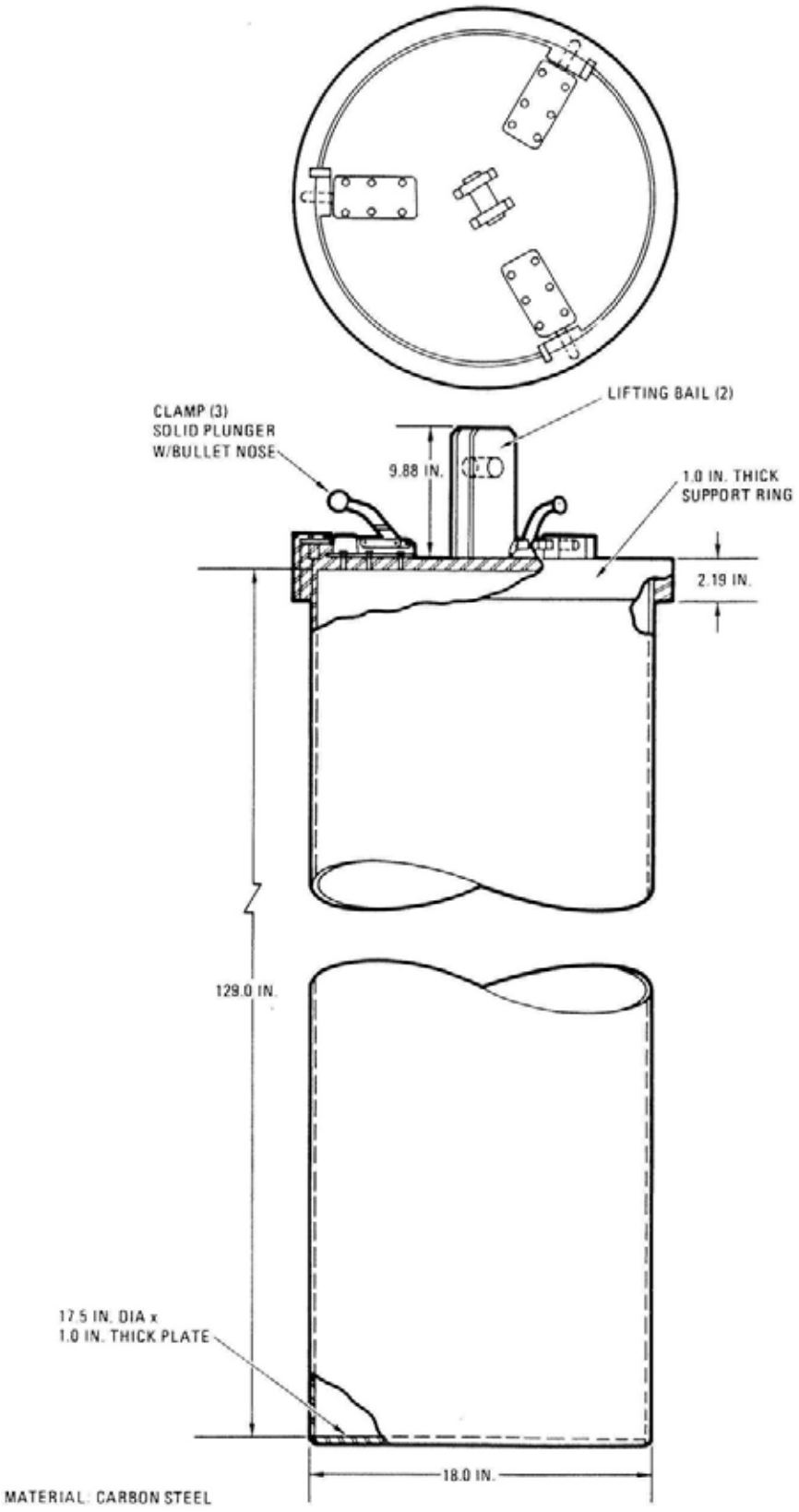

FIG. 11.18. Peach Bottom core 2 storage container.

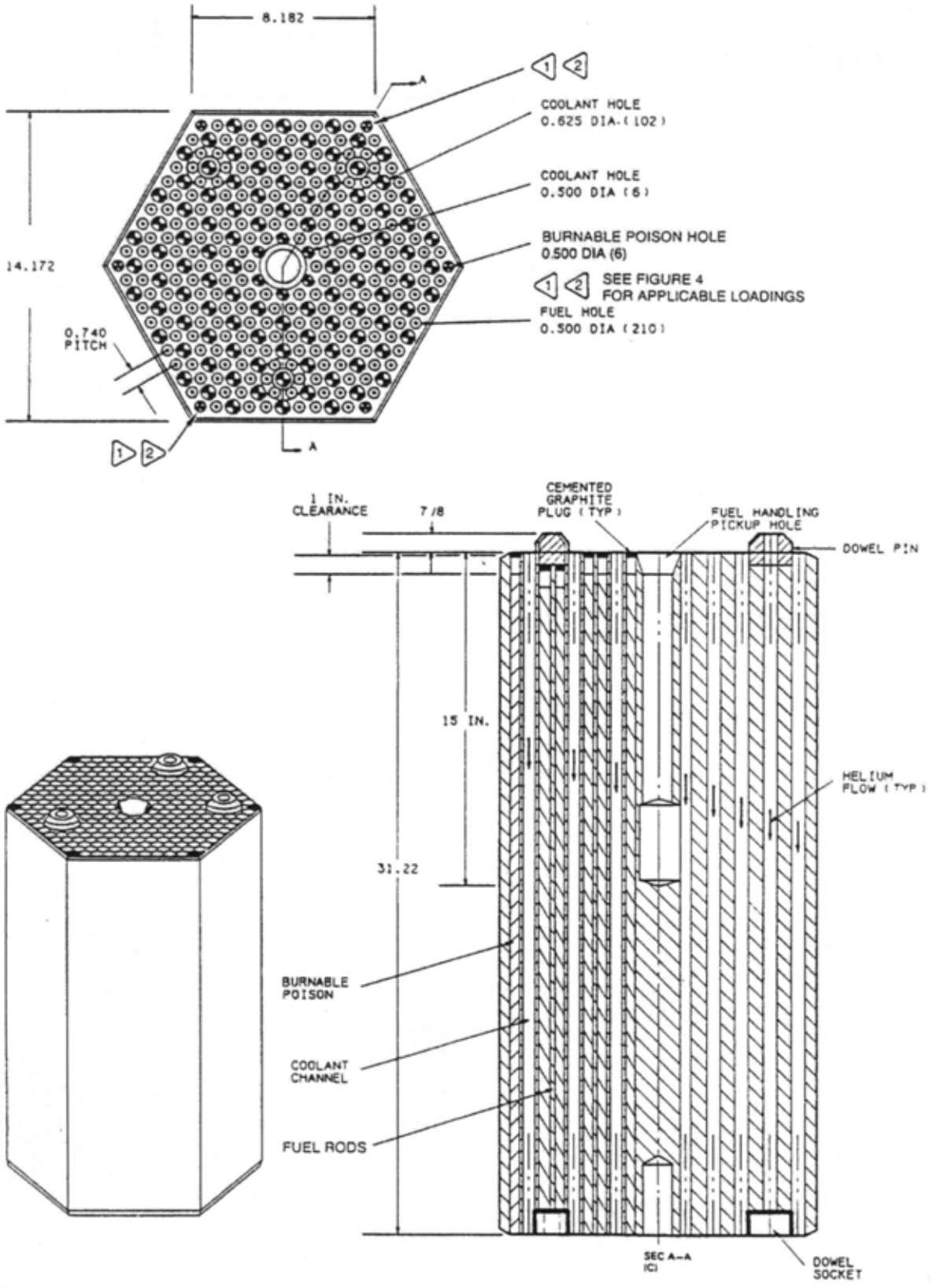

FIG. 11.19. Fort St. Vrain standard fuel element.

TABLE 11.7. COMPARISON OF FSV AND GT-MHR CORE DESIGNS

Parameter	FSV	GT-MHR
Reactor power (MW(th))	842	600
Power density in the core (MW/m^3)	6.3	6.0
Columns in the core	247	102
Fuel elements per column	6	10
Fuel elements in core	1482	1020
Core volume (m^3)	131.80	91.28
Core geometry	Cylindrical	Annular
Rows of elements in the inner reflector	0	5
Rows of elements in the core	10	3
Different radial/azimuthal loadings in core	6	6
Number of control rods		
Inner reflector	n.a.	0
Core	74 (37 pair)	12
Outer reflector	37	24
Number of shutdown holes in the core	37	12
Fissile material	93% enriched U	19.8% enriched U
Fertile material	Thorium	Natural uranium
Average loading per element (g) at time point:	BOIC [a]	BOEC [b]
Th-232	10 738	0
U-235 + other fissile	486	555
U-238 + other heavy metal	36	3716
Average heavy metal enrichment (%)	4.3	13.0
Radial leakage from core	2.0	10.5

[a] BOIC = beginning of initial cycle.
[b] BOEC = beginning of equilibrium cycle.

Fort St. Vrain was the first US nuclear power plant to be fully decommissioned following a substantial commercial operating history (e.g. [388, 389]. After decommissioning the nuclear portion of the site, PSCo re-employed the turbines and other non-nuclear buildings to generate natural gas-fired electricity [390].

(a) Plant D&D

Brief summaries of the successful FSV D&D project are given, e.g. in Refs. [388, 389, 391, 392]; of these, the paper by Fisher [388] is the most comprehensive. Nevertheless, it only provides an overview of the project, and the specific 'lessons learned' that could be applicable to a future D&D project for an advanced HTGR, such as the GT-MHR, are therefore limited. One of the reasons for the limited availability of detailed FSV D&D information is probably the intention of PSCo and the Westinghouse D&D team to patent and market some of the innovations developed during the FSV D&D project for future decommissioning efforts [389].

(b) Defueling

Defueling was the first step in the decommissioning process. There had been an agreement between PSCo and DOE to ship all of the FSV spent fuel to INL for long term storage prior to

a final disposition to be determined at a future date. Initially, spent FSV fuel was shipped to INL without incident, but political developments soon foreclosed that option. Consequently, PSCo chose to construct an on-site interim storage facility. The disposition of FSV spent fuel is described in more detail in a following subsection.

(c) Primary circuit component removal

Following the defueling, the most challenging phase of the FSV D&D project began: the removal of contaminated primary circuit components from the PCRV and then the destructive removal of the PCRV itself. Those components that had been contacted by the helium coolant were moderately contaminated by plated out fission products, such as ^{134}Cs and ^{137}Cs that had been released from the reactor core [393]. However, the dominant source of radioactivity was in-situ neutron activation of the primary circuit components, including the metallic reactor internals and (somewhat surprisingly) the PCRV concrete. To minimize occupational exposure, the PCRV was flooded with water to shield the workers from radioactivity. Using two circulating loops of 32 litres/s (500 gallons per minute) each and a side stream demineralizer, the water was filtered and processed to improve water cleanliness and clarity for the divers.

The major phases of the PCRV removal are shown schematically in Fig. 11.20 [391]. First, the 1200 t, 4.57 m (15 ft) thick, reinforced concrete top head was removed to provide access to the internal PCRV cavity. This step was accomplished by using diamond wire cutting cables and cutting the top head concrete into 12 pie shaped wedges. Each of these 100-ton wedges were radioactive due to neutron activation and read approximately 0.015 Sv (1.5 rem) per hour at the bottom of the wedge (Fig. 11.21, left). After removal from the PCRV, the wedges were placed in a large segmenting tent, cut into three pieces, placed in special steel cans and shipped as low level waste to Hanford. The ~25 mm (1 inch) thick steel PCRV liner was then cut using oxilance cutting tools, removed and also shipped as low level waste. At the completion of the top head removal effort, which took approximately nine months, the upper plenum of the reactor was open, and PCRV internals were accessible.

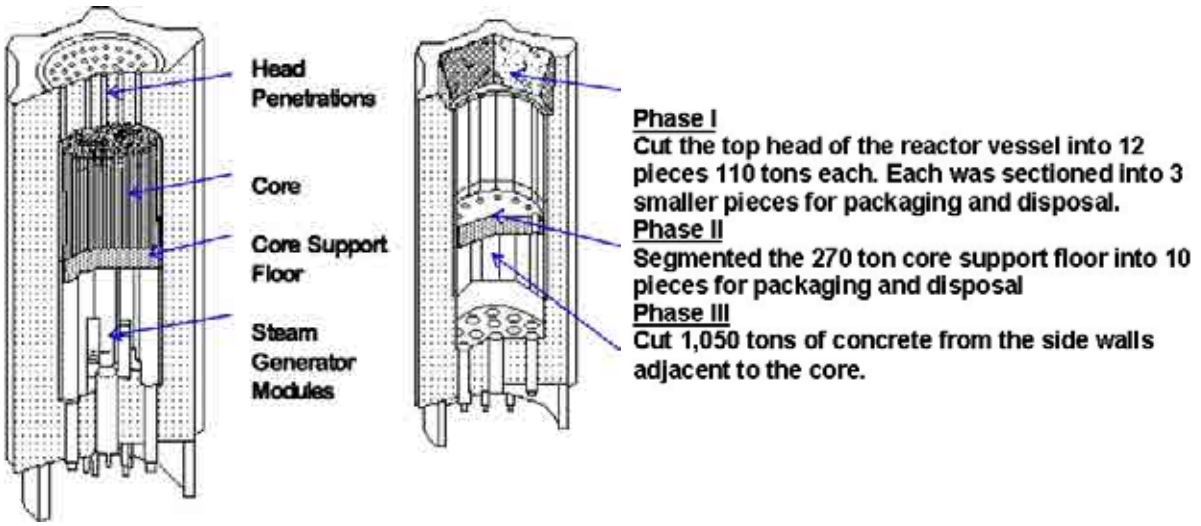

FIG. 11.20. Destructive removal of PCRV.

A rotating work platform was then installed on top of the PCRV. From this platform, more than 5000 graphite components were removed from the upper cavity. These components, some of which read as high as 0.3 Gy (30 rad) per hour, were removed and placed into a transfer basket that had been lowered into the water. The basket was then drawn into a lead-shielded bell and was subsequently taken to a hot cell. There, the basket was lowered into a shipping cask for shipment as low level waste to Hanford.

To expose the lower plenum, the core support floor (CSF) had to be raised and removed. The CSF was a 1.52 m thick, 9.45 m diameter, concrete structure encased in a carbon steel liner. Since the CSF was radioactive, steel shielding plates were positioned above the floor prior to its removal with a hydraulic jacking system. Shield water in the PCRV protected underwater divers which entered into the steam generator ducts that went through the core support floor. Once inside these ducts the divers cut their way to access the underside of the CSF where they severed all the connections so it could be raised and removed [392]. The CSF — due to the added weight of the shield plates, the attachments on the underside, and any entrained water — weighed 313 t during its removal. Again using diamond wire cutting technology, the CSF was sectioned, removed from the building, and shipped off site as low level active waste.

Once the CSF was extracted, all components within the PCRV were removed, including 12 steam generators and four helium circulators. Then, the activated concrete ringing the inside of the PCRV beltline and lower plenum areas was removed using diamond wire cutting technology (Fig. 11.21, right). The upper beltline concrete sidewall blocks were approximately 2.4 m wide, 0.76 m thick, and 12.8 m long. The lower plenum concrete blocks were approximately 2.4 m wide, 0.69 m thick, and 7.9 m long.

Steps also were required to radioactively decontaminate the entire PCRV cavity, the reactor building and the support buildings to meet the final acceptance criteria. Decontamination was also required on plant piping and the balance-of-plant systems and equipment. Depending on their levels of contamination, these systems either were cleaned and left in place or removed for disposal as low level waste (LLW).

During the dismantlement, decontamination and system removal process, 511 shipments, containing 2.6×10^6 GBq (~71 412 Ci) of LLW and weighing approximately 6800 t, were made without incident to the LLW burial site at Hanford. This effort was required to meet the NRC's release criteria of 0.05 μSv (5 μrem) per hour exposure rate above background 1 meter from previously activated surfaces and components, and less than 5000 disintegrations per minute (83 Bq) per 10 cm^2 for previously contaminated surfaces and components. The dose from all sources of residual activation had to be less than 0.1 mSv (10 mrem) per year based on an occupancy factor of 2080 hours per year.

(d) Final site survey

The final radiological survey process began in late 1994 and continued throughout 1995 and into 1996. The final survey plan, which required NRC approval, took more than six man-years to complete. The objective of the survey was to allow for unrestricted release of FSV from the NRC license. The actual survey consisted of characterization, final survey, investigation, and remediation measurements which accounted for the more than 400 000 physical measurements taken throughout the facility. This effort took more than 900 man-months over a period of one and a half years to complete. The final survey areas for the entire FSV site were divided in to 10 survey groups. Each area was evaluated to determine its classification as unaffected, suspect affected or non-suspect affected. By the end of the survey, over 300 areas had been surveyed.

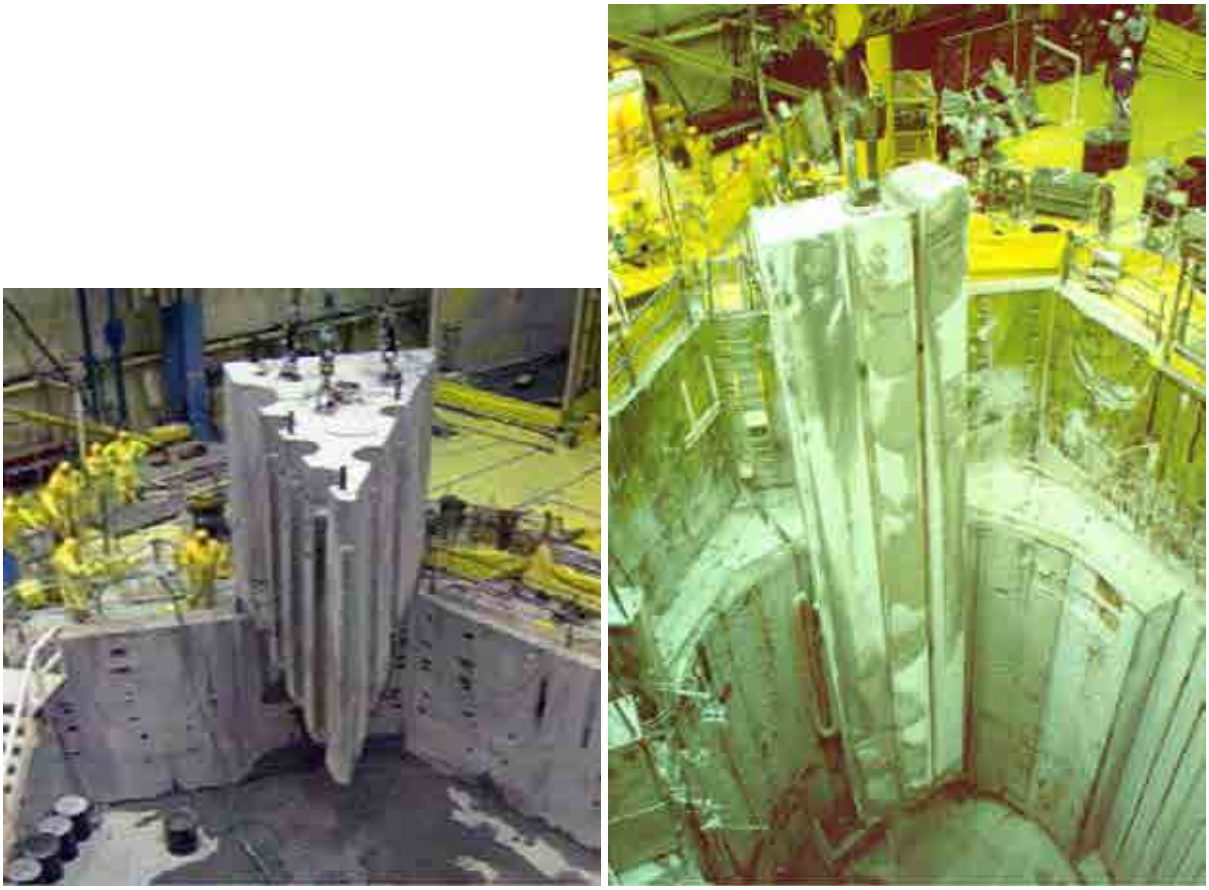

FIG. 11.21. Removal of PCRV top head (left) and side wall (right).

To confirm the accuracy of the final survey results, PSCo contracted for an independent verification survey, and the NRC conducted its own verification survey. Two specific issues that had to be addressed were hard to detect radionuclides and background determination. Hard to detect radionuclides identified at FSV were tritium and iron-55. Since these two nuclides cannot be easily measured as part of a general survey, site specific release criteria were determined for FSV. These release criteria were lower than the regulatory numbers to include the effects of the hard to detect radionuclide contribution. The background determination was important as well because the release criteria was $\leq$ 0.05 μSv/h above background. Background measurements both onsite and offsite varied between 0.02 and 0.35 μSv/h. Permission was obtained from the NRC to use gamma spectroscopy to directly measure exposure rate from licensed material in selected areas. This effort cost approximately $20 million (more than 10% of the total D&D project cost).

During the four-year decommissioning period, and despite the fact that personnel spent 340% more time in the radiologically controlled areas than originally forecast, the project experienced a total radiation exposure of only 3.8 man-Sv (380 man-rem). This number, approximately 12% under the original radiation exposure estimate, is roughly equivalent to the expected man-Sv exposure during one year of operation for an LWR. In addition, the FSV personnel contamination rates were only 54% and 24% of the contamination rates for typical pressurized water reactor and boiling water reactor outages, respectively. Moreover, the project maintained (including all subcontractors) a remarkably low lost-workday incident rate of 0.70 per 200 000 man-hours.

Of particular interest here are the potential 'lessons learned' from the FSV D&D project for the D&D of future MHRs, such as the GT-MHR. Some of the FSV experience is only marginally applicable because of the PCRV used in FSV as opposed the steel pressure vessels used in MHRs. However, two important areas that should be of direct relevance is the amount and distribution of radionuclides in the graphite structures, especially the permanent reflectors, and the efficacy of the various decontamination protocols used during the FSV D&D. Unfortunately, little quantitative information on these topics is provided in the available open literature references. Presumably, considerable data on these topics were generated during the comprehensive final site survey.

In recognition of the potential future value of these final survey data, EPRI funded the preparation of a report describing the FSV final site radiation survey process, the methods and techniques used, and particularly lessons learned [394].

(e) Spent fuel storage/disposal

The FSV active core was made up of 1482 hexagonal fuel elements stacked in columns six blocks high. Each fuel compact was formed by binding two types of TRISO coated fuel particles, so-called fissile and fertile particles, with a carbonaceous matrix: $(Th,U)C_2$ fissile particles, containing thorium and 93.15% enriched ^{235}U, and the ThC_2 fertile particles. The standard FSV fuel element had no metallic components. A few fuel elements also contained neutron sources which were contained in stainless steel canisters, and selected surveillance and test elements contained small dosimeters. In addition, numerous fuel elements had blind holes at the corners of the block that contained burnable poison in the form of boron carbide particles bonded together in a carbonaceous matrix analogous to the fuel compacts.

Prior to the final shutdown of the FSV reactor, there were three refuelings of one segment each; each segment consisted of about one sixth of the core. The first 726 discharged fuel elements were shipped to the INL [395] and stored in a special convection cooled facility built for that purpose at the ICPP facility. There is still unused storage space, but in 1988 the governor of Idaho blocked any further receipts of FSV spent fuel in the state of Idaho. The remainder of the fuel is now stored in an independent storage facility [396] which was built on the FSV site. Other details on the FSV spent fuel can be found in [397].

The FSV spent fuel elements stored at the ICPP are in 6.4 mm (0.25 in) thick carbon steel canisters with a diameter of 457 mm (18 in) and a length of 3.35 m (11 ft). They have ungasketed lids that are held in place by remotely operable clamps. Each canister contains four FSV fuel elements with a total of 182 canisters at the INL site.

The FSV 'independent spent fuel storage installation' (ISFSI) shown in Fig. 11.22 is a 'modular vault dry store' (MVDS) facility which was designed for interim storage of FSV spent fuel for 40 years [396]. Each fuel storage container can accommodate up to six fuel elements or up to 12 half-height reflector elements stacked vertically. A matrix of 45 fuel container storage positions is provided within each of six concrete vault modules that were designed for shielding and criticality control. The medium within the storage container is ambient air, and the decay heat is removed by once-through, buoyancy-driven air flowing across the exterior of the storage containers. The entire end-of-life FSV core was transferred to the ISFSI during the December 1991, to June 1992, time frame. It is planned that this FSV spent fuel will eventually be transferred to a geologic repository for permanent disposal.

FIG. 11.22. FSV independent spent fuel storage installation.

11.2. WASTE CONCEPTS FOR PRESENT AND FUTURE HTGR DESIGNS

11.2.1. China (HTR-10)

11.2.1.1. HTR-10 fuel storage

The site of HTR-10 is located in the Institute of Nuclear Energy Technology (INET). INET itself is located in the northwestern suburb of Beijing city, about 40 km from the city centre. The storage of the spent fuel elements in the HTR-10 reactor building is surely the intermediate storage. The issues of handling, intermediate and final storage of the spent fuel elements remain to be studied.

The fuel elements are designed to pass the reactor five times in average to reach an average burnup of 80 GW•d/t U after about 1080 efpd. According to calculations, the discharged spent fuel elements have a burnup distribution between 74.3 and 87.1 GW•d/t U. In the case of full power operation, 25 spent fuel elements per day are generated. The concrete compartment inside the reactor building is big enough to store all spent fuel elements of the HTR-10, about 90 000 fuel spheres, which are expected to accumulate over 20 years of operation on an average load factor of 50%.

The spent fuel elements are discharged into containers [398]. Each container is designed to receive 1000 spent fuel elements. The container is made of stainless steel and has an outer diameter of 622 mm and a height of 1000 mm. Thee spent fuel containers are stored in a concrete compartment inside the reactor building and cooled by natural air convection.

The intermediate storage system in the reactor building consists mainly of receiving the spent fuel elements, transporting and storing the container with the spent fuel elements. The intermediate storage system is located at the bottom of HTR-10 reactor building at the height level of -18m. There are 45 storage wells in the spent fuel store. These wells are arranged in a 5×9 array. The distance between the well centres is one meter. Two spent fuel storage containers are perpendicularly stacked in each well.

11.2.1.2. Treatment and storage of radioactive wastes

The waste management strategy for the HTR-10 is guided by the following objectives:

- Prevention of the generation of waste;
- Minimization of the generation of waste;
- Clearance of waste for re-use and recycling;
- Disposal of waste.

(a) Treatment of radioactive solid waste

The radioactive solid waste from HTR-10 mainly consists of

- evaporated residuals and concrete solidification waste;
- worn ion-exchange resin from wastewater disposal facilities;
- filters and other absorbing components in helium purification system and its regeneration system as well as ventilation system;
- worn equipment and parts;
- graphite powder caused by the abrasion of fuel balls;
- other low active solid wastes.

The quantity of the above mentioned radioactive solid wastes will be approximately 5 m^3. The treatment strategy of the radioactive solid wastes is that

- the radioactive waste will be classified and collected into the 200 L standard waste barrels according to their kind and radioactive level;
- the evaporated residuals and loose solid waste such as molecular sieve and active carbon will be disposed of by concrete solidification method;
- the used ion exchange resin will be temporarily stored;
- the compactable dry solid waste will be compressed, packed, and collected in the 200 L standard waste barrels;
- the radioactive solid waste will be temporarily stored at the HTR-10 site and transported at regular intervals to the nation′s regional waste repositories.

(b) Treatment of radioactive liquid waste

The radioactive liquid waste from the HTR-10 mainly consists of

- condensed liquid from helium purification system;
- leakage liquid waste;
- waste water from the decontamination rooms, solidification system, and laboratories;
- waste water from decontaminating equipment and flushing floor;
- waste water from the laundry and shower, etc.

Liquid radioactive wastes are classified into three categories based on their origin, radioactive level, and chemical composition. Category I mainly consists of condensed liquid from helium purification system under normal operation and at accident condition. Category II mainly consists of leakage liquid waste, waste water from decontamination rooms, solidification system, and laboratories, and from decontaminating equipment and flushing floor. Category III mainly consists of the waste water from the laundry and shower, etc.

The waste water quantity of category I is approx. 0.2 m^3 per year. It will not be treated, but rather collected in a container for temporary storage. The waste water quantity of categories II and III is approximately 60 and 600 m^3 per year, respectively. They will be collected in containers that have a net capacity of 5 m^3 each, then transported to the INET waste water treatment workshop if the radioactive level in the waste water is greater than the level prescribed for release to the environment. The system of radioactive waste water treatment consists of the following components: waste water receiving pool, filter, evaporation facility, cooler, ion exchange units, clear water pool, and other auxiliary facilities.

If a decision sampling determines that the activity concentration of the treated waste water is lower than 1.85 Bq/L, it is possible to discharge it under control. If quality permits, the regenerated and treated waste water will be recycled.

(c) Treatment of radioactive gaseous waste

The gaseous radioactive waste from HTR-10 primary circuit, helium purification system, fuel handling system as well as ventilation system and others will be treated prior to release to the atmosphere via the high stack. Treatment comprises pre-filtration, absorbing and final absolute filtration to remove the entrained reaction gases, vapours and particulate matter.

11.2.1.3. Decommissioning consideration

Decommissioning of the HTR-10 is subject to the Chinese national standards and codes for research and test reactors [399]. China′s national nuclear safety authority has issued the following documents which are applicable to the decommissioning work of HTR-10:

- Nuclear safety regulation HAF 1000-1 ‘Safety Regulations on the Design of Research Reactors’;
- Nuclear Safety Regulation 1000-2 ‘Safety Regulations on the Operation of Research Reactors’;
- Regulatory Guide HAF 1004 ‘Decommissioning of Research Reactors and Critical Facilities’.

Regulations require that the issues of decommissioning a reactor should be considered already in its design and operation stages. Technical approaches of decommissioning HTR-10 depend on a number of aspects, but mainly on the national strategies. The designed life of the HTR-10 is 20 years. Until its decommissioning, much development is expected in the national nuclear strategies, including the fuel cycle/waste disposal strategies. But also INET will conduct much development work. The decommissioning programme for the HTR-10 will be strongly dependent on the status of these developments then.

Independent of the above strategic development, the following activities will be performed when HTR-10 is to be put out of service:

(1) After sufficient cooling time, the fuel elements will be removed from the reactor core into the storage containers. All spent fuel storage containers are supposed to be transported to places designated by the nation for further treatment or storage.

(2) Removable radioactive materials will be removed from the HTR-10 site and transported to the nation′s regional waste repositories. The following radioactive materials are relevant to the decommissioning work of HTR-10:

- Metallic materials: the reactor pressure vessel and metallic core internals, the steam generator and its pressure vessel, the components of the fuel handling system and the reactor shutdown system, components and pipes of some auxiliary systems, mainly of the helium purification system and its regeneration system;

- Graphite and carbon bricks of the core internals including dust;

- Filters and other absorbing components of the helium purification system and its regeneration system as well as the ventilation system.

- Routine liquid and solid radioactive materials which were produced during reactor normal operation.

(3) For the remaining components and structures, decontamination will be made as much as reasonably possible.

(4) Radioactive site and components will be sealed or blocked, the facility being under appropriate monitoring and surveillance.

11.2.2. Japan (HTTR)

11.2.2.1. Fuel storage system for the HTTR fuel

The fuel assembly of the HTTR is discharged from the core after 660 efpd. The maximum bumup is designed to be 33 GW•d/t as a block average value [98]. A flow diagram of fuel treatment of the HTTR facility [400] is shown in Fig. 11.23. Fuel handling and storage systems in the HTTR building are shown in Fig. 11.24. The fuel handling machine moves new fuel assemblies from the new fuel storage cell to the reactor before operation. Upon reaching the final burnup, the fuel assemblies are transferred by the fuel handling machine to the spent fuel storage pool in the reactor building.

The spent fuel storage system in the reactor building consists of a spent fuel storage pool, pool water cooling and purification system, etc. The spent fuel storage pool in the reactor building, which is fabricated of ferroconcrete with sufficient shielding for personnel, includes 63 storage racks as shown in Fig. 11.25 [400]. It can store spent fuel assemblies of about two core inventories. The spent fuel storage pool is lined inside the pool with stainless steel to prevent pool water leakage. When pool water leaks, the leakage can be detected by monitoring the water from the leakage check ditch which is located within the lining. The storage rack forms a vertically arranged cylindrical vessel with a shielding plug, and has sufficient distance to the adjacent storage racks to maintain subcriticality. The pool water cooling and purification system removes the decay heat from the spent fuel assemblies. The maximum decay heat from the two core inventories of spent fuel assemblies is evaluated to be 55 kW and the cooler is designed to keep the water temperature below 65°C.

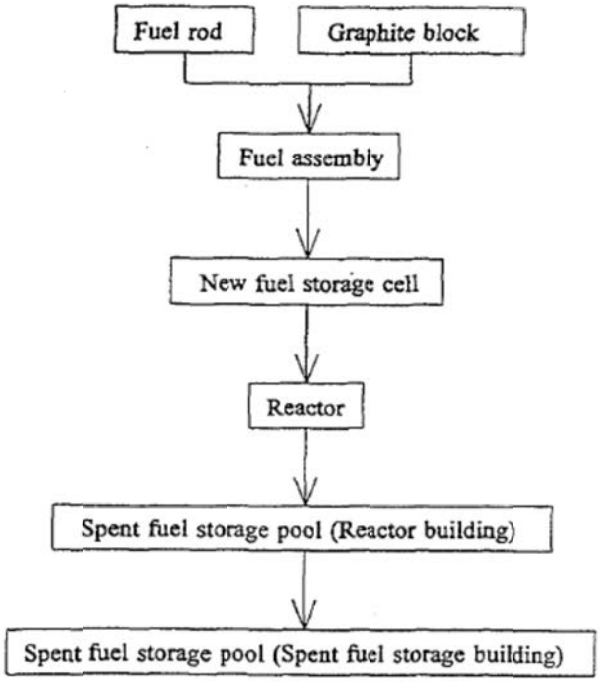

FIG. 11.23. Fuel treatment flow in the HTTR facility.

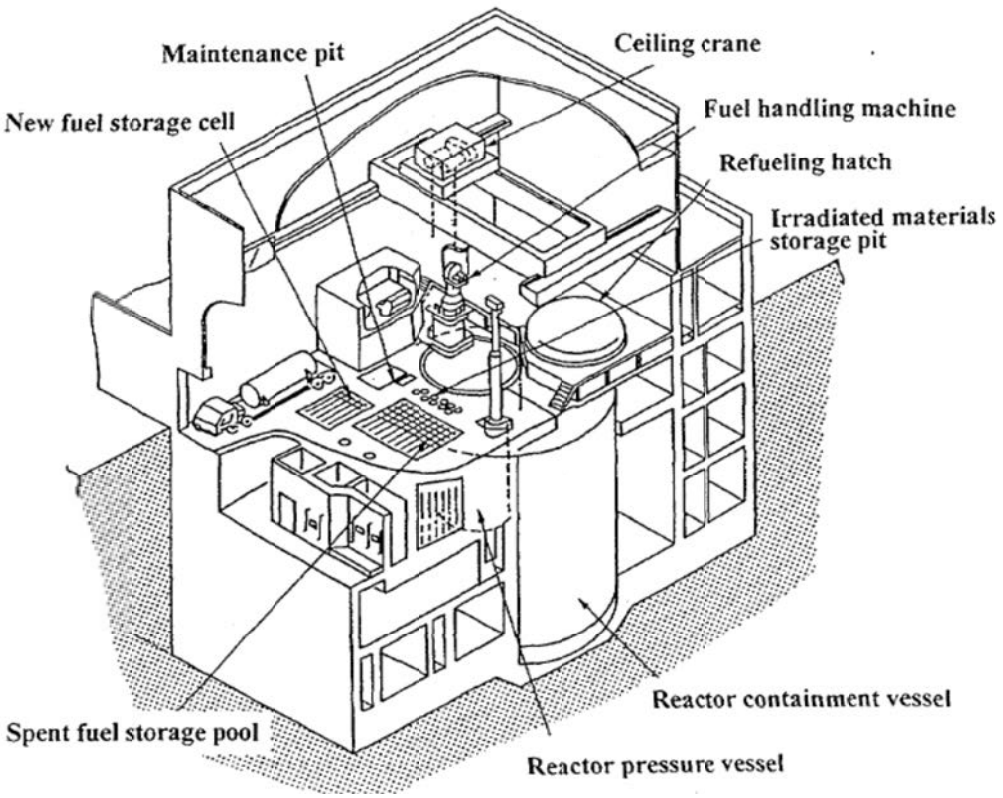

FIG. 11.24. Fuel handling and storage systems in the HTTR.

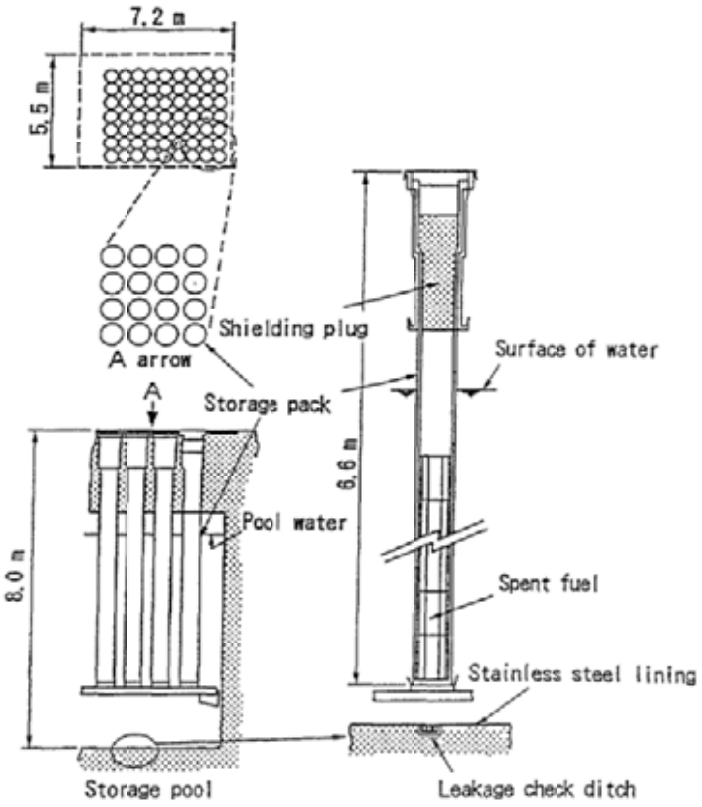

FIG. 11.25. Spent fuel storage system in the HTTR reactor building.

After more than two years of cooling in the fuel storage pool, the spent fuel will be transferred from the reactor building to the air cooled spent fuel storage racks in the spent fuel storage building. Storage capacity of the air cooled spent fuel storage pool will be about ten core inventories.

11.2.2.2. Reprocessing procedures for HTTR fuel

According to the basic Japanese concept, all spent fuels including the HTTR fuel shall finally be reprocessed. Estimated quantities of radioactivity in the HTTR are listed in Table 11.8 [400].

TABLE 11.8. QUANTITIES OF RADIOACTIVE NUCLIDES IN AN HTTR CORE LOADING

	Quantity (Bq/fuel assembly)
Actinides (and daughters)	8.1×10^{15}
Fission products	3.5×10^{16}
Carbon-14	2.1×10^{9}
Tritium	8.0×10^{7}

JAEA's studies on HTGR fuel reprocessing were focused on the applicability of the graphite–CO_2 reaction technique and jet grind method to head end reprocessing. A block diagram of JAEA's head end reprocessing is illustrated in Fig. 11.26 [400]. The graphite–CO_2 reaction technique has been developed to reduce CO gas release in the burning process of the fuel compacts and fuel kernel. The jet grind method was investigated to reduce maintenance works of roll-gap clearance of the roll grinder which was used to remove the SiC layer from burned

SiC particles. The feasibility of these methods was approved through laboratory scale experiments and the research and development work was terminated. Pilot scale tests will be carried out to confirm the applicability of these methods to the HTTR spent fuel in future.

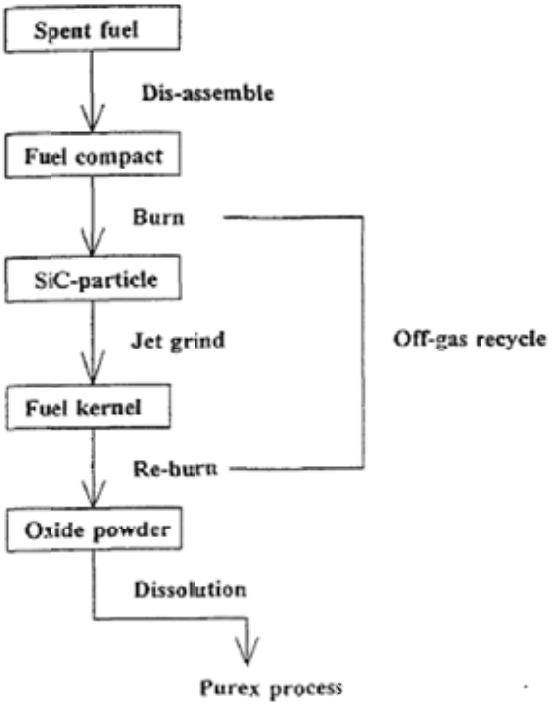

FIG. 11.26. Block diagram of JAEA head end reprocessing.

(a) Uranium recovery experiences in fuel fabrication process

In the fuel fabrication process, uranium in the as-fabricated fuel compact is recovered by the process illustrated in Fig. 11.27 [400]. Since this process is almost the same as burn-grind-leach method in the head end reprocessing method of the spent fuel, useful data can be obtained to investigate the head end reprocessing method.

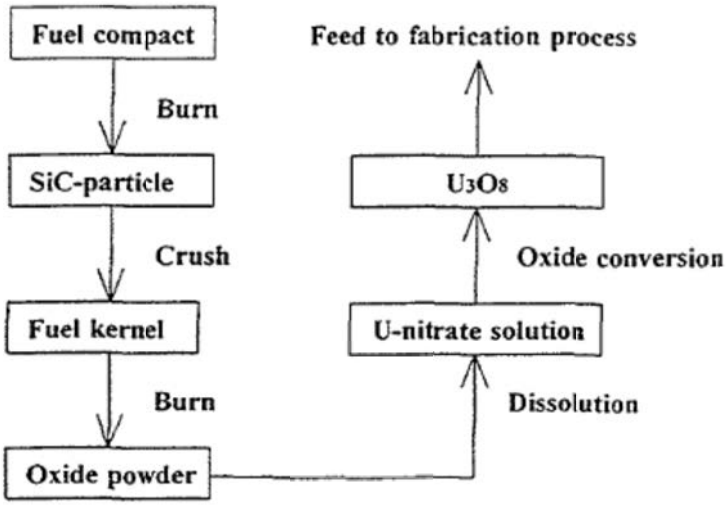

FIG. 11.27. Block diagram of uranium recovery in fuel fabrication process.

The SiC layer is removed from burned SiC particles by the grind–crush method. For this purpose, a hard disk crusher is used in the recovery process as is shown in Fig. 11.28. The crushing gap was selected to meet the following criteria: (i) crush efficiency of coated fuel particle should be as high as 100%; and (ii) UO_2 kernels should not be crushed in order to prevent uranium contamination in the crusher. The crush efficiencies were investigated as a function of the crushing gaps. In the recovery process, a 0.60 mm crushing gap was selected. Through the fabrication of the HTTR first loading fuel, about 100 kg of UO_2 was recovered. The experience shows that 100% of crush efficiency could be obtained and no re-adjustment of the crushing gap was needed during the fabrication.

JAEA studied the graphite–CO_2 reaction and jet grind method as a head end reprocessing technique to reduce CO gas release and maintenance for controlling roll-gap clearance in the roll grinder. The feasibility of this method was approved through laboratory scale experiments.

The reprocessing of HTGR fuel has also been studied by the Japanese company NFI under the condition that the same process be applied as that for LWR fuels [401].

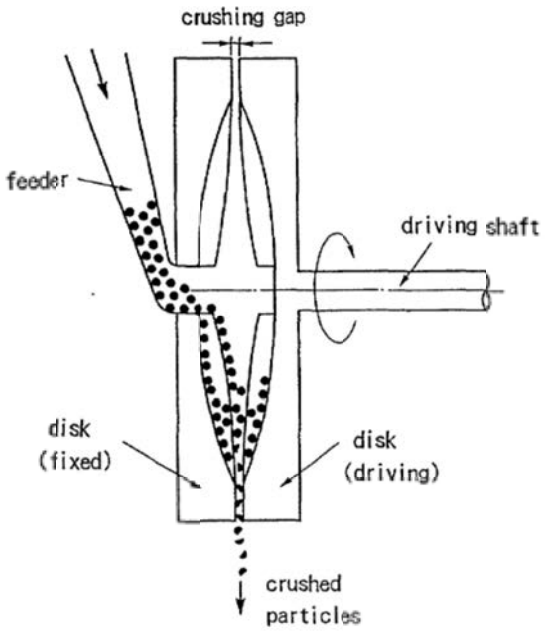

FIG. 11.28. Hard disk crusher in recovery process.

(b) Separation of coated fuel particles from fuel compact

The first step of the head end process is to take out the coated particles from the fuel compacts. Some techniques, such as electrical method, chemical method, mechanical crushing method, or combustion method, were already proposed for this step. A complete separation of particles and graphite is not possible by the electric method. Drawbacks of the chemical method are the low separation efficiency, difficulties in the recovery of chemicals, and corrosion of materials. The recovery rates of graphite and fuel particles are also low in the mechanical crushing method. After consideration of these features of each method, the combustion method with burning of graphite in an air environment was selected as reference method for the further investigations. This method has been already adopted, on a smaller scale, in the recovery of faulty coated particles in the HTTR fuel production plant.

(c) Removal of the silicon carbide layer from the coated particles

After removal of graphite by burning, the second step of the head end process is to take out the fuel kernels from the chemically stable SiC layer. Some mechanical methods for crushing the SiC layer, such as roller method, jet mill method, or rotating disk method, were already proposed. The roller method shows the problem of maintaining the gap width to crush the SiC layer. Maintenance ability and confinement of radioactive materials are other problems in this method. In the jet mill method, the coated particles are accelerated in a fluidized bed and collide with a plate to crush the SiC layer. A facility for separation of small fragments of SiC from exhaust gas is necessary in this method. The rotating disk method is to crush the SiC in the gap between a static disk and a rotating disk. This method has been adopted in the recovery of faulty coated particles in the production of HTTR fuels, and its availability was established. The rotating disk method was therefore selected as the reference method for further investigations.

(d) Removal of inner graphite layers from fuel kernels

The third step is to remove the two remaining graphite layers, iPyC and buffer layer, by roasting in an air envronment. A mixture of oxidized fuel (U_3O_8) and small fragments of SiC is obtained after the third step.

11.2.2.3. Conditioning process

After the head end process, the HTGR fuels are supplied to the separation process of the reprocessing plant for LWR fuels. The solution of spent fuel must meet the acceptable conditions of the reprocessing plant in Rokkasho as listed in Table 11.9 [401]. These are conditions in order to ensure the safe condition of subcriticality. Sampling and analysis of the solution are conducted upstream of the separation process to certify that the solution meets the acceptable conditions.

TABLE 11.9. ACCEPTABLE CONDITIONS OF SEPARATION PROCESS FOR CRITICALITY SAFETY

	Limitation
Enrichment of U-235	< 1.6 wt%
Isotopic composition of Pu-240	> 17 wt%
Concentration of uranium	< 300 g/L of U
Concentration of plutonium	< 3.5 g/L of Pu

Enrichment of ^{235}U of HTGR spent fuel was calculated to be 4.5%. If the concentration of uranium in the solution of spent fuel of HTGRs is adjusted to be 250 g/L of U, the concentration of plutonium becomes 6.6 g/L of Pu. Both values do not meet the acceptable conditions.

Therefore, a process for conditioning of the spent fuel solution is necessary after the head end process. In this conditioning process, the U_3O_8 is dissolved with nitric acid and fragments of SiC were removed. The nitric solution of spent fuel is diluted with depleted uranium solution in order to meet the condition for ^{235}U enrichment. When the solution is diluted by a factor of 3.5 with depleted uranium solution with an enrichment of 0.2 wt%, the enrichment of both ^{235}U and Pu becomes 1.43 wt%. This diluted solution meets the acceptable condition.

On the other hand, the isotopic composition of ^{240}Pu is calculated to be 17.4% which would meet the acceptable condition. However, it will be possible to have smaller value due to the dispersion of burnup distribution in each fuel batch during reactor operation. In order to solve this problem, the solution of HTGR fuel is mixed with a solution of LWR fuel which has higher composition of ^{240}Pu than 17% in the measurement and adjustment tank of the reprocessing plant.

Figure 11.29 shows the outline of the conditioning process. HTGR spent fuel (a mixture of U_3O_8 and fragments of SiC) after the head end process is accepted by the spent fuel supply hopper from the head end process and supplied to the dissolver tank to be dissolved by nitric acid. SiC fragments are left as undissolved residue and removed by a screw conveyor to the washing tank. The nitric solution of spent fuel is moved to the solution catch tank and supplied to the centrifugal clarifier to remove the undissolved residue. The clarified solution is supplied to the mixing tank. The residual enrichment of ^{235}U and the concentration of uranium are adjusted by mixing with a solution of depleted uranium. The adjusted solution of spent fuel is supplied to the separation process of the Rokkasho reprocessing plant.

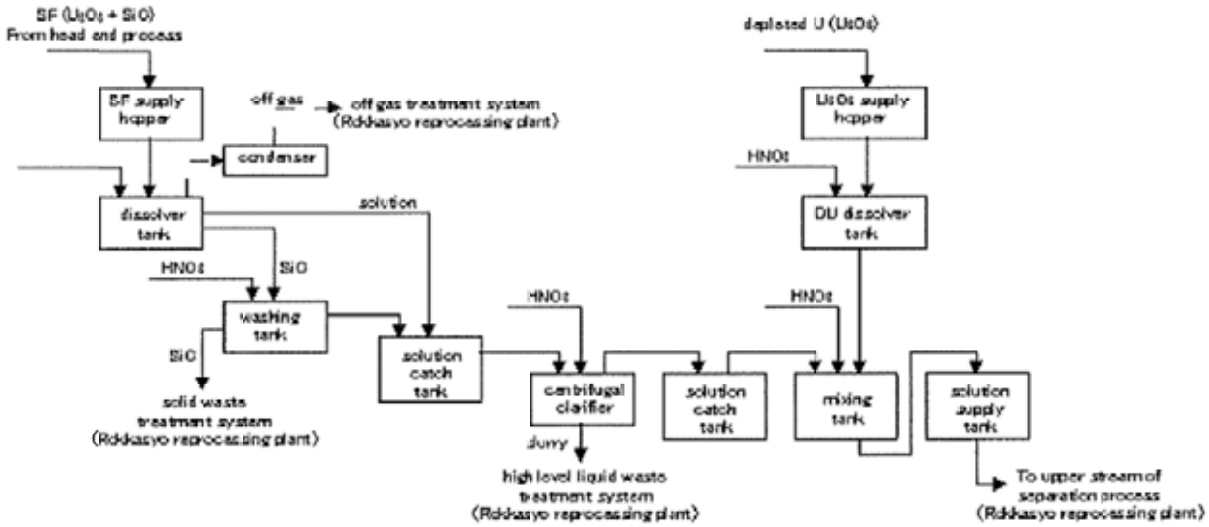

FIG. 11.29. Process flow of conditioning process.

In the separation and waste treatment processes, radioactivity and decay heat in HTGR fuels are approximately 30% larger than those in LWR fuels, and they are 20% larger in the process of Pu treatment. This problem can be solved by a prolongation of the cooling period of the HTGR fuel up to four years, i.e. the same as the cooling period as LWR fuels. Mixing with a solution of LWR fuels in the measurement and adjustment tank is another way to solve this problem [401].

11.2.3. South Africa (PBMR)

11.2.3.1. Storage tank

Different from the HTR-Modul (casks) or THTR-300 (drums), spent fuel storage for the PBMR has been considered to be done in tanks. The PBMR uses an arrangement with twelve storage tanks (Fig. 11.30), capable of storing a total of more than six million spheres [402, 403]. The spheres can be either spent fuel, used fuel (average burnup sphere from an equilibrium core), or graphite spheres. All storage tanks have the same design, although a

distinction is made between a spent fuel tank, a used fuel tank and a graphite tank. This distinction describes the predefined contents of the tank. The cooling design is the same for all tanks and will be adjusted to the heat load inside the tank. A storage tank is a large cylindrical pressure vessel, 18 m high with a 3.1 m inner diameter. It is made of thin-walled carbon steel and can sustain an internal pressure of 1 MPa. Inside the tank are a number of vertically arranged cooling tubes. The fuel spheres are stored in an inert gas environment at atmospheric pressure. The decay heat is transferred from sphere to sphere to the tank surfaces, and then via convection to the outside air. No heat is actively removed from inside the tank.

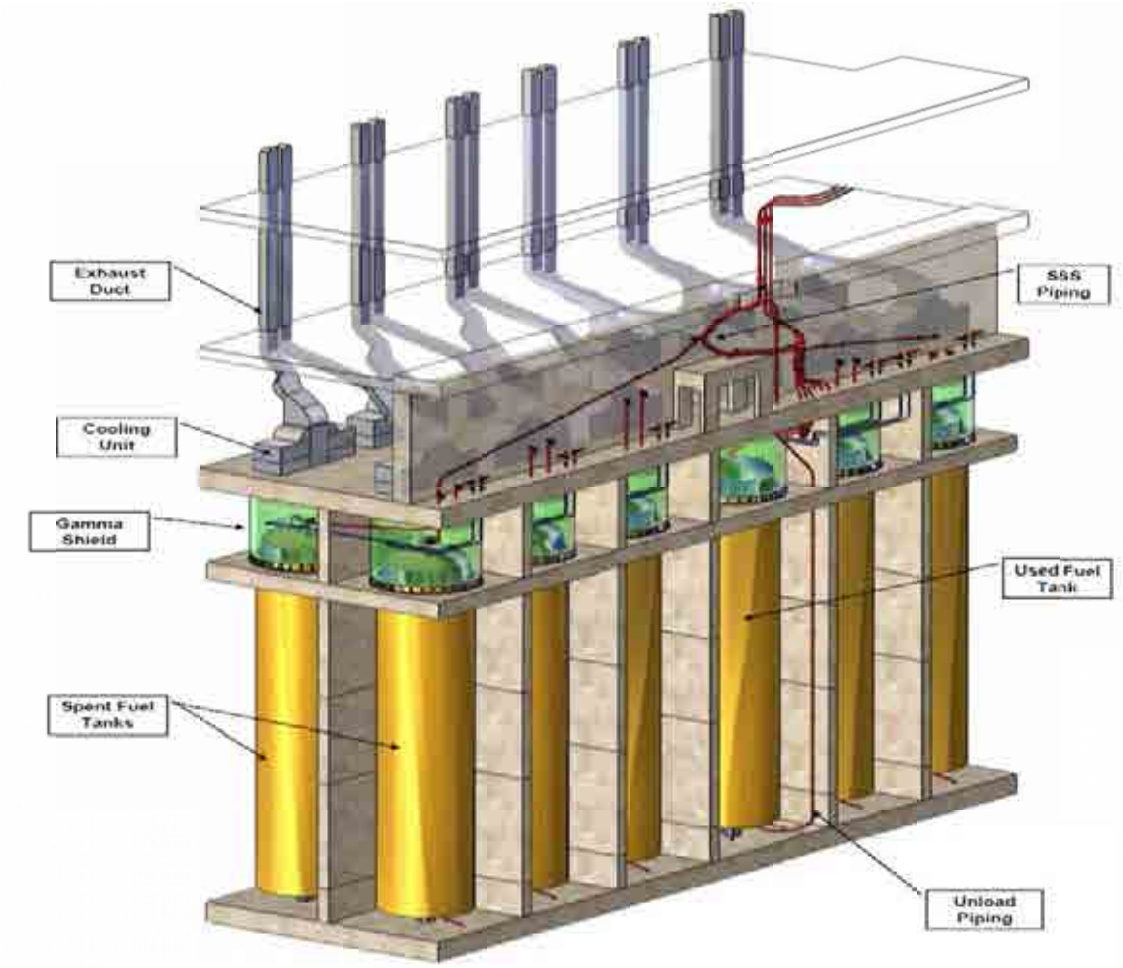

FIG. 11.30. Storage tank arrangement for PBMR spent and used fuel and graphite spheres.

11.2.3.2. Tank cubicle layout and airflow

Each storage tank is located in its own concrete cubicle (Fig. 11.31). The cubicle is split into an upper and lower cavity at the level of the tank support. At the upper cavity is the gamma shield which allows human access, even when the tank contains fuel, and also separates the inlet from the outlet airflow. A thermal shield is located around the tank extending from the ring support down to the bottom preventing thermal radiation from the tank to the surrounding concrete structures, and also directs the cooling air downwards from the top of the cavity and upwards along the tank. At the bottom of the tank cubicle, the cooling air splits up into the cooling tubes inside the tank and the gap between the tank and the thermal shield. All decay heat is absorbed by the cooling air as it flows upward along the tank. The flow collects above

the tank, moves past the horizontal part of the gamma shield and exits at the central outlet in the upper floor.

The tubes inside the tank, along with the gap between the thermal shield and the tank act as vertical heated chimneys. As a result, the storage tank has a strong passive cooling ability. The flow path as described above and depicted in Fig. 11.31 will exist for active and passive cooling, and for all heat loads that could exist inside the tank.

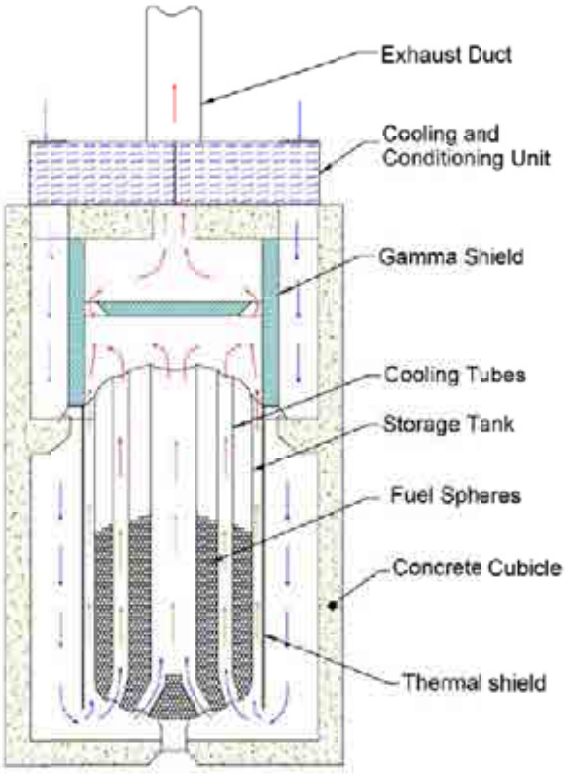

FIG. 11.31. Layout of the storage tank in its concrete cubicle.

11.2.3.3. Cooling modes

The storage tanks can be cooled in three different modes. The primary cooling mode is closed loop active cooling. In this mode, the cooling air is circulated in a closed loop around the tank cubicle. The two cooling and conditioning units condition the closed loop air to a purity level such as to prevent any significant corrosion on the tank over the 80-year storage. The heat is transferred from the internal loop to the atmosphere via an air-to-air heat exchanger. If the active cooling fails for some reason, louvres will automatically open to bypass the heat exchanger and filters. This allows air from outside to directly enter the tank cubicle, cool the tank, and exit at the exhaust duct. Heat removal is then achieved in an open loop passive cooling mode. This mode can be sustained indefinitely. Passive cooling is therefore the ultimate decay heat removal mechanism, while active cooling is only employed to protect the tanks from corrosion.

11.2.4. USA (GT-MHR)

Spent fuel elements discharged from a GT-MHR are considered ideal waste forms for permanent disposal in a geologic repository The graphite fuel elements and the ceramic

coatings on the fuel particles are as-manufactured engineered barriers that provide excellent near field containment of radionuclides. Because of the high level of plutonium destruction and degradation achieved by GT-MHR, the isotopic composition of residual plutomum in spent fuel elements would not be practical for use in nuclear weapons and for energy production Dilution of plutomum within the relatively large volume of GT-MHR fuel elements provides excellent resistance to diversion throughout the fuel cycle.

Based on previous studies conducted at ORNL [395] and in Germany [404], whole fuel elements disposal of GT-MHR spent fuel has been recommended as the preferred option because of advantages related to ease of implementation, proliferation risks, safeguards requirements, cost and schedule [405]. which concluded that whole elements of HTGR spent fuel containing uranium and thorium coated fuel particles repository and should perform better than unreprocessed LWR spent fuel.

According to the current conception of management with spent fuel from GT-MHR, the spent fuel is moved to the on-site long term storage. Storage methods considered are concrete storage casks (current the preferred choice), dual-purpose casks, an expanded in-plant storage facility, or a modular vault dry storage (as is currently used at Fort St. Vrain).

As a preferable spent fuel disposal method the following operations are considered:

- Place spent fuel in multi-purpose canisters (MPC) in reactor service building;
- Load canister into concrete cask;
- Move cask to storage facility;
- Store 10 years or until final disposal facility is available;
- Load MPC into shipping cask;
- Ship spent fuel in MPC to final disposal facility.

A conceptual design has been developed for an MPC (Fig. 11.32) which would be used for storage, transportation, and permanent disposal of spent fuel [405]. The GT-MHR MPC would contain 42 fuel hexagonal graphite elements of 0.8 m in length and 0.36 m across the flats, arranged as seven columns with six fuel elements per column. Each fuel element contains ~20 million coated fuel particles.

The following results have been obtained from evaluations of whole elements disposal:

- Graphite comprises most of the volume of GT-MHR spent fuel. Because of very low level of impurities in nuclear-grade graphite and excellent irradiation performance of coated particle fuel, the graphite does not become highly radioactive during irradiation. The high purity, nuclear-grade graphite fuel elements are non-combustible by conventional standards, and oxidation of graphite and other fuel element components at repository temperatures would be negligible over geologic time periods.
- Because of the relatively low volumetric decay heat for GT-MHR waste packages, the peak fuel/graphite temperatures will not exceed ~220°C.

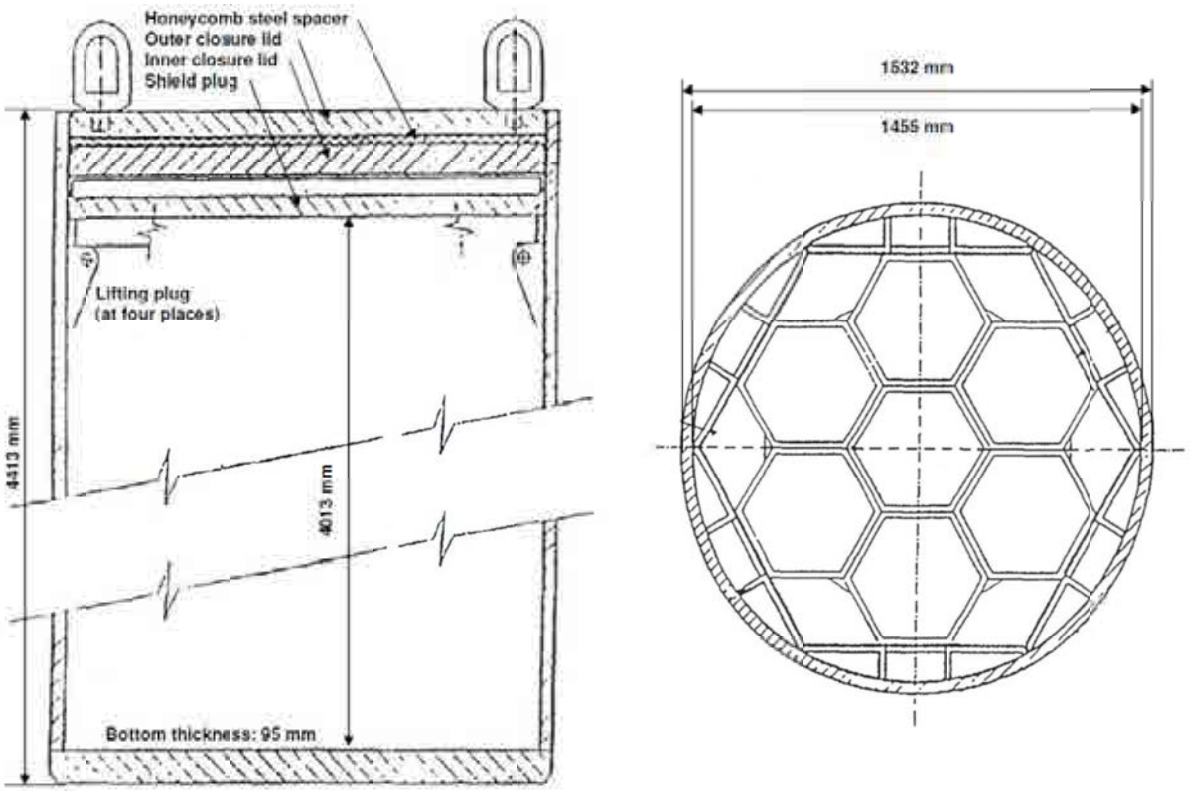

FIG. 11.32. Multi-purpose canister (MPC).

- GT-MHR TRISO coated particle fuel offers the benefit of long term containment for radionuclides without having to rely on performance of the waste package or geologic media. Quantitative assessment show that the TRISO coating is capable to maintain its integrity for hundreds of thousands to millions of years in a repository environment. Previous experimental studies [406, 407] have shown that the corrosion rates of pyrocarbon, SiC, and nuclear-grade graphite are very low (even relative to waste glass) and are ideal components of an engineered barrier for a waste management system. A key conclusion from the ORNL study [406] was that coated particle waste provides much better long term containment of radionuclides than glassified waste forms.
- For release by groundwater transport, only nuclides with high mobility are expected to reach the accessible environment within the 10 000 year time period currently specified by the US Environmental Protection Agency (EPA). The nuclide of most concern is carbon-14, because nearly all of the inventory is external to the coated particles and can be released by groundwater leaching of the graphite. Conservative estimates of release and transport show that the dose rates resulting from aqueous ^{14}C release are well below the applicable EPA criteria for any anticipated GT-MHR spent fuel disposition strategy. Preliminary estimations show that ^{14}C activity may reach up to 55.5 GBq/m^3 (1.5 Ci/m^3), more than five times less of criterion given in EPA requirements of 8 Ci/m^3 (~296 GBq/m^3) for low level waste.
- Preliminary evaluations of a GT-MHR MFC conceptual design show that all regulatory requirements for storage, transportation and disposal are met with significant margin. The GT-MHR MFC containing 42 fuel elements has overall dimensions nearly identical to those for an LWR MFC designed for 21 pressurized water reactor (PWR) fuel assemblies, but the weight with spent fuel is be about

one half of that of the PWR MFC. The GT-MHR MFC decay heat load is significantly lower: 760 W for GT-MHR vs. 13.200 W for the LWR MFC (with both values based on a decay time of 10 years following discharge from the reactor). These advantages allow storage of the MPC without active cooling. The estimated maximum dose rate determined by of actinides activity after 1000 years disposal is amount to ~10 mrems/year that is less than dose rate limit from EPA requirement for controlled area of fuel storage (~25 mrems/year).

- The large volume of GT-MHR spent fuel relatively to that of the LWR, which results primarily from dilution of the plutonium within the graphite fuel elements and results in significant safeguards and security advantages for the GT-MHR, does not adversely affect repository land requirements. Land requirements are determined primarily by decay heat load and not by physical volume of spent fuel. On a per unit electrical energy basis, the GT-MHR MFCs and thermal/mechanical design requirements for the repository itself, the GT-MHR will requires less repository area. For the current reference areal power density limit of ~14 kW/m (57 kW/acre), GT-MHR spent fuel requires about one half of the repository land area of LWR spent fuel per MW(e) and year. The corresponding number of waste package that can be loaded into the repository per a square meters are about 19 for the GT-MHR vs. only one for the LWR.

11.3. ADVANCED APPROACHES FOR HTGR specific WASTE MANAGEMENT IN FUTURE SYSTEMS

HTGR waste management includes the management of both spent fuel and irradiated graphite [408]. Regarding the spent fuel, current research activities deal with long term repository/direct disposal for SiC particles. Confirmatory tests which prove the long term integrity of the coating layers are needed. But also the reprocessing of fuel is investigated, which would result in a significant reduction of waste volumes and potential. An important issue is here to access the particle kernels for dissolution. Regarding graphite management, works deal with technologies to separate high activity from low activity fractions and evaluate the feasibility to reuse the graphite.

VHTR can also be used for minor actinide incineration or transmutation due to the high burnup capabilities of coated particle fuel. These features can be used in symbiosis with other reactor types to reduce mnor actinide contents and decay heat. The deep-burn potential of VHTR avoids multi-recycling of spent fuel as it would be needed for alternative routes. Although a once-through uranium cycle is being envisioned initially for a VHTR, the potential for deep-burn of plutonium and minor actinides as well as the use of thorium based fuels will be accounted for as evolutionary steps towards a closed cycle. To answer these questions, an international collaborative programme has been set up between the USA, Japan, Republic of Korea, the European Union and France, under the GIF umbrella. The 'VHTR/Fuel and Fuel Cycle' (VHTR/FFC) Project Arrangement (PA) became effective in 2008 [408].

11.3.1. Project DEEP-BURN: development of transuranic fuel for HTGRs

11.3.1.1. Background

Studies of the VHTR fuel cycle must involve: (i) use of light water cooled reactor (LWR) spent fuel as kernel feedstock; (ii) recycle of spent VHTR fuel; (iii) use of the VHTR in the management of transuranics (TRU); and, (iv) the geologic storage performance of spent

VHTR fuel. Examination of these aspects of the fuel cycle and defining a resolution path for any technology gaps is essential for determining future deployment options of the VHTR.

The deep-burn project has been initiated by the Office of Nuclear Energy (NE) to establish the technological foundations supporting the role of the VHTR in the nuclear fuel cycle. The project will include a quantitative assessment of the scope, cost, and schedule implications of incorporating various fuel cycle considerations into a prototype VHTR project.

The concept of destruction of spent fuel TRU in a TRISO fueled gas cooled reactor is known as deep-burn. The term 'deep-burn' reflects the large fractional burnup of up to 60–70% FIMA that may be achievable with a single-pass, multi-cycle irradiation in VHTRs. Spent TRISO fuel from deep-burn can be either placed directly into geologic storage to provide long term containment of the residual radioactivity, or recycled into fast reactor fuel. Deep-burn rapidly and effectively reduces the inventory of TRU from spent fuel without the need for repeated re-cycles, destroys weapons-usable materials contained in spent fuel, and precludes the possible weapons-related use of the residuals thereby providing strong proliferation barriers. The DB-VHTR concept is particularly attractive because it employs the same reactor design that is used for the NGNP programme with the same potential for highly efficient electricity and hydrogen production.

During deep-burn irradiation, the various TRU constituents of the deep-burn TRISO (DB-TRISO) fuel particle are progressively destroyed according to their cross-section for fission or capture of neutrons. For instance, already at the 50% FIMA burnup level, almost all the ^{239}Pu (~90%) has already been destroyed thereby eliminating the risk of future diversion of spent fuel for weapons production. Of crucial importance to the deep-burn concept is the interplay between ^{239}Pu, ^{240}Pu and ^{241}Pu. Plutonium-239 is a strong fissile isotope, while ^{240}Pu is a strong burnable poison that is also a fertile isotope producing ^{241}Pu. The utilization of the short-lived ^{241}Pu in the high burnup TRISO fuel without reprocessing is a special feature of deep-burn. The sequence 239–240–241 produces a very steady reactivity behaviour over long periods of time leading ultimately to the achievement of better than 60% FIMA burnup without exceeding allowable TRISO fuel fluence limits.

Different from the 'classical' TRISO fuel production, manufacturing of DB-TRISO will require the additional implementation of remote handling techniques and the development of fuel designs specifically geared to very high burnup. Preliminary studies show that up to 20 times more energy can be extracted from DB-TRISO fuel in VHTRs than from mixed oxide (MOX) fuel in LWRs. If these results can be validated, the deep-burn concept would create a completely different paradigm for the near term economics of closed fuel cycles. The cost of spent LWR fuel reprocessing would be partially or fully offset by the value of the recovered TRU in a deep-burn VHTR (DB-VHTR) producing power at competitive cost.

11.3.1.2. Objectives

The current project aims at establishing the technological foundations supporting the role of the VHTR in the nuclear fuel cycle. This includes a quantitative assessment of the scope, cost, and schedule implications of incorporating various fuel cycle considerations into a prototype-VHTR project. The medium term objectives, which would take several years to achieve, are:

- Analysis of the DB-VHTR as a TRU burner, including neutronics, thermo-hydraulics and safety aspects;
- First-principle model of DB-TRISO fuel for incorporation in the VHTR design tool;

- Production of sufficient amounts of high quality TRU-bearing DB-VHTR fuel to begin irradiation experiments;
- Flowsheet development for aqueous and pyro-chemistry reprocessing methods for VHTR spent fuel;
- Quantitative assessment of waste management and geologic storage options for VHTR spent fuel;
- Cost analysis and roadmap development for the VHTR fuel cycle options, including recommended interfaces with NGNP and GNEP/AFCI programmes.

11.3.1.3. Scope of work

Preliminary assessments of the DB-VHTR indicate that fuel cycle lengths of 1 to 1.5 years are feasible and that the reactivity swing over the cycle could be managed. There is a need for additional analysis to develop a self-consistent fuel management, thermal-hydraulic, and fuel performance approach, including burnable poisons, for the DB-VHTR to determine that the TRU burnups of such magnitude are achievable with sufficient margins of power peaking, peak fuel temperature, and fast fluence to acceptable limits.

Using generic NGNP type prismatic and pebble bed reactor cores, the project will perform physics calculations to evaluate the capabilities of this reactor to perform destruction and utilization of LWR spent fuel TRU and to improve the performance of the geologic repository or synergistically complement fast recycling reactors.

While DB-TRISO fuel can in principle be irradiated to very high burnups of 40–50% FIMA within previously achieved fluence limits of TRISO fuel, DB-TRISO fuel is expected to greatly exceed historically achieved burnups. The chemical and physical changes to the fuel kernel during deep-burn will be extreme and necessitate a deeper understanding of the fuel behaviour during irradiation. Kernel, coatings, and fission product transport behaviour will be modeled using leading edge computational methods to provide predictive capabilities for integration with high fidelity nuclear models of the gas cooled reactor.

There is a long history of international TRISO coated particle fuel fabrication up to and including production scale. Remote fabrication at each step (kernel, coating, compacting) of such fuels has been studied as part of other DOE fuel programmes. Both MOX fuel and curium targets have been made via sol-gel technology. A pilot scale remote operating coater was designed and operated ‘cold’ as part of the U/Th gas reactor fuel programme. Automated compacting technology was developed as part of Fort St. Vrain development. These technologies have been demonstrated at the proof of principle stage and designs exist for larger scale remote systems. Engineering scale demonstrations are needed to assess technical and economic feasibility of remote fabrication of DB-VHTR fuel. Of specific concern is the ability to perform remote maintenance on the CVD coaters and the need to produce high quality, low defect fuel in the remote environment.

The project will initiate steps towards the manufacture of testable amounts of DB-TRISO fuel and to establish the processes for large scale fabrication. Designs and plans for permitting and installation of coating and compacting facilities for TRU fuel will be developed. The project will establish surrogate coating operations and functional and operational requirements for the Pu and ^{241}Am equipment. The use of zirconium carbide (ZrC) will be considered, either on the kernel itself or on the buffer layer, or as a replacement for silicon carbide. The project will produce the first ‘sparse’ kernels containing TRU materials (a few particles with the required

amounts of americium among many kernels) and perform hot tests, though not in the first year.

Small quantities of TRISO fuel containing limited quantities of radioactive TRU such as ^{239}Pu and ^{237}Np have been successfully fabricated and tested in the past. Studies on the disposition of weapons-grade plutonium indicate that extremely high burnup can be achieved by using oxide fuels, oxygen getters and perhaps dilution with inert materials. LEU and HEU TRISO fuel have been extensively tested both with respect to fluence and burnup.

The project will establish a similar database for the deep-burn fuel by irradiating DB-TRISO fuel manufactured in the course of this programme in high flux facilities in statistically significant sample sizes and perform post-irradiation testing to provide feedback to the fuel designers. The project will perform an analysis of existing irradiation facilities and develop a plan for irradiation and accident testing. This plan will include plans for the required irradiation campaigns, the testing at off-normal conditions, and the modifications to test equipment and facilities needed to test DB-TRISO fuel.

(a) Recycle of actinides from VHTR fuel

In the early days of VHTR technology, a crush-burn-leach process was proposed to reprocess VHTR fuel. This process produced large quantities of carbon dioxide that needed to be trapped. A new head end process consistent with the UREX+ separation technologies has been identified and demonstrated at the proof of principle level for TRISO fuel in the past few years. The process flow consists of separation of the compacts from the graphite block, disposal of the graphite block as low level waste, grinding and jet-milling of the compact components (matrix, coatings, fuel kernels) into a fine powder to support chemical separation, and leaching, to dissolve the TRU for aqueous separation or a novel electrochemical process, termed METROX, for the pyroprocessing separation.

The project will develop a full flowsheet for TRISO recycling using both aqueous and non-aqueous reprocessing, particularly as it pertains to spent DB-TRISO fuel. The process of crushing the ceramic coatings and exposing the spent fuel kernels to dissolving agents will be brought up to today's standards of low secondary waste streams and process losses. The project will study the crush–leach flowsheet to minimize waste, establish and test a laboratory filtering system, and study the suitability of the fuel solution for liquid separation. Laboratory scale tests of the equipment for separation of the solid coating and compact material from the fuel solutions will be performed.

The project will investigate the METROX process, a promising head end coupling for TRISO fuel into pyroprocessing for metallic reactor fuel. Early studies successfully demonstrated process feasibility with uranium based fuel but additional study is required to qualify the process for TRU-bearing fuel. The project will construct a complete mass balance flowsheet including identification of waste form types and quantities, and conduct experimental studies needed to validate process chemistry.

(b) Waste management and repository performance of VHTR spent fuel

TRISO fuel provides very strong barriers to the dispersal of the long-lived components of radioactive spent fuel. The TRISO SiC coating acts as a pressure vessel to contain the helium produced during storage from the alpha decay processes. Preliminary measurements have indicated that the corrosion rate of both pyrocarbon and silicon carbide coatings in the repository are extremely slow in air, moist air and water, to the point that there is reasonable

expectation for containment of radioactivity over millions of years. Also, the use of a DB-VHTR to recycle LWR spent fuel could reduce the heat load to the repository by a factor of 2 to 3, given the high destruction rate of TRU in the deep-burn irradiation. Additional testing is needed to characterize degradation of the fuel compact and fuel particle under repository conditions and long term modeling of repository behaviour.

The project will study the long term behaviour of spent TRISO in dry and wet environments and develop a strategy for the geologic storage of DB-TRISO. The project will develop a plan for measuring corrosion rates of pyrocarbon and silicon carbide coatings in repository atmospheres. Relevant tests representing coating corrosion in the repository will be defined and exploratory testing to refine protocols will be performed.

(c) Integration of the VHTR in the overall nuclear fuel cycle

The most likely role of the VHTR is to operate on LEU fuels for nuclear power or process heat and hydrogen production applications. In this mode, the VHTR offers some fuel cycle advantage compared to LWRs because the rate of TRU production per energy generated is reduced by a factor of 2 to 3; this behaviour is attributed to improved thermal efficiency, together with higher fuel enrichment and burnup in the VHTR.

The current TRU destruction scenario adopted by GNEP/AFCI is termed the single-tier approach; it is the simplest demonstration of closing the fuel cycle. In this case, spent fuel from LWRs is sent directly to the advanced burner reactor (ABR) for destruction. Our studies suggest that DB-VHTRs can have a synergistic relationship with the ABR when operated in dual-tier mode. This synergy allows relaxed operating parameters for the two reactor types and a smaller inventory of recycling TRU relative to the single-tier approach. It would also reduce the number of fast reactors by a factor of 3 as compared to the LWR two-tier scenario (i.e. thermal to fast reactor ratio of 9 to 1 rather than a 3 to 1 ratio).

The project will assess the future role for VHTRs in delivering energy products including consideration of its fuel cycle and TRU-management function. As gas cooled reactors may play an important role in the sustainable expansion of nuclear energy and in the TRU-management for the whole nuclear energy system, the project will perform a dynamic analysis of the evolution from today's reactor park to future reactor parks. Such dynamic analysis will focus on the correct assessment of the mass flows, waste inventory and arisings, separated-TRU inventories, the delay times in deployment, and the overall economic impacts.

The project will assess the role of Pu and Minor Actinide burning in DB-VHTRs in the context of a fuel cycle that includes LWR and fast reactor fuels. The role of DB-VHTRs in burning Pu both from the stockpile and LWR reprocessing will be examined. The project will formulate a range of scenarios in which the VHTR burner are operated in conjunction with today's reactors to achieve fuel cycles in which waste discharges for geological disposal are minimized.

As part of the dynamic analysis, the project will explore the economic viability of the whole fuel cycle infrastructure required to support the introduction of the VHTR. Based on the mass flow analysis and the technical description of fuel cycle infrastructure, proliferation and physical security risks will be evaluated.

11.3.2. Project PUMA: utilisation and transmutation of plutonium and minor actinides

The project PUMA, 'Plutonium and Minor Actinide Management in Thermal high temperature gas cooled reactors', was a Specific Targeted Research Project (STREP) within the Euratom 6th Framework Programme running from 2006 to 2009 [409]. The project's main objective was to investigate the possibilities for the utilisation and transmutation of plutonium and especially minor actinides in contemporary and future (high temperature) gas cooled reactor designs which are promising tools for improving the sustainability of the nuclear fuel cycle. Earlier projects already indicated favourable characteristics of HTRs with respect to Pu burning. The PUMA project tasks included the investigation of

- core physics of Pu/MA fuel cycles for HTGRs to optimize the coated particle fuel and reactor characteristics and to ensure nuclear stability of a Pu/MA HTGR core;
- requirements and design of innovative fuel forms for Pu and Minor Actinide incineration in HTGRs;
- analysis of the VHTR's impact on the entire nuclear fuel cycle and economics, its role in a future nuclear energy park, the implications on fuel cycle, economics and socio-political aspects.

The reference systems chosen were contemporary representatives of the two main HTGR designs, the PBMR-400 as pebble bed HTGR with continuous reload of fuel elements and the GT-MHR prismatic block HTGR.

Fuel compositions studied were Pu as a first reference fuel composition with the isotope vector of first-generation plutonium; PuMA, a mixture of plutonium and minor actinides; Pu2xMA, a fuel composition with double minor actinide content compared to PuMA; IMX, an inert matrix fuel with isotope content identical to PuMA; and WP, so-called 'wallpaper' fuel with the same isotope content as PuMA where the fuel kernels are condensed to the outer diameter of the fuel zone leaving the central part of the pebble free of fuel. The IMX fuel features a fuel kernel diameter of 500 μm, while others have fuel kernel diameters of 200 μm. The total heavy metal loading per fuel pebble is 2 g.

Recent FZJ activities were dealing with a fuel composition of plutonium with thorium to satisfy safety regulations. To combine this requirement with a high burnup of the total plutonium content of the fuel and in particular the amount of the fissionable isotopes, the fuel composition should be optimized. The combination of plutonium with an additional amount of thorium has in general many positive effects as the reduction of peak fuel temperature, power per pebble, power density and because of the Doppler broadening at higher temperatures a negative temperature reactivity effect. In addition, the breeding effect generates an additional amount of the fissionable isotope ^{233}U. A negative effect is seen in the additional mass of thorium increasing the total heavy metal load per pebble which reduces the moderation ratio to an under moderated stage — and therefore criticality — of the core.

Although none of the computer models applied has been specifically validated for Pu and/or MA fuels, most of the codes have the potential to be successfully used for complex and detailed HTGR Pu/MA investigations. Calculations have been carried out to determine the equilibrium state of the core in each case, the power density distribution and core inventory of actinides and selected fission products at equilibrium, the amount and composition of fresh and discharged fuel, temperatures at nominal conditions, temperature reactivity coefficients, control rod worth, and reactivity effects of water ingress.

The results obtained demonstrate the excellent plutonium and minor actinide burning capabilities of the high temperature reactor. The largest degree of incineration is attained in the case of an HTGR fueled by pure plutonium fuel as it remains critical at very deep burnup of the discharged pebbles. Addition of minor actinides to the fuel leads to decrease of the achievable discharge burnup and therefore smaller fraction of actinides incinerated during reactor operation. The inert matrix fuel design improves the transmutation performance of the reactor, while the 'wallpaper' fuel does not have advantage over the standard fuel design in this respect. For validation purposes, it was recommended to examine the possibility of using low/zero power critical facilities, such as the Petten low flux reactor, to yield experimental data on the reactor physics properties of HTGR Pu/MA based fuel.

Prior to any modeling of helium behaviour in fuel particles, the production of helium itself must be calculated. In the evolution of a fissionable nuclide, a higher neutron flux imposes higher total reaction rates which comprise fission and neutron capture, thus enhancing both burnup and transmutation to an alpha emitter. At lower burnup rates, the process of alpha emitter formation, particularly of ^{241}Am, is more efficient.

Alpha decay of heavy metal nuclides is an overwhelming contributor to helium production in all locations. This term is responsible for differences in helium production depending on locations. Second contributing term of ternary fission is, due to its nature, proportional to the burnup but its contribution is below 10%. The alpha emission from oxygen is very small due to deeply moderated neutron flux. The highest values of helium production on discharge occurs when fuel is kept in the reactor core for a long residence time under relatively lower burnup rates in order to reach the target burnup, as it is generally the case for pebble bed fuel.

Experiments have shown that He will be released from the kernel, but not from fresh kernels. Indeed, fresh fuel has shown a remarkable stability up to 2500°C. For modelling purposes, 100% release of helium from the kernel is justified. The diluted kernel concept was first invoked by Belgonucleaire brings many benefits. The fuel modelling studies have clearly indicated the advantages that can be gained by dilution. Essentially, for a given buffer layer thickness, more volume is available to accommodate the CO and He released. Chemical thermodynamic models have been deployed to design a kernel that will show limited CO production. The most important point here is that substoichiometric Pu or Am oxides are essential. Further improvement can be achieved by chemical buffering of the fuel by the addition of Ce sesquioxide which takes up oxygen to form the dioxide. Ultimately any coated particle design must be validated in an irradiation test.

Pu/MA transmuters are envisaged to operate in a global system of various reactor systems and fuel cycle facilities. The integrated LWR–HTR–GCFR system basically aims at closing the current nuclear fuel cycle. LWR spent fuel along with depleted uranium becomes valuable material to both produce energy and drastically reduce the natural uranium demand as well as the mass of the long term radiotoxic component in the nuclear waste to be geologically stored. Also a strong reduction of Pu (and, if necessary, Np) stockpiles can be achieved due to the HTGR loaded with fertile-free fuel, in parallel with an important change of its isotopic composition, which becomes highly proliferation resistant. Fuel cycles become long due to the very favourable neutron economy that is typical for helium cooled reactors.

A study on proliferation resistance has taking into account several possible proliferation pathways: (i) diversion of unirradiated fuel for the purpose of constructing a fissile device; (ii) undeclared access to fissile material in irradiated fuel for the purpose of constructing a fissile device; (iii) clandestine irradiation of fertile targets; and (iv) postulated threat of a sub-

national organisation stealing radioactive material for use in a dispersal weapon. The study highlights that a prismatic VHTR core would be amenable to conventional safeguards accounting and verification procedures with fuel blocks accounted for individually in the same way as LWR fuel assemblies. However, a modified approach would be needed in pebble bed cores because of the impracticability of accounting for individual fuel spheres.

11.3.3. Project CARBOWASTE: Improved fuel treatment methods

A characteristic feature of HTGRs is the vast amount of graphite that is being used in a plant mainly serving as structural and moderator material. Looking at the active core of a pebble bed HTGR, a fraction of 93.6% of the mass (or 96.6% of the volume) consists of graphitic matrix material (Fig. 11.33). In contrast, the fuel elements in a block type HTGR are mainly composed of highly graphitized standard nuclear graphite with only little matrix material used for the compacts.

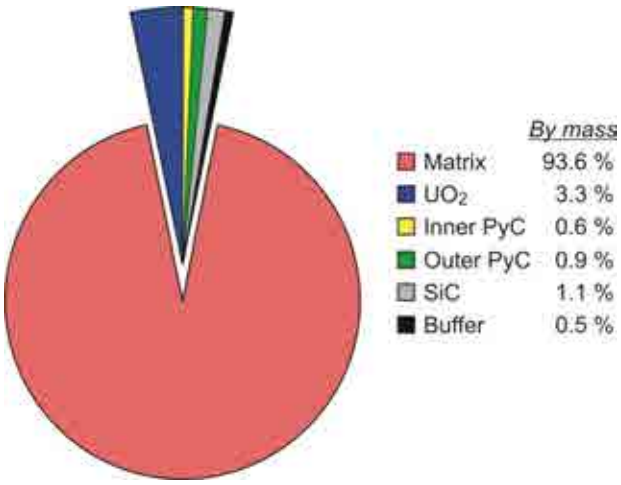

FIG. 11.33. Mass fractions of the different HTGR fuel materials.

Alternative approaches on the retrieval of irradiated graphite from the reactors under decommissioning are currently under discussion within the EU project CARBOWASTE [410]. A characterization programme has been started to localize the contamination in the micro-structure of the irradiated graphite and to better understand their origin and the release mechanisms during treatment and disposal.

It has been discovered that a significant part of the contamination (including ^{14}C) can be removed by thermal, chemical, electrochemical or micro-biological treatment. The feasibility of the associated processes is experimentally investigated to determine and optimize the decontamination factors. Re-use of the purified material is also addressed either to find alternative applications in nuclear technology or to close the 'graphite cycle' for future graphite moderated reactors. Other objectives are the disposal behaviour of graphite and carbonaceous wastes and the improvement of suitable waste packages. Different disposal and treatment strategies need to be analysed for a future VHTR. Figure 11.34 illustrates the different choices for HTGR spent fuel management (e.g. for block type fuel):

- Direct disposal (Path A);
- Separation of moderator and fuel compacts or coated particles (Path B);
- Separation of graphite, coatings and kernels with reprocessing of the UO_2 fuel (Path C).

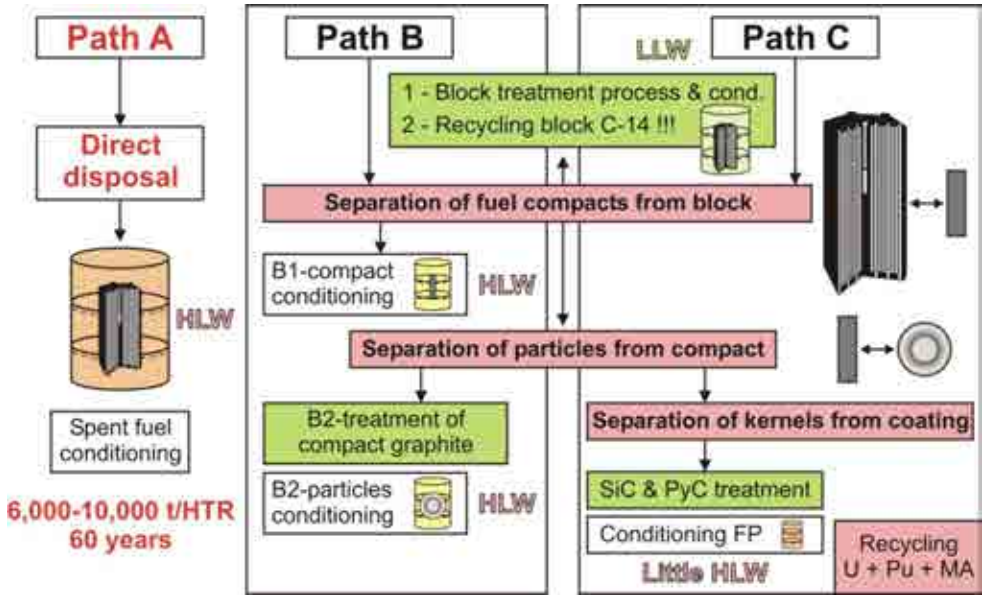

FIG. 11.34. Spent fuel management options for VHTRs.

A significant reduction of disposal volume can be achieved if the spent fuel (coated particles or compacts) can be separated from the matrix and these waste streams being treated either as high level waste (HLW) with regard to the coated particles or as long-lived low level waste (LLW) or medium level active waste (MLW) with regard to bulk of the moderator graphite. If the UO_2 fuel will be reprocessed another waste stream of carbonaceous waste would arise from the pyrocarbon and SiC coatings.

Reprocessing of spent HTGR fuel has formerly been developed in USA and Germany based on incineration and mechanical technologies. These combustion processes to extract the coated particles from the HTGR fuel element matrix cannot be used anymore, in particular due to the release of ^{14}C to the environment. In addition, the mechanical methods like grinding and crushing, which have been investigated and used in the 1970's, lead to a cross contamination of the moderator graphite with the HLW from the spent fuel particles.

Therefore future processes have to separate graphite from coated particles without damaging them and without significant contamination transfer. Different technical options are under development for separating the coated particles from the matrix of HTGR fuel elements:

- A maturing technology is based on pulsed high voltage discharges which enable selective fragmentation of fuel elements and coated particles. Significant progress with this technology has been achieved by the JRC and SelFrag AG which produces the equipment. CEA has pursued research in this area at laboratory scale.
- NECSA is performing deconsolidation tests with plasma, laser, molten salt, and electrochemistry.
- Subatech has studied intercalation methods.
- In the past, FZJ has developed a process based on homogeneous oxidation to weaken the strength of the graphite and to ease its decomposition.

At CEA, the fragmentation tests have been continued with pulsed power equipment by using unirradiated compacts containing different amounts of dummy TRISO particles. Energy, frequency and the number of pulses, the geometry of electrodes, the liquid medium within the

reaction vessel and the number of compacts per run have been varied to optimize the process, e.g. to minimize undesired fines. Segregation of particles from compacts appears to be easier than fragmentation of massive graphite as fragmentation takes place at the interface between particles and graphite.

JRC and SelFrag have performed tests with surrogate pebble fuel elements and coated particles in commercially available high voltage discharge installations (Fig. 11.35) [411, 412]. The product to be fragmented is poured into a vessel, which is filled with water. An electrode delivering repetitive HV discharges under water is plunged into the vessel creating shock waves. Coated particles were liberated intact from their matrix.

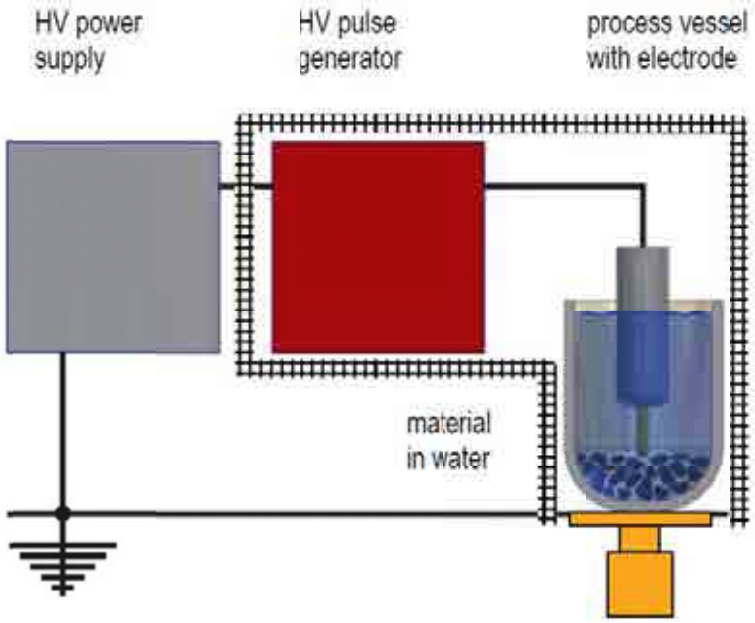

FIG. 11.35. Pulsed Power Defragmentation (from www.selfrag.com).

The energy consumption of the process is low and the installation is suitable for a hot cell environment and industrially relevant material streams. After further fragmentation of coated particles, the fragmentation product can directly be fed into classical aqueous reprocessing.

Complementary tests were made by Subatech using HTGR compact fuel with surrogate ZrO_2 TRISO particles to test two separation methods: low (H_2SO_4+H_2O_2) and high (H_2SO_4+HNO_3) temperature acid treatments applying micro-waves. In both cases, the TRISO separation was complete but some TRISO layers oxidized at high temperature. At low temperature, the segregation of graphite grains is facilitated by intercalation of sulphuric acid between the graphene layers. The obtained acid–graphite intercalation compounds (GIC) consist of pure phases of high quality suggesting their potential for industrial recycling. Figure 11.36, top left, shows some GICs after treatment and extracted coated particles can be seen in Fig. 11.36, top right.

Additional deconsolidation tests at NECSA on HTGR fuel pebbles performed with plasma, laser, molten salt and electrochemistry were also successful and are further optimized. Another method is the homogeneous oxidation of the fuel matrix, as formerly developed in Germany.

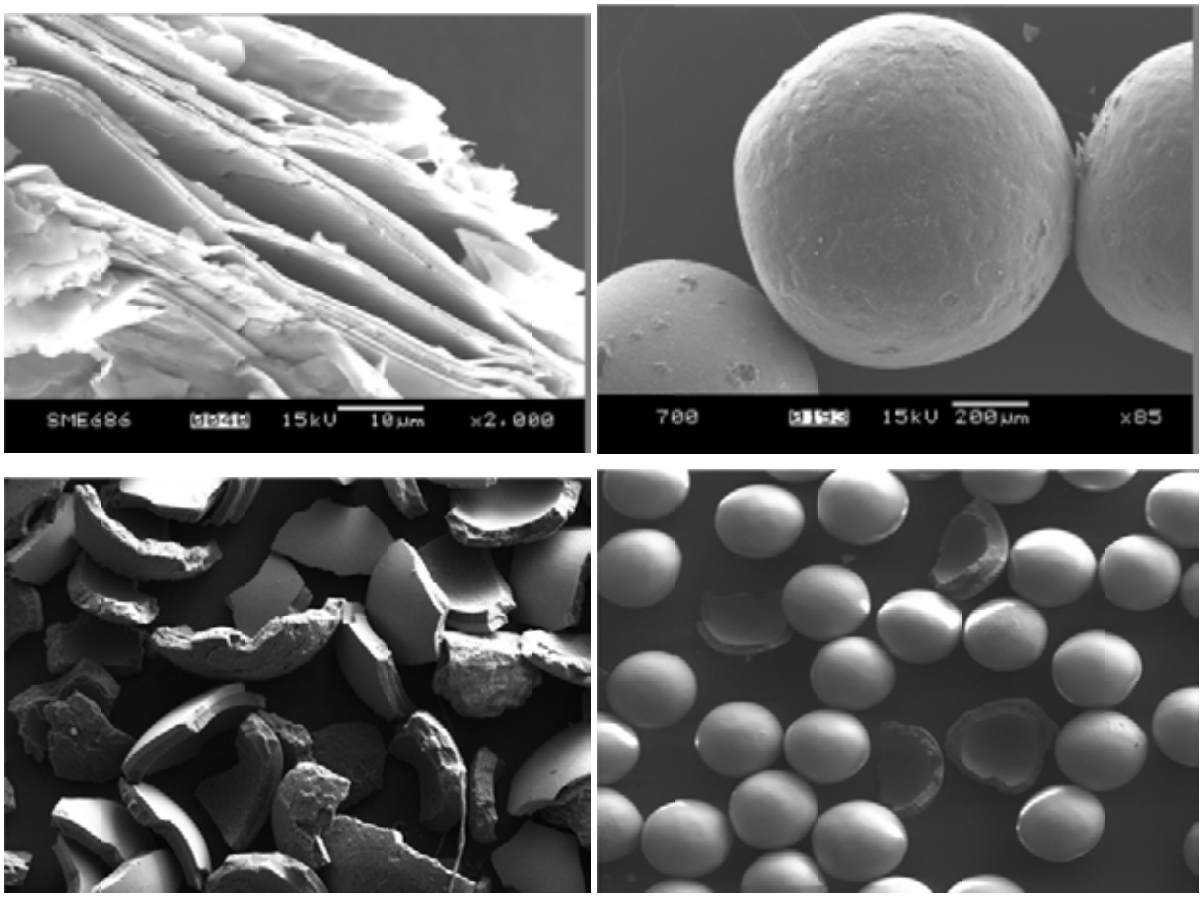

FIG. 11.36. Graphite intercalation compounds, GICs (top left); extracted coated particles from compacts (top right); fragmented coatings (bottom left); retrieved surrogate fuel kernels (bottom right).

JRC and SelFrag have cracked the coatings of isolated (dummy) fuel kernels in the same device as already described above, only with different operating characteristics. Figure 11.36, bottom left, shows the fragmented coatings and Fig. 11.36, bottom right, the separated (non-irradiated) kernels. Alternate processes for the separation of the fuel kernel from the coatings are studied such as mechanical milling, jet stream processes, molten salt, plasma, combustion, fluorination etc.

Conditioning processes were also investigated for the disposal of fractured TRISO coated particles layers. SiC–glass composites from glass frit have been examined. For the choice of the glass, low viscosity and low temperatures (to limit RN volatility) and limited reactivity with SiC (to avoid bubbling) were the most important parameters.

The recent progress in the area of waste management confirms feasibility of closed HTGR fuel cycles, with some further technology development pending. Separation of spent fuel from the irradiated matrix material is feasible and enables reprocessing and recycling of these materials. However, this still needs to be confirmed for irradiated fuel.

11.3.4. China activities on HTGR fuel disintegration

11.3.4.1. Electrochemical disintegration of matrix graphite from spherical fuel elements

With the rapid development of pebble bed HTGR in China, it will also become important to consider the treatment and disposal of spent spherical fuel elements before establishing a large number of commercial HTGR plants. If the large amount of the graphite matrix could be removed and be disposed of as LLW, a significant reduction of disposal volume of HLW would be achieved. Therefore, a proper technique is needed to disintegrate the graphite matrix from the spent fuel elements without damage to the SiC layer, leaving the option of reprocessing the coated fuel if necessary [413]. In this way, the radioactive contamination of the graphite matrix can be controlled and the graphite matrix can be finally disposed of as MLW, or even LLW.

The general methods to disintegrate the fuel element, i.e. mechanical separation (by grinding) and chemical separation (by burning) require some modifications under the principles of the IAEA radioactive waste safety standards (RADWASS). The mechanical grinding [414] would produce a large quantity of radioactive dust and gases due to the breakage of the coated fuel particles leading to cross-contamination of the graphite material [411, 415]. The option of incineration of graphite matrix could produce the release of great amounts of off-gas, such as CO_2, noble gases and other fission products. The CO_2 would have to be fixed into stable carbonate in order to control the release of ^{14}C. This would lead to a remarkable increase in volume of the solid waste [411, 415–417].

In the 1970s, Merz and his co-workers [418, 419] concentrated on studies of an electrochemical method to remove the graphite matrix with strong oxidizing acids as electrolyte, like concentrated sulphuric acid. In sulphuric acid, the cause of disintegration of graphite matrix is mainly due to the formation of graphite intercalation compounds and oxidation of carbon at the grain boundaries of the graphite body. Merz considered it as a very good method in analytical application. However, it was assumed that this method was not suitable for head end process, mainly due to a high degree of damage to the coated particles, a significant formation of secondary waste and corrosion of the reaction vessel materials, as well as a slow speed of the process [418, 419].

The disadvantages of the electrochemical method described above were mainly due to the electrolyte of concentrated oxidizing acids. If the concentrated acid were replaced with a mild solution which is also capable of disintegrating the graphite matrix, then the disadvantages of concentrated acid would be avoided. Up to now, no ideal option to remove the graphite matrix from spherical HTGR spent fuel elements has been presented. Scientists have to reconsider other noninvasive method to separate graphite and fuel, such as the electrolytic method [395]. In this section, the development of an improved electrochemical method with salts as electrolyte and the study of the disintegration of HTGR fuel elements is described [420].

Graphite is composed of a series of stacked parallel hexagonal layer planes, with much weaker van der Waals bond with the adjacent planes [421]. In nitrate solution, the graphite matrix could be disintegrated by the electrochemical method. The disintegration process was composed of an intercalation part of nitrate anion and further an oxidation part of carbon which effected together to lead to the collapse of graphite crystals. Disintegration of graphite in nitrate solution could be realized without any trouble in dealing with large quantities of radioactive dust, or secondary radioactive waste. Furthermore, the electrochemical method could avoid the extra damage to the coated fuel particles and unexpected dissolution of radioactive elements.

(A) Disintegration of graphite matrix from a simulative fuel element

The simulative HTGR fuel elements, which were fabricated with reactor-grade graphite according to the production procedure for HTGR fuel elements at INET, were previously used to investigate the disintegration of graphite matrix by the electrochemical method [16]. The simulative fuel element served as the anode during the electrolysis, and it was disintegrated gradually from the surfacce as graphite particles.

The graphite particles had a certain width of size distribution with the volume-averaged hydrodynamic diameter of about 100 μm. The maximum diameter was smaller than 900 μm which was less than the diameter of coated fuel particle (920 μm).

After disintegration, the graphite particles got a weight gain more than 20% owing to the partial oxidation of the graphite in the electrochemical process. The weight gain mainly resulted from the increase of oxygen. The oxygen element of the graphite particles obtained in $NaNO_3$ solution was about 19% concluded from elemental analysis results. Therefore, it implied that graphite matrix might have been oxidized to some extent during the disintegration process.

Figure 11.37 shows the X ray diffraction of graphite particles obtained by the electrochemical process in nitrate solution. As can be seen in the figure, the peak of graphite oxide from the graphite particles was observed besides the strong peak of graphite material, compared with the curve of original graphite material which indicated that the graphite matrix was disintegrated as a mixture of graphite and graphite oxide.

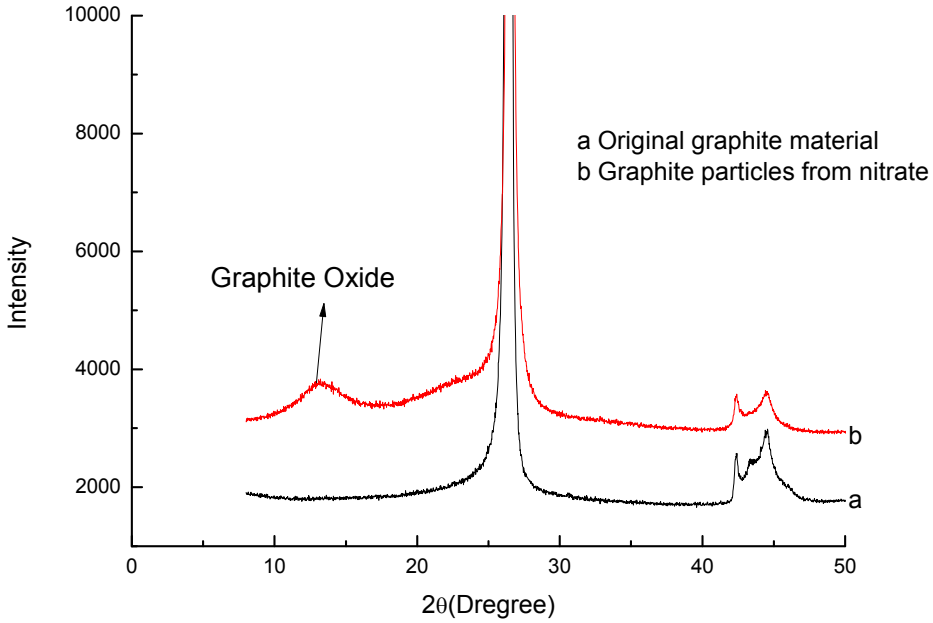

FIG. 11.37. Powder XRD patterns of graphite samples.

The variation of concentration of $NaNO_3$ from 2 mol/L to 6 mol/L did not have a great influence on the rate of graphite disintegration. Therefore, the rate of disintegration was not sensitive of solution concentration which could be of benefit to the practical application due to a large controllable excess for the concentration. The experimental results showed that the temperature variation between 15 and 40°C had no obvious influence on the rate of graphite disintegration.

Current density was a key parameter to influence the disintegration rate. The rate of graphite disintegration (RGD) was defined as the mass of disintegrated graphite particles per hour per square centimeter, (g/(h·cm^2)). Figure 11.38 shows that RGD increased with current density. In general, the RGD and current density exhibit a linear relationship in the regression result from 0.1 to 0.5 A/cm^2. Therefore, an appropriately higher current density was recommended in order to achieve a larger RGD.

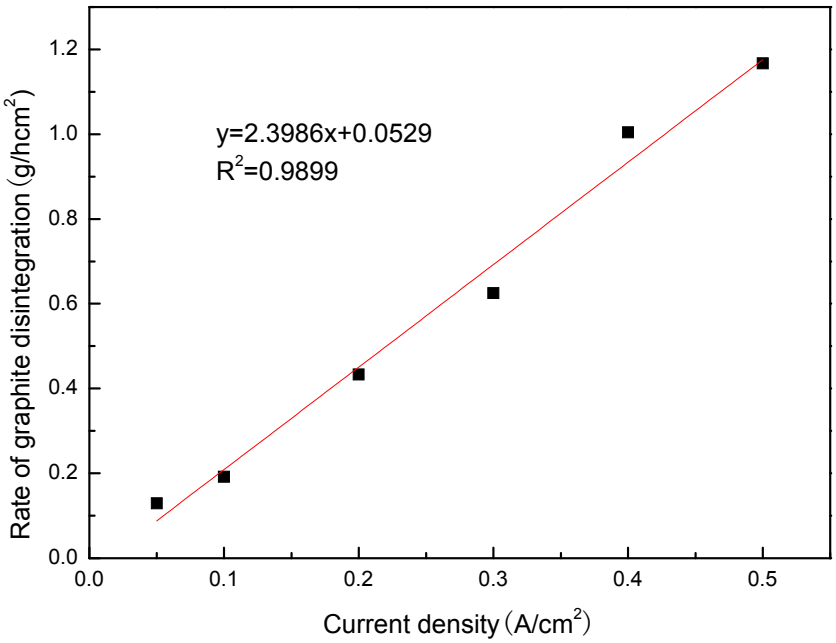

FIG. 11.38. Relationship between the RGD and current density.

(B) Disintegration of graphite matrix from an HTGR fuel element

In the experiments with genuine HTGR fuel elements, a columnar stainless steel electrode was used as the cathode, and the spherical fuel element served directly as the anode. Three experiments were carried out including currents of 5.6 A for 20 h, 11.3 A for 10 h and 17.0 A for 7.3 h, respectively. During the process of bulk electrolysis, the anodic fuel element was disintegrated gradually from the surface into graphite particles together with the coated fuel particles. After disintegration, the mixed particles were collected and split into the following three fractions: < 0.5 mm, 0.5–0.9 mm, and > 0.9 mm.

To avoid radioactive contamination of the graphite material, it is important to guarantee no damage to the SiC layer or the dissolution of fuel kernels. Therefore, the graphite particles and coated fuel particles were examined to verify the integrity of the coated fuel particle after disintegration.

(i) Evaluation on coated fuel particles and graphite particles

Some overcoatings were found detached from the coated fuel particles and some part of the coating was still left on the fuel particles after the disintegration of fuel element (Figs 11.39 and 11.40). The fuel particles shown in Fig. 11.39 are examples with some coatings left. Figure 11.39 (a)-(c), at a magnitude of 65, are images of different fuel particles obtained under 11.3 A. Figure 11.39 (d) is the image of the same particle as (c) at the magnitude of 45 to exhibit the overcoating scaled off. It can be seen that the overcoating of coated particles could even be scrapped off occasionally.

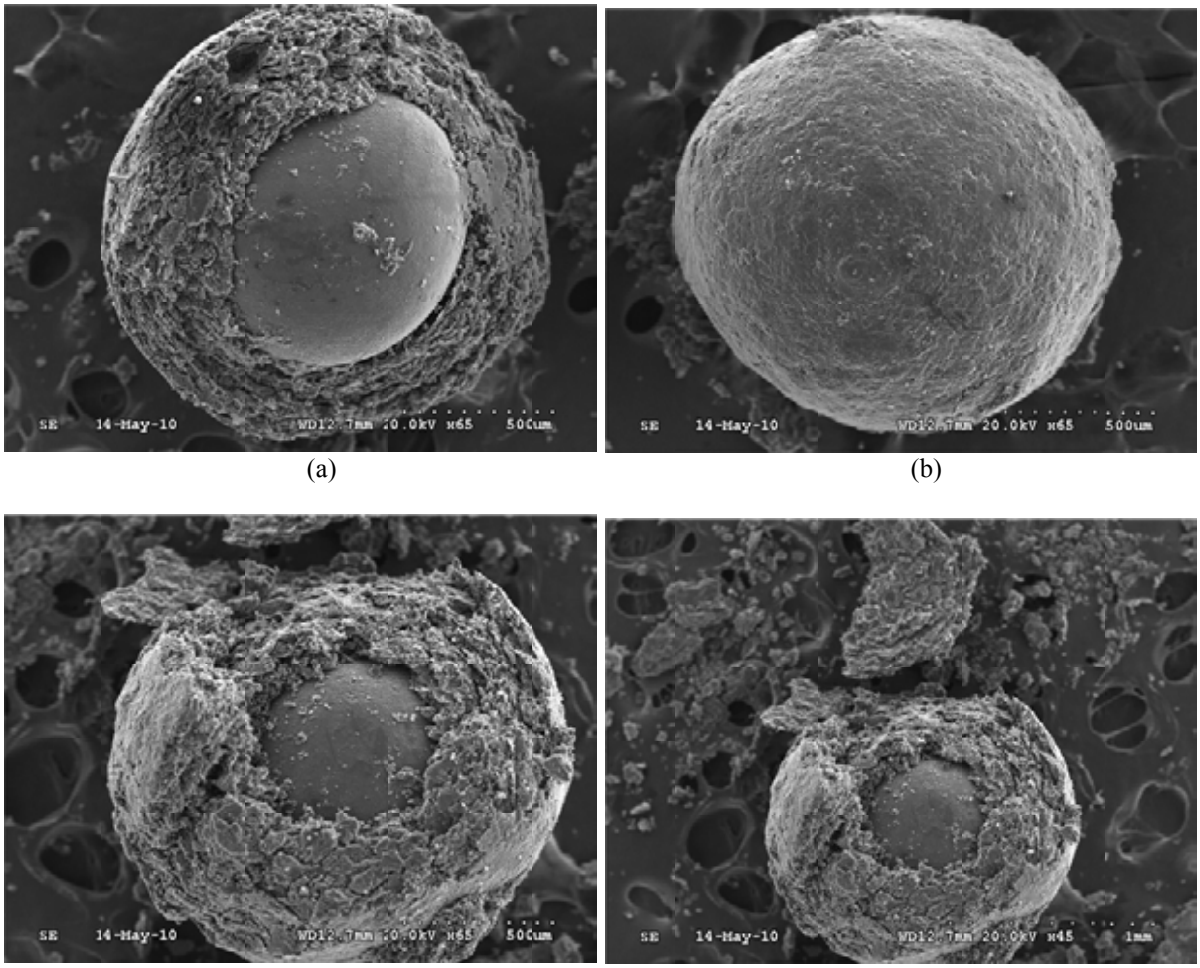

(a) (b)

(c) (d)

FIG. 11.39. TRISO coated particles with overcoating.

Figures 11.40 (a) and (b) exhibit SEM of the original standard TRISO coated fuel particle with a diameter of ~0.9mm at a magnitude of 90 and 500, respectively. Figures 11.40 (c) and (d), at a magnitude of 90 and 500, respectively, are images of a coated particle (~0.9 mm diameter) without most of its overcoating. The raffinate overcoating could also be observed obviously in Fig. 11.40 (c), however it could suggest that the fuel particle by the electrochemical method and the original fuel particle had the same dense surface of outer pyrocarbon layer and the same diameter after comparison of the SEM images.

The plane analyses of the chemical compositions by the energy dispersive system (EDS) are shown in Fig. 11.41 for different coated particle samples. The EDS spectra show X ray peaks of the carbon element. Because the measurement were carried out with an aluminum specimen mount, small spectra of Al were recorded in some EDS spectra. Most importantly, no peak of silicon was observed before and after the electrochemical process for the fuel particles which implies that no SiC layer was exposed.

Accordingly, the nuclear particles obtained by electrochemical method were TRISO coated particles with an outer high density carbon layer and no exposure of the SiC layer.

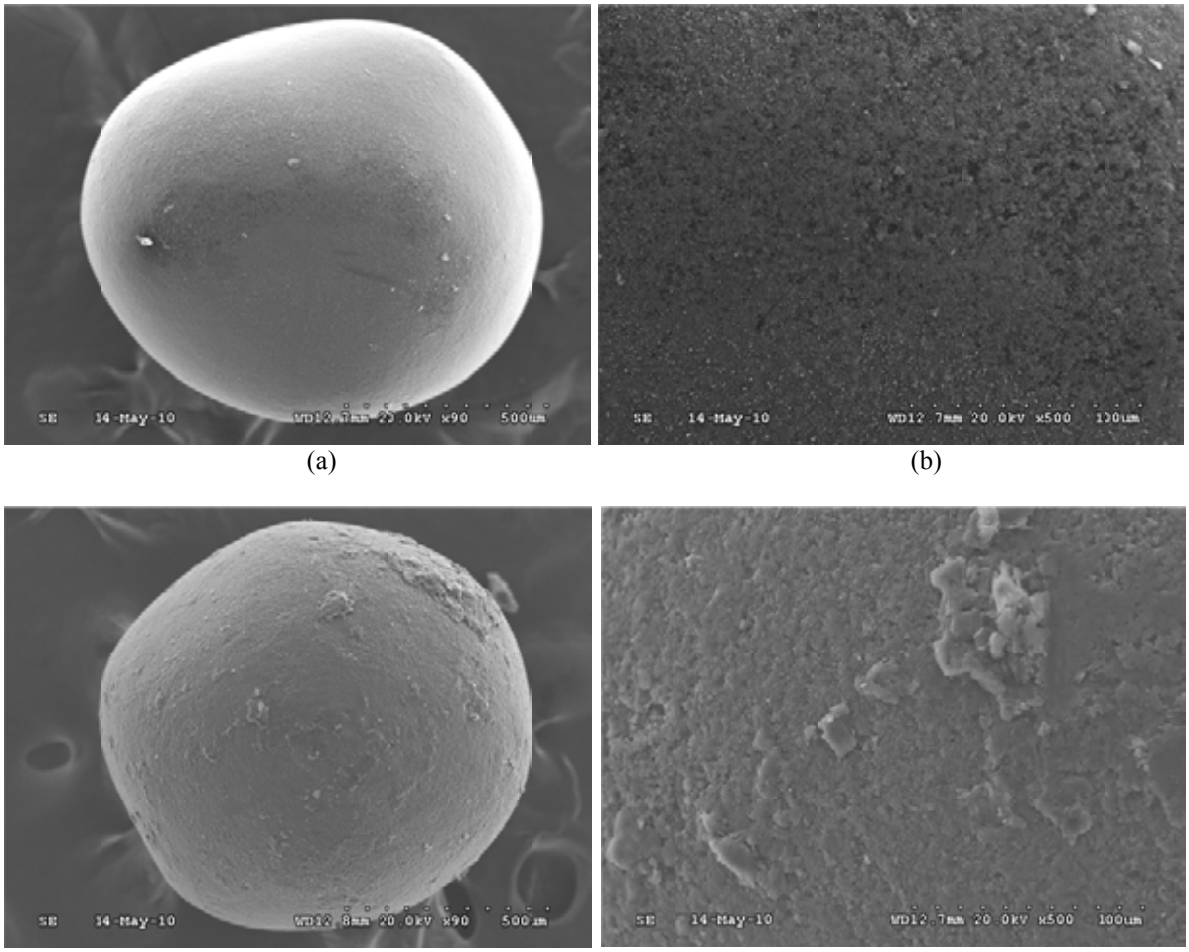

FIG. 11.40. TRISO coated particles.

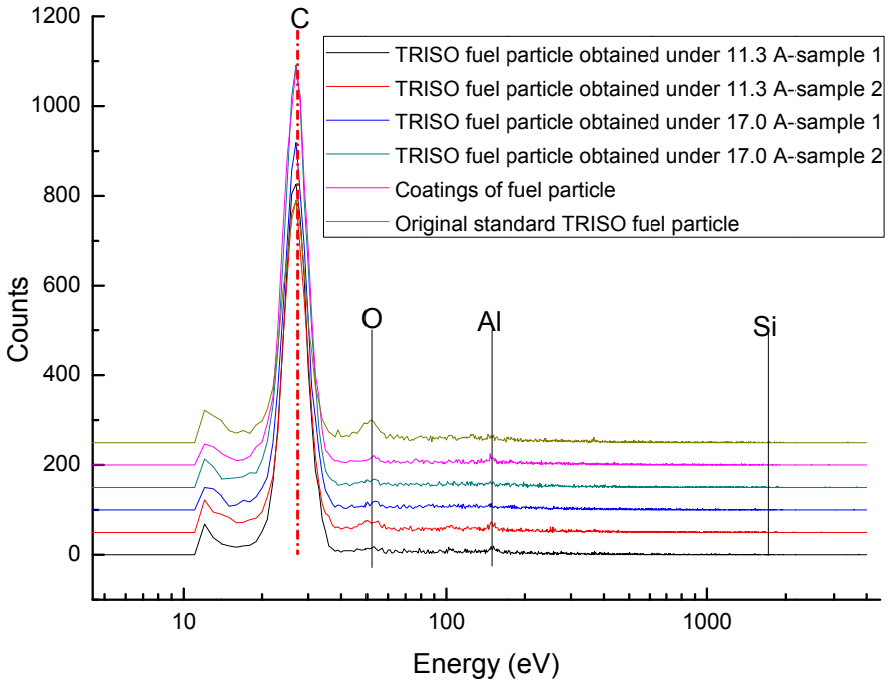

FIG. 11.41. EDS spectra of surfaces of the particles.

The plane analyses of the chemical compositions by the energy dispersive system (EDS) are shown in Fig. 11.41 for different coated particle samples. The EDS spectra show X ray peaks of the carbon element. Because the measurement were carried out with an aluminum specimen mount, small spectra of Al were recorded in some EDS spectra. Most importantly, no peak of silicon was observed before and after the electrochemical process for the fuel particles which implies that no SiC layer was exposed.

Accordingly, the nuclear particles obtained by electrochemical method were TRISO coated particles with an outer high density carbon layer and no exposure of the SiC layer.

From the experimental results of simulative fuel elements, the graphite matrix was disintegrated as graphite and graphite oxides by the electrochemial method in nitrate solution. The X ray diffraction spectra of graphite particles from HTGR fuel elements are shown in Fig. 11.42. Different patterns of graphite particles of different current densities illustrate the strong peaks of graphite and the peaks of graphite oxides [422, 423]. Therefore, graphite particles from fuel elements have similar components as the graphite particles from the simulative fuel elements.

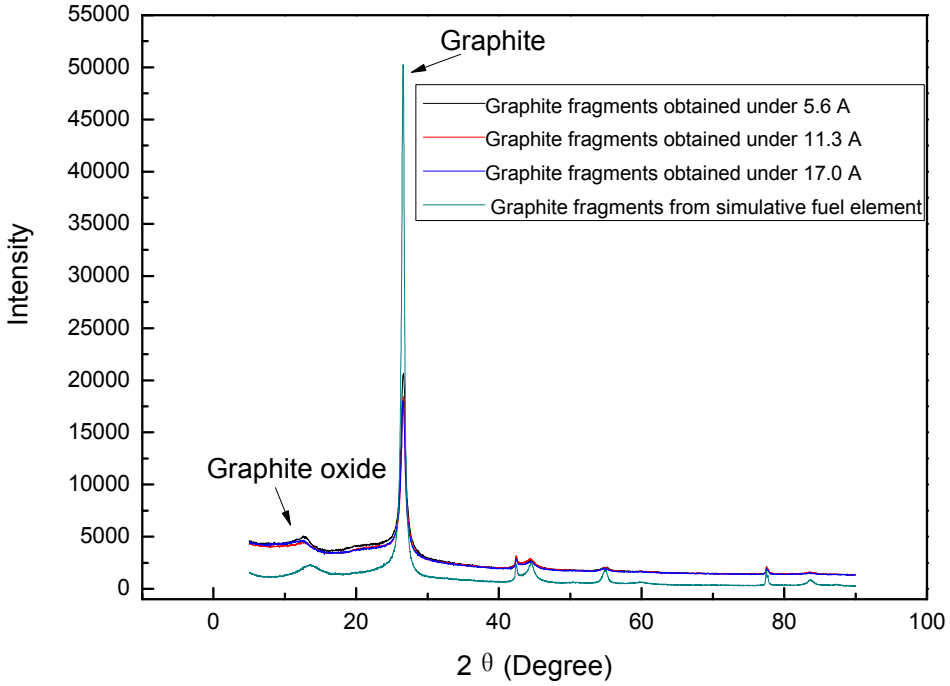

FIG. 11.42. X ray diffraction spectra of different graphite particles samples.

The carbon contents of the graphite particles are listed in Table 11.10. As could be concluded from the results of elemental analysis and the XRD spectra, the graphite particles from HTGR fuel elements by electrochemical method were also generated by partial oxidation. The carbon covered about 72 wt% of the graphite particles which was close to the carbon content of the graphite particles from the simulative fuel element.

TABLE 11.10. CARBON CONTENT OF GRAPHITE PARTICLES FROM HTGR FUEL ELEMENTS

Current (A)	5.6	11.3	17.0
Carbon content (%)	72.9	72.9	72.4

(ii) Integrity of coated fuel particles

In order to verify whether or not the TRISO coated particles got damaged and the graphite particles got contaminated by uranium, the microwave heating leaching method was used to study the dissolution of uranium from graphite particles and TRISO particles [424, 425].

About 0.5 g graphite particles, 0.4 g TRISO coated particles obtained under different densities were tested by the microwave heating leaching method in 8 mol/L HNO_3, and about 70 mL of solution was collected. These leaching solutions diluted by 10 times were examined for the uranium by ICP-MS, and the graphite particles from simulative fuel element were treated according to the same procedure to allow a comparison. The results of ICP-MS are listed in Table 11.11, and the uranium concentrations from solutions of nuclear particles and graphite particles are around the result from the simulative fuel element.

TABLE 11.11. ICP-MS RESULTS OF URANIUM CONCENTRATION OF DISSOLUTION SOLUTIONS

Solutions	Graphite particles			TRISO particles			Graphite particles from simulative element
Current (A)	5.6	11.3	17.0	5.6	11.3	17.0	—
U concentration (ppb)	< 0.7	1.7	< 0.7	< 0.7	< 0.7	< 0.7	1.3

— data not available.

After the electrolysis, the spent electrolyte solutions were recovered, and these solutions diluted by 10 times were tested by ICP-MS. The original electrolyte solution (8 mol/L $NaNO_3$) was also examined by ICP-MS for comparison. The results are shown in Table 11.12. It could be seen the uranium concentrations in the electrolyte solutions have the same level as in the original solution which implies that no obvious radioactive contamination to the electrolyte solutions occurred.

TABLE 11.12. URANIUM CONCENTRATION OF DISSOLUTION SOLUTIONS AND SPENT ELECTROLYTE BY ICP-MS

Solutions	Spent electrolyte			Original 8 mol/L HNO_3
Current (A)	5.6	11.3	17.0	—
U concentration (ppb)	< 0.7	2.8	< 0.7	2

— data not available.

The testing of the leaching solutions and the spent electrolyte solutions demonstrated the integrity of the coated fuel particles after the electrochemical disintegration process, which could avoid contamination of the graphite particles and the electrolyte solutions.

(iii) Influence of current

From the experimental results of simulative fuel elements, current density had an obvious influence on the rate of graphite disintegration. It took different times to disintegrate the fuel element under different currents. Fuel elements of 200 g, which were disintegrated under currents of 5.6 A for 20 h, 11.3 A for 10 h and 17.0 A for 7.3 h, were left at a weight of

37.0 g, 30.3 g and 41.8 g, respectively. The mixed particles were split into three fractions, < 0.5 mm, 0.5 to ~0.9 mm, and > 0.9 mm, respectively. The results of mass fractions obtained under different currents are listed in Table 11.13.

The fraction of < 0.5 mm consisted of graphite particles only. The other two fractions were mixtures of graphite and nuclear coated particles. For the current of 5.6 A, the fraction of > 0.9 mm mainly consisted of fuel particles with overcoating (Fig. 11.43 (a)), while only a small volume of nuclear particles could be found in the fraction of 0.5 to ~0.9 mm. For the current of 11.3 A, mainly coated fuel particles existed in the fraction of 0.5 to ~0.9 mm (Fig. 11.43 (b)), and the fraction of > 0.9 mm mainly consisted of graphite particles. From the experimental results, a larger current could cause finer graphite particles and detach the overcoating from the coated particles more easily.

(a) obtained under 5.7 A (> 0.9 mm) (b) obtained under 11.3 A (0.5 to ~0.9 mm)

FIG. 11.43. TRISO coated particles by electrochemical method.

TABLE 11.13. MASS FRACTIONS OF PARTICLES OBTAINED UNDER DIFFERENT CURRENTS

Current (A)	> 0.9 mm (%)	0.5 to ~0.9 mm (%)	< 0.5 mm (%)
5.6	6.9 [a]	27.0 [c]	66.1 [b]
11.3	3.1 [b]	8.8 [c]	88.0 [b]
17.0	0.79 [b]	14.2 [c]	85.0 [b]

[a] coated particles.
[b] graphite.
[c] mixture of graphite and coated particles.

(C) Conclusions

The graphite particles got partial oxidation with the oxygen element about 19% after the disintegration of graphite matrix, and the determined distribution of graphite particles from simulative fuel elements showed the promising potential to separate graphite particles from coated fuel particles. The nitrate concentration and system temperature had no obvious

influence on the rate of graphite disintegration. However, the current greatly affected the rate of graphite disintegration, which was increasing under a higher current, leaving graphite particles with a finer distribution.

After the disintegration of HTGR fuel elements, the characterization analysis of coated fuel particles and the determination of uranium concentration in the leaching solutions and spent electrolyte demonstrated that the electrochemical process can effectively disintegrate the fuel elements without any damage to the coated particles. This could avoid unexpected radioactive contamination of the graphite particles and electrolyte solutions.

Although this is an experimental basic study of the electrochemical method in nitrate solution proceeding at a slow rate, it exhibits the advantages of mild conditions without any corrosion to the reaction vessels, and any damage to the coated particles. Follow-on studies should explore assistant pretreatment to accelerate the disintegration process and develop the equipment which allows the continuous disintegration of fuel elements.

11.3.4.2. Dissolution of UO_2 from TRISO coated particles by microwave heating

In the head end process, the efficient dissolution of UO_2 kernel is a very important step. The UO_2 kernel can be dissolved in concentrated nitric acid by conventional heating [426].

The applications of microwave energy in mineral processing were widely investigated after 1970. Microwave-assisted leaching has been studied to improve the yield of extracted metal and reduce the process time. The unique microwave heating advantages such as short processing time, direct, selective and volumetric heating, and a more controllable heating process are the main drivers for potential implementation in metal extraction [427].

In order to explore a new concept of head end process for the treatment of spent fuel from HTGRs, the dissolution of UO_2 pellets and kernels in nitric acid solution by microwave heating has been studied.

(A) Experimental

The ceramic UO_2 pellets for high temperature gas cooled reactors were made from $UO_2(NO_3)_2$ solutions by the method called total gelation process (TGU) [428] which includes the following steps: preparation, gelation, drying, reduction and sintering at 1773 K. The characteristics of the UO_2 pellets were described in previous work [425]. The UO_2 pellets are 450–550 μm in diameter. The density is ≥ 10.4 Mg/m^3 and the element ratio of O to U is 1.99–2.01.

The TRISO coated isotropic fuel particles (0.92 mm diameter) with UO_2 kernel (0.5 mm diameter) used in the study have been manufactured by INET, Tsinghua University. Before dissolution, the TRISO coated particles were mechanically crushed.

A MARS 5 (microwave-assisted reaction system) with Teflon (PTFE) vessels was used to study the dissolution of UO_2 pellets and kernels under a 600 W, 2.45 GHz microwave field. The temperature of the solution in the vessel was automatically controlled by regulating the microwave power output according to a temperature feedback signal. The dissolution by conventional heating was carried out in an oil bath.

The concentrations of UO_2^{2+} in the dissolution solution were determined by the absorbance at 652 nm using spectrophotometry, with arsenazo III as the color-producing reagent.

(B) Results and discussion

(i) Microwave absorption property of UO_2

Under 300 W microwave heating, the surface temperature of 30 g ceramic UO_2 pellets was measured by infrared thermometer. Figure 11.44 shows the temperature evolution. It can be seen that the temperature increased quickly with a temperature rising rate of about 2.7 K/s, which implies that the ceramic UO_2 pellet has a very good ability to absorb microwave energy.

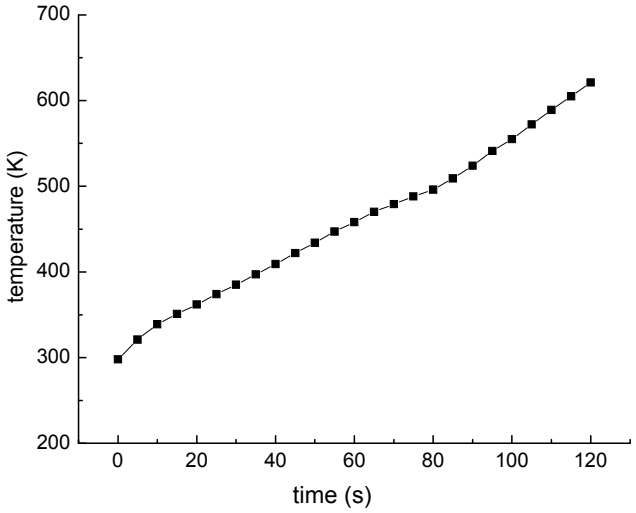

FIG. 11.44. Temperature of ceramic UO_2 pellets vs. microwave heating time.

(ii) Dissolution kinetics of UO_2 pellet

The dissolution kinetics of UO_2 pellet [425] in nitric acid (from 4 to 8 mol/L) by microwave heating was studied at different temperatures (from 363 to 383 K). The dissolution of UO_2 particles in the acidic media is a heterogeneous reaction, so the dissolution reaction kinetic model of UO_2 particles in HNO_3 can be associated with the well known shrinking core models which can be classified into the diffusion control through liquid film, the surface reaction control and the diffusion control through product layers. In the case of spherical particles, these models can be expressed as follows:

$$x = k_F \times t \qquad \text{for film diffusion control} \qquad (11.1)$$

$$1 - (1-x)^{1/3} = k_S \times t \qquad \text{for surface reaction control} \qquad (11.2)$$

$$1 + 2(1-x) - 3(1-x)^{2/3} = k_D \times t \qquad \text{for product layer diffusion} \qquad (11.3)$$

where x is the reacted fraction at time t and k_F, k_S, k_D are apparent rate constants given in the following equations:

$$k_F = \frac{3\, b\, k\, C_{HNO3}}{\rho} \qquad (11.4)$$

$$k_S = \frac{b\,k\,M\,(C_{HNO3})^n}{\rho\,r_0} \tag{11.5}$$

$$k_D = \frac{2\,b\,D_e\,M\,C_{HNO3}}{\rho\,r_0^{\,2}} \tag{11.6}$$

where

b	is the stoichiometric coefficient;
M	is the molecular weight of reacted substance;
ρ	is the density of reacted particle;
r_0	is the initial particle radius;
k	is the intrinsic rate constant;
D_e	is the effective diffusivity;
C_{HNO3}	is the bulk concentration of HNO_3;
n	is the reaction order in the term of HNO_3 concentration.

Although these models are derived from the assumption that the particles are spherical, they are applicable for variously shaped particles.

In the experiments, the film diffusion was eliminated by strong stirring during the dissolution process. The data of dissolution rate vs. time were analyzed by the above shrinking core models (surface reaction control and product layer diffusion control). The results fit very well with the product layer diffusion control model other than surface reaction control model because the correlation coefficients are above 0.99 (see Fig. 11.45, an example of 6 mol/L HNO_3). Within the reaction temperatures, the dissolution of UO_2 particles is controlled by product layer diffusion under a 600 W microwave field in 4–8 mol/L HNO_3 solution.

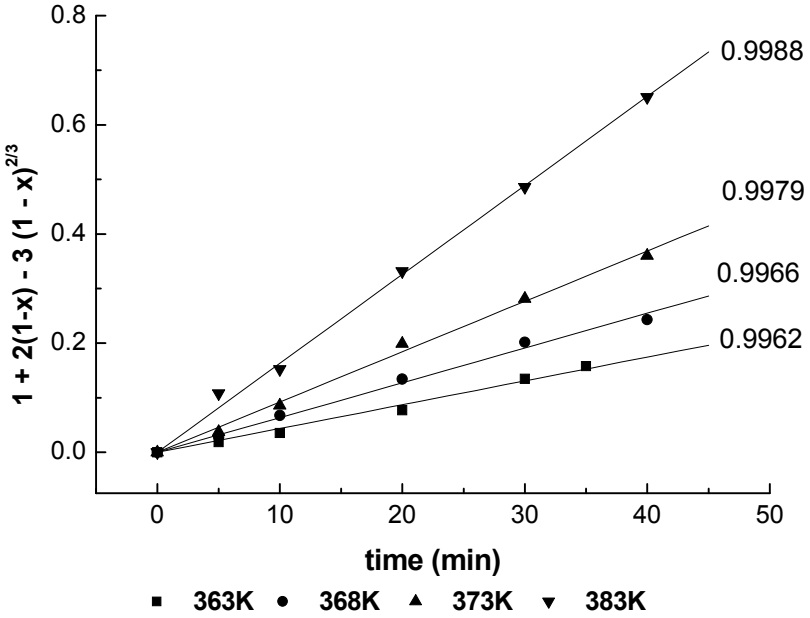

FIG. 11.45. Plot of equation (11.3) vs. reaction temperature in 6 mol/L HNO_3.

According to equation (11.6), assuming that $k_D = f(T, r_0, C_{HNO3})$, where r_0 is the initial particle radius in the experiment (450–550 μm), k_D can be expressed as follows:

$$k_D = k_0 \exp\left\{\frac{E_a}{R\,T}\right\} \times C_{HNO3}{}^{\alpha} \qquad or \tag{11.7}$$

$$\ln(k_S) = \ln(k_0) - \frac{E_a}{R\,T} + \alpha \ln(C_{HNO3}) \tag{11.8}$$

where k_0 and α are the constants to be determined.

The activation energy was calculated by the Arrhenius equation. The Arrhenius plots can be obtained from the values of reaction rate constant k_D which can be derived from the slopes of the plots at different temperatures and given in Fig. 11.46. The average activation energy for the dissolution of UO_2 particles is 73.2 ± 1.8 kJ/mol.

From plots of $\ln(k_D)$ vs. $\ln(CHNO_3)$, an average slope is given as 1.58 ± 0.05. By using the stepwise linear regression method, the values of E_a, k_0 and α, respectively, can be obtained. Hence, the reaction rate constant can be expressed as

$$k_D = 9.10 \times 10^6 \exp\left\{\frac{73\,200}{R\,T}\right\} \times C_{HNO3}{}^{1.58} \tag{11.9}$$

Thus, according to equation (11.3), the dissolution of the ceramic UO_2 pellets under the present experimental conditions can be expressed as

$$1 + 2(1-x) - 3(1-x)^{2/3} = 9.10 \times 10^6 \exp\left\{\frac{73\,200}{R\,T}\right\} \times C_{HNO3}{}^{1.58} \times t \tag{11.10}$$

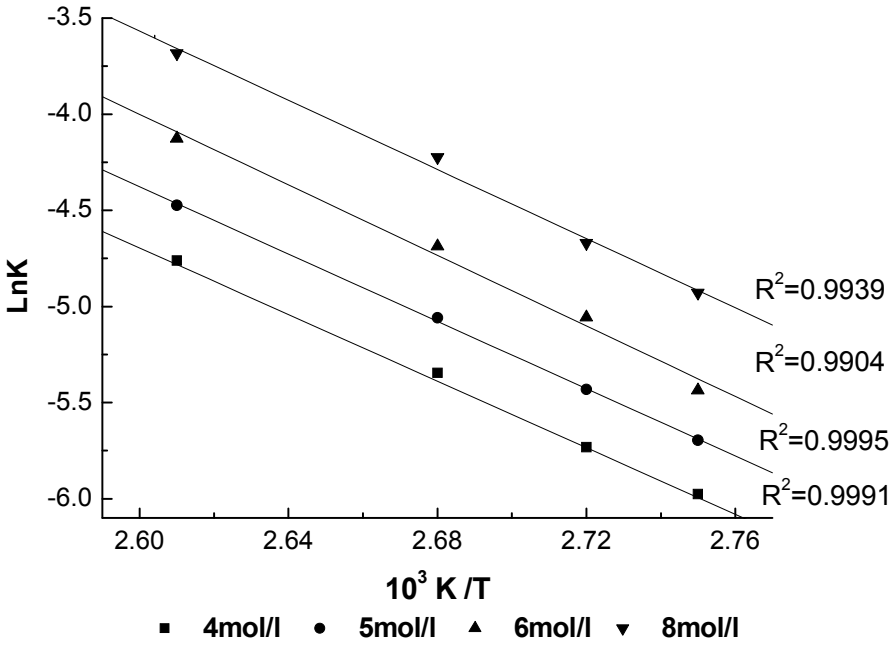

FIG. 11.46. Kinetic constants as a function of 1/T in various HNO_3 concentrations.

(iii) Dissolution of UO_2 kernels from crushed fuel particles

The TRISO coated fuel particles were crushed by a squeeze roller. Figure 11.47 gives the size distribution of the fragments obtained. More than 99% of the fuel particles could be broken up and about 70% fragments were in the diameter range of 0.4 to 0.6 mm.

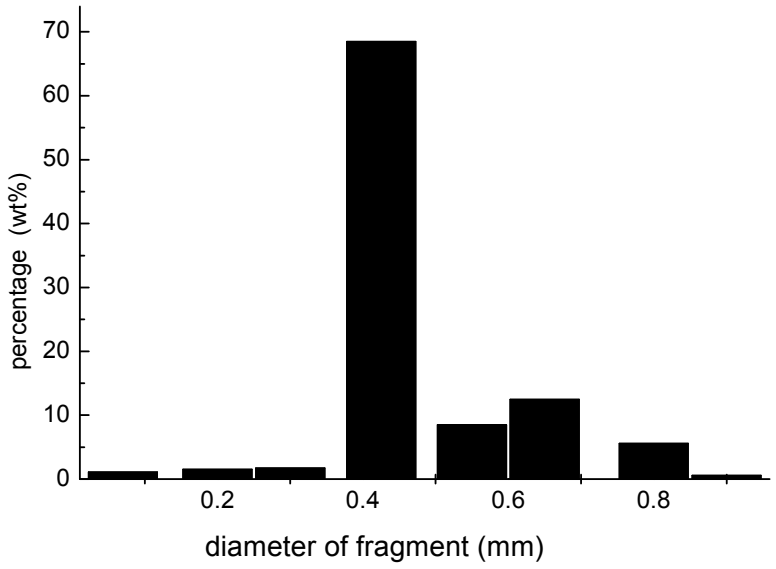

FIG. 11.47. Size distribution of fragments.

Table 11.14 lists the results of the dissolution of the crushed fuel particles. Compared to conventional heating, the microwave heating could remarkably reduce the dissolution time for the same dissolution percentage. The possible reason is that the nitric acid and the uranium dioxide are both polar molecules with a high value of the dielectric loss factor and the microwave can directly heat the uranium dioxide and the nitric acid solution allowing the temperature to rise much faster.

TABLE 11.14. DISSOLUTION OF CRUSHED FUEL PARTICLES BY CONVENTIONAL HEATING AND MICROWAVE HEATING (8 mol/L HNO_3, 100°C, INITIAL RATIO OF SOLID TO LIQUID = 1.2 g/mL)

Heating	Conventional heating		Microwave heating	
Dissolution time (min)	90	150	30	40
Dissolution percentage (%)	69.4	71.1	63.4	67.4

The effects of nitric acid concentration, initial ratio of solid to liquid, and dissolution temperature were studied. The appropriate technology parameters have been proposed for the dissolution of UO_2 kernel as: 8 mol/L HNO_3, temperature 100°C, initial ratio of solid to liquid 1.2 g/mL.

A cross-flow dissolution experiment was conducted to investigate the dissolution efficiency. First, 1.2 g fragments were dissolved using the above technology parameters for 40 min. Then the raffinate was dissolved by 1 mL 8 mol/L HNO_3 three times. Table 11.15 gives the experimental results. After three times of cross-flow dissolution, the total dissolution percentage of UO_2 kernel was more than 99.99% which indicates a high dissolution efficiency.

TABLE 11.15. RESULTS OF CROSS-FLOW DISSOLUTION EXPERIMENT

Turn	1	2	3	4
U concentration (g/L)	505.3	193.9	2.0	0.0137
Total U content (mg)	505.3	699.2	701.18	701.20
Dissolution percentage (%) [a]	> 72.1	> 99.7	> 99.99	> 99.999

[a] The dissolution percentage is defined as: (total U content/fourth total U content) × 100%.

(C) Conclusion

The HTGR spent fuel has a special structure with ceramic UO_2 kernel which is sintered at 1600°C during manufacture. The microwave technique was applied to dissolve the UO_2 kernel from the TRISO coated fuel particle.

The results of the temperature rise by microwave heating show that the ceramic UO_2 as the solute has a good ability to absorb the microwave energy demonstrating that it is possible to dissolve UO_2 with nitric acid by microwave heating.

Studies on the dissolution dynamics for UO_2 pellets have shown that microwave heating can increase the dissolution rate of UO_2 to a great extent compared with traditional heating. The dissolution of UO_2 pellets by microwave heating is a product diffusion control process.

The results of UO_2 kernel dissolution from crushed TRISO coated particles by microwave heating show that the dissolution percentage of UO_2 decreases with the initial ratio of solid to liquid (over 0.4 g/mL), increases with temperature and changes slightly above 120°C. The appropriate process parameters are: 8 mol/L HNO_3, temperature 100°C, initial ratio of solid to liquid 1.2 g/mL. The total dissolution percentage of UO_2 is more than 99.99% after three times of cross-flow dissolution.

11.3.5. Treatment of irradiated matrix (and structural) graphite

Radioactivity in graphite and carbonstone results from the neutron capture reaction on carbon itself and on impurities like chlorine, cobalt, iron, lithium, nitrogen, etc. Besides the activation of carbon and of stable impurities there are also the fission products from natural uranium present in the graphite as an impurity and from surface contamination via the coolant gas.

Whereas it appears principally possible to purify graphite from other radioactive elements by applying e.g. methods as already used during the fabrication of high purity nuclear graphite, the question still remains on the possibility for the removal of ^{14}C from the bulk material consisting of ^{12}C (88.89%) and ^{13}C (1.11%) in natural carbon.

It has been observed that, thermal and chemical treatment showed a significant selective release of ^{14}C, whilst the bulk material was only slightly corroded. In the first experiments, different graphite grades were heated up (or ‘roasted’) to 1060°C, in an inert atmosphere (Fig. 11.48). The fractional release of ^{14}C went up to about 10% although the mass loss of the samples was rather low (0.16–1.36%). A release up to 20% was found for a test, which experienced a minor air ingress corresponding to the mass loss of 1.36%. These experiments provided first indications that higher selective removal of ^{14}C may be possible.

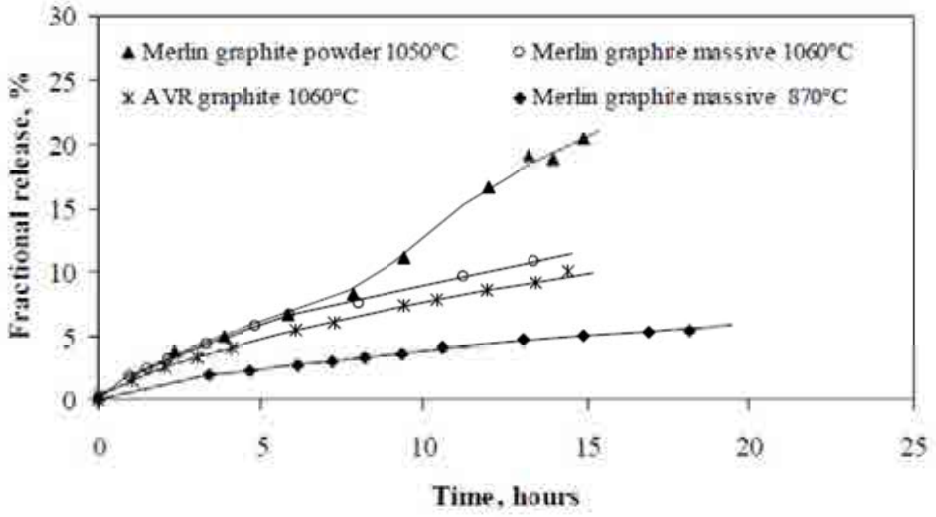

FIG. 11.48. Carbon-14 release during heating in an argon atmosphere.

These results have been explained by the assumption that most ^{14}C is created via the neutron activation of ^{14}N which might have been adsorbed within the pore system of the fuel matrix in case of the AVR, or has been provided by the air environment during neutron irradiation of the MERLIN sample taken from the thermal column of the FRJ-1 material test reactor at FZJ.

Meanwhile, there are indications that also ^{14}C stemming from neutron activation of ^{13}C is not part of the graphite lattice anymore, because the recoil energy during the activation process exceeds the energies of the chemical and crystal bonds. Thus, most ^{14}C may exist in more reactive chemical bonds as compared to the regular ^{12}C and ^{13}C atoms, in the graphite structure. During the heating in an inert atmosphere, the adsorbed oxygen preferentially reacts with the loosely bond ^{14}C atoms and releases the ^{14}C as ^{14}CO and/or $^{14}CO_2$. Once this oxygen reservoir is depleted, the release of ^{14}C slows down.

Further experiments with injection of water steam or oxygen were performed in the facility as illustrated in Fig. 11.49. The carbon monoxide and carbon dioxide produced during the heat and chemical treatment was captured in washing bottles. Samples were stepwise taken from these bottles and analysed with liquid scintillation counters (LSC) to determine ^{14}C and tritium releases.

These experiments achieved much higher fractional ^{14}C releases as e.g. shown in Fig. 11.50, whilst the total mass loss kept in the range of some percent. Complementary to argon, nitrogen was also used as carrier gas. The HTGR A3 fuel matrix material was taken from flakes of the particle-free zone from broken AVR fuel pebbles. The ^{14}C release reached nearly 80%, whereas the related mass loss was only 3%.

It must be noted that such experiments need to be repeated and optimized, but they provide first indications that purification of i-graphite seems to be possible even for most of the ^{14}C content.

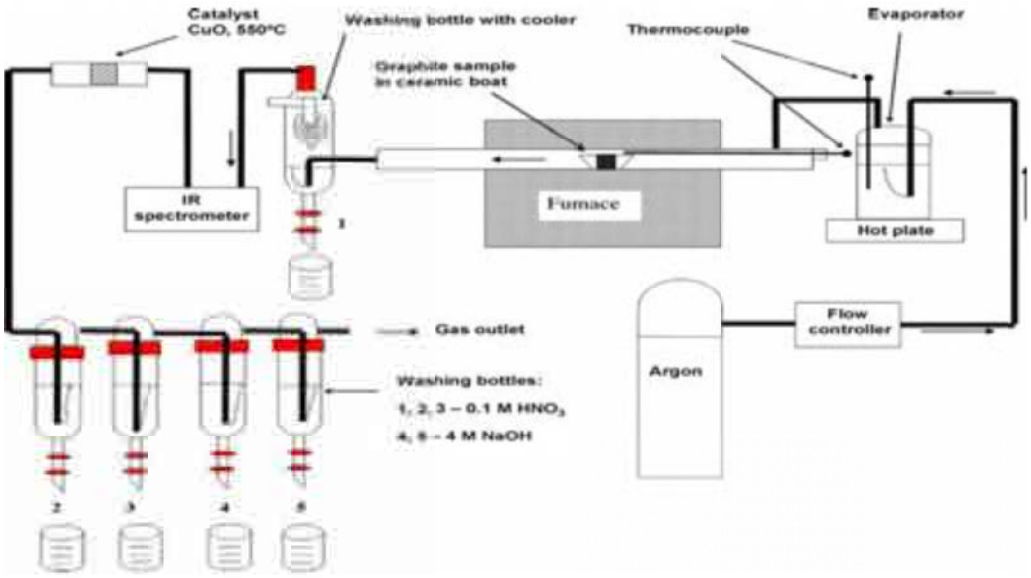

FIG. 11.49. Facility for thermal and chemical treatment.

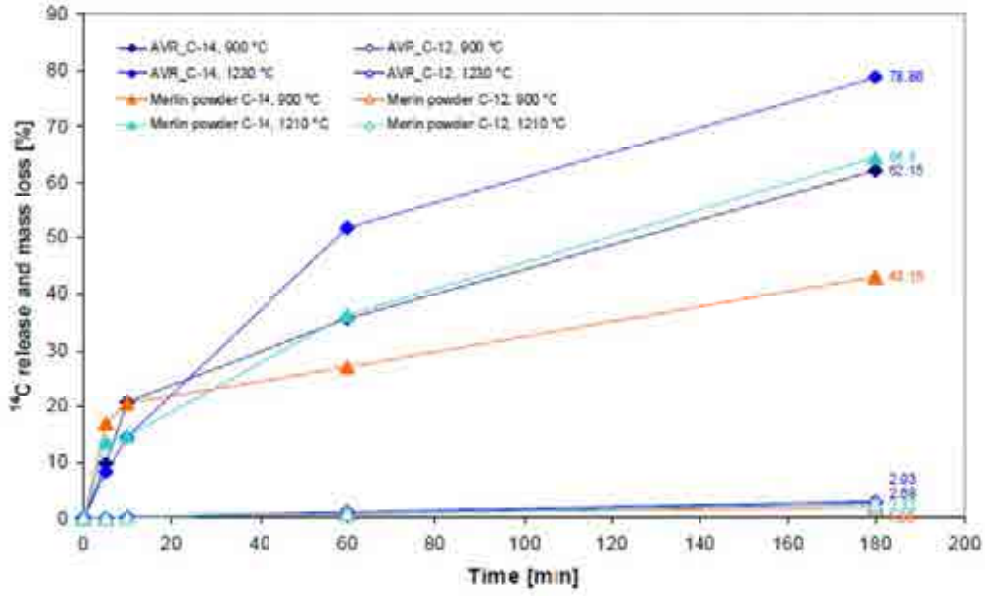

FIG. 11.50. Carbon-14 releases in oxidizing atmosphere.

A viable strategy for the recycle/reuse of graphite is the establishment of a process which takes the graphite from its retrieved form and converts it into a suitable intermediate (i.e. carbon black) for its inclusion into products for use within the nuclear industry.

To maximize the benefits of the initial roasting phase, the graphite should be in a particulate form to increase the surface area and conversely reduce the closed pore volume of the graphite. This is achieved as a byproduct of the fragmentation and segregation process for separating the graphite from the fuel particles.

The roasting phase enables the release of the majority of the ^{14}C (up to 90%) from the graphite with minimal conversion of the graphite to the gas phase (< 10%). This ^{14}C rich gas stream might then be used for other purposes. Once the majority of the ^{14}C has been removed, it is then converted by means of steam into carbon monoxide which can be separated or

further oxidized to carbon dioxide. The water involved can be recycled to collect the tritium released from the graphite. The residue can be packaged and grouted for long term storage.

In terms of maximizing the recycle opportunity of the graphite, the reversal process (through the Sabatier or Bosch reactions) enables the production of carbon black to be incorporated into the production of carbon based products for applications in the nuclear industries. These may include the production of (i) silicon carbide for use in disposal sites as a backfill or encapsulant, (ii) absorbent material to remove nuclides from liquid/gaseous waste, (iii) new graphite for use in graphite moderators, (iv) graphite electrodes for use in waste vitrification. The use of these recycled products aims at minimizing the requirement for the use of similar virgin graphite products, thereby minimising waste generation.

The production of the various carbon based artefacts is currently underway, with the evaluation of these being undertaken towards the end of the CARBOWASTE programme. This evaluation phase will address the viability of using recycled graphite for production of new reactors, moderators and fuel components, through detailed assessment of the candidate products properties, characteristics and fitness for purpose.

In addition to the work being undertaken under the CARBOWASTE programme, other work in this field is being performed internationally, which supports the viability of graphite recycle. One of these activities is the above described Deep-Burn project in the USA.

Initial results of the work taking place in this field are very encouraging and exhibit the significant potential for the recycling of pre-existing irradiated graphite to be an increasingly viable and considered option compared to the previously considered packaging and burial [410].

11.3.6. Conditioning of waste for disposal in final repository

Disposal of irradiated graphite imposes specific issues due to the porosity of the material and significant contents of long-lived activation products like ^{14}C and ^{36}Cl. Leach experiments are undertaken to clarify the radioactive releases under disposal conditions. Also the chemical form of the ^{14}C releases has an impact on the retention within the waste packages and potential releases to the environment.

Deep or shallow geological disposal of irradiated graphite is studied in many countries. Long-lived ^{14}C and ^{36}Cl complicate the disposal of carbonaceous wastes and graphite. The disposal performance might be enhanced by specific conditioning techniques in adequate waste packages, e.g. by confining the waste in stable matrices emplaced inside containers resistant to radiation, corrosion and mechanical damage. Recycled carbon based products may contribute to the packaging and confinement function. Decontamination will also lead to new waste streams with corresponding disposal needs for new carbonaceous waste products. An important point of the experimental programme within the EU project CARBOWASTE [410] is the development of new ceramic or vitreous waste matrices for graphite dust. High waste loadings can be achieved without loosing stability in aqueous solutions.

The mobility of long-lived radionuclides like ^{14}C and ^{36}Cl under repository conditions prior to and after groundwater access is an important concern. It has been shown that ^{36}Cl exists already under reactor conditions in two chemical forms, an inorganic very mobile one and an organic one more fixed. Only the latter is expected to resist under disposal conditions. Access of groundwater to the pore space in graphite has been studied as first step for the release of radionuclides from graphite. The results show that small hydraulic gradients are sufficient for

water infiltration into the pore space. Water saturation of a significant fraction of the pore volume is rapid even at low pressures. Water saturation rates increased with irradiation. Water access leads almost instantaneously to leaching of > 60% of the ^{36}Cl inventory. Both diffusive and advective transport properties for radionuclide transport in graphite were studied.

Radionuclides released from graphite may in principal be retained by engineered barrier materials surrounding the waste. However, first project results show that ^{36}Cl retention on cementitious barriers is rather weak. Performance analyses have shown that clay barriers are beneficial for reducing ^{36}Cl release while ^{14}C release is slow in presence of cementitous barriers. Dose contributions of radionuclides originating from irradiated graphite are very low, so that for, e.g. 100-year old graphite, radiolytic effects are not very relevant anymore.

12. REGULATORY PERSPECTIVES ON HTGR FUEL SAFETY AND LICENSING

As for any nuclear power plant design, fuel safety performance[4] and fuel fission product retention capability are important elements of the nuclear safety and licensing review conducted by a national nuclear safety regulator. For high temperature gas cooled reactor plants, regulators consider the performance and fission product retention capability of the fuel to be singularly important elements of the nuclear safety and licensing reviews. Accordingly, fuel performance and fuel fission product retention are areas of focus and emphasis for HTGR safety and licensing reviews conducted by national nuclear regulators. The reasons for this are multiple and include: the central importance of fuel performance and fuel fission product retention in the overall HTGR safety case; reliance on the fuel as the most important and essential barrier to prevent unacceptable releases of fission products from the facility during normal operation and potential accident conditions; the desire on the part of HTGR plant designers to utilize a vented, low pressure, fission product confinement building rather than an essentially leak-tight, pressure retaining, fission product containment building; the use of an event specific mechanistic approach, rather than a bounding approach, for calculating radiological accident source terms and; the significant differences between HTGR fuel and LWR fuel with respect to design, manufacture, performance, fission product retention characteristics and analytical modeling.

The purpose of this section is to present, at a high level, the safety performance objectives, the expectations and potential safety research issues bearing on regulatory assurance of HTGR fuel performance and fuel fission product retention capability for HTGR safety and licensing. The expectations and R&D issues described in this section are drawn from the licensing safety review conducted by the South African National Nuclear Regulator (NNR) for the PBMR as well as the pre-licensing safety reviews conducted by the US Nuclear Regulatory Commission (NRC) for the PBMR, the GT-MHR, and the NGNP VHTR. Additionally, regulatory research that has been conducted by NNR and NRC provide input and context to these expectations and related potential safety research issues.

Expectations will differ somewhat depending on whether the HTGR designer or license applicant references and places significant reliance on the design, manufacture, performance experience and established data base for a specific historical (i.e. reference) fuel design or whether the designer or license applicant relies mostly on the design, manufacture process

[4] As used in this section 'fuel safety performance' is the capability of the high density layers of the coated fuel particles in the fuel element to maintain integrity during fuel fabrication and the reactor specific core conditions associated with normal operations and the licensing-basis events (i.e. transients and accidents).

development, performance experience and data base developed specifically for the proposed fuel design.

In general, the expectations and potential safety research issues associated with HTGR fuel safety and licensing can be catalogued into one of several interrelated technical review areas. These are: fuel design, fuel fabrication development, fuel qualification testing, fuel performance analysis, accident source term analysis, production fuel fabrication quality assurance and in-reactor fuel performance monitoring. The following sections document the identified expectations and selected safety R&D issues. These expectations and issues reflect the current status of ongoing HTGR regulatory reviews as of 2010.

12.1. FUEL DESIGN

The contents of this section is discussed in Refs [429–437].

12.1.1. Safety performance objective

The fuel design specifications (together the fuel manufacture specifications) are adequate to achieve the required fuel safety performance and the required fuel fission product retention for the design service conditions associated with normal operations and the licensing basis events for the reactor design specific application.

12.1.2. Expectations

The full scope of fuel design specifications (i.e. key fuel design parameters/characteristics and related acceptance criteria), including the design parameters and associated design acceptance criteria, which are important to the safety case, are documented.

The full scope of fuel design specifications which are important to ensure fuel particle failure rates stay within the design fuel particle failure rates for fuel fabrication and the design specific service conditions of normal operations and licensing basis events, are documented.

The full scope of fuel design specifications which are important to ensure fuel fission product transport rates (i.e. fission product diffusion rates) in the kernels and the coatings of fuel particles and in the fuel matrix material remain within the design basis fission product transport rates for the design specific service conditions of normal operations and licensing basis events, are documented.

The full scope of the fuel design specific service conditions (e.g. maximum operating temperature, maximum fast fluence, maximum particle power, maximum burnup, maximum helium impurity levels) which are important to ensure fuel safety performance and fuel fission product retention for normal operations are documented.

The full scope of fuel design specifications needed to ensure integrity of the fuel element (compact, pebble) for the service conditions of normal operations and licensing basis events, are documented.

The full scope of fuel design specifications needed to control the rate of dust generation by the fuel for the service conditions of normal operations are documented.

12.1.3. Fuel design based on a reference fuel design

The reference fuel is clearly identified.

The fuel design specifications do not differ from the reference fuel design specifications.

The qualification and experience data of the reference fuel envelopes the fuel design specifications or is supported and justified by additional qualification data.

12.1.4. Potential safety research issues

HTGR designers seek to use the SiC layer fission product diffusion coefficients and associated supporting experimental data of a reference fuel design for their design specific fuel. In this regard, the effects of the SiC coating layer micro-structure (e.g. grain size, grain structure, grain orientation, grain boundaries) are well recognized as important to affecting the diffusion rates of radiologically important metallic fission products, (e.g. Cs, Ag) in the SiC layer. However, the effects of micro-structure are not yet completely understood or quantified. Accordingly, SiC micro-structures developed to be equivalent to a reference fuel SiC micro-structure is currently accomplished by using the SiC coating process specifications of the reference fuel and a qualitative comparison and acceptance of equivalency of the resulting micro-structure. The absence of an extensive theoretical and quantitative understanding of the effects of SiC micro-structure on SiC diffusion rates has resulted in the lack of a quantified acceptance criteria for equivalency of SiC micro-structures. Research could be conducted to adequately understand the theoretical and quantitative relationship between SiC micro-structure to fission product diffusion rates to assure and confirm the equivalency of SiC micro-structures and the diffusion rates associated with the reference fuel.

12.2. FUEL FABRICATION DEVELOPMENT

The contents of this section is discussed in Refs [429, 433–436, 438–441].

12.2.1. Safety performance objective

The fuel fabrication development programme provides the necessary and sufficient fuel fabrication requirements and quality control requirements needed to assure that the production fuel performance and fission product retention behaviour during the conditions of normal operations and potential licensing basis events for the reactor specific application are consistent with the manufacture, fuel performance and fission product retention behaviour demonstrated by the fuel used for the fuel qualification irradiation and accident condition testing programme.

12.2.2. Expectations

The fuel fabrication development programme provides the necessary and sufficient fuel manufacturing specifications, including the important manufacturing process parameters and related acceptance criteria and, the important fuel product parameters and related acceptance criteria used in production fuel manufacture.

The fuel fabrication development programme develops the necessary and sufficient fuel manufacture inspection methods, procedures and related acceptance criteria and the fuel manufacture testing methods, procedures and related acceptance criteria needed to show that the fuel manufacture product specifications are met.

The fuel manufacturing specifications together with the fuel manufacture inspection and tests methods assure that the fuel particle defect rate from manufacture and the fuel particle failure rates that could occur during the conditions of normal operation and licensing basis events are within the design fuel particle failure rates demonstrated by the fuel qualification programme.

The fuel fabrication development programme establishes sufficient fuel manufacturing knowledge and experience to support effective evaluation of the impact of variations of fuel manufacture on fuel quality and fuel safety performance.

The development of the fuel fabrication and quality control requirements are based on the use of prototypical production scale fuel fabrication equipment and processes and quality control The developed fuel fabrication process equipment, monitoring and control systems are highly reliable in ensuring that the important fuel fabrication process parameters stay within the acceptable ranges. Features are developed to continuously record the operating values of the important process parameters and preclude operation outside the acceptable range.

Inspection, calibration and preventive maintenance methods and procedures are developed or referenced for the fuel fabrication process equipment, monitoring and control systems. The appropriate frequency for implementation is established or referenced to ensure proper operation of the equipment.

Appropriate sampling methods, mixing methods, statistical analysis methods and acceptance criteria are developed to show, at a high confidence level, that the fuel meets the fuel product specifications.

Training is developed to ensure a high level of human performance of the production fuel fabrication facility personnel.

If a production fuel fabrication facility is not yet operational to provide fuel for fuel qualification testing in support of a plant operating license, the fuel used for the fuel qualification irradiation and accident condition simulation testing is provided by ‘production scale’ fuel fabrication equipment and methods. In this regard the production scale fuel used for fuel qualification testing is to:

- Use the same fuel manufacturing equipment (e.g. design, process control system) and processes (e.g. automation software) that are be used in the production fuel fabrication facility
- Use the same fuel manufacturing process specifications and fuel product specifications that are used in the production fuel fabrication facility
- Use the same fuel characterization methods that are used in the production fuel fabrication facility
- Meet the same fuel manufacturing process specifications and fuel product specifications that are used in the production fuel fabrication facility
- Use the same sampling, mixing, statistical analysis methods and acceptance criteria that are used in the production fuel fabrication facility
- Use the same calibration testing equipment, calibration inspection procedures and maintenance procedures for the fuel fabrication equipment as used for the production fuel fabrication facility equipment.

12.2.3. Fuel fabrication based on the fabrication of the reference fuel

Fuel fabrication specifications are equivalent to the reference fuel specifications.

The fuel meets the fuel manufacturing specifications of the reference fuel.

Fuel fabrication process is equivalent to the reference fuel process; fuel fabrication process development is sufficient to enable the effect of deviations from the reference fuel process on fuel quality to be effectively evaluated.

Any change to the fabrication process used for the manufacture of the reference fuel, based on advances in state-of-the-art of fuel manufacture methods or the state-of-knowledge of the effects of fuel manufacturing methods on fuel properties, is fully evaluated.

12.2.4. Potential safety research issues

Before deployed for use in production fuel characterization, a new state-of-the-art fuel characterization method is benchmarked against the existing fuel characterization method and calibrated against a standard.

Before deployed for use in production fuel fabrication, the efficacy of a potential new fuel product specification (e.g. SiC strength) is demonstrated and the effectiveness and reliability of the associated characterization method (e.g. crush strength) is validated.

12.3. FUEL QUALIFICATION TESTING

The contents of this section is discussed in Refs [429, 430, 434–436, 441, 442].

12.3.1. Safety performance objective

The fuel qualification test programme provides the necessary and sufficient data needed to demonstrate the safety performance and the fission product transport and release behaviour of the qualification fuel during the conditions of normal operations and the licensing basis events for the reactor specific application. The data is sufficient to develop and validate the fuel safety performance and fuel fission product transport and release models used for predicting the fission product release from the fuel for the conditions of normal operations and the licensing basis events for the reactor specific application.

12.3.2. Expectations

The fuel qualification irradiation test conditions (e.g. neutron flux energy spectrum and intensity, fuel burnup, fast neutron dose, irradiation temperature, helium impurity levels) conservatively bound the design conditions of normal operations for the reactor specific application.

- The rate of irradiation is either realistic or conservative (with respect to fuel performance) relative to the rate of irradiation predicted for the fuel operating in the reactor specific application.
- The neutron flux energy spectrum is either realistic or conservative (with respect to fuel performance) relative to the rate of irradiation predicted for the fuel operating in the reactor specific application.

The fuel qualification irradiation tests provide fuel margin data on fuel performance (i.e. particle failure fraction) and fuel fission product transport and release (e.g. fission product diffusion rates) for conditions beyond the design conditions for normal operations (e.g. fuel burnup, fast neutron dose, irradiation temperature).

The fuel qualification accident simulation testing is conducted to provide data on fuel performance and fuel fission product transport and release for each type of licensing basis event (e.g. core heatup, core heatup with air ingress, core moisture ingress, core reactivity increase) which is applicable to the reactor specific application.

The fuel qualification accident simulation test conditions (e.g. fuel burnup, fast neutron dose; time–temperature accident heatup profile, maximum accident temperature, fuel oxidation) conservatively bound the conditions for the licensing basis events for the reactor specific application.

The fuel qualification accident simulation tests provide fuel margin data on fuel performance (i.e. particle failure fraction) and fuel fission product transport and release (e.g. fission product diffusion rates) for conditions beyond the predicted maximum accident conditions (e.g. maximum transient accident temperature, maximum fuel oxidation).

During the fuel irradiation and accident conditions simulation tests fuel fission product releases are monitored and recorded. After completion of the fuel irradiation tests and accident condition simulation tests, fuel particle mechanical, geometrical, and chemical characteristics which are important to understanding, quantifying and confirming fuel particle performance and fuel fission product transport are examined and characterized.

The fuel qualification irradiation and accident condition testing facility includes instruments that accurately and continuously monitor and record test conditions, and fuel performance and fission product release.

A sufficient quantity of manufactured fuel particles are characterized (e.g. defect rate), irradiation tested and accident condition tested to obtain a statistically significant database, for developing analytical models for fuel predicting fuel performance (e.g. fuel particle failure fraction curve or response surface) and predicting fuel fission product transport and release (e.g. fission product diffusion rates).

Applicable nuclear quality assurance requirements are implemented for the fuel qualification test programme, including fuel manufacture, irradiation testing, accident condition testing and post-irradiation examinations and analyses

12.3.3. Fuel qualification based in part on fuel qualification testing of the reference fuel

To utilize the fuel irradiation test data, accident condition test data and operating experience data for a reactor specific application, the reference fuel:

- design and manufacture are equivalent to the design and manufacture of the fuel for the reactor specific application.
- physical, materials, structural and micro-structural characteristics are equivalent to the physical, materials, structural and micro-structural characteristics of the fuel for the reactor specific application
- irradiation test conditions conservatively envelope the operating conditions of the fuel for the reactor specific application.

- accident simulation test conditions conservatively envelope the fuel accident conditions for the reactor specific application
- behaviour and failure mode(s) that are observed in post-irradiation examinations are equivalent to the behaviour and failure mode(s) of the fuel for the reactor specific application.

Where one or more parameters of the reference fuel qualification envelope (i.e. irradiation conditions, accident conditions) does not bound the required fuel qualification envelope for the reactor specific application (i.e. gaps exist), fuel qualification test data are obtained for the fuel for the reactor specific application.

Notwithstanding the applicability of the reference fuel data to the fuel for the reactor specific application, supplemental fuel performance and fission product transport and release data from fuel irradiation and accident condition testing is provided for the fuel for the reactor specific application to confirm and further support the fuel performance and the analytical models developed from the reference fuel data.

12.3.4. Potential safety research issues

To model the effects of fuel oxidation on the local rate of fuel particle failure during a core heatup accident with air ingress, integral effects test data for the specific fuel design and manufacture for the reactor specific accident conditions is needed. Margin data on fuel performance (i.e. particle failure fraction) for fuel oxidation beyond the design basis oxidation conditions will be needed.

To model the effects of hydrolysis of fuel particles of exposed kernels on fission product release from the kernel during a moisture ingress accident, integral effects test data for the specific fuel design and manufacture for the reactor specific accident conditions will be needed. Margin data on fission product release from exposed fuel kernels for fuel kernel hydrolysis beyond the design basis hydrolysis conditions will be needed.

HTGR fuel qualification irradiations are typically performed in material test reactors (MTRs). As such, consideration needs to be given to the differences between the HTGR design specific neutron energy spectra and MTR neutron energy spectra. Differences could potentially result in differences in fuel particle failure probability. For low enriched uranium (LEU) fuel, neutron spectral differences affect uranium-to-plutonium conversion, isotopic fission ratios, and the resulting inventories of fission products within the fuel. These have the potential to affect fuel performance. The following observations bear noting in this context:

- Plutonium fission generally accounts for a large and variable fraction of the total burnup in LEU fuel. For a given initial uranium enrichment and total fuel burnup, the magnitude of the plutonium fission fraction will vary with changes in the neutron energy spectrum. An HTGR spectrum may tend to convert more uranium to plutonium than a water cooled MTR spectrum. Furthermore, for a given inventory of ^{239}Pu in relation to ^{235}U, the harder thermal neutron spectrum in an HTGR, typically peaked around the 0.3 eV fission resonance of ^{239}Pu, will favour ^{239}Pu fission over ^{235}U fission.
- The different fissionable nuclides (mainly ^{235}U, ^{238}U, ^{239}Pu, ^{241}Pu) that undergo fission in LEU fuel have very different yields of certain fission products that can affect TRISO fuel failure particle mechanisms and fission product release rates. In particular, the fission yields of palladium and various rare earths are many times higher from

plutonium fission than from ^{235}U fission. Therefore, the total production of these fission products may be more a function of plutonium burnup than initial heavy metal burnup.

- It is known that palladium and various rare earth fission products can degrade particle coating layer integrity. For palladium in particular, the following has been noted: "Fission product palladium is known to attack SiC at localized reaction sites. In high burnup LEU fuels, 25 to 50 times more Pd is produced than in either high burnup HEU fuels or LEU low burnup fuels because of the large fraction of fissions from Pu that are expected at high burnup. As a result, the potential for Pd attack of the SiC could be higher in LEU high burnup fuels. A review of the international database shows no strong dependence on burnup or the composition of the kernel, although theoretically this could be important."

Initial information needed for evaluating the effects of differences in the MTR neutron energy spectra and the HTGR design specific neutron energy spectra. The would include calculating or measuring the following quantities as functions of total burnup and irradiation time: (a) fissions of ^{235}U, ^{238}U, ^{239}Pu, and ^{241}Pu, and (b) inventories of palladium, selected rare earth fission products. The integral effects of the resulting inventory differences in palladium and selected rare earths on particle failure probability would then involve conducting sensitivity studies. The sensitivity studies would involve the use of a mechanistic fuel performance code (that models the effects of palladium and rare earth attack on the SiC layer integrity and particle failure probability) comparing the predicted failure rates between irradiations in the MTR and the specific HTGR for the design fast neutron fluence and design burnup conditions.

12.4. FUEL PERFORMANCE ANALYSIS

The contents of this section is discussed in Refs [433–436, 441, 443, 444].

12.4.1. Safety performance objective

Analytical models and methods used for predicting fuel particle failure and fuel fission product transport and release in the safety analysis evaluation model are adequately developed, verified validated and assessed.

12.4.2. Expectations

If a mechanistic fuel performance code (i.e. fuel particle failure is based on a mechanistic failure criteria) is used in the safety analysis evaluation model, the code is developed and assessed in accordance with regulatory requirements and guidance for the development and validation of safety analysis codes that are used in the licensing basis safety analysis evaluation model.

If an empirical fuel performance model (i.e. fuel particle failure is based on fuel particle failure test data) is used in the safety analysis evaluation model, the fuel performance model is to provide very high confidence that the actual particle failure rate would not exceed the predicted particle failure rate.

The fission product transport and release data obtained from the fuel qualification irradiation tests and fuel qualification accident condition tests and the fission product data from post-irradiation examinations are analysed to develop either conservative models for predicting

fuel fission product transport and release or best estimate models with uncertainties for predicting fuel fission product transport and release.

12.4.3. Potential safety research issues

If a mechanistic fuel performance code is used as part of the safety analysis evaluation model, separate effects test data on important material properties would be needed for the modeling of such properties in the fuel performance code. It is expected that data for the specific fuel design and manufacture, as appropriate would be obtained. Data on material properties, such as SiC strength, PyC strength, PyC irradiation-induced shrinkage, PyC irradiation-induced creep, bond strength between layers, kernel swelling and PyC thermal expansion coefficient could be required.

If a mechanistic fuel performance code is used as part of the safety analysis evaluation model, integral effects test data on the effects of irradiation conditions and accident conditions on the number of fuel particle failures and fission product releases will be needed to validate the predictions of the fuel performance code.

Metallic fission product (e.g. Cs) release data obtained from accident heat up simulation tests is used for predicting metallic fission product diffusion coefficients for the fuel temperatures associated with a core heatup accident. Because these heatup tests are conducted as part of the post-irradiation testing and therefore do not include the effects of irradiation on bulk diffusion within the grains of the coating layers or along the grain boundaries of the coating layers. The use of this data, especially for SiC layer, as 'margin data' used for predicting fission product diffusion for fuel operations at irradiation temperatures above the design operating fuel iradiation temperature could be non-conservative. Such post-irradiation data would not account for the effect of increased diffusion due to neutron irradiation causing a continuous production of defects in the layer lattice and grain boundaries. The Cs diffusion rate would miss this effect and thus potentially underpredict the Cs diffusion rate during irradiation. It would be expected that margin data for metallic fission product diffusion for fuel operating irradiation conditions above the maximum fuel operating conditions would be obtained by irradiation rather than by post-irradiation testing.

Metallic fission product (e.g. Cs) release data obtained from accident heatup simulation tests are used for predicting metallic fission product diffusion coefficients for the fuel temperatures associated with a core heatup accident. Because these heatup tests are conducted as part of post-irradiation testing, they do not address any diffusion-related phenomena that are present during irradiation and absent afterward. The additional use of such post-irradiation heatup data as 'margin data' for predicting fission product diffusion during irradiation at operating temperatures above those addressed by the fuel qualification irradiations could therefore be non-conservative. For example, recent experiments and multi scale (e.g. atomic level) simulations suggest that lattice vacancies in the grains and grain boundaries play an important role in both the solubility and the diffusion of Cs in SiC. Further, it is well known that neutron irradiation produces not only extended defects such as dislocation loops and voids but also temporary lattice vacancies and interstitials that disappear soon after irradiation stops. These non-equilibrium vacancies and interstitials would be expected to increase the solubility of Cs in SiC and accelerate Cs diffusion during neutron irradiation conditions. Post-irradiation measurements would miss this effect and thus potentially underpredict Cs diffusion during irradiation. In general, the evaluation of diffusion effects during irradiation should consider how the concentration of lattice vacancies increases with both irradiation intensity and temperature. In this regard, a statistical comparitive analysis should be conducted for the

diffusion coefficients based on irradiation conditions and the diffusion coefficients based on post-irradiation conditions for the same temeratures. The comparison would be used to assess whether or not the effect of irradiation on the diffusion rates is significant.

12.5. ACCIDENT SOURCE TERM ANALYSIS

The contents of this section is discussed in Refs [429, 434, 435, 440, 441, 445–447].

12.5.1. Safety performance objective

Analytical models and methods used for predicting the core-wide release of fission products from the fuel during normal operations and licensing basis events for the reactor specific application are adequately developed, verified, validated and assessed.

12.5.2. Expectations

The expectations documented in Section 12.4 apply to this section.

The fuel particle design failure fraction curve (or response surface) is to provide 95% confidence that the particle failure fraction would not exceed the design particle failure fraction curve (or response surface).

The fuel particle design failure fraction curve (e.g. particle failure fraction versus fuel temperature) or failure fraction 'response surface' (e.g. particle failure fraction versus fuel temperature and fuel burnup) is to include the fuel particle defect fraction from fuel manufacture, the fuel particle failure fraction due to normal operating conditions (e.g. fuel temperature, burnup) and the fuel particle failure fraction due to accident conditions (e.g. fuel temperatures associated with core heatup, fuel oxidation associated with air ingress, kernel energy deposition and temperature increase associated with reactivity insertion).

The fuel particle design failure fraction curve (or response surface) and is based on the fuel failure data from fuel qualification irradiation tests and fuel accident condition tests and associated post-irradiation examinations of the design specific fuel.

The fuel fission product transport models (e.g. fission metal diffusion in the fuel kernel, coating layers and matrix; fission gas release from the kernel) are based on data from irradiation testing, accident condition testing and post-irradiation examinations for the design specific fuel.

The test data for developing the fuel fission product transport models are to span the predicted range of fuel operating conditions (e.g. temperature, burnup) and accident conditions (e.g. fuel accident temperature, fuel oxidation) for the reactor design specific application.

Fission product transport for intact coated particles, coated particles with failed coating layers and defective coated particles (from manufacture) are modeled.

The analytical models and methods developed for predicting core-wide fission product release from the fuel during normal operation and accidents are validated against integral fuel irradiation and accident condition fission product release tests.

The integral tests are to involve a significant number of failed fuel particles and significant fission product releases from the fuel form (i.e. fuel compacts, fuel spheres) associated with

the reactor design specific application. Potential biases and uncertainties in the predictions are assessed and quantified.

The fuel fission product transport models and methods are validated against integral fuel irradiation tests and accident condition tests.

The fuel fission product transport models are to account for all radiologically important fission products (e.g. Cs, Sr, I, Ag, Kr, Xe) and include the effects of radionuclide decay.

The time dependent fission product releases from the fuel in the core are based on the local fuel conditions (e.g. fuel temperature, fuel burnup) and the timing of fuel particle failures in the different regions in the core.

12.5.3. Source term models based on reference fuel source term models

The fuel fission product transport models (e.g. fission metal diffusion in the fuel kernel, coating layers and matrix; fission gas release from the kernel) for the reference fuel are confirmed and supplemented by data from irradiation testing, fuel accident condition testing and fuel post-irradiation examinations for the fuel for the reactor specific application.

12.5.4. Potential safety research issues

While iodine-131 is an important radionuclide for modeling the dose consequences of HTGR accidents, it has a half-life of only about 8 days. As such, accident simulation heatup tests which take place several months after fuel irradiation ends do not attempt to measure ^{131}I release from failed fuel particles since there is no longer a detectable concentration of ^{131}I in the particles. To obtain accurate data on ^{131}I releases for modeling accidents which result in fuel particle failures, the irradiated fuel should be re-irradiated just prior to the accident testing to re-establish a known ^{I31}I concentration in the intact particles. ^{131}I released from particles that fail during the accident heatup tests should be collected (via cold plates) and analysed.

Metallic fission products released by the fuel and adsorbed in carbonaceous (e.g. graphite, matrix) dust that is generated by the fuel during normal reactor operation can significantly contribute to the magnitude of metallic fission product release outside the plant during a rapid depressurization event due to the mobility of the dust. Currently, there is only limited operational data and no significant experimental separate effects data available to accurately model the magnitude and the physical characteristics of carbonaceous dust that is generated by the fuel during normal power operation. Research could be conducted to obtain data on the rate and characteristics of carbonaceous dust generated during normal operations to reduce the uncertainties associated with the accident source term calculation modeling in this area. The results of such testing could also be used to develop a specific test and acceptance criteria for fuel manufacture (i.e. Section 12.2).

12.6. PRODUCTION FUEL FABRICATION QUALITY ASSURANCE

The contents of this section is discussed in Refs [429, 436, 441].

12.6.1. Safety performance objective

The production fuel to be loaded in the reactor core is fabricated to the required level of quality established by the fuel fabrication development programme and will have fuel

performance and fission product retention behaviour demonstrated by the fuel qualification testing programme.

12.6.2. Expectations

Production fuel fabrication uses the identical/equivalent equipment and the same fabrication methods, procedures, acceptance criteria and know-how established by the fuel fabrication development programme. These include the:

- same manufacturing specifications (fuel product specifications and fuel process specifications) and related acceptance criteria;
- same inspection methods, procedures and related acceptance criteria and the fuel manufacture testing methods, procedures and related acceptance criteria;
- identical/equivalent fuel fabrication process equipment, monitoring and control systems;
- inspection, calibration and preventive maintenance methods, equipment, procedures and acceptance criteria for the fuel fabrication process equipment, monitoring and control systems;
- sampling methods, mixing methods, statistical analysis methods and acceptance criteria.

The fabricated fuel meets the full scope of fuel manufacturing specifications.

Training is provided for the production fuel fabrication facility staff that has a role in fuel quality.

Significant deviations in fuel quality are fully evaluated by staff with adequate knowledge and experience.

Changes to implement advances in the state-of-the-art of fuel manufacture are fully evaluated for acceptability

12.7. IN-REACTOR FUEL PERFORMANCE MONITORING

The contents of this section is discussed in Ref. [448].

12.7.1. Safety performance objective

The systems and analysis methods that monitor the performance of the fuel in the reactor core during reactor operations is capable of assessing core-wide fuel fission product barrier performance and detecting if core-wide fuel fission product barrier performance degradation places fuel barrier performance outside the envelop assumed in the safety analysis.

12.7.2. Expectations

The systems and analysis methods provided to monitor the performance of the fuel in the core during reactor operations are expected to provide for reliable and accurate monitoring.

The systems and analysis methods continuously monitor (e.g. continuous activity, grab sample) the non-condensable fission products circulating in the helium coolant.

The systems and analysis methods monitor (e.g. plateout probes) the condensable fission products circulating in the helium coolant.

The systems and analysis methods measure the condensable fission products that have plated out or settled out on surfaces within the reactor system.

The systems and analysis methods measure the condensable fission products absorbed in carbonaceous dust that is circulating in the helium coolant or has settled out on surfaces within the reactor system.

The systems and analysis methods monitor radiologically important isotopes (e.g. iodine, caesium, krypton, silver) released from the fuel.

Threshold action levels are established for monitored parameters indicating when fuel fission product barrier performance is approaching the envelope for fuel fission product barrier performance assumed in the safety analysis.

For the initial fuel core load associated with a new reactor design specific application a representative sample of irradiated fuel at end-of-life burnup is subject to accident condition heatup testing and post-irradiation examination to confirm fuel fission product barrier performance during operation was within the fuel fission product barrier performance assumed in the safety analysis.

12.7.3. Potential safety research issues

If the measured fuel performance is below the fuel performance assumed in the safety analysis, it is expected that a full evaluation, including fuel safety research as needed, will be implemented to establish the root causes and corrective actions that may be associated with the technical areas in this section.

REFERENCES

[1] INTERNATIONAL ATOMIC ENERGY AGENCY, Fuel performance and fission product behaviour in gas cooled reactors, IAEA-TECDOC-978, IAEA, Vienna (1997).

[2] GAUTHIER, J.C., HITTNER, D., CARRÉ, F., "ANTARES: Ready for the combined heat and power market", Proc. 3rd Int. Top. Meeting on High Temperature Reactor Technology HTR2006, Johannesburg (2006).

[3] KUNITOMI, K., et. al., Reactor core design of Gas Turbine High Temperature Reactor 300, Nucl. Eng. Des. **230** (2004) 349.

[4] KUNITOMI, K., et. al., "GTHTR300 for hydrogen cogeneration", Proc. 2nd Int. Top. Meeting on High Temperature Reactor Technology HTR2004, Beijing (2004).

[5] KODOCHIGOV, N., et al., "The international GT-MHR fuel development program", Proc. IAEA-TM on Current Status and Future Prospects of Gas Cooled Reactor Fuels, International Atomic Energy Agency, Vienna (2004).

[6] RICHARDS, M., et al., H2-MHR conceptual designs based on the sulphur-iodine process and high-temperature electrolysis, Int. J. Nuclear Hydrogen Production and Applications **1** (2006) 36.

[7] KODOCHIGOV, N., et al., "Program of GT-MHR fuel development and justification", Proc. 2nd Int. Top. Meeting on High Temperature Reactor Technology HTR2004, Beijing (2004).

[8] LABAR, M.P., et al., The Gas Turbine Modular Helium Reactor, Nuclear News **46**(11) (2003) 28.

[9] HARVEGO, E.A., et al., "Hydrogen production using the Modular Helium Reactor", Proc. Int. Conf. on Nuclear Engineering ICONE13, Beijing (2005).

[10] SMITH, C., BECK, S., GALYEAN, W., Separation requirements for a hydrogen production plant and high-temperature nuclear reactor, Rep. INL/EXT-05-00137, Rev.1, Idaho National Laboratory, ID (2005).

[11] RICHARDS, M.B., et.al., "Conceptual designs for MHR-based hydrogen production systems", Proc. Int. Conf. on Nuclear Energy Systems for Future Generation and Global Sustainability GLOBAL2005, Tsukuba (2005).

[12] REUTLER, H., LOHNERT, G.H., Advantages of going modular in HTR, Nucl. Eng. Des. **78** (1984) 129.

[13] PETTI, D., "Fuel failure mechanisms", IAEA, High Temperature Gas Cooled Reactor Fuels and Materials, Rep. IAEA-TECDOC-1645, International Atomic Energy Agency, Vienna (2010) 70–78.

[14] HEIT, W., HUSCHKA, H., RIND, W., KAISER, G.G., Status of qualification of high-temperature reactor fuel element spheres, Nucl. Technol. **69** (1985) 44.

[15] GONTARD, R., NABIELEK, H., Performance evaluation of modern HTR TRISO fuels, Internal Report HTA-IB-05/90, Research Center Jülich (1990).

[16] TANG, C.H., et al., Design and manufacture of the fuel element for 10 MW high temperature gas cooled reactor, Nucl. Eng. Des. **218** (2002) 91.

[17] TANG, C.H., et al., Research and development of fuel element for Chinese 10 MW high temperature gas-cooled reactor, J. Nucl. Sci. Technol. **37** (2000) 802.

[18] SAWA, K., et al., Fabrication of the first-loading fuel of the High Temperature Engineering Test Reactor, J. Nucl. Sci. Technol. **36** (1999) 683.

[19] FÖRTHMANN, R., Die Chemie des Hydrolyseverfahrens zur Herstellung sphärischer Kernbrennstoffteilchen, Rep. Jül-950-RW, Research Center Jülich (1973).

[20] XU, Z.C., et al., "A total gelation process for the preparation of dense UO_2 microspheres for HTGR", Proc. 1st Pacific Rim International Conference on Advanced Materials and Processing PRICM-1, Hangzhou (1992).
[21] FUKUDA, K, et al., Research and development of HTTR coated particle fuel, J. Nucl. Sci. Eng. **28** (1991) 570.
[22] HACKSTEIN, K.G., et al., Stand der Brennelement-Technologie für Hochtemperatur-Kugelhaufenreaktoren, Atomkernenergie-Kerntechnik **47** (1985) 163.
[23] LAUF, R.J., BRASKI, D.N., Dependence of silicon carbide coating properties on deposition parameters, Preliminary Rep. ORNL/TM-7209, Oak Ridge National Laboratory, TN (1980).
[24] DEGALTSEV, Y.G., "Fuel properties with combined SiC-PyC layers", Proc. 2nd Soviet/German Seminar on Fuel and Graphite for HTR, Research Center Jülich (1991) 49–75.
[25] HROVAT, M.H., et al., Über die Entwicklung eines Matrix Materials zur Herstellung gepresster Brennelemente für Hochtemperatur-Reaktoren, Rep. Jül-969, Research Center Jülich (1973).
[26] GUILLERMIER, P., PHELIP, M., "CEA & AREVA R&D on HTR fuel technology", Proc. IAEA-TM on Current Status and Future Prospects of Gas Cooled Reactor Fuels, International Atomic Energy Agency, Vienna (2004).
[27] GUILLERMIER, P. PHELIP, M., "AREVA and CEA fuel development and qualification program of HTR fuel", Proc. 3rd Int. Top. Meeting on High Temperature Reactor Technology HTR2006, Johannesburg (2006).
[28] CHAROLLAIS, F., et al., "CEA and AREVA R&D on HTR fuel fabrication & presentation of the GAIA experimental manufacturing line", Proc. 2nd Int. Top. Meeting on High Temperature Reactor Technology HTR-2004, Beijing, China (2004).
[29] BENDOTTI, S., et al., "HTR and VHTR fuel irradiation program in the OSIRIS material testing reactor and codes", Proc. 2nd Int. Top. Meeting on High Temperature Reactor Technology HTR2004, Beijing (2004).
[30] PHELIP, M., et al., "First results from HTR-F&F1 projects: HTR fuel technology", Proc. Int. Congr. on Advanced Nuclear Power Plants ICAPP'03, Cordoba (2003).
[31] PHELIP, M., et al., "European programme on HTR fuel technology", Proc. 2nd Int. Top. Meeting on High Temperature Reactor Technology HTR-2004, Beijing (2004).
[32] HOWARD, R.M., PRICE, M.S.T., SHEPHERD, L.R. (Eds.), A summary and evaluation of the achievements of the Dragon project and its contribution to the development of HTR, D.P.1000, Dragon Project, Winfrith (1978).
[33] RAGONE, D.V., "Fuel fabrication techniques for HTGR fuel", Proc. Euratom Conference on Fuel Cycles of HTGR, Brussels (1965).
[34] BEATTY, R.L., et al., Gel-sphere-pac fuel for thermal reactor – Assessment of fabrication technology and irradiation performance, Rep. ORNL/TM-5469, Oak Ridge National Laboratory, TN (1979).
[35] NICKEL, H., et al., Long time experience with the development of HTR fuel elements in Germany, Nucl. Eng. Des. **217** (2002) 141.
[36] CHAROLLAIS, F., DUHART, A., FELINES, P., GUILLERMIER, P., PERRAIS, C., "Effect of thermal treatment conditions on microstructure and composition of HTR fuel kernel - CEA and AREVA R&D on HTR fuel fabrication & presentation of the GAIA experimental manufacture line", Proc. 106th American Ceramic Society Conference, Indianapolis, USA, *Ceramics Transactions* **168** (2004).

[37] GYARMATI, E., NICKEL, H., Beschichtung von Kernbrennstoffteilchen durch Propenpyrolyse im 1 Zoll- und 3 Zoll-Flieβbett, Rep. Jül-686-RW–1614, Research Center Jülich (1970).
[38] MINATO, K., et al., Fission product release from ZrC-coated fuel particles during post- irradiation heating at 1800°C and 2000°C, J. Nucl. Mater. **249** (1997) 142.
[39] MINATO, K., et al., Fission products release from ZrC coated particles during post-irradiation heating at 1600°C, J. Nucl. Mater. **224** (1995) 85.
[40] WAGNER, P., High-temperature fuel technology for nuclear process heat: ZrC-containing coated particle fuels and high density graphite fuel matrices, Rep. LA-6984, Los Alamos National Laboratory, NM (1977).
[41] WAGNER, P., et al., Chemical vapor deposition of ZrC made by reactions of $ZrCl_4$ with CH_4 and with C_3H_6, Nucl. Technol. **35** (1977) 527.
[42] HOLLABAUGH, C.M., et al., Factors influencing the chemical vapor deposition of ZrC, J. Nucl. Mater. **62** (1976) 221.
[43] CHAROLLAIS, F., "Caractérisation de combustibles HTR par analyse d'images", Proc. MATERIAUX 2002, Tours (2002).
[44] HELARY, D., et al., "Microstructures of silicon carbide and pyrocarbon coatings for fuel particles for high temperature reactors (HTR)", Proc. 2nd Int. Top. Meeting on High Temperature Reactor Technology HTR-2004, Beijing (2004).
[45] PHELIP, M., et al., "High-temperature reactor technology in the European projects HTR-F1 and RAPHAEL", Proc. 3rd Int. Top. Meeting on High Temperature Reactor Technology HTR-2006, Johannesburg (2006).
[46] NABIELEK, H., et al., Development of advanced HTR fuel elements, Nucl. Eng. Des. **121** (1990) 199.
[47] IVENS, G., WIMMERS, M., "The AVR as test bed for fuel elements, In: AVR-Experimental High-Temperature Reactor", 21 Years of Successful Operation for a Future Energy Technology, VDI-Verlag, Düsseldorf (1990) 170–185.
[48] POHL, P., Betrachtung der aufgelaufenen Buchabweichungen nach Abschluss der bisherigen Brennelement- und Brennstoffbuchführung, Eine Geschichte der Brennelementerkennung am AVR, Technical Note E-6509, Arbeitsgemeinschaft Versuchsreaktor, Düsseldorf (2002).
[49] VERFONDERN, K., "Status of German spent HTGR fuel research", Proc. IAEA-TM on Safety Aspects of Modular HTGRs, Beijing (2007).
[50] RÖLLIG, K., "The THTR coolant gas activity, an indicator of fuel performance behaviour", Behaviour of Gas Cooled Reactor Fuel under Accident Conditions (Proc. IAEA Specialists' Meeting, Oak Ridge, 1990), Rep. IWGGCR/25, International Atomic Energy Agency, Vienna (1991b) 99–108.
[51] WOLF, L., BALLENSIEFEN, G., FRÖHLING, W., Fuel elements of the high temperature pebble bed reactor, Nucl. Eng. Des. **34** (1975) 93.
[52] HOMAN, F., NABIELEK, H., YANG, L., Low-enriched fuel particle performance review, Rep. Jül-1502, Research Center Jülich, and Rep. GA-A14759, General Atomics, San Diego, CA (1978).
[53] KANIA, M.J., NICKEL, H., Performance assessment of the $(Th,U)O_2$ HTI-BISO coated particle under PNP/HHT irradiation conditions, Rep. Jül-1685, Research Center Jülich (1980).
[54] MEHNER, A.W., et al., Spherical fuel elements for advanced HTR manufacture and qualification by irradiation testing, J. Nucl. Mater. **171** (1990) 9.
[55] NABIELEK, H., et al., Fuel for pebble-bed HTRs, Nucl. Eng. Des. **78** (1984) 155.
[56] GULDEN, T.D. NICKEL, H., Coated particle fuel, Nucl. Technol. **35** (1977) 206.
[57] HUSCHKA, H., VYGEN, P., Coated fuel particles: Requirements and status of fabrication technology, Nucl. Technol. **35** (1977) 239.

[58] KADNER, M., BAIER, J., Production of fuel kernels for high-temperature reactor fuel elements, Kerntechnik **18** (1976) 413.
[59] SCHULZE, R.-E., et al., Graphitic matrix materials for spherical HTR fuel elements, Rep. Jül-Spez-167, Research Center Jülich (1982).
[60] HACKSTEIN, K.G., Herstellung von Brennelementen für den THTR und AVR-Reaktor, Atomwirtschaft **16** (1971) 245.
[61] YAMASHITA, K. et al., Nuclear design of the High-Temperature Engineering Test Reactor (HTTR), Nucl. Sci. Eng. **122** (1996) 212.
[62] JAPAN ATOMIC ENERGY RESEARCH INSTITUTE (now JAEA), Present Status of HTTR Research and Development, HTTR R&D Bulletin, Oarai (1990).
[63] KATO, S., et al., "Fabrication of HTTR first loading fuel", Safety Related Design and Economic Aspects of HTGRs (Proc. IAEA-TCM, Beijing, 1998), Rep. IAEA-TECDOC-1210, International Atomic Energy Agency, Vienna (2001) 187–199.
[64] MINATO, K., et al., Improvements in quality of as-manufactured fuels for high-temperature gas-cooled reactors, J. Nucl. Sci. Technol. **34** (1997) 325.
[65] ODA, T., et al., "Fabrication characteristics of first-loading fuel compact of the HTTR", Proc. Fall Meeting of the Atomic Energy Society of Japan, Fukui (1998).
[66] SAWA, K. et al., Evaluation method and prediction result of fuel behavior during the High Temperature Engineering Test Reactor operation, Rep. JAERI-Research 98-016, Japan Atomic Energy Research Institute, Oarai (1998).
[67] LEE, Y.-W., et al., "Development of HTGR coated particle fuel technology in Korea", Proc. 3rd Int. Top. Meeting on High Temperature Reactor Technology HTR2006, Johannesburg (2006).
[68] PETTI, D.A., MAKI, J.T., BUONGIORNO, J., HOBBINS, R., MILLER, G.K., Key differences in the fabrication, irradiation and safety testing of U.S. and German TRISO-coated particle fuel and implications on fuel performance, Rep. INEEL/EXT-02-00300, Idaho National Engineering and Environmental Laboratory, Bechtel BWXT Idaho, ID (2002).
[69] MATZNER, D., "PBMR project status and the way ahead", Proc. 2nd Int. Top. Meeting on High Temperature Reactor Technology HTR-2004, Beijing (2004).
[70] VENTER, F., "The PBMR fuel development laboratories at NECSA", Contribution to IAEA-CRP on Advances in HTGR Fuel Technology, International Atomic Energy Agency, Vienna (2004).
[71] VENTER, F., "The PBMR fuel development laboratories at NECSA", Proc. IAEA-TM on Current Status and Future Prospects of Gas Cooled Reactor Fuels, International Atomic Energy Agency, Vienna (2004).
[72] VENTER, F., "The progress in fuel development laboratories", Proc. IAEA-TM on Current Status and Future Prospects of Gas Cooled Reactor Fuels, International Atomic Energy Agency, Kharkov (2005).
[73] BARRY, J.C., "Commissioning experience with both the laboratory coater and the initial full size coater at the PBMR fuel laboratories", Proc. 3rd Int. Top. Meeting on High Temperature Reactor Technology HTR2006, Johannesburg (2006).
[74] MÜLLER, A., "Establishment of the technology to manufacture uranium dioxide kernels for PBMR fuel", Proc. 3rd Int. Top. Meeting on High Temperature Reactor Technology HTR2006, Johannesburg (2006).
[75] PRICE, M.S.T., "The Dragon project origins, achievements and legacies", Proc. 5th Int. Top. Meeting on High Temperature Reactor Technology HTR2010, Prague (2010).

[76] PRICE, M.S.T., GOUGH, J. R. G., HORSLEY, G.W., Fuel element fabrication for the Dragon reactor experiment, Proc. BNES Symposium on High Temperature Reactors and the Dragon Project, London, UK, 1966, Rep. D.P.425, Part III, Paper 10, Dragon Project, Winfrith (1966).
[77] PRICE, M.S.T., SMITH, E., Safety aspects of the replacement elements in the second charge of the Dragon reactor, Rep. D.P.489, Dragon Project, Winfrith (1966).
[78] STANSFIELD, O.M., Evolution of HTGR coated particle fuel design, Energy **16** (1991) 33.
[79] GOEDDEL, W.V., Coated-particle fuels in high-temperature reactors: A summary of current application, Nuclear Applications **3** (1967).
[80] SIMON, R.H., A history of and prospects for gas-cooled reactors in the United States, Rep. GA-A16637, General Atomics, San Diego, CA (1982).
[81] TURNER, R.F., NEYLAN, A.J., MHTGR design and development status, Rep. GA-19391, General Atomics, San Diego, CA (1988).
[82] TURNER, R.F., et al., Selection of LEU/Th reference fuel for the HTGR-SC/C lead plant, Rep. GA-A17123, General Atomics, San Diego, CA (1983).
[83] McEACHERN, D.W., et al., "Manufacture and irradiation of Fort St. Vrain fuel", Proc. HTR-TN Int. HTR Fuel Seminar, Brussels (2001).
[84] DAHLBERG, R.C., TURNER, R.F., GOEDDEL, W.V., Fort St. Vrain core design characteristics, Nucl. Eng. Int. **14** (1969) 1073.
[85] DAHLBERG, R.C., JOHNSTON, T.A., Fort St. Vrain nuclear power station, Nucl. Eng. Int. **14** (1969).
[86] WALKER, R.E., JOHNSTON, T.A., Fort St. Vrain nuclear power station, Nucl. Eng. Int. **14** (1969) 1069.
[87] HOFFMAN, B.L., SCARBOROUGH, J.C., "Quality assurance aspects of the Fort St. Vrain fuel", Proc. Int. Conf. on Nuclear Fuel Performance, London (1973).
[88] OEHME, H., "Comparative HTGR-design", Proc. ANS Topical Meeting on Gas-Cooled Reactors: HTGR and GCFBR, Gatlinburg (1974).
[89] SPENSE, R., "Sol gel spherical fuel", Proc. Conf. of the American Society for Metals on Metallurgical Technology of Uranium and Uranium Alloys, Gatlinburg, TN (1981).
[90] BESENBRUCH, G. et al., "HTR fuel compacts without defective particles", Proc. HTR-TN Int. HTR Fuel Seminar, Brussels (2001).
[91] GOODIN, D.T., MHTGR fuel performance and supporting date base, Energy **16** (1991) 187.
[92] US DEPARTMENT OF ENERGY, A technology roadmap for Generation IV nuclear energy systems, US-DOE Nuclear Energy Research Advisory Committee and the Generation IV International Forum, Report GIF-002-00, Washington, DC (2002).
[93] MAKI, J.T., PETTI, D.A., KNUDSON, D.L., MILLER, G.K., The challenges associated with high burnup, high temperature and accelerated irradiation for TRISO-coated particle fuel, J. Nucl. Mater. **371** (2007) 270.
[94] MILLER, G.K., MAKI, J.T., KNUDSON, D.L., PETTI, D.A., "Current capabilities of the fuel performance modeling code PARFUME", Proc. 2nd Int. Top. Meeting on High Temperature Reactor Technology HTR2004, Beijing (2004).
[95] BULLOCK, R.E., KAAE, J.L., Performance of coated UO_2 particles gettered with ZrC, J. Nucl. Mater. **115** (1983) 69.
[96] KETTERER, J.W., KANIA, M.J., BULLOCK, R.E., SIMAN-TOV I.I., Capsule HRB-15A postirradiation examination, Rep. GA-A16758, General Atomics, San Diego, CA (1984).

[97] KETTERER, J.W., MYERS, B.F., Capsule HRB-16 postirradiation examination report, Rep. HTGR-85-053 and GA-908012 N/c, General Atomics, San Diego, CA (1985).
[98] SAWA, K., et al., Development of a coated fuel particle failure model under high burnup irradiation, J. Nucl. Sci. Technol. **33** (1996) 712.
[99] SAWA, K., MINATO, K., An investigation of irradiation performance of high burnup HTGR fuel, J. Nucl. Sci. Technol. **36** (1999) 781.
[100] MINATO, K., FUKUDA, K., "Thermodynamic analysis of behavior of HTGR fuel and fission products under accident air or water ingress conditions", Response of Fuel, Fuel Elements and Gas Cooled Reactor Cores under Accidental Air or Water Ingress Conditions (Proc. IAEA-TCM, Beijing, 1993), Rep. IAEA-TECDOC-784, International Atomic Energy Agency, Vienna (1995) 86–91.
[101] OGAWA, T., FUKUDA, K., Quick analysis of free carbon in metal carbide by plasma oxidation, J. Am. Ceram. Soc. **73** (1990) 2558.
[102] SAWA, K., et al., Safety criteria and quality control of the High Temperature Engineering Test Reactor fuel, Nucl. Eng. Des. **208** (2001) 305.
[103] FU, X., et al., Comparison of HTGR fuel design, manufacture and quality control methods between Japan and China, Rep. JAERI-Tech 2002-049, Japan Atomic Energy Research Institute, Oarai (2002).
[104] DELLE, W.W., KOIZLIK, K., LUHLEICH, H., NICKEL, H., Quality control procedures for HTGR fuel element components, Rep. Jül-1333, Research Center Jülich (1976).
[105] DELLE, W.W., KOIZLIK, K., PRICE, M.S.T., WALLURA, E., Quality control techniques of pyrocarbon, Nucl. Technol. **35** (1977) 284.
[106] NABIELEK, H., et al., Silver release from coated particle fuel, Nucl. Technol. **35** (1977) 483.
[107] SCHENK, W., et al., Fuel accident performance testing for small HTRs, J. Nucl. Mater. **171** (1989) 19.
[108] HANTKE, H.-J., Performance of high quality HTR-LEU fuel elements with TRISO coated particles, Internal Report HTA-IB-7/92, Research Center Jülich (1992).
[109] BACON, G.E., A method for determining the degree of orientation of graphite, Journal of Applied Chemistry **6** (1956) 477.
[110] WIMMERS, M., Das Verhalten kugelförmiger HTR-Brennelemente bei der Massenerprobung im AVR-Reaktor, Report, Arbeitsgemeinschaft Versuchsreaktor, Düsseldorf (1977).
[111] RAGOß, H., Description of fuel behavior performance used in the German licensing procedures for the HTR-Module, Technical Note 38.07247.9, Interatom, Bergisch-Gladbach (1989).
[112] NABIELEK, H., TANG, C.H., UETA, S., VERFONDERN, K., Burn-leach: the most important test in the manufacture of HTR fuel, T. Am. Nucl. Soc. **94** (2006) 651.
[113] SCHENK, W., PITZER, D. KNAUF, H., KUNITZ, J., Jod- und Xenonfreisetzung aus kurz bestrahlten Brennelementen bei 1000 bis 1600°C (FRJ2-KA2), Technical Note KFA-IRW-TN-9/91, Research Center Jülich (1991).
[114] KOBAYASHI, F., et al., An inspection standard of fuel for the High Temperature Engineering Test Reactor, Rep. JAERI-M 92-079, Japan Atomic Energy Research Institute, Oarai (1992) (in Japanese).
[115] KOBAYASHI, F., et al., An examination on the determination precision of uranium content in the HTGR fuel compacts, Rep. JAERI-M 92-046, Japan Atomic Energy Research Institute, Oarai (1992) (in Japanese).

[116] KASHIMURA, S., et al., Automatic size analysis of coated fuel particles, Rep. JAERI-M 84-196, Japan Atomic Energy Research Institute, Oarai (1984) (in Japanese).
[117] IKAWA, K., et al., Density determination of the coating layers of fuel particles, Rep. JAERI-M 5674, Japan Atomic Energy Research Institute, Oarai (1974) (in Japanese).
[118] KASHIMURA, S., et al., Non-destructive inspection of the coated fuel particles by contact X-ray microradiography, Rep. JAERI-M 4749, Japan Atomic Energy Research Institute, Oarai (1972) (in Japanese).
[119] TOBITA, T., et al., Detection of ruptured fuel particles in the fuel compact by acid leach techniques, Rep. JAERI-M 5265, Japan Atomic Energy Research Institute, Oarai (1973) (in Japanese).
[120] KOBAYASHI, F., et al., On the disintegration and acid leaching method for measuring free uranium in HTGR fuel compacts, Rep. JAERI-M87-023, Japan Atomic Energy Research Institute, Oarai (1987) (in Japanese).
[121] KOBAYASHI, F., Determination of defective SiC fraction and free uranium fraction in the HTGR fuel compacts, Rep. JAERI-M 88-265, Japan Atomic Energy Research Institute, Oarai (1988) (in Japanese).
[122] SOWDER, W.K., Quality assurance program plan for AGR fuel development and qualification program, Rep. INEEL/EXT-04-01825, Idaho National Laboratory, ID (2003).
[123] HUNN, J.D., "Quality assurance and quality control for coated particles and fuel compacts", Presentation at the Eurocourse on Coated Particle Fuel, EU-RAPHAEL Project, Petten (2007).
[124] JELLISON, Jr. G.E., HUNN, J.D., LOWDEN, R.A., Optical characterization of tristructural isotropic fuel particle cross-sections using generalized ellipsometry, J. Nucl. Mater. **352** (2006) 6.
[125] JELLISON, Jr. G.E., HUNN, J.D., Optical anisotropy measurements of TRISO nuclear fuel particle cross-sections: The method, J. Nucl. Mater. **372** (2008) 36.
[126] ASTM INTERNATIONAL, Standard test method for density of plastics by the density gradient technique, ASTM D1505-98, West Conshohocken, PA (1999).
[127] KIM, W.K., et al., "Non-destructive measurement of the coating thickness in the simulated TRISO-coated fuel particle for the HTGR", Proc. 3rd Int. Top. Meeting on High Temperature Reactor Technology HTR2006, Johannesburg (2006).
[128] PRICE, J.R., et al., "New developments in image-based characterization of coated particle nuclear fuel", Proc. Machine Vision Applications in Industrial Inspection XIV, SPIE **6070** (2006) 153.
[129] WALLISCH, K., KOSS P., Automatic size analysis of coated fuel particles, Nucl. Technol. **35** (1977) 279.
[130] BASINI, V., CHAROLLAIS, F., New techniques dedicated to the characterization of future nuclear fuels, Revue de Métallurgie **96** (1999) 641.
[131] LE HOUËDEC, H., ROCHAIS, D., ENGUEHARD, F., JUMEL, J., LEPOUTRE, F., Microscopic thermal characterization at temperatures up to 1000°C by photoreflectance microscopy, Superlattices and Microstructures **35** (2004) 401.
[132] ROCHAIS, D., LE MEUR, G., BASINI, V., DOMINGUES, G., "Microscopic thermal characterization of HTR particle layers", Proc. 3rd Int. Top. Meeting on High Temperature Reactor Technology HTR2006, Johannesburg (2006).
[133] ROCHAIS, D., LE MEUR, G., BASINI, V., DOMINGUES, G., Microscopic thermal characterization of HTR particle layers, Nucl. Eng. Des. **238** (2008) 3047.
[134] BARIN, I., KNACKE, O., Thermochemical properties of inorganic substances, Springer-Verlag, Berlin and New York (1973).

[135] HOFMANN, G., et al., An investigation of the relationship between position within coater and pyrolytic carbon characteristics using nanoindentation, Carbon **38** (2000) 645.
[136] MARTIN, D.G., SAWA, K., UETA, S., SUMITA, J., A study of fuel failure behavior in high burnup HTGR fuel – Analysis by STRESS3 and STAPLE codes, Rep. JAERI-Research 2001-033, Oarai (2001).
[137] MILLER, G.K., et al., Consideration of the effects of partial debonding of the IPyC and particle asphericity on TRISO-coated fuel behavior, J. Nucl. Mater. **334** (2004) 79.
[138] KIM, W.K., et al., Nondestructive measurement of the coating thickness for simulated TRISO-coated fuel particles by using phase contrast X-ray radiography, Nucl. Eng. Des. **238** (2008) 3285.
[139] BANCHET, J., et al., "Innovative non destructive evaluation methods on HTR fuel at AREVA NP: Towards a 100% non invasive control strategy", Proc. Int. Conf. on Advanced Nuclear Fuel Cycles and Systems GLOBAL2007, Boise, ID (2007).
[140] GUILLERMIER, P., et al., "Application of X-ray imaging for HTR fuel characterization", Proc. Int. Congr. on Advances in Nuclear Power Plants ICAPP'09, Tokyo (2009).
[141] CLOETENS, P., et al., Observation of microstructure and damage in materials by phase sensitive radiography and tomography, J. Appl. Phys. **81** (1997) 5878.
[142] LE MEUR, G., ROCHAIS, D., DOMINGUES, G., BASINI, V., "Microscopic thermal characterization of HTR particle layers", Proc. 3rd Int. Top. Meeting on High Temperature Reactor Technology HTR2006, Johannesburg (2006).
[143] KRAPEZ, J.-C., LEGRANDJACQUES, L., LEPOUTRE, F., BALAGEAS, D., "Optimization of the photothermal camera for crack detection", Quantitative Infrared Thermography QIRT'98 (Proc. Seminar, Lodz, 1998), Eurotherm Series 60 (1998) 305–331.
[144] HANIA, P.R., et al., "Qualification of HTR pebbles by X-ray tomography and thermal analysis", Proc. 5th Int. Top. Meeting on High Temperature Reactor Technology HTR2010, Prague (2010).
[145] OUGOUAG, A.M., KLOOSTERMAN, J.L., VAN ROOIJEN, W.F.G., GOUGAR, H.D., TERRY W.K., Investigation of bounds on particle packing in pebble-bed high temperature reactors, Nucl. Eng. Des. **236** (2006) 669.
[146] HOCKEY, R.L. et al., "Advances in automated QA/QC for TRISO fuel particle production", Proc. Int. Congr. on Advances in Nuclear Power Plants ICAPP'04, Pittsburgh, PA (2004).
[147] XU, Y.H., QIN, Z.Y. WU, Z.X., Design of the 10 MW high temperature gas-cooled reactor, Journal of Tsinghua University **34** (1994), No. ES2.
[148] TANG, C.H., "HTR fuel R&D activities in China", Contribution to 3rd CRP-6 Meeting on Advances in HTGR Fuel Technology, International Atomic Energy Agency, Vienna (2005).
[149] NICKEL, E., BALTHESEN, E., Status of HTR fuel element development in the FRG and its potential for nuclear process heat reactor, Kerntechnik **17** (1975) 205.
[150] HU, S.Y., WANG, R.P., GAO, Z.Y., "Safety demonstration tests on HTR-10", 2nd Int. Top. Meeting on High Temperature Reactor Technology, Beijing (2004).
[151] HU, S.Y., WANG, R.P., "Power operation commissioning tests of HTR-10", 2nd Int. Top. Meeting on High Temperature Reactor Technology, Beijing (2004b).
[152] DERZ, H., GOTTAUT, H., POHL, P., POTT, G., Experiment HTA-8: The determination of the maximum coolant temperatures in the AVR core, Internal Report HTA-IB-3/90, Research Center Jülich (1990).

[153] GOTTAUT, H., KRÜGER, K., Results of experiments at the AVR reactor, Nucl. Eng. Des. **121** (1990) 143.
[154] NABIELEK, H., VERFONDERN, K., KANIA, M.J., "Fuel and fission products in the Jülich AVR pebble-bed reactor", Presentation at the 4th Int. Top. Meeting on High Temperature Reactor Technology HTR2008, Washington, DC (2008).
[155] POHL, P., Experimental evaluation of the AVR melt-wire test, AVR Report, Arbeitsgemeinschaft Versuchsreaktor GmbH, Düsseldorf (2009).
[156] STOKER, C.C., OLIVIER, L.D., STASSEN, E., REITSMA, F., VAN DER MERWE, J.J., PBMR radionuclide source term analysis validation based on AVR operating experience, Nucl. Eng. Des. **240** (2010) 2466.
[157] VILJOEN, C.F., et al., "The re-evaluation of the AVR melt-wire experiment using modern methods with specific focus on bounding the bypass flow effects", Proc. 4th Int. Top. Meeting on High Temperature Reactor Technology HTR2008, Washington, DC (2008).
[158] VILJOEN, C.F., SEN S., "The re-evaluation of the AVR melt-wire experiment with specific focus on different modeling strategies and simplifications", Proc. 5th Int. Top. Meeting on High Temperature Reactor Technology HTR2010, Prague (2010).
[159] BEN, M.G., YOHAI, V.J., Quantile-quantile plot for deviance residuals in the generalized linear model, J. Comput. Graph. Stat. **13** (2004) 36.
[160] WEBER, J., Einbeziehung der Spaltproduktfreisetzung in die numerische Simulation des AVR-Abbrand-Umwälzgeschehens und Vergleich mit den VAMPYR-Resultaten, Rep. Jül-1570, Research Center Jülich (1979).
[161] HOCHTEMPERATUR-KERNKRAFTWERK GMBH, The commissioning of the THTR 300, A performance report, Publication No. HKG 002 89 E, Hamm-Uentrop (1989).
[162] SAITO, S., et al., Design of High Temperature Engineering Test Reactor (HTTR), Rep. JAERI-1332, Japan Atomic Energy Research Institute, Oarai (1994).
[163] SAWA, K., UETA, S., SUMITA, J., VERFONDERN, K., Prediction of fuel and fission gas release behavior during the High Temperature Engineering Test Reactor operation by JAERI and FZJ modeling approach, J. Nucl. Sci. Technol. **38** (2001) 411.
[164] UETA, S., SUMITA, J., EMORI, K., TAKAHASHI, M., SAWA, K., Fuel and fission gas behavior during rise-to-power test of the High Temperature Engineering Test Reactor (HTTR), J. Nucl. Sci. Technol. **40** (2003) 679.
[165] UETA, S., et al., An investigation of fuel and fission product behavior in rise-to-power test of HTTR (No. 2: Results up to 30 MW operation), Rep. JAERI-Research 2003-025, Japan Atomic Energy Research Institute, Oarai (2003b) (in Japanese).
[166] MEEK, M.E., RIDER, B.F., Compilation of fission product yields, Rep. NEDO-12154-1, General Electric Co., Vallecitos Nuclear Center, CA (1974).
[167] PRICE, M.S.T., ASHWORTH, F.P.O., GRAHAM, L.W., Fuel element fabrication, Proc. Dragon-THTR Assessment Meeting, held at Brussels, Belgium, May 22-24, 1967, Rep. D.P.475, Part II, Paper 3.2, Dragon Project, Winfrith (1967).
[168] GRAHAM, L.W., et.al., HTR fuel development and testing in the Dragon project, Rep. D.P.885, Dragon Project, Winfrith (1974).
[169] STEWARD, K.P., Final summary report on the Peach Bottom end-of-life program, DOE Rep. GA-Al4404, General Atomic, San Diego, CA (1978).
[170] MALINAUSKAS, A.P., et al., "Fission product behaviour during operation of the second Peach Bottom core", Gas-Cooled Reactors with Emphasis on Advanced Systems (Proc. IAEA Int. Symp., Jülich, 1975), Paper IAEA-SM-200/50, International Atomic Energy Agency, Vienna (1976).

[171] HANSON, D.L., JOVANOVIC, V., BURNETTE, R.D., "Comparison of predicted and measured fission product behavior in the Fort St. Vrain HTGR during the first three cycles of operation", Fission Product Release and Transport in Gas-Cooled Reactors (Proc. IAEA Specialists' Meeting, Berkeley, 1985), Rep. IWGGCR--13, International Atomic Energy Agency, Vienna (1985) 2–14.
[172] Decommissioning costs for German pebble bed reactor escalating, Nucleonics Week, Issue of July 4 (2002) 7.
[173] ZIERMANN, E., IVENS, G., Abschlussbericht über den Leistungsbetrieb des AVR-Versuchskernkraftwerkes, Rep. Jül-3448, Research Center Jülich (1997).
[174] BALDWIN, C.A., KANIA, M.J., IMGA examination of set #4 fuel under Project Work Statement FD-20, Rep. ORNL/TM-11455, Oak Ridge National Laboratory, TN (1990).
[175] WAWRZIK, U., IVENS, G., "Operational monitoring of the release behaviour of the AVR core", Fission Product Release and Transport in Gas-Cooled Reactors (Proc. IAEA Specialists' Meeting, Berkeley, 1985), Rep. IWGGCR--13, International Atomic Energy Agency, Vienna (1985) 15–26.
[176] EL-MASRI, M.A.A., EL-SAYED, A.A., Distribution on fission products in the fuel free zone of AVR irradiated fuel elements, Internal Report KFA-IRW-IB-10/89, Research Center Jülich (1989).
[177] SCHENK, W., PITZER, D., NABIELEK, H., Fission product release profiles from spherical HTR fuel elements at accident temperatures, Rep. Jül-2234, Research Center Jülich (1988).
[178] NABIELEK, H., VERFONDERN, K., KANIA, M.J., Irradiation testing of HTR fuels in AVR and in material test reactors, Proc. 5th Int. Top. Meeting on High Temperature Reactor Technology HTR2010, Prague (2010).
[179] OGAWA, T., et al., Performance of ZrC-coated particle fuel in irradiation and post-irradiation heating tests, J. Am. Ceram. Soc. **75** (1992) 2985.
[180] MINATO, K., et al., Irradiation experiment of ZrC coated fuel particles for high-temperature gas-cooled reactors, Nucl. Technol. **130** (2000b) 272.
[181] INO, H., UETA, S., SUZUKI, H., TOBITA, T., SAWA K., Design of high temperature irradiation materials inspection cells (spent fuel inspection cells) in the High Temperature Engineering Test Reactor, Rep. JAERI-Tech 2001-083, Japan Atomic Energy Research Institute, Oarai (2001) (in Japanese).
[182] SAWA, K., et al., Fabrication experience and integrity confirmation tests of the first-loading-fuel of the HTTR, Rep. JAERI-Conf 99-006, Japan Atomic Energy Research Institute, Oarai (1999).
[183] SAWA, K., et al., Integrity confirmation tests and post-irradiation test plan of the HTTR first-loading fuel, J. Nucl. Sci. Technol. **38** (2001) 403.
[184] SAWA, K., et al., Acceleration irradiation test of first-loading fuel of High Temperature Engineering Test Reactor (HTTR) up to high burnup (Joint research), Rep. JAERI-Research 2002-012, Japan Atomic Energy Research Institute, Oarai (2002) (in Japanese).
[185] US-NUCLEAR REGULATORY COMMISSION, Termination of Fort St. Vrain nuclear generating station operating license, SECY-97-138, Rockville, MD (1997).
[186] PUBLIC SERVICE COMPANY OF COLORADO, Fort St. Vrain Nuclear generating station, Final safety analysis report" (updated), Docket No. 50-267, Golden, CO (1997).
[187] BAXTER, A.M., McEACHERN, D., HANSON, D.L., VOLLMAN, R.E., FSV experience in support of the GT-MHR reactor physics, fuel performance, and graphite, Rep. GA-A21925, General Atomics, San Diego, CA (1994).

[188] COPINGER, D.A., MOSES, D.L., Fort Saint Vrain gas cooled reactor operational experience, Rep. NUREG/CR-6839, ORNL/TM-2003/223, Oak Ridge National Laboratory, TN (2004).
[189] HAWARI, A.I. CHEN, J.W., Computational investigation of on-line interrogation of pebble ped reactor fuel, IEEE Transactions on Nuclear Science **52** (2005) 1659.
[190] QUANDT, X., Weiterentwicklung der Coreinstrumentierung, Abbrandmessung an Brennelementen, Final report 61.0447.8, 04.02, Siemens/Interatom, Bergisch-Gladbach (1988).
[191] GERHARDS, E., Untersuchung zu Verfahren der Abbrandmessung an HTRs, Diploma thesis, Technical University RWTH Aachen (1988).
[192] WIMMERS, M., POHL, P., KRÜGER, K., Inbetriebnahme der neuen Abbrandmessanlage, Report, Arbeitsgemeinschaft Versuchsreaktor, Düsseldorf (1982).
[193] PUTSCH, F., et al., Experiment FRJ2-KA2, Bestrahlungsbericht, Technical Note KFA-ZBB-TN-6/90, Research Center Jülich (1990).
[194] KÜHNLEIN, W., SCHRÖDER, R., FRJ2-KA2: Inventar- und Abbrandbestimmung durch gammaspektrometrische Messung und Rechnung, Technical Note IRW-TN-48/91, Research Center Jülich (1991).
[195] QUADE, U., Abschlußbericht HTR-Meßgeräte EA Nr. 4: Prototyperprobung einer Abbrandmeßanlage, Internal Report KWU R263/92/029, Siemens/Interatom, Bergisch-Gladbach (1992).
[196] ORTEC, The next generation in Digital Gamma Spectroscopy, ORTEC (2011).
[197] CANBERRA, A Practical Guide to High Count Rate Germanium Gamma Spectroscopy; CANBERRA Corporate, Meriden, CT (2002).
[198] ZHANG, L.G. SHANG, R.C., Analysis of influence of decay-cooling time on on-line burnup measurement of HTR-PM, Nuclear Power Engineering **30**(3) (2009) 43.
[199] FACHINGER, J., et al., Behaviour of spent HTR fuel elements in aquatic phases of repository host rock formations, Nucl. Eng. Des. **236** (2006) 543.
[200] HENSEL, W., HOINKIS, E., The diffusion of cesium in the graphitic matrix A3-3 in the presence of helium at pressures up to 10^7 Pa, J. Nucl. Mater. **224** (1995) 1.
[201] HOINKIS, E., The diffusion of silver in the graphite matrices A3-3 and A3-27, J. Nucl. Mater. **209** (1994) 132.
[202] HENSEL, W., HOINKIS, E., The diffusion of Sr in the graphite matrix A3-3 in vacuum and in the presence of hydrogen, J. Nucl. Mater. **184** (1991) 88.
[203] SERAN, J.L., et al., "Metallic and graphite materials for out-of-core and in-core components of the VHTR: First results of the CEA R&D program", Proc. 2nd Int. Top. Meeting on High Temperature Reactor Technology HTR2004, Beijing (2004).
[204] SUMITA, J., et al., Characteristics of first loaded IG-110 graphite in HTTR core, Rep. JAEA-Technology 2006-048, Japan Atomic Energy Agency, Oarai (2006) (in Japanese).
[205] ISHIHARA, M., SUMITA, J., SHIBATA, T., IYOKU, T., OKU, T., Principle design and data of graphite components, Nucl. Eng. Des. **233** (2004) 251.
[206] TOYOTA, J., et al., An inspection standard of graphite for the High Temperature Engineering Test Reactor, Rep. JAERI-M-91-102, Japan Atomic Energy Research Institute, Oarai (1991) (in Japanese).
[207] GREBENNIK, V.N., et al., "Analysis and choice of characteristics of the HTGR spherical fuel elements", Gas-Cooled Reactor Fuel Development and Spent Fuel Treatment (Proc. IAEA Specialists Meeting, Moscow, 1983), Rep. IAEA-IWGCR/8, International Atomic Energy Agency, Vienna (1985) 5–18.
[208] CHERNIKOV, A.S., HTGR fuel and fuel elements, Atomnaya Energiya **65** (1988) 32 (in Russian).

[209] CHERNIKOV, A.S., et al., Matrix graphites of HTGR fuel elements. Variants of manufacture properties radiation behaviour, Atomnaya Energiya **72** (1992) 360 (in Russian).
[210] CHERNIKOV, A.S., "Matrix materials", IAEA Consultancy on Graphite Issues in High Temperature Gas Cooled Reactor Development, Manchester (2005) (in Russian).
[211] AVRAMENKO, P.Ya., et al., Manufacture of fine-grained graphite of MPG type on the base of non-traditional cokes, Journal of Chemistry of Solid Fuel **1** (1998) 67 (in Russian).
[212] ODEYCHUK, M.P., et al., "The current state of HTGR core component fabrication technologies in Ukraine and some properties of materials and products", Proc. IAEA-TM on Current Status and Future Prospects of Gas Cooled Reactor Fuels, International Atomic Energy Agency, Vienna (2004).
[213] ODEYCHUK, M.P., "Graphites and CCCM for nuclear reactor plants: Ukraine's experience", Ceramic Processing PROCER (Proc. Int. Conf. Mumbai, 2004), Bombay Metropolitan Regional Chapter, Indian Ceramic Society (2004) 103–123.
[214] PAPPANO, P.J., BURCHELL, T.D., TRAMMELL, M.P., HUNN, J.D., A novel approach to fabricating fuel compacts for the Next Generation Nuclear Plant (NGNP), J. Nucl. Mater. **381** (2008) 25.
[215] HUNN, J.D., Product inspection plan, coated particle composites, Rep. AGR-CHAR-PIP-04, Oak Ridge National Laboratory, TN (2005).
[216] RÖLLIG, K., Release of rare fission gases from spherical elements with coated fuel particles, Nucl. Technol. **35** (1977) 516.
[217] THIEL, J., Gasfreisetzung aus Defektpartikeln im Experiment FRJ2-P25, Rep. DB 1583, 1.10.1982, Hochtemperatur-Reaktorbau GmbH, Mannheim (1982).
[218] RÖLLIG, K., Final report of the R&D project: Brennelemente unter Normal- und Störfallbedingungen, Rep. HTR-M-0210-BA-GHRA 006910, 30.4.1993, Hochtemperatur-Reaktorbau GmbH, Mannheim (1993).
[219] THIEL, J., THTR-300: Kühlgasaktivität bis 423 VLT, Rep. 422-210-BF 3501, 10.01.1989, Hochtemperatur-Reaktorbau GmbH, Mannheim (1989).
[220] KASTEN, P.R., Research on fuel performance in modular high-temperature gas-cooled reactors, Final Report to the US Nuclear Regulatory Commission under Grant Number NRC-04-92-092 (RES-C92-231) (1994).
[221] KROHN, H., FINKEN, R., FRESCO-II: Ein Rechenprogramm zur Berechnung der Spaltproduktfreisetzung aus kugelförmigen HTR-Brennelementen in Bestrahlungs- und Ausheizexperimenten, Rep. Jül-Spez-212, Research Center Jülich (1983).
[222] SCHENK, W., et al., The behavior of spherical HTR fuel elements under accident conditions, J. Nucl. Mater. **124** (1984) 25.
[223] BOOTH, A.H., A method of calculating fission gas release from UO_2 fuel and its implication to the X-2-f loop test, Report-496, Atomic Energy of Canada Limited, Chalk River Laboratories (1957).
[224] NABIELEK, H., et al., Performance limits of coated particle fuel; Part III: Fission product mgration in HTR fuel, Rep. D.P.828, Part 3, Dragon Project, Winfrith (1974).
[225] KESHAW, J.B., VAN DER MERWE, J.J., "GETTER – A model for fission product release from spherical HTR fuel elements", Proc. 3rd Int. Top. Meeting on High Temperature Reactor Technology HTR2006, Johannesburg (2006).
[226] KROHN, H., Freisetzung von Spaltprodukten aus dem Core eines Kugelhaufenreaktors bei Störfällen mit Core-Aufheizung, Rep. Jül-1791, Research Center Jülich (1982).

[227] VERFONDERN, K., et al., Methods and data for HTR fuel performance and radionuclide release modeling during normal operation and accidents for safety analysis, Rep. Jül-2721, Research Center Jülich (1993).
[228] VERFONDERN, K., NABIELEK, H., PANAMA Ein Rechenprogramm zur Vorhersage des Partikelbruchanteils von TRISO-Partikeln unter Störfallbedingungen, Rep. Jül-Spez-298, Research Center Jülich (1985).
[229] NABIELEK, H., GOODIN, D.T., SCHEFFEL, W.J., "Criteria for a high performance particle", Proc. HTR-TN Int. HTR Fuel Seminar, Brussels (2001).
[230] NABIELEK, H., BROWN, P.E., "The release of ^{110m}Ag in HTRs", Proc. Jahrestagung Kerntechnik, Nürnberg (1975) 370–373.
[231] VAN DER MERWE, J.J., Evaluation of silver transport through SiC during the German HTR fuel program, J. Nucl. Mater. **305** (2009) 99.
[232] MARTIN, D.G., The mathematical basis of STRESS3 and STAPLE, Unpublished report, Oxon, UK (2003).
[233] REDLICH, O., KWONG, J.N.S., On the thermodynamics of solutions. V. An equation of state, Fugacities of gaseous solutions, Chemical Reviews **44** (1949) 233.
[234] HARRISON, J.W., An extrapolated equation of state for xenon for use in fuel swelling calculations, J. Nucl. Mater. **31** (1969) 99.
[235] KUBASCHEWSKI, O., et al. Metallurgical thermochemistry, 4th Edition, Pergamon, London (1967).
[236] MARTIN, D.G., An analytical method of calculating, to a reasonable accuracy, stresses in the coatings of HTR fuel particles, J. Nucl. Mater. **44** (1973) 35.
[237] MARTIN, D.G., "An analysis of stresses created in the layers of coated fuel particles by temperature changes", Proc. 3rd Int. Conf. on Structural Mechanics in Reactor Technology, London (1975).
[238] MARTIN, D.G., Considerations pertaining to the achievement of high burn-ups in HTR fuel, Nucl. Eng. Des. **213** (2002) 241.
[239] MARTIN, D.G., Modelling the performance of coated particles in the NPR-1 irradiation using the STRESS3 and STAPLE codes, Appendix C of INEEL FY 2002 Annual Report INEEL/EXT-02-01545, Idaho National Laboratory, ID (2002).
[240] HICK, H., NABIELEK, H., HARRISON, T.A., Performance limits of coated particle fuel, Part II: Mechanical failure of coated particles due to internal gas pressure and kernel swelling. D.P.828 Part II, Dragon Project, Winfrith (1973).
[241] SAYERS, J.B., et al., "Nuclear fuel performance", Proc. B.N.E.S. Int. Conf. London (1973) 32.1–32.6.
[242] AHLF, J., CONRAD, R., TARTAGLIA, G.P., TSOTRIDIS, G., The HFR Petten as a test bed for fusion materials and components, J. Nucl. Mater. **212-215** (Part 2) (1994) 1635.
[243] AHLF, J., CONRAD, R., CUNDY, M., SCHEURER, H., Irradiation experiments on high temperature gas-cooled reactor fuels and graphites at the High Flux Reactor Petten, J. Nucl. Mater. **171** (1990) 31.
[244] AHLF, J., ZURITA, A., High Flux Reactor (HFR) Characteristics of the installation and the irradiation facilities, Rep. EUR 15151 EN, Joint Research Center Petten (1993).
[245] RÖLLIG, K., Nachuntersuchung HFR-K5/K6, Rep. HTR-M-210-BF-GHRA 006903, Hochtemperatur-Reaktorbau GmbH, Mannheim (1992).
[246] VAN DER MERWE, J.J., Verification and validation of the PBMR models and codes used to predict gaseous fission product releases from spherical fuel elements, MSc Thesis, Rand Afrikaans University (2003).

[247] NABIELEK, H., CONRAD, R., RÖLLIG, K., MEYERS, B.F., "Fuel irradiation experiments on HFR-K6 and HFR-B1 with intermittent water vapour injections", Response of Fuel, Fuel Elements and Gas Cooled Reactor Cores under Accidental Air or Water Ingress Conditions (Proc. IAEA-TCM, Beijing, 1993), Rep. IAEA-TECDOC-784, International Atomic Energy Agency, Vienna (1995) 17–24.
[248] VAN DER MERWE, J.J., COETZEE, P.P., Development of a model to predict fission product behaviour in spherical fuel elements during water ingress events, Nucl. Eng. Des. **237** (2007) 47.
[249] FÜTTERER, M.A., et al., Results of AVR fuel pebble irradiation at increased temperature and burn-up in the HFR Petten, Nucl. Eng. Des. **238** (2008) 2877.
[250] DE GROOT, S., et al., Modelling of the HFR-EU1bis experiment and thermomechanical evaluation, Nucl. Eng. Des. **238** (2008) 3114.
[251] DE GROOT, S., BAKKER, K., VAN HEEK, A.I., "Modelling of the HFR-EU1bis experiment and thermomechanical evaluation", Proc. 3rd Int. Top. Meeting on High Temperature Reactor Technology HTR2006, Johannesburg (2006).
[252] FÜTTERER, M.A., et al., Next generation fuel irradiation capability in the High Flux Reactor Petten, J. Nucl. Mater. **392** (2009) 184.
[253] VAN DER MERWE, J.J., VENTER, J.H., "A method to evaluate fission gas release during irradiation testing of spherical fuel", Proc. 4th Int. Top. Meeting on High Temperature Reactor Technology HTR2008, Washington, DC (2008).
[254] KELLERBAUER, A., BOTTOMLEY, D., FREIS, D., RONDINELLA, V., VAN UFFELEN, P., "High-temperature reactor fuel element characterization with the Küfa device", Presentation at the 5th Int. Top. Meeting on High Temperature Reactor Technology HTR2010, Prague (2010).
[255] MARMIER, A., FÜTTERER, M.A., LAURIE, M., TANG, C.H., "Preliminary results of the HFR-EU1 fuel irradiation of INET and AVR pebbles in the HFR Petten", Proc. 4th Int. Top. Meeting on High Temperature Reactor Technology HTR2008, Washington, DC (2008).
[256] LAURIE, M., et al., "Results of the HFR-EU1 fuel irradiation of INET and AVR pebbles in the HFR Petten", Proc. 5th Int. Top. Meeting on High Temperature Reactor Technology HTR2010, Prague (2010).
[257] LAURIE, M., et al., "JRC's on-line fission gas release monitoring system in the High Flux Reactor Petten", Proc. 5th Int. Top. Meeting on High Temperature Reactor Technology HTR2010, Prague (2010).
[258] DE GROOT, S., et al., "RAPHAEL-FT & Generation IV PYCASSO-I irradiation", Proc. 4th Int. Top. Meeting on High Temperature Reactor Technology HTR2008, Washington, DC (2008).
[259] VAN DER MERWE, H., OLIVIER, D., "Modeling silver: Evaluation of German experience", Proc. 4th Int. Top. Meeting on High Temperature Reactor Technology HTR2008, Washington, DC (2008).
[260] DE GROOT, S., et al., "The European ARCHER project proposal: HTR research towards demonstration", Proc. 5th Int. Top. Meeting on High Temperature Reactor Technology HTR2010, Prague (2010).
[261] DE GROOT, S., et al., HTR fuel coating separate effect test PYCASSO, Nucl. Eng. Des. **240** (2010) 2392.
[262] KNOL, S., et al., "PYCASSO: Irradiation of HTR particles at high temperatures", Proc. 5th Int. Top. Meeting on High Temperature Reactor Technology HTR2010, Prague (2010).
[263] HAYASHI, K., et al., Irradiation experiments of the 6th–12th OGL-L fuel assemblies, Rep. JAERI-Research 94-017, Japan Atomic Energy Agency, Oarai (1994).

[264] HAYASHI, K., et al., Irradiation experiments of the 13th–15th OGL-l fuel assemblies, Rep. JAERI-Research 2000-001, Japan Atomic Energy Agency, Oarai (2000).
[265] HAYASHI, H., SAWA, K., KOMORI, Y., "Irradiation experiences and the future plan in the HTTR project", Report on International Symposium on Research Reactor and Neutron Science — In Commemoration of the 10th Anniversary of HANARO, Daejeon (2005) 215–220.
[266] SAWA, K., FUJIKAWA, S., OGAWA, M., "Present status of HTTR project in Japan", Proc. IAEA-TM on Current Status and Future Prospects of Gas Cooled Reactor Fuels, International Atomic Energy Agency, Vienna (2004).
[267] TSUYUZAKI, N., et al., "Fission product plate-out measurtement of Oarai Gas Loop OGL-1", Fission Product Release and Transport in Gas-Cooled Reactors (Proc. IAEA Specialists' Meeting, Berkeley, 1985), Rep. IWGGCR--13, International Atomic Energy Agency, Vienna (1985) 363–370.
[268] SAWA, K., UETA, S., Research and development on HTGR fuel in the HTTR project, Nucl. Eng. Des. **233** (2004) 163.
[269] MAKI, J.T., et al., NP-MHTGR fuel development program results, Rep. INEEL/EXT-2002-1268, Idaho National Engineering and Environmental Laboratory, Bechtel BWXT, Idaho, ID (2002).
[270] KAAE, J.L., Irradiation-induced microstructural changes in isotropic pyrolytic carbons, J. Nucl. Mater. **57** (1975) 82.
[271] PRICE, R.J., Properties of silicon carbide for nuclear fuel particle coatings, Nucl. Technol. **35** (1977) 320.
[272] KANIA, M.J., FUKUDA, K., Experimental test plan: USDOE/JAERI collaborative program for the coated particle fuel performance test, Rep. ORNL/ITM-11346, Oak Ridge National Laboratory, TN (1989).
[273] SAWA, K., YOSHIMUTA, S., Design of coated fuel particle for high burnup high temperature gas-cooled reactor, Rep. JAERI-Tech 98-025, Japan Atomic Energy Research Institute, Oarai (1998) (in Japanese).
[274] MONTGOMERY, F.C., HRB22 irraditaion phase test data, Rep. ORNL/M-4080, Rev 0, Oak Ridge National Laboratory, TN (1995).
[275] MINATO, K., et al., HRB-22 capsule irradiation test for HTGR fuel (JAERI/USDOE collaborative irradiation test, Rep. JAERI-Research 98-021, Japan Atomic Energy Research Institute, Oarai (1998).
[276] FUJIKAWA, S., et al., Rise-to-power test of the HTTR (High Temperature Engineering Test Reactor), Transactions of the Atomic Energy Society Japan **1** (2002) 361.
[277] BELL, G.L., et al., Technical program plan for the Advanced Gas Reactor fuel development and qualification program, Rep. ORNL/TM-2002/262, Oak Ridge National Laboratory, TN (2003).
[278] PETTI, D.A., et al., Technical program plan for the Advanced Gas Reactor fuel development and qualification program, Rep. INL/EXT-05-00465, Revision 1, Idaho National Laboratory, ID (2005).
[279] GROVER, S.B., "Final assembly and initial irradiation of the first Advanced Gas Reactor fuel development and qualification experiment in the Advanced Test Reactor", Proc. Int. Congr. on Advances in Nuclear Power Plants ICAPP'07, Nice (2007).
[280] PETTI, D.A., GROVER, S.B., MAKI, J.T., "Status of the first Advanced Gas Reactor fuel irradiation experiment in the Advanced Test Reactor", Proc. 4th Int. Top. Meeting on High Temperature Reactor Technology HTR2008, Washington, DC (2008).

[281] MAKI, J.T., AGR-1 irradiation experiment test plan, Rep INL/EXT-05-00593, Idaho National Laboratory, ID (2005).
[282] REMPE, J.L., et al., "Evaluation of specialized thermocouples for high-temperature in-pile testing", Proc. Int. Congr. on Advances in Nuclear Power Plants ICAPP'06, Reno, NV (2006).
[283] GROVER, S.B., PETTI, D.A., "Initial irradiation of the first Advanced Gas Reactor fuel development and qualification experiment in the Advanced Test Reactor", Proc. Int. Conf. on Advanced Nuclear Fuel Cycles and Systems GLOBAL2007, Boise, ID (2007).
[284] SCATES, D.M., et al, "Fission product monitoring of TRISO coated fuel for the Advanced Gas Reactor-1 experiment", Proc. 4th Int. Top. Meeting on High Temperature Reactor Technology HTR2008, Washington, DC (2008).
[285] MARTIN, R.C., Compilation of fuel performance and fission product transport models and database for MHTGR design, Rep. ORNL/NPR-91/6, Oak Ridge National Laboratory, TN (1993).
[286] DEMKOVICZ, P., MORRIS, R., "Post-irradiation of the AGR-1 experiment: Plans and preliminary results", Proc. 5th Int. Top. Meeting on High Temperature Reactor Technology HTR2010, Prague (2010).
[287] KOSHCHEEV, K.N., "Testing of fuel elements of high-temperature gas-cooled reactors", Presentation at the Meeting of PBMR (Pty) Ltd and FSUE "INM" on October 16-20 (2006).
[288] TANG, C.H., ZHOU, Y.W., LI, Z.Q., "Irradiation testing of matrix material for spherical HTR-10 fuel elements", Proc. 3rd Int. Top. Meeting on High Temperature Reactor Technology HTR2006, Johannesburg (2006).
[289] TANG, C.H., et al., Fuel irradiation of the first batches produced for the Chinese HTR-10, Nucl. Eng. Des. **236** (2006) 107.
[290] TANG, C.H., et al., "The behavior of HTR-10 fuel under irradiation", Proc. 2nd Int. Top. Meeting on High Temperature Reactor Technology HTR2004, Beijing (2004).
[291] KANIA, M.J., VALENTINE, K.H., The irradiated-microsphere gamma analyzer (IMGA) – An integrated system for HTGR coated particle fuel performance assessment, Rep. ORNL-5606, Oak Ridge National Laboratory, TN (1980).
[292] PARK, J.K., "Nuclear hydrogen project in Korea", Presentation at the Int. Congr. on Advances in Nuclear Power Plants ICAPP'05, Seoul (2005).
[293] CHO, M.-S., KIM, Y.M., LEE, B.C., Design of a capsule for an irradiation test of TRISO fuels in compact form, Transactions of the Korean Nuclear Society, Autumn Meeting, Gyeongju (2009).
[294] SCHENK, W., Nachbestrahlungsausheizverfahren für Kugelbrennelemente und andere Brennstoffproben, Rep. Jül-1454, Research Center Jülich (1977).
[295] SCHENK, W., NABIELEK, H., Kugelbrennelemente mit TRISO Partikeln bei Störfalltemperaturen, Rep. Jül-Spez-487, Research Center Jülich (1989).
[296] SCHENK, W. GONTARD, R., NABIELEK, H., Performance of HTR fuel samples under high-irradiation and accident simulation conditions with emphasis on test capsules HFR-P4 and SL-P1, Rep. Jül-3373, Research Center Jülich (1997).
[297] FREIS, D., Störfallsimulationen und Nachbestrahlungsuntersuchungen an kugelförmigen Brennelementen für Hochtemperaturreaktoren, PhD Thesis, Technical University RWTH Aachen (2010).
[298] FREIS, D., et al., "Post irradiation testing of high temperature reactor spherical fuel elements under accident conditions", Proc. 4th Int. Top. Meeting on High Temperature Reactor Technology HTR2008, Washington, DC (2008).

[299] CORINO, X., et al., “Assessment of coated-particle failure with the IMGA device”, Proc. 5th Int. Top. Meeting on High Temperature Reactor Technology HTR2010, Prague (2010).
[300] UMEDA, M., et al., Behavior of coated fuel particle of high-temperature gas-cooled reactor under reactivity-initiated accident conditions, J. Nucl. Sci. Technol. **47** (2010) 991.
[301] UMEDA, M., UETA, S., SUGIYAMA, T., “Behavior of HTGR particle fuel under reactivity initiated accident condition”, Presentation at the Conf. on Nuclear Fuels and Structural Materials for the Next Generation Nuclear Reactors (NFSM), Anaheim, CA (2008).
[302] MINATO, K., et al., Fission product release behavior of individual coated fuel particles for high-temperature gas-cooled reactors, Nucl. Technol. **131** (2000) 36.
[303] HANSON, D.L., SAURWEIN, J.J., Development plan for advanced high temperature coated-particle fuels, Rep. PC-000513, Rev. 0, General Atomics, San Diego, CA (2004).
[304] BONGARTZ, K., GYARMATI, E., SCHUSTER, H., TÄUBER, K., The brittle ring test: A method for measuring strength and Young’s modulus on coatings of HTR fuel particles, J. Nucl. Mater. **62** (1976) 123.
[305] MONTGOMERY, F.C., Fission product – SiC reaction in HTGR fuel, Rep. GA-905837/1, General Atomics, San Diego, CA (1981).
[306] ALLELEIN, H.J., et al., “The behavior of HTR fuel under irradiation”, Proc. 7th Int. Conf. on Structural Mechanics in Reactor Technology SMIRT, Chicago, IL (1983).
[307] PROKSCH, E., et al., Production of carbon monoxide during burnup of UO_2 kerneled HTR fuel particles, J. Nucl. Mater. **107** (1982) 280.
[308] SAWA, K., SUMITA, J., WATANABE, T., Fuel failure and fission gas release analysis code in HTGR, Rep. JAERI-DATA/Code 99-034, Japan Atomic Energy Research Institute, Oarai (1999).
[309] BONGARTZ, K., Status of the fuel stress and failure rate calculations at KFA, Rep. Jül-1686, Research Center Jülich (1980).
[310] KOVACS, W.J., et al., TRISO coated HTGR fuel pressure vessel performance models, Rep. GA-A 16807, GA Technologies, San Diego, CA (1983).
[311] KIM, Y.M., CHO, M.S., LEE, Y.W., LEE, W.J., “Development of a fuel performance analysis code COPA”, Proc. 4th Int. Top. Meeting on High Temperature Reactor Technology HTR2008, Washington, DC (2008).
[312] NAKAMURA, S., Computational methods in engineering and science, John Wiley & Sons, Inc., Hoboken, NJ (1977).
[313] APPEL, J., ROOS, B., A study of the release of radioactive metallic isotopes from high-temperature gas-cooled reactors, Nucl. Sci. Eng. **34** (1968) 201.
[314] KIM, Y.M., CHO, M.S., A stress analysis for a coated fuel particle of a HTGR using a Finite Element method, Nucl. Eng. Technol. **41** (2009) 1087.
[315] GOLUBEV, I.E., KURBAKOV, S.D., CHERNIKOV, A.S., Experimental and computational study of the pyrocarbon and silicon carbide barriers of HTGR fuel particle, Atomic Energy **105** (2008) 14.
[316] US-NUCLEAR REGULATORY COMMISSION, TRISO-coated particle fuel phenomenon identification and ranking tables (PIRTs) for fission products transport due to manufacturing, operations, and accidents, Main Report NUREG/CR-6844, Vol. 1, Office of Nuclear Regulatory Research, Washington DC (2004).
[317] SINJAREV, G.B., et al., Primenenie EVM dlja termodinamicheskich raschetov metallurgicheskich processov, Moscow, Nauka (1982) (in Russian).

[318] LINDEMER, T.B., Thermochemical analysis of gas-cooled reactor fuels containing Am and Pu oxides, Rep. ORNL/TM-2002/133, Oak Ridge National Laboratory, TN (2002).
[319] WALTHER, H., On mathematical models for calculating the mechanical behaviour of coated fuel particles, Nucl. Eng. Des. **18** (1972) 11.
[320] CEGA, NP-MHTGR material models of pyrocarbon and pyrolytic silicon carbide, CEGA-002820, Rev. 1, CEGA Corporation, San Diego, CA (1993).
[321] REID, R.C., et al., The properties of gases and liquids, Fourth Edition, McGraw-Hill, New York (1987).
[322] KOVACS, W.J., et al., High-temperature gas-cooled reactor fuel pressure vessel performance models, Nucl. Technol. **68** (1985) 344.
[323] OUTOKUMPU RESEARCH OY, Chemistry user's guide, version 5.0, Espoo, Finland (2002).
[324] MOORE, R.L., et al., MOCUP: MCNP-ORIGEN2 coupled utility program, Rep. INEL-95/0523, Idaho National Laboratory, ID (1995).
[325] BRIESMEISTER, J.F., et al., MCNP — A general Monte Carlo N-particle transport code, Rep. LA-13709-M, Los Alamos National Laboratory, NM (2000).
[326] CROFF, G., A user's manual for the ORIGEN2 computer code, Rep. ORNL/TM-7175, Oak Ridge National Laboratory, TN (1980).
[327] LITTMARK, U., ZIEGLER, J.F., Handbook of range distributions for energetic ions in all elements, Pergamon Press, Oxford (1980).
[328] TURNBULL, J. A., et al., The diffusion coefficient of gaseous and volatile species during the irradiation of uranium dioxide, J. Nucl. Mater. **107** (1982) 168.
[329] OLANDER, D.R., Fundamental aspects of nuclear reactor fuel elements, Rep. TID-26711-P1, ERDA Technical Information Center, Oak Ridge, TN (1976).
[330] RÖLLIG, K., Release of noble gases and halogens from the PBMR core, Rep. GBRA 052 336, Westinghouse Reaktor GmbH, Ladenburg, Germany (2001).
[331] HOCHTEMPERATURREAKTOR-BRENNSTOFFKREISLAUF, Projektbericht 1984, Internal Report HBK-IB-1/85, Research Center Jülich (1985).
[332] LAUF, R.J., et al., Out-of-reactor studies of fission product – Silicon carbide interactions in HTGR fuel particles, J. Nucl. Mater. **120** (1984) 6.
[333] MINATO, K., et al., Fission product palladium – silicon carbide interaction in HTGR fuel particles, J. Nucl. Mater. **172** (1990) 184.
[334] TIEGS, T.N., Fission product Pd-SiC interaction in irradiated coated-particle fuels, Nucl. Technol. **57** (1982) 389.
[335] MILLER, G.K., BENNETT, R.G., Analytical solution for stresses in TRISO-coated particles, J. Nucl. Mater. **206** (1993) 35.
[336] MILLER, G.K., PETTI, D.A., VARACALLE, D.J., MAKI, J.T., Statistical approach and benchmarking for modeling of multi-dimensional behavior in TRISO-coated fuel particles, J. Nucl. Mater. **317** (2003) 69.
[337] MILLER, G.K., PETTI, D.A., VARACALLE, D.J., MAKI, J.T., Consideration of the effects on fuel particle behavior from shrinkage cracks in the inner pyrocarbon layer, J. Nucl. Mater. **295** (2001) 205.
[338] MILLER, G.K., et al., "Development of an integrated performance model for TRISO-coated gas reactor particle fuel", Proc. 1st Int. Top. Meeting on High Temperature Reactor Technology HTR2002, Petten (2002).
[339] PELESSONE, D., PISA: A one-dimensional spherically symmetric computer program to perform thermal and stress analysis of irradiated fuel particles, General Atomics Unpublished report CEGA-M-92-2052, San Diego, CA (1992).

[340] BRADLEY, J.S., RICHARDS, M.B., Software design description and user's manual for CAPPER irradiation capsule performance computer code, Rep. CEGA-002309, General Atomics, San Diego, CA (1992).
[341] GENERAL ATOMICS, Fuel design data manual, Document 901866, Issue F, San Diego, CA (1987).
[342] MARTIN, D.G., How well can we model kernel coating mechanical interaction (KCMI)? Contribution to EU Project HTR-F WP3/DGM/04/04 (2004).
[343] GUILLERMIER, P., LANSIART, S., "AREVA and CEA R&D program on HTR fuel", Proc. Int. Congr. on Advances in Nuclear Power Plants ICAPP'09, Tokyo (2009).
[344] CRANK, J., The mathematics of diffusion, 2nd Edition., Oxford University Press, New York (1975).
[345] JOST, W., Diffusion in solids, liquids, gases, 3rd Printing with Addendum, Academic Press, New York (1960).
[346] KIM, Y.M., CHO, M.S., Development of the fission product release analysis code COPA-FPREL, Nucl. Technol. **170** (2010) 231.
[347] PEPPER, D.W., HEINRICH, J.C., The Finite Element method, Hemisphere Publishing Corporation, New York and Washington, DC (1992).
[348] SMITH, P.D., TRAFIC, A computer program for calculating the release of metallic fission products from an HTGR core, Rep. GA-A14721, General Atomics, San Diego, CA (1978).
[349] HILPERT, K., et al., Sorption of cesium and its vaporization from graphitic materials at high temperatures, High Temp. High Press. **20** (1988) 157.
[350] ALLELEIN, H.J., Spaltproduktverhalten — Speziell Cs-137 — in HTR-TRISO-Brennstoff-teilchen, Rep. Jül-1695, Research Center Jülich, Germany (1980).
[351] MYERS, B.F., Cesium diffusion in silicon carbide during post irradiation anneals, Technical Note HBK-TN-01/84, Research Center Jülich (1984).
[352] CHRIST, A., Nachrechnung von Ausheizexperimenten, Technical Note HBK-5125-BF-GHRA 001555, Hochtemperatur-Reaktorbau GmbH, Mannheim (1985).
[353] VERFONDERN, K., MÜLLER, D., Code development for fission product behavior in HTR fuel for safety assessments, Internal Report KFA-ISF-IB-10/89, Research Center Jülich (1989).
[354] MARNET, C., WIMMERS, M., BIRKHOLD, U., "Decommissioning of the AVR reactor concept for the total dismantling", Technologies for Gas Cooled Reactor Decommissioning, Fuel Storage and Waste Disposal (Proc. IAEA-TCM, Jülich, 1997), Rep. IAEA-TECDOC-1043, International Atomic Energy Agency, Vienna (1998) 17–39.
[355] POHL, P., "Short review of lessons learned from AVR mass fuel testing", Proc. HTR-TN Int. HTR Fuel Seminar, Brussels (2001).
[356] POHL, P., "AVR decommissioning achievements and future programme", Technologies for Gas Cooled Reactor Decommissioning, Fuel Storage and Waste Disposal (Proc. IAEA-TCM, Jülich, 1997), Rep. IAEA-TECDOC-1043, International Atomic Energy Agency, Vienna (1998) 41–53.
[357] KRUMBACH, H., DUWE, R., RÖDIG, M., "Handling and behaviour of AVR fuel elements for interim storage", Proc. HOTLAB 2004, Halding (2004).
[358] RÖLLIG, K., et.al., "Entsorgung von Hochtemperaturreaktoren", High Temperature Reactor Fuel Elements, Graphite, and Disposal (Proc. Status Seminar, Jülich, 1987), Rep. Jül-Conf-61, Research Center Jülich (1987) 109–134.
[359] SCHRÖDER, G., DIETRICH, G., HEESEN, W. von, „Aspekte der Entsorgung des THTR-300", Fortschritte in der Energietechnik, Monographien des Forschungszentrums Jülich, Vol. 8, Research Center Jülich (1993) 301–308.

[360] BÄUMER, R., DIETRICH, G., THTR commissioning and operating experience, Energy **16** (1991) 59.
[361] KNIZIA, K., Der THTR-300 – Eine vertane Chance? ATW **47** (2002) 110.
[362] NIEPHAUS, D., Referenzkonzept zur direkten Endlagerung von abgebrannten HTR-Brennelementen in CASTOR THTR/AVR Transport- und Lagerbehältern, Rep. Jül-3734, Research Center Jülich (2000).
[363] BÄUMER, R., KALINOWSKI, I., Decommissioning concept for the high temperature reactor THTR-300, Kerntechnik **56** (1991) 362.
[364] PLÄTZER, S., MIELISCH, M., "Unloading of the reactor core and spent fuel management of THTR-300", Technologies for Gas Cooled Reactor Decommissioning, Fuel Storage and Waste Disposal (Proc. IAEA-TCM, Jülich, 1997), Rep. IAEA-TECDOC-1043, International Atomic Energy Agency, Vienna (1998) 143–150.
[365] DIETRICH, G., Hochtemperatur-Kernkraftwerk GmbH, Hamm, personal communication, 2006.
[366] BRINKMANN, U., et.al., "Entsorgung des AVR-Versuchskraftwerks und Untersuchungen an abgebrannten Brennelementen für trockene Zwischenlagerung", Proc. Jahrestagung Kerntechnik, Berlin (1980) 497–500.
[367] DUWE, R., MÜNSTERMANN, H., Experimentelle Untersuchungen zum Freisetzungs-verhalten von HTR-BE unter Trocken-Lagerbedingungen, Internal Report KFA-IRW-IB-7/80, Research Center Jülich (1980).
[368] DUWE, R., MÜLLER, H., Begleitende Messungen im AVR-Trockenlager – Freisetzung gasförmiger Radionuklide – Temperaturverlauf, Internal Report KFA-IRW-IB-3/86, Research Center Jülich (1986).
[369] RÖLLIG, K., C-14 Freisetzung von abgebrannten THTR-BE, Technical Note 413-211-BF3521, Hochtemperatur-Reaktorbau, Mannheim (1989).
[370] POHL, P., Endlagergerichtete CASTOR-Dokumentation: Bestimmung des Nuklidinventars der AVR-Brennelemente nach einem Referenzbrennelement-Verfahren, Technical Note E-7562 (corrected version), Arbeitsgemeinschaft Versuchsreaktor, Düsseldorf (2003).
[371] POHL, P., Nuklidaktivitäten der bestrahlten AVR-Brennelemente zum Jahresende 2003, Technical Note E-8039, Arbeitsgemeinschaft Versuchsreaktor, Düsseldorf (2003).
[372] BRINKMANN, H.U., et.al., Contributions towards the development of a packaging concept for the final disposal of spent HTGR pebble bed Fuel, Nucl. Eng. Des. **118** (1990) 107.
[373] BRODDA, B.G., MERZ, E.R., Leachability of actinides and fission products from spent HTR fuel, Radiochimica Acta **44/45** (1988) 3.
[374] KIRCH, N., BRINKMANN, H.U., BRÜCHER, P.H., Storage and final disposal of spent HTR fuel in the Federal Republic of Germany, Nucl. Eng. Des. **121** (1990) 241.
[375] GANSER, B., et.al., "FuE-Arbeiten zur Endlagerung von HTR-Brennelementen", Works on High Temperature Reactor Fuel Elements, Graphite, and Disposal (Proc. Status Seminar, Jülich, 1987), Rep. Jül-Conf-61, Research Center Jülich (1987) 147–160.
[376] DUWE, R., SCHRÖDER, R., Auslaugverhalten von HTR-Brennelementen und -Brennstoffteilchen in Salzlauge, Internal Report KFA-IWE-IB-1/93, Research Center Jülich (1993).
[377] REBMANN, A., DUWE, R., Das Belastungsverhalten von HTR-Brennelementen im salinären Endlager, Internal Report KFA-IRW-IB-3/88, Research Center Jülich (1988).

[378] WOLF, J., Endlagerung verbrauchter Brennelemente aus dem AVR-Versuchskernkraftwerk im Salzbergwerk Asse, Rep. Jül-1163, Research Center Jülich (1975).
[379] MERZ, E., BRÜCHER, H., HALASZOVICH, S., "Lösung der Entsorgungsfrage beim Hochtemperaturreaktor", Fortschritte in der Energietechnik, Monographien des Forschungszentrums Jülich, Vol. 8, Research Center Jülich (1993) 336–348.
[380] BUTTLER, R., "Kernmaterialüberwachung beim rückholbaren Einlagerversuch mit verbrauchten AVR-Brennelementen", MAW und HTR-BE-Versuchseinlagerung in Bohrlöchern (Proc. Status Seminar, Jülich, 1986), Rep. Jül-Conf-60, Research Center Jülich (1987) 187–200.
[381] DEPARTMENT FOR ENVIRONMENT, FOOD AND RURAL AFFAIRS, The 2004 UK radioactive waste inventory, DEFRA/RAS/05.002, Nirex Report N/090, London (2005).
[382] SCHEFFEL, W.J., et al., Operating history of the Peach Bottom HTGR, Rep. GA-A13907, General Atomic, San Diego, CA (1976).
[383] STOUKY, R.J., KOHLER, E.J., "Planned decommissioning of the Peach Bottom Unit No. 1 HTGR", Proc. ASME Winter Ann. Meeting, 73-WA/NE-7, Detroit, MI (1973).
[384] US-NUCLEAR REGULATORY COMMISSION, Fact sheet on decommissioning nuclear power plants, http://www.nrc.gov/reading-rm/doc-collections/fact-sheets/decommissioning. html, Rockville, MD (2008).
[385] KOHLER, E.J., et al., Peach Bottom decommissioning and component removal, Rep. GA-A14297, General Atomic Company, San Diego, CA (1977).
[386] CATALYTIC Inc., Removal of primary circuit components from the Peach Bottom HTGR, ERDA Report GA-A14369, General Atomic Company, San Diego, CA (1977).
[387] MORISETTE, R.P., et al., Characterization of Peach Bottom Unit 1 fuel, Rep. ORNL/SUB-86-22047/2 and GA-C18525, GA Technologies, San Diego, CA (1986).
[388] FISHER, M., "Fort St. Vrain decommissioning project", Technologies for Gas Cooled Reactor Decommissioning, Fuel Storage and Waste Disposal (Proc. IAEA-TCM, Jülich, 1997), Rep. IAEA-TECDOC-1043, International Atomic Energy Agency, Vienna (1998).
[389] NUCLEAR ENERGY INSTITUTE, Decommissioning of nuclear power plants. NEI Fact Sheet, Washington, DC, (2007).
[390] UTILITY ENGINEERING CORPORATION, Fort St. Vrain repowering project, Denver, CO (2005).
[391] TRENTEC INC., Fort St. Vrain decommissioning diamond wire concrete cutting nuclear facility decommissioning, http://www.trentec.com/decom/projects/fsvls. PDF, Cincinnati, OH (2005).
[392] UNDERWATER CONSTRUCTION CORPORATION, Decommissioning services - FORT ST. VRAIN, http://www.uccdive.com/Underwater%20Plasma%20Arc%20Cutting%20Services.htm, Essex, CT (1994).
[393] JOVANOVIC, V., et al., FSV plateout analysis for decommissioning study, Rep. 909658/B, General Atomics, San Diego, CA (1992).
[394] ELECTRIC POWER RESEARCH INSTITUTE, Fort St. Vrain decommissioning: Final site radiation survey: Summary report and lessons learned, TR-107979, Palo Alto, USA (1998).
[395] LOTTS, A.L., et al., Options for treating high-temperature gas-cooled reactor fuel for repository disposal, Rep. ORNL/TM-12027, Oak Ridge National Laboratory, TN (1992).

[396] PUBLIC SERVICE COMPANY OF COLORADO, Fort St. Vrain independent spent fuel storage installation safety analysis report, Docket No. 72-09, Golden, CO (1991).
[397] MORISETTE, R.P., TOMISO, N., Characterization of Fort St. Vrain fuel, Rep. ORNL/SUB-86-22047/2 and GA-C18511, GA Technologies, San Diego, CA (1986).
[398] XIAO, H.L., LIU, J.G., Storage and safety analysis of HTR-10 fuel elements, Journal of Tsinghua University **41**(10) (2001) 49.
[399] SUN, Y.L., XU, Y.H., "On the issues of fuel storage and decommissioning of the HTR-10 test reactor", Technologies for Gas Cooled Reactor Decommissioning, Fuel Storage and Waste Disposal (Proc. IAEA-TCM, Jülich, 1997), Rep. IAEA-TECDOC-1043, International Atomic Energy Agency, Vienna (1998) 133–139.
[400] SAWA, K., et al., "Study on storage and reprocessing concept of the High Temperature Engineering Test Reactor (HTTR) fuel", Technologies for Gas Cooled Reactor Decommissioning, Fuel Storage and Waste Disposal (Proc. IAEA-TCM, Jülich, 1997), Rep. IAEA-TECDOC-1043, International Atomic Energy Agency, Vienna (1998) 177–189.
[401] KATANISHI, S., TAKEI, M., KUNITOMI, K., "Study on reprocessing method of high temperature gas cooled reactor fuels", Innovative Technologies for Nuclear Fuel Cycle and Nuclear Power (Proc. IAEA Int. Conf. Vienna, 2003), Rep. IAEA-CSP-24, International Atomic Energy Agency, Vienna (2004) 676–686.
[402] FULS, W.F., MATHEWS, E.H., Passive cooling of the PBMR spent and used fuel tanks, Nucl. Eng. Des. **237** (2007) 1354.
[403] CASPERSSON, S., PBMR Conceptual Design, Presentation at the VHTR R&D FY10 Technical Review Meeting, Denver, CO (2010).
[404] BRÜCHER, H., NIEPHAUS, D., BARNERT, E., KROTH, K., "Disposal of spent HTR fuel elements", Proc. 2nd Ann. Int. Conf. on High Level Radioactive Waste Management, Las Vegas, NV (1991).
[405] KIRYUSHIN, A.I., et al., "GT-MHR spent fuel storage disposal without processing", Technologies for Gas Cooled Reactor Decommissioning, Fuel Storage and Waste Disposal (Proc. IAEA-TCM, Jülich, 1997), Rep. IAEA-TECDOC-1043, International Atomic Energy Agency, Vienna (1998) 191–199.
[406] STANTON, D.P., et. al., "Coating of crystalline nuclear waste form to improve inertness", Proc. 83rd Ann. Meeting of the American Society, Washington, DC (1981) 394–398.
[407] GRAY, W.J., A study of the oxidation of graphite in liquid water for radioactive storage applications, Radioactive Waste Management and the Nuclear Fuel Cycle **3** (1982) 137.
[408] BROSSARD, P., et al., "The VHTR fuel and fuel cycle project: Status of on-going research and results", Report of GIF Symposium, Paris (2009).
[409] KUIJPER, J.C., et al., Plutonium and minor actinide management in thermal high-temperature gas-cooled reactors, PUMA Project Final Activity Report. Contract Number: FP6-036457, European Commission, Brussels (2010).
[410] VON LENSA, W., et al., CARBOWASTE: "Closing the fuel and graphite cycles for HTR", Proc. 5th Int. Top. Meeting on High Temperature Reactor Technology HTR2010, Prague (2010).
[411] FÜTTERER, M.A., BLUHM, H., HOPPÉ, P., SINGER, J., Head-end process for the reprocessing of reactor core material, International Patent WO/2006/087360, European Patent EP1849164, publication 24.08.2006, http://www.wipo.int/pctdb/en/wo.jsp?wo=2006087360 (2006).

[412] FÜTTERER, M.A., VON DER WEID, F., KILCHMANN, P., "A high voltage head-end process for waste minimization and reprocessing of coated particle fuel for high temperature reactors", Proc. Int. Congr. on Advances in Nuclear Power Plants ICAPP'10, San Diego, CA (2010).
[413] DAI, W.Z, ZHAO, J.J., The model and optimization of HTGR nuclear fuel cycle (I) Multi-reactor model, China Nuclear Science and Technology Rep. CN1C-00516, China Nuclear Information Centre, Atomic Energy Press, Beijing (1991).
[414] SPENCER, B.B., DEL CUL, G.D., MATTUS, C.H., COLLINS, E.D. "TRISO-coated spent fuel processing using a grind-leach head-end", Proc. Int. Conf. on Nuclear Energy Systems for Future Generation and Global Sustainability GLOBAL2005, Tsukuba (2005).
[415] DEL CUL, G.D., SPENCER, B.B., FORSBERG, C.W., COLLINS, E.D., RICKMAN, W.S., TRISO-coated fuel processing to support High-Temperature Gas-Cooled Reactors, Rep. ORNL/TM-2002/156, Oak Ridge National Laboratory, (2002).
[416] WICKHAM, A.J., NEIGHBOUR, G.B., DUBOURG, M., "The uncertain future for nuclear graphite disposal: crisis or opportunity?", Nuclear Graphite Waste Management (Proc. IAEA-TCM, Manchester, 1999), International Atomic Energy Agency, Vienna (2001) 13–28.
[417] FORSBERG, C.W., DEL CUL, G.D., SPENCER, B.B., COLLINS, E.D., "A new repository Waste Form: Graphite-Carbon High-Level Waste", Presentation at the International HLW Management Conference, Las Vegas, NV (2003).
[418] MERZ, E., On the disintegration of graphite by the formation of electrolytic graphite intercalation compounds, Kerntechnik **12** (1970) 341.
[419] HOOGEN, N.G., MERZ, E.R., Evaluation of potential head-end procedures for graphite-containing fuel elements, Nucl. Technol. **61** (1983) 380.
[420] TIAN, L.F., WEN, M.F., LI, L.Y., CHEN, J., Disintegration of graphite matrix from the simulative high temperature gas-cooled reactor fuel element by electrochemical method, Electrochimica Acta, 54 (2009) 7313.
[421] PIERSON, H.O., Handbook of carbon, graphite, diamond, and fullerenes: properties, processing, and applications, William Andrew Inc., Norwich, NY (1993).
[422] KANG, F., ZHANG, T.Y., LENG, Y., Electrochemical behavior of graphite in electrolyte of sulphuric and acetic acid, Carbon **35** (1997) 1167.
[423] HAN, Z.D., WANG, J.Q., XRD/XPS Study on Oxidation of Graphite, Chin. J. Inorg. Chem. **19** (2003) 1366.
[424] HUANG, J.H., ROWSON, N.A., Hydrometallurgical decomposition of pyrite and marcasite in a microwave field, Hydrometallurgy **64** (2002) 169.
[425] ZHAO Y.F., CHEN J., Studies on the dissolution kinetics of ceramic uranium dioxide particles in nitric acid by microwave heating, J. Nucl. Mater. **373** (2008) 53.
[426] KAISER, G., et al., "Head-end Processing of HTR Fuel Elements, Specialists' meeting on gas-cooled reactor fuel development and spent fuel treatment", Gas-cooled reactor fuel development and spent fuel treatment (Proc. IAEA Specialists' Meeting, Moscow, 1983), Rep. IWGGCR--8, International Atomic Energy Agency, Vienna, and the USSR State Committee for Utilization of Atomic Energy, Moscow (1985) 357–368.
[427] AL-HARAHSHEH, M., KINGMAN, S.W., Microwave-assisted leaching — a review, Hydrometallurgy **73** (2004) 189.
[428] TANG, Y.P., et al., Total gelation process for the preparation of UO_2 fuel kernel and its progress, Journal of Tsinghua University (Sci&Tech) **37** (1997) 61.

[429] Overview of key issues and guidelines for regulatory oversight and inspection of high temperature gas reactor fuel fabrication and quality control activities. Rep. ORNL/TM-2009/041, Oak Ridge National Laboratory, TN (2009).
[430] US design certification PBMR fuel performance envelop and test program, Document No. 039116, PBMR Pty., Centurion (2007).
[431] "PBMR nuclear fuel" Revision 2, Document No. 010520-425, Non-proprietary version, PBMR, Centurion (2002).
[432] HANSON, D.L., Logic for deriving fuel quality specifications, Project 30058, Rep. PC-000498/0, General Atomics, San Diego, CA (2001).
[433] US-NUCLEAR REGULATORY COMMISSION, Requests for additional information on the Gas Turbine Modular Helium Reactor (GT-MHR), Logic for deriving fuel quality specifications; design data needs; and fuel process and quality control description, Rockville, MD (2003).
[434] MORRIS, R., PETTI, D., POWERS, D., BOYAK, B., TRISO coated particle fuel phenomena identification and ranking tables (PIRTs) for fission product transport due to manufacturing, operations, and accidents, Rep. NUREG/CR-6844, Vol 1-3, US-Nuclear Regulatory Commission, Rockville, MD (2004).
[435] IDAHO NATIONAL LABORATORY, Technical program plan for the Next Generation Nuclear Plant/Advanced Gas Reactor fuel development and qualification program, Rep. PLN-3636, Rev 0, Idaho Falls, ID (2010).
[436] IDAHO NATIONAL LABORATORY, NGNP fuel qualification White Paper, Rep. INL/EXT-10-17686, Rev. 0, Idaho Falls, ID (2010).
[437] ALLEN, T., et al., Semi-annual report to the Nuclear Regulatory Commission on the Cooperative agreement for research on advanced VHTRs, University of Wisconsin, Madison, WI (2010).
[438] Submittal of fuel fabrication quality control measures and performance monitoring plans for the Pebble Bed Modular Reactor (PBMR) fuel, Nonproprietary Version, Exelon Generation, Kennett Square, PA (2002).
[439] GENERAL ATOMICS, MHTGR fuel process & quality control description, Rep. DOE-HTGR-90257/0, General Atomics, San Diego, CA (1991).
[440] GENERAL ATOMICS, 600 MW(t) Gas Turbine Modular Helium Reactor design data needs, Rep. DOE-GT-MHR-100217 (draft), San Diego, CA (2003).
[441] US-NUCLEAR REGULATORY COMMISSION, Request for additional information No. 5772 Revision 0, June 2, 2011 NGNP pre-application activities, Department of Energy, Idaho National Laboratory, Docket No. PROJ 0748, SRP Section: ARP FDQ-Fuel Design and Qualification, Rockville, MD (2011).
[442] Fuel irradiation qualification report, Document No. 000570-34 submitted to NRC, PBMR Pty., Centurion (2002).
[443] HOBBS, L.W., CLINARD Jr., F.W., ZINKLE, S.J., EWING, R.C., Radiation effects in ceramics, J. Nucl. Mater., **216** (1994) 291.
[444] SCHILLING, W., Properties of Frenkel defects, J. Nucl. Mater., **216** (1994) 45.
[445] PETTI, D., MAKI, J., The challenges associated with high burnup and high temperature for UO_2 TRISO coated particle fuel, Presentation at the MIT NGNP Symposium, Preprint INL/CON-05-00038, Idaho National Laboratory, ID (2005).
[446] IDAHO NATIONAL LABORATORY, Mechanistic source terms White Paper, INL/EXT-10-17997, Rev. 0, Idaho Falls, ID (2010).

[447] US-NUCLEAR REGULATORY COMMISSION, Request for additional information No. 5771 Revision 0 June, 2, 2011, NGNP pre-application activities, Department of Energy, Idaho National Laboratory, Docket No. PROJ 0748 SRP Section: ARP MST-mechanistic source term, Rockville, MD (2011).
[448] US DEPARTMENT OF ENERGY, Next Generation Nuclear Plant Licensing Strategy, A Report to Congress, Washington, DC (2008).

ABBREVIATIONS

ACS	auxiliary cooling system
ADU	ammonium diuranate
ADUN	acid deficient uranyl nitrate
ALARA	as low as reasonably achievable
ASME	American Society of Mechanical Engineers
ASTM	American Society for Testing and Materials
ATR	advanced test reactor
AWD	ageing, washing and drying vessel
BAF	bacon anisotropy factor
BEST	code name for sample holder at HFR Petten
BET	Brunauer, Emmett, Teller
CAPRI	CEA AREVA production integrated
CCCM	carbon-carbon composite material
CCCTF	core conduction cooldown test facility
CCD	charge-coupled device
CEA	Commissariat à l'Energie Atomique
CERCA	Compagnie pour l'Etude et la Réalisation de Combustibles Atomiques
CPS	counts per second
CSF	core support floor
CTE	coefficient of thermal expansion
CVI	chemical vapour infiltration
CUP	carbonization under pressure
D&D	decontamination & decommissioning
CVD	chemical vapour deposition
DPA	displacements per atom
EFPD	equivalent full power days
EPMA	electron probe micro analysis
EPR	European pressurized reactor
ESRF	European synchrotron research facility
FACS	fuel accident condition simulator
FFD	fuel failure detection
FIMA	fissions per initial metal atom

FMPS	fission product monitoring system
FP	framework programme
FSV	Fort St. Vrain
FWHM	full width at half maximum
FZJ	Forschungszentrum Jülich
GA	General Atomics
GAIA	lab scale experimental manufacturing line for coated particles
GenIV	generation IV nuclear reactor
GSP	gel-supported precipitation
GTHTR	gas turbine high temperature reactor
GT-MHR	gas turbine- modular helium reactor
HEU	high enriched uranium
HFEF	hot fuel examination facility
HFIR	high flux isotope reactor
HFR	high flux reactor, Petten
HLW	High level active waste
HMTA	hexamethylenetetraamine
HTE	high temperature electrolysis
HTGR	high temperature gas cooled reactor
HTR-PM	high temperature reactor-pebble modular
HTTR	high temperature engineering test reactor
IAEA	International Atomic Energy Agency
ICP-MS	inductively coupled plasma mass spectrometer
ICPP	Idaho chemical processing plant
IHX	intermediate heat exchanger
IMGA	irradiated microsphere gamma analyzer
INET	Institute for Nuclear and New Energy Technology
IPyC	inner pyrocarbon layer
ITU	Institute for Transuranium Elements, Karlsruhe
JAEA	Japan Atomic Energy Agency
JMTR	Japan materials test reactor, Oarai
KAERI	Korea Atomic Energy Research Institute
KCMI	kernel coating mechanical interaction
KÜFA	Kühlfinger Apparatur

LEU	low enriched uranium
LEUCO	low enriched uranium oxycarbide
LLW	low level active waste
LOFC	loss of forced convection
LWR	light water reactor
MHTGR	Modular High Temperature Gas cooled Reactor
MLW	medium level active waste
MTR	material test reactor
MTS	methyltrichlorosilane
NGNP	next generation nuclear plant
NHDD	Nuclear Hydrogen Production Technologies Development and Demonstration Project
NIIAR	State Scientific Center – Research Institute of Atomic Reactors
NRAD	neutron radiography
NRG	Nuclear Research and Consultancy Group, Petten
OAF	optical anisotropy factor
OECD	Organisation for Economic Co-operation and Development
OGL	Oarai gas loop
OKBM	Experimental Mechanical Engineering Construction Office
OPTAF	optical anisotropy factor
OPyC	outer pyrocarbon layer
PBMR	pebble bed modular reactor
PCI	phase contrast imaging
PCR	primary coolant radioactivity
PCRV	prestressed concrete reactor vessel
PCS	power conversion system
PFP	pilot fuel plant
PHP	process heat plant
PIE	post-irradiation examination
PLC	programmable logic controller
PSA	particle size analyzer
PVA	polyvinyl alcohol
PYCASSO	pyrocarbon irradiation for creep and swelling/shrinkage of objects
QC	quality control

QUATTRO	code name for sample holder at HFR Petten
RAPHAEL	ReActor for Process heat, Hydrogen And ELectricity generation
RB	removable beryllium
REFA	code name for sample holder at HFR Petten
RGD	rate of graphite disintegration
RIAR	Russian Institute forAtomic Reactors, Dimitrovgrad
RPV	reactor pressure vessel
RRE	round robin exercise
RT	room temperature
SEM	scanning electron microscopy
SGL	Sigri Great Lakes, Bad Godesberg
SI	sulphur-iodine
SLF	sweep loop facility
SMR	small and medium-sized reactor
SPN	self powered neutron detector
TC	thermocouple
TEC	thermal expansion coefficient
TEM	transmission electron microscopy
THFA	tetrahydrofurfuryl alcohol
TRIO	code name for sample holder at HFR Petten
VHTR or V/HTR	very high temperature reactor
VNIIMN	A.A. Bochvar All Russian Institute of Inorganic Materials
XRD	X ray diffraction

CONTRIBUTORS TO DRAFTING AND REVIEW

Abram, T.	University of Manchester, United Kingdom
Bakker, K.	Nuclear Research and Consultancy Group (NRG), Petten, the Netherlands
Chen, J.	Institute of Nuclear and New Energy Technology (INET), Beijing, China
Chernikov, A.	SIA Lutch, Podolsk, Russian Federation
Colak, U.	Hacettepe University, Ankara, Turkey
Demkowicz, P.	Idaho National Laboratories, Idaho Falls, USA
Dittrich, W.	AREVA NP, Erlangen, Germany
Feltus, M.	US Department of Energy, Germantown, USA
Fütterer, M.	Joint Research Center, Petten, The Netherlands
Golubev, I.	A.A. Bochvar All Russian Research, Moscow, Russian Federation
Groot, S. de	Nuclear Research and Consultancy Group (NRG), Petten, the Netherlands
Guillermier, P.	AREVA NP, Lyon, France
Hania, P.R.	Nuclear Research and Consultancy Group (NRG), Petten, the Netherlands
Hanson, D.	General Atomics, San Diego, USA
Hunn, J.	Oak Ridge National Laboratory, USA
Kadak, A.	Massachussetts Institute of Technology, Boston, USA
Kadarmetov, I.	A.A. Bochvar All Russian Research, Moscow, Russian Federation
Kania, M.J.	Averill Park, NY, USA
Kellerbauer, A.	Institute for Transuranium Elements, JRC, Karlsruhe, Germany
Kendall, J.M.	Global Virtual LLC, Prescott, USA
Kercher, A.	Oak Ridge National Laboratory, USA
Kim, Y.-M.	Korea Atomic Energy Research Institute, Daejeon, Republic of Korea
Kupitz, J.	International Atomic Energy Agency, Vienna
Lee, Y.-W.	Korea Atomic Energy Research Institute, Daejeon, Republic of Korea
Lohnert, G.	University Stuttgart, Germany
Maki, J.T.	Idaho National Laboratories, Idaho Falls, USA
Martin, D.G.	Oxon, United Kingdom
Methnani, M.	International Atomic Energy Agency, Vienna, Austria
Nabielek, H.	Research Center Jülich, Jülich, Germany
Nawada, H.	International Atomic Energy Agency, Vienna, Austria
Odeychuk, M.	Kharkov Institute of Physics and Technology, Kharkiv, Ukraine
Petti, D.A.	Idaho National Laboratories, Idaho Falls, USA
Phelip, M.	Commissariat à l'Energie Atomique, Cadarache, France
Ramlakan, A.	South Africa

Rubin,S.	US National Regulatory Commission, Washington, DC, USA
Sawa, K.	Japan Atomic Energy Agency, Oarai, Japan
Tang, C.	Institute of Nuclear and New Energy Technology (INET), Beijing, China
Tian, L.F.	Institute of Nuclear and New Energy Technology (INET), Beijing, China
Toscano, E.	Institute for Transuranium Elements, JRC, Karlsruhe, Germany
Ueta, S.	Japan Atomic Energy Agency, Oarai, Japan
Van d. Merwe, H.	South Africa
Venter, J.	South Africa
Verfondern, K.	Research Center Jülich, Jülich, Germany
Versluis, R.M.	US-DOE, Germantown, USA
Wen, M.F.	Institute of Nuclear and New Energy Technology (INET), Beijing, China
Werner, H.	Research Center Jülich, Jülich, Germany
Zhang, L.	Institute of Nuclear and New Energy Technology (INET), Beijing, China

RESEARCH COORDINATION MEETINGS

Vienna, Austria, December 9-12, 2002

Vienna, Austria, October 18-22, 2004

Vienna, Austria, October 17-21, 2005

Vienna, Austria, June 18-22, 2007

Vienna, Austria, December 1-5, 2008

Vienna, Austria, May 3-7, 2010

CONSULTANTS MEETINGS

Petten, Netherlands, April 21-25, 2002

Vienna, Austria, July 4, 2003

Vienna, Austria, December 3-5, 2003

Daejeon, Republic of Korea, May 19, 2005

IAEA
International Atomic Energy Agency

Where to order IAEA publications

In the following countries IAEA publications may be purchased from the sources listed below, or from major local booksellers. Payment may be made in local currency or with UNESCO coupons.

AUSTRALIA
DA Information Services, 648 Whitehorse Road, MITCHAM 3132
Telephone: +61 3 9210 7777 • Fax: +61 3 9210 7788
Email: service@dadirect.com.au • Web site: http://www.dadirect.com.au

BELGIUM
Jean de Lannoy, avenue du Roi 202, B-1190 Brussels
Telephone: +32 2 538 43 08 • Fax: +32 2 538 08 41
Email: jean.de.lannoy@infoboard.be • Web site: http://www.jean-de-lannoy.be

CANADA
Bernan Associates, 4501 Forbes Blvd, Suite 200, Lanham, MD 20706-4346, USA
Telephone: 1-800-865-3457 • Fax: 1-800-865-3450
Email: customercare@bernan.com • Web site: http://www.bernan.com

Renouf Publishing Company Ltd., 1-5369 Canotek Rd., Ottawa, Ontario, K1J 9J3
Telephone: +613 745 2665 • Fax: +613 745 7660
Email: order.dept@renoufbooks.com • Web site: http://www.renoufbooks.com

CHINA
IAEA Publications in Chinese: China Nuclear Energy Industry Corporation, Translation Section, P.O. Box 2103, Beijing

CZECH REPUBLIC
Suweco CZ, S.R.O., Klecakova 347, 180 21 Praha 9
Telephone: +420 26603 5364 • Fax: +420 28482 1646
Email: nakup@suweco.cz • Web site: http://www.suweco.cz

FINLAND
Akateeminen Kirjakauppa, PO BOX 128 (Keskuskatu 1), FIN-00101 Helsinki
Telephone: +358 9 121 41 • Fax: +358 9 121 4450
Email: akatilaus@akateeminen.com • Web site: http://www.akateeminen.com

FRANCE
Form-Edit, 5, rue Janssen, P.O. Box 25, F-75921 Paris Cedex 19
Telephone: +33 1 42 01 49 49 • Fax: +33 1 42 01 90 90
Email: formedit@formedit.fr • Web site: http://www. formedit.fr

Lavoisier SAS, 145 rue de Provigny, 94236 Cachan Cedex
Telephone: + 33 1 47 40 67 02 • Fax +33 1 47 40 67 02
Email: romuald.verrier@lavoisier.fr • Web site: http://www.lavoisier.fr

GERMANY
UNO-Verlag, Vertriebs- und Verlags GmbH, Am Hofgarten 10, D-53113 Bonn
Telephone: + 49 228 94 90 20 • Fax: +49 228 94 90 20 or +49 228 94 90 222
Email: bestellung@uno-verlag.de • Web site: http://www.uno-verlag.de

HUNGARY
Librotrade Ltd., Book Import, P.O. Box 126, H-1656 Budapest
Telephone: +36 1 257 7777 • Fax: +36 1 257 7472 • Email: books@librotrade.hu

INDIA
Allied Publishers Group, 1st Floor, Dubash House, 15, J. N. Heredia Marg, Ballard Estate, Mumbai 400 001,
Telephone: +91 22 22617926/27 • Fax: +91 22 22617928
Email: alliedpl@vsnl.com • Web site: http://www.alliedpublishers.com

Bookwell, 2/72, Nirankari Colony, Delhi 110009
Telephone: +91 11 23268786, +91 11 23257264 • Fax: +91 11 23281315
Email: bookwell@vsnl.net

ITALY
Libreria Scientifica Dott. Lucio di Biasio “AEIOU”, Via Coronelli 6, I-20146 Milan
Telephone: +39 02 48 95 45 52 or 48 95 45 62 • Fax: +39 02 48 95 45 48
Email: info@libreriaaeiou.eu • Website: www.libreriaaeiou.eu

JAPAN
Maruzen Company, Ltd., 13-6 Nihonbashi, 3 chome, Chuo-ku, Tokyo 103-0027
Telephone: +81 3 3275 8582 • Fax: +81 3 3275 9072
Email: journal@maruzen.co.jp • Web site: http://www.maruzen.co.jp

REPUBLIC OF KOREA
KINS Inc., Information Business Dept. Samho Bldg. 2nd Floor, 275-1 Yang Jae-dong SeoCho-G, Seoul 137-130
Telephone: +02 589 1740 • Fax: +02 589 1746 • Web site: http://www.kins.re.kr

NETHERLANDS
De Lindeboom Internationale Publicaties B.V., M.A. de Ruyterstraat 20A, NL-7482 BZ Haaksbergen
Telephone: +31 (0) 53 5740004 • Fax: +31 (0) 53 5729296
Email: books@delindeboom.com • Web site: http://www.delindeboom.com

Martinus Nijhoff International, Koraalrood 50, P.O. Box 1853, 2700 CZ Zoetermeer
Telephone: +31 793 684 400 • Fax: +31 793 615 698
Email: info@nijhoff.nl • Web site: http://www.nijhoff.nl

Swets and Zeitlinger b.v., P.O. Box 830, 2160 SZ Lisse
Telephone: +31 252 435 111 • Fax: +31 252 415 888
Email: infoho@swets.nl • Web site: http://www.swets.nl

NEW ZEALAND
DA Information Services, 648 Whitehorse Road, MITCHAM 3132, Australia
Telephone: +61 3 9210 7777 • Fax: +61 3 9210 7788
Email: service@dadirect.com.au • Web site: http://www.dadirect.com.au

SLOVENIA
Cankarjeva Zalozba d.d., Kopitarjeva 2, SI-1512 Ljubljana
Telephone: +386 1 432 31 44 • Fax: +386 1 230 14 35
Email: import.books@cankarjeva-z.si • Web site: http://www.cankarjeva-z.si/uvoz

SPAIN
Díaz de Santos, S.A., c/ Juan Bravo, 3A, E-28006 Madrid
Telephone: +34 91 781 94 80 • Fax: +34 91 575 55 63
Email: compras@diazdesantos.es, carmela@diazdesantos.es, barcelona@diazdesantos.es, julio@diazdesantos.es
Web site: http://www.diazdesantos.es

UNITED KINGDOM
The Stationery Office Ltd, International Sales Agency, PO Box 29, Norwich, NR3 1 GN
Telephone (orders): +44 870 600 5552 • (enquiries): +44 207 873 8372 • Fax: +44 207 873 8203
Email (orders): book.orders@tso.co.uk • (enquiries): book.enquiries@tso.co.uk • Web site: http://www.tso.co.uk

On-line orders
DELTA Int. Book Wholesalers Ltd., 39 Alexandra Road, Addlestone, Surrey, KT15 2PQ
Email: info@profbooks.com • Web site: http://www.profbooks.com

Books on the Environment
Earthprint Ltd., P.O. Box 119, Stevenage SG1 4TP
Telephone: +44 1438748111 • Fax: +44 1438748844
Email: orders@earthprint.com • Web site: http://www.earthprint.com

UNITED NATIONS
Dept. I004, Room DC2-0853, First Avenue at 46th Street, New York, N.Y. 10017, USA
(UN) Telephone: +800 253-9646 or +212 963-8302 • Fax: +212 963-3489
Email: publications@un.org • Web site: http://www.un.org

UNITED STATES OF AMERICA
Bernan Associates, 4501 Forbes Blvd., Suite 200, Lanham, MD 20706-4346
Telephone: 1-800-865-3457 • Fax: 1-800-865-3450
Email: customercare@bernan.com · Web site: http://www.bernan.com

Renouf Publishing Company Ltd., 812 Proctor Ave., Ogdensburg, NY, 13669
Telephone: +888 551 7470 (toll-free) • Fax: +888 568 8546 (toll-free)
Email: order.dept@renoufbooks.com • Web site: http://www.renoufbooks.com

Orders and requests for information may also be addressed directly to:

Marketing and Sales Unit, International Atomic Energy Agency
Vienna International Centre, PO Box 100, 1400 Vienna, Austria
Telephone: +43 1 2600 22529 (or 22530) • Fax: +43 1 2600 29302
Email: sales.publications@iaea.org • Web site: http://www.iaea.org/books

For further information on this publication, please contact:

Nuclear Power Technology Development Section
International Atomic Energy Agency
Vienna International Centre
PO Box 100
1400 Vienna, Austria
email: Official.Mail@iaea.org

EDITORIAL NOTE

This CD-ROM has been prepared from the original material as submitted by contributors. Neither the IAEA nor its Member States assume any responsibility for the information contained on this CD-ROM.

The use of particular designations of countries or territories does not imply any judgement by the publisher, the IAEA, as to the legal status of such countries or territories, of their authorities and institutions or of the delimitation of their boundaries.

The mention of names of specific companies or products (whether or not indicated as registered) does not imply any intention to infringe proprietary rights, nor should it be construed as an endorsement or recommendation on the part of the IAEA.

ADVANCES IN HIGH TEMPERATURE GAS COOLED REACTOR FUEL TECHNOLOGY
IAEA, VIENNA, 2010
IAEA-TECDOC-CD-1674
ISBN 978–92–0–186810–7
ISSN 1684–2073

Produced by the IAEA in Austria
December 2012